

PROTECTIVE COATINGS TECHNOLOGY

**Papers presented at the 1999 E-MRS
Conference, Symposium B: Protective Coatings
and Thin Films, Strasbourg, France
June 1-4, 1999**

Editors

**B. D. Sartwell
A. Matthews**

Proceedings Editors

**W. Gissler
A. Matthews
Y. Pauleau
T. Pieczonka
V. Valvoda**



ELSEVIER

SURFACE AND COATINGS TECHNOLOGY

Editors

B. D. Sartwell (*Washington, DC, USA*)
A. Matthews (*Hull, UK*)

Editorial Board

S. Bull (*Newcastle upon Tyne, UK*)
G. Dearnaley (*San Antonio, TX, USA*)
H. Herman (*Stony Brook, NY, USA*)
H. Hintermann (*Ins, Switzerland*)
A. Inspektor (*Latrobe, PA, USA*)
H. Jehn (*Schwabisch Gmund, Germany*)
A. Kinbara (*Ishikawa, Japan*)
A. S. Korhonen (*Espoo, Finland*)

G.W. Marshall (*Wakefield, UK*)
P. Martin (*Sydney, Australia*)
W.-D. Munz (*Sheffield, UK*)
A. R. Nicoll (*Wohlen, Switzerland*)
Y. Pauleau (*Saint Martin d'Heres, France*)
L. Pranevicius (*Kaunas, Lithuania*)
D. S. Rickerby (*Derby, UK*)
S. Schiller (*Dresden, Germany*)
W. D. Sproul (*Evanston, IL, USA*)
K. N. Strafford (*London, UK*)
J.-E. Sundgren (*Linkoping, Sweden*)
R. C. Tucker (*Indianapolis, IN, USA*)
J. von Stebut (*Nancy, France*)
R. P. Walters (*Albany, OR, USA*)

Scope

The increasing requirement for high technology materials with specific performance characteristics in various types of environments has dictated that these materials possess near-surface properties different from their bulk properties. This journal is a principal forum for the interchange of information on the science, technology and applications of thin and thick coatings and modified surfaces which alter the properties of materials. The scope includes all types of coatings and surface modification techniques (including physical vapour deposition, chemical vapour deposition, electroplating and surface modification by directed energy techniques). Of particular emphasis are the emerging advanced processes such as thermal spraying, sputter deposition, activated reactive evaporation, ion plating, molecular beam epitaxy, ion implantation and pulsed laser surface deposition. Contributions range from original scientific articles concerned with applied research or direct applications of coatings to reviews of current technology in specific areas. Papers are solicited on topics which include one or more of the following areas: (1) characterization of coatings and modified surfaces, which includes the determination of composition, structure, adhesion, and internal stresses; (2) the application of coatings and modified surfaces to alter the mechanical, chemical or optical properties of materials. Mechanical properties include friction, wear, erosion, hardness and load bearing capacity. Chemical properties include corrosion and oxidation. Optical and electro-optical properties include reflectivity, selective absorption and electroluminescence. Particular emphasis is also placed on the emerging surface engineering technologies and coatings with a diversity of applications such as diamond, diamond-like carbon, and cubic boron nitride. Other interdisciplinary areas include thermal barrier coatings and coatings for biomedical applications and materials conservation.

Abstracting/Indexing Services

This journal is cited by the following services: Engineering Index, FIZ Karlsruhe, Metal Finishing Abstracts, Current Contents — Engineering, Technology and Applied Sciences, Physikalische Berichte, Cambridge Scientific Abstracts, Chemical Abstracts, Fluid Abstracts, Metals Abstracts, Physics Abstracts, PASCAL/Centre National de Recherche Scientifique, Solid State Abstracts.

Pre-publication abstracts of articles in *Surface and Coatings Technology* and other related journals are now available weekly in electronic form via CoDAS, a new direct alerting service in condensed matter and materials science run jointly by Elsevier Science and Institute of Physics Publishing. For details on a free one-month subscription contact Paul Bancroft on fax +44 1179 294318 or e-mail bancroft@ioppublishing.co.uk.

Publication Information: *Surface and Coatings Technology* (ISSN 0257-8972). For 2000 volumes 122–134 are scheduled

for publication. Subscription prices are available upon request from the Publisher or from the Regional Sales Office nearest you or from this journal's website (<http://www.elsevier.nl/locate/surfcoat>). Further information is available on this journal and other Elsevier Science products through Elsevier's website: (<http://www.elsevier.nl>). Subscriptions are accepted on a prepaid basis only and are entered on a calendar year basis. Issues are sent by surface standard mail (surface within Europe, air delivery outside Europe). Priority rates are available upon request. Claims for missing issues should be made within six months of the date of dispatch.

Orders, claims and product enquiries: please contact the Customer Support Department at the Regional Sales Office nearest you:

New York: Elsevier Science, PO Box 945, New York, NY 10159-0945, USA;
phone: (+1) (212) 633 3730 [toll free number for North American customers: 1-888-4ES-INFO (437-4636)];
fax: (+1) (212) 633 3680;
e-mail: usinfo-f@elsevier.com

Amsterdam: Elsevier Science, PO Box 211, 1000 AE Amsterdam, The Netherlands;
phone: (+31) 20 4853757; fax: (+31) 20 4853432;
e-mail: nlinfo-f@elsevier.nl

Tokyo: Elsevier Science, 9-15 Higashi-Azabu 1-chome, Minato-ku, Tokyo 106-0044, Japan;
phone: (+81) (3) 5561 5033; fax: (+81) (3) 5561 5047;
e-mail: info@elsevier.co.jp

Singapore: Elsevier Science, No. 1 Temasek Avenue, #17-01 Millenia Tower, Singapore 039192;
phone: (+65) 434 3727; fax: (+65) 337 2230;
e-mail: asiainfo@elsevier.com.sg

Rio de Janeiro: Elsevier Science, Rua Sete de Setembro 111/16 Andar, 20050-002 Centro, Rio de Janeiro - RJ, Brazil;
phone: (+55) (21) 509 5340; fax: (+55) (21) 507 1991;
e-mail: elsevier@campus.com.br [Note (Latin America): for orders, claims and help desk information, please contact the Regional Sales Office in New York as listed above]

US mailing notice: *Surface and Coatings Technology* (ISSN 0257-8972) is published semimonthly by Elsevier Science S.A. (PO Box 211, 1000 AE Amsterdam, The Netherlands). Annual subscription price in the USA US\$ 4969.00 (valid in North, Central and South America), including air speed delivery. Periodical postage rate paid at Jamaica, NY 11431.

USA POSTMASTER: Send address changes to *Surface and Coatings Technology*, Publications Expediting, Inc., 200 Meacham Avenue, Elmont, NY 11003.

AIRFREIGHT AND MAILING in the USA by Publications Expediting Inc., 200 Meacham Avenue, Elmont, NY 11003.

REPORT DOCUMENTATION PAGE			Form Approved OMB No. 0704-0188	
Public reporting burden for this collection of information is estimated to average 1 hour per response, including the time for reviewing instructions, searching existing data sources, gathering and maintaining the data needed, and completing and reviewing the collection of information. Send comments regarding this burden estimate or any other aspect of this collection of information, including suggestions for reducing this burden to Washington Headquarters Services, Directorate for Information Operations and Reports, 1215 Jefferson Davis Highway, Suite 1204, Arlington, VA 22202-4302, and to the Office of Management and Budget, Paperwork Reduction Project (0704-0188), Washington, DC 20503.				
1. AGENCY USE ONLY (Leave blank)		2. REPORT DATE March 2000		3. REPORT TYPE AND DATES COVERED June 1-4, 1999 Conference Proceedings
4. TITLE AND SUBTITLE E-MRS Conference, Symposium B: Protective Coatings and Thin Films, Strasbourg, France, June 1-4, 1999.			5. FUNDING NUMBERS	
6. AUTHOR(S) B.D. Sartwell and A. Matthews, Editors				
7. PERFORMING ORGANIZATION NAME(S) AND ADDRESS(ES) European Materials Research Society (E-MRS) 23 rue du Loess - BP 20 67037 Strasbourg Cedex 02 - France http://www-emrs.c-strasbourg.fr/index.html			8. PERFORMING ORGANIZATION REPORT NUMBER ISSN -0257-8972	
9. SPONSORING/MONITORING AGENCY NAME(S) AND ADDRESS(ES) Office of Naval Research, European Office PSC 802 Box 39 FPO AE 09499-0039			10. SPONSORING/MONITORING AGENCY REPORT NUMBER	
11. SUPPLEMENTARY NOTES Published in Surface & Coatings Technology, Vol. 125 Nos. 1-3, March 2000. Published by Elsevier Science, S.A., PO Box 211, 1000 AE Amsterdam, The Netherlands. This work relates to Department of the Navy Grant issued by the Office of Naval Research International Field Office. The United States has a royalty free license throughout the world in all copyrightable material contained herein.				
12a. DISTRIBUTION/AVAILABILITY STATEMENT Approved for Public Release. U.S. Government Rights License. All other rights reserved by the copyright holder. (Code 1, 20)			12b. DISTRIBUTION CODE A	
12. ABSTRACT (Maximum 200 words) This symposium belongs to a series of E-MRS symposia started in 1993. The title "Protective Coatings and Thin Films" adopted for the 1999 symposium will be maintained for the foreseeable future to ensure a desirable continuity required for members of the European scientific community/ For the 1999 symposium, emphasis was placed on fundamental aspects of vapor deposition technology, in particular on relationships between physical and/or chemical phenomena involved in vapor deposition processes and progress in surface treatments, energy beam processing, ion implantation processing, ion beam and plasma processing, wear-resistant coatings, multilayer coatings, nitride coatings, hard and protective coatings, physical and chemical vapor-deposited coatings, polymer coating and oxide coatings.				
13. SUBJECT TERMS ONRIFO, EOARD, Foreign reports, Conference proceedings, Reprints, E-MRS, Thin Films, Protective coatings, Materials science, Chemistry			15. NUMBER OF PAGES	
			16. PRICE CODE	
17. SECURITY CLASSIFICATION OF REPORT UNCLASSIFIED	18. SECURITY CLASSIFICATION OF THIS PAGE UNCLASSIFIED	19. SECURITY CLASSIFICATION OF ABSTRACT UNCLASSIFIED	20. LIMITATION OF ABSTRACT UL	

***SURFACE
& COATINGS
TECHNOLOGY***

Volume 125 (2000)

SURFACE & COATINGS TECHNOLOGY

Vol. 125 (2000)

Papers presented at the E-MRS Conference, Symposium B:
Protective Coatings and Thin Films,
Strasbourg, France,
June 1-4, 1999

EDITORS

B. D. Sartwell (*Washington, DC, USA*)
A. Matthews (*Hull, UK*)

PROCEEDINGS EDITORS

W. Gissler (*Ispra, Italy*)
A. Matthews (*Hull, UK*)
Y. Pauleau (*Saint Martin d'Herès, France*)
T. Pieczonka (*Cracow, Poland*)
V. Valvoda (*Prague, Czech Republic*)

EDITORIAL BOARD

S. Bull (*Newcastle upon Tyne, UK*)
G. Dearnaley (*San Antonio, TX, USA*)
H. Herman (*Stony Brook, NY, USA*)
H. Hintermann (*Ins, Switzerland*)
A. Inspektor (*Latrobe, PA, USA*)
H. Jehn (*Schwäbisch Gmünd, Germany*)
A. Kinbara (*Tokyo, Japan*)
A. S. Korhonen (*Espoo, Finland*)
G.W. Marshall (*Wakefield, UK*)
P. Martin (*Sydney, Australia*)
W.-D. Münz (*Sheffield, UK*)
A. R. Nicoll (*Wohlen, Switzerland*)
Y. Pauleau (*Saint Martin d'Herès, France*)
L. Pranevičius (*Kaunas, Lithuania*)
D. S. Rickerby (*Derby, UK*)
S. Schiller (*Dresden, Germany*)
W. D. Sproul (*Evanston, IL, USA*)
K. N. Strafford (*London, UK*)
J.-E. Sundgren (*Linköping, Sweden*)
R. C. Tucker (*Indianapolis, IN, USA*)
J. Vogel (*Vaduz, Liechtenstein*)
J. von Stebut (*Nancy, France*)
R. P. Walters (*Albany, OR, USA*)

20011130 011



ELSEVIER

AMSTERDAM — LAUSANNE — NEW YORK — OXFORD — SHANNON — TOKYO

U.S. Government Rights License

This work relates to Department of the Navy
Grant or Contract issued by Office of Naval
Research (ONR) International Field Office-
Europe. The United States Government has a
royalty-free license throughout the world in all
copyrightable material contained herein.

AQ F02-02-0258

Abstracting Services

This journal is cited by the following Abstracting/Indexing Services: Automatic Subject Citation Alert, Cambridge Scientific Abstracts, Chemical Abstracts, Current Contents-Physical, Chemical & Earth Sciences, Engineering Index, FIZ Karlsruhe, Metals Abstracts, PASCAL/Centre National de la Recherche Scientifique, Physics Abstracts, Physikalische Berichte, Science Citation Index.

International Standard Serial Number 0257-8972

© 2000 Elsevier Science S.A. All rights reserved.

This journal and the individual contributions contained in it are protected by the copyright of Elsevier Science S.A., and the following terms and conditions apply to their use:

Photocopying

Single photocopies of single articles may be made for personal use as allowed by national copyright laws. Permission of the publisher and payment of a fee is required for all other photocopying, including multiple or systematic copying, copying for advertising or promotional purposes, resale, and all forms of document delivery. Special rates are available for educational institutions that wish to make photocopies for non-profit educational classroom use.

Permissions may be sought directly from Elsevier Science Rights & Permissions Department, PO Box 800, Oxford OX5 1DX, UK; phone: (+44) 1865 843830, fax: (+44) 1865 853333, e-mail: permissions@elsevier.co.uk. You may also contact Rights & Permissions directly through Elsevier's home page (<http://www.elsevier.nl>), selecting first 'Customer Support', then 'General Information', then 'Permissions Query Form'.

In the USA, users may clear permissions and make payments through the Copyright Clearance Center, Inc., 222 Rosewood Drive, Danvers, MA 01923, USA; phone: (978) 7508400; fax: (978) 7504744, and in the UK through the Copyright Licensing Agency Rapid Clearance Service (CLARCS), 90 Tottenham Court Road, London W1P 0LP, UK; phone: (+44) 171 436 5931; fax: (+44) 171 436 3986. Other countries may have a local reprographic rights agency for payments.

Derivative Works

Subscribers may reproduce tables of contents or prepare lists of articles including abstracts for internal circulation within their institutions. Permission of the publisher is required for resale or distribution outside the institution.

Permission of the publisher is required for all other derivative works, including compilations and translations.

Electronic Storage or Usage

Permission of the publisher is required to store or use electronically any material contained in this journal, including any article or part of an article. Contact the publisher at the address indicated.

Except as outlined above, no part of this publication may be reproduced, stored in a retrieval system or transmitted in any form or by any means, electronic, mechanical, photocopying, recording or otherwise, without prior written permission of the publisher.

Address permissions requests to: Elsevier Science Rights & Permissions Department, at the mail, fax and e-mail addresses noted above.

Notice

No responsibility is assumed by the Publisher for any injury and/or damage to persons or property as a matter of products liability, negligence or otherwise, or from any use or operation of any methods, products, instructions or ideas contained in the material herein. Because of rapid advances in the medical sciences, in particular, independent verification of diagnoses and drug dosages should be made.

Although all advertising material is expected to conform to ethical (medical) standards, inclusion in this publication does not constitute a guarantee or endorsement of the quality or value of such product or of the claims made of it by its manufacturer.

Advertising information. Advertising orders and enquiries may be sent to: **USA, Canada and South America:** Mr Tino de Carlo, The Advertising Department, Elsevier Science Inc., 655 Avenue of the Americas, New York, NY 10010-5107, USA; phone: (+1) (212) 633 3815; fax: (+1) (212) 633 3820; e-mail: t.decarlo@elsevier.com. **Japan:** The Advertising Department, Elsevier Science K.K., 9-15 Higashi-Azabu 1-chome, Minato-ku, Tokyo 106-0044, Japan; phone: (+81) (3) 5561 5033; fax: (+81) (3) 5561 5047. **Europe and ROW:** Rachel Leveson-Gower, The Advertising Department, Elsevier Science Ltd, The Boulevard, Langford Lane, Kidlington, Oxford OX5 1GB, UK; phone: (+44) (1865) 843565; fax: (+44) (1865) 843976; e-mail: r.leveson-gower@elsevier.co.uk.

Printed in The Netherlands

∞ The paper used in this publication meets the requirements of ANSI/NISO Z39.48-1992 (Permanence of Paper)

U.S. Government Rights License

This work relates to Department of the Navy Grant or Contract issued by Office of Naval Research (ONR) International Field Office-Europe. The United States Government has a royalty-free license throughout the world in all copyrightable material contained herein.

Sponsors

It is our pleasure to acknowledge with gratitude the financial assistance provided by:

- the French Ministry of Defense (DGA/DPS)
- the Office of Naval Research International Field Office (ONRIFO)
- Europe together with the European Office of Aerospace Research and Development, UK.
- the French Ministry of National Education, Research and Technology

Contents

Preface	xii
<i>Materials Surface Treatments</i>	
Microstructural characterisation and properties of thermochemically treated iron-based alloys	1
J. Kazior, A. Molinari, C. Janczur and T. Pieczonka	
Modification of composite nitrided layers by phosphorus compounds	9
J. Nowacki	
Laser cladding and erosive wear of Co–Mo–Cr–Si coatings	13
J. Przybylowicz and J. Kusinski	
Surface activation of polyimide with dielectric barrier discharge for electroless metal deposition	19
H. Esrom, R. Seeböck, M. Charbonnier and M. Romand	
Diamond-like films formed by pulsed laser irradiation of phenylcarbyne polymer	25
S.M. Huang, Y.F. Lu, Z. Sun and X.F. Luo	
Influence of surface pretreatment on case formation during gaseous nitriding	30
J. Baranowska and M. Wysiecki	
Pre-treatment of large area strips with the aid of a high power Hall current accelerator	35
N. Vershinin, R. Dimitriou, M. Benmalek, B. Straumal, W. Gust, J. Vivas and J. Shulga	
Laser induced Cu/alumina bonding: Microstructure and bond mechanism	40
L. Shepeleva, B. Medres, W.D. Kaplan, M. Bamberger, M.H. McCay, T.D. McCay and M. Sharp	
Laser cladding of turbine blades	45
L. Shepeleva, B. Medres, W.D. Kaplan, M. Bamberger and A. Weisheit	
<i>Energy Beam Processing</i>	
Physical foundations for surface treatment of materials with low energy, high current electron beams	49
D.I. Proskurovsky, V.P. Rotshtein, G.E. Ozur, Y.F. Ivanov and A.B. Markov	
Effect of energy on direct ion beam deposition of carbon thin films: induced defects and graphitization	57
H.-A. Durand, K. Sekine, K. Etoh, K. Ito and I. Kataoka	
Structural stability of irradiated metallic and non-metallic films	61
P.M. Ossi and R. Pastorelli	
The interface between TiAlN hard coatings and steel substrates generated by high energetic Cr ⁺ bombardment	66
C. Schönjahn, M. Bamford, L.A. Donohue, D.B. Lewis, S. Forder and W.-D. Münz	
<i>Ion Implantation Processing</i>	
Ion implantation by plasma immersion: interest, limitations and perspectives	71
F. Le Cœur, J. Pelletier, Y. Arnal and A. Lacoste	
AlN formation by direct nitrogen implantation using a DECR plasma	79
N. Duez, B. Mutel, O. Dessaux, P. Goudmand and J. Grimblot	
Raman study of titanium oxide layers produced with plasma immersion ion implantation	84
S. Mändl, G. Thorwarth, M. Schreck, B. Stritzker and B. Rauschenbach	
Protection of γ -based TiAl against high temperature oxidation using ion implantation of chlorine	89
U. Hornauer, R. Günzel, H. Reuther, E. Richter, E. Wieser, W. Möller, G. Schumacher, F. Dettenwanger and M. Schütze	
Plasma immersion ion implantation of cold-work steel	94
G. Thorwarth, S. Mändl and B. Rauschenbach	
<i>Ion Beam and Plasma Processing</i>	
Production of stable and metastable phases of zirconium nitrides by NH ₃ plasma nitridation and by double ion beam sputtering of zirconium films	100
A. Straboni, L. Pichon and T. Girardeau	
Deposition of c-BN by ion beam assisted CVD	106
G. Schwarz, F. Friess and G.K. Wolf	
Influence of ion induced surface defects on the nucleation and formation mechanisms of metallic thin films	111
H.-A. Durand, K. Sekine, K. Etoh, K. Ito and I. Kataoka	

<i>Structure of Coatings</i>	
Amorphisation and related structural effects in thin films prepared by ion beam assisted methods	116
A.R. González-Elipé, F. Yubero, J.P. Espinós, A. Caballero, M. Ocaña, J.P. Holgado and J. Morales	
Structural properties and surface morphology of laser-deposited amorphous carbon and carbon nitride films	124
E. Riedo, F. Comin, J. Chevrier, F. Schmithusen, S. Decossas and M. Sancrotti	
A phenomenological study of the initial stages of film growth	129
C. Templier, S. Muzard, A. Galdikas, L. Pranevicius, J. Delafond and J.C. Desoyer	
Influence of the structure of the composite: 'nitrided layer/PVD coating' on the durability of tools for hot working	134
J. Smolik, J. Walkowicz and J. Tacikowski	
Influence of carbon content on the crystallographic structure of boron carbide films	141
O. Conde, A.J. Silvestre and J.C. Oliveira	
Formation of polycrystalline and microcrystalline composite thin films by codeposition and surface chemical reaction	147
P.B. Barna, M. Adamik, J. Lábár, L. Kövér, J. Tóth, A. Dévényi and R. Manaila	
Early stage growth structure of indium tin oxide thin films deposited by reactive thermal evaporation	151
A. Amaral, P. Brogueira, C. Nunes de Carvalho and G. Lavareda	
<i>Characterization of Coatings</i>	
Vacuum arc deposition of Ti coatings	157
B. Straumal, W. Gust, N. Vershinin, R. Dimitriou and E. Rabkin	
Spatial distribution of microdroplets generated in the cathode spots of vacuum arcs	161
K. Miernik and J. Walkowicz	
Pure Al thin film protective layer to prevent stress migration in Al wiring for thin-film transistors	167
H. Takatsuji, K. Haruta, S. Tsuji, K. Kuroda and H. Saka	
XPS investigation of ion beam treated MoS ₂ -Ti composite coatings	173
I. Bertóti, M. Mohai, N.M. Renevier and E. Szilágyi	
<i>Mechanical Characteristics of Coatings</i>	
Mechanical properties of hard chromium tungsten nitride coatings	179
P. Hones, R. Consiglio, N. Randall and F. Lévy	
Mechanical behaviour of hard PVD multilayered coatings	185
E. Harry, M. Ignat, Y. Pauleau, A. Rouzaud and P. Juliet	
Correlation between stress values of cubic boron nitride thin films and intrinsic film properties or the infrared peak position	190
A. Klett, R. Freudenstein, M.F. Plass and W. Kulisch	
Mechanical properties of Al/Al ₂ O ₃ nanolaminated films: correlation to microstructure	196
M. Ben Daia, P. Aubert, S. Labdi, C. Le Paven-Thivet, P. Houdy and J.L. Bozet	
A comparative study of the nanoscratching behavior of amorphous carbon films grown under various deposition conditions	201
C. Charitidis, S. Logothetidis and M. Gioti	
<i>Corrosion-Resistant Coatings</i>	
Morphologies and corrosion properties of PVD Zn-Al coatings	207
M.A. Baker, W. Gissler, S. Klose, M. Trampert and F. Weber	
Improvement of the corrosion resistance of PVD hard coating-substrate systems	212
H.A. Jehn	
Vapour deposited Zn-Cr Alloy coatings for enhanced manufacturing and corrosion resistance of steel sheets	218
L. Guzman, M. Adami, W. Gissler, S. Klose and S. De Rossi	
Corrosion resistance of the vacuum arc deposited Ti, TiN and TiO ₂ coatings on large area glass substrates	223
N. Vershinin, K. Filonov, B. Straumal, W. Gust, R. Dimitriou, A. Kovalev and J. Camacho	
Corrosion behaviour of the protective and decorative TiN coatings on large area steel strips	229
N. Vershinin, K. Filonov, B. Straumal, W. Gust, I. Wiener, E. Rabkin and A. Kazakevich	
<i>Wear-Resistant Coatings</i>	
Application of hard coatings in aluminium die casting — soldering, erosion and thermal fatigue behaviour	233
C. Mitterer, F. Holler, F. Üstel and D. Heim	
New coatings on metal sheets and strips produced using EB PVD technologies	240
S. Schiller, C. Metzner and O. Zywitzki	
Sputtered silicon carbide thin films as protective coating for MEMS applications	246
N. Ledermann, J. Baborowski, P. Mural, N. Xantopoulos and J.-M. Tellenbach	
Pulsed electron-beam treatment of WC-TiC-Co hard-alloy cutting tools: wear resistance and microstructural evolution	251
Y.F. Ivanov, V.P. Rotshtein, D.I. Proskurovsky, P.V. Orlov, K.N. Polestchenko, G.E. Ozur and I.M. Goncharenko	

<i>Multilayer Coatings</i>	
Structure and hardness of vacuum arc deposited multi-component nitride coatings of Ti, Zr and Nb R.L. Boxman, V.N. Zhitomirsky, I. Grimberg, L. Rapoport, S. Goldsmith and B.Z. Weiss	257
Localised oxidation defects in TiAlN/CrN superlattice structured hard coatings grown by cathodic arc/unbalanced magnetron deposition on various substrate materials M.I. Lembke, D.B. Lewis and W.-D. Münz	263
<i>Nitride Coatings</i>	
Properties of various large-scale fabricated TiAlN- and CrN-based superlattice coatings grown by combined cathodic arc-unbalanced magnetron sputter deposition W.-D. Münz, L.A. Donohue and P.E. Hovsepian	269
Physical properties of carbon nitride films synthesized using atomic transport reactions C. Popov, M.F. Plass, L. Zambov, J. Bulir, M.-P. Delplancke-Ogletree and W. Kulisch	278
Correlation between bonding structure and mechanical properties of amorphous carbon nitride thin films C. Quirós, R. Núñez, P. Prieto, I. Vergara, D. Cáceres, L. Soriano, G.G. Fuentes, E. Elizalde and J.M. Sanz	284
Magnetron sputtered carbon nitride: composition and chemical bonding of as-grown and post-annealed films studied with real-time and in situ diagnostic techniques M. Gioti, S. Logothetidis, P. Patsalas, A. Laskarakis, Y. Panayiotatos and V. Kechagias	289
Carbon nitride thin films deposited by reactive plasma beam sputtering P.Y. Tessier, R. Kre N'guessan, B. Angleraud, V. Fernandez, N. Mubumbila and G. Turban	295
Synthesis and characterization of carbon nitride thin films obtained by laser induced chemical vapour deposition A. Crunteanu, M. Charbonnier, M. Romand, F. Vasiliu, D. Pantelica, F. Negoita and R. Alexandrescu	301
Chemical analysis of pulsed laser deposited a-CN _x films by comparative infrared and X-ray photoelectron spectroscopies T. Szörényi, C. Fuchs, E. Fogarassy, J. Hommet and F. Le Normand	308
X-ray photoelectron spectroscopy study of carbon nitride films V. Krastev, P. Petrov, D. Dimitrov, G. Beshkov, C. Georgiev and I. Nedkov	313
Near-edge X-ray absorption fine structure study of carbon nitride films C. Lenardi, M.A. Baker, V. Briois, G. Coccia Lecis, P. Piseri and W. Gissler	317
<i>Hard and Protective Coatings</i>	
Hard and superhard nanocomposite coatings J. Musil	322
Electron beam physical vapour deposition of protective films on carbon reinforced carbon E. Roos, K. Maile, A. Lyutovich, S. Lauf, H. Kockelmann and A. Gusko	331
The effect of substrate temperature and biasing on the mechanical properties and structure of sputtered titanium nitride thin films P. Patsalas, C. Charitidis and S. Logothetidis	335
Pulsed-plasma assisted magnetron methods of depositing TiN coatings J. Walkowicz, K. Miernik, A. Zykov, S. Dudin and V. Farenik	341
<i>PVD and CVD Coatings</i>	
Hard lubricating coatings for cutting and forming tools and mechanical components V. Fox, A. Jones, N.M. Renevier and D.G. Teer	347
PVD coating of plastic webs and sheets with high rates on large areas S. Schiller, V. Kirchhoff, N. Schiller and H. Morgner	354
Condensation of silver-copper alloys in a solid-liquid domain of the phase diagram S. Leroux, J. Le Ny, C. Guéneau and D. Camel	361
Determination of resputtering yields in carbon nitride films grown by dual ion beam sputtering C. Quirós, P. Prieto, E. Elizalde, R. Pérez-Casero, V. Gómez, P. Herrero and J.M. Sanz	366
<i>Polymer Coatings</i>	
Plasma polymer films and their future prospects H. Biederman and D. Slavinská	371
The protection of metallic archaeological objects using plasma polymer coatings L. Favre-Quattrapani, P. Groening, D. Ramseyer and L. Schlapbach	377
Mechanical properties of plasma deposited polymer coatings F. Benítez, E. Martínez, M. Galán, J. Serrat and J. Esteve	383
Pulsed laser deposition of crystal polyaniline thin films Z.M. Ren, Y.F. Lu, Z.H. Mai, S.C. Ng, P. Miao, S.I. Pang, J.P. Wang and T.C. Chong	388
<i>Oxide Coatings</i>	
Catalytic behavior of plasma-sprayed Al-Al ₂ O ₃ coatings doped with metal oxides L.L. Pranevicius, P. Valatkevicius, V. Valincius and C. Montassier	392

Temperature and substrate influence on the structure of TiN_xO_y thin films grown by low pressure metal organic chemical vapour deposition	396
F. Fabreguette, L. Imhoff, J. Guillot, B. Domenichini, M.C. Marco de Lucas, P. Sibillot, S. Bourgeois and M. Sacilotti	
CVD of ZrO_2 , Al_2O_3 and Y_2O_3 from metalorganic compounds in different reactors	400
M. Pulver, W. Nemetz and G. Wahl	
Deposition of layered bioceramic hydroxyapatite/ TiO_2 coatings on titanium alloys using a hybrid technique of micro-arc oxidation and electrophoresis	407
X. Nie, A. Leyland and A. Matthews	
Microstructure and properties of laser treated arc sprayed and plasma sprayed coatings	415
A. Pokhmurska and R. Ciach	
Al_2O_3 coatings on stainless steel from Al metal-organic chemical vapor deposition and thermal treatments	419
L. Dumitrescu and F. Maury	
Titanium dioxide films prepared by photo-induced sol-gel processing using 172 nm excimer lamps	424
N. Kaliwoh, J.-Y. Zhang and I.W. Boyd	
Author index	428
Subject index	430

The publisher encourages the submission of articles in electronic form thus saving time and avoiding rekeying errors. A leaflet describing our requirements is available from the publisher upon request. For more information on Surface and Coatings Technology please visit our website which is accessible via the Elsevier Surfaces & Interfaces HomePage at <http://www.elsevier.nl/locate/surfaces>

Preface

This symposium belongs to a series of E-MRS symposia started in 1993 (symposium C on “Ion Beam, Plasma, Laser, and Thermally-stimulated Deposition Processes”, Proceedings Volume 41, published by Elsevier in 1994) and containing symposia subsequently organized every two years, in 1995 (“Advanced Deposition Processes and Characterization of Protective Coatings”, Proceedings Volume 53, published by Elsevier in 1996) and 1997 [“Coatings and Surface Modifications for Surface Protection and Tribological Applications”, *Surf. Coat. Technol.*, 100–101, (Nos. 1–3), March 1998].

The title “Protective Coatings and Thin Films” adopted for the 1999 symposium will be maintained for the foreseeable future to ensure a desirable continuity required for members of the European scientific community involved in this field of research. The program of these symposia was focused on the characterization, properties and applications of advanced ceramic, metallic and polymeric coatings or thin films produced by vapor deposition processes for surface protection against various phenomena (corrosion, oxidation, diffusion, wear, friction) resulting from interactions with hostile environments and leading to the detrimental damage of materials.

For the 1999 symposium, a specific emphasis was placed on fundamental aspects of vapor deposition technology, in particular on relationships between physical and/or chemical phenomena involved in vapor deposition processes and major characteristics of functional protective coatings and thin films. This symposium covered recent trends and progress in surface treatments, energy beam processing, ion implantation processing, ion beam and plasma processing, structure of coatings, characterization of coatings (mechanical properties, composition, morphology, stresses, etc.), wear-resistant coatings, multilayer coatings, nitride coatings (in particular carbon nitride films), hard and protective coatings, physical and chemical vapor-deposited coatings, polymer coatings and oxide coatings. These various topics were presented and discussed during 13 oral sessions and two poster sessions. The scientific program featured 13 invited speakers and 94 contributed papers (45 presented orally and 49 for the poster sessions). More than 100 participants attended this meeting.

The invited talks included the presentations of J. Kazior (Cracow University of Technology, Poland) on “Microstructural characterization and properties of thermochemically surface treated P/M iron based alloys”, D.I. Proskurovsky (Institute of High Current Electronics, Tomsk, Russia) on “The physical foundations for surface treatment of materials with low-energy, high-current electron beams”, J. Pelletier (CNRS, Grenoble, France) on “Ion implantation by plasma immersion: interest, limitations and perspectives”, A. Straboni (University of Poitiers, France) on “Plasma and ion beam nitridation of surfaces”, P.B. Barna (RITP, Budapest, Hungary) on “Mechanisms of texture evolution in polycrystalline thin films”, A.R. Gonzalez-Elipe (ICM de Sevilla, Spain) on “Structural amorphization in thin films prepared by ion beam assisted methods”, C. Mitterer (University of Leoben, Austria) on “The application of hard coatings in aluminum die casting — soldering, erosion and thermal fatigue behavior”, R. Boxman (University of Tel Aviv, Israel) on “Deposition of multi-layer and multi-component hard coatings using a multi-cathode vacuum arc deposition system”, W.D. Münz (Sheffield Hallam University, UK) on “Properties of various large scale fabricated TiAlN and CrN based superlattice coatings grown by combined cathodic arc/unbalanced magnetron deposition”, J. Musil (University of West Bohemia, Plzen, Czech Republic) on “Hard and superhard nanocomposite coatings”, A. Figueras (ICM de Barcelona, Spain) on “Preparation of hard ceramic coatings by plasma-enhanced chemical vapor deposition and laser ablation to improve surface properties of metallic materials”, H. Biederman (Charles University, Praha, Czech Republic) on “Plasma polymer films and their future prospects”, and J. Schneider (University of Linköping, Sweden) on “Deposition and properties of physically vapor deposited (PVD) alumina thin films”.

The special oral session organized for the graduate student award (GSA session) was composed of six oral presentations. The winners were Peter Hones (EPFL, Lausanne, Switzerland) and Cornelia Schönjahn (Sheffield Hallam University, UK) who talked about “Mechanical properties of hard chromium tungsten nitride coatings” and “The interface between TiAlN hard coatings and steel substrates generated by high energetic chromium ion bombardment”, respectively.

The 107 contributions were presented by authors coming from 19 European countries (including nine from the European Union) and five other countries (Argentina, Israel, Japan, Singapore and the USA). The participation of scientists and researchers from central and eastern European countries was particularly encouraged by a financial support offered by the grant from the French Ministry of National Education, Research and Technology. It is our pleasure to acknowledge with gratitude the financial support provided by the French Ministry of Defense (DGA/DPS), the Office of Naval Research International Field Office (ONRIFO) — Europe together with the European Office of Aerospace Research and Development, UK, and the French Ministry of National Education, Research and Technology. In addition to W. Gissler (Italy), A. Matthews (UK) and Y. Pauleau (France), two symposium organizers, V. Valvoda and T. Pieczonka, were from the Czech Republic and Poland. Five invited speakers were from Russia, the Czech Republic, Poland and Hungary and six scientific committee members were from Poland, Lithuania and Hungary. Many thanks to the invited speakers, chairpersons, scientific committee members and all the participants who contributed actively to the success of this symposium. This meeting was an appropriate opportunity to create new links and improve or spur scientific collaborations between European scientists of the surface engineering community.

W. Gissler

A. Matthews

Y. Pauleau

T. Pieczonka

V. Valvoda

Commission of The European Union,
Institute for Health & Consumer Protection,
Joint Research Centre,
Ispra (VA), Italy

Microstructural characterisation and properties of thermochemically treated iron-based alloys

J. Kazior ^{a,*}, A. Molinari ^b, C. Janczur ^c, T. Pieczonka ^d

^a Institute of Materials Science and Metal Technology, Cracow University of Technology, Warszawska 24, 31-155 Cracow, Poland

^b Department of Materials Engineering, University of Trento, Via Mesiano 77, 38050 Trento, Italy

^c Institute of Automobiles and Internal Combustion Engines, Cracow University of Technology, Warszawska 24, 31-155 Cracow, Poland

^d Faculty of Metallurgy and Materials Engineering, Academy of Mining and Metallurgy, Mickiewicza 30, 30-059 Cracow, Poland

Abstract

Some results of a gaseous thermochemical treatments based on nitrogen, sulphur and oxygen on an Astaloy Mo alloy and AISI 316L austenitic stainless steel are discussed in order to show the importance of the chemical composition and the microstructure of the base material on the wear resistance of the treated specimens. In order to reduce the case depth and to increase the microhardness of the diffusion layers, boron was added to the base material. In this way, it is possible to close porosity, due to the liquid phase sintering. The treated specimens underwent a specific characterisation in order to investigate the microstructure and the constitution of the hardened layers as well as the tribological properties in dry sliding conditions. Both the microhardness measurements and the nitrogen concentration depth profile indicate that boron is able to reduce the nitrogen penetration. Furthermore, the combined surface thermochemical treatments improves the tribological behaviour of the material, and in particular, sulphuration significantly changes the morphology of the treated specimens, and consequently, the dry sliding wear of the sintered material is decreased. © 2000 Elsevier Science S.A. All rights reserved.

Keywords: Nitriding; Oxidation; Sintered materials; Sulphurising; Thermochemical surface treatment

1. Introduction

Manufacturing of steels by powder metallurgy (P/M) technology has been used in the industrial field owing to their low cost of production coming from the near-net shape process, which eliminates any machining, thus reducing energy consumption and ensuring the high material utilisation [1].

However, for specific applications, as in the case of mechanical parts subjected to a severe wear, it is necessary to improve their surface features. Choosing a surface treatment for powder metallurgy components can be a difficult task. The main problem in surface treatment of PM steels is porosity. The presence of interconnected pores increases the surface area and enhances the penetration of the gaseous medium into the bulk of materials. Among various surface treatments, ion nitriding is a well-known surface treatment technique to improve

properties like hardness, corrosion resistance and tribological characteristics [2]. Due to the particular mechanism of nitrogen enrichment of the surface, the ion nitriding process is less sensitive to porosity than the others gaseous surface treatments [3]. However, ion nitriding is more expensive than gas nitriding and does not appear to be suitable for the treatment of small pieces or of pieces of different geometry [4]. Besides, it is well known that for gaining benefits from nitriding, the base material has to contain alloying elements with a high affinity for nitrogen, like V, Cr, Al in order to favour the formation of a well-defined, thick and hard diffusion layer. However, these elements introduce noticeable problems during sintering, owing to their high affinity with oxygen and therefore require the use of a specific sintering atmosphere consisting of pure dry hydrogen with a very low dew point or applied of high sintering temperatures in order to reduce the stable oxides that cover the surface of powder particles. For this reason, these specific steels are not currently produced by powder metallurgy technology, because all the requirements increase the production cost and economic

* Corresponding author. Tel.: +48-12-648-0170;
fax: +48-12-648-4463.

E-mail address: m-2@mech.pk.edu.pl (J. Kazior)

advantages of powder metallurgy technology in comparison to alternative technologies can be greatly reduced.

Thus, it is very important to study the applicability of the gaseous thermochemical treatment to a suitable PM material and to be hardened by means of nitrogen surface enrichment, at the same time. A particular treatment was studied and patented by some of the authors [5], which combines nitrogen, oxygen and sulphur in one batch only. The treatment was applied to a sintered alloy, and the results are presented here. From the different P/M structural steels, the prealloyed Fe–1.5% Mo and AISI 316L austenitic stainless steels were selected. The chemical composition of the base material was modified by boron for two main reasons. From a theoretical point of view, boron influences the hardenability of steel, and its high affinity for nitrogen allows the formation of boron nitrides that may increase the hardness of the diffusion layer. Furthermore, boron is an α -stabilising element and activates the sintering process of iron alloys by the formation of liquid phase, and consequently the near full density may be obtained [6]. This last effect is very important because it may strongly reduce the nitrogen penetration during nitriding, which is one of the greatest problems in gas nitriding of porous sintered steels [7].

In the present paper, some results of a gaseous thermochemical treatments based on nitrogen, sulphur and oxygen on an P/M Astaloy Mo alloy and P/M AISI 316L austenitic stainless steel are discussed in order to show the importance of the chemical composition and the microstructure of the base material on the wear resistance of the treated specimens.

2. Experimental

The specimens were produced by blending a prealloyed Fe–1.5% Mo powder and separately water-atom-

ised AISI 316L austenitic stainless-steel powder (both Astaloy Mo and AISI 316L were supplied by Höganäs) and elemental boron powder with an average grain size of 2.4 μm with two different compositions: 0.2 wt% B, 0.4 wt% B. Boron-free specimens were also produced for comparison. The chemical compositions of the commercial powders used in this study are shown in Table 1.

The specimens $\varnothing 20 \times 5$ mm were compacted at 600 MPa with die-wall lubrication in an uniaxial press. Sintering was carried out at 1200°C (Astaloy Mo) or at 1240°C (AISI 316L) in a laboratory furnace under pure dry hydrogen. The time of isothermal sintering for both sintered alloys was 30 min. The density, total porosity and interconnected open porosity were measured by the usual water-displacement method. The sintered density depends on the chemical composition of specimens and on the boron concentration.

The gaseous thermochemical treatment of sintered materials comprises three steps, each related to one specific chemical element used to modify the surface of the pieces; nitrogen, sulphur and oxygen. It should be noted that austenitic stainless steels contain elements with a high affinity for nitrogen to favour the formation of hard and stable nitrides in the surface layer. These elements however, also form stable oxides, and for this reason, they are not particularly suitable for nitriding since transport phenomena responsible in inducing the formation of the external compound layer and diffusion layer require destabilisation of oxide covering the surface of powder grains. To overcome these drawbacks, depassivation of sintered specimens has been performed. In order to protect against repassivation, the austenitic stainless steels have to be coated by the iron galvanic layer, which simultaneously enhances the nitriding process. The surface treatment is carried out in an industrial furnace. The detailed description of the treatment parameters is protected by the patent and is not available. The treatment temperature ranges between 400 and 560°C, and the complete treatment time is about 15 h. Different treatment procedures were carried out on the sintered materials, as summarised in Table 2, where the codes used for their identification are also reported.

The treated specimens have been characterised by means of light and scanning electron microscopy, micro-

Table 1
Chemical compositions of powders

Powder	Nominal chemical composition (%)						
	Cr	Ni	Mo	Si	Mn	C	Fe
Astaloy Mo	–	–	1.5	–	–	–	Balance
AISI 316L	16.3	12.75	2.28	0.87	0.17	0.019	Balance

Table 2
Material and surface treatments

Material	No treatment	Nitriding	Nitriding and oxidation	Nitriding and sulphurising	Nitriding oxidation and sulphurising
Astaloy Mo	A	AN	ANO	ANS	ANSO
Astaloy Mo + 0.2% B	A2	A2N	A2NO	A2NS	A4NSO
Astaloy Mo + 0.4% B	A4	A4N	A4NO	A4NS	A4NSO
AISI 316L	L	LN	LNO	LNS	LNSO
AISI 316L + 0.2% B	L2	L2N	L2NO	L2NS	L2NSO
AISI 316L + 0.4% B	L4	L4N	L4NO	L4NA	L4NSO

hardness measurements, the X-ray diffraction analysis of surface layers and the concentration depth profile of oxygen and nitrogen by using a LECO GDS 750 instrument. Furthermore, in order to confirm the constitution of the surface layers, some specimens were characterised by means of wavelength dispersion X-ray spectroscopy (WDXS) and energy dispersion X-ray spectroscopy (EDXS). In order to determine the surface roughness, a Hommelwerke Profilometer T1000 was used. Wear tests were carried out on an Amsler tribotester with a block-on-disk configuration, in dry sliding condition, by using 100Cr6 steel as the counterface material (63HRC). The wear tests were performed under a load of 20 N and with a surface sliding speed of 0.8 m/s.

3. Results and discussion

The values of density ρ_s (g/cm³), total porosity ϵ (%) and interconnected open porosity ϵ_i (%) are reported in Table 3.

For Astaloy Mo powders, boron tends to increase the sintered density and to close the residual porosity; however, while the density starts to increase in correspondence with 0.4% B, just at 0.2% B, an effect on the closure of pores is observed. On the contrary, for AISI 316L powders, boron increases the sintered density and closes the interconnected pores just at 0.2% B.

The unalloyed sintered Astaloy Mo has a homogen-

Table 3

Density ρ_s (g/cm³), total porosity ϵ (%) and open porosity ϵ_i (%) of sintered materials

Material	ρ_s (g/cm ³)	ϵ (%)	ϵ_i (%)
Astaloy Mo	7.1	10	9
Astaloy Mo + 0.2%B	7.1	10	7
Astaloy Mo + 0.4%B	7.3	7.4	1
AISI 316L	6.6	16.2	13
AISI 316L + 0.2%B	7.1	8.5	1.5
AISI 316L + 0.4%B	7.8	1.0	0

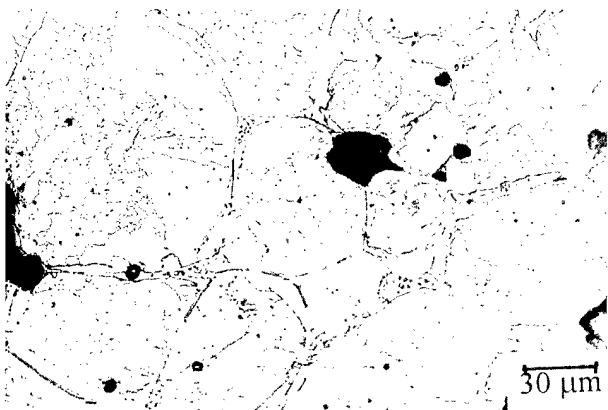


Fig. 1. Microstructure of material A4.



Fig. 2. Microstructure of material L4.

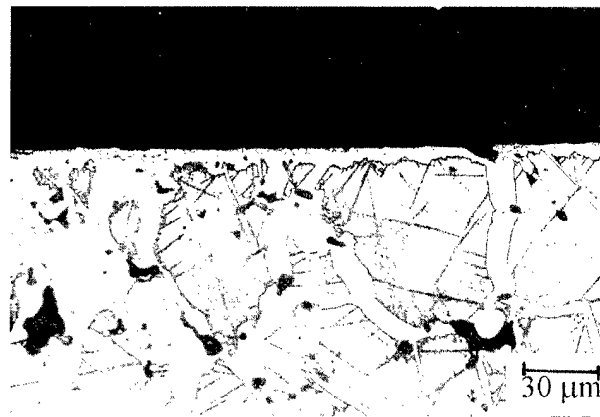


Fig. 3. Microstructure of material AN.

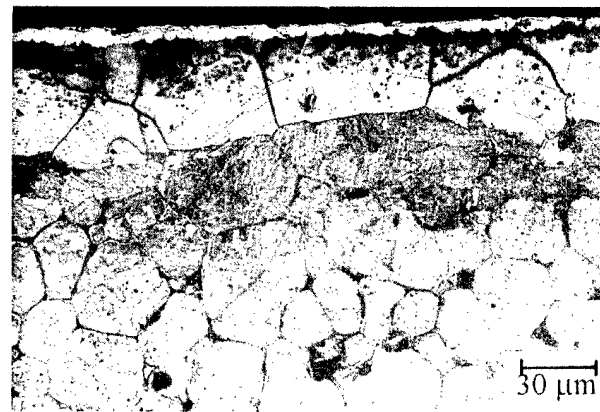
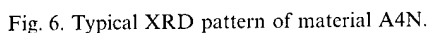
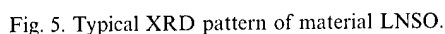


Fig. 4. Microstructure of material A4N.

eous ferritic microstructure. The boron-alloyed materials have a heterogeneous microstructure consisting of an almost continuous eutectic constituent surrounding the hard matrix grains in the bulk and near-full dense ferritic surface layer [8]. The microstructure of sintered boron alloyed AISI 316L is similar to that obtained with the Astaloy Mo alloy powder. Whereas the unalloyed AISI 316L presents the usual austenitic microstructure with an irregular and interconnected porosity, the alloyed



The thermochemical treatment of P/M-based iron steel has first been pointed out on nitriding, because it is the base treatment of all specimens. Figs. 3 and 4

[illegible]

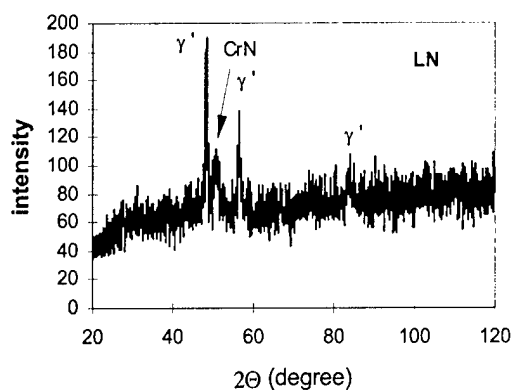


Fig. 9. Typical XRD pattern of material LN

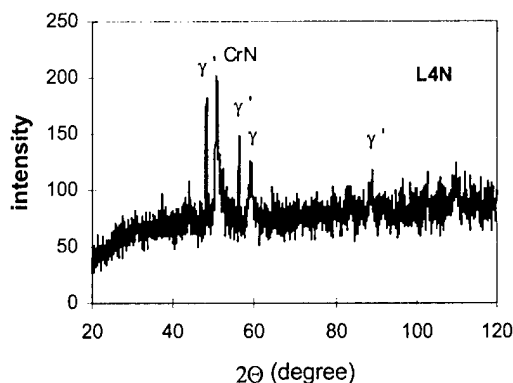


Fig. 10. Typical XRD pattern of material L4N

350 and 500 HV_{0.05}. The white network consists of a mixture of the γ' and ϵ -Fe₂₋₃N nitrides, as confirmed by XRD analysis, as shown, for instance, in Fig. 5 for a graph showing the results from Table 4. The low hardness of this constituent is due to the presence of micropores. Concerning the other boron-free materials, the

microstructure and the microhardness are the same as for AN material. Only a very thin external surface layer with a thickness of about 1–4 μ m of FeS in material ANS can be observed. A similar thin oxide layer in material ANO and a very thin oxide layer with a thin sulphide layer in material ANSO can be seen.

On the contrary, the microstructure of the A4N material shows a typical thick compound layer that consists of both the nitrides γ' and ϵ -Fe₂₋₃N, as shown in Fig. 6. The microhardness of this compound layer is about 800 HV_{0.01}. The near full-dense subsurface boron-free layer shows large needles like γ' nitrides in the ferritic grains. By moving towards the bulk, the microhardness decreases from 550 HV_{0.05} to about 420 HV_{0.05}. The microhardness of the matrix where the eutectic constituent is present is about 280 HV_{0.05}. The other boron-alloyed materials show a similar thick compound layer, and the same diffusion layer and bulk microstructure as the A4N material. The sintered austenitic stainless AISI 316L steel shows the CrN nitride in addition to γ' and γ -phases. The characteristic microstructures of material LNSO and L4NSO are shown in Figs. 7 and 8, respectively.

From these results it is clearly evident that boron, present in the iron base alloys, modifies the nitrogen diffusion, decreasing the penetration depth of nitrogen and increasing the average surface hardness. Finally, the thermochemically nitrided boron-alloyed specimens demonstrated typical characteristics of a nitrided case depth: a distinct compound layer and a well-defined diffusion layer, consisting of a dispersion of submicroscopic nitrides in a nitrogen-enriched solid solution. However, the BN precipitation is not confirmed because the microhardness values measured in the diffusion layer of A4N and in the ferritic grains of AN are very similar.

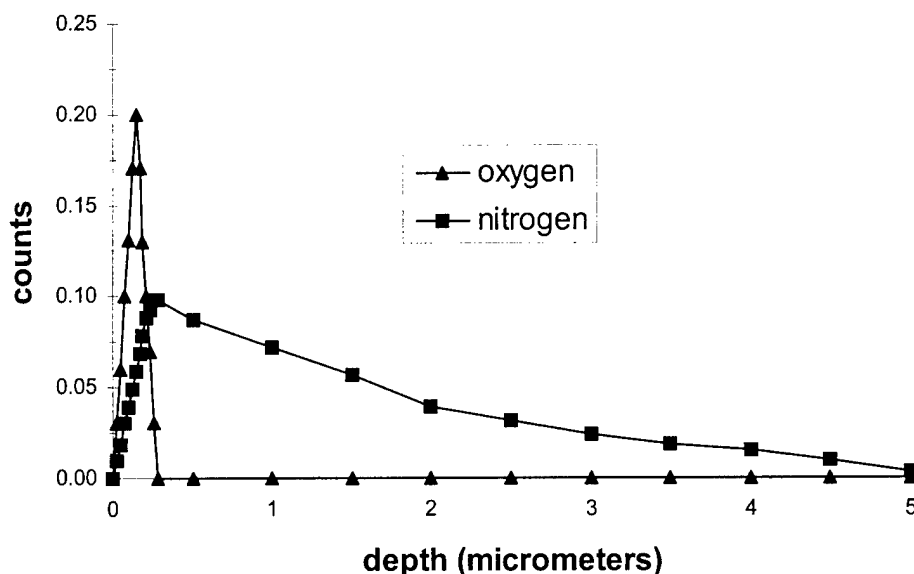


Fig. 11. Semiquantitative concentration depth profile of oxygen and nitrogen in material ANO.

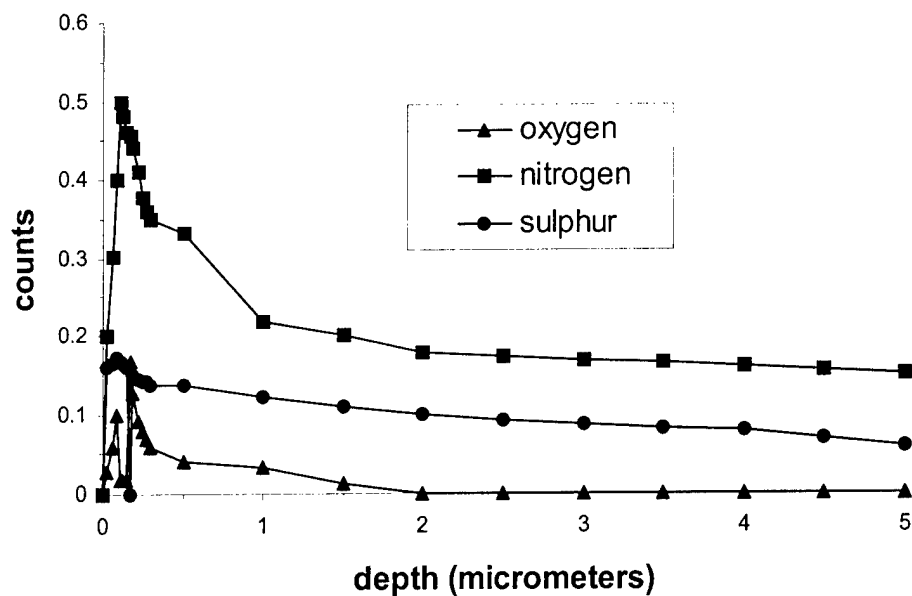


Fig. 12. Semiquantitative concentration depth profile of oxygen, nitrogen and sulphur in material ANSO.

The results of XRD analyses of specimens A, L and A4, L4 (Figs. 9 and 10) treated in all the experimental conditions can be summarised as follows:

- oxidation of the previously nitrided surface forms magnetite, but is not able to transform the whole compound layer in material A4, L4, as demonstrated

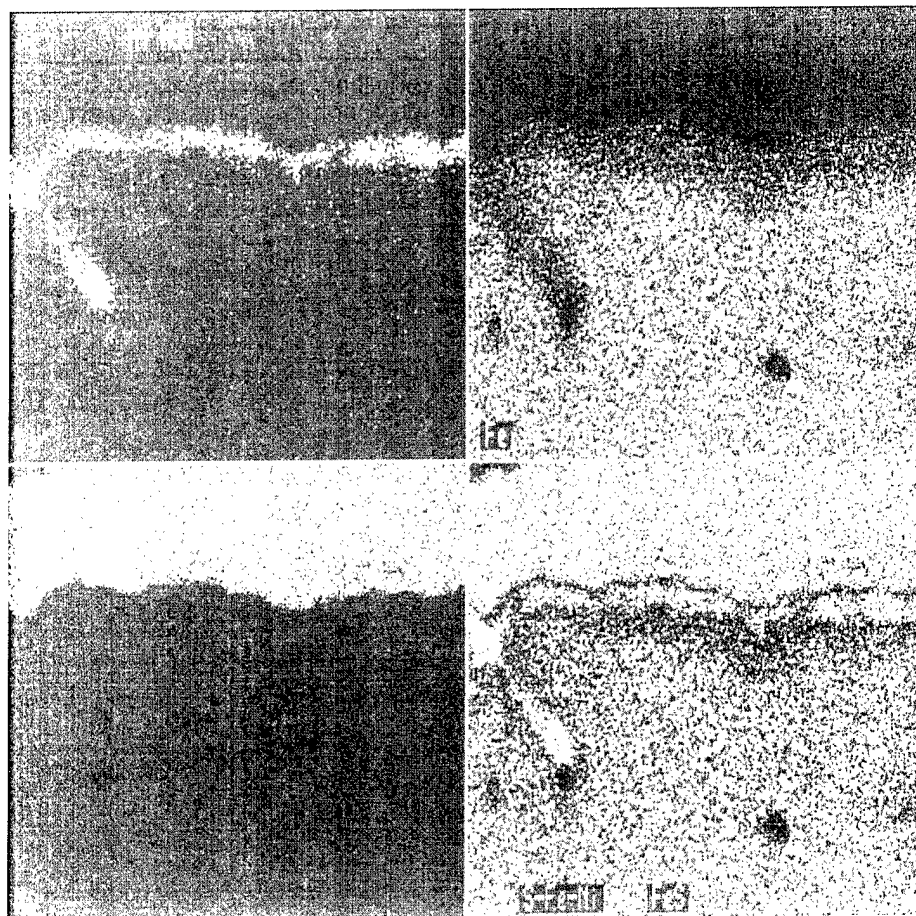


Fig. 13. WDXS analysis of material A4NSO.

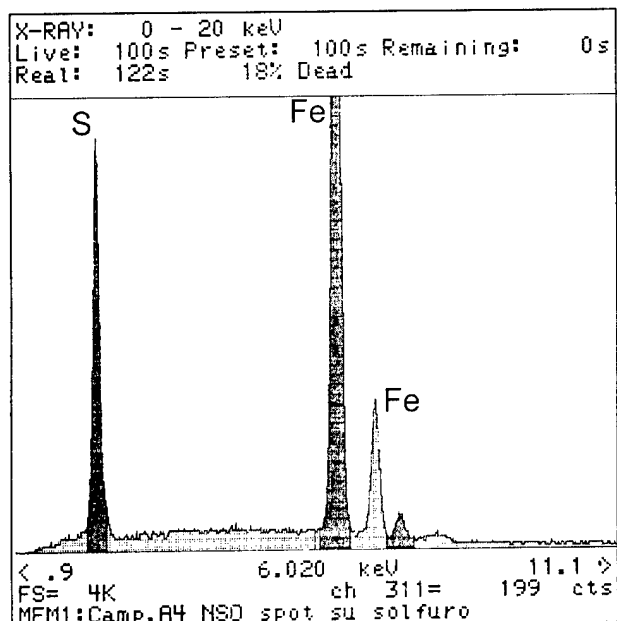


Fig. 14. EDXS characterisation of material A4NSO.

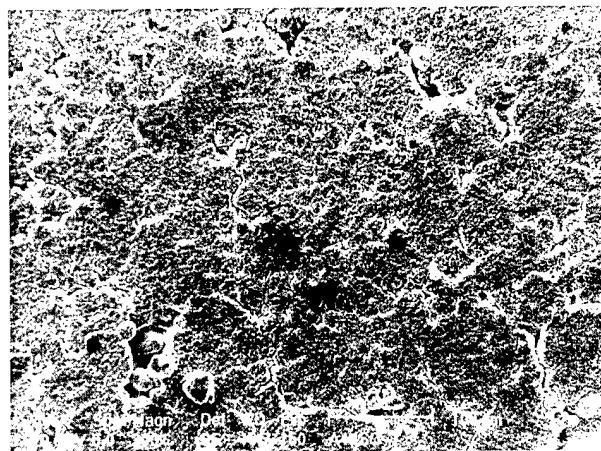


Fig. 17. Surface morphology of material A4NSO.

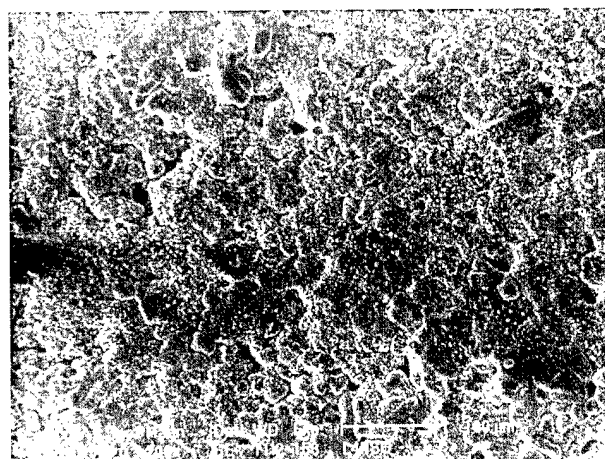


Fig. 18. Surface morphology of material L4NSO.

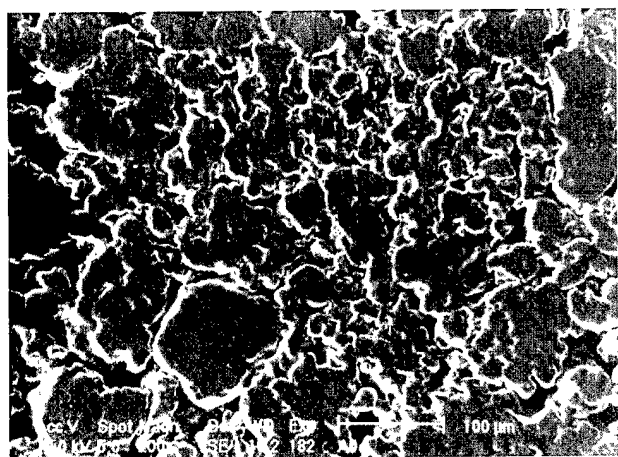


Fig. 15. Surface morphology of material A.

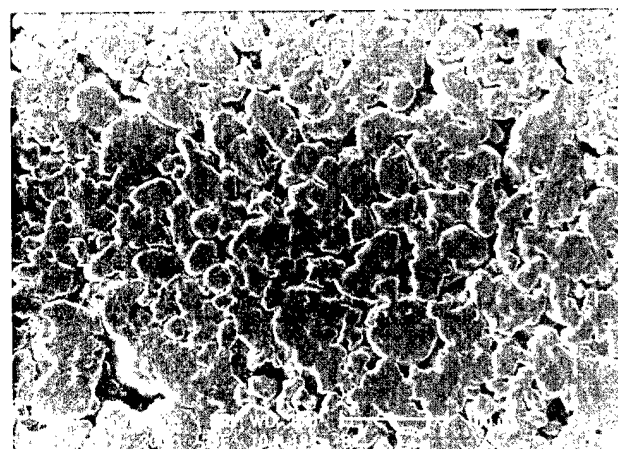


Fig. 16. Surface morphology of material A4N.

by the diffraction peaks of nitrides in XRD patterns of samples A4NO or L4NO;

- sulphuration of the nitrated surface is able to modify the compound layer and forms FeS and Fe₃O₄;
- the nitriding, sulphuration and oxidation form a mixture of FeS and iron oxides in the compound layer; these last dominate in comparison with the NS treatment, as expected.

The above results confirm the concentration depth profiles. Figs. 11 and 12 show the depth profile of oxygen and nitrogen in specimens ANO and ANS, respectively. While oxidation produces a sharp oxygen segregation on the surface as a consequence of a very thin oxide layer on the external surface, sulphuration induces the interdiffusion of sulphur, nitrogen and oxygen, from which a mixture of sulphides, oxides and nitrides is formed. The semiquantitative concentration depth profile in Fig. 12 is representative of specimens ANSO, too, and the depth profiles in the specimens with the other base composition are quite similar to those reported in the above figures.

In order to confirm the constitution of the surface

Table 5

Roughness (R_a , μm) of surface-treated sintered materials

A	AN	ANO	ANS	ANSO	A4N	A4NO	A4NS	A4NSO
3.42	3.11	2.81	2.37	1.94	2.27	1.96	1.68	1.53
L	LN	LNO	LNS	LNSO	L4N	L4NO	L4NS	L4NSO
2.89	2.26	1.91	1.61	1.22	2.76	2.1	2.03	1.63

layers, a detailed characterisation by WDXS spectroscopy and an EDXS analysis were carried out on A4NSO specimens. From these results (Figs. 13 and 14), one can conclude that FeS is formed in the compound layer.

Figs. 15–18 show the surface morphology of the materials A, A4N, A4NSO, L4NSO, respectively. It is clear that only after nitriding, sulphuration and oxidation is a noticeable modification of the surface morphology obtained. This observation agrees with the XRD analyses. As predicted, nitriding does not change the surface morphology, which is maintained after oxidation, too, because of the very low thickness of the oxide layer. In contrast, sulphuration tends to eliminate all the surface irregularities of the nitrided pieces. The specimen A4NS has the same surface morphology as A4NSO, and the above figures are representative of the other base materials, too. The roughness of a sintered part is highly dependent on the surface porosity (open porosity). Due to these pores, the classical parameters R_a and R_z and so on, measured with a normal roughness meter, appear to be much larger for the sintered surface than for that of the wrought part with identical functional properties. With a sintered or sized surface, excellent friction behaviour can be obtained, even at high R_a and R_z values (Table 5).

Finally, Fig. 19 shows the results of the preliminary dry sliding wear test of five different samples: untreated, A4N, A4NO, A4NS, A4NSO. The weight loss in Fig. 19 is the average value obtained from three successive and similar wear tests on a given sample. It is clear from these results that all the treatment are able to increase the wear resistance of the base material; moreover, sulphuration is more effective than oxidation. This is

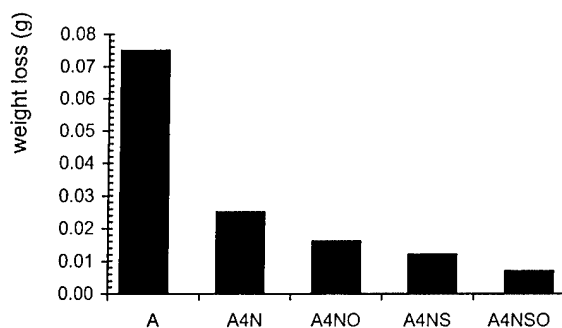


Fig. 19. Results of wear tests. The test duration was 60 min.

due to the combined contribution of the well-known influence of FeS on the sliding behaviour and the very low thickness of the magnetite layer formed by oxidation. However, when oxidation is carried out after sulphuration, a further increase in the wear resistance is attained. The results of the wear test are only indicative.

4. Conclusion

It has been shown that with pore closure caused by the addition of boron, the disadvantage of deep gas nitriding can be eliminated. Furthermore, boron is able to reduce the nitrogen penetration because it activates the sintering process and closes the residual porosity. However, during sintering, a depletion from external layers of the base material occurs, and the added element cannot be exploited to form a fine precipitation of hard and stable nitrides in the diffusion layer. Therefore, the microhardness of this layer is not high because the needle-like γ' nitrides do not harden the matrix. The effect of boron is then limited to the control of nitrogen penetration. The combined treatment induces the formation of a surface layer consisting of FeS, magnetite and iron nitrides. In particular sulphuration significantly changes the surface morphology of the treated specimens. As a consequence, the dry sliding wear resistance of the material increased.

References

- [1] Metals Handbook, ninth ed., American Society for Metals, 1984, p. 7.
- [2] P.C. Borges, N.C. Nilton, C. Franco, A.N. Klein, Adv. Powder Metallur. Partic. Mater. 2 (1994) 61.
- [3] G.F. Bocchini, A. Molinari, B. Tesi, T. Bacci, Metal Powder Rep. 11 (1991) 772.
- [4] A. Molinari, Proc. Int. Conf. Powder Metall., Cluj-Napoca 1 (1996) 27.
- [5] Surface strengthening of metals and alloys by electrolytic alloying and nitriding, European Patent No. 0248431.
- [6] A. Molinari, J. Kazior, G. Straffellini, Mater. Character. 34 (1995) 271.
- [7] J. Kazior, C. Janczur, B. Stolarski, M. Pellizzari, A. Molinari, Adv. Powder Metallur. Partic. Mater. 3 (1997) 17.
- [8] A. Molinari, J. Kazior, T. Pieczonka, G. Straffellini, Proc. Eur. Conf. PM97, Advances in Structural Powder Metall. Component Production, Munich 1 (1997) 327.
- [9] A. Molinari, G. Straffellini, J. Kazior, T. Pieczonka, Adv. Powder Metall. Partic. Mater. 5 (1996) 17.



ELSEVIER

Surface and Coatings Technology 125 (2000) 9–12

**SURFACE
& COATINGS
TECHNOLOGY**

www.elsevier.nl/locate/surfcoat

Modification of composite nitrided layers by phosphorus compounds

J. Nowacki *

Institute of Materials Engineering, Technical University of Szczecin, Al. Piastow 19, 70-310 Szczecin, Poland

Abstract

Composite diffusive nitrided layers with precipitates of iron phosphides are considered. They are generated in the process of nitriding in an atmosphere of partly dissociated ammonia with a slight admixture of gaseous phosphorus. The addition of small quantities of gaseous phosphorus to the nitriding atmosphere influences the structure and properties of the nitrided layer. The layers consists of: a zone of phosphides of Fe_3P and Fe_2P , a zone of nitrides of Fe_{2-3}N and Fe_4N , and a zone of precipitates of iron phosphide Fe_3P in the zone of nitrides of Fe_{2-3}N and Fe_4N . The relations between chemical contents of the atmosphere, as well as the parameters of the process, structure and properties of the layer, have been defined. Iron phosphide reinforcement in the diffusive nitrided layer increases its hardness and resistance to wear. © 2000 Elsevier Science S.A. All rights reserved.

Keywords: Iron nitrides; Iron phosphides; Nitriding of short duration; Phospho-nitriding; Phosphorus in steel

1. Introduction

Modifying the structure and properties of diffusive layers, e.g. carburized and nitrided ones, is required in numerous special applications. It is possible through their alternation with fine ceramic or intermetallic particles, e.g. borides, oxides, sulphides or phosphides. The particles in such layers are generated as a result of polyphase diffusion; lattice diffusion or precipitation processes accompanied the process of generating the base diffusive layer. Additions of some chemical elements or compounds, e.g. sulphur, phosphorus, oxygen or H_2O , H_2S , SO_2 , to the active atmosphere enabled synthesis of the ceramic or intermetallic particles. Thus a diffusive layer on steel plays the role of a matrix, whereas ceramic precipitates are an addition, modifying the structure and properties of the layer. Such layers and their particular reinforcement may be regarded as composite diffusive layers reinforced by particles. In this paper the structure and properties of such a layer are considered, with the example of a nitrided layer modified by iron phosphides. So far, not much attention has been paid to the role of phosphorus as a component of the nitriding atmosphere. The beneficial influence of phosphorus on the properties of the surface of machine elements made of steel, especially on the increase of

hardness and wear resistance in the process of friction, is also underestimated. The profitable influence of phosphorus on surface properties of iron alloys has been proved [1,2]. There are many possibilities to modify the structure and properties of a surface of iron alloys as a function of the phosphorus concentration. When the phosphorus concentration in iron is small, a solid solution of phosphorus in iron may be formed. An increase of the phosphorus concentration in iron gives a chance to precipitate hardening of its surface. Further increase of the phosphorus concentration in iron alloys makes it possible to form iron phosphides Fe_3P and Fe_2P according to the Fe–P equilibrium system. It was found that the presence of phosphorus in the nitrided layer exerts a substantial influence on its structure and properties [3,4]. As a result of phospho-nitriding, precipitates of fine particles of iron phosphides in the nitrided layer, as well as a continuous zone of iron phosphides, may be formed. The presence of iron phosphides in the nitrided layer increases its hardness and wear resistance in the process of dry sliding friction. The essential significance of the course of phospho-nitriding lies in the notable solubility of phosphorus in ferrite at the temperature of nitriding. The hitherto existing research results are a convincing justification to search for the technical possibilities of introducing phosphorus to the nitriding layer, and defining the relations between the parameters of the phospho-nitriding and the structure, as well as the properties of layers.

* Tel.: +48-91-449-4751. fax: +48-91-434-0558.

E-mail address: jnowacki@safona.tuniv.szczecin.pl (J. Nowacki)

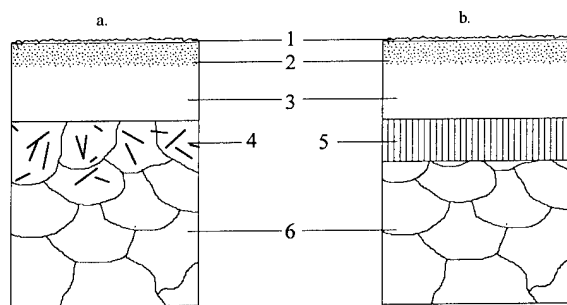


Fig. 1. Types of structure of composite phospho-nitrided layers according to the process temperature T : (a) $T < 863$ K (590°C); (b) $T > 863$ K (590°C). 1, Compact $\text{Fe}_2\text{P} + \text{Fe}_3\text{P}$ phosphides zone; 2, ϵ (Fe_{2-3}N) nitride zone with Fe_3P phosphide precipitates; 3, ϵ (Fe_{2-3}N) and γ' (Fe_4N) nitride zone; 4, Fe_4N nitride precipitates in ferrite; 5, braunite; 6, ferrite base.

2. Method of investigation

Preparation of the composite nitrided layers with particles of iron phosphides was carried out on a base of Armco iron, 0.4% C, 1.1% Cr steel and 0.4% C, 1.6% Cr, 1% Al steel in an atmosphere of partly dissociated ammonia with the addition of gaseous phosphorus. Phosphorus vapours were deposited by means of ammonia from an evaporator into the working chamber of the reactor, in which the process of generating the layer was executed. The phosphorus pressure was calculated from the dependence derived from the equation of state of the perfect gas [4,5]. During the process the following parameters were applied: temperature $T = 843\text{--}923$ K ($570\text{--}650^\circ\text{C}$), ammonia volume flux $V_a = 5.6 \times 10^{-6} \text{ m}^3/\text{s}$, phosphorus partial pressure $p = 10\text{--}300$ Pa, process duration $t = 10.8\text{--}21.6$ ks (3–6 h). The diffusive layers were investigated by several methods: metallographic, X-ray structural analysis, microanalysis, measurement of Vickers hardness, measurements of resistance

to wear by Falex test at a load of 450 N and linear velocity of friction 1 m/s.

3. Structure and properties of the layer

As a result of the experiments carried out, layers of a silver-grey colour were formed on the surface of the specimens. The structure of the layers is presented in Figs. 1 and 2. The investigations proved that, owing to the addition of phosphorus to the nitriding atmosphere, the structure of the diffusive layer is subject to an essential change. Depending on the partial pressure of phosphorus in the nitriding atmosphere, it is possible to differentiate two basic types of structure. In the case of low partial pressure of phosphorus, i.e. below 120 Pa [Fig. 2(a)], a stripe of iron phosphide Fe_3P precipitates in the zone of nitrides ϵ (Fe_{2-3}N), and $\epsilon + \gamma'$ (Fe_{2-3}N and Fe_4N) of the nitrided layer is created. The size and concentration of these precipitates depend on the parameters of the process, and they first increase with an increase of phosphorus partial pressure in the nitriding atmosphere. Higher partial pressure of phosphorus in the ammonia atmosphere causes the formation of a compact layer of iron phosphides $\text{Fe}_3\text{P} + \text{Fe}_2\text{P}$ above the zone of nitrides. The quantity relation of Fe_3P to Fe_2P in the compact layer depends on the partial pressure of phosphorus in the ammonia atmosphere and the process temperature. At process temperature above $T = 923$ K (650°C) only iron phosphide Fe_3P is created (Fig. 3). The qualitative distribution of the phosphorus, nitrogen and iron in the phospho-nitrided layer is shown in Fig. 4. The phosphorus concentration in the layer, determined by X-ray microanalysis, is presented in Table 1. The layer of phosphides is compact only until a thickness of about 0.01–0.02 mm, dependent on the size and shape of the sample. For greater thickness a gap between the

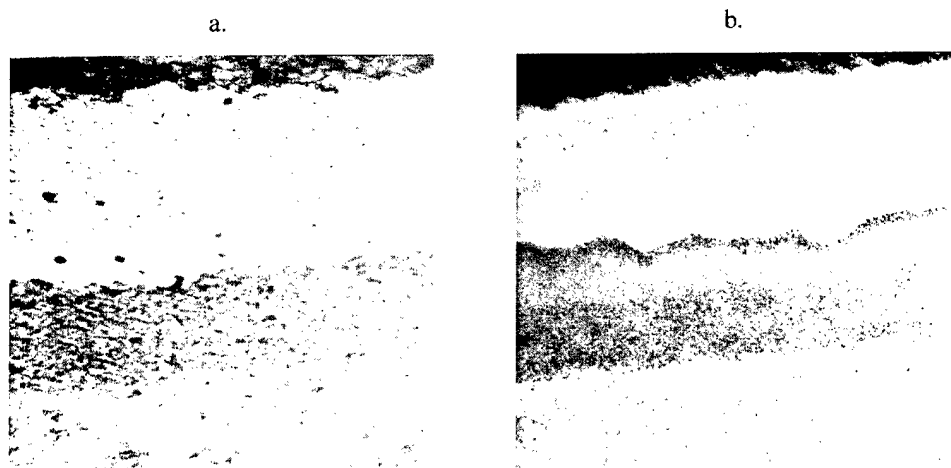


Fig. 2. Microstructure of composite phospho-nitrided layer, process parameters: (a) $T = 893$ K (620°C), $p = 60$ Pa, $t = 21.6$ ks (6 h); (b) $T = 893$ K (620°C), $p = 130$ Pa, $t = 21.6$ ks (6 h).

Table 1

Limits of phosphorus concentration in the phospho-nitrided layer determined by X-ray quantitative microanalysis

Zone of the phospho-nitrided layer	Phosphorus concentration (wt%)
Compact $\text{Fe}_2\text{P} + \text{Fe}_3\text{P}$ zone	15–21
Porous Fe_3P zone	10–12
Fe_3P zone	1–3

compact $\text{Fe}_2\text{P} + \text{Fe}_3\text{P}$ phosphides zone and the ϵ (Fe_{2-3}N) nitrides zone with Fe_3P phosphide precipitates is created. In the advanced stages of the process of phospho-nitriding the gap is filled by porous Fe_3P . The process of creating the gap and porous Fe_3P is similar to the process of the growth of oxide layers, and is described in Ref. [6]. The layer structures with the gap or porous Fe_3P are not used in technical applications.

The addition of phosphorus to the nitriding atmosphere alters the geometry of the phospho-nitrided surface to a small degree, in comparison with classic nitriding (Figs. 5 and 6). Some increase of the surface

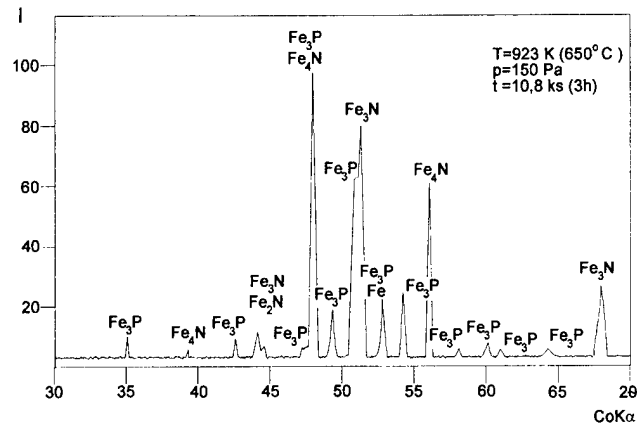


Fig. 3. Diffraction pattern of phospho-nitrided layer formed on Armco iron with process parameters $T=923\text{ K}$ (650°C), $p=150\text{ Pa}$, $t=10.8\text{ ks}$ (3 h).

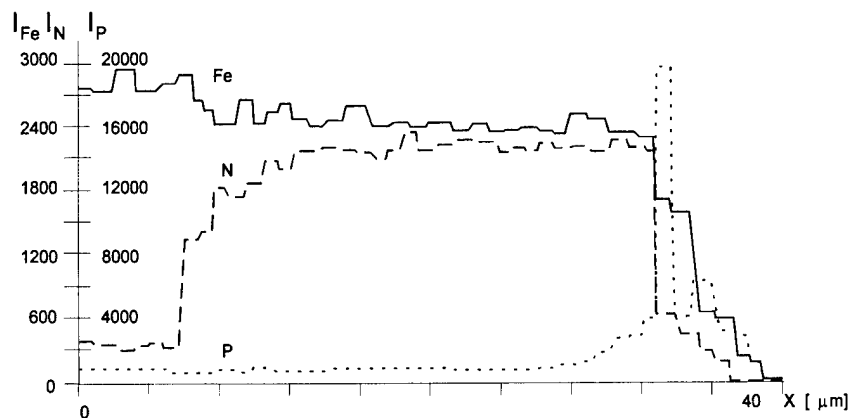


Fig. 4. Distribution of the phosphorus P, nitrogen N and iron Fe in the phospho-nitrided layer, process parameters: $T=853\text{ K}$ (580°C), $p=130\text{ Pa}$, $t=21.6\text{ ks}$ (6 h).

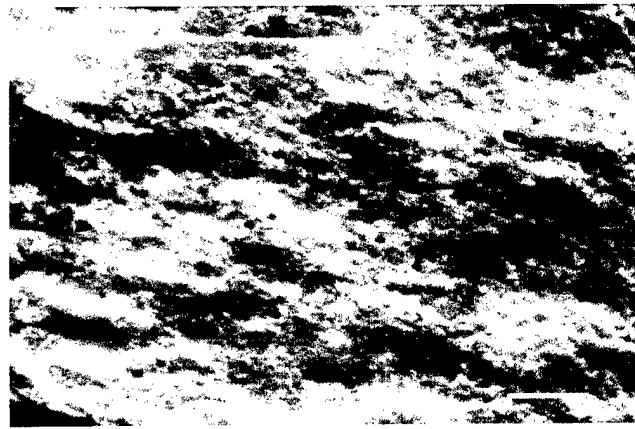


Fig. 5. Scanning image of the phospho-nitrided Armco iron surface, process parameters: $T=843\text{ K}$ (570°C), $t=10.8\text{ ks}$ (3 h), $p=10\text{ Pa}$; space bar 0.005 mm .

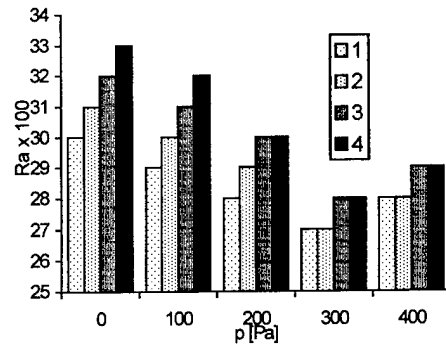


Fig. 6. Influence of phosphorus partial pressure p on the surface roughness R_a of 0.4% C, 1.1% Cr steel after phospho-nitriding with process parameters: 1, $T=843\text{ K}$ (570°C), $t=10.8\text{ ks}$ (3 h); 2, $T=843\text{ K}$ (570°C), $t=21.6\text{ ks}$ (6 h); 3, $T=893\text{ K}$ (620°C), $t=10.8\text{ ks}$ (3 h); 4, $T=893\text{ K}$ (620°C), $t=21.6\text{ ks}$ (6 h).

smoothness is visible for phosphorus partial pressures $100 < p < 300\text{ Pa}$. The presence of iron phosphides in the nitrided layers increases their hardness (Figs. 7 and 8). The effect is stronger at lower temperatures of phospho-

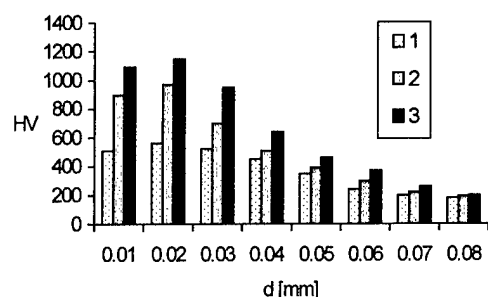


Fig. 7. Hardness HV 0.01 of nitrided layers formed with process parameters $T=843$ K (570°C), $t=21.6$ ks (6 h) at distance from the surface d : 1, Armco iron; 2, 0.4% C, 1.1% Cr steel; 3, 0.4% C, 1.6% Cr, 1% Al steel.

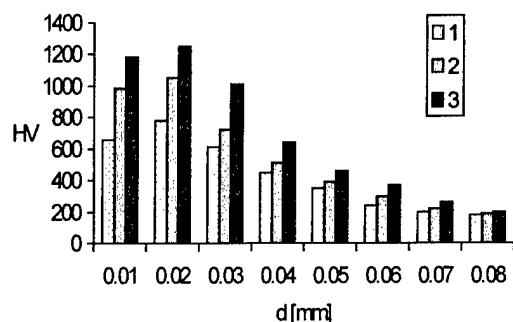


Fig. 8. Hardness HV 0.01 of phospho-nitrided layers formed with process parameters $T=843$ K (570°C), $p=100$ Pa, $t=21.6$ ks (6 h) at distance from the surface d : 1, Armco iron; 2, 0.4% C, 1.1% Cr steel; 3, 0.4% C, 1.6% Cr, 1% Al steel.

nitriding. An increase in the layer hardness is especially distinct on Armco iron and carbon steels, in which there are no components forming hard nitrides. The nitrided layers with iron phosphides show greater resistance to wear in the process of dry friction than layers made in an atmosphere of pure NH_3 (Fig. 9). The increase of the layer hardness and the wear resistance is caused by a solid solution strengthening and precipitation hardening as a result of the Fe_3P reinforcement presence.

4. Conclusions

The obtained layers are an example of composite diffusive layers with iron phosphide particles generated as a result of polyphase diffusion, lattice diffusion and

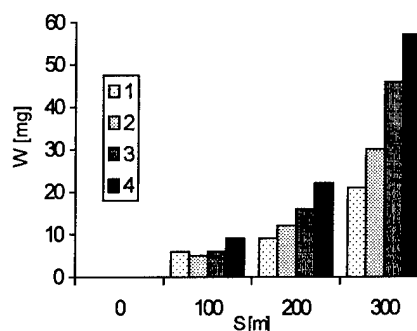


Fig. 9. Dependence of weight wear W on path of friction S of: 1, phospho-nitrided 0.4% C, 1.6% Cr, 1% Al steel; 2, phospho-nitrided 0.4% C, 1.1% Cr steel; 3, nitrided 0.4% C, 1.6% Cr, 1% Al steel; 4, nitrided 0.4% C, 1.1% Cr steel, in accordance with the Falex test; nitriding parameters as in Fig. 7 and phospho-nitriding parameters as in Figs. 7, 8.

precipitation processes accompanying the phospho-nitriding. The type, form and concentration of iron phosphides appearing in the phospho-nitrided layer correspond, first of all, to the partial pressure of phosphorus in the ammonia atmosphere and then to the remaining parameters of the process. Depending on the partial pressure of phosphorus in the nitriding atmosphere, the formation of a compact layer of phosphides with adjustable relation of Fe_3P to Fe_2P , or controlled phosphide precipitate concentrations in the nitride zone, is possible. The presence of phosphorus in the nitrided layer increases its hardness and tribological properties owing to the solid solution strengthening and precipitation hardening as a result of the Fe_3P presence. The best tribological properties have phospho-nitrided layers obtained in the lower than 100 Pa partial pressure of phosphorus in ammonia atmosphere.

References

- [1] A. Wustenfeld, Verfahren zur Eindiffusion der Elemente Bor, Silizium und Phosphor in Metalloberfläche, German Patent 2429948, 1972.
- [2] A.W. Schluchter, Method of rust-proofing iron or steel, US Patent 1,761,963, 1964.
- [3] J. Nowacki, Harterei-Technische Mitteilungen 47 (1991) 47–51.
- [4] J. Nowacki, S. Strzelecki, Optimisation of tribological properties of phosphorised layers, Eurotrib'93, Proc. 6th Int. Congress on Tribology, Budapest, Hungary (1993) 303–307.
- [5] J. Nowacki, Harterei-Technische Mitteilungen 44 (1989) 107–112.
- [6] J. Nowacki, Wear 173 (1994) 51–55.

Laser cladding and erosive wear of Co–Mo–Cr–Si coatings

J. Przybylowicz, J. Kusinski *

Faculty of Metallurgy and Materials Science, University of Mining and Metallurgy, 30 Mickiewicza Ave., 30-059 Krakow, Poland

Abstract

Defect free coatings, made of Tribaloy T-400 powder, deposited by laser cladding on iron and nickel based substrates are described. The proper selection of the cladding process parameters allowed us to get coatings with low dilution of the base material. Cross-sections of such coatings have been examined to reveal their microstructure using optical, scanning electron and transmission electron microscopy, chemical analysis (EDS microanalysis), phase composition (XRD), hardness and microhardness testing methods. Compared with other deposition techniques the microstructure of the laser coatings showed a high degree of refinement and chemical homogeneity. Grain coarsening was observed in the heat-affected zones and was explained as being due to the overlapping of subsequent tracks during the coatings deposition. The erosive wear resistance of the coatings has been investigated. In general, the laser deposited coatings turned out to be susceptible to extensive erosive wear. This effect was explained by lack of feasibility of the coated material to plastic deformation during erosion. © 2000 Elsevier Science S.A. All rights reserved.

Keywords: Erosive wear; Laser cladding; Microstructure

1. Introduction

In modern technology hardfacing is often used to produce surface coatings protecting parts against different kinds of wear, including sliding, abrasion or erosion. In addition, depending on coating material selection, chemical or high temperature corrosion protection can be provided to the surface. Hardfacing is a method to obtain desired surface properties and allow for economical consumption of expensive wear resistant alloys.

Materials particularly useful in wear applications and often used in as-cast condition are Triballoys (trademark of Delloro Stellite Ltd.). The alloy Tribaloy T-400 contains about 50 vol.% of CoMoSi Laves phase of hardness up to 1300 HV providing adhesive wear resistance. The Mo addition gives high temperature strength to the Co based matrix. The Cr content in both matrix and Laves phase contributes to their corrosion resistance [1]. The matrix fcc crystal structure is stabilized by Ni and Fe addition [2]. This lattice type is desirable for better strength and ductility due to more active slip systems over the hcp type [3]. On the other hand, Mo

and Cr, by reducing the stacking fault energy, enhance the plastic deformation induced fcc→hcp crystal structure transformation in the Co based matrix [2,4]. This increases the alloy work hardening rate reported to be beneficial for abrasive wear resistance of other Co based alloys [5]. In the work by Halstead and Rawlings T-400 alloy in a cast and heat treated form is said to be erosion resistant owing to the combination of brittle intermetallic embedded in the softer Co solid solution matrix [6].

The solid particle erosion (SPE) effect occurs whenever solid particles carried in a gas or liquid jet at a speed exceeding 1 m/s impinge on the component surface. Particularly susceptible for SPE are components of steam and gas turbines (vaness, disks, rivets, valves), helicopter rotor blades, fluidized bed heat exchanger elements and others. There are three basic groups of erosion parameters: referring to particle flow, abrasive material properties and eroded material properties. The third group comprises primarily: material microstructure, hardness, toughness, plasticity, work hardenability, residual stresses and others. Numerous parameters affecting the SPE process make it difficult to establish a uniform model quantifying the erosion effects. In practice most cases have to be evaluated individually based on empirical data [7]. All the properties can be widely affected by the deposition technology selection of protective coatings.

* Corresponding author.

E-mail address: kusinski@metal.agh.edu.pl (J. Kusinski)

Laser cladding is a modern technology oriented on producing, among others, wear resistant coatings. The process objective is to use a laser beam to melt the coating material in the form of continuously fed powder or wire or a pre-deposited paste together with a substrate layer of controlled thickness [8]. As a result of using the high power density accomplished by the laser beam, a high temperature gradient at the coating–substrate interface and rapid cooling of the coating material can be achieved [7]. The result is a strong microstructure refinement, solid solution supersaturation in alloying elements and high residual stresses in the coating. An important feature is the ability to control the coating from the substrate dilution in laser cladding. Numerous tests indicated superior sliding and abrasive wear resistance of Co based alloys deposited by laser cladding, compared with other welding techniques [5,7,9]. On the other hand, there is little data available regarding the erosion resistance of laser deposited coatings.

This paper shows the results of an investigation carried out to study the microstructure and properties of laser clad Tribaloy T-400 coatings as well as their solid particle erosion behaviour.

2. Experimental procedure

The alloy T-400 of chemical composition listed in Table 1 was deposited as coatings on 0.45% C structural steel and IN 718 substrates by means of laser cladding.

The laser treatment was performed on $25 \times 6 \text{ mm}^3$ steel coupons using a 1500 W continuous wave CO_2 laser with generated beam power of 1000 W. The scanning speed of 8 mm/s was applied during deposition. The laser beam in TEM₀₀ mode (with Gaussian energy density distribution) was defocused on the surface to a spot about 2.6 mm in diameter. The Tribaloy T-400 powder of 45 μm grade was pneumatically fed into argon, providing oxidation protection of the coating material. The subsequent laser tracks were overlapped by 30%, to obtain a coating exceeding 1 mm in thickness. Pre-heating of IN 718 samples up to 500°C was required in order to avoid the coating cracking upon cooling after laser cladding.

The cross-sections for metallography were prepared in the plane normal to the cladding direction. The microstructure was examined using optical and scanning

electron microscopy (SEM). Chemical composition analysis were carried out by means of electron dispersive spectroscopy (EDS). The alloy phase composition was determined by X-ray diffraction (XRD). The cross-sectional microhardness was measured at a load of 2 N. The coatings hardness tests were performed using a Rockwell type tester.

The coatings erosion resistance was examined using a nozzle type apparatus described in detail elsewhere [10]. The samples were prepared by surface grinding of a 0.25 mm thick layer down to no. 600 abrasive paper. The eroding material used was corundum of about 200 μm particle size fed into a compressed air jet at room temperature. The particles speed was about 100 m/s at a flow rate of 30 g/min. Three independent tests were performed at each erosion angle α (measured as the nozzle to eroded surface tilt): 20, 30, 40, 50, 60 and 90° for both tested coatings. An average value of sample relative mass decrement (per abrasive mass unit) was plotted against α to obtain the erosion curves. The mass measurements were carried out using an analytical scale precise to 10^{-4} g.

In order to determine the erosion mechanisms for each coating, single craters were produced in tested samples. This was accomplished by introducing about 10 to 15 corundum particles into the air jet projected at polished and slightly etched surface. The effects of surface erosion for single particle impacts, as well as for multi-particles stream impingement, were investigated by means of SEM.

Thin foils for transmission electron microscopy (TEM) analysis were obtained from the material after erosion both parallel and across the surface layer as 3 mm diameter disks. After mechanical thinning and dimpling, foils were ion milled till perforation. The foils from the eroded surface were processed by ion milling from one side, preserving the surface layer.

In order to estimate the degree of material work hardening due to erosion, the microhardness at 0.2 N load was measured near the surface on suitable sample cross-sections.

3. Results and discussion

The cross-section of Tribaloy T-400 coating laser deposited on structural carbon steel substrate is pre-

Table 1
Nominal chemical composition of experimental materials (wt%)

Alloy	C	Co	Cr	Fe	Mo	Ni	Nb	Si	Other
T-400	0.08	balance	8.5	1.5	28.5	1.5	—	2.6	—
IN718	0.04	—	18.6	18.5	3.1	balance	5.0	—	Al, Ti
Steel	0.4	—	2.0	balance	—	—	—	0.25	—

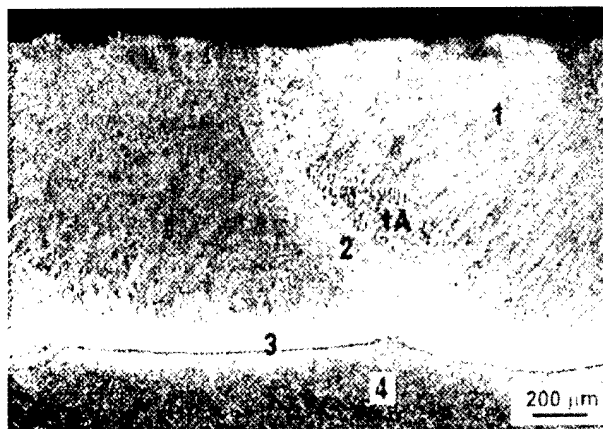


Fig. 1. Cross-section of Tribaloy T-400 layer laser cladded on steel substrate: (1) cladded track center; (1A) grain growth zone; (2) inter-track heat-affected zone; (3) transition zone; (4) substrate.

sented in Fig. 1. The layer of 1.15 mm average thickness was crack and porosity free. The structure was not uniform on the coating cross-section with heat-affected zones due to laser track overlapping effect. The microstructure of the cladded track center consisted of a fine lamellar eutectic mixture of Laves and Co based phases forming colonies of 7–15 μm in diameter, elongated in the direction of heat flow with a different orientation in relation to the microsection. Fig. 2 shows the eutectic morphology with Co phase crystallizing between eutectic colonies, indicating the slightly hypoeutectic character of the alloy. Eutectic colonies adjacent to the heat-affected zone were larger and spherical in shape. The structure of the corresponding zone in the coating on IN 718 substrate contained less Co based phase along grain boundaries and few precipitations of primary Laves dendrites. Heating by successive passes up to eutectic temperature caused spheroidization of Laves phase in the inter-track heat-affected zones, the effect of which is shown in Fig. 3. The width of the spheroidized

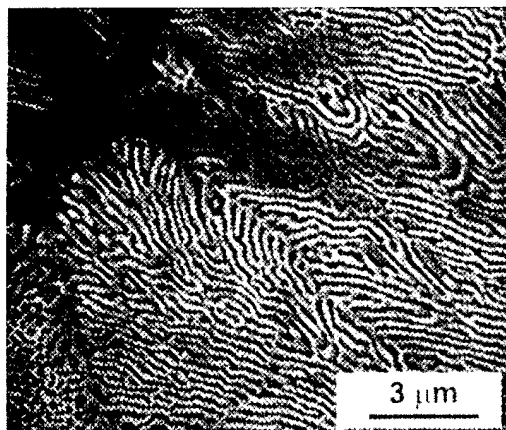


Fig. 2. SEM view of fine lamellar eutectic and Co solid solution precipitations in the cladded track center zone.

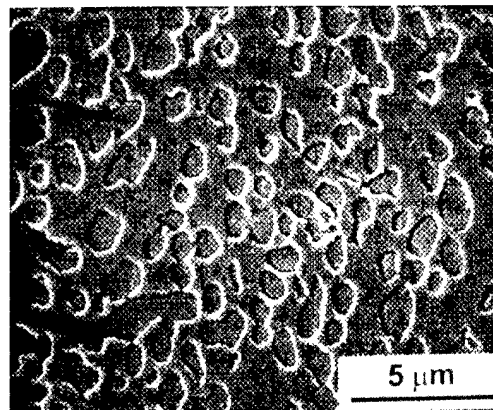


Fig. 3. Laves phase spheroidization in the inter-track heat-affected zone.

material zone in the coating on steel substrate was twice as much as in the case of Ni based substrate, ranging up to 120 μm .

The phase composition of T-400 laser coatings varied depending on the substrate material. In the case of steel substrate, using XRD, the Laves phase present was determined to be $\text{Co}_3\text{Mo}_2\text{Si}$. When the substrate contained Ni, CoMoSi Laves phase was found. In both cases the matrix was fcc Co based solid solution.

Using EDS the coating material dilution from the substrate during processing was estimated as 4% and over 12%, respectively, for Fe and Ni based substrates, with the difference resulting from pre-heating of IN 718 substrate.

The hardness of laser deposited T-400 coating was high, reaching 63 HRC. The coating showed uniform cross-sectional microhardness distribution, leveling at 800 HV2 with a drop by 5% in heat-affected zones. This has been attributed to a substantial microstructure change in those regions.

The quantitative results of erosion tests are shown in Fig. 4. As can be seen from erosion curves, plotted as sample relative mass decrement E against the erosion angle α , laser deposited T-400 alloy was eroded with the highest erosion intensity at the angle α of 90° , irrespective of substrate type. The E value at 30° was less than 7% smaller than that at 90° . For typical brittle materials (e.g. mullite) such a difference can reach up to 290%, as pointed out by Morrison et al. [11]. According to Bitter's erosion theory [12], such results suggest mixed ductile and brittle material erosion mechanism, with the predominance of ductile microcutting at low erosion angles and brittle material chipping at high α values.

A corundum particles stream impinging at the T-400 coating surface resulted in a severe deformation. Typical surface effects caused by a solid particles stream impingement at $\alpha = 90^\circ$ are shown in the SEM images of Fig. 5 and Fig. 6. Platelets formation (as arrowed in Fig. 5)

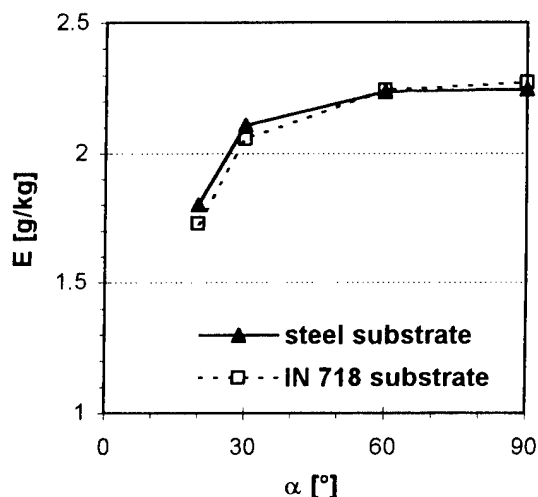


Fig. 4. Erosive wear of Tribaloy T-400 alloy laser coatings plotted as a relative mass decrement E against the erosion angle α .

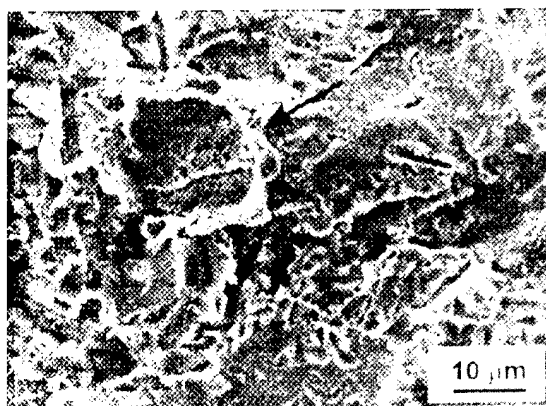


Fig. 5. SEM view of Tribaloy T-400 surface deformed by solid particles impingement showing platelet erosion mechanism.

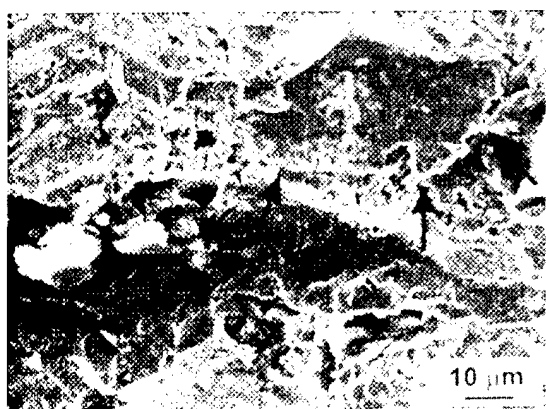


Fig. 6. SEM view of Tribaloy T-400 surface deformed by solid particles impingement showing brittle cracking erosion mechanism.

indicates the ductile mechanism of erosion proposed by Levy [13]. On the other hand, the extensive cracks observed in Fig. 6 (as arrowed) prove the material to be removed in a brittle way as well. Characteristic uplifts

of material formed upon particle impacts at the laser coating surface tended to crack and delaminate, being moved if not separated at first contact. Both observations are in agreement with the mass loss on impact angle dependence for the tested material presented in Fig. 4.

Typical craters together with deformation zones produced by single particle impacts are presented in Fig. 7 and Fig. 8. The material extruded using active slip systems formed stacks of plates to be forged and removed by subsequent particles impacts. The microstructure distortion in the crater vicinity indicated a



Fig. 7. Typical surface effects resulting from single particle impingement including the material extruding into stacks of plates as well as material cracking.

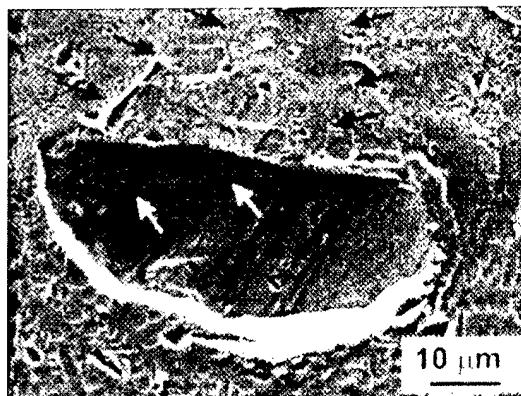


Fig. 8. SEM view of a typical crater formed after single particle impingement indicating immediate material chipping and delamination.

high degree of alloy plastic deformation. Considering the large radial crack linking adjacent craters (as arrowed in Fig. 7), relatively large portions of material could be lifted up with no adherence to the matrix. Another typical crater produced by single particle impact is shown in Fig. 8. On the crater walls and bottom characteristic shearing bands can be seen. Cracks in extruded material indicate the poor bonding to the original surface. Coarse deformation twins in coagulated Laves phase in the craters vicinity have also been observed. Microstructure refinement after laser cladding promoted crystallographic defects piling up at grain boundaries, that led to microcrack formation. Other factors promoting material cracking could be the supersaturation of solid solution in alloying elements as well as the residual stresses after laser treatment.

Cross-sectional SEM observations of the eroded alloy microstructure next to the surface revealed the presence of a narrow material layer, showing a high degree of plastic deformation (defined by a dashed line in Fig. 9). The deformed material lost the two-phase eutectic character specific to the matrix. Beyond the surface layer, the material maintained the original two-phase microstructure.

In order to further examine the microstructure changes in material subjected to intensive erosive wear, the TEM method has been applied. After erosion, regarding microstructural effects, three zones could be distinguished across the surface layer. Down to 4–5 μm below the surface the structure turned nearly amorphous, as confirmed by a ring diffraction pattern [Fig. 10(A)]. Based on ring diameter measurements, Co fcc solid solution as a matrix and fine precipitates of recrystallized Laves phase have been identified. The second zone situated roughly at 5 to 15 μm beneath the surface appears strongly dislocated, with fragments of highly deformed grains of Laves phase cut by slip bands and displaced [Fig. 10(B)]. Coarse, intersecting slip

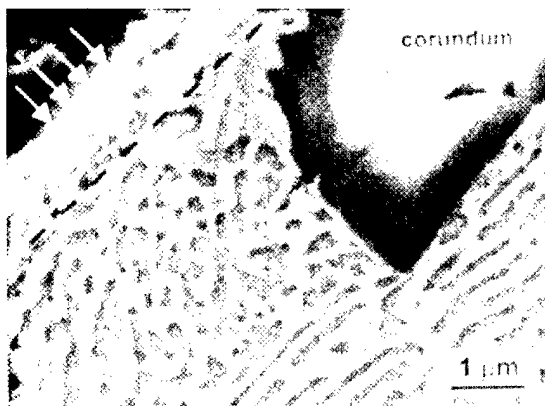


Fig. 9. Cross-sectional SEM view of material deformation next to the surface (arrowed) due to erosion (the deformation zone approximate range is determined by a dashed line).

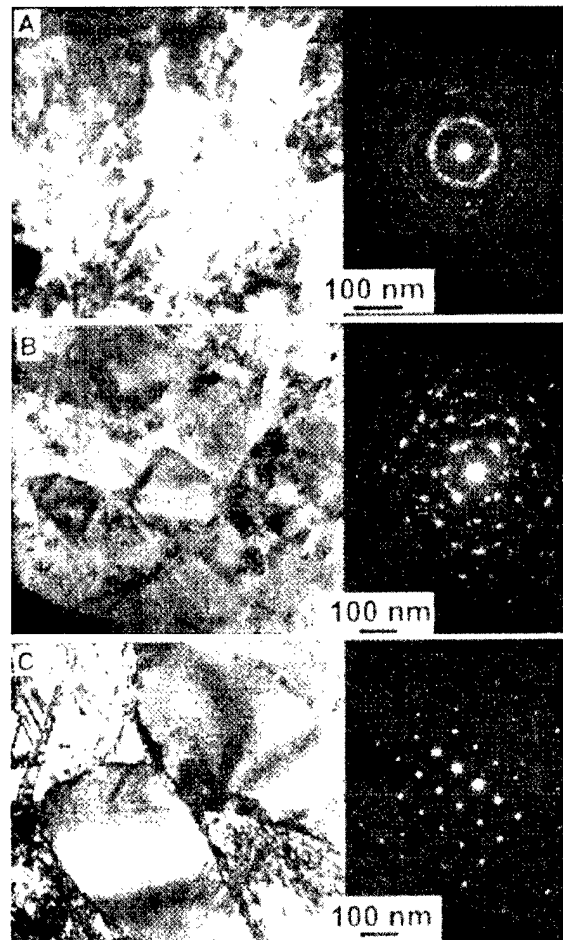


Fig. 10. TEM bright field view of the microstructure and related electron diffraction patterns from three zones formed in the surface layer of T-400 alloy during erosion: (A) 2 μm , (B) 10 μm , (C) 30 μm below the surface.

bands favourable for crack nucleation have also been spotted, as well as twinning in some Laves phase grains. The presence of both fcc and hcp type Co solid solution in this zone was stated upon the diffraction patterns solution, even if no stacking faults were observed in the area [Fig. 10(B)]. In the third zone, lying about 30 μm below the surface, stacking faults dominated in the matrix and micro-twins in Laves phase grains [Fig. 10(C)]. Some slip bands crossing the Laves phase grains could also be seen.

The low load (0.2 N) microhardness was tested next to the surface on the samples cross-section with the aim of estimating the alloy strain hardening due to erosion. It was found that the strain hardening of T-400 alloy in the laser track center zone was small, reaching about 14% compared with the original alloy. In the inter-track heat-affected zone a microhardness increase of about 30% was observed. In both cases the microhardness increase zone measured about 60 μm below the eroded surface.

4. Concluding remarks

Proper selection of laser cladding parameters allows us to obtain high quality and low dilution Tribaloy T-400 coatings on different substrates. Such a material is characterized by high hardness due to microstructure refinement, supersaturation of phases by alloying elements and presence of highly dispersed and brittle Laves phase. At the same time, however, the plastic properties of the alloy deteriorates, which may have a negative effect on the erosion behavior of T-400 alloy by promoting the material cracking and chipping that in consequence leads to extensive surface wear.

Acknowledgement

This project was supported by KBN under Grant No. 7 T08C 005 12.

References

- [1] R.D. Schmidt, D.P. Ferriss, *Wear* 32 (1975) 279.
- [2] C.T. Sims, *J. Metals* 12 (1969) 36.
- [3] S.C. Agarwal, H. Ocken, *Wear* 140 (1990) 223.
- [4] K.C. Anthony, *J. Metals* 35 (1983) 52.
- [5] S. Atamert, H.K.D.H. Bhadeshia, *Metall. Trans. A* 20 (1989) 1037.
- [6] A. Halstead, R.D. Rawlings, *Proc. Int. Conf. on Science of Hard Materials* (1986) 989.
- [7] A. Frenk, W. Kurz, *Mater. Sci. Eng. A* 173 (1993) 339.
- [8] G.J. Bruck, *Proc. Laser Beam Surface Treating and Coating*, Dearborn, MI (1988) 14.
- [9] A. Tiziani, L. Giordano, P. Matteazzi, B. Badan, *Mater. Sci. Eng.* 88 (1987) 171.
- [10] J. Przybylowicz, *Structure and wear properties of cobalt based coatings by laser cladding*, Ph.D. Thesis, AGH, 1999.
- [11] C.T. Morrison, J.L. Routbort, R.O. Scattergood, *Wear* 115 (1985) 19.
- [12] J. Bitter, *Wear* 6 (1963) 5.
- [13] A.V. Levy, *Solid Particle Erosion*, ASM, Metals Park, OH, 1995, p. 16.

Surface activation of polyimide with dielectric barrier discharge for electroless metal deposition

Hilmar Esrom ^{a,*}, Robert Seeböck ^a, Marlène Charbonnier ^b, Maurice Romand ^b

^a *Fachhochschule Mannheim, University of Applied Sciences, Windeckstraße 110, 68163 Mannheim, Germany*

^b *Laboratoire de Sciences et Ingénierie des Surfaces, Université Claude Bernard-Lyon 1, 69622 Villeurbanne Cedex, France*

Abstract

Electroless plating of non-conducting materials needs, prior to the metal deposition itself, to make the sample surface catalytically active. The route involving the chemical reduction of a thin solid metal–organic coating has, for this purpose, a significant potential in reducing the number of steps which are required today in conventional wet chemical metallization processes. In this work, a novel activation process using a dielectric barrier discharge (DBD) is described for the first time. This process is based on the plasma-induced chemical reduction at atmospheric pressure in air of palladium acetate (PdAc) layers resulting in the formation of palladium (Pd) on non-active surfaces. Fast surface activation of polymers like polyimide (PI) was found to occur in only a few seconds using a simple DBD device instead of expensive excimer UV lamps or complicated laser systems. The DBD-induced Pd layers on PI exhibit high activity with regard to initiation of the electroless copper plating. Indeed, copper deposition starts immediately after dipping the activated PI samples in the electroless solution without any inhibition time. Homogeneous copper coatings on PI were achieved under optimal plasma treatment conditions. The results are compared to those achieved with excimer UV lamps and excimer UV lasers. © 2000 Elsevier Science S.A. All rights reserved.

Keywords: Dielectric barrier discharge (DBD); Electroless copper plating; Excimer UV lamps; Palladium; Palladium acetate; Photo-induced reduction; Plasma-induced reduction; Polyimide (PI)

1. Introduction

Electroless metal deposition is one of the most frequently used industrial processes for metallizing non-conductors like polymers [1,2]. The need for new techniques which allow a reduction in environmental problems led to the use of new direct deposition methods like laser chemical vapour deposition (LCVD) [3] and plasma enhanced chemical vapour deposition (PECVD) [3,4], and also to the simplification of the electroless methods by using plasma [5], laser [6–8] and excimer UV laser [9–16] or VUV/UV excimer lamps [17–26] induced surface pre-treatment and activation. In order to reduce the number of wet chemical surface conditioning steps, the surface activation of polymers and ceramics was performed by chemical reduction of thin solid metal–organic films using the intense radiation of excimer UV lasers and lamps, besides several other techniques involving gaseous and liquid chemical precursors.

Especially, pre-nucleation of non-catalytic surfaces with Pd from Pd–organic films has been carried out by using excimer lasers at $\lambda=193$ nm (ArF⁺) and $\lambda=248$ nm (KrF⁺) and novel incoherent excimer sources. The UV/VUV generation of excimer lamps is based on the excimer formation using a dielectric barrier discharge in an atmosphere of rare gas, halogen or rare gas/halogen mixture. A large number of different excimer spectra can then be obtained. In our experiments we used preferentially the incoherent excimer radiation at $\lambda=172$ nm (Xe₂⁺) and $\lambda=222$ nm (KrCl⁺). For some years, excimer lamps of this type have been commercially available. Lately, a new photo-processor including a KrCl⁺ excimer lamp (Excimet[®] from J.I.P.ELEC) [27] has been developed to perform a photo-selective metallization. This process is an additional UV excimer-assisted process allowing the photo-selective activation of substrates for electroless plating.

The objective of our present work consists of using the dielectric barrier discharge directly for pre-treating and activating polymeric materials for electroless plating in order to achieve a higher throughput compared to that achieved with excimer lamp processing.

* Corresponding author. Fax: +49-621-292-6237.

E-mail address: h.esrom@fh-mannheim.de (H. Esrom)

2. Experimental

Commercially available square shaped ($25 \times 25 \text{ mm}^2$) PI foils (Du Pont; Kapton[®]), 50 μm in thickness, were used. The PdAc films to be investigated were spin-coated on the substrates from a solution of palladium (II) acetate at a concentration of 0.15 mol dm^{-3} in chloroform. During the spin-on process the chloroform evaporates immediately and uniform solid films with thicknesses between 0.01 and 0.3 μm are obtained almost instantaneously. The pre-nucleation of the PI surface with Pd is performed by decomposition of the PdAc film by UV processing with the excimer lasers and lamps or via direct plasma treatment in a dielectric barrier discharge in air. For the laser experiments a KrF⁺ excimer laser (Lambda Physik, Model EMG 103) was used. The excimer laser pulse energy was measured with a joulemeter (Gen Tec PRJ-D).

The VUV lamp processing was performed with a dielectric barrier discharge operating in xenon [17,18] and emitting an incoherent radiation around $\lambda = 172 \text{ nm}$. For these experiments a cylindrical VUV source was mounted in a small reactor [17] which could be evacuated and flooded with nitrogen or argon. Air cannot be tolerated for such experiments because oxygen absorbs the VUV radiation and is dissociated. This would lead to ozone formation, which also attenuates this radiation. In such experiments, the substrate was mounted at a distance of 1 cm from the VUV source and was irradiated with an estimated flux of about $5 \times 10^{16} \text{ photons cm}^{-2} \text{ s}^{-1}$ (about 60 mW cm^{-2}). Under these conditions, the decomposition of PdAc was achieved in a few minutes and resulted in the formation of a continuous palladium film. The patterning of the metal layers was obtained using contact metal masks.

The DBD plasma experiments for surface modification of polymers were performed in air at atmospheric pressure with the electrode arrangement shown schematically in Fig. 1. The lower electrode of the arrangement was a circular copper disk 25 mm in diameter. The PI samples themselves served as the dielectric barrier for the discharge. The samples under treatment were put

on top of the lower grounded electrode. The upper electrode was a 6 mm rod in diameter with a rounded lower edge, leading to a 3 mm in diameter circular plane electrode area. For the DBD treatment of larger PI surfaces a larger upper planar electrode with a diameter of 20 mm was used. The axial position of the lower electrode could be varied in order to adjust the discharge gap length. The two electrodes were connected to a low-frequency generator (ENI HRG-2) without additional matching network. The minimum frequency of the generator was 125 kHz. The discharge power was read at the generator output. Only a very limited range of discharge gap lengths between 0.1 and 0.25 mm was accessible for discharge ignition with the power and frequencies available from the generator. The load power was typically between zero and 80 W. At 0.5 mm no discharge could be ignited. The frequencies used were 125 kHz and 135 kHz, since at higher frequencies discharge ignition was harder to accomplish if not impossible.

The topography of the irradiated polyimide surfaces was investigated using scanning electron microscopy (SEM) (JEOL JXA-733). Thicknesses of PdAc, Pd and Cu films were estimated using electron probe microanalyses (EPMA). For calibration different film thicknesses were deposited on glass substrates and determined by interference microscopy (Carl Zeiss instrument).

X-ray photoelectron spectroscopy (XPS) analyses were performed with a Riber SIA 200 spectrometer equipped with a non-monochromatic Al X-ray source and a Mac 2 analyser. Survey scans were recorded at overall resolution of 2.3 eV and core-level spectra at 0.9 eV with a take-off angle of 65° with respect to the sample surface. All spectra were referenced to the C 1s signal at 285 eV representative of the C–C and C–H bonds. Additional analyses by X-ray fluorescence spectrometry (XRFS) were carried out using a Philips PW 1220 instrument.

3. Results and discussion

3.1. Experiments with the dielectric barrier discharge

The steps of the simple deposition process are shown schematically in Fig. 2. A DBD pre-treatment for about 10 s cleans the PI surfaces and generates a micro-roughness. As seen in a previous work [28], surface cleaning is accompanied by a moderate surface oxidation. The latter is observed through slight variations of the atomic surface concentrations, namely a decrease of C and an increase of O when the treatment time increases from 2 to 60 s. The most striking feature concerns a new component located at about 407 eV, which appears on the N 1s spectrum of the DBD-treated samples. This component characterizes NO_2 – NO_3 -type groups whose

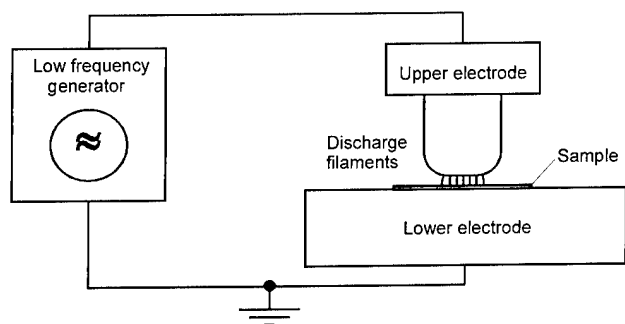


Fig. 1. Schematic view of the experimental set-up used for surface modification of PI with the dielectric barrier discharge.

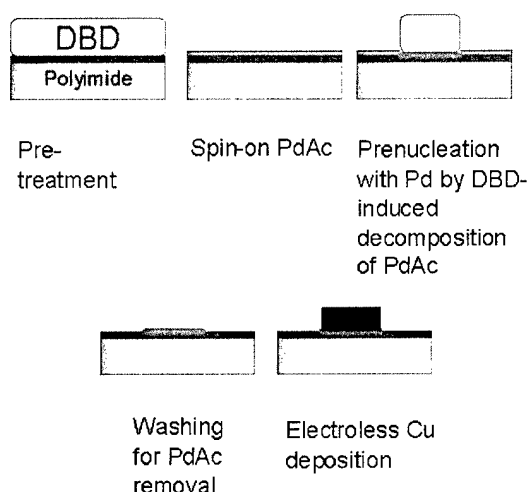


Fig. 2. Schematic diagram of the deposition process.

formation results from the strong oxidizing power of ozone molecules (O_3) and atomic oxygen (O) created in the silent discharge operating in air.

The PdAc films were then spin-coated onto the so-modified PI surfaces and their complete decomposition was achieved through a DBD treatment for a few seconds, resulting in a well-adherent Pd layer on the PI surface. The non-decomposed parts of the PdAc film were removed by rinsing in chloroform and the pre-nucleated PI surfaces were electrolessly coated using a commercially available electroless copper bath. All process steps were carried out in air at room temperature. Concerning this sequence, the palladium amount uptaken by spin-coating as a function of the number of PdAc droplets deposited on the PI substrate was determined. Such measurements were performed using XRFs. In this particular case, for which the PdAc thickness is very low, the intensity of the X-ray signal characteristic of Pd is directly proportional to the deposit thickness. Fig. 3 represents the intensity variation of the Pd $L\beta_1$ signal due to PdAc films deposited on such as-received samples (curve a) and samples previously DBD-treated for 4 s (curve b), respectively. In both

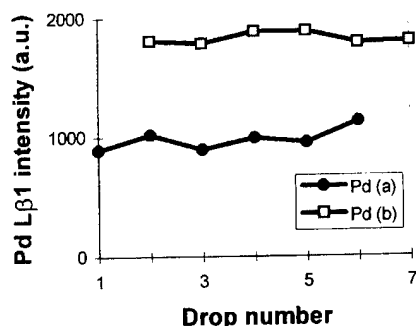


Fig. 3. XRFs experiments: Pd $L\beta_1$ intensity variation as a function of the droplet number of spin-deposited PdAc: (a) on as-received substrates; (b) on DBD-cleaned PI substrates.

cases, the Pd $L\beta_1$ signal intensity can be considered as constant whatever the number of droplets deposited. This result means that, for the high spin-frequency of about 10^3 rpm used, the centrifugation effect leaves on the substrate surface only a low material amount similar in thickness. The Pd signal is about twice as high in the case where PdAc is deposited on DBD-treated substrates as in the case where it is deposited as a non-homogeneous film on non-treated substrates. This emphasizes the need for surface pre-treatment, which allows us to make the surface more 'reactive' towards the PdAc deposit and consequently to form thin films much more uniform in thickness. In addition, XPS investigations of the PdAc films were undertaken. However, no quantitative analysis is provided here given that a spectral interference exists between the O 1s and Pd 3p $3/2$ peaks which prevents us from evaluating the oxygen atomic concentration. The use of the O 2s peak for this purpose is obviously possible but its very low intensity would lead to very large uncertainties. On the other hand, interesting information on the chemical state of Pd can be drawn from the Pd 3d $3/2$, $5/2$ spectra. Indeed, the DBD treatment of the PdAc layers causes a partial chemical reduction of the deposited Pd^{2+} species. This reduction gives rise to a chemical shift of the spin doublet towards the low binding energy side (Fig. 4) at an intermediate value between those of the Pd^{2+} and $Pd(0)$ states [29]. However, it appears that the complete chemical reduction of the palladium species present on the PI substrate after the DBD treatment occurs in the plating bath thanks to the action of the reducing agent (formaldehyde in the present case). This is confirmed by spectrum c in Fig. 4 obtained after a short immersion time (10 s) in the plating bath of the DBD-treated sample. Indeed, the

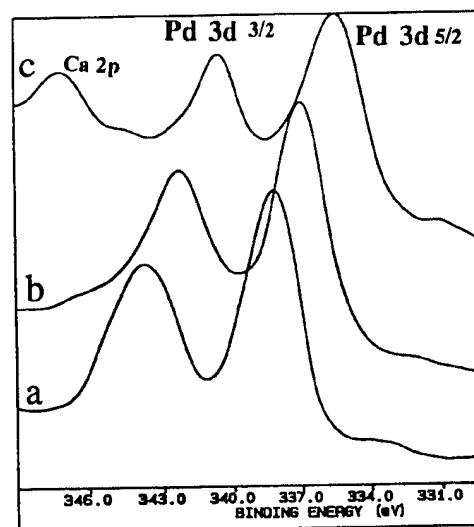


Fig. 4. Pd 3d XP spectra of: (a) a spin-deposited PdAc film; (b) the same as (a) after a DBD treatment; (c) the same as (b) after immersion for 10 s in the plating bath.

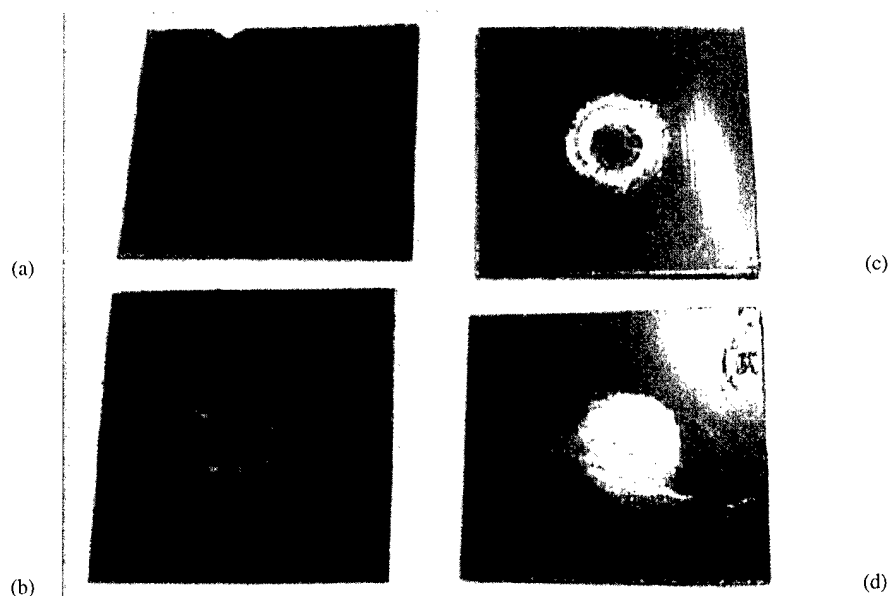


Fig. 5. Copper deposits on PI (Kapton[®]) after electroless plating (2 min) of pre-treated PI samples (pre-treatment time 10 s, DBD power 60 W) and DBD-induced decomposition of PdAc (treatment time 5 s) at different powers: (a) 40 W, (b) 50 W, (c) 60 W, and (d) 70 W. Discharge gap 175 μm .

binding energy of the spin doublet is again shifted towards the low binding energy side and reaches the energy value of the Pd(0) species (metallic Pd).

In Fig. 5 are shown copper deposits on PI (Kapton[®]) produced with the described method using different powers of the DBD. First of all, a DBD power of about 40 W is necessary to initiate the decomposition of the PdAc film [Fig. 5(a)]. At higher DBD powers, ring-shaped copper layers are obtained due to the higher electrical field strengths at the edges of the upper electrode of the DBD device [Fig. 5(b) and (c)]. Finally, at about 70 W circular copper coatings are achieved with high reproducibility [Fig. 5(d)]. Contrary to the discontinuous copper layer shown in the SEM image of Fig. 6, which is a magnified view of Fig. 5(a), the copper

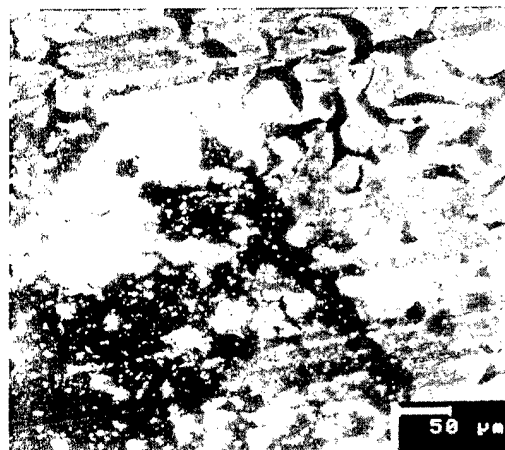


Fig. 6. SEM image of the sample of Fig. 5(a); scale 50 μm .

pads produced at optimal conditions (70 W) consist of a continuous layer (Fig. 7).

Fig. 8 shows the thickness variation determined by XRF of the electroless copper film deposited on PI as a function of the dipping time. As can be seen, the deposition starts immediately (no inhibition time) and the rate of formation of the copper layers is higher at the beginning of the deposition process. The typical deposition rate in the copper bath used is about 0.1 $\mu\text{m}/\text{min}$.

3.2. Experiments with excimer lasers and excimer lamps

In order to study the UV-induced decomposition of PdAc with the excimer laser and lamp UV radiation, the PI foils were spin-coated as already described. The average thickness measured by EMPA of the PdAc films was determined to be about 90 nm. In the case of the incoherent excimer lamp irradiation, the formation of the palladium film proceeds almost linearly with the exposure time. The final thickness of about 6 nm is reached in about 180 s, after which time no further changes are observed. Excimer lamp-induced Pd layers were smooth and continuous and were electrolessly coated with copper. All copper coatings have a good adhesion and pass the Scotch[®] tape test.

Different results were obtained with pulsed excimer laser irradiation. To perform these experiments we used a cylindrical quartz lens to obtain a focal line. As found in previous works, decomposition of PdAc with pulsed excimer laser radiation (typical pulse width 20 ns) is only possible above a certain threshold fluence value of

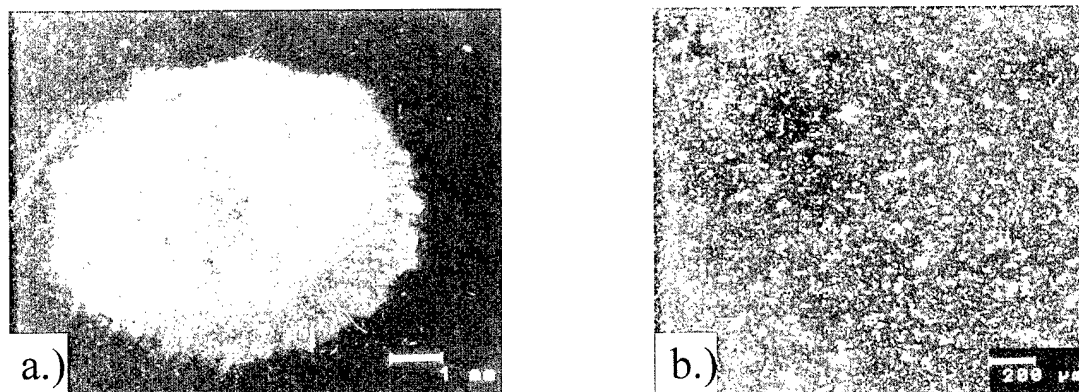


Fig. 7. SEM pictures of a copper film deposited under optimum conditions [same parameters as in Fig. 5(d)]: (a) overview, scale 1 mm; (b) centre, scale 200 μm .

about 15 mJ/cm^2 at $\lambda = 248 \text{ nm}$. Palladium formation on PI from the thin solid PdAc films shows a very complex behaviour compared to that obtained using the incoherent excimer lamp radiation. First of all, for fluences below 30 mJ/cm^2 no palladium can be detected. Indeed, as the laser treatment is inefficient to reduce Pd^{2+} to Pd, the whole PdAc film is removed by rinsing in the chloroform solution. PI, which is a strong absorbent material, presents a relatively low ablation threshold fluence of about 30 mJ/cm^2 . Adherent palladium layers are obtained for fluences above 30 mJ/cm^2 . Evidently, higher pulse energies have a beneficial influence on the Pd chemical transformation and on its adhesion to the substrate. This is a consequence of the strong interaction of the UV radiation with the polyimide surface. Furthermore, the number of pulses has a decisive influence on the process. For a fluence of about 75 mJ/cm^2 , the first pulse allows us to obtain a 0.8 nm thick discontinuous palladium layer while the following pulse causes its complete removal due to ablation. The strong influence of the substrate material on the film deposition is typical for a pyrolytic decomposition mechanism of the thin solid layer in which the extent of the transient temperature rise is determined by the thermal properties of the coated substrate [30]. Therefore, in

our experiments two processes, namely Pd chemical reduction and ablation, are in competition during the excimer laser irradiation. During the first laser pulse (for a fluence of about 75 mJ/cm^2) nearly the whole UV radiation is absorbed by the initial PdAc film, leading to the removal of a certain amount of PdAc and therefore to the formation of only a very thin Pd layer on the PI surface. The energy of the second pulse leads to a fast heating of the PI surface, resulting in a complete ablation of the initial PdAc layer so that copper plating is no longer achievable. Additional experiments have shown that at high fluences (roughly above 0.3 J/cm^2) the first pulse already causes the complete removal of the PdAc layer.

4. Conclusions

A simple electroless plating method was investigated using excimer lasers, excimer lamps and DBDs with a view to pre-activating PI surfaces. We found that the characteristics of the UV source have a decisive influence on the nature of the decomposition process of thin solid PdAc films. Excimer laser-induced formation of Pd films is a pyrolytic process which depends strongly on the thermal properties of the substrate material. The thickness of the discontinuous Pd films depends sensitively on the fluence and the number of pulses. Therefore, excimer lasers do not seem to be well-suited to make use of the proposed metallization method.

With the incoherent xenon VUV lamp, decomposition of PdAc is achieved resulting in smooth and continuous Pd films on the PI surfaces which can be plated without any problems. However, the low efficiency of the excimer lamps presently in use, in addition to the necessarily long UV processing time, stimulates the search for new and more efficient activation techniques.

Pre-treatment of the PI surfaces and activation of the PdAc films for subsequent electroless copper deposition

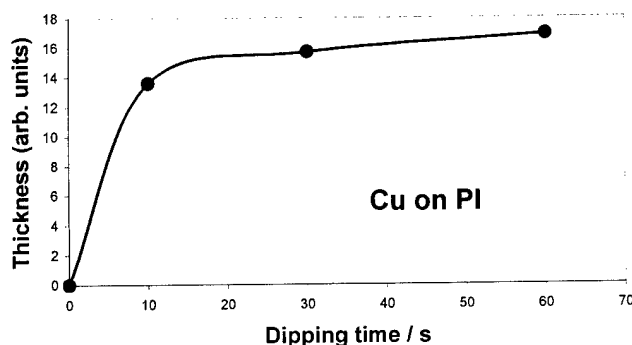


Fig. 8. Thickness changes of the electroless copper films deposited on PI as a function of the dipping time.

using DBDs at atmospheric pressure have been shown for the first time. Surprisingly, we found that the surface activation through the DBD-induced decomposition of the PdAc precursor layer is possible only in a few seconds compared to long-term exposure required in the case of excimer lamps. The use of DBDs for surface treatment and activation by Pd of polymeric substrates for electroless metal plating instead of expensive excimer lamp and laser systems provides an interesting alternative from an economical point of view.

Acknowledgements

The authors gratefully acknowledge financial support by the Karl Völker-Stiftung and the assistance of Ingo Deppner in performing experiments and SEM investigations.

References

- [1] G.O. Mallory, J.B. Hajdu (Eds.), *Electroless Plating: Fundamentals and Applications*, American Electroplaters and Surface Finishers Society, Orlando, FL, 1990.
- [2] A.F. Karam, G. Stremsdoerfer, in: K.L. Mittal (Ed.), *Metallized Plastics 5 and 6: Fundamental and Applied Aspects*, VSP, Utrecht, 1998, pp. 137–144.
- [3] I.W. Boyd, J. Perriere, M. Stuke (Eds.), *Surface Processing: Laser, Lamp, Plasma Vol. 82*, Elsevier, Amsterdam, 1999.
- [4] A. Ricard, R. Kassing, H.K. Pulker, K.-T. Rie (Eds.), *Plasma Surface Engineering, Part I and II*, Elsevier, Amsterdam, 1997.
- [5] M. Romand, M. Charbonnier, M. Alami, J. Baborowski, in: K.L. Mittal (Ed.), *Metallized Plastics 5 and 6: Fundamental and Applied Aspects*, VSP, Utrecht, 1998, pp. 3–23.
- [6] M.E. Gross, *Chemtronics* 4 (1989) 197.
- [7] Y.S. Liu, H.S. Cole, *Chemtronics* 4 (1989) 209.
- [8] G.A. Shafeyev, A.V. Simakin, A.A. Lyalin, E.D. Obratsova, V.D. Frolov, *Appl. Surf. Sci.* 138/139 (1999) 461.
- [9] H. Esrom, G. Wahl, *Chemtronics* 4 (1989) 216.
- [10] A. Bauer, J. Ganz, K. Hesse, E. Köhler, *Appl. Surf. Sci.* 46 (1990) 113.
- [11] H. Esrom, *Mater. Res. Soc. Symp. Proc.* 204 (1991) 457.
- [12] A.J. Pedraza, J.-Y. Zhang, H. Esrom, *Mater. Res. Soc. Symp. Proc.* 285 (1993) 209.
- [13] H. Niino, A. Yabe, *Appl. Surf. Sci.* 69 (1993) 1.
- [14] J.-Y. Zhang, I.W. Boyd, H. Esrom, *Appl. Surf. Sci.* 109/110 (1997) 253.
- [15] J. Bekesi, K. Kordas, C. Beleznaï, K. Bali, R. Vajtai, L. Nanai, *Appl. Surf. Sci.* 138/139 (1999) 613.
- [16] K. Kolev, A. Jadin, S. Benbakoura, L.D. Laude, *Appl. Surf. Sci.* 138/139 (1999) 434.
- [17] H. Esrom, J. Demny, U. Kogelschatz, *Chemtronics* 4 (1989) 202.
- [18] H. Esrom, U. Kogelschatz, *Thin Solid Films* 218 (1992) 231.
- [19] T. Okamoto, K. Hatao, T. Shimizu, M. Aoike, M. Murahara, *Mater. Res. Soc. Symp. Proc.* 397 (1997) 555.
- [20] J.-Y. Zhang, I.W. Boyd, *J. Mater. Sci. Lett.* 16 (1997) 996.
- [21] J.-Y. Zhang, I.W. Boyd, *Thin Solid Films* 318 (1998) 234.
- [22] D.J. Macauley, K.F. Mongey, P.V. Kelly, Mc. Crean, *Surf. Coat. Technol.* 100/101 (1998) 238.
- [23] J.-Y. Zhang, I.W. Boyd, S. Draper, *Surf. Coat. Technol.* 100/101 (1998) 469.
- [24] J.-Y. Zhang, I.W. Boyd, H. Esrom, *J. Mater. Sci. Lett.* 17 (1998) 2037.
- [25] D.J. Macauley, P.V. Kelly, K.F. Mongey, Mc. Crean, *Appl. Surf. Sci.* 138/139 (1999) 622.
- [26] M. Romand, M. Charbonnier, in: D.R. Speth (Ed.), *Proc. 22nd Annual Meeting of the Adhesion Society, The Adhesion Society, Blacksburg, VA, 1999*, pp. 94–97.
- [27] J.I.P. ELEC, Meylan, France, *Brochure: Excimet®*, 1999.
- [28] H. Esrom, R. Seeböck, M. Charbonnier, M. Romand, in: K.L. Mittal (Ed.), *Polymer Surface Modification: Relevance to Adhesion*, VSP, Utrecht, 2000.
- [29] C.D. Wagner, W.M. Riggs, L.E. Davis, J.F. Moulder, G.E. Muilenberg, *Handbook of X-ray Photoelectron Spectroscopy*, Perkin-Elmer Corporation, Eden Prairie, MN, 1979, pp. 110–111.
- [30] H. Esrom, U. Kogelschatz, *Appl. Surf. Sci.* 46 (1990) 158.

Diamond-like films formed by pulsed laser irradiation of phenylcarbyne polymer

S.M. Huang ^a, Y.F. Lu ^{a,*}, Z. Sun ^b, X.F. Luo ^c

^a *Laser Microprocessing Laboratory, Department of Electrical Engineering and Data Storage Institute, National University of Singapore, 10 Kent Ridge Crescent, Singapore 119260, Singapore*

^b *School of Electrical and Electronic Engineering, Nanyang Technological University, Nanyang Singapore 639798, Singapore*

^c *Department of Chemistry, National University of Singapore, 10 Kent Ridge Crescent, Singapore 119260, Singapore*

Abstract

Growth of diamond-like films at room temperature by Nd:YAG laser ($\lambda=532$ nm) irradiation of a polymer precursor is presented. The morphologies of the resulting samples were examined by scanning electron microscopy (SEM). The structures of films were investigated by Raman spectra. The mechanism of diamond-like phase conversion from the polymer is discussed. Our results indicate that the polymer is converted into sp^3 diamond phases in amorphous carbon matrix phases by pulsed laser irradiation in an argon atmosphere. Raman spectroscopy analysis provides evidence for the conversion from this polymer to diamond-like phases. SEM micrographs reveal the crystalline structures. It is proposed that the conversion of diamond-like phases may be related to the unique structure of the polymer and the thermal energy provided by the laser beam. © 2000 Elsevier Science S.A. All rights reserved.

Keywords: Diamond; Polymer precursor; Pulsed laser; Pyrolysis

1. Introduction

Diamond thin films offer a large variety of possible applications due to their unique material properties such as hardness, chemical inertness, excellent tribological properties, optical transparency, high thermal conductivity and high electrical resistivity. Diamond can be doped and used as a wide band-gap (5.4 eV) semiconductor. Low temperature growth of diamond films is important for extending these applications. A variety of techniques have been successfully applied in deposition of diamond films. Among them, pulsed laser deposition (PLD) using suitable target materials in a vacuum is an emerging technology for forming diamond films.

Of the various possible target materials, graphite has received the most attention. Using graphite targets in high vacuum, PLD can be applied to produce nanophase and microphase diamond films [1,2] at temperatures higher than 600°C. However, during the deposition of diamond and diamond-like (DLC) films [3] it was found that the use of such targets resulted in splashed graphite

particles in films. The deposition rates were initially slow and decreased rapidly if the target was not continuously moved.

As graphite proves to be a disadvantageous material for deposition of crystalline diamond by PLD, more acceptable targets have been investigated. Recently, PLD was adopted in the synthesis of diamond films using liquid organic [4,5] and solid polymeric targets [6,7]. Using suitable organic and polymeric targets, the deposition rates can be effectively increased and splashed material from graphite targets can be avoided.

One possible polymeric target is phenylcarbyne. This is a carbon based random network polymer [8]. This polymer could be converted to diamond-like carbon phases at atmospheric pressure after thermal decomposition [8]. By plasma treatment of the polymer precursor in a hydrogen or hydrocarbon atmosphere, diamond crystals were formed at low temperature with high growth rates [9]. The polymer is readily soluble in organic solvents, which can be applied to various substrates by spinning, dipping or draining. In addition, the polymer precursor undergoes a photo-oxidation reaction so that it may be photo-patternable [8]. By laser irradiation of the polymer, very small size features

* Corresponding author. Tel.: +65-874-2118; fax: +65-779-1103.
E-mail address: eleyflu@nus.edu.sg (Y.F. Lu)

suitable for direct writing can be formed, which is very useful in microelectronic or micromechanical processes. Although this polymer has these possible advantages, no report on treatment by laser-based methods is available. In this article, we report on the synthesis of diamond-like films using phenylcarbyne polymer as a precursor by a pulsed Nd:YAG laser ($\lambda = 532$ nm) irradiation at low temperature with a high growth rate.

2. Experimental

The polyphenylcarbyne polymer was inexpensively synthesized by reductive condensation of 1,1,1-trichlorotoluene monomer with an ultrasonically generated NaK alloy emulsion in tetrahydrofuran (THF) under an inert atmosphere [8]. The polymer solution was prepared by dissolving polymer powder in THF, and the solution was applied on single crystal silicon (100) substrates by spin-coating. After evaporation of the THF, polymer films were formed on the substrates.

A schematic diagram of the experimental configuration is shown in Fig. 1. The laser beam was focused with a quartz lens and guided through a quartz window to irradiate the polymer surface. The three valves allowed evacuation of the cell, introduction of argon to various pressures, and measurement of the vacuum pressures. The cell was evacuated to a pressure of 10^{-2} Torr, and argon gas was used to further suppress the photo-oxidation reaction [8] and to reduce evaporation of the polymer. The pressure of the cell was maintained at about 250 Torr during the experiment. An Nd:YAG laser (B.M. industries 5022 D. Ns. 10) operating in its second harmonic mode ($\lambda = 532$ nm, $\tau = 7$ ns) was used for growing diamond with a fluence of 950 mJ/cm^2 at a repetition of 1 Hz, and irradiating the polymer surface with one or two pulses.

The films were investigated using SEM (Hitachi S-4100) and micro-Raman spectroscopy. The micro-Raman measurements were made with a Renishaw

Ramanscope, which offers a resolution of 1 cm^{-1} , and uses Ar^+ laser ($\lambda = 514.5$ nm, laser power on the sample was less than 2 mW). Thermal analysis was done on the polymer. The glass transition temperature (T_g) of the polymer was measured with a thermal analysis TA Instruments 2920 differential scanning calorimeter.

3. Results and discussion

The typical SEM morphologies of a film/crystal formed on the surface of silicon substrate after laser irradiation are shown in Fig. 2, which is considerably different from the SEM image of the precursor polymer film. The precursor polymer film is smooth and featureless, mainly consisting of an amorphous phase. In Fig. 2(a), the film consists of different crystallites with sizes from several tens of nanometers to several microns. Fig. 2(b) displays crystallites of microns in size. In most cases, the converted carbon film consists of nanocrystals

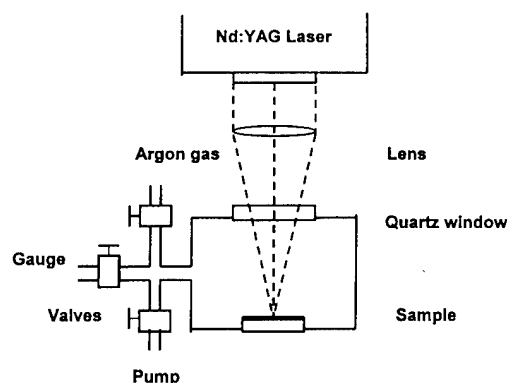
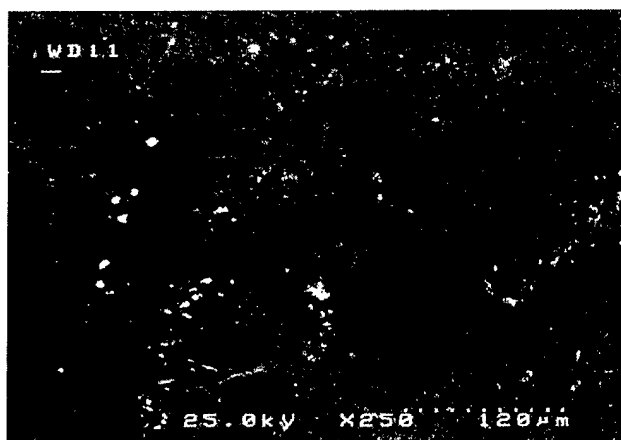
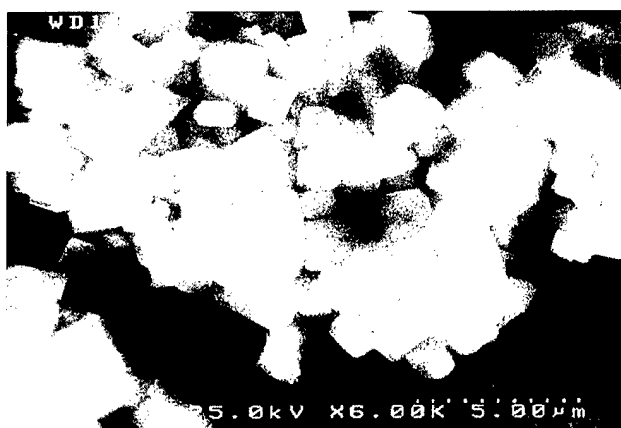


Fig. 1. A schematic diagram showing the experimental setup.



(a)



(b)

Fig. 2. SEM images of the film and crystals formed on Si substrate by laser irradiation with a fluence of 950 mJ/cm^2 : (a) a film, (b) crystals with different sizes.

and amorphous matrix, only a few micron crystals can be observed.

A micro-Raman spectrum of a crystal region in the film is shown in Fig. 3, which is significantly different from that of the original polymer film. There is a strong luminescence without detectable features in Raman spectrum of the original polymer film. The peak at 1333 cm^{-1} is a characteristic for sp^3 bonding in diamond film [10], although it is broadened by the presence of contaminating sp^2 amorphous carbon. Further, the broadening can also be due to small grain size [11] and defects in the diamond structure. The broad peak at 1582 cm^{-1} (G band) shows that some sp^2 amorphous carbon exists in the carbon. For nanocrystal graphite (glassy carbon), besides the G band at around 1580 cm^{-1} , another peak at about 1355 cm^{-1} which is assigned to the D band also appears in the Raman spectrum. Therefore we assume that the broad peak at 1333 cm^{-1} in our Raman spectrum may be contributed to the diamond phase and sp^2 cluster carbon (D band). Associated with the SEM observation, we concluded that the film converted from the polymer consisted of sp^3 diamond phases with some sp^2 amorphous carbon.

Two mechanisms, photochemical and thermal, have been considered for the UV laser ablation of polymers. On absorbing laser light, polymer molecules are excited into high energy electronic states which may decay through direct bond dissociation [12] or rapid conversion of photon energy into vibrational energy to produce heat [13]. In general, a distinction between these two mechanisms depends on the identity of polymers and experimental conditions such as laser fluence, wavelength and pulse duration. For the thermal mechanism, the subsequent decomposition is a pyrolysis of the polymer that is not quite different from the processes observed with laser irradiation at visible or infrared

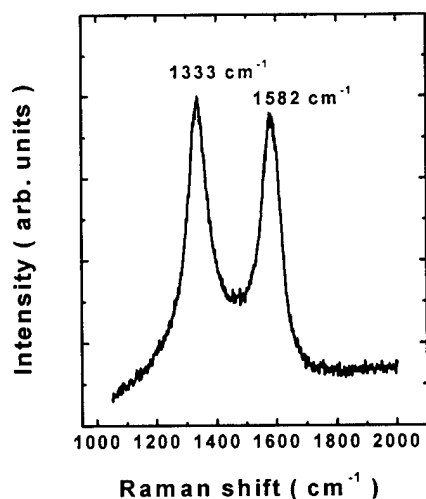


Fig. 3. Raman spectrum of the film formed on Si substrate by laser irradiation with a fluence of 950 mJ/cm^2 .

wavelengths [14,15]. In our experiment, the polymer $[\text{C}_6\text{H}_5\text{C}]_n$ is a hydrocarbon network and is mainly composed of tetrahedral hybridized carbon atoms which bear one phenyl group and are linked through three single C—C bonds into a random network of fused rings [8]. The bond energies in the ground electronic states in the polymer could be estimated in a range from 4.0 to 7.4 eV. This range assumes that tabulated C—H, C=C, C— C_6H_5 bond energies [16] are similar to those formed in the polymer, and the single C—C bonds in the polymer are close to the C—C bond in diamond. The photon energy for 532 nm laser light is 2.3 eV. Consequently, for this laser, it appears unlikely that bond breaking occurs as a direct result of absorption of a single photon with a large cross-section. Thus, we think that the thermal process plays a more major role in the formation of diamond-like phases.

When a pulsed laser irradiates the sample surface, the temperature distribution in the sample can be described by the one-dimensional heat equation. The temperature at any point inside the sample $T(x,t)$ is a function of the distance from the sample surface x and time t , and is governed by the one-dimensional heat equation:

$$\rho c \frac{\partial T(x,t)}{\partial t} = k \frac{\partial^2 T(x,t)}{\partial x^2} + (1-R)\alpha I(t) \exp(-\alpha x), \quad (1)$$

where ρ , c , K , R , α and $I(t)$ represent density, specific heat, thermal conductivity, reflectivity, absorption coefficient of the sample and laser intensity on the sample surface respectively. Since the dependence of ρ , c and K on temperature is not known for the phenylcarbyne film, its temperature distribution cannot be obtained. However, estimation for the temperature change ΔT in the irradiated polymer film can be made. For this polymer film, its reflectivity, transmissivity and absorption coefficient for the laser at 532 nm wavelength were 0.06, 0.42, $2.6 \times 10^3\text{ cm}^{-1}$, respectively, and its thickness was $2.6\text{ }\mu\text{m}$ measured in the experiment. The mass m of the polymer film within a spot size was $2.0 \times 10^{-4}\text{ g}$. The laser spot size was about 0.1 cm^2 . When the incident laser fluence was 950 mJ/cm^2 , the energy absorbed by the spotted polymer film was 447 mJ/cm^2 . From thermal analysis for the polymer, the heat capacity c of the polymer is $0.2305\text{ J/g}^\circ\text{C}$ in the glass range. If the heat capacity c of the polymer film is assumed to be $0.2305\text{ J/g}^\circ\text{C}$, the temperature in the spotted polymer film will rise by about 880°C , which is much higher than required in conventional pyrolysis [17]. Therefore, we believe that visible pulsed laser absorbed by the phenylcarbyne polymer in our system provides an efficient thermal source. The thermal process must have great importance in the growth of diamond-like phases.

Table 1
The physical properties of silicon

Properties	Silicon
Thermal conductivity (W/cm K)	1) $T < 1370$ K: $1585T^{-1.229}$ 2) 1370 K $< T < 1685$ K: 0.221 3) $T > 1685$ K (liq.): 0.70
Volume heat capacity (J/cm ³ K)	1) $T < 1685$ K: $1.98 + 2.54 \times 10^{-4}T - 3.68 \times 10^{-7}T^2$ 2) $T > 1685$ K (liq.): 2.4
Reflectivity	0.37 ($\lambda = 532$ nm)
Absorption coefficient (cm ⁻¹)	1.06×10^4 ($\lambda = 532$ nm)

When a pulsed laser irradiates the sample surface, the visible laser photons are absorbed not only by the polymer film but also by the silicon substrate. For the silicon surface, the laser intensity $I(t)$ in Eq. (1) is the fluence transmitted by the polymer film, and approximates to a constant value throughout a pulse duration of 7 ns and zero after the pulse. The initial temperature T_0 in the silicon substrate is assumed to be the ambient temperature. Substituting the parameters [18,19,21] of the silicon in Table 1 into Eq. (1), the temperature distribution in the substrate can then be obtained.

Fig. 4 shows the temperature distribution with time at the top surface of the silicon substrate by laser irradiation of polymer films with a fluence of 950 mJ/cm². From Fig. 4, the top surface temperature of the substrate increases with time during laser irradiation, reaching 810 K at 3.0 ns, and peaking to a maximum of 1413 K at the end of the pulse (7 ns). This temperature range is much higher than required in conventional pyrolysis [17]. In addition, the top surface temperature decreases rapidly after peaking at the maximum and reaches 530 K at 300 ns. Therefore, we believe that visible pulsed laser in our system provides an

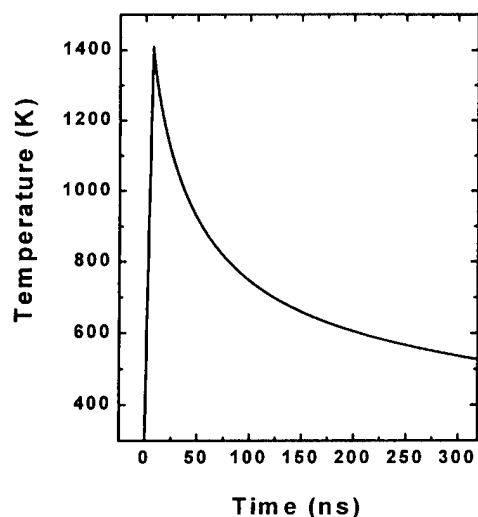


Fig. 4. Temperature rises as a function of time at silicon substrate surface by laser irradiation with an incident fluence of 950 mJ/cm².

efficient thermal source. The thermal process, in which temperatures higher than required in thermolysis and high cooling velocities occurred, must have a great influence on the formation of diamond-like phases.

With a laser fluence of 950 mJ/cm², the local temperature was high enough for decomposition to occur in the spotted polymer. Most of the phenyl substituents would be removed from the spotted polymer and the C—C bonded amorphous network would be resulted in [20]. In the conversion process, some phase transition from an amorphous network to a crystalline structure may occur, and some hydrogen and hydrocarbon radicals created from the hydrocarbon polymer by the laser irradiation may be beneficial to depress the sp² graphite phase and increase the sp³ diamond phase to form crystalline diamond. Due to the unique structure of the polymer, i.e. tetrahybridized carbon network, it is easier to form diamond with high conversion efficiency at lower temperatures by laser irradiation on the polymer than the conventional laser ablation process. The exact mechanism for diamond synthesis via this process is yet to be investigated further.

4. Conclusions

In summary, diamond-like phases have been converted from phenylcarbyne polymer precursor at room temperature by pulsed Nd:YAG laser ($\lambda = 532$ nm) irradiation of the polymer in argon atmosphere. The film/crystal has been confirmed by Raman spectroscopy studies. It is proposed that the conversion of diamond-like phases may be related to the unique structure of the polymer. The thermal process induced by laser irradiation on the polymer has a great influence on the formation of diamond-like phases.

References

- [1] J. Seth, R. Padiyath, D.H. Rasmussen, S.V. Babu, Appl. Phys. Lett. 63 (1993) 473.
- [2] M.C. Polo, J. Cifre, G. Sánchez, R. Agüer, M. Varela, J. Esteve, Appl. Phys. Lett. 67 (1995) 485.
- [3] T. Sato, S. Furuno, S. Iguchi, M. Hanabusa, Appl. Phys. A 45 (1988) 355.
- [4] F.X. Rong, Appl. Phys. Lett. 67 (1995) 3117.
- [5] Y.F. Lu, S.M. Huang, X.B. Wang, Z.X. Shen, Appl. Phys. A 66 (1998) 543.
- [6] S. Lätsch, H. Hiraoka, J. Metals 46 (1994) 64.
- [7] H. Hiraoka, J. Photochem. Photobiol. A Chem. 92 (1995) 129.
- [8] T. Visscher, D.C. Nesting, J.V. Badding, P.A. Bianconi, Science 260 (1993) 1496.
- [9] Z. Sun, X. Shi, B.K. Tay, D. Flynn, X. Wang, Z. Zheng, Y. Sun, Diamond Relat. Mater. 6 (1997) 230.
- [10] D.S. Knight, W.B. White, J. Mater. Res. 4 (1989) 385.
- [11] Y. Namba, E. Heidarpour, M. Nakayama, J. Appl. Phys. 72 (1992) 1748.
- [12] R. Srinivasan, Science 234 (1986) 559.

- [13] J.H. Branon, J.R. Lankard, A.I. Baise, F. Burns, J. Kaufman, *J. Appl. Phys.* 58 (1985) 2037.
- [14] T.F. Deutsch, M.W. Geis, *J. Appl. Phys.* 54 (1983) 7201.
- [15] G. Koren, J.T.C. Yeh, *Appl. Phys. Lett.* 44 (1984) 1112.
- [16] A.J. Gordon, R.A. Ford, *Chemist's Companion*, Wiley, New York, 1972, pp. 113–113.
- [17] R.W. Lenz, *Organic Chemistry of Synthetic High Polymers*, Wiley-Interscience, New York, 1967.
- [18] E.D. Palik, *Handbook of Optical Constants of Solids*, Academic Press, Orlando, 1985, pp. 556–569.
- [19] Y.S. Touloukian, *Thermophysical Properties of Matter Vol. 1*, IFI/Plenum, New York, 1978, pp. 326–329.
- [20] Z. Sun, Y. Sun, Z. Zheng, X. Wang, Q. Yang, *Surf. Coat. Technol.* 79 (1996) 108.
- [21] Y.S. Touloukian, *Thermophysical Properties of Matter Vol. 4*, IFI/Plenum, New York, 1978, pp. 204–207.

Influence of surface pretreatment on case formation during gaseous nitriding

J. Baranowska *, M. Wysiecki

Institute of Material Engineering, Technical University of Szczecin, al. Piastów 19, 70-310 Szczecin, Poland

Abstract

The results of studying the influence of cathode sputtering on surface layer formation during gas nitriding will be presented in this paper. Specimens of iron have been cathode sputtered before nitriding in controlled ammonia–hydrogen and/or nitrogen gas mixtures. The cathode sputtering process was performed in a separated chamber in argon or nitrogen atmospheres. The thickness and microhardness of the compound case and internal diffusion zone and their structure were compared for specimens pre-treated and non-pre-treated before gas nitriding.

The increased number of active centres caused by cathode sputtering has a very important influence on the kinetics of surface layers formation. The thickness measurements of nitride layers show the significant growth of thickness for all the ranges of atmospheres used. After cathode sputtering, a compound layer developed rapidly on the iron surface during the subsequent nitriding. After 10 min, the closed compound case was noticed. This phenomenon has an important influence on the conditions of the diffusion zone formation. Its higher thickness achieved through cathode sputtering was also measured.

The results were controlled by metallographic testings (scanning and light microscopy) and microhardness measurements. The phase compositions of the layers were evaluated by X-ray diffraction. © 2000 Elsevier Science S.A. All rights reserved.

Keywords: Cathode sputtering; Gaseous nitriding; Nitrides nucleation; Nitriding kinetics; Surface activation

1. Introduction

Gaseous nitriding is a thermo–chemical surface treatment of great importance. It leads to the improvement of the surface quality (hardness, wear and corrosion resistance). During the nitride layer build-up several stages can be distinguished:

1. diffusion of nitrogen carrier (ammonia) towards the iron surface;
2. ammonia adsorption and dissociation on the surface; and
3. nitrogen absorption and its diffusion into the sample.

The global rate of the total nitriding process will be then determined by the duration of the slowest of the above mentioned stages. The formation and growth of the surface layer will depend on the relationship between the nitrogen supply and nitrogen demand. The nitrogen supply is regulated by the composition of the nitriding atmosphere, which is the fundamental parameter of the

nitriding process. Nitrogen demand mainly depends on the diffusion process (e.g. temperature and time).

The build-up of the nitriding layer starts from nitrogen absorption and the layer develops by nitrogen diffusion into the bulk material. Nitrogen diffusion in iron is thought to limit the kinetics of nitriding layer formation [1]. When the quantity of nitrogen atoms produced from the gas atmosphere is smaller than its capability to be absorbed in those conditions then only a solid solution $\text{Fe}(\text{N})$ with nitrides (γ' — Fe_4N or α'' — Fe_{16}N_2) is formed in the surface layer. But if the nitrogen supply exceeds that capability, besides the diffusion zone, the compound layer (consisting of nitrides γ' and ϵ) is present [1–5]. In this case, after a period of time (the so called the incubation time) the surface nitrogen content reaches the solubility limit [6,7]. In such a saturated area, the nucleation of nitrides takes place. Further growth of the compound layer proceeds by growth of the nuclei until they connect [8–10]. The nucleation starts in some energetically preferred places such as grain boundaries, structural defects or inclusions (e.g. oxides) [7,9].

Activation of the surface before or during nitriding

* Corresponding author. Tel.: +48-91-449-4779;
fax: +48-91-434-0558.

Table 1
Conditions of the nitriding treatment

Atmosphere	Ammonia (10, 20, 30, 40, 50%) + H ₂ and/or N ₂
Temperature	843 K
Time	10, 30, 60, 120, 180 min

is a very common treatment, which enables the intensification of surface reactions occurring during nitriding — ammonia adsorption and dissociation. Techniques such as mechanical treatment or oxidation are very often used [9–11]. In the present paper cathode sputtering is suggested as an activation process, and its influence on the kinetics and conditions of nitriding layer formation is investigated.

2. Experimental

The experiments were carried out on the samples made of α -Fe $2 \times 6 \times 20$ mm in size. Before the treatment, samples were ground ($Re = 0.12 \mu\text{m}$). Some of them were additionally polished ($Ra = 0.05 \mu\text{m}$). Two series of samples were gas nitrided: I — without and II — with cathode sputtering as a surface pre-treatment. The nitriding conditions are listed in Table 1.

The process of cathode sputtering was carried out in a separated chamber. The sample was connected as a cathode. The parameters of the treatment were as follows: voltage 1200 V, pressure 13 Pa, time 20 min, nitrogen or argon was used as a sputtering gas. The whole stand for pre-treatment and nitriding was presented in the previous papers [8,12]. The sample immediately after sputtering was introduced into the reaction zone of the furnace.

For every sample the following investigations were made:

1. Metallography of cross-section of nitrided layers and layer thickness measurements (the compound layers) with a Reichert light microscope; the diffusion zone thickness was estimated from microhardness measurements on cross-sections of nitrided layers. The distance from the outer surface where the microhardness was 50 HV higher than that in matrix was recognised as a thickness of diffusion zone. 0.02 HV microhardness was measured using a Boehler 2000 microhardness tester.
2. Surface observation by a scanning microscope JEOL 6100.
3. Phase identification by X-ray diffraction (CoK α).
4. Roughness measurements using profilometer Mitutoyo Surftest 301.

3. Results

3.1. Cathode sputtering

The cathode sputtering process leads to an increase in the number of surface defects [13]. Its influence on macrochanges of surface shape causing the roughness increase was also observed [14]. SEM observation confirmed that even after a very short time of sputtering (30 min: Fig. 1(a) and (b)) the surface changes very distinctly. Some increase in surface roughness is also observed (Fig. 1(c)).

Cathode sputtering was carried out with two types of gases: argon and nitrogen. The XRD surface analysis results reveal significant (Fig. 2) differences in phase composition between the samples which had undergone cathode sputtering and ones which had not. But there are no differences between the samples scattered with nitrogen or argon. Both samples have the same nitriding layer thickness and similar morphology.

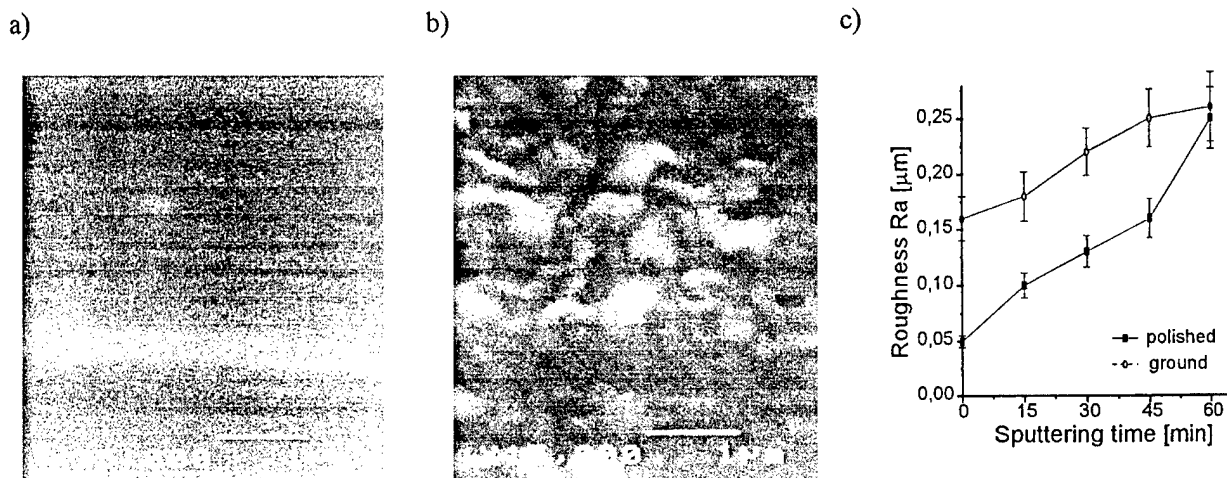


Fig. 1. (a) Surface of sample in the initial stage; (b) surface after 30 min cathode sputtering (1200 V, 13 Pa), SEM; (c) change of surface roughness versus time of cathode sputtering.

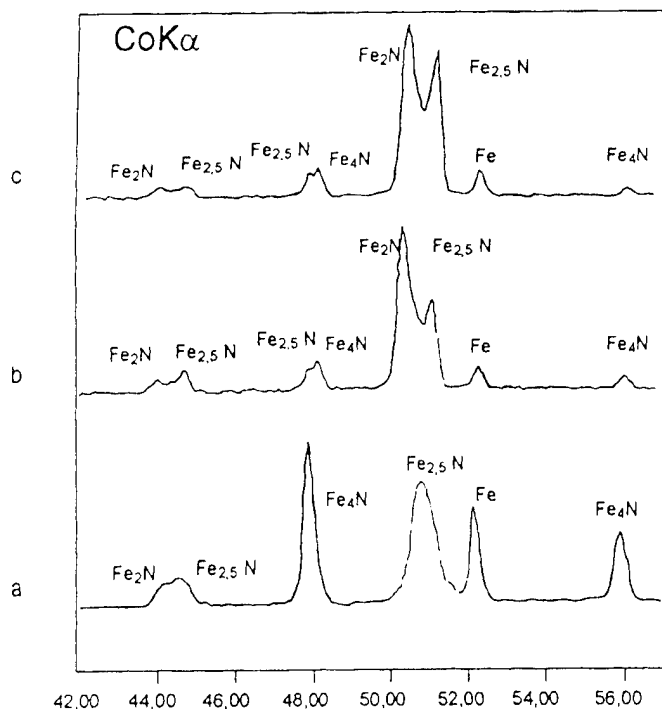


Fig. 2. X-Ray diffraction patterns of the samples: (a) without cathode sputtering; (b) with cathode sputtering with argon; (c) with cathode sputtering with nitrogen (XRD, $\text{CoK}\alpha$). All the samples were nitrided in a 30% $\text{NH}_3 + \text{N}_2$ atmosphere, for 3 h, at 843 K.

3.2. Nitriding process

Cross-section (LMA) and surface (SEM) observations for samples after a very short time of nitriding (Fig. 3) revealed that in the case of pre-treated samples a close compound nitride layer is observed at the very beginning of nitriding (after 10 min) even for low nitrogen potential atmospheres. For samples which have not been pre-treated close layer formation takes at least 60 min (Figs. 3, 4(a) and (b)). Also the diffusion zone for cathode sputtered samples is twice as big as for non-pretreated samples.

The influence of cathode sputtering on the kinetics of nitride layer formation is also observed only after a considerably longer period of time (3 h) – see Fig. 5.

Moreover the XRD investigations of phase composition showed that cathode sputtered samples have higher ϵ/γ' ratio than samples without this pre-treatment.

4. Discussion

Taking into account the stages of nitriding layer formation (saturation, nucleation and nucleus growth)

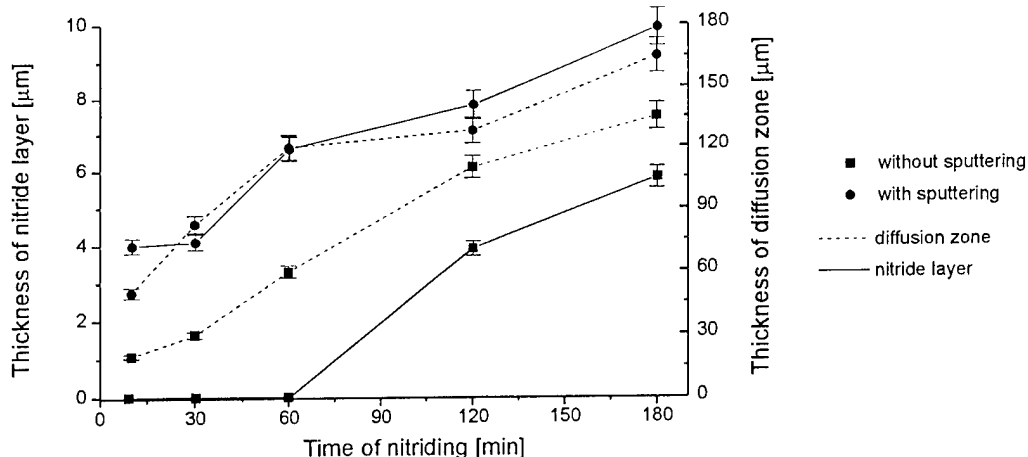


Fig. 3. Thickness of compound case and diffusion zone versus duration of nitriding for samples with and without cathode sputtering. Nitriding conditions: 20% $\text{NH}_3 + \text{H}_2$, 843 K.

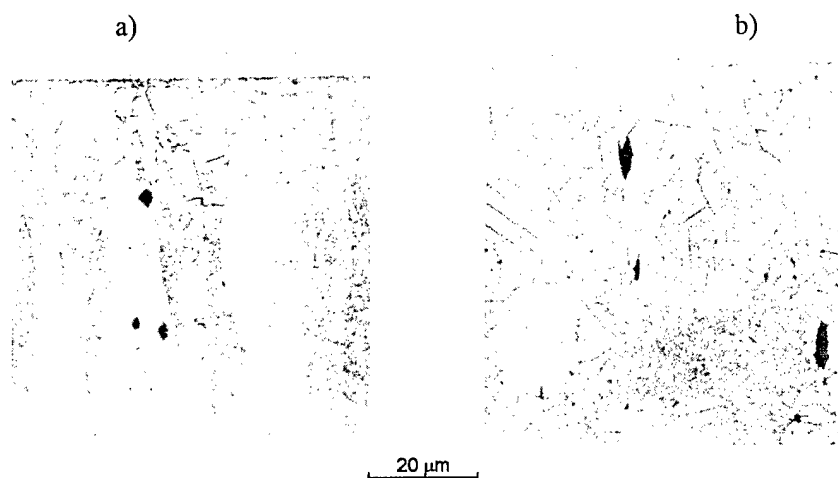


Fig. 4. Cross-section of layers after gaseous nitriding in an atmosphere 50% $\text{NH}_3 + \text{N}_2$, 843 K after 10 min of treatment: (a) without, (b) with cathode sputtering.

during gaseous nitriding the following statements can be made. Either:

1. The process of surface saturation with nitrogen is not constant on the whole surface. Therefore some parts reach the solubility limit more quickly than others do and the nucleation of nitrides in these places is possible. Or:
2. The saturation is even on the surface but some areas are more preferred for nitride nucleation. It means that the nitride is not always formed on the saturated basis.

If the saturation was equal on the whole surface, the nitride phase should not have any influence on the diffusion zone. The diffusion range should depend only on temperature (diffusion coefficient) and nitriding potential of the atmosphere (lower incubation time). As we can see from the present investigation for pre-sputtered samples, which developed a close compound layer just after 10 min treatment, the thicker diffusion zone is also observed. It was also observed that for both kinds of the samples (sputtered and not) the thickness

differences between the diffusion zones obtained are very big and vary depending on the nitriding atmosphere composition. The higher nitrogen potential of the atmosphere is the smaller difference is measured. This is in good accordance with the changes of the incubation time versus nitriding potential [7].

The above indicates that these active centers in which the nitrides nucleation takes place, play a crucial role in one of the surface reactions which are responsible for mass transfer during gaseous nitriding (ammonia adsorption, its dissociation or nitrogen absorption). The cathode sputtering process which activates the upper surface of the sample enables nitrogen to penetrate into iron through the whole of its surface.

After the formation of the close compound layer has been completed, the case growth is limited by nitrogen diffusion through the nitrides. Because the diffusion coefficient of nitrogen in γ' is much lower than in iron [1–3,5] the ϵ nitride in pre-activated samples is formed very quickly. Therefore if we compare samples treated in the same nitriding conditions, those which have been

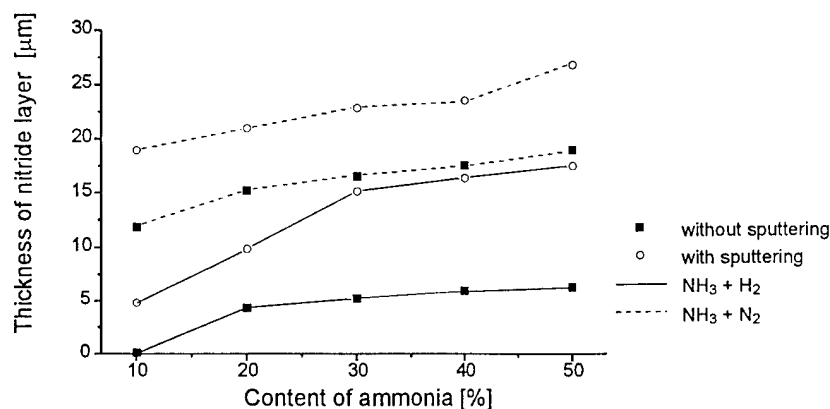


Fig. 5. Thickness of compound cases after 3 h of treatment for various nitriding atmospheres.

pre-treated must have a higher ϵ nitride content than those which have not undergone the process.

Moreover, the large differences between the thickness of the diffusion zone for both series of the samples can indicate that diffusion is not necessarily responsible for limiting the kinetics of nitriding at an early stage of treatment.

5. Summary

The cathode sputtering process which increases the number of active centers on the iron surface has an important influence on layer formation kinetics for gas nitriding. Rapid formation of the continuous nitride layer in pre-treated samples increases the thickness both of the compound layer and the diffusion zone. Comparing the kinetics and the conditions of nitriding layer formation for samples with and without cathode sputtering, our attention is drawn to the importance of activating treatment for the initial stage of nitriding. It is suggested that before the close nitride layer is formed it is not diffusion but the surface reaction kinetics which determines the rate of the total process.

References

- [1] L. Torchane, P. Biliger, J. Dulcy, M. Gantois, *Metall. Mater. Trans. A* 27 (1996) 1823.
- [2] L. Maldziński, J. Tacikowski, *Inżynieria Powierzchni* 2 (1998) 49.
- [3] E.J. Mittemeijer, A.A.J. Sommers, *Surf. Eng.* 13 (6) (1997) 483.
- [4] H. Du, *J. Phase Equilibria* 14 (6) (1993) 682.
- [5] M.A.J. Sommers, J. Mittemeijer, *Metall. Mater. Trans. A* 26 (1995) 57.
- [6] H.C.F. Rozendaal, E.J. Mittemeijer, P.F. Colijn, *Metal. Trans. A* 14 (1983) 395.
- [7] H. Du, N. Lange, J. Ågren, *Surf. Eng.* 11 (4) (1995) 301.
- [8] J. Baranowska, K. Szczeciński, M. Wysiecki, *Mat. Conf. Obróbka Powierzchniowa*, Częstochowa, Poland, Kule 9–12 October (1996) 59–64.
- [9] W.D. Jentzsch, S. Böhmer, *Kristall und Technik* 14 (5) (1979) 617.
- [10] C. Kozaryn, PhD Thesis, Technical University of Szczecin, 1979.
- [11] G.S. Kaplina, G.L. Zhunkovskij, *Schutzschichten auf Metallen* 6 (1972) 73.
- [12] J. Baranowska, K. Szczeciński, *EUROMAT'98*, Lisboa, 22–24 July Vol. II (1998) 329–334.
- [13] *Ionic Bombardment Theory and Application*, Gordon and Breach, New York-London, 1962.
- [14] Z.W. Kowalski, J. Wilk, 5th Eur. Conf. on Advanced Materials and Processes and Applications, *EUROMAT'97*, Maastricht, 21–23 April (1997) 379–382.

Pre-treatment of large area strips with the aid of a high power Hall current accelerator

N. Vershinin ^{a,b}, R. Dimitriou ^c, M. Benmalek ^c, B. Straumal ^{b,d,*}, W. Gust ^d, J. Vivas ^e,
J. Shulga ^f

^a SONG Ltd., P.O. Box 98, Chernogolovka, Moscow District, 142432 Russia

^b I.V.T. Ltd., P.O. Box 47, 109180 Moscow, Russia

^c PECHINEY CRV, BP 27, 38340 Voreppe, France

^d Institut für Metallkunde, Seestrass 92, D-70174 Stuttgart, Germany

^e Universidad Nacional del Comahue, Av. Buenos Aires 1400, 8300 Neuquen, Argentina

^f Institute of Chemical Physics, Chernogolovka, Moscow District, 142432 Russia

Abstract

A large aperture Hall current accelerator has been developed for ionic cleaning of glass and metallic strips before vacuum arc deposition of protective and decorative layers. The accelerator has a large aperture of 1400 mm and power up to 10 kW. Various gases can be used for sputter cleaning: argon, nitrogen, oxygen, etc. The advantages of the Hall current source towards that of Kaufman in industrial processes are emphasized. The source sputter rates were measured. The maximal sputter rate is 7.5 nm/min for glass and 100 nm/min for poly(methyl metacrylate). The quality of ionic etching was demonstrated with the aid of Auger electron spectroscopy. The current–voltage characteristics for argon and oxygen are presented. © 2000 Elsevier Science S.A. All rights reserved.

Keywords: Hall current accelerator; Ionic etching; Kaufman source; Sputter cleaning

1. Introduction

Ion beam processing is an established method for surface treatment [1]. It includes techniques like sputtering, thin film deposition and ion implantation. Though the principle is the same in all cases, a given application requires a specific source design according to the ion energy range and uniformity needed. By the coating of large substrates like glass sheets or steel strips for architectural and structural applications, the substrate cleaning before coating is of particular importance for the adhesion and corrosion resistance of the further deposited layers and, therefore, for the long-term stability of properties and of the appearance of coated parts in various environments. Ion beam sputter precleaning proved to be an efficient method to ensure high quality coatings on glass, metal and plastic sheets. For sputtering purposes, Kaufman sources [2–4] are usually chosen. These sources

are very attractive in the sense that a neutralized beam is generated with independently controllable ion energy and current density. The ion production is also separated from the substrate and target used. However, inherent design considerations limit the use of such sources in production applications [5]. The source cathode and grid optics are critical components which sometimes require excessive maintenance. Local heating or presence of reactive gases (such as oxygen) dramatically reduce the source lifetime by damaging the cathode. Depending on the cathode type, the source lifetime ranges from a few hundred to one thousand hours. Grid optics of Kaufman sources limit the ion beam current that can be extracted from the chamber. In architectural and structural applications the source design must also meet the requirement of a large area treatment.

2. Experimental

In this work, a large aperture Hall current accelerator was developed for sputter cleaning of large area glass,

* Corresponding author. Present address: Institut für Metallkunde, Seestrass 92, D-70174 Stuttgart, Germany. Tel.: +49-711-1211276; fax: +49-711-1211280.

E-mail address: straumal@mf.mpi-stuttgart.mpg.de (B. Straumal)

metal and plastic sheets. Though less controllable than Kaufman sources, a Hall current accelerator appears better suited for sputter cleaning production requirements [4]. Of greater significance is the lack of any space charge flow limitation on the ion current density. Furthermore, the reliability in etching is improved through the absence of any delicate structures like cathode or grid optics. The Hall current accelerator requires little maintenance, and the sputter cleaning can be performed with reactive gases such as oxygen, nitrogen and carbon dioxide. The scheme of the Hall current accelerator is shown in Fig. 1. It has the shape of a very elongated loop. The large aperture (1400 mm in the vertical direction) allows one to use it in the multi-purpose 'Nikolay' apparatus for deposition on large area glass and plastic sheets by vacuum arc deposition [6–8] and magnetron sputtering. Sheets to be treated are successively transported under the Hall discharge accelerator at a given translation speed, the substrate surface being perpendicular to the ionic flux axis. Changing the speed and accelerator power, one can control the sputter dose received by the substrate. The aperture of the Hall current accelerator can be scaled up to 3000 mm without significant changes in design and, therefore, adjusted to a deposition apparatus. A twin aperture has two slots, 55 mm away from one another. Two juxtaposed permanent magnets act as cathode. The water cooled anode of tubular shape runs inside the groove made by the cathode. The whole apparatus is set under vacuum in the presence of a sputter gas (usually argon). Gas ionization and the subsequent ion acceleration is made through the presence of crossed electric and magnetic fields. The electric field is created by the cathode-to-anode potential drop whereas a quasi-uniform magnetic field is set between the two pole pieces of the cathode. In the presence of a low pressure gas and an electric field, a glow discharge plasma is initiated. The magnetic field traps the plasma electrons and, together with the electric field, causes

them to precess circumferentially along the anode surface. Through their cycloid path, they collide with argon atoms and ionize them. The high difference of potential accelerates the argon ions away from the anode and towards the substrate to be sputter cleaned.

In production of materials for architectural and structural needs, the sputter requirements are less demanding than in microelectronics or optics; nevertheless, the cleaning profile of the source must be known in order to estimate the sputter dose received by the substrates. A simple method was used to derive the source cleaning profile. Two hundred millimetre wide samples were sputter cleaned fixed to the source for different exposition times. Before cleaning, pen mark lines were drawn at a regular spacing interval on the sample surface. The pen marks provided masking against sputter cleaning of the sample surface. After cleaning treatment, they were removed with alcohol, leaving a step between the sputtered and non-sputtered parts. The step height was measured using a Taylor–Hobson profilometer. The measures along the width of the sample give the cleaning distribution of the source for a given exposition time. Such experiments were carried out on samples made of silicate glass and organic glass [poly(methyl metacrylate)]. The samples were placed 300 mm away from the source.

Cleaning of aluminium has been assessed in terms of impurity content after treatment. Al 5182 samples were sputter cleaned with oxygen at a pressure of 1.5×10^{-2} Pa at different doses and immediately coated with a thin TiO_2 film less than 300 nm thick. The samples were placed in the industrial scale deposition 'Nikolay' apparatus. The cleaning conditions correspond for each gas to a maximum cleaning at a low frame velocity (0.15 m/min), to medium cleaning at higher frame velocity (0.3 m/min) and no cleaning at all. The cleaning was performed through one return of the frame. The deposition parameters for the thin TiO_2 film were the same for all samples: Ti was evaporated under an oxygen pressure of 2.4×10^{-2} Pa. The samples were then analysed using Auger electron spectroscopy (AES) in order to derive the carbon content, considered to be the main source of impurity. The analysis was carried out with the excitation beam normal to the specimens. The spectra were taken during argon ion sputtering which produced a relatively clean surface of the sample under study without baking the system. The etching rate was considerably faster than the adsorption rate of the active residual gases. The Auger spectra were measured on a PHI-551 spectrometer with a double-pass cylindrical mirror analyzer. The base pressure was less than 2×10^{-8} Pa. The spectra were excited by an electron beam with an energy of 3 keV and a current of 8 μA through the sample. The peak-to-peak modulation was 3 V. The sputtering was accomplished using a 5 keV Ar^+ ion beam. An ion gun was mounted to give a beam

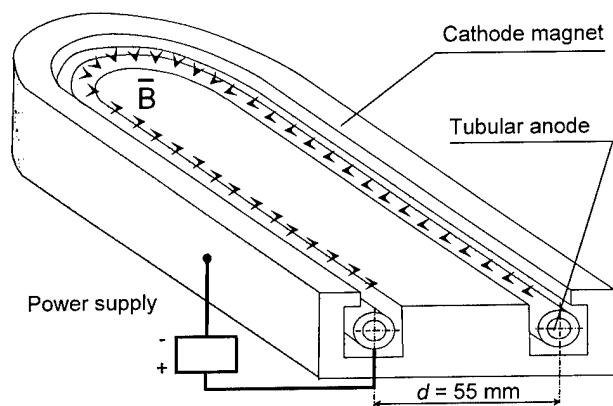


Fig. 1. Hall current accelerator (section through the middle plane). The total length is 1400 mm.

incidence angle of 70° and, in order to minimize possible crater effects, it was rastered. The pressure of argon during sputtering was equal to 3×10^{-3} Pa. In order to provide a basis for comparison, a very pure aluminium polycrystal and chemically cleaned 5182 aluminium samples were also analysed.

3. Results and discussion

Cleaning profile for silicate glass is shown in Fig. 2. Similar profiles for an organic glass were published elsewhere [9]. As would be expected, the form of the profile depends on the material cleaned because silicate and organic glasses have a different behaviour towards sputtering. Silicate glass has a more reproducible cleaning profile with time in comparison to organic glass. Two distinct peaks appear in the distribution (Fig. 2). They correspond to two parallel parts of the elongated anode loop (Fig. 1). The twin construction of the source can thus be resolved in the cleaning profile of silicate glass. In the region of maximum sputter cleaning (corresponding to the two peaks), the sputter rate for glass almost reaches 7 nm/min. Organic glass has a lower thermal resistance compared to silicate glass. As a result, by sputtering longer than 5 min deterioration of the organic glass occurs. Below this value, the material is sputtered at a maximum rate of 100 nm/min [9]. The sputter cleaning of two materials of interest showed that the source cleaning profile is highly non-uniform and material dependent. The source profile for organic glass is difficult to interpret as the ion bombardment produces a combined effect of physical and thermal sputtering of the polymer with a low thermal resistance. Material deterioration similar to the damage induced by ionizing radiation can be expected [10].

The source cleaning profile for glass shows a distribution in agreement with the twin aperture source design. In a first approximation, the source profile can be modelled with a two-peak Gaussian profile distribution. Three hundred millimetres away from the source, the

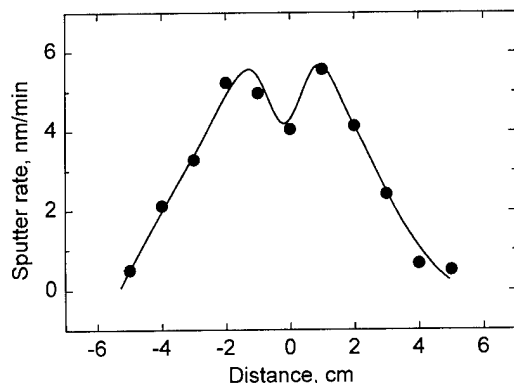


Fig. 2. Sputter profile for silicate glass. The line is a visual guide.

spacing between the Gaussian peaks (30 mm) is smaller than the distance d between the axes of the elongated parts of the anode loop (Fig. 1). This shows that the source beam is convergent and that a complete beam description would imply the derivation of the source cleaning profile for different distances from the source. As far as the process is concerned, silicate glass substrates, when cleaned, are moved relative to the source at a given translation speed. It ensures a uniform cleaning treatment over the glass panel surface. An estimation of the layer sputtered when moving at a given speed can be obtained by integrating the cleaning profile (expressed in cleaning rate units, e.g. nm/min) along the source width. For the speed range used in the industrial process, the silicate glass sputtered layer varies from 13 nm at low speed to 0.6 nm at high speed. At the most widely used speed, the thickness of the removed layer is 2 nm.

Usual values for the source power are the discharge voltage $U=6$ kV and current $I=0.5$ A under an argon pressure P of about 0.01 Pa. The resulting ion beam has an average energy of 6 keV. The current–voltage characteristic for argon at $P=2.4 \times 10^{-2}$ Pa is presented in Fig. 3. At high voltages the current changes slowly. Below 3 kV the current starts to decrease, and the discharge becomes unstable. The parameters of discharge are rather independent of the method of gas input (into vacuum chamber or directly into Hall accelerator). The current–voltage characteristic for oxygen at $P=3.8 \times 10^{-2}$ Pa is presented in Fig. 4. The interval of stable discharge is much broader in this case (discharge current up to 6 A). The measured current–voltage characteristics allow one to optimize the regime of sputter cleaning by finding the maximum power value at a stable discharge.

The AES depth profiles for the 5182 Al alloy without any precleaning (Fig. 5) and with maximal oxygen cleaning (Fig. 6) were measured. They show that at the surface of the samples, the carbon contamination is high

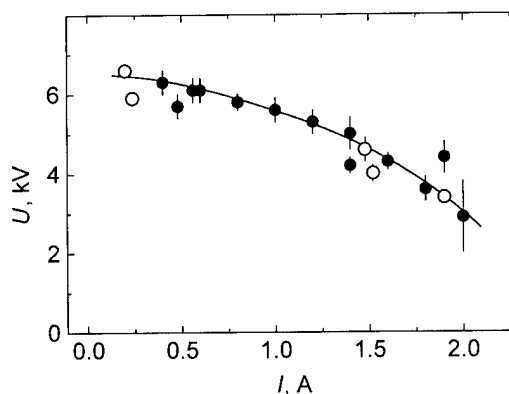


Fig. 3. Current–voltage characteristic for Ar at a pressure of 2.4×10^{-2} Pa. Gas input into the vacuum chamber (full symbols) and into the Hall accelerator (open symbols). The line is a visual guide.

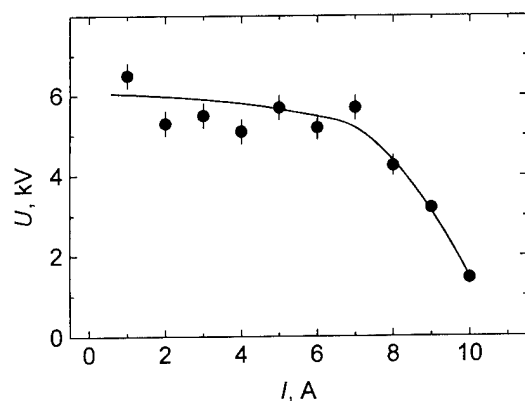


Fig. 4. Current–voltage characteristic for oxygen at a pressure of 3.8×10^{-2} Pa. The line is a visual guide.

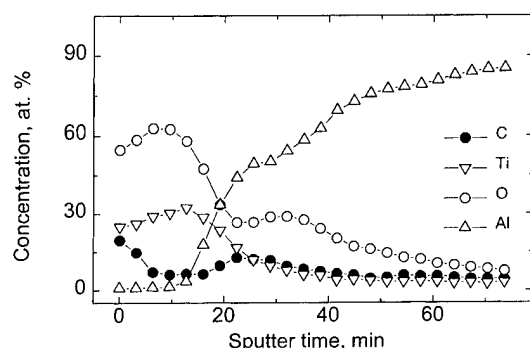


Fig. 5. AES depth profile for the 5182 Al alloy coated with TiO_2 without preliminary cleaning. The lines are visual guides.

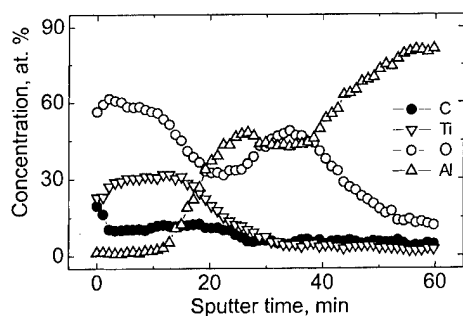


Fig. 6. AES depth profile for the 5182 Al alloy coated with TiO_2 after maximal oxygen ionic sputter cleaning. The lines are visual guides.

and decreases deeper into the substrate. For large sputtering times, which correspond to the material bulk, the values of carbon content is still rather high (5 to 10 at.%) even for the very pure 99.999 at.% Al polycrystal. (This may be explained by the surface finish of both samples.) In the experimental set-up the surface sputtering is accomplished using a 5 keV Ar^+ ion beam at an incidence angle of 70° . The Auger electrons are excited by an electron beam having an other incidence than the sputtering beam. The high surface roughness may provide some shadowing making the removal of all surface contamination impossible. The oxygen content also

shows a surface contamination and some implantation in the neighbourhood. In the bulk of the material, the oxygen content is equivalent to the carbon one. These preliminary spectra underline that without any treatment, the bulk of the 5182 aluminium contains around 5 at.% carbon which must be considered as the background content when reading the cleaning spectra. The spectra (Figs. 5 and 6) show at the beginning the presence of the thin TiO_2 film with some carbon content. The film/substrate interface is revealed by the sharp augmentation of the Al content. In this region, the carbon concentration increases in the case of the non-cleaned sample while it decreases for the oxygen cleaned sample. In the bulk of the material, a 5 at.% background content is found. The second noticeable cleaning effect is observed for the oxygen content. The sputtering induces implantation close to the interface. It is revealed by a significant peak for oxygen after 30 min sputtering (Fig. 6). The same behaviour is observed in the case of cleaning with argon. The carbon content peak at the interface disappears when the sputtering is performed. However, no oxygen implantation occurs by sputtering with argon.

4. Conclusions

A large aperture Hall current accelerator is presented. The absence of any lifetime critical components makes it very attractive for industrial applications in comparison to Kaufman sources. Little or no maintenance is needed, and active gases such as oxygen, carbon dioxide and nitrogen can be used for sputter cleaning. The source sputter profile under argon was determined for silicate glass and poly(methyl metacrylate) treated 300 mm away from the source. In both cases, the cleaning distribution is highly inhomogeneous and presents only a narrow area of maximal sputtering. Silicate glass has a cleaning rate about 12 times lower than that of poly(methyl metacrylate). The cleaning profiles are rather complicated, whereas for silicate glass the two-peak distribution induced by the twin aperture source can be resolved. This type of characterization enables one to give an estimate of the sputtered glass layer when the substrate is moved relative to the source at a given speed. The current–voltage characteristic measured for argon is presented. It allows one to optimize the regime of sputter cleaning by finding the maximum power value at a stable discharge. The quality of the sputter cleaning is demonstrated with the aid of AES depth profiling of uncleaned and cleaned Al alloy strip.

Acknowledgements

The financial support of the NATO Linkage Grant (contract HTECH.LG.970342 + CN.SUPPL 973216),

the Isopress-Inter Programme of the Russian Ministry of Science and Technology and the Copernicus Network (contract ERB IC15 CT98 0815) is heartily acknowledged.

References

- [1] R.F. Bunshah (Ed.), *Handbook of Deposition Technologies for Films and Coatings* Noyes Publications, Park Ridge, NJ, 1994, 350 pp.
- [2] H.R. Kaufman, *Adv. Electronics Electron Phys.* 36 (1974) 265.
- [3] H.R. Kaufman, J.M.E. Harper, J.J. Cuomo, *J. Vac. Sci. Technol.* 21 (1982) 764.
- [4] H.R. Kaufman, J.J. Cuomo, J.M.E. Harper, *J. Vac. Sci. Technol.* 21 (1982) 725.
- [5] H.R. Kaufman, *J. Vac. Sci. Technol. A* 4 (1986) 764.
- [6] N. Vershinin, B. Straumal, W. Gust, *J. Vac. Sci. Technol. A* 14 (1996) 3252.
- [7] N.F. Vershinin, V.G. Glebovsky, B.B. Straumal, W. Gust, H. Brongersma, *Appl. Surf. Sci.* 109 (110) (1996) 437.
- [8] B.B. Straumal, W. Gust, N.F. Vershinin, M. Friesel, M. Willander, *Surf. Coat. Technol.* 100–101 (1998) 316.
- [9] N. Vershinin, B. Straumal, K. Filonov, R. Dimitriou, W. Gust, M. Benmalek, *Thin Solid Films* 190 (1999) 351.
- [10] D. Evans, M.A. Crook, *MRS Bulletin* 22 (1997) 36.

Laser induced Cu/alumina bonding: Microstructure and bond mechanism

L. Shepeleva ^{a,*}, B. Medres ^a, W.D. Kaplan ^a, M. Bamberger ^a, M.H. McCay ^b,
T.D. McCay ^b, M. Sharp ^b

^a Department of Materials Engineering, Technion — Israel Institute of Technology, Haifa, Israel

^b University of Tennessee, Space Institute, Tullahoma, TN, USA

Abstract

The results of laser cladding of Cu to alumina under different treatment conditions and gas medium are presented. The laser surface treatment of alumina substrates was conducted by injection of copper powder into the laser–substrate interaction region. Processing parameters included the laser power, the scan speed of the laser beam, the copper feed rate and heat treatments following the laser treatment. Laser treated alumina substrates and the alumina–copper system, which was treated in air and under argon, were studied. Possible reactions at the metal–ceramic interface were investigated. Sub-micron Cu particles were formed in the amorphous grain boundary glass, and CuAlO₂ phases were found in the alumina substrate after laser treatment. © 2000 Elsevier Science S.A. All rights reserved.

Keywords: Alumina; Copper cladding; Laser treatment; Microstructure

1. Introduction

Interfacial reactions between Cu and Al₂O₃ have been the subject of several investigations. The eutectic reaction of copper has been used to bond copper to oxides, especially to alumina, in order to fabricate substrates for power electronic applications. There are several studies which demonstrated by sessile drop experiments that oxygen-containing molten copper wets alumina, forming a layer of cuprous aluminate (CuAlO₂) [1]. Cu–Cu₂O eutectic bonding was reported by Donald [2]. Solid-state bonding has also been studied for copper–sapphire and copper–diamond systems by Klomp et al. [5] and Dewar et al. [6]. There is no doubt that CuAlO₂ forms between copper and alumina at the temperatures above 1500 K and high oxygen partial pressures. However, as indicated by Yoshino and Shibata [7], it is not certain if the same reaction takes place at temperatures slightly above the eutectic temperature. The reactions taking place at the Cu/alumina interface during laser processing under different atmospheres are presented.

2. Experimental methods

2.1. Processing

Alumina (α -Al₂O₃) substrates of 96% purity were used in the study. The alumina substrates were 25 mm in length and 10 mm in width, with a thickness of 30 mm. The process was accomplished by feeding copper powder (average particle diameter of 100 μ m) into the work-zone at rates of 0.125 g/s and 0.225 g/s.

A CO₂ laser with a maximum power of 3 kW was used for the process. The laser beam was scanned across the substrate at a speed in the range of 0.66–4.0 cm/s. It was found that it is important to supply the powder in front of the moving laser beam. Specimens were prepared at laser powers ranging from 200 W to 800 W, with a constant beam diameter of 0.2 cm. The substrates were preheated to 400°C before laser treatment, in order to minimize thermal shock effects.

2.2. Characterization

Cross-sections of the metal/ceramic interfaces were characterized by optical and electron microscopy.

* Corresponding author.

Electron microscopy included both scanning electron microscopy (SEM) and transmission electron microscopy (TEM). For SEM, cross-sections were metallographically polished to a surface roughness of 0.25 μm , and etched in $\text{H}_3\text{PO}_4 + \text{NH}_4\text{OH}$. SEM was conducted on a JEOL 840 SEM, routinely operated at 10 kV. Chemical analysis of the interface region was conducted by energy dispersive spectroscopy (EDS) (Link-Oxford) mounted on the SEM. TEM was conducted on a JEOL 2000FX operated at 200 kV. The 2000FX also includes a Link EDS system which was used for micro-elemental analysis. Specimens for TEM were prepared by slicing 300 μm thick cross-sections, mechanical thinning to $\sim 100 \mu\text{m}$, mechanical dimpling to $\sim 25 \mu\text{m}$, and ion-milling with Ar at 6 kV and 0.5 mA to perforation. TEM specimens were coated with carbon to prevent charging in the TEM.

3. Results and discussion

3.1. Laser treatments in air

Laser cladding of Cu to alumina in air resulted in the agglomeration of molten Cu close to the edges of the melt pool (Fig. 1). Fig. 2 presents a SEM micrograph of the alumina/Cu interface region and the corresponding Cu and Al EDS linescans.

The linescans reveal that the chemical composition changes abruptly at the alumina/Cu interface. These results indicate that no reaction took place between the Cu and the alumina substrate when the molten Cu is located on the solid alumina. All joints revealed cracks

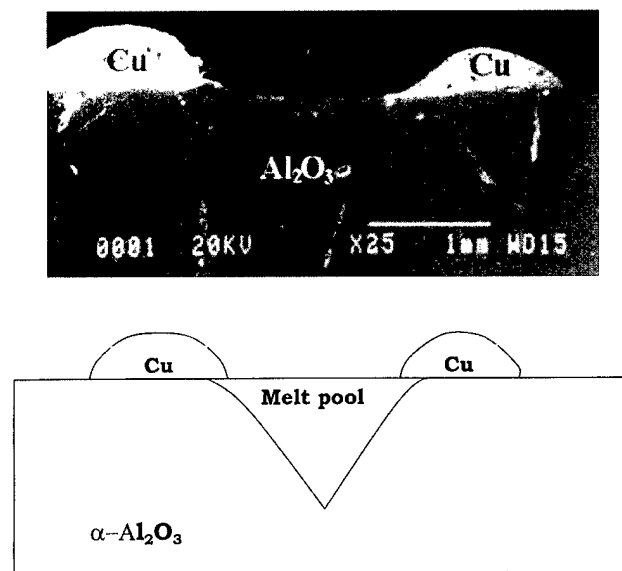


Fig. 1. SEM micrograph of the Cu/Al₂O₃ interface (laser treatment in air) and a scheme drawing showing the relative size and position of the alumina melt-pool.

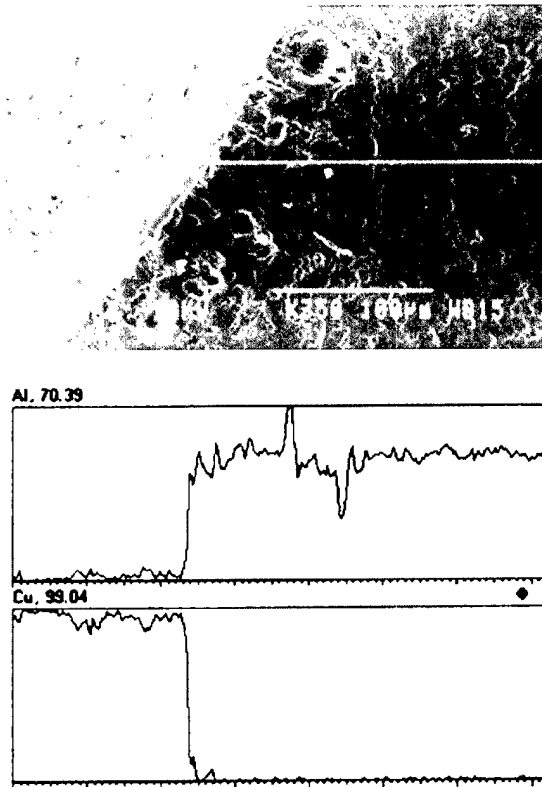


Fig. 2. SEM image of the Al₂O₃/Cu interface region and corresponding Cu and Al EDS linescans.

due to weak interfacial bonds [8]. These results imply that a reaction might be essential to obtain a crack-free Cu/alumina interface with strong chemical bonds between the Cu and alumina. In order to access the thermal stability of the joints, heat treatments were conducted in air at 900–1000°C for 6–24 h. After heat treatments, the copper agglomerates spread over the Al₂O₃ substrate (see Fig. 3).

This can be correlated with a high interfacial energy between liquid copper and liquid Al₂O₃, which promotes

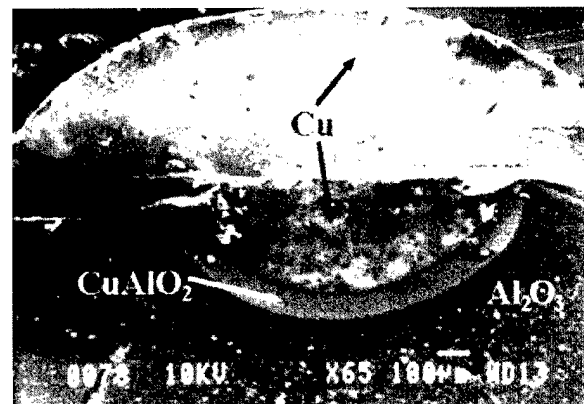


Fig. 3. SEM micrograph of a heat-treated (950°C for 20 h) laser processed Cu—alumina bond (800 W, 800 mm/min) (laser treatment in air).

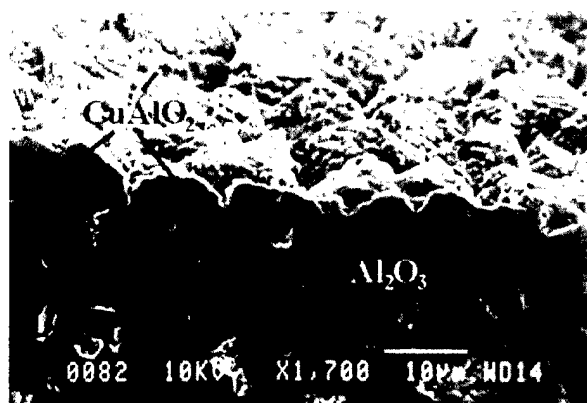


Fig. 4. SEM micrograph of a Cu–alumina joint, showing the presence of CuAlO_2 which forms between the alumina and metal (laser treatment in air).

Cu agglomeration, whereas the low interfacial energy between liquid Cu and solid Al_2O_3 results in the formation of a Cu layer on the substrate. In addition an interlayer, approximately $80\text{ }\mu\text{m}$ thick, was found between the Cu and the alumina (Figs. 3 and 4).

This layer was identified by EDS as CuAlO_2 (28.1 wt.% Cu, 35.6 wt.% Al, 33.3 wt.% O).

Fig. 5 is a TEM micrograph of the alumina near the melt-pool, formed during laser treatment at 800 W at 800 mm/min followed by heat treatment for 20 h at 930°C .

The microstructure is characterized by small sub-micron particles of Cu located at alumina grain boundaries. The particles are surrounded by glass, which exists at the boundaries. In some regions Cu particles at the grain boundaries were much smaller than those shown in Fig. 5. Fig. 6 presents bright-field micrographs of nano-sized particles of Cu located in the glass at the alumina grain boundaries and triple junctions. These particles are in the form of small dendrites. These results indicate that during the laser treatment Cu is transported to the base region of the melt-pool, most probably in the liquid state [9].



Fig. 5. TEM micrograph of the heat-treated alumina near the melt pool. A Cu particle is located at a grain boundary (laser treatment in air).

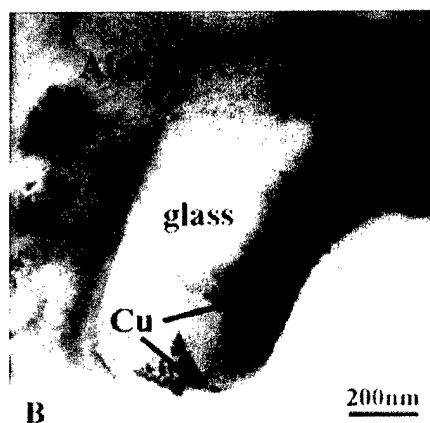
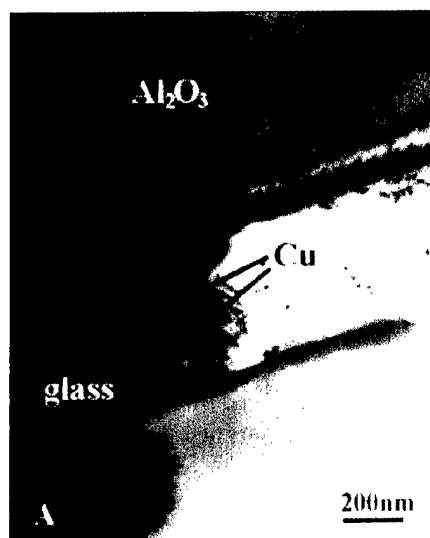


Fig. 6. Bright-field TEM micrographs of nano-Cu-dendrites located in the glass (laser treatment in air): (A) at grain boundaries; (B) at triple junctions.

3.2. Laser treatment in argon

Laser treatments in argon at lower scan speeds resulted in a melted zone which consists of two regions: a zone of melted copper and a zone of melted alumina (Fig. 7).

A chemical compound between Cu and Al_2O_3 at the interface between the two zones is shown in Fig. 8. The compound located in this region is CuAl_2O_4 , which was determined by EDS in SEM. The width of the CuAl_2O_4 region is $12\text{--}14\text{ }\mu\text{m}$. TEM of the alumina located directly below the CuAl_2O_4 compound also showed the presence of Cu. However, in these regions the Cu grains are adjacent to pockets of glass (Fig. 9).

3.3. Possible reactions at the metal-ceramic interface

The reaction of copper and cuprous oxide is a practical means to wet alumina. It is used to manufacture

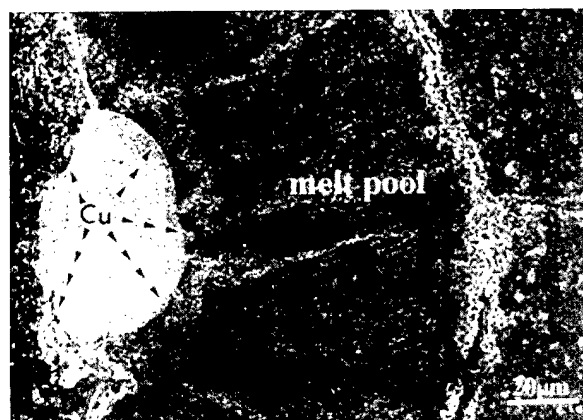


Fig. 7. SEM image of the Cu/alumina interface (laser treatment under argon).

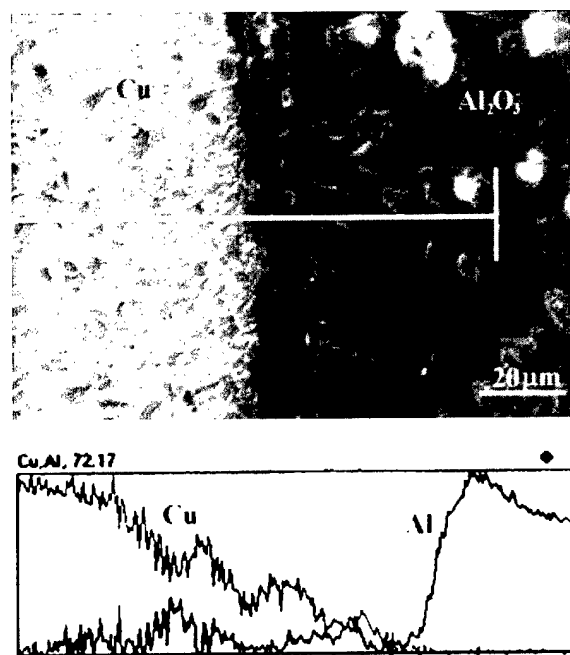


Fig. 8. SEM image of the Cu/alumina interface (laser treatment in argon).

copper-bonded alumina substrates for power semiconductor applications. The bonding of copper to alumina is carried out at a temperature slightly above the eutectic temperature, 1065°C, in a properly controlled oxygen-containing atmosphere. Oxygen-rich liquid copper is known to form a CuAlO₂ layer when it is in contact with alumina [5]. A CuAlO₂ phase is known to form between oxygenated liquid copper and alumina by the reaction:



It is known from the literature that the adhesion at the copper–alumina interface varies reversibly with the concentration of the oxygen at the interface, and there

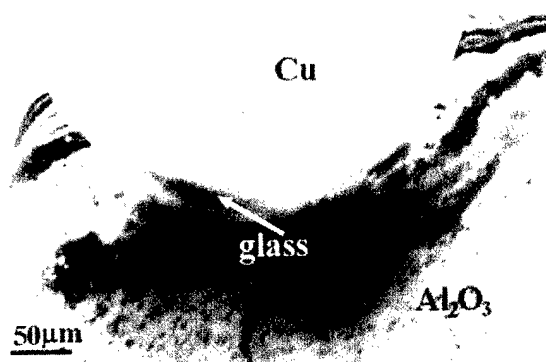
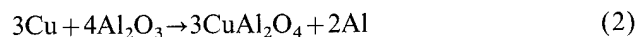


Fig. 9. Bright-field TEM micrograph of the Cu grains (laser treatment in argon).

is a critical oxygen concentration above which the bond energy shows no further increase [3,4].

The critical value corresponds to the solubility limit at 850°C, and is about one-tenth of the solubility limit for the eutectic temperature, according to the latest Cu–O phase diagrams [5].

The absence of the CuAlO₂ phase after the laser treatment can be attributed to the formation of a very thin oxide layer on the molten Cu which hinders the diffusion of Al into the Cu. Hence the very short laser treatment, compared with the exposure to 930°C for 20 h required to form this phase during the hear treatment, is insufficient to form CuAlO₂. For samples processed in Ar the CuAl₂O₄ should form according to reaction (2)



The absence of Cu oxide on the Cu particles, which are in contact with the Al₂O₃, enables this reaction to form CuAl₂O₄ even during short interaction times characteristic of the laser treatment. The presence of Al in the resolidified Cu and the CuAl₂O₄ layer in the samples treated under Ar confirms this reaction.

4. Conclusions

The characterization of the joints has resulted in a number of important conclusions.

- Sub-micron Cu particles form in the amorphous grain boundary glass at the base of the melt-pool. The presence of Cu at these grain boundaries would be expected to influence the mechanical properties of the ceramic substrate.
- No CuAlO₂ is formed during laser treatment in air due to an oxide layer formed on the copper particles.
- Heat treatments following the laser process result in

the formation of CuAlO_2 between the alumina and the Cu (laser treatments in air).

- In the case of laser treated alumina under argon, CuAl_2O_4 was formed due to good contact between the Cu and Al_2O_3 . Regions containing small Cu particles adjacent to pockets of glass were found.

Acknowledgements

Dr. L. Shepeleva and Dr. B. Medres acknowledge the Center for Absorption in Science, Ministry of Immigrant Absorption State Israel for its financial support. This work was conducted with the support of a bi-national Israel–USA grant (BSF).

References

- [1] A.C.D. Chaklader, A.M. Armstrong, S.K. Misra, *J. Am. Ceram. Soc.* 51 (11) (1968) 630–633.
- [2] I.W. Donald, *J. Am. Ceram. Soc.* 60 (2) (1977) 89–90.
- [3] E.J. Gonzalez, K.P. Trumble, *J. Am. Ceram. Soc.* 79 (1) (1996) 114–120.
- [4] A. Amirfazli, D. Chatain, A.W. Neumann, *Colloids and Surfaces A (Physicochemical and Engineering Aspects)*, vol. 142, no. 2–3. The Russian Academy of Science, Moscow, 1998. pp. 183–188.
- [5] J.T. Klomp, *J. Am. Ceram. Soc.* 51 (9) (1972) 683–688.
- [6] B. Dewar, M. Nicholas, P.M. Scott, *J. Metal Sci.* 11 (1976) 1083–1090.
- [7] Y. Yoshino, T. Shibata, *J. Am. Ceram. Soc.* 75 (10) (1992) 2756–2760.
- [8] L. Shepeleva, B. Medres, W.D. Kaplan, M. Bamberger, *J. Laser Appl.* 11 (1) (1999) 38–41.
- [9] M. Bamberger, W.D. Kaplan, B. Medres, L. Shepeleva, *J. Laser Appl.* 10 (1998) 29–33.

Laser cladding of turbine blades

L. Shepeleva ^{a,*}, B. Medres ^a, W.D. Kaplan ^a, M. Bamberger ^a, A. Weisheit ^b

^a Department of Materials Engineering, TECHNION - Israel Institute of Technology, Technion City, 32000 Haifa, Israel

^b Institute für Werkstoffkunde und Werkstofftechnik, Agricolastraße 6, D-38678 Clausthal-Zellefeld, Germany

Abstract

A comparative study of two different techniques for the application of wear-resistant coatings for contact surfaces of shroud shelves of gas turbine engine blades (GTE) has been conducted. Wear-resistant coatings were applied on In713 by laser cladding with direct injection of the cladding powder into the melt pool. Laser cladding was conducted with a TRUMPF-2500, CW-CO₂ laser. The laser cladding was compared with commercially available plasma cladding with wire. Both plasma and laser clad zones were characterized by optical and scanning electron microscopy. It was found that the laser clad zone has a higher microhardness value (650–820 HV) compared with that of the plasma treated material (420–440 HV). This is a result of the significant reduction in grain size in the case of laser cladding. Unlike the plasma clad zones, the laser treated material is free of micropores and microcracks. © 2000 Elsevier Science S.A. All rights reserved.

Keywords: Laser cladding; Plasma cladding; Shroud shelf; Turbine blade

1. Introduction

The operational stability of turbine blades with shroud shelves depends on the wear resistance of the shroud shelves. [1,2]. It is known that during operation, as a result of dynamic contact as well as vibration and heat, the contact surfaces of shroud shelves undergo intensive wear. This leads to the formation of a gap between them and, as a result, increases the amplitude of alternating loads on the blade critical cross-section [2]. Thus, the wear of the blade shroud shelves' contact area determines the overall service life of the GTE [2,3]. To increase the service life of turbine blades with shroud shelves, plasma cladding of cobalt stellites supplied in the form of wire is used. These materials exhibit sufficiently high tribological properties [1,3].

In spite of a significant increase in wear resistance for clad blades (compared with non-clad blades) plasma cladding technology has some essential drawbacks:

- plasma cladding is performed manually, and does not provide the required uniformity of the coating;
- the layer contains cracks and pores both at the layer–substrate interface and in its entire volume;
- the plasma clad layer has a sharp boundary with

the substrate, where high stress concentration leads to the formation of cracks and pores under loading; and

- plasma cladding increases the hardness of the coating by 20–40 HV above that of the substrate.

These limitations can be overcome by applying coating techniques, such as laser cladding [3–5].

This paper presents a comparison between the microstructure and properties of plasma cladding in which the clad material is supplied via a wire, and laser cladding with direct injection of clad powder into the melt pool.

2. Experimental methods

Commercially available blades with plasma cladding were investigated, as well as wear-resistant coatings produced by laser cladding, using the method of direct injection of cladding powder into the melt pool. All tests were performed with alloy In713.

Laser cladding was conducted with a TRUMPF-2500 CW-CO₂ laser operated at a laser power density in the range of 2.8×10^4 – 3.6×10^4 W/cm² and scanning velocities of 0.5–0.7 cm/s. The powder feed rate was 0.015–0.02 g/s. Both plasma and laser cladding zones were

* Corresponding author.

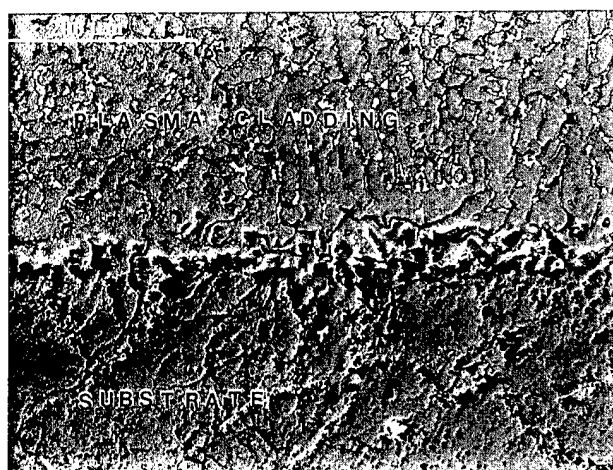


Fig. 1. SEM micrograph of the plasma cladded zone and its interface with the substrate.

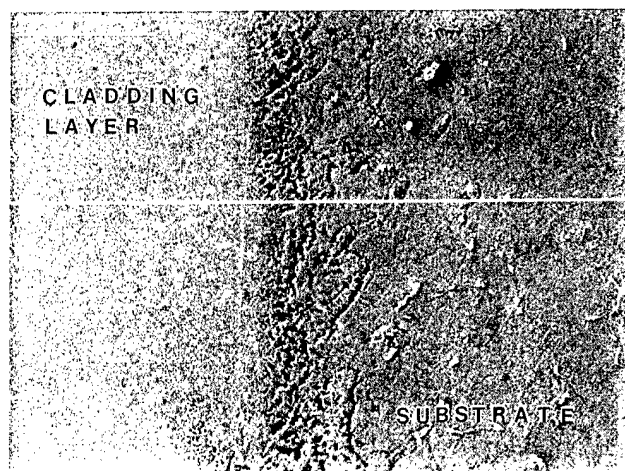
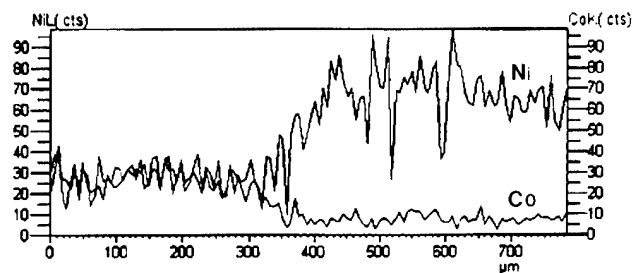


Fig. 2. EDS line-scan analysis of the major elemental distribution across the plasma clad–substrate interface

characterized by optical and scanning electron microscopy (SEM).

3. Results and discussion

3.1. Plasma cladding zone

The plasma-cladding zone and its interface with the substrate are shown in Fig. 1. In this figure one can see

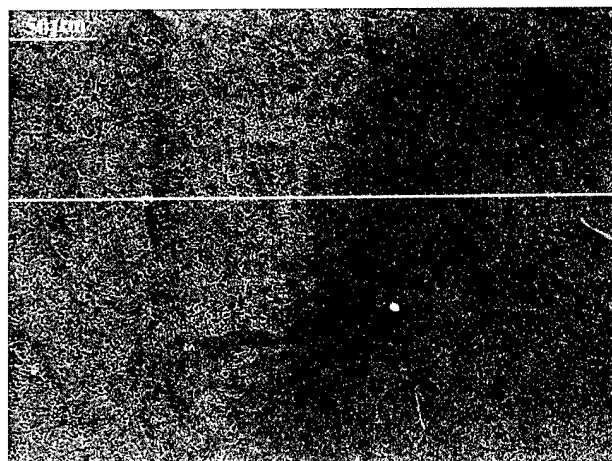
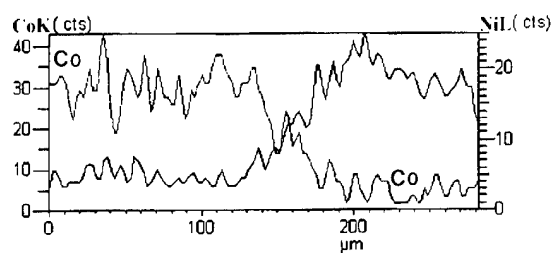
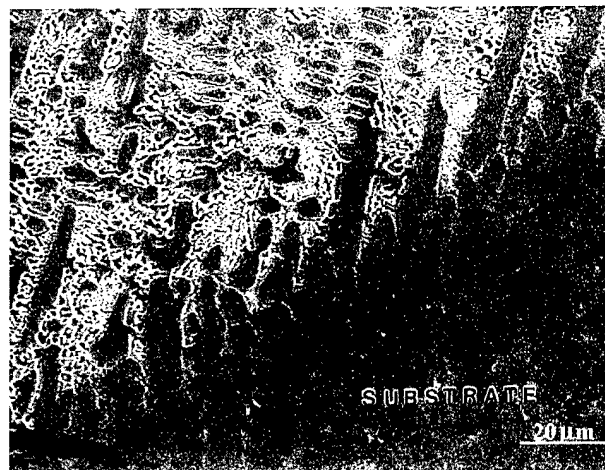


Fig. 3. (a) SEM micrograph of a laser cladded substrate region. (b) EDS line-scan analysis of the major elemental distribution across the laser clad–substrate interface.

that the plasma cladded zone is characterized by the presence of microcracks and pores, which might adversely affect the wear resistance of contact surfaces of blades [2]. The low content of Ni, which originates from the substrate, in the cladding is evident in Fig. 2. From Figs. 1 and 2 it can be concluded that the boundary between the clad and substrate is very sharp and contains a large quantity of microcracks and pores. The sharp boundary can be correlated with the processing characteristics — e.g. the relative size of the plasma-heating source compared with that of the wire and the

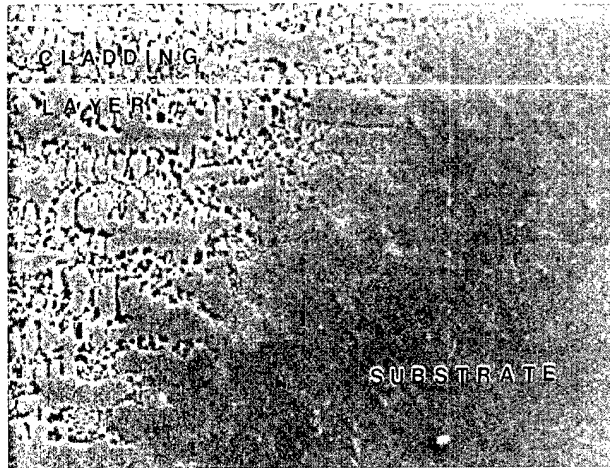


Fig. 4. EDS line-scan analysis of concentration changes of basic elements of a laser clad layer and substrate in interdendritic regions.

substrate. Therefore, the melted wire, which spreads on the unmelted surface of the substrate, is not sufficiently overheated to ensure mixing and/or mutual dissolution of elements from both components.

This is reflected in the concentration profiles seen in Fig. 2. The porosity seen in Fig. 1 results from gas entrapped in the high viscosity melt [6]. The microhardness of the plasma clad layer is 420–440 HV. The microhardness of the substrate is 400 HV.

3.2. Laser clad layer

The laser clad layer has a uniform microstructure with a smooth boundary between the clad layer and the substrate (Fig. 3(a) and (b)).

The crack- and pore-free interface between the laser clad layer and the substrate, at higher magnification, and the enrichment of the cladding with Ni from the substrate are evident in Fig. 4. The formation of a smooth interface by laser cladding can be explained by the fact that the laser beam causes significant heating of the injected powder and essential overheating of the molten surface of the substrate, and hence the hot particles melt on hitting the melt bath. The high temperatures prevail in the melt and the gradient in the surface tension throughout this melt pool result in dissolution of constituents from the substrate, and their distribution

Table 1

The microhardness at various locations in the laser clad blades by various power densities

Sample group	Laser treatment conditions $\times 10^4$ (W/cm ²)	Microhardness (HV)		
		Base	Boundary	Clad layer
1	3.6	400	572	824
2	3.2	400	522	680–724
3	2.8	400	464	542

in the melt due to the intensive mixing. The low viscosity of the melt bath and the directional dendritic growth, which nucleated on the cold substrate, result in the crack- and pore-free interface [6] seen in Fig. 4. Table 1 presents the microhardness at various locations in the laser treated blades by various power densities.

The microhardness for both interface and laser clad zones increase as a function of laser radiation power density. The laser clad zones reveal a significant grain refinement (Fig. 5) which raises their microhardness values.

4. Conclusions

1. Laser cladding of the contact surfaces of shroud shelves by direct powder injection provides a cladding layer with a higher hardness than plasma treated surfaces.
2. Laser clad zones, unlike the plasma treated surfaces, are free of microcracks and pores.
3. The laser clad layer has a smooth interface with the substrate, which prevents stress concentration at the clad-substrate interface during operation.

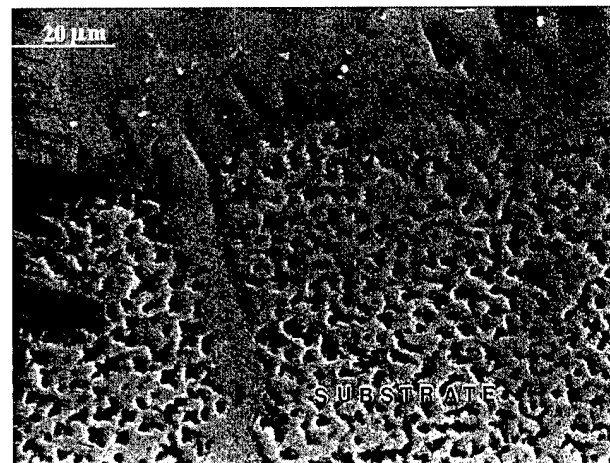


Fig. 5. SEM micrograph of a laser clad-substrate interface.

Acknowledgement

Dr. B. Medres and Dr. L. Shepeleva acknowledge the Center for Absorption in Science, Ministry of Immigrant Absorption State, Israel for its financial support.

References

- [1] S.T. Kyshkin, A.V. Logunov et al., Scientific background for alloying of heat-resistant nickel alloys, *Aviazionnie Materialy* 00 (1987) 387.
- [2] A.I. Cosov, B.S. Medres et al., Laser alloying of contact surfaces of GTE blades, *Aviazionaya Promishlennost Mag.* 2 (1984) 8.
- [3] A.A. Soloviov, B.S. Medres et al., Laser alloying of GTE blades made of EP-109 alloy, Reports of 1st All-Union Conference on Laser Metallurgy and Laser-plasma Treatment, USSR, IMET, Academy of Sciences of the USSR, Moscow, 1984, p. 98.
- [4] W.M. Steen, *Laser Material Processing*, Springer-Verlag, 1991, p. 266.
- [5] M. Bamberger, W.D Kaplan, B. Medres, L. Shepeleva, Calculation of processes parameters for laser alloying and cladding, *J. Laser Applications* 10 (1) (1998) 29–33.
- [6] M. Boaz, M. Bamberger, G. Revesz, Laser alloying of a plasma sprayed WC/Co layer to enhance wear properties, *Surf. Coat. Technol.* 42 (1990) 175–186.



ELSEVIER

Surface and Coatings Technology 125 (2000) 49–56

**SURFACE
& COATINGS
TECHNOLOGY**

www.elsevier.nl/locate/surfcoat

Physical foundations for surface treatment of materials with low energy, high current electron beams

D.I. Proskurovsky, V.P. Rotshtein *, G.E. Ozur, Yu.F. Ivanov, A.B. Markov

High Current Electronics Institute, SD of RAS, 4, Akademicheskoy Ave., Tomsk 634055, Russia

Abstract

The paper presents a review of original investigations on the surface modification of metallic materials with low energy (up to 40 keV), high current (up to 40 J/cm²) electron beams of microsecond duration. Based on materials research and on simulations of temperature and stress fields, the regularities and mechanisms for the changes in the defect structure and in the strain–stress state of pure metals (Fe) on pulsed heating are considered. The peculiarities of the formation of non-equilibrium structure-phase states and graded structures on pulsed melting of film–substrate (Fe–Ta, Al–Si, and Al–C) systems have been studied. For a broad spectrum of structural and tool materials (steels, aluminum and titanium alloys, hard alloys) it has been shown that the most pronounced changes in the structure-phase state occur in the near-surface layer quenched from the liquid state, where the velocity of the crystallization front reaches its maximum. In this layer, the second phases are partially or completely dissolved, and oversaturated solid solutions and nanosized second-phase segregates are formed. This substantially improves the electrochemical and strength properties of the surface layer. It has been established that the action of dynamic stresses has the result that the modified layer with enhanced strength properties is substantially thicker than the heat-affected zone. © 2000 Elsevier Science S.A. All rights reserved.

Keywords: Pulsed electron beams; Surface thermal treatment

1. Introduction

In the last few decades, new methods have been developed for surface modification of metallic materials which are based on the use of intense pulsed laser [1], electron [1–5] and ion beams [6,7]. Irradiation induces dynamic temperature fields in the surface layers giving rise to superfast heating, melting and evaporation, followed by superfast solidification of the material. The dynamic stress fields formed cause intense deformation processes in the material. As a result, metastable structure-phase states may appear in the surface layers, which are capable of providing improved physical, chemical and strength properties of the material unattainable with conventional surface treatment techniques.

We began our studies on the action of pulsed electron beams on metals in the mid 1970s [8]. In the 1980s, a series of experiments was performed by Follstaedt and Knapp [9,10] on pulsed melting of pure materials and

film-substrate systems, and by Demidov et al.[2] on surface treatment of iron-base alloys. In recent years, considerable success has been achieved in the creation of sources of low energy high current electron beams (LEHCEBs) [3,4]. The sources contain an electron gun with an explosive emission cathode and a plasma anode, placed in a guide magnetic field. The LEHCEB operating parameters are as follows: electron energy 0.5–40 keV; pulse duration 0.5–5 μs; energy density 0.5–40 J/cm²; beam cross-section area 10–50 cm²; and pulse repetition rate 0.2 Hz. These sources, because of their simplicity and reliability, have essential advantages over the pulsed lasers and high power ion beam sources used for surface treatment of materials. This paper reviews the results of original studies of the features and mechanisms of the LEHCEB modification of the structure and properties of a broad spectrum of metallic materials.

2. Modification of the structure and properties of metallic materials

The major factors which determine the state and properties of a material in the beam-affected zone are

* Corresponding author. Tel.: +7-3822-259709;

fax: +7-3822-259410.

E-mail address: rvp@lve.hcei.tsc.ru (V.P. Rotshtein)

the non-stationary temperature fields appearing in the surface layers as a result of absorption of the beam energy, and the stress fields caused by pulsed heating of the surface. The techniques and results of the calculations of temperature fields and stress waves are described elsewhere [4]. We used the results of these calculations in interpreting experimental data.

2.1. Pure metals

It has been shown that pulsed heating of pure ($\sim 10^{-3}$ at.% C) recrystallized iron near the melting threshold (~ 20 keV, $0.8 \mu\text{s}$, $2\text{--}2.5 \text{ J/cm}^2$) leads to plastic deformation of the surface layer and the formation of an extended ($\sim 100 \mu\text{m}$) non-uniformly hardened zone with a microhardness maximum located at a depth of $\sim 20 \mu\text{m}$ [11]. The microhardness (Vickers) profile $H_\mu(x)$ follows the dislocation density depth distribution $\rho(x)$ (Fig. 1).

In the surface layer of thickness up to $\sim 5 \mu\text{m}$, plastic deformation is accompanied by primary recrystallization with the recrystallization nuclei ($2\text{--}5 \mu\text{m}$) appearing at grain boundaries. From thermal calculations and stress field estimates, it follows that the non-monotonic depth change in the material substructure and microhardness are related to the plastic deformation caused by compressing (in the surface plane) quasi-static thermoelastic stresses and to the recrystallization processes caused by the heat transfer into the material bulk. The stress wave, because of its low amplitude [4], has a minor effect on the material structure and properties.

The character of the bending of thin ($\sim 0.5 \text{ mm}$) specimens have confirmed that compressive stresses acted in the surface plane in the process of irradiation. Estimates based on measuring plastic microstrain curves have shown [12] that on single irradiation these resulting stresses are as high as $\sim 400 \text{ MPa}$, i.e. far exceeding the dynamic yield limit for Fe.

As the pulse is completed, the near-surface layer is cooled and then compressed; therefore, residual tensile stresses are formed here. Measurements have shown that for the number of pulses $N=1\text{--}50$ these stresses

make up $40\text{--}80 \text{ MPa}$, i.e. they are about an order of magnitude lower than the compressive stresses acting on irradiation. The residual stresses have a maximum at a depth of $\sim 5 \mu\text{m}$ and are effective within the heat affected zone (HAZ) whose thickness is $\sim 20 \mu\text{m}$. The existence of a maximum agrees with the data on recrystallization in the surface layer of $\sim 5 \mu\text{m}$. The monotonic decrease in the residual stresses beyond the recrystallized layer correlates with the $H_\mu(x)$ and $\rho(x)$ distributions (see Fig. 1).

As the melting threshold is achieved, the dominant effect on the microstructure of the surface layer is exerted by the processes of rapid crystallization from melt and plastic deformation in dynamic stress fields. It follows from thermal calculations that as the energy density is increased in the range $E_s = 2.3\text{--}5.2 \text{ J/cm}^2$, the melt thickness and lifetime increase in the ranges $0.7\text{--}2.5 \mu\text{m}$ and $0.5\text{--}3 \mu\text{s}$, respectively. The increase in melt thickness decreases the melt cooling rate from $\sim 10^{10}$ to $\sim 10^9 \text{ K/s}$ and the crystallization front velocity from ~ 5 to $\sim 2 \text{ m/s}$.

An analysis of the spectra of positron lifetimes (slow positron annihilation spectroscopy) in the surface layer of recrystallized iron ($\sim 10^{-2}\%$ C) has shown that as a result of quenching from melt vacancy-type defects, mainly, vacancy clusters (divacancies and trivacancies) are formed [13]. Fig. 2 presents the S parameter of Doppler broadening of the annihilation peak as a function of positron energy for specimens irradiated with various E_s values (S parameter defined as the ratio of the central area to the total area of the annihilation peak). The increase of the S parameter is directly correlated with the increase of the vacancy-like defect concentration. Thus, the dependencies given in Fig. 2 correspond to the vacancy concentration profiles. It can be seen that quenching from melt increases the defect concentration against the initial state. The dependence of the degree of defectiveness of this layer (at depths $x \geq 500 \text{ nm}$) on E_s is represented by a curve with a maximum at $E_s = 4.2 \text{ J/cm}^2$. This regularity can be

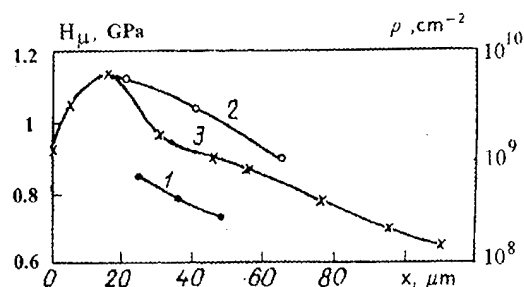


Fig. 1. Depth distribution of dislocation density (1, 2) and microhardness (3) for iron after irradiation (2.2 J/cm^2 , $0.8 \mu\text{s}$): Pulse number: $N=5$ (1,3); $N=300$ (2). The Vickers diamond pyramid load was 0.2 N .

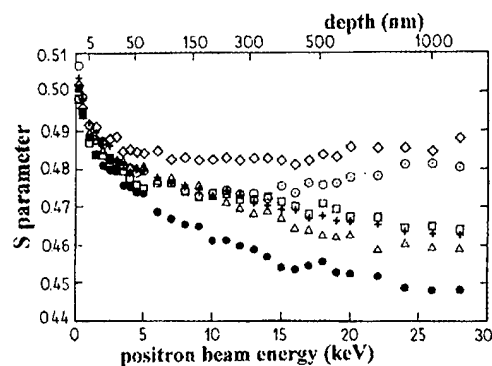


Fig. 2. Depth distributions of the S parameter for iron before and after pulsed melting: untreated (●); 2.3 J/cm^2 (Δ, +); 4.2 J/cm^2 (◇, ○); 5.2 J/cm^2 (□).

accounted for as follows. The concentration of quench vacancies is determined by their nucleation at the crystallization front and recombination at the dislocations formed under the action of dynamic stress fields. As E_s is increased and correspondingly increases the melt thickness and lifetime, the vacancy concentration decreases. The dependence of the dislocation density on E_s has the same character. This is associated with the decrease in the temperature gradients, with an increase in the thickness of the energy release zone and, hence, with the reduction of the quasi-static stresses. For low E_s (2.3 J/cm²), a significant fraction of non-equilibrium vacancies may recombine at dislocations since the dislocation density is high. As E_s is increased, the probability of recombination falls because of the decrease in dislocation density. Thus, there exists a critical energy density at which the concentration of vacancies is a maximum.

The $H_\mu(x)$ distribution is shown in Fig. 3. An increase in microhardness is accompanied by an increase in the wear resistance of the surface layer [14]. As follows from thermal calculations, the near-surface hardened layers are formed on quenching from the liquid state. The increased microhardness in these layers is due to strain hardening under the action of quasi-static stresses formed at the stage of cooling after the completion of crystallization. This is evidenced by the presence of slipping marks and by the formation of a dislocation substructure [9]. The amplitude of the stress wave, as for the pre-melting irradiation mode, is low. Moreover, within the melt lifetime this wave propagates over a considerable distance from the surface and, therefore, it has only a slight effect on the formation of the affected zone. The intricate character of the hardening at 5.2 J/cm² might be associated with the combined effect exerted on the material microstructure by the deformation processes in the HAZ and by the processes of redistribution of dislocations and recrystallization in the near-surface layers where the temperature reaches its maximum.

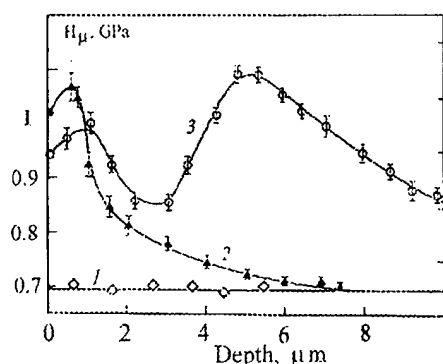


Fig. 3. Depth distributions of microhardness for iron: (1) untreated, (2) 3.3 J/cm², (3) 5.2 J/cm². The Vickers diamond pyramid load was 0.002 N [13].

2.2. Microcraters

On irradiation of previously deformed metals, the uniform melting of the near-surface layer is preceded not by plastic deformation but by the formation on the surface of microcraters of size 10^{-4} – 10^{-3} cm [15]. Crater formation is also observed on irradiation of almost all metallic alloys. The microcrater size and distribution density depend on the material purity, the grain size, etc., and on the beam parameters. As the melting threshold is achieved, microcraters show up as well on the background of the complicated relief of the molten surface. On going to the evaporation mode, microcraters are, as a rule, not observed. It should be noted that crater formation is also observed on metals and alloys treated with pulsed ($\sim 10^{-7}$ s) laser and ion beams [16].

The specific symmetry of the microcraters testifies to a local melting of the metal. A reason for the local melting may be the irregularity of the microstructure in the near-surface layer and/or the discrete cross-sectional structure of the electron beam (presence of individual microjets with an elevated current density). Experiments have shown [16,17] that the dominant reason is the first, namely, the presence of microirregularities of the chemical and phase composition which are responsible for local melting at temperatures below the melting threshold for the matrix. For instance, in copper these impurities are insoluble Pb and Bi which form eutectics at 326 and 270°C as well as O and S present as intermediate phases of Cu₂O and Cu₂S which enter into the eutectics, whose thermal conductivity is more than two orders of magnitude lower than that of copper.

The consequences of crater formation are the increased roughness of the surface and the formation in the near-surface layer of local regions with highly non-uniform structure-phase and strain-stress states. Obviously, these changes should deteriorate the tribotechnical characteristics and impair the strength properties and corrosion resistance of the material. This makes the search for efficient methods for combatting this unwanted effect an urgent problem.

2.3. Film–substrate systems

The pulsed melting of these systems is of considerable interest since it makes it possible to form metastable states, amorphous states included, such that the thickness of the modified layer may be about an order of magnitude greater than that achievable on high-dose ion implantation [1,9,10]. Detailed investigations were performed for single layer (Ta–Fe) and multilayer (Al–Si and Al–C) systems. These systems are characterized by a limited solubility of the components in the solid state, and the system Al–C is inconsistent in the liquid state.

On irradiation of the Ta–Fe system (0.8–1.5 μs and 1.5–6 J/cm^2), as shown by thermal calculations, the presence of a refractory Ta film (100 nm) increases severalfold the thickness and lifetime of the molten layer of the substrate (Fe) and decreases the velocity of the crystallization front as compared to pure Fe. With the RBS and Auger spectroscopy methods it has been shown that the liquid phase component mixing has the result that the thickness of the Ta-doped layer is two or three times greater than that of the film. Increasing beam energy density favors the mixing and increases the thickness of the mixed layer. The effective coefficient of the liquid phase diffusion of Ta into Fe is $\sim 5 \times 10^{-5} \text{ cm}^2/\text{s}$. With transmission electron microscopy (TEM) it has been established that the structure formed as a result of quick quenching from the melt has a complex phase composition and is inhomogeneous in depth (Fig. 4). In the close vicinity of the surface (at a depth of $\sim 0.2 \mu\text{m}$), particles ($\leq 0.3 \mu\text{m}$) of undissolved Ta, the Fe–Ta amorphous phase and dispersed segregates of the intermetallic compound Fe_2Ta are observed. The deeper layers consist predominantly of Fe_2Ta particles and $\text{Fe}(\text{Ta})$ solid solution grains with a high dislocation density. The layer-by-layer disposition of the structures is due to the decrease in Ta concentration with depth, resulting from Ta diffusion in the liquid phase, and to the difference in the cooling rates at the surface and in deeper layers of the melt. In the process of thermal cycling realized on multiple pulsed heating, the presence of the refractory Ta film has the result that, in the near-surface layer, a microstructure is formed with the dislocation density and long range stresses elevated compared to pure iron [17].

In the original state, the multilayer (Al/Si/Al/Si/Al/Si/Al) system on an Al substrate consists of four polycrystalline Al layers ($\sim 350 \text{ nm}$) separated with amorphous silicon interlayers ($\sim 50 \text{ nm}$). According to Auger electron spectroscopy data carbon (up to 5 at.%) is present at the Al–Si interfaces. On irradiation in the

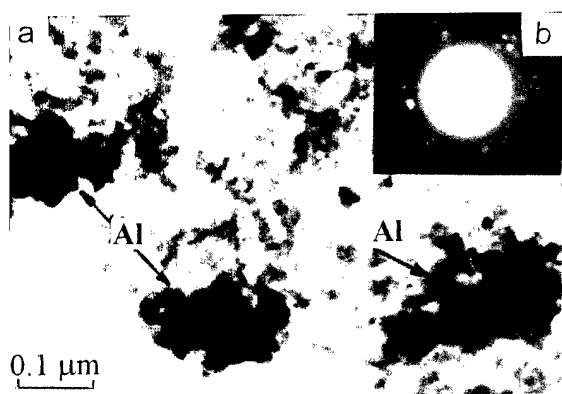


Fig. 4. Microstructure of a multilayer (Al/Si/Al/Si/Al/Si/Al) system on an Al substrate after pulse melting of Al: (a) bright-field image, (b) diffraction pattern.

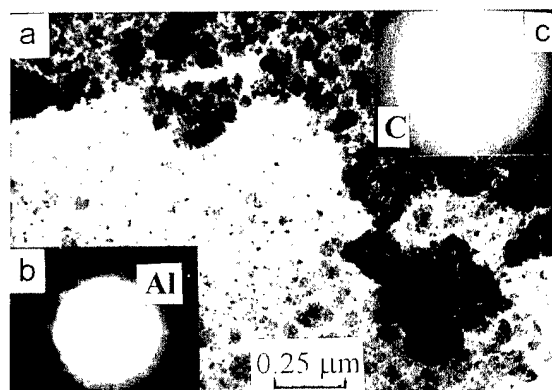


Fig. 5. Microstructure of a multilayer (Al/C/Al/C) system on an Al substrate after pulse melting of Al: (a) bright-field image; (b) and (c) diffraction patterns for top and bottom parts of (a).

mode of melting of the Al layers preceding the melting threshold for Si (2.5 μs , 2.3–3.1 J/cm^2), the multilayered texture is retained: however, the concentration of Si in the Al layers increases abruptly due to the diffusion of Si atoms into the liquid Al. The superfaster crystallization of the Si-enriched Al layers from the liquid state results in the formation of nanosized ($\sim 30 \text{ nm}$) Al crystallites combined in complexes $\sim 100 \text{ nm}$ in size. At the Al crystallite boundaries, nanosized particles of the second phase $\text{Al}_4\text{Si}_2\text{C}_5$ are segregated (Fig. 4). In the amorphous Si–Al–C interlayers, partial crystallization with the formation of nanosized Si particles takes place. As the melting threshold for Si is achieved ($E_s \geq 4 \text{ J}/\text{cm}^2$), the efficiency of mixing decreases abruptly because of ablation of the coating.

The unaffected (Al/C/Al/C) system on an Al substrate consists of alternating two polycrystalline Al layers (~ 700 and $\sim 500 \text{ nm}$) and two amorphous carbon layers (~ 200 and $\sim 100 \text{ nm}$). On irradiation in the mode of melting of the Al layers (2.5 μs , 1.8 J/cm^2), the following structures are formed: coarse (up to $\sim 20 \mu\text{m}$) molten-off Al particles; regions consisting of submicron Al grains with nanosized (2–3 nm) particles of cubic lattice carbon segregated along the grain boundaries; regions consisting of 50–100 nm cells of amorphous carbon with nanosized (3–5 nm) Al segregates (major type structures, Fig. 5), and, finally, amorphous carbon particles (a few micrometers) formed on destruction of the original carbon layers. The formation of these structures points to the stratification of Al and C on pulsed melting under the given conditions. As distinct from the previous system, the second phases (Al_4C_3) are absent, which may be related to the insufficiently high temperature ($< 1700^\circ\text{C}$) and short lifetime ($\sim 10^{-6} \text{ s}$) of the Al melt.

2.4. Carbon steels

Let us consider the features of the hardening on the example of Steel 45 (0.45% C). In doing this, we also

use the results we have obtained with electron beams whose duration was longer than that of the LEHCEBs. Experiments have shown that with $\tau \geq 10 \mu\text{s}$ and $E_s \geq 10 \text{ J/cm}^2$ sufficient to melt a surface layer of thickness $\geq 5 \mu\text{m}$, irrespective of the original state of the steel, a quench structure (martensite and residual austenite) with enhanced microhardness and wear resistance is formed in this layer. Metallographically, this structure shows up as a weakly etchable ('white') layer. In the layer heated to a temperature over the quench temperature, the microhardness decreases gradually with distance from the surface. The highest degree of hardening is achieved on irradiation of the pre-quenched steel.

As the pulse duration is shortened to $\sim 1 \mu\text{s}$ (LEHCEB), the martensitic transformation of the steel on quenching from the liquid state and, hence, efficient hardening of the surface layer are realized only at energy densities such that the melt thickness is over the critical value equal to $\sim 5 \text{ mm}$. This is related to the existence of a minimum critical grain size for the original phase ($\sim 1 \mu\text{m}$) necessary for the nucleation of martensitic crystals [18]. This criterion is in good agreement with the data on the effect of the grain size on the temperature at which martensitic transformation begins, M_s , available in the literature and allows an interpretation of both our results and the data on laser treatment of steels available in the literature.

For $\tau \sim 1 \mu\text{s}$ and $E_s = 2.5 \text{ J/cm}^2$, when the melt thickness is noticeably below the critical value, a steel originally having a ferritic–pearlitic structure is not hardened for the above reason. As for the pre-quenched steel, its hardening is substantially different in character. In this case, an extended ($\sim 200 \mu\text{m}$) hardened zone with two microhardness maxima is formed (Fig. 6) with the microhardness reaching abnormally high values (up to $\sim 16 \text{ GPa}$) on multiple irradiation [3,4,19].

As the number of pulses is increased, accumulation of the γ -phase occurs in the HAZ ($\sim 15 \mu\text{m}$), which is associated with the increase in carbon concentration.

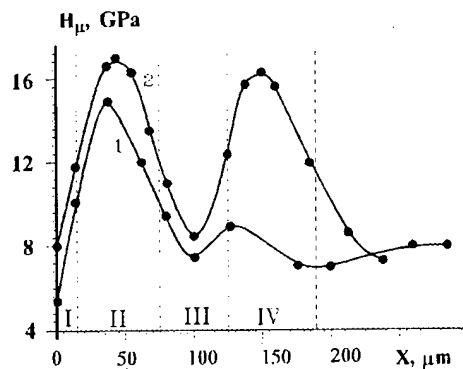


Fig. 6. Depth distributions of microhardness for pre-quenched carbon steel 45 after irradiation (2.5 J/cm^2 , $0.8 \mu\text{s}$): (1) pulse number $N=1$; (2) $N=300$. For untreated steel $H_v=7.5 \text{ GPa}$. The Vickers diamond pyramid load was 0.5 N .

Layer-by-layer TEM examination has shown that a graded structure is formed in the HAZ, and in the near-surface layer quenched from melt a nanocrystalline structure consisting of grains of α - and γ -phases and containing no martensite crystals is formed. The formation of nanostructures correlates with the fact that the rate of quenching from the melt and the velocity of the crystallization front reach their maxima ($\sim 10^{10} \text{ K/s}$ and $\sim 5 \text{ m/s}$ respectively) at the surface.

At the microhardness maxima located beyond the HAZ, fragmentation and twinning of the original martensite crystals and segregation of dispersed cementite particles are observed. These effects may be related to the action of stress waves and/or quasi-static stresses. To eliminate the quasi-static stresses, a $10 \mu\text{m}$ thick Ta foil was pasted on the surface. After irradiation of this three-layer structure, the character of hardening did not change [15]. It follows that the formation of the hardened layers is related to the action on martensite of low amplitude cyclic stress waves. A feature of these waves, as distinct from ordinary bipolar waves formed under the action nanosecond electron beams, is that the stress changes its sign several time [4], i.e. the loading is quasi-periodic. With this type of loading, the dominant role in hardening is played by the carbon present in the martensitic structure. As distinct from the original ferritic–pearlitic structure, the carbon in the martensite is in a weakly bound state (mainly, at dislocations). Therefore, even at low amplitudes of the stress wave, it is prone to diffusion, segregation in some places and, eventually, to the formation of dispersed segregates of cementite.

On irradiation of previously quenched structural and tool steels, their hardening is similar in character to that described above. Testing has shown that irradiation increases about twofold the operating life of drills, cutters and other tools subjected to standard hardening thermal treatment, and this correlates with the increase in microhardness.

2.5. Stainless steels

For type 304 austenitic steel it has been shown [20] that multiple pulsed melting produced with the use of an LEHCEB is accompanied by a smoothing of the surface microrelief and substantially enhances the corrosion resistance of the material. A more detailed investigation using samples of Steel 440 A (Fe-0.65 C-16.6 Cr) and Steel 304 (Fe-0.04 C-18.3 Cr-8.5 Ni) have shown that on pulsed melting, in the near-surface layer of thickness $0.2 \mu\text{m}$, the concentration of chromium increases due to its liquid phase diffusion from the deeper layers of the melt to the carbonized surface. Depending on the energy density and, hence, on the conditions for crystallization, the original particles of second phases (carbides and intermetallic compounds)

dissolve in this layer partially or completely. Fast crystallization of the liquid phase enriched with chromium and carbon has the result that the matrix phase grains become much smaller, namely, a non-disoriented nanosized (up to 100 nm) structure is formed in Steel 440A and a submicron ($\sim 0.5 \mu\text{m}$) structure in Steel 304. The stability of this structure is due to the presence of disperse segregates of second phases at the intraphase boundaries [4].

Corrosion tests have shown that these structure–phase changes lead to significant (by 1–3 orders of magnitude) decrease in passivation current density, for a long time and to a substantially reduced tendency to pitting corrosion. This testifies to the formation of a strong passive film on the irradiated surface [4].

2.6. Aluminum alloys

Investigations were performed with specimens of type Al2024 (Al-4.3 Cu) and type Al6061 (Al-0.6 Si-0.7 Fe) alloys. For Al2024 alloy irradiated in the melting mode (melt thickness $\sim 7 \mu\text{m}$), complete dissolving of coarse ($\sim 1 \mu\text{m}$) particles takes place in the near-surface layer of thickness up to $\sim 0.4 \mu\text{m}$, and the second phase segregates become smaller as compared to the original state. For Al6061 alloy, a similar dispersion of second-phase particles is observed, but coarse inclusions are dissolved incompletely [4].

After irradiation of Al2024 alloy in a more intense mode (with the melt thickness $\sim 25 \mu\text{m}$), an ordered structure is formed as a result of the dissolving of second phase coarse particles, followed by the decay of the oversaturated solid solution. This structure consists of non-disoriented matrix phase grains of size 200–300 nm with nanosized CuAl_2 segregates coherently bound with the matrix and localized along the grain boundaries. Microcracks are also observed which can be related to the shrinkage of the molten surface layer on solidification. For Al6061 alloy irradiated under similar conditions, complete dissolving of all original second phase particles (nanosized segregates included) is observed. With that, an Al_2O_3 film uniform in thickness ($\sim 30 \text{ nm}$) is formed on the surface, while for the original specimens the thickness of such a film varies in the range from 5 to 40 nm. These two effects substantially enhance the corrosion resistance of the material which is evidenced by corrosion resistance measurements [4].

Irradiation of these alloys in both modes results in the formation of an extended ($\sim 400 \mu\text{m}$) zone non-uniformly hardened in depth, which shows enhanced wear resistance. This is accounted for by the formation of high strength quenched states in the near-surface layer and by the strain hardening of the material at larger depths under the action of stress fields.

2.7. Titanium alloys

Experiments were performed on specimens of BT8M (Ti-5.8 Al-3.7 Mo) and BT18Y (Ti-6.3 Al-4.5 Mo) alloys subjected to preliminary annealing at 920 and 940°C and aging at 550 and 600°C, respectively. It has been found [4] that pulsed melting makes it possible to clean the surface of oxygen and carbon impurities, to increase the aluminum content in the near-surface layer to 20%, to make the component distribution in this layer more uniform, and to reduce the surface roughness to $0.1 \mu\text{m}$. With that, however, the phase composition changes to some extent: tensile weak residual stresses are induced in the near-surface layer, and microcraters appear on the surface. When irradiating these materials in optimum modes, crater formation can be suppressed and the annealing following makes it possible to restore the original phase composition and to enhance substantially the operating properties of the materials, namely, the endurance limit by more than 20%, the cyclic durability by more than tenfold, the resistance to dust erosion at low loads by more than twofold, and the short term strength by up to 8%, with the plasticity also being substantially improved. With that, the surface microhardness and the heat resistance are retained at the original level.

The enhancement of the strength properties of the materials is related to the smoothing of the surface due to its melting, to the cleaning of the surface of impurities, and to the increase in aluminum content in the near-surface layer. Fractography has shown that on static loading, pulsed melting changes the fracture mechanism from intercrystallite, or quasi-viscous, to viscous. Under cyclic loading, the fracture of original specimens is initiated at the surface of sharp edges, while characteristic of irradiated specimens is subsurface nucleation of cracks. It is just this circumstance which determines the improvement of the fatigue properties of the irradiated specimens.

3. Hard alloys

It has been shown [4] that irradiation of cemented carbide inserts in the surface melting modes ($2.5 \mu\text{s}$, $1\text{--}7 \text{ J/cm}^2$) increases about threefold the wear resistance of the inserts at high cutting speed. TEM investigation of irradiated T15K6 (WC-15 TiC-6 Co) inserts has shown that in the near-surface layer ($\leq 1 \mu\text{m}$) a subgrain ($0.1\text{--}0.2 \mu\text{m}$) structure is formed in the binding phase, nanosized ($\sim 10 \text{ nm}$) particles of new carbide phases are segregated in the near-boundary regions, and the transformation $\alpha\text{-WC} \Rightarrow \text{WC}(\text{fcc})$ occurs in part. In the process of cutting, intense plastic deformation of the material takes place which is accompanied by annealing of defects in the near-surface contact zone. In unirradi-

ated tools, relaxation of stresses leads to the formation in the cobalt binder of a relatively depth-homogeneous dislocation structure with a low dislocation density, and to the formation of micropores at the interphase boundaries. In irradiated inserts, immediately beneath the wearing surface layer, a substructure is formed which is characterized by a high dislocation density in the cobalt and carbide (WC) phases and by the presence of microtwins in the carbide phase (Fig. 7(a)) and of nanosized second carbide segregates in the binder and at the interphase boundaries (Fig. 7(b)). It follows that the main reason for the enhancement of the wear resistance of the inserts is dispersion and grain boundary hardening of the cobalt binder on pulsed melting. Because of this, in the process of cutting, a dislocation structure stable to high thermomechanical loads is continuously being formed beneath the wearing surface. The stability of this structure is due to the fact that dislocations are fixed by the nanosized segregates formed in the process of cutting.

Experiments were performed [21] to study the action of an LEHCEB (2.5 μ s, 5–40 J/cm², 1–50 pulses) on a hard alloy of WC-30% Steel 110G13 (Fe-1.1 C-13 Mn). The binder had a γ -lattice (fcc) which is characterized, as distinct from cobalt, by an elevated structural instability in deformation. The experiments have shown that, beginning from ~ 40 J/cm² and $N \geq 3$, along with surface hardening, quasi-periodic hardening is observed throughout the thickness (up to 7 mm) of the specimen. The distance between the microhardness maxima is 0.25–1 mm with the microhardness reaching ~ 15 GPa (as against 7.5 GPa in the original state). Similar effects are observed in a carbon steel with martensitic structure irradiated with an LEHCEB (Fig. 6) and with a megavolt high current electron beam [15]. At the same time, in WC-Co hard alloys there are no changes in microhardness on LEHCEB irradiation, and this points to the dominant role of the binder in hardening.

Investigations have shown that the surface hardening is due to the formation on quenching from a melt of a

nanocrystalline structure consisting of particles of WC (fcc and hcp lattice) and of type $M_{23}C_6$ and M_7C_3 complex carbides and to the decrease in the fraction of the binder caused by its selective evaporation. The formation of hardened layers in the bulk is related to the increase in dislocation density and to the partial $\gamma \Rightarrow \alpha$ martensitic transformation in the binder, as well as to the increase in dislocation density and twinning in WC. The material structure in the layers located between the microhardness maxima is weakly distinct from the original one.

The reason for the spatial changes in microhardness is the action on the material of the stress wave formed due to the effect of thermoelasticity and the recoil pulse of the scattering material vapor. Estimates show that the amplitude of this wave is not over 200 MPa, which is far below the yield limit of the material. However, because of the effects similar to those realized in the Bridgeman chamber, the local stresses at the carbide–binder–carbide contact may be an order of magnitude or more greater than the stress wave amplitude. The results obtained suggest that to realize spatial hardening under the given conditions, it is necessary that the structure-phase state of the material (or some its phases) be unstable. In carbon steels and hard alloys with a structurally unstable binder, this state is attained by quenching.

The effect of irradiation with an LEHCEB (2.5 μ s, 3–5 J/cm², 5 pulses) on the microstructure and wear resistance of TiN coatings deposited by the PVD method on carbide (WC–TiC–TaC–Co) inserts is described elsewhere [22]. The lower level of E_s corresponded to the initial melting of the coating. The experiments have shown that, after irradiation, the coating is cracked because of the high intensity of tensile stresses formed at the stage of cooling. Notwithstanding this, the coating retains its good adhesion to the substrate. The stoichiometry and phase composition of the coating, except the surface itself, remain unchanged. However, the residual compressive stresses reduce to zero and the concen-

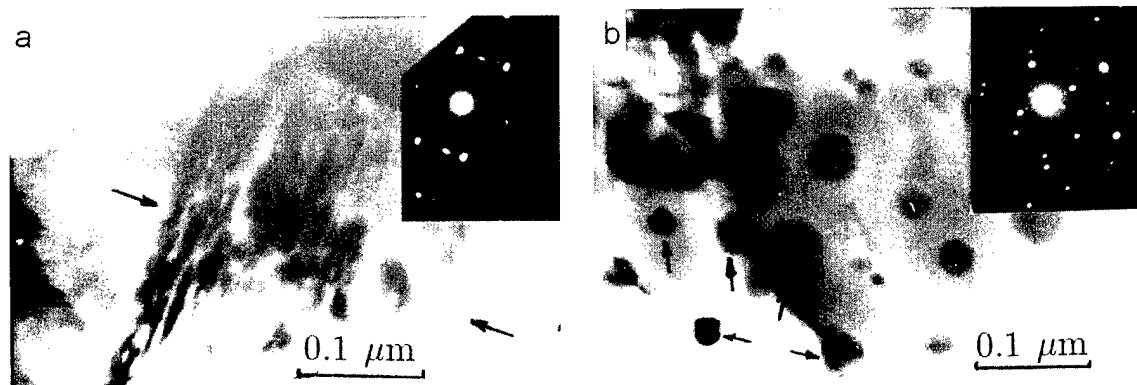


Fig. 7. Microstructures of the sublayer of cutting edge of a pre-irradiated T15K6 carbide insert. The cutting time was 120 s. The arrows indicate (a) microtwins, and (b) nanosized carbide segregates.

tration of vacancies noticeably decreases, indicating that pulsed annealing of defects took place. These substructural changes make it possible (at 3 J/cm²) to double the wear resistance of the inserts in steel cutting.

4. Conclusion

The principal peculiarities and mechanisms of the changes in the structure-phase state, and in the strength and electrochemical properties of the surface layers of metallic materials occurring on pulsed melting with an LEHCEB have been discussed. The results obtained suggest that the LEHCEB sources show promise for the development of new and highly efficient technologies for surface treatment of materials.

References

- [1] J. Poate, G. Remini, D. Jacobson (Eds.), *Surface Modification and Alloying by Laser Ion and Electron Beams*, Plenum Press, New York (London), 1983.
- [2] L. Rudakov, B. Demidov, V. Uglov, *Fiz. i Himiya Obrab. Mater.* 5 (1989) 11–15.
- [3] D. Proskurovsky, V. Rotshtein, G. Ozur, *Surf. Coat. Technol.* 96 (1) (1997) 115–122.
- [4] D. Proskurovsky, V. Rotshtein, G. Ozur, A. Markov, D. Nazarov, V. Shulov, Yu. Ivanov, R. Buchheit, *J. Vac. Sci. Technol. A* 1694 (1998) 2480–2488.
- [5] G. Muller, G. Shumacher, D. Straus, V. Engel'ko, A. Andreev, K. Koval'ov, *Proc. 10th Int. Conf. on High Power Particle Beams*, Prague Vol. 2 (1996) 809–812.
- [6] G. Remnev, I. Isakov, M. Opekunov, G. Kotlyarevsky, V. Kutuzov, V. Lopatin, V. Matvienko, M. Ovchinnikov, A. Potyomkin, V. Tarbokov, *Surf. Coat. Technol.* 96 (1) (1997) 103–109.
- [7] R. Stinnett, R. Buchheit, F. Greulich, C. Hills, A. Kilgo, D. McIntyre, J. Greenly, M. Thomson, G. Johnson, D. Rej, *J. Mater. Res. Soc. Symp. Proc.* 316 (1994) 521–532.
- [8] V. Rotshtein, L. Bushnev, D. Proskurovsky, *Izv. Vyssh. Uchebn. Zaved. Fiz.* 3 (1975) 130–131.
- [9] J. Knapp, D. Follstaedt, in: B. Appleton, G. Celler (Eds.), *Laser and Electron Beam Interaction with Solids*, North-Holland, New York, 1982, pp. 407–412.
- [10] D. Follstaedt, J. Knapp, in: B. Appleton, G. Celler (Eds.), *Laser and Electron Beam Interaction with Solids*, North-Holland, New York, 1982, pp. 377–387.
- [11] E. Dudarev, L. Kornienko, C. Lykov, A. Markov, G. Pochivalova, V. Rotshtein, T. Chubenko, *Izv. Vyssh. Uchebn. Zaved. Fiz.* 5 (1993) 42–47.
- [12] E. Dudarev, G. Pochivalova, D. Proskurovsky, V. Rotshtein, A. Markov, *Izv. Vyssh. Uchebn. Zaved. Fiz.* 3 (1996) 126–132.
- [13] A. Zecca, R. Brusa, M. Duarte Naia, J. Paridaens, A. Pogrebnjak, A. Markov, G. Ozur, D. Proskurovsky, V. Rotshtein, *Phys. Lett. A* 175 (6) (1993) 433–440.
- [14] A. Pogrebnjak, R. Oshner, A. Zecca, V. Rotshtein, A. Mihalyov, *Fiz. i Him. Obrab. Mater.* 1 (1996) 29–37.
- [15] V. Rotshtein, PhD Thesis, Institute of High Current Electronics, Tomsk, 1995.
- [16] B. Wood, A. Perry, L. Bitteker, W. Waganaar, *Surf. Coat. Technol.* 108/109 (1998) 171–176.
- [17] Yu. Ivanov, Yu. Kryuchkov, A. Markov, D. Nazarov, G. Ozur, A. Pogrebnjak, D. Proskurovsky, V. Rotshtein, *Poverhnost'* 10/11 (1994) 95–102.
- [18] Yu. Ivanov, M. Kashchenko, A. Markov, V. Rotshtein, *Zh. Tekhn. Fiz.* 65 (3) (1995) 98–101.
- [19] Yu. Ivanov, V. Itin, S. Lykov, A. Markov, G. Mesyats, G. Ozur, D. Proskurovsky, V. Rotshtein, A. Tuchvatullin, *Izvestiya RAN Metall.* 3 (1993) 130–140.
- [20] I. Goncharenko, V. Itin, S. Isichenko, C. Lykov, A. Markov, O. Nalesnik, G. Ozur, D. Proskurovsky, V. Rotshtein, *Zashchita Metallov.* 29 (6) (1993) 932–937.
- [21] Yu.F. Ivanov, S.F. Gnyusov, *Izv. Vyssh. Uchebn. Zaved. Fiz.* 8 (1996) 104–110.
- [22] A. Perry, J. Matossian, S. Bull, D. Proskurovsky, P. Rice-Evans, T. Page, D. Geist, J. Taylor, J. Vajo, R. Doty, V. Rotshtein, A. Markov, *Metall. Mater. Trans.*, in press.

Effect of energy on direct ion beam deposition of carbon thin films: induced defects and graphitization

H.-A. Durand *, K. Sekine, K. Etoh, K. Ito, I. Kataoka

Japan Aviation Electronics Industry Ltd., Central Research Laboratory, Musashino 3-1-1, Akishima-shi, Tokyo 196-8555, Japan

Abstract

The direct deposition of ions at low energy enables fine control of the fundamental processes of thin film formation. Using a source of carbon and nickel ions with energy ranging from a few tens to a few hundreds of electron volts, combined with an ultra-high vacuum scanning electron tunneling microscope, we have studied the formation of thin films for thicknesses equivalent to less than one atomic layer. We have revealed the influence of ion-induced defects on the formation mechanisms of the thin film as a function of ion energy using the dynamic scaling analysis of the roughness of the thin film terminal surfaces. In the case of carbon ions we acknowledge the formation of an sp^2 bonded layer at 300°C, that is above the critical temperature where the formation of a diamond-like carbon sp^3 layer recess as described by the subimplantation model [4]. © 2000 Elsevier Science S.A. All rights reserved.

Keywords: Carbon; Fractal surface; Ion beams; Nickel; Scanning tunneling microscope; Thin films

1. Introduction

The direct deposition of ions at low to medium energy enables full control of deposition parameters. A wide range of isotopically selected materials, including metals, can be deposited using an ionized beam. Despite very low yields, the direct deposition of ions has proved to be an excellent tool to control the density of deposited atoms on a substrate surface accurately. By coupling such a source with an ultra-high vacuum scanning tunneling microscope (STM) one may investigate the early moments of thin film formation. These fundamental studies are instrumental in clarifying the growth mechanisms of materials. A comprehensive understanding of thin film formation, nucleation and island growth is critical for several industrial fields. Results will be applied to the fabrication of future generations of materials whose properties might be tuned through nanoparticles' size effects, such as quantum confinement.

We present here some of our results concerning the growth of carbon and nickel thin films by direct deposition of ions at energy up to 100 eV.

2. Experiments

In direct ion beam deposition (DIBD) ions are directly impinged on the substrate at low energy. The experimental configuration is very similar to industrial ion implanters except for the energy of ions reaching the substrate: in DIBD ions do not penetrate deep inside the substrate material. For ion implantation it is necessary to use a high energy of several keV for extraction and acceleration in order to generate a reasonable current in the ion beam. Mass selection requires highly accelerated ions as well. Therefore, for direct deposition at low energy, an additional deceleration electrode is necessary.

Our experimental setup consisting of a low energy DIBD coupled with an ultra-high vacuum (UHV) STM has been extensively described in Ref. [1]. It is entirely dedicated to the study of initial thin film formation as the design provides only a very low ion current, equivalent to less than an atomic monolayer per hour. With the system, the attainable energy of landing ions ranges from a few tens of electron-volt (eV) up to 300 keV. C^+ ions were generated from ionized carbon dioxide. Ni^+ ions were generated from nickel chloride placed in the oven of a Colutron G2 ion gun surrounded by ionized argon. Substrates were bombarded with average densities ranging from 1 to about 40 ions/nm², while the

* Corresponding author. Tel.: +81-425-49-9216;
fax: +81-425-49-9572.
E-mail address: hadurand@jae.co.jp (H.-A. Durand)

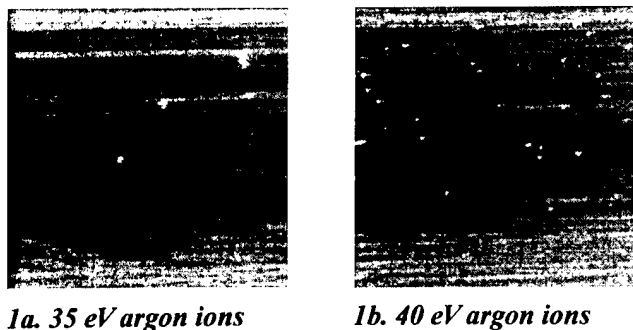


Fig. 1. (100 × 100 nm) STM images of defects induced by argon ions (a) below, and (b) above the energy threshold.

pressure was kept at 10^{-4} Pa. Highly oriented pyrolytic graphite (HOPG) substrates were cleaved just before being put in the deposition chamber in the 1000 class clean room where the whole system is installed — no contamination of the surface was been detected using this process. STM observations were conducted at 10^{-8} Pa in a separate UHV chamber.

3. Observation and discussion

3.1. Effects of argon ions on HOPG surface

In regular molecular beam epitaxy (MBE) the particles impinging on substrates have an energy of only a few eV. This energy is not usually controlled, as opposed to DIBD where adjustment is enabled through the deceleration voltage of the ion beam. For very low energy, ions have no effect on the substrate. There is a threshold where the energy of the incoming particles start to disturb the lattice structure of the substrate. This threshold is reported to be 38.7 eV for the c plane of HOPG [2]. In the case of an argon beam, ions will neutralize when reaching the substrate surface, they will immediately desorb and be pumped out. Argon ions are not to be observed by STM after irradiation, nevertheless the defects they induce on the HOPG surface will be visible.

Fig. 1 presents two STM images of samples which have been identically irradiated, at room temperature,

by an argon beam at 30 eV and 40 eV, that is just below and just above the damaging energy threshold. While the surface of the first sample is virtually unchanged from a cleaved HOPG, the second image is protruded by several hillocks of several nanometers in size. These are the symptoms of induced damages to the HOPG surface. The most probable defects for energy just above the damaging threshold are single ion vacancies in the surface lattice, when an incoming ion pushes out one atom from a crystal cell.

The fine tip of an STM picks the partial electronic density of charge at the surface. Noting this fact is crucial as the images obtained are not a true representation of the surface morphology, as would be obtained from an atomic force microscope (AFM) for instance. As a consequence it is difficult to assert the type of defect induced in Fig. 1(b), even at the highest resolution of our instrument.

3.2. Deposition of carbon ions

Fig. 2 presents several STM images taken for samples irradiated with carbon ions with energy ranging from 25 to 100 eV. Above the 38.7 eV threshold, the defects become numerous and their number increases with ion energy. Again, in Fig. 2 most hillocks have undefined edges, and in most cases it is difficult to identify the type of defects induced in the surface.

In contrast to argon ions, carbon ions are adsorbed on the substrate surface after they have been neutralized. These carbon atoms will diffuse on the surface and probably settle in preferential sites, form islands and eventually a thin film. Moreover, carbon atoms pushed out of the surface lattice by incoming ions will have the same fate and will migrate on the surface.

For low densities of defects, when the surface is still in 'good condition', a few atoms settled in particular sites may induce a perturbation of the electronic density of charge with a very large extension (of more than 10 nm). While single atoms are not visible in images, the perturbation they induce is very sharply revealed. Fig. 3 shows a singular feature where two such electronic perturbations interfere to form a geometrical figure with an attractive

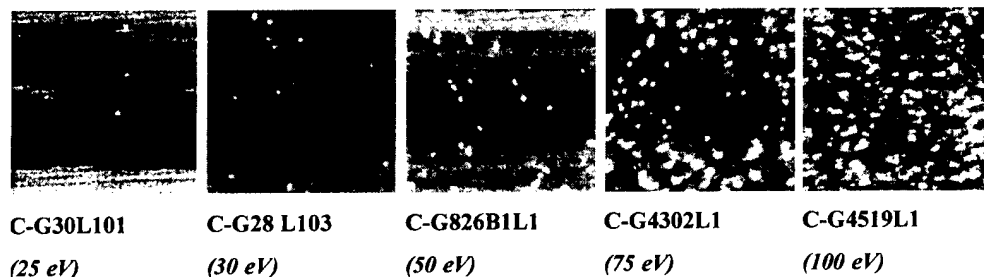


Fig. 2. (100 × 100 nm) STM images of defects induced and islands created on HOPG by carbon ions as a function of energy below and above the threshold.

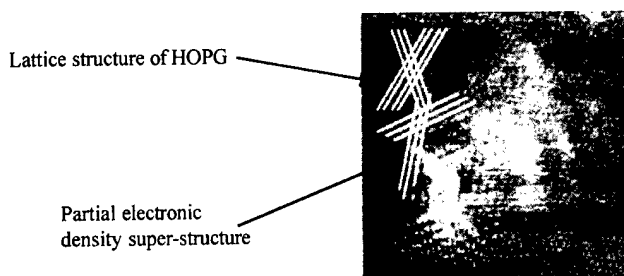


Fig. 3. (10×10 nm) STM image of a complex superstructure induced by carbon ions (CG83F4M1).

periodic pattern [1,3]. The periodicity is $\sqrt{3}$ larger than that of graphite and the directions of symmetry are tilted 60° with respect to the underlying HOPG lattice.

When ions are deposited at high density (equivalent to several atomic layers), graphitization occurs only above a critical substrate temperature T_c . Below this critical temperature, which is a function of ion energy ($T_c = 150^\circ\text{C}$ for 120 eV C^+ ions [4]; $T_c = 250^\circ\text{C}$ for 92 eV C^+ ions [5]), the growth of a dense, mostly sp^3 bonded film was reported. The subimplantation model suggests that ions with low energy, but just enough to penetrate below the surface, induce stress. The growth of a diamond film is attributed to the formation of sp^3 bounds in these stressed sublayers. In our experiments it is probable that a majority of the 100 eV ions actually penetrate below the surface as shown in a previous molecular dynamics study [6], but they also generate numerous defects in the surface. Nevertheless, having deposited only very low densities of a few ions at low energy (it is very time consuming as the ion current is very low) there was no clear confirmation of the formation of a diamond-like thin film or islands.

We could prepare samples with a large density equivalent to a monolayer (~ 38 ions/ nm^2) only for higher energy, or above the corresponding critical temperature T_c , when defects induced by ions seriously damage the surface stress is released and the process of creating sp^3 bounds recess: only a rough, low density, sp^2 bounded graphite film is formed. The temperature of 300°C during deposition in our experiments at high density is certainly above the critical temperature T_c for 100 eV ions when compared to reported values of T_c for 92 eV ions and 120 eV ions. The rough, rather disordered, layer observed for these samples is compatible with the graphitization process as clarified by the subimplantation model.

3.3. Deposition of Ni ions

The deposition of carbon ions on HOPG supposes a homogenous growth as both the deposit and the substrate are made of the same material. It is also interesting to study a heterogeneous growth, such as the deposition

of a metal on carbon graphite. The effects of nickel ions on the HOPG surface also depend on energy, with a threshold implying displacement in the lattice structure. In the following we present results concerning the formation of islands and their growth for 100 eV ions.

The image in Fig. 4 is an atmospheric AFM image of the HOPG surface after irradiation by 100 eV at a density of 2 ions/ nm^2 at room temperature. As the image scale is much larger than for previous figures ($1 \times 1 \mu\text{m}$) the atomic layers finishing the surface of cleaved HOPG are clearly revealed. Nickel islands have a uniform distribution on free surfaces, but one notices numerous islands aligned along the atomic steps. Despite neutralized nickel ions have the freedom to diffuse a few tens of nanometers on the surface at room temperature, they tend to be captured by edges where there are perturbations of the surface free energy.

3.4. Scaling study

We computed the dynamic scaling function of roughness (DSFR) [7] by dividing each STM or AFM image



Ni⁺ (100 eV, 2 ions/ nm^2). File Ni06.000 L10

Fig. 4. ($1 \times 1 \mu\text{m}$) AFM image on nickel deposited by DIBD on cleaved HOPG.

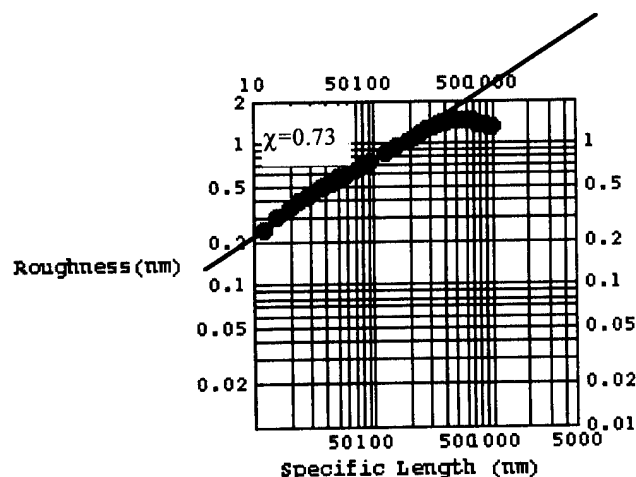


Fig. 5. Plot of the dynamic scaling function as computed from Fig. 4.

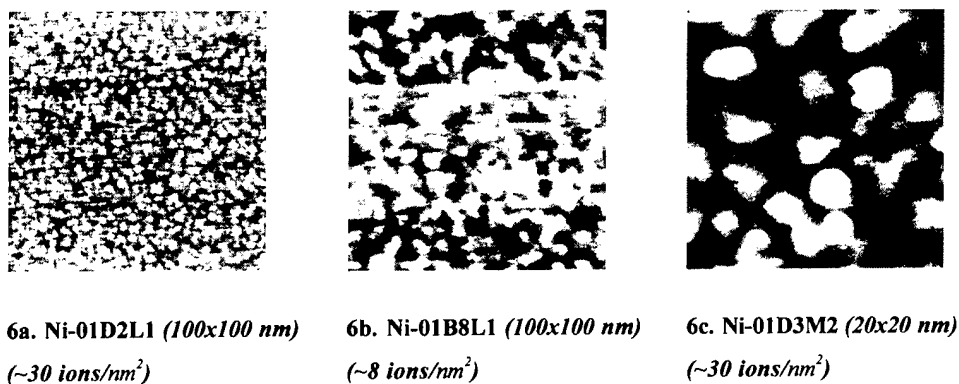


Fig. 6. STM images of Ni deposits prepared by DIBD: (c) is an image of the same sample as in (a) but scanned at a smaller scale.

(256×256 pixels) in smaller boxes of specific length L (128×128 , 64×64 , ..., 2×2 pixels). The 'specific roughness' $\sigma(L)$ is the roughness for a specific length scale L and is then obtained by first calculating the root mean square roughness inside each $L \times L$ box, then averaging over the ensemble of boxes of the same size in one STM image. This function describes the degree of self-scaling (degree of fractality) of the surface and it embodies the growth mechanisms of the thin film. The rising slope of the DSFR (χ , called the scaling exponent of roughness) is particularly representative of the growth mode. In brief, the value of χ would be zero for an ideal layer-by-layer growth, and tends to a value of unity for three-dimensional growth (pyramidal islands growth). Fig. 5 is a plot of the DSFR for the AFM image shown Fig. 4. The slope in the first part of the curve is $\chi_{\text{Ni-AFM}} = 0.73 \pm 0.05$.

From a large number of STM images of nascent films, the scaling exponent of roughness stabilize around $\chi_{\text{Ni-STM}} = 0.78 \pm 0.05$ for the DIBD of Ni. The values obtained from STM images (such as in Fig. 6) and AFM images (such as in Fig. 4) are remarkably close, despite the scales differing by one order. This is very satisfactory as the DSFR is an intrinsic property of the surface and embodies the characteristic of growth, therefore the scaling parameters are constant within the domain of the surface fractality.

This intermediate value of $\chi_{\text{Ni-ions}} = 0.75$ (average of $\chi_{\text{Ni-STM}}$ and $\chi_{\text{Ni-AFM}}$) has to be compared to the value of χ close to that obtained for evaporation [8]. Defects induced by incoming ions on the HOPG surface generate nucleation centers for islands and consequently reduce the mean free path of neutralized nickel atoms on the surface of the substrate. This phenomena is also qualitatively seen in Fig. 6. The number of ions bombarded in Fig. 6(a) is about five times larger than that in Fig. 6(b) and consequently the island network is much more dense. If no defects were created during growth, as in a simple evaporation, one would simply expect existing islands to grow, in contrast to the present situation where many small islands can be seen.

4. Conclusion

In this paper we have presented several experiments concerning the deposition of materials by direct low energy ion beam. Our observations by UHV-STM at atomic resolution confirm the existence of an energy threshold below 40 eV where the lattice of the HOPG is damaged and vacancies are created. Defects induced by incoming ions of moderate energy (~ 100 eV order) generate perturbations of the partial density of charge at the surface. These perturbations extend far away from the defect they originate in. Our experiments show the graphitization of the deposit and we could not observe the formation of a diamond-like thin film. The defects on the HOPG surface play a crucial role in the subsequent growth mechanisms and probably reduce diffusion by enhancing the spatial distribution nucleation centers.

Acknowledgement

Authors would like to thank Dr. Yonosuke Makita of the Electrotechnical Laboratory, AIST, MITI (Tsukuba Science City, Japan) for fruitful discussions and support.

References

- [1] H.-A. Durand, K. Sekine, K. Etoh, K. Ito, I. Kataoka, *J. App. Phys.* 84 (5) (1998) 2591.
- [2] H.J. Steffen, D. Marton, J.W. Rabalais, *Nucl. Inst. and Meth. B* 67 (1992) 308.
- [3] J. Yan, *J. Appl. Phys.* 75 (3) (1994) 1390.
- [4] Y. Lifshitz, G.D. Lempert, E. Grossman, *Phys. Rev. Lett.* 72 (1994) 2753.
- [5] S. Sattel, J. Robertson, H. Ehrhardt, *J. Appl. Phys.* 82 (1997) 4566.
- [6] K. Nordlund, J. Kejonen, T. Mattila, *Phys. Rev. Lett.* 77 (1996) 699.
- [7] R.S. Williams, W.M. Tong, T.T. Ngo, *Symp. on Fractal Aspects of Materials, Proc. Mat. Res. Soc., Pittsburgh MA* 273 (1995).
- [8] H.-A. Durand et al., (submitted for publication).

Structural stability of irradiated metallic and non-metallic films

P.M. Ossi *, R. Pastorelli

INFM-Dipartimento di Ingegneria Nucleare, Politecnico di Milano, via Ponzio 34/3, 20133 Milan, Italy

Abstract

The segregation charge transfer model allows the interpretation of the nucleation of either crystalline or vitreous phases in binary non-metallic as well as metallic compounds, ion bombarded under conditions favourable to the formation of dense collision cascades. At the cascade–matrix interface a non-equilibrium electronic density profile forms and it is re-equilibrated by charge transfer reactions (CTRs), each involving a couple of dissimilar atoms, which undergo single ionization. The energy cost associated with a single CTR and the local volume change provoked by CTR products are evaluated. Thresholds in the values taken by the above physical quantities are found for both families of irradiated materials. Those thresholds separate the compounds amorphized from those remaining crystalline under ion bombardment. © 2000 Published by Elsevier Science S.A. All rights reserved.

Keywords: Radiation effects; Structural stability; Surface binary compounds

1. Introduction

The use of energetic ion beams to favour the deposition or the modification of surface films with specific (e.g. mechanical and transport) properties is becoming widespread. The possible amorphization of the surface layer is associated with the use of ion-assisted techniques; the capability to control surface structure evolution under irradiation is crucial, given the different behaviour of a crystalline or a vitreous system with respect to the above properties.

It is generally accepted that quite different characteristics, such as bond directionality and non-uniform charge distribution in ceramics [1], as well as chemical disordering, and excess of point defect production and accumulation in metallic systems [2], promote structural destabilization. In this work the main features of the segregation charge transfer (SCT) atomistic model, able to interpret and predict the structural stability of ion bombarded films, are discussed. Both metallic and non-metallic binary compounds are considered, taking into account the detailed evolution of collision cascades, which is largely independent of the chemical nature of the material. Cascade formation is dominated by ballistic processes and their history is determined by the evolu-

tion of thermodynamic quantities towards free energy minimization. The history of a prototypical cascade includes a ‘ballistic’ stage, of about 0.1 ps, in which projectile slowing down involves nuclear stopping, and causes atomic displacements, which deeply alter the crystalline nature of the region surrounding the ion path; in the cascade core, atomic density is strongly lowered (vacancy enrichment) just after the very first evolution stage [3]. The ‘thermal spike’ stage, with a lifetime of some picoseconds, begins once no more recoils can occur, i.e. when the deposited energy has been distributed among all atoms in the cascade (see Fig. 1). Energy dissipation is provided both by a temperature gradient and by an atomic density wave propagating from the centre to the periphery of the spike [4]. The wave is caused by the inhomogeneous radial atomic distribution around the ion track, which is a direct consequence of the initial ballistic processes. A typical density increase associated with the matter wave is about 20% with respect to core values [4]. Considering a binary A_xB_y system, towards the end of the ballistic stage the energy of higher-order recoils lies between the displacement energies $E_d(A)$ and $E_d(B)$ [e.g. $E_d(A) < E_d(B)$] of compound constituents, so that displacements can involve only atoms of the species with lower E_d value (i.e. A atoms). Thus, at the end of the ballistic stage the fraction of displaced A atoms, with respect to all displaced atoms, is higher than the initial fraction of A atoms, namely x . For this reason the

* Corresponding author. Tel.: +39-02-2399-6319;
fax: +39-02-2399-6309.
E-mail address: paolo.ossi@polimi.it (P.M. Ossi)

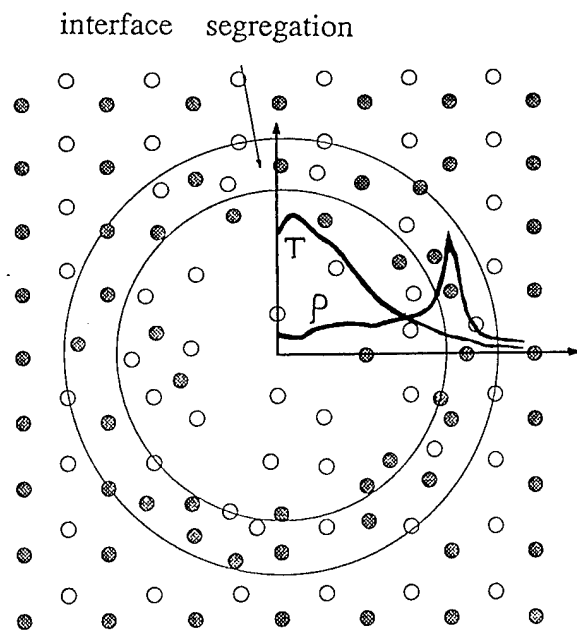


Fig. 1. Schematic view of the temperature and density evolution across a thermal spike (adapted from Ref. [4]). Enrichment at the spike–matrix interface of one compound constituent is shown.

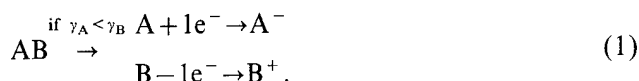
atomic density wave is progressively enriched in A atoms with respect to bulk stoichiometry on moving away from the spike centre [5]. In the last ‘relaxation’ stage, residual defects relax towards an equilibrium configuration over times of the order of 10 ps [6]; the SCT model interprets such a relaxation, pointing at those phenomena that occur at the spike–matrix interface.

2. Theory

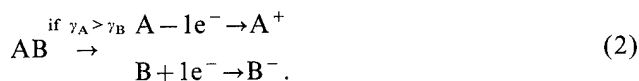
In a binary A_xB_y compound, SCT model analysis concentrates on the spike–crystalline matrix interface (Fig. 1), where bombardment-driven preferential migration of one compound constituent is assumed to occur. In agreement with the indication by Gibbsian segregation in irradiated systems [7], the constituent with lower surface energy γ is taken to segregate to the interface. The same criterion is also adopted for compounds for which segregation data is lacking. As γ values scale with E_d values along the Periodic Table [8], a coherent explanation for the interface enrichment is provided: in our example $E_d(A)$ is lower than $E_d(B)$ and γ_A is lower than γ_B , and the spike–matrix interface is thereby enriched in A constituent. The temperature range spanned by the spike is wide enough to secure that propagation of the matter wavefront is related to a meaningful compositional enrichment. Thus, localized segregation events induce (i) lowering of system energy, (ii) compositional gradient formation, and (iii) develop-

ment of a non-equilibrium electronic charge density profile.

In the SCT model the re-equilibration of such a profile is taken to occur via localized charge transfer reactions (CTRs). This *assumption* [9] is a generalization of electronic re-equilibration mechanisms observed in many ion-irradiated systems, both metallic and non-metallic [10,11], in which the charge transfer, experimentally ascertained by electron energy loss spectroscopy, is correlated [12] with the short-range order (SRO) of the amorphous compound and its (meta)stability. Supposing again that the starting compound is A_xB_y , and that γ_A is lower than γ_B , in each CTR one A atom and one B atom, which constitute the *starting dimer*, are involved and one electron is assumed to be transferred from the B atom of the non-segregating constituent to the A atom of the segregating species, according to the scheme:



Conversely, if γ_A is higher than γ_B



Here A and B are neutral atoms with atomic number Z_A and Z_B ; such a rather crude atomistic approximation is justified by the high energy of the spike. Indeed, although the local coordination in a liquid at high temperature is often the same as in the corresponding crystal (the SRO is the same), yet that value is an *average* value with large fluctuations, increasing with temperature, which are specifically responsible for system fluidity. A^- , B^+ , A^+ , B^- are singly charged ions. In the SCT model they are defined as *effective* elements.

Referring to Eqs. (1) and (2), both CTRs go in the direction of shell closing in both atoms. Indeed, γ values are progressively lower in elements with progressively filled electronic shells, so one electron is gained, via charge transfer, by the constituent with lower surface energy.

In the framework of the SCT model it is possible to calculate physical quantities whose values are interpreted in terms of structural stability of an irradiated system. Among the considered quantities [1,13], in this work we focus on the two that best characterize the charge transfer process.

Referring for example to Eq. (1), the energy cost ΔE_e^- associated with a single CTR consists of the algebraic sum of the positive term ΔE_{-e^-} , needed to extract one electron from the free B atom, plus the negative term ΔE_{+e^-} , needed to add the same electron to the free A atom [1,2]. When ΔE_e^- is positive, formation of effective elements is structure destabilizing

Table 1

Calculated SCT model parameters for ion-bombarded binary non-metallic compounds: a-, amorphized under ion beam; c-, crystalline under ion beam

Starting compound	Ref.	Segregant	Ref.	Ions (CTR)	ΔE_e^a (eV)	$ \Delta V _{rel}^b$
a-Cr ₇ C ₃	[14]	Cr	[15]	Cr ⁻ C ⁺	8.16	0.70
a-Cr ₃ C ₂	[14]	Cr	[15]	Cr ⁻ C ⁺	8.16	0.65
a-Fe ₈ N	[16]	N	[17]	Fe ⁺ N ⁻	3.69	0.35
a-GaN	[18]	N	[17]	Ga ⁺ N ⁻	10.29	1.90
a-NbN	[19]	N	[17]	Nb ⁺ N ⁻	-1.34	1.17
a-Si ₃ N ₄	[20]	N	[17]	Si ⁺ N ⁻	1.52	1.65
a-TaN	[19]	N	[17]	Ta ⁺ N ⁻	11.48	1.01
a-TiB ₂	[21]	Ti	[17]	Ti ⁻ B ⁺	6.25	0.65
c-Cr ₂ N	[22]	N	[17]	Cr ⁺ N ⁻	-0.91	0.13
c-Fe ₂ B	[23]	B	[17]	Fe ⁺ B ⁻	n.a.	0.40
c-HfC	[24]	C	[15]	Hf ⁺ C ⁻	~0	0.18–0.30
c-MoN	[22]	N	[17]	Mo ⁺ N ⁻	-0.44	1.22
c-TaC	[25]	Ta	[15]	Ta ⁻ C ⁺	7.77	0.6
c-TiC	[21]	C	[15]	Ti ⁺ C ⁻	0.93	0.17
c-Ti ₂ N	[21]	N	[17]	Ti ⁺ N ⁻	~0	0.13
c-W ₂ N	[22]	N	[17]	W ⁺ N ⁻	0.89	0.21–0.80
c-ZrC	[24]	C	[15]	Zr ⁺ C ⁻	~0	0.36
c-ZrN	[26]	N	[17]	Zr ⁺ N ⁻	-0.88	1.17

^a Electron binding energies from Ref. [27]; absolute electronegativities from Ref. [28]; n.a.: not available.^b Crystallographic data from Ref. [29]; neutral atom, positive ion and negative ion radii from Refs. [30,31].

and the dimer of effective elements, e.g. A⁻B⁺, is considered an amorphization nucleus. Conversely, when ΔE_e is negative, the effective element dimer plays the role of a crystallization nucleus.

It is conceivable that the target suffers a local deformation as a consequence of a CTR; this is likely to be associated with volume changes. Given the prototypical A_xB_y unit, with starting volume per atom V_s , if, for example, $x < y$, the CTRs involved yield $x(A^- + B^+)$ ions and $(y - x)B$ neutral atoms, with an average volume per atom V_{CTR} . In non-metallic compounds V_{CTR} includes both ion volumes V_{A^-} and V_{B^+} and neutral volume V_B . In metallic alloys the neutrals are not taken into account, given the system ability to withstand ionization effects due to bond non-directionality.

The local volume changes are evaluated by comparing V_s with the pertinent V_{CTR} . In non-metallic compounds the absolute value of the relative volume variation $|\Delta V|_{rel}$ is calculated

$$|\Delta V|_{rel} = |(V_{CTR} - V_s)/V_{CTR}|. \quad (3)$$

In metallic alloys, given the exiguity of volume changes

$$|\Delta V| = |(V_{CTR} - V_s)|. \quad (4)$$

In both kinds of material a high local volume change favours structure destabilization. In the following data analysis the threshold $|\Delta V|$ values are identified that separate amorphizing from crystalline systems.

3. Results and discussion

In Tables 1 and 2 starting compounds, segregants, ions resulting from CTR, ΔE_e , $|\Delta V|_{rel}$ and $|\Delta V|$ are listed respectively for 18 non-metallic compounds, and for 33 metallic alloys. In the SCT model a given system is considered amorphized (a-) when in one kind of experiment it has been amorphized.

ΔE_e values are positive among amorphized non-crystalline compounds, with one exception (NbN) (Table 1); calculated $|\Delta V|_{rel}$ values are greater than 0.60, with one exception (Fe₈N). For crystalline compounds, three ΔE_e values (for TaC, TiC and W₂N) are positive and two $|\Delta V|_{rel}$ values are greater than 0.60 (for MoN and ZrN). Concerning W₂N, $|\Delta V|_{rel}$ lies across a range of values including the threshold value, corresponding to the widest range of values of ion radii. It is remarkable that model predictions for amorphized compounds are largely in agreement with experimental results [47]; we expect that among those systems presently considered crystalline under irradiation, which, however, are exceptions with respect to model predictions, some could be amorphized under proper experimental conditions.

ΔE_e values are positive for all amorphized alloys, for which $|\Delta V|$ values are greater than $15 \times 10^{-3} \text{ nm}^3$ with four exceptions (Cr₆₇Ti₃₃, Fe₆₇Cr₃₃, Nb₅₀Cr₅₀, Ni₆₇Si₃₃). For crystalline alloys the $|\Delta V|$ values are negative, in agreement with the model, and $|\Delta V|$ is lower than $15 \times 10^{-3} \text{ nm}^3$, with two exceptions (Al₅₅Co₄₅ and

Table 2

Calculated SCT model parameters for ion bombarded binary metallic alloys: a-, amorphized under ion beam; c-, crystalline under ion beam

Starting alloy	Ref.	Segregant	Ref.	Ions (CTR)	ΔE_e^a (eV)	$ \Delta V ^b$ ($\times 10^{-3}$ nm ³)
a-Co ₅₀ Ti ₅₀	[32]	Ti	[33]	Co ⁺ Ti ⁻	0.091	21
a-Co ₄₈ Zr ₅₂	[34]	Zr	[33]	Co ⁺ Zr ⁻	0.083	22
a-Cr ₆₇ Ti ₃₃	[35]	Ti	[33]	Cr ⁺ Ti ⁻	0.280	14
a-Cr ₆₇ Zr ₃₃	[36]	Zr	[33]	Cr ⁺ Zr ⁻	0.426	22
a-Cu ₅₅ Ta ₄₅	[9]	Cu	[33]	Cu ⁻ Ta ⁺	0.070	30
a-Cu ₅₀ Zr ₅₀	[35]	Zr	[33]	Cu ⁺ Zr ⁻	0.283	21
a-Fe ₆₇ Cr ₃₃	[35]	Fe	[33]	Fe ⁻ Cr ⁺	0.390	11
a-Fe ₇₅ Mo ₂₅	[37]	Fe	[33]	Fe ⁻ Mo ⁺	0.080	17
a-Fe ₆₈ Nd ₃₂	[13]	Nd	[38]	Fe ⁺ Nd ⁻	0.310	23
a-Fe ₆₇ Ti ₃₃	[32]	Ti	[33]	Fe ⁺ Ti ⁻	0.095	21
a-Gd ₇₅ Co ₂₅	[13]	Gd	[38]	Gd ⁻ Co ⁺	0.320	18
a-Nb ₅₀ Cr ₅₀	[39]	Cr	[33]	Nb ⁺ Cr ⁻	0.800	14
a-Nb ₇₅ Ir ₂₅	[40]	Nb	[33]	Nb ⁻ Ir ⁺	0.030	22
a-Nb ₈₆ Zr ₁₄	[41]	Nb	[33]	Nb ⁻ Zr ⁺	0.100	17
a-Ni ₆₇ Si ₃₃	[42]	Ni	[38]	Ni ⁻ Si ⁺	0.075	9–10
a-Ni ₇₅ Sn ₂₅	[43]	Sn	[38]	Ni ⁺ Sn ⁻	0.270	15
a-Ni ₅₀ Ta ₅₀	[44]	Ni	[33]	Ni ⁻ Ta ⁺	0.090	26
a-Ni ₆₅ Ti ₃₅	[43]	Ni	[33]	Ni ⁻ Ti ⁺	0.300	17
a-Zr ₆₇ Ni ₃₃	[45]	Zr	[33]	Zr ⁻ Ni ⁺	0.200	18
c-Al ₅₅ Co ₄₅	[40]	Al	[38]	Al ⁻ Co ⁺	-0.130	20
c-Al ₅₀ Sb ₅₀	[9]	Sb	[38]	Al ⁺ Sb ⁻	-0.020	0–3
c-Au ₆₇ Al ₃₃	[34]	Au	[38]	Au ⁻ Al ⁺	-0.850	0
c-Co _{98–80} Ta _{2–20}	[46]	Co	[33]	Co ⁻ Ta ⁺	-0.040	6
c-Cr ₅₀ Ni ₅₀	[9]	Cr	[33]	Cr ⁻ Ni ⁺	-0.030	15
c-Cu ₇₅ Pd ₂₅	[44]	Cu	[33]	Cu ⁻ Pd ⁺	-0.155	3–6
c-Fe ₆₇ Mo ₃₃	[44]	Fe	[33]	Fe ⁻ Mo ⁺	-0.220	9
c-Fe ₆₅ Ni ₃₅	[39]	Ni	[33]	Fe ⁺ Ni ⁻	-0.030	6
c-Fe ₅₅ V ₄₅	[40]	Fe	[33]	Fe ⁻ V ⁺	-0.070	9
c-Fe ₈₀ Yb ₂₀	[13]	Yb	[38]	Fe ⁺ Yb ⁻	-0.190	15
c-Mo ₅₀ W ₅₀	[32]	Mo	[33]	Mo ⁻ W ⁺	-0.295	14–19
c-Nb ₅₀ Mo ₅₀	[32]	Mo	[33]	Nb ⁺ Mo ⁻	-0.340	15
c-Pd ₇₅ Ta ₂₅	[13]	Pd	[33]	Pd ⁻ Ta ⁺	-0.120	6
c-Pd ₇₅ V ₂₅	[44]	Pd	[33]	Pd ⁻ V ⁺	-0.175	6
c-Ru ₅₀ Ti ₅₀	[32]	Ti	[33]	Ru ⁺ Ti ⁻	-0.250	20–24
c-Zr ₆₇ Ni ₃₃	[35]	Ni	[33]	Zr ⁺ Ni ⁻	-0.200	0

^a Electron binding energies from Ref. [27].^b Crystallographic data from Ref. [29]; neutral atom and negative ion radii from Refs. [30,31].

Ru₅₀Ti₅₀). Notice that two exceptions among $|\Delta V|$ values for amorphized alloys (Cr₆₇Ti₃₃ and Nb₅₀Cr₅₀) are marginally at variance with respect to the threshold value. For some alloys an interval of $|\Delta V|$ values is reported; this corresponds to the widest range of values of ion radii.

In conclusion, the SCT model, which is based on the evolution of collision cascades, shows a good degree of interpretative success with a reasonably large set of irradiated compounds, both non-metallic and metallic.

Acknowledgement

This work was supported by CNR — *Progetto Finalizzato Materiali Speciali per Tecnologie Avanzate II*.

References

- [1] P.M. Ossi, R. Pastorelli, J. Appl. Phys. 85 (1999) 1387.
- [2] P.M. Ossi, Riv. Nuovo Cimento 15 (5) (1992)
- [3] H. Zhu, R.S. Averback, M. Nastasi, Philos. Mag. A 71 (1995) 735.
- [4] H. Van Swygenhoven, A. Caro, Phys. Rev. Lett. 70 (1993) 2098.
- [5] F. Gao, D.J. Bacon, Philos. Mag. A 71 (1995) 65.
- [6] H. Hsieh, T. Diaz de la Rubia, R.S. Averback, R. Benedek, Phys. Rev. B 40 (1989) 9986.
- [7] R. Kelly, Surf. Sci. 100 (1980) 85.
- [8] B.J. Garrison, N. Winograd, D. Lo, T.A. Tombrello, M.H. Shapiro, D.E. Harrison Jr., Surf. Sci. 180 (1987) L129.
- [9] P.M. Ossi, Surf. Coat. Technol. 83 (1996) 22.
- [10] K. Saito, K. Yabe, O. Nishimura, Nucl. Instr. Meth. Phys. Res. B: 39 (1989) 623.
- [11] U. Mizutani, M. Sasaura, Y. Yamada, T. Matsuda, J. Phys. F: Met. Phys. 17 (1987) 667.
- [12] E.S.K. Menon, K.M. Krishnan, Philos. Mag. Lett. 66 (1992) 271.
- [13] P.M. Ossi, J. Non-Cryst. Solids 232–234 (1998) 219.

- [14] T. Fujihana, Y. Okabe, M. Iwaki, *Nucl. Instr. Meth. Phys. Res. B*: 127–128 (1997) 660.
- [15] T. Fujihana, Y. Okabe, M. Iwaki, *Surf. Coat. Technol.* 66 (1994) 419.
- [16] H. Shinno, K. Saito, *Surf. Coat. Technol.* 103–104 (1998) 129.
- [17] A. Zangwill, *Physics at Surfaces*, Cambridge University Press, Cambridge, UK, 1988.
- [18] C. Liu, B. Mensching, M. Zeitler, K. Voltz, B. Rauschenbach, *Phys. Rev. B* 57 (1998) 2530.
- [19] K. Baba, R. Hatada, K. Udoh, K. Yasuda, *Nucl. Instr. Meth. Phys. Res. B*: 127–128 (1997) 841.
- [20] S.J. Zinkle, L.L. Snead, *Nucl. Instr. Meth. Phys. Res. B*: 116 (1996) 92.
- [21] M. Soltani-Farshi, H. Baumann, D. Rück, E. Richter, U. Kreissig, K. Bethge, *Surf. Coat. Technol.* 103–104 (1998) 299.
- [22] W. Ensinger, M. Kiuchi, *Surf. Coat. Technol.* 84 (1996) 425.
- [23] J.A. Davis, P.J. Wilbur, D.L. Williamson, R. Wei, J.J. Vajo, *Surf. Coat. Technol.* 103–104 (1998) 52.
- [24] T. Fujihana, M. Taniguchi, Y. Okabe, M. Iwaki, *Surf. Coat. Technol.* 83 (1998) 120.
- [25] Q.Y. Zhang, X.X. Mei, D.Z. Yang, F.X. Chen, T.C. Ma, Y.M. Wang, F.N. Teng, *Nucl. Instr. Meth. Phys. Res. B*: 127–128 (1997) 664.
- [26] Y. Miyagawa, S. Nakao, K. Baba, R. Hatada, M. Ikeyama, S. Miyagawa, *Surf. Coat. Technol.* 103–104 (1998) 323.
- [27] F. Hermann, S. Skillman, *Atomic Structure Calculations*, Prentice-Hall, Englewood Cliffs, NJ, 1963.
- [28] J.E. Huheey, R.L. Keiter, *Inorganic Chemistry: Principles of Structure and Reactivity*, Harper Collins, New York, 1993.
- [29] *Metals and Alloys Indexes*, International Center for Diffraction Data, Swarthmore, PA, 1992.
- [30] *Periodic Table of the Elements*, IUPAC, 1998.
- [31] K.D. Sen, P.J. Politzer, *Chem. Phys.* 91 (1989) 5123.
- [32] P.M. Ossi, *Rad. Eff. Def. Solids* 108 (1989) 61.
- [33] P.M. Ossi, *Surf. Sci.* 201 (1988) L519.
- [34] P.M. Ossi, *Mater. Sci. Eng.* 90 (1987) 55.
- [35] P.M. Ossi, *Comput. Mater. Sci.* 1 (1993) 428.
- [36] L.M. Howe, D. Phillips, H. Zou, J. Forster, R. Siegele, J.A. Davies, A.T. Motta, J.A. Faldowski, P.R. Okamoto, *Phys. Res. B* 118 (1996) 663.
- [37] Z.J. Zhang, *J. Appl. Phys.* 81 (1997) 2027.
- [38] F.R. de Boer, R. Boom, W.C.M. Mattens, A.R. Miedema, A.K. Niessen, *Cohesion in Metals, Transition Metal Alloys*, North-Holland, Amsterdam, 1989.
- [39] P.M. Ossi, *Phys. Status Solidi A* 135 (1993) 169.
- [40] P.M. Ossi, *Phys. Status Solidi A* 119 (1990) 463.
- [41] A. Cavalleri, F. Giacomozzi, L. Guzman, P.M. Ossi, *J. Phys. Condens. Matter* 1 (1989) 6685.
- [42] P.M. Ossi, *Z. Phys. B: Condens. Matter* 77 (1989) 321.
- [43] P.M. Ossi, *Mater. Sci. Eng.* 90 (1987) 55.
- [44] P.M. Ossi, *Thin Solid Films* 275 (1996) 235.
- [45] M.J. Griffiths, *J. Nucl. Mater.* 159 (1988) 190.
- [46] Z.J. Zhang, B.X. Liu, *J. Phys. Condens. Matter* 6 (1994) 9065.
- [47] P.M. Ossi, R. Pastorelli, *Nucl. Instr. Meth. Phys. Res. B* 147 (1999) 202.

The interface between TiAlN hard coatings and steel substrates generated by high energetic Cr^+ bombardment

C. Schönjahn ^{*}, M. Bamford, L.A. Donohue, D.B. Lewis, S. Forder, W.-D. Münz

Sheffield Hallam University, Materials Research Institute, Howard Street, Sheffield S1 1WB, UK

Abstract

The microstructure of TiAlN coatings deposited by reactive unbalanced magnetron (UBM) sputtering after substrate bombardment with Cr ions, generated by a cathodic arc, and compositional changes of the ferritic steel substrate have been investigated for different bias voltages (U_b) during the Cr bombardment. Analysis was carried out using cross-sectional transmission electron microscopy (XTEM) and conversion electron Mössbauer spectroscopy (CEMS). The aim of the Cr bombardment is a substrate sputter cleaning effect. This is achieved when a bias voltage of -1200 V is applied. In this case subsequent UBM deposition of TiAlN leads to the growth of dense coatings exhibiting local epitaxy. For lower bias voltages CEMS indicates Cr deposition resulting in an open columnar structure of the subsequently grown TiAlN film, although small areas with oriented growth can still be observed. © 2000 Elsevier Science S.A. All rights reserved.

Keywords: Cathodic arc; Epitaxy; Interface; Mössbauer spectroscopy; Sputter cleaning

1. Introduction

Substrate sputter cleaning is an important step in all PVD processes. An alternative approach to the sputter cleaning in an argon glow discharge prior to sputter deposition is metal ion etching where a cathodic arc serves as an ion source as used prior to arc deposition. This provides high ion energies and fluxes and it has been shown that PVD coatings deposited after metal ion etching give better results in adhesion testing [1].

It has been shown that metal ion etching modifies the bombarded substrate surface [2] and the microstructure of the initial growth region of the coating deposited immediately after metal ion etching [3]. Local epitaxy in the coating has been observed for $\text{Ti}_{0.5}\text{Al}_{0.5}$ etching indicating that a relatively clean growth surface with well preserved crystalline order has been achieved. The presence of heavier and more energetic Nb ions during the $\text{Ti}_{0.85}\text{Nb}_{0.15}$ etching led to the formation of an amorphous interface layer and subsequent competitive columnar growth.

A drawback of the cathodic arc metal ion etching technique is the deposition of droplets on the substrate

surface, which produce subsequent growth defects in the coating. Earlier investigations have shown that high melting point materials, which also have high vapour pressure, should be used as etching materials in order to minimise this effect [4,5]. This and the findings in Ref. [3] make chromium, with its medium atomic mass, relatively high melting point and extremely high vapour pressure [6], attractive for use in metal ion etching.

A special feature of metal ion etching with a cathodic arc is that, besides multiply ionised metal ions, metal atoms are present. This makes the bias voltage applied to the substrate during metal ion etching a crucial process parameter, because high bias voltage levels may cause substrate surface overheating whereas low bias voltages may result in metal deposition rather than substrate sputter cleaning [7].

The present study investigates the influence of the bias voltage during cathodic arc ion etching of steel substrates on the interface region between a TiAlN coating deposited by unbalanced magnetron sputtering and the Cr etched mild steel substrate. The substrate surface modification has been investigated using conversion electron Mössbauer spectroscopy and cross-sectional transmission electron microscopy. The latter technique has also been employed for the microstructure investigation of the TiAlN coating.

^{*} Corresponding author. Tel.: +44-114-225-3500;
fax: +44-114-225-3501.

E-mail address: c.schonjahn@shu.ac.uk (C. Schönjahn)

2. Experimental procedure

Cr ion etching and coating deposition has been performed employing a combined CA/UBM deposition system [8] as shown in Fig. 1. The chromium cathode is operated in the CA mode during metal ion etching. For coating deposition the cathodes are coupled via electromagnetic coils to form a closed magnetic field and the $\text{Ti}_{0.5}\text{Al}_{0.5}$ targets are operated in the UBM mode. The substrates are undergoing three-fold rotation during substrate sputter cleaning and coating deposition (see Fig. 1 with $\tau_1 = 7.5$ rpm, $\tau_2 = 27$ rpm, $\tau_3 = 4.5$ rpm) and have an average distance of 250 mm from the targets. The chamber was evacuated to a pressure of 6×10^{-5} mbar and heated to 400°C (measured with a thermocouple attached to a dummy substrate). The pump down and heating is followed by a Cr metal-ion bombardment. The etching of the substrate is carried out over a period of 20 min by biasing the substrates at -1200 V, -1000 V, -800 V or -600 V and operating the steered cathodic Cr arc at an arc current of 100 A. The Ar working pressure was kept at 6×10^{-4} mbar for stable arc operation. During the Cr-ion etching step the substrate temperature is raised to 450°C either by high-energy ion impact at high bias voltages (-1200 V and -1000 V) or in the other cases additional radiant substrate heating. The temperature is kept constant by radiant substrate heating during TiAlN reactive deposition at a working gas pressure of 3.4×10^{-3} mbar (50:30 Ar: N_2 gas mixture). The target power on both TiAl targets was set to 8 kW and the unbalancing coil current was 6 A. The bias voltage during coating growth is reduced to -75 V. UBM deposition has been performed for 10 min giving a coating thickness of ~ 100 nm in order to stay below the escape depth of conversion electrons used in Mössbauer spectroscopy.

The substrate material was mild steel

($25 \times 25 \times 0.7$ mm³). All substrates were polished using $1 \mu\text{m}$ diamond paste in the final step resulting in a roughness $R_a = 5$ nm. The substrates were wet cleaned in an automatic 10 station industrial cleaning line containing a range of aqueous based alkali detergents, de-ionised water and vacuum radiant heating.

The XTEM samples were prepared using a diamond saw to obtain 2×0.5 mm² slabs which were further thinned to $20 \mu\text{m}$ by mechanical polishing. The samples were mounted on a Cu slot grid and Ar^+ (5 keV, 16 mA, 5°) ion milled to electron transparency. The transmission electron microscopy has been carried out using a Philips CM20 microscope operated at 200 kV acceleration voltage. Chromium etched mild steel samples were studied using conversion electron Mössbauer spectroscopy in a gas flow proportional counter with an anode wire potential of 1500 V. A 25 mCi cobalt 57 radionuclide source in a rhodium matrix was placed on a Wissel velocity transducer, and data was collected by an EG&G ORTEC multi-channel analyser.

3. Results and discussion

3.1. Compositional changes of the substrate

The CEMS studies of the various etched samples show a reduction in relative counts when the bias voltage is reduced, showing that the overall coating thickness (TiAlN+Cr) is increased due to increasing chromium deposition. The effect of the etching process suggests the presence of the iron rich $\alpha\text{-FeCr}$ phase. As the bias voltage is decreased the amount of FeCr similarly reduces (see Table 1 and Fig. 2).

The presence of the FeCr phase is shown by the change in isomer shift δ and quadrupole interaction ΔE_Q (see Table 2) at the substrate surface.

For an untreated mild steel sample a symmetrical sextet with little or no quadrupole interaction would be expected. For Cr etched samples it was found that the line half-widths at half-maximum height were uneven, showing the presence of a second sextet at a similar position to the substrate.

The isomer shift becomes less negative showing a reduction in the 's' electron density at the iron nuclei coupled with an increase in electric field gradient shown by the increase in the quadrupole field. This represents

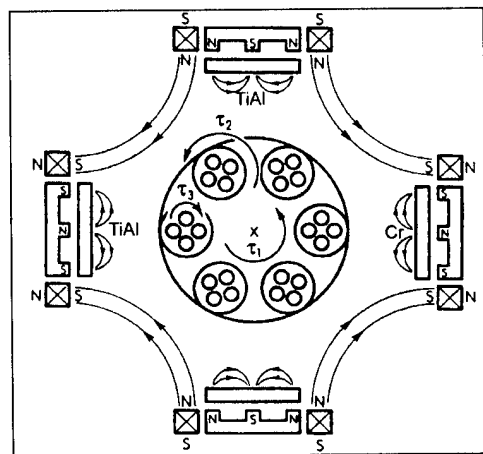


Fig. 1. Schematic drawing of the combined CA/UBM four-target deposition system.

Table 1
Observed parameters of the substrate and interface for all bias voltages

Bias voltage U_b (V)	Relative area of FeCr to Fe (%)
-1200	16
-1000	13
-800	10
-600	8

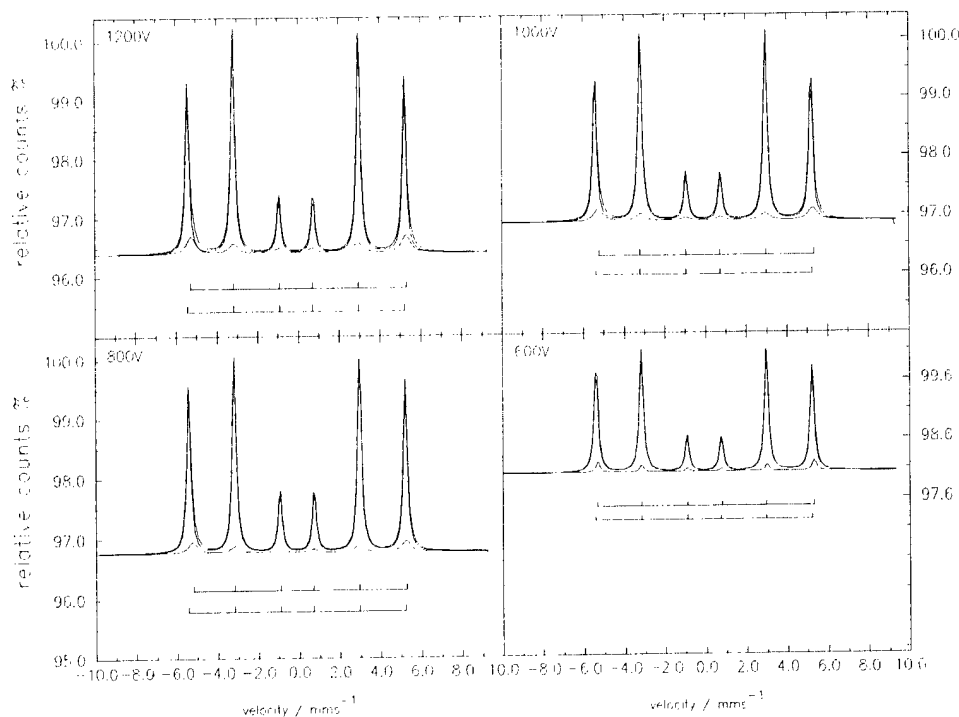


Fig. 2. Comparison of CEMS studies at varying bias voltages. The more intense sextet of mild steel substrate overlays the sextet of the interface region.

Table 2

Change in relative peak area of interface to substrate material for different bias voltage

	Substrate steel	Interface material
δ (mm s ⁻¹)	-0.11 ± 0.02	-0.05 ± 0.02
ΔE_0 (mm s ⁻¹)	0.00 ± 0.01	0.06 ± 0.01
H (T)	33.0 ± 0.1	32.5 ± 0.1

a change in the surroundings of the iron sites due to the presence of chromium. There is a slight reduction in the magnetic field strength H also, showing the presence of Cr, since alloys of FeCr with high levels of Cr are paramagnetic as opposed to ferromagnetic iron. These parameters remain constant throughout the range of bias voltages showing that the same phase is formed each time although in smaller amounts at lower bias voltages.

3.2. Microstructure of the interfacial region

Figs. 3–5 show bright field images of the interfacial region for samples etched at different bias voltages. In Fig. 4(a) a typical interface region of a sample etched at a bias voltage of -600 V, taken in underfocused conditions, is shown so that regions of low-density material appear bright. These regions were only found for substrates etched at -600 V. Fig. 4(b) shows such an area at higher magnification. The dark layer presumably formed during the substrate cleaning varies in thick-



Fig. 3. Bias voltage during cathodic Cr arc: (a) $U_b = -800$ V; (b) $U_b = -1000$ V.

ness considerably. CEMS suggests that this layer is a deposited chromium layer.

Fig. 5 presents the interface region for a bias voltage of -1200 V. In Fig. 5(c) evidence of removal of substrate material of ~ 100 nm is visible. The substrate beneath the droplet is ~ 100 nm thicker than the surrounding substrate, which was exposed to further ion impact indicating that an etch rate of at least 5 nm/min is obtained under these cleaning conditions. Therefore, the marked area in Fig. 5(f) can be identified as the modified substrate in contrast to the deposition layer in Fig. 4. Because of the similarity of Cr and Fe in the atomic mass (atomic number 24 and 26, respectively), the visible contrast is not attributed to atomic number but is believed to be due to local strain fields caused by

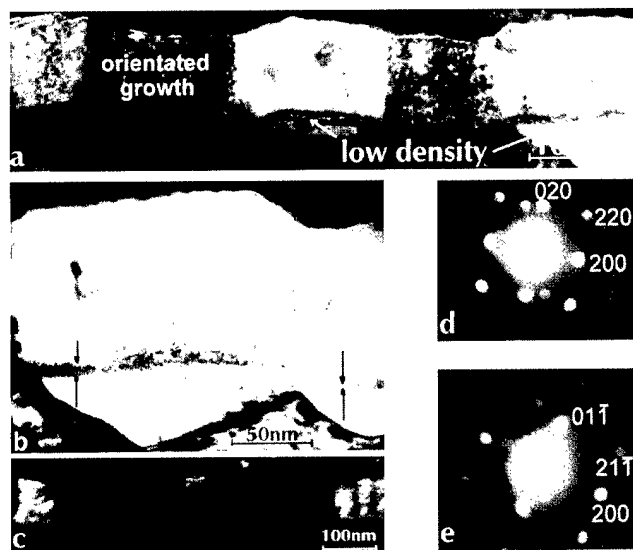


Fig. 4. Bias voltage during cathodic Cr arc $U_b = -600$ V: (a) bright field image (BF) (underfocused); (b) BF at higher magnification (overfocused); (c) dark field image (DF); (d) convergent beam diffraction pattern from TiAlN; (e) CBED from steel substrate.

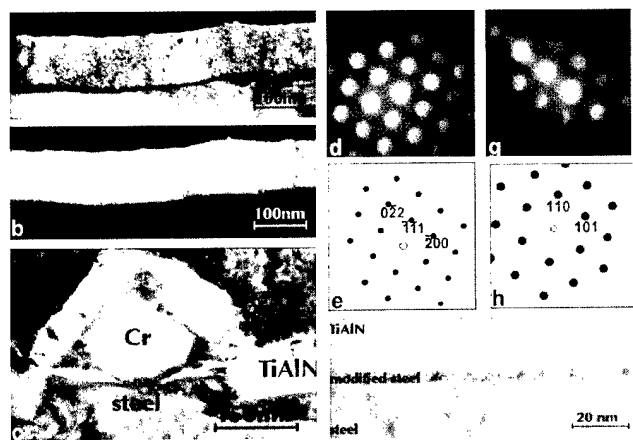


Fig. 5. Bias voltage during cathodic Cr arc $U_b = -1200$ V: (a) BF; (b) DF from (220) reflection; (c) BF showing droplet and protected steel; (d) CBED TiAlN; (e) schematic DP of TiAlN; (f) BF higher magnification; (g) CBED from steel substrate; (h) schematic DP of steel.

dislocation cores or defect clusters generated by highly energetic Cr ion impact. The thickness of the modified region was measured by XTEM imaging to be ~ 5 nm. TRIM [9] simulation assuming an acceleration potential of 1.2 kV applied to the Fe substrates and a maximum charge state of Cr^{3+} [10] shows that target displacement events and vacancy production takes place in a depth of up to 6 nm.

Because the described surface modification due to metal ion etching leads to modified initial nucleation conditions, the microstructure of the TiAl coating is expected to be affected by the substrate pre-treatment. Indeed, an increase in grain size is found for high etching bias voltages as demonstrated in Fig. 3(a), (b) and

Fig. 5(a). Here the grain boundaries of the coating match the grain boundaries of the substrate, as can most clearly be seen in Fig. 3(b). This indicates local epitaxial growth of the coating (fcc, $a = 0.417$ nm [11]) on the ferritic steel (bcc, $a = 0.286$ nm [12]). The dark field image taken from the (220) reflection shown in Fig. 5(b) demonstrates the large dimension of areas with the same orientation. In Fig. 5(d) and (g) convergent beam diffraction patterns (CBED) of the TiAlN coating and the steel substrate are presented, showing that the [011] zone axis of the coating is parallel to the $[\bar{1}11]$ zone axis of the steel substrate. This shows that although some damage has been induced in the substrate surface during the Cr ion bombardment, the crystallinity of the substrate surface is preserved so that local epitaxial growth can occur [bright almost structureless area in Fig. 5(b)].

In contrast the low etching bias voltage of -600 V gives rise to finer grain size as can be seen from Fig. 4(a) and (c). Porosity between the grains is observed. On some areas local orientated growth can still be observed. This is confirmed in Fig. 4(d) and (e) showing a [001] zone axis CBED pattern of the coating and a [011] CBED pattern of the underlying steel grain, respectively.

The presence of the above described film porosity can be avoided when the substrates are treated at higher bias voltages ($U_b = -800$ to -1200 V). It is thought that the improved nucleation conditions of a 'cleaner' substrate surface stimulate void free film growth in contrast to the possibly gas bubble containing Cr deposits as shown in Fig. 4(a) labelled 'low density'.

4. Conclusions

CEMS and XTEM investigations on ferritic steel samples coated with TiAlN after Cr ion bombardment at different bias voltages ($U_b = -600$ V, -800 V, -1000 V and -1200 V) have been carried out. Significant differences in substrate surface modification, such as substrate material removal for $U_b = -1200$ V (etching) and deposition of low density material for $U_b = -600$ V, have been observed. This led to substantial changes in microstructure of the subsequently grown TiAlN coating, ranging from columnar growth with an open structure for $U_b = -600$ V to local epitaxial growth at $U_b = -1200$ V. In the latter case an improved adhesion of the coating on the steel is expected. For verification thicker TiAlN coatings should be deposited in order to perform adhesion tests.

References

- [1] W.-D. Münz, J. Schroeder, H. Pechterstein, G. Håkansson, L. Hultman, J.-E. Sundgren, in: A. Czichos, L.G. Vollrath (Eds.), Proc. SURTEC, Berlin, Hanser, Munich, 1989, p. 61.

- [2] G. Håkansson, L. Hultman, J.-E. Sundgren, J.E. Green, W.-D. Münz, *Surf. Coat. Technol.* 48 (1991) 51–67.
- [3] I. Petrov, P. Losbichler, D. Bergstrom, J.E. Greene, W.-D. Münz, T. Hurkmans, T. Trinh, *Thin Solid Films* 302 (1997) 179–192.
- [4] W.-D. Münz, I.J. Smith, D.B. Lewis, S. Creasey, *Vacuum* 48 (1997) 473–481.
- [5] S. Creasey, D.B. Lewis, I.J. Smith, W.-D. Münz, *Surf. Coat. Technol.* 97 (1997) 163–175.
- [6] *Surface Engineering* ASTM Handbook Vol. 51, ASTM International, Materials Park, OH, 1994, p. 558.
- [7] J. Musil, J. Vyskocil, S. Kadlec, *Physics of Thin Films* 14 (1993) 79–144.
- [8] W.-D. Münz, D. Schulze, F.J.M. Hauzer, *Surf. Coat. Technol.* 50 (1992) 169–178.
- [9] J. Ziegler, J.A. Biersack, *The Stopping and Ranges of Ions in Matter*, Pergamon, New York, 1985.
- [10] I.G. Brown, B. Feinberg, J.E. Galvin, *J. Appl. Phys.* 63 (1988) 4889–4897.
- [11] I.J. Smith, D. Gillibrand, J.S. Brooks, W.-D. Münz, S. Harvey, R. Goodwin, *Surf. Coat. Technol.* 90 (1997) 164–171.
- [12] G.V. Raynor, *Metal Physics and Physical Metallurgy* Vol. 4, Pergamon Press, Oxford, 1964, p. 125.

Ion implantation by plasma immersion: interest, limitations and perspectives

F. Le Cœur, J. Pelletier *, Y. Arnal, A. Lacoste

Laboratoire d'Electrostatique et de Matériaux Diélectriques, UMR C5517, CNRS and Université Joseph Fourier, 38042 Grenoble Cedex 9, France

Abstract

Plasma-based ion implantation (PBII) is a recent method to implant ions into materials for modifying surface properties. Negative high voltage pulses are applied to the substrate to extract ions from the plasma and accelerate them directly onto the substrate surface. The main advantages of PBII over ion beam implantation are its simplicity for processing large surfaces or three-dimensional objects and the possibility of preparing surfaces *in situ* prior to the implantation process. The two general specifications required for PBII are low pressure, large size plasmas and high voltage–high current pulse generators. Multipolar discharges excited by distributed electron cyclotron resonance, which can operate with reactive gases and can be easily scaled up, are thus well adapted to the PBII process. In order to produce the high voltage–high current pulses with rise and fall times of the order of the inverse ion plasma frequency necessary for PBII processing, generators using pulse transformers, where the voltage at the primary is provided by transistor switches and where the energy is stored at a low voltage level, have been developed. Then, before discussing the various limitations of the process, PBII in plasmas is illustrated through few selected examples. © 2000 Published by Elsevier Science S.A. All rights reserved.

Keywords: High voltage pulse; Ion implantation; Materials processing; Plasma immersion; Plasma sheath; Pulse generator

1. Introduction

Ion implantation was first used in the 1960s to dope semiconductor materials for the electronics industry [1]. Then, the idea of using ion beams to enhance the surface properties of metals emerged in the early 1970s [2]. It was found that implantation of nitrogen, carbon, or boron into steel and other alloys resulted in increased wear and corrosion resistance and enhanced surface properties.

In conventional ion implantation, an ion source is used to create an ion beam of the species to be implanted. The ion beam is accelerated through a potential of from tens to hundreds of kilovolts and transported to the substrate. Since the beam spot size is usually smaller than the wafer size, mechanical and electrostatic scanning are used to achieve dose uniformity. The relatively low beam currents, limited by the source optics, lead to high costs for high-dose applications. Lower-energy implantation (energies less than 10 keV) can also be limited by ion beam optics, especially if high doses are required. Conventional ion implantation is a line-of-

sight process, and the objects being processed generally require manipulation in order to implant the desired surfaces. The limitation of this approach is that, for large size and three-dimensional (3-D) objects, the ability to implant their surfaces uniformly becomes difficult and, at times, cost prohibitive.

Plasma immersion ion implantation (PIII) or plasma-based ion implantation (PBII) was initially developed by Conrad and Castagna [3] in 1987 to circumvent the beam line restrictions. In this PBII technique, substrates are immersed directly in the plasma and are then pulsed biased to high negative voltages. As the sheath conformably surrounds the substrate, all surfaces are implanted at the same time, so that rastering and manipulation of the substrate are not necessary. PBII eliminates the intermediate stages of beam extraction, focusing, scanning, and wafer manipulation. The PBII technique has many advantages over the conventional implantation, such as high dose rates ($10^{16} \text{ cm}^{-2} \text{ s}^{-1}$), wide ion energy range starting from 0 up to 100 keV or more, large implant areas, and treatment of 3-D workpieces with complex shapes.

However, a few limitations and disadvantages of PBII in comparison with beam-line ion implantation can be

* Corresponding author.

pointed out: (i) no ion mass separation; all the ions in the plasma (monatomic and molecular ions) are implanted; (ii) not strictly monoenergetic, mainly depending on gas pressure and pulse shape; (iii) in situ dose monitoring is difficult and requires calibration; (iv) the production of secondary electrons under ion impact and their acceleration in the sheath leads to high current densities and X-ray formation; (v) biasing of thick dielectric objects is not possible. Despite these disadvantages, PBII appears particularly attractive for mass production in metallurgy and in the semiconductor and flat panel display industry.

The aim of this article is to present the plasma and pulse generator specifications generally required for PBII processing. In particular, we will demonstrate the necessity to dispose of low pressure and large size, scalable plasmas up to square or cubic meters. Such plasma dimensions can be easily provided by discharges confined with multipolar magnetic field structures. Also, new concepts of pulse generators able to fulfill the requirements assigned to the high voltage pulses for PBII processing are being developed. Finally, before concluding, we will discuss the physical and technological limitations of PBII and plasma-based ion implantation and deposition (PBIID) through selected examples of surface treatments.

2. PBII basic mechanisms

2.1. Evolution of the plasma sheath

The evolution of the plasma sheath when a negative high voltage pulse is applied to a substrate immersed in a plasma has already been extensively studied [4–6]. According to the time scale, three different phases, as shown in Fig. 1, must be distinguished. (1) On the time scale of the inverse plasma frequency $\omega_{pe}^{-1} = (\epsilon_0 m_e / n_e e^2)^{1/2} \approx 2 \times 10^{-10}$ s for $n_e = 10^{10}$ cm⁻³, electrons are repelled, whereas ions, much more massive than electrons, are left back. Therefore, an ion ‘matrix’ sheath that is free of electrons is formed around the substrate. (2) On the time scale of the inverse ion plasma frequency $\omega_{pi}^{-1} = (\epsilon_0 m_i / n_i e^2)^{1/2} \approx 3 \times 10^{-8}$ s for $n_i = 10^{10}$ N⁺ ions/cm³, the ions in the matrix sheath close to the substrate are accelerated towards the substrate. The energy distribution of ions depends of course on their initial position in the ion ‘matrix’ and the ion current density reaches a sharp maximum before decreasing. Then, once the ions in the matrix are collected, new ions are extracted from the plasma edge and the plasma sheath expands. (3) On a large time scale, typically tens of ω_{pi}^{-1} , the sheath and the current density evolve to the steady state (static sheath) given by the Child–Langmuir law. The theoretical evolution [6] of the ion current collected on the substrate as a function

of time is shown in Fig. 2 and the experimental corresponding evolution of the ion current is reported in Fig. 3. In the above expressions giving the electron and ion plasma frequencies, ϵ_0 is the permittivity of free space, $-e$ the electron charge, n_e and n_i are respectively the electron and ion densities, and m_e and m_i their masses.

2.2. Sheath thickness

Since, in PBII, the duration of negative pulses is much longer than the inverse ion plasma frequency (see Fig. 3), we can generally consider that the sheath thickness g is that given by the steady-state Child–Langmuir law, i.e.

$$g = \frac{2^{5/4} \epsilon_0^{1/2}}{3 \exp(-1/4)} \frac{V_0^{3/4}}{e^{1/4} n_i^{1/2} (kT_e)^{1/4}} \approx \lambda_{De} (eV_0/kT_e)^{3/4}, \quad (1)$$

where $-V_0$ is the potential of the substrate during the pulse (as a first approximation, the plasma potential is assumed equal to the ground potential), T_e the electron temperature of the plasma, k the Boltzmann constant, and λ_{De} the electron Debye length. As shown in Eq. (1), the thickness g of the sheath, independent of the mass of ions, is poorly dependent on the electron temperature and varies proportionally with the inverse of the square root of the plasma density. Accordingly, the amplitude E_0 of the electric field at the substrate surface (the highest amplitude in the sheath) is given by

$$E_0 = \frac{2^{3/4} \exp(-1/4) e^{1/4}}{\epsilon_0^{1/2}} n_i^{1/2} V_0^{1/4} (kT_e)^{1/4}. \quad (2)$$

The amplitude of the electric field, poorly dependent on the pulse voltage and on the electron temperature, is proportional to the square root of the ion density.

The numerical evolution of the thickness g of the static sheath as a function of the pulse voltage is shown in Fig. 4, when considering a plasma with a density $n_e = 10^{10}$ cm⁻³ and an electron temperature $kT_e = 1$ eV. For example, the sheath thickness exceeds 40 cm for $V_0 = 100$ kV. Such a result has strong implications on the specifications of PBII systems, as discussed below.

3. Plasma specifications

A first specification concerns the size of the plasma, which must be much larger than the sheath thickness in order to avoid total depletion of the plasma between the substrate and the plasma walls. As an example, at $V_0 = 100$ kV, the sheath thickness (40 cm) is such that the implantation of a 30 cm wafer requires reactor dimensions more than 1 m in diameter and 40 cm high.

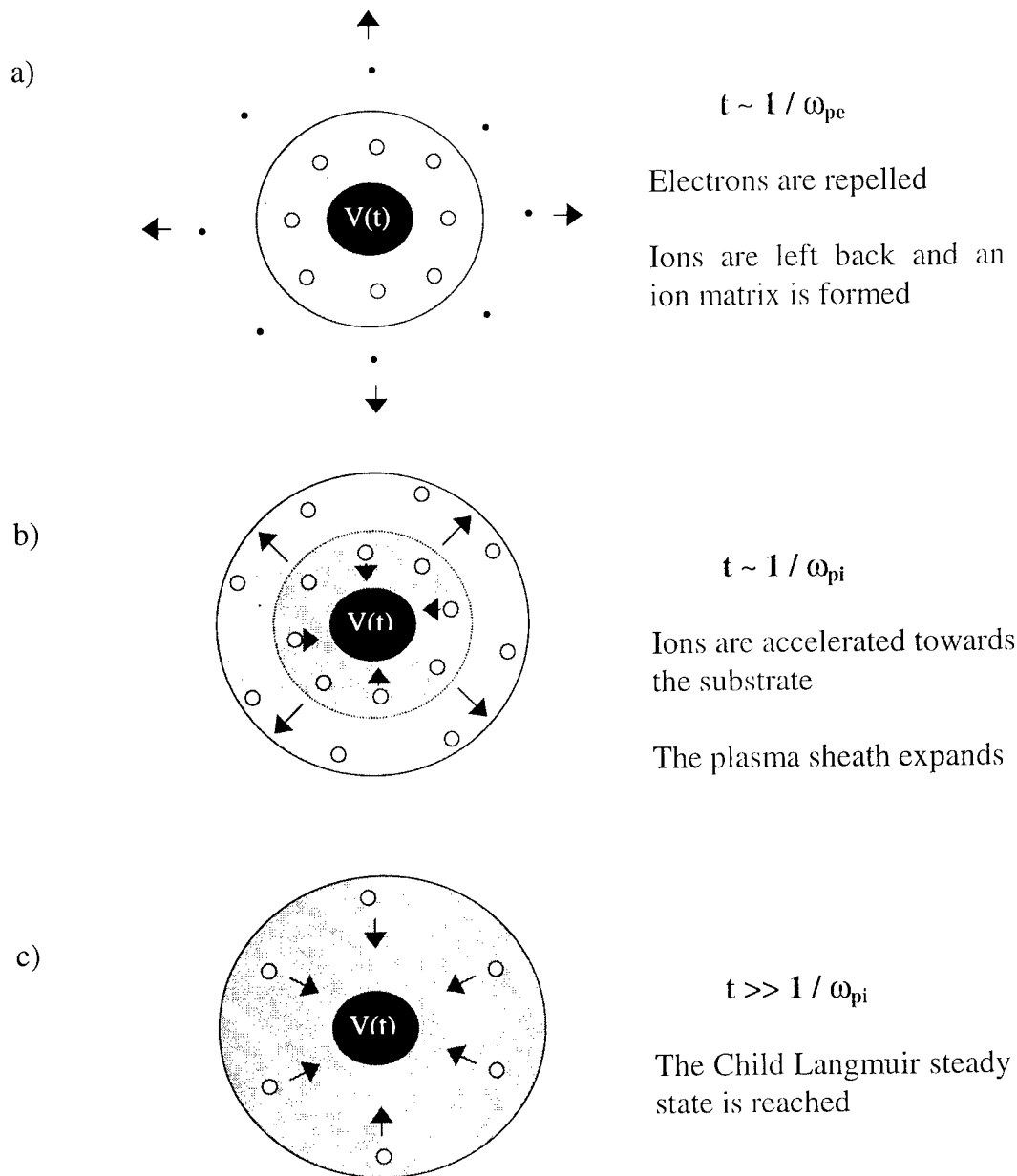


Fig. 1. Evolution of the plasma sheath with time when a negative voltage pulse $V(t)$ is applied to a substrate.

The other plasma specifications mainly concern the *energy distribution function* of the ions being implanted. Since, for a given application, the energy of implanted ions is generally predetermined, the control of the energy distribution function is necessary. Implantation of monoenergetic ions using PBII requires different conditions. As deduced from the above description of the sheath dynamics, this goal first requires a large pulse length compared with ω_{pi}^{-1} , so that the fraction of ions implanted from the initial matrix (accelerated under a potential difference less than V_0), is small with respect to the fraction of ions extracted from the plasma at the sheath edge (accelerated under the applied potential difference V_0) [6]. Secondly, the ion transit in the sheath

must be collisionless, i.e. an ion mean free path on the order or longer than the sheath thickness. Under these conditions, monoenergetic ion bombardment can be obtained. Otherwise, the effect of ion–neutral collisions in the sheath is to reduce significantly the ion energy below the expected value. Unfortunately, even in the ideal case of a monoenergetic ion bombardment, owing to the presence in the plasmas of several ionic species, the different ion populations reach the substrate surface with distinct velocities and, hence are implanted with distinct projected depths.

However, despite the difficulty of achieving a perfect control of the *velocity distribution function* of ions at the substrate surface, low pressure plasmas would be prefer-

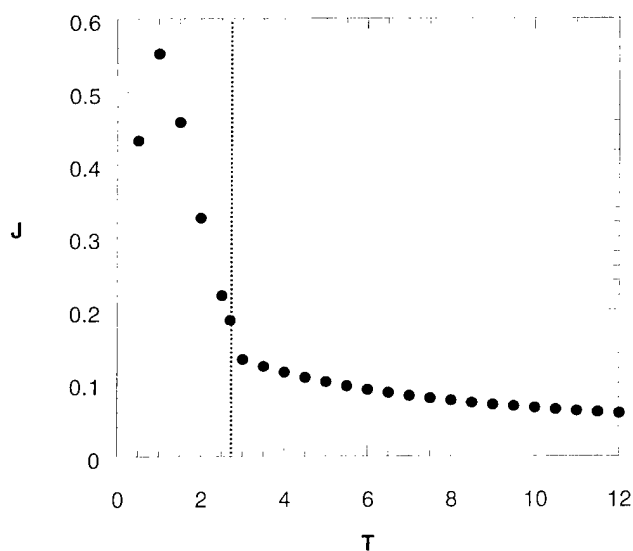


Fig. 2. Normalized implantation current density as a function of reduced time $T = \omega_{pi} t$. The lines show the analytical solutions for $T < 2.7$ and $T > 3.0$ (from Ref. [6]).

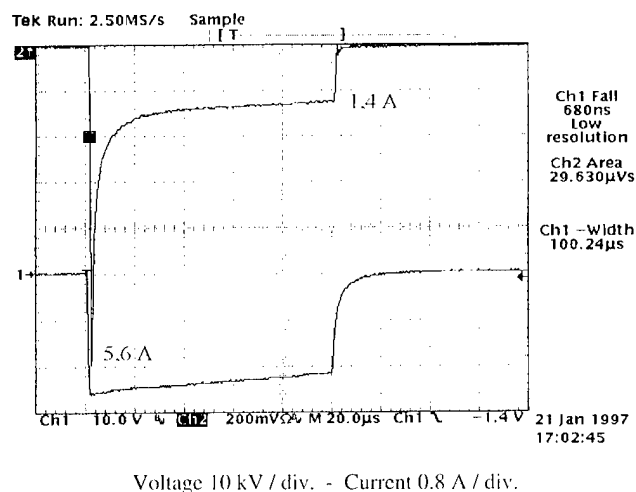


Fig. 3. Typical voltage and current experimental waveforms at -25 kV.

able in order to exploit the total capabilities of the voltage pulse supplier.

Finally, too dense a plasma, which leads to shorter sheath thickness and higher ion current densities, is not attractive owing to enhanced risks of arcing in the sheath [7,8] (higher electric field intensity) and increased substrate heating.

4. Pulse generator specifications

The specifications for the pulse generators in PBII processing directly follow from the sheath dynamics described above. Firstly, the pulse generator must be able to provide enough current in order to clear the

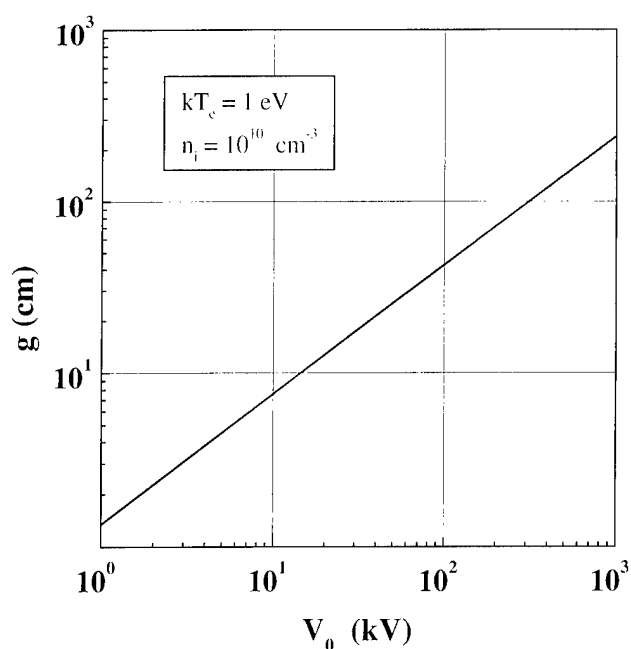


Fig. 4. Sheath thickness as a function of the voltage amplitude V_0 of the negative pulse.

initial current peak after the application of the pulse. In addition, as the sheath thickness (geometrical factor for non-planar substrates) and secondary electron yield both increase with the pulse voltage, the required maximum peak current also increases with the pulse voltage. Consequently, when the pulse generator cannot provide enough current, the rise time of the pulse voltage becomes huge compared with the pulse duration (see Fig. 5) and the ion energy distribution of the ions cannot be kept under control.

As already discussed in Section 3, the second specification corresponds to the necessity to reach a quasi-monoenergetic energy distribution for the implanted ions. To achieve this goal, it is necessary to apply pulses with rise and fall times of the order of ω_{pi}^{-1} and a duration time τ much larger than ω_{pi}^{-1} . In this way, the time during which the ion energy distribution is not monoenergetic is restricted to the minimum and is thus much shorter than the total pulse duration τ . Since ω_{pi}^{-1} is typically of the order of $1 \mu\text{s}$ in the low-density plasmas used for PBII, rise and fall times of less than $1 \mu\text{s}$ and pulse durations of more than a few tens of microseconds are required in most cases. At a given plasma density, the dose per pulse is controlled by its duration length τ , whereas the dose rate is controlled by the product of pulse duration τ and its repetition rate f . The final dose is then proportional to the total duration of the PBII process.

Another important requirement is to avoid any reverse positive voltage, in particular at the end of the pulse. In this way, ion bombardment of reactor walls

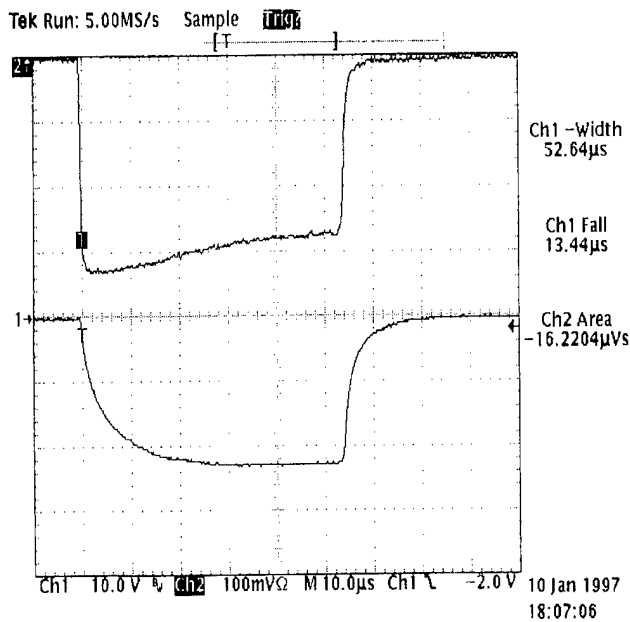


Fig. 5. Typical voltage and current waveforms when the pulse generator cannot clear the initial peak current.

and contamination of the substrate from reactor wall sputtering is thus avoided.

Finally, additional requirements for the pulse generator, in particular in terms of reliability and safety, are also important: the generator must be protected against short-circuits in the load (arcing protection) and also energy storage at the lowest voltage level is highly desirable.

5. Multipolar plasmas for large-area PBII processing

The above discussions have shown the necessity to generate low-pressure, large-sized plasmas for PBII. Discharges confined by multipolar magnetic fields exhibit these two characteristics. In addition, the scaling up of these plasmas is possible up to several cubic meters without any difficulty [9,10].

5.1. Multipolar magnetic field confinement

Conventional multipolar magnetic field structures [11] generally consist of parallel magnet bars with alternating polarities. Such magnetic fields are well known to be very efficient in providing homogeneous plasmas at low pressure (typically between 10^{-2} and 1 Pa) with densities of up to two orders of magnitude higher than that obtained without magnetic confinement [12]. However, the confinement effect of a multipolar magnetic field on the plasma itself is weak. In fact, the improved uniformity and the enhanced density of the plasma mainly result from the very efficient confinement of fast electrons that, once trapped in the magnetic field,

produce the peripheral ionization of the plasma. Then, from this region, the plasma, i.e. the ions and the slow thermal electrons, diffuses perpendicularly to the magnetic field lines under the influence of the density gradients

5.2. Fast electrons in a multipolar magnetic field

At low pressure, the fast electrons behave like free energetic particles in motion in the external fields, including the multipolar magnetic field and the space charge electric field of the plasma. However, as the variation of the potential inside the plasma usually does not exceed a few electron-volts, the trajectory of the fast electrons is, in contrast to that of the slow plasma electrons, only weakly influenced by the space charge electric field.

Neglecting the influence of the space charge electric field with respect to the action of the magnetic field, the study [13,14] of the trajectories demonstrates that the motion of the fast electrons trapped in the multipolar magnetic field is confined between two field lines and oscillates between two opposite poles until they suffer elastic or inelastic ionizing collisions.

A more complete description of the motion of fast electrons also shows that, besides the oscillations between mirror points in front of two successive cusps, these electrons undergo a drift velocity along the magnets due to the magnetic field curvature and magnetic field gradient [13,14]. The direction of this drift velocity changes with the direction of either the magnetic field, or the curvature radius vector.

Because of the magnetic drift of the fast electrons along the multipolar magnetic structure, leakage of these electrons inevitably occurs at the extremities of the magnet bars that constitute an open, non-closed magnetic field configuration. Loss of fast electrons can be overcome by adding magnets at the extremities of the magnet bars in such way as to close the magnetic structures onto themselves according to ring, racetrack or comblike configurations [15]. These magnetic structures are the same as those currently realized in the *magnetron* plasmas used worldwide for sputtering applications.

5.3. Production of the fast electrons in the multipolar magnetic fields

For more than a decade following the initial study of Limpacher and MacKenzie [12], the excitation of multipolar plasmas was almost exclusively ensured by electron emission from heated filaments located in the central volume (free from magnetic field), and biased negatively with respect to the multipolar magnetic structure and the chamber wall. At low pressure, the fast electrons can reach the multipolar magnetic sheath,

become trapped and produce the peripheral ionization of the plasma. Another attractive solution is to produce the fast electrons directly in the multipolar magnetic field by placing the filaments directly in the magnetic sheath [16].

Unfortunately, hot filaments cannot be used to sustain plasmas in reactive gases (O_2 , FH , Cl_2). Thus, at very low pressure, another attractive solution is to transfer high frequency (HF) energy to the electrons by electron cyclotron resonance (ECR) within the confining magnetic field. The development of this excitation, called distributed ECR or DECR, is based on two ideas [17]:

1. the permanent magnet rows intended for multipolar magnetic field confinement are also used to provide the magnetic field intensity B_0 needed for the ECR coupling

$$B_0 = 2\pi(m_e/e)f_0, \quad (3)$$

where f_0 is the microwave frequency;

2. the HF electric field required for ECR is provided by linear applicators (or antennas) running along and close to the magnet rows [17]. This scheme results in the generation of the plasma in the multipolar magnetic field, where the fast electrons (accelerated through ECR) are trapped and oscillate between two successive cusps until they ionize the gas.

The evolution of plasma density as a function of microwave power and excitation frequency [15,18] shows that, when the microwave power increases, the plasma density at first varies proportionally to the microwave input power. Next, the plasma density reaches a maximum value of the order of the critical density:

$$n_c = \epsilon_0 m_e \omega_0^2 / e^2 \quad (4)$$

with $\omega_0 = 2\pi f_0$. Since the critical density varies according to the square of the excitation frequency, the highest densities are obtained at the highest excitation frequency [18]. However, for PBII applications, on the one hand the substrate heating due to the power deposited by the ion bombardment and, on the other hand, arcing due to the high electric fields developed in the sheaths [7,8] do not argue in favor of too dense a plasma. Thus, the 2.45 GHz excitation frequency is high enough to provide the plasma densities required for PBII, i.e. of the order of 10^{10} cm^{-3} .

Finally, another possibility commonly used to accelerate electrons in a multipolar magnetic field is to bias the magnetic structure negatively with respect to the walls by applying radio frequency (RF) or negative DC voltages. The ions are accelerated through the sheath towards the surface above the magnetic structure, yielding sputtering of the surface and emission of secondary electrons. These secondary electrons are then accelerated in the ion sheath surrounding the magnetic structure; outside the sheath, these electrons, trapped in the

multipolar magnetic field, oscillate between two opposite adjacent magnetic poles until they ionize the plasma. This scheme is currently applied in the well-known *magnetron* plasmas used for direct or reactive sputtering of solid, non-volatile materials.

Clearly, plasmas confined by multipolar magnetic fields and excited at very low pressure are perfectly well suited to large-area PBII processing. In particular, the scaling up of these plasma sources is possible up to square or cubic meters without any difficulty or limitation. As a confirmation, the large volume PBII system developed at the Hughes Research Laboratory (1.2 m in diameter, 2.4 m long) allows the implantation of large substrates with 250 keV ions [19]. In this reactor, the plasma is excited with an array of hot filaments and can thus be operated only with non-reactive gases. In contrast, with hot cathode multipolar discharges, DECR plasmas can operate with highly reactive gases such as oxygen or fluorine. Such a reactor, 60 cm in diameter, 70 cm high, previously described [20–22], allows PBII processing without arcing up to 60 keV. Of course, higher voltages would require larger reactor dimensions.

Another possibility of multipolar structures is illustrated by *magnetron* plasmas excited by DC or RF voltages. In this way, an array of *magnetrons* surrounding a pulsed biased substrate can, by sputtering, produce the partially ionized metallic vapors involved in PBIID processing. As for multipolar plasmas, such reactors can be scaled up without any difficulty, as is already the case for *magnetrons* at the industrial level.

Considering the aforementioned plasma specifications, it clearly appears that, at low pulse voltages, typically less than 30 kV (sheath thickness less than 10 cm), all kinds of plasma can be used for PBII processing. In contrast, at high pulse voltages, the plasma requirements are much more difficult to meet. Multipolar discharges, which can be excited in different ways according to the application, are particularly well suited to applications of ion implantation up to 100 kV or more.

6. Pulse generators for large-area PBII processing

As discussed above, the pulse generator is a central component in PBII processing since it has to deliver very high instantaneous power, to present rise and fall times within a microsecond and finally to resist sudden short circuits in the load.

The most commonly used high voltage pulse generator described in the literature combines a high voltage power supply and a high voltage switch [22,23]. A conventional system includes a positive DC high voltage supply (typically a few tens of kilovolts, a few milliamps) connected to a capacitor (tens of nanofarads or more) through a charging resistor (100 to 200 k Ω). The pulse

duration, controlled by a tetrode (the positive electrode of the capacitor is switched down to ground through the tetrode by grid control), can reach 100 μ s with a repetition rate of up to a few 100 Hz. The target bias voltage and current during implantation can be monitored with a voltage divider and a current transformer. However, the main limitation of most vacuum tubes is the maximum current being emitted by current hot cathodes.

Since the currents delivered by vacuum tubes are generally limited to values of the order of 10 A, other solutions must be developed to provide the high currents required for PBII processing at the industrial level. For this purpose, a 100 kV/100 A generator (10 MW power) using a pulse transformer [24] is presented in Fig. 6. A magnetic core is used as step-up pulse transformer. Voltage duration at the primary is provided by transistor switches that can achieve rise and fall times of less than 1 μ s and maximum pulse currents of 100 A. The primary of the transformer consists of 96 turns wired up in parallel and the secondary of 96 turns wired up in series. The performances reported with this type of pulse generator have been obtained on a test resistor and then on a substrate immersed in a plasma [24]. An example of pulse characteristics obtained with a load constituted by a substrate immersed in a DECR nitrogen plasma [20–22] is presented in Fig. 7(a). In this example, the average voltage is 60 kV and the initial peak current reaches 95 A. In Fig. 7(b), the waveform of a pulse with intentional arcing is shown. The other characteristics are such that all the requirements for PBII processing are fulfilled [24].

The high current pulse generator described above appears particularly well suited for large-area PBII processing. The absence of a vacuum tube and of a high voltage power supply makes this pulse generator of comparatively low cost with respect to other conventional systems. In addition, energy storage at low voltage

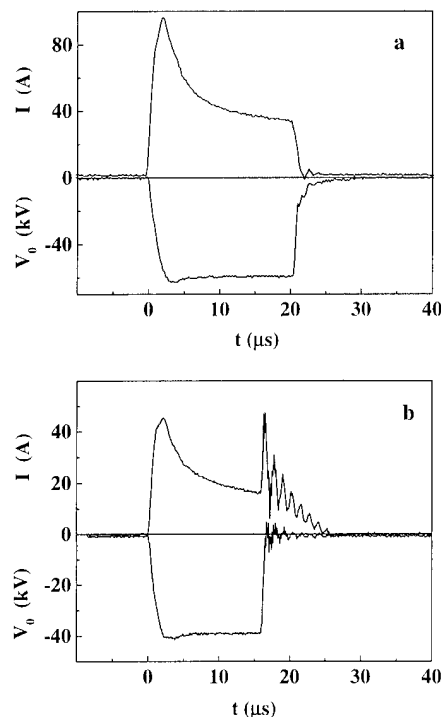


Fig. 7. Typical voltage and current waveforms obtained on a nitrogen plasma using a 100 kV–100 A pulse transformer: (a) pulse without short circuit; (b) pulse with arcing.

level (1 kV) is quite attractive for safety purposes. Also, the possibility to extend the available voltage and current ranges to much higher values opens interesting perspectives for PBII processing at the industrial level.

7. Limitations and perspectives for PBII

Up to now, the physics and the possible applications of PBII have already been extensively studied [25]. However, the transfer of processes from the laboratory to industry is mainly limited to very specific and low-energy applications. In fact, mass production using PBII processing requires production tools still under development. Large-volume multipolar plasma reactors, on the one hand, and high power pulse supplies (100 kV–1000 A/100 MW), on the other hand, are mandatory for the rise of PBII at the industrial scale. Nevertheless, considering the sheath thickness as a function of the pulse voltage (Fig. 4), it is obvious that operating much above 250 kV is unrealistic and would lead to plasma dimensions and plasma production means requiring very high investments.

The great disadvantage of PBII compared with beam-line ion implantation is the absence of mass separation. Consequently, all the ions (atomic, molecular, ionic impurities) present in the plasma are implanted. As examples, in oxygen or nitrogen plasmas, the density of monatomic ions (O^+ or N^+) is of the same order of

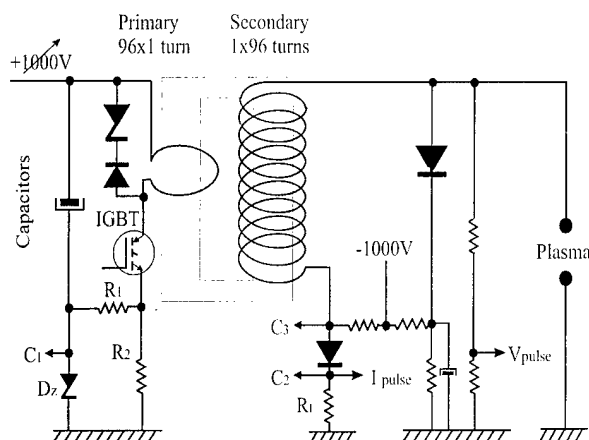


Fig. 6. Schematic circuit diagram of a pulse transformer.

magnitude as diatomic ions (O_2^+ or N_2^+), so that equivalent doses of atoms (O or N) are implanted at two distinct projection depths. A possible way to circumvent this drawback is the careful choice of the parent gas. In general, provided the implantation of hydrogen ions is not cumbersome, the hydrogenated compounds (when they exist) of the elements to be implanted appear as fairly good candidates: NH_3 for nitrogen implantation, H_2O for oxygen, H_2S for sulfur, FH for fluorine, etc. In the case of a nitrogen plasma, the projected depths $520R_p$ in Si of N atoms from 90 keV N^+ and N_2^+ ions are 2010 Å and 1090 Å respectively. In the case of an ammoniac (NH_3) plasma, the projected depths of N atoms from 90 keV N^+ , NH^+ and NH_2^+ ions are 2010 Å, 1970 Å and 1855 Å respectively [26]. Since the corresponding longitudinal stragglings are of the order of 600 Å, the implantation profile is practically that of nitrogen atoms implanted with the same velocity. In this way, using gas mixtures, controlled multispecies ion implantation can be achieved in one step.

Finally, a very great advantage of PBII over other techniques lies in achieving sequential processing in the same reactor, such as cleaning, etching and deposition prior or after PIII. Such a possibility opens new fields of applications and new perspectives for the PBII technique.

Acknowledgements

This work was supported by a grant from the Région Rhône-Alpes, France. Frédéric Le Cœur thanks the Région Rhône-Alpes for a doctoral fellowship.

References

- [1] S.T. Picraux, Phys. Today 37 (1984) 38.
- [2] N.E.W. Hartley, Wear 34 (1975) 427.
- [3] J.R. Conrad, T. Castagna, Bull. Am. Phys. Soc. 31 (1986) 1479.
- [4] J.R. Conrad, J. Appl. Phys. 62 (1987) 777.
- [5] I.J. Donnelly, P.A. Watterson, J. Phys. D 22 (1989) 90.
- [6] M.A. Lieberman, J. Appl. Phys. 66 (1989) 2926.
- [7] S. Mändl, J. Brutscher, R. Günzel, W. Möller, Nucl. Instrum. Methods B: 112 (1996) 252.
- [8] S. Mändl, J. Brutscher, R. Günzel, W. Möller, J. Vac. Sci. Technol. B: 14 (1996) 2701.
- [9] J. Pelletier, Y. Arnal, R. Debric, L. Pomathiod, J.C. Rifflet, Rev. Sci. Instrum. 55 (1984) 1636.
- [10] L. Pomathiod, R. Debric, Y. Arnal, J. Pelletier, Phys. Lett. A 106 (1984) 301.
- [11] K.N. Leung, T.K. Samec, A. Lamm, Phys. Lett. A 51 (1975) 490.
- [12] R. Limpaecher, K.R. MacKenzie, Rev. Sci. Instrum. 44 (1973) 726.
- [13] C. Gauthereau, G. Matthieussent, J. Phys. (Paris) 45 (1984) 1113.
- [14] J. Pelletier, G. Matthieussent, Homogeneity in multipolar discharges: the role of primary electrons, in: M. Moisan, J. Pelletier (Eds.), Microwave Excited Plasmas, Elsevier, Amsterdam, 1992, pp. 351–384.
- [15] T. Lagarde, J. Pelletier, Y. Arnal, Plasma Sources Sci. Technol. 6 (1997) 53.
- [16] C. Courteille, J. Bruneteau, F. Valckx, Z. Zleziwski, M. Bacal, Rev. Sci. Instrum. 64 (1993) 3265.
- [17] M. Pichot, A. Durandet, J. Pelletier, Y. Arnal, L. Vallier, Rev. Sci. Instrum. 59 (1988) 1072.
- [18] T. Lagarde, Y. Arnal, J. Pelletier, Plasma Sources Sci. Technol. 6 (1997) 386.
- [19] J.N. Matossian, J. Vac. Sci. Technol. B: 12 (1994) 850.
- [20] F. Le Cœur, Y. Arnal, R. Burke, O. Lesaint, J. Pelletier, Surf. Coat. Technol. 93 (1997) 265.
- [21] J. Pelletier, T. Lagarde, Y. Arnal, R. Burke, J. Cocagne, Surf. Coat. Technol. 76–77 (1995) 770.
- [22] F. Le Cœur, T. Lagarde, J. Pelletier, Y. Arnal, R. Burke, M. Brunel, Rev. Sci. Instrum. 69 (1998) 831.
- [23] J. Brutscher, Rev. Sci. Instrum. 67 (1996) 2621.
- [24] O. Maulat, M. Roche, F. Le Cœur, O. Lesaint, Y. Arnal, J. Pelletier, J. Vac. Sci. Technol. B: 17 (1999) 879.
- [25] W. Möller, Plasma based ion implantation, in: H. Schlüter, A. Shivarova (Eds.), Advanced Technologies Based on Wave and Beam Generated Plasmas, Kluwer, Dordrecht, 1999, pp. 191–244.
- [26] J.P. Biersack, L.G. Hagmark, Nucl. Instrum. Methods 174 (1980) 257 The TRIM program is being continuously updated by J.F. Ziegler.

AlN formation by direct nitrogen implantation using a DECR plasma

N. Duez^{a,*}, B. Mutel^a, O. Dessaux^a, P. Goudmand^a, J. Grimblot^b

^a *Laboratoire de Génie des Procédés d'Interactions Fluides, Réactifs Matériaux (UPRES-EA No. 2698),
Université des Sciences et Technologies de Lille, 59655 Villeneuve d'Ascq, France*

^b *Laboratoire de catalyse de Lille (UPRESA 8010), Université des Sciences et Technologies de Lille, 59655 Villeneuve d'Ascq, France*

Abstract

Nitriding of aluminum was carried out successfully using a distributed electron cyclotron resonance (DECR) nitrogen plasma without RF bias voltage or heating of the substrate. The surface compositions and chemical environments of the treated samples were characterized by X-ray photoelectron and Auger spectroscopy (XPS-XAES). AlN formation was evidenced. Ar⁺ etching sequences in the ultra high vacuum chamber of the spectrometer allowed us to investigate the internal nature of the samples, and to estimate the nitride layer thickness. It is shown that the residual oxide layer acts as a diffusion barrier. An efficient in situ preliminary cleaning was researched in order to get a high nitriding rate. An [Ar(90%)+H₂(10%)] plasma followed by a [N₂(96%)+Ar(4%)] plasma allowed us to nitride 60% of the whole detected aluminum. For this sample, the nitride layer thickness was estimated to 22 Å. © 2000 Elsevier Science S.A. All rights reserved.

Keywords: Aluminum nitride; Electron cyclotron resonance; Nitridation; Plasma

1. Introduction

Nitriding is one of the processes which enables an increase in the hardness of metal surfaces without affecting their bulk properties. Nitriding of aluminum has already been carried out by direct thermal nitriding [1], reactive RF sputtering in a nitriding atmosphere [2], and direct current nitrogen plasma [3]. Recently, the electron cyclotron resonance (ECR) plasma has become a very attractive energy source for material processing as a result of its relatively high degree of ionization in the low pressure range in comparison with other conventional discharges [4]. Nitriding of Al by ECR was demonstrated to be possible, but high temperature and substrate polarization were always required [5,6]. In the present work, Al surfaces were nitrided by an ECR nitrogen plasma without external heating or RF bias voltage of the substrate. Optimum process conditions were determined by a spectroscopic characterization of the nitrogen plasma.

2. Experiment

2.1. Nitridation reactor

The DECR reactor with a multipolar magnetic field is shown Fig. 1. The plasma chamber was a stainless steel cylinder (200 mm height × 250 mm diameter). The vacuum system included a turbomolecular pump (500 l/s) allowing a low base pressure (10⁻⁷ Torr) and operating pressure around 10⁻³ Torr. The pressure (*p*) was measured by a Pirani–Penning gauge and baratron manometer. Six injectors allowed the introduction of the gas along the whole height of the reactor. The gas flow (*Q*) was regulated by a mass flow controller. The microwave (2450 MHz) power (*P*) was fed through six antenna rods located inside the periphery of the chamber and close to its wall. Six pairs of permanent magnets with alternated polarities, settled in front of the antenna, created resonant field cusps next to the antenna. The energetic electrons were trapped in the magnetic cusps and were sufficiently accelerated to ionize the gas inside them. These cusps behave like local sources, from which a cold plasma diffuses towards the center of the reactor, where the substrate is settled.

* Corresponding author.

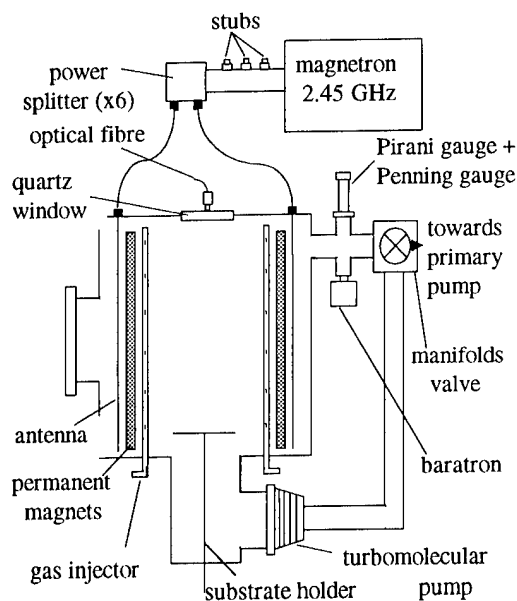


Fig. 1. DECR plasma reactor.

2.2. Plasma diagnostics

The gas phase was studied by UV-visible optical emission spectroscopy. The measurements were performed using a monochromator Jobin Yvon HR460 equipped with a CCD detector. An optical fibre could collect the emission through a quartz window located above the vertical axis of the reactor (Fig. 1).

2.3. Surface characterization

The surface compositions and chemical environments of the treated samples were characterized by X-ray photoelectron spectroscopy (XPS, Leybold LHS 10 spectrometer, AlK α source operating at 13 kV and 20 mA). The samples were always exposed to the ambient air before analysis. The binding energies (BE) were calculated taking as reference either the C1s peak at BE=285.0 eV or the oxidized Al2p peak at BE=74.8 eV when carbon is absent. The integrated peak ratio I_A/I_B can be converted into the corresponding A/B ratio using the cross sections relative to each core level [7]. Atomic percentages (denoted by x_i for the element i) were then evaluated, assuming a homogeneous distribution within the analyzed depth. The precision of these values is about 5%. In addition, a depth profile was achieved with Ar⁺ etching sequences (about 1 Å/min) in the XPS spectrometer, the duration of which is denoted by τ .

2.4. Nitridation procedure

Aluminum always has a dense surface oxide layer; so before nitriding, aluminum samples were previously in situ cleaned by a DECR argon plasma (with or without

hydrogen) for 1 h. This pre-treatment was immediately followed by the DECR nitrogen plasma (with or without argon and/or hydrogen) used without polarization or external heating of the substrate. Two gas qualities were used: 'U' level (purity $\geq 99.998\%$; O₂=3 ppm; H₂O = 3 ppm) and 'GC' level (purity $\geq 99.999\%$; O₂=5 ppb; H₂O = 20 ppb).

3. Results and discussion

3.1. Spectroscopic study

A nitrogen (GC quality) DECR plasma is created ($Q=13$ sccm, $p=1$ mTorr and $P=700$ W). In these conditions, a global spectrum recorded between 300 and 1015 nm consists of three emission systems: the first positive system N₂ ($B^3\Pi_g \rightarrow A^3\Sigma_u^+$) denoted (1+), the second positive system N₂ ($C^3\Pi_u \rightarrow B^3\Pi_g$) denoted (2+), and the first negative system N₂⁺ ($B^2\Sigma_u^+ \rightarrow X^2\Sigma_g^+$) denoted (1−). The optical emissions of bands located at 380.5, 391.4 and 762.6 nm and corresponding respectively to the vibrational transitions (0−2) of (2+), (0−0) of (1−) and (3−1) of (1+) are measured versus various experimental parameters. These transition intensities respectively denoted by I_{2+} , I_{1-} and I_{1+} correspond to the dominant emission peak in each studied system. For given p and Q values, I_{2+} , I_{1-} and I_{1+} increase with P ranging from 300 to 900 W. For given P and Q values, the evolutions of I_{2+} , I_{1-} and I_{1+} versus p give evidence for a maximum value appearing around 2 mTorr. Whatever the experimental conditions, I_{2+}/I_{1+} remains approximately constant while I_{2+}/I_{1-} and I_{1+}/I_{1-} decrease when P increases (for given p and Q) and increase when p increases (for given P and Q). So low pressure and high microwave power are required to favour the N₂⁺ ($B^2\Sigma_u^+$) concentration [8]. Taking into account these results, the experimental conditions used for the nitriding process were $p=2$ mTorr, $QN_2=16$ sccm and $P=800$ W. In these conditions, the gas temperature estimated from the rotational temperature of the N₂($C^3\Pi_u$) is approximately equal to 500 K. The vibrational temperature calculated from the vibrational distribution function deduced from the emission of (2+) is estimated to be around 8000 K.

The influence of an argon addition to nitrogen is studied from the evolution of (2+), (1+) and (1−) versus the QAr/QN_2 ratio for a given pressure equal to 1 mTorr. I_{2+} and I_{1-} increase until a QAr/QN_2 value around 0.05. Then by increasing the argon addition, these intensities decrease. This maximum shows the contribution of the atomic argon in the nitrogen plasma formation as it was already explained by Aleksandrov et al.[9]. The I_{1+} intensity decreases on the whole QAr/QN_2 range. So a weak quantity of argon (4%)

Table 1

Evolution of the surface composition (at.%) versus the nitriding duration (t) and the Ar^+ etching duration (τ)

τ	Samples A									Sample B	Sample C
	$t = 30 \text{ min}$			$t = 1 \text{ h}$			$t = 6 \text{ h}$			$t = 1 \text{ h}$	$t = 1 \text{ h}$
	0	5 min	15 min	0	5 min	15 min	0	5 min	15 min	0	0
$x\text{Al}$	36.0	41.9	41.4	33.0	39.7	43.5	38.0	42.8	44.8	39.8	38.6
$x\text{O}$	33.5	41.6	44.9	25.4	35.7	42.8	25.1	31.7	38.7	31.6	31.6
$x\text{N}'$	19.0	12.9	9.9	24.8	17.5	10.4	25.1	23.2	14.6	21.5	25.9
$x\text{N}''$	2.2	0.0	0.0	2.3	0.0	0.0	1.5	0.0	0.0	0.0	0.0
$x\text{C}'$	2.9	0.0	0.0	4.6	0.0	0.0	6.5	0.0	0.0	3.8	3.1
$x\text{C}''$	0.0	0.0	0.0	1.0	0.0	0.0	0.0	0.0	0.0	0.0	0.0
$x\text{F}$	3.6	3.6	3.8	3.3	3.7	3.3	1.9	2.3	1.9	3.3	0.8
$x\text{Si}$	2.8	0.0	0.0	5.6	3.4	0.0	1.9	0.0	0.0	0.0	0.0

added to the nitrogen DECR plasma enables an increase in the $\text{N}_2^+(\text{B}^2\Sigma_u^+)$ concentration.

3.2. XPS results

3.2.1. Characterization of a commercial reference

A study was carried out on a commercial sample of AlN (Goodfellow) in order to get reference values for binding energies (BE). The Al2p photopeak shows two components located at $BE = 73.7 \text{ eV}$ and $BE = 74.8 \text{ eV}$ and corresponding, respectively, to the nitrided and oxidized components. The nitride component of the N1s photopeak is located at $BE = 396.8 \text{ eV}$. Oxygen and carbon detected are certainly due to the exposure of the ambient air, but could also be provided by the elaboration procedure of the sample. The O1s photopeak, approximately symmetrical, is located at $BE = 532 \text{ eV}$. The C1s photopeak shows two components around 285.0 eV (contamination carbon) and 288.3 eV (oxidized carbon).

3.2.2. Characterization of nitrided Al samples

Before nitridation, the aluminum substrate was always cleaned by an Ar (U quality) pre-treatment for 1 h ($Q = 9 \text{ sccm}$, $p = 1 \text{ mTorr}$ and $P = 800 \text{ W}$) in order to

eliminate the oxide layer. But, as a transfer to ambient air between this pretreatment and the analysis can not be avoided, it is impossible to control the surface of the sample before the nitridation step. So, samples were only analyzed after nitridation. The Al2p, N1s, O1s, C1s, F1s and Si2p were detected. The evolution of the atomic percentage of each element versus the nitriding time (t) and the ionic etching sequences (τ) in the spectrometer are shown in Table 1. For the pre-treatment with Ar (U quality) plasma and nitridation with N_2 (GC quality) plasma (sample A), a contamination by fluorine appears in the bulk of the material, while silicon and carbon are only surface contaminants. The contaminations by Si and F are not similarly distributed because of the different diffusion kinetics for this two elements. The amount of oxygen ($x\text{O}$) increases with τ , which shows that the cleaning pre-treatment is not efficient enough to eliminate the native oxide layer.

The N 1s photopeak shows a nitride component (as N') and an oxide component (N''). The BE of the nitride component (397.0 eV) as well as the kinetic energy of the NKLL Auger peak (378.0 eV), unambiguously shows the formation of AlN independent on t and τ . The BE values agree with those observed in the literature [6,10–12]. The AlN nitride rate ($x\text{N}'$) increases from $t =$

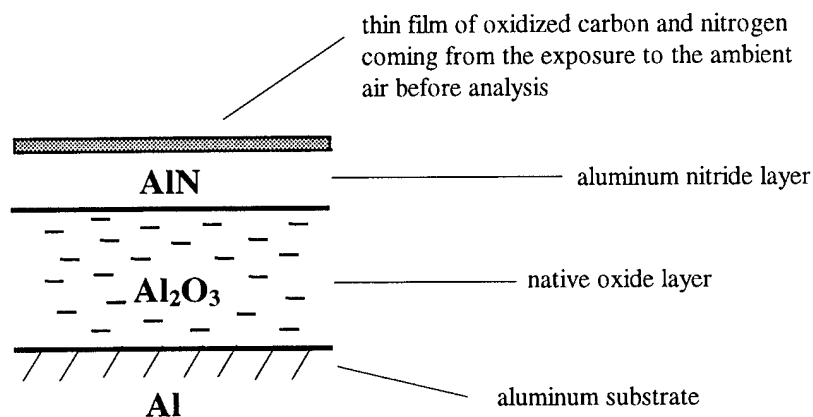


Fig. 2. Scheme of the treated sample layers.

Table 2

Influence of hydrogen addition to the argon cleaning, and argon or hydrogen addition to the nitrogen treatment

		xAl	xN	xO	xC	xF	xAlI	xAl2	xAl3	d_{ox} (Å)	d_{nit} (Å)
C	Ar-N ₂	38.6	25.9	31.6	3.1	0.8	49.2	49.0	1.8	100	15
D	Ar + H ₂ (10%)-N ₂	42.7	25.2	22.7	7.7	1.3	34.2	59.0	6.8	56	21
E	Ar + H ₂ (30%)-N ₂	44.5	25.3	24.0	4.4	0.9	34.8	56.8	8.3	52	20
F	Ar + H ₂ (50%)-N ₂	45.9	23.8	22.5	7.3	0.5	31.8	51.9	16.3	35	18
G	Ar + H ₂ (70%)-N ₂	41.3	22.7	21.1	12.0	2.9	34.1	55.0	10.9	45	19
H	Ar + H ₂ (10%)-N ₂ + H ₂ (10%)	42.2	22.8	28.3	5.5	0.8	44.0	54.0	2.0	95	18
I	Ar + H ₂ (10%)-N ₂ + Ar(4%)	40.8	24.5	22.0	11.5	0.8	35.3	60.0	4.7	66	22

30 min to 1 h and seems to reach a limiting value approximately equal to 25% for $t \geq 1$ h. The native aluminum oxide layer which was not eliminated before the nitriding step, seems to act as a diffusion barrier. Si contamination was eliminated by removing the quartz window located on the reactor side (sample B). For $t = 1$ h and $\tau = 0$, a comparison between samples A and B shows that xSi and xN' decrease simultaneously, suggesting that the silicon was nitrided; on the other hand SiO bonding is probably not involved as xO does not decrease with the removal of the window. The elimination of fluorine is more difficult as it is provided by teflon parts present in the reactor which are difficult to substitute. Contrarily, the carbon contamination can not be provided by teflon parts as the CN emission bands, very strong, are not detected by emission spectroscopy. Contamination during exposure to the ambient air is more likely. The C1s photopeak, which shows two components around 285 eV (contamination carbon C') and 288.5 eV (oxidized carbon C''), disappears for $\tau \geq 5$ min giving evidence for surface contamination by carbon.

As no influence was noticed using Ar (GC quality — sample C) instead of Ar (U quality — sample B), the

oxygen contamination can be attributed either to the reactor or to a diffusion from the inner oxide layer towards the surface. The presence of residual oxygen in the reactor can not be excluded even if the base pressure is 10^{-7} Torr.

In order to reduce the native oxide layer, a cleaning procedure using a mixture [Ar(GC) + $a\%$ H₂(U)] was used followed by a nitriding step with N₂(GC — sample D to G in Table 2). Whatever the ' $a\%$ ' value, results are improved as xO decreases from 31.6% (for $a = 0$) to a mean value approximately equal to 23% whatever ' $a\%$ ' ranging from 10% to 70%. In this ' $a\%$ ' range of values, xN' remains constant. After a pre-treatment by [Ar(GC) + 10%H₂(U)] plasma, the addition of H₂(U) to the N₂(GC) plasma is harmful (sample H): xO increases and xN decreases in comparison with the sample D. This may be provided by a preferential etching of nitrogen atoms by hydrogen, but reactive nitrogen species can also react with H₂ instead of being implanted on the Al sample: NH radicals and H atoms were already identified in a [N₂ + 25%H₂] ECR plasma by Matsumoto and Takemura [6].

The determination of relative oxide (d_{ox}) and nitride (d_{nit}) thicknesses of different samples can be obtained

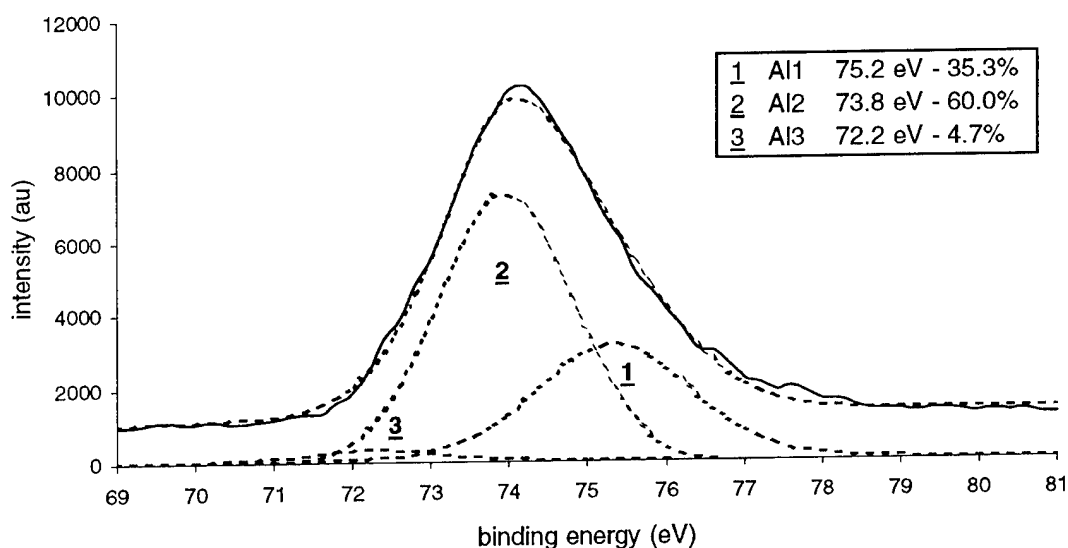


Fig. 3. Spectral Al2p decomposition of sample I.

from the comparison of the relative intensities of the oxide, nitride and metal components of the Al2p photopeak [7] considering the layers as homogeneous as in the scheme proposed in Fig. 2 (in fact, the structure may be more complex and the nitrided layer may contain oxygen atoms). In this aim, the Al2p band, broad and dissymmetrical, was decomposed assuming a gaussian profile in three peaks whose BE are 75.2, 73.8 and 72.2 eV and which correspond respectively to oxide (Al1), nitride (Al2) and metal (Al3) components. These binding energy values agree with the commercial reference values. Results of the decomposition and layer thickness values are shown in Table 2, and Fig. 3 shows the Al2p decomposition of the sample I, for which the best nitrogen rate is obtained. Whatever d_{ox} , ranging from 100 Å (sample C) to 35 Å (sample F), d_{nit} remains approximately constant and equal to 20 Å. This very thin thickness suggests that the oxide layer acts as a diffusion barrier for nitrogen atoms in the aluminum. This hypothesis could be confirmed by the elimination of this oxide layer. On the other hand, the AlN layer could also act as a diffusion barrier for nitrogen atoms. The weak addition of argon (4%) during the nitridation, in a quantity corresponding to the maximum $N_2^+(B^2\Sigma_u^+)$ concentration determined by optical emission spectroscopy, does not seem to improve the nitridation efficiency.

Aluminum samples previously in situ cleaned by an [Ar(GC)+10%H₂(U)] plasma shows a nitrided aluminum rate equal to 60% of the whole analyzed aluminum after a nitridation by a [N₂(GC)+4%Ar(GC)] plasma over 1 h.

4. Conclusion

An oxidized aluminum sample, previously in situ cleaned for 1 h by a DECR argon+hydrogen (10%)

plasma, can be nitrided by a DECR nitrogen+argon (4%) plasma. The nitrided layer thickness obtained after 1 h of nitriding is estimated to be 22 Å. The nitridation is achieved without external heating or substrate polarization. Removal of the native oxide layer from the surface of the aluminum substrate before nitriding is not completely achieved by the procedure described. It is probable that a more efficient etching of the native aluminum oxide layer will favour a more efficient nitriding of the aluminum substrate. However, due to possible diffusion limitation of nitrogen atoms within the AlN layer, its thickness could also reach a limiting value. Studies are presently in progress to improve the AlN layer thickness and composition.

References

- [1] P. Sthapitanonda, J.L. Margrave, *J. Phys. Chem.* 60 (1956) 1268.
- [2] E.V. Geroval, N.A. Ivanov, K.I. Kirov, *Thin Solid Films* 81 (1981) 201.
- [3] T. Jung, *Phys. Stat. Sol. A* 93 (1986) 479.
- [4] S. Miyake, W. Chen, *Mat. Sci. Eng. A* 139 (1991) 294–301.
- [5] I. Fujita, T. Hino, T. Yamashina, *Shinku* 35 (1992) 117.
- [6] O. Matsumoto, K. Takemura, *Proc. 11th International Symposium on Plasma Chemistry, Loughborough, August Vol. 3* (1993) 1053–1058.
- [7] J. Grimblot, *L'analyse de Surface des Solides par Spectroscopies Électroniques et Ioniques*, Masson, Paris, 1995, pp. 44–47.
- [8] N. Duez, B. Mutel, O. Dessaux, P. Goudmand, *Proc. 24th International Conference on Phenomena in Ionized Gases, Warsaw, July 1999, J. Tech. Phys.*, (submitted for publication).
- [9] S.E. Aleksandrov, A.Y. Kovalgin, A.Y. Rybnikov, *Rus. J. Appl. Chem.* 66 (1993).
- [10] P.W. Wang, S. Sui, W. Wang, W. Durrer, *Thin Solid Films* 295 (1997) 142–146.
- [11] D. Byun, J. Jeong, H.J. Kim, S.K. Koh, W.K. Choi, D. Park, D.W. Kum, *Thin Solid Films* 326 (1998) 151–153.
- [12] R. Vanden Berghe, R. Vlaeminck, *Surf. Interf. Anal.* 10 (1987) 316–318.

Raman study of titanium oxide layers produced with plasma immersion ion implantation

S. Mändl *, G. Thorwarth, M. Schreck, B. Stritzker, B. Rauschenbach

Institut für Physik, Universität Augsburg, 86135 Augsburg, Germany

Abstract

Raman spectroscopy was used to study thin titanium oxide (TiO_2) layers obtained by oxygen plasma immersion ion implantation (PIII) at rather low temperatures between 265 and 550°C. A pulse voltage of -30 kV and different pulse numbers between 5×10^5 and 4×10^6 were used. The phase composition was investigated with Raman spectroscopy, showing that rutile is present for all temperatures and doses used in this investigation. The results were corroborated with glancing angle X-ray diffraction (XRD). The grain size, as determined by scanning electron microscopy (SEM), changed from 40–100 to 10–30 nm when the temperature was decreased from 430 to 380°C. The retained dose and the layer thickness were determined by elastic recoil detection (ERD), yielding an incident dose of 6×10^{11} oxygen atoms per pulse and a maximum layer thickness beyond 100 nm. © 2000 Elsevier Science S.A. All rights reserved.

Keywords: Elastic recoil detection; Plasma immersion ion implantation; Raman spectroscopy; Titanium Oxide; X-ray diffraction

1. Introduction

TiO_2 thin films have been widely studied due to their peculiar optical and chemical properties [1]. The refractive index of TiO_2 in the optical region, in combination with a low refractive index material such as SiO_2 , makes it an ideal material for multilayer antireflection coatings. Another widely investigated application is its use as a biocompatible protective coating on medical implants [2], where a protective surface layer of TiO_2 increases the wear resistance and hardness considerably [3]. Additionally, they exhibit bioinertness and act as a diffusion barrier for metals such as Ti and Ni [4]. However, low treatment temperatures between 250 and 400°C are necessary to avoid changes in the bulk properties, especially to retain the transformation temperature of TiNi shape-memory alloys.

Various techniques, such as chemical vapor deposition (CVD), sputtering and laser ablation have been used to prepare TiO_2 thin films on different substrates [1,5,6]. At lower temperatures mainly amorphous TiO_2 or the metastable anatase phase are obtained [7]. Between 400 and 800°C a transformation into rutile, the

energetically favoured phase at higher temperatures, is observed with the exact transformation temperature depending on the fabrication method [8].

In a previous experiment, oxygen PIII into Ti6Al4V and pure titanium was investigated using XRD and RBS [9]. For temperatures between 550 and 600°C the formation of TiO and rutile was observed in pure Ti, while in the alloy Ti6Al4V additional anatase was detected. At lower temperatures no phase identification was possible, which could indicate either an amorphous phase or very small crystals which are not detectable for layers below 100 nm by XRD. The dissolution of Ti metal ions from rutile is one order of magnitude lower than from anatase [2], so that rutile is the preferred phase for biomedical applications. Using Raman spectroscopy, it is possible to identify the phases in an optically transparent material, like titania, with thicknesses down to some 50 nm [10], making it a much more sensitive characterisation tool than XRD.

In this paper we present Raman spectra of thin layers produced by oxygen PIII into pure Ti at temperatures between 265 and 550°C, and deduce the phase composition of these films. For comparison glancing angle XRD was performed. ERD was used to measure the dose and layer thickness, while SEM was used for characterising the grain structure of the titanium oxide.

* Corresponding author. Tel.: +49-821-598-3417;
fax: +49-821-598-3425.

E-mail address: S.Maendl@physik.uni-augsburg.de (S. Mändl)

2. Experiment

PIII treatments were performed in an HV system using an ECR plasma source [11] with a base pressure of 2×10^{-6} mbar and a working pressure of 3×10^{-3} mbar. High voltage pulses of -30 kV with a rise time of less than $0.5 \mu\text{s}$ [12] were used. A repetition rate of 1 kHz was used until the process temperature, between 265 and 550°C , was reached then the frequency was lowered to maintain this temperature until the end of the process. Pulse numbers between 0.5 and 4×10^6 were used, resulting in total process times between 8 min and 8 h.

The micro-Raman spectra were recorded in back-scattering configuration by the Instruments S.A. T64000 triple Raman spectrometer equipped with a microscope. For the excitation the 514.5 and 488.0 nm lines of an Ar^+ ion laser were used. The laser intensity at the sample surface was between 3 and 5 mW for all measurements, so that no thermal heating of the sample occurred during the measurements.

Glancing angle XRD measurements were performed on a Siemens D500 with a copper anode using the $\text{CuK}\alpha$ -line, a fixed incident angle $\theta = 5^\circ$, a step size of 0.1° and a measuring time of 60 s per step. Additionally, to obtain a higher sensitivity for selected samples, measurements using synchrotron radiation were performed. At the DESY-B2 beamline in Hamburg the parameters were a wavelength of 1.2026 \AA , $\theta = 5^\circ$, stepsize 0.05° and 2 s per step. ERD measurements were performed using $210 \text{ MeV } ^{197}\text{Au}^{15+}$ ions with 19° incident angle and a detector placed at a scattering angle of 37° . SEM micrographs were taken by a LEO DSM 982 Gemini scanning electron microscope equipped with a Schottky field emission cathode.

3. Results

Fig. 1 presents the Raman spectra for selected samples. In Fig. 1(a) the spectra for 488.0 and 514.5 nm laser excitation measured on a sample treated with 4×10^6 pulses at 550°C are compared, confirming that the observed features result from Raman scattering. For rutile single crystals, four Raman active modes at 143 , 447 , 612 and 826 cm^{-1} are reported in the literature [13,14]. They are all observable in the present spectra. In contrast, no structures which could be associated with other titania phases, such as anatase or brookite (the less common low temperature phase) have been detected [15]. The positions where the, respective, four and six Raman active lines from rutile and anatase should appear are indicated in Fig. 1(a). In addition to the first order Raman lines, broad structures around 250 cm^{-1} , as well as between 320 and 360 cm^{-1} , are

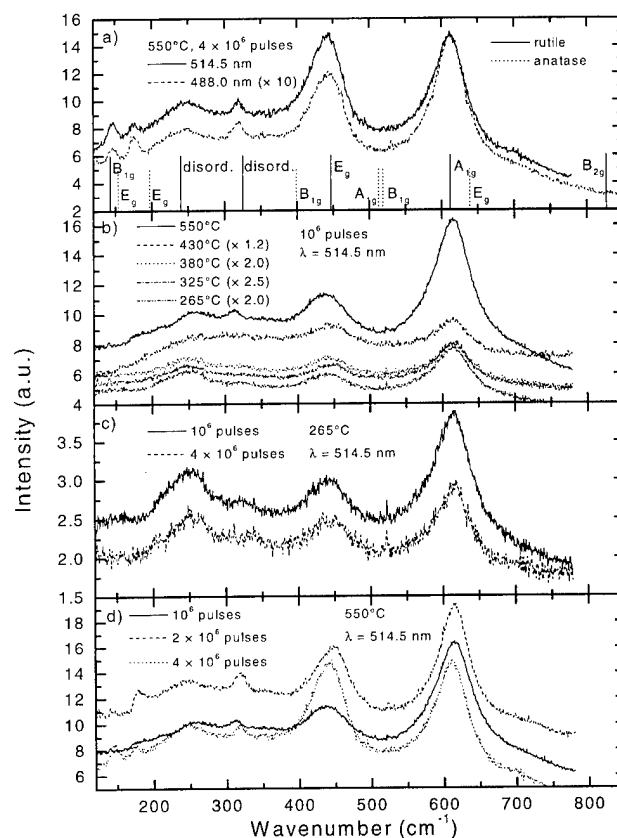


Fig. 1. Raman spectra for different samples: (a) using two different excitation wavelengths; (b) spectra for different treatment temperatures; (c) evolution of the spectra for increasing dose at 265°C ; (d) evolution for 550°C .

observed. They can be traced back either to disorder induced scattering or second order processes [13].

Fig. 1(b) shows five different spectra corresponding to samples treated at different temperatures between 265 and 550°C with 10^6 pulses. The E_g and A_{1g} modes at 447 and 612 cm^{-1} are present in all spectra, while the B_{1g} mode and the bands around 250 and 320 cm^{-1} are extremely weak. For the structure at 250 cm^{-1} , a weak shift towards lower wavenumbers is observed with decreasing temperature. The evolution of the spectra with increasing dose is shown in Fig. 1(c) and (d) for samples treated at 550 and 265°C respectively. At 265°C no significant difference is found for the samples with 1 and 4×10^6 pulses, while changes can be seen at 550°C for increasing dose. The signal/noise ratio increases for all three rutile modes and an additional structure around 175 cm^{-1} appears for the highest dose (Fig. 1(a)).

The diffractograms depicted in Fig. 2(a), which were measured using synchrotron radiation, show the formation of rutile for all samples. In contrast, only for the high temperature high dose sample was a positive identification possible using $\text{Cu K}\alpha$ radiation from a laboratory X-ray tube. The phase identification was done using the PDF files 44-129 and 21-1276 for α -Ti and rutile

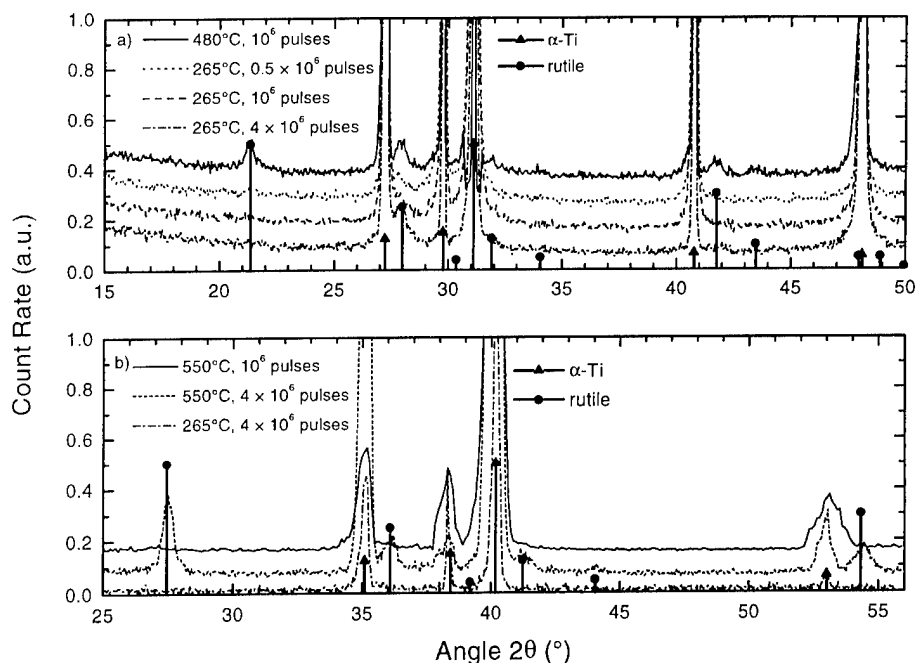


Fig. 2. X-ray diffractograms of different samples: (a) measured with synchrotron radiation at a wavelength of 1.2026 nm; (b) using Cu K α radiation.

respectively. No additional peaks corresponding to other TiO_x phases were found. The relative peak intensities point to a random orientation distribution for rutile, whereas a strong fibre texture was found for the α -Ti substrate.

The ERD spectra for four samples are shown in Fig. 3. The three sample implanted at 265°C show stoichiometric TiO₂ on top of Ti with the sharpness of the transition limited by the depth resolution of ERD, i.e. about 25 nm in the present case. The retained

dose increases from 2.7 via 3.7 to 5.3 × 10¹⁷ oxygen atoms/cm² for 0.5, 1 and 4 × 10⁶ pulses respectively. For the sample implanted at 480°C with 10⁶ pulses, a TiO₂ layer of 80 nm followed by a broad diffusion tail down to more than 250 nm was found, corresponding to a total dose of 5.6 × 10¹⁷ O/cm².

Fig. 4 shows SEM micrographs of two samples implanted at 480 and 265°C respectively. Interpreting the dimensions of the observed structures in terms of different grain sizes, a reduction of the mean grain size

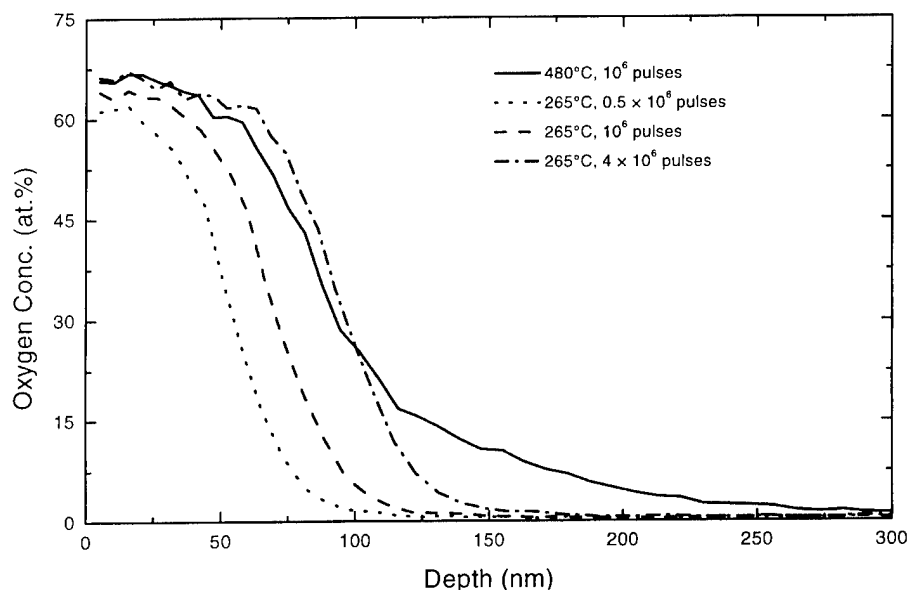


Fig. 3. ERD spectra for four samples: one high temperature and three low temperature with different doses.

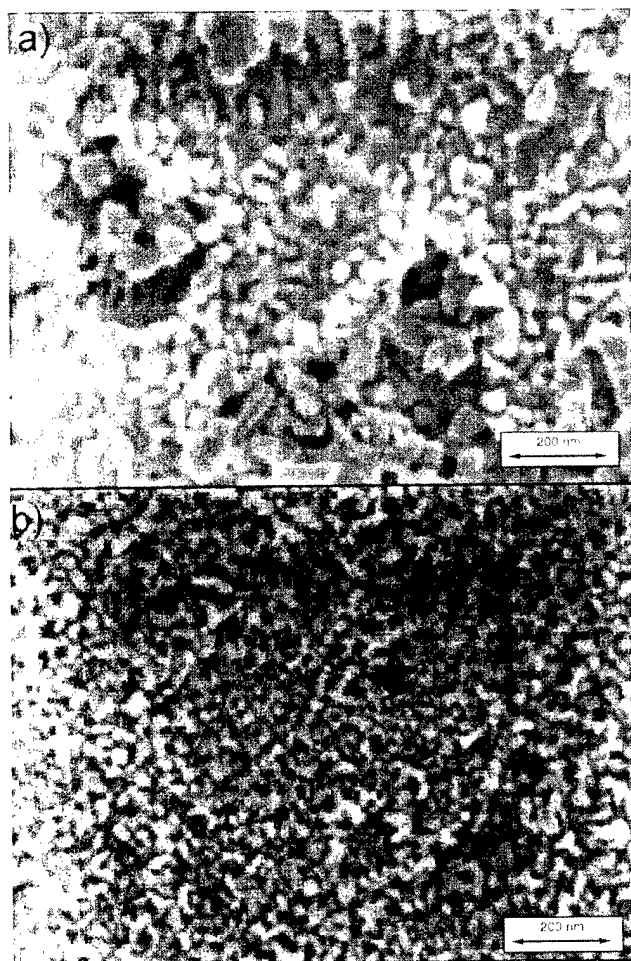


Fig. 4. SEM micrographs for two samples implanted at (a) 480°C and (b) 265°C.

from 40–100 nm at 480°C down to 10–30 nm at 265°C can be deduced.

4. Discussion

Using oxygen PIII for the formation of titania films, only rutile has been observed by Raman spectroscopy in the temperature range between 265 and 550°C, which is also confirmed by XRD measurements. Recently, calibration curves for stoichiometry of $\text{TiO}_{2-\delta}$ based on the shift of the E_g mode have been reported [14]. In our case, small non-systematic peak shifts between 447 and 435 cm^{-1} , indicating minor stoichiometry variations within the samples between $\delta=0.0$ to 0.02, have been observed. ERD results corroborate this observation.

Towards lower temperatures, the scattering intensities for XRD, as well as for Raman, decrease strongly. We interpret this in terms of smaller grain size and decreasing crystal quality, maybe even a transition towards an amorphous structure. The size of the surface structures observed by SEM, decreasing from 40–100 nm down to

10–30 nm with decreasing temperature, confirm this tendency. Two features in the Raman spectra require further comments. While all lines decrease in intensity with lower temperature, the band around 215–260 cm^{-1} is relatively increased. Correlating this band with disorder, as proposed in Ref. [13], may indicate a weaker annealing of the defects induced by the energetic oxygen ions. A new structure is observed at 175 cm^{-1} for the high temperature samples, increasing with implanted dose (Fig. 1(d)). An unequivocal assignment would require further studies. Considering the possibility of disorder induced transitions, we want to point to a high density of states for an infrared active A_{2u} mode at this energy [16].

Box-shaped profiles were found even beyond the depth of 30 nm given by the sputter saturation limit, indicating a strong tendency for titania phase formation and appreciable diffusion at all temperatures. Albeit, the formation of TiO_2 by diffusion of Ti and O proceeds more slowly at lower temperatures, yielding a lower retained dose for the same pulse number.

5. Summary and Conclusions

After oxygen PIII into titanium, stoichiometric rutile was found in the whole temperature range from 265 to 550°C, with no indication of the alternative TiO_2 phases anatase and brookite. Two different morphologies, large grains at high temperature and smaller grains at low temperatures, were found in SEM micrographs and correlated with XRD and Raman results. Using XRD it is extremely difficult to detect rutile for samples of 100 nm or less, whereas Raman spectroscopy allows the phase analysis of layers with thicknesses down to 50 nm. PIII is suitable for treating medical titanium implants at temperatures below 300°C, resulting in the formation of the high temperature rutile phase, which is preferred over anatase due to better biocompatibility.

Acknowledgements

W. Assmann and J.W. Gerlach are acknowledged for assistance during the ERD measurements. We are indebted to C. Hammerl, S. Six and P. Huber for performing the XRD measurements at DESY. This research was performed within the framework of Sonderforschungsbereich 438.

References

- [1] L. Escobar-Alarcón, E. Haro-Poniatowski, M.A. Camacho-López, M. Fernández-Guasti, J. Jiménez-Jarquín, A. Sánchez-

- Pineda, *Appl. Surf. Sci.* 137 (1999) 38.
- [2] N. Huang, Y. Chen, J. Luo, J. Yi, R. Lu, J. Xiao, Z. Xue, X. Liu, *J. Biomater. Appl.* 8 (1994) 404.
- [3] A. Loinaz, M. Rinner, F. Alonso, J.I. Oñate, W. Ensinger, *Surf. Coat. Technol.* 103/104 (1998) 262.
- [4] T. Kim, J.H. Han, I.S. Lee, K.H. Lee, M.C. Shin, B.B. Choi, *Biomed. Mater. Eng.* 7 (1997) 253.
- [5] G.A. Battiston, R. Gerbasi, M. Porchia, *Thin Solid Films* 239 (1994) 186.
- [6] N. Martin, C. Rousselot, D. Rondot, F. Palmino, R. Mercier, *Thin Solid Films* 300 (1997) 113.
- [7] C.M. Dai, C.S. Su, D.S. Chu, *Appl. Phys. Lett.* 57 (1990) 1879.
- [8] R.D. Shannon, J.A. Pask, *J. Am. Ceram. Soc.* 48 (1965) 391.
- [9] M. Rinner, B. Stritzker, W. Ensinger, *Proc. 4th Int. Workshop on Plasma-Based Ion Implantation*, Dearborn (1998).
- [10] W.T. Pawlewicz, G.J. Exarhos, W.E. Conaway, *Appl. Optics* 22 (1983) 1837.
- [11] W. Ensinger, J. Klein, P. Usedom, B. Rauschenbach, *Surf. Coat. Technol.* 93 (1997) 175.
- [12] J. Brutscher, *Rev. Sci. Instrum.* 67 (1996) 2621.
- [13] U. Balachandran, N.G. Eror, *J. Solid State Chem.* 42 (1982) 276.
- [14] J.C. Parker, R.W. Siegel, *Appl. Phys. Lett.* 57 (1990) 943.
- [15] P.P. Lottici, D. Bersani, M. Braghini, A. Montenero, *J. Mat. Sci.* 28 (1993) 177.
- [16] J.G. Traylor, H.G. Smith, R.M. Nicklow, M.K. Wilkinson, *Phys. Rev. B* 3 (1971) 3457.

Protection of γ -based TiAl against high temperature oxidation using ion implantation of chlorine

U. Hornauer ^{a,*}, R. Günzel ^a, H. Reuther ^a, E. Richter ^a, E. Wieser ^a, W. Möller ^a,
G. Schumacher ^b, F. Dettenwanger ^b, M. Schütze ^b

^a Forschungszentrum Rossendorf e.V., FWII, PO Box 510119, D-01314 Dresden, Germany

^b Karl-Winnacker-Institut der DECHEMA e.V., Theodor-Heuss-Allee 25, D-60486 Frankfurt, Germany

Abstract

The effect of ion beam implantation and plasma immersion ion implantation of chlorine on the high temperature oxidation of titanium aluminides above 800°C in air was investigated. Thermogravimetric oxidation tests (TGA) were performed to examine the long term protection. Depth profiling with Auger electron spectroscopy (AES) was used to investigate Cl diffusion and oxide formation during the first stage of oxidation. A microscopic model of the 'Cl-effect' will be discussed. A systematic variation of the implantation energy and fluence shows that there is a narrow regime of Cl concentration for optimum protective effect. The time to form a protective Al₂O₃ layer depends on the local Cl concentration. The oxidation rate after this incubation time is reduced by about two orders of magnitude compared to untreated Ti50Al and is nearly independent of the fluence. The implantation energy is not a sensitive parameter because the implanted chlorine profile changes very quickly during high temperature oxidation. © 2000 Elsevier Science S.A. All rights reserved.

Keywords: Chlorine; Implantation; Oxidation; Plasma immersion; TiAl

1. Introduction

γ -TiAl based intermetallic compounds are very promising as structural materials in high temperature applications because of the low density of 3.6 g/cm³. The problems which hinder the use of this material are its low ductility at room temperature and oxidation above 700°C. The basic effects of alloying ternary elements on the oxidation kinetics of TiAl are still not understood completely. Because the equilibrium oxygen partial pressure of Ti/TiO and Al/Al₂O₃ is very similar [1], a mixed oxide layer is formed during oxidation. Whether a dense protective layer of Al₂O₃ is formed or a fast growing scale depends on the local activities of the metals and the oxides, which are influenced mainly by the oxygen partial pressure, and also by alloying elements [2,3]. In Ref. [4] it is reported that very small amounts of halogenides improve the oxidation behavior dramatically. Chlorine is found to have the strongest effect. The 'Cl-effect' protects TiAl at very low concentration below

500 ppm. The underlying mechanism and the influence of Cl concentration is discussed in Ref. [5]. Briefly, a catalytic process involving volatile AlCl leads to Al enrichment in the oxide scale, which forms a protective, dense Al₂O₃ layer. Ion implantation of Cl is useful to study this microalloying effect. Systematic screening of the implantation parameters of Cl⁺ shows [6] that there is a narrow regime of the fluence (1×10^{16} cm⁻²) for optimum oxidation protection. The implantation energy is not a sensitive parameter in the range 200 keV up to 1 MeV. It has been shown that the important processes take place in the first minutes of oxidation [6,7]. Long term oxidation tests have proved that Ti50Al can be protected at 900°C in air for at least 1000 h [8].

In this study, low energy beam line implantation is used to investigate the Cl-effect for implantation into the very near surface layer. Conventional beam line ion implantation is not without drawbacks, prior to scanning complexity and efficiency. Moreover, sometimes it is impossible to implant shadowed areas of the work-piece even by the use of highly sophisticated systems for target movement. A positive result of low energy beam line implantations encouraged experiments using plasma

* Corresponding author. Tel.: +49-351-260-3674;
fax: +49-351-260-2703.

E-mail address: u.hornauer@fz-rossendorf.de (U. Hornauer)

immersion ion implantation (PI^3). PI^3 was developed as an alternative technology to conventional beam line ion implantation [9–11]. A plasma is generated in a sufficiently large vacuum chamber surrounding the workpiece on all sides. By applying negative high voltage pulses to the sample, positively charged ions are extracted from the plasma through the plasma sheath and implanted into the surface. First results and an assessment of the applicability of PI^3 will be given.

2. Experimental

A binary alloy Ti50Al was used to compare the effect of 15 keV implantation with results obtained for higher implantation energies. Specimen of dimension of approximately $1 \times 1 \text{ cm}^2$ with a thickness of 1 mm were prepared. The surface was ground using 4000 grit SiC paper. Beam line implantations were performed at the DANFYSIK 1090 implanter. Three different fluences (5×10^{15} , 1×10^{16} and $2.5 \times 10^{16} \text{ cm}^{-2}$) were implanted at an energy of 15 keV. For the fluence $1 \times 10^{16} \text{ cm}^{-2}$, the influence of an enhanced implantation temperature of 500°C was studied. The surface quality of the samples was not changed by beam line implantation. PI^3 was done in a high vacuum chamber (stainless steel). A detailed description of the system can be found in Ref. [12]. Prior to treatment, the system was pumped to a pressure of 10^{-6} mbar to minimize contamination by hydrogen, oxygen and nitrogen. The chamber was then filled with Ar and pumped again. Dry Cl_2 gas was filled into the chamber up to the working pressure of 0.3 Pa. This high pressure was chosen to have a stable plasma and to minimize the dissociation of Cl_2 [13]. The plasma was maintained by an ECR source. High voltage pulses of 30 keV with a duration of 5 ms were applied to the samples, leading to an effective implantation energy of 15 keV for Cl (30 keV Cl_2^+). In order to vary the implanted fluence, the number of pulses was varied over a wide range (3×10^5 , 6×10^5 and 3×10^6) at a fixed repetition rate of 1500 Hz. This variation overlaps the optimum Cl fluence ($1 \times 10^{16} \text{ cm}^{-2}$) found at higher energies [8]. The temperature was measured using a pyrometer. It rose during implantation within a time of approximately 10 min. Therefore it was not constant for the low pulse numbers, where the treatment took only 3.5 min and 7 min respectively. The longest treatment was 70 min leading to a final temperature of approximately 500°C . The heating due to implantation was controlled by the repetition rate of the pulses. The influence of temperature was checked by reducing the repetition rate to 150 Hz, which led to a temperature of $T = 100^\circ\text{C}$.

The surface was analyzed using SEM. The element distribution was measured by depth profiling with Auger electron spectroscopy (AES, MICROLAB 310F).

Thermal treatment for 10 min at 800°C and 24 h at 900°C in a conventional furnace was used to study the first stage of oxidation and the mass gain due to oxidation. Isothermal TGA tests were performed at 900°C in air for 100(TGA)h using a thermobalance to continuously record the mass gain.

3. Results and discussion

3.1. Beam line implantations

AES depth profiling (Fig. 1) shows that the implantations into Ti50Al result in non-gaussian depth profiles. Cl is distributed partially in the oxide layer. Implantation of a high dose at elevated temperature leads to a growth of the oxide during implantation [Fig. 1(d) and (e)]. Therefore, a significant amount of Cl is found in the oxide. A sufficient concentration of Cl [6] is found in the bulk close to the oxide at a depth of approximately 30 nm for the implantation of $1 \times 10^{16} \text{ cm}^{-2}$ [Fig. 1(c)].

In order to study the first stage of oxidation, the samples were oxidized for 10 min at 800°C in air. In Fig. 2 the corresponding AES depth profiles are compiled. The sample with the lowest fluence shows a similar structure in the oxide scale compared to an untreated control sample [Fig. 2(a) and (b)]. Therefore no protective effect is expected. For the fluence of $1 \times 10^{16} \text{ cm}^{-2}$,

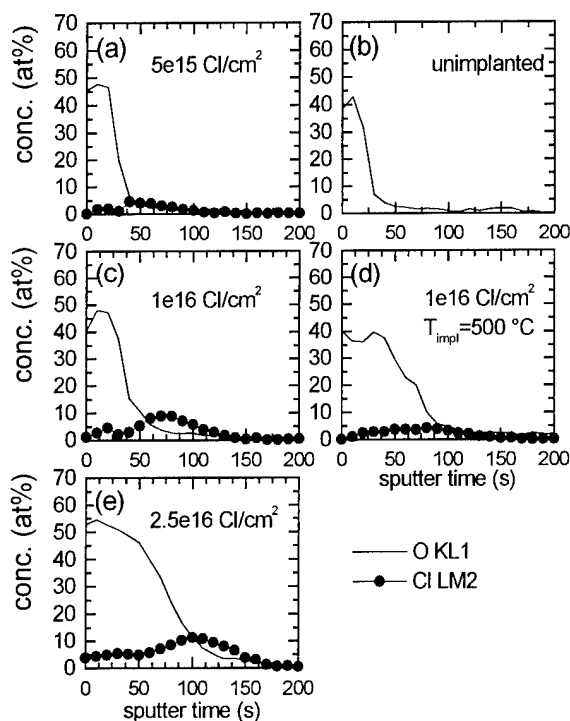


Fig. 1. AES depth profiles of oxygen and chlorine of the as-implanted state for 15 keV beam line implantation into Ti50Al with three different fluences (a, c and e) and at $T = 500^\circ\text{C}$ (d).

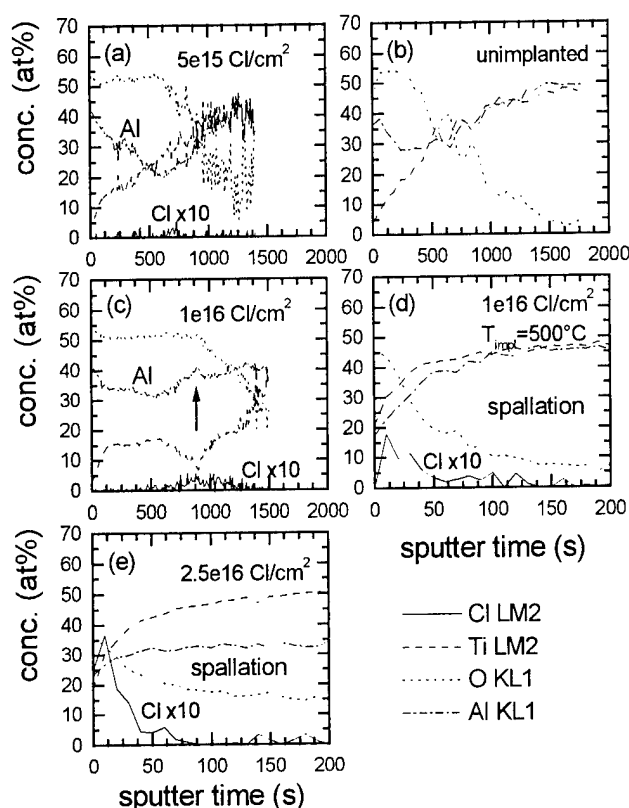


Fig. 2. AES depth profiles after 10 min at 800°C for different samples (a, c and e). Implantation at RT for given fluences (b); unimplanted reference sample (d): implantation at 500°C.

an enrichment of Al in the scale can be found [Fig. 2(c)] close to the remaining Cl content. This indicates the formation of a protective Al_2O_3 layer induced by Cl, similar to prior experiments [6]. The adhesion of the scale is good and no relevant spallation occurs. The higher Cl fluence and the implantation at higher temperature [Fig. 2(d) and (e)] leads to spallation after cooling. Only a very thin oxide scale of approximately 15 nm is detectable (different depth scale). Therefore the implantation of $1 \times 10^{16} \text{ cm}^{-2}$ was studied using continuous TGA for 100 h.

Fig. 3 shows the very good protective behavior measured using TGA. After a short incubation period with fast oxidation, the oxidation follows Al_2O_3 kinetics for at least 100 h. This is an decrease of the oxidation rate by two orders of magnitude compared to untreated Ti50Al. The oxidation kinetics is the same as for implantations at higher energies. For the thick scales no AES measurements were possible due to charging effects of the surface.

3.2. Plasma immersion ion implantation

Fig. 4 shows that the surface is etched strongly by the PI^3 treatment using a Cl_2 plasma. A reference sample, which was in the plasma for 7 min without HV

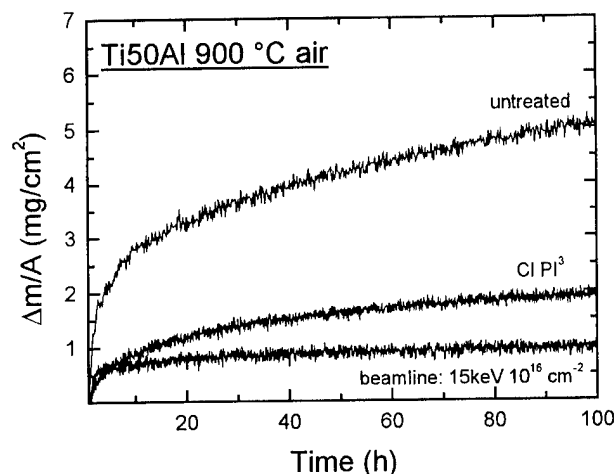


Fig. 3. TGA results: beam line implantation at 15 keV into Ti50Al leads to a very good protection for 100 h in comparison to untreated Ti50Al.

pulses was not etched significantly. Therefore, it is assumed that there is only minor etching in the pulse pauses. Measuring the etch step gives, on average, about 700 nm etch loss for all samples. The projected range (TRIM95 [14]) is $R_p = 20 \text{ nm}$ for 15 keV implantation of Cl^+ into TiAl. Therefore the retained dose is governed by the equilibrium between implantation and etching. Fig. 5 shows the exemplary AES depth profile of one sample. The depth distribution is comparable to simulated profiles assuming a strong etching (sputter saturation). The Cl is distributed in the first 20 nm of the sample. A high content of Fe is found close to the surface. This is due to etching of the chamber walls and contamination of the plasma. Integrating the Cl profile with an approximate sputter rate of 3 Å/s gives a small dependence of the retained Cl dose on the number of pulses, as shown in Fig. 6. A retained dose in the order of $1 \times 10^{16} \text{ cm}^{-2}$ is achieved with the high repetition rate. The lower rate gives a dose of $2.1 \times 10^{16} \text{ cm}^{-2}$. The main parameter controlling the Cl content is the temperature during implantation. This is probably due to a lower etch rate.

Continuous TGA was performed on the sample implanted with 6×10^5 pulses at 150 Hz, which exhibited the highest Cl content (Fig. 3). The mass gain is reduced strongly in the first stage of oxidation. The difference between beam line implanted and PI^3 treated Ti50Al may also be due to non-optimized process parameters of the PI^3 treatment.

4. Conclusions

In continuation of previous work, it has been shown that implantation of chlorine into a binary Ti50Al alloy has a very good protective effect on the high temperature

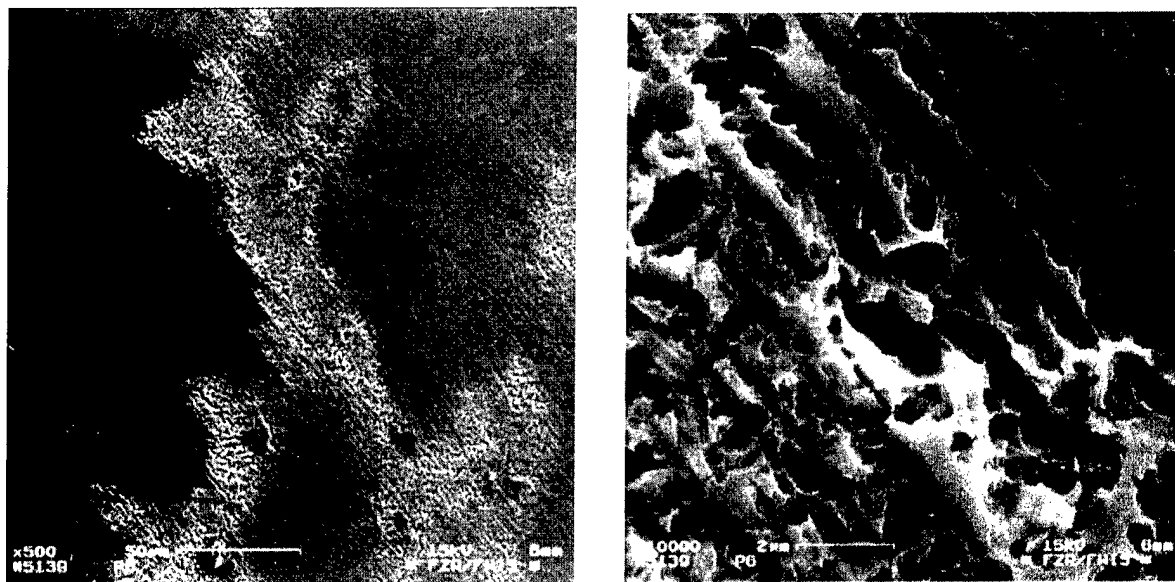


Fig. 4. Surface after plasma immersion ion implantation of 6×10^5 pulses of 30 kV at 1500 Hz. The magnification $\times 500$ shows selective etching of different grains. Higher magnification ($\times 10\,000$) of the boundary between two grains.

oxidation behavior in air, even at low ion energy. The protective effect is almost independent of the energy between 1 MeV and 15 keV and depends on the retained Cl dose. A narrow regime of the fluence for optimum protection is found ($1 \times 10^{16} \text{ cm}^{-2}$). The ion energy of 15 keV seems to be the lower limit since the projected range falls into the oxide scale.

In order to treat non-planar surfaces and to use the Cl-effect for application, first experiments with Cl_2 plasma immersion ion implantation were presented. A short time PI^3 treatment for protection of TiAl alloys against high temperature oxidation is possible using the Cl-effect. Ion enhanced etching leads to an increased surface roughness, which may be positive for the adher-

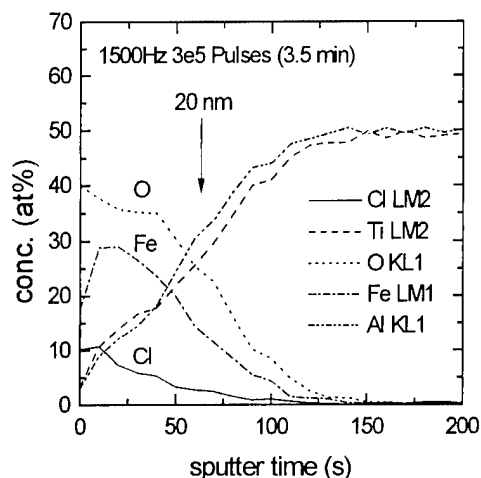


Fig. 5. AES depth profile after implantation using PI^3 . The treatment took only 3.5 min using 3×10^5 pulses at 1500 Hz. Cl is found close to the surface. Contamination with Fe is due to etching of the chamber walls.

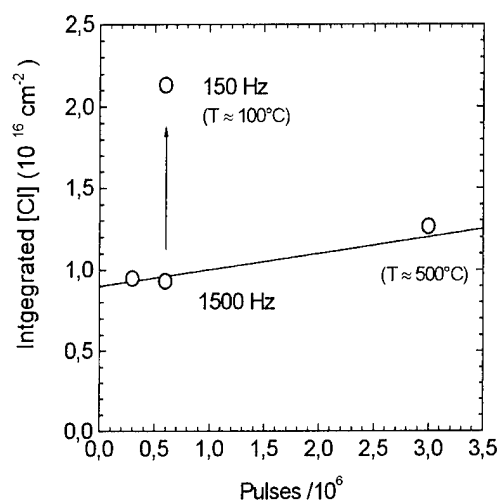


Fig. 6. Integrated Cl profiles show only a small dependence of the retained Cl dose from the number of pulses. The influence of temperature is more pronounced.

ence of the scale. The Cl depth distribution is very close to the surface and is limited by the equilibrium between etching and implantation. The main parameter controlling the retained Cl dose is the temperature during the treatment. Optimization of the plasma properties, the processing window and the reduction of contaminations are necessary in order to approach the excellent effect of beam line implantations.

Acknowledgements

This work is financially supported by the Volkswagen Stiftung. The authors would like to thank Mr. Winkler,

Dr. Schöneich, Dr. Pham, Dr. Dobler, Mrs. Quaritsch, Mrs. Aniol, Mrs. Christalle, Mrs. Iseke and Mr. Betzl for their help.

References

- [1] A. Rahmel, W.J. Quadackers, M. Schütze, *Materials and Corrosion* 46 (1995) 217.
- [2] K. Maki, M. Shioda, M. Sayashi, T. Shimizu, S. Isobe, *Mat. Sci. Eng. A* 153 (1992) 591.
- [3] Y. Shida, H. Anada, *Mater. Trans.* 35 (1994) 623.
- [4] M. Kumagai, K. Shibue, K. Mok-Soon, Y. Makoto, *Intermetallics* 4 (1996) 557.
- [5] M. Schütze, M. Hald, *Mat. Sci. Eng. A* 239/240 (1997) 847.
- [6] U. Hornauer, E. Richter, E. Wieser, W. Möller, G. Schumacher, C. Lang, M. Schütze, *Nucl. Instrum. Meth. B* 148 (1999) 858.
- [7] C. Lang, M. Schütze, *Materials and Corrosion* 48 (1997) 13.
- [8] G. Schumacher, C. Lang, M. Schütze, U. Hornauer, E. Richter, E. Wieser, W. Möller, *Materials and Corrosion* 50 (1999) 162–165.
- [9] J.R. Conrad, J.R. Radke, *J. Appl. Phys.* 62 (1987) 4591.
- [10] J. Tendys, I.J. Donnelly, M.J. Kenny, J.T.A. Pollock, *Appl. Phys. Lett.* 53 (1988) 2143.
- [11] R. Günzel, E. Wieser, E. Richter, J. Steffen, *J. Vac. Sci. Technol. B* 12 (1994) 927.
- [12] D. Korzec, V. Raiko, J. Engemann, R. Günzel, J. Brutscher, W. Möller, *Surf. Coat. Technol.* 93 (1997) 217.
- [13] G.A. Gaddy, S.F. Webb, R. Blumenthal, *Appl. Phys. Lett.* 71 (22) (1997) 3206.
- [14] J. Ziegler, J. Biersack, U. Littmark, *The Stopping of Ions in Solids: Program Version*, Pergamon Press, New York, 1995.

Plasma immersion ion implantation of cold-work steel

G. Thorwarth, S. Mändl *, B. Rauschenbach

Institut für Physik, Universität Augsburg, 86135 Augsburg, Germany

Abstract

Plasma immersion ion implantation can be used to modify the near surface region of steels at temperatures lower than 400°C. Hence even the surface properties of heat-sensitive steels like cold-work steels, which are not accessible for conventional nitriding, can be enhanced by reducing the friction coefficient and improving wear behaviour. Subsequent implantation of nitrogen and carbon into X155CrVMo12.1 steel using voltage pulses of –30 kV with combined doses up to $2.7 \times 10^{18} \text{ cm}^{-2}$ was performed at different temperatures between 300 and 400°C. Layers of $\epsilon\text{-Fe}_{2+x}(\text{C},\text{N})$ of several micrometers were detected using X-ray diffraction and glow discharge optical spectroscopy. Wear tests were performed with an oscillating ball-on-disc tribometer using a stainless steel ball and contact pressures between 0.7 and 1.4 GPa. For the lower contact pressure, a reduction of the abrasive wear by one order of magnitude was observed while the friction coefficient was reduced by 75%. At the higher contact pressures the wear mechanism changed from adhesive wear to slightly abrasive wear after nitrogen/carbon implantation, eliminating the cold welding between a stainless steel ball and the untreated sample completely. An optimum treatment temperature of 350°C was found. © 2000 Elsevier Science S.A. All rights reserved.

Keywords: Carbonitriding; Plasma immersion ion implantation; Steel; Wear

1. Introduction

Thermal treatment and quenching of iron and steel has been used for a long time to increase the hardness and the lifetime of tools. In recent times, other methods such as gas nitriding or plasma nitriding [1] have been introduced for selectively improving the surface without changing the bulk properties. Another recent technique is ion implantation to form new phases, even far away from the thermal equilibrium in the surface region [2,3]. Plasma immersion ion implantation (PIII) combines the advantages of plasma nitriding and ion implantation, namely treatment of the whole surface at the same time and penetration of the ions below surface barriers [4,5], and allows the introduction of this method into commercial ventures.

Tool steels are still the backbone of the machining industry where they are used for different purposes such as forming, cutting and transforming. During the last century their properties and lifetime were continuously improved by advanced thermal cycling and adding new alloying elements. For cold-work steels, plasma or gas

nitriding is not a viable method, as the last annealing/quenching cycle for this class of steels is around 300–400°C, and renewed heating to 500°C or above would change the bulk properties and lead to increased embrittlement. PIII, with moderate temperatures around 300°C, can induce further improvements.

In this work, we have investigated the influence on wear behaviour of nitrogen or combined nitrogen/carbon implantation using PIII into X155CrVMo12.1 steel (DIN 1.2379). Nitrogen is known to reduce the wear [6,7] while carbon reduces the friction coefficient by forming solid lubricants [8]. No pure carbon or carbon/nitrogen treatment was used as it is known that the formation of cementite can lead to a phase segregation into Fe and graphite, drastically reducing the hardness [9]. The goal of this investigation was to find an optimal set of parameters for treating transforming tools, reducing the cold welding tendency as well as the wear, and increasing their lifetime.

2. Experiment

Flat samples were prepared from X155CrVMo12.1 steel with a diameter and height of 10 mm and subjected

* Corresponding author. Tel.: +49-821-598-3417;

fax: +49-821-598-3425.

E-mail address: s.maendl@physik.uni-augsburg.de (S. Mändl)

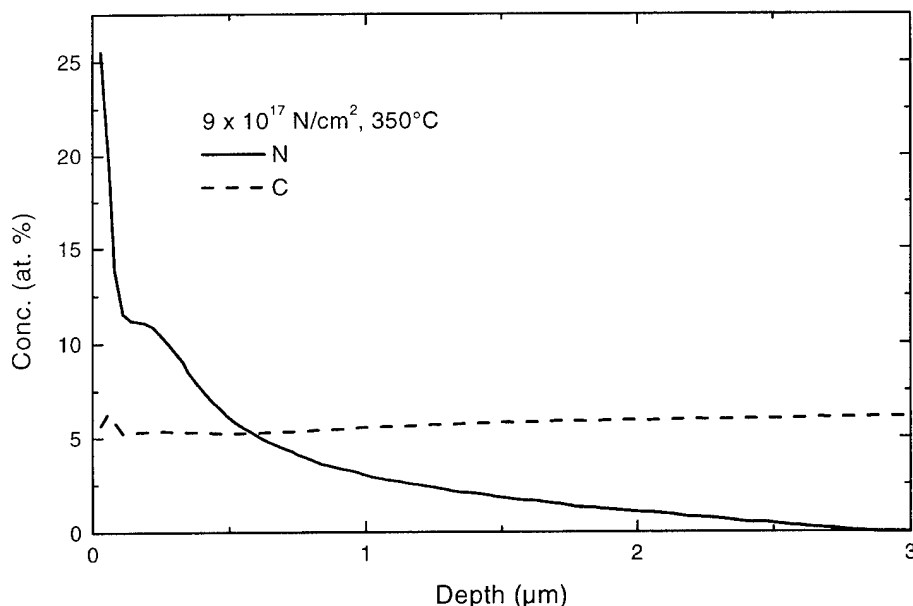


Fig. 1. GDOS depth profiles for nitrogen and carbon after treatment with $9 \times 10^{17} \text{ N/cm}^2$ at 350°C .

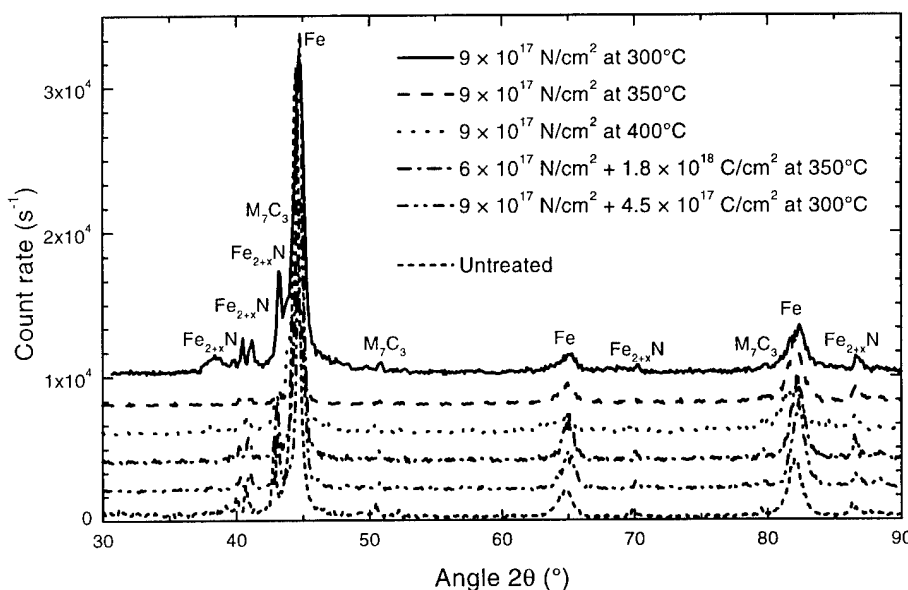


Fig. 2. X-ray diffractograms for untreated and different treated samples.

to a standard hardening procedure with a final annealing temperature of 450°C to allow treatments up to 400°C . The dimensions of the samples were chosen to avoid buckling during pre-treatment. Before the PIII experiments, they were polished to a mirror finish and cleaned with acetone and isopropanol.

PIII treatments were performed in an HV system using an ECR plasma source [10] with a base pressure of 2×10^{-6} mbar and a working pressure of 3×10^{-3} mbar. High voltage pulses of -30 kV with a rise time of less than $0.5 \mu\text{s}$ [11] were used. The repetition rate was varied between 230 and 500 Hz to maintain

process temperatures of 300, 350 or 400°C . For the pure nitrogen PIII treatment, total pulse numbers ranged between 2 and 6×10^6 , corresponding to doses between 0.6 and $1.8 \times 10^{18} \text{ cm}^{-2}$. The dose per pulse was obtained in a separate experiment [12]. For the combination treatment, first nitrogen was implanted and in a second step methane gas was used for subsequent carbon implantation with similar incident doses.

Implantation profiles of the samples were obtained to a depth of a few micrometers with glow discharge optical spectroscopy (GDOS). Structure and phase formation was analysed with X-ray diffraction (XRD).

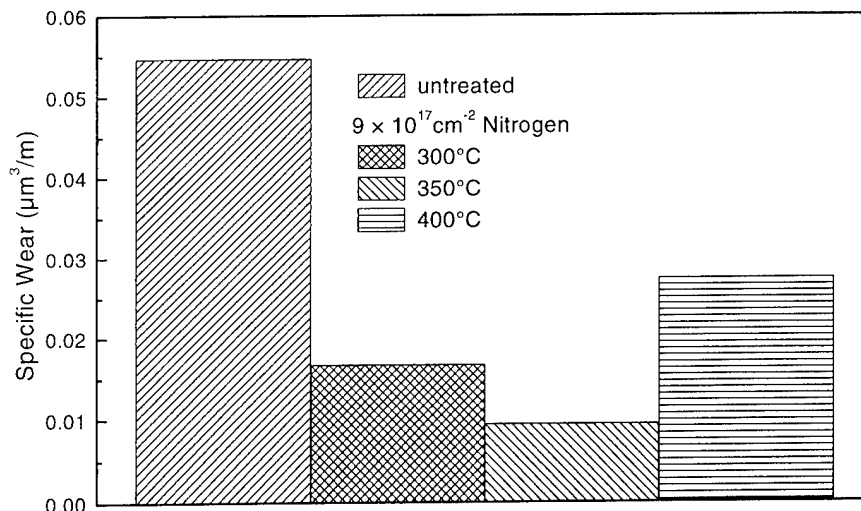


Fig. 3. Specific wear as measured with an oscillating ball-on-disk tribometer at a contact pressure of 0.7 GPa after a wear path of 56 m.

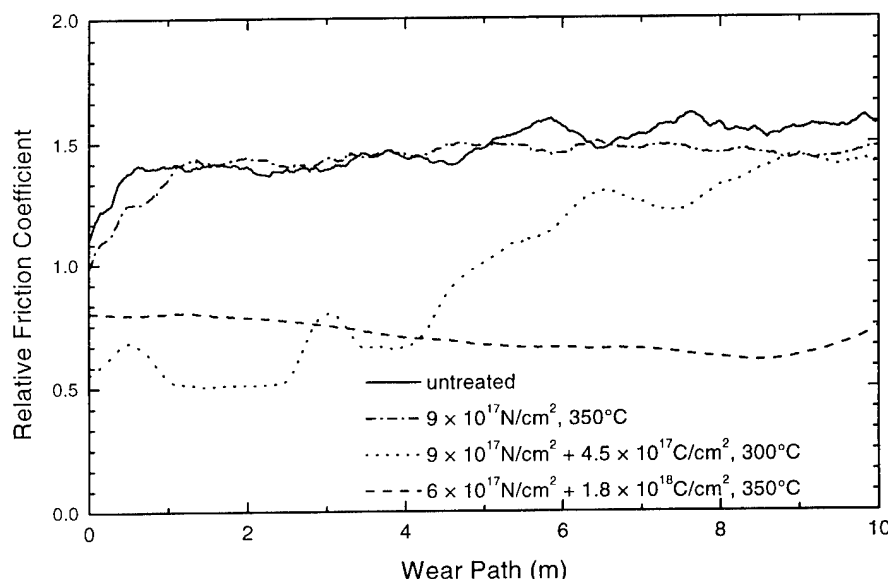


Fig. 4. Relative friction coefficient for an untreated sample, and three different treatments as measured during the wear tests with 1.4 GPa contact pressure.

The wear and relative friction coefficient were simultaneously determined using an oscillating pin-on-disc tribometer with a 5.0 mm stainless steel ball (DIN 1.4541) using an oscillation amplitude of 2.9 mm and a frequency of 4.0 Hz, resulting in a maximum velocity of 46.4 mm/s. A controlled temperature and humidity of 22°C and 45% respectively were used during the tests. After the tests the wear tracks were investigated with an optical microscope and a DEKTAK profilometer.

3. Results

The nitrogen implantation profile is shown in Fig. 1 as an example for a sample treated with 9×10^{17} ions/cm²

at 350°C. A 100 nm layer with a nitrogen concentration of up to 25 at.%, corresponding to a compound layer, followed by a 3 μm thick diffusion layer was obtained. Also shown in Fig. 1 is the carbon, which was mostly bound in carbides and partially in solid solution. The free carbon diffused along with the nitrogen, leaving a carbon deriched surface layer.

X-ray diffractograms for an untreated sample and samples treated at different temperatures and for different doses are presented in Fig. 2. The untreated sample consisted of α-Fe and M₇C₃ carbide phases. For the treated samples, irrespective of the temperature, dose or carbon content, only additional peaks corresponding to ε-Fe_{2+x}N [or ε-Fe_{2+x}(C,N)] were found. No peaks corresponding to cementite could be found.

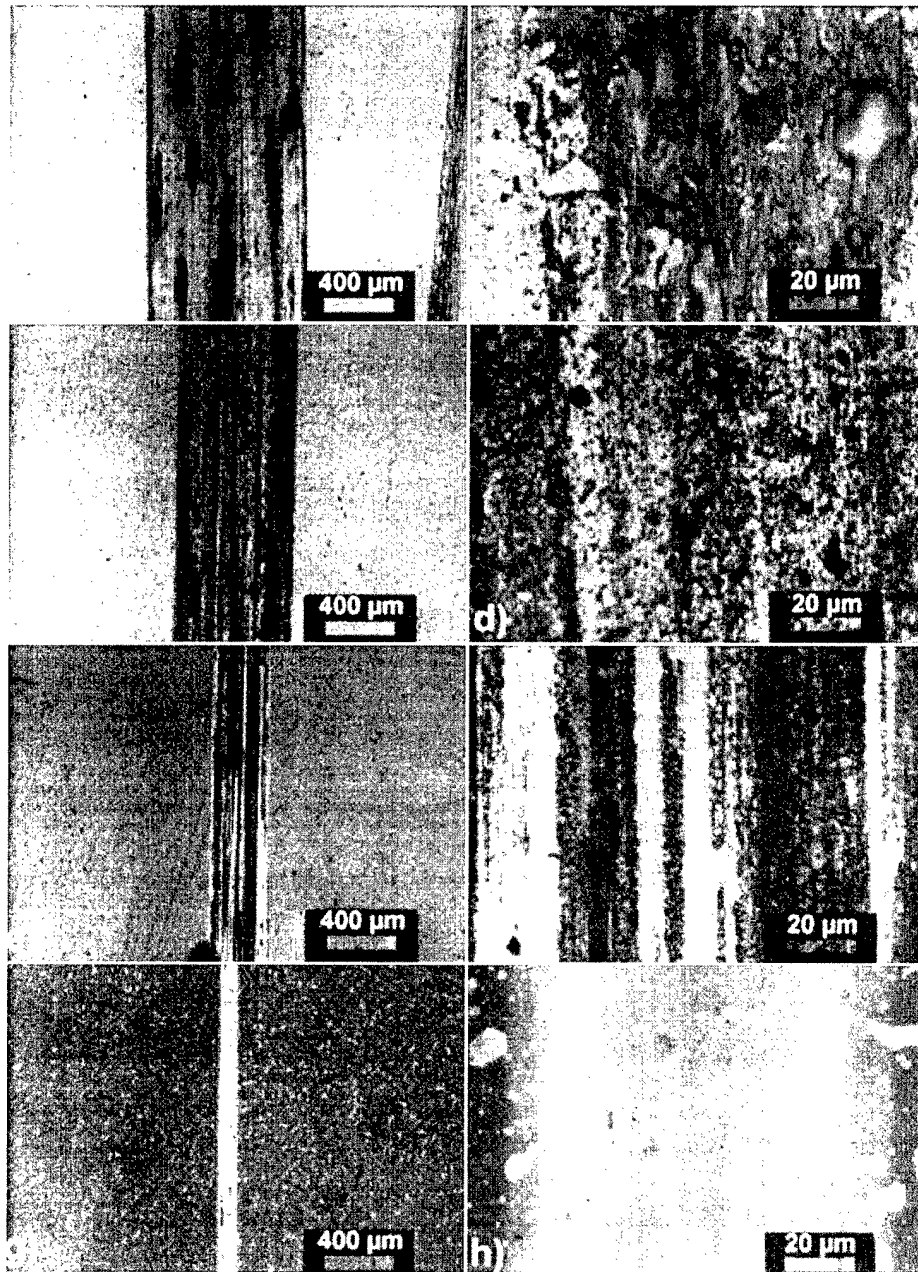


Fig. 5. Optical micrographs of the wear tracks obtained at a contact pressure of 1.4 GPa for different treatments in low and high magnification: (a) and (b) untreated; (c) and (d) $9 \times 10^{17} \text{ N/cm}^2$ at 350°C ; (e) and (f) $9 \times 10^{17} \text{ ion/cm}^2 + 4.5 \times 10^{17} \text{ C/cm}^2$ at 300°C ; (g) and (h) $6 \times 10^{17} \text{ N/cm}^2 + 1.8 \times 10^{18} \text{ C/cm}^2$ at 350°C .

The wear experiments were performed with two different loads, 1 and 7 N, yielding contact pressures of 0.7 and 1.4 GPa, respectively. The results for the lower load and samples implanted with the same dose of nitrogen are shown in Fig. 3. At 350°C a decrease in the specific wear by a factor of six was obtained, while at 300 and 400°C a smaller decrease was obtained. The depth of the wear tracks was around $1 \mu\text{m}$. For longer tests, an increase of the specific wear was observed when the wear track is getting deeper than the modified layer. For $9 \times 10^{17} \text{ ions/cm}^2$ this occurred after a total wear

path of 168 m and a wear track depth of $3 \mu\text{m}$, in accordance with the nitrogen depth profile of Fig. 1. Additional carbon implantation further reduced the wear.

For a load of 7 N a completely different picture was obtained. While for 0.7 GPa abrasive wear was observed for the untreated as well as the treated samples, the mechanism changed to adhesive wear at a contact pressure of 1.4 GPa for the untreated sample. After nitrogen treatment, no significant change was observed. Albeit, after a combined nitrogen/carbon treatment a

drastic reduction of the adhesive wear was observed. Material was no longer deposited on the wear tracks — instead a smooth surface with minor grooves, pointing to slightly abrasive wear, was measured using the DEKTAK profilometer.

The relative friction coefficient, obtained during the wear tests is presented in Fig. 4 for the high load and different treatments. For the untreated sample, a constant high friction coefficient was obtained after a short settling period. For the sample implanted only with nitrogen, the same behaviour was observed. After adding carbon in a subsequent implantation, a reduction of the friction coefficient was observed. For a dose of $4.5 \times 10^{17} \text{ C/cm}^2$ this reduction lasted until a wear path of 5 m was reached, then an increase in the original friction was observed. Increasing the carbon dose to $1.8 \times 10^{18} \text{ C/cm}^2$ further stabilised the low friction until a wear path of 11 m was reached.

Finally, in Fig. 5 optical micrographs at two magnifications, $50\times$ and $1000\times$, of the wear tracks are presented after a total wear path of 56 m. The same samples used for the relative friction coefficient measurements in Fig. 4 are presented. For the untreated sample, a broad wear track with large spots of material deposited from the stainless steel ball were observed. With increasing nitrogen and carbon dose, the width of the wear tracks decreased and less material was deposited. Finally, in Fig. 5(h) the base structure of the steel with carbide precipitates is observed, indicating almost no damage during the wear test.

4. Discussion

The two layer structure of compound and diffusion layer obtained after nitrogen treatment is similar to that observed at higher temperatures or conventional nitriding. Ion implantation is known to lower the phase formation temperature in several systems. Here no $\gamma\text{-Fe}_4\text{N}$, the high temperature phase, was observed, indicating that this effect has no role in cold-work steel. The layer thickness of $3 \mu\text{m}$, as shown in Fig. 1, corresponds to a diffusion constant $D = 4.2 \times 10^{-12} \text{ cm}^2/\text{s}$. As the steel used contained 12 wt.% Cr, reducing the diffusion of nitrogen, the difference compared to literature values of $4.7 \times 10^{-10} \text{ cm}^2/\text{s}$ for $\alpha\text{-Fe}$ can be explained [13]. The subsequently implanted carbon diffuses along the same sites with the same speed as nitrogen [6] so that only one diffusion constant is necessary to calculate the final layer thickness.

The loads, and the respective contact pressures, were chosen to simulate the operating conditions of tool application where the real contact pressure is between 0.7 and 1.4 GPa. Pure nitrogen treatment is an excellent method of reducing purely abrasive wear for steel, while

the use of carbon reduces the friction coefficient and the abrasive wear. Hence, the combination treatment of nitrogen followed by carbon implantation proved to be the best treatment for the complex wear behaviour of the cold-work steel in contact with stainless steel. The main wear mechanism determined from investigations of untreated worn tools is cold welding leading to deposition of material on the tool and not the abrasive wear removing material from the tool. Hence, the treatment depth of $6\text{--}8 \mu\text{m}$ for the dose of $6 \times 10^{17} \text{ N/cm}^2 + 1.8 \times 10^{18} \text{ C/cm}^2$ at 350°C is deep enough to increase the lifetime of the tools.

5. Summary and conclusions

PIII is a suitable low temperature treatment for improving the mechanical properties of tools made from cold-work steel. The wear behaviour was significantly improved as determined in oscillating ball-on-disc test using a stainless steel ball. For a contact pressure of 0.7 GPa, a reduction in the specific wear by a factor of six was obtained using nitrogen implantation at 350°C . Furthermore, the friction coefficient was decreased by a factor of two by adding a second treatment with carbon after the nitrogen treatment. At a contact pressure of 1.4 GPa the dual nitrogen/carbon treatment changed the wear mechanisms from adhesive to slightly abrasive, and improved the mechanical behaviour considerably.

An optimal treatment for X155CrVMo12.1 steel was found to be $6 \times 10^{17} \text{ N/cm}^2$ followed by $1.8 \times 10^{18} \text{ C/cm}^2$ at a temperature of 350°C . Industrial tests using tools treated with these parameters are in progress and the results on the effect on their lifetime will be reported in a further publication.

Acknowledgement

The support of the Bayerische Forschungsförderung (AZ:237/97) is gratefully acknowledged.

References

- [1] K. Höck, G. Leonhardt, B. Bücken, H.-J. Spies, B. Larisch, *Surf. Coat. Technol.* 74/75 (1995) 339.
- [2] J.N. Matossian, J.J. Vajo, J.A. Wysocki, M.E. Bellon, *Surf. Coat. Technol.* 62 (1993) 595.
- [3] G. Dearnaley, *Surf. Coat. Technol.* 65 (1994) 1.
- [4] J.R. Conrad, J.L. Radtke, R.A. Dodd, F.J. Worzala, N.C. Tran, *J. Appl. Phys.* 62 (1987) 4591.

- [5] G.A. Collins, R. Hutchings, J. Tendys, M. Samandi, *Surf. Coat. Technol.* 68/69 (1994) 285.
- [6] S. Mändl, R. Günzel, E. Richter, W. Möller, *Surf. Coat. Technol.* 100/101 (1998) 372.
- [7] S. Mändl, E. Richter, R. Günzel, W. Moller, *Nucl. Instrum. Meth. B* 148 (1999) 846.
- [8] K. Baba, R. Hatada, *Surf. Coat. Technol.* 103/104 (1998) 235.
- [9] D. Babonneau, T. Cabioch, M.-F. Denanot, A. Naudon, *Appl. Phys. Lett.* 74 (1999) 800.
- [10] W. Esinger, J. Klein, P. Usedom, B. Rauschenbach, *Surf. Coat. Technol.* 93 (1997) 175.
- [11] J. Brutscher, *Rev. Sci. Instrum.* 67 (1996) 2621.
- [12] T. Höchbauer, W. Esinger, G. Schrag, J. Hartmann, B. Strizker, B. Rauschenbach, *Nucl. Instrum. Meth. B* 127 (128) (1997) 869.
- [13] J.R.G. da Silva, R.B. McLellan, *Mater. Sci. Eng* 26 (1976) 83.

Production of stable and metastable phases of zirconium nitrides by NH_3 plasma nitridation and by double ion beam sputtering of zirconium films

A. Straboni *, L. Pichon, T. Girardeau

Laboratoire de Métallurgie Physique, Université de Poitiers, SP2MI, UMR 6630 CNRS, BP 179, 86960 Futuroscope cedex, France

Accepted 13 October 1999

Abstract

Nitrided surfaces and nitrogen composition gradients in thin films exhibit interesting mechanical, electrical and optical properties. Metal, semiconductor or oxide surfaces can be transformed into a nitrided compound via interactions of nitrogen species issued from a plasma or an ion beam. The thermal activation is a key factor in both cases to ensure chemical reactions and short/long-range diffusion necessary to allow the growth of stable or metastable structures. In this work, we focus our attention on zirconium nitrides prepared under controlled temperature through reaction and diffusion, in Zr films, of low energy NH_x species produced in NH_3 plasma and through the implantation–diffusion of energetic N_2^+ ions during Zr deposition by using double ion beam sputtering. Zirconium nitrides show optical and electrical properties that depend on the conditions and on kinetics of the nitrogen take-up; the material exhibits a transition from the stable metallic ZrN to a metastable phase Zr_3N_4 that appears transparent and insulating. The influence of the energy of the nitriding species and of the temperature on nitride compositions and phases are addressed. A model using coupled implantation and thermal diffusion mechanisms is proposed to explain the phases produced. In relation with the described phenomena, a temperature-controlled plasma-immersion ion-implantation system is proposed for tailoring in-depth stable/metastable ceramic structures such as nitrides, oxides and carbides. © 2000 Published by Elsevier Science S.A. All rights reserved.

Keywords: Growth modelling; Ion beam deposition; Optical properties of thin films; Zirconium nitrides

1. Introduction

Being generally more covalent than oxides, metal and semiconductor nitrides are hard and dense materials. When used as ceramic coatings, they act as barriers withstanding diffusion and resisting oxidation [1,2]. Native growth of nitride on a metal generally requires high temperatures and long durations because of retarded diffusion due to the film growth itself [3]. In the case of refractory metals these severe conditions lead to partial oxidation due to the interaction with residual water vapour [4]. Nitridation of metals using plasma or low energy ion beams has been used to enhance the reaction rates or to decrease the temperatures, like in steel nitridation. When thermal diffusion is predominant, the resulting film material is generally a stable phase; this is the case for TiN [5], ZrN [6] and Fe_4N [7],

which are respectively obtained after native nitridation of titanium, zirconium and Fe–C alloys. Metastable phases have been observed, especially when using implantation or low energy ion-beam bombardment coupled with sputtering [8–11]. To emphasise the role of diffusion and implantation on the nitridation, this paper reports on the production of stable and metastable phases of zirconium nitrides by NH_3 plasma nitridation of Zr films and by double ion beam sputtering (DIBS).

2. Experimental

Plasma nitridation experiments were conducted using the thermally assisted plasma reactor URANOS (unit of reaction assisted for the nitridation and oxidation of surfaces) [12,13]. The system is composed of a silica tube 2 m long, with 0.3 m diameter, in which the plasma is created by surfatron coupling. The external and

* Corresponding author.

circular electrode around the tube excites surface waves at the end of the insulating vessel. Their propagation along the walls results in an homogeneous and cold plasma in the entire volume. A three-zone furnace around the centre part of the tube allows one to control the substrate temperature between room temperature and 1000°C. The mean electron energy is around 3 eV. Neutrals and radicals are in thermal equilibrium with silica walls and the ion energy is around 10 eV, which is determined by the difference between the plasma and floating potential $V_p - V_f$. For plasma nitridation a 100 nm thick zirconium film deposited on silicon by argon sputtering at 1200 eV was used. The silicon wafer itself was nitrided to a depth of 5 nm to ensure that no interaction, such as silicidation, occurs between substrate and film. Nitridation was performed at 700°C for 2 and 7 h in low-pressure (93 μ bar) ammonia using plasma-assisted reaction and for comparison using pure thermal nitridation with the same conditions.

For reactive deposition, DIBS was used with RF excitation of the ion gun sources. The first beam was used to sputter a Zr target with ionised argon at 1.2 keV with a current of 80 mA. The second beam was used to bombard the substrate by nitrogen ions during deposition with an energy varying between 50 and 300 eV. The substrate temperature was controlled during deposition between room temperature and 450°C. The ionised nitrogen fluence was maintained constant for all the experiments by controlling the current at 40 mA. Nuclear reaction analysis (NRA) and Rutherford backscattering (RBS) were used to determine the N/Zr and O/Zr relative concentrations. Auger electron spectrometry (AES) with in situ profilometry was dedicated to diffusion gradient determinations in nitride films. The Auger peaks monitored during sputtering are as following: 120 eV (Zr), 385 eV (N), 510 eV (O) and 90 eV (Si). The N and O concentrations as a function of depth were determined by plotting the N/Zr and O/Zr atomic ratios. Spectrometric ellipsometry was performed on specific samples to compare their electronic properties.

3. Results

3.1. Plasma nitridation of Zr films

The N/Zr and O/Zr atomic ratios are plotted in Fig. 1 as a function of the sputtering time for zirconium nitride films grown after 7 h at 700°C in NH_3 plasma (a) and after a pure thermal treatment under the same conditions (b). For the sample nitrided in plasma, the film is entirely converted into zirconium nitride. The N/Zr ratio is close to unity over the whole thickness; it corresponds to the expected stoichiometry of the stable material ZrN. Oxygen contamination is clearly observed; this is

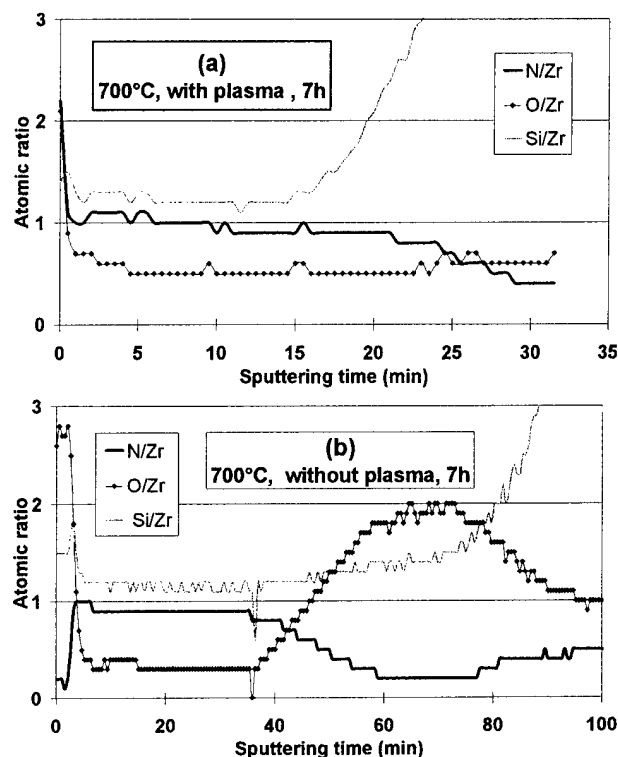


Fig. 1. Comparison of plasma and thermal AES profiles of native growth zirconium nitrides.

due to the strong reaction of zirconium at this temperature with residual oxidising species produced by water vapour outgassing of walls and substrate holders. When the film is nitrided under same conditions but without igniting the plasma, the nitride conversion is limited to the upper part of the zirconium. Underneath, the metal has been totally transformed into zirconium oxide. Fig. 2(a) illustrates the way the two elements O and N enter the metal during the initial step where temperature was ramping from room temperature up to the working temperature. During this step, which is common to all sample treatments, the temperature is linearly increased at about 25°C/min. This means that for the sample treated 15 min, the NH_3 plasma treatment was performed at a maximum temperature of 400°C. The AES profile shows that after 15 min of ramping temperature, oxygen and nitrogen present diffusion gradients close to the surface. Oxygen has penetrated deeper and shows higher concentration values. This may indicate that, in this low temperature range, the nitridation rate is lower than that of oxidation. Fig. 2(b) shows the same O and N profiles after a 2 h plasma nitridation at 700°C. In the surface region the nitrogen content is higher and approaches ZrN stoichiometry whereas oxygen is nearly absent. This can be interpreted by a reaction of nitriding species with oxidised zirconium that results in an exchange between nitrogen and oxygen. In the deeper part of the film, and up to the interface, the metal is

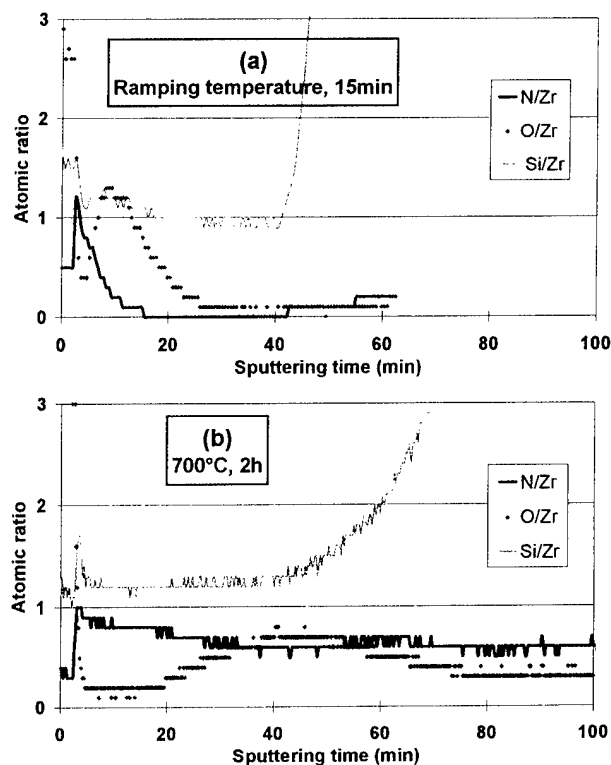


Fig. 2. AES profiles of plasma-nitrided zirconium films.

partially nitrided and partially oxidised. For longer times, as shown in Fig. 1, an increase of nitrogen in the deepest regions occurs in conjunction with oxygen rejection. Compared with thermal nitridation, the reaction of nitridation of the oxidised zirconium is clearly enhanced with plasma. NH_x species are thought to play a major role in the enhancements of nitrogen diffusion and reduction of the oxide.

The optical constants obtained using spectroscopic ellipsometry in the $[0.2\text{--}0.8\text{ }\mu\text{m}]$ spectral range are presented in Fig. 3. The n and k values are very similar to those of gold, the refractive index n being less than 1.0 in a major part of the visible spectrum ($0.45\text{--}0.7\text{ }\mu\text{m}$) and the k extinction coefficient increasing with the wavelength up to very high values in the infrared region. This behaviour, due to free electrons, is characteristic of a good conducting sample. Optical index variations have been well simulated by the free-electron Drude model, giving an electron plasma energy of 7.27 eV and an electron energy relaxation of about 0.57 eV. A static electrical resistivity of $73 \times 10^{-4}\text{ }\Omega\text{ cm}$ has been deduced, which is in good agreement with four-probes resistivity measurements.

3.2. Reactive deposition using DIBS

In Fig. 4 the atomic ratio N/Zr of the nitride film is plotted as a function of the substrate temperature (a) and of the nitrogen ion energy (b). The composition of

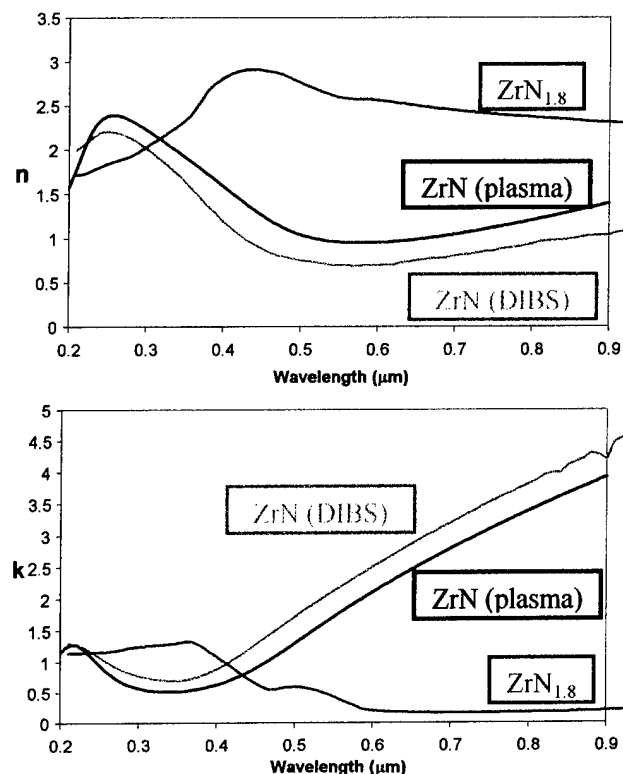


Fig. 3. Optical indices of zirconium nitrides produced by plasma nitridation at 700°C , 7 h (ZrN plasma), reactive deposition by DIBS at 450°C , 50 eV (ZrN DIBS) and at room temperature, 200 eV ($\text{ZrN}_{1.8}$).

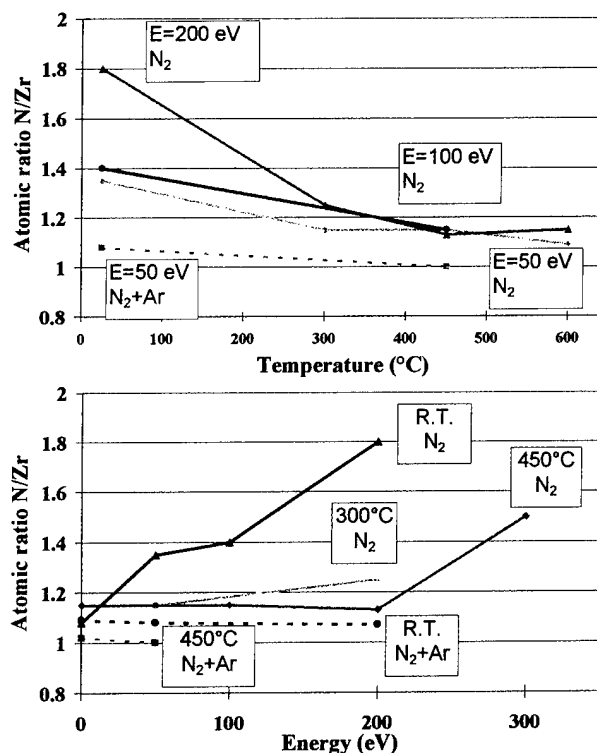


Fig. 4. Nitrogen composition of DIBS-deposited nitrides as a function of the substrate temperature and of the nitrogen ion energy.

the film obtained by reactive sputtering of Zr in N_2 atmosphere is given in Fig. 4(b) at $E=0$ eV. This '0 eV' sample was deposited without igniting the second ion source at a N_2 pressure of around 10^{-4} mbar. A stoichiometry and optical indexes (Fig. 3) that are very similar to the stable phase ZrN are obtained. This shows that Zr deposition in the N_2 atmosphere due to the feeding of the ion source leads to ZrN films. These conditions of reactive sputtering in N_2 and under thermal conditions constitute the ground level of ion beam deposition. Thus, this means that, when using the secondary ion source, the accelerated nitrogen ions are bombarding a nitrated material with N/Zr close to unity. The following results deal with such sputter-deposited films assisted by nitrogen ion beams with energies ranging from 50 to 300 eV. At a low energy of 50 eV similar ZrN -like films are obtained in the whole range of temperature studied from room temperature to 450°C . At higher energies, the films are overstoichiometric with N/Zr ranging between 1.3 and 1.8. At room temperature with the energies of 50 and 100 eV, N/Zr ratios are near 1.33. This stoichiometry is that of Zr_3N_4 . Superior values are obtained at higher energies. With increasing temperature the N/Zr ratio tends towards unity [Fig. 4(a)]. At the maximum energy studied of 300 eV, sputtering predominates with rates close to deposition rates. For these films the resultant growth rates are

nearly null. Spectroscopic ellipsometry characterisation of samples prepared at room temperature and with 200 eV nitrogen ion energy is presented in Fig. 3. The nitride film shows an insulating transparent behaviour with low k extinction coefficient values of about 0.3 for wavelengths up to $0.4\ \mu\text{m}$; this increases to 1.0, due to bound electron contribution, in the UV region ($0.2\text{--}0.4\ \mu\text{m}$). The n values are larger than two over the whole range explored.

4. Discussion and implantation–diffusion growth model

Growth of nitride films using sputtered metal by a first beam and irradiation of the film being deposited by a second nitrogen-ion beam is the result of numerous interacting mechanisms. One such mechanism is point defect diffusion, which is particularly active in surface regions subjected to implantation. A model taking into account enhanced diffusion under irradiation has been established for explaining the experimental results. As illustrated by Fig. 5, the nitride growth has been separated into the four following steps. Step 1 (a) corresponds to sputter deposition at low-pressure nitrogen and leads to ZrN type films more easily when temperature is high. This is the well-known reactive sputtering process whose mechanisms are generally described as

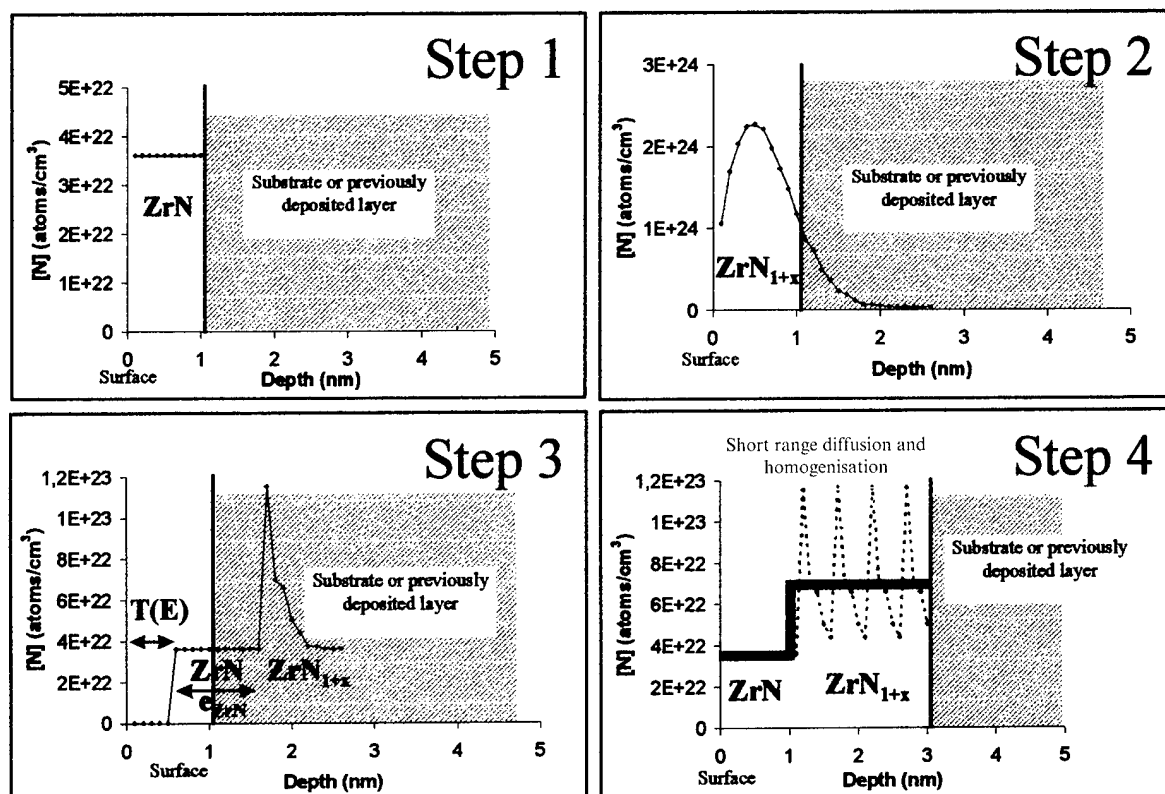


Fig. 5. Growth modelling of DIBS-deposited zirconium nitrides.

sputtered metal atoms adsorbing on the substrate and reacting with the incoming reactive species, which are mainly neutral molecular N_2 . As a matter of fact, in most of the sputtering systems, the base pressure is principally composed of neutrals. Then, in our case, a ZrN film was grown whose thickness was chosen to be equal to 1 nm. Growth rates corresponding to this step have been calculated using thickness measurements on samples deposited under low pressure N_2 (‘0 eV’ sample). These growth rates have been used to determine the time necessary to grow the 1 nm initial layer and then to determine the corresponding fluence and thicknesses used in further steps. Step 2 (b) refers to low energy implantation. Nitrogen ions are implanted in the subsurface region at a depth related to the ion projected range R_p . The implanted nitrogen profiles have been calculated using TRIM code. Step 3 (c) deals with implantation-enhanced diffusion, which is thought to play a major role in assisted deposition. We assume that atomic displacements due to collisions largely improve the nitrogen diffusivity allowing the material to tend very rapidly to equilibrium, which is the stable ZrN phase in our case. We defined the thickness e_{ZrN} as the depth corresponding to a complete relaxation of the film into stoichiometric ZrN. As the diffusivity is strongly enhanced by the ion interactions, the e_{ZrN} depth might be related to the ion projected range R_p . It must also be increased for deposits realised at high temperature. The e_{ZrN} depth value is the only variable parameter of the simulations. Classical sputtering by nitrogen ions striking the surface is included in this step, leading to a sputtered thickness $T(E)$ depending on the ion energy. The sputtering rates have also been estimated using TRIM and verified by measuring etching rates of ZrN films subjected to the secondary N_2 ion beam, with the primary Ar beam being switched off. After this step the nitrogen profile (c) is composed of two regions: a surface region with stoichiometric ZrN followed by a tail with a nitrogen composition largely superior to the first one. Homogenisation by classical thermal diffusion occurring during the whole deposit time is described by step 4 (d). As only short-range diffusion is necessary to smooth the nitrogen profiles, homogeneous layers may be obtained at low temperature. The first three steps are, in reality, simultaneous. However, our model considers them as occurring sequentially. We assume that this does not make a difference unless the different thicknesses used for the calculations are too thin. This is the case for the 1 nm value chosen for the reactive sputter deposited initial layer, for the ion projected range R_p at low energy implantation, and for the $T(E)$ sputter etched layer. By simulating step by step the nitride growth, we could calculate the evolution of the N/Zr ratios during growth. The results are shown in Fig. 6 for nitrides deposited with different energies of the nitrogen beam at room temperature. When compared with the obtained experi-

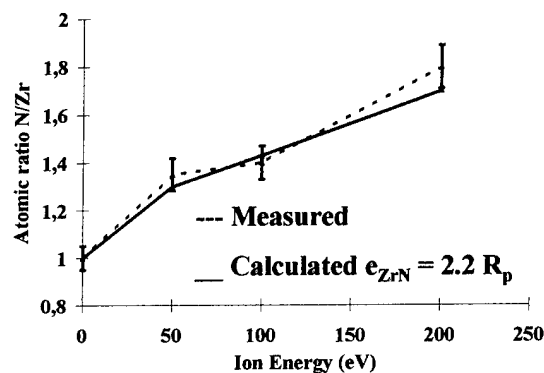


Fig. 6. Numerical results of N/Zr ratios as a function of nitrogen ions energy using implantation–diffusion model and comparison with experimental data.

mental values, the best fit was obtained using an e_{ZrN} value equal to $2.2R_p$. This agrees with the above assumption that diffusion is predominant at low temperature in the region where numerous atomic displacements occur. It would not be the case for deposition performed at higher temperature where the e_{ZrN} value must be increased with thermal diffusion length. Such coupled implantation and thermal diffusion mechanisms are the determining factor for the growth of ceramic coatings in plasma-immersion ion-implantation (P3I) systems. In order to realise a better control of both mechanisms, and to take advantage of the plasma efficiency in improving surface reactivity, we have recently developed a thermally controlled P3I system that enables implantation in the 2–70 keV range between room temperature and 1000°C. This temperature-controlled plasma-immersion ion-implantation offers the opportunity to tailor in-depth stable/metastable ceramic phases such as nitrides, oxides and carbides.

5. Conclusion

This study shows that it is possible to produce stable and metastable zirconium nitrides by native nitridation in NH_3 plasma and by reactive double ion-beam deposition. Plasma nitridation improves the diffusion of nitrogen species and their reaction with metallic Zr. It allows a faster reduction of partially oxidised regions by increasing the exchanges between oxygen and nitrogen. This leads to a stable ZrN phase that is goldish and conductive. Double ion beam deposition enables the production of overstoichiometric nitrides. Keeping the two ion-beam currents constant, the nitrogen ion energy and the temperature determine the composition and phase of the deposited nitride layers. A phase close to Zr_3N_4 was produced that appears transparent and insulating. To explain the appearance of such metastable structures, a model was proposed that considers low

energy implantation and short-range diffusion as the two relevant mechanisms. The combination of the plasma efficiency to enhance surface reactions with the ability of ion implantation to produce non-equilibrium phases has been proposed in a temperature-controlled P3I system.

References

- [1] P. Panjan, B. Navinsek, A. Cvelbar, A. Zalar, I. Milosev, *Thin Solid Films* 298 (1996) 281–282.
- [2] L.C. Zang, C.L. Liang, S.K. Cheung, N.W. Cheung, *J. Vac. Sci. Technol. B*: 5 (1987) 1716–1722.
- [3] L.E. Toth, *Transition Metal Carbides and Nitrides*, Academic, New York, 1971.
- [4] J.P. Langeron, in: P. Pascal (Ed.), *Nouveaux Trait  de Chimie Min rale Tome IX*, Masson, 1963, pp. 402, 403 628–634.
- [5] L. Pichon, A. Straboni, T. Girardeau, M. Drouet, P. Widmayer, *J. Appl. Phys.* (2000) submitted for publication.
- [6] T. Hino, I. Fujita, M. Nishikawa, *Plasma Sources Sci. Technol.* 5 (1996) 424–428.
- [7] L. Marot, L. Pichon, M. Drouet, R. Holtz, A. Straboni, *Appl. Phys. Lett.* (2000) submitted for publication.
- [8] B.O. Johansson, H.T.G. Hentzell, J.M.E. Harper, J.J. Cuomo, *J. Mater. Res.* 1 (1986) 442–451.
- [9] D.S. Yee, J.J. Cuomo, M.A. Frish, D.P.E. Smith, *J. Vac. Sci. Technol. A*: 4 (1986) 381–385.
- [10] L. Pichon, T. Girardeau, A. Straboni, F. Lignou, P. Gu rin, J. Perri re, *Appl. Surf. Sci.* 150 (1999) 115–124.
- [11] R.P. Netterfield, P.J. Martin, D.R. McKenzie, *J. Mater. Sci. Lett.* 9 (1990) 972–974.
- [12] A. Straboni, B. Vuillermoz, A. Vareille, *Proceedings of the 163rd Meeting of Electrochemical Society* (abstract 867 RNP), San Francisco (1983).
- [13] J. Perri re, J. Siejka, N. Remili, A. Laurent, A. Straboni, B. Vuillermoz, *J. Appl. Phys.* 59 (1986) 2752–2759.

Deposition of c-BN by ion beam assisted CVD

G. Schwarz, F. Friess, G.K. Wolf *

Universität Heidelberg, Physikalisch-Chemisches Institut, Im Neuenheimer Feld 500, D-69120 Heidelberg, Germany

Abstract

The main problem in growing c-BN rich films in the past has been their very high intrinsic stress, leading to partial or complete detachment from the substrate after reaching a critical thickness of 200 nm. The process we are using is closely related to IBAD or IAE. However, in addition to the evaporation of boron atoms and simultaneous nitrogen ion bombardment by an ion gun, the films were grown in a highly reactive gas (SF_6 , BF_3) atmosphere, provided by a nozzle close to the Si substrate [chemically modified ion assisted evaporation (CMIAE)]. Reactive gases were used to verify preferential etching of impurities and different phases of boron nitride. SF_6 represents a pure etchant, BF_3 , in addition, is a boron source.

With this modification it was possible to grow films at 450°C with a c-BN content of 85% up to a thickness of 800 nm. The films showed very good adhesion and could be deposited over a wide range of ion/neutral (I/N) ratios (0.4–1.2), depending on gas flux and geometrical condition. Furthermore, c-BN films could also be grown at much lower temperatures down to 120°C.

The analysis of the films was performed by IR and AES spectroscopy. The film thickness was measured independently by Talystep and Dektak. Although the details of the mechanism are not yet understood, the reactive gas assistance is very promising for obtaining rather thick films with high c-BN content and good adhesion. Further experiments on CMIAE deposition on iron and steel substrates are in preparation. © 2000 Elsevier Science S.A. All rights reserved.

Keywords: Adhesion; BF_3 ; c-BN; SF_6

1. Introduction

The main problem preventing the practical use of c-BN coatings for tools or work pieces [1] is the high compressive stress in the films. Independent of the method of deposition, the film thickness is limited to less than 200–300 nm and the films tend to delaminate. There have been many attempts to improve the situation by using multilayers or, for example, postbombardment with energy rich ions [2]. However, they were not very successful up to now. We developed a different deposition technique to prepare c-BN coatings with improved adhesion and reduced stress. The normal IAE deposition technique was modified by injection of reactive gases to the target surface. Their influence on the enrichment of c-BN and the properties of the synthesised coatings were investigated. Boron evaporation and irradiation with a mixture of nitrogen and argon ions was done in the presence of reactive gases like SF_6 and BF_3 using a nozzle which could be arranged at different geometrical positions. By this investigation we were able to verify

that it is possible to grow c-BN rich films at much lower temperatures (120°C) using the CMIAE technique.

2. Experimental

All BN-films were prepared by evaporation of boron and by ion bombardment with a low energy ion source (Anatech Ltd.) delivering a Gaussian beam profile. Owing to this profile it was possible to synthesise films with various ion to neutrals ratio (I/N) on the same substrate and under similar conditions in a single experiment (Fig. 1a and b).

Silicon wafers (100) were used as substrate material. Before the BN deposition started we deposited a 20 nm thick boron layer [3] on the substrate. The depositions were made in the Heidelberg IBAD facility ALLIGATOR [4]. The position of the gas nozzle for the reactive process gases relative to the ion beam centre on the target and the gas flow were varied to investigate the influence of reactive gas concentration at the surface on the formation of the cubic phase. Also, the ion energy and the ion current density in the beam centre

* Corresponding author.

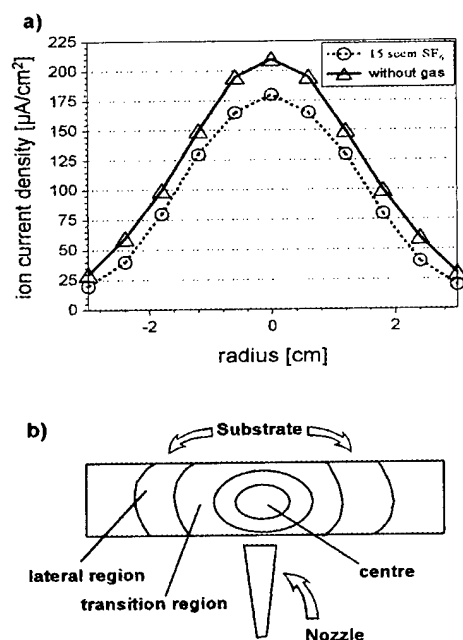


Fig. 1. (a) Ion beam profiles of the low energy ion source Anatech with and without reactive gas flux. (b) Scheme of a deposited substrate and gas nozzle.

were altered. Other parameters like the angle of ion incidence (20°), the N_2 -Ar mixture (65/35) in the ion source and the distance between the ion source and the growing film (20 cm) were kept constant. The rate of thermal boron (neutrals) during deposition was measured by a quartz crystal monitor. The pressure in the vacuum chamber was between 4×10^{-5} and 1.5×10^{-4} mbar depending on the amount of the chemical additives (BF_3 or SF_6). The ion current density was measured with a Faraday cup before deposition with and without gas flow (see Fig. 1a). To calculate the I/N ratio in the different substrate regions (Fig. 1b), measurements of ion current density under simultaneous gas flow were performed. Another set-up, where the gas nozzle was positioned further from the ion beam centre while keeping the gas flux constant, showed that the ion current density decreases with decreasing distance between nozzle and beam centre (Fig. 2). This results in a moderate increase in pressure on the substrate surface and correspondingly an increasing number of neutrals in the beam if the nozzle is near the beam centre. Furthermore, the film growth was studied at different temperatures from 120°C up to 450°C .

3. BN-film characterisation

A Fourier transformed infrared spectrometer (brucker IFS 66 V) in the wavenumber range between 600 and 1700 cm^{-1} was used to identify the h-BN and c-BN-phases (see Fig. 3). The absorption peak at

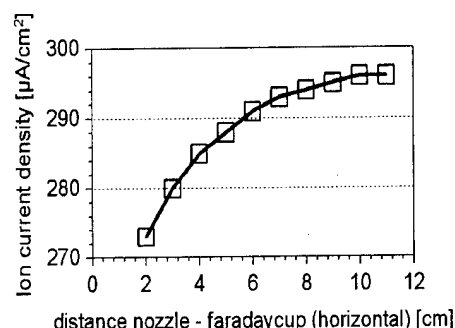


Fig. 2. Ion current density as a function of the horizontal distance between gas nozzle and ion beam centre.

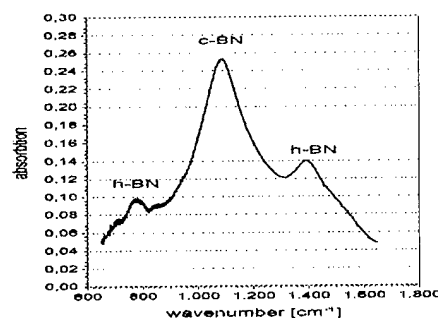


Fig. 3. Infrared spectra of a BN coating containing h-BN and c-BN prepared by BF_3 -CMIAE

1390 cm^{-1} correlates with the B-N in plane stretching vibrations of hexagonal BN. Also, the B-N-B out of plane bending vibrations at 780 cm^{-1} are associated with hexagonal BN. Cubic Boron Nitride shows a transversal optical peak in the region between 1057 and 1100 cm^{-1} . By comparing areas under these peaks, the c-BN content was estimated. The c-BN peak shifts with increasing intrinsic stress up to higher wavenumbers [5]. Great care must be taken to calculate the value of compressive stress from this peakshift because it is also dependent on other parameters such as contamination, crystallite size and stoichiometry effects [6,7]. Auger depth profiling (AES) was carried out to estimate the elemental concentrations in the film and was verified by photoelectron spectroscopy (XPS). The thickness of the film was measured with a Talystep and Dektak instrument and compared with scanning electron microscopy (SEM) cross-sections.

4. Results and discussion

The formation of cubic boron nitride by using the ion assisted evaporation (IAE) technique depends on a high ion to neutral ratio (>1) [8] up to the threshold of resputtering ($\text{I/N} \sim 1.5$) and requires ion energies between 500 and 700 eV [8].

Fig. 4 shows the c-BN content as a function of the

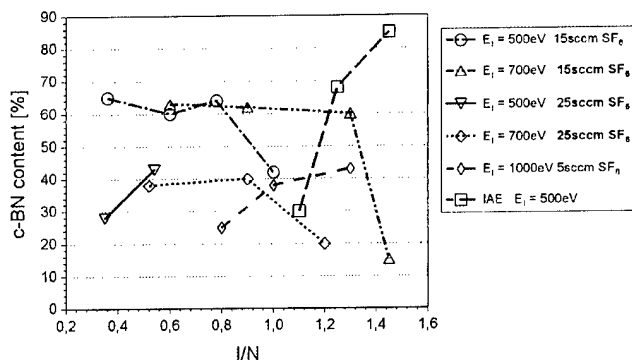


Fig. 4. c-BN content as a function of the ion to neutral ratio for SF_6 -CMIAE films prepared by different gas flow and ion energies compared with the c-BN content of an IAE film.

I/N ratio of samples that were coated with chemically modified IAE under SF_6 flow compared with conventional IAE technique. The results show clearly that it is possible to prepare coatings with high amounts of the cubic phase at drastically lower I/N ratios if SF_6 is used as the chemical additive rather than without SF_6 . So far the highest amount (60–70%) was found by using a gas flux of 15 sccm. The c-BN content decreases considerably with higher flux (25 sccm) of SF_6 when the ion energy (500 eV; 700 eV) is kept constant. The films synthesised under the same geometric conditions under BF_3 flow contain an even higher percentage of the cubic phase (70–85%) for the same I/N ratio. Fig. 5 shows the c-BN content as a function of the I/N-ratio for different ion energies and a constant gas flux of 10 sccm.

Substantial higher ion energy has to be used to get a reasonable amount of the cubic phase in comparison to the normal IAE or SF_6 treated CMIAE films. An important parameter for the growth of c-BN at low I/N ratios is the position of the gas nozzle relative to the beam centre near the substrate (Fig. 1b). If no

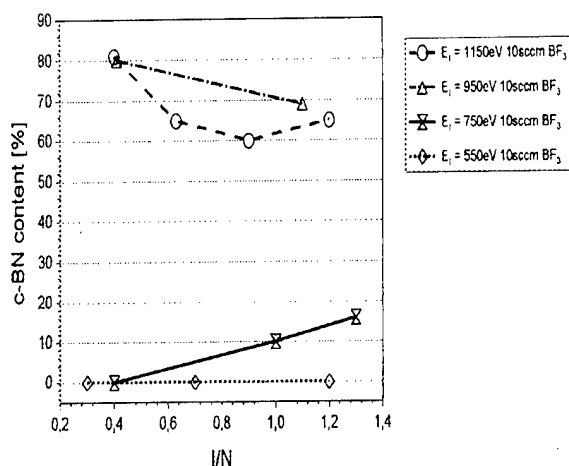


Fig. 5. c-BN content as a function of I/N for different ion energies and a constant gas flux of 10 sccm BF_3 .

nozzle is used but the pressure in the deposition chamber is equal to that with nozzle, no c-BN can be found in the lateral regions of the substrate. This must be caused by a decreasing concentration of the chemical additive or its decomposition products near the substrate surface. Furthermore, the ion density in the beam centre must be kept high ($>200 \mu\text{A}/\text{cm}^2$) to obtain c-BN formation at low I/N ratios. This leads to the conclusion that dissociation products like ions or radicals of the used gas (BF_3 or SF_6) are generated by collisions with ions. Another important question is whether energy rich neutral particles may be produced in these collisions. These particles must be added to the number of ions in the I/N ratio because of their additional impulse transfer to the growing film. To study this problem we measured the ion beam profile with and without gas flux (Fig. 1a). The ion density in the beam centre ($210 \mu\text{A}/\text{cm}^2$) decreases by less than 10% using a gas flux of 15 sccm. Furthermore, the I/N ratio threshold of film growth (resputter region) does not change drastically compared to IAE films [≈ 1.5 (500 eV); ≈ 1.3 (1100 eV)]. Another possibility that would increase the 'effective' I/N ratio is preferential etching of the condensing thermal boron. This should equally lead to a lower I/N threshold for resputtering as well as to a decreasing film thickness at similar I/N ratios compared to IAE films. However, this could not be verified experimentally. The films prepared with normal IAE and SF_6 added CMIAE technique were deposited up to a film thickness of 300 nm in situ measured on the quartz crystal monitor. This measurement naturally only relates to boron, and does not relate to nitrogen or resputtering. Therefore, some of the films also underwent thickness measurements by profilometry.

The thickness of SF_6 added CMIAE films is comparable or lower than that of normal IAE films at similar I/N ratios (Fig. 6). If selective etching of h-BN or boron was the reason for the high amount of c-BN at lower I/N ratios using the CMIAE technique, there should be a decrease of film thickness compared to IAE films, which is not the case. The thickness of deposited boron

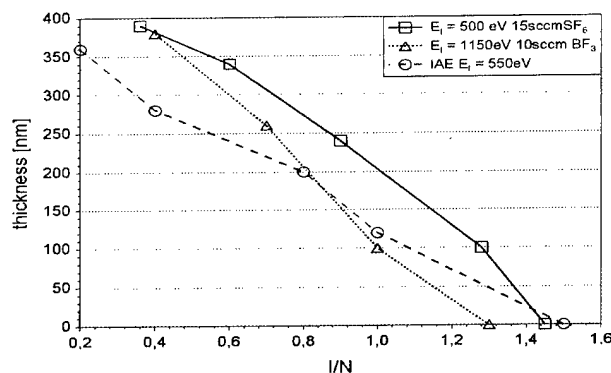


Fig. 6. Talystep thickness measurements of SF_6 -CMIAE, BF_3 -CMIAE and IAE films as a function of the I/N ratio.

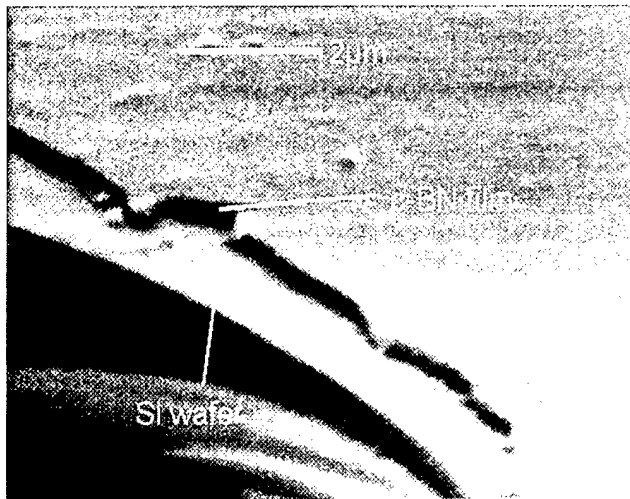


Fig. 7. SEM representation of an 85% c-BN film prepared at an I/N of 0.4 and 1150 eV ion energy and a gas flux of 10 sccm BF_3 .

measured on the quartz crystal monitor during the deposition under BF_3 gas flow was about 160 nm. The thickness obtained by profilometry was 200–380 nm at I/N ratios between 0.4 and 0.8. The thickness of the c-BN film at the I/N ratio of 0.4 was measured by SEM as 400 nm. Fig. 7 also shows that there is no film detachment. In another case, 800 nm film thickness could be measured by profilometry, while boron was deposited up to 480 nm on the quartz crystal monitor. It was also found that the ratio of deposited boron to the real film thickness changes with the substrate temperature. This means an increase of thickness must be caused by the additional boron delivered via BF_3 and/or a radiation induced transfer of nitrogen radicals from the residual gas into the growing film.

4.1. Adhesion and stress

BN-films prepared by IAE and similar PVD techniques with a high amount of c-BN normally crack off if the critical film thickness of 200–300 nm is reached [6]. This is caused by the high intrinsic, compressive stress (>10 Gpa)[6,9]. This process starts immediately after deposition or if the films are exposed to air. In contrast, c-BN films prepared at low I/N ratios (0.3–0.8) using the CMIAE technique have good adhesion and do not show any cracks even though the film thickness is much higher than 200 nm. It was possible to synthesise c-BN films (80–85%) up to a thickness of 800 nm without any signs of cracking or detachment. In Fig. 8 the AES depth profiles of films prepared by normal IAE, SF_6 and BF_3 added CMIAE are shown. The depth profile in the case of SF_6 -CMIAE (Fig. 8b) shows, in contrast to the normal IAE film, a broadened interface that might be responsible for the good adhesion at lower I/N ratios. The interface region of

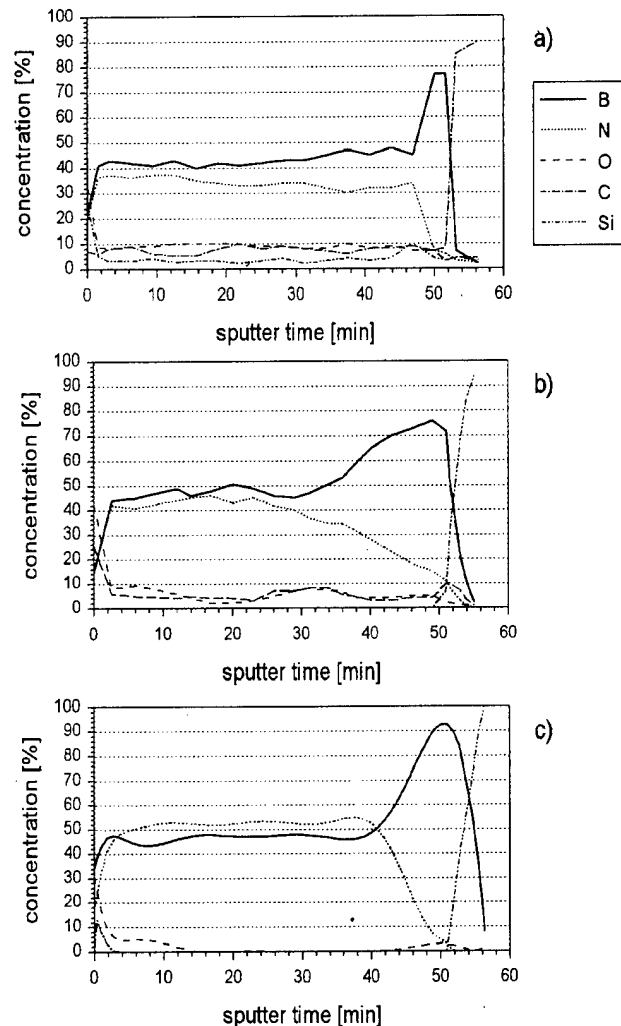


Fig. 8. Auger depth profiles: (a) IAE film (87% c-BN); (b) SF_6 -CMIAE film (65% c-BN); (c) BF_3 -CMIAE film (85% c-BN).

BF_3 -CMIAE films, however, is not as broad as that of the SF_6 -CMIAE films (Fig. 8c), but they also show a good adhesion. A detailed study is not yet available and further investigations are necessary. Remarkable is the absence of substantial amounts of oxygen, fluorine, sulfur or carbon in the BF_3 -CMIAE coating in contrast to the other two samples.

5. Conclusions

The IAE process was modified by leading reactive gases to the substrate chamber through a nozzle. The presence of SF_6 and BF_3 molecules had a distinct effect on the c-BN formation. Whereas in the normal IAE process I/N ratios of >1 were necessary to achieve a content of 85% cubic boron nitride in the deposited layer, in the deposition with reactive gases an I/N ratio as low as 0.4 led to a c-BN content of 65% in the case

of SF₆ and 85% using BF₃. The optimal c-BN formation took place at 500 eV ion energy for SF₆ addition and 1050 eV and 450°C for BF₃. However, even at 120°C, films with 55% c-BN could be synthesised. The decomposition products of the reactive gases, produced by collision with ions, are thought to be responsible for this effect. BN films synthesised by IAE show very poor adhesion even with low concentration of c-BN (40%). They often delaminate after deposition even without load. This could be greatly improved by the CMIAE process. Films with 85% c-BN and a thickness of 800 nm show no cracks even after long exposure to air, probably because of the reduced film stress caused by etching and the lower I/A ratio. The detailed mechanism of the influence of the reactive gases on the growth and quality of the coatings is not fully understood yet. However, the results bear interesting perspectives for the future production of c-BN coatings with reduced stress on various substrates.

Acknowledgements

The authors thank the 'Deutsche Forschungsgemeinschaft' and Prof. Grunze, PCI, University of Heidelberg for supporting this work.

References

- [1] S. Myake, R. Kaneko, Y. Kikuya, I. Sugimoto, *Trans. ASME J. Tribol.* 113 (1991) 384.
- [2] M. Murakawa, S. Watanabe, S. Myake, *Diamond, Heidelberg*, 1992.
- [3] G. Sene, Ph.D. thesis, University of Paris-Sud, France, 1995.
- [4] H. Wituschek, M. Barth, W. Ensinger, G. Frech, D. Rück, K. Leible, G.K. Wolf, *Rev. Sci. Instrum.* 63 (4) (1992) 2441.
- [5] J.A. Sanjurjo, E. Lopez, P. Vogl, M. Cardona, *Phys. Rev. B* 28 (1983) 8.
- [6] S. Reinke, M. Kuhr, R. Beckmann, W. Kulisch, R. Kassing, *Proc. of 3rd International Symposium in Diamond Materials*, May 1993, Honolulu, Hawaii.
- [7] G.P. Lamaze, R.G. Downing, L.B. Hackenberger, L.J. Pilione, R. Messier, *Diamond Relat. Mater.* 3 (1994) 728.
- [8] D.J. Kester, K.S. Ailey, R.F. Davis, K.L. More, *J. Mater. Res.* 8 (1993) 6.
- [9] M.A. Douadj, D. Bouchier, P. Müller, G. Sene, *9th Int. Colloq. Societe Francaise du Vide*, (1993).

Influence of ion induced surface defects on the nucleation and formation mechanisms of metallic thin films

H.-A. Durand *, K. Sekine, K. Etoh, K. Ito, I. Kataoka

Japan Aviation Electronics Industry Ltd, Central Research Laboratory, Musashino 3-1-1, Akishima-shi, Tokyo 196-8555, Japan

Accepted 13 October 1999

Abstract

Using an in situ ultra high vacuum (UHV) electron tunneling microscope, we have studied the influence of ion induced defects on highly oriented pyrolytic graphite on metallic thin film formation. The impact of ions with energy ranging from 10 to 300 eV induces several kinds of defects on the substrate surface. We classified defects according to impinging energy of ions and this correlates well with atomic resolution images of bombarded surfaces. More precisely, we will present here the influence of these defects on the initial formation of nickel and molybdenum thin films. We have analyzed thin films deposited by both direct ion beam and electron beam evaporation. We reveal clear differences and prove the dramatic influence of surface defects on the nucleation of thin films. These investigations have specific importance for the control and production of materials enclosing metallic and semiconducting nanoparticles used in a new generation of magnetic and optoelectronic devices. © 2000 Elsevier Science S.A. All rights reserved.

Keywords: Fractal surface; Ion beams; Molybdenum; Nickel; Scanning tunneling microscopy; Thin films

1. Introduction

An understanding the fundamental mechanisms of thin film formation is essential where ‘ultra smooth’, ‘ultra thin’ films are to be used. Applications of thin films for high accuracy interferometric sensors and optoelectronic devices are of crucial importance in many industries. Furthermore, basic formation mechanisms may lead to the natural construction of networks of metallic islands which can be embedded in a matrix material. This is advantageous for adjusting the properties of functional materials using quantum confinement in nanoparticles. Using a scanning tunneling microscope (STM) in UHV, we show that the influence of low energy ion induced defects on a surface enables direct control of the morphology of a network of metallic nano-islands. Ion irradiation at a macroscopic scale enables control of the nanoscale morphology of the surface.

2. Experiments

In the following experiments, graphite substrates were irradiated by 100 eV Ar⁺ ions in order to induce defects in the surface. Subsequently, we deposited Ni and Mo by electron beam evaporation on these prepared substrates, and on virgin substrates for comparison.

The ion beam deposition system consisted of a beam line directly attached to the UHV-STM chamber. This system has been extensively described in Ref. [1]. It is dedicated to the study of initial thin film formation because the design provides only a very low ion current — equivalent to less than 1 ML/h. It should be noticed that larger scale direct ion beam deposition (DIBD) systems [2] allowing practical yields of the order of 1 Å/min are available and are used for the preparation of films with complex compositions. Ion energy can range from a few eV to 1 keV, although all experiments presented here were performed with 100 eV ions. In our experiments Ni⁺ ions were generated from nickel chloride placed in the oven of a Colutron G2 ion gun and the substrates were bombarded with average densities ranging from 1 to about 40 ions/nm², while the pressure was kept at 10⁻⁴ Pa. Highly Oriented Pyrolytic

* Corresponding author. Tel.: +81-425-49-9216;
fax: +82-425-49-9572.

E-mail address: hadurand@jae.co.jp (H.-A. Durand)

Graphite (HOPG) substrates were cleaved just before placement in the deposition chamber in the 1000 class clean room where the whole system was installed; no contamination of the surface was been detected using this process.

For evaporation we used a commercially available electron beam evaporator (Oxford Instruments EGN4). The Ni and Mo sources were commercially available 99.9% pure metal rods placed in the sockets of the evaporator. The distance between the evaporation point and the substrate was 150 mm conducted at 10^{-8} Pa in a separate UHV chamber.

3. Observation of nanostructures and discussion

In the following we will discuss: (i) the formation of defects induced by low energy ions on HOPG; (ii) the initial formation of Ni and Mo films by evaporation; (iii) the formation of an Ni film on an HOPG surface which included defects; and (iv) a comparison with films prepared using Ni^+ ions directly.

3.1. Defects induced by ions on an HOPG surface

We have previously classified ion induced defects as a function of ion energy [3]. In short, for 100 eV Ar^+ ions most of the defects induced on the HOPG surface are vacancies, interstitials and ‘settled ato-clusters’. Indeed, a few carbon atoms are removed from the surface lattice by incoming energetic ions. These recoil carbon atoms migrate on the surface by diffusion, even at low deposition temperature, and settle alone or in groups of two or three on several preferential sites on the graphite surface lattice: they form ‘settled ato-clusters’. We assumed that all these surface defects are

nucleation centers and influence thin film formation drastically.

Fig. 1 shows the influence of annealing at 200 and 300°C on the reconstruction of the HOPG surface. By tuning the annealing temperature and duration, one may eliminate some categories of defects — such as vacancies and interstitials. The remaining defects visible on STM images presented in Fig. 1 are settlements of a few atoms on a unique graphite cell [3]. This particular type of defect generates a perturbation of the electronic density surrounding the defects and extends to several nanometers around each settled ato-cluster. This electronic density perturbation is beautifully revealed by the electron scanning microscope by a periodic pattern. By comparison with computer simulations [4], the symmetry of these patterns reveals the number of atoms and their respective position in the crystal network [3].

3.2. Formation of evaporated films on virgin HOPG

Fig. 2 presents STM images on the atomic scale of the early stages of the formation of Mo and Ni thin films. In Fig. 2(b) (compare with Fig. 2(e)) the virgin HOPG substrate has received eight times more Ni (or Mo) particles than in Fig. 2(a) (compare with Fig. 2(d)), and so on for Fig. 2(c) (compare with Fig. 2(f)). For increasing density, many more islands are visible and the substrate is almost covered by the Ni (or Mo) films. Nevertheless, many more islands exist for Mo than for Ni. This significant difference in morphology results from the diverse behavior of elements regarding thin film growth. For each material, growth mechanisms are driven by the balance between sticking and cohesion energy. Assuming a macroscopic equilibrium between the condensed phases and their vapors, the theory of wetting [5] predicts the nucleation of bulk phase clusters

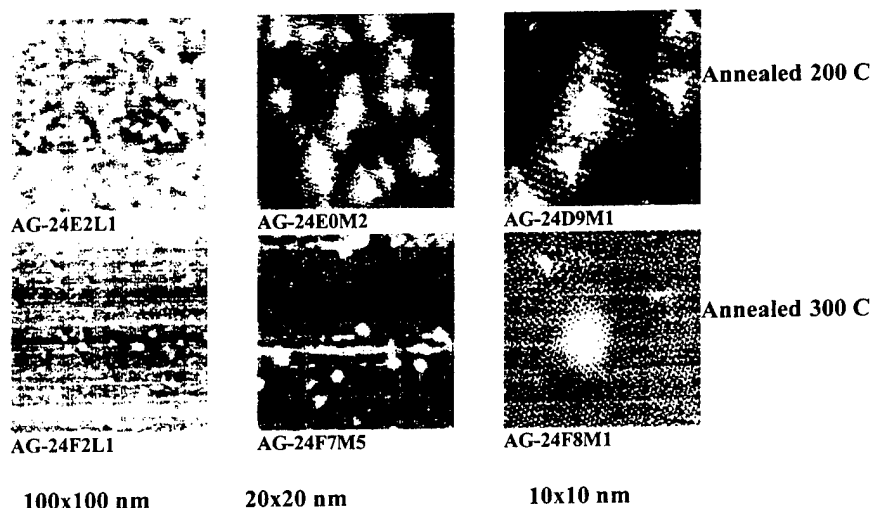


Fig. 1. STM images of annealed HOPG surfaces protruded by Ar^+ 100 eV ion induced defects at different scales up to atomic resolution.

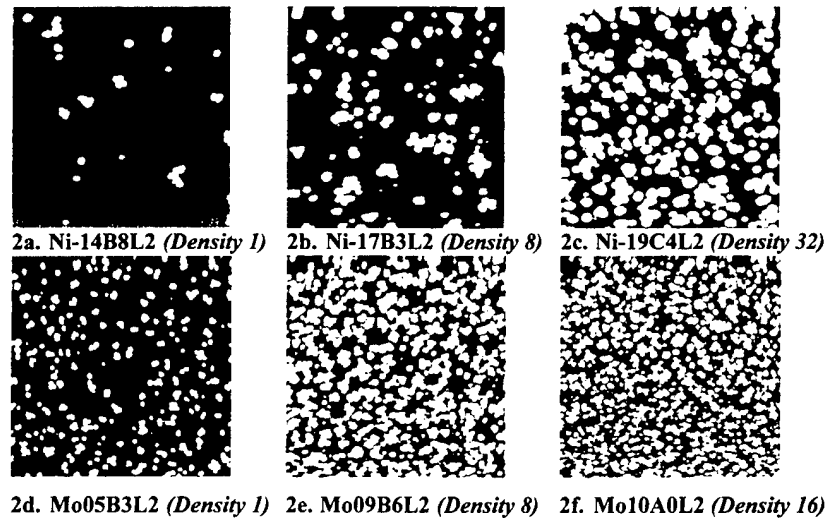


Fig. 2. STM image of Ni and Mo films evaporated on virgin HOPG (200 × 200 nm).

(Volmer–Weber growth mode) or a total wetting of the substrate by the adsorbate (van der Merwe growth mode).

It is difficult to draw conclusive remarks regarding growth mechanisms simply from visual inspection of STM images, even using three dimensional representations. Therefore several ways of representing complex surfaces as a one dimensional function have been proposed. Notably, the powerful theory concerning the dynamic evolution of fractal surfaces allows the reduction of images to unidimensional functions [6], while the parameters embodied in the dynamic scaling function of roughness [2] (DSFR) are characteristic of the growth mechanisms. This theory has already been presented extensively [7] and the following summarizes features relevant to the present work. One can easily compute [1] the DSFR from digitized images of the surface obtained by STM.

For most growth models, the DSFR log–log plots give two distinct regions separated by a crossover length L_0 [7]. For $L < L_0$ the diffusive terms dominate, and the DSFR increases with a slope of χ ; for $L > L_0$, the adsorption/desorption terms govern and leads to $\chi = 0$ in three dimensions. χ is called the roughness scaling exponent and it is characteristic of the growth mechanisms. Therefore, the plots of the DSFR calculated from experimental images lead to a graphical reading of the roughness exponent χ , giving indications of the mechanisms of growth of the surface. Several models have been proposed for an established steady growth of a solid thin film [7]. These models balance the roughening caused by the ballistic arrival of incoming particles with the smoothing effect of transport processes on the surface. For example, in the simplest Wolf–Villain [8] model of growth for three dimensions $\chi = 1$. Lai–Das Sarma [9] formed a characteristic function of growth with the

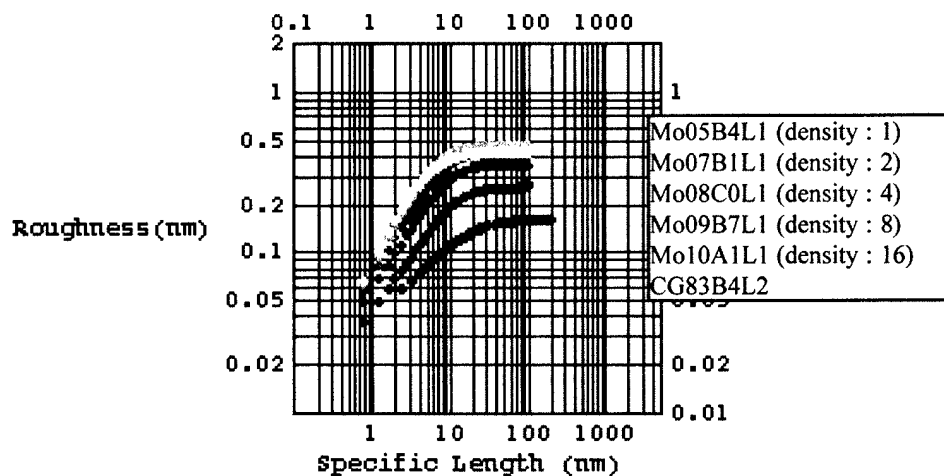


Fig. 3. Evolution of the dynamic function of roughness as a function of density Mo deposits (100 × 100 nm). The DSFR for the HOPG surface is also presented for comparison (STM 200 × 200 nm scan, CG83B4L2).

Table 1

Experimental values of the roughness scaling exponent for Mo and Ni grown by evaporation and DIBD and corresponding interpretation

Material	Deposition	χ	Remarks on growth mechanisms
HOPG	Virgin	0.2–0.3	Cleaved HOPG — this represents atomic corrugation.
Argon	100 eV ions	0.6–0.7	Diffusion driven of recoil atoms at initial stage on HOPG
Molybdenum	Electron beam	0.67	Diffusion driven at the initial stage
Nickel	Electron beam	Steady growth, stabilizing at 1	Three dimensional growth
Nickel	Ar ⁺ on irradiated HOPG	0.7–0.4	Enhanced nucleation of islands
Nickel	100 eV ions	0.73	Self-enhanced nucleation of islands

first term representing surface diffusion, while a second term takes into account the incident flux of particles. The theoretical value of the scaling exponent is then $\chi = 2/3$ in three dimensions.

All these models were developed for steady growth under low energy particle (or ion) flux of a material identical to the substrate, that is homogenous growth. In contrast, our experiments concerned the heterogeneous growth of metals on HOPG. The growth of ultra thin films starts from the virgin, flat substrate surface and is not steady, at least until the coalescence of islands. Before reaching the steady homogeneous growth, that is after the full coverage of the HOPG substrate, the value of the scaling exponents evolves with density of deposits.

Fig. 3 shows the evolution of the DSFR for the increasing density of evaporated Mo particles. At coalescence, the DSFR saturates and the scaling exponent becomes steady. Further evolution follows the

characteristics of a growing fractal interface while the scaling exponent will be kept at the value of saturation. This roughness scaling exponent saturates at a value of $\sim 2/3$ for Mo and 1 for Ni for evaporation (see Table 1).

3.3. Surface defects and thin film formation

In Fig. 4 one can compare the island networks of Ni grown by evaporation on virgin HOPG (Fig. 4(a)), Ni grown by evaporation on 100 eV Ar⁺ bombarded HOPG (Fig. 4(b)), and Ni grown by direct deposition of 100 eV Ni⁺ ions on HOPG (Fig. 4(c)). The number of Ni atoms on the surface is approximately the same. Ar⁺ induced defects on the HOPG surface in Fig. 4(b) have an enormous influence on the number and size of islands. Fig. 4(c) represents an intermediate state as incoming 100 eV Ni⁺ ions themselves induce defects which will lead to subsequent Ni island formation. The latter case allows less controllability as the processes of

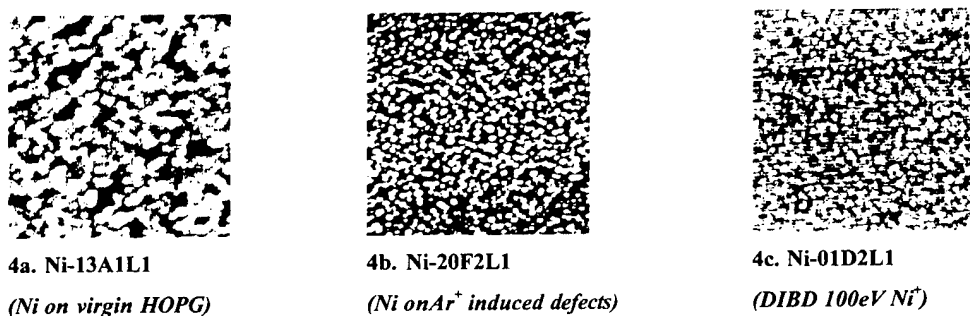


Fig. 4. STM (100 × 100 nm) images of Ni films deposited by: (a) evaporation on a virgin HOPG substrate; (b) evaporation on a 100 eV Ar⁺ irradiated substrate; and (c) by direct 100 eV Ni⁺ ion beam on virgin HOPG.

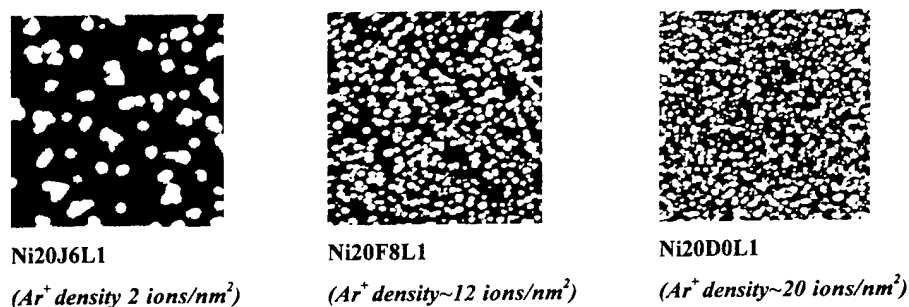


Fig. 5. STM images of Ni film deposited on Ar⁺ 100 eV ion irradiated HOPG for various ion densities from 2 to 20 ions/nm² (100 × 100 nm).

defect creation and island formation occur at the same time.

Fig. 5 shows STM images of Ni evaporated at an equivalent and constant density of eight arbitrary units (similar to image Fig. 2(b)) on HOPG substrates prepared by 100 eV Ar⁺ irradiation with densities varying from 2 to 20 ions/nm². The conclusion is easy — the more Ar⁺ ions irradiated on HOPG, the more islands generated for Ni thin film during the subsequent evaporation. The average size of islands is logically smaller as they become numerous. From these three STM images it is already clear that ion induced defects have a dramatic influence on nucleation.

Creating nucleation centers has a similar effect to reducing diffusion, meanwhile growth is shifting from a three dimensional mode to a mode close to the Laï-Das Sarma model. For DIBD of Ni the scaling coefficient has an intermediate value of $\chi \sim 0.73$ — these show the great influence of Ni⁺ ion induced defects in thin film formation.

4. Conclusion

We believe that such a method of inducing defects using medium energy Ar⁺ ions for controlling island size at the nanometer scale can have a significant impact

on the technology of thin film growth. Our experiments were conducted on a carbon graphite substrate, but the same effects can be expected for materials such as silicon or arsenide monocrystals which are important in the electronic and optoelectronic industry.

Acknowledgement

The authors would like to thank Dr Yonosuke Makita of the Electrotechnical Laboratory, AIST, MITI (Tsukuba Science City, Japan) for fruitful discussion and support.

References

- [1] H.-A. Durand, K. Sekine, K. Etoh, K. Ito, I. Kataoka, *J. App. Phys.* 84 (5) (1998) 2591.
- [2] K. Ito, T. Yonemitsu, K. Etoh, H. Sekiguchi, I. Yamada, I. Kataoka, H.-A. Durand, *Nucl. Instrum. Meth. B* 59/60 (1991) 321.
- [3] H.-A. Durand, K. Sekine, K. Etoh, K. Ito, I. Kataoka, *Thin Solid Films* 336 (1998) 42.
- [4] H.A. Mizes, J.S. Foster, *Science* 244 (1989) 559.
- [5] F. Gautier, D. Stoeffler, *Surf. Sci.* 249 (1991) 265–280.
- [6] F. Family, T. Vicsek, *J. Phys. A* 18 (1985) L75.
- [7] A.-L. Barabasi, H.E. Stanley, *Fractal Concepts in Surface Growth*, Cambridge University Press, 1995, p. 23. Parts 1–2.3.
- [8] D. Wolf, J. Vilain, *Europhys. Lett.* 13 (1990) 389.
- [9] Laï-Das Sarma, *Phys. Rev. Lett.* 66 (1991) 2348.

Amorphisation and related structural effects in thin films prepared by ion beam assisted methods

A.R. González-Elipe *, F. Yubero, J.P. Espinós, A. Caballero, M. Ocaña, J.P. Holgado, J. Morales

Instituto de Ciencia de Materiales de Sevilla (CSIC-Univ. Sevilla) and Dpto. Q. Inorgánica, Avda. Américo Vespucio s/n, 41092 Sevilla, Spain

Abstract

Amorphisation of thin films is a very common phenomenon when their synthesis is assisted by a beam of ions. In this case, X-ray diffraction or related diffraction procedures do not provide a complete description of the phase structure of the films, and alternative methods have to be used to get information about the atom distribution within the lattice. This paper presents some approaches using X-ray absorption and infrared spectroscopy to account for the local structure and other crystallographic effects which may appear in thin films prepared by ion beams. Tin, iron and zirconium oxide thin films, all prepared by ion beam induced CVD, have been selected to show the possibilities of the different characterisation methods. The local distribution of atoms and the evolution of the crystal structure upon annealing are studied as a function of the type of ion species (i.e. O_2^+ or Ar^+) used for the preparation of the films. © 2000 Published by Elsevier Science S.A. All rights reserved.

Keywords: Amorphisation; Crystal orientation; IBAD; IR; Thin films; XAS

1. Introduction

Ion beam assisted deposition procedures (IBAD), used for the synthesis of thin films, have become very popular during the last few years because of the optimal characteristics of the films prepared by assisting the film growth with accelerated ion species [1,2]. Generally, these methods are preferred when thin films with a high densification, homogeneity and adhesion are required [3]. A common effect of assisting the growth of thin films by bombardment with ions is the appearance of compressive stress that can be a problem for certain applications [4]. It is also generally found that in these films the crystallographic structure is also modified. Amorphisation, preferential growth of some crystallographic planes, etc. are some of the phenomena attributed to the assistance of the bombardment with low energy ions [5,6].

In bulk materials changes in composition, amorphisation, crystallisation, preferential growth of certain crystallographic planes and other structural effects have been widely reported [7,8]. With thin films prepared by IBAD methods, systematic studies on the modifications

of the crystallographic structure are less numerous, probably because in most cases only X-ray diffraction is used to structurally characterise the films. As a consequence, no direct information is accessible about amorphisation or other related phenomena.

The present paper constitutes an attempt to investigate the structural modifications, in particular amorphisation, induced by the ion bombardment of growing films. The use of alternative methodologies based on X-ray absorption spectroscopy (XAS) and infrared (IR) spectroscopy is proposed as a complement to the classical investigation of the structure by X-ray diffraction (XRD). The possibilities of these methods are illustrated with examples of oxide thin films (i.e. SnO_2 , Fe_2O_3 and ZrO_2) prepared by means of the ion beam induced CVD (IBICVD) procedure [9]. These thin film materials are interesting because of their optical, magneto-optical and heat resistance applications [10–12]. It is shown that the use of Ar^+ ions for assisting the film growth has a clear influence on the structure of the films.

2. Experimental

The basic principles of the IBICVD procedure have been discussed previously [9]. The procedure consists of

* Corresponding author. Fax: +34-9544-606-65.

E-mail address: agustin@cica.es (A.R. González-Elipe)

bombarding a suitable substrate with an ion beam while a flow of a volatile metal precursor is directed onto its surface. Typically, O_2^+ ions are used for the preparation of oxide thin films, although synthesis is also possible using mixtures of ions such as $\text{O}_2^+ + \text{Ar}^+$. All the examples presented in this paper correspond to thin film oxides prepared with ion kinetic energies of 400 eV and beam currents at the sample position of $\sim 100 \mu\text{A cm}^{-2}$.

The present paper focuses on the structural effects in thin films of Fe_2O_3 , SnO_2 and ZrO_2 materials, taken as examples. Surface morphology and other properties of these thin films will not be discussed here. Nevertheless, it is worth mentioning that all the films were dense and presented a very low roughness. No significant amount of impurities, such as C or Cl atoms, existing in the precursors, were incorporated into the film during preparation. All the films had good optical properties and presented good adhesion to the substrate.

XRD spectra were recorded using $\text{Cu K}\alpha$ radiation with a Siemens D5000 diffractometer at an incidence angle of 0.5° to increase the sensitivity. Films were deposited on fused quartz or silicon wafers. No influence of the support could be detected by XRD for the different films. Crystallite size was determined from the XRD pattern using the Scherrer formula.

X-ray absorption spectra at the Sn L_I and L_{III} edges of SnO_2 thin films were recorded using synchrotron light at LURE, Orsay (France). Monochromatisation of the light was carried out through a $\text{Si}(111)$ double crystal monochromator. The system for collecting data consisted of an ionisation chamber in front of the sample to monitor the incident beam and a conversion electron yield detector [13]. XA spectra at the Fe K-edge of Fe_2O_3 samples were taken, using a similar set-up, in the SERC synchrotron at the Daresbury Laboratory (UK). Although data will not be shown here, all spectra were first treated by the usual procedures consisting of extraction of the extended X-ray absorption fine structure (EXAFS) oscillations, Fourier transformation (FT) and fitting. A systematic analysis of the spectra has also been attempted by means of the FEFF code [14]. This procedure consists of simulating the EXAFS and the FT curves of atom clusters representing the actual structure of the studied samples. These clusters are typically constructed by incorporating successive atom spheres (cations and anions) around a central atom. Then, the EXAFS oscillations corresponding to these structures are simulated by calculating and averaging the individual EXAFS curves of the cation atoms within the cluster. Comparison of experimental and calculated curves provides a way to define the cluster whose structure better describes the experimental results. X-ray absorption near-edge structure (XANES) spectra have been treated mathematically by means of the mathematical method of factor analysis [15]. This technique has

been previously used to assess the percentage of amorphous and crystalline components contributing to the shape of experimental XANES spectra of SnO_2 nanoparticles [16].

IR spectra were recorded in the transmission mode in a Nicolet 510 FT-IR spectrometer for samples grown on KBr pellets or silicon substrates. Apart from the total transmission, no differences were observed depending on the substrate used for the deposition of the films.

3. Results and discussion

In this paper we present the structural characterisation of several oxide thin films by means of XRD, XAS and IR spectroscopy. We have focused our study on the following issues: determination of the degree of amorphisation, effect of ion bombardment on crystal nucleation and subsequent crystal growth, preferential orientation of crystallographic axis and control of the structure by the type of ion species used for the preparation of the films.

3.1. Quantitative evaluation of the amorphisation degree in thin films

Fig. 1 shows the XRD patterns of an original SnO_2 thin film prepared at room temperature and of this film after annealing in air at 573 and 773 K for 8 h. From these diagrams it can be determined that the crystalline

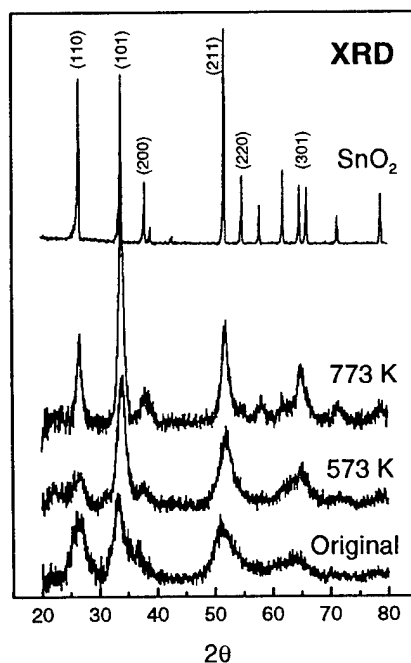


Fig. 1. XRD diagrams of a SnO_2 thin film prepared by IBICVD at 300 K and then annealed at 573 and 773 K. The diagram of a reference sample is included for comparison.

domains existing in the original and 773 K annealed films have an average size of 35 and 100 Å, respectively. Simultaneously, the height of the diffraction peaks increases and their relative intensity changes as a result of the annealing treatments. This evolution is consistent with a progressive crystallisation of the film with the preferential growth of certain crystallographic planes. However, from these results no quantitative estimation can be inferred about the amorphisation degree of the films. On this point, a more complete structural characterisation is furnished by XAS, a technique that proves the local order around a given atom. Fig. 2 shows the Sn L_{III} XANES spectra of SnO₂ thin films equivalent to those studied above by XRD. For comparison, the figure also shows, as a reference, the spectrum of a crystalline sample of SnO₂ (cassiterite). At a first glance it appears that the XANES spectra of the original sample depict a less defined shape than the rest. Calculation by FA of an ample series of experimental XANES spectra shows that the number of principal components (PCs) that by lineal combination reproduce the whole set is two. FA also provides a way to determine the spectral shape of these PCs. Here, one of these two PCs was equivalent in shape to the experimental spectrum of the SnO₂ reference and, therefore, is attributed to the crystalline phase existing in the films. The other, also plotted in Fig. 2, had no direct correspondence with any of the experimental spectra and is attributed tentatively to amorphous SnO₂. As shown in Fig. 2, the experimental spectra are well reproduced by a lineal combination of these PCs. The partition coefficient of these two compo-

nents for each experimental spectrum, also determined by FA, can be taken as a measure of the amorphous/crystalline contributions to the structure of the films. The values for the amorphous component were 57, 29 and 10% for the original and the 573 and 773 K annealed samples, respectively. So, it appears that in the original sample there is a majority amorphous contribution and that this phase decreases with the annealing treatments.

3.2. Nucleation and growth of crystal domains in thin films

The crystal nuclei formed during bombardment of the growing film must have been created in tight association with the atom tracks generated by the impinging ions. An important issue is the description of such nuclei in terms of size, atomic structure, etc. Here, we propose a simple methodology consisting of the analysis of the experimental EXAFS spectra and FT curves by means of the FEFF methodology. Fig. 3(left) shows the FTs of a reference sample and SnO₂ thin films in their original form and after annealing at 573 and 773 K. Fig. 3(middle) also shows several FEFF simulations of increasingly large clusters of this material with the cassiterite structure. These clusters are built by considering successive coordination spheres around a central atom of tin. Comparison of the calculated and experimental spectra reveals that at least four-sphere clusters are necessary to reproduce the intense peak at $R \sim 3.7$ Å, and that at least 14-sphere clusters are required to reproduce all the experimental features appearing for $R < 6$ Å. The evolution of the experimental spectra with the annealing temperature is characterised by a relative increase of the features between 2 and 5 Å. It is also worth noting that these peaks at $R < 6$ Å already exist, although with very small intensity, in the as-deposited film. So, it can be concluded that in the original films there are already small crystallites reproducing the cassiterite structure and that the minimum size of these crystallites is equivalent to that of 14-sphere clusters (i.e. ~ 12 Å, a value that is smaller than the size of 35 Å determined by XRD for the crystalline domains existing in this sample). Moreover, it can be deduced that no order beyond the second/third sphere exists in the amorphous component, otherwise the very intense peak at ~ 3.6 Å appearing for the four-sphere cluster would be more intense in the spectrum of the original sample. A good description of this amorphous component is a cluster formed by an atom of tin surrounded by just one coordination sphere of oxygen atoms (i.e. no order at a scale larger than the first Sn–O distance would exist in that structure as described above). Fig. 3(right) shows that the best agreement of the relative intensities of the peaks in the experimental FTs of the original and 773 K annealed samples is

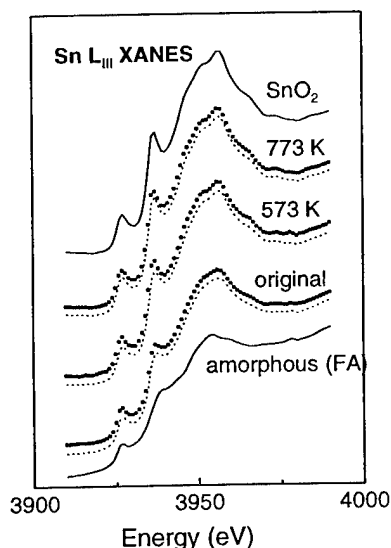


Fig. 2. Sn L_{III} XANES spectra of a SnO₂ thin film prepared by IBICVD at 300 K and then annealed at 573 and 773 K. The spectrum of a reference sample is included for comparison. Points: experimental spectra. Dashed line (displaced with respect to the experimental curves): spectra calculated by FA. Thin line: principal components calculated by FA.

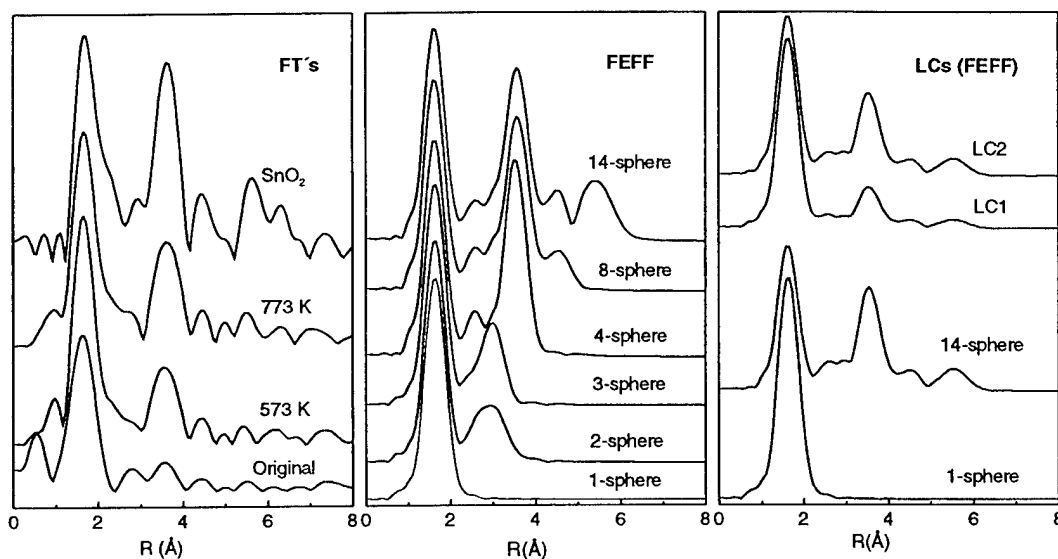


Fig. 3. (Left) Experimental FT curves of the SnO_2 thin film prepared by IBICVD at 300 K and then annealed at 573 and 773 K; the curve of a reference sample is included for comparison. (Middle) FT curves calculated with the FEFF code for clusters of increasing size reproducing the cassiterite structure of SnO_2 . (Right) Analysis of experimental spectra as lineal combinations of FEFF curves: LC1 = 0.6 (one-sphere) + 0.4 (14-spheres). LC2 = 0.2 (one-sphere) + 0.8 (14-spheres).

obtained by lineal combinations of the FEFF curves of one-sphere and 14-sphere clusters. By analysis of the XANES spectra it has been shown that in the original films there is a 57% contribution of an amorphous phase. From the FEFF analysis it also results that annealing increases the relative contribution of the crystalline component from about a 40% in the 'as-deposited' sample to 80% in the sample annealed at 773 K, in good agreement with the values deduced above from the FA analysis of the XANES spectra.

3.3. Amorphisation and crystal orientation

The previous analysis has stressed the importance of amorphisation phenomena in thin films prepared by ion beams and how XAS can be used to study such processes. Now we would like to illustrate the possibilities of a more conventional technique such as IR to get structural information from thin films. Typically, IR is used on a 'fingerprint' basis for the characterisation of thin films. However, a systematic analysis of IR spectra may also provide a deep insight into their structure. In particular, it is well known that IR spectra of a film contain information not only on the crystalline structure but also on the orientation of the crystallographic axis with respect to the film surface [17–20]. Fe_2O_3 thin films prepared by IBICVD were analysed by FT-IR. Fig. 4 shows a series of IR spectra for thin films prepared at room temperature and after annealing at 773 K. Two sets of samples have been studied, the first one prepared using O_2^+ for decomposition of the precursor and deposition of the film and the second using a mixture $\text{O}_2^+ + \text{Ar}^+$. The IR spectrum of the sample prepared

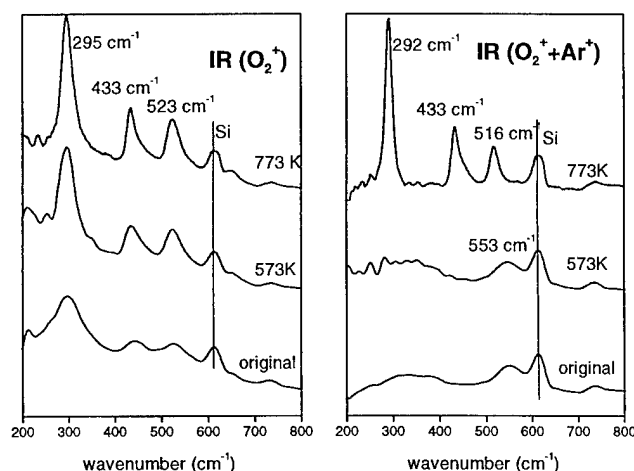


Fig. 4. FT-IR spectra of Fe_2O_3 thin films prepared by IBICVD using O_2^+ or mixtures $\text{O}_2^+ + \text{Ar}^+$ for their synthesis. Spectra are shown for samples 'as-prepared' and after annealing at 573 and 773 K.

with O_2^+ presents three intense bands at 295, 433 and 523 cm^{-1} that can be related to $\text{Eu} (E \perp c)$ vibrational modes of hematite (Table 1).

It should be noted that although the $\text{A}_{2u} (E \parallel c)$ modes of hematite lie at frequencies close to those of two Eu modes (i.e. 299 and 526 cm^{-1}), the relative

Table 1
IR transverse modes for $\alpha\text{-Fe}_2\text{O}_3$ taken from Ref. [21]

Symmetry	$\nu_T (\text{cm}^{-1})$
$\text{Eu} (E \perp c)$	524, 437, 286, 227
$\text{A}_{2u} (E \parallel c)$	526, 299

intensity of the bands observed for the O_2^+ prepared sample is consistent with that expected for the Eu modes [22], thus suggesting that the A2u modes do not contribute significantly to the spectra. In an experiment of this kind, only the IR transverse modes parallel to the film surface can be observed at normal incidence of the radiation. Thus, since the Eu modes vibrate perpendicular to the c -axis of hematite, the presence of these modes in the absorption spectrum indicates that, in this case, the crystal c -axis is preferentially oriented perpendicular to the film surface. The enhancement of the intensity of the (110) diffraction peak with respect to the powder pattern agrees with this preferential orientation of the c -axis (Fig. 5). Annealing of the film at 773 K yields a spectrum with only the Eu bands, which become sharper after this treatment. This suggests a progressive crystallisation of the structure. A similar conclusion can be derived from the width and intensity of the XRD peaks of the pattern for these samples in Fig. 5. The use of $O_2^+ + Ar^+$ mixtures for the synthesis of the films produces dramatic changes in their structure. In fact, the IR spectrum of the original film in Fig. 4 is characterised by a broad band at 553 cm^{-1} and an even broader structure between 250 and 400 cm^{-1} . Since the XRD diagram of this film does not present any peak (cf. Fig. 5), it can be concluded that the IR spectrum in Fig. 4 might respond to a badly ordered phase. Rutherford backscattering (RBS) analysis of the samples reveals that all of them have an Fe_2O_3 stoichiometry, the sole difference in composition being the fact that in the $O_2^+ + Ar^+$ prepared samples there are 4% of Ar atoms distributed homogeneously through the whole thickness. So, it appears that the Ar atoms, incorporated

within the lattice during bombardment, constitute lattice defects that contribute to the amorphisation of the structure in the original sample. RBS also showed that Ar remains incorporated upon annealing. XRD analysis of the annealed $O_2^+ + Ar^+$ sample shows the appearance of a limited set of well-defined diffraction peaks of hematite (cf. Fig. 5). The almost complete disappearance of the (110), (116) and (300) reflections from this pattern might be due to the incorporation of Ar in positions of those planes, a phenomenon that would lead to the loss of diffraction coherence along the corresponding crystallographic directions. However, further work is needed to prove this assumption. After annealing at 773 K, IR shows that the amorphous phase of the original sample renders the $\alpha\text{-Fe}_2O_3$ phase with the c -axis preferentially oriented perpendicular to the film surface (cf. Fig. 4).

Further structural characterisation of the Fe_2O_3 thin films can be obtained by means of XAS. Fig. 6 shows the FT curves of the samples already studied by IR and XRD, as well as the results of an analysis with the FEFF code similar to that previously carried out for the SnO_2 thin films. The most significant effect in the experimental spectra is the relative change in intensity of the peak at $R \sim 3\text{ Å}$, in particular for the original $O_2^+ + Ar^+$ sample where this peak depicts the minimum intensity. FEFF calculations with an increasing number of coordination spheres show a progressive increase of the second peak that reaches its maximum intensity for seven-sphere clusters. Comparison of experimental FT and calculated FEFF curves confirms that the $O_2^+ + Ar^+$ sample is poorly ordered even at the second coordination sphere, since the relative intensity of the

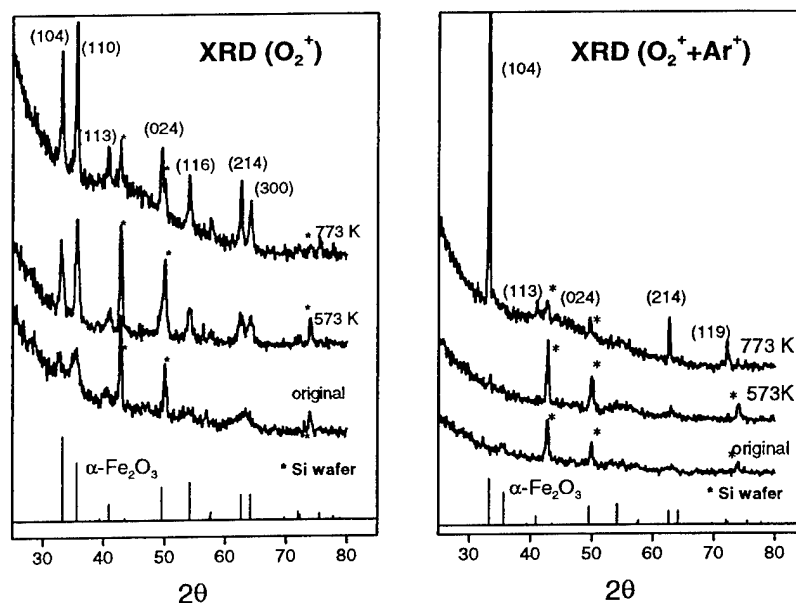


Fig. 5. XRD patterns of Fe_2O_3 thin films prepared by IBICVD using O_2^+ or mixtures $O_2^+ + Ar^+$ for their synthesis. Spectra are shown for samples 'as-prepared' and after annealing at 573 and 773 K. Powder patterns are also included for comparison.

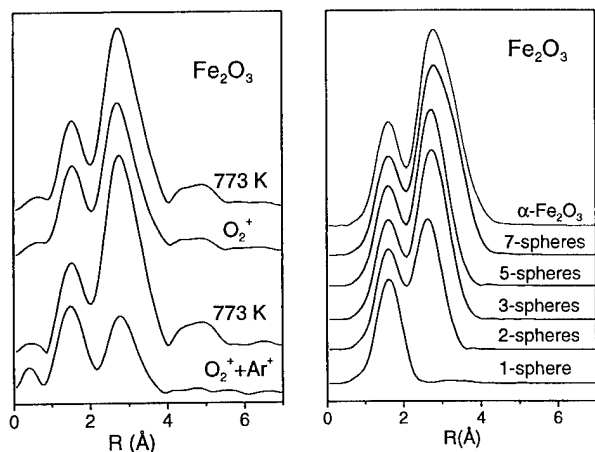


Fig. 6. (Left) FT curves for Fe_2O_3 thin films prepared by IBICVD using O_2^+ or mixtures $\text{O}_2^+ + \text{Ar}^+$ and then annealed at 773 K. FTs calculated with the FEFF code for clusters of increasing size reproduce the structure of hematite.

second peak is smaller than in the two-sphere FEFF simulation. An additional conclusion from these results is that, in the original sample prepared with O_2^+ ions and the two annealed samples, the crystal structure has already reached a local order similar to that existing in bulk $\alpha\text{-Fe}_2\text{O}_3$, since the second peak in the FT curves depicts, in all cases, a similar intensity. This result is consistent with the IR and XRD data and discards the existence of an amorphous phase in these samples (cf. Fig. 4 and 5).

3.4. Type of ion species and control of crystal structure

In the experiments described above with Fe_2O_3 thin films it has been shown that, by using a mixture

$\text{O}_2^+ + \text{Ar}^+$, the crystallographic structure of the films was badly ordered. So, it could be interesting to check whether similar phenomena are also produced in other systems. ZrO_2 in the form of thin films is a very interesting material for many applications [11,23]. As bulk material it was one of the first reported systems where crystallisation was induced by Ar^+ bombardment [8]. The possibility of obtaining different crystallographic phases in ZrO_2 thin films subjected to ion bombardment was already reported by Martin [24]. So, we have studied the structure of ZrO_2 thin films prepared by IBICVD using O_2^+ or mixtures $\text{O}_2^+ + \text{Ar}^+$. As in the previous case with Fe_2O_3 , it was found that ca. 4% Ar remained incorporated within the ZrO_2 lattice when the films were prepared with the mixture of ions. Here, this particular experimental procedure also had a dramatic influence for the control of the structure. Fig. 7 shows XRD patterns of thin films prepared with O_2^+ or mixtures $\text{O}_2^+ + \text{Ar}^+$ for the 'as-deposited' films and after annealing at increasingly higher temperatures. For the $\text{O}_2^+ \text{-ZrO}_2$ sample the patterns reveal the existence of at least two phases: monoclinic and cubic or tetragonal. It is worth mentioning that conventional XRD is unable to distinguish between these latter two phases due to the similarity of their patterns. Annealing leads to a relative increase of the monoclinic phase, a process that increases with the annealing temperature. Simultaneously, the peaks become narrower, a fact which is consistent with a progressive crystallisation of the lattice. On the contrary, for $(\text{O}_2^+ + \text{Ar}^+) \text{-ZrO}_2$ films the XRD pattern of the 'as-deposited' and the sample annealed at 573 K only depict two broad structures at diffraction angles which might indicate the existence of a badly ordered cubic or tetragonal structure of ZrO_2 . After

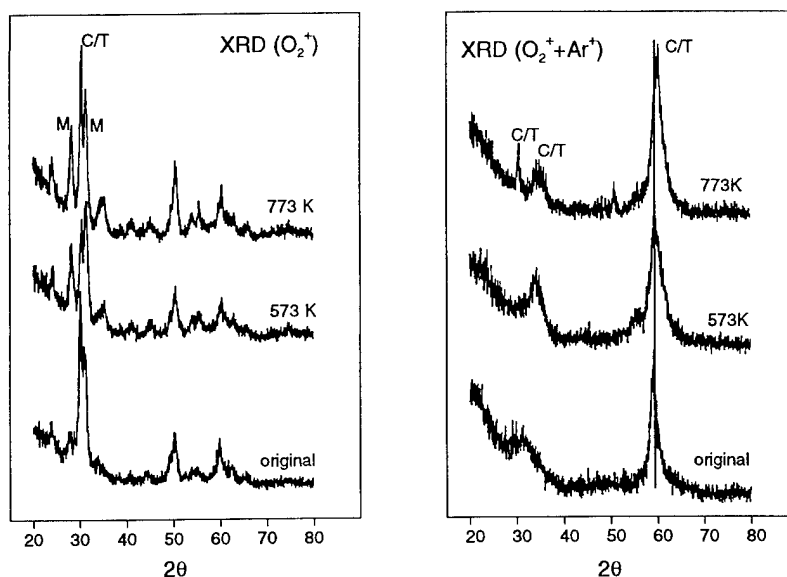


Fig. 7. XRD patterns of ZrO_2 thin films prepared by IBICVD using O_2^+ or mixtures $\text{O}_2^+ + \text{Ar}^+$. Patterns are shown for samples 'as-prepared' and after annealing at 573 and 773 K.

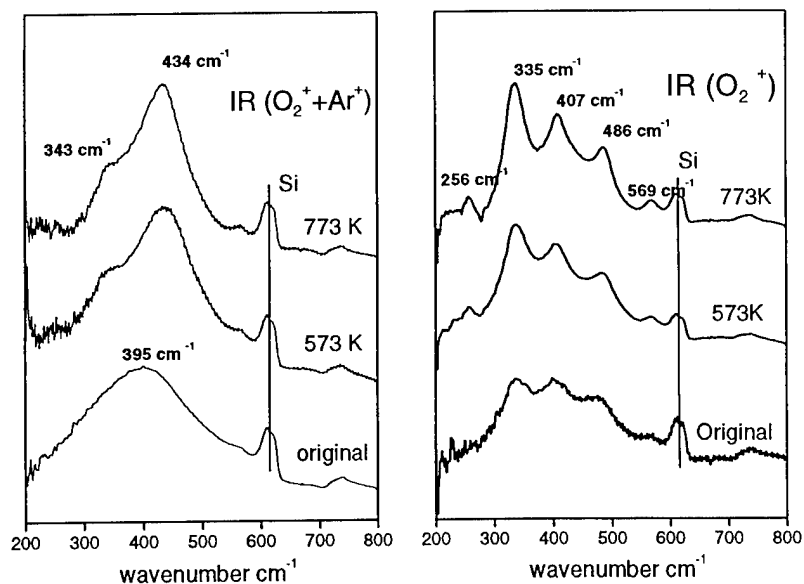


Fig. 8. FT-IR spectra of ZrO_2 thin films prepared by IBICVD using O_2^+ or mixtures $\text{O}_2^+ + \text{Ar}^+$. Spectra are shown for samples 'as-prepared' and after annealing at 573 and 773 K.

annealing at 773 K a relatively more defined diffraction pattern appears, consistent with the cubic or tetragonal phases. It is interesting to note that, for the sample annealed at 773 K, the observed peaks depict different broadening, indicating that some planes have less crystalline order than others. As in the previous case with F_2O_3 , in this sample Ar remained incorporated within the lattice after annealing, a phenomenon that could account for the different crystalline order according to each crystallographic direction.

IR spectroscopy can be used for a more accurate description of the structure of ZrO_2 thin films. Fig. 8 shows IR spectra for the samples whose XRD patterns are shown in Fig. 7. Typical frequencies of the transverse vibrational modes of the Y_2O_3 stabilised cubic and tetragonal phases of ZrO_2 are reported in Table 2.

By comparison of our spectra with the reported values, it is clear that after annealing at $T \geq 573$ K the $(\text{O}_2^+ + \text{Ar}^+) - \text{ZrO}_2$ sample has a tetragonal structure. In the original sample the corresponding IR spectrum only displays a broad band at $\sim 400 \text{ cm}^{-1}$ which could be attributed to the Flu mode of a badly ordered cubic phase. The IR spectra of the $\text{O}_2^+ - \text{ZrO}_2$ films are characterised by several bands that become sharper when the annealing temperature increases. According to XRD

these new bands must correspond to some of the 15 vibrational modes of the monoclinic phase of ZrO_2 [26]. It should be noted that hidden by this sharp pattern in Fig. 8 there must be the broader features corresponding to the tetragonal ZrO_2 phase observed by XRD. These bands would contribute to the intensity of the spectrum in the zone around $\nu \sim 434 \text{ cm}^{-1}$ (i.e. at the position of the maximum of the spectrum of the tetragonal phase), thus modifying the relative intensities of the bands of the monoclinic phase.

Stabilisation at low temperature of the cubic or tetragonal phase of ZrO_2 ceramic materials without doping with cations such as Y^{3+} , Ca^{2+} , etc. is possible when the particles have a small size ($d \sim 300 \text{ \AA}$) [27]. However, although a particle size effect cannot be discarded here, the fact that a similar effect is not found by bombardment with O_2^+ ions suggests that the main cause leading to the stabilisation of the cubic or tetragonal phases is the incorporation of Ar within the ZrO_2 structure (in principle no differences in particle size should be expected for the samples prepared under O_2^+ or $\text{O}_2^+ + \text{Ar}^+$ bombardment). Crystallisation of ZrO_2 thin films by ion bombardment was already reported by Martin [24], although this author only reported the formation of the monoclinic and cubic phases, perhaps because for his study he only used XRD. Our results show that the combined use of XRD and IR is a more powerful approach for the structural characterisation of thin films.

Table 2
IR vibrational modes for tetragonal and yttria stabilised cubic ZrO_2 taken from Ref. [25]

Phase	Symmetry	ν_T (cm^{-1})
Tetragonal	Eu ($E \perp c$)	164, 467
	A _{2u} ($E \parallel c$)	339
	Flu	358
Yttria stabilised cubic	Flu	358

4. Conclusions

From the previous results and discussion, it appears that a deeper understanding of the amorphisation pro-

cesses induced in thin films prepared by ion beam assisted methods is possible by applying characterisation procedures other than XRD. It has been shown that the degree of amorphisation of SnO_2 thin films can be estimated by FA of their XANES spectra. Furthermore, a description (i.e. size, type of atom structure, etc.) of the crystal nuclei formed in these films during bombardment is possible by analysing the EXAFS spectra with the FEFF code. The obtained data are congruent with those provided by XRD with respect to the evaluation of the size of the crystal domains existing in these films. However, a significant advantage of the proposed methodology is that it proves the existence of an amorphous phase, which cannot be inferred by XRD.

IR spectroscopy can be used to characterise structurally thin films. A careful analysis in terms of vibrational modes of the lattice can serve to get information about preferential orientations of crystal axes and their dependence on the preparation parameters of the films. Thus, we have shown that in Fe_2O_3 thin films prepared by IBICVD the atoms are arranged as in an $\alpha\text{-Fe}_2\text{O}_3$ phase with different degrees of amorphisation and a preferential orientation of the crystallographic c -axis with respect to the film surface.

Finally, it has been shown that Ar may become incorporated within the lattice network of thin film oxides prepared by ion beam assisted methods. The incorporated atoms of Ar have a strong influence in enhancing the amorphisation degree of the lattice and favouring the development of certain crystallographic structures. Examples of these effects are discussed for Fe_2O_3 and ZrO_2 thin films prepared by IBICVD. IR has proved to be a valuable technique to characterise the different phases of ZrO_2 .

Acknowledgements

We thank the CICYT for financial support (Project No. MAT97-0689). The XA spectra have been recorded in the LURE (France) and Daresbury (UK) synchrotrons thanks to grants provided by the TMR Program of the EU.

References

- [1] E. Kay, S.M. Rossnagel, in: J.J. Cuomo, S.M. Rossnagel, H.R. Kaufman (Eds.), *Handbook of Ion Beam Processing Technology*, Noyes Publications, New Jersey, 1989.
- [2] Th. Koch, P. Ziemann, *Thin Solid Films* 303 (1997) 122.
- [3] J. Baglin, in: J.J. Cuomo, S.M. Rossnagel, H.R. Kaufman (Eds.), *Handbook of Ion Beam Processing Technology*, Noyes Publications, New Jersey, 1989.
- [4] R.W. Knoll, E.R. Bradley, *Thin Solid Films* 117 (1984) 201.
- [5] E.C. Baranova, V.M. Gusev, Y.V. Martynenko, C.V. Starinin, I.B. Haitullin, *Radiat. Eff.* 18 (1973) 21.
- [6] J.M.E. Harper, J.J. Cuomo, H.T.G. Hentzell, *Appl. Phys. Lett.* 43 (1983) 547.
- [7] R. Kelly, in: O. Auciello, R. Kelly (Eds.), *Ion Bombardment Modification of Surfaces*, Elsevier, New York, 1984.
- [8] H.M. Naguib, R. Kelly, *J. Nucl. Mater.* 35 (1970) 293.
- [9] J.P. Espinós, A. Fernández, A. Caballero, V.M. Jiménez, J.C. Sánchez-López, L. Contreras, D. Leinen, A.R. González-Elipe, *Chem. Vapor Depos.* 4 (1997) 219.
- [10] L.A. Dawar, A. Kumar, S. Sharma, K.N. Tripathi, P.C. Mathur, *J. Mater. Sci.* 28 (1993) 639.
- [11] H. Guerrero, G. Rosa, E.M. Moreno, R. Páez del Real, D. Levy, C. Aroca, P. Sánchez, M.P. Morales, F. Del Monte, C.J. Serna, M.C. Sánchez, E. López, *Nanospace 98*, 2nd NASA Conference on Nano/Microtechnology for Space Applications, Houston, TX, November 1–6 (1998).
- [12] H.C. Chen, E. Pfender, J. Heberlain, *Thin Solid Films* 315 (1998) 159.
- [13] C.E. Bouldin, R.A. Fornan, M.I. Bell, *Phys. Rev. B* 35 (1987) 1429.
- [14] J.J. Rehr, S.J. Zabinsky, R.C. Albers, *Phys. Rev. Lett.* 69 (1992) 3397.
- [15] E.R. Malinowski, D.G. Howery, *Factor Analysis in Chemistry*, Wiley, New York, 1990.
- [16] V.M. Jiménez, A. Caballero, A. Fernández, J.P. Espinós, M. Ocaña, A.R. González-Elipe, *Solid State Ionic* 116 (1999) 117.
- [17] D.W. Berreman, *Phys. Rev.* 130 (1963) 2193.
- [18] G.L. Bottger, A.L. Geddes, *J. Chem. Phys.* 46 (1967) 3000.
- [19] F. Proix, M. Balkanski, *Phys. Status Solidi* 32 (1969) 119.
- [20] J.S. Ahn, H.S. Choi, T.W. Noh, *Phys. Rev. B* 53 (1996) 10310.
- [21] S. Onari, T. Arai, K. Kudo, *Phys. Rev. B* 16 (1997) 1717.
- [22] C.J. Serna, J.L. Rendon, J.E. Iglesias, *Spectrochim. Acta A38* (1982) 797.
- [23] G. García, J. Casado, J. Llibre, M. Doudkowski, J. Santiso, A. Figueras, S. Schamm, D. Dornignac, Ch. Grigis, M. Aguiló, *J. Phys.* 5 (1995) 439.
- [24] P.J. Martin, *J. Mater. Sci.* 21 (1986) 1.
- [25] C. Pecharrromán, M. Ocaña, C.J. Serna, *J. Appl. Phys.* 80 (1996) 33479.
- [26] E. Anastassakis, B. Papanicolaou, I.M. Asher, *J. Phys. Chem. Solids* 36 (1975) 667.
- [27] B.E. Yoldas, *J. Mater. Sci.* 21 (1986) 1080.

Structural properties and surface morphology of laser-deposited amorphous carbon and carbon nitride films

E. Riedo ^{a,b,*}, F. Comin ^a, J. Chevrier ^{a,c}, F. Schmithusen ^a, S. Decossas ^a, M. Sancrotti ^d

^a ESRF, BP220, F-38043, Grenoble Cedex, France

^b INFN-Dipartimento di Scienze dei Materiali, Università di Milano, Milan, Italy

^c LEPEP, CNRS, Grenoble, France

^d Laboratorio Nazionale TASC-INFN, Trieste, Italy

Abstract

A study of the relationship between structure and growth parameters for existing and candidate carbon-based protective coatings has been carried out. In particular, diamond-like carbon (DLC) and carbon nitride thin films were deposited on silicon wafers by pulsed Nd:YAG laser (wavelength 532 nm) ablation of graphite in high vacuum ($p = 1.5 \times 10^{-7}$ Pa) and in a nitrogen atmosphere ($p = 13$ Pa). The composition (N/C ratio), the structural and electronic properties and the surface morphology of the deposited films were investigated as a function of laser fluence ($1\text{--}12\text{ J/cm}^2$). The highest N/C ratio 0.40 was obtained with a laser fluence of 12 J/cm^2 ; for this nitrogen concentration X-ray photoelectron spectroscopy (XPS) reveals an increase of C–N bonds instead of C=N bonds with respect to lower concentrations.

Electron energy loss spectroscopy (EELS) and XPS show an increase of sp^2 carbon bonded sites in the DLC films deposited with lower laser fluences in agreement with the theory of the so-called sub-implantation model. EELS also reveals a gradient in the chemical nature of the films through the thickness. Atomic force microscopy analysis shows that the root-mean-squared roughness of the DLC samples is about 3 Å over the laser fluence range investigated. © 2000 Elsevier Science S.A. All rights reserved.

Keywords: AFM; CN_x films; Diamond-like carbon films; EELS; Pulsed laser deposition; XPS

1. Introduction

Amorphous carbon films with diamond-like properties are good materials for a wide range of technological applications. In particular, diamond-like carbon (DLC) films are currently used in the production of hard coatings because of their extreme hardness, chemical inertness and excellent tribological, corrosion and adhesive properties. However, a tendency toward CN_x films in carbon coatings is taking place because of improved wear durability, lower coefficient of friction, and compatibility with existing lubricants [1].

DLC and CN_x films have been grown using different methods, mainly sputter deposition, cathodic arc, direct ion beam deposition [2] and pulsed laser deposition (PLD). This last method is particularly interesting because of the high adhesion and low substrate temperature during film growth [3].

There still exist several unanswered questions regarding how the process of growth influences the resulting structure in DLC and CN_x films. All these films usually contain a mixture of carbon sites characterized by ‘diamond’ sp^3 , ‘graphite’ sp^2 and, to a lesser extent, sp^1 hybrid configurations. The improvement of the quality of the films such as hardness is strictly correlated with the increase of the sp^3 concentration in the films. An important parameter characterizing the films prepared under different depositions conditions is, hence, the sp^3/sp^2 ratio.

Since nitrogen is a weak dopant in carbon, techniques like core-level analysis are required to establish the chemical bond of nitrogen with carbon. In this paper X-ray photoelectron spectroscopy (XPS), electron energy loss spectroscopy (EELS), and atomic force microscopy (AFM) are used to investigate how the laser fluence changes the structural, electronic and morphological properties of DLC and CN_x films grown with PLD.

* Corresponding author. Tel.: +33-476-88-2666.

E-mail address: riedo@esrf.fr (E. Riedo)

2. Experimental

DLC and CN_x films were deposited in the PLD system shown in Fig. 1. This system consists of an ultrahigh vacuum (UHV) chamber with a base pressure of 1.5×10^{-7} Pa, a Q-switched Nd:YAG laser with a wavelength of 532 nm, a pulse duration of 20 ns and a frequency of 10 Hz. The distance between the target and the substrate was 3 cm. The laser beam was moved by an oscillating mirror attached to two loudspeakers in order to provide each pulse with a fresh surface. Much attention was paid to measuring the power of the laser on the target, while the laser spot on the target was determined from a scanning electron microscope image of the hole left on the target by the laser. The laser fluence so measured ranged from 1 to 35 J/cm². During the growth of CN_x films we used a nitrogen pressure of 13 Pa. Silicon wafers, cleaned with acetone, were used as substrates. XPS and EELS were used to characterize the electronic and structural properties of the deposited thin films. Core levels were measured using an Al K α 1486 eV X-ray source. Charging effects were not observed on the samples during measurements. The resulting experimental resolution, including the width of the X-ray line and the energy resolution of the analyzer, is about 1.1 eV. The Si 2p core level of an uncovered part of the silicon substrate was used to calibrate the scale of binding energies (BEs), whereas to calculate the chemical composition at the surface we used standard sensitivity values. EELS measurements were performed using an EG5 VSW Scientific Instruments electron gun. The energy losses were studied in the range from zero loss (at primary electron energy) up to 50 eV loss. The energy resolution as deduced from the width of the primary peak is 2 eV. For both XPS and EELS measurements we utilized a hemispherical analyzer. A Digital Instruments Nanoscope III atomic force microscope operating in the tapping mode was utilized to measure the surface roughness of the deposited films. A DEK TEK profilometer was used to measure the thickness of the samples. The average thickness of the deposited films is 100 nm. The growth rate changes significantly

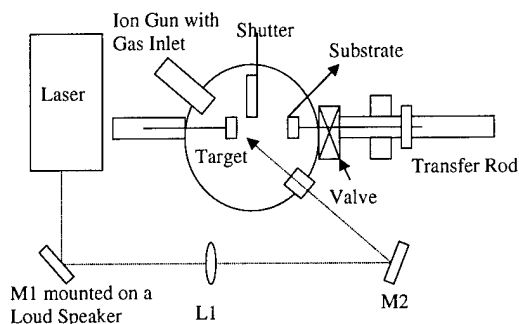


Fig. 1. The experimental set-up for growth of the films. M1 and M2 are mirrors and L1 is a lens.

with the laser fluence, going from 200 Å/min for $I_L = 35$ J/cm² to 6 Å/min for $I_L = 1$ J/cm². All the characterizations were performed ex situ. The O 1s/C 1s intensity ratio, evaluated by taking into account the O 1s and C 1s sensitivity factors, is 0.03 for all the DLC samples and 0.1 for the CN_x samples.

3. Results and discussion

Fig. 2(a) and (b) shows the C 1s core-level XPS spectra of two DLC samples grown with two different laser fluences: 12 J/cm² and 1 J/cm² respectively. The full-width at half-maximum of both our samples is about 1.8 eV. The C 1s core-level shifts by 0.6 eV towards lower energies in the sample grown with lower laser fluence. A quantitative indication of the population ratio between sp^2 and sp^3 hybridization can be evaluated by fitting the C 1s core-level spectra with two components [4]. The first one at lower BE is related to sp^2 hybridization, the second one to sp^3 hybridization. This is in accordance with the shift of 0.9 eV between the C 1s core levels of diamond and graphite [5]. Each component is a convolution of a Gaussian and a Lorentzian

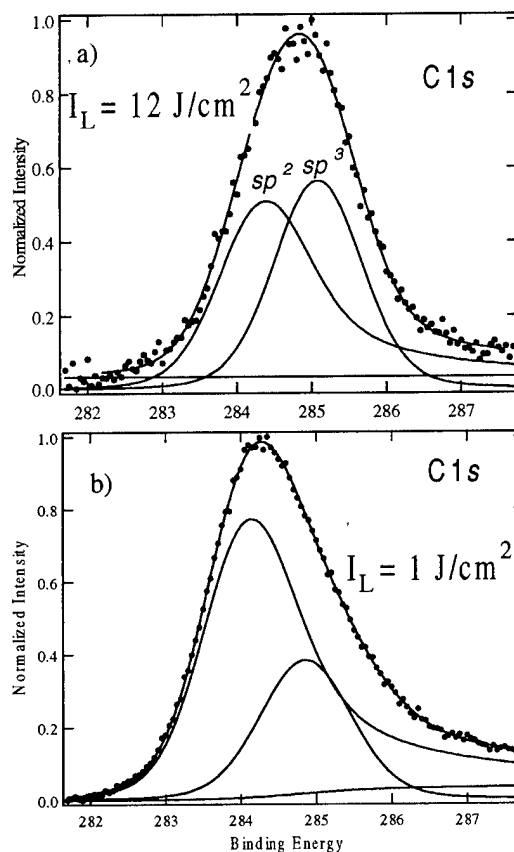


Fig. 2. C 1s XPS spectra of two DLC films grown with fluences of (a) 12 and (b) 1 J/cm². The subtracted Shirley background and the components in which the spectra have been decomposed are shown. The resulting fit is superimposed on the data.

and a Shirley background is subtracted. The Gaussian component accounts for the instrumental broadening and the chemical disorder, and the Lorentzian accounts for the finite core hole lifetime of the photoionization process. The Lorentzian lifetime is fixed in both components as 215 meV [4]. Because of the semi-metallic character of the graphite the sp^2 component is fitted including the Doniac–Sunjic function. The asymmetry parameter for the C 1s of graphite was set at 0.14 in agreement with the literature [4]. The C 1s spectra were fitted with five parameters: the BE and the Gaussian width of each component and the singularity index for the sp^2 component. The Gaussian widths were 1.25 ± 0.05 eV for all the resulting components and the singularity index results were 0.16 ± 0.02 , in agreement with values in literature [4]. This Gaussian width is larger than the width predicted by the instrumental broadening of 1.1 eV. This further broadening is probably due to the chemical disorder and to the phonon broadening. The components related to sp^2 and sp^3 hybridizations result in each sample being shifted by 0.9 ± 0.05 eV, in agreement with previous results [5]. We remark that changes of the free fitting parameters within reasonable ranges do not affect the overall conclusions drawn in this paper. Our analysis shows that the sample grown with higher laser fluence has 53% sp^3 , whereas the other sample has 34% sp^3 .

The decrease of sp^2 hybrid carbon atoms in the sample grown with higher laser fluences is also confirmed by EELS. In Fig. 4 the EELS spectra of the same two samples normalized at the intensity of the elastic peak are shown. The first peak at about 6 eV, called the π -plasmon peak, is related to π electrons; it is not present in a pure sp^3 configuration, whereas it is present at 6.6 eV in the graphite [6]. The second peak at about 28 eV is related to $\sigma + \pi$ electrons [6]. This peak is located at about 27.6 eV in graphite and at 33 eV in diamond [6]. The energy of this plasmon excitation is predicted by the free electron model to be equal to [6]:

$$\omega_p = \left(\frac{4\pi n_e e^2}{m^*} \right)^{1/2}, \quad (1)$$

where n_e is the electron density of the material and m^* and e are the electronic effective mass and charge respectively. From Fig. 3 it is evident that there is a decrease in intensity of the π -plasmon peak in the sample grown with higher laser fluences. These results indicate a decrease of sp^2 sites in this sample with respect to the other one. XPS and EELS experimental results on DLC films are in accord with the sub-implantation model [7] taking into account that the laser fluence growth changes almost linearly with the energy of the carbon ions [8]. This model indicates for carbon ion energies greater than 30 eV a low density sp^2 -rich surface layer below which a dense sp^3 -rich layer develops, whereas for

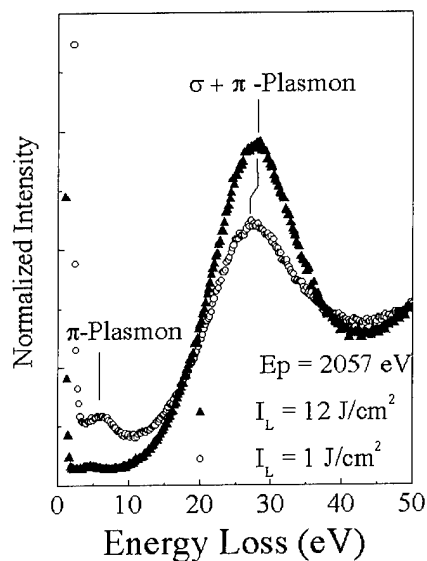


Fig. 3. EELS spectra of two DLC films grown with fluences of 1 and 12 J/cm².

energies lower than 30 eV one obtains just an sp^2 -rich film.

The possibility of an inhomogeneous pattern of properties as a function of depth was explored by exploiting the energy-dependent electron mean free path of the primary electron beam in EELS. In Fig. 4 we report some EELS spectra normalized at the intensity of the elastic peak for three different primary energies: 2057, 993.2, 617.2 eV. From Fig. 4 it is possible to observe the growth of the π -plasmon peak and the shift of almost 2 eV of the $\sigma + \pi$ plasmon peak for the lowest primary

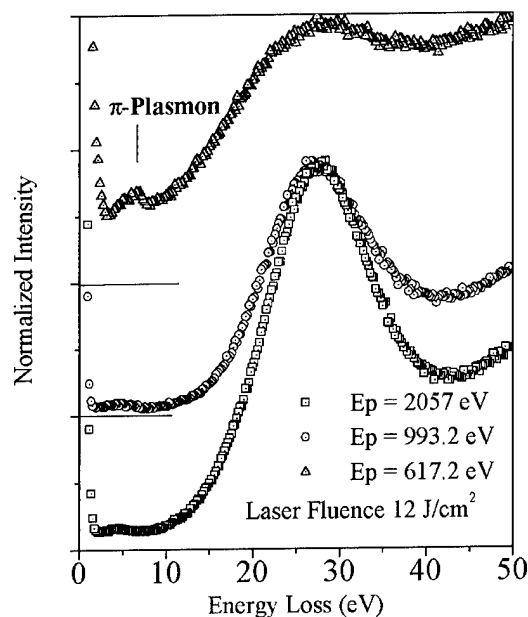


Fig. 4. EELS spectra of a DLC film for different primary energies. The spectra are shifted on the y-axis.

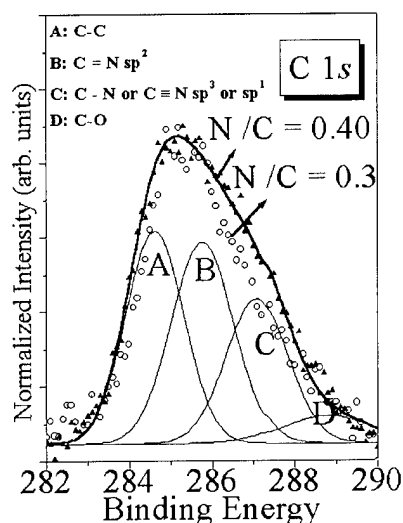


Fig. 5. C 1s core-level spectra of two CN_x films with $\text{C/N}=0.30\text{--}0.40$.

energy, suggesting the presence of a very thin sp^2 layer at the surface.

The N/C ratio of the deposited thin films was measured by XPS. The N/C ratio is 0.30 for a laser fluence of 5 J/cm^2 and 0.40 for 12 J/cm^2 . Figs. 5 and 6 show the XPS C 1s and the N 1s spectra of two CN_x films with varying nitrogen content. The C 1s peak broadens and becomes more asymmetric with increasing nitrogen concentration. These effects are a clear indication that nitrogen atoms are involved in chemical bonds with carbon in three possible distinct chemical states: C–N, C=N, C≡N bonds. A clear image of the possible chemical bonds between nitrogen and carbon can be deduced from the deconvolution of the individual C 1s and N 1s lines into Gaussian lineshapes [1]. The best Gaussian fits to the XPS lines resulted in four different peaks for the C 1s line and three peaks for the N 1s line. Fig. 5 shows the deconvolution of peak C 1s of the sample with the ratio $\text{N/C}=0.4$. The deconvoluted

spectrum exhibits peaks at 284.7 eV (A), 285.9 eV (B), 287.1 eV (C) and 289.17 eV (D) that are attributed to C–C, C=N, C–N or C≡N, and C–O bonds, respectively [1]. Likewise, the deconvolution of the N 1s line for the same sample, shown in Fig. 6, gives three peaks at 399.6 eV (A), 401.3 eV (B), and 402.1 eV (C) which are assigned to C–N or C≡N, C=N and N–O bonds, respectively [9]. These values agree quite well with organic polymers containing nitrogen [1]. Pyridine (C=N, sp^2 hybridization) has a C 1s BE at 285.5 eV and an N 1s BE at 400.6 eV. Urotropine or HMTA (C–N, sp^3 hybridization) exhibits a C 1s BE at 286.9 eV (287.3 eV for HMTA) and an N 1s BE at 399.4 eV. Polyacrylonitrile (C≡N, sp) has a C 1s BE at 286.4 eV and an N 1s BE at 399.6 eV. From Fig. 5 it is evident that the sample with higher nitrogen content ($\text{N/C}=0.4$) has a greater contribution coming from peak C, which is related to sp or sp^3 hybridization. Also, the N 1s spectra in Fig. 6 show that this film has a large contribution from peak A, which is related to sp or sp^3 hybridization. This contribution clearly decreases in favor of a greater contribution coming from peak B related to C=N bonds in the sample with lower nitrogen content ($\text{N/C}=0.3$). There still exists debate in the literature on whether the deconvoluted peaks from the C 1s spectra at $\sim 286 \text{ eV}$ and from the N 1s spectra at $\sim 399 \text{ eV}$ are assigned to C–N, C≡N, or $\beta\text{-C}_3\text{N}_4$ bonding. In this study the $\beta\text{-C}_3\text{N}_4$ bonding is not expected because our films contain less than the required $\text{N/C}=1.33$. We suggest that in the sample with $\text{N/C}=0.4$ there is a considerable number of N– $\text{sp}^3\text{-C}$ bonded sites (C–N bonds) because the corresponding BE, peak C in Fig. 6, is at 287.1 eV, which is much closer to the values 286.8 and 287.3 eV of materials with sp^3 configuration with respect to the value 286.4 eV of polyacrylonitrile (C≡N bonds).

In Fig. 7 the EELS spectra of the DLC sample grown

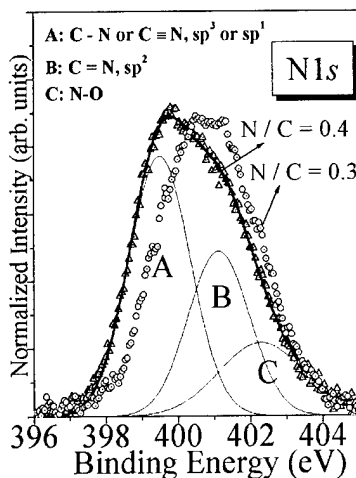


Fig. 6. N 1s core-level spectra of two CN_x films with $\text{C/N}=0.30\text{--}0.40$.

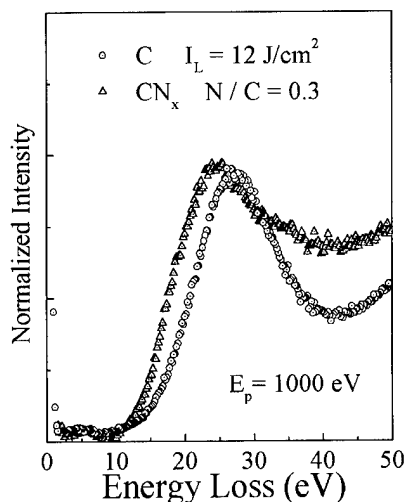


Fig. 7. EELS spectra of a CN_x film and a DLC film.

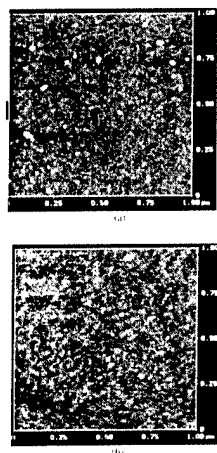


Fig. 8. AFM images of two DLC samples grown with a laser fluence of (a) 1 and (b) 3 J/cm².

with a laser fluence of 12 J/cm² and of the CN_x film with N/C=0.3 normalized at the intensity of the elastic peak are shown. It is possible to observe that the π plasmon peak is depressed in the CN_x sample as in the DLC sample grown with high laser fluences, suggesting that the fraction of sp² C bonds is almost equal in the two samples, whereas the $\sigma + \pi$ plasmon energy is shifted towards lower energies. If we suppose the same density in the two materials and if we consider that nitrogen contributes three electrons instead of the four of carbon, from Eq. (1), with the composition N/C=0.3, we obtain the energy shift of the $\sigma + \pi$ plasmon in Fig. 7.

AFM images of a 1 × 1 μm² DLC surface are shown in Fig. 8(a) and (b) for laser fluences of 32 J/cm² and 1 J/cm² respectively. Even though the root-mean-squared (rms) roughnesses of all the samples grown from laser fluences of 1 to 35 J/cm² are about 3 Å (the same of the silicon substrate), we can observe in Fig. 8(a) and (b) the appearance of small particulates of nanometer size on the surface of the sample grown with a laser fluence of 1 J/cm². The same particulates are observed on the sample grown with a laser fluence of 35 J/cm².

4. Conclusions

In this paper we have presented a study of the structural, electronic and morphological properties of

DLC and CN_x thin films deposited by PLD. In particular, the CN_x films were grown by laser ablation of graphite in a nitrogen atmosphere. The N/C ratio of the films can reach a value of 0.4. XPS analysis shows that in the DLC films the fraction of sp³ C sites doubles when the laser fluence increases from 1 to 12 J/cm². This result is confirmed by EELS measurements and it is in accord with the so called 'sub-implantation model' developed to explain the growth of DLC films.

More importantly, the XPS analysis shows that in the CN_x films the carbon and nitrogen atoms form stable bonds instead of simple mixing. There is a considerable amount of N–sp³-C bonded sites in a predominant N–sp²-C bonded matrix in the film with N/C=0.4. Decreasing the nitrogen (N/C=0.3) results in a decrease of N–sp³-C bonded sites. EELS analysis seems to indicate that the DLC film grown with laser fluences of 12 J/cm² and the CN_x film with N/C=0.30 have the same density and the same fraction of sp²-C bonded sites.

AFM shows an rms roughness of 3 Å on a surface of 1 × 1 μm² for all the DLC films grown with laser fluences in the range: 1–35 J/cm². Small particles of nanometer size are visible for the lowest laser fluences.

Acknowledgement

The authors would like to thank the Progetto Ricerca Avanzata CLASS of the INFN.

References

- [1] T.W. Scharf, R.D. Ott, D. Yang, J.A. Barnard, *J. Appl. Phys.* 85 (1999) 3142.
- [2] J.C. Angus, *Plasma Deposited Thin Films*, CRC Press, Boca Raton, FL, 1986, p. 89.
- [3] A. Kumar, R.B. Inturi, *Advanced Laser Processing of Materials MRS Symposium Proceeding vol. 397* (1996) 289.
- [4] J. Diaz, G. Paolicelli, S. Ferrer, F. Comin, *Phys. Rev. B* 54 (1996) 8064.
- [5] Y. Mizokawa, T. Miyasato, S. Nakamura, M. Geib, C.W. Wilmsen, *J. Vac. Sci. Technol. A* 5 (1987) 2809.
- [6] P. Kovarik, E.B.D. Bourdon, R.H. Prince, *Phys. Rev. B* 48 (1993) 12123.
- [7] S. Uhlmann, Th. Frauenheim, Y. Lifshitz, *Phys. Rev. Lett.* 81 (1998) 641.
- [8] Pappas, K. Saenger, J. Bruley, W. Krakow, J. Cuomo, T. Gu, R. Collins, *J. Appl. Phys.* 71 (1992) 5675.

A phenomenological study of the initial stages of film growth

C. Templier ^{a,*}, S. Muzard ^a, A. Galdikas ^b, L. Pranevicius ^c, J. Delafond ^a, J.C. Desoyer ^a

^a *Laboratoire Métallurgie–Physique, Université de Poitiers, BP179, 86960 Futuroscope Cedex, France*

^b *Physics Department, Kaunas University of Technology, 50 Studentu, 3041 Kaunas, Lithuania*

^c *Physics Department, Vytautas Magnus University, 28 Daukanto, 3000 Kaunas, Lithuania*

Abstract

The kinetics of island nucleation, coalescence and growth during deposition of Au atoms on amorphous carbon are studied experimentally and the obtained results are analysed using rate equations. Rutherford backscattering spectroscopy (RBS), transmission electron microscopy (TEM), grazing-incidence small angle scattering (GISAXS) and atomic force microscopy (AFM) techniques are used to measure the quantity of deposited Au, density, size and average height of the islands as a function of time. Parameters used in rate equations are deduced from a quantitative comparison between calculated and experimental evolution of the above dependencies. Suggested rate equations take into account the adsorption rate on a bare substrate as well as on existing islands, the mobility of adatoms, possible redistribution of atoms between islands and bare substrate and coalescence of islands. The rate equations are used to study the kinetics of the coverage of a carbon substrate by gold atoms and the kinetics of the island density. It is shown that experimental and calculated dependencies are in agreement if the mobility of islands is included. © 2000 Elsevier Science S.A. All rights reserved.

Keywords: Film; Gold; Growth; Initial stages; Island; Modelling

1. Introduction

Many theoretical and experimental studies of gold deposition on non-oriented substrates, including amorphous carbon, have been performed in the past, trying to obtain detailed knowledge of the prevailing processes taking place at the initial stages of film growth. It becomes clear that our understanding of the processes is rendered difficult by the large variety and complexity of physical and chemical interactions involved. Different modelling approaches of these processes are developed based on the analysis of rate equations and lattice gas models [1–3], taking into account islands of all sizes. Analysis of the scaling of the island density as a function of the coverage and deposition rate is able to explain the observed experimental results for a limited number of variables, which include the variety of processes defining the complex behaviour of adatoms and islands on the surface. It seems that in this situation the most efficient way to obtain an understanding of the funda-

mental processes driving the thin film growth process during the initial stages is not through an increase in complexity of models, but a simplification of the models in the limited range of experimental parameters with following analysis of the prevailing processes. Our goal is to recognise characteristic features of the different processes which can be identified from the analysis of the experimental results of time dependence of coverage, island density and mean size of islands obtained in highly controlled Au deposition conditions on the surface of amorphous carbon.

2. Experimental technique and results

A gold target was ion sputtered using a Kaufmann source with argon ions and an accelerating voltage equal to 1.2 kV at a pressure of residual gases equal to 5×10^{-2} Pa. As a preliminary, the substrate (TEM carbon-coated copper grid or silicon wafer) was covered with a 20 nm thick amorphous carbon film. The amount of deposited gold was measured after deposition using the Rutherford backscattering (RBS) technique. The fractional coverage, mean density of islands and their

* Corresponding author. Tel.: +33-5-4949-6660;

fax: +33-5-4949-6692.

E-mail address: claude.templier@lmp.univ-poitiers.fr

(C. Templier)

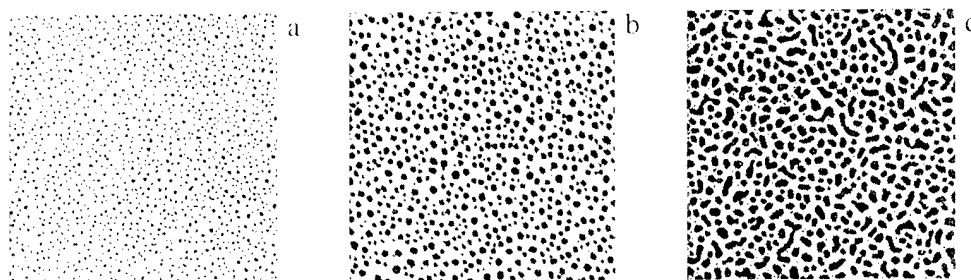


Fig. 1. TEM images showing the gold islands for different equivalent deposited thicknesses: (a) 0.4 nm, (b) 0.8 nm and (c) 1.6 nm. The area is $220 \times 220 \text{ nm}^2$.

size distribution were obtained from transmission electron microscopy (TEM) images using an image processor. The atomic force microscopy (AFM) and grazing-incidence small angle scattering (GISAXS) techniques were used for complementary analysis of island morphology and mean height [4]. A set of TEM images displayed in Fig. 1 shows the evolution of the 2D geometry of the gold islands for various gold deposited amounts. One can observe that the number density of islands is decreasing as the deposition proceeds.

Fig. 2(a) includes the dependence of the amount of deposited gold on amorphous carbon as a function of time. The observed linear dependence indicates that the condensation rate of Au does not depend on coverage and is approximately equal to $1.2 \times 10^{14} \text{ cm}^{-2} \text{ s}^{-1}$. It is equivalent to a film growth rate of 0.02 nm s^{-1} or 0.08 ML s^{-1} .

The evolution of the coverage is plotted in Fig. 2(b) as a function of the deposited amount of gold. Up to a coverage value of ~ 0.5 , it is seen that the coverage increases quite linearly with increase of deposited Au. With an increase in deposited amount of Au, the coverage approaches one as the Au deposited amount equals $3.7 \times 10^{16} \text{ cm}^{-2}$, equivalent to 24 ML. The decrease in island number density and the quite linear increase in mean radius versus deposited amount of Au are shown

in Fig. 3(a). The island height remains quite constant over that range of deposited amount as observed in Fig. 3(b).

3. Phenomenological description

The theoretical analysis is based on the approach provided by mean-rate equations. It includes the basic steps in the irreversible processes of nucleation and growth and presents the rate equation formalism with the emphasis on the analysis of the role of island migration on the coalescence process. Atoms are randomly deposited on a periodic array of adsorption sites at a rate per site of $i_0 = I_0/N_a$, where I_0 is the flux of arriving atoms and N_a is the surface concentration of atoms. Adatoms either meet other adatoms, irreversibly nucleating islands, or aggregate with existing islands. Let us denote by $\tilde{\lambda}$ the mean distance at which diffusing atoms aggregate with islands. Then, the mean island capture zone of adatoms arriving on the bare substrate may be expressed as

$$S_c^* = N\pi(R + \tilde{\lambda})^2 - N\pi R^2 = N\pi\tilde{\lambda}^2 + 2\pi\tilde{\lambda}\sqrt{\frac{NS_c}{\pi}} \quad (1)$$

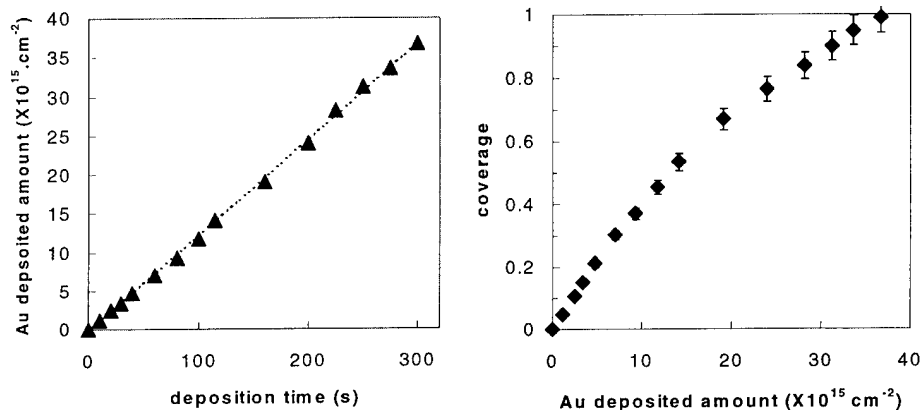


Fig. 2. (a) Measured deposited amount of gold as a function of deposition time and (b) coverage of the amorphous carbon substrate by gold islands versus the Au deposited amount.

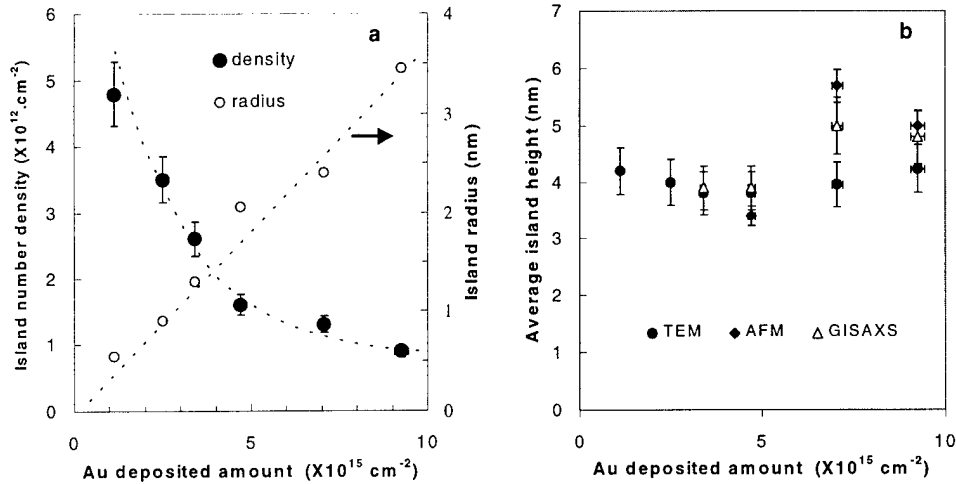


Fig. 3. The evolution of (a) island number density and average island radius and (b) average island height deduced from TEM, AFM and GISAXS as a function of gold deposited amount.

where N is the island density, R is the mean radius of islands assuming that they have a circular shape and S_c is the coverage of the surface by gold islands. Eq. (1) may be presented in dimensionless units as $n = N/N_a$, $\lambda = \tilde{\lambda}/a$ where a is the mean distance between adatom nucleation sites, approximately equal to the mean distance between atoms in bulk Au, and $\varphi_c = S_c/N\pi a^2$. This gives

$$\varphi_c^* = n\lambda^2 + 2\lambda\sqrt{n\varphi_c}. \quad (2)$$

The capture zone around adatoms on the surface is calculated using the same approach with n_s being the relative concentration of adatoms

$$\varphi_s^* = n_s\lambda^2 + 2\lambda\sqrt{n_s\varphi_s} = n_s\lambda(\lambda + 2). \quad (3)$$

During deposition the surface coverage increases and $\varphi_s + \varphi_c$ approaches one. When λ is large, $\varphi_s + \varphi_s^* + \varphi_c + \varphi_c^*$ can be more than one. So, φ_s^* and φ_c^* are replaced by $a(t)\varphi_s^*$ and $a(t)\varphi_c^*$, where $a(t)$ is a normalisation parameter which takes the following values

$$a(t) = \begin{cases} 1 & \text{if } \varphi_s + \varphi_s^* + \varphi_c + \varphi_c^* \leq 1 \\ \frac{1 - \varphi_s(t) - \varphi_c(t)}{\varphi_s^*(t) + \varphi_c^*(t)} & \text{if } \varphi_s + \varphi_s^* + \varphi_c + \varphi_c^* > 1. \end{cases} \quad (4)$$

Adatoms falling on the islands can initiate an additional flux of adatoms from the island to the bare substrate. It is either due to the migration distance of adatoms being larger than the size of the island, or due to the partial dissociation of islands on the impact of energetic adatoms. This flux is added to the flux i_0 so that the final flux is $i_0^* = i_0(1 + \eta\varphi_c)$, where η is the adatom yield, i.e. the number of adatoms produced by an atom deposited on an island. Then, the final equation for the

kinetics of coverage by adatoms is

$$\frac{d\varphi_s}{dt} = \frac{dn_s}{dt} = \alpha_{A0}i_0^*\varphi_L - \alpha_{AA}i_0^*[\varphi_s + a(t)\varphi_s^*] \quad (5)$$

where $\varphi_L = 1 - [\varphi_s + a(t)\varphi_s^* + \varphi_c + a(t)\varphi_c^*]$ is the free surface of the substrate available for nucleation and α_{A0} and α_{AA} are the sticking probabilities of an adatom to the bare substrate and to another adatom, respectively.

The coverage by islands is the sum of the following terms. The first describes the formation of new islands resulting from the capture of an adatom by adatoms. The second results from the adatoms falling within the island capture zone and sticking to the edge of islands with sticking probability α_{AC} . This gives

$$\frac{d\varphi_c}{dt} = 2\alpha_{AA}i_0^*[\varphi_s + a(t)\varphi_s^*] + \alpha_{AC}i_0^*a(t)\varphi_c^*. \quad (6)$$

The equation for the kinetics of island number density may be written as

$$\frac{dn}{dt} = \left(\frac{dn}{dt}\right)_n + \left(\frac{dn}{dt}\right)_c = \alpha_{AA}i_0^*[\varphi_s + a(t)\varphi_s^*] - B\left(\frac{ds^*}{dt}\right)n^2. \quad (7)$$

The first term on the right-hand side of the equation is the island nucleation rate which is expressed as the sticking rate of the arriving adatoms to adatoms. The second term is the island coalescence rate, where B is a frequency probability of coalescence which depends on the geometry of the islands (for circular islands, $B = 2\text{ s}^{-1}$) and s^* is an effective area. When the mobility of the islands is not included, $s^* = s$, where s is the mean surface of the islands in relative units [5,6]. If the island mobility is included, then s^* may be rewritten using $s^* = [r + \beta(r)]^2$, where $\beta(r)$ is an effective distance around

an island of radius r which characterises the island motion.

4. Results and discussion

The calculated results for coverage obtained after numerical integration of Eq. (6) are presented in Fig. 4(a) and are compared with experimental ones using $I_0 = 1.2 \times 10^{14} \text{ cm}^{-2} \text{ s}^{-1}$, $N_a = 1.5 \times 10^{15} \text{ cm}^{-2}$, $i_0 = 0.08 \text{ s}^{-1}$ and $a = 0.146 \text{ nm}$. The set of parameters has been adjusted to obtain the best quantitative agreement. It gives $\alpha_{A0} = 1$, $\alpha_{AA} = \alpha_{AC} = 0.06$, $\tilde{\lambda} = 1.25a$ and $\eta = 1$.

In the range of deposition times between 10 and 80 s, the flux of adatoms from the island has a minor effect, so the value of η is not a major parameter. The observed linear increase with time of the calculated coverage can be understood since after 10 s, the density of adatoms is negligible and $a(t)\phi_c^*$ is essentially equal to $1 - \phi_c$. This implies that Eq. (6) has an analytical solution of the form $\phi_c = 1 - \exp(-\alpha_{AC}i_0t)$, reasonably equivalent to $\alpha_{AC}i_0t$ in the time interval 10–80 s. It corresponds to a power law behaviour of coverage which is characteristic of 2D growth [7]. This is in agreement with the experimentally observed constant height of islands which does not depend on island radius, thereby reducing the island growth mode from 3D to 2D.

The experimental time dependence of island density [Fig. 3(a)] shows that the island number density decreases as soon as the coverage is larger than 0.05. This means that the process of island coalescence cannot be ignored even at the initial stages of deposition. The mechanism of coalescence which can be expected at such a low value of surface coverage is the mobility coalescence of islands, prior to the mechanism of immobile islands in which the coalescence occurs at high value of surface coverage when the islands touch each other [8].

Fig. 4(b) shows the calculated island number density without coalescence (a), with coalescence and immobile islands (b), with coalescence and a constant mobility parameter $\beta = 9$ (c), and with coalescence and a decreasing mobility parameter (d). The best fit is obtained if the island mobility parameter β decreases with time from ~ 8.2 at $t = 10 \text{ s}$ to ~ 3.2 at $t = 80 \text{ s}$.

The major conclusion that may be drawn from the results presented above is that diffusion of adatoms and islands on the surface plays a major role in the first stages of film growth. In the present work, these processes are characterised by the parameters λ and β defining adatom capture and island migration zones, respectively.

According to Lennard–Jones calculations, an atom which arrives at the substrate surface loses its excess energy in a few nanoseconds and travels only a few atomic distances during the period of accommodation which is determined by both its kinetic energy and the substrate temperature. The average energy of the sputtered gold atoms leaving the target is around 10 eV and is almost independent of the target temperature. The mean time between hops τ_H is determined by the substrate temperature T_s and is obtained according to the equation $\tau_H = \omega^{-1} \exp(E_H/kT_s)$, where E_H is the energy needed for a hop and ω ($\sim 2.0 \times 10^{12} \text{ s}^{-1}$) is the vibration frequency of an adatom at a normal binding site. The mean time before re-evaporation is determined by the same equation as for τ_H using the activation energy E_E for the escape of an adatom from the surface. E_H and E_E depend on the surrounding of adatoms. This means that a distinction has to be drawn between adatoms migrating on the substrate surface (amorphous carbon) and on the islands (gold). This is very important during the nucleation stage since it determines the properties of the growing film, like column size, crystal orientation, formation of defects, etc.

Unfortunately, little is known about hop and escape energies of gold on amorphous carbon. The only remark

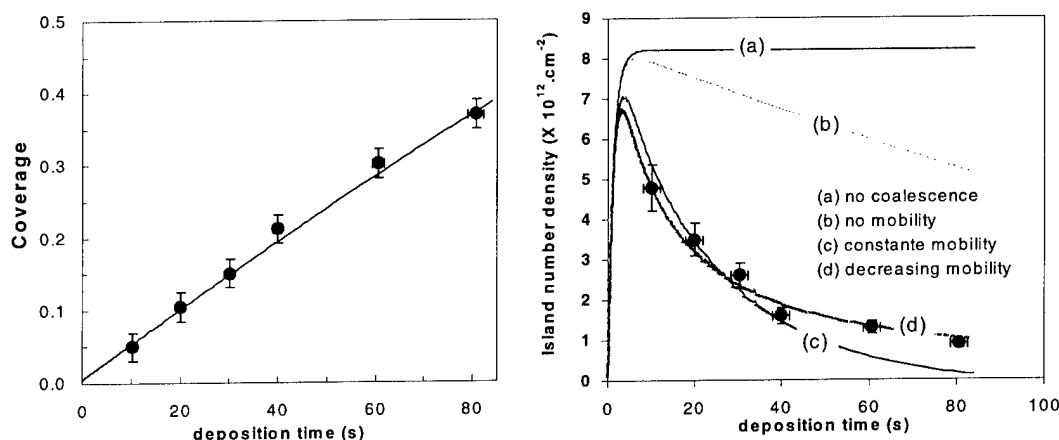


Fig. 4. Calculated (lines) and experimental (circles) evolution of (a) coverage and (b) island number density as a function of deposition time.

which may be made is that surface diffusion of gold on amorphous carbon is larger than surface diffusion of gold adatoms on gold islands since the gold–gold bonds are stronger than the gold–amorphous carbon ones. It is shown that the energy for surface diffusion is about 20% of the escape energy [9]. This implies that, at room temperature, the process of re-evaporation of adatoms may be neglected and is consistent with the observed constant deposition rate in time. With every jump, the adatoms move over a distance equal to the average distance between adsorption sites and perform a random walk over the substrate surface and diffuse away from their impingement spot. The average diffusion distance can be expressed as $\tilde{\lambda} = 0.5a(\tau_M/\tau_H)^{1/2}$ [10]. A rough estimation of $\tilde{\lambda}$ can be done using the given experimental conditions ($I_0 = 0.02 \text{ nm s}^{-1}$, $T_s = 300 \text{ K}$, $a = 0.15 \text{ nm}$ and $E_H = 0.22 \text{ eV}$ [11] and $\omega = 2 \times 10^{12} \text{ s}^{-1}$). This gives $\tilde{\lambda} \approx 10a$, which is very close to the value of $12.5a$ used in calculations.

The island mobility in the present work was introduced employing the parameter β defining an equivalent area available for island migration. The experimental results are in agreement with the calculated ones only in the case when this parameter differs from zero and decreases with time, keeping in the mind that the mean radius of islands increases linearly with time as follows from experimental results presented in Fig. 3(a). Island mobility may be considered as a result of the gradual translation of the island centre of mass as a consequence of atomic motion in the island, and is expected to be characterised by an activation energy of the order of those for adatom atom surface diffusion [12]. In some cases, the term defining island nucleation rate is presented in a way including the diffusion coefficient [13] with σ_c and D_c as the capture rate and diffusion coefficient of islands

$$\left(\frac{dn}{dt}\right)_c = -\sigma_c D_c n^2. \quad (8)$$

Experimental results suggest that, for gold on amorphous carbon with given experimental conditions of deposition, $\sigma_c D_c$ is independent of time, i.e. of the island size. The capture rate σ_c of the island depends on the island size and may be calculated by using a classical model of diffusion driven growth [14]. For quantitative estimation, the capture rate may be chosen to be proportional to the radius of the island as $\sigma_c(s) = \sigma_{c0}r$ [3]. This tells us that, in a limited range of deposition time, the diffusion coefficient of the island decreases as r^{-1} . The

characteristic diffusion length, assuming that the lifetime of the island before capture does not depend on the size of the island, is then proportional to $r^{-1/2}$. This is in satisfactory agreement with experimental results, since in the time interval between 20 and 60 s the island mean radius is multiplied by 2.5 while the parameter β is reduced by a factor of about $\sqrt{2.5}$. This indicates that the approaches of the coalescence processes using Eqs. (7) and (8) are equivalent. However, when the mobility of adatoms is described by the parameter λ and the island mobility by the parameter β , it simplifies the analysis of island growth and coalescence process.

5. Conclusions

It has been shown that a deeper knowledge of processes occurring in the early stages of film deposition on a non-oriented substrate can be obtained in terms of a simplified set of rate equations for the coverage and island number density as a function of time. Parameters required to obtain agreement with experimental results are the sticking coefficients α , the parameter λ which defines the adatom capture zone and the parameter β which defines the island migration zone. It is shown that all parameters needed to describe the coalescence behaviour are physically reasonable. The rate equations were applied to recent experimental data on gold deposited on amorphous carbon and it was shown that island mobility was required in order to understand the behaviour of the island number density.

References

- [1] S. Stoyanov, D. Kashchiev, in: E. Kaldis (Ed.), Topics in Material Science Vol. 7, North-Holland, Amsterdam, 1981, p. 71.
- [2] O. Biham, G.T. Barkema, M. Breeman, Surf. Sci. 324 (1995) 47.
- [3] J. Sillanpää, I. Koponen, Nucl. Instrum. Meth. Phys. Res. B 142 (1998) 67.
- [4] A. Naudon, D. Thiaudiere, J. Appl. Crystallogr. 30 (1997) 822.
- [5] J.A. Venables, Surf. Sci. 299/300 (1994) 798.
- [6] S. Liu, L. Bönig, H. Metiu, Surf. Sci. 392 (1997) L56.
- [7] J.A. Blackman, Physica A 220 (1995) 85.
- [8] M.C. Bartelt, J.W. Evans, Surf. Sci. 314 (1994) L229.
- [9] L. Abelman, C. Lodder, Thin Solid Films 305 (1997) 1.
- [10] B. Lewis, G.J. Rees, Philos. Mag. 29 (1974) 1253.
- [11] J.A. Venables, G.D.T. Spiller, M. Hanbücken, Rep. Progr. Phys. 47 (1984) 399.
- [12] J.L. Levine, J.B. Cohen, Y.W. Chung, Surf. Sci. 248 (1991) 215.
- [13] A.D. Gates, J.L. Robins, Thin Solid Films 149 (1987) 113.
- [14] G.S. Bales, D.C. Chrzan, Phys. Rev. B 50 (1994) 6057.

Influence of the structure of the composite: ‘nitrided layer/PVD coating’ on the durability of tools for hot working

Jerzy Smolik ^{a,*}, Jan Walkowicz ^a, Jan Tacikowski ^b

^a Institute for Terotechnology, Pullaskiego 6/10, 26-600 Radom, Poland

^b Institute of Precision Mechanics, Duchnicka 3, 00-967 Warsaw, Poland

Accepted 30 June 1999

Abstract

The paper presents research results of the influence of the ‘nitrided layer/PVD coating’ composite on the durability of tools for hot plastic working. Four structures of the composite differing in the PVD coating material were investigated. They were: TiN, CrN, (Ti,Cr)N and Ti(C,N). The composites investigated were created by means of the surface ‘duplex’ treatment method in a two stage separable cycle (the nitriding process and the PVD coating deposition were carried out with different devices). The nitriding process was executed with the use of the regulated gas nitriding method, whereas the PVD coating was executed by means of the arc-vacuum method. The tools tested were forge dies made of ISO steel 35CrMoV5 (0.4%C, 0.4%Mn, 1.0%Si, 5.0%Cr, 1.3%Mo, 0.3%V) designed for the plastic working of automotive half-shafts.

The paper presents the results of maintenance investigations, executed under manufacturing conditions, obtained for tools used for hot forging which were covered with different composites. The investigations proved that the best durability was achieved for tools covered with the composite ‘nitrided layer/CrN coating’, for which the increase in durability was almost 90%. The smallest durability was noted for tools covered with the composite ‘nitrided layer/TiN coating’. The results obtained proved that a proper choice of the composite ‘nitrided layer/PVD coating’ structure may increase the durability of tools considerably for hot plastic working. © 2000 Elsevier Science S.A. All rights reserved.

Keywords: Composite layer; Duplex treatment; Physical vapor deposition coating

1. Introduction

Large cyclic mechanical loads and thermal shocks caused by the contact of a tool with hot treated material are characteristic features of hot plastic working. Apart from the abrasive wear dominant in the wearing process of cutting tools, in the case of tools used for hot plastic working it also causes plastic strain and thermal fatigue of the tool material. The processes of gas and ion nitriding are commonly used to give good antiwear properties to tools for hot working. The rapid development of plasm-chemical technologies to modify the antiwear properties of cutting tools prompted trials in using them for plastic working tools to be undertaken. The use of PAPVD methods to coat the working surfaces of cutting tools with thin antiwear coatings promotes a considerable increase in their durability. However, this effect has not been confirmed for hot working tools. Research works performed in the 1990s concerning the

use of the PAPVD technology in the treatment of tools for hot working have resulted in elaboration of the ‘duplex’ surface treatment technology [1–3] assisting in creation of the composite ‘nitrided layer/PAPVD coating’.

On the basis of research results described in the literature [4–8] it was stated that the nitrided layer structure created significantly influences the composite properties. It also determines quality of the PAPVD coating adhesion to the nitrided substrate. It turns out that appearance of only the $\text{Fe}_x(\text{N})$ phase on the nitrided surface is essential for achieving a good adhesion of the PAPVD coating to the substrate. In the literature, it has been proved that a layer of iron nitrides $\epsilon\text{-Fe}_{2-3}\text{N}$ and $\gamma\text{'-Fe}_4\text{N}$, in addition to a thin layer of titanium [9,10], often occurring directly on the nitrided element surface under the PAPVD coating, have a harmful influence on the PAPVD coating adhesion in the composite’s ‘nitrided layer/PAPVD coating’. However, the majority of experiments were carried out concerning the TiN coating.

According to this paper’s authors, the PAPVD coating adhesion to the nitrided substrate, as well as the

* Corresponding author. Tel.: +48-48-43884; fax: +48-48-44760.

E-mail address: jerzy.smolik@itec.radom.pl (J. Smolik)

Table 1
'Duplex' treatment parameters

Nitriding					
Temperature (°C)	Atmosphere	Flow (l/min)	Time (h)		
450	NH ₃	150	0.5		
510	NH ₃	80	7		
Surface mechanical treatment					
Type of treatment	Abrasive material	Carrier (MPa)	Time (min)		
Shot blasting	Elektrokorund 150	Air: 0.6	6		
Shot blasting	Interminglas 40–70	Air: 0.6	4		
Polishing	Paste: Cr ₂ O ₃	Felt target	Till attainment of a uniform polish		
PVD coating deposition					
Coating	Atmosphere	Pressure × 10 ^{−2} mbar	Temperature (°C)	Ubias (V)	Current (A)
TiN	100% N ₂	1.2	400	−150	80
CrN	100% N ₂	2.0	400	−150	80
(Ti,Cr)N	100% N ₂	2.0	400	−150	80
Ti(C,N)	25%C ₂ H ₂ + 75% N ₂	0.8	400	−200	80

Table 2
PVD coating parameters

Coating	Thickness (μm)	Ra (μm)	Chemical composition	Phase structure	HV0.05	Young's modulus (GPa)
TiN	3.0	0.35	70%Ti, 30%N	TiN-fcc	2200	421
CrN	4.3	0.15	78%Cr, 22%N	CrN-fcc, Cr ₂ N-hex	2410	314
(Ti,Cr)N	3.8	0.23	33%Ti, 39%Cr, 28%N	TiN-fcc, CrN-fcc	2250	384
Ti(C,N)	2.8	0.39	58%Ti, 15%C, 27%N	Ti(C,N)-fcc	2800	508

resistance to thermal fatigue of the whole composite, is significantly determined, not only by the nitrided layer structure, but also by the chemical composition and the structure of the PAPVD coating material. This paper presents research results on the influence of different materials in PAPVD coatings, produced by the reactive arc-vacuum sputtering method, on the maintenance properties of the composite's 'nitrided layer/PAPVD coating'.

2. Experimental

2.1. Preparation of composites

The composites investigated were created by means of the 'duplex' surface treatment method in a two stage separable cycle (the nitriding process and the PVD coating deposition were carried out with different devices). The nitriding process was carried out by means

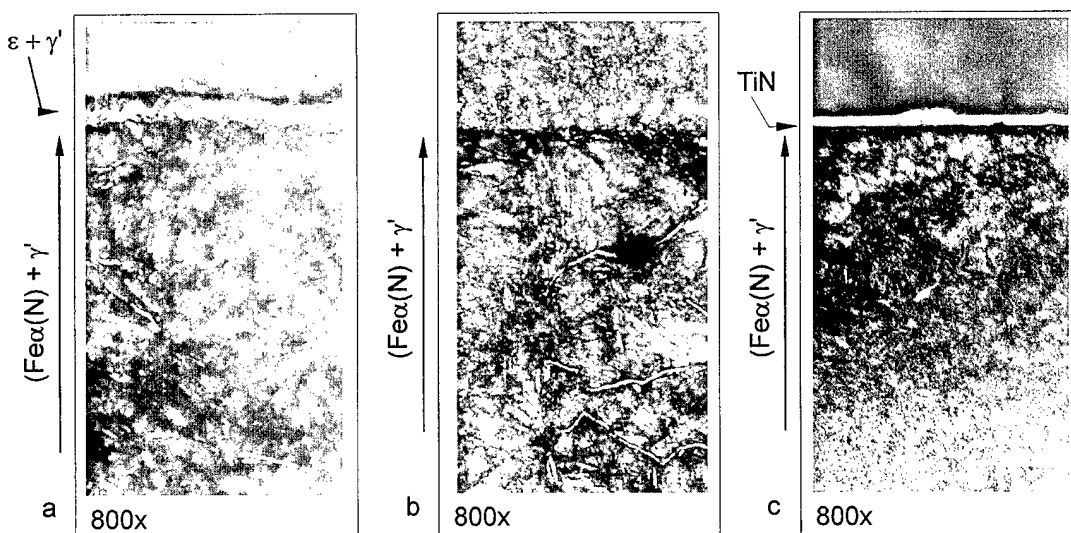


Fig. 1. The structure of the composite 'nitrided layer/TiN coating' at successive stages of its creation: (a) nitrided layer created in Stage 1; (b) nitrided layer after mechanical surface treatment; (c) the composite 'nitrided layer/TiN coating'.

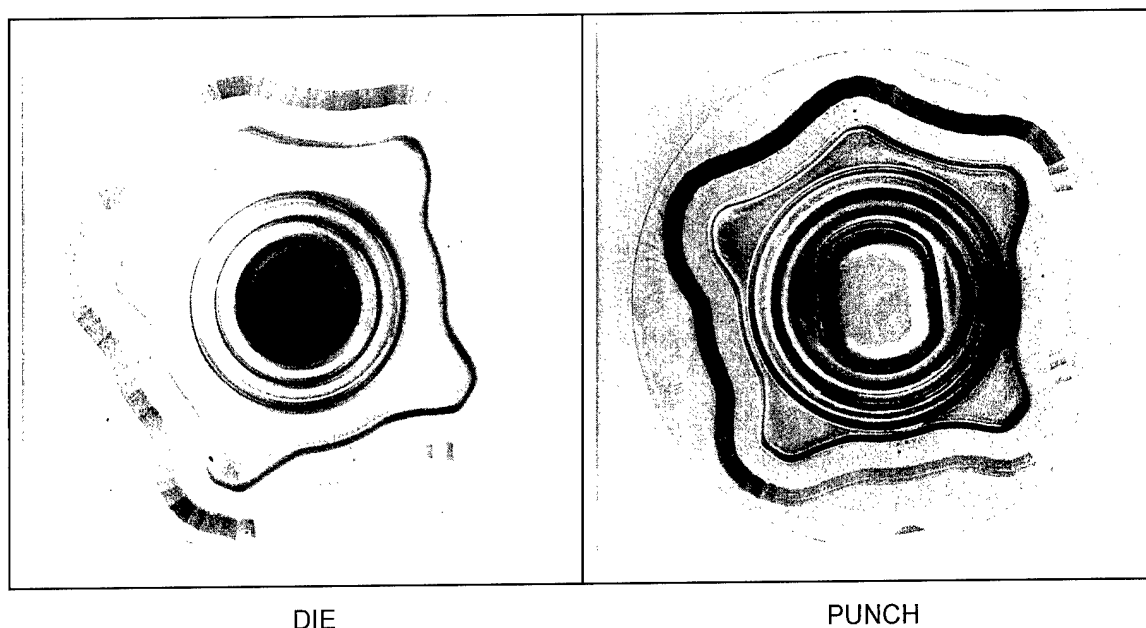


Fig. 2. Tools for hot-forging designed for maintenance investigations.

of regulated gas nitriding and was the first stage of 'duplex' treatment. The second stage was to produce the PVD coating by means of the arc-vacuum method using an MZ383 arc-vacuum device (Metaplas Ionon GmbH). Mechanical surface treatment aimed at removing the superficial zone of $\epsilon\text{-Fe}_{2-3}\text{N}$ and $\gamma'\text{-Fe}_4\text{N}$ iron nitrides was carried between the two main stages of the 'duplex' treatment. The parameters of the individual stages of the surface 'duplex' treatment are presented in Table 1.

2.2. Characterization of the composites

The nitrided layer created in the Stage 1 of 'duplex' treatment contained a diffusion layer $\text{Fe}_x(\text{N})$ of thickness 0.085 mm and a zone of iron nitrides $\epsilon\text{-Fe}_{2-3}\text{N}$ and $\gamma'\text{-Fe}_4\text{N}$ of thickness 5.5 μm . As a result of the mechanical surface treatment executed after the nitriding stage, a nitrided layer of the thickness 0.080 mm and surface hardness $\text{HV1} = 1265$ was created. The high value of the surface hardness is the result of the residual amount of iron nitrides γ' left on the surface after the mechanical surface treatment. The metallographic investigations carried out after the mechanical surface treatment revealed that only the $\text{Fe}_x(\text{N})$ structure and the γ' structure issued at grain boundaries in the cooling process. The parameters of four different PVD coatings are presented in Table 2. The chemical composition of the investigated coatings was determined by the EDS method using an X-ray microanalyser (Noran Instruments) installed on a scanning microscope (Hitachi-S2460N). Values of Young's modulus for the materials of particular layers in the composites investigated were measured by means of the indentation test

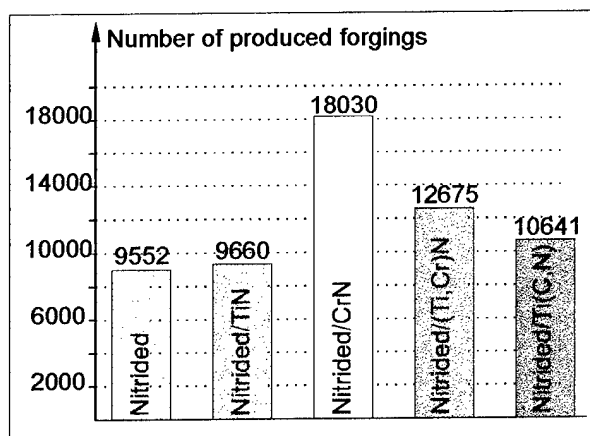


Fig. 3. Results of maintenance investigations.

method. To achieve this, the nano-hardness tester made by the Swiss firm Centre Suisse d'Electronique et de Microtechnique S.A. was used. Measurements were carried out with a Vicker's indenter in a single cycle without stopping using the following parameters: $F = 10 \text{ mN}$, $dF/dt = 20 \text{ mN/min}$. To eliminate the influence of the substrate material on the measurement of Young's modulus of the layer material, the range of the indenter's penetration depth was limited to $g \leq 0.1d$; (d = layer thickness). X-ray investigations to determine the coating phase composition were carried out using the Philips Analytical PW1840 diffractometer with a cobalt anode.

The structure of the composite 'nitrided layer/TiN coating' in successive stages of creation is presented in Fig. 1.

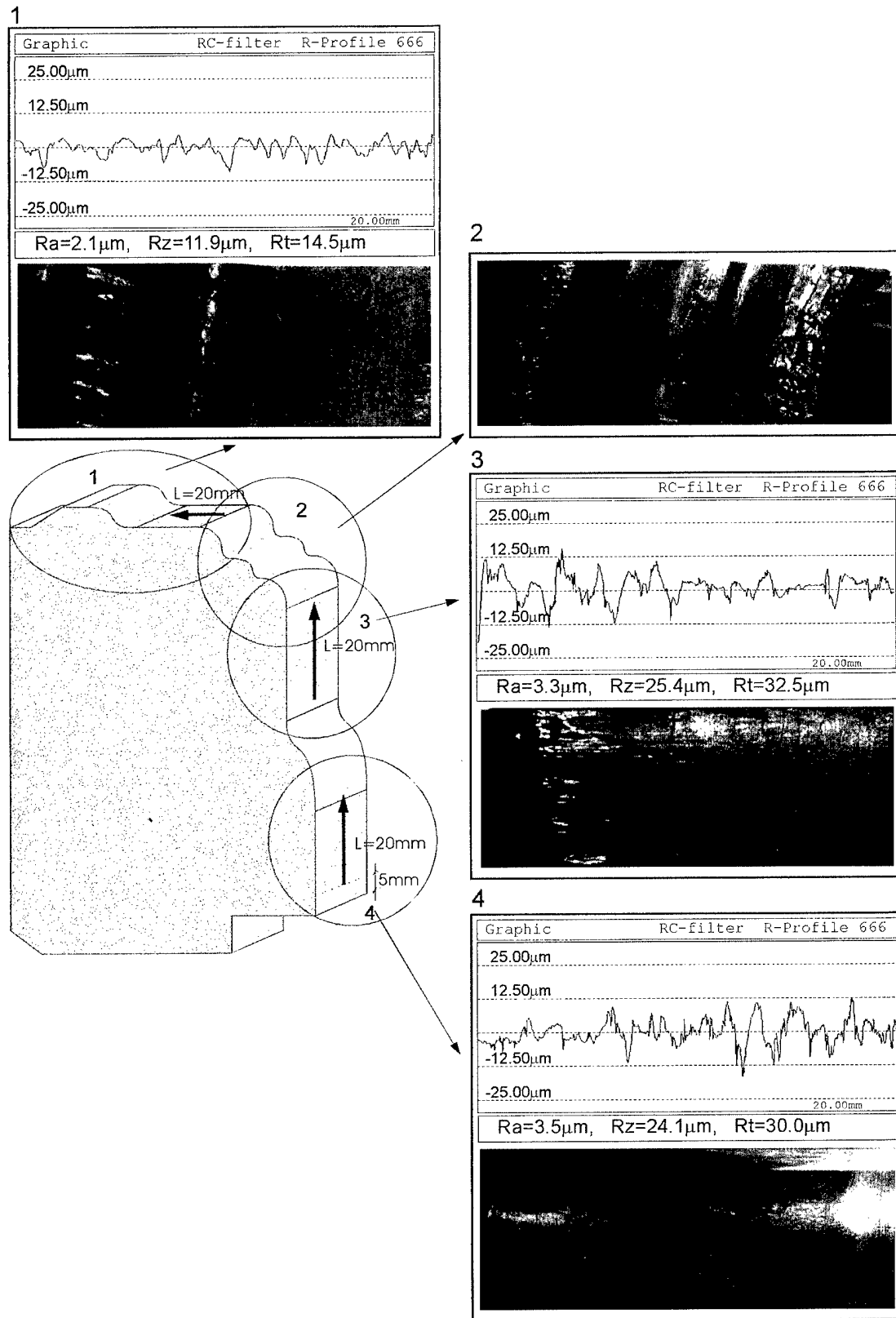


Fig. 4. Results of microscope observations and roughness measurements for the working surfaces of the die covered with the composite 'nitrided layer/TiN coating'.

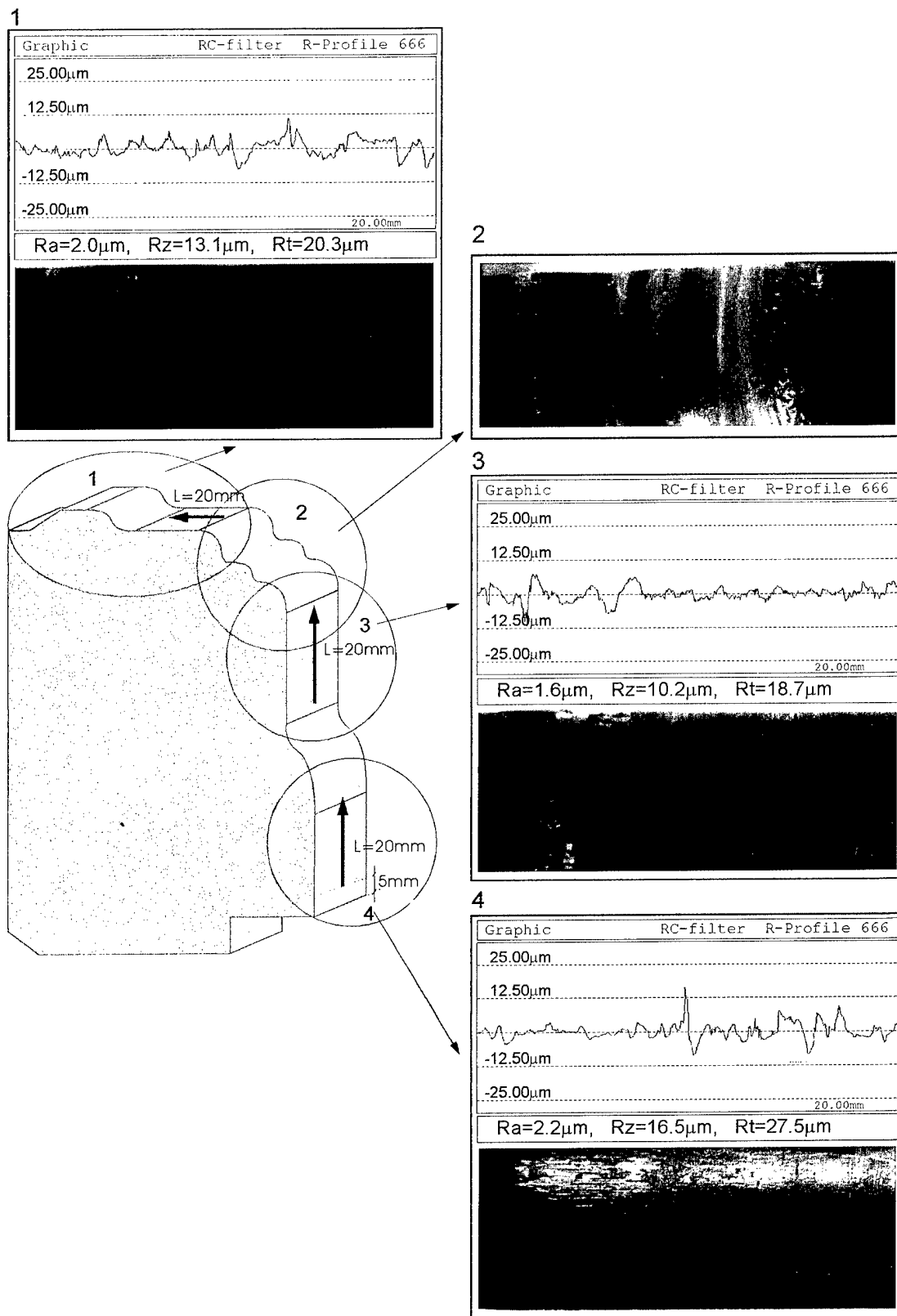


Fig. 5. Results of microscope observations and roughness measurements for the working surfaces of the die covered with the composite 'nitrided layer/CrN coating'.

2.3. Antiwear performance test

Four sets of hot-forging tools made of ISO steel 35CrMoV5 (0.4%C, 0.4%Mn, 1.0%Si, 5.0%Cr, 1.3%Mo, 0.3%V) which is used for production of automotive half-shafts (constructed from material 25CrMo4) were investigated. Tools selected for investigations (Fig. 2) belonged to a group of tools working in long-production series. The shape of required forgings meant that the dies and punches used were characterised by a complex shape in the working surfaces which are used in the forging process. It also meant that during work with large loads they had to ensure a considerable degree of plastic strain on the forged material.

Maintenance tests on tools covered with the composites examined were carried at the forging hammer, type VES1600 (Vesterman and Cleaver) with the following parameters: the die's temperature before forging was in the range 250–300°C; the forged material's temperature was 1150°C; and the lubricant was Delta 31 at concentration 1:7

3. Results

The results of the maintenance tests showing the number of forgings made by respective sets of tools are presented in Fig. 3.

Microscope analysis of the intensity of the investigated forge dies destruction, because of their shape (centrally situated port), required a proper preparation of the samples to ensure access to the frontal surface of the die as well as to the port surfaces. The way the samples were prepared also enabled us to measure roughness in three different places of the die working areas — the frontal surface; and the port surface at two depths from the die front. The analysis of the dies' surfaces wear was carried out on tools covered with two composites — 'nitrided layer/TiN coating' and 'nitrided layer/CrN coating' i.e. for those which in the maintenance test made the smallest and the biggest number of forgings. The way in which the investigated samples' preparation and the results of the analysis are presented in Figs. 4 and 5.

Microscope observations revealed that longitudinal grooves created as a result of the abrasive wear process and a grid of cracks — a result of fatigue processes — are the main forms of the analysed surfaces' destruction. The abrasive wear is predominant in the die frontal part and in the port upper part, i.e. in places where the forging process is accompanied by the biggest pressures of the treated material on the tool surface. In the lower part of ports, the abrasive wear is minimal. However, a dense grid of cracks is visible there, which points to the predominance of fatigue processes. Conclusions from the microscope observation also seem to be confirmed

by the results of the substrates' roughness measurements. As can be seen in Figs. 4 and 5 the substrates' roughness indexes R_a , R_z , R_t for the dies' frontal surfaces with TiN and CrN coatings are similar. It points to a similar intensity of destruction of this part of both dies. So, it should be true that resistance of the investigated composites to mechanical loads, a dominant destruction factor in this part of the tools, is comparable.

On the other hand, the further from the die frontal area, the smaller the abrasive wear intensity and the larger intensity of fatigue cracks. The crack intensity is smaller in the case of a die with a CrN layer than in the case of one with a TiN layer, which is proved by the roughness measurement. Thus, this points to a considerably bigger resistance to thermal shock of dies with the composite 'nitrided layer/CrN coating' than those with the composite 'nitrided layer/TiN coating'.

4. Conclusions

These results enable us to formulate the following conclusions:

1. use of 'nitrided layer/PVD coating' composites offers the potential to increase the durability of tools for hot plastic working;
2. correct choice of the PVD coating material significantly influences the durability of the 'nitrided layer/PVD coating' composite in hot plastic working; and
3. the destruction intensity of investigated tools for hot plastic working which were covered with various composites 'nitrided layer/PVD coating' was different in different parts of the tool. The degree of frontal area destruction in dies covered with the composites 'nitrided layer/TiN coating' and 'nitrided layer/CrN coating' was comparable, which testifies to their similar resistance to mechanical loads. Smaller wear of the ports' surfaces in forging tools covered with the 'nitrided layer/CrN coating' composite testifies to their significantly bigger resistance to thermal shocks.

Acknowledgement

The work is a part of the research project European Concerted Action COST 516.

References

- [1] M. Van Stappen, M. Kerkhofs, C. Quaeys, *Surf. Coat. Technol.* 62 (1993) 655.
- [2] T. Gredić, M. Zlatanović, N. Popović, Ž. Bogdanov, *Thin Solid Films* 228 (1993) 261.

- [3] J. Walkowicz, J. Smolik, K. Miernik, J. Bujak, *Surf. Coat. Technol.* 97 (1997) 453.
- [4] K. Hock, H.J. Spies, B. Larisch, G. Leonhardt, B. Buecken, *Surf. Coat. Technol.* 88 (1996) 44.
- [5] F.D. Lai, J.K. Wu, *Surf. Coat. Technol.* 88 (1996) 183.
- [6] A. Matthews, A. Leyland, *Surf. Coat. Technol.* 71 (1995) 88.
- [7] N. Dingremont, E. Bergmann, P. Collignon, H. Michel, *Surf. Coat. Technol.* 72 (1995) 163.
- [8] F. Sanchette, E. Damond, M. Buvron, L. Henry, P. Jacquot, N. Randall, P. Alers, *Surf. Coat. Technol.* 94/95 (1997) 261.
- [9] Y. Sun, T. Bell, *Trans. Inst. Metal Finish.* 70 (1992) 38.
- [10] J. Walkowicz, J. Smolik, J. Tacikowski, Optimization of nitrided case structure in composite layers created by duplex treatment on the basis of PVD coating adhesion measurement, Sixth International Conference on Plasma Surface Engineering — PSE'98, Garmisch-Partenkirchen (1998).

Influence of carbon content on the crystallographic structure of boron carbide films

O. Conde ^{a,*}, A.J. Silvestre ^b, J.C. Oliveira ^{a, 1}

^a Departamento de Física, Faculdade de Ciências, Universidade de Lisboa, Campo Grande, Ed. C1, 1749-016 Lisbon, Portugal

^b Instituto Superior de Transportes, R. Castilho no. 3, 1250 Lisbon, Portugal

Abstract

Boron carbide thin films were synthesised by laser-assisted chemical vapour deposition (LCVD), using a CO₂ laser beam and boron trichloride and methane as precursors. Boron and carbon contents were measured by electron probe microanalysis (EPMA). Microstructural analysis was carried out by Raman microspectroscopy and glancing-incidence X-ray diffraction (GIXRD) was used to study the crystallographic structure and to determine the lattice parameters of the polycrystalline films. The rhombohedral–hexagonal boron carbide crystal lattice constants were plotted as a function of the carbon content, and the non-linear behaviour observed was interpreted on the basis of the complex structure of boron carbide. © 2000 Elsevier Science S.A. All rights reserved.

Keywords: Boron carbide; Crystallographic structure; Laser CVD; Micro-Raman spectroscopy

1. Introduction

Rhombohedral boron carbide, often denoted B₄C since its composition was established by Ridgway in 1934 [1], is the most stable compound in the boron–carbon system and exists as a single-phase material over a wide range of solubility, generally accepted to be from about 9 to about 20 at% carbon.

From the technological point of view, boron carbide exhibits many attractive properties, such as low specific weight and high hardness, even surpassing diamond and cubic boron nitride at temperatures over 1100°C [2]. Moreover, it presents a high melting point (2450°C) and modulus of elasticity, and has great resistance to chemical attack. These properties make boron carbide an interesting wear- and corrosion-resistant ceramic material for thin film applications. In addition, the B₄C has been utilised as a neutron-absorbent material in the nuclear industry since it has a high neutron capture cross-section, and is also a good candidate for high-temperature thermoelectric energy converters owing to its high-temperature stability [3].

The combination of all these properties in one unique material reflects the complex structure of boron carbide, over which some uncertainty still persists [4,5]. The most accepted model for the rhombohedral structure of boron carbide considers B₁₁C icosahedra clusters directly linked by covalent bonds and indirectly linked by a C–B–C chain along the main diagonal of the rhombohedron [5–7]. On the basis of this model, boron carbide has a B₁₂C₃ stoichiometry with 20 at% carbon. The wide range for carbon content characteristic of boron carbide is made possible by the substitution of boron and carbon atoms for one another within both B₁₁C icosahedra and C–B–C chains.

The aim of this paper is to present experimental results on the microstructure, chemical composition, deposition rate and structure of boron carbide films deposited by laser-assisted chemical vapour deposition (LCVD), and to discuss the influence of carbon content on the crystallographic structure of the films deposited.

2. Experimental procedure

Boron carbide films were deposited on silica substrates using a CO₂ laser beam as heat source and a dynamic reactive gas mixture of BCl₃, CH₄ and H₂. The experimental apparatus used for the experiments has been described previously [8].

* Corresponding author. Tel: +351-21-750-0035;
fax: +351-21-757-3619.

E-mail address: oconde@fc.ul.pt (O. Conde)

¹ Present address: Faculdade de Ciências e Tecnologia, 3030 Coimbra, Portugal.

The CO₂ laser was operated in cw TEM₀₀ mode at a wavelength of 10.6 μm and impinges on the substrate surface at perpendicular incidence, with a diameter of 13 mm. No focusing lens was used since fused silica substrates absorb approximately 84% of the laser radiation. The reactor was pumped to a base pressure of less than 2×10^{-6} torr before introduction of the reaction gas mixture, which consisted of BCl₃ (purity 99.99%), CH₄ (purity 99.9995%), H₂ (purity 99.9995%) and Ar (purity 99.9995%). Mass flow controllers regulated the reactant flow rates while the total pressure was measured by a capacitance manometer and kept constant by means of a throttle valve. Fused silica plates with dimensions 15 mm \times 15 mm \times 2 mm were used as substrates. They were ultrasonically cleaned in acetone and ethanol prior to insertion in the reactor.

Since the substrates were always kept stationary under the laser irradiation, the experimental variables of the set-up are the laser output power (P), the interaction time (t_{int}), the total pressure (p_t) and the partial flow rates of each gas (ϕ_i). In this study, total pressure, hydrogen flux and argon flux were kept constant at 100 torr (1.33×10^4 Pa), 200 sccm and 430 sccm, respectively. The other experimental parameters were varied in the ranges listed in Table 1.

The relative amount of carbon and boron precursors in the reactive atmosphere can be characterised by the parameter $\phi = \phi_{\text{CH}_4} / (\phi_{\text{CH}_4} + \phi_{\text{BCl}_3})$. In this study, ϕ took values between 0.15 and 0.29, which were optimised to achieve homogeneous deposits of B₄C, as reported previously [8,9].

Thickness profiles were obtained by optical profilometry and the microstructure was examined by scanning electron microscopy (SEM). Quantitative chemical analysis was performed by electron probe microanalysis (EPMA). Structural analyses were carried out with a micro-Raman spectrometer (Ar⁺ laser, 488 nm excitation line) and glancing-incidence X-ray diffraction (GIXRD, glancing angle of 1°) using Cu K α radiation.

3. Results and discussion

3.1. Morphology and microstructure

According to visual observation, all the films deposited are homogeneous, exhibit the characteristic B₄C

light grey shining colour and good adherence. Since the laser beam has a nearly Gaussian energy profile the deposits are approximately circular in shape, with diameters between 5.5 and 7.4 mm. Results of EPMA revealed that the coatings are chemically homogeneous, showing evidence of carbon concentration profiles almost flat with distance from spot centre, and that the stoichiometry of the films (9–20 at% carbon) is mainly determined by the composition of the gas phase [9].

SEM analyses of different films showed that their morphology is nodular with a fine and uniform grain structure all over the deposits. A typical microstructure is illustrated in Fig. 1(a), where an SEM micrograph of a film deposited with $P=150$ W, $t_{\text{int}}=30$ s and $\phi=0.25$ is shown. The film presents a polycrystalline structure that seems to have originated from a high density of nucleation centres yielding a mean grain size of a few tenths of a μm . The micrograph also shows some cracks formed during cooling of the samples, arising from the difference between the thermal expansion coefficients of the film ($4.5 \times 10^{-6} \text{ K}^{-1}$) and the silica substrate ($0.5 \times 10^{-6} \text{ K}^{-1}$).

Concerning the topography of the deposited material,

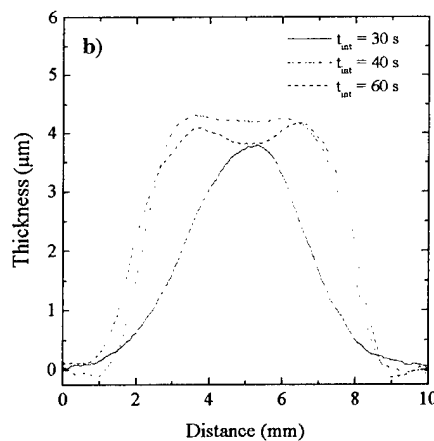
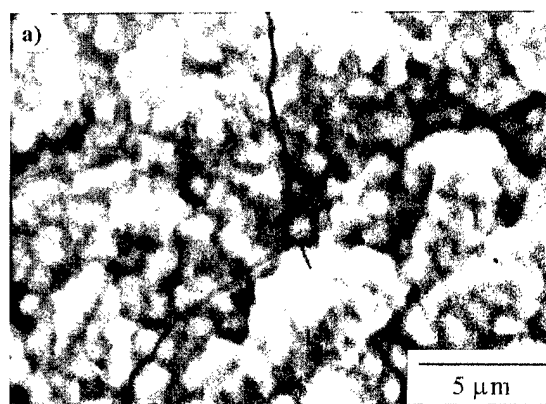


Fig. 1. (a) SEM micrograph of a film deposited with $\phi=0.25$, $P=150$ W and $t_{\text{int}}=30$ s; (b) thickness profiles of films deposited with $\phi=0.25$, $P=150$ W and different interaction times.

Table 1

Process parameters for LCVD of boron carbide films

Experimental parameter	Range of values
Laser output power (W)	125–175
Interaction time (s)	30–90
Partial flux of BCl ₃ (sccm)	34–40
Partial flux of CH ₄ (sccm)	7.2–14

three different thickness distributions were found; namely, Gaussian, top-flat and volcano-like profiles. Fig. 1(b) shows thickness profiles measured on spots deposited with $\phi=0.25$, $P=150$ W and different interaction times. As can be seen, for $t_{\text{int}}=30$ s the spot presents a broad Gaussian profile; by increasing the irradiation time up to 40 s the thickness distribution of the deposited material evolves to a quasi top-flat profile. The film processed with $t_{\text{int}}=60$ s presents a central depression associated with a lack of film material, yielding a volcano-like profile. The series of coating profiles plotted in Fig. 1(b) also illustrates an important observed behaviour: for constant ϕ and P values, the thickness of the films, defined as the maximum height above the substrate surface, does not show any significant dependence on the laser irradiation time. However, the amount of material deposited is an increasing function of the irradiation time, as can be determined from the increasing area of the region limited by the thickness profiles.

3.2. Growth kinetics

The thickness profiles were very useful to investigate the growth kinetics of the B_4C films, providing not only a means to estimate the total amount of material deposited but also the values of surface temperature induced by the laser–material interaction. The apparent deposition rate for the boron carbide films was evaluated in terms of the total mass deposited per unit time, following the method described in [10] and assuming the bulk density of B_4C to be 2.52 g cm^{-3} . Apparent deposition rate values in the range 2.3 to $9.4 \mu\text{g s}^{-1}$ were obtained. Following the calculation technique described elsewhere [9], the surface temperature achieved at the centre of the films during deposition was estimated to be between 800 and 1080 K.

Fig. 2 shows an Arrhenius diagram where the apparent deposition rates and temperatures are those referred to above. The fact that only one straight line is needed to fit the data indicates that only one mechanism is responsible for B_4C film growth. From the slope of the straight line, the apparent activation energy was calculated to be $27.5 \pm 7.8 \text{ kJ mol}^{-1}$. The low magnitude of the activation energy indicates a small dependence of the deposition rate on temperature, which means that mass transport of reactive gaseous species is the rate-limiting step for the growth of the boron carbide film.

3.3. Structural analysis

The GIXRD diffractograms show narrow diffraction lines which are all matched by rhombohedral boron carbide, JCPDS card no. 33-0225. This result confirms that only one polycrystalline phase was formed during the LCVD process. Fig. 3 displays a series of spectra

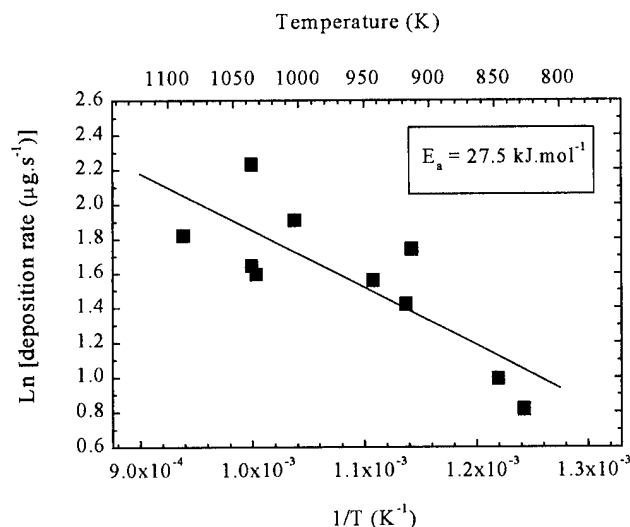


Fig. 2. Logarithm of the apparent deposition rate as a function of reciprocal temperature: ■, measured values; line, curve fitting.

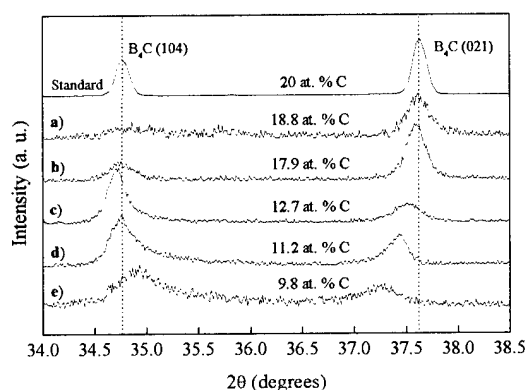


Fig. 3. GIXRD spectra of boron carbide films with different carbon contents, as measured by EPMA.

recorded over samples with varying carbon content, from 9.8 to 18.8 at%, and also a standard bulk sample with 20 at% carbon, for comparison. The 2θ region selected is the one comprising the two strongest boron carbide diffraction peaks, i.e., the (104) and (021) reflections. When carbon concentration is high (Fig. 3, spectra a and b) the experimental intensity distribution pattern follows the relative intensities of the standard polycrystalline B_4C sample with randomly oriented grains. For films with low carbon contents an inversion of the relative intensities of the (104) and (021) peaks was always observed, suggesting the development of a (104) texture (Fig. 3, spectra c–e). A strong continuous shift of the (021) peak to lower angles is also observed when the atomic carbon concentration decreases.

Based on the d_{hkl} values inferred from the angular position of the two major peaks in the GIXRD patterns, we estimated the B_4C equivalent hexagonal lattice

parameters c_h and a_h using the following equations

$$c_h = \sqrt{\frac{63d_{104}^2 d_{021}^2}{4d_{021}^2 - d_{104}^2}} \quad \text{and} \quad a_h = \sqrt{\frac{4c_h^2 d_{104}^2}{3(c_h^2 - 16d_{104}^2)}}, \quad (1)$$

which were deduced from the spacing formulae given by Warren [11]. The constants c_h and a_h are correlated with the B_4C rhombohedral lattice parameters a_r and α_r by the relationships [11]

$$a_r = \frac{1}{3}\sqrt{3a_h^2 + c_h^2} \quad \text{and} \quad \sin \frac{\alpha_r}{2} = \frac{3}{2\sqrt{3 + (c_h/a_h)^2}}. \quad (2)$$

Fig. 4 shows c_h and a_h parameters as a function of the carbon content of the films. The non-linear correlation found between the lattice constants and the carbon concentration suggests analysis of the whole graph in terms of three distinct zones, which can be related to the way carbon atoms are preferentially substituted in the lattice as the carbon content is reduced. Between 20 and about 17.5 at% carbon (zone I), both c_h and a_h increase when the carbon concentration decreases. This behaviour may be explained by the exchange of carbon atoms by boron atoms in the central C–B–C chain, leading to a C–B–B chain in the main diagonal of the rhombohedral structure. Since boron atoms have a higher covalent radius (0.82 Å) than carbon atoms (0.77 Å), these substitutions induce an increase in volume of the hexagonal lattice, expanding the unit cell in both a and c dimensions. Between about 17.5 and 13.5 at% carbon (zone II), the parameters c_h and a_h present almost constant values. This zone could be interpreted on the basis of substitutions of carbon atoms by boron atoms in the $B_{11}C$ icosahedral units, since this kind of substitution does not affect the volume of the unit cell significantly. For carbon contents lower than 13.5 at% (zone III), a decrease in carbon concentration yields a decrease in c_h and an increase in a_h .

The results found in zone I and zone II and the intrinsic carbon→boron substitution sequence agree

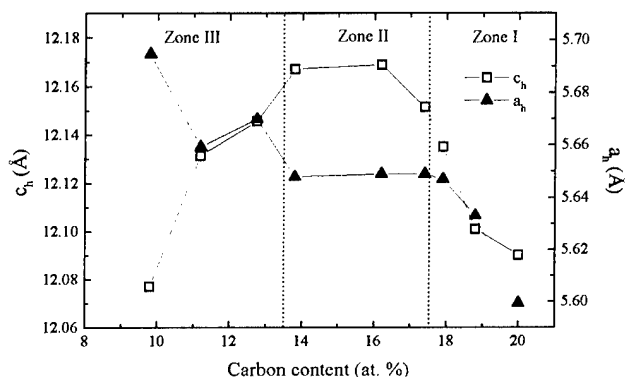


Fig. 4. Hexagonal lattice parameters, c_h and a_h , as a function of carbon content of the boron carbide films.

qualitatively with the evolution of the lattice parameters inferred by Aselage et al. [7]. However, these authors extend zone I to about 13.5 at% carbon and zone II to about 9 at% carbon. Zone III is absent in the results of Aselage et al., probably due to the discrepancy in the measured carbon concentration. When converted to the rhombohedral lattice parameters, the measured values of c_h and a_h in zone III follow the trend reported by Yakel [12] for low carbon concentrations. Unlike the trends observed in zones I and II, the behaviour in zone III seems hard to explain considering only the prolonged replacement of carbon atoms by boron atoms on the main diagonal and/or in the icosahedral units. Therefore, one may attempt to interpret this stage of further carbon depletion by considering the replacement of C–B–C and/or C–B–B chains by a new intericosahedra linking component, whose existence was proposed earlier by Yakel [12] and seems to be consistent with our micro-Raman results, as will be seen in the following discussion.

Fig. 5 shows a series of micro-Raman spectra obtained in the centre region of different boron carbide films. All the Raman spectra were normalised to the broad peak at 700 cm^{-1} and the background was removed by empirical procedures. As a reference, Fig. 5 also displays the micro-Raman spectrum obtained with a bulk standard sample of B_4C with 20 at% carbon. The spectrum of the sample with 18.8 at% carbon (Fig. 5, spectrum a) presents three broad peaks at 720, 840 and 1070 cm^{-1} in the high-frequency region. The broad peak at 1070 cm^{-1} has a clearly developed shoulder between 900 and 1000 cm^{-1} , which can be fitted by two peaks at 930 and 980 cm^{-1} . These peaks match the peaks assigned by Tallant et al. [6] to the breathing modes of the icosahedral $B_{11}C$ structures. In the low-frequency region, spectrum a in Fig. 5 presents three narrower peaks at 320, 480 and 530 cm^{-1} . The peak at 320 cm^{-1} is an experimental artefact which appears in all Raman spectra. The other two peaks at 480 and 530 cm^{-1} were reported by Tallant et al. as due to the

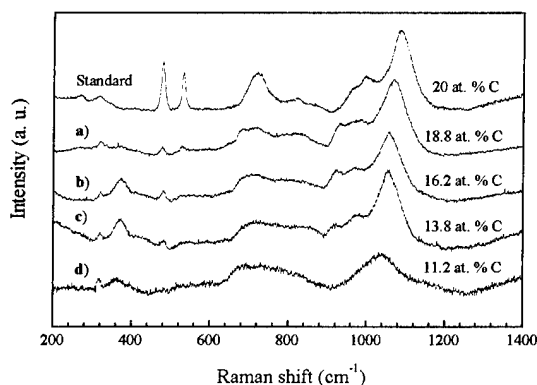


Fig. 5. Raman spectra of boron carbide films with different carbon contents, as measured by EPMA.

vibration modes of C–B–C chains. By comparing this micro-Raman spectrum (Fig. 5, spectrum a) with that of the standard sample (20 at% carbon) it can be observed that the Raman bands between 600 and 1200 cm^{-1} , which are associated with the icosahedral modes, are relatively unaffected by the decrease in carbon content of the samples. However, in the low-frequency region assigned to the vibrations of C–B–C chains, the doublet at 480/530 cm^{-1} decreases in intensity while a new peak at 380 cm^{-1} tends to develop. These results are consistent with replacement, during the initial stages of carbon depletion, of the C–B–C chains along the main diagonal by C–B–B chains, and support the behaviour of the lattice parameters found in zone I of Fig. 4. For the same type of vibrational mode, the less stiff C–B–B chains will have a lower vibration frequency [6,7].

The micro-Raman spectra b and c in Fig. 5 concern films with carbon concentration values of 16.2 and 13.8 at%, respectively. The carbon content of these two samples corresponds to zone II of Fig. 4. By comparing both spectra with Fig. 5, spectrum a we can observe that the peaks at 480 and 530 cm^{-1} become less intense while the 380 cm^{-1} peak is enhanced as the carbon content decreases. Also, in the high-frequency range, the 1070 cm^{-1} peak is shifted to lower frequency, from 1070 to 1055 cm^{-1} , while the intensity of the shoulder of this peak also decreases. These results indicate that the icosahedral B_{11}C units are also affected by the decreasing amount of carbon, leading to B_{12} icosahedra [6,7]. By comparing spectrum b with spectrum c, both related to samples inside zone II of Fig. 4 but with decreasing carbon content, the most affected bands are clearly the high-frequency ones. Therefore, it can be concluded that the most probable carbon \rightarrow boron substitution in zone II occurs in the B_{11}C icosahedra.

Fig. 5, spectrum d was recorded over the centre region of a film with carbon concentration of 11.2 at%, corresponding to zone III of Fig. 4. By analysing this spectrum and comparing it with the ones described above, we can conclude that a further decrease in carbon content leads to a substantial modification of the micro-Raman spectra of boron carbide samples. In the high-frequency region, the peaks at 1055 cm^{-1} become broader, less intense and shift to lower frequency by about 15 cm^{-1} . In the low-frequency region the peaks at 480 and 530 cm^{-1} vanish and the intensity of the broad peak at 380 cm^{-1} decreases strongly, eventually disappearing at lower carbon concentration. These Raman results are a clear indication that, for carbon atomic concentration in zone III, the C–B–C and/or C–B–B chains are strongly affected, and can even disappear at low carbon content values. This seems to be consistent with the hypothesis of Yakel [12]; i.e., the random replacement of the main diagonal chains by a new linking component consisting of four boron atoms

located at the centre of the unit cell in a plane perpendicular to the c_h axis. As a result of the substitution of the C–B–C and/or C–B–B chains by these (B_4) planar groups, Yakel anticipated an increase in the rhombohedral unit cell angle (α_r) with little effect on cell edge (a_r). Our results are in good agreement with these predicted trends: after converting the hexagonal lattice parameters into rhombohedral lattice parameters by using relations (2), the values found in zone III show an increase of α_r of about 2% while the a_r values are almost constant, with a fluctuation of less than 0.15% when the carbon content decreases from 13.5 to 9.8 at%.

4. Conclusions

Boron carbide films were deposited on fused silica substrates by CO_2 laser CVD, using a gas mixture of BCl_3 , CH_4 , H_2 and Ar. The deposited films present good adherence, a fine grain morphology and a mean carbon concentration in the range from 9 to about 20 at%. Growth rates in the range of 2.3 to 9.4 $\mu\text{g s}^{-1}$ were deduced from the thickness profiles of the films. The Arrhenius equation for the deposition rate yields an apparent activation energy of $27.5 \pm 7.8 \text{ kJ mol}^{-1}$, showing that, for the experimental conditions used in this study, the mass transport of reactive gaseous species is the rate-limiting step for boron carbide film growth.

The crystallographic lattice constants, c_h and a_h , were plotted as a function of the carbon content in the films, showing a non-linear dependence for these two quantities. The trends found are consistent with micro-Raman spectra of the samples and allow us to interpret the way in which carbon atoms are preferentially substituted by boron atoms in the lattice as the carbon content is reduced. As the carbon concentration starts to decrease, C–B–C chains are the units preferentially affected, by replacement by C–B–B chains. Between about 17.5 and 13.5 at% carbon, the most affected structures are the B_{11}C icosahedra, leading to the formation of B_{12} structure units. Below 13.5 at% carbon, the C–B–C and/or C–B–B diagonal chains are affected and probably disappear at low carbon concentrations.

Acknowledgement

This work was partially funded by the EU under contract BRE2-CT93-0451. J.C. Oliveira gratefully acknowledges an MSc research grant from JNICT (P).

References

- [1] R.R. Ridgway, Trans. Am. Electrochem. Soc. 66 (1934) 117.
- [2] R. Telle, in: M.V. Swain (Ed.), Structure and Properties of Ceram-

- ics, Materials Science and Technology vol. 11, VCH Publishers, Weinheim, 1994, pp. 173–266.
- [3] M. Olsson, S. Soderberg, B. Stridh, U. Jansson, J.-O. Carlsson, *Thin Solid Films* 172 (1989) 95.
- [4] I. Jiménez, D.G.J. Sutherland, T. van Buuren, J.A. Carlisle, L.J. Terminello, F.J. Himpsel, *Phys. Rev. B* 57 (1998) 13167.
- [5] D. Emin, *Phys. Rev. B* 38 (1988) 6041.
- [6] D.R. Tallant, T.L. Aselage, A.N. Campbell, D. Emin, *Phys. Rev. B* 40 (1989) 5649.
- [7] T.L. Aselage, D.R. Tallant, J.H. Gieske, in: R. Freer (Ed.), *The Physics and Chemistry of Carbides, Nitrides and Borides*, Kluwer Academic Publishers, Dordrecht, 1990, pp. 97–111.
- [8] J.C. Oliveira, M.N. Oliveira, O. Conde, *Surf. Coat. Technol.* 80 (1996) 100.
- [9] J.C. Oliveira, O. Conde, *Thin Solid Films* 307 (1997) 29.
- [10] M.L.F. Paramês, O. Conde, *J. Physique IV, Coll. C 3* (1993) 217.
- [11] B.E. Warren, *X-ray Diffraction*, Dover Publications, New York, 1990.
- [12] H.L. Yakel, *Acta Crystallogr. B* 31 (1975) 1791.

Formation of polycrystalline and microcrystalline composite thin films by codeposition and surface chemical reaction

P.B. Barna ^{a,*}, M. Adamik ^a, J. Lábár ^a, L. Kövér ^b, J. Tóth ^b, A. Dévényi ^c, R. Manaila ^c

^a *Research Institute for Technical Physics and Materials Science, Konkoly Thege 29-33, 1121 Budapest, Hungary*

^b *Institute of Nuclear Research, PO Box. 51, H-4001 Debrecen, Hungary*

^c *National Institute of Materials Physics, RO-76900 Bucharest-Magurele, PO Box MG-7, Romania*

Abstract

The formation mechanisms of nanocrystalline composite structures are discussed, and results on co-deposited material system of C_{60} -Au, C_{60} -Cu as well as Al-SiO_x are presented. Three type of structures are distinguished in the composite films, depending on the concentration of the additive. The decisive structure-forming phenomena are the kinetic segregation of the minority species and the chemical reaction of the deposited components. © 2000 Published by Elsevier Science S.A. All rights reserved.

Keywords: Grain boundary; Impurity; Segregation; Structure

1. Introduction

Because of the novelty of their physical and chemical properties, nanocomposite material structures in thin films have received an increasing amount of interest during the last decades. These structures are two- or multicomponent systems containing additive(s) of varying concentration beside the film material and are generally composed of segregated phases. Their thermal stability has been discussed in the literature in details and attributed to the reduction of the specific grain boundary (GB) energy by the solute species segregated to the GB and/or to the large driving force for segregation [1–3]. Less attention has been paid, however, to the description and understanding of the evolution of nanocrystalline structures during preparation. It should be mentioned that pure elemental polycrystalline solids are thermodynamically unstable with respect to grain growth [1], while nanocomposite structures with a high concentration of additives and, consequently, with a small grain size have a high thermal stability.

The present paper discusses the possible formation mechanisms of as-prepared nanocomposite thin film structures prepared by co-deposition. Experimental results will be presented and referred for the illustration of various nanocomposite structures developed by the

different formation mechanisms. It will be also shown that the chemical reaction among the components taking place on the growth surface can be used for the preparation of artificial structures.

2. Formation mechanism of nanocomposite thin films prepared by codeposition

Nanocomposite thin film structures are produced either by the post-deposition heat treatment of an amorphous mixture phase of the components prepared at a low temperature [4] or in situ (as-prepared form) by the co-deposition (or reactive deposition) of the components at elevated temperatures [5–8]. In the first case, the thermodynamic segregation of the components and, in some material systems, the simultaneous compound formation are the active structure-forming phenomena during the heat treatment. In the second case, the films should be considered as a specific type of polycrystalline thin films due to a higher concentration of active additive(s). The whole process of structure evolution can be described by the fundamental structure-forming phenomena of polycrystalline thin films, and their structure can be interpreted according to the theoretical structure zone models [9–12].

In cases of nanocomposite structures the self-surface mobility of the film material is high, while the self surface

* Corresponding author.

mobility of the additive or its compound phase (e.g. amorphous phase) is low at the given preparation parameters. Consequently, three-dimensional crystals of the film material develop during the condensation while the additive or its compound develop bidimensional layers or a bulk of their tissue phase. The crystals of a nanocomposite thin film of high thermal stability are surrounded and separated by tissue phase(s) [9,13,14]. In one of these types of structures, the tissue phase is situated at the grain boundaries of the polycrystalline film structures, while in the other type, the crystals of the film material are dispersed in the bulk of the tissue phase(s). The tissue phase is in many cases an amorphous compound.

The fundamental structure-forming phenomena of polycrystalline films are the nucleation, the crystal growth, the grain growth by GB migration, the process-induced kinetic segregation of the species of insoluble minority component and the chemical reaction of the codepositing components developing new compound(s) on the growth surface or within the top layer. In the case of nanocomposite structure evolution, the process-induced kinetic segregation of the minority component together with a possible compound formation has a decisive role. This kinetic segregation and the resulting surface-covering tissue layer limiting the growth of film crystals have been shown directly by in-situ transmission electron microscopic experiments [15,16] and analysed in various material systems [6–8,14,17]. The kinetic segregation means that the species of the minority component condensing on the growth surface of the majority component's phase are segregated by the atom-by-atom building process of that phase by replacement and develop either their own or a compound solid phase on the growth surface [18]. When the tissue-forming additive is the minority component, the kinetic segregation develops a high concentration of additive species or, at a higher concentration, a layer covering the growth surface of the film grains (crystals) limiting their growth and coalescence as well. The concentration of the tissue-forming material species in the condensing vapour beam will determine the size of the film crystals at which their surface will be covered completely and their growth will be limited. At this stage, the condensation proceeds by repeated nucleation of the film material on the surface-covering tissue layer, and the whole process repeats itself. The grain size of the film material decreases with increasing concentration of tissue material and can be as low as 1–10 nm. This process is illustrated in Fig. 1(a) and (b). At a low concentration of the tissue forming component ($c_t < 0.05$) [Fig. 1(a)], large film material crystals can grow with segregated tissue material species on their surface. The GBs developing upon the impingement of neighbouring crystals, and incorporating these segregated species, will have a decreased specific energy; therefore, their migration rate is lower than that of pure GBs. The GB migration rate can also be decreased kinetically if the clusters or nuclei

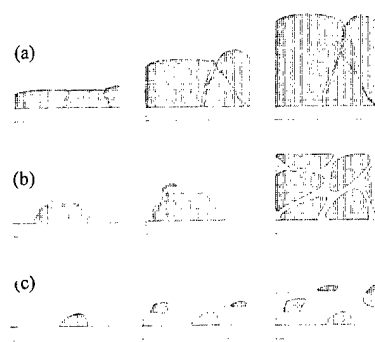


Fig. 1. Schematic figures of composite structure in the case of (a) a low and (b) a high concentration of the minority additive component, as well as in the case of additives giving the majority component (c).

of the segregated phase act as pinning sites for the GBs. At a higher concentration of the tissue forming component (e.g. $0.05 < c_t < 0.4$) [Fig. 1(b)], the surface concentration of segregated species can be enough for the nucleation and development of its own phase forming a layer on the growth surface. This layer can cover the crystals completely and will be incorporated at the developing GBs. The thickness of this layer can increase with increasing concentration of the tissue component.

At a high concentration of the tissue-forming additive ($c_t > 0.4–0.5$), when it is the majority component, the conditions of structure formation can be changed completely. Its matrix will grow primarily, and the species of film material will be segregated on/to the growth surface [Fig. 1(c)]. With this material having a high self-surface mobility, the segregated species will form three-dimensional crystals, which will be incorporated into the bulk of the growing tissue phase. The nanocrystals of the film material will be dispersed in the bulk of the tissue phase, which can also be a compound of the components.

The mechanisms of structure evolution discussed above can describe both the continuous decrease in grain size and the increase in thermal stability of the composite thin films with increasing concentration of the codeposited additive, as detected in various systems [1]. The thermal stability is related namely to the decreased GB energy due to the solute concentration developed by the process-induced kinetic segregation during film deposition at a low additive concentration. At a high concentration, the nanocrystals of the film material are well separated by the tissue phase of the additive. The high thermal stability of these films is related to the large driving force for the segregation [3].

It is easy to understand that the tissue phase is hardly detectable at the low additive concentration either by diffraction techniques or by microchemical analysis.

This structure evolution, based on the kinetic segregation of the minority species, will be shown at the co-deposition of fullerene gold and copper as well as aluminium and SiO_x .

Table 1
Relative oxide and metal content of SiO_x-doped Al films

Sample		Al 2p XPS		Si KLL XAES	
T _{substr} (°C)	Si (at.%)	Metal (%)	Oxide (%)	Metal (%)	Oxide (%)
350	30	44 ± 5	56 ± 5	75–80	20–25
450	30	37 ± 5	63 ± 5	95–100	0–5
450	50	28 ± 5	72 ± 5	95–100	0–5

3. Experimental

The films were prepared by thermal evaporation of C₆₀ Au and Cu as well as Al and SiO_x at a background pressure of 10^{−4} Pa. The composition of the films was controlled by the deposition rates of the components measured by a quartz crystal monitor. An evaporated a-C layer was supported by transmission electron microscopic (TEM) microgrids, air-cleaved NaCl, KCl and mica single crystals for thin films, while thermally oxidised Si single crystals for cross-sectional TEM investigation, X-ray photoelectron spectroscopic (XPS), Auger electron spectroscopic (AES) and X-ray diffraction (XRD) measurements of thick films were applied as substrates. Deposition temperatures were selected between room temperature and 450°C. The structure of the films was investigated by plan-view and cross-sectional high-resolution and analytical TEM, X-ray diffraction, as well as by ESCA and AES.

The results of these detailed investigations have been published recently and are referred to. The present paper contains complementary results confirming the coexistence and distribution of different phases and the role of chemical reaction in their development.

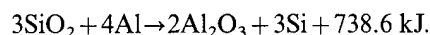
4. Results and discussion

4.1. Codeposited Al–SiO_x films

At substrate temperatures lower than 250°C Al–SiO_x composite structures form. By increasing the concentration of SiO_x up to 50 at% Si, the SiO_x is segregated by the growing Al crystals, and a polycrystalline structure with decreasing grain size will develop. In that case, the SiO_x tissue phase is situated at the grain boundaries. At concentrations of SiO_x > 50 at.%, the tissue of SiO_x grows and the Al species are segregated, forming Al micro- and nanocrystals dispersed in the bulk of the SiO_x tissue phase [14].

At deposition temperatures higher than 300°C, a completely new process sets in, the decomposition of SiO_x by the codeposited Al, forming elemental Si and aluminium oxide according to the reaction [19] taking

place during the deposition on the growth surface



This reactive deposition results in the formation of a composite structure of crystalline Al and Si with amorphous Al₂O₃ (and SiO_x) tissue phase(s). By increasing the concentration of SiO_x, increasing amounts of Al are consumed by the reaction. The concentration of metallic Al decreases while that of elemental Si increases, as indicated by the selected area electron diffraction patterns published in [14]. The XPS and XAES analysis of the samples provided information on the oxidation states of Al and Si. Spectra of the Al 2p XPS measurements are shown in Fig. 2. The peaks at the lower kinetic energy correspond to the oxide, whereas the peaks at a higher kinetic energy correspond to the metallic phase. The oxidised parts of Al and Si in the composite films are listed in Table 1. According to these results, Al is consumed more rapidly at a higher temperature.

4.2. Codeposited Au–C₆₀ and Cu–C₆₀ films

In these experiments, C₆₀ and Au as well as Cu were codeposited at room temperature when the Au and Cu were the minority components. The development of metal nanocrystals in the bulk of C₆₀ matrix and the interaction between Au and C₆₀ were investigated. The X-ray diffraction patterns of films with Au atomic concentrations higher than 1.5 at.% detected the presence of finely dispersed metallic Au particles. The FCC

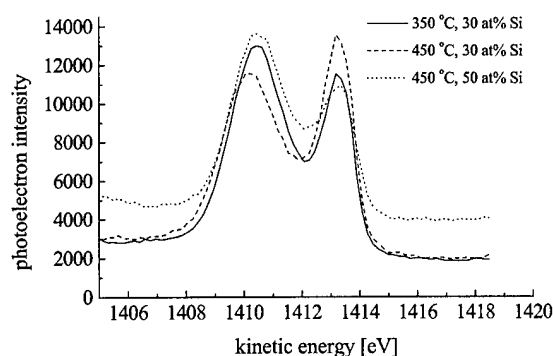


Fig. 2. Al 2p XPS spectra of SiO_x doped Al films prepared by codeposition.

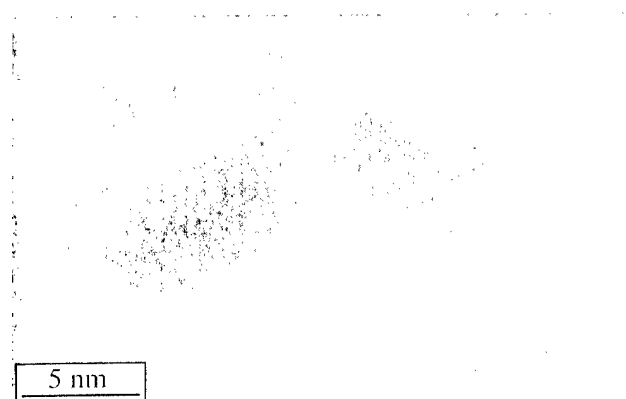


Fig. 3. HR-TEM image of crystalline Cu particles embedded in the amorphous C_{60} matrix.

lines of C_{60} fullerite, as well as two broad maxima close to the positions of the (111) and (200) lines of Au, were present in the diffraction pattern [17].

The measured C_{60} lattice parameter fits well with the reported value $a_{C_{60}} = 1.419$ nm. The diffraction patterns with two very broad and partially superposed maxima show the presence of finely dispersed Au. The lattice parameter values of the Au phase in films with 1.65 and 4.5 at.% Au [0.40725 nm and 0.40552 nm from (111) while 0.42078 nm and 0.41694 nm from (200)] are at variance, much beyond the experimental precision. These observations suggest that long-range order is heavily affected in the Au nanoparticles, due to the very high density of local lattice distortions. Thereby, the structure of Au is closer to quasi-amorphous than to the crystal lattice affected by static phonon disorder. The formation of nanocrystalline, distorted Au in these co-deposited Au- C_{60} films could be attributed to the Au- C_{60} interface interaction, in the first place to the electron transfer from Au to fullerene. Fig. 3. shows the lattice fringe image of Cu nanocrystals in the C_{60} -Cu composite film with 5 at.% Cu concentration.

5. Conclusions

The codeposition of immiscible additive(s) with the film material at well selected preparation parameters is an important tool for tailoring as deposited artificial thin film composite structures. The characteristics of these structures of good thermal stability is that the nanocrystals are well separated by a tissue phase. Two ranges of concentration of the tissue-forming component can be distinguished in which the structure evolution is completely different. This is related to the conditions of the kinetic segregation of the minority component during the growth of the film. When the tissue-forming component is the minority component, the species of the tissue are segregated by the growing crystals of the film material. The segregated tissue species develop a layer on the surface of the growing crystals and at the grain bound-

aries. In the resulting structure, the crystals of the film material are separated by grain boundaries covered by the tissue phase. When the film material is the minority component, the phase of the tissue material grows primarily segregating the species of the film material. These segregated film material species will form the three-dimensional crystals. It is important to note that both the nanocrystals of the film material and the tissue phase can develop by the chemical reaction(s) among the codeposited components on the growing surface or within the surface layers, as in the cases of the structures composed of Si (and Al) nanocrystals and Al_2O_3 (and SiO_x) tissue phase with codeposition of Al and SiO_x .

Acknowledgements

The authors thank G. Glázer and E. Hajmássy for their technical assistance. This work has been financially supported by the Hungarian National Foundation OTKA under contract No. T015878.

References

- [1] J. Weissmüller, W. Krauss, T. Haubold, R. Birringer, H. Gleiter, *Nanostruct. Mater.* 1 (1992) 439.
- [2] T.R. Marlow, C.C. Koch, *Mater. Sci. Forum* 225 (1996) 227–295.
- [3] A. Niederhofer, P. Nesládek, H.-D. Männling, K. Moto, S. Veprek, M.J. Ilek, *Surf. Coat. Technol.* (1999) in press.
- [4] D. Das, *Solid State Phenom.* 44 (1995) 227.
- [5] R. Hayashi, M. Yamamoto, K. Tsunetomo, K. Kohno, Y. Osaka, H. Nasu, *Jpn. J. Appl. Phys.* 29 (1990) 756.
- [6] P.B. Barna, M. Adamik, U. Kaiser, S. Laux, K.A. Pischow, M. Pulliainen, H. Bangert, *Surf. Coat. Technol.* 100–101 (1998) 72.
- [7] M. Adamik, P.B. Barna, I. Tomov, *Thin Solid Films* 317 (1998) 64.
- [8] P.B. Barna, M. Adamik, U. Kaiser, H. Hobert, *J. Noncryst. Solids* 227–230 (1998) 1063.
- [9] P.B. Barna, in: L. Eckertova, T. Ruzicka (Eds.), *Diagnosis and Application of Thin Films*, Inst. Phys. Publ., Bristol, 1992, p. 295.
- [10] P.B. Barna, M. Adamik, in: F.C. Mataracotta, G. Ottaviani (Eds.), *Science and Technology of Thin Films*, World Scientific, Singapore, 1995, p. 1.
- [11] P.B. Barna, M. Adamik, *Protective Coatings and Thin Films: Synthesis — Characterisation and Application*, Y. Pauleau, P.B. Barna (Eds.), NATO ASI Series, 3 — High Technology Vol. 21, Kluwer Academic, Dordrecht, 1997, p. 279.
- [12] P.B. Barna, M. Adamik, *Thin Solid Films* 317 (1998) 27.
- [13] S. Veprek, R.S. Reiprich, *Thin Solid Films* 268 (1996) 64.
- [14] P.B. Barna, M. Adamik, J.L. Lábár, *Proc. 4th Special Symp. Advanced Materials*, Nagoya, Japan, 1998.
- [15] P.B. Barna, Ph.D. thesis, Budapest, 1966.
- [16] J.F. Pócsa, Á. Barna, P.B. Barna, I. Pozsgai, G. Radnóczy, *Jpn. J. Appl. Phys.* 2 (1) (1974) 525.
- [17] A. Dévényi, R. Manaila, A. Belu-Marian, D. Macovei, M. Manciu, E.M. Popescu, M. Tanase, D. Fratiloiu, N.D. Mihai, P.B. Barna, J. Lábár, G. Sáfrán, A. Kovács, T. Braun, *Thin Solid Films* 335 (1998) 258.
- [18] P.B. Barna, G. Radnóczy, F.M. Reicha, *Vacuum* 38 (1988) 527.
- [19] R.J. Blattner, A.J. Braundmeister Jr., *J. Vac. Sci. Technol.* 20 (1982) 320.

Early stage growth structure of indium tin oxide thin films deposited by reactive thermal evaporation

A. Amaral ^{a,b,*}, P. Brogueira ^b, C. Nunes de Carvalho ^{a,c}, G. Lavareda ^{a,c}

^a Centro de Física Molecular, Complexo Interdisciplinar do IST-UTL, Av. Rovisco Pais, 1049-001 Lisboa, Portugal

^b Departamento de Física, IST-UTL, Av. Rovisco Pais, 1049-001 Lisboa, Portugal

^c Departamento de Ciências dos Materiais, FCT-UNL, Quinta da Torre, 2825-114 Caparica, Portugal

Abstract

The initial stage of indium tin oxide (ITO) thin film growth, deposited by reactive thermal evaporation (RTE), was investigated using atomic force microscopy (AFM) measurements. Five ITO thin films were deposited by RTE of an In:Sn alloy in the presence of added oxygen on heated oxide substrates ($T_s = 440$ K), with film thickness as the deposition variable. Surface imaging as well as statistical analysis were applied to obtain information about the structure of the samples from AFM measurements. In the initial stages of the deposition it was possible to distinguish the presence of individual features randomly distributed with characteristic dimensions of up to 100 nm. Subsequently, the ITO films appeared to grow uniformly as a continuous film deposited over the entire surface. As the ITO films were formed under the low-nucleation barrier regime, which involved small critical nucleus with low positive free energy of formation, the films consisted of many small aggregates. The small minimum stable size of the aggregates and the high nucleation frequency gave rise to a fine-grained film. The grain size of the ITO films increased as the film thickness increased until a maximum value of $t = 80$ nm was reached. © 2000 Elsevier Science S.A. All rights reserved.

Keywords: Atomic force microscopy; Grain size; Indium tin oxide; Surface roughness; Thin films growth

1. Introduction

Indium tin oxide (ITO) thin films, as well as the other transparent conductive oxides (SnO_2 and ZnO) are often used as transparent electrodes and wave-selective coatings for their ease of efficient doping. This characteristic, along with good etchability, hardness and good adherence to many types of substrates, permits a wide range of applications of ITO in a variety of optoelectronic/photovoltaic devices, liquid crystal displays, etc. [1–3]. The electrical characteristics of ITO thin films are dependent on the presence of oxygen vacancies and substitutional tin created during or after growth. ITO are also valued because their fundamental properties (optical, electrical and structural) can be controlled by deposition techniques which employ a careful optimization of the main production parameters for reproducible properties. ITO thin films can be prepared by different deposition techniques: reactive thermal evaporation (RTE) [4], r.f. sputtering [5], electron beam evaporation [6] and spray pyrolysis [7]. Our work

advances a further step in the systematic study of ITO films produced by RTE of an In:Sn alloy in the presence of oxygen [8]. The initial stage of ITO film growths were studied by means of AFM measurements. Surface imaging, as well as statistical analysis, was used to

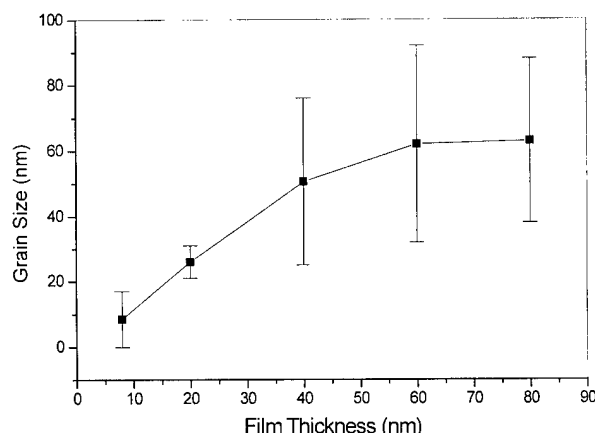
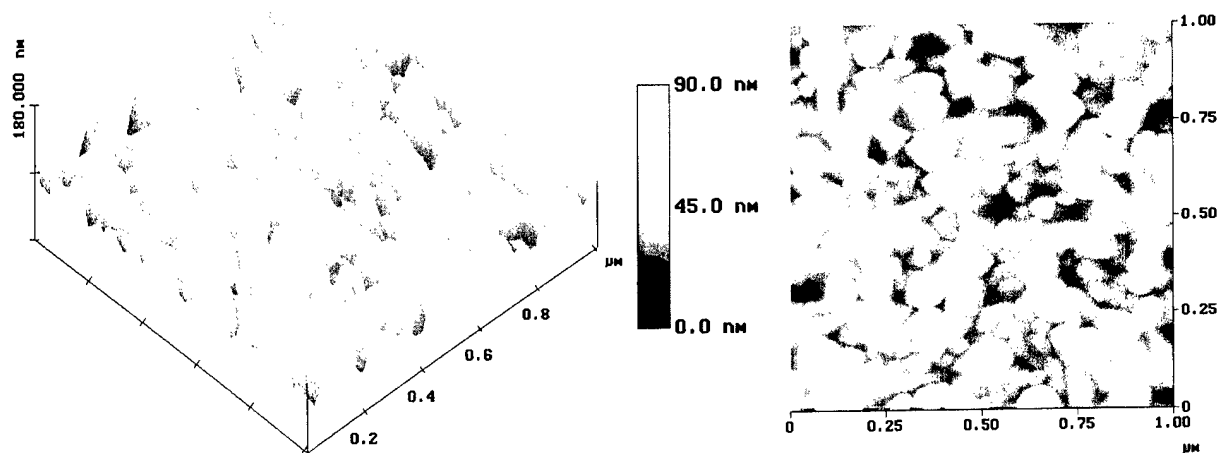


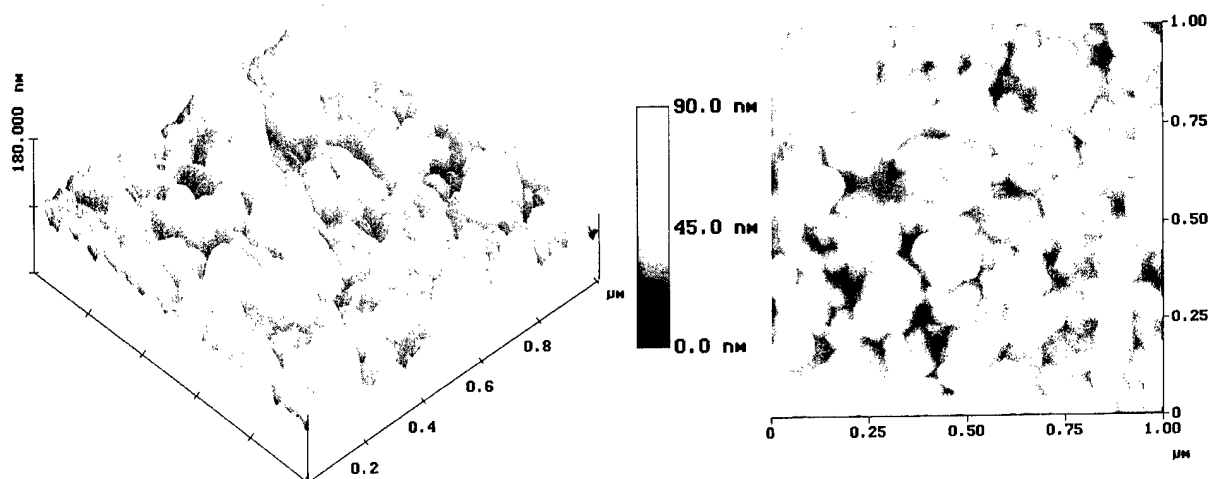
Fig. 1. Variation of the grain size with film thickness.

* Corresponding author.

Sample A



Sample B



Sample C

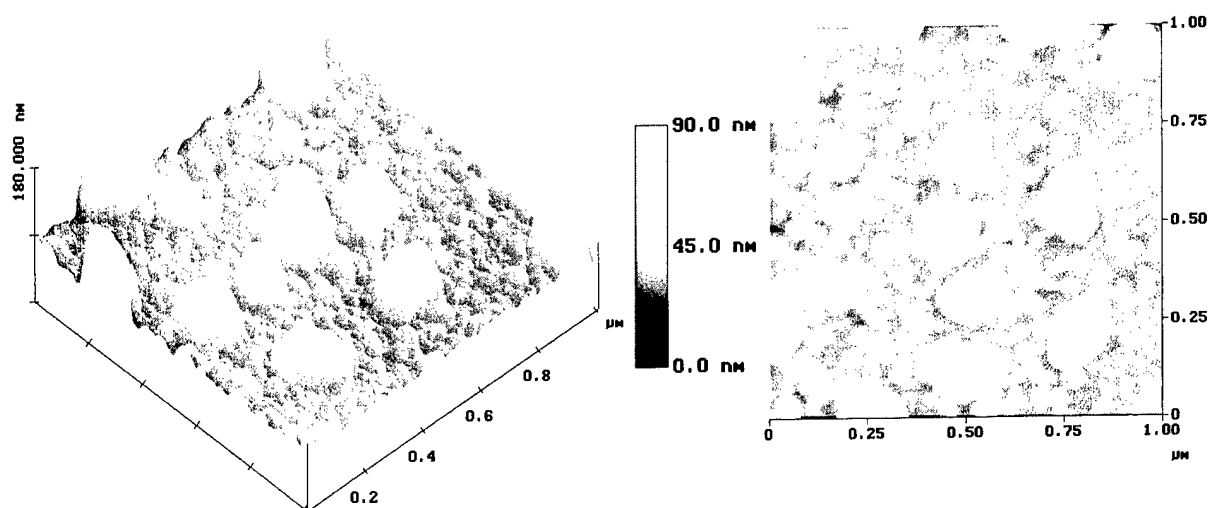
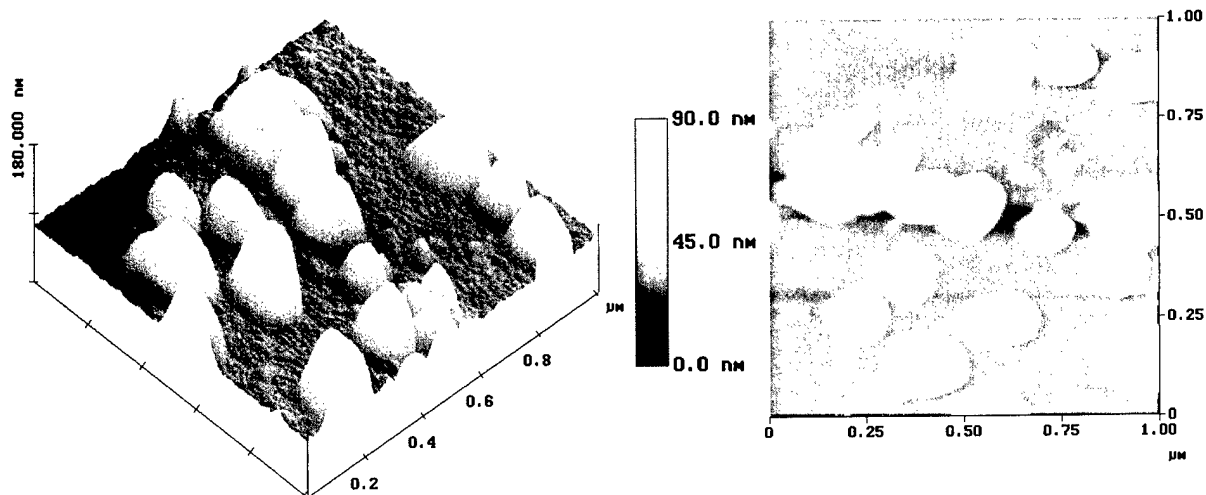


Fig. 2. (a) 3-D and (b) top view AFM surface imaging using tapping mode of ITO thin films: A 80 nm; B 60 nm; C 40 nm; D 20 nm; and E 8 nm. Scanned areas: $1 \times 1 \text{ mm}^2$. Height color scale: 90 nm.

Sample D



Sample E

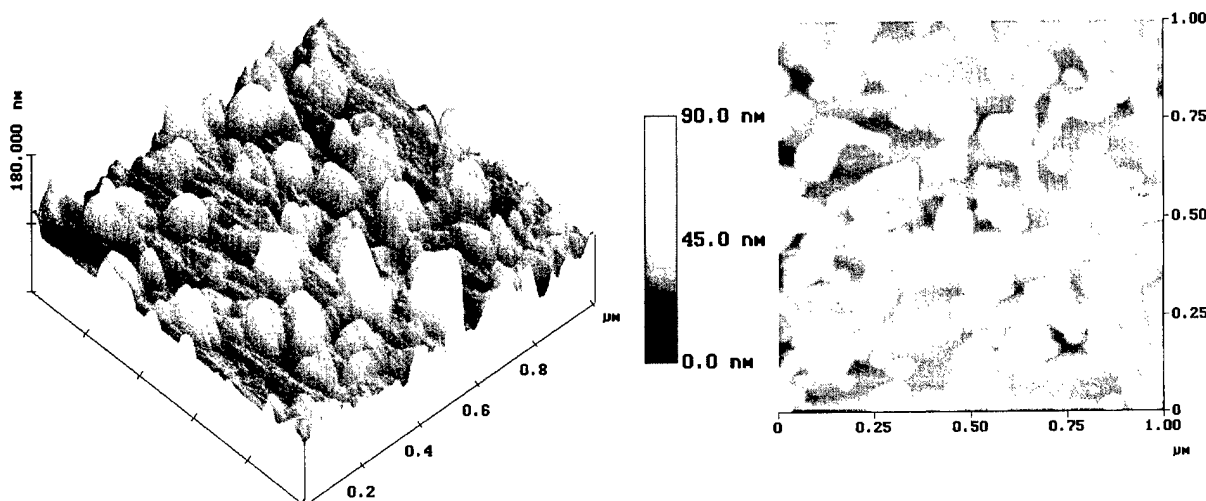


Fig. 2. (continued)

characterize the local and overall roughness and the mean grain size of the deposited films.

2. Experimental procedures

2.1. Sample preparation

The $\text{In}_2\text{O}_3\text{-Sn}$ films were deposited by RTE on $2.5 \times 2.5 \text{ cm}^2$ glass substrates. A Balzers tungsten boat was used for the alloy evaporation and the source–substrate distance was approximately 30 cm. To measure substrate temperature accurately, a thermocouple was embedded in the dummy glass substrates. Five samples of varying film thickness, $t=8\text{--}80 \text{ nm}$, were prepared. The experimental conditions found to optimize the ITO thin films properties[8] were: substrate temperature,

$T_s=440 \text{ K}$; deposition pressure, $p \approx 6 \times 10^{-2} \text{ Pa}$; alloy chemical composition of 90% In:10% Sn; and deposition rate, $r_d=0.1\text{--}0.2 \text{ nm/s}$.

2.2. Sample characterisation

The transmittance of the ITO thin films was measured with a Shimadzu UV-3100 spectrophotometer equipped with an integrating sphere attachment (wavelength range: $400 \text{ nm} \leq \lambda \leq 800 \text{ nm}$) without a bare substrate as the optical reference. The sheet resistance was measured using a Veeco FPP-500 four point probe. A quartz crystal thickness monitor (Edwards FTM5) monitored the thickness of the films. The AFM of the ITO films was performed by a Multimode with a Nanoscope IIIa controller from Digital Instruments. The imaging was performed in *tapping mode* using commercial tapping

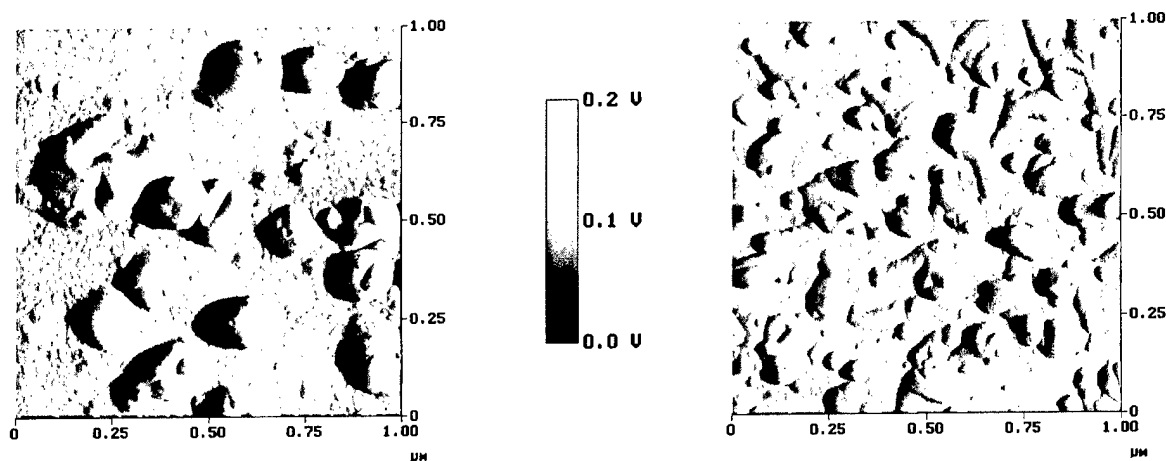


Fig. 3. Amplitude imaging of samples D and E. Scanned areas: $1 \times 1 \text{ mm}^2$. Height color scale: 0.2 V.

mode etched silicon probes and a $10 \times 10 \text{ μm}^2$ scanner. In tapping mode, a stiff crystal silicon probe at the end of a cantilever was oscillated to its resonant frequency (200–400 kHz) so that the tip possessed sufficient energy to break free of surface tension forces during the scan. The feedback loop kept the vibrating cantilever at a constant amplitude by changing the height of the sample to maintain a constant tip surface interaction throughout the measurement. High values of the feedback gains allowed minimal changes in the tip vibrational amplitude while tracking the sample surface to collect accurate height data. Images consisted of raster-scanned, electronic renderings of sample surfaces. The images were obtained with a resolution of 512×512 pixels. All measurements were performed on $1 \times 1 \text{ μm}^2$ areas under ambient conditions. The Multimode was mounted on an optical table in order to isolate vibration. The root mean square (rms) roughness, R_q , of the sample surface was calculated from,

$$R_q = \sqrt{\sum_i (z_i - \bar{z})^2 / N}, \quad (1)$$

where \bar{z} is the average height of the scanned area and z_i is the height value of each point. The typical diameter of the grains was measured with the AFM software after choosing a non-biased cross-section of the sample by putting the cursors at the identified grain boundaries and simultaneously measuring the horizontal distance between the cursor positions.

3. Results

Fig. 1 shows the mean grain size, d , as a function of the film thickness, t , for the five ITO samples obtained under the deposition conditions described above. The mean grain size increased from 10 to 65 nm as the film thickness increased from 8 to 80 nm. The major variation of the grain size values occurred in the film thickness

range $t = 10\text{--}40 \text{ nm}$. For a thickness higher than 70 nm the mean grain size value remained practically constant.

Table 1 summarises the deposition conditions, as well as some of the optical and electrical properties characteristic of the five ITO samples. For the thickest sample, the wavelength range of the transmittance measurements was insufficient for an accurate calculation of $\langle T \rangle$, which is affected by the interference fringes. An upper value was estimated.

Fig. 2 shows 3-D and top view AFM images of five ITO thin films with different thickness: A - 80 nm; B - 60 nm; C - 40 nm; D - 20 nm; and E - 8 nm. A 3-D AFM image of sample A shows two different scales. One furnished by a random distribution of aggregates with mean grain size around 100 nm, and the other consisting of a smoother texture lying between these aggregates with a structure characterised by a mean grain size value of 63 nm, with a calculated local surface roughness, R_q , of 7.923 nm and a overall value, R_q , which includes the coarser structure of 14.410 nm. In sample B we observe the same coarse structure as in sample A, while the underlying structure now shows a decrease in the average size of the grain (62 nm). The local surface roughness ($R_q = 7.269 \text{ nm}$) has decreased slightly. Inversely, the total R_q has increased up to 16.170 nm. The topography of sample C shows a decrease in the grain size of the underlying structure of up to $\sim 50 \text{ nm}$, while keeping a roughly similar nuclei density. The local surface roughness, R_q , is now 5.055 nm and the total R_q is 20.295 nm. Sample D

Table 1
Optical and electrical properties of ITO thin films

Sample	E	D	C	B	A
$\langle T \rangle$ (%)	88	86	83	75	<80
t (nm)	8	20	40	60	80
R_s (Ω/sq)	1.8×10^5	9×10^2	3.8×10^2	2×10^2	1.2×10^2

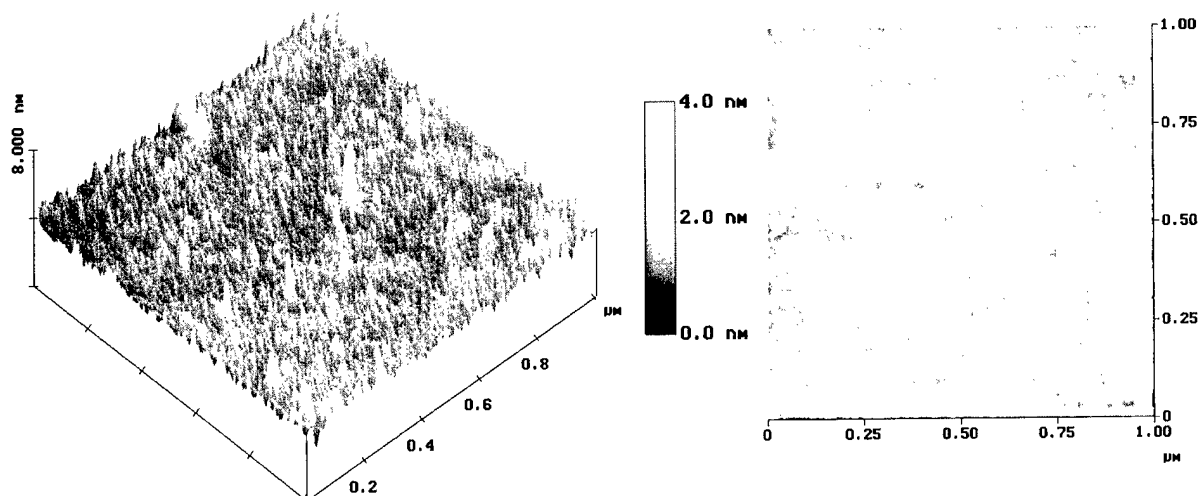


Fig. 4. 3-D and top view AFM surface imaging using tapping mode of the bare glass substrate.

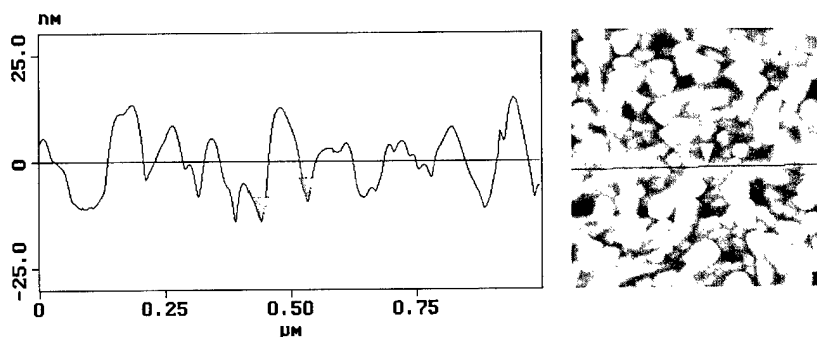


Fig. 5. Cross-section of the sample A.

exhibits the presence of individual nuclei with an average diameter of the order of 26 nm. The calculated local surface roughness, R_q , is 2.299 nm and the total R_q is 23.880 nm. Sample E exhibits a fine-grained underlying film. These crystalline-like features exhibit diameters lower than 17 nm. The calculated local surface roughness, R_q , is 1.8 nm while the total R_q is 18.993 nm. The presence of the big spikes, when taken together with the thinner grained underlying structure of samples D and E produces, under flattening of the sample, an oscillatory output which is spurious. Consequently, it is useful to observe the amplitude image, i.e. the sample error signal, in which this artifact is absent. Fig. 3 shows the amplitude image of samples D and E.

Fig. 4 shows 3-D and top view AFM images of the bare glass substrate. Local fluctuations around 5 nm were observed on the 3-D AFM image.

Fig. 5 shows the cross-section of sample A. The position of the pointers was chosen to allow the determination of the diameter of the identified grain.

4. Discussion

To study the initial stage of ITO growth, the evaporation was done without the use of a shutter. The surface

topography analysis of the samples suggests that, after starting to heat the crucible, the fusion of the material was incomplete but the energetic balance allowed the release of chunks of material and later deposition on the substrate. These solid aggregates were responsible for the features seen in the AFM topographic imaging with characteristic dimensions of up to 100 nm on nominal thickness films of about 7 nm. To oxidize the film it was necessary for the presence of a monolayer of a metal film to be deposited on the substrate, to induce the chemical bonding between the oxygen in gas phase and the metal [9]. It appears that these aggregates were able to induce this oxidation without decreasing the average transmittance of the sample due to an a posteriori oxidation process which took place on the heated substrate to 440 K. After the initial heating of the crucible, the film deposition became uniform on the surface and the pre-deposited material was oxidized. Experiments on post-deposition annealing, in the presence of oxygen, of ITO samples deposited at low substrate temperature showed a significant increase of the mean transmittance $\langle T \rangle$, suggesting the presence of bulk diffusion of oxygen in thick ITO films [10]. As the thickness increased, the initial features began to merge in the deposited ITO matrix, as was verified by the

diminution of the total surface rms roughness of the thicker samples (in contrast with the CVD material growth).

It is also possible to attribute the formation of these aggregates to the presence of a spiky surface on the bare glass, as observed in the AFM imaging, which could induce local nucleation. However the PVD-like characteristics of RTE deposition do not favor this interpretation.

5. Conclusions

The initial stage of ITO thin film growth deposited by RTE was investigated by means of AFM measurements. We found that in the initial stages of the deposition it was possible to distinguish the presence of individual features randomly distributed, with characteristic dimensions around 100 nm. Subsequently the ITO films appeared to grow uniformly as a continuous structure deposited over the entire surface. The mean grain size increased as the film thickness increased. The maximum grain size value of 63 nm was reached for film thickness $t=80$ nm. Local roughness increased, and total roughness decreased as the sample thickness increased.

Acknowledgements

This work was supported by Fundação para a Ciência e Tecnologia through Pluriannual Contracts with CFM (IST) and by project PRAXIS3/3.1/CEG/2620/95.

References

- [1] G. Lavareda, E. Fortunato, C.N. Carvalho, R. Carrapa, R. Martins, Proc. Int. Semiconductor Device Research Symposium Conference (ISDRS) 1 (1993) 161.
- [2] R. Keough, Vacuum Solutions 4 (1998) 31.
- [3] I. Rusing, M.H. Godinho et al., J. Polym. Sci.: Part B Polym. Phys. 32 (1994) 1907.
- [4] W. Spence, J. Appl. Phys. 38 (1967) 3767.
- [5] R. Tueta, M. Braguier, Thin Solid Films 80 (1981) 143.
- [6] R. Banerjee, D. Das, S. Ray, A. Batabyal, Solar Energy Materials 13 (1985) 11.
- [7] W. Sieffert, Thin Solid Films 121 (1984) 275.
- [8] N. Carvalho, O. Figueiredo, E. Fortunato, R. Martins, L. Guimarães, in: I. Solomon, B. Equer, P. Helm (Eds.), Proc. 8th EC-PVSEC, Italy (1988) 801.
- [9] R.W. Hewitt, N. Winograd, J. Appl. Phys. 51 (1980) 2620.
- [10] H. Kobayashi, T. Ishida, K. Nakamura, Y. Nakato, H. Tsubomura, J. Appl. Phys. 72 (1992) 5288.

Vacuum arc deposition of Ti coatings

B. Straumal^{a,b,*}, W. Gust^a, N. Vershinin^{b,c}, R. Dimitriou^d, E. Rabkin^e

^a Institut für Metallkunde, Seestrass 92, D-70174 Stuttgart, Germany

^b I.V.T. Ltd, PO Box 47, 109180 Moscow, Russia

^c SONG Ltd., PO Box 98, Chernogolovka, Moscow District, 142432, Russia

^d Pechiney CRV, BP 27, 38340 Voreppe, France

^e Technion — Israel Institute of Technology, Department of Materials Engineering, Haifa 32000, Israel

Abstract

Ti coatings on silicate glass substrates have been produced using a nonfiltered vacuum arc deposition technique. The dependence of the deposition rate and average roughness R_a on the discharge current and distance from the cathode was investigated. The deposition rate decreases monotonically with the distance and increases nonlinearly with the discharge current. R_a also increases with increasing discharge current. R_a decreases with the distance, showing a transition area between the microparticle-containing and microparticle-free Ti films. R_a depends strongly on the number of microparticles. A linear dependence of R_a on the distance was obtained only for substrates far enough from the cathode. For substrates close to the cathode the dependence is governed by the microparticle density. Therefore, the roughness can be changed in a very broad interval by changing the deposition parameters. © 2000 Elsevier Science S.A. All rights reserved.

Keywords: Deposition rate; Roughness; Titanium; Vacuum arc deposition

1. Introduction

Titanium is a transition metal mainly characterized by its high specific modulus and its good resistance to corrosion. Ti coatings are mainly attractive owing to their biocompatibility, which makes them reliable for the design of medical instruments or implants in the human body. The chemical and morphological modification of metallic implant materials has been shown by in vivo tests to influence their biocompatibility. The control of the surface roughness is an important factor for the implants [1,2]. Rougher surfaces have been shown to result in firmer bone fixation [3,4]. Vacuum arc deposition of titanium, though less documented than sputter deposition, offers a wide range of microstructural and morphological properties for coatings [5,6]. The cathodic arc plasma deposition process enables one to generate a much higher degree of ionization than other ion-plating processes, providing a better film adhesion and higher densities. Some 30 to 80% of the material that is evaporated from the cathode surface is ionized,

including multiply charged states [7,8]. The kinetic energies of the ions typically are in the 10 to 100 eV range. These features result in deposits of superior quality in comparison with other physical vapour deposition processes. High deposition rates can be achieved with an excellent coating uniformity. As a result of the arc process, microparticles are emitted at a very high velocity towards the substrate and contribute to the film formation. Though often considered as a disadvantage for applications in optics and electronics, the microparticles also represent a good way to create films of a given roughness [9]. The following study presents the main coating characteristics of vacuum arc deposited titanium on silicate glass as a function of deposition parameters. It gives a quantitative overview of the deposition rate and roughness values available for widely used titanium coatings.

2. Experimental

The vacuum arc apparatus used in this work is described elsewhere [10]. The facilities for magnetic filtering of the microparticles were not used in this work. Ti was deposited on a $450 \times 470 \times 4$ mm³ silicate glass

* Corresponding author. Tel.: +49-711-121-1276;
fax: +49-711-121-1280.

E-mail address: straumal@mf.mpi-stuttgart.mpg.de (B. Straumal)

plate. The glass plate was positioned horizontally, at the middle of the round cathode, perpendicular to the cathode surface plane, 50 mm away from it. The round cathode has a diameter of 180 mm. Before coating, a grid was drawn on the glass surface with the aid of an overhead pen. The grid provided a set of nodes located at a definite position relative to the cathode surface. The grid also acted as a mask and its removal after deposition made it possible to determine of the film thickness at each node. After deposition, the plate was cut into $40 \times 30 \text{ mm}^2$ samples suitable for the measurements. This experimental procedure ensures the similarity of the process conditions for each sample, the absence of sample shadowing and a large quantity of samples through one experiment. All data given in this work were obtained on the top surface of the substrate. The vacuum arc source voltage was maintained constant at $U = 22 \text{ V}$ while the discharge current I varied ($I = 110, 140, 160, 175$ and 220 A). No bias was applied to the substrate. The coating time t was the same for all samples ($t = 420 \text{ s}$) except for $I = 160 \text{ A}$ ($t = 240 \text{ s}$). To prevent overheating of the surfaces, the 420 s coating process was divided into two coating periods (210 s each) separated by a 60 s interruption.

The sample surface was observed using a Zeiss Axiophot optical microscope and an Autoprobe CP AFM atomic force microscope (AFM) from Park Scientific Instruments. The thickness of the coatings d was measured with the aid of both a Taylor–Hobson Polystep profilometer and the AFM. During the thickness determination using profilometry six consecutive measurements of the step height between the coated and non-coated part were averaged. The average roughness R_a also was derived from profilometry measurements. The AFM was operated in the contact mode, using sharpened gold-coated microlevers with a nominal radius of the tip curvature of less than 20 nm. For the film thickness measurements $50 \times 50 \mu\text{m}^2$ scans were positioned in such a way that the border between coated and uncoated glass was approximately in the middle of the scanned area. The thickness was then determined as an average from four line scans that were not disturbed by the particles or contaminations at the coated/uncoated glass border. The profilometer thickness measurements were known within a 5% accuracy, and the AFM enabled one to measure the thickness with an accuracy of 5 nm.

3. Results and discussion

Figs. 1–3 display the microstructure of the Ti coatings. During vacuum arc deposition, the flux of material coming from the cathode to the substrate contains multiply charged ions and microdroplets [11]. The microdroplets are thought to be ejected from the liquid

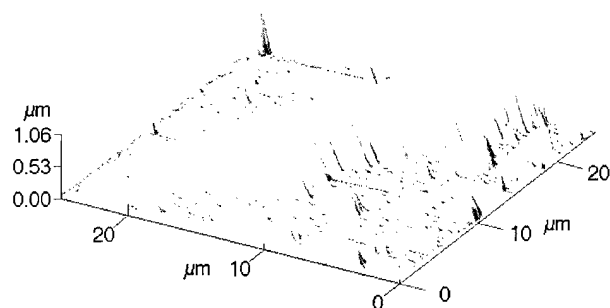


Fig. 1. AFM low magnification micrograph of vacuum arc deposited Ti coating on the silicate glass substrate ($L = 80 \text{ mm}$, $I = 160 \text{ A}$, $t = 240 \text{ s}$) showing the 'tail' of a big droplet, smaller droplets and smooth film formed from ionic flux.

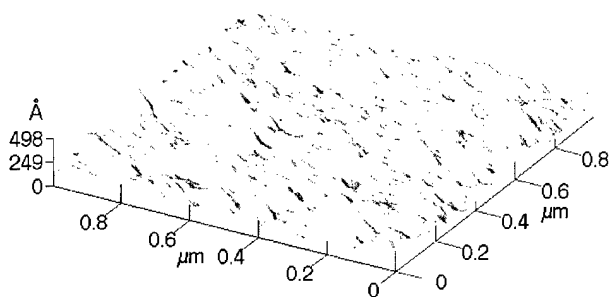


Fig. 2. AFM high magnification micrograph of vacuum arc deposited Ti coating on the silicate glass substrate ($L = 80 \text{ mm}$, $I = 160 \text{ A}$, $t = 240 \text{ s}$) showing the topography of a film between droplets.

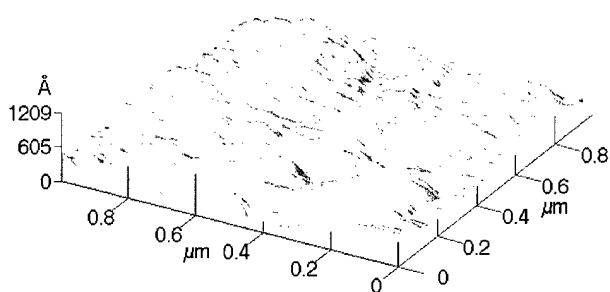


Fig. 3. AFM high magnification micrograph of vacuum arc deposited Ti coating on the silicate glass substrate ($L = 80 \text{ mm}$, $I = 160 \text{ A}$, $t = 240 \text{ s}$) showing the surface topography of a droplet.

pool of the cathode (created by the arc impact) by the ionic flux accelerated back towards the target [12]. The microdroplets are usually emitted at low angles relative to the cathode surface [13], but some are also found normal to the cathode surface [14]. Their shape depends mostly on the angle between their trajectory and the substrate plane. In our case, the microdroplets fly almost parallel to the substrate plane. Their resulting shape is thus ellipsoidal and can be characterized by their aspect ratio. The surface morphology is driven mainly by the microparticle density. Close to the cathode, the Ti film has a very rough surface made of overlapping microparticles. In this zone, the dark grey coating has a poor

adherence to the glass substrate. The droplets have various sizes and shapes, from nearly circular to elongated. Further away from the cathode, both droplets and a homogeneous film formed by deposition of individual ions can be clearly seen. The microdroplets are still of various sizes but their shape is more uniform. The average aspect ratio is higher and leads to a standard elongated shape. In the AFM picture made with a low magnification the 'tail' of a large microdroplet is visible together with some smaller particles on the rather smooth surface of a film formed by the flux of individual ions. The homogeneity in droplets shape and direction reveals a better uniformity of the particle flux compared with the near-cathode zone. High-magnification AFM pictures show the smooth film between the droplets (Fig. 2) and the surface morphology of the microdroplets (Fig. 3). The average roughness R_a measured profilometrically on the length of 80 μm includes both big and small droplets and a smooth surface among them and, therefore, is rather high (about 350 nm on the sample shown in Figs. 1–3). R_a measured microscopically is much lower (3.6 nm for the location shown in Fig. 2 and 5.5 nm for Fig. 3). If the deposition process is carried on, the microdroplets become a part of the coating. Their structure may or may not differ from the film itself [9,15]. At the largest distance from the cathode, the microdroplets occurrence is very low and the coating consists of a homogeneous film formed by deposition of individual ions and which can be considered as microparticle free. The AFM measurements reveal that the film among the particles is atomically smooth ($R_a = 1 \text{ nm}$) at $L > 200 \text{ mm}$.

The dependence of deposition rate R_d on the transverse distance d_t is shown in Fig. 4 for different distances $L = 170$ and 230 mm from the cathode. Both curves are symmetric, having the maximum at the middle of the substrate where $d_t = 0$. R_d decreases monotonically with increasing d_t . The dependence of deposition rate

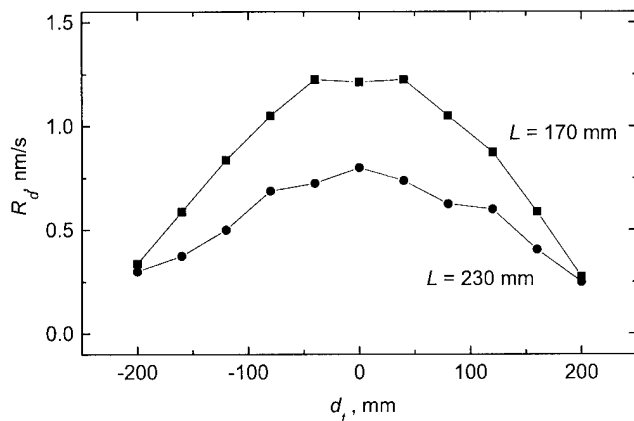


Fig. 4. Dependence of the Ti deposition rate R_d on the transverse distance d_t from the symmetry axis of the substrate for different distances L to the cathode. Deposition time $t = 240 \text{ s}$.

R_d on discharge current I is shown in Fig. 5 for various distances L from the cathode. The R_d values were measured along the middle line of the substrate ($d_t = 0$), being, therefore, the maximal values for each L . The $R_d(I)$ curves show linearity only for samples far enough from the cathode. Close to it, the microparticles presence boosts the deposition rate and a sharp variation with the discharge current I is observed. As can be seen from Fig. 5, R_d decreases monotonically with increasing L at a fixed discharge current I . The decrease is rather slow, especially at high I . The low variation of R_d with increasing distance illustrates the high throwing power of the arc process [5]. It has been already noticed [16] that for cathodic arc evaporation R_d decreases slower with increasing L than in the case of magnetron sputtering. This allows one to coat effectively three-dimensional parts having a complicated form. The slow $R_d(L)$ dependence is also advantageous for the coating of planar large-area substrates, allowing one to transport the frames with substrates at various distances from the cathode. This feature allowed one to simplify the construction of the vacuum arc deposition apparatus for large-area substrates [17]. The deposition rates for Ti close to the cathode surface are quite high, with values up to 9 nm/s for $I = 220 \text{ A}$ and $L = 80 \text{ mm}$. For Ti films deposited on stainless steel plates placed 160 mm from the cathode, Martin et al. [6] found $R_d = 5 \text{ nm/s}$ at $I = 90 \text{ A}$. In our case an estimated value $R_d = 2 \text{ nm/s}$ is found. The difference may be explained by the fact that the substrates in Ref. [6] are oriented parallel to the cathode surface, whereas here the substrates lie perpendicular to it, and R_d values for substrates parallel to the cathode surface are usually much higher than for those oriented perpendicular to the cathode plane [10,16].

The dependence of R_d (measured by profilometry at a length of 80 μm) on the distance L from the cathode for various values of the discharge current I is shown in

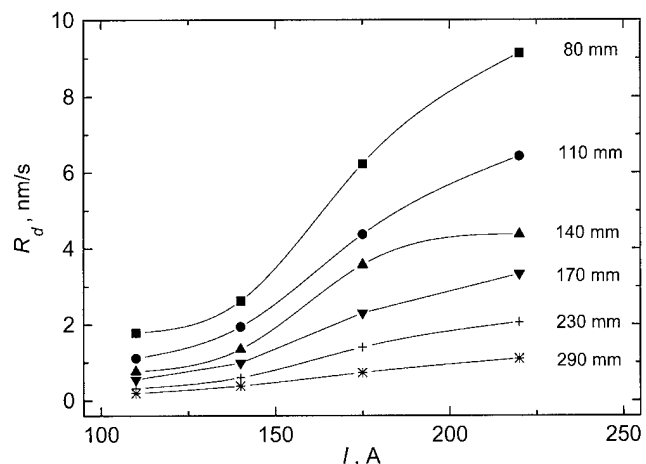


Fig. 5. Dependence of the Ti deposition rate R_d on the discharge current I for different distances L to the cathode along the symmetry axis of the substrate ($d_t = 0$). Deposition time $t = 420 \text{ s}$.

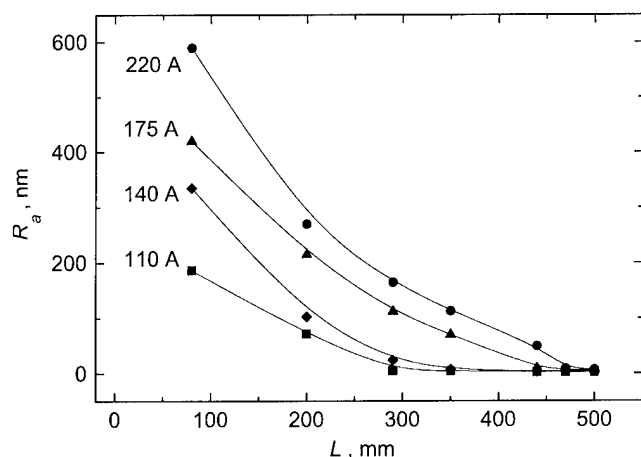


Fig. 6. Dependence of the average roughness R_a on distance L to the cathode for different values of discharge current I measured along the symmetry axis of the substrate ($d_t=0$). Deposition time $t=420$ s.

Fig. 6. These data were also measured along the middle line of the substrate ($d_t=0$). For samples close to the source, R_a sharply decreases with the distance L . The surface is built of micrometre-sized overlapping particles. Values up to 600 nm are found. Further away, as the film begins to be free from microparticles, R_a goes down to about 4 nm, which is the initial roughness of the glass substrate. The numerical significance of R_a for these samples is the average of a rather smooth background on which the microparticles are randomly dispersed. A more detailed description of the surface morphology would imply a bimodal roughness description [18]. An increase of the discharge current I increases the roughness and widens the choice of available roughnesses. The higher the discharge current, the larger the microparticle-free zone. For comparison, in the biomedical field, reported R_a values needed for bone anchoring on implants range from 460 to 8400 nm [19,20]. The deposition time t is the third parameter that enables one to produce a given roughness, but its influence has not been studied here. Comparison of the data given in Figs. 5 and 6 shows that there is no linear correlation between R_d and R_a . Namely, the deposition rate decreases much more slowly with increasing L and decreasing I than the average roughness. This is very important from the technological point of view, because it allows one to obtain very smooth coatings on a substrate with a reasonable deposition rate simply by increasing the distance from the cathode.

Acknowledgements

The financial support of the NATO Linkage Grant (contract HTECH.LG.970342 + CN.SUPPL 973216), the Isopress-Inter Programme of the Russian Ministry of Science and Technology, Royal Swedish Academy of Sciences and the Copernicus Networks (contracts ERB IC15 CT98 0815 and ERB IC15 CT98 0812) is acknowledged.

References

- [1] T. Albrechtsson, P.-I. Brenemark, H.-A. Hansson, J. Lindström, *Acta Orthop. Scand.* 52 (1981) 155.
- [2] T. Peltola, M. Patsi, R. Viitala, I. Kangasniemi, A. Yli-Urpo, S. Kothari, P. Hatton, in: L.A.J.L. Sarton, H.B. Zeedijk (Eds.), *Materials Functionality and Design* vol. 3, The Netherlands Society for Materials Science, Zwijndrecht, 1997, p. 569.
- [3] D. Buser, R.K. Schenk, S. Steinemann, J.P. Fiorellini, C.H. Fox, H. Stich, *J. Biomed. Mater. Res.* 25 (1991) 889.
- [4] L. Carlsson, T. Rustlund, B. Albrektsson, T. Albrektsson, *Int. J. Oral Maxillofac. Implants* 3 (1988) 21.
- [5] P.J. Martin, D.R. McKenzie, R.P. Netterfield, P. Swift, S.W. Filipeczuk, K.H. Müller, G. Pacey, B. James, *Thin Solid Films* 153 (1987) 91.
- [6] P.J. Martin, P. Netterfield, D.R. McKenzie, I.S. Falconer, C.G. Pacey, P. Tomas, G. Sainty, *J. Vac. Sci. Technol. A* 5 (1987) 22.
- [7] I.G. Brown, J.E. Galvin, *IEEE Trans. Plasma Sci.* 17 (1989) 679.
- [8] I.G. Brown, X. Godechot, *IEEE Trans. Plasma Sci.* 19 (1991) 713.
- [9] B. Straumal, N. Vershinin, V. Semenov, V. Sursaeva, W. Gust, *Defect Diff. Forum* 143–147 (1997) 1637.
- [10] N. Vershinin, B. Straumal, W. Gust, *J. Vac. Sci. Technol. A* 14 (1996) 3252.
- [11] R.L. Boxman, P.J. Martin, D.M. Sanders (Eds.), *Handbook of Vacuum Arc Science and Technology*, Noyes Publications, Park Ridge, NJ, 1995, p. 367.
- [12] G.W. McClure, *J. Appl. Phys.* 45 (1974) 2078.
- [13] J.E. Daadler, *J. Phys. D* 8 (1975) 1647.
- [14] J.E. Daadler, *J. Phys. D* 9 (1976) 2379.
- [15] B.B. Straumal, N.F. Vershinin, R. Dimitriou, W. Gust, T. Watanabe, Y. Igarashi, X. Zhao, *Thin Solid Films* 319 (1998) 127.
- [16] N.F. Vershinin, V.G. Glebovsky, B.B. Straumal, W. Gust, H. Brongersma, *Appl. Surf. Sci.* 109–110 (1997) 437.
- [17] B. Straumal, N. Vershinin, K. Filonov, R. Dimitriou, W. Gust, *Thin Solid Films* 351 (1999) 190.
- [18] H.G. Pfaff, G. Willmann, *Interceramics* 43 (1994) 73.
- [19] T.J. Vijayaraghavan, A. Bensalem, *J. Mater. Sci. Lett.* 13 (1994) 1782.
- [20] K. Hayashi, T. Inadome, H. Tsumura, Y. Nakashima, Y. Sugiooka, *Biomaterials* 15 (1994) 1187.

Spatial distribution of microdroplets generated in the cathode spots of vacuum arcs

K. Miernik *, J. Walkowicz

Institute for Terotechnology, ul. Pullaskiego 6/10, 26-600 Radom, Poland

Accepted 29 June 1999

Abstract

Results of research on the spatial distribution of aerosol generated by the cathode spots of the vacuum-arc evaporators used for wear-resistant coatings deposition are presented in the paper. Research was carried out on four arc plasma sources differing in the cathode's structure and the arc ignition system. The spatial angular distribution for different fractions of microdroplets is presented. The influence of the cathode's shape on conditions of the microdroplets generation is described. © 2000 Elsevier Science S.A. All rights reserved.

Keywords: Angular distribution; Arc discharge; Coatings; Microdroplets

1. Introduction

The vacuum arc method is at present widely used for hard, wear-resistant coating deposition [1]. Apart from many advantages, such as the simplicity of the deposition process and plasma source structures, the method also has several disadvantages. The most important of these is the occurrence of the microdroplet phase in the plasma, from which crystallization takes place [2–4]. Microdroplets of the cathode's metal, molten and thrown out of the cathode spot's area, are deposited on the substrate's surface and take part in the coating creation equally as evaporated and ionized atoms (Fig. 1). This causes a significant increase in the roughness of deposited coatings (by an order of magnitude) at the same time worsening the homogeneity of their structure and chemical composition. Moreover, they become the source of the coating's cracks and lead to the creation of open pinholes considerably worsening its anti-corrosive properties [5,6]. This disadvantage disqualifies the described method in some fields of application (e.g. microelectronics, optics). It necessitates the use of special filtration systems of the microdroplet phase, which generally lead to a decrease in the deposition rate [7,8].

Plenty of features influence the share of the micro-

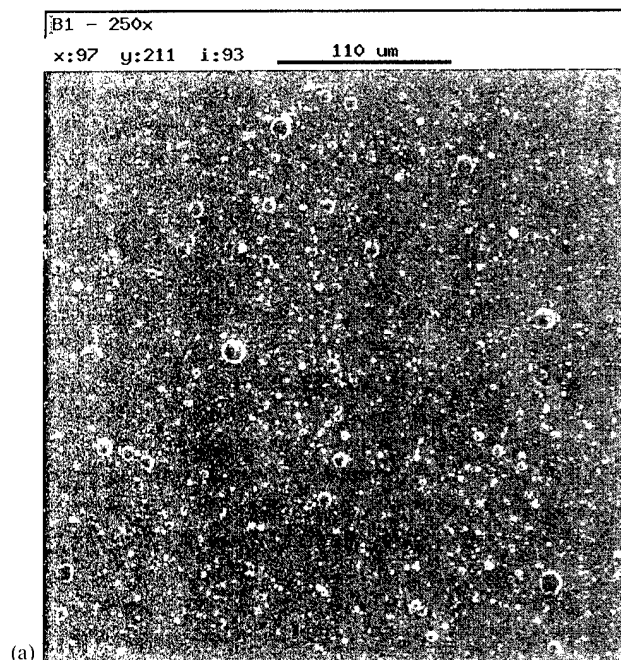
droplet phase in the deposited coating: the melting point of the cathode's material, the average temperature of the cathode's evaporated surface and the average cathode energy dissipation [9] should be mentioned. It was stated that the number and the average size of the droplet monotonically increase together with the increase in discharge current, cathode temperature and working gas pressure [10–12].

From a practical point of view, a spatial distribution of the droplet phase is of great importance. It appears from the literature that the spatial distribution of the microdroplet phase is anisotropic, and microdroplets are thrown out at a low angle to the cathode's surface (Fig. 1c) [4,13]. The speed at which the microdroplets are thrown out is in the range of 10^2 – 10^3 m/s, and it depends on the kind of evaporated material, in particular its melting point [9,12]. Depending on the substrate's temperature, its position against the source and its size, the deposited droplets are shaped like a ball, a lens or a tear.

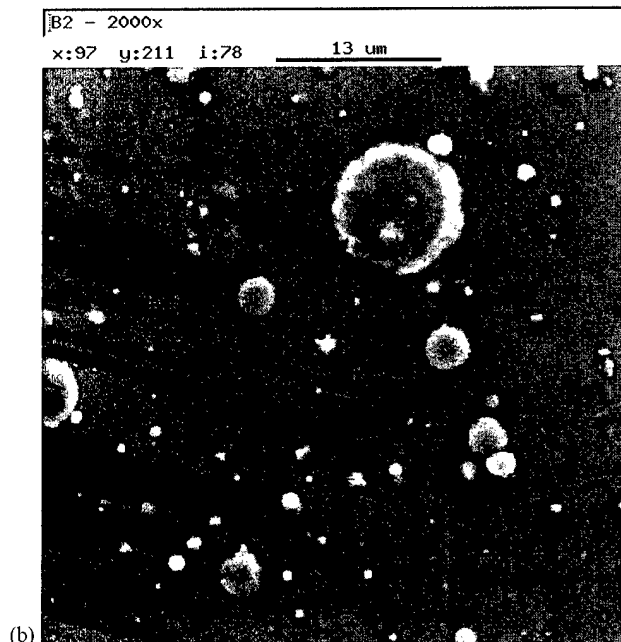
2. Experimental

Experiments were carried out with four considerably different constructions of arc sources. The sources differed in their ignition systems, the system of the cathode spot localization, the cathode thickness, the

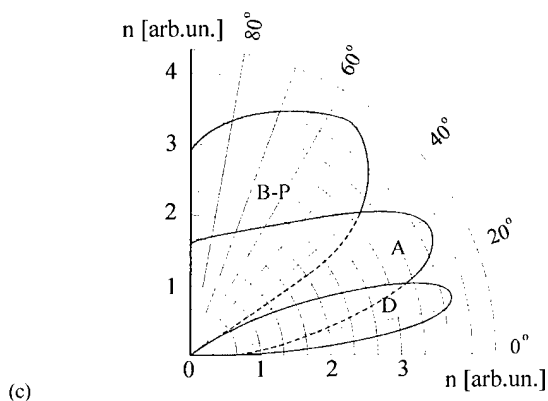
* Corresponding author.



(a)



(b)



(c)

shape of the eroding surfaces (Fig. 2a) and the cooling systems. The industrial arc source of the device NNW6,6I4 [14,15] and the MZ383 device's source (Metaplas Ionon) [16,17] described in the literature were used in the investigation. Moreover, two sources, with construction schemes presented in Fig. 2b and c were investigated. Basic values of the source parameters are presented in Table 1.

The arc source device NNW6,6I4 has a high-voltage discharge ignition and a directly cooled cathode. Magnetic localization of discharge on the cathode's frontal surface based on the acute angles law (Robson's law) was utilized. Because of that, the cathode's lateral surfaces are inclined at an angle of about 8° in relation to the source's axis. Two coils create an axial magnetic field. As a result, the whole construction could be related to systems with a linear separation of microdroplets described in the literature [19]. The MZ-383 device's cathode is fixed to a copper cooler with a central pin and uses an indirect way of cooling. The set has a mechanical system of arc discharge initiation and electrostatic (with the use of a shield) localization of discharge supported by a weak axial magnetic field created by a permanent magnet. Initiation of discharge occurs as a result of touching the cathode's frontal surface with a molybdenum starting electrode.

In the arc source, ITeE 65EM² discharge initiation takes place mechanically. A mixed magnetic–electrostatic localization of arc discharge is used there. A small, axially centered magnet creates a dome-shaped magnetic field over the cathode's surface. The source's target has direct water-cooling. The cathode set of the device ITeE 55 E²M also has a mechanical initiation of arc discharge. The cathode spot has a mixed magnetic–electrostatic type of localization. An exclusively electrostatic way of localization (without the creation of an additional axial magnetic field) was used in the investigations. The target's cooling was direct.

In the investigations of the microdroplet fraction's distribution, a steel, semicircular holder with a radius of 250 mm was used. As substrates, polished belts of stainless steel, with a width of 10 mm and a thickness of 1 mm, were fixed to the holder. These substrates were placed horizontally to eliminate the influence of gravitation on the distribution of microdroplets. In the course of investigations, the holder was under the floating potential. Because of the specific construction features of both the sources and the vacuum chambers of particular devices, it was impossible to make measurements in the angular range of $0-180^\circ$. In each device, a 'dead visual field' occurred; the smallest was in the MZ383

Fig. 1. (a) Substrate surface covered with microdroplets, (b) picture of microdroplets and (c) angular distribution of microdroplets in the arc method according to Baouchi and Perry (B-P), Daarler (D) and Aksenov et al. (A) [11,13,18].

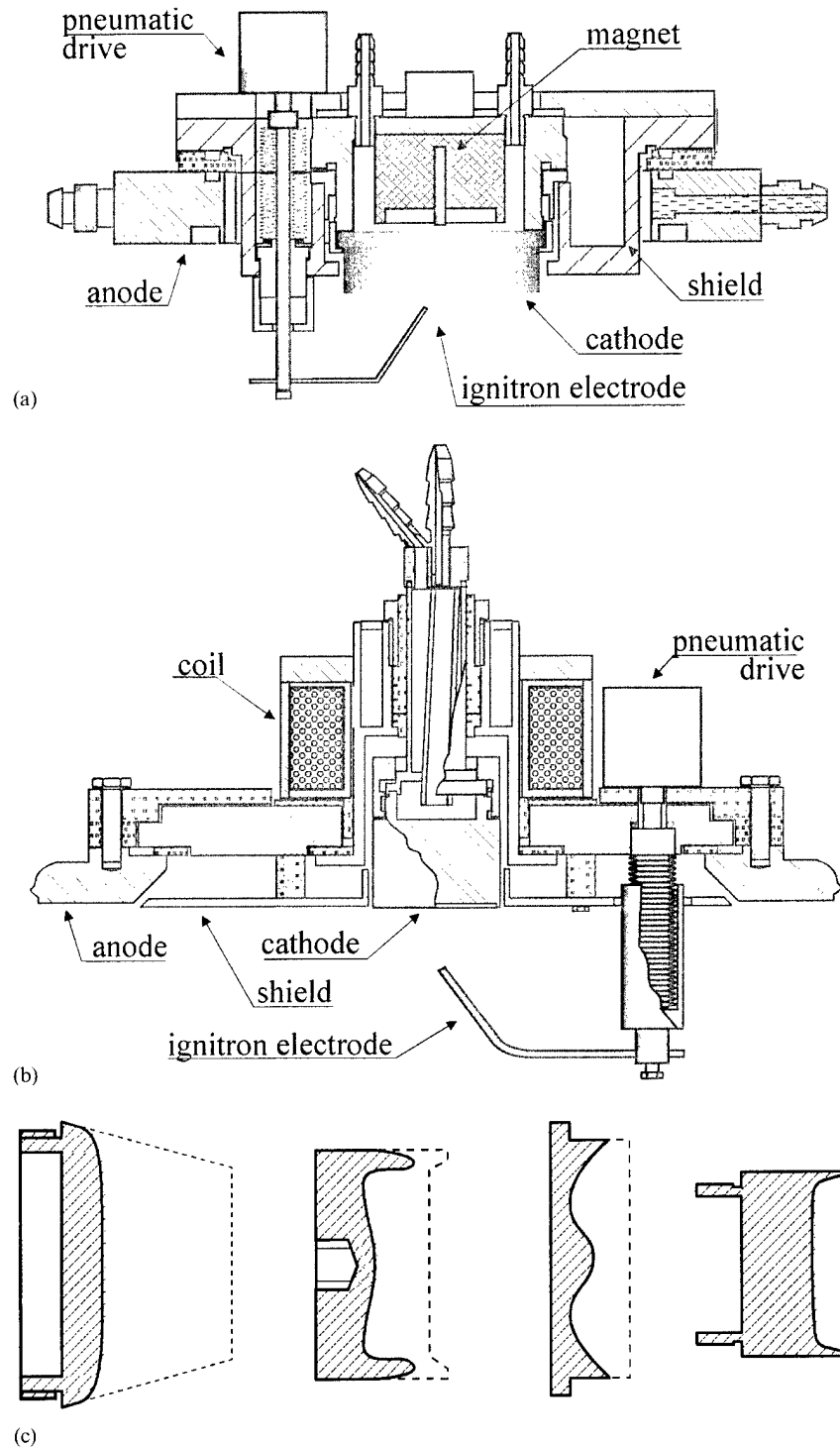


Fig. 2. Shapes of the targets' intersection of investigated arc sources (a): (from the left) NNW6,6 I4, MZ383, ITeE 65EM², ITeE55E²m (the shape of a new target is marked with a broken line) and schemes of arc sources of the devices ITeE 65EM² (b) and ITeE55E²m (c) [20].

device (16°) and the largest was in the NNW6,6 I4 device (44°).

The time of coating deposition in all cases amounted to 10 min. The evaporation process was carried out using titanium cathodes with an arc current of 100 A and at a pressure below 10^{-3} Pa. Reactive gas was not

used in the investigations to eliminate the creation of a coating of chemical compounds on the cathode's surface [21]. Partly worn out cathodes with a stabilized shape of the erosion sphere were used in experiments.

Measurements of the droplet distribution on the belt surface were made every 3 cm, which gave an average

Table 1
Basic parameters of investigated arc sources

	NNW6,6 14	MZ383	ITeE 65EM ²	ITeE55E ² m
Cathode diameter (mm)	80	63	65	55
Cathode thickness (mm)	35	26	18	45
Cathode thickness during experiments (mm)	30	21	13	41
Magnetic field induction (mT)	5	3	8	–
Arc current (A)	100	100	100	100

angular resolution of about 6–7°. The results obtained from the whole angular range were averaged to the range of 0–90°, assuming a symmetric microdroplet

emission distribution in a horizontal plane. In this paper, we will use the term ‘microdroplet diameter’ to denote the diameter of the object visible in the picture [12,22].

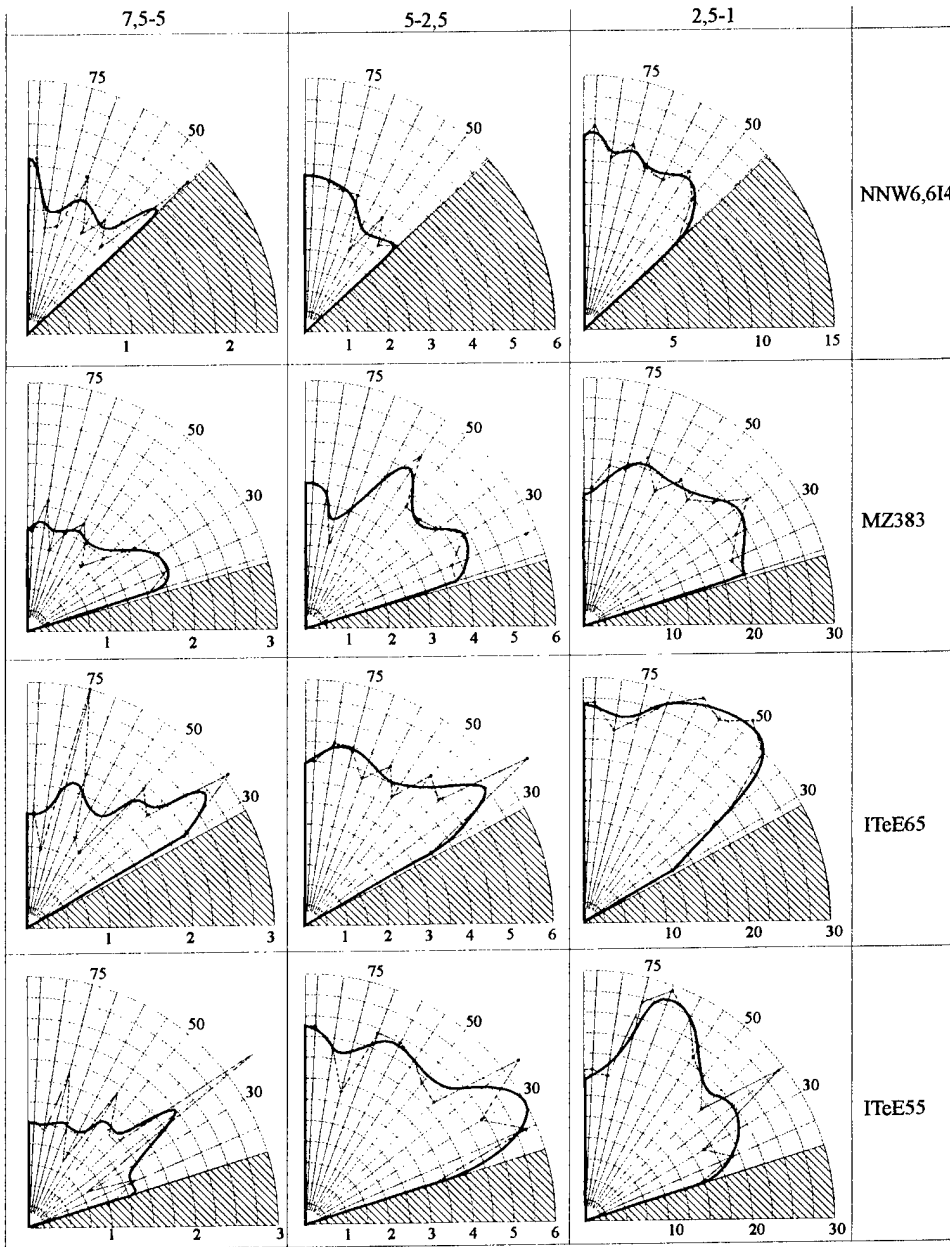


Fig. 3. Angular distribution of the microdroplet phase fraction for different sources. (The radial scale is the average number of droplets per analyzed area of $4.3 \times 10^4 \mu\text{m}^2$.)

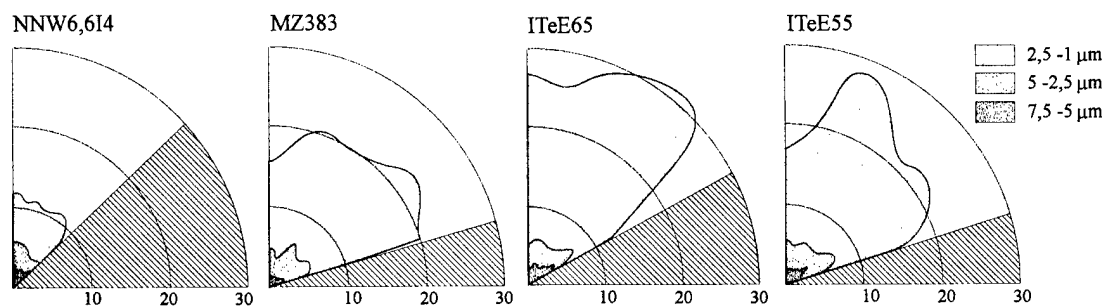


Fig. 4. Normalized angular distribution of the microdroplets for different sources.

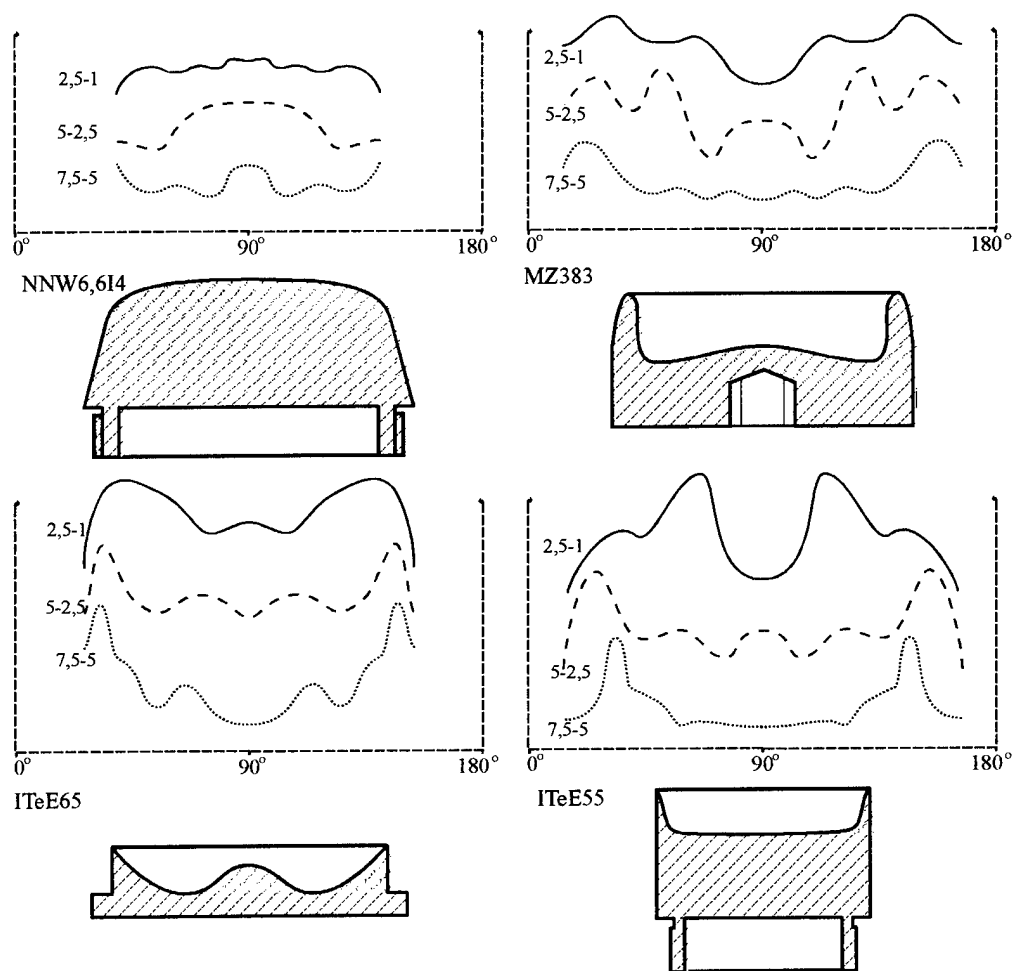


Fig. 5. Correlation between spatial distribution of microdroplet and the shape of the cathode surface.

The majority of investigated microdroplets, in particular small microdroplets, had a regular, round shape, irrespective of the type of source, which means that they were crystallized during the passage from the cathode to the substrate. Larger droplets became flattened, which means that the cooling phase had finished on the substrate surface (Fig. 1a and b).

3. Results

The investigations proved that each source has a characteristic distribution of microdroplet emission. Radial angular distributions of different fractions of microdroplets (1–7.5 μm) for different sources are presented in Fig. 3.

In the NNW6.614 device, we observed that in the investigated angular range, the fraction of the smallest microdroplets ($<2.5\text{ }\mu\text{m}$) is in practice emitted isotropically. Greater differences in the microdroplet distribution were observed for the fraction with larger droplets ($2.5\div 5\text{ }\mu\text{m}$), for which the maximal emission angle was $\approx 90^\circ$. As distinct from the previously described source NNW6.6, two angles can be distinguished in the fraction of the smallest microdroplets emission of the MZ383 and the ITeE 55EM² devices, with local maxima: ≈ 35 and $\approx 70^\circ$.

The distribution of microdroplets emitted by arc source ITeE65E²m was close to the distribution given by Baouchi and Perry [11]. The largest amount of microdroplets was emitted at the angle $\approx 55^\circ$ (Fig. 4).

The source NNW6.6 emitted the smallest amount of microdroplet phase from among all the investigated arc sources. This amount was more than two times smaller than in the other sources. This fact can be explained by the source's structure, which is a simplified version of a rectilinear plasma-optical filter described in the literature [19]. Moreover, the source's cathode is localized deeply in the tubular anode, which also influences the decrease in the number of microdroplets. As a result, the fraction of microdroplets emitted at the acute angle is deposited on the anode surface and is not involved in the process of coating creation. Furthermore, the impact of a directed stream of ions on microdroplets can be another possible feature decreasing their amount [23,24]. The occurrence of two maxima for the arc source of the MZ383 device and ITeE 55EM² source can be explained with the phenomena of the microdroplet's rebounding from a relatively high edge of the cathode or microdroplets emission from these edges. Distributions of microdroplet emission for all discussed sources in rectangular coordinates are presented in Fig. 5.

Comparing their courses with the cathode's shape, we can see that the spatial distribution of the microdroplet emission is indisputably influenced by the shape of the cathode's emitting surface, which is closely associated with the shape of magnetic and electric fields over the cathode [25].

4. Conclusions

Investigations of the influence of the arc source's structure proved a direct dependence of the spatial distribution of microdroplet emission and the shape of the target's surface, from which their emission takes place. No visible influence of the method of discharge localization, type of cooling and its intensity (the cathode's thickness) on the amount of the droplet phase emitted by the source was found. The shape of the

cathode's emitting surface has the biggest influence on the spatial distribution of the microdroplets emission, fraction $1\text{--}2.5\text{ }\mu\text{m}$. This observation is also proved by the fact that the presence of two local maxima lying in a similar angular range was also observed for sources with a similar shape of the cathode's erosion sphere (MZ383 and ITeE55). The number of large microdroplets (fraction over $5\text{ }\mu\text{m}$) for the investigated sources is at a similar level, which proves that the phenomenon responsible for their creation occurs with an identical intensity independently of the arc source construction. The most probable explanation of their creation is the passing of the cathode spot through microdroplet conglomerates deposited on the cathode's surface.

One can observe a significant difference among results of microdroplets distribution given in this paper and in the papers of other authors [11,18,22]. It can be explained by the fact that authors of those papers

References

- [1] R.L. Boxman, S. Goldsmith, *IEEE Trans. Plasma Sci.* 17 (1989) 705.
- [2] R.L. Boxman, S. Goldsmith, *Surf. Coat. Technol.* 52 (1992) 39.
- [3] B. Rother, J. Vetter, *Wiss. Z.D. TU Karl-Marx-Stadt* 31 (1989) 433.
- [4] H.M. Gabriel, *IEEE Trans. Plasma Sci.* 21 (1993) 416.
- [5] R.R. Aharonov, M. Chhowalla, S. Dhar, R.P. Fontana, *Surf. Coat. Technol.* 82 (1996) 334.
- [6] M. Keidar, I. Beilis, R.L. Boxman, S. Goldsmith, *Surf. Coat. Technol.* 86–87 (1996) 415.
- [7] R.L. Boxman, P.J. Martin, D.M. Sanders, *Handbook of Vacuum Arc Science and Technology*, Noyes, NJ, 1995.
- [8] J.P. Martin, Cathodic arc deposition, in: D.A. Glocker, S.I. Shah (Eds.), *Handbook of Thin Film Processes Technology*, Institute of Physics, Bristol, UK, 1995.
- [9] J. Vyskocil, J. Musil, *Surf. Coat. Technol.* 43–44 (1990) 299.
- [10] S. Anders, A. Anders, K.M. Yu, X.Y. Yao, I.G. Brown, *IEEE Trans. Plasma Sci.* 21 (1993) 440.
- [11] A.W. Baouchi, A.J. Perry, *Surf. Coat. Technol.* 41 (1991) 253.
- [12] T. Utsumi, J.H. English, *J. Appl. Phys.* 46 (1975) 126.
- [13] J.E. Daalder, *Physica* 104C (1981) 91.
- [14] D.A. Karpov, I.F. Kislov, A.I. Ryabchikov, A.A. Ganenko, *Surf. Coat. Technol.* 89 (1997) 58.
- [15] D.A. Karpov, *Surf. Coat. Technol.* 96 (1997) 22.
- [16] M. Mack, *Surface Technology*, Verlag Moderne Industrie, Landsberg, 1990.
- [17] S. Falabella, D.A. Karpov, Continuous cathodic arc sources, in: R.L. Boxman, P.J. Martin, D.M. Sanders (Eds.), *Handbook of Vacuum Arc Science and Technology*, Noyes, NJ, 1995, p. 404.
- [18] I.I. Aksenov, I.T. Kononov, E.E. Kudriavceva, V.V. Kunchenko, V.G. Padalka, V.V. Khoroshih, *J. Tech. Phys.* 54 (1984) 1530.
- [19] I.I. Aksenov, V.G. Padalka, V.T. Tolok, V.V. Khoroshih, *Plasma Phys.* 6 (1980) 918.
- [20] K. Miernik, *Elektronika* 4 (1999) 5.
- [21] B.F. Coll, M. Chhowalla, *Surf. Coat. Technol.* 68–69 (1995) 131.
- [22] J.E. Daalder, *J. Phys. D: Appl. Phys.* 9 (1976) 2379.
- [23] R.L. Boxman, S. Goldsmith, *J. Appl. Phys.* 52 (1981) 151.
- [24] Z. Cheng, M. Wang, *Surf. Coat. Technol.* 92 (1997) 50.
- [25] B.F. Coll, D.M. Sanders, *Surf. Coat. Technol.* 81 (1996) 42.

Pure Al thin film protective layer to prevent stress migration in Al wiring for thin-film transistors

H. Takatsuji ^{a,*}, K. Haruta ^b, S. Tsuji ^a, K. Kuroda ^b, H. Saka ^b

^a Display Technology, IBM Japan, Ltd., Shimotsuruma, Yamato-shi, Kanagawa 242, Japan

^b Department of Quantum Engineering, Nagoya University, Nagoya 464-01, Japan

Accepted 28 June 1999

Abstract

The anti-stress migration property of layered structure aluminum (Al) thin films overcoated with pure Al was investigated for application of such films as interconnect materials in large arrays of high-resolution thin-film transistor liquid crystal displays (TFT-LCDs). It was found that no hillock or whisker generation occurred in a pure Al thin film with a sputter-deposited fine-grained polycrystalline pure Al layer after exposure to mechanical and 300°C thermal stresses. Atomic force microscopy (AFM) and cross-sectional transmission electron microscopy (TEM) analyses revealed the morphology of the layered structure thin film and the mechanism for the prevention of stress migration in the film. © 2000 Elsevier Science S.A. All rights reserved.

Keywords: Nanoindentation techniques; Overcoated pure aluminum thin film; Sputtering; Stress migration; Thin-film transistor liquid crystal displays

1. Introduction

The performance of thin-film transistor liquid crystal displays (TFT-LCDs) has improved over the past several years with a change in standard display size from 10.4 to 12.1 or 13.3 inches, and the resolution has also improved with the transition from VGA to SVGA, XGA, and SXGA. Consequently, pure aluminum (Al) and Al alloys have attracted much attention for their potential use as interconnect materials in high-performance TFT-LCD arrays formed on glass substrates, because of their low resistivity and good patterning ability [1]. However, stress migration due to the thermal expansion mismatch between Al films and the glass substrate, which leads to phenomena such as the growth of hillocks (including whiskers), is a major concern, because it affects the yield loss during TFT device fabrication. There are several ways to protect against stress migration, of which one using Al alloys with rare earth or transition metals has been the subject of many reports [2–5]. However, two shortcomings of such alloys for TFT-LCD applications are their higher electrical resistivity and the higher cost of the sputtering target than in the case of pure Al. Other methods coat clad or

capped thin-film layers with transition metals (Ti, Mo, etc.) on Al interconnects, or form anodized Al₂O₃ layers on Al interconnects [6,7]. The shortcoming of these techniques is that they need an additional photolithographic or special anodizing process step, which increases the manufacturing cost. Accordingly, to reduce the thermal expansion stress, we focus on Al interconnects with a layered structure using only pure Al.

In this work, we demonstrate the anti-stress migration property of overcoated pure Al thin film (thickness = 40–200 nm) sputter-deposited on several kinds of pure Al thin film (thickness = 350 nm) and Al–indium (Al–In) thin film (thickness = 270 nm) with a weak anti-stress migration property, formed on LCD grade large glass substrates [8]. We investigated the anti-stress migration property of these thin films by means of our nanoindentation techniques [9]. As a result, we found that the overcoated layer is effective in preventing stress migration in layered Al thin films. We also investigated the nanostructure of the layered pure Al thin film by means of atomic force microscopy (AFM) and cross-sectional transmission electron microscopy (TEM).

2. Experiment

Two kinds of pure Al thin film [(a) and (b), thickness = 350 nm] were deposited on an LCD grade glass

* Corresponding author. Tel.: +81-462-73-2427;
fax: +81-462-77-0382.
E-mail address: takatsuji@jp.ibm.com (H. Takatsuji)

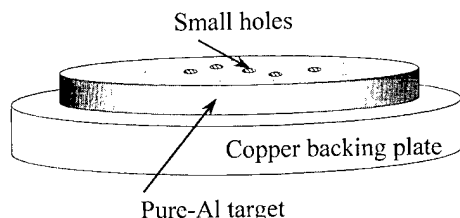


Fig. 1. Schematic diagram of a modified sputtering target for deposition of Al–In thin film.

Table 1
Sample configurations and crystallographic texture^a

Sample ID	(111)	(200)	(220)	(311)
Pure Al (a)	3122	119	51	22
Pure Al (b)	356	138	96	96
Pure Al (c)	513	252	396	129

^a The unit of intensity is counts per second (cps).

substrate ($300 \times 400 \text{ mm}^2$) using two types of single substrate transfer cluster type d.c. magnetron sputtering apparatus [(a) using multi-magnet type and (b) using a single bar magnet scan type] at a rate of 400 nm/min, with an argon pressure of 0.4 Pa and a substrate temperature of 120°C. Pure Al (c) and Al–In thin films (thickness = 270 nm) were deposited on LCD grade glass substrate ($125 \times 125 \text{ mm}^2$) by means of a d.c. magnetron sputtering apparatus at a rate of 36 nm/min, with an argon pressure of 0.4 Pa and a substrate temperature of 120°C. To deposit Al–In thin film, we modified the pure Al target to make indium ooze from the bonding material, as shown in Fig. 1. [Bonding material (In solder) oozed through the small hole in the target.] The indium content was measured using a CAMECA time-of-flight secondary ion mass spectrometry (TOF-SIMS) model 4 at analysis energies of 25 keV with a Ga gun, and at

sputter energies of 3 keV with an Ar gun. We confirmed that the Al–In thin film contains 0.19 wt.% indium.

After deposition of the above-mentioned Al-based thin films, the substrates were exposed to the atmosphere, and a pure Al layer (with a thickness of 40 nm or 200 nm) was deposited by means of an RF sputtering apparatus at a rate of 40 nm/min, with an argon pressure of 0.6 Pa and a substrate temperature of 100°C, on Al-based thin films deposited by means of a d.c. magnetron sputtering apparatus. The resistance to stress migration was investigated by means of our nanoindentation techniques for various stress temperatures (200°C, 250°C, and 300°C). The films' crystallographic texture was measured with θ –2 θ XRD using Cu K α radiation at 50 kV/150 mA, with a scanning speed of 1°/min and a scanning range of 30–80°. Nanostructures were observed by means of AFM and cross-sectional TEM operated at 200 kV.

3. Results and discussion

3.1. Properties of Al–In and pure Al thin films deposited on glass substrate

The crystallographic textures of pure Al (a), pure Al (b), and pure Al (c) deposited on LCD grade glass substrates were investigated, with the results shown in Table 1. These indicate that pure Al (a) is a highly (111) textured film, while pure Al (b) and (c) are only slightly (111) textured (i.e. nearly random) films. The crystallographic texture of Al thin film and its anti-stress migration property are strongly correlated, and we confirmed in a previous study that the former type of Al thin film has a strong anti-stress migration property, while the

Table 2
Anti-stress migration property results obtained by nanoindentation techniques

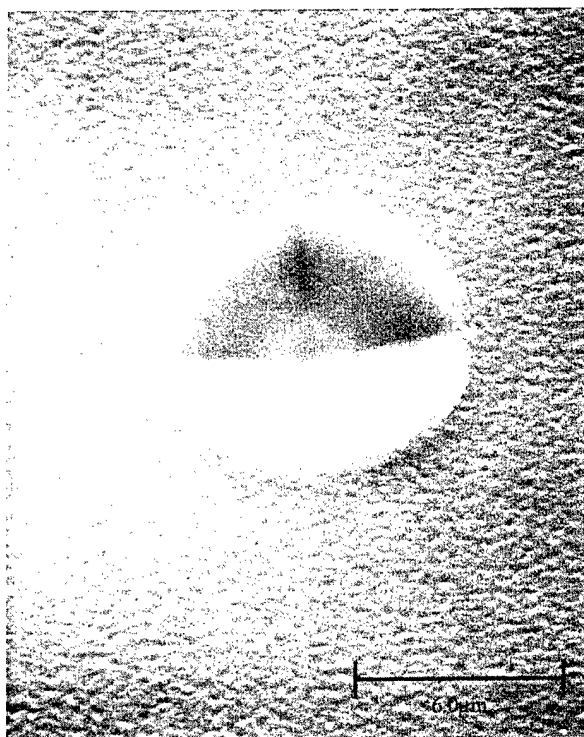
Sample ID	200°C		250°C		300°C	
	Number of whiskers	Number of hillocks	Number of whiskers	Number of hillocks	Number of whiskers	Number of hillocks
Al–In	4	54	5	47	13	103
Pure Al (c)	0	28	3	39	6	41

Table 3
The effects of the pure Al overcoated layer in preventing hillock generation

Sample ID	No overcoated layer		40 nm thick overcoated layer		200 nm thick overcoated layer	
	200°C	300°C	200°C	300°C	200°C	300°C
Pure Al (a)	3	9	0	0	0	0
Pure Al (b)	7	67	1	0	0	0
Al–In	54	102	13	8	0	0



(a) non-overcoated layer (sample A)

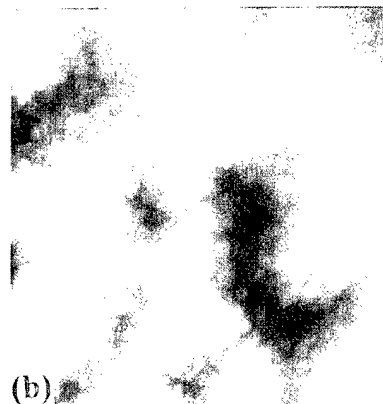


(b) layer with a 200-nm-thick overcoat (sample B)

Fig. 2. SEM images after nanoindentation techniques in the Al–In thin films corresponding to the samples: (a) non-overcoated layer (sample A); (b) layer with a 200 nm thick overcoat (sample B).



(a) before (sample 3a) annealing



(b) after (sample 3b) annealing at 300°C in vacuum for 60 min

Fig. 3. AFM top views of the overcoated pure Al layer on the pure Al (b) thin films: (a) before (sample 3a); (b) after (sample 3b) annealing at 300°C in vacuum for 60 min; scale 1000 × 1000 nm².

latter type has a weak anti-stress migration property [10].

Table 2 compares the anti-stress migration properties of Al–0.19 wt.% In (Al–In) and pure Al (c) thin films deposited by the same sputtering apparatus. Whisker generation was observed in the Al–In thin-film samples

at a stress temperature of 200°C, but was not observed in the pure Al (c) thin film at the same temperature. More whiskers and hillocks were generated in the Al–In thin film than in the pure Al (c) thin film at all stress temperatures. These results indicate that the use of Al–In thin film leads to the generation of whiskers and

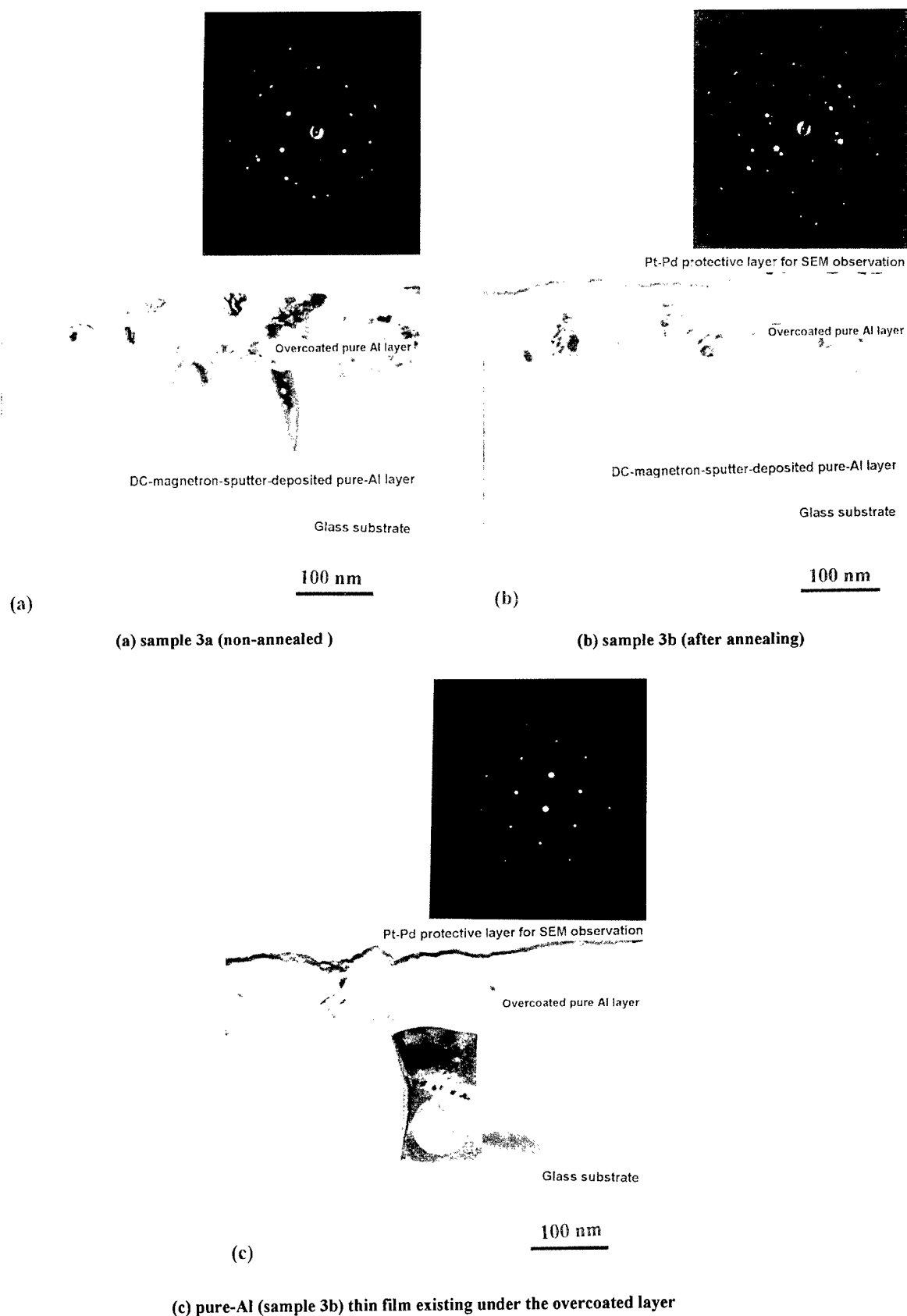


Fig. 4. Cross-sectional TEM images and analyses of the grain orientation caused by electron diffraction: (a) sample 3a (non-annealed); (b) sample 3b (after annealing); (c) pure Al (sample 3b) thin film existing under the overcoated layer.

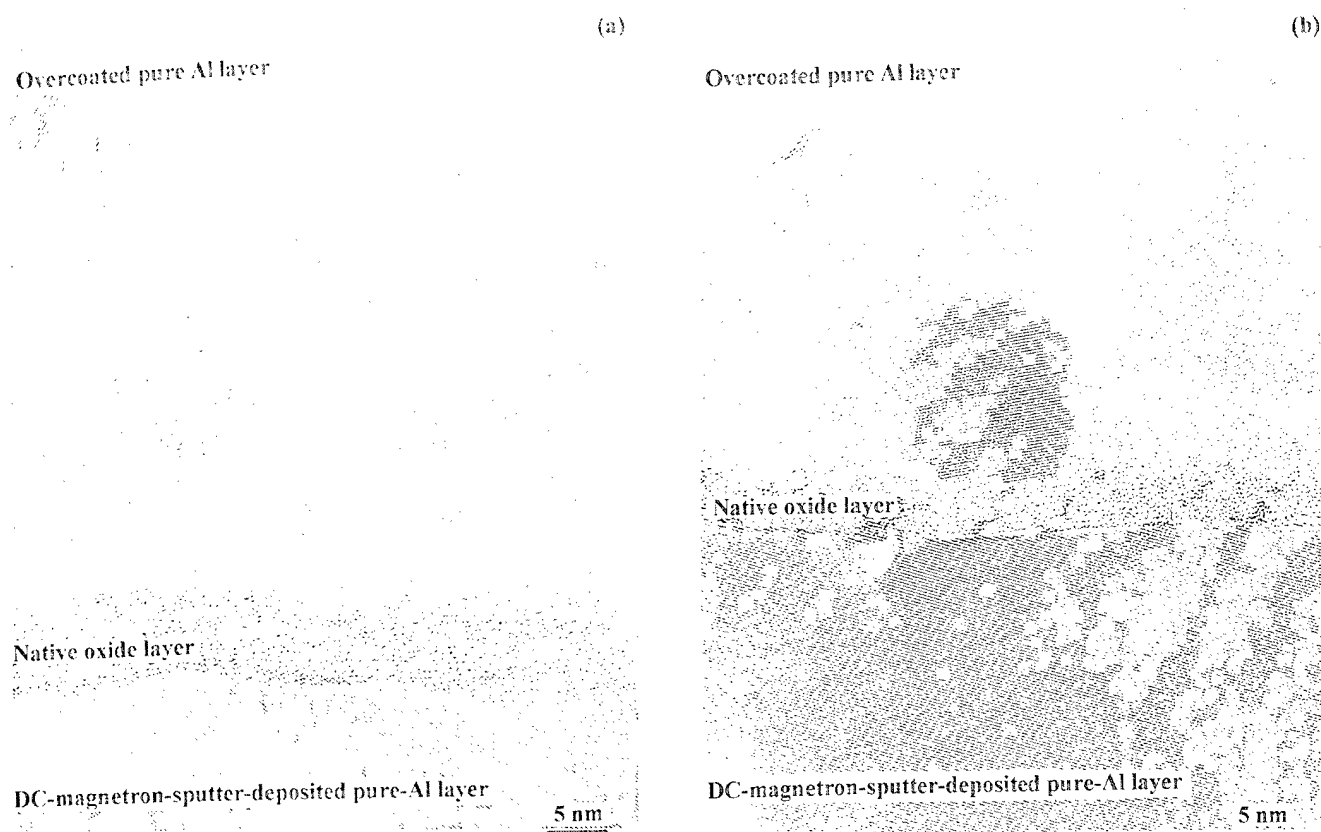


Fig. 5. Detailed nanostructure micrographs obtained by means of cross-sectional TEM corresponding to: (a) sample 3a; (b) sample 3b.

hillocks by nanoindentation techniques at lower stress temperatures than when pure Al (c) thin film is used. We conclude that the Al–In film in this study has a weaker anti-stress migration property than pure Al (c). According to the results shown in Tables 1 and 2, Al–In film has the weakest anti-stress migration property of all these samples.

3.2. Effect and properties of an overcoated pure Al thin film layer

The effect of a pure Al overcoated layer in preventing hillock generation is shown in Table 3, which indicates that the largest number of hillocks was generated in the Al–In thin film by our nanoindentation technique when no overcoated layer was used, and that both (40 nm and 200 nm thick) overcoated layers completely prevented the generation of hillocks in pure Al (a) and pure Al (b) thin films. The table also indicates that the 40 nm thick overcoated pure Al layer reduced the generation of hillocks, while the 200 nm thick layer completely prevented the generation of hillocks in the Al–In thin film, which has the weakest anti-stress migration property of the three samples. We conclude that the overcoated pure Al layer (200 nm) is very effective in preventing hillock generation, while the overcoated pure

Al layer (40 nm) has an unstable effect on the Al–In thin film, since the number of hillocks generated in the Al–In thin film with the overcoated pure Al layer (40 nm) at a stress temperature of 200°C is greater than at 300°C.

Fig. 2(a) and (b) shows SEM images after nanoindentation techniques (300°C thermal stress) which correspond to the samples: Al–In thin films with a non-overcoated layer (sample A) and with a 200 nm thick overcoated layer (sample B). Whiskers and hillocks are observed on the nanoindentation marks in sample A, whereas no whiskers or hillocks are observed in sample B. A comparison of these micrographs reveals that the overcoated layer is very effective in preventing stress migration.

To investigate the characteristics of overcoated pure Al thin film, we performed AFM surface analysis and cross-sectional TEM observation. Fig. 3(a) and (b) shows AFM top views of the overcoated pure Al layer on the pure Al (b) thin films before (sample 3a) and after (sample 3b) annealing at 300°C in vacuum for 60 min. They indicate that there is no significant change in either sample, and that their grain sizes are fine.

The results of cross-sectional TEM observation of sample 3a (non-annealed) and 3b (after annealing) are shown in Fig. 4(a) and (b), which also shows the results

of electron diffraction analysis in both overcoated pure Al layers. These images reveal that the morphology of the overcoated layer is fine-grained polycrystalline, and that there is little change in the grain size after annealing, as seen in Fig. 3(a) and (b). This indicates that the overcoated layer is robust to the thermal stress. Fig. 4(c) also shows the result of electron diffraction analysis in the pure Al (sample 3b) thin film existing under the overcoated layer. It indicates that the grain is (111) oriented.

Detailed nanostructural observation was performed by means of cross-sectional TEM, as shown in Fig. 5(a) and (b), which corresponds to samples 3a and 3b. A very thin (about 3 nm thick) native oxide layer is visible between the d.c. magnetron sputter-deposited pure Al thin film and the overcoated pure Al thin film in both TEM images. We consider that this oxide layer grew in the atmosphere between the periods of d.c. magnetron sputtering and RF sputtering. Aluminum lattice patterns are sporadically observed in the overcoated layers of both samples. Judging from this result and Fig. 4(a) and (b), we conclude that the overcoated pure Al layer has a fine-grained polycrystalline structure. Fig. 5(a) and (b) also reveals that there is no significant difference between the two samples. This indicates that the morphology of the pure Al/Al₂O₃/pure Al layered structure thin film in this study was little changed by annealing.

We consider that the Al/Al₂O₃/fine-grained polycrystalline pure Al layered structure thin film prevents stress migration from being caused by the thermal expansion mismatch between the glass substrate and itself, by absorbing the stress throughout the layered thin film. As regards application of the layered structure pure Al to interconnects in TFT arrays, since a resistivity of 3.12 Ω cm was obtained in the layered thin film by means of the four-point probe method, such a thin conductive film is suitable for low-resistivity interconnect materials in large high-resolution TFT-LCD arrays.

4. Conclusions

We confirmed that layered Al thin films with overcoated fine-grained polycrystalline pure Al thin film

have a strong anti-stress migration property. With the 200 nm thick overcoated thin film, no hillocks or whiskers were generated in an Al–In thin film with a weak anti-stress migration property. By means of cross-sectional TEM analysis, we confirmed that the morphology of the layered thin film was changed little by annealing. We consider that the Al/Al₂O₃/fine-grained polycrystalline pure Al layered structure thin film prevents stress migration by absorbing the thermal stress throughout the layered thin film. Consequently, we conclude that the layered structure thin film can be used as an interconnect material in large high-resolution TFT-LCD arrays.

Acknowledgements

The authors wish to thank T. Yoshioka of JEOL Hightech Co., Ltd. for TEM observation, H. Okuhira of Hitachi Science Systems, Ltd. for TOF-SIMS analysis, S. Takeuchi and T. Hashimoto of IBM Display Business Unit for encouragement, and M. McDonald of IBM Yamato Laboratory for his comments on this article.

References

- [1] G.L. Schnable, R.S. Keen, *Proc. IEEE* 57 (9) (1969) 1570.
- [2] T. Onishi, E. Iwamura, K. Takagi, K. Yoshikawa, *J. Vac. Sci. Technol. A* 14 (5) (1996) 2728–2735.
- [3] S. Takayama, N. Tsutsui, *Thin Solid Films* 289 (1996) 289–294.
- [4] E. Iwamura, T. Ohnishi, K. Yoshikawa, *Thin Solid Films* 270 (1995) 450–455.
- [5] H. Takatsuji, H. Iiyori, S. Tsuji, K. Tsujimoto, K. Kuroda, H. Saka, *Mater. Res. Soc. Symp. Proc.* 471 (1997) 99–104.
- [6] T. Tsujimura, H. Kitahara, A. Makita, P. Fryer, J. Batey, *Proc. 1994 International Display Research Conference and International Workshops on AMLCD and Display Materials* (1994) 424–427.
- [7] T. Arai, Y. Hiromasu, S. Tsuji, *Mater. Res. Soc. Symp. Proc.* 424 (1997) 37–42.
- [8] K. Hazama, Y. Nakamura, O. Nittono, *Jpn. J. Appl. Phys.* 27 (1988) 1142.
- [9] H. Takatsuji, S. Tsuji, H. Kitahara, K. Tsujimoto, K. Kuroda, H. Saka, *Mater. Res. Soc. Symp. Proc.* 441 (1997) 415–420.
- [10] H. Takatsuji, K. Tsujimoto, K. Kuroda, H. Saka, *Thin Solid Films* 343/344 (1999) 461–464.

XPS investigation of ion beam treated MoS₂–Ti composite coatings

I. Bertóti ^{a,*}, M. Mohai ^a, N.M. Renevier ^b, E. Szilágyi ^c

^a *Research Laboratory for Materials and Environmental Chemistry, Chemical Research Center, Hungarian Academy of Sciences, PO Box 17, H-1525 Budapest, Hungary*

^b *Teer Coatings Ltd., 290 Hartlebury Trading Estate, Hartlebury, Worcs. DY10 4JB, UK*

^c *Research Institute for Particle and Nuclear Physics, Hungarian Academy of Sciences, PO Box 49, H-1525 Budapest, Hungary*

Accepted 8 June 1999

Abstract

MoS₂ coatings incorporating Ti were deposited on Si substrates primarily for compositional characterisation and chemical structure studies. For comparison, MoS₂ layers and natural molybdenite crystals were also involved in this work. The MoS₂ and the MoS₂–Ti composite layers were co-deposited by unbalanced close field DC magnetron sputtering using simultaneously operating MoS₂ and Ti targets in Ar plasma. The coatings are almost amorphous by XRD. The overall composition and the in-depth homogeneity of the coatings were determined by NBS. XPS studies show that the surface of the coatings stored in ambient air was partially oxidised and carbon contaminated. The majority of Mo and S were found to be in sulphide environment and part of the Ti in oxide (TiO₂) and part in sulphide states. A small part of the S proved to be in a newly discovered sulphidic environment, different from that found in MoS₂. No evidence of such state could be detected for the molybdenite crystal but developed in it at Ar⁺ treatment. The major effect of the Ar⁺ ion bombardment was the severe preferential sputtering of the sulphide type S lowering the ratio of sulphide S to Mo–S states from the initial value of 2 down to approx. 1.5 for molybdenite. This effect was more pronounced for both coatings lowering the S/Mo–S ratio to about 1. The experimental results demonstrate that the atomic scale chemical structure of the MoS₂ coatings was also affected by energetic particles in agreement of their amorphous microstructure. © 2000 Elsevier Science S.A. All rights reserved.

Keywords: Composite coatings; Ion bombardment; Molybdenum sulphide; MoST[®]; MoS₂–Ti; XPS

1. Introduction

MoS₂ has received distinguished attention as a solid lubricant in extreme conditions. Recent results show that MoS₂ coatings incorporating Ti have not only better adhesion to various substrates but also improved friction and wear properties [1]. As previously reported [2,3], MoST[®] coatings are MoS₂–Ti composites formed by co-deposition of small amounts of titanium in an MoS₂ based matrix. These composite coatings, produced by closed field unbalanced magnetron sputtering (CFUBMSIP), are harder, more resistant to wear and less sensitive to atmospheric water vapour than MoS₂ and possess excellent industrial performance in a wide range of cutting and forming applications. The properties are dependent on the titanium content. Two types

of MoS₂–Ti composite coatings have been developed with ‘low’ and ‘high’ titanium content (10 and 15–20 at.% Ti respectively). The ‘low’ titanium content composite coating shows hardness of 500 HV, a coefficient of friction of 0.02 during 100 N applied load reciprocating wear testing and a low wear rate, while the ‘high’ titanium composite coating exhibits hardness similar to TiN, a coefficient of friction of 0.04 at 100 N reciprocating wear testing and an extremely low wear rate. These latter high titanium self-lubricating coatings are utilised today in large-scale production.

Molybdenum and titanium as multivalent cations can be consolidated in various valence states both in sulphide and oxide environments. Microanalysis and short range chemical structure studies have been the subject of several early and recent publications [4–10]. Special attention was made to spontaneous and to forced oxidation of such coatings [9]. It was shown that only the Mo is oxidised while no evidence of oxidised sulphur products, e.g. sulphite or sulphate states, could be

* Corresponding author. Tel.: +36-1-319-8147;
fax: +36-1-319-7892.

E-mail address: bertoti@chemres.hu (I. Bertóti)

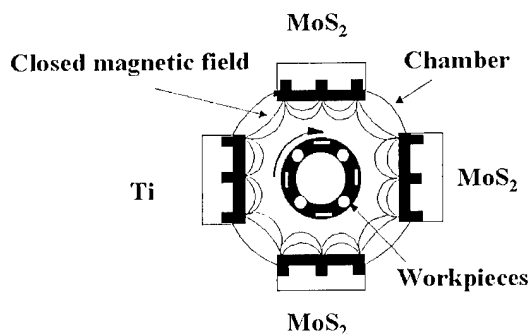


Fig. 1. Schematic representation of a four magnetron coating chamber configured with the closed field unbalanced magnetron sputter ion plating.

detected [4,5]. Hints to the appearance of elemental S has also been reported [4]. In a recent study, formation of sulphuric acid was demonstrated leading to corrosion of the metallic substrates [8]. Recently the super-low friction of MoS₂ has been associated with the extremely high purity (low O level) and stoichiometry of the coatings [7]. These and other literature sources equivocally point out the importance of a close control of composition, impurity level and chemical structure of the constituents in the coatings of high performance.

The purpose of this work was to evaluate the composition and chemical state of the elements in the MoS₂ and MoS₂-Ti composite coatings with 18 at. % Ti content deposited by DC magnetron sputtering. In order to mimic the possible short range chemical transformations caused by the energetic particles of the plasma environment, Ar⁺ ion bombardment was applied to various coatings as well as to a natural molybdenite crystal. The chemical states of the main constituents

were determined by detailed XPS studies and, in addition, short range chemistry of minor contaminants (O and C) were also discovered. The modification of the composition of the constituents due to Ar⁺ bombardment was also widely demonstrated.

2. Experimental

2.1. Sample preparation

The coatings were deposited by DC magnetron sputtering in a Teer CFUBMSIP equipment [11]. The magnetrons in the chamber were arranged so that three MoS₂ and one Ti targets were used and substrates rotated among them (Fig. 1). The procedure starts with the deposition of a thin Ti interface layer.

2.2. XPS measurements

X-ray photoelectron spectra were recorded on a Kratos XSAM 800 spectrometer operated at fixed retarding ratio of 20 using MgK_{α1,2} (1253.6 eV) excitation. Spectra were referenced before ion bombardment experiments to the C1s line of the residual carbon set at 284.6 eV binding energy (BE). For Ar⁺ bombarded states, the position of the sulphidic S2p_{1/2} BE was used set at 162.0 eV. At the applied resolution, the line energy positions could be determined with an accuracy better than ±0.2 eV. The pressure of the analysis chamber was lower than 10⁻⁷ Pa. Peak synthesis was performed by the KRATOS VISION 2000 software. Quantitative analysis, based on peak area intensities, was performed by

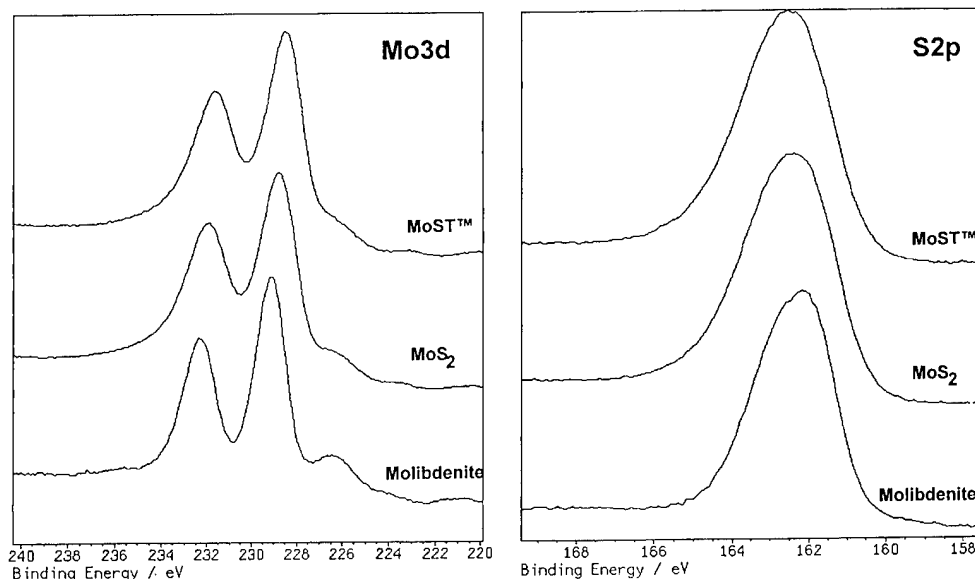


Fig. 2. XP spectra of Mo3d and S2p regions after prolonged air exposure representing gross differences in the chemical states.

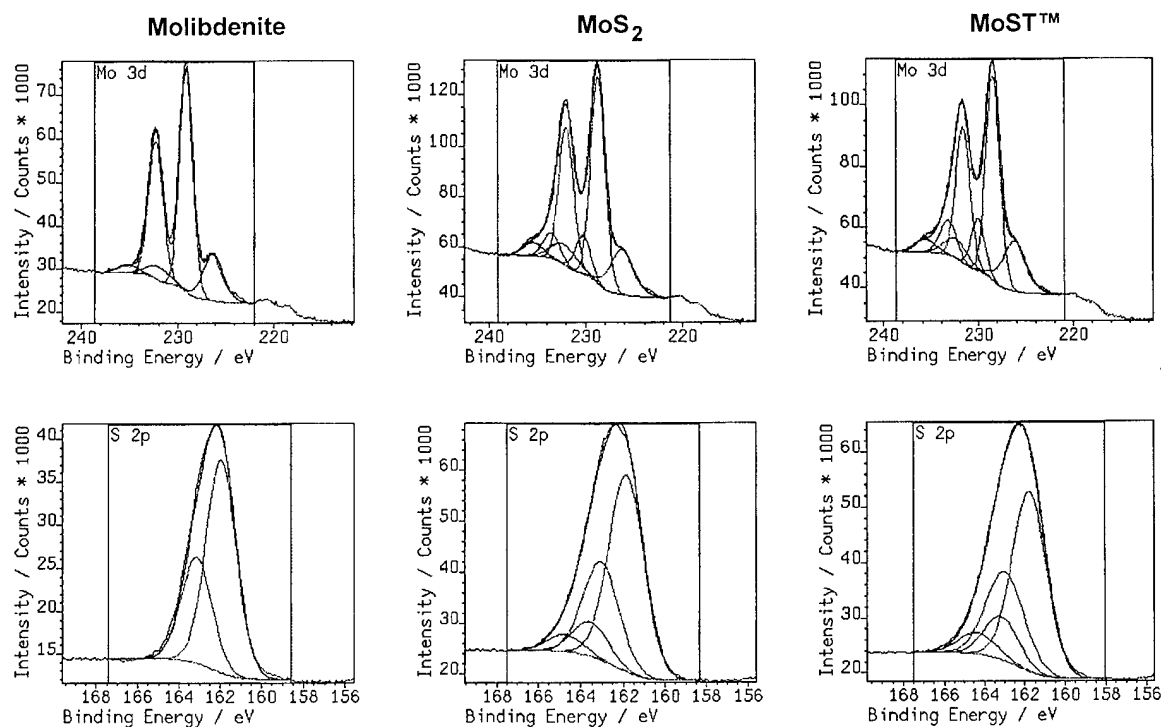


Fig. 3. Decomposition of the Mo3d and S2p spectral regions in as-received states.

the XPS MULTIQUANT program [12] using experimentally determined photo-ionisation cross-sections [13].

2.3. XRD analysis

XRD measurements were performed with Philips equipment between 10° and 60° 2θ angles using $\text{CuK}\alpha$ radiation.

2.4. NBS measurements

Nuclear backscattering spectrometry (NBS) measurements were performed with $^4\text{He}^+$ beam of 3560 keV energy obtained from a 5 MeV Van de Graaff accelerator; using a 25 mm^2 ORTEC detector at 165° scattering angle with a solid angle of 2.5 msr. The spectra were analyzed by the RBX program [14].

Table 1
XPS line positions (eV, BE) and chemical state assignments

Sample	Line	As-received		After Ar^+ bombardment	
		Position	Assignment	Position	Assignment
Molibdenite	Mo3d _{5/2}	229.2	MoS ₂	228.5	MoS _{2-x}
		232.1	MoO _{3-x}	231.7	MoO _{3-x}
		-	-	229.9	Mo ⁺ -S ⁺
	S2p _{3/2}	162.0	MoS ₂	162.0	MoS ₂
MoS ₂ coating	Mo3d _{5/2}	-	-	163.7	S ⁺ -Mo ⁺
		228.8	MoS ₂	228.6	MoS _{2-x}
		232.5	MoO ₃	-	-
		230.4	Mo ⁺ , MoO ₂	230.2	Mo ⁺
	S2p _{3/2}	161.9	S ²⁻	162.0	MoS ₂
MoS ₂ -Ti composite coating	Mo3d _{5/2}	163.6	S ⁺	163.5	S ⁺
		228.8	MoS ₂	228.2	MoS _{2-x}
		232.7	MoO ₃	-	-
		230.4	Mo ⁺ , MoO ₂	229.7	Mo ⁺
	S2p _{3/2}	162.0	S ²⁻	162.0	S ²⁻
		163.4	S ⁺	163.8	S ⁺ -(Mo,Ti)
	Ti2p _{3/2}	455.8	Ti-S	455.0	Ti-S
		458.9	TiO ₂	458.3	TiO _{2-x}
		-	-	456.7	Ti ⁺ -S ⁺

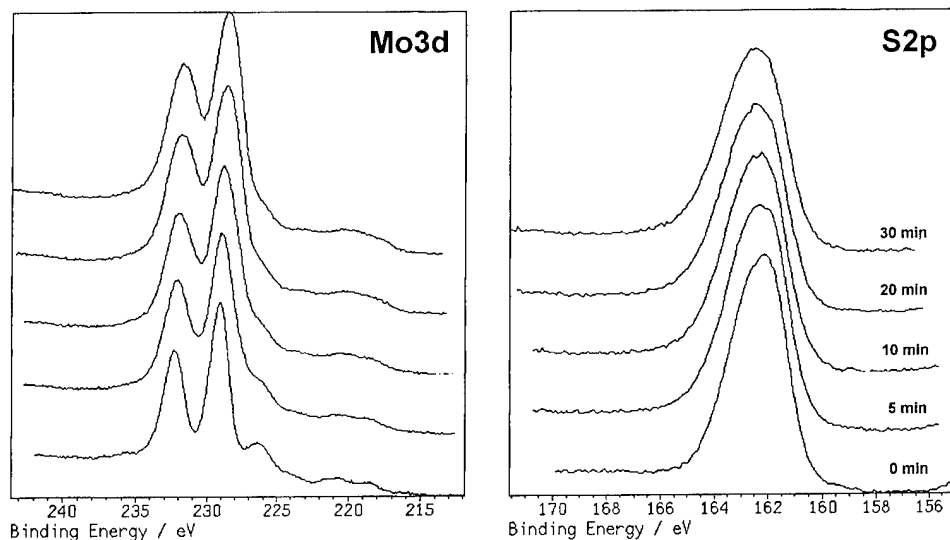


Fig. 4. Alteration of the Mo3d and S2p lines of the molibdenite due to successive Ar^+ bombardment.

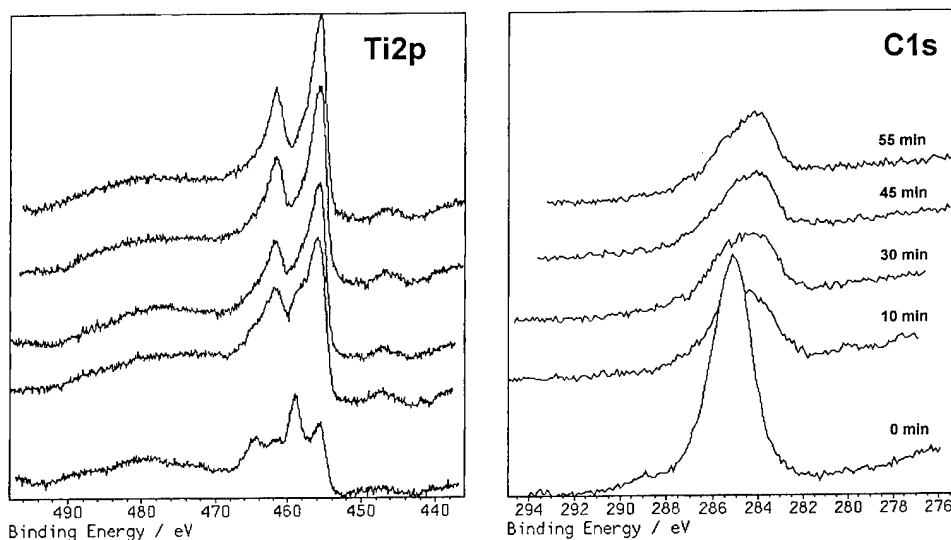


Fig. 5. Changes of the Ti2p and C1s lines of the MoST[®] coating due to Ar^+ bombardment steps.

3. Results and discussion

3.1. Crystallinity

XRD analysis showed that the structure of the coatings was quasi-amorphous. The pure MoS_2 coating shows some broad reflections characteristic of small crystallites lower than 10 nm dimensions.

3.2. Overall chemical composition

In accordance with the applied standard coating procedure, the following layered structures were produced as determined for the coatings by NBS. The MoS_2 coating consists, from the top inwards, of an ≈ 480 nm thick $\text{MoS}_2\text{C}_{0.6}$ and an ≈ 300 nm thick

$\text{MoS}_{2.2}\text{C}_{0.6}$ layers, and of two thin interface layers $\text{Mo}_1\text{Ti}_1\text{S}_2 \approx 6$ nm and $\text{Ti} \approx 60$ nm. The MoS_2 -Ti composite coating consists of a homogeneous $\text{MoS}_2\text{Ti}_{0.7}\text{C}_{0.25}$ layer of ≈ 3000 nm thickness and of two thin interface layers of $\text{MoS}_2\text{Ti}_{1.7}\text{C}_{0.25} \approx 130$ nm and $\text{TiO}_2\text{C}_{0.25} \approx 210$ nm. The fairly constant S/Mo ratio, close to the expected stoichiometry, and also the constancy of Ti/Mo ratio indicative of the stable operation of the deposition system.

3.3. Surface chemical structure and composition

3.3.1. Molibdenite

The Mo3d and S2p spectral regions taken from the surface of a natural molibdenite crystal are depicted in

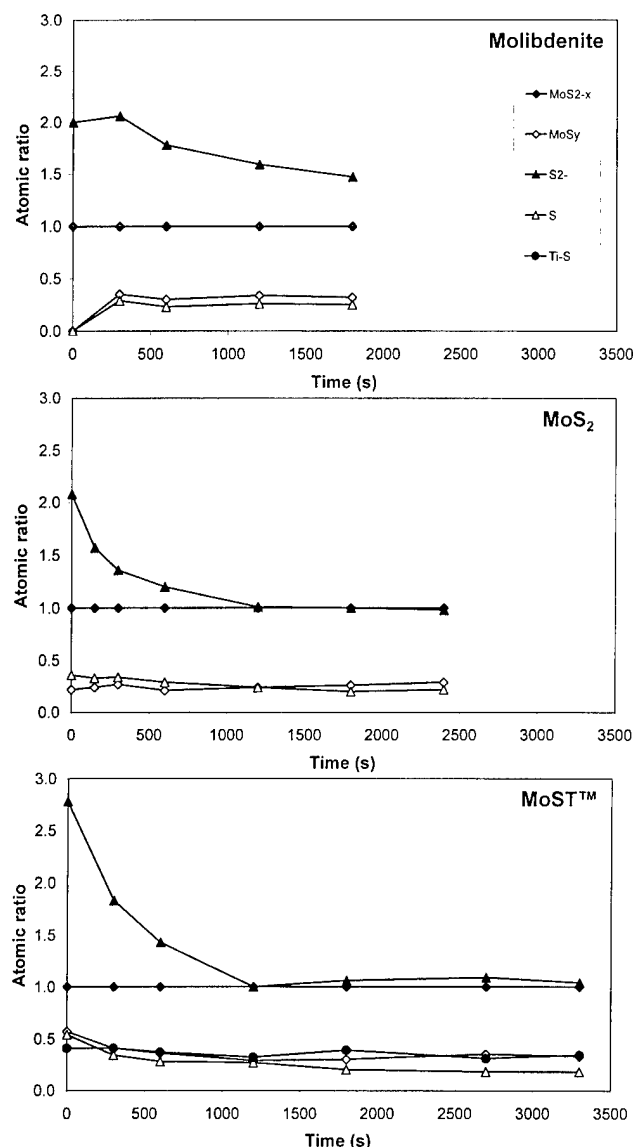


Fig. 6. Alteration of the ratios of the different chemical states (normalised to MoS_2) vs. Ar^+ bombardment time.

Figs. 2 and 3 (together with those from MoS_2 and MoS_2 -Ti composite (MoST^{TM}) coatings). The sharp Mo doublet and the narrow $\text{S}2\text{p}$ line represent essentially one single chemical state assigned to MoS_2 [5,9,15] (Table 1). Additional doublet of negligibly low intensity represents an oxidised state as a sign of slight oxidation of the sample.

3.3.2. MoS_2 and MoS_2 -Ti composite (MoST^{TM}) coatings

As witnessed by Figs. 2 and 3 significantly broader signals of $\text{Mo}3\text{d}$ and $\text{S}2\text{p}$, manifesting more than one chemical state, were recorded for the two coatings. The results of the peak decomposition applied to these lines are also indicated in Table 1 together with the chemical state assignment. The components Mo^* and S^* were

assigned by us to $\text{Mo}(\text{Ti})\text{S}_x$ with $x \approx 1$ on the basis of composition data.

Alterations of the $\text{Mo}3\text{d}$ and $\text{S}2\text{p}$ signals from molibdenite due to Ar^+ bombardment are depicted in Fig. 4. It is obvious that the signals became significantly broadened with increasing bombardment time. These broadened peaks could be fitted with those components which were applicable to fit the corresponding signals of the coatings shown in Fig. 3. Accordingly, Ar^+ bombardment resulted in similar short range chemical structures of Mo and S in the molibdenite crystal as were detected in the coatings. These observations lead us to the conclusion that the unusual $\text{Mo}(\text{Ti})\text{S}_x$ structure in the coatings also developed due to bombardment with energetic species from the plasma during the layer growth.

Alterations of the $\text{Ti}2\text{p}$ and $\text{Cl}1\text{s}$ signals with Ar^+ bombardment time for the MoS_2 -Ti composite coating are shown in Fig. 5. The Ti on the surface of the coating is heavily oxidised and also remains partly oxidised in the detected depth (≈ 60 – 80 nm). The chemical states of Ti are given in Table 1. The assignment of the major (lowest energy) $\text{Ti}2\text{p}_{3/2}$ component to Ti-S bonding state and the Ti^* component to $\text{Mo}(\text{Ti})\text{S}_x$ (or TiO_x before bombardment) derived by us on the basis of both chemical shift and composition data. The C in this coating, in addition to the usual graphitic or adventitious carbon (C-H and C-O) environments, found also in the MoS_2 coating, includes a carbide type component at ≈ 283 eV which is bound, most probably, to titanium.

3.4. Compositional changes caused by Ar^+ bombardment

Changes of the ratios of the major chemical structure units (normalised to sulphide type Mo) vs. Ar^+ exposure time are depicted in Fig. 6. As can be seen, the molibdenite crystal surface is less affected by Ar^+ impact than the MoS_2 and MoST^{TM} coatings. The stoichiometric $\text{S}/\text{Mo} = 2:1$ ratio for molibdenite decreases to ≈ 1.5 . The initial S content on the surface of MoS_2 and MoST^{TM} is significantly reduced by stepwise Ar^+ bombardment to the $\text{S}/\text{Mo} \approx 1$ level. This can be interpreted by the preferential removal of S at Ar^+ impact as being the lightest constituent in these systems. In addition, the maximum energy transfer from Ar^+ projectiles to target atoms, calculated as $E_{\text{max}}/E_{\text{Ar}} = (4M_{\text{Ar}} \times M_{\text{i}}) / (M_{\text{Ar}} + M_{\text{i}})^2$ is largest (0.99) for S and Ti, and is much smaller (0.83) for Mo. Interestingly, the ratio of the $\text{S}^*/\text{Mo}^*(\text{Ti}^*)$ components seems to remain constant with the above indicated $\text{Mo}(\text{Ti})\text{S}_x$ ($x \approx 1$) stoichiometry.

4. Conclusions

- The applied magnetron sputtering technique proved to produce coatings with overall composition very close to MoS_2 stoichiometry.

- The atomic scale chemical structure proved to be complex. XP spectroscopic evidence is given that a new MoS_x ($x \approx 1$) chemical environment was formed at Ar^+ bombardment differing from the undisturbed stoichiometric MoS_2 .
- Chemical states, similar to those observed in Ar^+ bombarded molybdenite, were detected on MoS_2 and MoST^{TM} coatings prepared by unbalanced DC magnetron sputtering.
- The majority of Ti was found bonded to sulphur and a small part to oxygen.
- Ar^+ ion bombardment decreased significantly the S/Mo ratio and, consequently, it can not be applied for depth profiling of MoS_2 type layer structures.

Acknowledgements

This work has been supported by the Hungarian Research Fund (OTKA T014934 and F019165). MoST^{TM} coatings were developed through a SMART and a SPUR program of UK DTI. The XPS experiments were performed in the ESCA Laboratory of the OTKA Materials Science Measuring Center (Budapest). Thanks are due to I. Sajó for the XRD measurements and L. Gulyás for technical assistance.

References

- [1] D.G. Teer, Surf. Coat. Technol. 94/95 (1997) 572.
- [2] V.C. Fox, N.M. Renevier, D.G. Teer, J. Hampshire, V. Rigato, Proceedings of the PSE Conference, Garmisch Partenkirchen, 14–18 September (1998).
- [3] D. G. Teer, V. Bellido-Gonzales, J. Hampshire, MoS_2 /Titanium Coatings, UK Patent GB9514773.2 (19/07/1995), EU Patent 0842306.
- [4] T.B. Stewart, P.D. Fleischauer, Inorg. Chem. 21 (1982) 2426.
- [5] W. Jaegermann, D. Schmeisser, Surf. Sci. 165 (1986) 143.
- [6] V. Buck, Surf. Coat. Technol. 57 (1993) 163.
- [7] T. Le Mogne, C. Donnet, J.M. Martin, A. Tonck, N. Millard-Pinard, S. Fayeulle, N. Moncofre, J. Vac. Sci. Technol. A 12 (1994) 1998.
- [8] D-Y. Yu, J-A. Wang, J-L. Ou Yang, Thin Solid Films 293 (1997) 1.
- [9] N.M.D. Brown, N.Y. Cui, A. McKinley, Appl. Surf. Sci. 134 (1998) 11.
- [10] L. Benoist, D. Gonbeau, G. Pfisterguillouzo, E. Schidth, G. Meunier, A. Levasseur, Thin Solid Films 258 (1995) 110.
- [11] D. G. Teer, Magnetron Sputter Ion Plating, US Patent 5.556.519 (1996), UK Patent GB2258343B.
- [12] M. Mohai, Surf. Interface Anal., (submitted for publication).
- [13] S. Evans, R.G. Pritchard, J.M. Thomas, J. Electron Spectrosc. Relat. Phenom. 14 (1978) 341.
- [14] E. Kótai, Nucl. Instr. and Meth. B 85 (1994) 588.
- [15] J.F. Moulder, W.F. Stickle, P.E. Sobol, K.D. Bomben, Handbook of X-ray Photoelectron Spectroscopy, Eden Prairie, Minnesota, 1992. Physical Electronics Division, Perkin-Elmer Corporation.

Mechanical properties of hard chromium tungsten nitride coatings

P. Hones^{a,*}, R. Consiglio^b, N. Randall^b, F. Lévy^a

^a EPFL-Institut de Physique Appliquée, Ecole Polytechnique Fédérale de Lausanne, CH-1015 Lausanne, Switzerland

^b CSEM Instruments, Jaquet-Droz 1, CH-2007 Neuchâtel, Switzerland

Abstract

Due to its excellent oxidation and wear resistance, CrN is a prominent material for protective coatings. Still, its comparatively low hardness prevents CrN from being widely used in industrial applications. Thin films of $\text{Cr}_{1-x}\text{W}_x\text{N}_y$ with $0 \leq x \leq 1$ were deposited on silicon, glass and steel substrates by reactive r.f. magnetron sputtering. The B1-NaCl phase is the only phase detected. In tungsten-rich films the compressive residual stress increases linearly with increasing tungsten content, but films with a high chromium content show tensile stresses. The morphology, examined by cross-section scanning electron microscopy, changed with increasing tungsten content from a columnar to a fine-grained microstructure. Hardness values, measured by nanoindentation, show a steep increase in hardness with only small additions of tungsten (hardness increases by 85% at a tungsten content of 10%). The maximum hardness value was measured for $\text{WN}_{0.7}$ (30 GPa). The ternary $\text{Cr}_{1-x}\text{W}_x\text{N}_y$ films with $0.1 \leq x \leq 0.8$ and $0.8 \leq y \leq 1$ were significantly harder (29–24 GPa) compared to CrN (13 GPa). In scratch tests with progressively increasing load, the films prove to have good adhesion and wear resistance, although some cracking is observed in films with tensile residual stress. In multi-pass scratch tests at low load, brittle flank wear is observed in films with moderate to high tungsten contents, while the softer CrN film exhibit cracks in the wear track. © 2000 Elsevier Science S.A. All rights reserved.

Keywords: Chromium nitride; Mechanical properties; Ternary compound; Transition metal nitride; Tungsten nitride

1. Introduction

Transition metal nitride coatings, mainly based on titanium and chromium, are nowadays essential in protection technologies against wear and corrosion [1–3]. Especially with regard to hot corrosion resistance, chromium nitride coatings show promising properties [4,5]. W–N thin films were examined mainly as diffusion barrier for Al and Cu metallizations in ultra large scale integrated circuits (ULSI) [6–8] due to their low reactivity and permeability for Al and Cu. This might also be of advantage in tribological applications as a low sticking coefficient of these metals is anticipated. Ternary compounds offer the opportunity to adjust parameters such as lattice constant, hardness, elasticity, thermal expansion and corrosion stability in order to optimize the overall performance of the coating. In addition, the effect of mixed crystal strengthening and phase separation can be applied [1]. In previous work, (Cr, Mo)N [9] and (Cr, Ti)N [10] compounds were investigated,

but the addition of Mo or Ti to CrN did not result in an increased hardness.

This paper reports on the characterization of the crystalline phase, residual stress and the morphology of $\text{Cr}_{1-x}\text{W}_x\text{N}_y$ thin films grown in the whole range of chromium to tungsten ratios ($0 \leq x \leq 1$). The mechanical properties were studied by nanoindentation and scratch tests. To the best of our knowledge, this was the first systematic examination of structural and mechanical of chromium tungsten nitride thin films.

2. Experimental

The chromium tungsten nitride thin films were deposited by reactive r.f. magnetron sputtering in an ultrahigh vacuum reactor with two confocal sources [11]. The residual pressure was in the range of 10^{-5} Pa before the introduction of the sputtering gases, namely argon and nitrogen. Disks (50 mm in diameter) of 99.99% pure chromium and 99.95% pure tungsten were used as target materials. The distance between the substrate and the

* Corresponding author. Tel.: +41-21-693-4438;
fax: +41-21-693-4666.

E-mail address: peter.hones@switzerland.org (P. Hones)

targets was fixed at 100 mm. The total pressure during the sputtering process was kept constant at 0.66 Pa and the nitrogen partial pressure p_{N_2} at 0.33 Pa. Silicon, glass and high speed steel were used as substrate materials. The substrate temperature was kept constant during deposition at 500 ± 20 K. This temperature was chosen in order to obtain films with zone T microstructures [12], which often exhibit favorable mechanical properties. The substrates were also electrically grounded. In order to produce films with different chromium to tungsten ratios a power between 0 and 150 W was applied to the different sputtering targets maintaining the total power ($P_{Cr} + P_W$) at 150 W.

The crystallographic phases were determined by X-ray diffraction (XRD) using monochromatized $CuK\alpha$ radiation at grazing incidence ($\omega = 4^\circ$) and preferential orientations by a $\theta/2\theta$ scan. The $\sin^2\psi$ method [13] was applied to determine the average biaxial residual stress. The measurements were performed in symmetric ($\theta/2\theta$) and asymmetric configuration (incidence angle $\omega = 4^\circ$). The shift of the [111] peak position as a function of the tilt angle ψ together with the elastic modulus, measured by nanoindentation, were used to calculate the residual stress. The Poisson ratio ν was assumed to be 0.25 for all films.

Electron probe microanalysis (EPMA) (Cameca SX 50) was used to determine the chemical composition. The measurements were performed at 8 kV (accelerating voltage) and 100 nA (beam current) for about 1 μ m thick films, limiting the penetration depth of the electron beam to less than 40% of the film thickness. The precision of the results is within ± 1 at. %.

Cross-sectional scanning electron microscopy (SEM) was performed on a Jeol 6300 F field emission SEM at an acceleration voltage of 30 kV.

The nanohardness was determined by nanoindentation (Nanoindenter XP, Nano Instruments). A Berkovich-type pyramidal diamond tip indented the films to a maximum depth of 700 nm. Constant stiffness data measurements were obtained by oscillating the tip during indentation with a frequency of about 62 Hz [14]. This kind of measurement provided hardness, elastic modulus and stiffness data throughout the whole indentation depth. Hardness values were taken at 150–200 nm depth to avoid a major influence of the surface roughness and of the substrate.

The adhesion and the wear resistance were tested with two different scratch test methods (Nanoscratch tester, CSEM Instruments). In single-pass experiments, a diamond tip (tip curvature radius 10 mm) scratched the surface with a linearly increasing load from 0 N to 300 mN over a distance of 2 mm with a scratch speed of 0.1 mm/s. In multi-pass experiments the diamond tip moved back and forth under the constant load of 40 mN in the same wear track with a scratch speed of 0.1 mm/s.

3. Results and discussion

3.1. Structural properties and morphology

Smooth (average roughness R_a below 2 nm) and well adhesive films were deposited with typical growth rates between 0.14 nm/s for pure W–N and 0.10 nm/s for pure Cr–N [10]. The measured film thickness was in the range 1.1–1.8 μ m. The face centered cubic (fcc) phase was the only phase observed in XRD for all the films. Fig. 1 shows the XRD pattern of $Cr_{1-x}W_xN_y$ films with various chromium to tungsten atomic ratios. Adding a small amount of tungsten to Cr–N, the texture changes from a [111] preferential orientation in the binary Cr–N compound to a weak [200] texture in the ternary films. The W–N compound crystallizes without a significant preferential orientation.

The apparent crystallite size can be estimated from the FWHM of the XRD peaks [15], and is shown in Fig. 2. It increases from 10 nm in W–N to 20 nm in Cr–N. Competition between nucleation and crystal growth

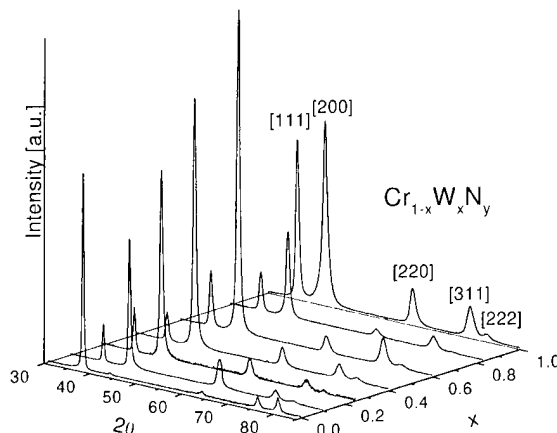


Fig. 1. X-ray diffraction pattern of $Cr_{1-x}W_xN_y$ films measured in grazing incidence configuration.

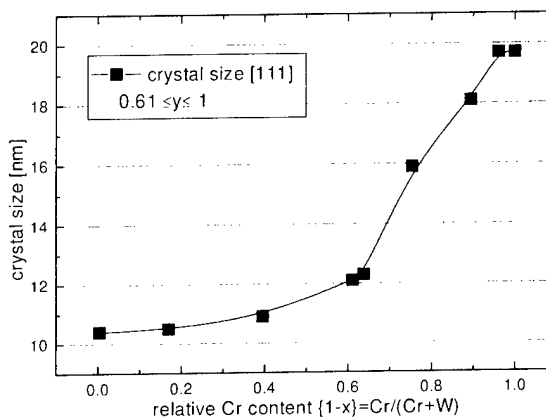


Fig. 2. Crystallite size in $Cr_{1-x}W_xN_y$ films as a function of the chromium content determined from the peak broadening of the [111] diffraction peak. The accuracy of the indicated values is within 1–2 nm.

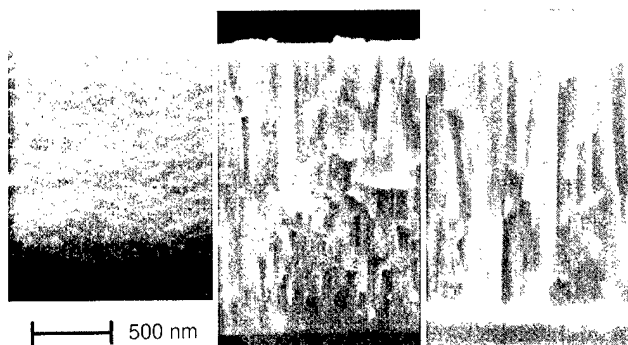


Fig. 3. Cross-section scanning electron micrographs of (from left to right) a $\text{Cr}_{0.6}\text{W}_{0.4}\text{N}$, a $\text{Cr}_{0.9}\text{W}_{0.1}\text{N}$, and a CrN film.

during the deposition causes these different behaviors. Nitrogen deficiency reduces the growth of the crystallites. The cross-section SEMs in Fig. 3 show a columnar crystal arrangement in both the Cr–N and the $\text{Cr}_{0.9}\text{W}_{0.1}\text{N}$ film. In contrast, the $\text{Cr}_{0.6}\text{W}_{0.4}\text{N}$ film exhibits a fine-grained dense morphology without apparent superstructure.

3.2. Chemical composition

The stoichiometric ratio of chromium, tungsten and nitrogen is represented versus the power on the chromium target during the sputtering process in Fig. 4. Both the decrease of the tungsten content and the increase of the chromium content run almost linearly with increasing power on the chromium target and decreasing power on the tungsten target, respectively. The nitrogen content increases steadily from a metal to nitrogen ratio of 5:3 for W–N, to a ratio of 1:1 for mainly chromium containing films. In order to grow stoichiometric W_2N films, the nitrogen partial pressure has to be lowered to 0.22 Pa. However, in order to grow the films under the same deposition conditions, we kept the nitrogen partial pressure constant at 0.33 Pa. At this

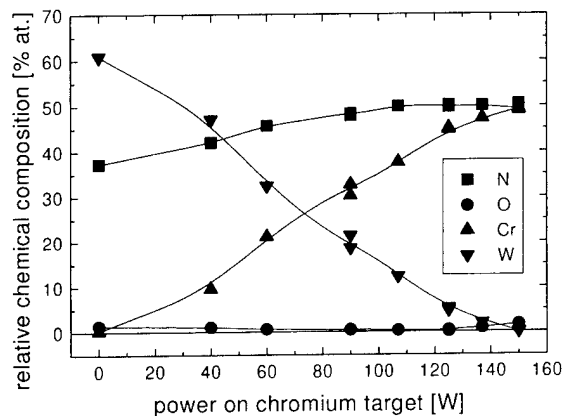


Fig. 4. $\text{Cr}_{1-x}\text{W}_x\text{N}_y$ thin films. Relative chemical composition vs. power on the chromium target; the total power on both targets (Cr and W) was constant at 150 W. The precision is within 1 at.%.

nitrogen partial pressure stoichiometric CrN films are deposited [16]. Only very low residual oxygen contents below 1.5 at.% are measured. Nitrogen vacancies can act as nucleation centers for grains with different orientations. Therefore, the nitrogen deficient tungsten-rich films exhibit more randomly oriented grains. This is also likely to be the reason for the smaller grain size of the films.

3.3. Mechanical properties

Hardness, elastic modulus and residual stress are important properties of hard coatings. In Fig. 5(a) we represent the nanohardness as a function of the chromium content $\{1-x\}$. Starting from W–N, with a high hardness value of 30 ± 1 GPa, the hardness stays at a high level over a large range of chromium to tungsten ratios. Only at $x < 0.1$ does the films hardness drop steeply. In the nanoindentation measurement, the CrN film yields a hardness of 13 ± 1.5 GPa (literature bulk value 11 GPa) which is in good agreement with the results from microindentation experiments on films deposited under similar conditions [16]. Fig. 5(b) represents the elastic modulus and the residual stress as a function of the chromium content $\{1-x\}$. The bulk elastic modulus value for CrN was reported [1] to be 400 GPa, which is substantially higher than our measured value of 205 ± 20 GPa. Nevertheless, this result is not unusual since thin films show different mechanical properties to bulk materials as the deformation mechanism differs considerably. For example, the dislocation mobility is hindered by a very high defects and grain boundary density [2] which are common features in thin films. The origin of the rather large inaccuracy in the elastic modulus measurements of about 10% is due to the influence of the surface roughness and of the substrate. It is generally observed that a high compressive residual stress accounts for high hardness values, whereas tensile stresses lead to softer films. The $\text{WN}_{0.61}$ film exhibits a relatively high compressive residual stress level (4.3 ± 5 GPa). With increasing chromium (and nitrogen) content the compressive stress decreases, in a first approximation, linearly. Chromium-rich films show low tensile stresses. Deviations from this linear behavior are due to differences in the elastic modulus of the films. The residual stress is not responsible for the strong hardness increase at low tungsten contents. Neither can changes in the microstructure account for the hardness increase with the addition of a small tungsten content in a CrN film. The hard $\text{Cr}_{0.9}\text{W}_{0.1}\text{N}$ film and the relatively soft CrN film show a very similar morphology and about the same grain size (Figs. 2 and 3).

It is commonly observed that covalent bonded materials are harder than metallic or ionic bonded compounds [1]. Correlated peak shifts in the X-ray photoelectron

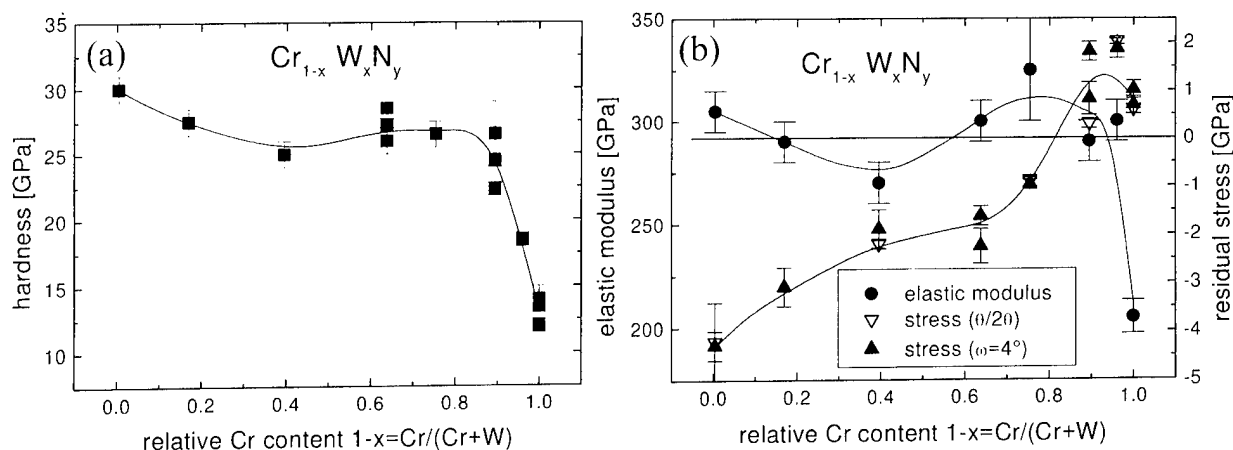


Fig. 5. (a) Nanohardness, and (b) elastic modulus and residual stress in $\text{Cr}_{1-x}\text{W}_x\text{N}_y$ thin films. Positive stress values signify a tensile biaxial stress, and negative values a compressive stress respectively.

spectrographs of nitrogen and metal electronic states show differences in the charge transfer from the metal to the nitrogen atoms as a function x . In other words, the bonding character is changed. In fact, tungsten-containing films exhibit a higher covalence level than CrN, which could account for the hardness difference. A similar correlation is also observed in CrTiN [10] and CrMoN [9] thin films. Details about the study of the electronic structure will be reported elsewhere.

The wear resistance depends strongly on intrinsic properties of the films such as morphology, hardness, friction coefficient and cohesion [17]. In addition, the stress state exerts an important influence. Low compressive residual stresses are preferable, as in most wear sensitive applications an additional tensile stress is induced in the film. This leads to tensile cracking foremost in films with tensile residual stresses.

Scratch tests allow probing the adhesion and the

wear resistance of the most promising films for industrial applications of the present study, the chromium-rich $\text{Cr}_{1-x}\text{W}_x\text{N}_y$ films. No indications of adhesive failure were detected in any of the films, which proved an excellent adhesion to Si. In a first row of experiments, the load on the diamond tip was linearly increased up to a maximum load of 300 mN. Comparing the wear tracks of $\text{Cr}_{0.6}\text{W}_{0.4}\text{N}$, $\text{Cr}_{0.9}\text{W}_{0.1}\text{N}$ and CrN films, the penetration depth (Fig. 6(a)) and the damage state (Fig. 6(b)) in the wear track change significantly. The films with a tensile residual stress ($\text{Cr}_{0.9}\text{W}_{0.1}\text{N}$ and CrN) show cracks in the wear track and also laterally to the track. The $\text{Cr}_{0.6}\text{W}_{0.4}\text{N}$ film with compressive residual stress shows no cracks even at highest load.

Surprisingly this film exhibits the largest residual depth of the wear track. As the depth exceeds, by far, the film thickness of 2.33–2.49 μm and optically no damage in the wear track is observed, it is concluded

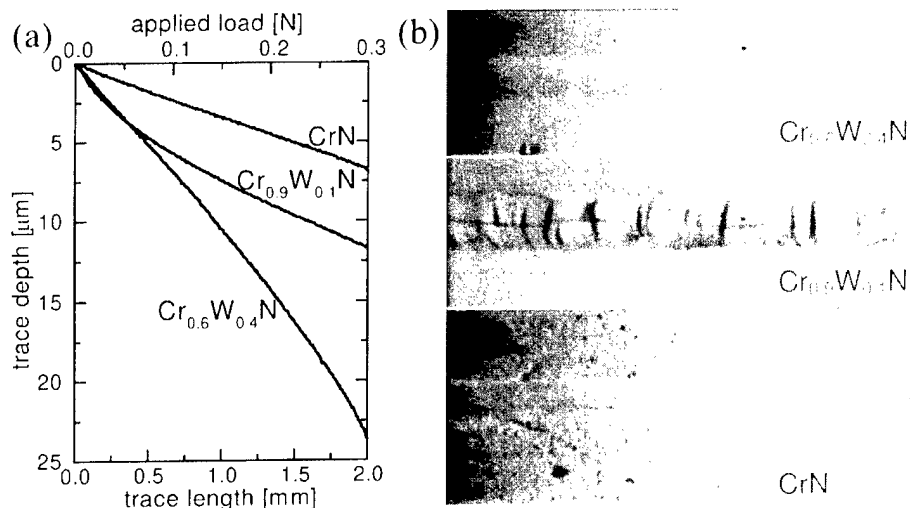


Fig. 6. (a) Depth, and (b) damage state of wear scars of $\text{Cr}_{0.6}\text{W}_{0.4}\text{N}$, $\text{Cr}_{0.9}\text{W}_{0.1}\text{N}$ and CrN thin films deposited on Si at maximum load in a single-pass experiment with increasing load on the scratching diamond tip.

that the energy dissipation by deformation takes place mainly in the relatively soft substrate ($H(\text{Si})=13$ GPa vs. $H(\text{Cr}_{0.6}\text{W}_{0.4}\text{N})=26$ GPa). In the case of $\text{Cr}_{0.9}\text{W}_{0.1}\text{N}$ and CrN , the depth of the wear track decreases with decreasing hardness and the damages in the wear scar indicate that the energy is increasingly dissipated in the film. In order to study the failure mechanism, multi-pass experiments were conducted at a comparatively low load. Contrary to the CrN film, films with a relatively high tungsten content show small particles along the scratch path (Fig. 7). These particles are split off the film, probably because of flank wear. This indicates that the toughness of CrN is reduced by the incorporation of tungsten. It is a common observation that the brittleness of the films is increased with increasing hardness [1]. By optical microscopy, no damage was observed in the scratch tracks of tungsten-containing films even after 500 scratch cycles. In the CrN film, tensile cracking was observed after only 20 cycles.

Reports on CrN films showed excellent wear resistance of fcc CrN films. Depending on the deposition and measurement technique, their wear resistance is reported to be superior to TiN thin films [17] — this is attributed to the commonly lower coefficient of friction and higher toughness. Some authors (e.g. Ref. [18]) claim that hardness and adhesion show opposing trends. However, if the film hardness, in relation to the hardness of the wear partner, is too small, abrasive wear results. Therefore, the lower hardness of CrN compared to TiN can be a disadvantage. Thus, the increase in the hardness of CrN by simple means is of great technological advantage if other functional properties of CrN are not degraded. The presented results suggest that $(\text{Cr}, \text{W})\text{N}$

films with compressive residual stress provide a superior wear resistance if high peak loads are applied in the application. However, compared to CrN they are inferior when performing under continuous load conditions due to their lower toughness.

Commonly, there is a large gap between results from wear tests and performance in practical applications. Costly field tests are more likely to give reliable information on wear protection; scratch test can only provide indications. The coatings were not optimized for tribological issues. If the bombardment of the growing film is increased (e.g. through a negative substrate bias) the tensile stresses can be altered in a compressive stress, which is then favorable for wear protection applications.

4. Conclusions

The addition of tungsten increases the comparatively low hardness of CrN , a prominent material for corrosion and wear protective coatings. The fcc phase is the only phase detected in $\text{Cr}_{1-x}\text{W}_x\text{N}_y$ thin films with $0 \leq x \leq 1$. In tungsten-rich films, the compressive residual stress linearly increases with increasing tungsten content, but films with a high chromium content show tensile stresses. The film morphology changes with increasing tungsten content from a columnar to a fine-grained microstructure. The chemical composition shows a decreasing nitrogen content from $y=1$ in CrN_y to $y=0.61$ in WN_y . The nitrogen stoichiometry strongly influences the evolution of the grain size, texture and residual stress. The hardness values show a steep increase in hardness with only small additions of tungsten (hardness increases by 85% at a tungsten content of 10%). The maximum

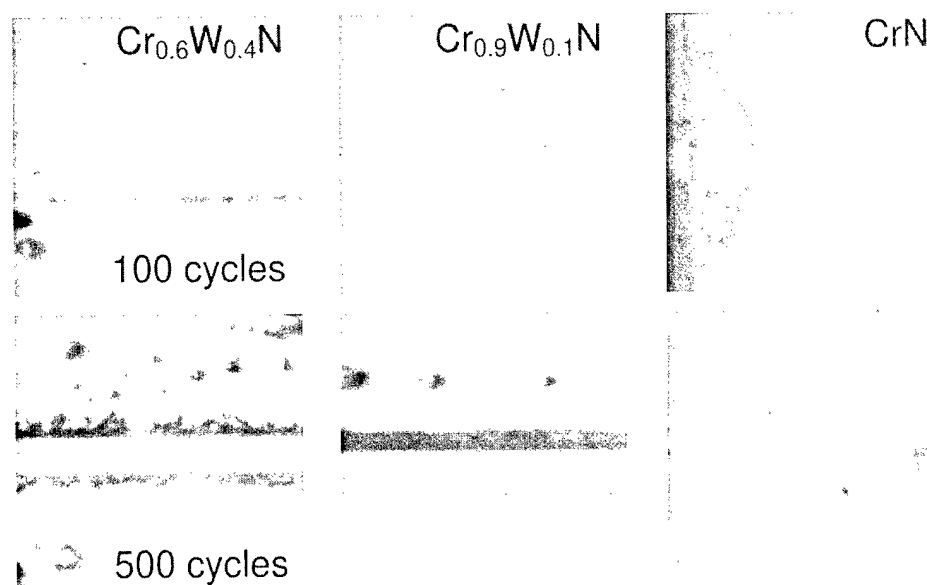


Fig. 7. Wear scars of $\text{Cr}_{0.6}\text{W}_{0.4}\text{N}$, $\text{Cr}_{0.9}\text{W}_{0.1}\text{N}$ and CrN thin films deposited on Si in multi-pass experiments at a load of 40 mN after 100 and 500 scratch cycles respectively.

hardness value was measured for $WN_{0.7}$ (30 GPa). The $Cr_{1-x}W_xN_y$ films with $0.8 \geq x \geq 0.1$ and $0.8 \leq y \leq 1$ also are significantly harder (29–24 GPa) compared to CrN (13 GPa). The evolution of hardness as a function of x can not be explained by changes in the microstructure and residual stress. In scratch tests the films show good adhesion and wear resistance, although some cracking is observed in films with tensile residual stress. An increasing tungsten addition in CrN embrittles the films progressively. Therefore, (Cr, W)N films with a low tungsten content are excellent candidates for wear protective coatings, combining the high hardness of W–N and the toughness of Cr–N.

References

- [1] H. Holleck, J. Vac. Sci. Technol. A 4 (1986) 2661.
- [2] J.-E. Sundgren, H.T.G. Hentzell, J. Vac. Sci. Technol. A 4 (1986) 2259.
- [3] I. Milosev, B. Navinsek, H.-H. Strehblow, Scientific Series of the International Bureau Vol. 37, Forschungszentrum Jülich GmbH, 1995, p. 1.
- [4] L. Swadzba, A. Maciejny, B. Formanek, P. Liberski, P. Podolski, B. Mendala, H. Gabriel, A. Poznanska, Surf. Coat. Technol. 78 (1996) 137.
- [5] P. Panjan, B. Navinsek, A. Cvelbar, A. Zalar, I. Milosev, Thin Solid Films 282 (1996) 298.
- [6] B.L. Park, D.H. Ko, Y.S. Kim, J.M. Ha, Y.W. Park, S.I. Lee, H.D. Lee, M.B. Lee, U.I. Chung, Y.B. Koh, M.Y. Lee, J. Electron. Mater. 26 (1997) L1.
- [7] M. Takeyama, A. Noya, Jpn. J. Appl. Phys. 36 (1997) 2261.
- [8] M. Uekubo, T. Oku, K. Nii, M. Murakami, K. Takahiro, S. Yamaguchi, T. Nakano, T. Ohta, Thin Solid Films 286 (1996) 170.
- [9] P. Hones, R. Sanjinés, F. Lévy, O. Shojaei, J. Vac. Sci. Technol. A 17 (1999) 1024.
- [10] P. Hones, R. Sanjinés, F. Lévy, Thin Solid Films 332 (1998) 240.
- [11] R. Luthier, F. Lévy, H. Jotterand, Proc. 7th Int. Conf. Ion and Plasma Assisted Techniques, CEP Consultants, Edinburgh, 1989, p. 37.
- [12] J.A. Thornton, Ann. Rev. Mater. Sci. 7 (1977) 239.
- [13] B.D. Cullity, Elements of X-ray diffraction, 2nd Edition, Addison-Wesley, Reading, MA, 1978, p. 447.
- [14] W.C. Oliver, G.M. Pharr, J. Mater. Res. 7 (1992) 1564.
- [15] A. Guinier, X-ray Diffraction, W. H. Freeman, San Francisco, CA, 1963, p. 143.
- [16] P. Hones, R. Sanjinés, F. Lévy, Surf. Coat. Technol. 94/95 (1997) 398.
- [17] Y. Chiba, T. Omura, H. Ichimura, J. Mater. Res. 8 (1993) 1109.
- [18] W.K. Grant, C. Loomis, J.J. Moore, D.L. Olson, B. Mishra, A.J. Perry, Surf. Coat. Technol. 86/87 (1996) 788.

Mechanical behaviour of hard PVD multilayered coatings

E. Harry ^{a,*}, M. Ignat ^b, Y. Pauleau ^b, A. Rouzaud ^c, P. Juliet ^c

^a *Laboratoire des Sciences & Ingenierie des Surfaces, Universite Claude Bernard Lyon 1,
43 boulevard du 11 Novembre 1918, Bat. 305, F-69622 Villeurbanne, France*

^b *ENSEEG, F-38402 Saint Martin d'Hères, France*

^c *CEA, F-38054 Grenoble Cedex 9, France*

Abstract

The aim of this work was to investigate the cracking behaviour and adhesion of tungsten–carbon-based multilayered coatings deposited on steel substrates by magnetron sputtering. Three-point bending experiments were performed on the coating-on-substrate systems until failure of the film. The systems were also strained uniaxially with a microtensile device adapted to a scanning electron microscope. The mechanical response is analysed from the evolution of the crack density in the coating and the fracture toughness. The results show that the rupture properties of the multilayered coatings are correlated to the film thickness and arrangement of the elementary layers. Scratch experiments on the systems revealed a strong adhesion of the multilayered coatings on steel substrates, and delamination at layer interfaces. Thus, graded coatings appear to be more attractive for mechanical applications. © 2000 Elsevier Science S.A. All rights reserved.

Keywords: Coatings; Cracking; Multilayers; Tungsten; Tungsten–carbon

1. Introduction

Tungsten carbide coatings prepared by chemical vapour deposition or physical vapour deposition appear to be attractive candidates for the protection of mechanical components (such as cutting tools) against wear or erosion [1]. However, these hard coatings exhibit brittle mechanical behaviour which can affect their reliability. To improve the erosion or wear resistance of hard coatings, a judicious combination of hardness and toughness should be favourable. Hence, hard multilayered coatings based on a stacking arrangement of ductile layers and hard layers have been developed [2,3]. Multilayered coatings produced by sputtering and composed of pure tungsten layers (W) and hard tungsten–carbon layers [W(C)] were found to be very promising erosion-resistant coatings for compressor blades in gas turbine engines [2]. The performance of these protective coatings appears to be governed by the cracking resistance and adhesion of the composites, and the by the mechanical behaviour of the elementary layers. Harry et al. reported that tungsten and W(C) layers deposited

by magnetron sputtering have quite different mechanical properties, since columnar tungsten films behave like a 'ductile' material compared with W(C) films, which are dense and brittle [4,5]. Indeed, tungsten layers exhibit a fracture toughness close to 2 MPa m^{1/2} and appear to adhere well to stainless steel substrates. By contrast, the cracking resistance of W(C) layers was found to be about two times lower than that obtained for tungsten layers; these films have also shown very poor adhesion on stainless steel substrates. The mechanical behaviour of multilayered coatings of this type layers has been investigated, and was found to depend on the nature of the layer at the interface between the substrate and the coating. In particular, a columnar tungsten interfacial layer appears to limit delamination of the coatings, through a contribution arising from motion of the columns.

The aim of this work was to investigate the mechanical response of multilayered coatings of this type submitted to an elongation. This includes determination of the critical deformation of the film corresponding to crack onset, and determination of the fracture toughness using an analytical approach. The fracture properties of the films are discussed through a Weibull analysis and the damage mechanisms examined with respect to coating architecture. Then, the adhesion of the multilayered coatings is characterised qualitatively.

* Corresponding author. Tel: +33-4-72-44-83-06;
fax: +33-4-72-43-12-06;

E-mail address: harry@cismcun.univ-lyon1.fr (E. Harry)

2. Experimental details

Coatings were deposited on stainless steel substrates by direct-current reactive magnetron sputtering. Experimental details of the procedure have been reported previously [4,6]. The multilayered coatings are based on the stacking arrangement of two or four successive layers of tungsten (W) and tungsten–carbon [W(C) with 14 at% of carbon]. The bilayer and four-layer coatings are named 2L-W(C)/W and 4L-W(C)/W, respectively. These multilayered coatings, of thickness ranging from 3.5 μm to 14 μm , are composed with a columnar tungsten layer located at the substrate/coating interface and a hard W(C) top layer.

The films were submitted to three different types of test:

- three-point bending tests [7], to determine the Young's modulus and to detect the onset of cracking of the coating;
- uniaxial tensile tests performed in a scanning electron microscope (SEM), supplying some new information in the analysis of the mechanical response of the deposited materials [8]. These experiments permit us to follow the evolution of the transverse crack density in the films when the applied strain is increased; and
- scratch tests performed under loads ranging from 0 to 100 N. The loading rate and displacement speed of the indenter are 100 N min⁻¹ and 10 mm min⁻¹, respectively. The objectives of this method are to evaluate the adhesion of the coatings to the substrate and to rank the coatings with respect to debonding resistance.

3. Mechanical properties

The hardness of the multilayered coatings was measured by classical Vickers microindentations under 50 g for films of thickness 14 μm . As a result, the effect of the hardness of substrates covered with relatively thick coatings can be neglected. The microhardness values lay between 26 GPa for the four-layer coatings and 28 GPa for the bilayer coatings. The microhardness of the multilayered coatings was close to that of the material deposited on top of the coating, i.e., W(C) [4].

The residual stresses in the films were determined by means of substrate curvature measurements before and after deposition of the coatings, using the Stoney formula. The multilayered coatings are found to be in a compressive state. The level of residual stress appears to be similar for both types of multilayered coating, and very high, close to -3 GPa, without any delamination of the films.

The Young's modulus of the coatings was determined through three-point bending experiments, performed on the substrate only and on the coated substrate. The device used and the experimental procedure are

described elsewhere [5,7]. Assuming perfect adhesion of the films on the substrates, when the sample is submitted to an elastic bending, calculations derived from an energy balance on the composite structure lead to the following simple equation:

$$E^f = E^s \frac{t^s}{3t^f} \frac{F_2 - F_1}{F_1}, \quad (1)$$

where E^s , t^s and E^f , t^f are the Young's modulus and thickness of the substrate and the film, respectively. F_1 and F_2 are the forces which correspond to bending of the substrate and the composite to the same deflection. The parameter $(F_2 - F_1)/F_1$ is determined experimentally, and the film's Young's modulus is then deduced.

The experimental mean value of Young's modulus is around 391 GPa for the multilayered coatings, whatever their architecture or thickness. This result shows that the Young's modulus of 2L-W(C)/W and 4L-W(C)/W coatings is close to the tungsten bulk value [9].

4. Cracking investigation

Techniques to determine fracture properties such as the fracture toughness of bulk materials are not suitable for determination of the same parameters in thin coatings. Therefore, new experimental methods have been developed [8,10,11]. In our case, we first performed three-point bending tests, and then in situ microtensile tests, both to determine the fracture parameters and to study the rupture properties of the coatings. Investigations of this type on the elementary tungsten and W(C) layers have been carried out previously [5]. Then, the results obtained for the multilayered coatings could be compared with those obtained for the single layers.

When a coatings on a substrate is submitted to tensile tests, the response of both the film and the substrate is entirely elastic at low strain (lower than 0.8%). At a critical longitudinal deformation of the substrate, $\epsilon_{xx,c}^s$, the coating begins to crack as it is much stiffer than the substrate. The critical cracking stress attained at coating failure is denoted $\sigma_{xx,c}^f$.

The cracking phenomenon can be described in successive stages. At crack onset, the coating will develop a series of regular and parallel spaced cracks, perpendicular to the loading direction. These initial cracks will multiply rapidly after the crack onset. With increasing deformation additional transverse cracks appear progressively and the distance separating two consecutive cracks decreases. This evolution can be followed by the crack density parameter D , which is defined as the number of transverse cracks over a given length. Continuing the longitudinal strain, this parameter — which grows at the beginning of the deformation — will

reach a constant value: the crack saturation density, D_{sat} , corresponding to a minimal length between two cracks. The vicinity of the crack-free surfaces lowers the global stress level in the coating under the critical cracking stress $\sigma_{xx,c}^f$ [4]. When saturation of the cracks is reached, if the deformation continues, no new cracks appear; but the existing ones will continue to open, with increasing plastic deformation in the substrate, concentrated at the crack tip [4].

The critical strain for the substrate is determined experimentally [4], and the critical cracking stress of the coating is deduced by taking into account the residual stresses pre-existing in the coating, σ_r^f . The critical cracking stress can be written as:

$$\sigma_{xx,c}^f = E^f \epsilon_{xx,c}^s + \sigma_r^f. \quad (2)$$

Experimental mean values of $\epsilon_{xx,c}^s$ and $\sigma_{xx,c}^f$ are reported in Table 1. When considering the existence of defects in sputtered coatings, resulting from the growth process or previously existing on the substrates, this cracking stress may be associated with the presence of singularities pre-existing in the coatings. This explains the very low measured values.

Determination of the fracture toughness of the films, K_{1c}^f , depends on the parameters mentioned above. It is based on the energy balance in the strained system when the coating cracks. The theoretical approach has been previously described in detail in the case of single layers [4,5]. It can be extended to our multilayered coatings since the elementary layers have the same Young's modulus and level of residual stress, and assuming perfect cohesion at layer interfaces. In fact, SEM observations of the cross-section of the multilayered coatings do not reveal any delamination or buckling at the interfaces between the tungsten and W(C) layers when the films are uniaxially strained. Therefore, the fracture toughness of the multilayered coatings can be written as:

$$K_{1c}^f = \sqrt{t^f (\sigma_{xx,c}^f)^2 \left[\pi F \left(\frac{E^f}{E^s} \right) + \frac{\sigma_{xx,c}^f}{3\sigma_y^s} \right]}. \quad (3)$$

F is a function of the elastic modulus ratio [12], and σ_y^s is the yield strength of the substrate. The mean values of the calculated fracture toughness are given in Table 1.

The low values of the cracking parameters character-

ise the brittleness of the multilayered coatings, as observed for the single layers. However, the multilayered coatings exhibit critical cracking stress and fracture toughness larger than those determined for the W(C) films. The combination of hardness [W(C) layers] and toughness (tungsten layers) in a multilayered structure appears to improve the failure properties of hard coatings. In the case of the four-layer coatings, the cracking parameters come close to those of the pure metal films. In addition, the results given in Table 1 reveal a higher fracture toughness for the four-layer coatings 4L-W(C)/W (with a total thickness of 14 μm and single layers 3.5 μm thick) than for the bilayer coatings 2L-W(C)/W#3 (14 μm thick and based on two layers of 7 μm thickness) and 2L-W(C)/W#1 (thickness 7 μm , with elementary layers 3.5 μm thick). The cracking behaviour of the coatings appears to depend on the arrangement of the films (single layers, multilayered structures), the total thickness of the coatings, and the thickness of the elementary layers. A judicious choice of the number and thickness of the single layers in multilayered structures should optimise the in-service performance of the coatings for a given application.

The experimental evolution of the transverse crack density (D) of the multilayered coatings is plotted against the applied strain in the substrate ($\epsilon_{xx,c}^s$) in Fig. 1. The following empirical relation, based on a Weibull-type

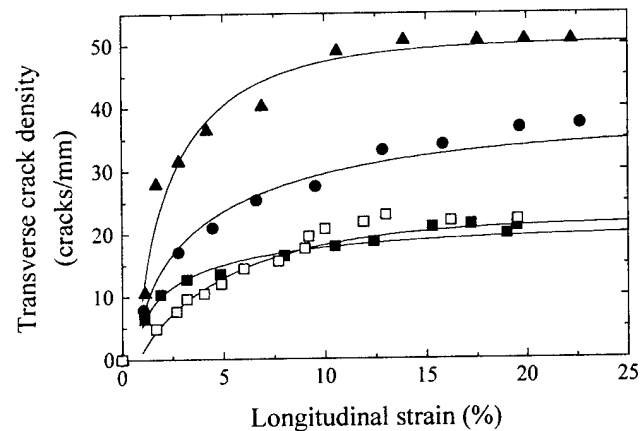


Fig. 1. Transverse crack density of the bilayer coatings 2L-W(C)/W #1 (Δ), #2 (\bullet) and #3 (\blacksquare), and of the four-layer coatings 4L-W(C)/W (\square), versus longitudinal strain applied to the substrate.

Table 1

Experimental values of critical strain of the substrate resulting in film cracking, $\epsilon_{xx,c}^s$, critical cracking stress of the coating, $\sigma_{xx,c}^f$, the fracture toughness, K_{1c}^f , and the scratch critical load, L_c , for the bilayer and four-layer coatings

Coating	Thickness (μm)	$\epsilon_{xx,c}^s$ (%)	$\sigma_{xx,c}^f$ (MPa)	K_{1c}^f (MPa $\text{m}^{1/2}$)	L_c (N)
2L-W(C)/W	#1	3.5	224	0.7	55
	#2	7	148	0.6	65
	#3	14	130	0.8	>100
4L-W(C)/W	14	0.824	297	1.9	>100

distribution function, was applied to describe the crack density D as a function of the deformation $\epsilon_{xx,c}^s$ [13]:

$$D(\epsilon_{xx}^s) = D_{sat} \{1 - \exp[-A(\epsilon_{xx}^s - \epsilon_{xx,c}^s)^\alpha]\}, \quad (4)$$

where A and α are constant parameters which depend on the film/substrate system. The exponent α is known as the Weibull modulus.

The transverse crack density D_{sat} is obtained from the experimental plot of $D(\epsilon_{xx,c}^s)$ at saturation (Fig. 1). Notice that A and α are also determined experimentally. They are respectively the ordinate at zero point and the slope of the line obtained from the plot of $\ln\{-\ln[1 - (D/D_{sat})]\}$ versus $\ln(\epsilon_{xx}^s - \epsilon_{xx,c}^s)$. The values of the parameters D_{sat} , α and A involved in Eq. (4) are reported in Table 2.

The values of the Weibull modulus range from 0.517 to 0.682 for the bilayer coatings layers, depending on the coating thickness; and appear to be much higher for the four-layer coatings, of the order of 0.873. We may recall that the Weibull modulus expresses the statistical scatter of events: a high Weibull modulus indicates a low scatter [11]. The Weibull analysis gives a mathematical tool for predicting the fracture probability of a structure. In our case, the Weibull modulus appears to be small, reflecting a high probability of cracking of the coating and then the presence of numerous defects. As a comparison, soda-lime glass has a Weibull modulus of 2–3 and polysilicon films have a value of 7–11 [11]. The Weibull modulus tells nothing about the severity of the defects or their location. However, the difference in Weibull modulus obtained for the multilayered coatings may indicate the existence of different types and/or densities of defects. In our case, a larger number of interfaces does not seem to generate a higher defect density or increase the fracture probability of the films, since the parameters characterising the cracking resistance of the films ($\sigma_{xx,c}^f$, K_{Ic}^f , α) are found to be higher for the four-layer coatings than for the bilayer coatings.

The cracking behaviour of multilayered coatings has been little investigated. In particular, the work of Marieb et al. [14] on coatings composed of a tungsten layer deposited on a titanium nitride layer which is deposited on aluminium substrates, shows that the transverse crack density of the multilayered coatings is similar to that obtained for a single layer of titanium nitride. This suggests that the mechanical behaviour of the multilay-

ered coatings is controlled by the layer at the interface between the film and the substrate. For our film/substrate systems, this does not seem to be verified. In fact, for the bilayer coatings, we noted that at saturation the corresponding crack densities D_{sat} decreased from 50.6 to 20.8 when the coating thickness increases from 3.5 μm to 14 μm , showing a larger average intercrack spacing for thicker films. This dependence can be described by an empirical equation, written as:

$$D_{sat} = \frac{B}{(t^f)^n}. \quad (5)$$

The parameters B and n obtained from the experiments are 110.3 and 0.63, respectively, for the bilayer coatings on the stainless steel substrates; they were found to be 43.9 and 0.33, respectively, for tungsten single layers on stainless steel substrate [5]. The empirical model for the bilayer coatings, describing the evolution of the saturation crack density as a function of coating thickness, differs from that obtained for the tungsten elementary layers. This result indicates that the cracking behaviour of the multilayered coatings is not affected only by the nature and thickness of the interfacial layer. This is supported by the value of D_{sat} obtained for the four-layer coatings (22 cracks mm^{-1}), which appears to be different from that of the tungsten layer of 3.5 μm thickness (50.6 cracks mm^{-1}).

The results show that the cracking properties of multilayered coatings depend mainly on the total thickness of the films and the arrangement of the elementary layers (number of layers, thickness of single layers, layer interactions).

When increasing the substrate strain to 25%, no debonding of the film is observed at layer interfaces and at the substrate/coating interface. This reveals that the adhesion between the film and the substrate is good, but cannot be characterised through tensile tests. Therefore, scratch experiments were performed on these coatings.

5. Adhesion characterisation

The objectives of performing scratch tests are to evaluate the adhesion of the coatings to the substrate and then to rank the coatings with respect to debonding resistance. This investigation was based on determination of the critical scratch load values, L_c , characterising the decohesion between the film and the substrate. Acoustic emission measurements allow detection of this load, corresponding to delamination of the coatings observed by optical examinations of the scratches and saturation of the acoustic burst.

The experimental values of the critical scratch load

Table 2

Experimental values of the saturation crack density, D_{sat} , the Weibull modulus, α , and the constant, A , for the multilayered coatings

Coating		D_{sat} (cracks mm^{-1})	α	A
2L-W(C)/W	#1	50.6	0.682	0.599
	#2	37.3	0.576	0.434
	#3	20.8	0.517	0.606
4L-W(C)/W		22	0.873	0.256

L_c are reported in Table 1. For the bilayer coatings 2L-W(C)/W#1 and 2L-W(C)/W#2, decohesion of the films from the substrates is found to occur at the loads 50 N and 62 N, respectively. As for the bilayer coating 2L-W(C)/W#3 and the four-layer coatings 4L-W(C)/W of 14 μm thickness, the critical scratch loads could not be determined since saturation of the acoustic burst was not reached under a load range of 0–100 N. The critical scratch load was found to be higher than 100 N. Our multilayered coatings appear to adhere very well to stainless steel substrates, according to the very high value of L_c . Indeed, a maximum adhesion can be reached for the thickest films. These results emphasise the effect of film thickness on the mechanical behaviour of the multilayered coatings.

Examinations of the cross-section of the scratches by SEM show that multilayered coatings are subjected to detachment at layer interfaces [6]. The remaining parts of the film still protect the substrate surface against interactions with the environment until complete removal of the coating. However, the progressive delamination of the multilayered coatings may result in a reduction of their reliability, which can affect the in-service performance of the coating/substrate system. Thus, graded coatings might appear to be more suitable candidates for protective coatings [6,15].

6. Conclusion

In situ microtensile tests were performed on systems consisting of multilayered coatings deposited by magnetron sputtering on stainless steel substrates. The multilayered coatings were based on the stacking arrangement of two or four tungsten and tungsten–carbon [W(C)] single layers. The rupture properties of the films were characterised by specific parameters, such as the critical cracking stress and the fracture toughness deduced from an analytical model, and by the evolution of transverse crack density with respect to applied strain. The cracking probability was analysed through a Weibull analysis. The calculated values of the Weibull modulus revealed a high probability of cracking, supported by the low measured values of the fracture toughness and the

existence of defects in the films. The analysis showed a significant effect of the number and thickness of the elementary layers on the fracture resistance of the multilayered coatings. Indeed, the coatings based on four thin layers exhibited the highest fracture toughness and Weibull modulus.

The adhesion of the coatings on substrates was characterised through scratch experiments. Our multilayered coatings appeared to adhere well on stainless steel substrates, and no delamination was observed and detected for the thickest films. However, delamination at layer interfaces could be observed, resulting in a reduction in the reliability of the films, before complete decohesion.

References

- [1] A. Cavaleiro, M.T. Veira, *Mater. Sci. Eng. A* 140 (1991) 631.
- [2] P. Monge Cadet, F. Pellerin, G. Farges, D. Rickerby, E. Quesnel, *Propulsion and Energetics Panel Symposium AGARD Conference Proceedings No. 558, Rotterdam vol. 31* (1994) 1.
- [3] D. Garg, P. Ndyer, D.B. Dimos, S. Sunder, *J. Am. Ceram. Soc.* 75 (4) (1992) 1008.
- [4] E. Harry, A. Rouzaud, M. Ignat, P. Juliet, *Thin Solid Films* 332 (1–2) (1998) 195–201.
- [5] E. Harry, M. Ignat, A. Rouzaud, P. Juliet, *Surf. Coat. Technol.* 111 (2–3) (1999) 177–183.
- [6] E. Harry, A. Rouzaud, P. Juliet, Y. Pauleau, *Thin Solid Films* 342 (1–2) (1999) 208–214.
- [7] A. Rouzaud, E. Barbier, J. Ernoult, E. Quesnel, *Thin Solid Films* 270 (1995) 270.
- [8] M. Ignat, *Key Eng. Mater.* 116–117 (1996) 279.
- [9] M.F. Asbhy, D.R.H. Jones, *Matériaux vol. 1* Dunod, Paris, 1991.
- [10] C.E. Kalmas, J.F. Mansfield, G.S. Was, J.W. Jones, *J. Vac. Sci. Technol. A* 12 (3) (1994) 883.
- [11] S. Greek, F. Ericson, S. Johansson, J.-A. Schweitz, *Thin Solid Films* 292 (1997) 247.
- [12] M.S. Hu, A.G. Evans, *Acta Metall.* 37 (3) (1989) 917.
- [13] A. Mezin, J.-P. Chambard, J. Lepage, M. Nivoit, *Thin Solid Films* 185 (1990) 57.
- [14] T. Marieb, M. Ignat, H. Fujimoto, P. Flinn, in: A.S. Oates W.F. Filter, R. Rosenberg, A. Lindsay Greer, K. Gadepally (Eds.), *Thin Films: Stresses and Mechanical Properties*, *Mater. Res. Soc. Symp. Proc. vol. 391*, Materials Research Society, Pittsburgh, PA, 1995, p. 85.
- [15] Y. Gachon, *Etude de l'érosion par des particules solides de revêtements multicouches obtenus par procédé PVD sur substrat métallique (base titane)*. Thesis, Ecole Centrale de Lyon, France, 1997.

Correlation between stress values of cubic boron nitride thin films and intrinsic film properties or the infrared peak position

A. Klett, R. Freudenstein, M.F. Plass *, W. Kulisch

Institute of Technical Physics, University of Kassel, Heinrich-Plett-Str. 40, 34109 Kassel, Germany

Abstract

Boron nitride thin films were ion beam assisted deposited on silicon substrates. The c-BN content was investigated with IR spectroscopy. The intrinsic film stress, studied by measuring the resulting bending of the substrate using a profilometer, increases generally with increasing c-BN content. In addition, the IR peak position of the c-BN reststrahlen band was determined for adherent coatings and after the films completely peeled off the substrate. This stress relief due to the peeling-off induces a shift of the IR peak position to smaller wavenumbers. However, no correlation between the total stress obtained by the bending experiments and the IR peak position for adherent films could be found. In contrast, the value of the shift of the c-BN peak position to smaller wavenumbers after peeling-off shows a good correlation with the stress values from the bending method. Several mechanisms which may influence the peak position, such as stress, coalescence and film thickness, will be discussed. Finally, we conclude that an estimate of c-BN film stress from IR data is only possible on the basis of the peak shift after peeling-off, which on the other hand means that stress measurement using the IR peak position has to be a destroying technique. © 2000 Elsevier Science S.A. All rights reserved.

Keywords: Boron nitride; Ion beam assisted deposition; IR spectroscopy; Stress

1. Introduction

The poor adhesion commonly observed for cubic boron nitride (c-BN) containing thin films is caused by the low adhesion strength at the interface as well as by the high compressive stress of these coatings, which is most probably due to the intense ion bombardment necessary to deposit the c-BN phase. As a consequence, experimental and theoretical work concerning the mechanism of intrinsic stress formation in order to achieve a stress reduction has been recently reported (see e.g. Ref. [1] and references therein).

The stress σ of thin coatings is commonly determined by directly measuring the deformation of a substrate coated on one side with a film and employing Stoney's equation [2]. The resulting curvature radius R can be determined using e.g. the Newton's rings technique [2], capacitance measurements [3], surface profilometry [4], or, if very thin substrates (i.e. cantilever structures with

$D \ll 100 \mu\text{m}$) are used, simply by optical microscopy [5,6]. In order to gain a depth-resolved characterization of the film stress, several of these techniques were applied in situ during film growth [2,3] or post-depositionally after several re-etching steps [7].

In addition, another possibility exists at least to estimate the stress of c-BN films. Raman experiments on c-BN bulk material [8] showed that the c-BN transversal optical (TO) mode exhibits a stress induced shift to higher energies. As a consequence, IR spectroscopy is frequently applied to determine the IR peak position of the c-BN reststrahlen band and to estimate the film stress [9–11].

As both the bending method and the IR technique are, up to now, used almost independently in the literature, we will systematically compare the stress data evaluated from bending experiments with stress values obtained from the peak position of the c-BN reststrahlen band. Surprisingly, it will turn out that only the shift $\Delta\omega_{\text{c-BN}}$ of the c-BN IR peak after the coating peeled off, but not the absolute c-BN peak position for an adherent film, correlates with the stress values determined by the bending method.

* Corresponding author.

E-mail address: plass@schottky.physik.uni-kassel.de (M.F. Plass)

2. Experimental details

2.1. Film deposition

The boron nitride thin films were prepared using an ion beam assisted deposition (IBAD) setup [6]. Boron was evaporated on (100) silicon substrates (substrate temperature $T_s = 350^\circ\text{C}$) and simultaneously bombarded with a mixture of nitrogen and argon ions from a Kaufman ion source. Typical boron deposition rates were in the range of 10 nm/min. A nitrogen to argon gas flow ratio of 3:1 was used. The ion energy E_{ION} and the ion to thermal boron atom (I/A) ratio were varied between 500 and 1200 eV and between 1.3 and 2.0, respectively. The dependence of the resulting phase on the deposition conditions, i.e. E_{ION} or I/A ratio, was in good agreement with literature data [1,12]. The c-BN containing films exhibited an atomic boron to nitrogen ratio close to one, as revealed by Auger electron spectroscopy or heavy ion elastic recoil detection analysis (see the description in Ref. [13]). The elemental fraction of light contaminations, such as carbon or oxygen, were in the range of a few percent which is typical for IBAD c-BN films [12,14,15]. The thickness d of the BN coatings was obtained using single wavelength ellipsometry and checked by profilometry on selected samples. A deposition time of 15 min resulted in a thickness of 90 ± 15 nm, depending on the deposition conditions (E_{ION} and I/A ratio).

2.2. IR measurement

All samples prepared were routinely studied with IR transmission spectroscopy. A characteristic IR spectrum is presented in the lower part of Fig. 1. The peaks of c-BN at 1093 cm^{-1} and of non-cubic BN material at 775 cm^{-1} (bending) and 1410 cm^{-1} (stretching) are clearly visible. The IR data were fitted using three pure Lorentzian peak functions (dashed lines) in order to determine the intensity of the c-BN peak $I_{\text{c-BN}}$ and of the non-cubic stretching peak $I_{\text{h-BN}}$. Using these intensities, a quick estimate of the c-BN fraction,

$$X_C = I_{\text{c-BN}} / (I_{\text{c-BN}} + I_{\text{h-BN}}), \quad (1)$$

of the sample is possible. However, one should keep in mind that for IBAD c-BN films X_C is mainly controlled by the thickness ratio of two layers with an almost pure phase composition [6,7,12]. Thus, for the film shown in Fig. 1, a c-BN toplayer thickness of 60 nm can be deduced.

In general, the fits agree well with the experimental data except for the h-BN stretching mode. This discrepancy between IR data and simulations has already been noticed and is probably due to either the anisotropic properties of h-BN material [14,16,17] or a two-phonon contribution [15]. Besides, the large scatter of the experi-

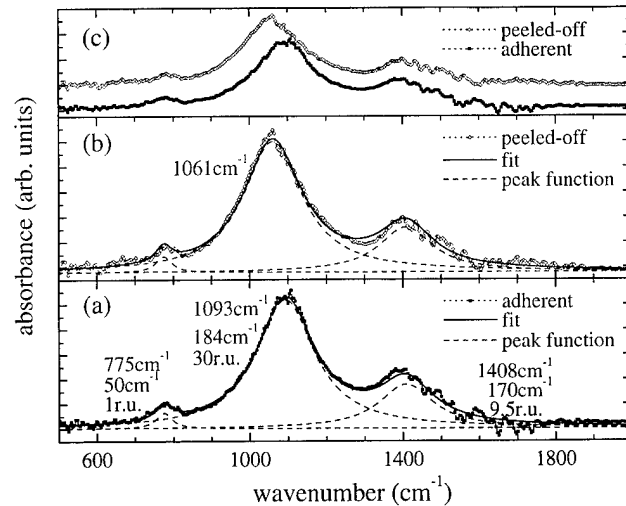


Fig. 1. IR transmission spectroscopy data using non-polarized light and a normal angle of incidence of a c-BN containing film (a) before and (b) after peeling-off. The fit parameter, e.g. peak positions $\omega_{\text{c-BN}}$ and the peak intensities $I_{\text{c-BN}}$ and $I_{\text{h-BN}}$, were obtained by a fit (full line) to the experimental data points using three pure Lorentzian curves (dashed lines). The resonance frequencies, the peak width and the intensities are given. In addition the two spectra are compared in (c). The sample was prepared using $E_{\text{ION}} = 500$ eV and an I/A ratio of 1.9.

mental data between 1500 and 1700 cm^{-1} is originated by water bands. For the c-BN reststrahlen band, on the other hand, an almost excellent fit could usually be obtained. As a consequence, the estimated error of measuring the peak position $\omega_{\text{c-BN}}$ of the TO mode of the reststrahlen band should be in the range of a few cm^{-1} . Thus, the requirement of a precise determination of peak positions for studying peak shifts is successfully achieved.

In addition, Fig. 1(b) shows the change of the spectrum when the c-BN film peeled off the substrate. This stress relief (see e.g. the SEM images in Refs. [4,18]) results in a shift of the c-BN peak of about 20 cm^{-1} to smaller energies, as often reported [2,6,18]. For a better comparison, the spectra of the film before and after delamination are presented in the upper part of Fig. 1(c).

2.3. Stress measurements

The internal stress of the adherent coatings was determined by the bending method and calculated from Stoney's equation (see e.g. Ref. [2]). For a film (thickness d) deposited on one side of a thin substrate (thickness D), the film stress is given by

$$\sigma = \frac{E_{\text{Si}}}{6(1-\nu)} \frac{D^2}{d} \frac{1}{R}, \quad (2)$$

where E_{Si} and ν are Young's modulus and Poisson's ratio of the silicon substrate, respectively. For the coated stripe-shaped Si substrates ($D = 350\text{ }\mu\text{m}$), the curvature

radius R was measured by a surface profilometer. The measuring length was 3–5 mm. The error of this procedure can be estimated to be less than 10%.

3. Results

3.1. Intrinsic stress σ vs. IR peak ratio X_C

For various IBAD conditions, the IR peak ratio X_C and the film stress σ obtained from the bending of the film–substrate system were determined. The results are presented in Fig. 2. For comparison, data taken from Ref. [2] are shown. Even after close examination, only a few superficial trends can be stated. Generally, the stress is increasing with increasing c-BN content, as already observed [5]. Films containing cubic BN exhibit a stress $\sigma > 3$ GPa.

3.2. Intrinsic stress σ vs. IR peak position $\omega_{\text{c-BN}}$ or IR peak shift $\Delta\omega_{\text{c-BN}}$

As some of the films presented in Fig. 2 peeled off the substrate, it was possible to compare the IR properties before and after delamination. The peak positions $\omega_{\text{c-BN}}$ before and after delamination are shown in Fig. 3 as a function of the stress σ determined by the bending method. The full symbols represent the peak position for adherent coatings, whereas the open symbols depict the IR peak position after the film completely peeled off. For adherent samples the IR peak position $\omega_{\text{c-BN}}$ almost constantly equals $1092(\pm 4) \text{ cm}^{-1}$ and does not depend on the stress of the coatings within the experi-

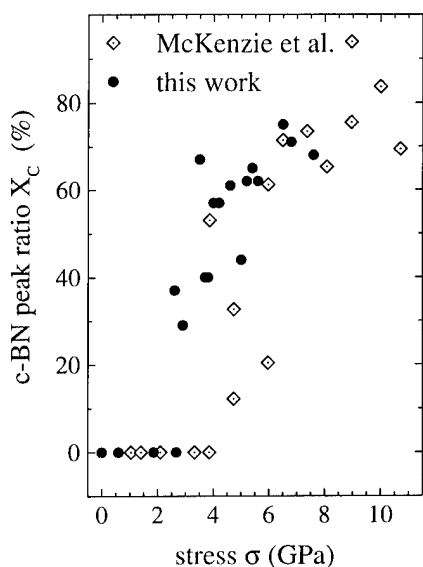


Fig. 2. Comparison between the film stress σ of the samples and the c-BN peak ratio X_C . The results of McKenzie et al. [2] are also shown for comparison.

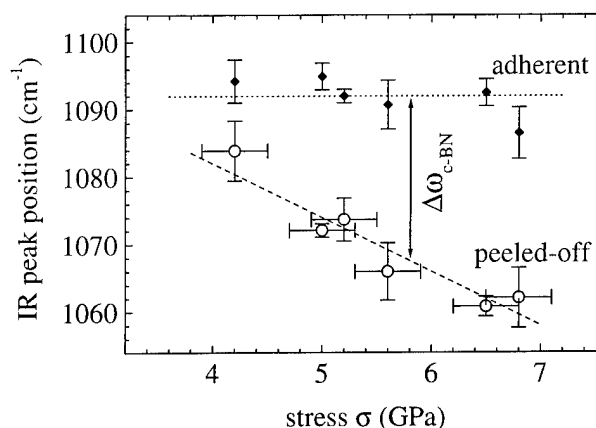


Fig. 3. IR peak position of c-BN mode for adherent films (full symbols) and after delamination (open symbols) as a function of stress σ obtained from the bending experiments.

mental uncertainty. Especially no indication for an increasing peak position with increasing stress can be found. On the contrary, a least-square fit would result in an almost marginal negative slope of $-1 \text{ cm}^{-1}/\text{GPa}$ including an error of almost 100%. For samples with a small cubic content ($X_C < 40\%$), the peak position even rises to wavenumbers between 1100 and 1120 cm^{-1} [6]. As these samples do not exhibit any delamination, they are not considered in Fig. 3.

In Fig. 3 it can be seen that the c-BN peak shifts to smaller energies after peeling-off. Analogue observations have frequently been reported by other groups, e.g. from 1090 to 1066 cm^{-1} [18]. An inverse linear relationship between the stress σ of the adherent films and the IR peak position after peeling-off is apparent. In Fig. 4 the IR peak shift $\Delta\omega_{\text{c-BN}}$ is plotted versus the film stress. A least-square fit is also shown resulting in a proportional factor of $4.0(\pm 0.2) \text{ cm}^{-1}/\text{GPa}$, assuming a linear relationship.

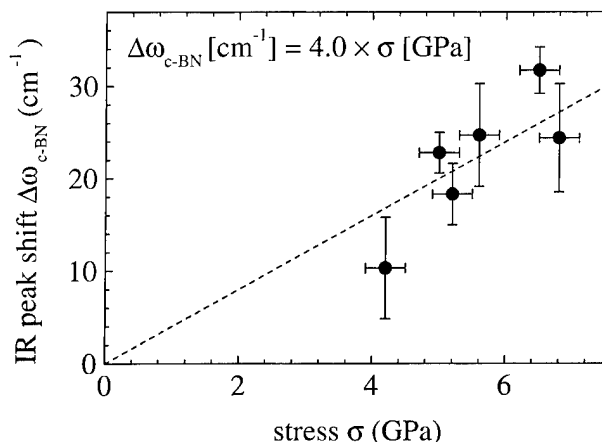


Fig. 4. Difference $\Delta\omega_{\text{c-BN}}$ of the peak position between adherent film and after peeling-off as a function of the total film stress.

4. Discussion

In the following, the results presented above will be discussed. For this purpose, the basic interdependencies between IR frequencies and various film properties, e.g. total film stress or film thickness, will be introduced. On the basis of these dependencies, the experimental observed relations between stress and IR data can conclusively be discussed.

4.1. Dependencies of the c-BN TO mode

For the c-BN reststrahlen band many parameter dependencies have been observed (see Fig. 5). Using Raman spectroscopy on bulk specimens, the shift of the c-BN TO mode with increasing pressure has been studied [8]. On the basis of these data, Reinke predicted, for thin film material, a value of $4.5 \text{ cm}^{-1}/\text{GPa}$ for the stress induced shift of the TO position [19]. Further insights concerning the interpretation of IR data of BN can be gained by monitoring the c-BN peak frequency as a function of the deposition time. With increasing film thickness, d , the IR peak position $\omega_{\text{c-BN}}$ moves to smaller energies. A shift from 1130 to 1065 cm^{-1} was observed during deposition [9], in accordance with results recently reported in Ref. [20]. Friedmann et al. already noticed that this shift cannot be explained by thickness effects alone [9]. In contrast, model calculations show that with increasing layer thickness the IR peak position should move to larger wavenumbers by 6 cm^{-1} per 100 nm increasing thickness (see Fig. 5) [9,21,22]. This disagreement led some authors to the assumption that the experimentally observed behavior is also stress induced, which would mean that for very thin c-BN films the stress is considerably higher than

for thicker films. Superficially, stress measurements [2,7] which observed a pronounced stress maximum for small thicknesses confirmed this interpretation. However, recent studies of the stress development [3,6,23] failed to support this explanation. Fahy et al. therefore suggested another mechanism, namely a coalescence or islanding induced dependence of the c-BN peak position (for details see Ref. [20]). In this model the c-BN peak position exhibits a shift towards larger wavenumbers for small layer thickness. According to Fahy et al. [20] a shift of up to 80 cm^{-1} can be explained. As the derivation $\partial\omega_{\text{c-BN}}/\partial d$ for this mechanism is negative, we also used a negative sign in the presentation in Fig. 5.

Finally, Hackenberger et al. mentioned that the atomic B/N ratio influences the c-BN peak position for delaminated c-BN films [24]. However, optical model calculations using a dielectric function described by an effective medium approximation (EMA) composed of c-BN and elemental boron demonstrated that the peak position does not depend on the boron fraction [21]. On the basis of these simulations, it can not be excluded that the elemental composition influences the peak position via the interstitial or vacancy defect concentration and, in turn, via the resulting stress of the coatings. For this reason, stoichiometry is not separately considered in the following.

4.2. Peak shift after peeling-off

After discussing the main parameters determining the IR peak position during film growth, we finally focus on the relationship between the c-BN peak position and the stress and/or stress relief, respectively. In general, the dependence between film stress σ and IR peak shift $\Delta\omega_{\text{c-BN}}$ after stress relief (Fig. 4) is in good agreement with the data of Fahy et al. [20] and the prediction of Reinke [19]. However, the results presented in Fig. 3 concerning the absolute peak position are in sharp contrast to this picture, which predicts a completely contrary behavior schematically depicted in Fig. 6(a). With increasing film stress, the peak position for adherent coatings (closed symbols) should shift to larger wavenumbers, whereas after stress relief (resulting in a shift $\Delta\omega_{\text{c-BN}} \propto \sigma$), a constant peak position is expected for stress free material (open symbols).

In contrast to this model, Fig. 6(b) takes coalescence effects also into account. Film thickness effects can be neglected for the samples studied, as a variation of 100 nm is necessary to yield a small shift of 6 cm^{-1} [21,22], which is almost the complete thickness of the film under consideration. As in Figs. 3 and 6(a) the full and open symbols denote the IR frequencies before and after delamination respectively. The experimentally obtained peak shift after peeling-off and stress relief (dashed arrow) is proportional to the stress σ . The difference (full arrow) between the position after stress

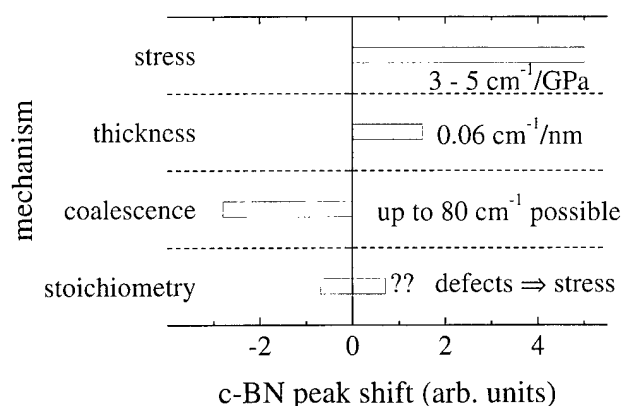


Fig. 5. Schematic presentation of the dependence of the IR peak position on different film properties. Stress, increasing film thickness, varying stoichiometry, and coalescence (islanding) induced shifts are considered. As the coalescence induced mechanism results in $\partial\omega_{\text{c-BN}}/\partial d < 0$ with increasing thickness, the bar reflects a shift to smaller wavenumbers. Regarding stoichiometry, the situation is not clear.

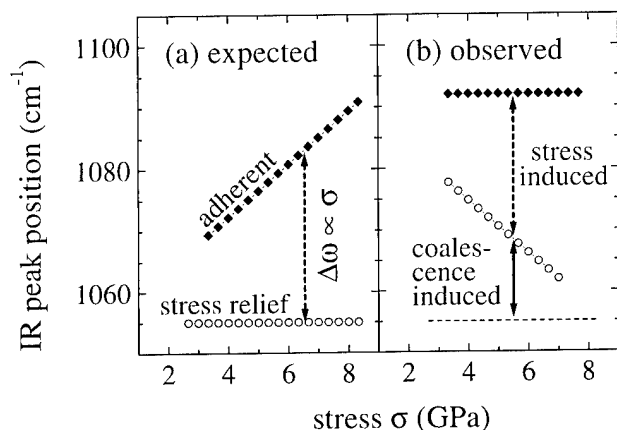


Fig. 6. Influence of stress σ and coalescence on the c-BN IR peak position and/or peak shift. The relation between stress and IR frequency before and after stress relief is shown schematically. In (a) only a stress induced shift is considered. In contrast, a coalescence induced shift is also taken into account in (b).

relief and the position at 1055 cm^{-1} [8], which is characteristic for stress free bulk material (horizontal dashed line), is mainly originated by coalescence or islanding induced effects. This description can be supported by a simple consideration being a crude representation of the physical interdependence. It has been shown [20] that the coalescence effect is maximal for small c-BN thicknesses. On the other hand, a small c-BN toplayer thickness is rather synonymous with a small IR ratio X_C , as the latter is determined by the thickness ratio of toplayer and non-cubic nucleation layer [6,7,12,23]. As can be seen from Fig. 2, there exists some dependence between X_C and the stress σ , at least for the examined range below 7 GPa. Moreover, a frequency $\omega_{\text{c-BN}} > 1100\text{ cm}^{-1}$ was observed for small $X_C < 40\%$, although the film stress was only marginal [6]. Therefore, a small film stress is directly related with a large coalescence induced peak shift and vice versa.

For large c-BN thicknesses and/or X_C , coalescence is marginal (see Fig. 6). Here, the peak position is to a large extent determined by the film stress. However, the contribution of thickness is no longer negligible. As a consequence, again not the peak position, but only the peak shift after stress relief is capable to estimate the stress σ .

5. Summary and concluding remarks

Thin BN films were deposited using IBAD. The resulting film stress σ was measured using the substrate bending method and compared with IR data. The c-BN peak exhibits a constant frequency $\omega_{\text{c-BN}}$ with no dependence on the film stress. The peak shift $\Delta\omega_{\text{c-BN}}$ after stress relief was found to be determined by σ . The

proportionality of $4\text{ cm}^{-1}/\text{GPa}$ is in excellent agreement with the value predicted by Reinke [19].

At first sight, the independence of the c-BN IR peak position, before delamination, of the stress is unexpected. Closely examined, however, this result is not surprising as the c-BN frequency is not only controlled by the stress. Here, additional optical effects such as the thickness of the layer (for large thicknesses) as well as a coalescence or islanding induced peak shift (for small thicknesses) must be taken into account. Regarding this latter mechanism, the experimentally observed behavior could be explained by a very crude model. Considering our results, a stress estimate based on IR spectroscopy is only possible after delamination.

Acknowledgements

Our work has been continuously supported by the European Community and the Deutsche Forschungsgemeinschaft. The authors would like to thank A. Bergmaier (TU Munich) for ERD investigations and M.A. Djouadi (ENSAM Cluny) for discussion.

References

- [1] S. Reinke, W. Kulisch, *Surf. Coat. Technol.* 97 (1997) 23.
- [2] D.R. McKenzie, W.D. McFall, W.G. Sainty, C.A. Davis, R.E. Collins, *Diamond Relat. Mater.* 2 (1993) 970.
- [3] M. Zeitler, S. Siem, H. Neumann, M. Zeuner, J.W. Gerlach, B. Rauschenbach, *Nucl. Instr. Meth. B* 139 (1998) 327.
- [4] N. Tanabe, M. Iwaki, *Nucl. Instr. Meth. B* 80/81 (1993) 1349.
- [5] G.F. Cardinale, D.G. Howitt, K.F. McCarty, D.L. Medlin, P.B. Mirkarimi, N.R. Moody, *Diam. Relat. Mater.* 5 (1996) 1295.
- [6] A. Klett, R. Freudenstein, M.F. Plass, W. Kulisch, *Surf. Coat. Technol.*, 1999 (in press).
- [7] S. Ilias, V. Stambouli, J. Pascallon, D. Bouchier, G. Nouet, *Diam. Relat. Mater.* 7 (1998) 391.
- [8] J.A. Sanjurjo, E. López-Cruz, P. Vogl, M. Cardona, *Phys. Rev. B* 28 (1983) 4579.
- [9] T.A. Friedmann, P.B. Mirkarimi, D.L. Medlin, K.F. McCarty, E.J. Klaus, D.R. Boehme, H.A. Johnsen, M.J. Mills, D.K. Ottesen, J.C. Barbour, *J. Appl. Phys.* 76 (1994) 3088.
- [10] P. Widmayer, P. Ziemann, S. Ulrich, H. Ehrhardt, *Diam. Relat. Mater.* 6 (1997) 621.
- [11] C. Ronning, E. Dreher, H. Feldermann, M. Gross, M. Sebastian, H. Hofäss, *Diam. Relat. Mater.* 6 (1997) 1129.
- [12] D.J. Kester, K.S. Ailey, D.J. Lichtenwalner, R.F. Davis, *J. Vac. Sci. Technol. A* 12 (1994) 3074.
- [13] R. Freudenstein, S. Reinke, W. Kulisch, R. Fischer, J. Zweck, A. Bergmaier, G. Dollinger, *Materials Science Forum* 287/288 (1998) 259.
- [14] M.F. Plass, W. Fukarek, A. Kolitsch, N. Schell, W. Möller, *Thin Solid Films* 305 (1997) 172.
- [15] J. Ullmann, J.E.E. Baglin, A.J. Kellock, *J. Appl. Phys.* 83 (1998) 2980.
- [16] E. Franke, M. Schubert, H. Neumann, T.E. Tiwald, D.W. Thompson, J.A. Woollam, J. Hahn, F. Richter, *J. Appl. Phys.* 82 (1997) 2906.

- [17] K.L. Barth, W. Fukarek, H.-P. Maucher, M.F. Plass, A. Lunk, *Thin Solid Films* 313/314 (1998) 697.
- [18] I.-H. Kim, S.-H. Kim, K.-B. Kim, *J. Vac. Sci. Technol. A* 16 (1998) 2295.
- [19] S. Reinke, PhD Thesis, University of Kassel, 1996.
- [20] S. Fahy, C.A. Taylor II., R. Clarke, *Phys. Rev. B* 56 (1997) 12 573.
- [21] M. Ben el Mekki, M.A. Djouadi, E. Guiot, V. Mortet, J. Pascal-
lon, V. Stambouli, D. Bouchier, N. Mestres, G. Nouet, (submitted
for publication).
- [22] M.F. Plass, PhD Thesis, Technische Universität Dresden, 1998.
- [23] Y. Yamada, Y. Tatebayashi, O. Tsuda, T. Yoshida, *Thin Solid
Films* 295 (1997) 134.
- [24] L.B. Hackenberger, L.J. Piliore, R. Messier, G.P. Lamaze, *J. Vac.
Sci. Technol. A* 12 (1994) 1569.

Mechanical properties of Al/Al₂O₃ nanolaminated films: correlation to microstructure

M. Ben Daia^{a,*}, P. Aubert^a, S. Labdi^a, C. Le Paven-Thivet^a, P. Houdy^a, J.L. Bozet^b

^a Laboratoire Multicouches Nanométriques (LMN), Université d'Evry, Bd F. Mitterand, 91023 Evry cedex, France

^b Université de Liège, Service d'Elements de Machine et de Tribologie, Rue E. Solvay 21, 4000 Liège, Belgium

Abstract

Wear resistance and the hardness of Al/Al₂O₃ nanolaminated films were investigated in this study. Monolithic films and multilayers were deposited on a silicon substrate with two different substrate temperatures: $T_s = 25^\circ\text{C}$ and $T_s = -90^\circ\text{C}$. The period thickness of multilayers was lowering from 40 to 2 nm. From nanoindentation measurements, it appears that the hardness of multilayers has an intermediate value between those of metal (Al) and ceramic (Al₂O₃). The tribological test was conducted by the pin-on-disc method. The $T_s = 25^\circ\text{C}$ deposited multilayers, as well as single films, demonstrated poor wear resistance. The best wear resistance was obtained for multilayers deposited at the lowest substrate temperature ($T_s = -90^\circ\text{C}$). The results are in good agreement with structural characterization. X-ray reflectometry demonstrated that the multilayer character of Al/Al₂O₃ is more pronounced for $T_s = -90^\circ\text{C}$. © 2000 Elsevier Science S.A. All rights reserved.

Keywords: Al/Al₂O₃ multilayers; Nanoindentation; Tribological properties

1. Introduction

In the field of research of new coatings for hard protective and wear resistance, multilayer films exhibit a large enhancement of mechanical properties compared to single layers. Wear resistance and hardness of multilayers are reported in many studies [1–3]. All these show a significant dependence of mechanical properties on the microstructure of multilayers.

According to Koehler [4], the strength of multilayers depends, in addition to layer thickness, on the difference in the shear moduli of the components. The metal–ceramic multilayers, in particular, are expected to demonstrate a high strength and hardness.

Only a few papers have been published on the investigation of the mechanical properties of Al/Al₂O₃ multilayers [5]. Our paper focuses on the mechanical behavior of multilayers of alternating amorphous alumina with polycrystalline aluminum, with period thickness λ less than 40 nm, correlated to morphological and structural properties.

2. Experimental details

The multilayers and monolithic films were produced by R.F. sputtering onto (100) silicon wafers. Two substrate temperatures were used, $T_s = 25^\circ\text{C}$ and $T_s = -90^\circ\text{C}$. For the two sets of multilayers, the period thickness ranged from $\lambda = 40$ nm to $\lambda = 2$ nm. Details of condition deposition can be found elsewhere [6]. Table 1 summarizes the physical characteristics of the samples.

The friction and test wear was carried out using a pin-on-disc device at room temperature and humidity controlled at 25%. The normal load, kept constant at 1 N, was applied through an alumina ball of 6 mm diameter. The specimen was mounted on a rotating specimen holder. The nominal diameter of wear track and rotation speed were chosen to give a sliding speed of 0.005 m/s. The experiment was stopped when the ball reached the silicon substrate. This is accompanied by a change in friction coefficient μ (0.6–0.7) and a specific silicon cracking sound. The wear track was checked by optical microscopy. The volume of material lost during wear was determined in order to compute the wear rate.

Investigation of the mechanical properties was also performed using an indentation load–depth sensing apparatus. The experimental procedure and analysis

* Corresponding author. Tel.: +33-1-69-763016.

E-mail address: mouloud.Ben-daia@mat.enscm.fr (M. Ben Daia)

Table 1
Physical characteristics of samples

Substrate temperature (°C)	Film type	Period (λ)	Individual film thickness ratio (nm) ^a	Total film thickness (nm) ^b
25	Monolithic Al	–	–	540
	Monolithic Al ₂ O ₃	–	–	75
	Al/Al ₂ O ₃ multilayers	40	20/20	215
		20	10/10	225
		10	5/5	195
		5	2.5/2.5	240
		2	1/1	280
–90	Monolithic Al	–	–	540
	Monolithic Al ₂ O ₃	–	–	73
	Al/Al ₂ O ₃ multilayers	40	20/20	140
		20	10/10	175
		5	2.5/2.5	130
		2	1/1	70

^a Individual thicknesses were estimated using deposition rate.

^b Thickness of films was measured using cross-section high resolution scanning electron microscopy.

used are described elsewhere [7]. Measurements of hardness were obtained with a Berkovich diamond indenter and the hardness was calculated using the true calibrated shape of the indenter. 10 indents were made on each sample and averaged. A simple cycle of loading and unloading was used in all the experiments, and the loading rate was equal to $2 \times P_{\max}/\min$ where P_{\max} was the maximum load (the time for one cycle was 1 min).

3. Results

3.1. Structural characterization

Alumina films are amorphous at any substrate temperature. The films are very smooth, which is suitable for multilayers film engineering.

Aluminium films are polycrystalline, with a weak (111) texture. As shown by high resolution scanning electronic microscope (SEM) surface observation, Al films are rough and granular, Fig. 1. We have studied the influence of substrate temperature on the morphology of aluminum films from low temperature ($T_s = -90^\circ\text{C}$) to high temperature ($T_s = 600^\circ\text{C}$) and found that the grain size increases with temperature [6]. Nevertheless, no significant difference was seen between films deposited at low temperature $T_s = -90^\circ\text{C}$ and at $T_s = 25^\circ\text{C}$. Equivalent diameters ϕ_e are of the same order: $\phi_e = 350$ nm for thick films (200 nm thick), Fig. 1(a); and $\phi_e = 30$ nm for thin films (10 nm thick), Fig. 1(b). The latter value is expected to arise in aluminium layers in Al/Al₂O₃ multilayers. Al/Al₂O₃ multilayers also exhibit a granular surface, in agreement with the Al one. Cross-section high resolution SEM has not shown any laminated structure [6]. In fact, big grains, characteristics of columnar growth, have been observed.

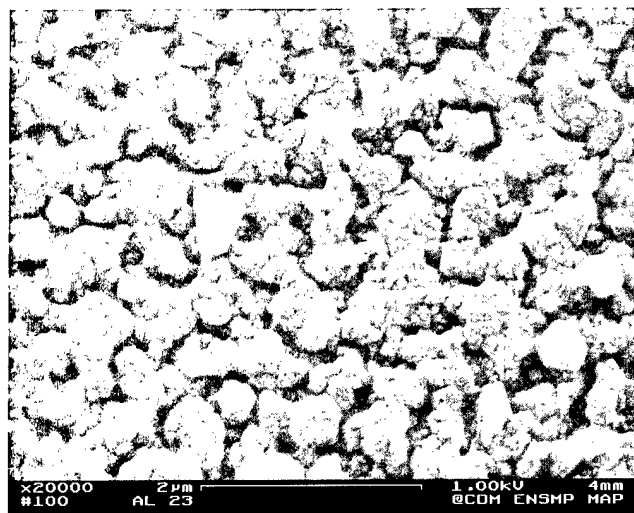
Since aluminum layers are very rough, no perfect

interfaces are expected in Al/Al₂O₃ multilayers. Nevertheless, the multilayering character of Al/Al₂O₃ structures occurs in some multilayers, as shown by X-ray reflectometry (XRR) experiments on 20 nm-periodic samples. In XRR, the appearance of Bragg peaks is the signature of a periodic structure. For $T_s = -90^\circ\text{C}$, four Bragg peaks are observed, Fig. 2(a), whereas at $T_s = 25^\circ\text{C}$ two peaks are seen Fig. 2(b). The existence of the multilayer structure in Al/Al₂O₃ has also been demonstrated by secondary ionic mass spectrometry (SIMS) [8]. It is clear that the multilayering character of Al/Al₂O₃ composites increases when the substrate temperature decreases. This is well correlated to the fact that aluminum grain size decreases with substrate temperature, leading to more and more abrupt interfaces. It can also be expected that diffusion of aluminum and oxygen atoms is reduced at low temperatures.

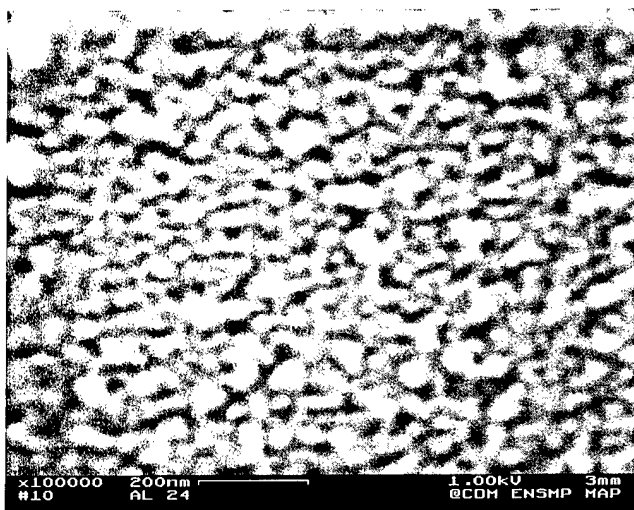
3.2. Tribological tests

The tribological tests were performed for all the samples. The wear rate was calculated as a function of period thickness for the two sets of multilayers and monolithic films. The results are summarized in Table 2. For monolithic films, a weak resistance to wear is seen for the two substrate temperatures. The multilayers deposited at $T_s = 25^\circ\text{C}$ demonstrate similar behavior. When comparing the two sets of multilayers, Fig. 3, it appears, on one hand, that there is no significant difference for multilayers with $\lambda \geq 10$ nm. On the other hand, the samples at $T_s = -90^\circ\text{C}$ $\lambda = 5$ nm and $\lambda = 2$ nm have a low wear rate and it seems that the wear resistance is greatly enhanced in these samples.

Fig. 4 (a) and (b) shows the evolution of friction coefficient μ with number of cycles during sliding for multilayers with $\lambda = 5$ nm and $\lambda = 2$ nm. In the case of $T_s = 25^\circ\text{C}$, the friction coefficient, initially started at 0.2–



(a)

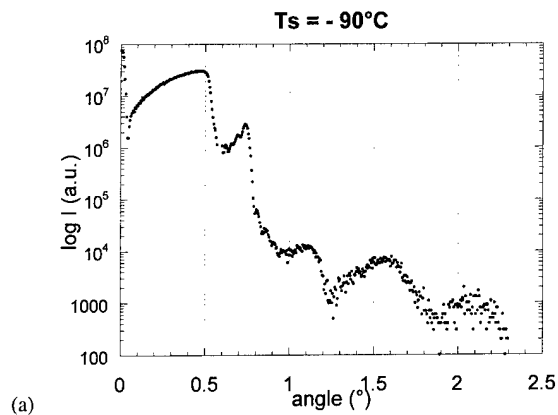


(b)

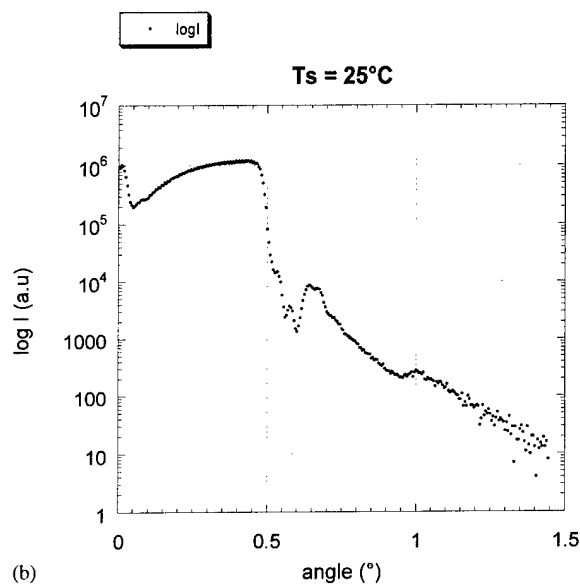
Fig. 1. Surface high resolution SEM observation of: (a) 200 nm thick Al films; (b) 10 nm thin Al film. The two thin films were deposited at $T_s = -90^\circ\text{C}$.

0.4, increased dramatically to achieve a value of $\mu = 1$. This was accompanied with severe mode of wear.

For $T_s = -90^\circ\text{C}$, there were two stages of wear. First the friction coefficient increased rapidly to achieve a



(a)



(b)

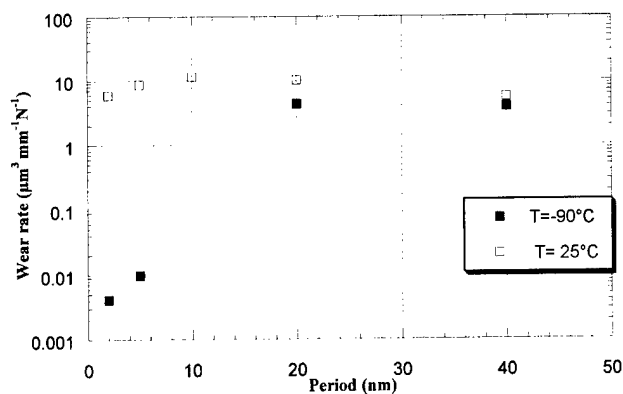
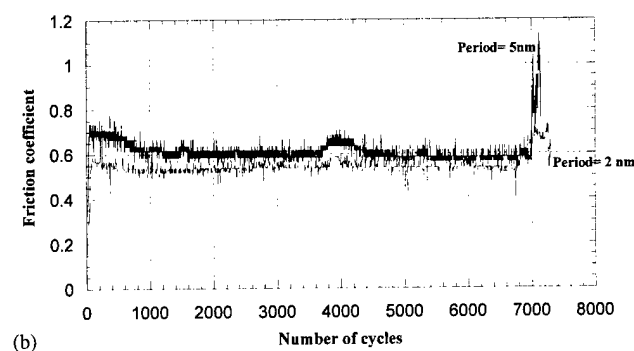
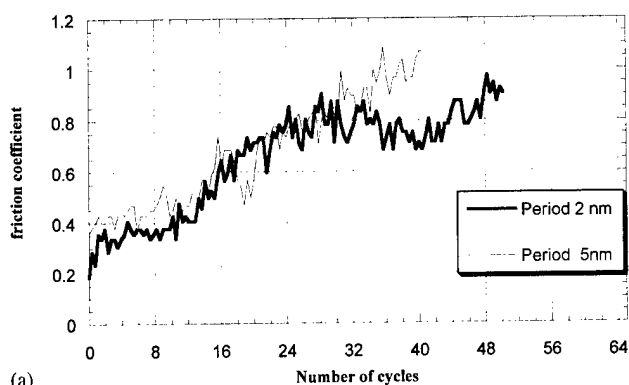
Fig. 2. X-ray reflectometry spectra of: (a) $T_s = -90^\circ\text{C}$ deposited Al/Al₂O₃ multilayers with $\delta = 20$ nm; (b) $T_s = 25^\circ\text{C}$ deposited Al/Al₂O₃ multilayers with $\gamma = 20$ nm.

maximum value of 0.7 for the $\lambda = 5$ nm sample and 0.55 for the $\lambda = 2$ nm sample. This initial stage was followed by a steady state. The steady friction coefficient was equal to 0.6 for the $\lambda = 5$ nm sample and 0.54 for the $\lambda = 2$ nm sample, and this slight difference can explain the difference in wear rate observed for these samples.

Table 2

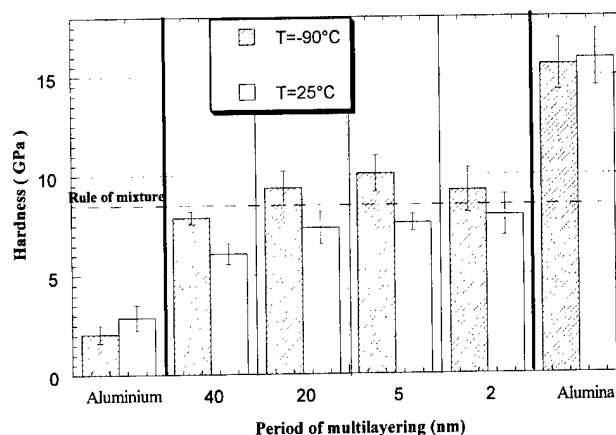
Wear rate and hardness measurements

$T_s = 25^\circ\text{C}$	Wear rate 10^{-2} ($\mu\text{m}^3 \text{mm}^{-1} \text{N}^{-1}$)	Hardness (GPa)	$T_s = -90^\circ\text{C}$	Wear rate 10^{-2} ($\mu\text{m}^3 \text{mm}^{-1} \text{N}^{-1}$)	Hardness (GPa)
Al	800	2.88 ± 0.64	Al	900	2.07 ± 0.45
Al ₂ O ₃	63	15.88 ± 1.4	Al ₂ O ₃	73	15.57 ± 1.32
$\lambda = 40$ nm	555	6.08 ± 0.51	$\lambda = 40$ nm	392	7.87 ± 0.32
$\lambda = 20$ nm	1012	7.36 ± 0.82	$\lambda = 20$ nm	443	9.35 ± 0.87
$\lambda = 10$ nm	1140	—	$\lambda = 5$ nm	1	10.08 ± 0.91
$\lambda = 5$ nm	863	7.60 ± 0.42	$\lambda = 2$ nm	0.4	9.23 ± 1.11
$\lambda = 2$ nm	588	7.98 ± 1.02			

Fig. 3. Wear rate vs. period thickness plotted for Al/Al₂O₃ multilayers.Fig. 4. Friction coefficient vs. number of cycles for multilayers deposited at: (a) $T_s = 25^\circ\text{C}$; (b) $T_s = -90^\circ\text{C}$.

3.3. Hardness measurements

Fig. 5 illustrates the hardness of multilayers compared to the monolith films hardness. The alumina films exhibited the highest value of hardness while the value of hardness of multilayers was between the aluminum hardness value and the alumina value. When comparing the $T_s = 25^\circ\text{C}$ deposited multilayers with the $T_s = -90^\circ\text{C}$ ones, it appears that the hardness of multilayers with $\lambda \geq 5$ nm is more important for the second group. In the case of $\lambda = 2$ nm, no conclusion is given due to experimental error. It should be noted that there

Fig. 5. Hardness of monolithic and multilayer Al/Al₂O₃ films.

is no large difference in hardness of $T_s = -90^\circ\text{C}$ multilayers as function of period λ .

The hardness of all multilayers has to be compared with the rule of mixture value of 8.82 GPa calculated with single layers hardness for $T_s = -90^\circ\text{C}$.

4. Discussion

The results of $T_s = 25^\circ\text{C}$ deposited multilayers is consistent with the reduced multilayering character of these samples. The hardness of Al/Al₂O₃ has been reported by Ding et al. [5], but the range of period thickness is very different from the range investigated in this study. The maximum hardness value from Ding's work (4.83 ± 0.08) was obtained for 70 nm (Al)/10 nm (Al₂O₃). This value is less than those obtained in this paper for multilayers with $\lambda \leq 40$ nm. The lack of hardness when decreasing the period of layering in this system of multilayers is in apparent contradiction with behavior reported for many multilayers with a well defined interface. If the multilayering structure is observed for $T_s = -90^\circ\text{C}$ for $\lambda = 10$ nm, the interface roughness is not yet known for these samples. Further work will be necessary to estimate the composition mixing in these samples.

The wear rate of $T_s = -90^\circ\text{C}$ deposited multilayers with $\lambda \leq 5$ nm was found to be the lowest. In particular, the wear resistance of $T_s = -90^\circ\text{C}$ deposited Al/Al₂O₃ with $\lambda = 2$ nm is 182% higher than the monolithic Al₂O₃ films ones. On the other hand, the hardness is $\approx 50\%$ lower. This is in negative correlation with the fact that in ceramic films, the wear resistance depends on its hardness. However, the metal phase in multilayers allows inhibition of microcracking in these materials during sliding compared with hard Al₂O₃ films. This can partially explain the apparent contradiction in correlation of hardness and wear resistance behavior of Al/Al₂O₃ multilayers.

5. Conclusion

Multilayers alternating polycrystalline aluminium and amorphous alumina were fabricated using RF-reactive sputtering. The temperature of substrate T_s during deposition greatly influenced the morphology and structure of the films. XRR experiments showed an improvement of the multilayering character with decreasing T_s , despite the granular surface of Al layers.

For $T_s=25^\circ\text{C}$ deposited Al/Al₂O₃ multilayers, no significant difference in wear resistance was seen when comparing to Al₂O₃ monolithic films.

A large enhancement of wear resistance was obtained for $T_s=-90^\circ\text{C}$ deposited multilayers with decreasing period thickness.

A comparison of the structure of the two sets of multilayers ($T_s=25^\circ\text{C}$ and $T_s=-90^\circ\text{C}$) suggests that tribological properties are greatly enhanced for films with good quality of multilayering which is Al/Al₂O₃ deposited at $T_s=-90^\circ\text{C}$.

Acknowledgements

We gratefully acknowledge M. Jeandin for useful discussion, M. Nélis for help on hardness measurements, P.A. Albouy for XRR experiments, and G. Renou for sample preparation.

References

- [1] W.D. Sproul, J. Vac. Sci. Technol. A 12 (1994) 4.
- [2] H. Kung, T.R. Jervis, J.-P. Hirvonen, J.D. Embry, T.E. Mitchell, M. Nastasi, Philos. Mag. A 71 (1995) 4.
- [3] S.J. Bull, A.M. Jones, Surf. Coat. Technol. 78 (1996).
- [4] J.S. Koehler, Phys. Rev. B 2 (1970) 547.
- [5] Y. Ding, Z. Farhat, D.O. Northwood, A.T. Alpas, Surf. Coat. Technol. 68 (1994) 459.
- [6] C. Le Paven-Thivet, C. Malibert, Ph. Houdy, P.A. Albouy, Thin Solid Films 336 (1998) 373.
- [7] N.X. Randall, C. Julia-Schmutz, J.M. Soro, J. von Stebut, G. Zacharie, Thin solid Films 308/309 (1997) 297–303.
- [8] C. Le Paven-Thivet et al., unpublished data.



ELSEVIER

Surface and Coatings Technology 125 (2000) 201–206

**SURFACE
& COATINGS
TECHNOLOGY**

www.elsevier.nl/locate/surcoat

A comparative study of the nanoscratching behavior of amorphous carbon films grown under various deposition conditions

C. Charitidis *, S. Logothetidis, M. Gioti

Department of Physics, Aristotle University of Thessaloniki, 54006 Thessaloniki, Greece

Abstract

Two types of amorphous carbon (a-C) films: one series with a layered structure (sequence of soft/hard carbon layers) resulting in thick, stable and sp^3 rich films, and another series of monolithic films rich in sp^2 , were deposited on Si substrates by magnetron sputtering and were investigated with respect to their nanoscratching behavior. The main purposes of this work are to investigate the scratch performance of a-C films developed in layered structure and to compare this with the films rich in sp^2 content. Ultra-low load scratch tests were performed in the load range from 2 to 20 mN to explore the deformation mechanisms of such thin films and their adhesion to the substrate. Below 5 mN, the scratches on layered structure films exhibit an almost full elastic response while on films rich in sp^2 content show massive brittle fragmentation. At 20 mN, the scratches on the former films reveal some areas which are completely elastic and some areas which were typical of a buckle failure. These areas may correspond to hard and soft carbon layers, respectively. The coefficient of friction varied from ~ 0.2 to ~ 0.3 , depending on the maximum normal load and being lower for films of the first type. Scratch testing results have shown that layered structured films are resistant to plastic deformation during contact and, together with the stability of the thick layered films, support their potential for protective overcoats. © 2000 Elsevier Science S.A. All rights reserved.

Keywords: Carbon; Nano-indentation; Scratch test; Sputtering

1. Introduction

Amorphous carbon (a-C) films rich in sp^3 content have been studied intensively during the last decade due to their outstanding properties, such as high hardness, high transparency, high resistance, low coefficient of friction, chemical inertness and biocompatibility. This unique combination of physical, chemical and mechanical properties makes them suitable for use in a wide range of technological and industrial applications, such as microelectronic, optical, biomedical applications, wear-resistant and protective overcoats for hard disks in the magnetic storage industry. Aspects which are important in assessing the potential use of all the a-C films are not only the elastic properties [hardness (H) and elastic modulus (E)] of the film, but also the adhesion of films onto the substrate, their deformation response and the presence of residual stresses.

The high internal stress observed in sputtered a-C films limits their maximum thickness below ~ 40 nm

because of poor adhesion to the substrate and subsequent delamination and cracking of the film. However, films with that thickness are useless for most practical applications. Therefore, the production of thicker and hard a-C films with low stress is technologically and scientifically important. Recently, it has been shown that reduction of the internal stress in thick a-C films with high hardness can be obtained by developing layer structured (consisting of sequential soft and hard layers) films [1].

The objective of this study was to investigate the elastic and tribological properties of films developed in layered structure (rich in sp^3 content) and their comparison with those rich in sp^2 content. The main focus was on the adhesion and deformation response of the films using the scratch test as the main experimental characterization tool. Film deformation response was studied in order to gain a better understanding of the mechanisms governing failure of thin films.

Sufficient adhesion of the film on the substrate is one of the basic properties of a functional film–substrate compound. Among techniques [2,3] utilized to evaluate the tribological properties of thin films, the nanoscratch

* Corresponding author. Tel.: +30-31-998129; fax: +30-31-246484.
E-mail address: cchar@skiathos.physics.auth.gr (C. Charitidis)

test [4,5] provides a simple, versatile and rapid means of assessing the adherence of thin films to the substrate. Although the scratch test has been widely used as an indicator of film adhesion strength [4,6,7] it was difficult, until recently, to perform such a test on films less than 1 μm thick. In order to perform a successful scratch test in sub-micron films the scratching apparatus has to satisfy two requirements: to apply controlled very low loads (nN) to the tip, and the precise movement of the tip relative to the film at controlled loads. An important requirement is the use of a procedure which can offer in situ monitoring of the induced scratch damage. The nanoscratch apparatus used in this work can make finely controlled low load scratches and provide coefficient of friction measurements as well as information about in situ surface elastic-plastic deformation depth during the test.

2. Experimental details

The sputtered a-C films were deposited in an Alcatel SCM 600 magnetron sputtering apparatus which has been described elsewhere [8,9]. Briefly, the a-C thin films were deposited on (100) c-Si substrates using a graphite (99.999% purity) target. During deposition we fixed the sputtering Ar gas at a partial pressure 2×10^{-2} mbar, the target to substrate distance at 65 mm and the discharge power at 100 W. The bias voltage applied to substrate (V_b) was either floating (positive) or negative. A phase modulated ellipsometer, mounted on the deposition system, allows in situ spectroscopic ellipsometry (SE) measurements in the energy region 1.5–5.5 eV, and was used to estimate the thickness and the composition (sp^2 and sp^3 content) of the deposited film [9].

To investigate the mechanical and tribological behavior of a-C thin films, two types of a-C films with thicknesses of 90, 280 and 200 nm respectively, were prepared. The first type of film was deposited in sequential layers with alternative (positive/negative) V_b . In detail, firstly a layer of ~ 10 nm was deposited with $V_b = +10$ V and subsequently a layer of ~ 20 nm with $V_b = -20$ V. This procedure was repeated three (nine) times in sequence for the development of films with total thickness ~ 90 (280) nm. Films with a thickness of 200 nm were deposited with positive V_b . We have found by analyzing SE (and also nano-indentation) measurements that films deposited with negative V_b are rich in sp^3 content (hard), while films deposited with positive V_b are rich in sp^2 content (soft) [10].

The elastic and tribological properties of the films were conducted using a Nano Indenter XP system with options for continuous stiffness measurements (CSM) and lateral-force measurements (LFM). A detailed description of the system has been presented elsewhere

[10]. H and E of each of the films were measured with a Berkovich, three-sided pyramid diamond indenter. Experiments were performed in a clean air environment with $\sim 45\%$ relative humidity and 22°C ambient temperature. In all CSM depth-sensing tests a total of 10 indents were averaged to determine the mean H and E values for statistical purposes, with a spacing of 50 μm .

A different diamond Berkovich indenter was used for scratch testing. Scratches were made with an edge of the indenter (point-on orientation). One potential criticism of scratch testing is that the tip itself may become increasingly blunt, making it difficult to quantitatively compare results for a series of tests. Therefore, prior to each scratch test, three indents were made in aluminum to clean the tip, and then two 100 nm indents were made in fused silica to evaluate the condition of the tip. A precision X – Y table with a resolution of 1 μm was used to slide the film under the tip with a minimum of vibration and electrical noise. Lateral deflection was measured using two separate capacitive displacement gauges to sense the lateral displacement of the indenter column in the X and Y directions. Lateral (friction) forces were then calculated from the stiffness of the column determined in calibration experiments. Coefficient of friction (μ) could be calculated afterwards [11]. Since scratch-induced damage of a film, specifically fracture or delamination, was monitored by in situ friction force measurements, there was no need to obtain an image of the scratch event but only to confirm the experimental results. Depths of scratches with increasing scratch depth or normal load were measured in situ by profiling the surface of the film before, during and after the scratch event, resulting in a total length of the test of 700 μm , while the scratch length was 500 μm long. The load for initial and post-scratch scan was 0.02 mN. In order to make effective use of the displacement data for production of a profile, it was assumed that regions associated with the pre-scratch scan and post-scratch scan were unaffected by the deformation achieved during the scratch itself. Data from these regions were used to account for both the slope and curvature of the sample surface so that the entire scratch could be viewed with the surface of the sample as the baseline for deformation [12].

3. Results and discussion

Fig. 1 shows the nano-indentation results for a-C films rich in sp^3 content (90 and 280 nm thick) and rich in sp^2 content (200 nm thick) where hardness and elastic modulus are plotted as a function of contact depth. Indentation was conducted by applying the CSM technique for different penetration depths. It can be clearly observed in Fig. 1 that the shape of hardness and elastic modulus strongly depends on the hardness of the film

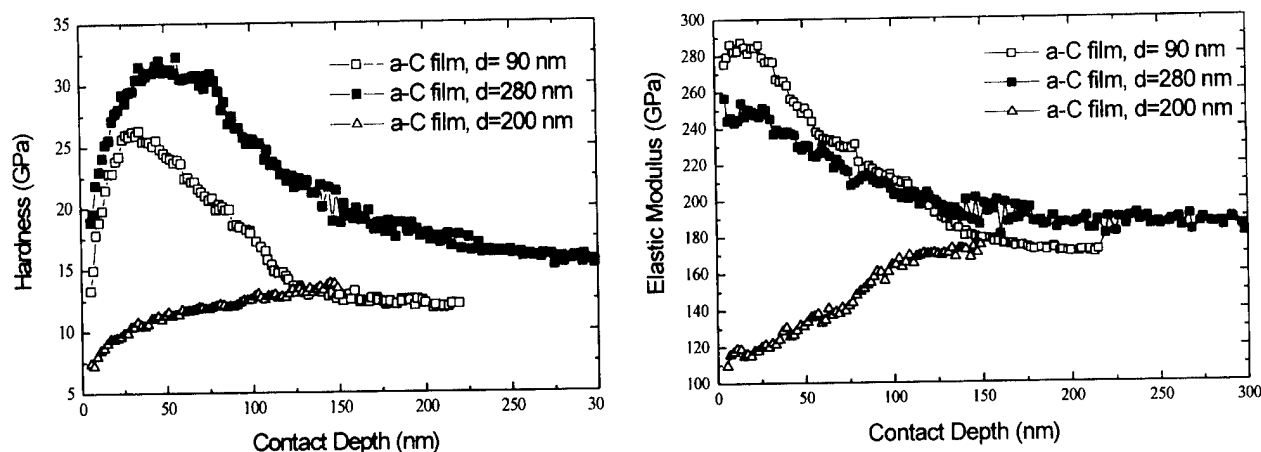


Fig. 1. Evolution of the hardness and elastic modulus of the three studied a-C films versus the indentation contact depth.

versus that of the substrate. More particularly, the films deposited in sequential layers appear to be harder than the substrate and reach values about 32 and 27 GPa, respectively, depending on the thickness of the deposited film. Films rich in sp^2 content appear to be softer than the Si substrate ($H=12.5$ GPa) and reach this value with increasing the contact depth. Values of the hardness, elastic modulus, plastic resistance parameter (H^3/E^2) [10] and coefficient of friction for the films examined in this work are included in Table 1.

Nanoscratch tests were conducted to examine the general scratching behavior of the a-C films and to quantify their scratch resistance. In Fig. 2 nanoscratch test results for a-C films, 90 and 280 nm thick respectively, at various normal loads are presented. Fig. 2 includes a plot of the vertical displacements of the diamond during the initial scan (prescan), the load-ramped scratch (scratch scan), and the post-scratch scan (post scan) for each film. The scratch proceeds from left to right in the figure. The initial scan profiles the unscratched surface of the film and the post-scratch scan is used to determine the surface damage due to the scratch event. Negative displacements correspond to the scratch tip being pushed into the specimen, and positive displacements, which appear in the post-scratch scan, indicate the outward blistering of the surface or the accumulation of debris in the scratch trace. Four scratches were made at each load at different areas of specimen.

Fig. 2(a) shows the surface profile of the 90 nm thick a-C film scratched with ramping load of 0.02–5 mN.

The resulting scratch shows a depth ~ 200 nm (more than double the film thickness), the film shows good adhesion to the substrate and recovers highly elastic ($\sim 90\%$). The abrupt changes of the coefficient of friction in Fig. 3(a) and the small scale fluctuations in the post scan for scratch lengths >450 μm reveal that it is likely that nano-scale fractures occur between the sublayers in the layered structure. The smoothness of the displacement curve during the scratch scan reflects the fact that no observable delamination or cracking was found in the scratch track. In the case of maximum normal loads below 5 mN, the scratches appear smooth, shallow and were undetectable over their entire length by optical microscopy and therefore it is expected that these scratches were completely elastic.

In Fig. 2(b) the scratch can be divided into two regimes based on differences in the appearance of the scratch profile. The first regime is defined by the first 300 μm of the scratch. In this regime, the scratch is extremely smooth and shallow, as can be seen both by comparing the post scan to the pre scan and by optical microscopy. A closer examination revealed that there are no remnants of the scratch, corresponding to fully recovered elastic contact. The second regime extends from 400 to 600 μm . In this regime, the film recovered highly elastic ($\sim 90\%$). It is marked by a change in the scratch displacement. In this regime the film blisters by partial delamination between layers [12]. Examination of the film by optical microscopy reveals some small particle debris surrounding the scratch trace in this regime, suggesting that damage was limited to cracking

Table 1
Summary of nano-indentation results of a-C films

	Thickness (nm)	H (GPa)	E (GPa)	H^3/E^2 (GPa)	μ
sp^3 -rich	90	27	290	0.235	0.25
sp^3 -rich	280	32	260	0.44	0.2
sp^2 -rich	200	8	100	0.05	0.35

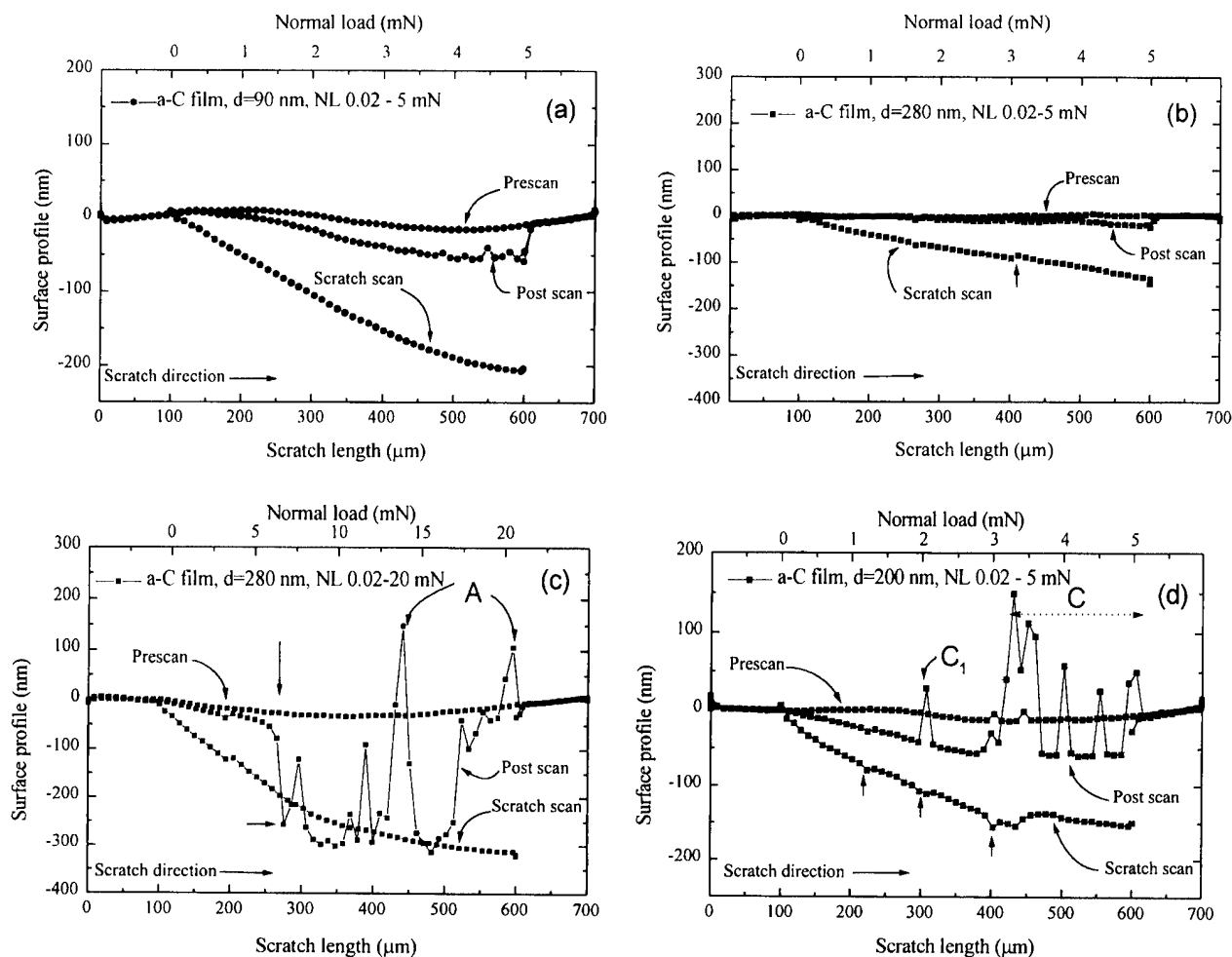


Fig. 2. Surface profiles of the a-C films rich in sp^3 content developed in layered structure (90 and 280 nm thick) scratched with ramping normal loads of (a) 0.02–5 mN, (b, c) 0.02–5 (20) mN respectively, and (d) a-C films rich in sp^2 content (200 nm thick) scratched with ramping normal loads of 0.02–5 mN.

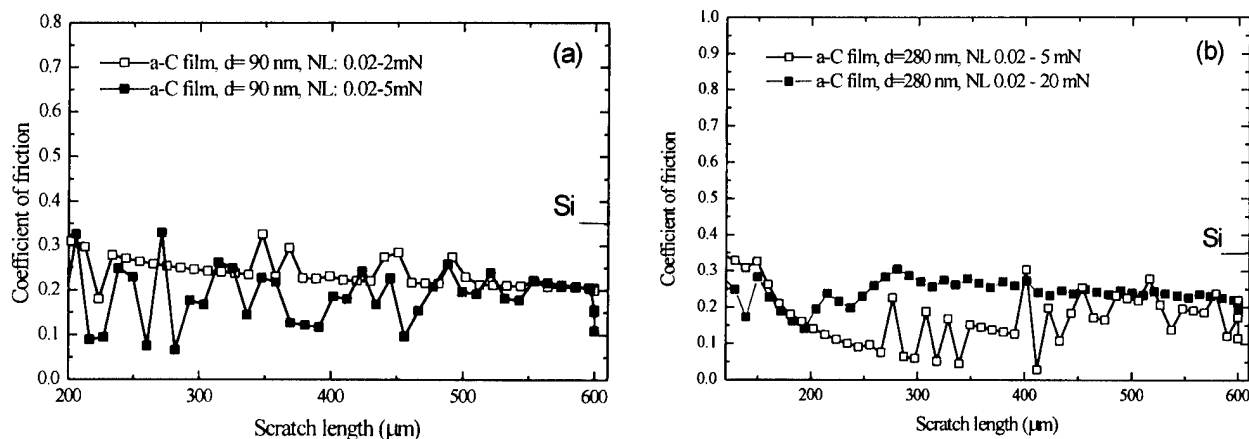


Fig. 3. Coefficient of friction profiles of a-C films rich in sp^3 content (a) 90 nm thick, and (b) 280 nm thick, as a function of scratching length (ramping normal load).

and small areas of pull-off contained entirely within the scratch track. In conclusion, the 280 nm thick a-C film remains intact and is resistant to scratch damage at loads up to 3 mN, but increasing the load further causes partial failure of the film by delamination and blistering. It is obvious that the 280 nm a-C film is harder than the 90 nm thick one, and it has almost recovered elastically. In the case of the 90 nm thick film, the maximum normal load (5 mN) results in a scratch depth of almost 200 nm. This means that the monitored response corresponds not to the film itself but to the film–substrate system. In the case of the film with a thickness of 280 nm, the scratch induced response is a pure film property. In general, the scratch test offers an alternative for characterizing thin films since the probed portion of the film is larger than it is in indentation tests. This is especially true when indentation alone yields measurements which are significantly affected by the substrate while the nanoscratch test can isolate the mechanical properties of the film.

The behavior of the 280 nm thick a-C film at loads up to 20 mN was examined to monitor the adhesion and strength of the film. As shown in Fig. 2(c), two distinct regimes are observed. The first extends from 100 to 250 μm and is characterized by almost fully elastic contact, as was also observed by optical microscopy. In the second one, above 250 μm , corresponding to a load above 5 mN there was a large change in the post scan, failure begins abruptly by brittle fragmentation in the film and substrate. The post scan trace shows that fragmentation occurred at a depth near the film thickness, indicating complete failure and removal of the film. Positions marked A in Fig. 2(c), where a sudden increase in depth occurred, are exactly correlated to the initiation of the delamination [13,14]. In detail, the height measured at position A is ~ 150 nm, and it is the half of the film thickness, which also implies the absence of a significant portion of the a-C film, at a load ~ 14 mN.

The scratch behavior of the a-C film rich in sp^2 content (Fig. 2(d)) is completely different from that of other films studied in this work. Film deformation is mainly plastic all over the scratch length and at ~ 400 μm of the scratch length (i.e. load 3 mN) failure begins abruptly by brittle fragmentation in the film. The ripple structures observed in the area marked C in Fig. 2(d) along the track seems to be influenced by tensile-type cracks. The depth measured in area C is ~ 150 nm, and it is more than the half of the film thickness which implies the absence of a-C film at loads > 3 mN and possibly is correlated to the delamination of the film. The poor adhesion of the a-C film to the substrate produced cracks and small regions of film pull-off at loads above 1 mN, which resulted in the displacement roughness at scratch track positions

between 200 and 300 μm (indicated by arrows in Fig. 2(d)). The large positive displacements observed in the post scan between 300 and 600 μm represent the positions at which the stylus was forced over the delaminated film which was piled up in its path. Friction coefficient values for these films were found to be ~ 0.35 .

Material removal, with the formation of surface material on the side of the scratch which were plastically torn away, indicates that scratching on films rich in sp^2 content occurred mainly by plastic deformation typical of soft materials. This type of deformation of soft layers is possibly responsible for the delamination and buckling effects observed in layered structure films when the former are subjected to high normal loads during the scratch test. A detailed examination of the scratch profiles in layered structure films supports the above speculation. For the design of tough layered structure a-C films we have to take into account the following mechanisms: (i) the stress relaxation in a hard layer by plastic deformation in a soft layer [1]; and (ii) the termination of cross-sectional cracks by their deflection at interfaces and braking in a soft layer with energy dissipation by plastic deformation. For a-C layered structure films, the important question is whether the termination of plastic deformation in a soft layer is required. From the strengthening mechanisms, (i) and (ii), interlayer plasticity is necessary to brake cracks and relax stresses in hard a-C bilayers. Thus, a minimum thickness of the soft layer is required to activate the strengthening mechanisms (i) and (ii) for a-C layered structure. However, for larger soft layer thicknesses, there is a probability of failure of the total film stack by buckling or crack propagation along the soft layer. In conclusion, an optimal thickness of the individual layers is thought to be critical in the design of layered structure films with good properties. On the other hand, a layered structure film with a high number of interfaces exhibits an increase in toughness and crack propagation resistance [15]. Interfaces in films with a layered structure are sites of energy dissipation and crack deflection leading to a toughening of the layer material. Further studies are in progress to determine the minimum thickness of soft layers and the number of interfaces in order to produce films with improved adhesion and toughness under high local loading, and to reduce the amount of residual compressive stresses associated with the kinetically forced formation of sp^3 bonds in hard layers.

Fig. 3 is a plot of the friction coefficient (μ) versus scratch length (normal load). μ is calculated by taking the ratio of the lateral force and normal load on the indenter [11]. Until the tip begins to slide with respect to the sample, μ is indeterminate. At the start of the scratch, the lateral force data is noisy indicating a stick-

slip phenomenon [16]. Once the normal load reaches about 0.5 mN, μ settles to nearly constant values. The fluctuation in friction coefficient values is promoted by point-on orientation of the tip or the layered structure of the films, or it could be due to nano-scale fracture events.

4. Conclusions

The results of the systematic investigation of scratch performance of sputtered a-C films in this work confirm the enhanced elastic behavior of the layered films. Layered films have better adhesion strength comparing to those which are rich in sp^2 content, so that they can sustain film cracking without debonding. Direct and in situ depth measurement can provide the elastic/plastic depth profile along the scratch track and useful information in scratch process modeling and understanding of fundamental mechanisms which could be used to increase the toughness and adhesion of hard a-C films.

References

- [1] M. Gioti, S. Logothetidis, C. Charitidis, *Appl. Phys. Lett.* 73 (1998) 184.
- [2] D.A. Hardwick, *Thin Solid Films* 154 (1987) 109.
- [3] V. Gupta, A.S. Argon, D.M. Parks, J.A. Cornie, *J. Mech. Phys. Solids* 40 (1992) 141.
- [4] T.W. Wu, *J. Mater. Res.* 6 (1991) 407.
- [5] S. Venkataraman, D.L. Kohlstedt, W.W. Gerberich, *J. Mater. Res.* 7 (1992) 1126.
- [6] P.J. Burnett, D.S. Rickerby, *Thin Solid Films* 157 (1990) 233.
- [7] J. Sekler, P.A. Steinmann, H.E. Hintermann, *Surf. Coat. Technol.* 36 (1988) 519.
- [8] S. Logothetidis, *Appl. Phys. Lett.* 69 (1996) 158.
- [9] S. Logothetidis, M. Gioti, *Mater. Sci. Eng. B* 46 (1997) 119.
- [10] C. Charitidis, S. Logothetidis, P. Douka, *Diamond Relat. Mater.* 8 (1999) 558.
- [11] T.W. Scharf, J.A. Barnard, *Thin Solid Films* 308/309 (1997) 340.
- [12] S.D. McAdams, T.Y. Tsui, W.C. Oliver, G.M. Pharr, *MRS Symp. Proc.* 356 (1995) 809.
- [13] H. Deng, T.W. Scharf, J.A. Barnard, *J. Appl. Phys.* 81 (8) (1997) 5396.
- [14] X. Li, B. Bhushan, *Thin Solid Films* 340 (1999) 210.
- [15] H. Holleck, V. Schier, *Surf. Coat. Technol.* 76/77 (1995) 328.
- [16] K. Li, B.Y. Ni, J.C.M. Li, *J. Mater. Res.* 11 (1996) 1574.

Morphologies and corrosion properties of PVD Zn–Al coatings

M.A. Baker¹, W. Gissler^{*}, S. Klose², M. Trampert, F. Weber³

Institute for Health and Consumer Protection, Joint Research Centre, Commission of the European Union, I-21020 Ispra(Va), Italy

Abstract

Physical vapour deposition (PVD) Zn alloy coatings are being considered as possible alternatives to conventional hot dip and electrochemically deposited coatings on steel substrates. Variation of the deposition temperature leads to very different microstructures being observed by SEM, primarily due to the low melting point of zinc. In the present study this phenomenon has been investigated in more detail. Zn + 5 at.% Al coatings were deposited by magnetron sputtering using a homogeneously alloyed Zn–Al target. As the substrate temperature is increased, the coating morphology changed from a compact to an open sponge/woollen-like microstructure and the coating thickness increased by up to a factor of 10. The Zn–Al coatings displayed a hexagonal structure corresponding to that of Zn. The corrosion properties were investigated by potential–time and salt bath immersion tests. Interestingly, both the barrier and sacrificial protection afforded by the coating were independent of the microstructure. © 2000 Published by Elsevier Science S.A. All rights reserved.

Keywords: Corrosion resistance; Microstructure; Physical vapour deposition; Zn–Al alloy

1. Introduction

For many years zinc and various zinc alloy coatings have been used to improve the corrosion resistance of steel sheets. Conventionally, these coatings are deposited by hot dip and electroplating processes (see e.g. Ref. [1]). A possible alternative coating process is PVD which includes the techniques of evaporation, ion beam, arc and sputter deposition [2–10]. These processes are environmentally friendly and have some additional advantages:

1. they allow the deposition of any type of Zn alloy without the restrictions inherent in electroplating processes due to different electrochemical potentials of the alloying materials;
2. there is no danger of steel embrittlement as a consequence of hydrogen evolution during the electrochemical process; and

3. PVD coatings can be produced with very compact microstructures which have been assumed to further increase the corrosion resistance [2], and might also advantageously influence steel sheet processing properties such as formability, weldability and paintability.

The disadvantage of PVD processes is the low deposition rate compared to electrochemical or hot dip methods.

This paper is concerned with the extent to which the microstructure of coatings, in particular their compactness, influences the corrosion resistance. It is well known that the microstructure of PVD coatings strongly depends on the melting point and on deposition parameters such as substrate temperature and ion bombardment during film growth and the pressure of the working gas [11]. Coatings with a low melting point such as Zn (420°C) assume an open microstructure if deposited without substrate cooling and ion bombardment. This is essentially due to a high surface mobility allowing the atoms to migrate immediately after deposition and to look for crystallographically favoured sites.

The influence of substrate bias voltage on the microstructure and surface morphology has been investigated by Li and Nowak [3] for Zn–Al alloy coatings of various composition, by Musil et al. [4] for pure Zn coatings, and by Bowden and Matthews [2] for Zn–Ni coatings. Applying a negative substrate bias voltage, compact and

^{*} Corresponding author. Tel.: +39-332-78-9906;
fax: +39-332-78-5036.

E-mail address: wolfram.gissler@jrc.it (W. Gissler)

¹ Present address: School of Mechanical and Materials Engineering, University of Surrey, Guildford, Surrey GU2 5XH, UK.

² Present address: Institut für Angewandte Physikalische Chemie, Universität Heidelberg, Im Neuenheimer Feld 500, D-69120 Heidelberg, Germany.

³ Present address: Gühring oHG, Lengederstrasse 29-35, D-13407 Berlin, Germany.

fine-grained coatings with a superior barrier protection have been obtained compared to electrodeposited, less compact coatings. The relationship between microstructure and corrosion resistance of hot-dip Zn–Al coatings has been investigated by Ling et al. [12,13].

In the present study Zn+5 at.% Al coatings have been deposited by magnetron sputtering. Zn alloys such as Zn–Al have a lower corrosion rate than pure Zn due to the higher electrochemical potential of the alloyed materials. However, the sacrificial protection deteriorates, which is important if the underlying steel is exposed locally as a result of stone chipping. The coatings were characterised with respect to their morphology, microstructure and corrosion behaviour.

2. Experimental

Film deposition was performed using a commercially available sputtering machine (MRC type 8667 A) in which a Zn–Al target of composition Zn+5 at.% Al (purity 99.99%) was mounted. Before deposition, the chamber was evacuated to a pressure of 1×10^{-4} Pa. During the deposition process, a gas flow of 137 sccm Ar was maintained by a mass flow controller. The total pressure was kept at 7×10^{-2} Pa during the coating process. Mild steel and Si(111) wafers were used as substrates. The steel substrates were degreased and ultrasonically cleaned in soap solution. Prior to film deposition the substrates were sputter etched for 5 min. A sputtering power of 600 W was used for the Zn–Al target and an r.f. generated bias voltage of -290 V was applied to the substrate. The substrate holder was rotated to obtain a homogeneous coating. Under these conditions a deposition rate of about 10^{17} atoms/cm² s was recorded. Samples were either placed in contact with the water cooled (8°C) substrate holder using a heat conduction paste or deliberately thermally isolated.

X-ray microstructural analysis of the samples was performed by glancing angle X-ray diffraction

(GAXRD) using an unmonochromated copper source at an incident angle of 0.5° (or in a conventionally θ – 2θ scan). The angular resolution was controlled by a high precision variable slit positioned between the source and sample and a Soller slit collimator mounted between the sample and detector. A solid state detector was used to isolate the CuK α doublet. The film morphology and composition was studied using a JEOL 5400 scanning electron microscope.

Potential–time plots were obtained by placing the Zn–Al coated specimen in a glass electrochemical cell and exposing an area of 1 cm² to an aerated 5% NaCl solution which was continuously stirred. The potential of the sample was measured with respect to a standard Ag/AgCl electrode. The immersion test was carried also out in a stirred aerated 5% NaCl solution. In this test, samples were spaced apart from each other in a flat bottomed glass vessel. The back side of the samples was painted, to avoid contact of the uncoated steel with the solution, and on the coated side a cross was scratched. At regular intervals the samples were inspected for the presence of red rust in the scratches or on the general surface.

3. Results and discussion

The Zn–Al coatings were highly reflective if deposited in good thermal contact, or opaque and of grey appearance if deposited in bad thermal contact with the cooled substrate holder. Fig. 1(a) and (b) show SEM fracture cross-sections of coatings in good (a) and in bad (b) thermal contact with the substrate holder plate. EDX analysis revealed a composition corresponding to Zn+5(\pm 1) at.% Al. The coatings were deposited onto Si substrates in adjacent positions on the substrate plate. The coating in Fig. 1(a) displays a typical columnar type structure (the droplets are due to arcing phenomena at the target), whereas the coating in Fig. 1(b) has an open woollen-like microstructure. Although both coat-

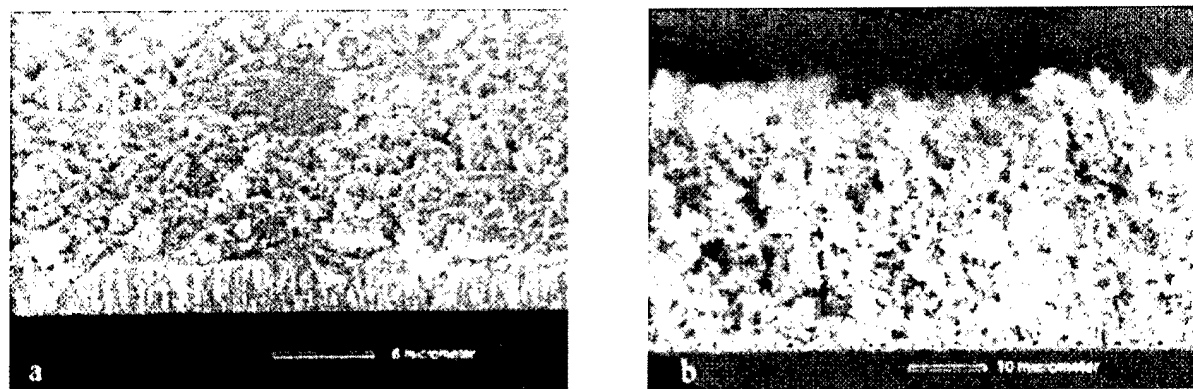


Fig. 1. SEM fracture cross-sections of two Zn–Al coatings of which one (a) was kept in good and the other (b) in bad thermal contact with substrate holder ($T \approx 8^\circ\text{C}$).

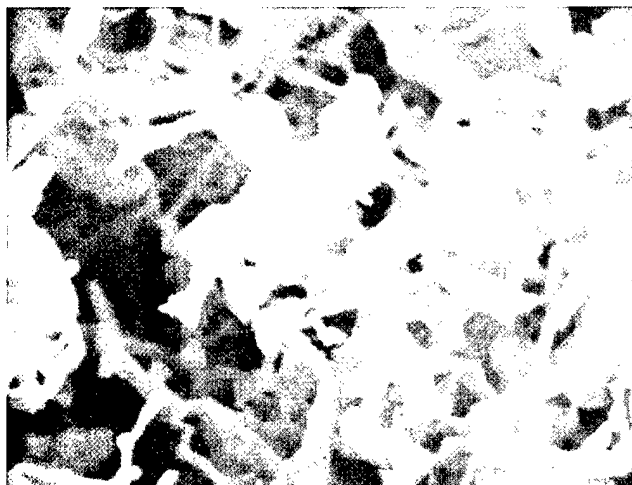


Fig. 2. Magnified view of a Zn+5 at.% Al coating deposited in bad thermal contact with the substrate holder displaying a woollen-like microstructure.

ings were deposited in the same batch and therefore had the same quantity of Zn–Al per unit area, their thickness of 3 and 30 μm , respectively, differs by a factor of 10. Fig. 2 shows a further magnified view of the surface of the coating of Fig. 1(b). The microstructure consists of a network of small dendrites arranged at angles typical for an hexagonal lattice structure.

The difference in the observed microstructures is due to different film growth temperatures as a consequence of the different heat transfer conditions for the coatings. We could not measure the actual surface temperatures of the growing film, but we can assume that the coating in good thermal contact with the cooled substrate holder plate was grown at a temperature significantly lower than the coating having bad thermal contact.

The growth mode of films is usually rationalised by structure-zone diagrams (see e.g. Refs. [12,13]) in which the different type of structures are schematically illustrated as a function of the normalised growth temperature T_s/T_m , where T_s is the film temperature and

T_m is the melting point of the coated material. In general, at $T_s/T_m < 0.5$, film growth is determined by low adatom mobility and atomic self-shadowing giving rise to columnar structures, whereas at $T_s/T_m > 0.5$ recrystallisation during deposition plays the dominant role and the film begins to form its 'intrinsic' microstructure independent of deposition parameters.

As the melting point of Zn is 693 K, at a substrate temperature of 281 K (8°C), the parameter $T_s/T_m \approx 0.4$, which is below the 'critical' value of 0.5. The film deposited in good thermal contact with the substrate holder plate exhibits a columnar type of microstructure in agreement with that expected. However, for the film grown in bad thermal contact a considerably higher growth temperature must be assumed. During deposition, there are several sources of heat at the surface, such as the kinetic energy of the depositing atoms, which is between 10 and 50 eV (for sputtered atoms), their heat of condensation, the plasma radiation and the energy of back-scattered neutralised Ar atoms. If the heat generated by these various sources cannot be transferred to the substrate holder, a considerable temperature rise must be expected and therefore a T_s/T_m ratio > 0.5 can be assumed. Consequently, the film microstructure is completely changed, as can be seen in Fig. 1(b). These different types of microstructure also influence the surface morphology which has been investigated by Musil et al. [4]. In agreement with Refs. [3,4] it has been found that films with a compact microstructure have a highly reflective and metallic appearance, whereas films with the open microstructure are grey and not reflective.

Fig. 3 shows the XRD spectra obtained from the good and bad thermally contacted coatings together with the standard line spectra [14] of zinc and iron. The peak positions of both coatings are only little different and agree quite well with the positions of the standard spectrum of Zn. The iron peaks come from the steel substrate. The coating deposited in good thermal contact

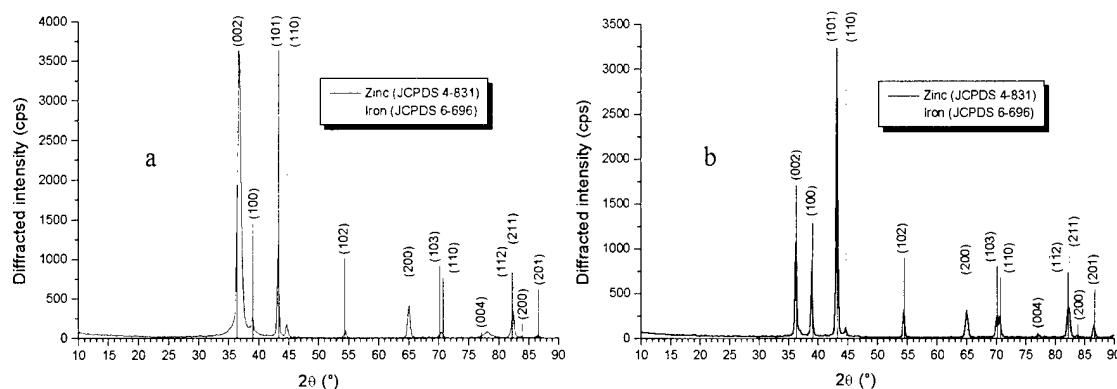


Fig. 3. XRD spectra obtained from the Zn+5 at.% Al coating in (a) good, and (b) bad thermal contact with the substrate holder plate, together with standard line spectra of zinc and iron.

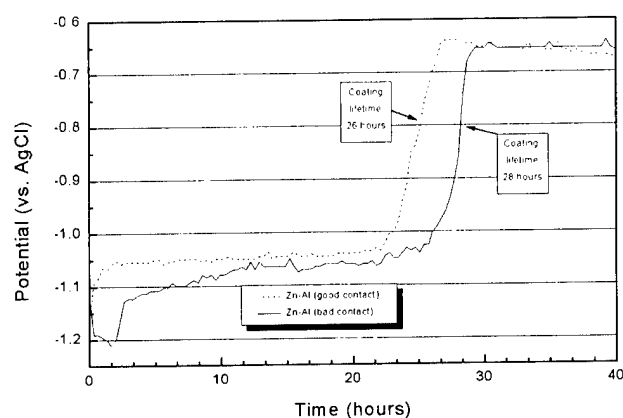


Fig. 4. Potential vs. time plot of Zn+5 at.% Al coatings with (a) a compact, columnar type and (b) an open woollen-like microstructure. No significant lifetime differences can be recognized.

displays a slightly shifted (002) peak towards larger angles, which might be due to compressive stress in the direction of the [002] axis. This coating is also characterised by a marked preferred orientation in the same crystallographic direction.

Both coatings consist of the same number of atoms per unit area, and have the same chemical and phase composition. Thus, the only difference between the two coatings is their microstructure and any differences in the corrosion behaviour should therefore be attributed to these different microstructures.

Fig. 4 shows the results obtained from the potential-time test. The lifetime of the coatings is nearly equal for both types of microstructure. This is an unexpected result since an open structure is generally assumed to be more porous than a compact one. Indeed, previous workers have reported for Zn–Ni that magnetron sputtered coatings have a lower corrosion rate than electroplated coatings [2]. The more compact microstructure of the sputtered coating was given as the reason for this behaviour.

The other important property of Zn-based coatings on steel is the sacrificial protection which they offer when the paint system is damaged, i.e. by stone chipping. The effectiveness of this sacrificial behaviour has been investigated by an immersion test. Both coatings resisted rust formation for approximately 150 h.

So, interestingly, the corrosion behaviour of the Zn+5 at.% Al coating on steel system appears to be independent of the microstructure. This result can be rationalised by considering that it is the total number of available Zn atoms and not microstructure which is the most important parameter regarding sacrificial protection of the steel.

4. Conclusions

Zn+5 at.% Al coatings were deposited by magnetron sputtering, using a homogeneously alloyed Zn–Al target.

Depending on the substrate temperature, two different microstructures were observed: at lower temperatures a compact and columnar type, and at higher temperatures an open woollen-like microstructure. Both coating types assumed similar crystal structures. The results of corrosion-potential vs. time measurements and of immersion tests did not reveal a significant difference between the corrosion behaviour of the two types of Zn–Al coatings. The corrosion resistance depends mainly on the number of deposited Zn atoms per unit area rather than the microstructure of the coating.

Acknowledgements

The authors wish to express their thanks to Dr. P.N. Gibson for helpful discussions in interpreting the X-ray diffraction experiments, and Messrs. A. Hoffmann and T. Sasaki for helpful technical assistance. The study was performed in the framework of the Brite-Euram project BE96-3073 of the European Union.

References

- [1] K. Kösters, M. Pimminger, Present state and future trends in surface coated steel sheets for automotive application, Proc. Int. Conf. on the 21st Century Steel Industry of Russia and CIS, Moscow 5 (1994) 9.
- [2] C. Bowden, A. Matthews, A study of the corrosion properties of PVD Zn–Ni coatings, Surf. Coat. Technol. 76/77 (1995) 508.
- [3] L. Li, W.B. Nowak, Biased magnetron sputter deposition of corrosion resistant Al–Zn alloy thin films, J. Vac. Sci. Technol. A 12 (1993) 1587.
- [4] J. Musil, J. Mattous, V. Valvoda, Effect of ion bombardment on the surface morphology of Zn-films sputtered in an unbalanced magnetron, Vacuum 46 (1995) 203.
- [5] R. Kuzel, V. Valvoda, M. Chladek, J. Musil, J. Matous, XRD microstructural study of Zn films deposited by unbalanced magnetron sputtering, Thin Solid Films 263 (1995) 150.
- [6] F. Alonso, V. Madina, J.L. Viviente, T. Mursell, J.I. Onate, Zn–Cr alloy coatings produced by ion beam assisted deposition, Surf. Coat. Technol. 103/104 (1998) 87.
- [7] C. Mitterer, R. Barbist, T. Björk, M. Sundqvist, J. Bergström, J. Hagler, A comparative study on the evaluation of the tribological behaviour of polymer/zinc coated steel sheets, Wear 210 (1997) 88.
- [8] Y. Fukui, H. Tanaka, M. Saito, T. Deguchi, Corrosion resistance of vapour-deposited Zn–Mn plated steel, Proc. 4th Int. Conf. on Zinc and Zinc Alloy Coated Steel Sheet (Galvatech'98), Chiba, Japan (1998) 443.
- [9] L. Guzman, M. Adami, E. Voltolini, Zn coatings on steel by advanced PVD techniques, Proc. 4th Int. Conf. on Zinc and Zinc Alloy Coated Steel Sheet (Galvatech'98), Chiba, Japan (1998) 763.
- [10] J. Kawafuku, J. Katoh, M. Toyama, K. Ikeda, H. Nishimoto, H. Satoh, Properties of zinc alloy coated steel sheets obtained by continuous vapor deposition pilot-line, Proc. 5th Automotive Corrosion and Prevention Conference, Dearborn (MI), USA (1991) 43.
- [11] R.F. Bunshaw, Evaporation: processes bulk microstructures and

- mechanical properties, in: R.F. Bunshaw (Ed.), *Handbook of Deposition Technologies for Films and Coating*, Noyes Publications, Park Ridge, NJ, 1994, p. 131.
- [12] K-L. Ling, C-F. Yang, J-T. Lee, Correlation of microstructure with corrosion and electrochemical behavior of the batch type hot-dip Al–Zn coatings, *Corrosion* 9 (1991) 47.
- [13] K-L. Ling, J.K. Ho, C.S. Jong, J.T. Lee, Growth behaviour and corrosion resistance of 5% Al–Zn coating, *Corrosion* 49 (1993) 759.
- [14] Powder Diffraction File 2, Version 2.14, Joint Committee on Powder Diffraction Standards, International Center for Diffraction Data, Swarthmore, PA. 1987–1993.

Improvement of the corrosion resistance of PVD hard coating–substrate systems

H.A. Jehn *

Forschungsinstitut für Edelmetalle und Metallchemie, D-73525 Schwäbisch Gmünd, Germany

Abstract

Hard coatings play a continuously increasing role in the field of tribology as well as for decorative applications. In both areas they are often exposed to corrosive environments. While especially hard coatings exhibit a high corrosion resistance for themselves, hard coating–substrate systems may suffer from a severe corrosion attack due to the defects in the coating structure (pores, pinholes) resulting from the PVD-typical film morphology. In contrast to the huge number of investigations on the structure, properties and tribological performance of hard coatings, only limited studies exist on the corrosion behaviour of hard coating–substrate systems and attempts to improve their corrosion resistance. This paper briefly describes the corrosion mechanisms and reports characteristic examples of the system behaviour. Special emphasis is put on recent investigations in order to improve the corrosion resistance by alloying, interlayers and multilayered coating structures. © 2000 Elsevier Science S.A. All rights reserved.

Keywords: Corrosion resistance; Hard coatings; Physical vapour deposition coatings

1. Introduction

The well known coating of tools and parts with hard materials results in a drastic increase in the lifetime of parts and tools and also in a strong reduction of the friction coefficient. Due to their attractive and variable colours, they are also frequently used for decorative applications such as watch cases, eye-glass frames, door plates and sanitary parts [1–3]. The gold- or brass-like colours of TiN and ZrN or the grey, dark blue or black colours of TiC, (Ti,Al)N or C films are the basis of modern design and technology. Hard coatings, furthermore, exhibit good biological compatibility; the basis for their use as coatings for prostheses or medical instruments [4,5]. Many of these applications are also connected with corrosive attack, e.g. by technical reagents or corrosive gaseous or liquid environments. This may reduce the lifetime of coated parts drastically, even if the coating materials themselves are characterised by a high corrosion resistance.

Vapour deposited coatings most often exhibit pores and pinholes through which a corrosive attack on the (less noble in most cases) substrate material takes place. In the following examples, the effects of processes and

process parameters will be shown, and also the possibility of improving corrosion resistance.

2. Corrosion and corrosion tests

Corrosion is defined as “attack on a material by its reaction with the environment and the resulting deterioration of the materials properties” [6,7]. Most often, it is related to an electrochemical reaction with a liquid or gaseous medium.

Concerning corrosion, generally a distinction has to be made between a homogeneous attack of the complete surface area and a local corrosion attack. This means, for coating–substrate systems, that either the total area of the coating is attacked (as in the case of so called sacrificial coatings) or the substrate is locally corroded at damaged areas, depending on the nobility ratio of coating and substrate material. As already mentioned, hard coatings mostly form the more noble component, and the substrate material or another less noble interlayer will face the corrosive attack, i.e. galvanic corrosion. The following reactions take place in an electrolyte (e.g. $\text{H}_2\text{O} + \text{NaCl}$): water and Cl^- ions penetrate through pores and the iron of the steel-based material is dissolved; Fe^{2+} ions diffuse towards the

* Tel.: +49-7171-100621; fax: +40-7171-100654.

E-mail address: jehn@fem-online.de (H.A. Jehn)

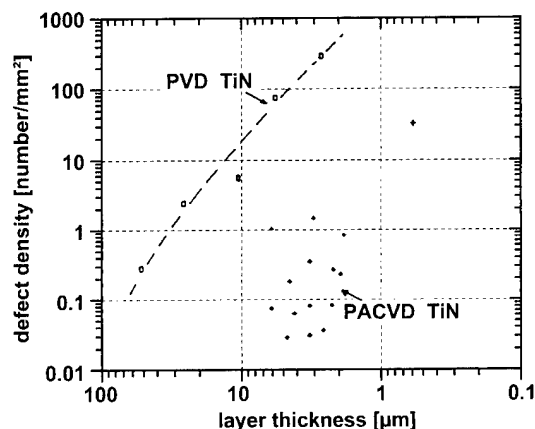


Fig. 1. Porosity of PVD and PACVD-TiN coatings given as the number of defects (after Ref. [9]).

coating surface forming rust by the reaction with OH^- ions; voids are formed underneath the coating [8]. This corrosion type is also observed with brass or zinc substrate materials.

The pores and pinholes known from the structure zone models exhibit a remarkable density. A strong increase of pore density with decreasing film thickness is observed. A similar, but lower, defect density has also been found in PACVD coatings. Fig. 1 illustrates this marked increase in defect density with decreasing film thickness [9]. The pinhole area for 0.1 μm magnetron-sputtered TiN was calculated to 3% [10].

The corrosion behaviour was studied on the one hand by application-oriented so called short-time tests representing the exposure to a specific gaseous climate or a liquid (salt spray test, Kesternich test, immersion tests, etc.) with subsequent qualitative or semi-quantitative evaluation of the corrosion damage [11]. On the other hand, electrochemical tests in corrosive media yield specific data on the behaviour of the system [12]. The advantage of the latter methods is that only the kinetics is changed and not the mechanism itself. In the following, the corrosion behaviour of the coating-substrate systems shall be especially characterised by current density-potential measurements. Earlier literature on hard coating-substrate systems is summarised in Ref. [13].

3. Corrosion studies with hard-coated parts

The above mentioned relations are well reflected by the corrosion potentials E_{corr} and corrosion current densities I_{corr} for some TiN and ZrN coatings on steel and glass substrates reported in Ref. [14]. All samples with hard coatings on glass show positive E_{corr} values, those of ZrN being lower than those of TiN. The nitride coatings on steel substrates show almost the same (negative) values given by the steel substrate. The corrosion

current is strongly increased too, when compared with coating-glass systems. This reflects the high contribution of the substrate corrosion to the total corrosion process.

The effect of the coating thickness is, as an example, illustrated for PACVD-TiN coatings in Fig. 2 [15]. Only thicknesses higher than about 14 μm guarantee a satisfying corrosion resistance. The $I-U$ curves for coatings $< 5 \mu\text{m}$ thick give only a partial corrosion resistance. Such lower thicknesses, however, are in the range of practical applications, especially decorative coatings which are most often about 1 μm . The strong increase of the pinhole defect density was recently proved for very thin magnetron-sputtered TiN coatings on SUS304 steel. A strongly increasing current density was observed correspondingly [10]. The total character of the $I-U$ curves, of course, depends strongly on the substrate material, as this is in contact with the corrosive medium through the coating defects.

The effect of the *PVD process* and its actual parameters can easily be described by the influence of these parameter values and the process characteristics. All means which lead to the deposition of denser coating structures improve the corrosion resistance of the system. Especially, the substrate temperature affects the coating morphology in accordance with the structure zone models of Movchan and Demchisin [16], Thornton [17] and Messier [18]. The $I-U$ curves of ion-plated TiN (hollow cathode arc discharge evaporation) on ball bearing steel shows a strong decrease in the current density with increasing substrate temperature (Fig. 3) [19]. Similarly, an ion plating process results in a denser structure of PVD coatings when compared with vacuum evaporation [20]. Such an improvement with respect to the corrosion current density by applying PVD processes which are characterised by a higher percentage of ions is also demonstrated by BN coatings on Al substrates when deposited by ion beam assisted deposition (IBAD) and sputtering respectively [21]. Another factor influencing the corrosion behaviour of coating substrate systems is the plasma power density, an increase of

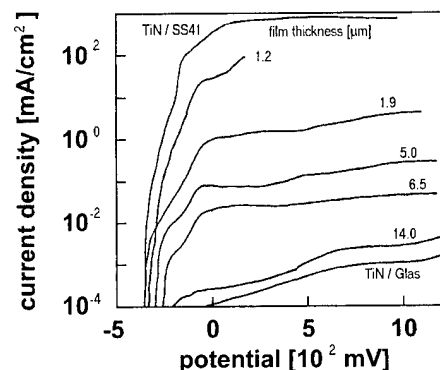


Fig. 2. Effect of coating thickness on $I-U$ curves for PACVD-TiN in HCl (after Ref. [15]).

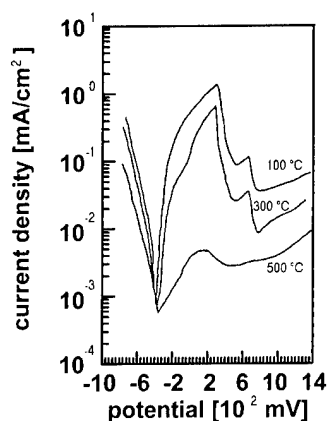


Fig. 3. Effect of substrate temperature on I - U curves of ion-plated TiN in 1 N H_2SO_4 (after [19]).

which reduces E_{corr} , I_{corr} and the corrosion current density [22]. Obviously this is caused by a change in the chemical composition of the coatings.

The *surface roughness* of the part to be coated also significantly influences the corrosion behaviour of the system. A higher substrate surface roughness results in a less complete coverage of the substrate with the coating material because of shadowing effects during PVD film growth. This is illustrated in Fig. 4 for TiN on aluminium [23]. A reduced number of coating defects with decreasing surface roughness was also observed for CrN on steel [24].

A large number of investigations have discussed the effect of *alloying additives* in binary (nitride) coatings. This effect can base on a 'chemical' interaction increasing the corrosion potential of the coating material. There is, however, also a 'physical' effect, i.e. denser and more fine grained coatings are formed. As examples, the following studies shall be cited: (Ti,Pd)N [25], (Ti,Si)N

[26], (Ti,Cr)N [27–30] and (Ti,Y)N [31]. In the case of (Ti,Al)N the Al-rich coatings, however, show a slightly increased porosity and, hence, poorer corrosion behaviour [32]. This was recently proved by Jiang et al. [33] with magnetron-sputtered TiN and (Ti,Al)N coatings. The addition of non-metallic elements also influences the corrosion behaviour, most probably because of their influence on the coating morphology.

4. Improvement of the corrosion behaviour by interlayers and multilayers

As illustrated above, the corrosion attack on hard-coated parts can be reduced by a denser coating structure resulting from well known and well defined variations of the vapour deposition process and its parameters. Another possibility for the improvement of corrosion resistance is the deposition of interlayers and/or multilayered coatings. Such interlayers may be deposited by physical or electrochemical processes (PVD, ECD). Some examples will be given in the following sections.

4.1. PVD interlayers

The deposition of PVD interlayers of metals more noble than the substrate material can reduce the corrosion attack. Such solutions are well known from electroplated multilayer systems. Additionally, the number of pores and pinholes can be reduced, when new structures of the hard coatings are formed on the top of the interlayer. Marked improvements are, for example, found for 4 μm thick Ti/TiN-PVD coatings when compared with 3 μm PVD-TiN [34]. Similar results are reported for Ti/TiN on iron substrates [35,36]. The benefit of the Ti layer is additionally attributed to its passivation. Other promising PVD-interlayers are PVD-Ni or PVD-Cr [37]. Very recently, Cr, CrN or Cr/CrN have been used as barrier layers against dezincification of Cu alloys during the corrosion reaction [38].

A marked improvement also results from an intermediate plasma etching of the PVD-TiN hard coating. Such a process additionally supports the new formation of nucleation sites, reducing the through-pores in the Ti/TiN layer system. Fig. 5 illustrates this effect showing the I - U curves of sputtered TiN coatings with a Ti interlayer with and without intermediate sputter etching, together with the brass substrate and TiN on glass [39].

4.2. PVD multilayers

The above mentioned reduction of the corrosion attack by an interlayer can even be improved by a multilayered coating, e.g. a modulation by a 'pulsed' N_2 flow during the triode sputtering process yields layers richer and poorer in their nitrogen content. Especially

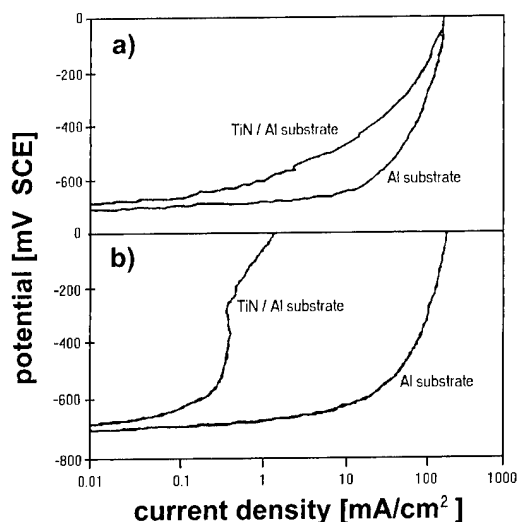


Fig. 4. I - U curves of TiN on Al substrates of different roughness: (a) incomplete and (b) complete coverage (after Ref. [23]).

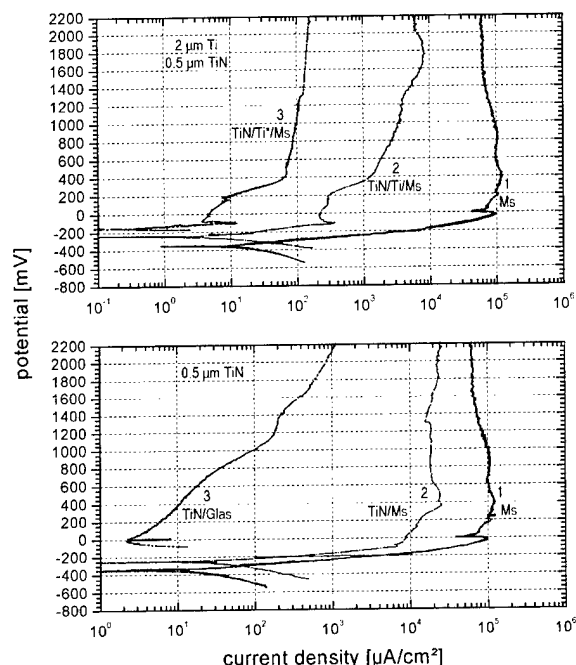


Fig. 5. Effect of intermediate plasma etching after Ti interlayer deposition determined by I - U curves in 0.8 M NaCl solution [39].

successful seemed e.g. to be layer sequences of ϵ -Ti₂N and TiN on C45 steel. Zr/ZrN multilayers, however, did not show an improvement when compared with a ZrN coating [40]. Other studies with Ti/TiN, Zr/ZrN, Hf/HfN and Nb/NbN multilayered coatings deposited by magnetron sputtering and electron beam evaporation show marked improvements [41]. More recently, the following systems have been studied to some extent: Ti/TiN [42–44], Cr/CrN [37,42,43] and TiN/C [45]. The number of multilayer sequences varies from three to several hundred for total coating thicknesses of few microns.

Current investigations were focused on reactive and non-reactive sputter-deposited multilayered Cr/CrN coating systems on high speed steel (HSS) substrates. On top of a 200 nm Cr interlayer for improving adhesion, CrN or CrN/Cr/CrN/... layers were deposited with a total thickness of about 2.8 μ m. The coatings were deposited with and without intermediate plasma etching with Ar⁺ ions (10 min, 1000 V). The coating–substrate systems were tested in 0.8 M NaCl solution (pH=7) potentiodynamically. The following behaviour can be deduced from the current–potential density curves (Figs. 6–8). The hard coating reduces the current density markedly by several orders of magnitude. Four intermediate etching steps result in a further decrease of the current density, but a higher number of intermediate etching steps (up to 16) yield no further change. For CrN/Cr/CrN/... multilayers, slightly lower values of I_{corr} are found, but practically no influence could be noticed for different thicknesses of the individual layers

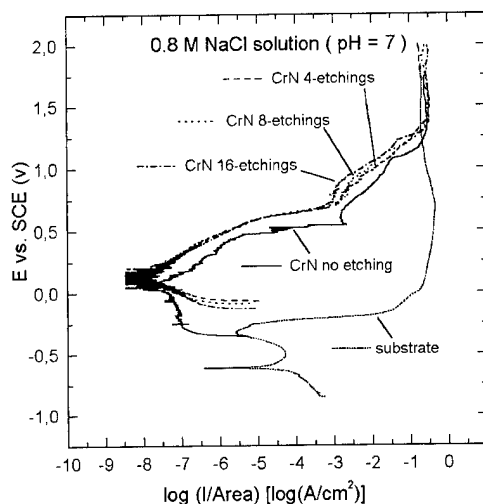


Fig. 6. Effect of intermediate plasma etching on I - U curves in 0.8 M NaCl (pH=7) for CrN coatings on HSS.

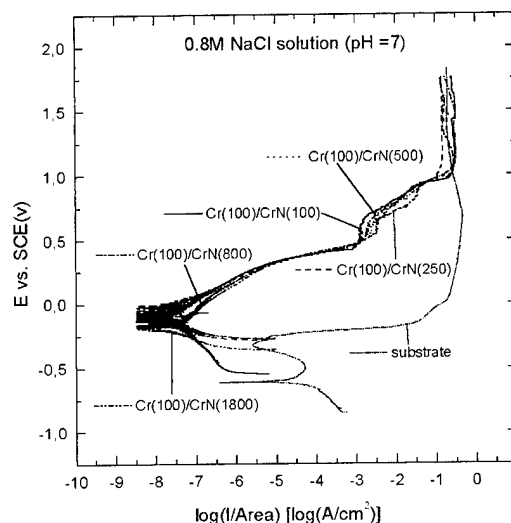


Fig. 7. Effect of multiple layer deposition of CrN/Cr/CrN/... with intermediate plasma etching on I - U curves in 0.8 M NaCl (pH=7).

and, hence, different numbers of etchings steps. Practically identical results were found for multilayers without intermediate etching. This means that the ‘physical’ effect of intermediate etching gives the same trend for the corrosion behaviour as the ‘chemical’ effect of multilayered structures [46]. Some further work has to be done to explain this, especially with respect to the changes in structure and morphology by the etching procedures.

4.3. ECD interlayers and substrate pretreatment

Two other factors improving or influencing the corrosion resistance of a coating–substrate system shall be discussed briefly to complete this review, i.e. the ECD

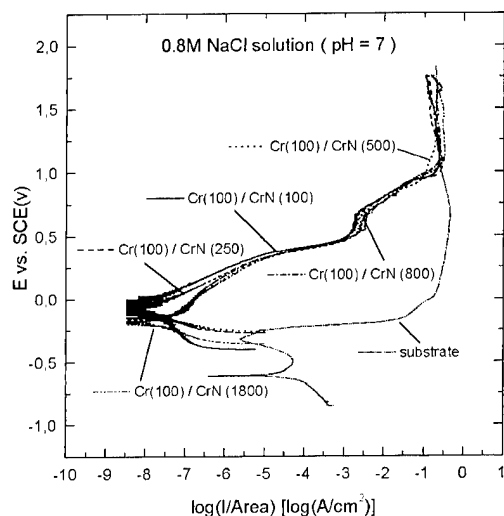


Fig. 8. Effect of multiple layer deposition of CrN/Cr/CrN/... without intermediate plasma on *I*–*U* curves in 0.8 M NaCl (pH = 7).

of interlayers and the substrate pre-treatment by nitriding.

Especially in the field of decorative hard coatings, ECD interlayers represent the state of the art. The substrate materials coated with ECD-Ni or ECD-Ni-Pd interlayers are brass, German silver, zinc die cast, as well as steel [47–50]. These ECD coatings show a lower porosity compared with PVD coatings. In most cases, however, they are thicker (5–20 µm) than the usual decorative PVD hard coatings (≤ 1 µm). A certain disadvantage is the need for two different deposition processes ('wet' electroplating and 'dry' PVD).

Substrate pretreatment by plasma nitriding is increasingly used to improve the load bearing properties of the steel substrate material when coated afterwards (duplex coatings). Combining both processes yields an improved corrosion resistance [51]. A positive effect of duplex coating was also found for PVD-deposited TiN, CrN and (Ti,Al)N coatings on prenitrided EN40B steel in 3.5% NaCl solution [52].

5. Conclusions

The corrosion behaviour of a material, or a composite, is generally a system effect based on the properties of the part and the medium interacting with its surface. Hard coating–substrate systems are normally characterised by the following:

- hard coating materials are normally relatively noble;
- in most cases the hard coatings are relatively thin and show pores and pinholes; and
- the corrosive medium can penetrate through the defects reacting with the substrate material causing galvanic corrosion.

All corrosion studies are difficult to compare because of the different test conditions. This holds especially for the solutions in electrochemical tests.

An improvement of the corrosion resistance of hard-coated parts can be obtained by the following measures:

- increased hard coating thickness;
- lower substrate roughness;
- denser coating morphology by suitable processes and process parameters including intermediate ion etching;
- 'alloying' of the hard coatings;
- PVD interlayer(s) including intermediate ion etching;
- PVD multilayers;
- ECD interlayer(s);
- duplex coatings.

Current research is especially focused on multilayer and structure modification effects.

References

- [1] P. Seserko, U. Kopacz, S. Schulz, *Galvanotechnology* 80 (1989) 4272.
- [2] R. Riedl, *Galvanotechnology* 80 (1989) 3391.
- [3] S. Bastian, *Galvanotechnology* 81 (1990) 2706.
- [4] A. Wisbey, P.J. Gregson, M. Tuke, *Biomaterials* 8 (1987) 477.
- [5] H. Brauner, *Surf. Coat. Technol.* 62 (1993) 618.
- [6] Corrosion education Manual, Swedish Corrosion Institut, Stockholm, 1974.
- [7] DIN 50 900 Blatt 1, Beuth Verlag Berlin, April 1982.
- [8] A. Korhonen, *Surface Modification Technologies Vol. IV TMS-AIME*, 1990.
- [9] H.A. Jehn, *Proc. Asian Finish*, Seoul, Korea, 1998.
- [10] H. Uchida, S. Inoue, K. Koterazawa, *Mater. Sci. Eng. A* 234–236 (1997) 649.
- [11] F. Altmayer, Choosing an accelerated corrosion test, in: M. Murphy (Ed.), *Metal Finishing: 65th Guidebook and Directory Issue 97*, Elsevier, New York, 1997, p. 559.
- [12] H.A. Jehn, A. Zielonka, *Corrosion Testing*, ASM Handbook Vol. 5: Surface Engineering, ASM, 1994, p. 635.
- [13] H.A. Jehn, I. Pfeiffer-Schäller, *Galvanotechnology* 84 (1993) 3283.
- [14] H.A. Jehn, I. Pfeiffer-Schäller, *Galvanotechnology* 84 (1993) 3669.
- [15] T. Kado, R. Makabe, S. Mochizuki, S. Nakajima, M. Araki, *Corros. Eng.* 36 (1987) 503.
- [16] B.A. Movchan, A.V. Demchisin, *Fiz. Metall. Metalloved.* 28 (1969) 653.
- [17] J.A. Thornton, *J. Vac. Sci. Technol.* 11 (1974) 666.
- [18] R. Messier, *J. Vac. Sci. Technol. A* 2 (1984) 500.
- [19] A. Erdemir, W.B. Carter, R.F. Hochman, in: T.S. Sudarshan, D.G. Bhat (Eds.), *Structure, Property and Performance Characteristics of HCD-ion plated TiN Coatings*, TMS/AIME, Warrendale, PA, 1989, p. 261.
- [20] Zh.J. Jin, Ch.-Q. Liu, L. Yu, W.-T. Wu, *Surf. Coat. Technol.* 46 (1991) 307.
- [21] L. Fedrizzi, S. Gialanella, M. Elena, M. Dabor, L. Guzmán, *Mater. Sci. Eng. A* 116 (1989) 47.
- [22] R.T. Carson, J.H. Givens, H.S. Savage, Y.W. Lee, J.M. Rigsbee, *Thin Solid Films* 204 (1991) 285.
- [23] J.H. Givens, J.M. Rigsbee, *Ceramic Thin and Thick Films*, American Ceramics Society, Westerville, OH, 1992, p. 59.

- [24] I. Milosev, B. Navisek, *Surf. Coat. Technol.* 63 (1994) 173.
- [25] J.M. Penttinen, et al., *ICMC*, 1990.
- [26] J.-W. He, C.-D. Bai, K.W. Xu, N.-S. Hu, *Surf. Coat. Technol.* 74/75 (1995) 387.
- [27] H.A. Jehn, F. Thiergarten, G. Ebersbach, D. Fabian, *Surf. Coat. Technol.* 50 (1991) 4.
- [28] A.A. Trufanov, K.B. Katsov, V.N. Zhitomirskii, *Fiz. Khim. Mekh. Mater.* 5 (1989) 94.
- [29] A.A. Trufanov, K.B. Katsov, V.N. Zhitomirskii, *Zashch. Met.* 24 (1) (1988) 127.
- [30] Y. Massiani, P. Gravier, L. Fedrizzi, F. Marchetti, *Thin Solid Films* 261 (1995) 202.
- [31] W. Brandl, C. Gendig, *Thin Solid Films* 290/291 (1996) 343.
- [32] J. Aromaa et al., *Mater. Sci. Eng. A* 150 (1991) 722.
- [33] S.-G. Jiang, D.-L. Peng, X.-Y. Zhao, L. Xie, Q. Li, *Appl. Surf. Sci.* 84 (1995) 373.
- [34] O. Forsen, K. Knuutila, M. Tavi, S. Yläsaari, *Proc. 10th Scand. Corrosion Congr., Stockholm* (1986) 221.
- [35] Y. Massiani, A. Medjahed, J. Crousier, P. Gravier, I. Rebatel, *Surf. Coat. Technol.* 45 (1991) 115.
- [36] B. Matthes, E. Broszeit, J. Aromaa, H. Ronkainen, S.-P. Hannula, A. Leyland, A. Matthews, *ICMC* (1990 PVD/Cr/Ni).
- [37] M. Herranen, U. Wicklund, J.O. Carlson, S. Hogmark, *Surf. Coat. Technol.* 99 (1998) 191.
- [38] N. Kitagawa, A. Kawana, S. Okabe, Y. Tottori, *Sumitomo Kinzoku Kozan Chuken Shoho* 11 (1996) 6.
- [39] M.E. Baumgärtner, H.A. Jehn, 4 Leybold Symposium Decorative Coatings, 1992, Bericht LH-II- S. 43.02.
- [40] U.K. Wiiala, I.M. Penttinen, A.S. Korhonen, J. Aromaa, E. Ristola, *Surf. Coat. Technol.* 41 (1990) 191.
- [41] E. Söderlund, P. Ljunggren, B. Johansson, *Int. Conf. Metall. ICMCTF 97, San Diego, CA* (1997), Paper E1.18.
- [42] L.A.S. Ries, D.S. Azambuja, I.J.R. Baumvol, *Surf. Coat. Technol.* 89 (1997) 114.
- [43] L. Swadzba, B. Mendala, *Mater. Funct. Des., Mater. Funct. Des.* 3 (1997) 75 *Proc. 5th Eur. Conf. Adv. Mater. Processes Appl.*
- [44] M. Bromark, M. Larsson, P. Hedenqvist, S. Hogmark, *Surf. Coat. Technol.* 90 (1997) 217.
- [45] H. Kupfer, F. Richter, S. Friedrich, H.J. Spies, *Surf. Coat. Technol.* 74/75 (1995) 333.
- [46] H.-S. Park, H. Kappl, H.A. Jehn, J.-J. Lee, unpublished results, 1998.
- [47] H. Erhart, *Metalloberfläche* 44 (2) (1990) 59.
- [48] U. Kopacz, Ch. Daube, S. Schulz, *Galvanotechnology* 83 (3) (1990) 844.
- [49] K. Reichel, *Development and Characterization of Corrosion and Wear Resistant Coatings Deposited by Arc PVD*, VDI Verlag, Düsseldorf, 1992. Reihe 5, Nr. 246.
- [50] J.L. He, M.H. Hon, *Surf. Coat. Technol.* 53 (1992) 92.
- [51] N. Dingemont, E. Bergmann, M. Hans, P. Collignon, *Surf. Coat. Technol.* 76/77 (1995) 218.
- [52] H. Dong, Y. Sun, T. Bell, *Surf. Coat. Technol.* 90 (1997) 91.

Vapour deposited Zn–Cr Alloy coatings for enhanced manufacturing and corrosion resistance of steel sheets ☆

L. Guzman ^{a,*}, M. Adami ^a, W. Gissler ^b, S. Klose ^{b,1}, S. De Rossi ^c

^a Ion Beam Group, University Trento, 38050 Povo (Tn), Italy

^b Joint Research Centre, 21020 Ispra (Va), Italy

^c Istituto Scientifico Breda, 21026 Milano, Italy

Accepted 22 June 1999

Abstract

In the present work, various Zn–Cr alloy coatings were deposited on automobilistic steels by a vacuum process, in which Zn and Cr are evaporated from resistance heated sources. After ion etching, different Zn:Cr evaporation rates were applied to produce several compositions in the films until a final coating thickness of 4 µm was obtained. The coatings were characterized with respect to morphology (SEM), structure (XRD) and hardness (by nanoindentation). The structure changed from the hexagonal Zn–Cr solid solution to a cubic (bcc) phase as the amount of Cr in the coating increased. Nanoindentation tests showed that the presence of Cr can significantly change coating hardness: this effect can be correlated with compositional and microstructural changes. To optimise the adhesion, the necessity of a multistage pre-treatment of the steel substrates was recognized. Further to Ar⁺ sputter cleaning of the substrates, the deposition of a thin Cr interlayer is necessary. It was observed that, without suitable pre-treatments, the coatings are poorly adherent.

Salt spray corrosion tests revealed that even small Cr additions are able to significantly improve the corrosion resistance of Zn coatings. The time for red rust to appear is very long (at least four times) when compared to pure Zn vapour deposited, or steel sheet electroplated with Zn (reference specimens). The generation of protective corrosion products which can suppress cathodic reaction is considered an important factor for that improvement. © 2000 Elsevier Science S.A. All rights reserved.

Keywords: Corrosion resistance; Mechanical resistance; Physical vapor deposition; Zinc alloy coatings

1. Introduction

Good adhesion is of prime importance in dictating the lifetime of a protective coating and a number of techniques have been developed to improve the adhesion coating/substrate based on such a requirement. Adhesion is clearly affected by the mechanical and chemical properties of the interfacial region. In order to improve the adhesion between coating and substrate, a number of techniques [1] have been developed which can be divided into three categories: (i) pre-treatments — cleaning and degreasing prior to loading; (ii) in situ treatments — such as heating, plasma or sputter cleaning; and (iii) bonding layers — to form strong interfacial

phases, minimise interfacial stresses and getter contaminants.

In neutral or close-to-neutral environments, corrosion products provide some degree of barrier protection against corrosion, giving Zn-coated steel better corrosion resistance compared to bare plate. Also, as the Zn has a lower corrosion potential than the steel plate, it also provides sacrificial cathodic corrosion protection and this is why Zn-plated steel sheet is so widely used. Recent developments to increase the corrosion behaviour include the use of Zn-alloys using Ni [2], Co [3], Al, Cr, Mg and Ti [4]. From among these developments, it has been reported that Zn-alloy coatings with a low concentration of a highly reactive alloying element are able to provide big improvements in corrosion resistance [5]. In our present project, several physical vapor deposited (PVD) Zn-alloy coatings (identified as possible alternatives to conventional Zn) are currently being deposited on different kinds of steel sheets using various processes. Among these are thermal, arc- and ion-beam-

☆ Performed in the framework of Brite/Euram Programme of the European Union, Project BE 96-3073.

* Corresponding author. Tel.: +39-461-881678;
fax: +39-461-881696.

¹ In leave of absence from Physikalisches Chemisches Inst., University Heidelberg, 69117 Heidelberg, Germany.

assisted evaporation. Such coating processes are carried out using different ion-cleaning pre-treatments. This paper describes the layer-by-layer construction of highly performant Zn–Cr coatings, as developed by using ion beam treatment and vapour co-deposition.

2. Experimental

Deposition of Zn–Cr alloys was accomplished by simultaneous evaporation of Zn and Cr. The alloy coatings were deposited on coupons of deep-drawing quality (DDQ) steel with the dimensions $100 \times 100 \times 1$ mm. A two crucible thermal evaporator and a low energy ion gun for carrying out ion beam bombardment were available inside an IBAD apparatus [6]. Once a vacuum level of better than 10^{-4} Pa was obtained inside the chamber, Ar^+ ions from a duoplasmatron-type source were used to sputter clean the surface. The best dose to clean the steel is of the order of 3×10^{16} ions/cm², suitable to erode about 20 nm of the (oxide+carbon) contaminated surface layer. The ion current density and energy of the Ar beam was 10 mA/cm² and 5 keV respectively, with a bombardment angle of 30° (relative to the etched surface). The amount of retained Ar was negligible. The aim of ion cleaning is to improve adhesion; therefore, Ar^+ bombardment was only applied at the beginning of the process. Further ion bombardment to achieve a dense coating was not carried out since the presence of pores in the coating does not greatly affect the corrosion resistance of Zn coatings [7].

As for the coating, the Zn was evaporated by heating a closed boat crucible with a small hole in the top, at a rate of 10 nm/s. Cr was evaporated by heating a Cr-coated W filament at varying rates from 0.1 to 1.0 nm/s. The first step consisted of ion etching and deposition of a 20 nm thin Cr layer. Then co-evaporation started until a theoretical thickness of about 4 µm was achieved, as measured by a crystal quartz monitor. Relative to the total coating layer, the Cr concentration in the different samples was varied between 1 and 15 at. %.

Morphology and fractography studies of the as-deposited coatings were performed by scanning electron microscopy (SEM). The elemental composition was determined by means of secondary neutrals mass spectrometry (SNMS), and the structure was analysed by conventional and glancing incidence X-ray diffraction (radiation source $\text{CuK}\alpha$). Friction tests were performed by scratch testing with an HS steel stylus of 200 µm diameter. Nanoindentations were carried out with a nanoindenter with a load range of 0.02–10 mN, used in constant displacement rate mode until a total depth of 250 nm was reached. Nanohardness and Young's modulus measurements were taken from loading and unloading curves by using a procedure reported previously [8].

The corrosion characteristics of the materials were investigated by using a salt spray test, with a 3.5% NaCl solution. Electrolytically deposited Zn-plated steel sheet was employed as the reference standard. The corrosion tested surfaces were further subjected to XRD analysis as well to SEM and EDX cross-sectional analysis.

3. Results and discussion

3.1. Microstructure and adherence

A general observation is that the coating morphology of evaporated Zn is strongly dependent on the substrate temperature, which can rise with deposition time. Experimental thicknesses obtained were in the range 2–8 µm. Typical grain size of the Zn crystallites was 1–2 µm. The growth was columnar at low deposition temperatures, in agreement with the well known Thornton diagram [9]. By SEM analysis of fractured coatings, it was established that the optimum growing temperature of PVD-Zn layers, with regard to adequate compacity of the microstructure, should be in the range 373–423 K in which the coatings have a more compact structure — films grown at lower temperatures are more porous. When temperature exceeds 423 K, Zn tends to form whiskers and other 'open' structures.

The pure Zn layers can be poorly adherent, which is generally due to insufficient substrate cleaning. Therefore, the need exists for adequate 'in situ' sputter etching. In order to solve the adhesion problem, a straightforward method has been devised which consists of ion etching and subsequent deposition of a thin Cr interlayer. The thickness and purity of the interlayer are critical and should match the native oxide parameters: the best value is about 20 nm Cr deposited in high vacuum conditions. For the optimized condition, adhesion was found to be generally in excess of 15–20 MPa, i.e. the limit of the pull-off testing method.

The interposition of a thin Cr film solves the problem of adhesion to the substrate, but the higher temperature resulting from the Cr evaporation source could lead to an excessive growth of grains of the subsequently deposited Zn, as can be seen in Fig. 1(a). However, once a Cr interlayer has been deposited, it is possible to extend the above Zn deposition process by co-evaporating a small quantity of Cr — in this way, a Zn–Cr alloy layer is obtained. The resulting coating microstructure is shown in Fig. 1(b). Evidently, the main effect of Cr-alloying is to refine the film microstructure and to increase its compacity.

3.2. XRD results

Fig. 2 shows the evolution of the Zn–Cr coating structure. The different X-ray patterns are shown

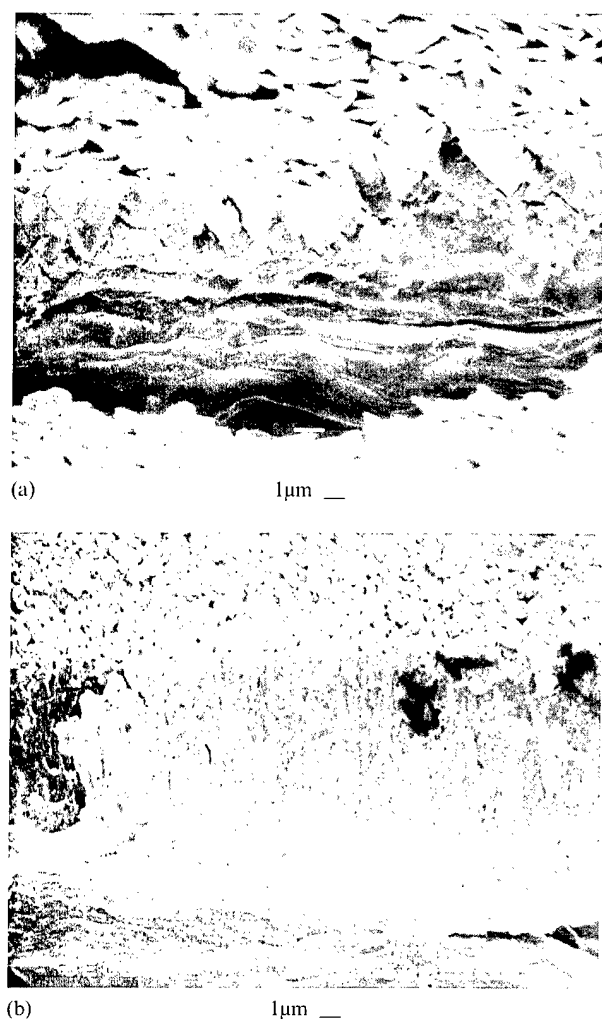


Fig. 1. SEM fractographs of: (a) evaporated Zn coating (with interposition of a thin Cr layer); (b) evaporated Cr/Zn–Cr alloy coating.

according to the different Cr contents and morphologies. The top pattern Fig. 2(a) represents the XRD pattern of a pure Zn coating, where all the peaks identify the hcp structure of Zn. PVD-Zn is textured with a [002] preferential orientation and a characteristic microstructure giving place to an opaque aspect. On the contrary, all Zn–Cr alloy coatings have a different [100] texture, or no texture at all, and have a glossy aspect. Fig. 2(b) corresponds to a Zn–2 at.% Cr coating, while Fig. 2(c) pertains to a Zn–5%Cr composition. Finally, in Fig. 2(d) corresponding to a Zn–15% Cr coating, a rather different XRD pattern can be seen, similar to the pattern of electrodeposited Zn–Ni or Zn–Cr layers [10]. The experimental reflections have been fitted to a phase with bcc structure, where the peaks are shifted to lower angles with respect to Cr implying a lattice constant of $a = 0.292$ nm, whereas the pure Cr has a lattice parameter of 0.284 nm.

Starting from the hexagonal Zn lattice, by increasing the Cr contents the peaks become multiple and are progressively shifted in both directions, meaning that the lattice assumes a higher compactness. The lattice gets compressed in the c -direction (perpendicular to the surface) and expands in the a -direction. The behaviour of the a/c fraction as a function of %Cr, is depicted in Fig. 3.

The changes in coating structure and morphology can explain significant changes in the mechanical properties of the coatings, such as hardness or elastic recovery, which are further reflected in their tribological and corrosion behaviour.

3.3. Nanoindentation results

The hardness of pure Zn coatings lies in the range 0.3–0.5 GPa. A significant change can be observed in the mechanical properties of the Zn–Cr coatings such

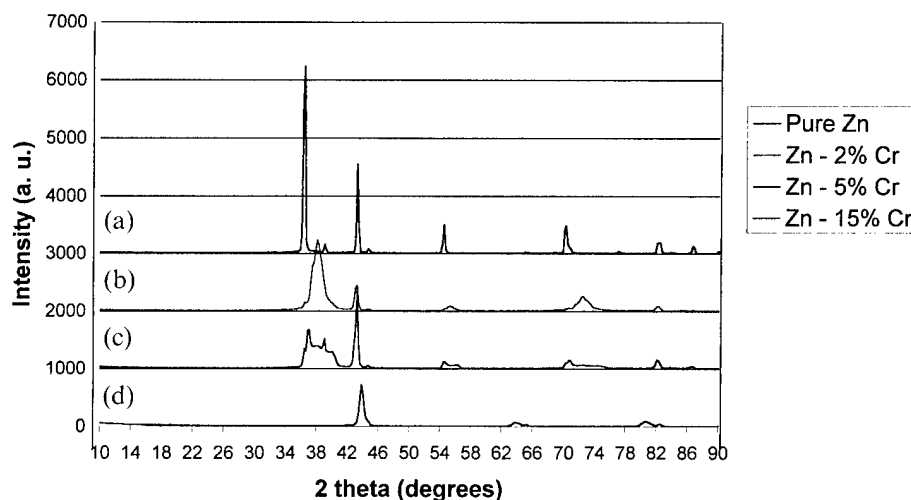


Fig. 2. XRD patterns of PVD coatings: (a) pure Zn; (b) Zn–2%Cr coating; (c) Zn–5%Cr coating; (d) Zn–15%Cr coating.

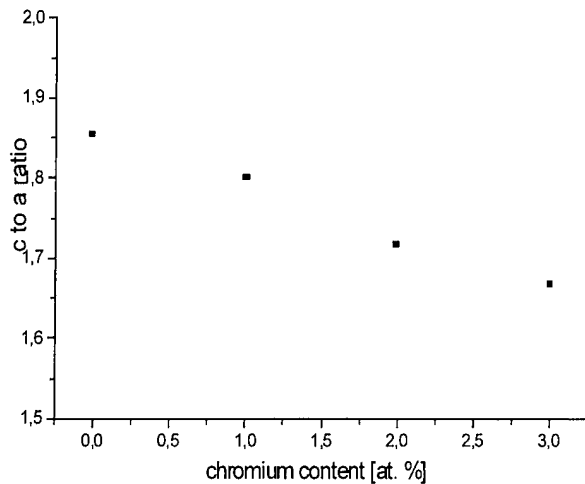


Fig. 3. Lattice parameters of Zn–Cr alloy coatings, as a function of Cr content.

as hardness or elastic recovery (see Table 1). Firstly, Cr-alloying is able to increase hardness (H) as well as stiffness (E) of the coatings, with up to five-fold improvement for the Zn-15%Cr alloy coating compared to the pure Zn. This fact could enhance abrasive wear (powdering) resistance.

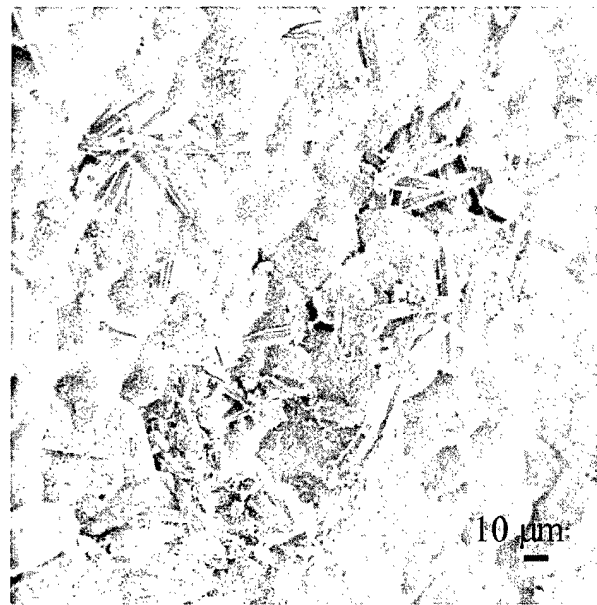
Secondly, optimised alloy coatings exhibit a lower E/H ratio, which means limiting plastic deformation and promoting elastic recovery, thus also conferring high adhesive wear resistance to the surface. This fact is reflected in a lower value of friction coefficient, as experimentally observed (Table 1).

Among the various Zn and Zn–Cr coatings, it is possible to distinguish between glossy and opaque coatings. It is difficult to quantify the microroughness of the coatings, because the steel substrate itself has a roughness of about 1.0 μm . As a general rule, glossy coatings are harder than their dark counterparts.

In any case, note that it is important to get optimized protective coatings which, while offering a reduced friction coefficient, should not be too hard with regard to conventional Zn in order to safeguard the integrity of the forming tools employed during the steel sheet manufacturing. To that regard, Zn–Cr alloy coatings of low Cr content are a good compromise, being tougher than pure Zn or high Cr content coatings.



(a)



(b)

Fig. 4. SEM micrographs of salt spray tested specimens: (a) Zn coating; (b) Zn–Cr alloy coating.

Table 1
Structural and mechanical properties of PVD-Zn and Zn-alloy coatings

Coating	Structure and texture	Aspect	H (Gpa)	E (Gpa)	E/H	Friction coefficient (against HSS steel)
PVD-Zn	Hexagonal [002]	Opaque	0.45	75	166	0.43
Zn-2%Cr	Hexagonal [100]	Glossy	0.81	95	117	0.30
Zn-5%Cr	Hexagonal no	Opaque	0.15	50	333	0.27
Zn-15%Cr	bcc cubic [110]	Glossy	1.86	47	25	0.37

3.4. Corrosion results

An outstanding corrosion resistance was observed for the Zn–Cr coatings in salt spray (SST) tests, ranging in the first place as compared to other Zn-alloy coatings forming part of the same study [11]. The corrosion rate, in terms of time-for-red-rust normalized to the thickness of the various coatings, decreased by a factor of between four and ten for all Zn–Cr coatings, whereas the pure Zn coatings were slightly inferior to the reference standard coating (electrodeposited Zn).

After 200 h of SST, diffraction analysis of the corroded samples showed the presence of basic zinc chloride, $\text{ZnCl}_2 \cdot 4\text{Zn}(\text{OH})_2$, and in some cases of basic zinc carbonates, $\text{Zn}_4\text{CO}_3(\text{OH})_6$ and $\text{Zn}_5(\text{CO}_3)_2(\text{OH})_6$. This observation was confirmed by SEM observation of the corroded Zn–Cr samples. The same corrosion products were found (with a different ratio) on other Zn-alloy coatings, e.g. Zn–Al, but not so on pure Zn coatings — see Fig. 4(a) and (b). Also the presence of zinc carbonates is clearly correlated with the subsistence of diffraction peaks corresponding to uncorroded coating and steel substrate. From these results, we conclude that higher corrosion resistance is afforded when the corrosion products are comprised of a mix of products as compared to the reference sample. We also believe that the relative amount of carbonates, and the enhanced barrier protection which they are able to afford, could explain the large scatter of time-to-red-rust values which can be found in round robin SST tests. The formation of protective Zn compounds depends critically on the corrosion atmosphere, it may not be relevant for tests in a ‘painted’ condition.

4. Conclusions

This paper describes the development of Zn–Cr coatings on steel by using ion beam etching and vapour co-deposition, and reports the results of their structural, microstructural, mechanical and corrosion resistance characteristics:

1. The Cr content in the coatings varied from 1% to 15 at.%. Columnar growth was observed in most of the evaporation conditions and the compacity of the coatings increased with Cr content.

2. XRD measurements showed a gradual change in the structure as the Cr concentration increased, from the hcp characteristic of Zn to a metastable bcc structure.
3. A significant change was observed in the mechanical properties of the coatings, such as hardness H or elastic modulus E . The former increased with Cr content up to a five-fold improvement for the 15%Cr coating as compared to the pure Zn, while the E/H ratio was optimized.
4. The time taken before the appearance of red rust is at least four times longer for Zn–Cr coatings as compared to equally thick pure Zn coatings. In the SST, when compared to other Zn-alloy and pure Zn-plated steel samples, the Zn–Cr coated steel produced higher quantities of protective corrosion products, and for this reason, the Zn–Cr coated steel exhibited superior corrosion resistance.

Acknowledgements

The authors wish to acknowledge the precious technical help of Mr. E. Voltolini and Ms. R. Belli.

References

- [1] H.K. Pulker, *Coatings on Glass*, Elsevier, Amsterdam, 1984, p. 59.
- [2] C. Bowden, A. Matthews, *Surf. Coat. Technol.* 76/77 (1995) 508.
- [3] J. Giridhar, W.J. van Ooij, *Surf. Coat. Technol.* 52 (1992) 17–30.
- [4] V. Leroy, *Proc. Galvatech '95 Conf.*, Iron and Steel Society, Chicago (1995) 508.
- [5] J. Kawafuku, J. Katoh, M. Toyama, K. Ikeda, H. Nishimoto, H. Satoh, *Proc. 5th Automotive Corrosion Prevention Conf.* (1991) 43.
- [6] M. Bonelli, L. Calliari, M. Elena, M.A. Ghabashy, L.A. Guzman, A. Miotello, P.M. Ossi, *Surf. Coat. Technol.* 49 (1991) 150.
- [7] F. Alonso, V. Madina, J.L. Viviente, T. Musell, J.I. Onate, *Surf. Coat. Technol.* 103/104 (1998) 87.
- [8] W. Gissler, J. Haupt, P.N. Gibson, T. Sasaki, L. Guzman, M. Elena, L. Ishizaki, in: M. Takata, K. Kamata (Eds.), *Title, The Institute of Metals*, London, 1994, p. 571.
- [9] J.A. Thornton, *J. Vac. Sci. Technol.* 11 (1974) 666.
- [10] S. Hashimoto, M. Nagoshi, S. Ando, T. Urakawa, M. Sagiya, *Proc. 4th. Int. Conf. Zinc and Zinc Alloyed Coated Steel Sheet*, ISIJ, 1998, p. 537.
- [11] G.M. Davies, Project BE96-3073, PVD alternatives to conventional zinc coatings, interim report, Rover Body Engineering, Oct. 1998.

Corrosion resistance of the vacuum arc deposited Ti, TiN and TiO₂ coatings on large area glass substrates

N. Vershinin ^{a,b}, K. Filonov ^a, B. Straumal ^{b,c,*}, W. Gust ^c, R. Dimitriou ^d, A. Kovalev ^e,
J. Camacho ^f

^a SONG Ltd., P.O. Box 98, Chernogolovka, Moscow, 142432 Russia

^b I.V.T. Ltd., P.O. Box 47, 109180 Moscow, Russia

^c Institut für Metallkunde, Seestr. 92, D-70174 Stuttgart, Germany

^d PECHINEY CRV, BP 27, 38340 Voreppe, France

^e Moscow State Institute of Steel and Alloys, Leninsky Prospekt 4, 117049 Moscow, Russia

^f Materials Science Institute, University of Valencia, P.O. Box 22085, 46071 Valencia, Spain

Accepted 9 August 1999

Abstract

An industrial installation for vacuum arc deposition is presented. Its potential in the field of decorative coatings for large area glass sheets is demonstrated. In particular it is possible to deposit patterned coatings through a polymeric textile mask. The ability to deposit uniform multilayer coatings having interference colours onto large silicate glass sheets is shown. Titanium, titanium nitride and titanium dioxide coatings on silicate glass have been characterized in terms of composition and corrosion resistance. Depth profiling was achieved with the aid of Auger electron spectroscopy. The corrosion resistance of TiN coatings is higher than that of TiO₂. The corrosion resistance of vacuum arc deposited TiN coatings on glass was higher than that of TiN coatings produced by direct current reactive sputtering and plasma assisted chemical vapour deposition. Mask-deposited TiN coatings do not show any signs of accelerated corrosion along the border between the coated and uncoated glass. © 2000 Elsevier Science S.A. All rights reserved.

Keywords: Corrosion; Titanium; Titanium dioxide; Titanium nitride; Vacuum arc deposition

1. Introduction

During recent years, the physical vacuum deposition technologies originally developed for microelectronics and optics have penetrated into the areas of low cost and large area coated products traditionally produced by metallurgical methods. This trend is strongly supported by the decrease in the cost of vacuum equipment and by the development of robust and inexpensive coating technologies. One such method is vacuum arc deposition [1]. The vacuum arc process became prominent since the technology of TiN deposition was developed in the 1970s. It is widely used for the deposition of hard and wear resistant coatings on tools, medical prostheses, etc. [2–4]. Another important application of

vacuum arc deposition is for diamond-like coatings on video recorder heads [5]. In both of these applications, the dimensions of the parts to be coated is rather small. The next step in the development of vacuum arc deposition was the development of equipment able to coat large area substrates of complicated form [6]. This opened the way for marketing materials for architectural applications. A very important sector of this market is coated glasses. They are used for glazing (with semi-transparent coatings), decoration (mirrors), etc. Vacuum arc deposition has several advantages in this area, particularly:

- a high deposition rate which does not depend on the sputter coefficient of the target material [7];
- the weak dependence of the deposition rate on the orientation of substrate and the distance between target and substrate, which allows easy coating of three-dimensional parts of complicated form [8];
- the possibility of coating non-conductive substrates; and

* Corresponding author. Tel.: +49-711-1211276;

fax: +49-711-1211280.

E-mail address: straumal@mf.mpi-stuttgart.mpg.de (B. Straumal)

- low temperature of the substrate during deposition [6].

These advantages facilitated the development of new coated glass products for architectural applications which is described in this paper.

Architectural outdoor application of these new glass products needs data concerning their corrosion resistance because the coated glasses are exposed to the aggressive atmosphere of a modern megalopolis. High corrosion resistance of TiN and TiO₂ coatings on steel and brass substrates is well documented [9,10]. Nevertheless, the corrosion properties of a system containing a substrate and a coating depend strongly on the electrochemical properties of both components. Unfortunately, data on corrosion resistance of TiN and TiO₂ coatings on electrochemical inert surfaces, such as glass, are very scarce and do not relate to vacuum arc deposited coatings [11,12]. The aim of this work is to present data on the properties of vacuum arc deposited decorative coatings on glass substrates which are important for outdoor applications.

2. Experimental

The 'Nikolay' industrial scale system used for the deposition of coatings on large area architectural glasses has the following characteristics — size: 6000 × 3000 × 3000 mm; mass: 15500 kg; maximum power consumed: 75 kW; ultimate vacuum: 5×10^{-4} Pa; maximum size of treated glass: 2100 × 1300 × 8 mm; output capacity: 30 glass sheets 2100 × 1300 × 5 mm in an 8 h cycle, up to 1000 m²/month. The standard procedure for glass decorative coating included three steps. Before being loaded into the machine the glass sheet was precleaned using hot distilled water. After this precleaning, the glass sheets were mounted on metallic frames and placed in the vacuum chamber. Each frame held two glass sheets, mounted back to back. The frames were inserted into a slot (15 slots were available) and allowed to move independently inside the machine in order to receive different treatment operations. The displacement velocity of the frame was monitored and could be controlled. Each pair of glass sheets was sputter cleaned immediately before coating using a Hall discharge accelerator having a form of a large elongated loop [13]. A twin aperture had two slots, 55 mm away from one another. Two juxtaposed permanent magnets acted as a cathode. The water cooled anode had a tubular shape and ran inside the groove made by the cathode. The whole apparatus was set under vacuum in the presence of a sputter gas (usually argon or oxygen; the gas inlet was directly in the source). Gas ionization and subsequent ion acceleration was achieved by crossed electric and magnetic fields. Sheets to be treated were successively transported under the Hall discharge accelerator at a given translation

speed, the substrate surface being perpendicular to the ionic flux axis. By changing the speed and accelerator power, we could control the sputter dose received by the substrate. Two Hall current accelerators were mounted in the machine. They were placed on both sides of the machine in order to clean the two sheets in the frame simultaneously. For Ar, the sputter voltage was typically 5 kV, the sputter current could vary from 1 to 6 A. The high power (up to 10 kW) provides sufficient cleaning of both surfaces in any circumstances.

Three sources with flat round targets of diameter 200 mm were placed on each side of the installation. The surfaces of the targets were parallel to the glass substrates. Only two sources were normally used during the deposition. Arc voltage was constant at $U=22$ V while the discharge current I on each source could be varied from 100 to 300 A. No bias was applied to the substrate. A reactive gas (oxygen or nitrogen) was introduced at a pressure of 0.05 Pa if an oxide or nitride coating was to be formed. The arc generation was continuous and random. The arc sources were placed a rather large distance (about 800 mm) from the sheets to be coated. The configuration of the machine provided shielding and increased the charged particle part of the beam using the fact that the microdroplets were ejected at small angles with respect to the target surface [14]. The distance of the glass sheet from the target depended on the position of a frame. Therefore, the thickness of the deposited layer was controlled by varying the translation speed of the frame. The translation speed varied from 0.5 to 3 m/min depending on the thickness of a coating (typically 300 to 500 nm). When decorative patterns had to be produced, light nylon patterned sheets were used to provide masking. Various colours can be produced depending on the gas and deposition parameters used. In this study Ti, TiN and TiO₂ coated silicate glass samples were cut from large glass sheets and the surface morphology, composition and corrosion resistance were analysed.

The microstructure of the TiN and TiO₂ coatings was studied using scanning electron microscopy (SEM) using the JEOL JSM-6300F with an electron beam microanalysis facility. The composition depth profile of TiN/TiO₂ coated silicate glass was performed by Auger electron spectroscopy (AES) on a Physical Electronics PHI-551 spectrometer with a double-pass cylindrical mirror analyzer. The analysis was carried out with the excitation beam normal to the specimens. The spectra were taken during argon ion sputtering which produced a relatively clean surface of the sample under study without baking the system. The etching rate was considerably faster than the adsorption rate of the active residual gases. The base pressure was less than 2×10^{-8} Pa. The spectra were excited by an electron beam with an energy of 3 keV and a current of 8 μ A to the sample. The peak-to-peak modulation was 3 V. The

sputtering was accomplished using a 5 keV Ar^+ ion beam. An ion gun was mounted to give a beam incidence angle of 70° and, in order to minimize possible crater effects, it was rastered. The pressure of argon during sputtering was 3×10^{-3} Pa. The sputter rates for SiO_2 were determined to be 25 nm/min. AES studies of the Ti-N system are complicated by the fact that the main Auger $\text{KL}_{2,3}\text{L}_{2,3}$ transition for nitrogen (379 eV) overlaps the titanium $\text{L}_{3}\text{M}_{2,3}\text{M}_{2,3}$ transition (383 eV) to produce a single peak at 385 eV [15]. Auger spectra of titanium nitride coatings hence include two peaks, one corresponding to the Ti $\text{L}_{3}\text{M}_{2,3}\text{M}_{4,5}$ transition (418 eV) and the TiN peak resulting from overlapping (385 eV). For quantitative analysis, one must be able to resolve the nitrogen peak by removing the titanium contribution to the 385 eV peak. This was performed using the method described previously [16] where the approach [15] was improved. The reflectivity, R , of coloured coatings was measured with standard lock-in techniques. White light from a halogen lamp was focussed on the entrance slit of a Jovin-Yvon H25 monochromator (with a 1200 grooves/mm grating) and monochromatic light was focused onto a silicon diode after reflecting on the sample. The signal was compared to the reflection of a high-reflectivity ($R=0.98$ at 500 nm) mirror in order to give the reflectance in absolute units.

The corrosion behaviour of both TiN and TiO_2 coatings on silicate glass was characterized. The standard accelerated tests on atmospheric corrosion were carried out according to the Russian standards RST 9.012, 9.017 and 9.020 (temperature 22–25°C, humidity 96–98%, no water condensation, under the influence of gaseous chlorides, NH_3 and SO_2). Accelerated tests in 3.5% NaCl solution at 22–25°C under both full and partial immersion were also carried out. Both uniform and mask-deposited TiN coatings were studied because on the border between coated and uncoated glass the TiN/glass interface is exposed to the corrosion medium. The polarization behaviour was measured potentiodynamically with the aid of a potentiostatic apparatus PI-50-1/PR8 of MSNP. All potential values are given versus an Ag/AgCl electrode ($E_{\text{Ag/AgCl}}=0$ corresponds to -200 mV on the hydrogen electrode scale). The scanning rate was 1 mV s^{-1} . The polarization was changed from -0.8 to $+1.5$ V. Before the potentiodynamic measurements, the corrosion potential E_c was monitored for 0.5 h. The measurements were carried out in the electrolytes 3.0% NaCl solution, and 3.0% NaCl+3.0% NH_4Cl solution with pH=4 and 2. The pH of the solutions was corrected by adding 0.05 mol of NH_4OH to the solutions containing NH_4Cl and by adding 0.05 mol of NaOH to the solutions without NH_4Cl . The pH value of the solution was controlled by a 'pH-121' pH-meter of MSNP. The solution was prepared from reagent-grade chemicals and distilled water.

The area exposed to the solution was 1 cm^2 , the remaining surface of the samples was isolated by a varnish layer. The test temperature was 22–25°C.

3. Results and discussion

Vacuum arc deposition produced architectural glass (with standard dimensions of $1300 \times 1600 \text{ mm}$) has the following coatings:

1. Thin semitransparent TiN coatings for glazing or thick non-transparent for mirrors. The colour of these coatings was determined mainly by the composition of TiN.
2. TiN patterned coatings. In this case the light polymeric mask was positioned between the vacuum arc source and the substrate. An example of a mask deposited coating is shown in Fig. 1. The natural coloured TiN coating was combined with uncoated transparent glass.
3. TiO_2 coatings having interferential colours defined by the thickness of the coating. TiO_2 coatings of three different thicknesses were characterized (blue, green and red). Reflectivity spectra for wavelength

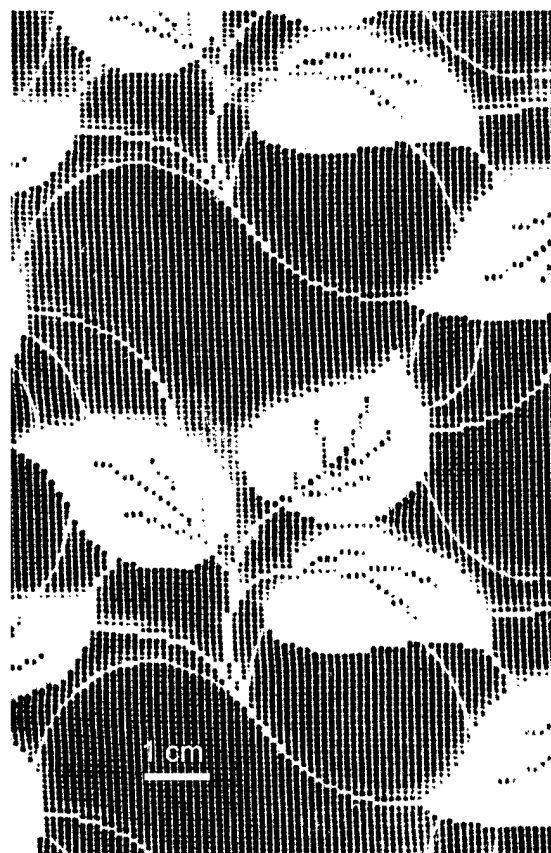


Fig. 1. Detail of a decorative pattern obtained by masking during TiN arc deposition on silicate glass.

from 400 to 800 nm (Fig. 2) characterized quantitatively the green and blue colours of the TiO_2 coatings.

4. TiN patterned coating deposited on an intermediate coloured TiO_2 coating. In this case the TiN coating of natural colour (goldish or yellow) was combined with a red, blue or green TiO_2 coating.

The depth concentration profile obtained from the AES for the TiN coating on silicate glass is shown in Fig. 3. The peak characteristics for titanium, nitrogen, oxygen, carbon and oxygen appeared in the spectra. The decreasing concentration of titanium and increasing concentration of Si mark the transition from the coating to the substrate. The nitrogen and oxygen content in the TiN coating was uniform except in the thin oxygen-rich layer close to the glass substrate (deliverably deposited for the better adhesion of TiN to the SiO_2 substrate). Quantitative analysis revealed that the Ti to N ratio in the TiN layer is about 1.2, very close to stoichiometric. The carbon concentration is nearly uniform in the whole coating (about 10 at.%). The uniformity of the composition of the TiN layer, which does not change significantly with depth, is comparable with that of TiN coatings obtained with the aid of the chemical vapor deposition (CVD) technique [17]. The TiN composition was similar to that obtained using plasma-assisted CVD (PACVD) deposited at 430°C substrate temperature, 60 W radio frequency power by Kim et al. [18]. They detected the stoichiometric composition for substrate temperatures

above 500°C. In our case, the substrate temperature was well below 100°C, which allowed the use of polymer masks for the deposition of patterned TiN and TiO_2 coatings. It was shown [19] that even a rather high residual carbon content did not drastically affect the properties of TiO_2 . In our case, the vacuum arc deposited coatings possessed high corrosion resistance, and the carbon contamination was obviously not detrimental to corrosion resistance.

The most important structural feature of both TiN and TiO_2 coatings is the Ti microdroplets present in the coating [7]. These microdroplets are so small that they are not visible to a naked eye, do not disturb the appearance of coated glasses and, therefore, do not resurrect their applicability as architectural materials. Nevertheless, in the case of a less corrosion resistant substrate (stainless steel instead of glass) the small pores surrounding these droplets can feed the corrosive agent to the substrate and active corrosion starts [20]. Visual examination of TiN and TiO_2 coatings before and after electrochemical corrosion testing in neutral solution revealed differences in the corrosion mechanism. The corrosion of TiO_2 coatings started at low E values (both positive and negative) and formed dark corroded regions around the Ti microparticles. The number and area of corroded places uniformly increased with increasing E . The TiN coatings were stable against corrosion and did not reveal any visual signs of damage up to rather high positive and negative E values -0.8 V and $+0.7$ V. Above $E = +0.7$ V, multiple corroded areas suddenly appeared all over the surface, destroying the coating almost simultaneously everywhere.

After 12 months of exposure to atmospheric corrosion, with conditions which correspond to the most aggressive type of industrial atmosphere (temperature 22–25°C, humidity 96–98%, no water condensation, under influence of gaseous chlorides, NH_3 and SO_2) neither the mass nor appearance changed. Likewise, neither full nor partial immersion in NaCl solution for 8 months produced any changes. The first signs of corrosion in these tests appeared only after 11 months. This high corrosion resistance is comparable with the properties of vacuum arc deposited TiN coatings on steel and brass substrates [10]. The mask-deposited TiN coatings did not show any signs of accelerated corrosion along the border between coated and uncoated glass. The data from electrochemical tests are displayed in Fig. 4 (NaCl solution, pH=4) and Fig. 5 (NaCl + NH_4Cl solution, pH=2). The dependence of the corrosion current i_c on the polarisation voltage E is shown for Ti, TiN and two different TiO_2 coatings of various thickness having red and green colours. Both TiN and TiO_2 were self-passivated. The corrosion potentials are given in Table 1. This data show that at a low pH value the corrosion resistance of TiN is much higher than that of Ti and TiO_2 in both solutions studied.

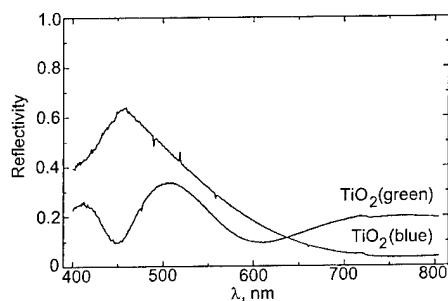


Fig. 2. Reflectivity spectra of green and blue TiO_2 coatings on silicate glass.

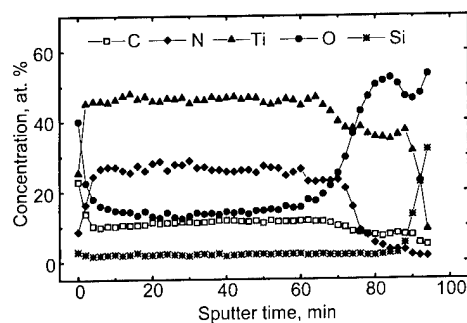


Fig. 3. AES depth profile for a TiN coating on silicate glass. The thickness was about 0.5 μm .

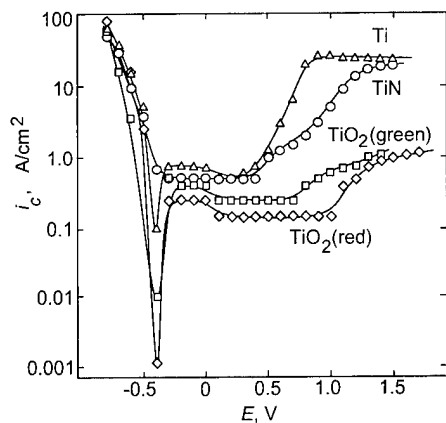


Fig. 4. The dependence of the corrosion current i_c on the polarisation voltage E in 3.0 at.% NaCl solution with pH=4.

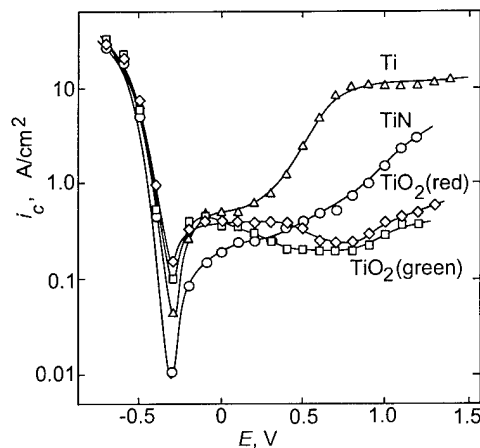


Fig. 5. The dependence of the corrosion current i_c on the polarisation voltage E in 3.0 at.% NaCl + 3.0 at.% NH_4Cl solution with pH=2.

Furthermore, the TiO_2 coating is more corrosion resistant than pure Ti. With increasing pH, E_c becomes more negative. Nevertheless, E_c in all cases remains more positive than the reduction potential for hydrogen. This indicates that the corrosion process for all coatings studied can proceed only with oxygen depolarization. The most negative E_c was measured for the Ti coatings, the most positive for TiN. It can be seen in Figs. 4 and 5 that both the cathodic and anodic processes are less pronounced on the surface of TiO_2 in comparison with TiN. The corrosion current i_c for TiN is smaller in the

NH_4Cl -containing solution. The values of i_c for Ti and TiO_2 remain at the same levels as those in NaCl solution without NH_4Cl . It is also important to mention that at anodic polarization voltages for TiO_2 , i_a oscillates. This reveals that the coating surface layer is repeatedly attacked and activated. The corrosion properties of a system containing a substrate and a coating depend strongly on the electrochemical properties of both components. To correctly discuss our results, we compare our data with the electrochemical properties of TiN deposited on electrochemically inert substrates (glass, Al_2O_3) by reactive direct current sputtering and PACVD [11,12]. The values of corrosion current density, i_c [11,12], are of the same order of magnitude as in this work. The corrosion potential E_c of TiN in NaCl solution with pH=6 in our work is about 0.09 mV more positive than E_c for nearly the same electrochemical conditions after results in [21]. For pH=1 [11], $E_c = -0.23$ V for sputtered films (recalculated for the Ag/AgCl electrode) and for pH=12, $E_c = -0.33$ V, which is much lower than both values obtained in this work. A pronounced anodic peak was present in all potentiodynamic curves [12]. In our work the coatings were self-passivated. Therefore, the corrosion resistance of TiN deposited by vacuum arc process is definitely higher than that of TiN coatings deposited on silicate glass substrates by reactive d.c. sputtering [12] and on Al_2O_3 substrates by PACVD [11].

The vacuum arc deposited naturally coloured Ti and TiN coatings, interferentially coloured TiO_2 coatings, and patterned TiN and TiN/ TiO_2 coatings on large area glass substrates were very uniform and exhibited high corrosion resistance. These properties, together with the unusual appearance, make vacuum arc coated glass very attractive for architectural applications.

Acknowledgements

The financial support of the NATO Linkage Grant (contracts HTECH.LG.970342 + CN.SUPPL973216), the Isopress-Inter Programme of the Russian Ministry of Science and Technology, the Copernicus Network (contract ERB IC15 CT98 0815), Royal Swedish

Table 1
Corrosion potentials E_c (V) for Ti, TiN and TiO_2 coatings vacuum arc deposited on silicate glass

Solution	3.0 at.% NaCl			3.0 at.% NaCl + 3.0 at.% NH_4Cl		
	pH=4	pH=6	pH=8	pH=2	pH=4	pH=6
Ti	-0.10	-0.22	-0.12	+0.05	-0.25	-0.26
TiO_2 (red)	+0.16	-0.10	-0.10	+0.23	0	-0.10
TiO_2 (green)	+0.10	-0.14	-0.07	+0.25	-0.05	-0.05
TiN	+0.28	+0.05	0	+0.35	+0.20	+0.15

Academy of Sciences, University of Valencia and the Generalitat Valenciana is acknowledged.

References

- [1] R.A. Andrievski, *J. Mat. Sci. Technol.* 14 (1998) 97.
- [2] A.A. Snaper, U.S. Patent No. 3,625,848, 1971.
- [3] B.K. Tay, X. Shi, H.S. Yang, E.L. Liu, L.K. Cheah, H.S. Tan, *Surf. Eng.* 15 (1999) 33.
- [4] J.S. Zabinski, A.A. Voevodin, *J. Vac. Sci. Technol. A* 16 (1998) 1890.
- [5] R.F. Bunshah (Ed.), *Handbook of Deposition Technologies for Films and Coatings*, Noyes Publications, Park Ridge, NJ, 1994.
- [6] B. Straumal, N. Vershinin, K. Filonov, R. Dimitriou, W. Gust, *Thin Solid Films* 351 (1999) 186.
- [7] N. Vershinin, B. Straumal, W. Gust, *J. Vac. Sci. Technol. A* 14 (1996) 3252.
- [8] N.F. Vershinin, V.G. Glebovsky, B.B. Straumal, W. Gust, H. Brongersma, *Appl. Surf. Sci.* 109/110 (1996) 437.
- [9] A. Giardini-Guidoni, V. Marotta, R. Teghil, T.M. DiPalma, A.M. Beccaria, L. Chiaruttini, *Surf. Coat. Technol.* 100/101 (1998) 437.
- [10] A.K. Vershina, I.A. Bel'chin, A.A. Pitel'ko, S.D. Izotova, *Fiz. Chim. Obr. Mat.* 5 (1990) 93 (in Russian).
- [11] E. Lunarska, J. Michalsky, *J. Mat. Sci.* 30 (1995) 4125.
- [12] Y. Massiani, A. Medjahed, P. Gravier, L. Argème, L. Fedrizzi, *Thin Solid Films* 191 (1990) 305.
- [13] N. Vershinin, B. Straumal, K. Filonov, R. Dimitriou, W. Gust, M. Benmalek, *Thin Solid Films* 351 (1999) 172.
- [14] J.E. Daadler, *J. Phys. D* 9 (1976) 2379.
- [15] P.T. Dawson, K.K. Tzatzov, *Surf. Sci.* 149 (1985) 105.
- [16] Ju.M. Shulga, A.N. Khodan, *Phys. Chem. Mech. Surf.* 5 (1989) 116 (in Russian).
- [17] D.W. Kim, Y.J. Park, J.G. Lee, J.S. Chun, *Thin Solid Films* 165 (1988) 149.
- [18] B. In, S.P. Kim, Y.I. Kim, W.W. Kim, I.H. Kuk, S.S. Chun, W.J. Lee, *J. Nucl. Mat.* 211 (1994) 223.
- [19] P. Babelon, A.S. Dequiedt, H., Mostéfa-Sba, S. Bourgeois, P. Sibillot, M. Sacilotti, *Thin Solid Films* 322 (1998) 63.
- [20] N. Vershinin, K. Filonov, B. Straumal, W. Gust, I. Wiener, E. Rabkin, A. Kazakevich, *Surf. Coat. Technol.* 123 (1999).
- [21] E. Lunarska, S. Al Ghanem, *Phys. Stat. Sol. A* 145 (1994) 587.

Corrosion behaviour of the protective and decorative TiN coatings on large area steel strips

N. Vershinin ^{a,b}, K. Filonov ^a, B. Straumal ^{b,c,*}, W. Gust ^c, I. Wiener ^d, E. Rabkin ^d,
A. Kazakevich ^e

^a SONG Ltd., P.O. Box 98, Chernogolovka, Moscow District 142432, Russia

^b I.V.T. Ltd., P.O. Box 47, 109180 Moscow, Russia

^c Institut für Metallkunde, Seestrasse 92, D-70174 Stuttgart, Germany

^d Technion-Israel Institute of Technology, Department of Materials Engineering, Haifa 32000, Israel

^e Moscow State Institute of Steel and Alloys, Leninsky Prospekt 4, 117049 Moscow, Russia

Accepted 29 June 1999

Abstract

Decorative and protective TiN coatings were vacuum arc deposited in an industrial installation 'Nikolay' allowing coating of strips with maximum size 2100 × 1300 × 8 mm. Titanium nitride (TiN) coatings on stainless steel strips have been characterized in terms of microstructure and corrosion resistance. The vacuum arc deposited TiN coatings have a higher corrosion resistance compared with TiN coatings on steel produced by plasma assisted chemical vapour deposition, glow discharge deposition, direct current magnetron sputtering or magnetron sputter deposition. © 2000 Elsevier Science S.A. All rights reserved.

Keywords: Corrosion resistance; Titanium nitride; Vacuum arc deposition

1. Introduction

TiN coatings are widely used due to their high hardness and wear resistance. Their goldish appearance makes them very attractive for decorative purposes. One of the most reliable technologies for the production of TiN coatings, together with magnetron sputtering, is vacuum arc deposition [1]. This technology has been applied since the 1970s for the production of coated tools, medical implants, furniture pieces, etc. [2]. Recently, a reliable vacuum arc deposition technology was developed for the coating of large-area substrates [3]. This robust and inexpensive process allows the production of coated materials for building and construction which are cheap enough to compete with materials prepared in a traditional metallurgical way. Particularly, in recent years stainless steel strips and rods coated with TiN by SONG Ltd. were used by building companies in Moscow for the rebuilding of the Cathedral of Christ The Saviour (2 m long elements for

the chains fixing the crosses on the domes), for the construction of the monument for Emperor Peter the Great, for the new roof for the Moscow Luzhniki Olympic Stadion (altogether about 2000 m², 1 × 2 m coated strips are used), and for the reconstruction of the roof of the Great Kremlin Palace (about 200 m long decorative grating, made of laser patterned and TiN coated 1 × 2 m strips).

Recently, the technology of vacuum arc deposition of TiO₂ coatings with interference colours (red, pink, green, etc.) was also developed for large-area glass substrates [4]. The transfer of this technology to steel substrates will allow the production of materials with very attractive decorative appearance for architectural needs.

This new outdoor application is a big challenge to the area of materials science and technology, because the coated metallic parts are exposed to the aggressive atmosphere of a northern megalopolis with 10 million inhabitants and 5 million cars. For about 6 months a year they are covered by (repeatedly melting) snow. Though TiN has a very high intrinsic corrosion resistance [5,6], the combination with electrochemically less positive substrates can, in principle, lead to an increase

* Corresponding author. Tel.: +49-711-1211276;

fax: +49-711-1211280.

E-mail address: straumal@mf.mpi-stuttgart.mpg.de (B. Straumal)

of the corrosion rate in comparison with an uncoated substrate [7]. High corrosion resistance of laser ablated TiO_2 coatings on steel was reported recently [8]. The aim of this work is to present data on the properties of vacuum arc deposited decorative coatings on steel substrates, which are important for their outdoor applications.

2. Experimental

The industrial scale setup 'Nikolay' (Fig. 1) used for the deposition of coatings on large-area stainless steel strips has the following characteristics: size = $6000 \times 3000 \times 3000$ mm; maximum power consumed = 75 kW; ultimate vacuum = 5×10^{-4} Pa; maximum size of treated strips = $2100 \times 1300 \times 8$ mm; output capacity for steel = 30 steel strips $2100 \times 1300 \times 5$ mm in an 8 h cycle, $1000 \text{ m}^2/\text{month}$.

The standard procedure for decorative steel coating consisted of three steps. Before being loaded into the machine, the steel strip was precleaned using hot distilled water. After precleaning, the steel strips were mounted on metallic frames and placed in the vacuum chamber. Each frame held two steel strips, mounted back to back. The frame was inserted into a slot (15 slots are available) and allowed to move independently inside the deposition chamber. The displacement velocity of the frame was monitored and could be controlled. Each frame received, in turn, a cleaning treatment followed

immediately by the coating process in order to prevent recontamination. The complete treatment involved one return of the frame for cleaning and another return for coating. Cleaning was performed using a large aperture Hall current accelerator [9] providing high energetic ions which impact and sputter the substrate surface. Coating in the industrial setup was performed using four circular targets of 200 mm diameter. Three sources were placed on each side of the installation. Only two sources were normally used during the deposition. A reactive gas (oxygen) was introduced at 0.05 Pa if oxide coating was to be formed. TiN coating was obtained by introducing nitrogen at a pressure of about 0.05 Pa. Because microdroplets are ejected at small angles [10] with respect to the target surface, this configuration provided shielding and only a very small number of microparticles was present in the coating (Fig. 2). These microparticles do not disturb the optical appearance of the decorative coatings. The TiN coatings studied in this work were deposited on H18N10T (18% Cr, 9% Ni, 0.5% Ti) stainless steel without an intermediate layer.

The samples' surface was observed using an atomic force microscope (AFM) Autoprobe CP AFM from Park Scientific Instruments. The AFM was operated in the contact mode using sharpened gold-coated microlevers with nominal radius of curvature of the tip less than 20 nm. The corrosion behaviour of TiN coatings on the H18N10T stainless steel was characterized. The standard accelerated tests on atmospheric corrosion were carried out according to the Russian standards RST 9.303-84 and 9.302-88 over 2 months by complete immersion in solution and in the humid atmosphere above the solution (humidity 96–98%). Two different solutions were used for these tests: (1) 30 g NaCl + 30 g NH_4Cl + 1 ml HCl; and (2) 30 g NaCl + 10 g Na_2S + 30 g NH_4Cl + 1 ml H_2SO_4 for 1000 cm^3 of aqueous solution. Electrochemical tests were carried out in two aqueous solutions: (3) 30 g NaCl; and (4) 30 g NH_4Cl for 1000 cm^3 of solution. The pH value was varied from 2.0 to 8.0. The correction of the pH value of the solutions was carried out by addition of 0.05 mol

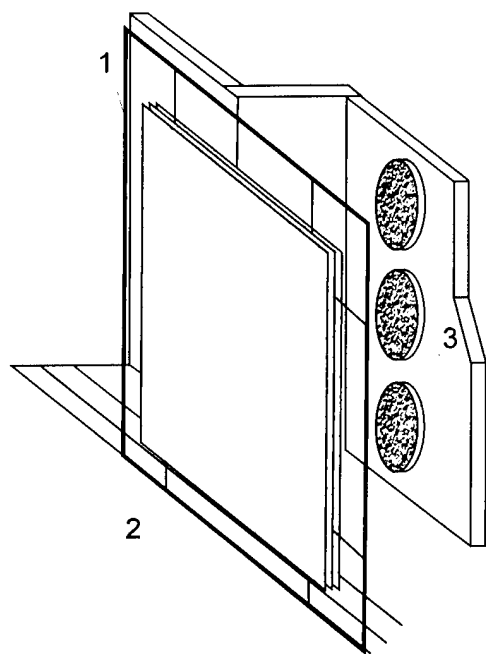


Fig. 1. Scheme of the 'Nikolai' apparatus for vacuum arc deposition on large-area substrates: (1) glass sheets mounted back to back; (2) mobile frame; (3) metallic cathodes.

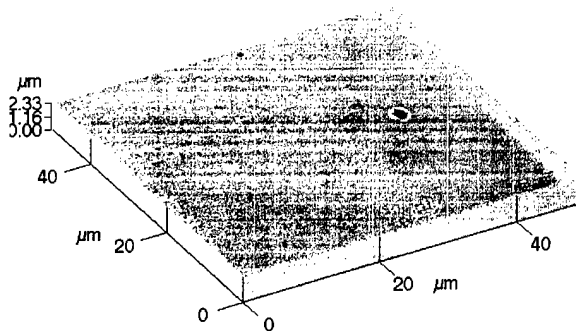


Fig. 2. AFM micrograph of a TiN coating showing Ti microparticles and point defects remaining after decohesion of the microparticles.

of HCl or NH_4OH (to the solutions containing NH_4Cl), and by addition of 0.05 mol of NaOH (to the solutions without NH_4Cl). The solution was prepared from reagent grade chemicals and distilled water. The area exposed to solution was 1 cm^2 , the rest of the samples' surface was isolated by a varnish layer. The test temperature was $22\text{--}25^\circ\text{C}$. The pH value of a solution was controlled by a 'pH-121' meter. The polarization behaviour was measured potentiodynamically with the aid of a potentiostatic apparatus PI-50-1/PR8. All potential values are given versus the Ag/AgCl electrode ($E_{\text{Ag/AgCl}}=0$ corresponds to -200 mV on the hydrogen electrode scale). The scanning rate was 1 mVs^{-1} . The polarization was changed from -1.3 to $+0.5\text{ V}$. Before potentiodynamic measurements, the corrosion potential E_c was monitored for 0.5 h.

3. Results and discussion

During the accelerated corrosion tests a coated sample immersed into solution 2 revealed the first signs of corrosion damage after 8 days: after 2 weeks about 32% of the surface area was corroded and after 2 months almost all the surface was corroded. No damage appeared on the sample immersed in solution 1 after 8 days and 2 weeks: only after 2 months did the first signs of damage appear, similar to the damage of the sample tested in the atmosphere above solution 2. The observed corrosion behaviour reveals the presence of pores in the coating. The AFM micrograph (Fig. 2) shows that such pores can exist in regions close to the Ti microdroplets.

The data from the electrochemical tests for coated and uncoated samples in solutions 3 (NaCl) and 4 (NH_4Cl) with various pH values are shown in Figs. 3 and 4, respectively. Generally, the pH value of a solution essentially influences the kinetics of the anode and cathode processes and the corrosion rate. The corrosion

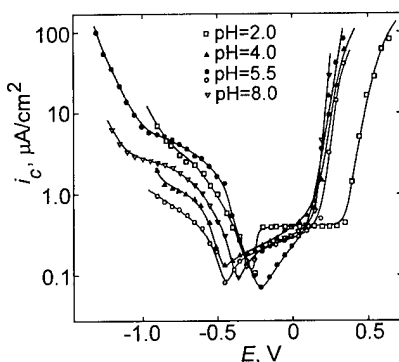


Fig. 3. The dependence of the corrosion current i_c on the polarisation voltage E in 3.0 at.% NaCl solution at various pH values for H18N10T stainless steel vacuum arc coated with a TiN layer (open symbols) and uncoated (full symbols). The lines are guides for the eye.

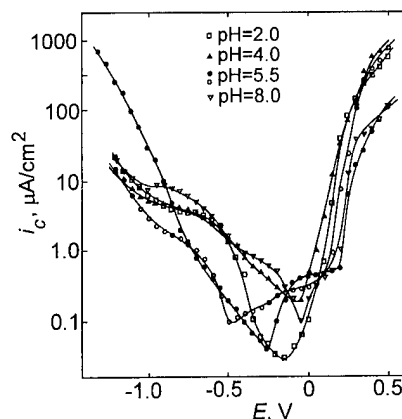
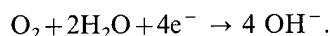


Fig. 4. The dependence of the corrosion current i_c on the polarisation voltage E in 3.0 at.% NH_4Cl solution at various pH values for H18N10T stainless steel vacuum arc coated with a TiN layer (open symbols) and uncoated (full symbols). The lines are guides for the eye.

process in NaCl solutions proceeds with the oxygen depolarisation. This follows from the form of the cathode curves at various pH values (Fig. 3). It means that the corrosion rate is controlled by the oxygen concentration in the solution and by the rate of the reaction:



Additionally, it is confirmed by the fact that the anodic polarization curves practically do not change by varying the pH value. Only at $\text{pH}=2$ in NaCl solution does the rate of the active dissolution increase by about 1.5 times, but the repassivation potential ($+0.35\text{ V}$) is about 0.2 V higher than for other pH values studied. The value of the repassivation potential ($+0.15\text{ V}$) and the rapid increase of the anodic current are typical of the local activation corrosion mechanism. It means that the coating is porous, and the steel surface is activated in the pores by anodic polarization. This fact is supported by the form of the anodic curve for the uncoated steel.

The anodic behaviour of the samples in NH_4Cl solutions practically does not depend on the pH value. The rate of the anodic dissolution increases slightly (about 10–15%) with increasing pH, and the repassivation potential at all pH values studied is $+0.15 \pm 0.05\text{ V}$. The stainless steel without a coating has similar behaviour. The corrosion in NH_4Cl solutions proceeds with oxygen depolarization, similar to the NaCl solutions. It means that the oxygen solubility in NH_4Cl solution practically does not depend on the pH value. The corrosion current estimated with the aid of the Tafel equation decreases by about one order of magnitude with increasing pH (Fig. 4). The minimal corrosion rate corresponds to the neutral solution. The data obtained reveal that both coated and uncoated steel is inclined to the pitting corrosion in an acidic environment ($\text{pH} < 4$). At high pH values uniform corro-

sion is more likely. The corrosion resistance of the TiN coating on stainless steel around $E=0$ V is comparable with the 'intrinsic' corrosion behaviour of TiN on electrochemically inert substrates (silicate glass, Al_2O_3) [3–6] and also very close to that of uncoated stainless steel. The vacuum arc deposited TiN coating on stainless steel is cathodic and ensures higher corrosion resistance only in the absence of pores. The stainless steel coated with TiN studied can be used under atmospheric conditions. The TiN coating conserves its decorative properties under normal atmospheric conditions, but does not enhance the corrosion resistance of stainless steel. If the environments contain sulphur, the multilayer coating must be used with additional intermediate layers (Ti, Ni) preventing contact with the substrate [11].

T. Wierzhon et al. [12] investigated TiN coatings deposited on 1H18N10T stainless steel (very similar to that studied in the present work) with the aid of glow discharge. The corrosion current i_a in our experiments is about five times lower than that obtained in [12] in 0.5 M NaCl neutral aqueous solution. In [6] TiN coatings were deposited on tool steel with the aid of the plasma assisted chemical vapour deposition process (PACVD). The corrosion current i_a in our experiments is more than one order of magnitude lower than that obtained in [6] in acidic solution (H_3PO_4). In [6] TiN coatings were deposited on M50 bearing steel with the aid of: (1) direct current (d.c.) magnetron sputtering; (2) magnetron sputter deposition; and (3) vacuum arc deposition. The samples were tested in 1 N acidic solution (H_2SO_4). The corrosion current i_a for coatings (1) and (2) is four to five orders of magnitude higher than in our experiments. But the corrosion curve for the vacuum arc deposited coatings is very similar to our curves for the vacuum arc deposited TiN on stainless steel. These facts reveal that vacuum arc deposition allows reaching a higher corrosion resistance of the TiN coating compared to other methods such as PACVD,

glow discharge deposition, d.c. magnetron sputtering or magnetron sputter deposition.

Acknowledgements

The financial support of the NATO Linkage Grant (contracts HTECH.LG.970342+CN.SUPPL 973216), the Isopress-Inter Programme of the Russian Ministry of Science and Technology, the Royal Swedish Academy of Sciences and the Copernicus Networks (contracts ERB IC15 CT98 0815 and ERB IC15 CT98 0812) is acknowledged.

References

- [1] R.L. Boxman, P.J. Martin, D.M. Sanders (Eds.), *Handbook of Vacuum Arc Science and Technology*, Noyes Publications, Park Ridge, NJ, 1995, p. 367.
- [2] P.J. Martin, R.P. Netterfield, T.J. Kinder, *Thin Solid Films* 193/194 (1990) 77.
- [3] B. Straumal, N. Vershinin, K. Filonov, R. Dimitriou, W. Gust, *Thin Solid Films* 351 (1999) 204.
- [4] N. Vershinin, K. Filonov, B. Straumal, W. Gust, R. Dimitriou, A. Kovalev, J. Camacho, *Surf. Coat. Technol.* (1999) this issue.
- [5] Y. Massiani, A. Medjahed, P. Gravier, L. Argème, L. Fedrizzi, *Thin Solid Films* 191 (1990) 305.
- [6] E. Lunarska, J. Michalsky, *J. Mater. Sci.* 30 (1995) 4125.
- [7] H.H. Uhlig, R.W. Revie, *Corrosion and Corrosion Control*, third ed., Wiley, New York, 1985. 464 pp.
- [8] A. Giardini-Guidoni, V. Marotta, R. Teghil, T.M. DiPalma, A.M. Beccaria, L. Chiaruttini, *Surf. Coat. Technol.* 100/101 (1998) 437.
- [9] N. Vershinin, R. Dimitriou, M. Benmalek, B. Straumal, W. Gust, J. Vivas, J. Shulga, *Surf. Coat. Technol.* (1999) this issue.
- [10] J.E. Daadler, *J. Phys. D* 9 (1976) 2379.
- [11] J.S. Zabinski, A.A. Voevodin, *J. Vac. Sci. Technol. A* 16 (1998) 1890.
- [12] T. Wierzhon, J. Michalski, J. Rudnicki, B. Kulakovska, N. Zyrinski, *J. Mater. Sci.* 27 (1992) 771.

Application of hard coatings in aluminium die casting — soldering, erosion and thermal fatigue behaviour

C. Mitterer ^{a,*}, F. Holler ^a, F. Üstel ^b, D. Heim ^c

^a *Institut für Metallkunde und Werkstoffprüfung, Montanuniversität, Franz-Josef-Straße 18, A-8700 Leoben, Austria*

^b *Department of Metallurgy and Materials Science, Sakarya University, TR-5400 Adapazari, Turkey*

^c *Rübig GmbH and Co. KG, Durisolstraße 12, A-4600 Wels, Austria*

Abstract

In aluminium die casting, tools are exposed to erosion, corrosion and soldering due to the frequent contact of the tool surface to the casting alloy, to heat checking and gross cracking due to thermal fatigue and to oxidation due to high pouring temperatures. The gradual destruction of die surfaces during service decreases casting piece quality and limits die lifetime. Hard coatings based on nitrides or carbides of transition metals may protect the steel surface from erosion and soldering of aluminium and improve the resistance against thermal cracking. Thus, they may replace the thick oxide-based die coatings nowadays used in foundries. Within this study, results obtained on the performance of coatings deposited onto die-casting dies by magnetron sputtering and plasma-assisted chemical vapour deposition are presented and discussed. TiN, Ti(C,N), Ti(B,N), and (Ti,Al)(C,N) coatings deposited onto hot-working tool steel have been evaluated in practical die-casting service. Results obtained are compared with those of simulation tests using thermal cycling immersion tests in liquid aluminium, thermo-gravimetric analysis, and stress measurements during thermal cycling. Maximum lifetime of the coated casting die is achieved for careful optimization of hardness, adhesion, oxidation resistance and high temperature stability, and internal stresses. © 2000 Elsevier Science S.A. All rights reserved.

Keywords: Aluminium die casting; Erosion; Hard coatings; Soldering; Thermal fatigue

1. Introduction

Today, high-quality aluminium castings are usually produced using permanent metallic moulds in gravity or pressure die-casting. Compared with sand casting, permanent moulds permit the high-volume production of more uniform castings, with closer dimensional tolerances, superior surface finish and improved mechanical properties [1] at relatively low cost — for example for automotive parts such as engine blocks, carburettor bodies, transmission cases, and valve bodies.

Chromium-alloyed or maraging hot-working tool steels heat treated to a hardness of typically 29 to 48 HRC are widely used for die-casting dies [2–4]. Die life is a major consideration in a die-casting process because, depending on the complexity of the part being produced, a die may cost more than US\$ 100 000. Die life may vary from 20 000 to over 250 000 parts depend-

ing on the casting produced. Thus, during service life, the die cavity and cores experience a large number of thermomechanical cycles. Usually, commercial die lubricants or mould release agents are sprayed each cycle on the die surface, which reduces wear, acts as a coolant, and facilitates the removal of the casting [5].

Wear and failure of die-casting dies involve a complex interaction between various mechanisms. The most important wear and failure modes can be seen in Fig. 1 and are summarized as follows [2].

(1) The so-called washout damages on working die surfaces are attributed to corrosion, erosion and soldering. They are the result of the exposure of the die surface to the liquid aluminium, the motion of the liquid aluminium and the solidification and ejection of the casting [6,7]. Corrosion is caused by the fact that iron and most of the alloying elements in the die steel are more or less dissolvable in liquid aluminium. In addition, the high pouring temperatures may cause oxidation of the die surface. Erosion takes place as a result of the motion of the aluminium melt, which can reach velocities within the range of 20 to 60 m s⁻¹ in gate areas [6]. Two basic

* Corresponding author. Tel.: +43-3842-402440;
fax: +43-3842-402737.

E-mail address: mitterer@unileoben.ac.at (C. Mitterer)

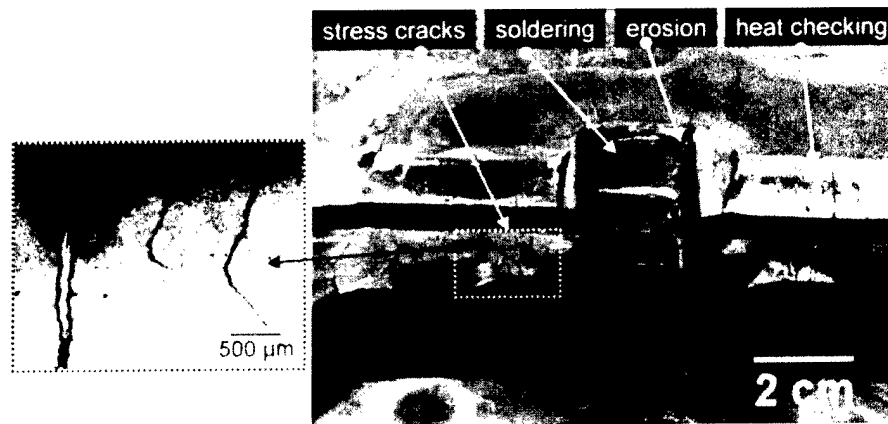


Fig. 1. Damage mechanisms in aluminium die casting (the inset on the left shows a scanning electron microscope cross-section of the mould on the right with thermal fatigue cracks).

erosion mechanisms are known, i.e. liquid-impingement and cavitation. Soldering of the casting to the steel surface inside the cavity takes place during solidification. On the one hand, this causes sticking problems when the casting is ejected. On the other hand, it can also give rise to adhesive wear when the casting is separated from the die.

(2) Thermal fatigue is the most important failure mode in die casting [2]. Thermal fatigue cracks may be classified by their appearance in heat checks and stress cracks [8] (see Fig. 1). The characteristic feature of heat checking is a net-shaped crack pattern that occurs predominantly on level surfaces. Stress cracks mainly appear as individual and clearly pronounced cracks as a result of stress concentrations due to the configuration of the die cavity [9]. Generally, thermal fatigue cracks will already have appeared after a few thousand cycles or even earlier, i.e. in the low cycle fatigue regime. The depth propagation and the opening of these cracks (which are sometimes filled with aluminium) can be seen from the inset in Fig. 1. Furthermore, gross cracking may be due to thermal shock or mechanical overloading, often leading to total failure of the die.

Die maintenance may be done by grinding or welding if the surface quality or dimensions of the castings are no longer sufficient [10]. However, the tool and service costs constitute a remarkable part of the production costs in die casting and there are numerous approaches to optimize the lifetime of the dies. In general, die life may be enhanced by geometric factors in die design (governing stresses and thermal gradients), die material considerations (e.g. machinability, heat treatment, toughness, resistance to wear and heat checking), processing conditions (e.g. preheating, heating and cooling cycles, machine closing force, lubricants, service intervals), and die surface considerations [2,11]. Surface treatments, such as nitriding, are often applied for casting dies to reduce abrasive wear and improve thermal fatigue resistance. In recent years, the application of

hard coatings deposited by physical vapour deposition (PVD) techniques has been reported in the literature [5,12–27]. It is the aim of this paper to present and discuss, within the background of the literature, results obtained in the authors' laboratories on hard coatings deposited onto die-casting dies using sputtering and plasma-assisted chemical vapour deposition (PACVD) and on their application in aluminium die casting.

2. Experimental details

Coating deposition was done using unbalanced d.c. magnetron sputtering in a laboratory plant [28] and by different commercial PACVD systems (diameter, 500 mm; height, 500 mm to diameter, 1000 mm; height, 1500 mm) with bipolar pulse generators [12,29]. The sputtering unit was used for deposition of specimens for the evaluation of application-related properties, whereas PACVD served as highly suitable technique for up-scaling of coatings for large and heavy die-casting cores and moulds. Within this work, coatings evaluated included TiN, Ti(C,N), Ti(B,N), and (Ti,Al)(C,N). These coatings were chosen because of their metallic character and expected good adhesion to hot-working steel substrates, and because of the comparatively low mismatch of thermal expansion coefficients of coating and substrate. This is assumed to be crucial for minimizing the possibility of thermal cracks in the substrate–coating interface [14]. Sputtered TiN coatings were deposited using non-reactive deposition from a TiN target and an ion-to-neutral flux ratio of approximately 0.7 [28], whereas TiN, Ti(C,N), Ti(B,N), and (Ti,Al)(C,N) coatings were grown by PACVD using H₂, Ar, N₂, CH₄, TiCl₄, BCl₃, and AlCl₃ gases. Typical deposition parameters can be seen in Table 1. The higher values for the PACVD discharge voltage have been used for the deposition of (Ti,Al)(C,N) films. Coating thickness was adjusted to 1.5–3.5 μm.

Table 1
Typical deposition conditions used in this work for magnetron sputtering and PACVD

Deposition parameter	Sputtering	PACVD
Total pressure (Pa)	0.7	50–300
Substrate temperature (°C)	300	480–500
Bias/discharge voltage (V)	–50	400–500
Deposition time (h)	1.5	8–10

Results from former experiments [12] and literature [19,30] showed that the tendency of building thermal fatigue cracks in aluminium die casting could be lowered significantly by plasma nitriding prior film deposition. It is also well known that plasma nitriding can improve coating adhesion significantly [31,32]. Within this work, plasma nitriding was performed in the PACVD units without white compound layer before coating deposition [19].

Substrates used within this study were die-casting core pins and moulds made of hot-working steel 1.2343 (quenched and tempered to a hardness of 48 HRC or 33 HRC for cores or moulds respectively), ground and polished specimens of the same steel, and (100) silicon sheets. Coating characterization was performed with respect to thickness (spherical abrasion test), morphology (scanning electron microscopy, SEM), chemical composition (wavelength dispersive electron-probe microanalysis, EPMA), microstructure (X-ray diffraction, XRD), hardness (Vickers microhardness), and adhesion (scratch test and VDI Rockwell indentation). Application-related properties have been evaluated using thermal cycling immersion tests in liquid aluminium, thermo-gravimetric analysis (TGA), and stress measurements during thermal cycling. The immersion tests were performed using a thermal cycling fatigue test, where one cycle consists of dipping the sample into a liquid aluminium alloy (AlSi7Mg) at 700°C and the subsequent cooling of the sample by pressurized air. No lubricating compounds were applied during the test. As samples, ground and polished truncated cones (height, 10 mm; larger diameter, 25 mm; smaller diameter, 15 mm) of

hot-working tool steel were used. The TGA tests were done in dry oxygen/argon at a flow ratio of 2/5 using a Netzsch TGA system. Samples (hot-working tool steel, size: diameter 5×1 mm) were heated at a rate of 5°C min^{-1} up to 925°C , and the mass gain was recorded with a sensitivity of $1.25 \mu\text{g}$. Film stresses were measured from the bending of coated silicon specimens ($20 \times 7 \times 0.42 \text{ mm}^3$) using the Stoney formula [33]. The bending was measured by the deflection of two parallel laser beams reflected from the sample surface. During the measurement, the sample was heated in vacuum (pressure $\leq 10^{-2} \text{ Pa}$) up to 720°C at a rate of 5°C min^{-1} and cooled down afterwards.

To evaluate the suitability of the coatings, coated core pins and moulds (size up to $520 \times 520 \times 300 \text{ mm}^3$) have been tested in industrial pressure die casting of the aluminium alloy AlSi9Cu3. Tenifer®-treated core pins [34] have been evaluated for comparison. The casting conditions and the spraying of the lubricating compound were not changed from the standard procedure. After service, cores, moulds, and test specimens were examined using SEM and optical microscopy.

3. Results and discussion

3.1. Coating characterization

The aim of this paper is to report on the application of hard coatings in aluminium die casting. Therefore, only essential data on characterization of film structure, hardness and adhesion are given here. Detailed results have been published in previous papers [12,28,29].

Typical composition ranges of the coatings investigated are shown in Table 2. Additions of small amounts of aluminium or boron are known to improve hardness as well as oxidation resistance of TiN-based coatings [35,36]. Owing to formation of a continuous solid solution [in the case of Ti(C,N)] or to the existence of a metastable phase in the case of alloying with Al [37] or low contents of B [38], all coatings show a single-phase fcc TiN structure. All films deposited have dense

Table 2
Chemical composition of the films deposited

Element (at.%)	Deposition method/coating system				
	Sputtering		PACVD		
	TiN	TiN	Ti(C,N)	Ti(B,N)	(Ti,Al)(C,N)
Ti	51	46–47	43–44	43–44	37–43
Al					2–8
B				10–11	
N	49	47–50	33–34	40–42	29–53
C			15–17		1–21
Cl		3–6	6–7	4–6	1–5

and fine-grained structures [12,28,29]. The chlorine content in the PACVD films, which is due to the comparatively low deposition temperatures (see Table 1), may hinder columnar growth of TiN-based hard coatings due to repeated nucleation [39]. Film hardness for sputtered TiN, PACVD TiN, Ti(C,N), Ti(B,N), and (Ti,Al)(C,N) coatings reached values of 2400 [28,40,41], 2050, 2400, 2500, and 2850 HV0.01 [12], respectively. On account of the low hardness of the hot-working tool steel used, the critical load determined using the scratch test for coating delamination varied between 20 and 30 N. The adhesion according to the VDI Rockwell indentation test was classified as HF1 to HF2.

3.2. Die casting application

The application of thin hard coatings instead of the commonly applied thick oxide-based die coatings in gravity die casting changes the thermal situation of the hot-working steel significantly. Fig. 2 shows the dependence of the temperature measured about 0.2 mm below the substrate–coating interface on the testing time during the thermal cycling immersion test. Using a sprayed die coating with a typical thickness of 200 μm , the average sample temperature for five cycles reached a value of $263 \pm 32^\circ\text{C}$. In contrast, for all PVD and PACVD hard coatings investigated within this study a value of about $322 \pm 46^\circ\text{C}$ was obtained, without significant influence of the coating material used. This difference is attributed to the porous structure and the higher thickness of the die coating with respect to the hard coatings. For example, the surface topography of the die coating with the characteristic high roughness and porosity is shown in Fig. 3. However, it should be noted at this point that, owing to the lack of application of a lubricating and parting compound and to a measuring point below the die surface, the actual surface temperatures are expected

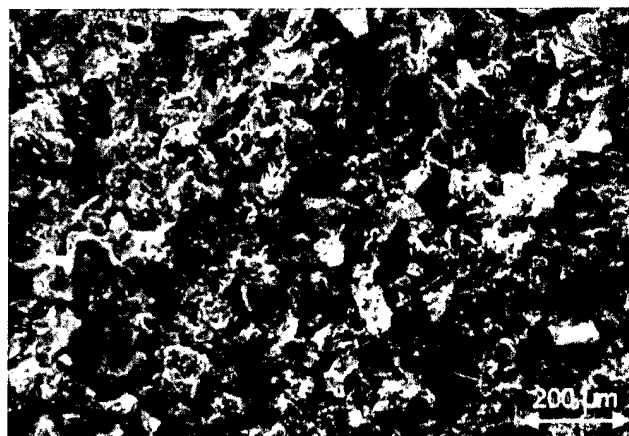


Fig. 3. SEM micrograph of the surface of an oxide-based die coating.

to show more pronounced extremes than those shown in Fig. 2. The decreasing temperature with increasing test time (see Fig. 2) is attributed to the formation of an oxide layer on the surface of the liquid aluminium. A first rough estimation of the performance of the samples was also achieved by the immersion test, where soldered aluminium had to be removed from time to time from the Ti(B,N) coatings.

Testing of PACVD-coated pin-cores in industrial application showed that all coatings increased the life-time significantly with respect to Tenifer®-treated cores (see Fig. 4 for the minimum and maximum numbers of shots achieved). On average, and excluding those data where failure occurred due to fracture of the core, TiN and Ti(C,N) coatings performed best. Fig. 5 shows an optical microscopy cross-section of a PACVD Ti(C,N)-coated core pin after service. As can be seen from the SEM inset showing a gap between coating and aluminium alloy, the coating is well suited to hinder soldering. In those areas where coating detachment has occurred, rapid erosion and corrosion has taken place. Reaction products of intermetallic phases consisting of Al, Cu,

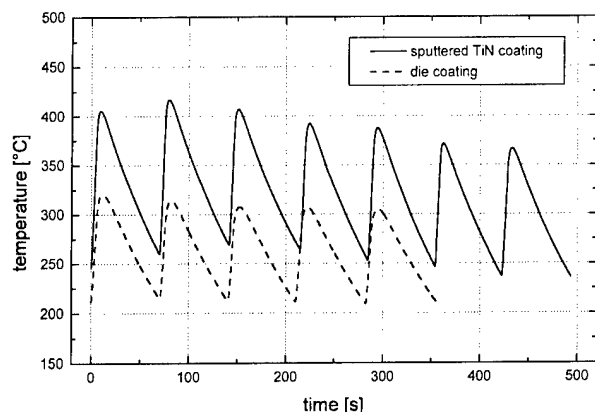


Fig. 2. Dependence of the sample temperature on testing time during cyclic immersion testing of a TiN-coated hot-working steel sample and a hot-working steel sample with die coating.

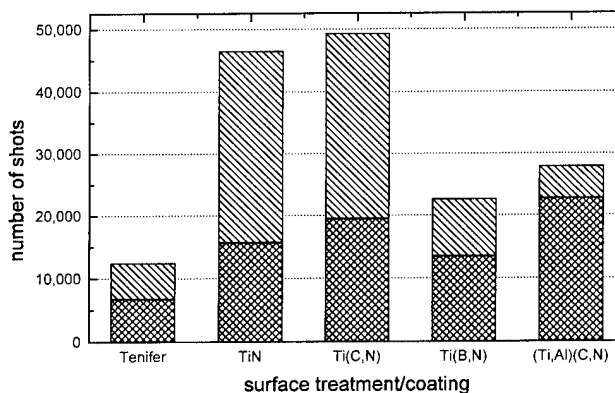


Fig. 4. Number of shots achieved in aluminium pressure die-casting for different surface treatments and PACVD coatings till an insufficient casting surface quality results.

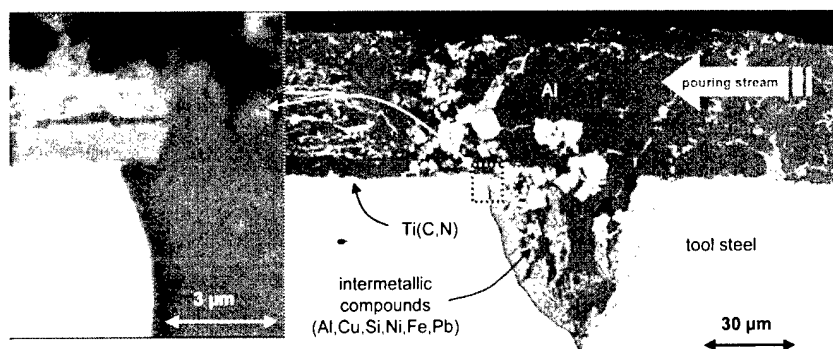


Fig. 5. Cross-section of the damage of a PACVD Ti(C,N)-coated core pin in aluminium pressure die-casting (the inset on the left shows the corresponding SEM cross-section).

Si, Ni, Fe, and Pb have been formed, which are easily washed out of the corrosion zone by the pouring stream.

3.3. Failure analysis

All coatings investigated proved to be suitable for enhancing the lifetime of aluminium die-casting dies. There are significant differences in the efficiency of the individual coatings that cannot be understood immediately. For example, it is well known that aluminium- or boron-containing coatings show superior oxidation resistance with respect to TiN or Ti(C,N) [35,36,42–47]; however, they seem to be less capable of protecting the tool steel (see Fig. 4). This result is also in contrast to the findings published by Pfohl and co-workers [13,15] who found that PACVD Ti(B,N) coatings with boron contents of up to 60 at.% had a superior performance with respect to TiN or (Ti,Al)N films in aluminium die casting. Within this investigation, the TGA oxidation rate measurements for the coatings investigated also confirmed the higher oxidation resistance of PACVD Ti(B,N) and (Ti,Al)(C,N) coatings with respect to TiN and Ti(C,N) coatings (see Fig. 6). The onset for rapid oxidation and rutile formation [46,47]

for Ti(B,N) and (Ti,Al)(C,N) during $5^{\circ}\text{C min}^{-1}$ thermal ramping occurs at $\sim 760^{\circ}\text{C}$, whereas the oxidation temperature for TiN and Ti(C,N) decreases to $680\text{--}690^{\circ}\text{C}$. It has to be noted that the oxidation temperature for both Ti(B,N) and (Ti,Al)(C,N) exceeds the maximum temperature in aluminium die casting and, consequently, formation of the protective rutile layer is hindered. The higher onset for rapid oxidation of the sputtered TiN coating is attributed to the lack of chlorine.

Intrinsic film stresses have been considered by several authors as showing a major effect on high-temperature properties of hard coatings [35,44,46,48]. For the formation of thermal fatigue cracks the dependence of stresses on the temperature is assumed to be crucial [49]. An example for this dependence is shown in Fig. 7 for the coatings used in this work deposited onto silicon substrates. Owing to the low thermal expansion coefficient of silicon ($3 \times 10^{-6} \text{ K}^{-1}$ [50]) with respect to the coatings investigated (exact data are to our knowledge only known for TiN, i.e. $9.4 \times 10^{-6} \text{ K}^{-1}$ [46,51]), almost all coatings are under tensile stress in the as-deposited condition. The compressive stress of (Ti,Al)(C,N) coatings is attributed to the higher discharge voltage used for deposition (see Table 1) and to the incorporation of aluminium atoms. As the film-substrate composite is heated, the tensile stress component is relaxed and the film may go into a state of compression. Temperatures above 600 to 650°C may result in (stress-induced) relaxation of lattice defects and grain boundary sliding [52,53], leading to the onset of a deviation from the thermoelastic loading line, i.e. plastic deformation. This is most prominent in the case of the (Ti,Al)(C,N) coating, where the highest compressive stresses have been measured. For those coatings reaching a considerable tensile stress state during cooling, i.e. PACVD TiN, Ti(C,N), and Ti(B,N), a tensile crack pattern is formed (see Fig. 8). The formation of these cracks is responsible for the flattening of the cooling portion of the curve and, in addition to the probable occurrence of microstructural changes during the high-temperature phase,

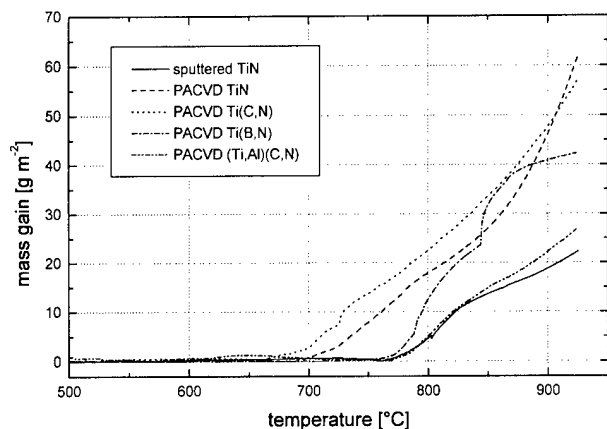


Fig. 6. Dependence of the mass gain on the annealing temperature in an argon-oxygen atmosphere for different coatings.

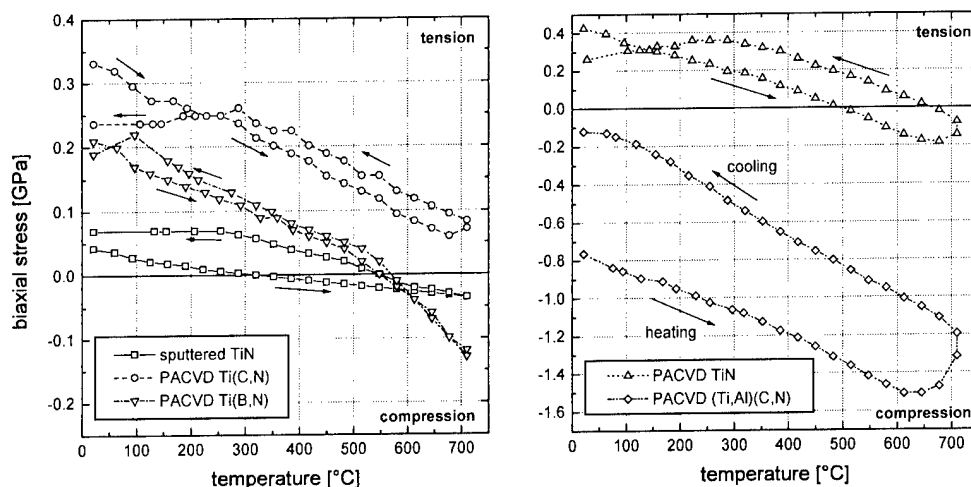


Fig. 7. Dependence of the biaxial film stress on the temperature for different coatings on silicon substrates.

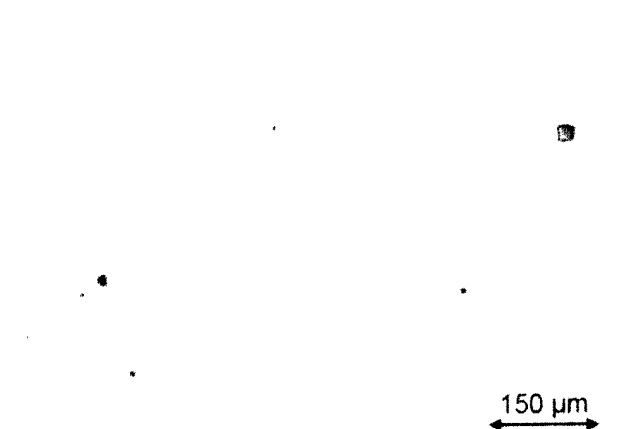


Fig. 8. Optical micrograph of the surface of a PACVD Ti(B,N) coating on a silicon substrate after one thermal cycle up to 720°C.

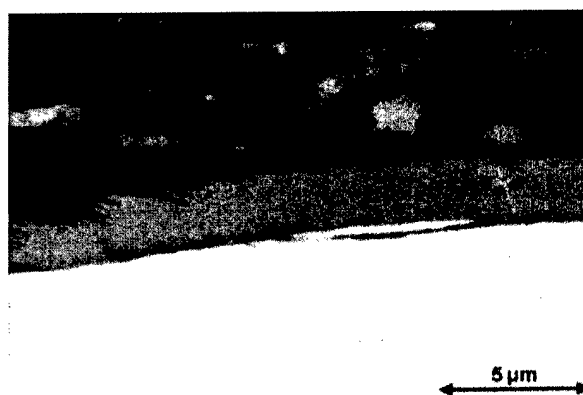


Fig. 9. SEM cross-section of a PACVD Ti(B,N) coated core pin after service.

4. Conclusions

for the final stress state reached at the end of the first cycle.

The thermal expansion coefficient of the hot-working tool steel used in this work is higher than that of silicon and increases from 11.5×10^{-6} to $13.2 \times 10^{-6} \text{ K}^{-1}$ in the temperature range between 20 and 700°C [54]. Therefore, it can be assumed that the curves shown in Fig. 7 are shifted towards the compressive stress region where tensile cracking is avoided [55]. This is also confirmed by Fig. 9, where crack propagation into the substrate and coating detachment due to high compressive stresses is shown for a coated core pin after service in aluminium die casting. According to the Coffin–Manson relationship for low cycle fatigue [56], where the plastic strain amplitude applied during thermal cycling governs the number of cycles to failure, those coatings showing the lowest compressive stresses can be assumed to perform in a superior manner.

Hard coatings based on TiN have been proven to increase the lifetime of aluminium die-casting dies by several hundreds of percent due to a reduction of erosion, corrosion and soldering processes and due to an increase of the thermal fatigue limit. The best performance has been obtained for TiN and Ti(C,N) coatings showing an optimum combination of hardness, adhesion, soldering behaviour, oxidation resistance, and stress state. Ti(B,N) and (Ti,Al)(C,N) coatings exhibited a superior oxidation resistance, but they showed a higher soldering tendency and/or higher compressive stresses leading to rapid thermal fatigue. In addition, for these coatings the pouring temperatures may not be sufficient to form a protective oxide layer during service. Finally, we have been able to show that the PACVD technology is very well suited to coating large and heavy dies of complex shape with a uniform coating thickness and homogeneity. Up to now, moulds with maximum

size of $520 \times 520 \times 300 \text{ mm}^3$ have been coated and tested in pressure die casting. However, although successfully transferred to industrial application, a lot of work is still necessary for further up-scaling of deposition processes, improving coating properties and re-designing casting geometry due to the changed solidification process.

Acknowledgements

The authors are grateful to the Forschungsförderungsfonds für die gewerbliche Wirtschaft for financial support of this work under contracts 6/850, 6/898, and 800335 and to the companies Georg Fischer Automobilguss AG, Herzogenburg, and Karl Fink GmbH, Kaindorf, for their co-operation. One of the authors (F.Ü.) acknowledges the support of the Österreichischer Akademischer Austauschdienst.

References

- [1] M.M. Gosh, S. Seshan, *Indian Foundry J.* 40 (6) (1994) 45.
- [2] R. Shivpuri, S.L. Semiatin, in: D. Olsen (Ed.), *Friction Lubrication and Wear Technology*, ASM Handbook vol. 18, ASM, Materials Park, OH, 1992, pp. 621–648.
- [3] K. Bengtsson, S. Pettersson, O. Sandberg, *Heat Treating* 24 (11) (1992) 18.
- [4] R. Danzer, Berg- Hüttenmänn. Monatsh. 129 (5) (1984) 135.
- [5] E. Lugscheider, C. Barimani, S. Guerreiro, K. Bobzin, *Surf. Coat. Technol.* 108–109 (1998) 109–408.
- [6] L.-Å. Norström, B. Klarenfjord, M. Svensson, *Gießerei-Praxis* 9 (1994) 204.
- [7] S. Malm, L.-Å. Norström, *Met. Sci.* 9 (1979) 544.
- [8] R. Danzer, F. Sturm, A. Schindler, W. Zleppnig, *Gießerei-Praxis* 19–20 (1983) 1287.
- [9] W. Young, *Gießerei-Praxis* 21 (1980) 325.
- [10] D. Sobol, *Die Cast. Eng.* 29 (11–12) (1985) 52.
- [11] J. Worbye, *Gießerei-Praxis* 1–2 (1987) 7.
- [12] D. Heim, F. Holler, C. Mitterer, *Surf. Coat. Technol.* 116–119 (1999) 497.
- [13] C. Pfohl, K.-T. Rie, *Surf. Coat. Technol.* 116–119 (1999) 911.
- [14] K.-T. Rie, A. Gebauer, C. Pfohl, *Galvanotechnik* 89 (10) (1998) 3380.
- [15] C. Pfohl, A. Gebauer-Teichmann, K.-T. Rie, *Mat.-wiss. Werkstofftech.* 29 (1998) 51.
- [16] K.-T. Rie, C. Pfohl, S.H. Lee, C.S. Kang, *Surf. Coat. Technol.* 97 (1997) 232.
- [17] K.-T. Rie, A. Gebauer, J. Wöhle, *Surf. Coat. Technol.* 86–87 (1996) 87–498.
- [18] K.-T. Rie, A. Gebauer, C. Pfohl, *J. Phys. IV* 5 (1995) 637.
- [19] J. Walkowicz, J. Smolik, K. Miernik, J. Bujak, *Surf. Coat. Technol.* 97 (1997) 453.
- [20] P. Hairy, M. Richard, *Gießerei-Praxis* 19–20 (1997) 405.
- [21] E. Bernacchi, A. Ferrero, E. Gariboldi, A. Korovkin, G. Pontini, *Metall. Sci. Technol.* 14 (1) (1996) 3.
- [22] Y. Wang, *Surf. Coat. Technol.* 94–95 (1997) 60.
- [23] O. Knotek, F. Löffler, B. Bosserhoff, *Surf. Coat. Technol.* 62 (1993) 630.
- [24] R. Wild, *Giesserei* 80 (20) (1993) 696.
- [25] F.J. Teeter, *Proceedings International Conference on Die Casting Technology*, North American Die Casting Association, Rosemont, 1993, pp. 233–237.
- [26] K.A. Pischow, S.O. Kivivuori, A.S. Korhonen, *J. Mater. Process. Technol.* 32 (1992) 55.
- [27] E. Ford, *Die Cast. Eng.* 34 (5) (1990) 36.
- [28] P. Losbichler, C. Mitterer, *Surf. Coat. Technol.* 97 (1997) 568.
- [29] D. Heim, R. Hochreiter, *Surf. Coat. Technol.* 98 (1998) 1553.
- [30] C.M.D. Starling, J.R.T. Branco, *Thin Solid Films* 308 (1997) 309–436.
- [31] T. Gredić, M. Zlatanović, N. Popović, Ž. Bogdanov, *Thin Solid Films* 228 (1993) 261.
- [32] T. Gredić, M. Zlatanović, N. Popović, Ž. Bogdanov, *Surf. Coat. Technol.* 54–55 (1992) 502.
- [33] G.G. Stoney, *Proc. R. Soc. London Ser. A* 82 (1909) 172.
- [34] F. Klein, *Giesserei* 22 (1992) 928.
- [35] C. Jarms, H.-R. Stock, P. Mayr, *Surf. Coat. Technol.* 108–109 (1998) 206.
- [36] C. Héau, R.Y. Fillit, F. Vaux, F. Pascaretti, *Surf. Coat. Technol.* 120–121 (1999) 200.
- [37] H.A. Jehn, S. Hofmann, V.-E. Rückborn, W.-D. Münz, *J. Vac. Sci. Technol. A* 4 (6) (1986) 2701.
- [38] J. Laimer, H. Karner, H. Störi, P. Rödhammer, *Mater. Sci. Forum* 140 (1993) 142–493.
- [39] P.B. Barna, in: L. Eckertova, T. Růžicka (Eds.), *Diagnostics and Applications of Thin Films*, Institute of Physics, Bristol, 1992, pp. 295–310.
- [40] E. Kelesoglu, C. Mitterer, M.K. Kazmanli, M. Ürgen, *Surf. Coat. Technol.* 116–119 (1999) 133.
- [41] C. Mitterer, P.H. Mayrhofer, E. Kelesoglu, R. Wiedemann, H. Oettel, *Z. Metallkde.* 90 (8) (1999) 602.
- [42] L.A. Donohue, I.J. Smith, W.-D. Münz, I. Petrov, J.E. Greene, *Surf. Coat. Technol.* 94–95 (1997) 226.
- [43] F. Vaz, L. Rebouta, M. Andrichky, M.F. da Silva, J.C. Soares, *J. Am. Ceram. Soc.* 17 (1997) 1971.
- [44] C.W. Kim, K.H. Kim, *Thin Solid Films* 307 (1997) 113.
- [45] S. Inoue, H. Uchida, Y. Yoshinaga, K. Koterazawa, *Thin Solid Films* 300 (1997) 171.
- [46] D. McIntyre, J.E. Greene, G. Håkansson, J.-E. Sundgren, W.-D. Münz, *J. Appl. Phys.* 67 (3) (1990) 1542.
- [47] M. Wittmer, J. Noser, H. Melchior, *J. Appl. Phys.* 52 (11) (1981) 6659.
- [48] R. Wiedemann, H. Oettel, *Surf. Eng.* 14 (4) (1998) 299.
- [49] W.D. Nix, *Metall. Trans. A*: 20 (1989) 2217.
- [50] R.C. Weast (Ed.), *Handbook of Chemistry and Physics*, 55th ed., CRC Press, Cleveland, OH, 1974, p. D152.
- [51] H. Holleck, *J. Vac. Sci. Technol. A* 4 (6) (1986) 2661.
- [52] J. Schiøtz, F.D. Di Tolla, K.W. Jacobson, *Nature* 391 (1998) 561.
- [53] C. Mitterer, P.H. Mayrhofer, M. Beschliesser, P. Losbichler, P. Warbichler, F. Hofer, P.N. Gibson, W. Gissler, H. Hruby, J. Musil, J. Vlček, *Surf. Coat. Technol.* 120–121 (1999) 405.
- [54] Böhler, *Edelstahl-Handbuch*, Böhler, Kapfenberg, 1989.
- [55] V. Tomala, T. Hirsch, P. Mayr, *Surf. Eng.* 15 (1) (1999) 59.
- [56] S. Suresh, *Fatigue of Materials*, Cambridge University Press, Cambridge, 1991.

New coatings on metal sheets and strips produced using EB PVD technologies

S. Schiller, Chr. Metzner *, O. Zywitzki

Fraunhofer-Institut für Elektronenstrahl und Plasmatechnik (FEP), Winterbergstraße 28, 01277 Dresden, Germany

Accepted 13 October 1999

Abstract

PVD coatings deposited by electron beam (EB) evaporation on large metal sheets and metal strips are discussed and have been used for many years. Recently developed plasma activated technology has opened up new potential applications. The new coatings produced by EB PVD represent an outstanding supplement to existing products. It is verified that the deposition costs are low enough in comparison to competitive technologies.

Dense Ti layers are produced with high deposition rates up to 1000 nm s^{-1} by EB evaporation in combination with effective plasma activation by a spotless arc (SAD-process). The corrosion resistance of the coatings deposited with this SAD process and an additional bias voltage can be drastically improved in comparison to deposition without plasma activation.

Aluminum oxide coatings were deposited by reactive EB evaporation at deposition rates between 50 and 100 nm s^{-1} . The influence of plasma activation using a hollow cathode low-voltage electron beam (HAD process) on the structure and properties of Al_2O_3 coatings have been investigated. It could be shown that the coatings deposited with the HAD process have a drastically increased hardness, higher density and an improved chemical stability in comparison to the coatings deposited without plasma activation.

Stone-blasting resistance can be improved and good formability of galvanised steel can be maintained by a thin Fe layer. The Fe layer is deposited by high rate EB evaporation and then via a subsequent annealing process an intermetallic compound top layer is created. © 2000 Elsevier Science S.A. All rights reserved.

Keywords: Al_2O_3 ; Electron beam evaporation; Galvanized steel; Plasma activation; Titanium

1. Introduction

The use of EB PVD processes for the coating of large areas, such as metal sheets and strips, has been investigated for many years. Some industrial applications are corrosion-resistant coatings, optical layer stacks and thermal barrier coatings. Further potential applications include anti-abrasive and wear-resistant coatings, lubricating coatings and conversion coatings for the replacement of chromating and phosphating [1–3].

High quality EB PVD coatings, which are not producible by conventional processes such as electrochemical deposition (ECD) or hot-dipping, stand the best chance for introduction into industrial applications. A further demand is that the coating costs are reasonable when compared with those of the competing processes.

Costs can be lowered through high deposition rates [4]. The ecological acceptability of the PVD technology is another reason for its future use.

The EB evaporation by axial guns allows very high deposition rates of up to several 1000 nm s^{-1} . Because of the low thermal energy of the vapor particles, the condensed particles have, however, only a limited mobility. This limited mobility leads to shadowing effects and to the formation of coatings with columnar microstructures and high porosity. The coatings are in most cases insufficient in their hardness, chemical resistance and adhesion [5,6].

It has long been known that through the application of ion assisted processes, such as ion plating (IP) and ion beam assisted deposition (IBAD), considerable improvements in the characteristics of the coatings can be achieved [7–12]. For high rate EB evaporation the plasma densities must be adapted to the high deposition rates and to the large coating areas. The activation of the plasma by a spotless arc (SAD process) and its

* Corresponding author. Tel.: +49-351-2586-240;
fax: +49-351-2586-105.

E-mail address: metzner.c@fep.fhg.de (C. Metzner)

activation by a hollow cathode low-voltage electron beam (HAD process) are presented here as possible solutions. The maximum ion current density reached on the substrate was 50 mA cm^{-2} with the HAD process, whilst the SAD process reached up to 400 mA cm^{-2} . These ion current densities are considerably higher than when conventional methods are used. The influence of plasma activating processes on the structure and the properties will be demonstrated using Ti and Al_2O_3 coatings as examples.

Another way in which the structure and properties of a surface can be tailored as desired is by the evaporation of a thin coating, followed by diffusion annealing. This is shown in the results achieved by coating of hot-dipped galvanized steel sheets with a thin iron layer deposited by EB evaporation. After an annealing procedure an intermetallic FeZn top layer is formed.

2. Experimental

2.1. EB evaporation with plasma activation by spotless arc (spotless arc deposition; SAD process)

Arc discharges are very well suited to plasma activation during high rate EB evaporation because of their high plasma density and high degree of ionization. A disadvantage of the conventional arc evaporation is the high energy density on the root of the arc. This leads to a high emission of droplets. The incorporation of droplets into the coating are not wanted and can only be avoided with great technical effort [13].

In some metals the so-called spotless arc with an extension of several centimeters appears after the evaporation material has melted. Owing to the decreased energy density on the root of the arc the emission of droplets is avoided.

The SAD process combines EB evaporation with the activation of the plasma due to a spotless arc (Fig. 1). The evaporation crucible is connected as the cathode of the spotless arc. The anode function will be taken on by an additional plasma electrode. The spotless arc is

guided by the electron beam. The arc follows the hottest area of the molten evaporation material. Typical discharge parameters of the spotless arc are between 15 and 40 V for U_{Arc} and between 600 and 2000 A for I_{Arc} . The maximum ion current density on the substrate is 400 mA cm^{-2} .

The appearance of the spotless arc is linked primarily to a sufficiently high thermal emission of electrons. Therefore the formation of spotless arc is limited to metals with a high melting point such as Ti, Mo, Zr and W [14,15]. For metals and alloys with lower melting points, such as FeCrNi for example, a further process has recently been developed which achieves plasma activation by spotless arc through the addition of a rod-shaped hot tungsten cathode (rod cathode activated deposition; RAD process) [16].

Ti coatings with thickness between 5 and $20 \mu\text{m}$ on steel of grade St14 will provide an example of the application of the SAD process for corrosion protection. Deposition rate was varied between 100 and 1000 nm s^{-1} and the substrate temperature (T_s) between 200 and 800°C .

2.2. Reactive EB evaporation with plasma activation by hollow cathode low-voltage electron beam (hollow cathode activated deposition; HAD process)

The HAD process combines high rate EB evaporation with plasma activation by a hollow cathode low-voltage electron beam (Fig. 2).

Typical discharge parameters for the hollow cathode low-voltage electron beam (LVEB) are U_{LVEB} 15 V and I_{LVEB} of 300 A. Plasma densities of 10^{12} cm^{-3} can be achieved. This allows an effective plasma activation even with high deposition rates. The maximum ion current density on the substrate is 50 mA cm^{-2} .

The effectiveness of plasma activation on structure and properties can be shown using the reactive deposition of Al_2O_3 coatings. The EB will therefore be generated in an axial gun and guided onto the aluminum evaporation material. The reactive oxygen gas will be let in a short distance above the crucible. On the way

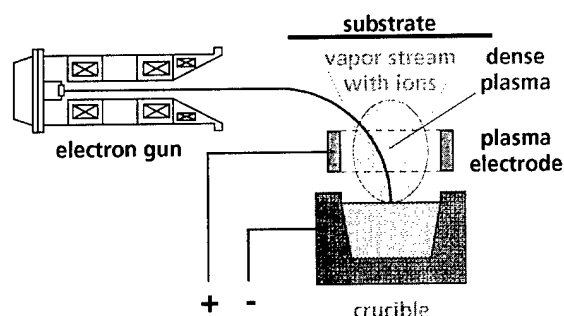


Fig. 1. Schematic arrangement of the EB evaporation with plasma activation using the SAD process.

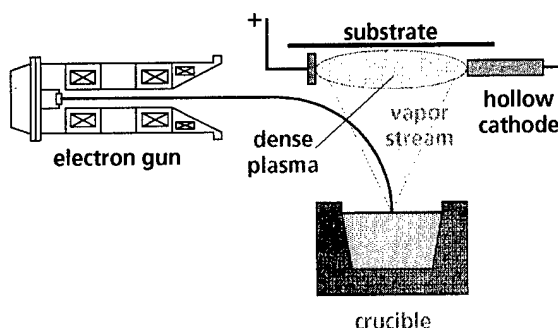


Fig. 2. Schematic arrangement of EB evaporation with plasma activation using the HAD process.

to the substrate both the Al vapor and the reactive O₂ gas must pass through the plasma zone of the LVEB. The coatings were deposited onto steel sheets of the grade X10CrAl24. The deposition rates varied between 50 and 100 nm s⁻¹. The substrate temperature was measured with a thermocouple and varied between 200 and 750°C. Coatings were deposited both with the HAD process and, to provide a comparison, with EB evaporation but without plasma activation.

2.3. Deposition of thin layer by EB evaporation, followed by annealing for diffusion

The deposition of a thin layer by EB evaporation, followed by annealing for diffusion will be explained using a thin iron layer on hot-dipped galvanized steel sheets.

The processes for deposition of zinc coatings are highly developed in ECD and in hot-dipping. A large proportion of the galvanized sheets is used in the varnished state in the automobile industry. Galvanized and varnished sheets, however, has only a slight mechanical resistance to stone-blasting, owing to the low hardness of zinc. As a consequence the varnish adhesion is often not sufficient in the case of stone-blasting.

An established process which improves the resistance to stone-blasting is the galvannealing process, in which iron diffuses from the steel substrate into the zinc coating. This produces a Zn alloy with 8–11 wt% Fe, which consists completely of the intermetallic FeZn phases. The galvannealed steel sheet is characterized by good varnish adhesion and good corrosion resistance. The disadvantage is the brittleness of the FeZn phases, which leads to a higher abrasion and to a deterioration of the further formability.

The aim is therefore to develop galvanized sheets with good corrosion resistance and stone-blasting resistance and with a simultaneously good formability. A solution is expected in the deposition of a thin iron layer by EB evaporation. This coating is then diffused into the zinc by a short annealing procedure. The annealing temperature and duration are controlled so that a FeZn top layer formation with a thickness of 1–2 µm is achieved, whilst the formation of intermetallic phases from the substrate can be almost completely avoided. The composite coating consists then of a sublayer of zinc and a top layer which consists of intermetallic FeZn phases. In this way the good formability of zinc and the greater hardness of the intermetallic FeZn phases are to be combined.

For an undisturbed diffusion of the Fe into the Zn it is necessary to carry out an intensive pretreatment by sputter etching, in order to completely remove oxides from the surface of the Zn coating. Then, without vacuum interruption, a 100–200 nm thick iron layer will be deposited by EB evaporation. The next step is a

short heating in an inert gas atmosphere to a maximum temperature of 400°C, which is also carried out without any vacuum interruption.

3. Results

3.1. Ti coatings deposited by EB evaporation with plasma activation by the SAD process

The influence of plasma activation by spotless arc on the microstructure can be shown with scanning electron microscopy (SEM) micrographs of the cross fractures and the topographies of ca. 5 µm thick Ti coatings, which were deposited, at a substrate temperature of 220°C, without and with plasma activation using the SAD process.

The Ti coating which was deposited without plasma activation has a columnar microstructure with a comparatively rough surface. The columnar grains can be seen over the whole coating and are orientated in the direction of the particles impinging on substrate. The pronounced columnar microstructure is probably caused by a high porosity along the grains [Fig. 3(a)].

In contrast the coating deposited by SAD process has a considerably smoother surface and a more compact, dense fracture [Fig. 3(b)].

In addition, the corrosion resistance of 5–20 µm thick Ti coatings was investigated. The coatings were deposited onto 0.8 mm thick steel sheets of grade St14 with an average roughness value of $R_a = 1.2$ µm. The substrate temperatures were between 600 and 800°C.

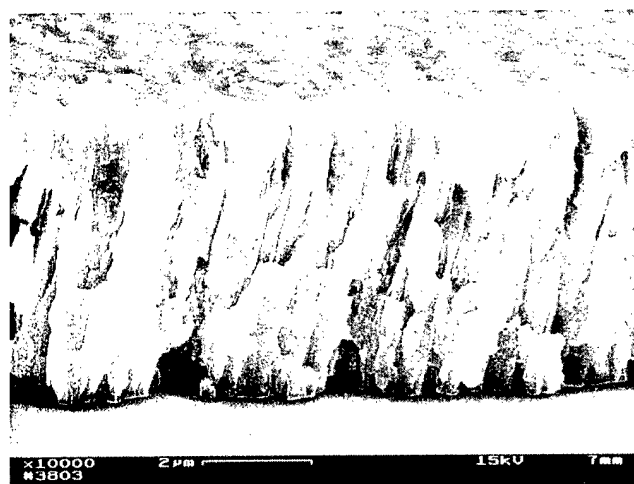
To test the corrosion resistance, the sulfur dioxide test with general condensation of moisture [17] was used. The criterion for sufficient corrosion resistance was that the red rust covering remained <50% after 60 test cycles.

When the spotless arc process was used, the coatings that achieved a sufficient corrosion resistance could be considerably thinner than without plasma activation. Further improvements were possible by raising the arc current from 600 to 2000 A and through the additional use of substrate bias voltage (Fig. 4).

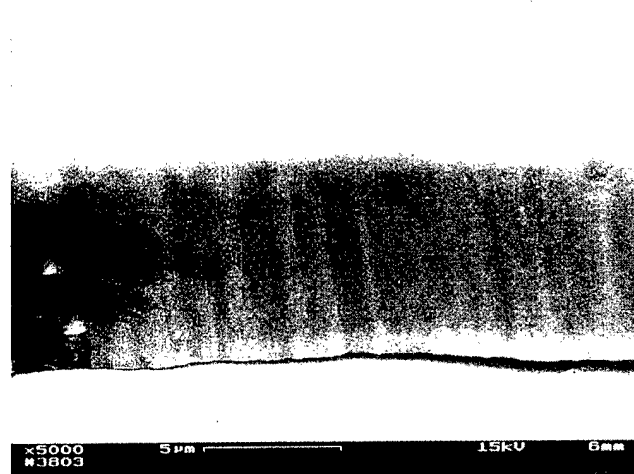
It is remarkable that the considerably higher corrosion resistance brought about by the use of plasma activation could still be found at very high coating rates of up to 1000 nm s⁻¹. This improvement in the corrosion resistance can be explained principally by the denser microstructure of the coatings which are deposited when using plasma activation.

3.2. Al₂O₃ coatings deposited by reactive EB evaporation with plasma activation by the HAD process

Plasma activation by hollow cathode low voltage electron beam causes a considerable increase in the



a)



b)

Fig. 3. SEM cross fracture and topography of titanium coatings deposited by EB evaporation at a substrate temperature of 220°C: (a) without plasma activation; (b) with plasma activation using the SAD process ($I_{Arc}=600$ A; $U_{Bias}=0$ V).

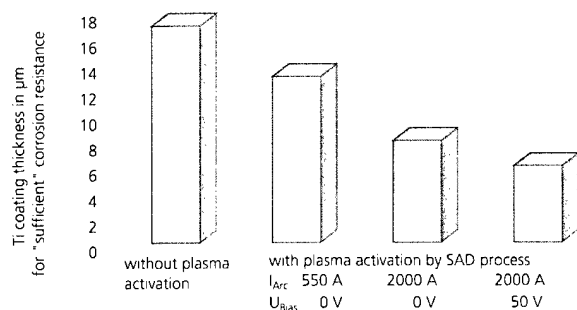
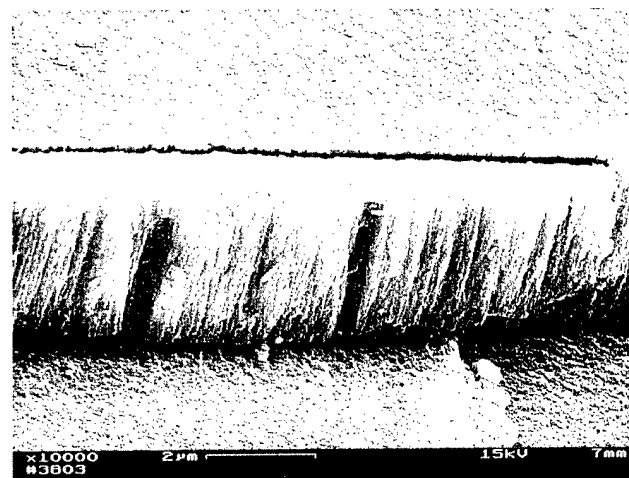


Fig. 4. The thickness of Ti coatings 'sufficient' for corrosion resistance can be drastically reduced with plasma activation using the SAD process. A further improvement can be achieved by increasing the arc current and additional substrate bias voltage (deposition rates 500–1000 nm s⁻¹; substrate temperature 600–800°C).

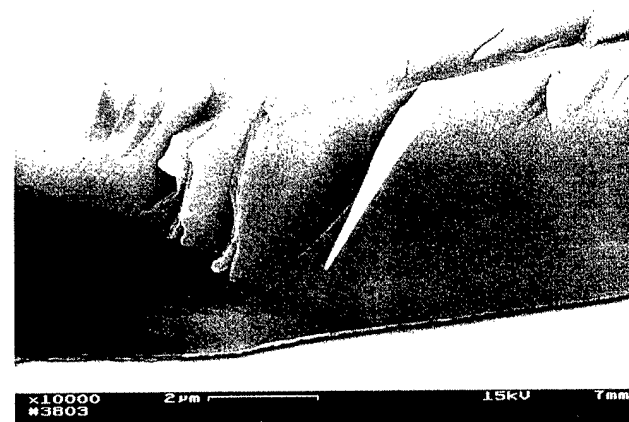
density of the Al₂O₃ coatings. In addition, the stoichiometric composition of the coatings deposited with plasma activation is nearly ideal, the Al/O ratio is 0.66–0.7, whereas the coatings without plasma activation have an Al/O ratio of 0.55–0.57, that is, they contain superfluous oxygen.

SEM micrographs of coatings are shown as examples of the microstructures which are produced without and with HAD process, both at a substrate temperature $T_s=500^\circ\text{C}$. Even at this rather high substrate temperature the coating deposited without plasma activation has a porous columnar microstructure and a relatively rough surface [Fig. 5(a)]. On the other hand, a coating produced with the HAD process has a glassy like, brittle fracture and a very smooth surface [Fig. 5(b)].

The structure of all coatings deposited at a substrate temperature of 600°C or lower is amorphous. At T_s of



a)



b)

Fig. 5. SEM cross-fracture and topography of Al₂O₃ coatings deposited by reactive EB evaporation of aluminum at a substrate temperature of 500°C: (a) without plasma activation and (b) with plasma activation using the HAD process.

700°C the coatings deposited with the HAD process are crystalline. The γ - Al_2O_3 phase with cubic spinel structure is identified by X-ray diffraction. However, a coating deposited at $T_s=700^\circ\text{C}$ without plasma activation is still amorphous to X-rays.

The plasma activation increases the hardness of the coatings by a factor of 2–3, depending on the substrate temperature (Fig. 6). The coatings which are deposited without plasma activation have up to a substrate temperature of 700°C an porous amorphous structure and their hardness is only between 4 and 7 GPa, depending on the substrate temperature. In contrast the hardness of the dense amorphous coatings deposited by the HAD process at substrate temperatures of 400–600°C is 12 GPa. The formation of the crystalline γ phase involves a drastic increase in hardness to 19 GPa.

A drastically increased chemical stability could simultaneously be achieved in the coatings prepared with plasma activation. The coatings produced without plasma activation had a etching rate, depending on the substrate temperature, of 430–2600 nm min^{-1} in phosphoric acid heated to 60°C. The etching rate on coatings deposited with the plasma activation was drastically reduced to 8–14 nm min^{-1} . The crystalline coating resulting from the deposition at T_s of 700°C with plasma activation is fully resistant to the heated phosphoric acid (Fig. 7).

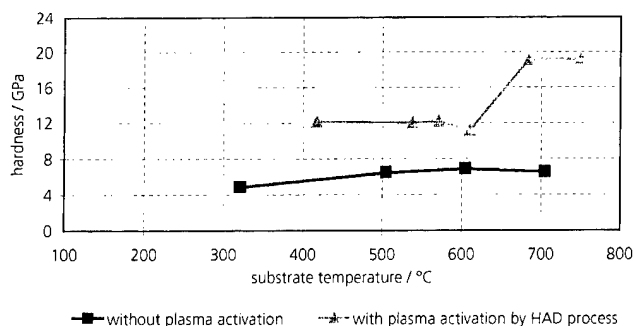


Fig. 6. Influence of substrate temperature and plasma activation using the HAD process on the hardness of reactive deposited Al_2O_3 coatings.

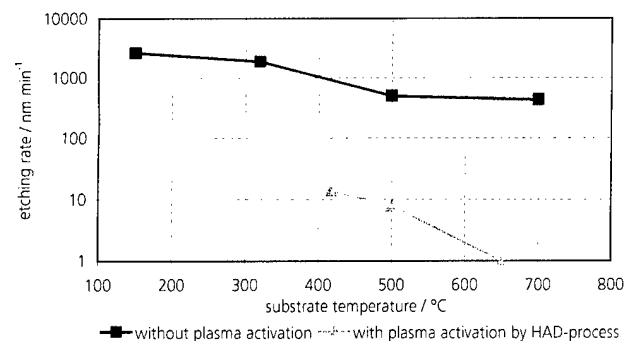


Fig. 7. Influence of substrate temperature and plasma activation using the HAD process on the etching rate of reactive deposition Al_2O_3 coatings in heated phosphoric acid.

3.3. FeZn coatings produced by EB evaporation onto hot-dipped galvanized steel with a subsequent annealing procedure

As a first process step the removal of oxides on the hot-dipped galvanized steel surface by an intense sputter etching is necessary. A 100–200 nm thick iron layer was then deposited by EB evaporation without an interruption to the vacuum. After that a flash annealing procedure up to a maximum temperature of 400°C was carried out in an inert gas atmosphere.

The result is a 1–2 μm thick intermetallic FeZn layer with a Fe content of ca. 8 wt.%, as can be seen in the GDOES Profile (Fig. 8). XRD phase analysis shows that the layer consists primarily of the intermetallic ξ phase (FeZn_{13}).

A metallographic cross-section (Fig. 9) clearly shows a 2 μm thick intermetallic FeZn layer which is formed by diffusion annealing. One can also see that the formation of FeZn phases arising in the steel substrate interface could largely be avoided. The hardness of the layers

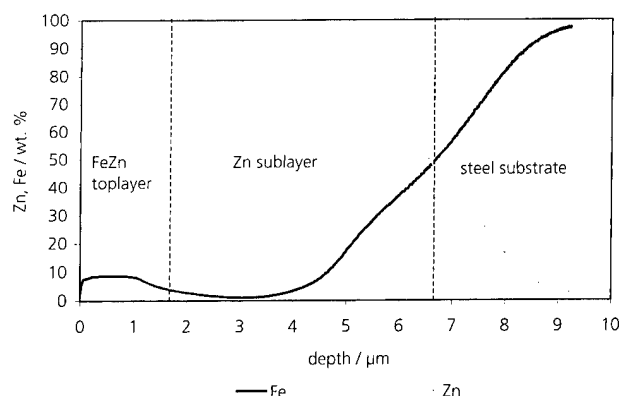


Fig. 8. GDOES composition depth profile after an annealing procedure of a 200 nm thick iron layer on hot-dipped galvanized steel. By a diffusion process an intermetallic FeZn top layer with ca. 8 wt.% Fe is formed.

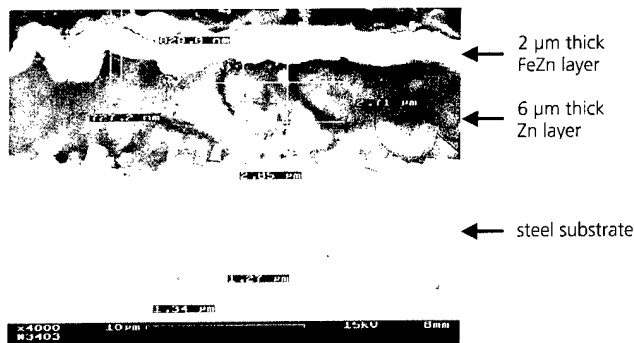


Fig. 9. SEM investigation and Vicker's hardness measurements with a constant load 0.1 gf on a metallographic cross-section. At the top an ca. 2 μm thick intermetallic FeZn layer above a 6 μm thick Zn sublayer can be recognized. The hardness for the FeZn layer is 3.0 GPa, that of the Zn sublayer is 0.25 GPa and that of steel substrate 1.1 GPa.

and the substrate were determined by indentations with a Vicker's indenter at a constant load of 0.1 gf. The size of the indentations were measured using SEM. For the intermetallic FeZn top layer the hardness is 3 GPa, that of the zinc sublayer 0.25 GPa, and that of the steel substrate 1.1 GPa.

The newly formed layer stack consists therefore of a 1–2 µm thick, hard intermetallic FeZn top coating above an ca. 6 µm thick soft zinc coating. The good formability of zinc and the stone-blasting resistance of the FeZn phases are thus combined in this new product.

The tests on stone-blasting resistance showed equally good results as those achieved with galvanized steel sheet, whose coating contains only intermetallic FeZn phases. The disadvantage of galvanized steel sheet, that is, the high abrasion during subsequent deformation is avoided in the new layer stack of ductile zinc and intermetallic FeZn. Further the new product has a good formability such as hot dipped galvanized steel.

4. Summary and conclusions

Possible new applications for high rate EB evaporation in connection with effective plasma processes have been demonstrated. The quality achieved in the coatings is promising.

The use of the SAD process, for example, leads to Ti coatings of a high density which are also very resistant to corrosion. The coating thickness required to provide sufficient protection from corrosion can therefore be dramatically reduced. Using the HAD process, Al₂O₃ coatings can be deposited which are two to three times harder than coatings deposited without the plasma activation, as well as being considerably more stable chemically.

New and improved properties could be achieved by the EB evaporation of a thin iron coating onto hot-dipped steel followed by annealing. The new product has a high stone-blasting resistance as well as good formability.

The processes introduced here offer great potential for new applications of EB PVD techniques and the

development of new products at reasonable coating costs. The next step must be the transfer of the results into industrial applications.

Acknowledgements

The investigations into the corrosion-protective action of Ti coatings on sheet steel were in part conducted within the framework of a project (14 N 6139) sponsored by the German Federal Government and in cooperation with the German steel industry. The authors are especially grateful to Dr. Steinhoff (Stahlwerke Bremen GmbH) for carrying out the comprehensive corrosion tests.

References

- [1] W. Duerr, G. Hoetzs, J. Kuhn, W. Schlump, *Stahl und Eisen* 113 (1993) 79.
- [2] Chr. Metzner, K. Goedicke, G. Hoetzs, B. Scheffel, J.-P. Heinss, *Surf. Coat. Technol.* 94–95 (1997) 663.
- [3] R.A. Haefer, *Oberflächen und Dünnschicht-Technologie*, Springer Verlag, Berlin, 1987.
- [4] S. Schiller, G. Hoetzs, K. Goedicke, O. Zywitzki, 1995. Proc. 38th Annual Technical Conference of the Society of Vacuum Coaters (SVC), Chicago, USA, April 1995, p. 401.
- [5] B.A. Movchan, A.V. Demchishin, *Phys. Met. Metallogr.* 28 (1969) 83.
- [6] H.K. Pulker, *Surf. Coat. Technol.* 112 (1999) 250.
- [7] R.F. Bunshah, A.C. Raghuram, *J. Vac. Sci. Technol.* 9 (1972) 1385.
- [8] D.M. Mattox, *J. Vac. Sci. Technol.* 10 (1973) 47.
- [9] A. Matthews, T.G. Teer, *Thin Solid Films* 80 (1981) 41.
- [10] J.R. Morley, H.R. Smith, *J. Vac. Sci. Technol.* 9 (1972) 1377.
- [11] R. Buhl, H.K. Pulker, E. Moll, *Thin Solid Films* 80 (1981) 265.
- [12] P.J. Martin, *J. Mater. Sci.* 21 (1986) 1.
- [13] R.L. Boxman, S. Goldsmith, *Surf. Coat. Technol.* 52 (1992) 39.
- [14] K. Goedicke, B. Scheffel, S. Schiller, *Surf. Coat. Technol.* 68/69 (1994) 799.
- [15] Chr. Metzner, B. Scheffel, K. Goedicke, *Surf. Coat. Technol.* 86/87 (1996) 86.
- [16] B. Scheffel, Chr. Metzner, K. Goedicke, J.-P. Heinss, O. Zywitzki, 1999. Paper presented at ICMCTF 99, San Diego, California, 12–16 April.
- [17] ISO, 1985. Metallic and other non-organic coatings: sulfur dioxide test with general condensation of moisture. ISO 6988.

Sputtered silicon carbide thin films as protective coating for MEMS applications

N. Ledermann^{a,*}, J. Baborowski^a, P. Muralt^a, N. Xantopoulos^b, J.-M. Tellenbach^c

^a *Laboratoire de Céramique (LC), Ecole Polytechnique Fédérale de Lausanne (EPFL), 1015 Lausanne, Switzerland*

^b *Laboratoire de Métallurgie Chimique (LMCH), Ecole Polytechnique Fédérale de Lausanne (EPFL), 1015 Lausanne, Switzerland*

^c *Mettler-Toledo GmbH, 8606 Greifensee, Switzerland*

Abstract

There is a need for chemically resistant coatings that protect the exposed surface of microfluidics components. Pinhole free films with low stress and a good uniformity on flat and inclined surfaces are required. In this study, amorphous silicon carbide (SiC) thin films have been deposited by RF magnetron sputtering on flat surfaces and into micromachined cavities of Si (100). The variation of RF power, deposition pressure and substrate bias voltage have been studied. Depending on the deposition conditions, the film stress can be adjusted from -1400 MPa to $+100$ MPa. Modifications of the deposition rate and the morphology between normal and inclined (54.7°) planes have been observed. Optimal chemical stability was found with slightly compressive (-100 MPa) SiC thin films. No degradation of the protective layer has been observed after 3 h in KOH at 80°C . © 2000 Elsevier Science S.A. All rights reserved.

Keywords: Film stress; MEMS; Protective coating; Silicon carbide

1. Introduction

In the advancement of micromachined transducers for life science or microfluidic applications [1], one particularly challenging area is the corrosion resistance of the devices in such media as caustic gases or biological systems. For this, inert protective coatings deposited at low temperature that do not deteriorate upon repeated or continual exposure are required. Silicon carbide has long been recognized as an ideal material for application where superior attributes such as hardness, high thermal conductivity, low coefficient of thermal expansion and chemical and oxidation resistance are of primary value. With heat conductivity three times greater than silicon, it is well suited for coatings in heat exchanger applications. Its potential in Micro-Electro-Mechanical Systems (MEMS) was reported for the first time by Klumpp et al. in 1994 [2]. Since then, it has been used as well as protective coating [3,4] or as new sensing material in harsh environment [5–8].

Deposition of SiC thin films can be done either by Physical Vapor Deposition (PVD) [9] or by Plasma

Enhanced Chemical Vapor Deposition (PECVD) [10]. As PVD is a highly directional deposition method, the covering of walls perpendicular to the substrate may not be guaranteed. Although, owing to the kinetic energy of the ions, PVD thins films may present a better adhesion to the substrate and a higher density. The aim of this study is to evaluate the potential of PVD SiC thin films as a protective coating for basic structures such as cavities of Si (100) and the influence of the substrate shape (convex or concave edge) on the protection behavior.

2. Experimental

Deposition of silicon carbide thin films was performed in a Nordiko 2000 magnetron sputtering equipment. RF cathode power was applied on an 80 mm diameter stoichiometric SiC target in a pure argon atmosphere. Amorphous SiC thin films were deposited at room temperature (25°C) on SiO_2/Si or Si substrates.

The measurement of the stress on (111) walls of (100) silicon cavities was realized on flat samples tilted by 54.7° during the deposition. The film stresses were measured on a Tencor FLX stress analysis instrument.

* Corresponding author.

E-mail address: nicolas.ledermann@epfl.ch (N. Ledermann)

Table 1
Process parameter ranges

Parameter	Range
Cathode RF power (W)	50, 100, 150, 200, 250, 300
Working pressure (Pa)	0.53, 1.07, 1.6, 2.13, 3.19, 4.26
Substrate bias voltage (V)	–13, –25, –48, –100

The influence of the shape of the substrate on the protection behavior of the film was evaluated by using micromachined cavities of Si (100). Etching resistance experiments were conducted in 40% KOH solution at 80°C. At this temperature, the etching rate of silicon along its (100) orientation is about 100 $\mu\text{m}/\text{h}$ [11].

3. Results and discussion

3.1. Deposition of SiC thin films on flat substrate, parametrical study

A parametrical study of PVD SiC thin films was carried out in order to evaluate the influence of different parameters such as the applied cathode RF power, the working pressure and the substrate bias voltage on the deposition rate, the film stress and the chemical composition. All the films were deposited at room temperature with 25 sccm pure argon flow. The parameter values are listed in Table 1.

Depending on the applied cathode RF power, the deposition rate ranged from 3.5 nm/min to 18 nm/min (see Fig. 1).

As the deposition rate decreases, the oxygen contamination increases. With a base pressure before deposition of 0.27 mPa, the contamination rate of oxygen can be

estimated to one monolayer per second. This is shown by the XPS analysis (see Fig. 2).

At low power (50 W), the atomic oxygen content is about 49 at.%. The analysis showed that oxygen is not just incorporated in the SiC thin films but bonded to silicon atoms to form silicon oxide. As silicon oxide is also etched by KOH, a lower protection capability of these films is expected. At high power (300 W), the atomic concentration of oxygen is less than 3 at.% and the peak position of C 1s at 283.5 eV corresponding to the C–Si bond was observed.

The film stress can be controlled by adjusting the working pressure as well as by applying a bias voltage on the substrate (see Fig. 3).

Above 1 Pa, stress tends to a slight compressive value of –60 MPa. At low pressure (0.5 Pa), high compressive stress (–800 MPa) was measured. The application of an external bias voltage on the substrate leads to densification of the film. The measured stress is then highly compressive (–1200 MPa) and the delamination of the film occurs. Due to the low concentration of silicon oxide and the weak compressive stress, the films deposited at high power (200–300 W) are expected to present better chemical stability.

3.2. Properties and morphology of SiC thin films deposited on inclined substrate

Real structures on devices often present a 54.7°-inclined (111) wall due to (100) silicon bulk micromachining. Thus, the transition zone between flat and inclined substrate can exhibit complex stress that can lead to the formation of singularities and cracks. In order to measure the stress on an inclined substrate, small flat samples were tilted by 54.7° during the deposition. Fig. 4 shows the variation of film stress as a function of the deposition angle.

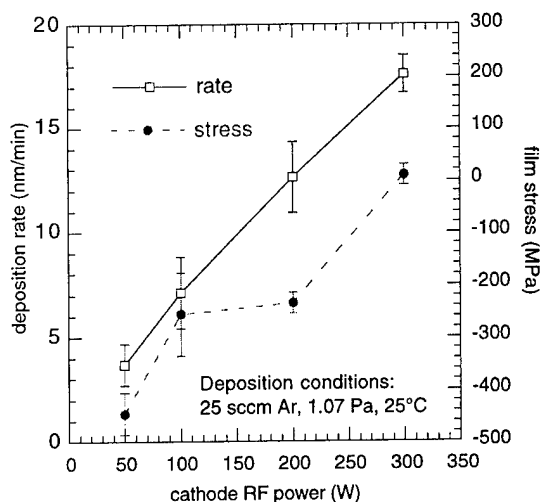


Fig. 1. Deposition rate and film stress as a function of the cathode RF power.

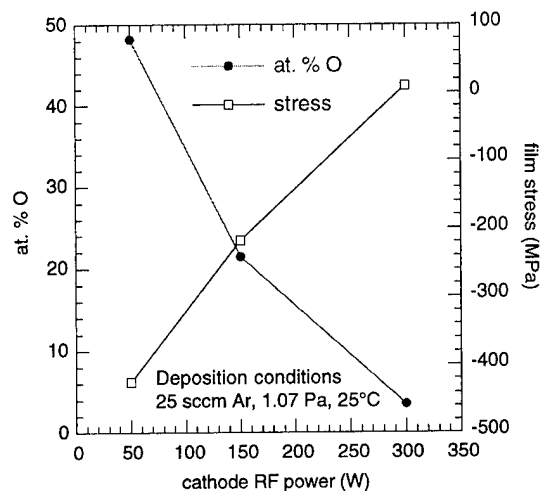


Fig. 2. At.% oxygen and film stress as a function of the cathode RF power.

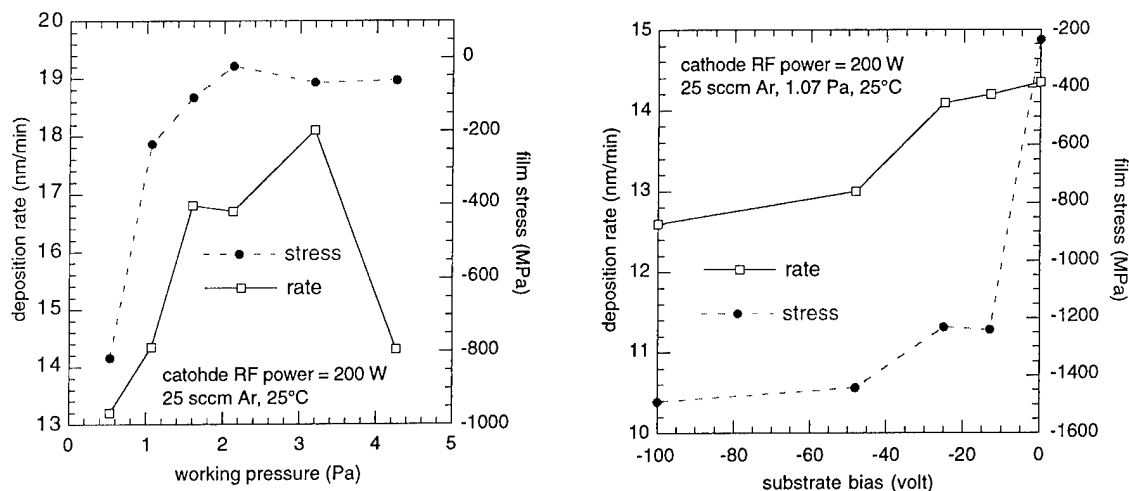


Fig. 3. Influence of (a) working pressure and (b) substrate bias voltage on the deposition rate and film stress.

The difference between the two curves may originate from the different intensity of ion bombardment and different distribution of incidence direction of atoms. The stress on inclined walls is the same as that on a flat substrate in an intermediate power range. SEM observations showed that the deposition on an inclined or flat substrate leads to different morphologies. Fig. 5(a) shows the junction point between flat and inclined wall of a (100) Si cavity. On the flat substrate, the SiC thin film (deposited at 200 W) is dense and no grain structure is found. On an inclined wall, a growth structure appears. This is shown in more detail by Fig. 5(b) where a 2.1 μm thick SiC film has been deposited on a 54.7°-tilted substrate. The film is also dense but a growth structure can be observed in this case. Finally, the thickness on inclined wall represents about 85% of the total thickness on the flat substrate.

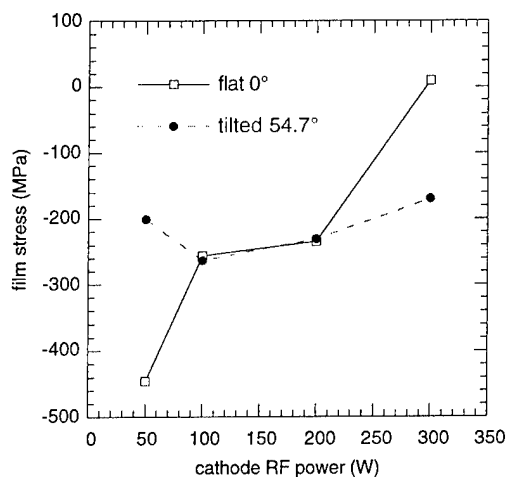


Fig. 4. Influence of the angle incidence and the cathode RF power on film stress (film thickness: 500 ± 40 nm).

3.3. Etching resistance of SiC thin films in KOH

First, the etching resistance of SiC thin films on the flat substrate was evaluated. Excellent chemical stability (5 h in KOH 40% at 80°C) was observed for low stress thin films (deposited at 200–300 W, 1.07 Pa, 25 sccm Ar, 25°C). On a polished substrate, only 200 nm thick films are sufficient for use as a masking layer during KOH bulk micromachining, with respect to the corrosion behavior. The use of low stress SiC thin films as masking layer can be a solution when there is a need to replace the high tensile stress (+1400 MPa) Low Pressure Chemical Vapor Deposition (LPCVD) silicon nitride [12,13].

Second, the etching resistance and the protective behavior of SiC thin films deposited on micromachined cavity of Si (100) were measured. As the roughness on the bottom of the cavity is about 70 nm, the deposition time was adjusted in order to obtain 2 μm thick films. The investigated samples are summarized in Table 2. The protection behavior was optically observed and the etching resistance time corresponds to the appearance of the first defect (pinholes, delamination) on the structure.

At low RF power (50 and 100 W), SiC thin films exhibit a high compressive stress and a concentration of atomic oxygen of about 40 to 50%. This leads to the delamination of the coating after several minutes in the KOH bath. As the deposition power is increased, the compressive stress is reduced and the concentration of silicon oxide also decreases. At 200 W, the stress is still compressive (-235 ± 20 MPa) and the atomic concentration of oxygen can be estimated to 15%. This high concentration can explain the fact that pinholes have been formed on the bottom of the (100) cavity after 15 min in KOH. At 300 W, the SiC thin film present a

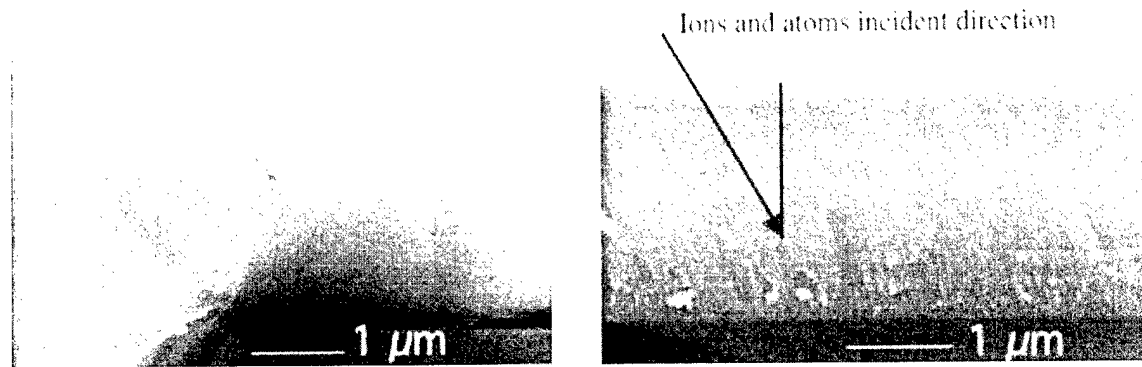


Fig. 5. (a) SEM cross-section of the junction point between flat and 54.7° inclined film (300 W, 1.07 Pa) (b) SEM cross-section of a SiC thin film deposited on a 54.7° tilted substrate (200 W, 1.07 Pa).

Table 2

Samples investigated for KOH etching test in (100) Si cavity

Cathode RF power (W)	Etching resistance time
50	delamination on top, 5 min
100	delamination on top, 5 min
200	Pinholes, 15 min
300	Resistant, 180 min

low stress in the range of ± 50 MPa with less than 3 at.% oxygen. Protective coating made using these conditions exhibits a high resistance in KOH and seems to be indefinitely resistant. No delamination and no pinhole were observed (see Fig. 6).

Finally, these results are similar to those obtained with amorphous hydrogenated silicon carbide (a-SiC:H) thin films deposited by PECVD [10]. In that case, an optimal protection behavior was also obtained with low compressive stress (-80 MPa) thin films. Although, for thin films deposited by PECVD, the substrate temperature was 350°C compared to room temperature for PVD.

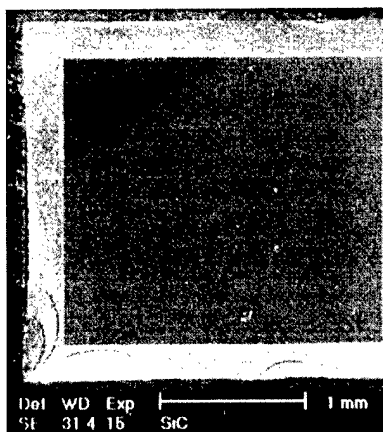


Fig. 6. SEM micrograph of a (100) Si cavity protected by a 2 μ m SiC layer after 180 min in KOH 40% at $80 \pm 2^\circ\text{C}$.

4. Conclusions

The parametric study of PVD silicon carbide thin films has shown that film stress is mostly compressive and can be adjusted from -1400 MPa to almost $+100$ MPa depending on the deposition conditions. It was demonstrated that PVD silicon carbide thin films offer superior protective capabilities of simple silicon microstructures in 40% KOH at 80°C. Thus, an excellent conformal deposition on (100) Si cavity was observed. The best protective behavior was obtained with 2 μ m low stress thin films deposited at 300 W cathode RF power, exhibiting a very low silicon oxide concentration (less than 3 at.% O). This work provides a new perspective in the development of sensors for harsh environment, such as heat exchangers or microevaporators. Further work will include evaluation of the mechanical properties of the films and adhesion/covering investigation on rough substrates.

Acknowledgements

Funding was provided by the Swiss Priority Program on Material. The authors would like to thank S. Hiboux (LC), G. Coullerez (LMCH) and the CIME for the SEM facilities.

References

- [1] A.K. Henning, 2nd Annu. IEEE Int. Conf. On Innovative Systems in Silicon, 8–10 October, 1997, IEEE, Austin, TX, 1999.
- [2] A. Klumpp, U. Schaber, H.L. Offereins, K. Kühl, H. Sandmair, Sensors and Actuators A 41–42 (1994) 310–316.
- [3] N. Rajan, C.A. Zorman, M. Mehregany, R. DeAnna, R. Harvey, Thin Solid Films 315 (1–2) (1998) 170–178.
- [4] G.F. Eriksen, K. Dyrbye, J. Micromech. Microeng. 6 (1) (1996) 55–57.
- [5] R. Ziermann, J.V. Berg, E. Obermeier, M. Eickhoff, G. Kroetz, Proceedings Transducers '97, Int. Conf. Sol. State Sens. Act., IEEE, 1997.

- [6] R.S. Okojie, A.A. Ned, A.D. Kurtz, Proceedings Transducers '97, Int. Conf. Sol. State Sens. Act., IEEE, 1997.
- [7] G.H. Kroetz, M.H. Eickhoff, H. Moeller, Sensors and Actuators 74 (1999) 182–189.
- [8] M. Mehregany, C.A. Zorman, N. Rajan, C.-H. Wu, Proc. IEEE 86 (8) (1998) 1596–1609.
- [9] T. Shikama, M. Kitajima, M. Fukutomi, M. Okada, Thin Solid Films 117 (3) (1984) 191–199.
- [10] A.F. Flannery, N.J. Mourlas, C.W. Storment, S. Tsai, H. Samantha, G. Kovacs, Proceedings Transducers '97, Int. Conf. Sol. State Sens. Act., IEEE, 1997.
- [11] W. Lang, Mater. Sci. Eng. R17 (1996) 1–55.
- [12] A.C. Adams, in: S.M. Sze (Ed.), VLSI Technology, second ed., McGraw-Hill, New York, 1988.
- [13] J.R. Hollahan, S.R. Rosler, in: J.L. Vossen, W. Kern (Eds.), Thin Film Processes, Academic Press, New York, 1978.

Pulsed electron-beam treatment of WC–TiC–Co hard-alloy cutting tools: wear resistance and microstructural evolution

Y.F. Ivanov ^a, V.P. Rotshtein ^{a,*}, D.I. Proskurovsky ^a, P.V. Orlov ^b, K.N. Polestchenko ^b,
G.E. Ozur ^a, I.M. Goncharenko ^a

^a High Current Electronics Institute, SD of RAS, 4 Akademicheskoy Ave., Tomsk, 634055 Russia

^b Omsk State University, 55a Mira Ave., Omsk, 644077 Russia

Accepted 13 October 1999

Abstract

The mechanisms for changes in the structure-phase state, microhardness, and wear resistance have been investigated for carbide inserts made of type T15K6 (WC–15TiC–6Co) hard alloy, irradiated with a low-energy (20–30 keV, high-current ($\sim 10^2$ A cm⁻²) electron beam of duration 2.5 μ s. Using transmission electron microscopy, it has been established that the pulsed melting of the near-surface (~ 1 μ m) layer results in the formation of a subgrain structure in the binding phase, segregation of nanosized carbide particles in the near-boundary regions, and the allotropic transformation of WC. The irradiation increases by about three times the durability of the inserts at elevated cutting rates for steels. The increase in durability is associated with the efficient hardening of the Co binder immediately on irradiation and with its high thermal stability being retained in the process of cutting due to the stability of the dislocation substructure provided by second-phase segregates. © 2000 Elsevier Science S.A. All rights reserved.

Keywords: Cemented carbides; Pulsed electron-beam treatment

1. Introduction

Enhancement of the wear resistance of hard-alloy (cemented carbides) inserts still remains an urgent problem. A possible way of solving this problem is pulsed thermal surface treatment with concentrated energy flows. This statement is based on the results obtained with the use of a laser (pulse duration $\tau = 10^{-2}$ s) [1] and high-power ion beams ($\tau = 10^{-7}$ s) [2]. It has been shown [3] that a promising technique for improving the performance of machine parts and tools (carbide inserts included) is treatment of the working surfaces with a low-energy (20–30 keV), high-current ($\sim 10^2$ A cm⁻²) electron beam (LEHCEB) of microsecond duration in surface melting modes. With this type of treatment (e.g. for iron), the following thermal treatment conditions are typically realized: the molten layer thickness is 10^{-4} – 10^{-3} mm; the melt lifetime is $\sim 10^{-6}$ s, and the maximum cooling rate from melt and the maximum velocity of the crystallization front, both achieved at the

surface, are $\sim 10^9$ K s⁻¹ and ~ 5 m s⁻¹, respectively. As a result of quick quenching from melt, highly dispersed metastable structure-phase states are formed which improve the performance of the material.

The goal of the study was to investigate the effect of LEHCEB treatment on the microhardness and durability of the inserts and to elucidate the mechanisms for the enhancement of its wear resistance by monitoring the evolution of the structure-phase state of the cutting edge in the process of cutting.

2. Experimental

Wear testing was performed for commercial pentahedral (11 \times 11 \times 5 mm) inserts made of type T15K6 (WC–15TiC–6Co) hard alloy. For microhardness (H_v) measurements and structural investigations the flat rear surfaces of the inserts, previously polished, were used. The evolution of the microstructure in the process of cutting was investigated for model inserts (2 \times 3 \times 15 mm). The commercial inserts and samples were irradiated on a set-up described elsewhere [3]. The electron beam

* Corresponding author. Fax: +7-3822-259410.

E-mail address: rvp@lve.hcei.tsc.ru (V.P. Rotshtein)

parameters were as follows: electron energy is 20–30 keV, $\tau = 2.5 \mu\text{s}$, energy density $E_s = 0.8\text{--}3 \text{ J cm}^{-2}$, and number of pulses $N = 5$. The signs of surface melting visible in an optical microscope were observed for $E_s = 1.2 \text{ J cm}^{-2}$. Wear testing for the commercial inserts was carried out using lathe machining of steel 40X (0.4% C, 1% Cr) at a speed of $v = 10\text{--}300 \text{ m min}^{-1}$, a feeding rate of $S = 0.14 \text{ rev min}^{-1}$, a depth of $d = 1.5 \text{ mm}$ and for $t \leq 10 \text{ min}$. To compare the wear of the inserts, curves of $h(L)$ (with h being the height of the wear area on the rear surface and L the cutting path length) were constructed. Using the normal wear portions of these curves, the dependencies of the relative linear wear T on v were constructed. The model inserts were irradiated with $E_s = 2.5 \text{ J cm}^{-2}$ and $N = 5$. Their testing was performed with $v = 100 \text{ m min}^{-1}$, $S = 0.14 \text{ rev min}^{-1}$ and $d = 1 \text{ mm}$. The testing time was 10, 20 and 120 s, which corresponded to the stage of running-in, normal wear, and the transition to the stage of fracture, respectively. Structural investigations were carried using optical metallography, scanning electron microscopy (SEM), X-ray diffraction (XRD) and transmission electron microscopy (TEM). Foils were prepared by one-sided electrolytical thinning of thin plates. The procedure of preparation of foils allowed an examination of the microstructure at various distances from the working surface.

The dislocation density $\langle \rho \rangle$ was measured by two methods: by the method of secant [4] for $\langle \rho \rangle \leq 5 \times 10^{10} \text{ cm}^{-2}$, and by the method described in Ref. [5] for $\langle \rho \rangle \geq 5 \times 10^{10} \text{ cm}^{-2}$.

The effect of irradiation on the strength properties and structure-phase state of the material.

Fig. 1 presents the relative wear as a function of speed. For $v \leq \sim 200 \text{ m min}^{-1}$, irradiation has an insignificant effect on the durability of the inserts. For $v = 300 \text{ m min}^{-1}$, the wear is observed to decrease about threefold. With that, the degree of enhancement of wear resistance depends on E_s only weakly. Given in Fig. 2 is the dependence $H_\mu(E_s)$ of the surface (in the initial state $H_\mu = 1700 \text{ kg mm}^{-2}$). Measurements performed on cross

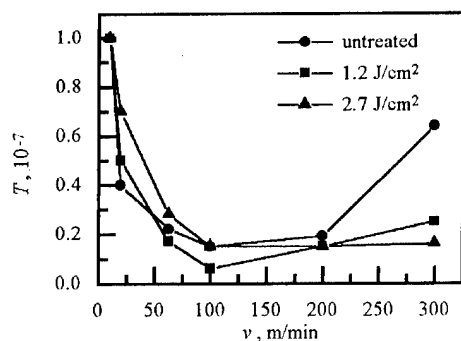


Fig. 1. Dependence of the relative wear of T15K6 carbide inserts on cutting speed.

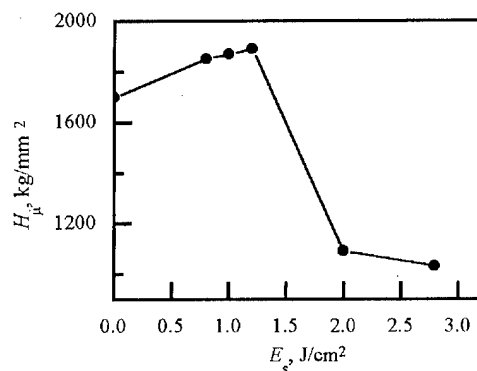


Fig. 2. Dependence of the surface microhardness of T15K6 carbide inserts on energy density.

sections have shown that the H_μ of irradiated specimens at depths over 5–10 μm corresponds to that of unaffected specimens, that is, variations in H_μ occur only in a thin surface layer. We call attention to the absence of any correlation between H_μ and the durability of the irradiated inserts, namely, notwithstanding the abrupt decrease in H_μ at $E_s \geq 2 \text{ J cm}^{-2}$, the durability of the inserts at $v = 300 \text{ m min}^{-1}$ is much in excess of the starting one (Fig. 1).

According to the data of optical metallography and SEM, there are three phases in the unaffected structure of the T15K6 alloy: WC (bright grains), solid solution of WC and TiC in cobalt playing the role of binding (dark grains), and solid solution of WC in TiC (grey grains) [Fig. 3(a)]. Even at $E_s = 1.2 \text{ J cm}^{-2}$ interphase boundaries are molten and separate microcracks appear [Fig. 3(b)]. For $E_s = 2 \text{ J cm}^{-2}$, intense melting of the surface layer is observed and microcraters of diameter up to 5 μm and long microcracks are formed [Fig. 3(c)]. An examination of cross-sections revealed changes in the microstructure only in a thin remelted surface layer of thickness no more than a few micrometers. This correlates with microhardness measurements.

According to the XRD data, being in agreement with Refs. [6,7], the diffraction pattern of the initial state contains the lines of α -WC (hex) and the lines of the (Ti, W)C with an fcc lattice as well as the lines of Co. After irradiation, the angular positions of the lines and their half-widths remained almost unchanged for both carbide phases. The intensity of the α -WC lines gradually decreased, while that of the cubic (Ti, W)C lines increased with increasing E_s as compared to the initial state. For $E_s \leq 1.2 \text{ J cm}^{-2}$, these changes were insignificant and might be related to extra dissolving of WC in (Ti, W)C. For $E_s \geq 2 \text{ J cm}^{-2}$, on the contrary, the intensity of the lines of α -WC was observed to abruptly decrease. This was accompanied by the appearance of metastable WC (fcc). Thus, the abrupt decrease of the volume fraction of α -WC, observed for $E_s \geq 2 \text{ J cm}^{-2}$, was related to its liquid-phase dissolving in the TiC

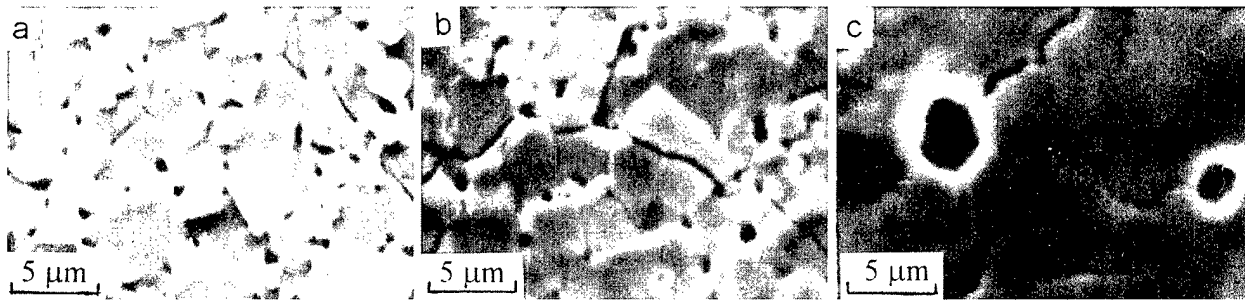


Fig. 3. SEM images of the surface of irradiated T15K6 carbide inserts: (a) 1, (b) 1.2 and (c) 2.7 J cm⁻².

lattice [7] and to the formation of the metastable cubic WC on rapid quenching from the melt. Note that the formation of WC (fcc) was observed on laser quenching of BK8 (WC-8Co) alloy from the liquid state [1].

TEM investigations have confirmed and supplemented the XRD data. The unaffected state contains micron-sized crystallites of carbides and interlayers of the binding material between the crystallites. The dislocation structure of the cobalt binder is highly inhomogeneous: the dislocation density $\langle\rho\rangle$ in the binder varies in the range of 5×10^9 – 5×10^{10} cm⁻². In the carbide phase (WC) $\langle\rho\rangle$ is low ($\sim 10^9$ cm⁻²). In the Co binder, regions with a maximum dislocation density are observed, as a rule, near the WC grain boundaries. Irradiation noticeably changes the structure-phase state only in the near-surface region of thickness < 1 μm. As the threshold for contact melting of the carbide and binding phases is achieved (1.2 J cm⁻²), only the binder is modified and a subgrain structure is observed to form: nanosized particles of the second phase (supposedly, Co₃W₉C₄ carbide) are found at interphase boundaries. These changes become more pronounced in the intense melting mode (2.0–2.7 J cm⁻²): almost the whole of the binding phase acquires subgrain (0.1–0.2 μm) structure [Fig. 4(a)]. The volume fraction of the Co₃W₉C₄ particles increases noticeably. With that, these particles are found not only along the carbide-binding interfaces, but also in the near-boundary regions of both the binder and the original carbide crystallites [Fig. 4(b)]. In addition, the micrographs also show reflexes corresponding to new disperse segregates which we failed to identify. After irradiation, the inhomogeneity of the original dislocation substructure of the material is retained.

3. Evolution of the substructure in the process of cutting

TEM studies have shown that in the cutting process, the substructure, in the cutting edge of both irradiated and unirradiated tools changes both in the Co binder and in the WC grains. In the binder, the dislocation density increases. In WC grains, strain occurs mainly by twinning. With that, the structures showing maximum $\langle\rho\rangle$ values in the binder and maximum density of

twins in the WC are formed at depths of 2–80 μm from the wear surface. Fig. 4(c–f) presents typical images of these microstructures. At a cutting time of 10 s (running-in stage), in an irradiated insert a developed grid dislocation structure is formed both in the binder and in the WC. The average dislocation density in the material is $\sim 4 \times 10^{10}$ cm⁻², which is noticeably higher than that in the unirradiated material. In crystallites of WC, along with the dislocation substructure, microtwins are observed which are arranged, in the main, without any order. The misorientation of the defect substructure, estimated by the relative smear of reflexes, is 4°. Inside the binder and at the interphase boundaries, nanosized segregates of second phases are detected. These structure-phase changes testify to an efficient strain hardening of the irradiated material in the process of cutting. In an unirradiated insert, the inhomogeneity of the defect structure inherent in the unaffected material is retained. An elevated $\langle\rho\rangle$ (up to $\sim 5 \times 10^{10}$ cm⁻²) is observed only in the binder regions bordering the carbide grains. In some cases, segregates of second phases are observed. Furthermore, micropores and microcracks are formed which are located along the binder–carbide interphase boundaries [Fig. 4(c)]. The absence of signs of strain hardening and the presence of micropores point to the reduced strength of the interphase boundaries and of the material as a whole as compared to the previously irradiated material.

Increasing the time to 20 s (normal wear stage) leads to further strain hardening of the cutting edge of the irradiated inserts. This shows up in the formation in the binder of a misoriented ($\sim 5^\circ$) dislocation structure with a high $\langle\rho\rangle$ ($\sim 7 \times 10^{10}$ cm⁻²) [Fig. 4(d)]. The misorientation regions are 70–90 nm in size. The characteristics of the defect substructure in WC (dislocation structure, presence of twins) are essentially the same as for the 10 s time. An increase in time results in an increase in the volume fraction of second phase segregates. In an unirradiated insert with the given time, the changes in the defect structure of the binding and carbide phases and in the volume fraction of the second phase segregates are insignificant as compared to the running-in stage (10 s). The decreased, compared to unirradiated inserts,

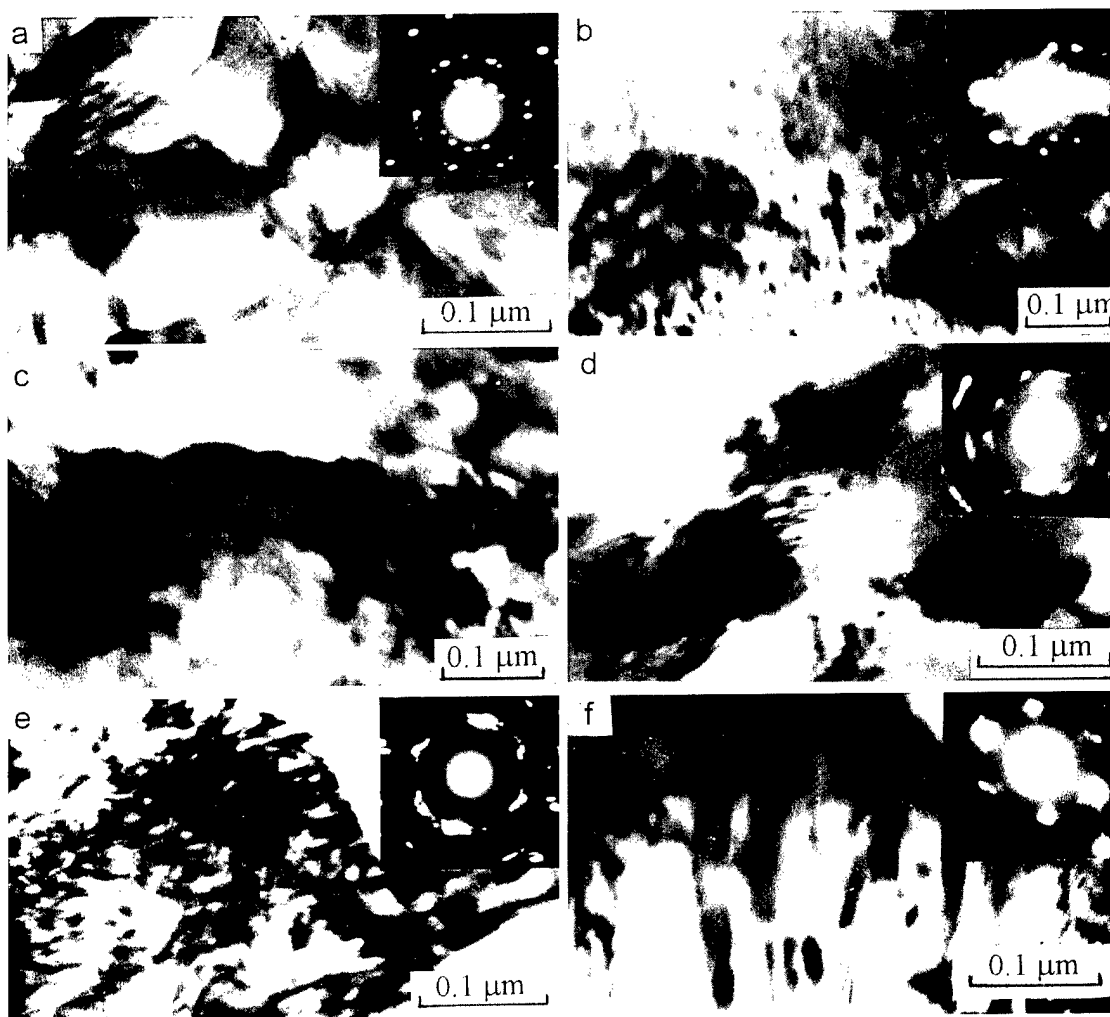


Fig. 4. TEM images of the cutting edge of T15K6 carbide inserts after irradiation (a and b) and cutting (c–f).

$\langle \rho \rangle$ ($3.5 \times 10^{10} \text{ cm}^{-2}$) testifies to a lesser strength of the material.

For an irradiated insert, increasing the time to 120 s was accompanied by further strain and dispersion hardening of the cutting edge. In the cobalt interlayer, the scalar dislocation density increases to $\sim 10^{11} \text{ cm}^{-2}$ and the misorientation of the substructure elements reaches $\sim 6^\circ$ [Fig. 4(e)]. In the carbide phase crystallites, multiple twinning is observed [Fig. 4(f)]. However, as distinct from the preceding case (20 s), signs of fracture of the material (micropores and microcracks) are observed. For an unirradiated insert, the defect substructure of the material for the given time is presented by dislocation grids with $\langle \rho \rangle \sim 4 \times 10^{10} \text{ cm}^{-2}$, which is substantially lower than that for an irradiated insert.

The results are given in Fig. 5 showing the dislocation density in the cobalt interlayer as a function of distance X from the cutting surface. The scale of depths is conventional (with the scale division being $\sim 5 \mu\text{m}$); however, the sequence of changes in the substructure is reflected adequately. Irrespective of the cutting time, the

depth distribution of dislocations in the cutting edge was highly nonmonotonic in character. This is most pronounced for irradiated inserts. The maximum of $\langle \rho \rangle$ is observed at a distance from the surface of the cutting edge, and, as the time is increased, this maximum shifts into the bulk. For irradiated inserts, the peak values of $\langle \rho \rangle$, irrespective of the time, are higher than those for unirradiated inserts. In addition, in irradiated inserts the thickness of the layer with an elevated $\langle \rho \rangle$ increases with time roughly linearly from $\sim 5 \mu\text{m}$ (at 10 s) to 50–70 μm (at 120 s), while in unirradiated inserts this thickness increases insignificantly.

4. Discussion

Let us consider the structural mechanisms that might be responsible for the change in surface microhardness on irradiation. In the mode of initial (contact) surface melting (1.2 J cm^{-2}), the modification of the Co binder occurs in the main. This modification consists, first, in

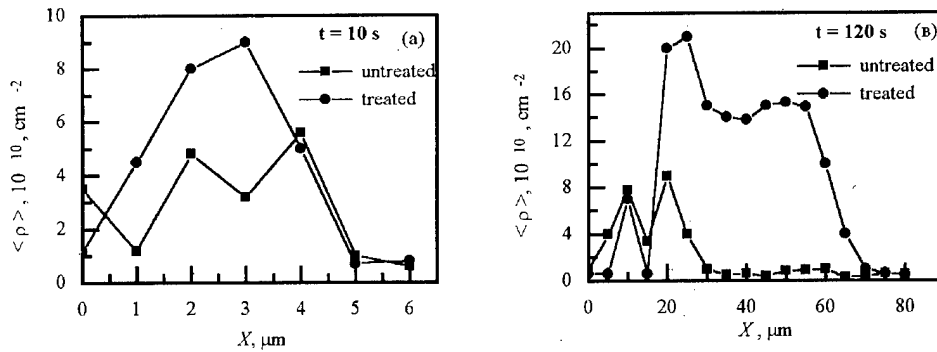


Fig. 5. The depth distribution of the dislocation density in the cutting edge of TiK6 carbide inserts before and after irradiation for various cutting times.

its saturation with W, Ti and C atoms due to partial dissolving of the carbide phases resulting in solid-solution hardening of the binder. The formation of an oversaturated Co-base solid solution is evidenced by the fact that the morphology of the crystallites changes from edged (in the original state) to oval (after irradiation) (see Fig. 3). Second, nanosized carbides of the $\text{Co}_3\text{W}_9\text{C}_4$ type are segregated which results in dispersion hardening of the binder [8]. Third, a subgrain structure is formed which is responsible for substructural hardening [see Fig. 4(a and b)]. The major mechanism for the binder hardening is solid-solution hardening. The contribution of the two other mechanisms is insignificant because of the small volume fraction of the binder where the relevant effects are observed. It follows that in this mode, solid-solution hardening of the binding phase is the main reason for the increase in H_μ (see Fig. 2).

In the mode of uniform melting of the near-surface layer ($2\text{--}2.7 \text{ J cm}^{-2}$), both the Co binder and WC change in state. In the binder, a subgrain structure is formed and $\text{Co}_3\text{W}_9\text{C}_4$ particles are segregated in noticeable amounts. These factors promote the hardening of the binder. WC experiences an allotropic transformation resulting, in the given irradiation modes, in a decrease in H_μ for the material as a whole, since the hardness of WC (fcc) is lower than that of α -WC.

Let us now analyse the reasons for the enhancement of the wear resistance of the inserts on irradiation. It is well known that at high speeds the diffusion wear mechanism is dominant [9]. Its essence is that the high temperature and intense plastic strain in the contact zone give rise to mutual dissolving of the components of the insert and the steel. The solubility of WC in the Co(Fe) substitutional solid solution is much higher than in Co in the original state [10,11]. This results in a decrease in α -WC fraction and in the formation of complex carbides of the FeW_3C type [10]. Moreover, the squeezing out of the pliable binder leads to its galling which has the result that the bonds between carbide grains weaken. Eventually, the cutting edge becomes brittle and fractures [12].

Irradiation of the material in the initial melting mode leads to saturation of the near-boundary regions of the Co binder with W, Ti and C atoms. This hampers the diffusion of iron atoms into the binder and prevents α -WC crystallites from decomposition [12]. The suppression of diffusion processes in the zone of contact of the insert with the steel should enhance the wear resistance of the insert.

In the process of high-speed cutting, there occurs intense plastic deformation of the cutting edge which is accompanied by annealing of defects in the near-surface contact zone. For unirradiated inserts, the relaxation of cutting stresses has the result that a comparatively depth-homogeneous dislocation structure with a low dislocation density is formed in the cobalt binder (see Fig. 4). This structure has reduced hardness and strength. At high temperatures and shear stresses, the binder is squeezed within a short time with the formation of micropores in the material and wears.

Preliminary pulsed melting hardens the Co binder due to the formation of a subgrain structure and segregation of second phase particles [see Fig. 4(b)]. Such a structure is known to show enhanced strength. It does not fracture for a certain time in the process of cutting. Within this time, owing to intense thermomechanical loading, a dislocation structure stabilized with new second phase segregates has time to form in the sublayer. This structure seems also to show elevated strength. As the cutting time increases, the sublayer modified in the process of cutting grows in thickness. The strength of this layer increases proportionally to $\langle \rho \rangle^{1/2}$ and to the density of nanosized second phase segregates [8]. Efficient hardening of the binder in the process of cutting is also shown by multiple twinning in the WC carbide phase [Fig. 4(f)]. Once the surface layer has worn, its functions are fulfilled by the sublayer formed in the process of cutting. This assures low wear of the irradiated inserts for a long time as compared on to unirradiated ones.

Thus, for high speeds, the main reason for the enhancement of wear resistance of inserts subjected to

preliminary pulsed melting is the modification of the Co binder in the near-surface layer through the formation of segregates of nanosized carbide particles and of a subgrain structure. In the process of cutting, as the near-surface layer wears, a dislocation structure resistive to high thermomechanical loading has time to form. Its stability is due to the fact that dislocations are fixed by nanosized second phase segregates formed in the process of cutting.

References

- [1] A.D. Gureev, S.I. Yares'ko, A.P. Laletin, A.L. Petrov, Proc. Lodedev Institute of Physics vol. 198, Nauka, Moscow, 1989, pp. 90–110.
- [2] G.E. Remnev, I.F. Isakov, M.S. Opekunov, G.I. Kotlyarevsky, V.L. Kutuzov, V.S. Lopatin, V.M. Matvienko, M.Yu. Ovsyannikov, A.V. Potemkin, V.A. Tarbokov, Surf. Coat. Technol. 96 (1997) 103–109.
- [3] D.I. Proskurovsky, V.P. Rotshtein, G.E. Ozur, A.B. Markov, D.S. Nazarov, V.A. Shulov, Yu.F. Ivanov, R.G. Buchheit, J. Vac. Sci. Technol. A 16 (4) (1998) 2480–2488.
- [4] P. Hirsch, A. Howie, R. Nickolson, D. Pashley, M. Whelan, Electron Microscopy of the Thin Crystals, Butterworths, 1965.
- [5] V.V. Rybin, V.F. Malyshevsky, V.N. Oleynik, Fizika Metallov i Memallov 42 (1976) 1042–1050.
- [6] L. Toth, Transition Metal Carbides and Nitrides, Academic Press, New York, 1971.
- [7] G. Kreimer, Strength of Hard Alloys, Metallurgia, Moscow, 1971.
- [8] J.W. Martin, Micromechanisms in Particle-hardened Alloys, Cambridge University Press, Cambridge, 1980.
- [9] T. Loladze, Strength and Wear Resistance of Hard Alloys, Mashinostroenie, Moscow, 1982.
- [10] O. Bannykh, M. Drits (Eds.), Phase Diagrams of Double- and Multicomponent Systems Based on Iron, Handbook, Metallurgia, 1986, pp. 206–207.
- [11] P. Kiffer, F. Benezovsky, Hard Alloys, Metallurgia, Moscow, 1971.
- [12] R. Edwards, T. Raine, Plansee Seminar “De re metallica”, Springer, Vienna, 1953, pp. 232–243.

Structure and hardness of vacuum arc deposited multi-component nitride coatings of Ti, Zr and Nb

R.L. Boxman ^{a,*}, V.N. Zhitomirsky ^a, I. Grimberg ^b, L. Rapoport ^c, S. Goldsmith ^a,
B.Z. Weiss ^b

^a *Electrical Discharge and Plasma Laboratory, Tel Aviv University, POB 39040, Tel-Aviv 69978, Israel*

^b *Department of Materials Engineering, Technion-Israel Institute of Technology, Haifa 32000, Israel*

^c *Center for Technological Education, 52 Golomb St., Holon 58102, Israel*

Abstract

Ternary transition-metal nitride coatings of (Ti,Zr)N, (Ti,Nb)N and (Zr,Nb)N were deposited using a triple cathode vacuum arc deposition system by simultaneously operating two cathodes of the appropriate metals in a low-pressure nitrogen background. The magnetically collimated plasma flux distribution was measured using a 13-element ion saturation current probe. The microstructure, composition, and hardness of the coatings were determined using X-ray diffraction, Auger electron spectroscopy, and Vickers indentation, respectively.

The plasma flux distribution had two peaks whose relative positions were related to the two cathodes. Coatings applied to extended substrates had a compositional gradient. In almost all cases, the ternary nitrides had a single-phase solid-solution microstructure, whose lattice constants had values intermediate between those of the parent binary nitrides. The ternary coatings were considerably harder than either of the parent binary nitrides. (Ti,Nb)N had the highest microhardness: ~50 GPa. © 2000 Elsevier Science S.A. All rights reserved.

Keywords: Hardness; Structure; Ternary nitrides; Transition metals; Vacuum arc deposition

1. Introduction

Hard coatings of TiN and similar materials are widely used to increase the work life and productivity of cutting and forming tools. Initially, simple binary materials such as TiN, CrN, and ZrN were favored for these applications. Increasingly, however, more complicated materials are being studied and used, including multi-layer coatings [1–3], and ternary materials including Ti(C,N) and (Ti,Al)N [4–6]. Coatings with multiple gas components are readily fabricated reactively, by admitting a mixture of the requisite gases into the deposition chamber. Deposition of coatings with multiple metallic components requires the use of an alloy source [5–7], a segmented source [8,9], or co-deposition from multiple sources [9,10].

Co-deposition of hard multi-component nitride coatings has been relatively little explored, albeit that it affords research flexibility. Various compositions can be fabricated by varying the relative strength of the various

sources in a sequence of deposition cycles, or by arranging the substrates within the deposition apparatus such that they are exposed to varying relative fluxes from the sources during a single deposition run. The present group, in a previous report, described the co-deposition of Ti–Zr–N and Ti–Nb–N coatings in a multi-cathode vacuum arc deposition apparatus, and their microstructure and morphology [10]. Solid solutions were found to form in both systems, with crystalline grain sizes in the 20–30 nm range. Although the configuration used led to a composition gradient across the coated substrate [11,12], the properties of the coatings as a function of the composition were not explored. In this paper we present the dependence of the structure and microhardness of multi-component coatings on composition. In addition, the previously developed methodology is extended to investigate also the Zr–Nb–N system.

2. Experimental setup and apparatus

The coatings were prepared in a triple-cathode vacuum arc deposition system [13,14]. The cathodes

* Corresponding author.

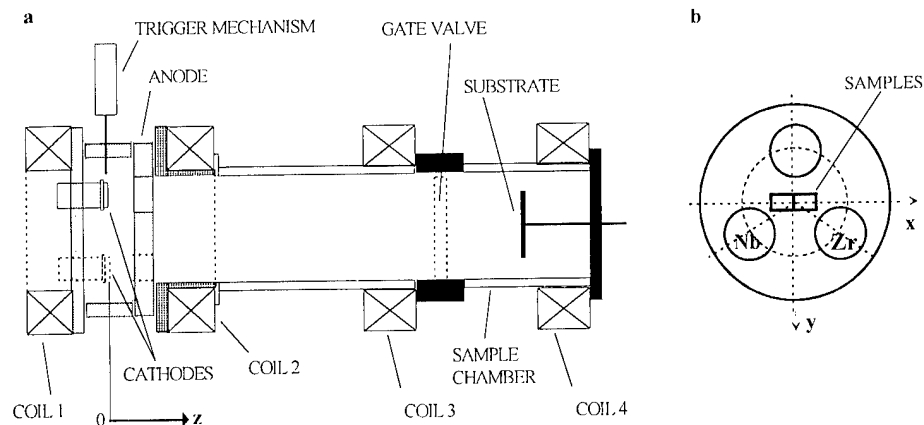


Fig. 1. Schematic diagram of the triple-cathode vacuum arc deposition system: (a) side view, (b) end view, showing the relative placement of the Nb and Zr cathodes in the cathode plane, and the substrate placement in the substrate plane.

were fabricated of Ti (99.9%), Zr (99.95%) and Nb (99.5%). Each cathode was 54 mm in diameter, and the three cathodes were equally spaced on a 50 mm diameter circle on the end flange of the system (Fig. 1). Each cathode had a separate trigger electrode that physically contacted the side of the cathode to ignite the arc. In any given experiment, one or two cathodes were operated simultaneously, with currents of 200 A each. The cathodes faced a common water-cooled anode having the form of a 40 mm thick plate with 54 mm diameter apertures aligned with the cathodes.

Plasma formed at cathode spots was transported through the anode apertures and along a 160 mm diameter duct to a substrate holder located 560 mm from the cathode plane. Four 250 mm average diameter magnetic field coils (Fig. 1) collimated the plasma beams. The axial locations and on-axis strengths are given in Table 1.

The substrates were mounted on a holder located 560 mm from the cathode plane. In some experiments, a 13-element probe was placed at the substrate plane to measure the distribution of ion flux. As shown in Fig. 2, the elements were arranged in three concentric circles of radii $(r_1, r_2, r_3) = (25, 37.5, 50)$ mm plus a central element. The probes were biased at -40 V with respect to the anode, and the currents to each of the probes were measured simultaneously.

The substrates were $20 \times 6.5 \times 5$ mm³ WC-Co bars. The surface to be coated was finely polished. Because

of the off-axial location of the cathodes and the magnetic field configuration, the centers of the various beams did not coincide [11,12]. The substrates were placed in the region generally between the beam centers, and thus generally received flux from both sources, and were thus coated with a multi-component film. Furthermore, the coating on extended substrates had a compositional gradient, with the relative contribution from a given source decreasing with the distance from its beam center. To study the composition distribution, two substrates were placed on the substrate plane parallel to the line connecting the active cathodes as shown in Fig. 1. Nitrogen gas was introduced into the system near the substrate. The gas flow was regulated to maintain a set pressure in the range of 0.67–2 Pa. The coatings were

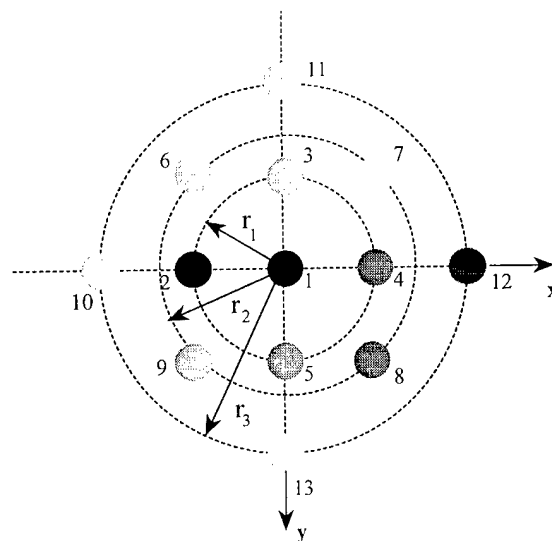


Fig. 2. Location of the individual elements in the 13-element ion flux probe. The relative darkness of each element is proportional to the average ion flux measured during simultaneous operation of Nb and Zr cathodes, as configured in Fig. 1.

Table 1
Location of magnetic field coils, and the magnetic field in their center

	<i>z</i> (mm)	<i>B</i> (mT)
Coil 1	−135	2
Cathode plane	0	
Coil 2	135	2
Coil 3	400	10
Substrate plane	560	
Coil 4	670	10

deposited at a substrate temperature of 400°C and with an applied bias voltage to the substrate of –40 V.

The compositional gradient was exploited to study the microhardness of the coatings as a function of composition. The composition was determined using Auger electron spectroscopy, and the hardness using Vickers indentation at loads of 0.5 to 1 N, both as a function of nitrogen pressure, and of position on the substrate. The coating thickness for the microhardness study was 2.4–3 µm.

3. Results

3.1. Plasma flux distribution

The plasma flux distribution obtained when operating the Nb and Zr cathodes shown in Fig. 1 is illustrated in Fig. 2 — the ‘gray level’ representing each element of the 13-element probe is proportional to the average ion current detected at that probe. The distribution apparently had a peak to the right of and below element 2, and a weaker peak below element 12. Presumably these peaks correspond to the center of the Nb and Zr plasma beams respectively.

3.2. Structure

The phase composition, angular positions of the diffraction maxima, texture and grain size of binary (TiN, ZrN, NbN), and ternary [(Ti,Zr)N, (Ti,Nb)N] coatings are summarized in Table 2. It may be seen that: (1) in all cases a single-phase composition was formed (except for Ti–Nb–N deposited at $P=2$ Pa); (2) the (Ti,Zr)N coating had a columnar structure, similar to that of binary TiN and ZrN, whereas in the case of (Ti,Nb)N the coating is built of equiaxed grains, i.e. a legacy from NbN which is also built of equiaxed grains; (3) the diffraction maxima of the ternary coatings lie between those of appropriate binary nitrides, and thus the lattice parameter of (Ti,Zr)N is between that of the

TiN and ZrN and similarly, that of (Ti,Nb)N is between that of TiN and NbN.

3.3. Microhardness

The Ti fraction and microhardness measured with a load of 0.5 N in Ti–Zr–N and Ti–Nb–N coatings as functions of deposition nitrogen pressure for samples placed on the system axis are shown in Fig. 3. The Ti fraction decreased with nitrogen pressure in both examples. However, the microhardness was minimized at the intermediate pressure of 1.33 Pa in Ti–Zr–N, whereas it was maximized there for Ti–Nb–N.

The microhardness of (Ti,Zr)N and (Ti,Nb)N coatings as a function of the Zr/(Zr + Ti) and Nb/(Nb + Ti) fractions is shown in Fig. 4. These results were obtained from binary nitride samples and from two different samples of ternary nitrides deposited using the same process, but having different compositions because of their different positions in the chamber. In both cases the microhardness is highest at some intermediate composition between pure TiN at the one extreme, and ZrN or NbN at the other.

3.4. Composition and microhardness hardness distribution

Fig. 5(a) presents the composition distribution of a (Nb,Zr)N coating deposited at $P=0.67$ Pa, and the microhardness distribution measured with a load of 1 N along the length of the samples, positioned as shown in Fig. 1. The Nb and Zr contents were highest at those positions closer to the respective beam centers (as seen in Fig. 2), as might be expected. The N content was somewhat higher in the Zr-rich coatings. The hardness data had considerable scatter. However, the maximum values were found in the Nb-rich portion of the sample.

Fig. 5(b) presents the dependence of the Vickers hardness on the Nb/(Nb + Zr) ratio. It was obtained by using the results from Fig. 5(a) by first fitting the Nb/(Nb + Zr) ratio dependence on position to a second-

Table 2
XRD peaks, structure, texture, and grain size of binary and related ternary nitrides

Coating	P (Pa)	Phase composition	2θ (111)	2θ (200)	2θ (220)	2θ (311)	Structure	Texture	Grain size (nm)
ZrN	0.67; 1.33	δ -ZrN	33.9	39.2	56.9	67.9	columnar	{111}	22–32
(Ti,Zr)N	0.67; 1.33	δ -(Ti,Zr)N	35.1	41.1	59.3	70.0	columnar	{111}	30
	2	δ -(Ti,Zr)N	35.0	41.0	59.0	69.7	columnar	{111}	30
TiN	0.67	δ -TiN	36.6	42.9	64.1	73.8	columnar	{111}, {200}	30–50
(Ti,Nb)N	0.67	δ -(Ti,Nb)N	35.6	41.7	60.5	71.5	equiaxed		20
	1.33	δ -(Ti,Nb)N	36.2	41.4	61.0	71.9	equiaxed		20–30
	2	δ -(Ti,Nb)N + δ -NbN	36.1	42.0	60.0	72.0	equiaxed		30
NbN	0.67–1.33	δ -NbN	35.1	40.7	59.4	70.5	equiaxed		25

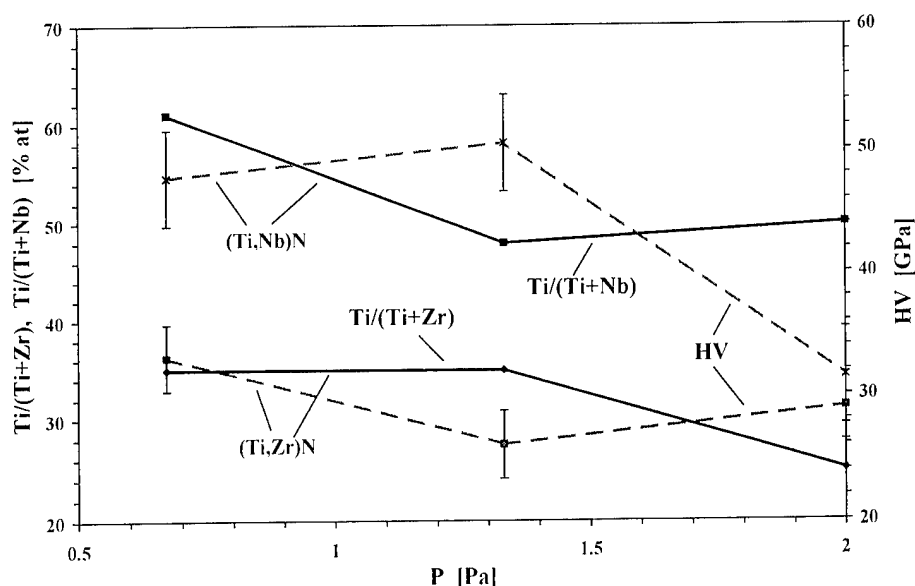


Fig. 3. Composition and microhardness of (Ti,Nb)N and (Ti,Zr)N coatings as functions of nitrogen pressure during deposition.

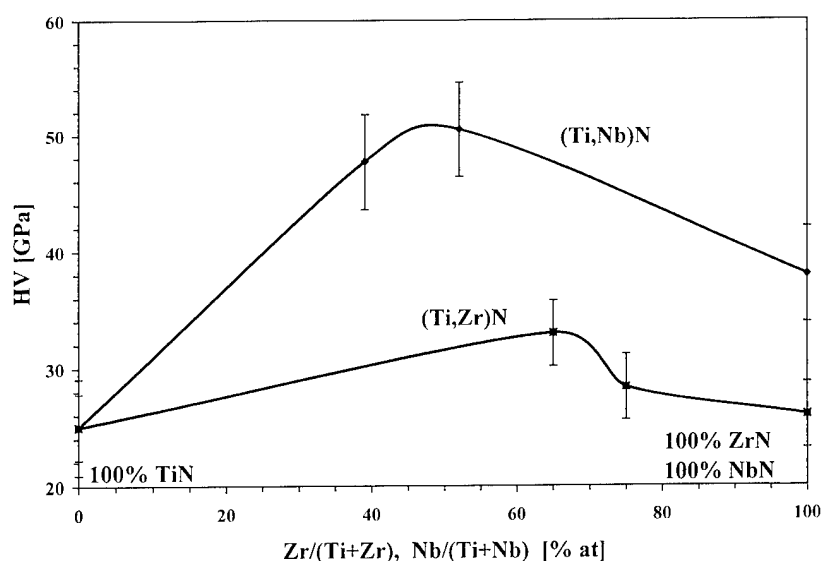


Fig. 4. Microhardness of (Ti,Nb)N and (Ti,Zr)N coatings, as a function of composition.

order polynomial in order to translate position to a single value of the ratio, and then plotting the measured microhardness (in general measured at slightly different positions than the composition) against the computed composition. The 0 and 100% points were obtained from separate binary ZrN and NbN samples deposited under the same conditions and having a thickness of 2.5–2.8 μm . The hardness versus composition data was fitted by third-order polynomial function, shown as the solid curve. It may be seen that the microhardness of the ternary nitride is higher than that of the corresponding binary nitrides, as was observed in the (Ti,Zr)N and (Ti,Nb)N coatings.

4. Discussion

It is known that in the ternary nitride systems of Group IV–VI transition metals, continuous ranges of solid solutions ($\text{MeI}_x\text{MeII}_{1-x}$)N with NaCl-type face-centered cubic structures exist. Such solid solutions may be considered as quasi-binary systems of two cubic nitrides, e.g. δ -(MeI)N and δ -(MeII)N [15].

In the Ti–Zr–N coatings, only single-phase ternary nitrides, with different Ti:Zr ratios depending on the nitrogen pressure and sample position, were found. Columnar grains with a strongly preferred (111) orientation were observed, similar to that in TiN and ZrN [13].

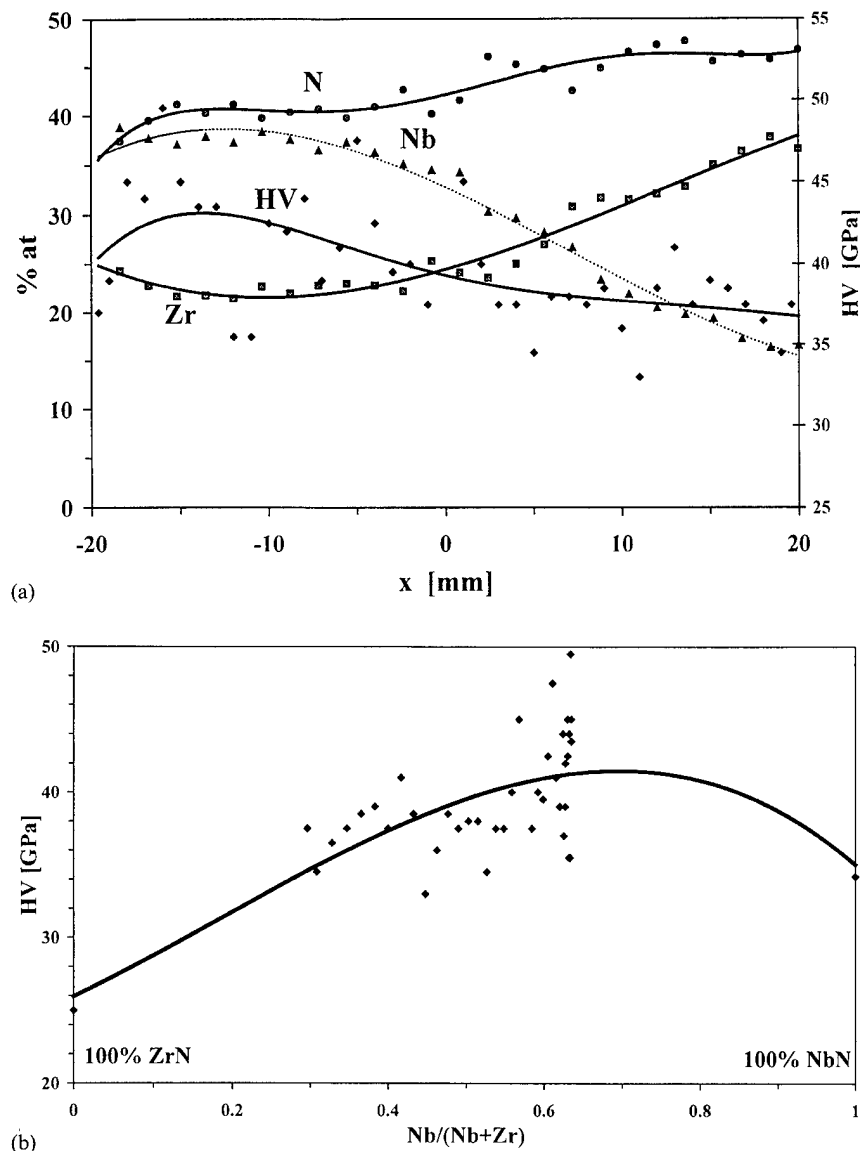


Fig. 5. Composition and microhardness of (Zr,Nb)N coatings: (a) as functions of position on the substrate; (b) microhardness as a function of composition.

Similarly, other researchers who studied Ti–Zr–N coatings deposited by different physical vapor deposition techniques reported the formation of the single-phase ternary nitride for a wide range of Ti:Zr ratios [8,9,16], and with a (111) oriented columnar structure [8,9]. The lattice parameter of $Ti_xZr_{1-x}N$ was between the values of that for binary TiN and ZrN and almost directly dependent on x (Vegard's rule) with slight positive deviation [9,16]. Knotek and Barimani [16] showed that single-phase (Ti,Zr)N coatings undergo spinodal decomposition after annealing at 1000°C for 3 h to form a solution of (Ti,Zr)N + (Zr,Ti)N, where the first is TiN enriched with Zr and the second is ZrN enriched with Ti. The spinodal decomposition is well described for bulk ternary nitrides [15].

As in our case, in most reported researches the

hardness of a ternary solid solution is higher than that of the appropriate binary nitrides [9,17], similar to that observed in the bulk ternary carbide and nitride systems [15]. The increased hardness is due to solid solution strengthening, possibly because of the energy barrier for dislocation movement through the crystals by the distortion of the lattice [9]. However, in the (Ti,Zr)N coatings deposited by Knotek et al. [17] using a cathodic arc, the Knoop microhardness measured on 5–7 μ m thick coatings were 25 GPa, 30 GPa, 33.5 GPa and 32 GPa (all ± 2 GPa) for TiN, $Ti_{0.5}Zr_{0.5}N$, $Ti_{0.25}Zr_{0.75}N$ and ZrN respectively. Thus the hardest ternary material was only slightly harder (i.e. within experimental uncertainty) than ZrN. They also observed that the increased hardness was accompanied by decreased scratch critical load of the ternary nitrides with respect to the parent

binary nitrides. Donohue et al. [9] also observed increased hardness for the ternary nitrides, but accompanied by increased scratch critical load. In most cases, the performance of cutting tools with the ternary coatings was enhanced relative to binary nitride coated tools [3,17–19].

In the Ti–Nb–N system, the phase composition depended on the deposition pressure. Thus, the high pressure (2 Pa) deposited coating had a two-phase composition consisting of ternary δ -(Ti,Nb)N and δ -NbN. It must be noted that the hardness of this two-phase coating was much less than that of the single-phase δ -(Ti,Nb)N coatings (Fig. 3). In contrast to (Ti,Zr)N, the (Ti,Nb)N coatings had an equiaxial structure (as did arc-deposited δ -NbN [14]). The ternary coatings exhibited a very high microhardness (~ 50 GPa), approximately the same as that of superlattice TiN–NbN coatings [20].

Few data on the physical, mechanical and tribological properties of (Ti,Nb)N coatings have been previously presented [4,21]. Coatings deposited using steered arc ion plating had a room temperature nanohardness of (28 ± 4 GPa), higher than that of TiN (23.8 ± 7 GPa). These values, however, are much less than those in the present study. The high temperature (900°C) nanohardness of (Ti,Nb)N was the highest among TiN, (Ti,Al)N, Ti(CN), and showed excellent cutting performance when drilling Cr–Mo steels, much higher than other coatings studied in that work [21].

5. Conclusions

Vacuum arc deposited ternary nitride coatings had a single-phase solid solution structure. Their lattice constants were between those of their parent binary compounds. The hardest of the ternary coatings was harder than either of the parent binary materials.

Acknowledgements

The authors gratefully acknowledge the technical assistance of Mr. H. Yaloz, and the financial support of

the Israel Ministry of Science, Strategic Infrastructure Program.

References

- [1] H. Holleck, V. Schier, *Surf. Coat. Technol.* 76 (77) (1995) 328.
- [2] H. Holleck, *J. Vac. Sci. Technol. A* 4 (1986) 2661.
- [3] O. Knotek, F. Löffler, G. Kramer, *Surf. Coat. Technol.* 54–55 (1992) 241.
- [4] E. Vancoille, J.P. Celis, J.P. Roos, *Thin Solid Films* 224 (1993) 168.
- [5] H. Freuller, H. Haessler, *Thin Solid Films* 153 (1987) 67.
- [6] O. Knotek, M. Bohmer, T. Leyendecker, *J. Vac. Sci. Technol. A* 4 (1986) 2695.
- [7] O. Knotek, M. Bohmer, C. Stoessel, *Surf. Coat. Technol.* 54–55 (1992) 249.
- [8] I. Sakamoto, S. Maruno, P. Jin, *Thin Solid Films* 228 (1993) 169.
- [9] L.A. Donohue, J. Cavley, J.S. Brooks, *Surf. Coat. Technol.* 72 (1995) 128.
- [10] I. Grimberg, V.N. Zhitomirsky, R.L. Boxman, S. Goldsmith, B.Z. Weiss, *Surf. Coat. Technol.* 108–109 (1998) 154.
- [11] V.N. Zhitomirsky, R.L. Boxman, S. Goldsmith, I. Grimberg, B.Z. Weiss, *Proceedings of the XVIIIth International Symposium on Discharges and Electrical Insulation in Vacuum*, Eindhoven, The Netherlands, August 17–21 vol. 2 (1998) 609–612.
- [12] V.N. Zhitomirsky, R.L. Boxman, S. Goldsmith, I. Grimberg, B.Z. Weiss, *IEEE Trans. Plasma Sci.* 27 (1999) 1049.
- [13] V.N. Zhitomirsky, I. Grimberg, R.L. Boxman, N.A. Travitsky, S. Goldsmith, B.Z. Weiss, *Surf. Coat. Technol.* 94–95 (1997) 207.
- [14] V.N. Zhitomirsky, I. Grimberg, L. Rapoport, N.A. Travitsky, R.L. Boxman, S. Goldsmith, A. Raihel, I. Lapsker, B.Z. Weiss, *Thin Solid Films* 326 (1998) 134.
- [15] H. Holleck, *Binäre und ternäre Carbide- und Nitridsysteme der Übergangsmetalle*, Gebrüder Borntraeger, Berlin, 1984. in German.
- [16] O. Knotek, A. Barimani, *Thin Solid Films* 174 (1989) 51.
- [17] O. Knotek, F. Löffler, G. Kramer, *Surf. Coat. Technol.* 49 (1991) 325.
- [18] H. Randhawa, P.C. Johnson, R. Cunningham, *J. Vac. Sci. Technol. A* 6 (1988) 2138.
- [19] O. Knotek, F. Löffler, G. Kramer, *Surf. Coat. Technol.* 59 (1993) 14.
- [20] X. Chu, S.A. Barnett, M.S. Wong, W.D. Sproul, *Surf. Coat. Technol.* 57 (1993) 13.
- [21] J.R. Roos, J.P. Celis, E. Vancoille, H. Veltro, S. Boelens, F. Jungblut, J. Ebberink, H. Homberg, *Thin Solid Films* 93–94 (1990) 547.

Localised oxidation defects in TiAlN/CrN superlattice structured hard coatings grown by cathodic arc/ unbalanced magnetron deposition on various substrate materials

M.I. Lembke, D.B. Lewis, W.-D. Münz *

Materials Research Institute, Sheffield Hallam University, Howard Street, Sheffield S1 1WB, UK

Abstract

TiAlN/CrN superlattice coatings show excellent surface oxidation resistance up to 900°C, with an as deposited hardness maximum of HK 3400 (bi-layer 3.8 nm). Coated M2 high speed steel and cemented carbide samples have been examined by scanning electron microscopy (SEM) and energy dispersive X-ray analysis (EDX) after heat treatment in air between 600°C and 1000°C to study the influence of the oxidation behaviour. X-ray diffraction (XRD) and thermogravimetric (TG) measurements were performed on the uncoated substrates to gain an overall picture of the oxidation stability of the plain substrate materials at high temperatures. Globular oxides were observed on coated cemented carbide at 700°C, while on M2 high speed steel similar oxides did not form below 800°C. The small globular oxides were gradually replaced by spherical oxides mainly formed out of substrate material. Initially oxidation starts at the bottom of pores or craters produced by small droplets or by growth defects grown on the droplets. The droplets were deposited during the cathodic arc metal ion step whereas the growth defects developed during film growth. Some detached growth defects formed craters through which oxidation products formed from the substrate material. Elements from the substrate penetrated to the coating surface at temperatures far below the actual oxidation temperature of TiAlN/CrN (900°C), namely at temperatures as low as 700°C (on cemented carbide). On M2 and stainless steel SS304, this type of localised oxidation was observed at temperatures equal to and above 900°C. © 2000 Elsevier Science S.A. All rights reserved.

Keywords: Cathodic arc deposition; Oxidation behaviour; PVD coatings; Superlattice structure; Unbalanced magnetron deposition

1. Introduction

Physical vapour deposited TiAlN coatings are used in dry cutting operations, because of their high oxidation temperature (850°C) and their wear resistance [1,2]. To further improve the hardness and the oxidation resistance, TiAlN/CrN multilayer coatings were produced leading to an increase in hardness up to HK_{0.25} 3400 and an increase in oxidation temperature of up to 900°C. Previous investigations showed that the oxidation resistance of this coating increases as the CrN component of the multilayer increases. The superlattice coating has an equal layer thickness of CrN and TiAlN of 3.8 nm [3]. The coating is produced by using the combined cathodic arc/unbalanced magnetron sputter technique (ABS®). The cathodic arc chromium metal ion-etching

step is an important step in the combined technique. It allows high and reliable adhesion values for PVD hard coatings on steel substrates [4]. One of the drawbacks of the cathodic arc deposition are macroparticles generated in the metal ion etching stage which result in the formation of growth defects [4–8]. In a previous paper [7], it was shown that the size and the number of droplets are substantially reduced by the cathodic arc Cr metal ion etch. However, the few remaining droplets are causing a shadowing effect underneath the droplet, which results in an attenuated ion and deposition flux. The defect structure that surrounds a droplet leaves a low-density zone or even a gap between the growth defect grain structure and the coating [8]. In other cases the droplets and the defects, grown on the droplets, may be expelled from the coating during film growth due to compressive stresses generated by the growing film, causing craters [5]. The influence growth defects on the localised oxidation behaviour of TiAlN/CrN superlattice coatings deposited on cemented carbide (CC) and M2

* Corresponding author. Tel.: +44-114-225-3500;
fax: +44-114-225-3501.

E-mail address: m.lembke@shu.ac.uk (W.-D. Münz)

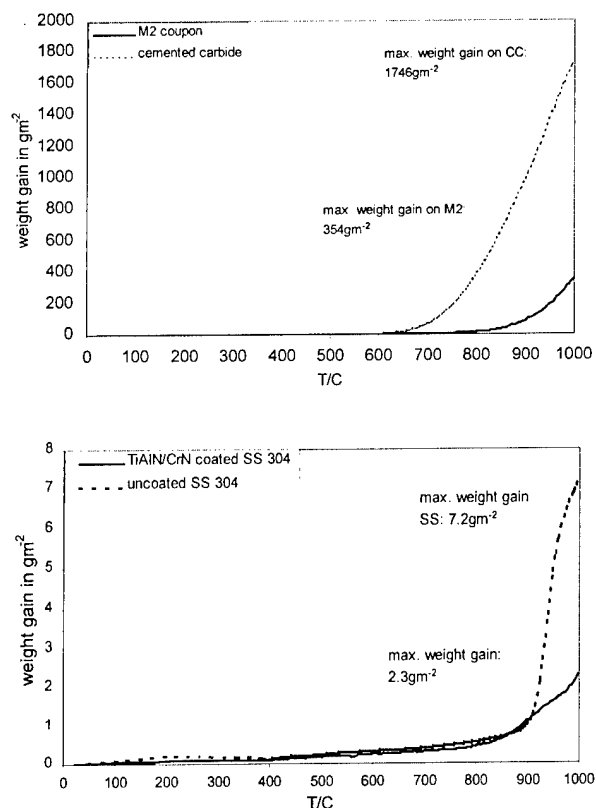


Fig. 1. (a) Continuous TG measurement on CC and M2 Fig. (b) Continuous TG measurement on coated SS and the uncoated substrate.

high speed steel substrates of the substrate materials was investigated using Scanning Electron Microscopy (SEM) and Energy Dispersive X-ray Analysis (EDX).

2. Experimental details

The TiAlN/CrN coatings were deposited by the ABS[®] technology using a Hauzer HTC 1000-4 physical vapour deposition machine. This machine comprises four targets operated simultaneously in a reactive atmosphere [1]. Prior to the coating step the substrates were exposed to high negative bias voltage (-1.2 kV) steered arc chromium metal ion etching treatment. The chromium metal ion etch minimises the number of droplets produced [6]. The remaining three targets were TiAl targets. All targets were operated at 8 kW in the coating step; details are given in Ref. [3]. Under these conditions, the coating was grown with approximately equally thick TiAlN and CrN layers with a bi-layer thickness of 3.8 nm [3]. The substrate materials used were M2 high speed steel (M2), cemented carbide (CC) and stainless steel 304 (SS), polished to a roughness of $R_a \approx 0.01$ mm finish.

The samples were heat treated in a furnace in air at 600, 700, 800, 900 and 1000°C for 1 h. The temperature

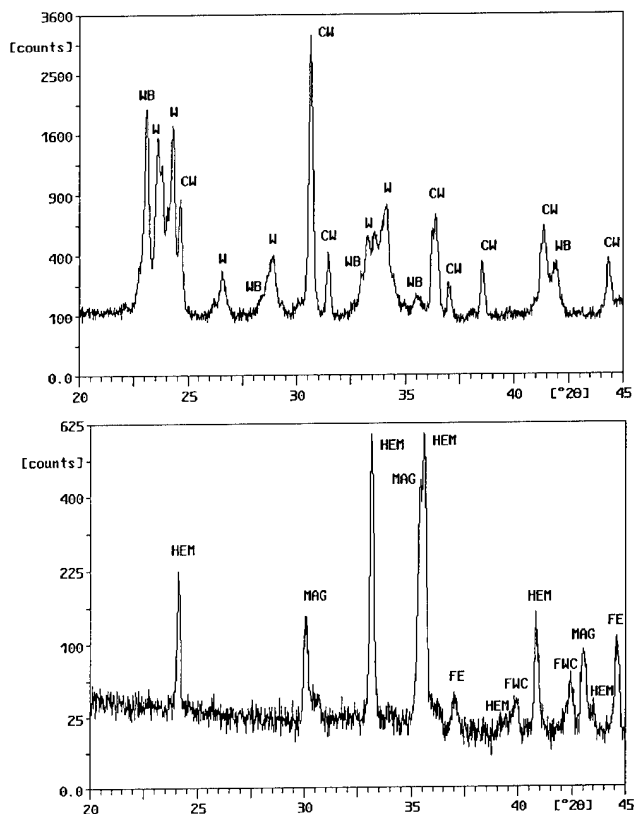


Fig. 2. (a) Oxidised CC substrate with W indicating the monoclinic version of WO_3 and WB the triclinic form. CW denotes $CoWO_4$. (b) Oxidised M2 substrate. MAG denotes Fe_3O_4 , HEM denotes Fe_2O_3 and FWC denotes the mixed $FeCr_2O_4$ oxide. FE is iron.

during the heat treatment was controlled with an accuracy of $\pm 3^\circ\text{C}$. After each heat treatment the samples were examined.

A Cahn TG 131 was used for the thermogravimetry work. The samples were continuously heated to 1000°C (at $50^\circ\text{C}/\text{min}$ to 400°C and from 400°C to 1000°C at $1^\circ\text{C}/\text{min}$) using a flow rate of 12.6 ml/min in dry air.

The specimens were examined by a SEM (Philips XL 40) at 20 kV accelerating potential for the imaging mode. The EDX analysis was performed using an ultra-thin window in front of the detector at a lower accelerating voltage of 10 kV.

The X-ray diffraction (XRD) was performed using monochromatic $Cu-K_\alpha$ radiation with Bragg–Brentano geometry. The phases present were identified using powder diffraction files data [9].

3. Results and discussion

The TG measurements in Fig. 1a revealed that the CC used starts to oxidise rapidly at temperatures above 700°C. In contrast to CC, rapid oxidation in M2 high speed steel does not occur before 900°C. The weight gain of cemented carbide is higher than that of M2 and

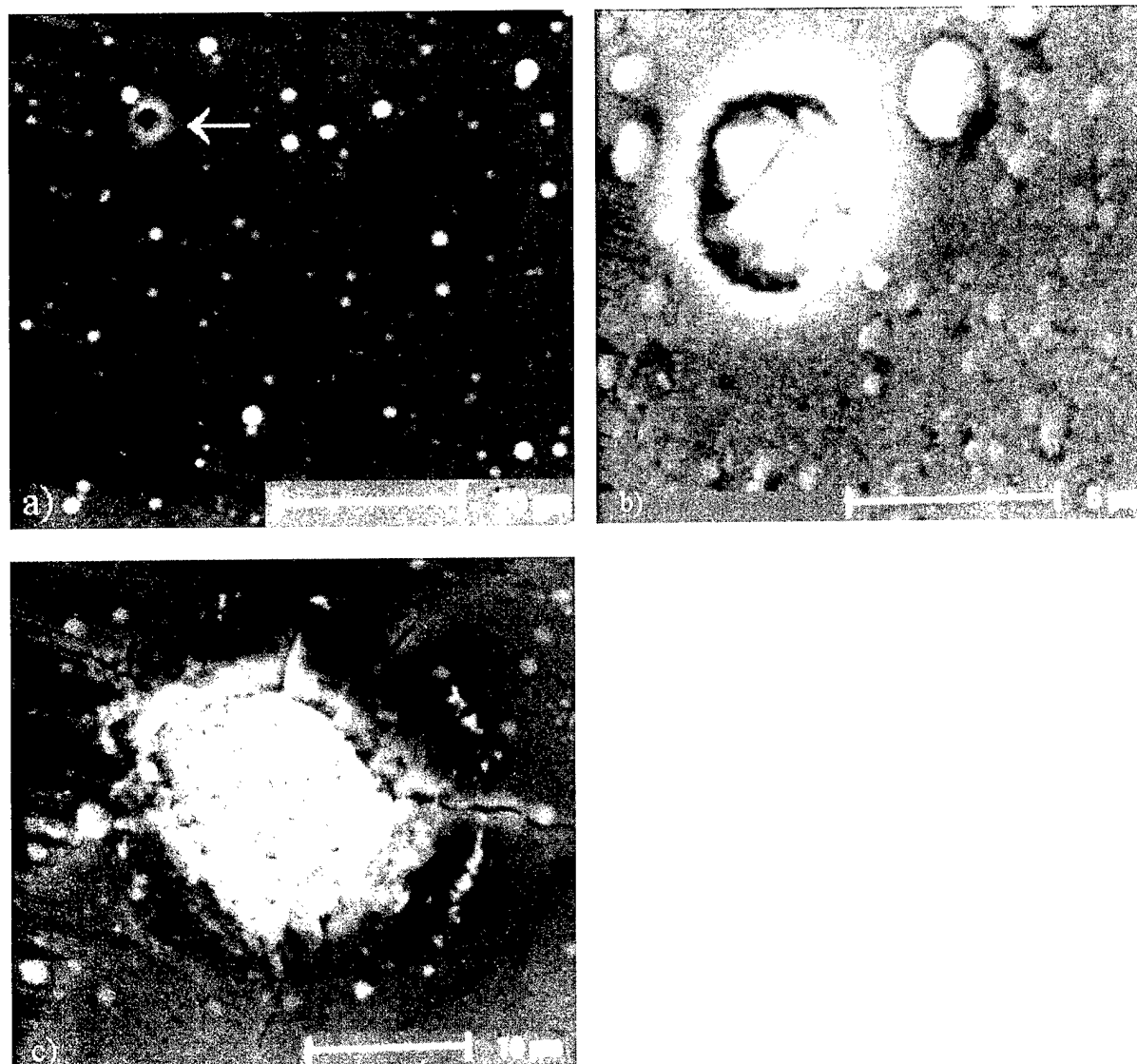


Fig. 3. (a) Low magnification survey from the as received coating surface. A crater is indicated through an arrow. (b) Oxides appear on the bottom of a crater on coated CC at 700°C. (c) Oxide formation on coated CC initiated local cracking of the coating at 800°C.

SS by factors of 5 and 100, respectively, when heated to 1000°C. Cemented carbide is well known for its rapid oxidation behaviour starting at temperatures as low as 600°C [10]. Therefore, it needs a protective coating to enable it to be used in high-speed cutting operations.

XRD diffraction patterns of the surface of CC and M2 heat treated at 900°C (CC) and 1000°C (M2) respectively are shown in Fig. 2. The oxides identified on CC were two different phases of tungsten oxide, WO_3 , one with a monoclinic crystal structure (JCPDS 24-747) and the other with a triclinic crystal structure (JCPDS 20-1323), together with a mixed tungsten cobalt oxide, CoWO_4 , with a cubic crystal structure (JCPDS 15-867) [9]. The mixed CoWO_4 oxide resulted from the oxidation of the cobalt binder used in liquid phase sintering of the tungsten carbide matrix. On M2, hematite (JCPDS 24-0072) Fe_2O_3 , magnetite (JCPDS

19-0629) Fe_3O_4 and a mixed FeCr_2O_4 (JCPDS 24-0512) oxide were identified. The M2 substrate material was not fully oxidised, as can be seen from the presence of the remaining iron (JCPDS 06-0696) peaks in the XRD pattern in Fig. 2b.

Examination at low magnification of the surface of the as deposited coating using SEM showed the presence of growth defects and craters (Fig. 3a). Droplets produced by the cathodic arc metal ion etch led to growth defects in the coating, which can extend from the substrate to the coating surface [8]. Because of the inherent high residual compressive stresses in the coating, some defects become detached [5] resulting in the formation of craters as pointed out by the arrow in Fig. 3a. After heat treatment of coated CC samples, oxides were formed at the bottom of craters at temperatures as low as 700°C (Fig. 3b). On CC, increasing the

temperature to 900°C leads to a significant increase in oxide formation in the crater, which results in cracking of the adjacent coating (Fig. 3c). EDX analysis of the oxidation product in the crater showed the presence of both tungsten and oxygen (Fig. 4a). The presence of the element tungsten in the oxides formed in the crater clearly shows that these oxides are formed by the oxidation of the substrate. Previous XRD measurements on the oxidised substrate would indicate that these were of WO_3 . A possible mechanism for the formation of cracks in the coating adjacent to craters containing oxide is the high volume expansion of tungsten oxide relative to that of tungsten (38% increase in volume). In contrast to CC local oxidation of substrate material in holes occurred at higher temperatures on M2. The first oxides were observed at 700°C on CC and at 900°C on M2. This result is not surprising as the TG analysis clearly showed that CC oxidises at a significantly lower temperature than M2.

Another form of oxidation is shown in the micrograph in Fig. 5a at 700°C on coated CC. At low magnifications, accumulations of very small globular defects

were observed on CC as pointed out by the arrows in Fig. 5a. At higher magnifications (Fig. 5b) a more or less continuous coating is observed covered with smaller and larger sized globular oxides. Only a small concentration of substrate elements are observed for coated CC oxidised at 800°C as shown in Fig. 4b. This special defect may be correlated to areas where the droplet and the growth defect were expelled during film growth and the crater created has been partially filled with coating material [5]. Pores formed in the under-dense region at the rim of the growth defect on the deposited film material allowed localised oxidation. Further oxidation led to the formation of spherical oxides as shown in the micrograph in Fig. 5c and the appearance of substrate materials as shown in the EDX spectrum in Fig. 4c at 800°C on coated CC. Similar shaped defects were observed on coated M2. An EDX spectrum in Fig. 4d taken at 900°C showed the occurrence of Fe and O on surface of the coated M2 steel. However, on coated M2 this defect formation was in general less pronounced than that on coated CC and the first defects containing substrate elements occurred at 900°C on M2. These

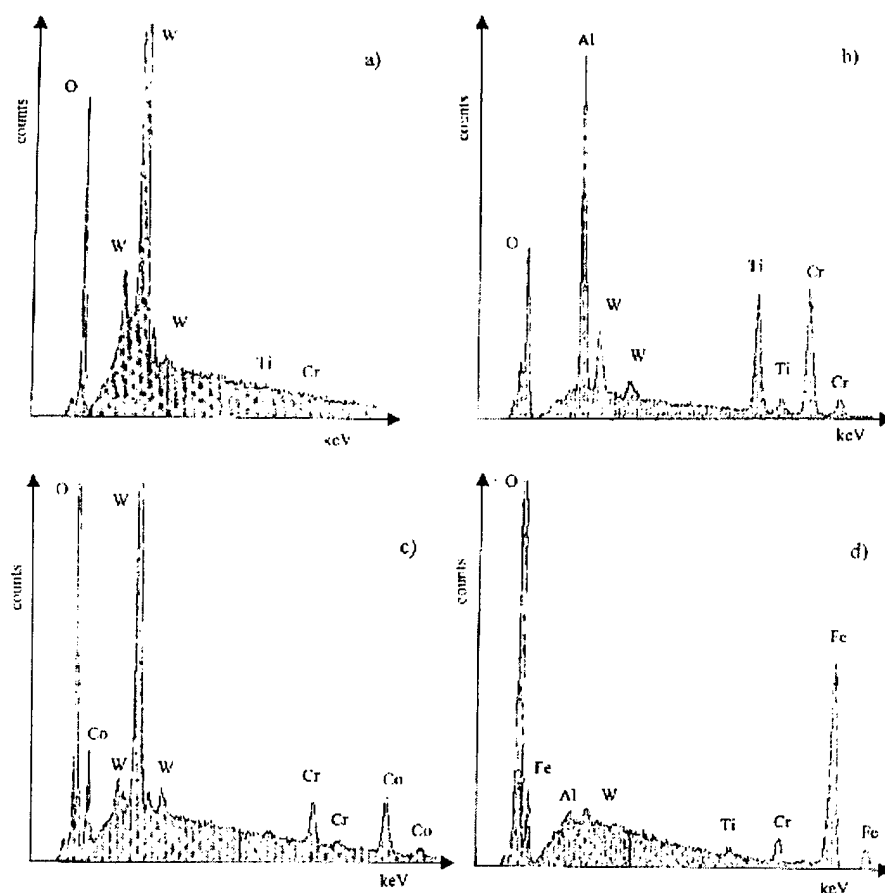


Fig. 4. (a) EDX analysis on oxide breaking through the surface on coated CC. Ti and Cr indicate the areas where the K_{α} lines of these elements would be observed. (b) EDX analysis of accumulated globular oxides on coated CC at 800°C. (c) EDX analysis of big oxide formed in the globular oxide region on CC at 800°C. (d) EDX analysis of big oxide formed in the globular oxide region on M2 at 900°C.

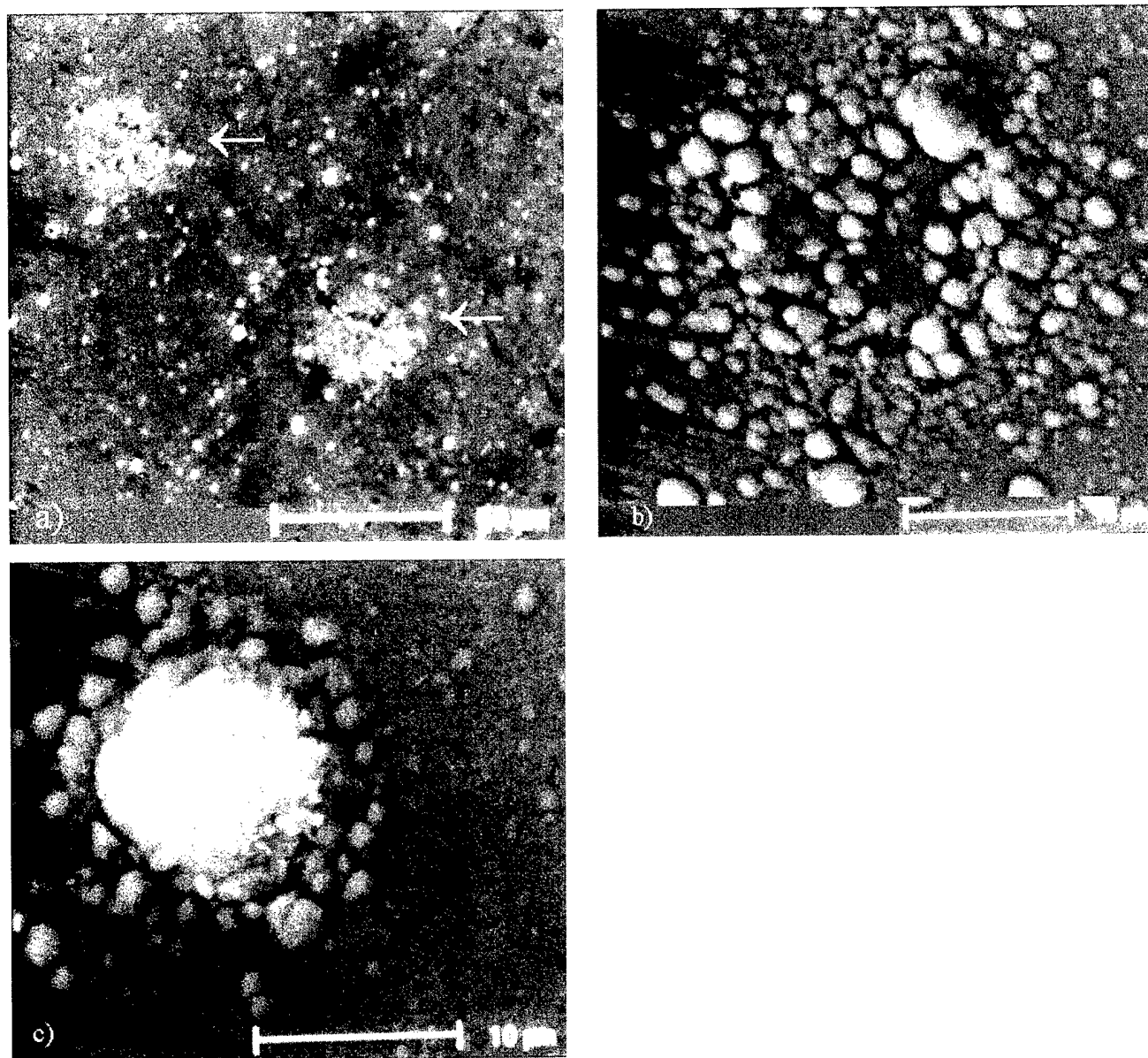


Fig. 5. (a) Low magnification survey on an oxidised coated CC at 700 °C. (b) Accumulated globular oxides in detail on CC at 800 °C. (c) Big oxide formed in globular oxides on CC at 800 °C

results are again reflected in the relative oxidation resistance of the M2 high speed steel in comparison to CC as can be seen in Fig. 1a.

4. Conclusion

(1) The oxidation behaviour of the substrate material influences directly the generation of growth defects through craters caused by droplet formation.

(2) Particularly in the case of WC substrates, severe oxide defect growth is observed already at 700 °C.

(3) These defects should be of significant influence in dry high speed cutting operations when cutting temperatures up to 1000 °C are expected.

(4) Conversely, in the case of M2 high speed steel substrates the oxide defect formation should be of less importance as tools fabricated from M2 are usually operated at temperatures below 600 °C.

References

- [1] W.-D. Münz, J. Vac. Sci. Technol. A4 (6) (1986) 2701.
- [2] I.J. Smith, D. Gillibrand, J.S. Brooks, W.-D. Münz, S. Harvey, R. Goodwin, Surf. Coat. Technol. 90 (1997) 164–171.
- [3] I. Wadsworth, I.J. Smith, L.A. Donohue, W.-D. Münz, Surf. Coat. Technol. 94–95 (1997) 315–321.
- [4] W.-D. Münz, D. Schulze, F.J.M. Hauzer, Surf. Coat. Technol. 50 (1992) 169–178.

- [5] W.-D. Münz, D.B. Lewis, S. Creasey, T. Hurkmans, T. Trinh, W. van Ijzendoorn, *Vacuum* 46 (4) (1995) 323–330.
- [6] W.-D. Münz, I.J. Smith, D.B. Lewis, S. Creasey, *Vacuum* 48 (5) (1997) 473–481.
- [7] S. Creasey, D.B. Lewis, I.J. Smith, W.-D. Münz, *Surf. Coat. Technol.* 97 (1997) 163–175.
- [8] I. Petrov, P. Losbichler, D. Bergstrom, J.E. Greene, W.-D. Münz, T. Hurkmans, T. Trinh, *Thin Solid Films* 302 (1997) 179–192.
- [9] JCPDS-ICDD Diffraction Data Database, International Centre for Diffraction Data, 1993.
- [10] E.M. Trent, *Metal Cutting*, Butterworths, London, 1977. p. 106.

Properties of various large-scale fabricated TiAlN- and CrN-based superlattice coatings grown by combined cathodic arc–unbalanced magnetron sputter deposition

W.-D. Münz*, L.A. Donohue, P.Eh. Hovsepien

Surface Engineering Research Group, Materials Research Institute, Sheffield Hallam University, Howard Street, Sheffield S1 1WB, UK

Accepted 13 October 1999

Abstract

TiAlN and CrN are gaining increasing importance in many industrial applications. To improve their mechanical and tribological properties further, these materials have been deposited to form 3 μm thick superlattice structures of TiAlN–CrN (period 3.8 nm). The structural and tribological characteristics of TiAlN–VN (period 3.0 nm) and CrN–NbN (period 3.7 nm) have also been studied in comparison with TiAlN–CrN and monolithic TiAlCrN and CrN alloys. All coating were deposited using the combined steered cathodic arc–unbalanced magnetron deposition method. The superlattice coatings generally showed increased hardness value and considerably reduced sliding and micro-abrasive wear compared with TiAlCrN and CrN. In the case of superlattice structured films TiAlN–VN films showed exceptional performance in dry sliding wear tests and, generally, all TiAlN-based films performed well in micro-abrasive wear trials. Corrosion tests revealed that CrN–NbN coatings exhibited clear passivation characteristics with considerably better corrosion resistance than stainless steel and significantly lower passive current density than electroplated hard chromium. © 2000 Elsevier Science S.A. All rights reserved.

Keywords: Arc; Evaporation; Multilayers; PVD; Sputtering; Superlattices

1. Introduction

The microstructure, microchemistry and enhanced mechanical properties of superlattice structures such as TiN–VN and TiN–NbN hard coatings have been reported for several years. In particular, hardness values up to Knoop hardness of 50 GPa (evaluated by 25 g load, $\text{HK}_{0.025}$) have raised the interest of the scientific community [1–3]. More recently, new materials combinations have been studied, among which have been TiN-based coatings, such as TiN–WN [4], TiN–CrN, TiN–Ta₂N, TiN–MoN [5] and TiN–AlN [6]. Initial efforts have also been undertaken to transfer process technology from the laboratory to an industrial scale to produce TiAlN-based superlattice coatings using commercial multi-target physical vapour deposition (PVD) equipment utilising the combined cathodic arc–unbalanced magnetron deposition technique [7,8] primarily for the coating of cutting tools. Early reports on TiAlN–ZrN

[8], TiAlN–CrN [9] and TiAlN–TiNbN [10] have shown that coatings can be deposited with clear superlattice characteristics without the use of complicated and economy-reducing shielding to avoid severe intermixing of the growing layers. Only recently, the scale of alloy combinations under evaluation has been enlarged by the introduction of CrN–NbN coatings [11,12] aimed at the development of a combined wear- and corrosion-resistant coating. The element Nb was chosen to be part of the coating system owing to its unique properties and performance in electrochemical tests [13]. When reactively deposited and constrained within a superlattice stack, high hardness values are expected that will allow competition with traditional 20 μm thick electroplated hard chromium coatings. In the following a comparative summary is presented on results obtained for monolithically grown TiAlCrN and CrN alloy coatings and superlattice structure TiAlN–CrN, TiAlN–VN and CrN–NbN hard coatings. The coatings have been evaluated with respect to their microstructure, mechanical and tribological properties and also the corrosion behaviour in the case of CrN–NbN.

* Corresponding author.

2. Experimental

All coatings were deposited using a Hauzer Techno Coating Europe B.V. HTC 1000-4 ABS PVD coating unit utilising the combined cathodic arc–unbalanced magnetron sputter deposition method [7]. Prior to deposition the substrates were exposed to an in vacuo pre-treatment with highly energetic Cr metal ions generated from a steered cathodic arc discharge. In the case of TiAlCrN–CrN, TiAlN–CrN and CrN–NbN the substrates [polished M2 high speed steel, diameter $30\text{ mm} \times 10\text{ mm}$ of $R_a = 0.01\text{ }\mu\text{m}$ and $30 \times 30 \times 8\text{ mm}^3$ coupons of austenitic 304 stainless steel (SS)] were metal ion etched at a substrate bias voltage of -1200 V and an exposure time of 20 min. By these means the steel substrate surface was conditioned for local epitaxial film growth [10,14], guaranteeing sufficiently high adhesion [10] and minimising the roughness of the coatings due to reduced macroparticle deposition on the substrate during the metal ion etching step [15]. In the case of TiAlN–VN, vanadium was used as the metal ion etchant.

The coatings were grown within a symmetrically arranged four cathode, large-scale chamber used in unbalanced magnetron sputter mode as shown in cross-section in Fig. 1. The cathodes could also be used in steered arc mode [7] by suitable mechanical movement of the permanent magnets (i.e. magnets positioned directly behind target for sputter mode or magnets withdrawn for steered arc mode). The unbalancing effect was achieved using electromagnets displaced around each cathode in such a manner that closed field magnetic field coupling could be accomplished to allow a high

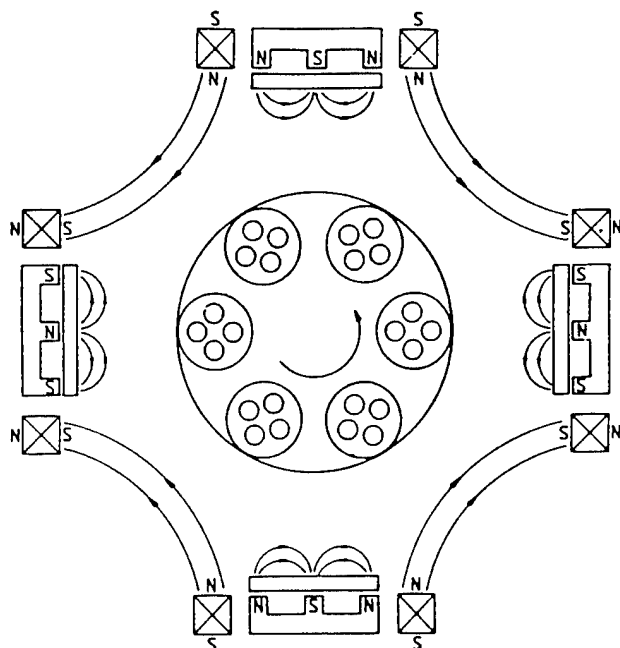


Fig. 1. Schematic cross-section of combined arc–magnetron PVD unit.

degree of ionisation and bias current density during unbalanced magnetron sputtering (typically $2\text{--}4\text{ mA cm}^{-2}$). The opposing linear cathodes were at a distance of 1 m. A planetary rotation substrate holder was placed in the centre of the chamber and rotated with a primary rotation frequency of 7.5 rpm. TiAlN was reactively ($\text{Ar} + \text{N}_2$ mixed discharge) sputtered from three TiAl targets of composition 50:50 at.% at a cathode power of 8 kW (each of dimension $60 \times 20 \times 1.2\text{ cm}^3$). Simultaneously, the Cr target was sputtered with 0.5 kW to maintain a surface that was essentially uncontaminated with scattered Ti and Al atoms. In the case of TiAlN–CrN superlattice films the same arrangement was used with accordingly higher power dissipation on the Cr target. TiAlN–VN coatings were formed using two TiAl targets (50:50 at.%) and two pure V targets; CrN–NbN films were fabricated by reactive sputtering two pure Cr and two pure Nb targets. During the complete cycle of superlattice deposition all the targets were operated simultaneously without the use of shutters or shieldings. It should be noted that this arrangement can clearly lead to a certain degree of cross-contamination and intermixing of the layers. If one uses different target materials simultaneously in one common reactive gas atmosphere, the effect of preferred poisoning of the more sensitive target material has to be considered. To avoid such a situation, a strong pumping system was used that included two unthrottled 2200 l s^{-1} turbomolecular pumps backed by a $250\text{ m}^3\text{ h}^{-1}$ roots pump and a $500\text{ m}^3\text{ h}^{-1}$ rotary vane pump. Under these conditions a rather flat and narrow hysteresis (poisoning curve formed by plotting N_2 partial pressure as a function of gas flow) characteristic may be expected (Fig. 2). As, in the relevant pressure range for reactive magnetron sput-

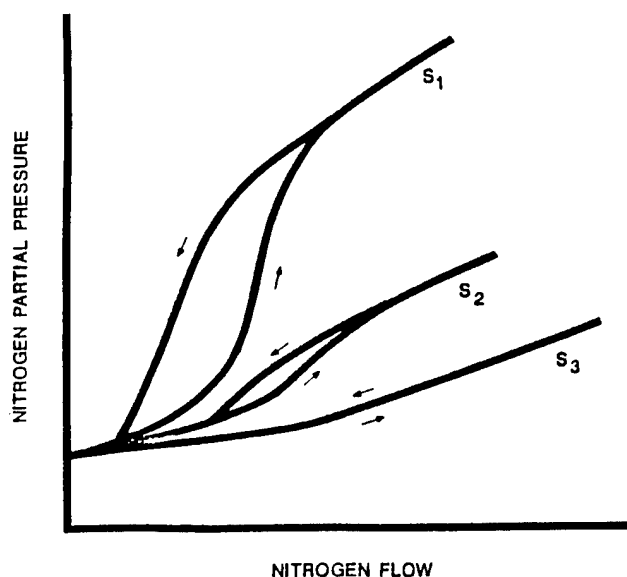


Fig. 2. Schematic of hysteresis behaviour as a function of pumping speed (after Ref. [16]).

tering, the turbo-pumps tend to exhibit a highly accurate and essentially pressure-independent pumping speed, the partial pressure of ΔP_{Ar} was adjusted by means of mass-flow controllers. The reactive gas was controlled by a feedback-controlled sensitive manometer (Leybold 'Viscovac') coupled to a flow control valve where the Viscovac accurately measured total pressure ($3\text{--}3.5 \times 10^{-3}$ mbar), whereas ΔP_{Ar} was set to $2\text{--}2.5 \times 10^{-3}$ mbar. The electromagnetic coils were usually operated at 6 A. Only in the case of low-temperature deposition of CrN were the coils reduced to 3 A to provide a substrate temperature as low as 250°C. The typical process data are summarised in Table 1. Further information on the simultaneous operation of the differently composed targets within a common gas atmosphere is given in Ref. [8].

3. Physical and structural properties of superlattice coatings

The various structural and physical properties, such as phase composition, lattice parameter, preferred orientation and residual stresses, of the films are summarised in Table 2). All of the coatings investigated were found to crystallise into a B1 NaCl fcc structure. As reported previously, monolithic $\text{Ti}_{0.44}\text{Al}_{0.53}\text{Cr}_{0.03}\text{N}$ [15] and CrN [17] films were grown with {111} and {220} preferred orientation respectively. All superlattice structured films examined so far have exhibited predominantly {111} or {200} orientation with {111} (occasionally mixed {111} and {220} for high CrN-containing films) preferred orientation observed typically for low lattice mismatched films demonstrating competitive columnar

growth, e.g. TiAlN–CrN, TiAlN–VN or TiAlN–TiN (not included in this study). However, {200} orientation (lowest energy state for an fcc structure) tends to become dominant for systems that grow via a continuous re-nucleation or interrupted grain growth mechanism (i.e. TiAlN–ZrN [8]). This effect is commonly found in TiAlN-based systems when large atomic radii or heavier atoms are involved in the growth, such as Nb [18], Y [19] and W [4,8]. All of the coatings exhibited compressive residual stress states, with the TiAlN-based superlattice systems generally considerably higher than that of $\text{Ti}_{0.44}\text{Al}_{0.53}\text{Cr}_{0.03}\text{N}$ and CrN. In contrast, the CrN–NbN superlattice has a comparatively low stress of -1.5 GPa. Similar low stress values have also been found for TiN–WN [4]. It is difficult at this stage to discuss the tabulated full-width at half-maximum (FWHM) data, as exact knowledge of the grain size has yet to be determined by plan view transmission electron microscopy (TEM). Complete separation of the influence of lattice strain and grain size contributions for each system is currently being determined. The phase composition of the coatings is further documented in Fig. 3(a)–(e). All the superlattice coatings [Fig. 3(c)–(e)] clearly identified single-phase character with peak positions coinciding with that predicted from the weighted average of the two components. It is also interesting to observe that the typical CrN orientation {220} loses its dominance in the CrN–NbN system to the {200} direction. The typical superlattice period of the coatings investigated in this study ranged between 3 and 4 nm. Figs. 4 and 5 outline the gradual change in bi-layer thickness that can be achieved within the TiAlN–CrN system at constant rotation velocity but increasing Cr content. On raising the cathode power of the Cr target steadily from

Table 1
Basic process details for PVD coating of the various films

	Metal ion etchant	Etching substrate bias (V)	Deposition temperature (°C)	Base layer and typical thickness (μm)	Total film thickness (μm)	Substrate bias (V)	R_a (μm)
TiAlCrN	Cr	–1200	450	None	3–5	–75	0.04
CrN	Cr	–1200	250	None	3–5	–100	0.04
TiAlN–CrN	Cr	–1200	450	TiAlN (0.1–0.3)	3–5	–75	0.04
TiAlN–VN	V	–1200	450	TiAlN (0.1–0.3)	3–5	–75	0.06
CrN–NbN	Cr	–1200	450	CrN (0.3)	3–5	–75	0.05

Table 2
Phase composition, lattice parameter and typical preferred orientation of the various films (data taken by low- and wide-angle Bragg–Brentano and glancing-angle parallel beam geometry X-ray diffraction)

	Preferred orientation	Structure	Typical lattice parameter (nm)	(111) peak FWHM ($2\theta^\circ$)	Typical superlattice period (nm)	Residual stress state and magnitude (GPa)
TiAlCrN	{111}	B1 NaCl fcc	0.418	0.34	none	–3.8 compressive
CrN	{220}	B1 NaCl fcc	0.419	0.75	none	–2.0 compressive
TiAlN–CrN	{111}	B1 NaCl fcc	0.420	0.93	3.8	–6.1 compressive
TiAlN–VN	{111}	B1 NaCl fcc	0.416	1.10	3.0	–4.0 compressive
CrN–NbN	{200}	B1 NaCl fcc	0.429	0.71	3.8	–1.5 compressive

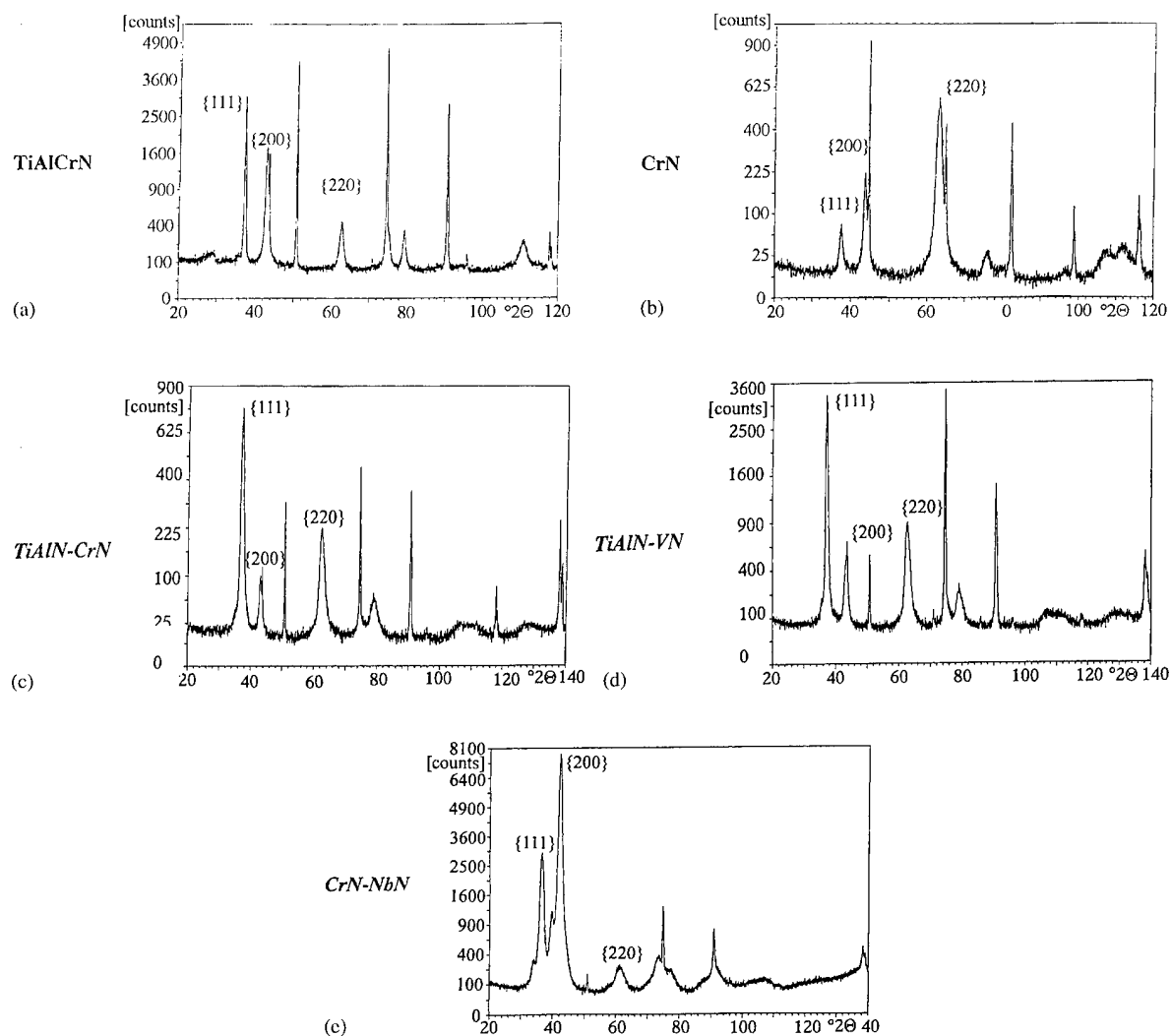


Fig. 3. Wide-angle Bragg-Brentano X-ray diffraction patterns: (a) TiAl-CrN; (b) CrN; (c) TiAlN-CrN; (d) TiAlN-VN; (e) CrN-NbN.

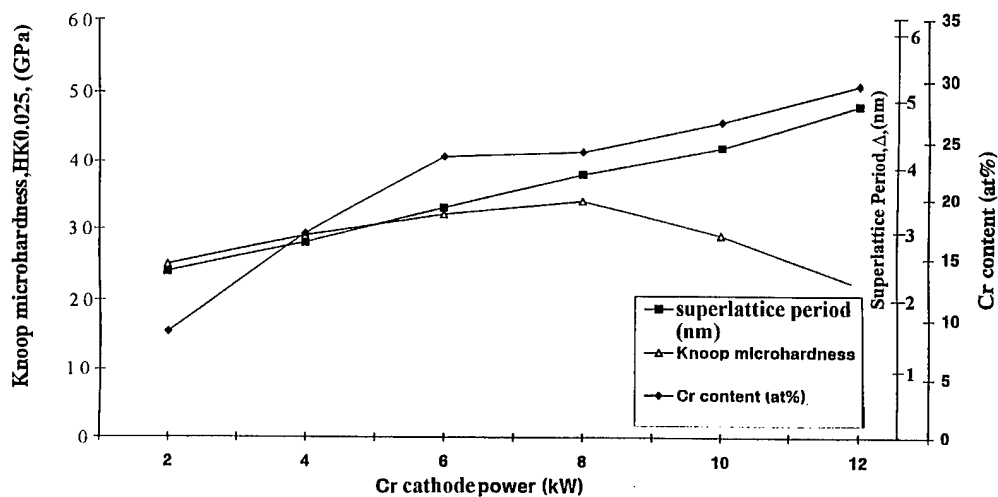


Fig. 4. Properties of TiAlN-CrN as a function of Cr content and superlattice period.

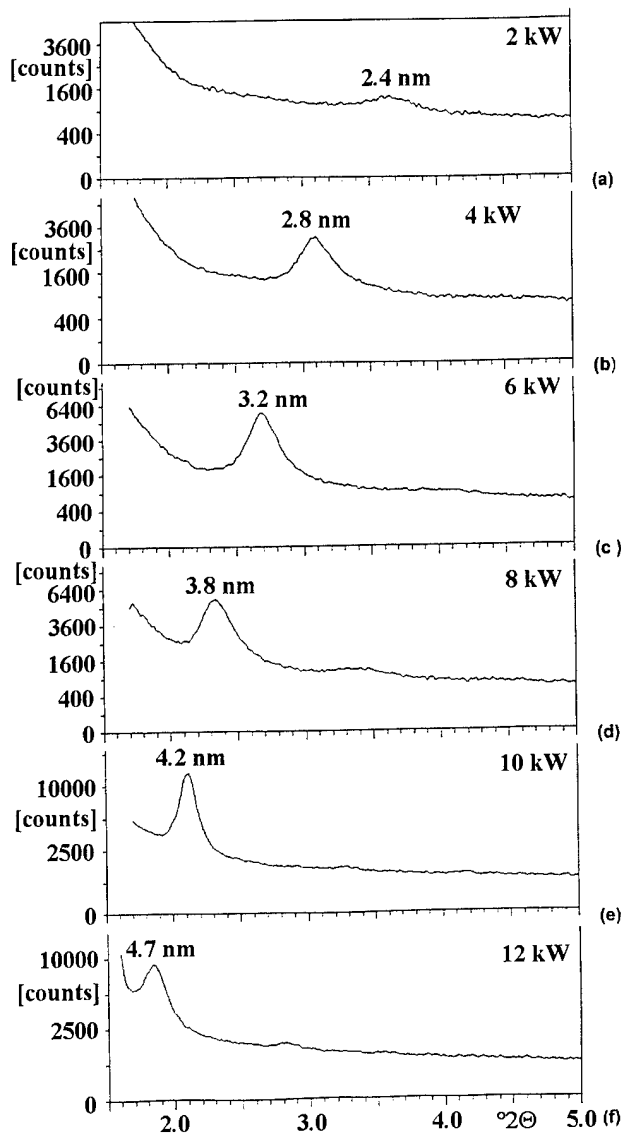


Fig. 5. Low-angle Bragg-Brentano X-ray diffraction patterns.

0 to 12 kW the bi-layer thickness shows a linearly increasing superlattice period from 0 to 4 nm. Fig. 4 also shows that at 8 kW the typical superlattice hardness maximum is attained, coinciding with equi-thickness layering. At a cathode power below 8 kW, a steady increase in hardness is achieved (from HK=25 GPa to HK=32 GPa) as a function of Cr content, followed by a hardness decay at power in excess of 8 kW approaching HK=20 GPa typical for CrN [17]. The bi-layer thickness may be measured by low-angle Bragg-Brentano X-ray diffraction analyses as illustrated in Fig. 5. The typical microstructure of the superlattice coatings can be illustrated using two systems using bright-field XTEM imaging in Figs. 6 and 7. Fig. 6 shows at low magnification the typical competitive columnar grain growth associated with {111} oriented TiAlN-VN. The micrograph also depicts clearly that a dense TiAlN base layer

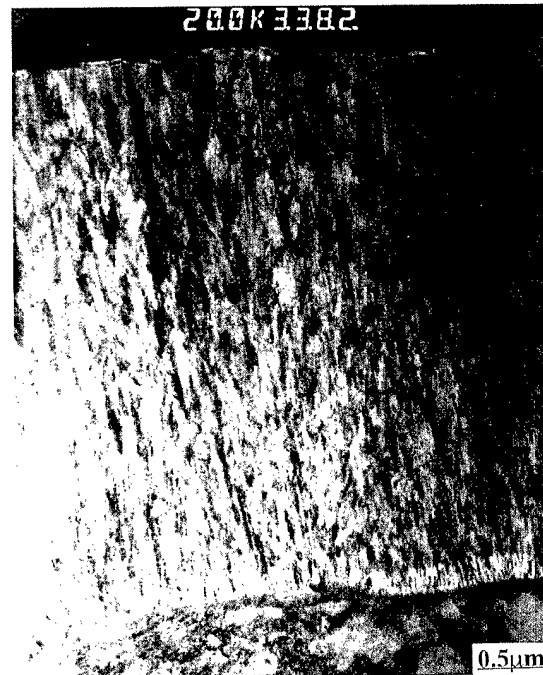


Fig. 6. Low magnification bright-field XTEM from TiAlN-VN superlattice.



Fig. 7. Higher magnification bright-field XTEM at base layer-superlattice interface of CrN-NbN and associated selected-area diffraction pattern.

of thickness approximately 0.2 μm is deposited above the polycrystalline steel substrate prior to superlattice deposition to a thickness in excess of 3 μm. The base layer is deposited primarily to control and set up a residual stress gradient between the superlattice film and steel substrate. The use of a base layer has also been found to be essential to achieve sufficiently high adhesion in highly stressed superlattice films such as TiAlN-ZrN. Fig. 7 describes at higher magnification the transition zone between the base layer and the CrN-NbN superlattice. The grains of the CrN base layer are found to extend into the superlattice in an undisturbed manner

unlike the case for {200}TiAlN–ZrN where continuous re-nucleation caused extensive grain refinement [8,10]. The image also shows the interesting detail of gradual poisoning of the Nb cathodes by the decrease in thickness of the deposited NbN layers (appearing dark). After deposition of approximately ten bi-layers a steady reactive sputtering condition has been reached and the thickness of the NbN layers remain constant throughout the remaining film thickness.

4. Mechanical and tribological properties

The mechanical and tribological properties of the various films are summarised in Table 3. The evaluated hardness values of the three superlattice coatings (typically around $HK=35$ GPa) were found to be consistently higher than the monolithically grown films (typically $HK=21$ GPa to $HK=25$ GPa). However, the hardness values measured using static load Knoop diamond indentation testing were lower than those recorded for various superlattice systems deposited under laboratory conditions and generally measured using dynamic nano-hardness apparatus [1,2]. One might speculate that a possible reason for the reduction in hardness could be a consequence of partial intermixing or reduced interface definition of the individual layers involved. This may be investigated further by exploring the introduction of shielding to stimulate sharper interface formation. On the other hand, all coatings show satisfactory adhesion-related results such as critical load L_c , or Rockwell-C indentation values (Daimler-Benz test).

The sliding wear represented by the sliding wear coefficient K_C , [20] Table 3, was found to depend strongly on the friction coefficient. The lowest friction coefficient was observed for the TiAlN–VN system. Earlier work indicated that VN tends to form lubricious surface oxides, which may reduce the friction coefficient [21]. Hence TiAlN–VN provides encouraging tribological behaviour through the complementary properties of surface oxide formation by VN, with high microhardness

given by the superlattice approach. Based on this assumption the wear coefficient of the CrN system should be expected to be lower than TiAlCrN. However, we must also correlate the morphology of the CrN to wear trials, as discussed later. With respect to the abrasive wear rate, all TiAlN-based coatings were found to be superior. This result may be attributed to the typically high oxidation resistance [19,21,22] of TiAlN coatings as the abrasive particles (in our case SiC) generate permanently new unprotected surfaces where tribo-oxidation may take place.

Examples of the wear tracks produced during the dry sliding wear tests are shown in Fig. 8(a)–(d). CrN coatings shown after 3 km of sliding (0.1 m s^{-1} , 6 mm Al_2O_3 , 33% humidity, 5 N) illustrate deep grooving along the wear direction. Growth defects developed above droplets generated during ion etching can be observed to be ejected from the coating to leave holes. In contrast, CrN–NbN films worn for an equivalent sliding distances show only marginal effects with a relatively smooth (polished) surface and significantly reduced wear. In the case of the TiAlN–CrN (and CrN–NbN) film after 500 000 cycles (equivalent to approximately 30 km) deep grooves were also found to appear as the wear depth within the track approached the coating–substrate interface and the distinctive role of the ploughed macroparticles reappears. In comparison, the TiAlN–VN coating after nearly 70 km of wear shows a wear depth within the track of less than $1 \mu\text{m}$. The wear track still appears rather smooth and only a few defects may be observed to have been extracted from the coating surface. On the contrary, the majority of the growth defects appear to have been smoothly polished, as indicated by bright spots. Fig. 9 represents the friction coefficient as a function of sliding distance. As expected from the wear rate measurements, the recorded friction coefficient was found to be relatively low at approximately 0.4 and to remain virtually constant over the entire 1.1×10^6 cycle duration of the test (a short run-in period may also be observed at initiation of the test).

Table 3
Mechanical properties of various PVD hard coatings^a

	Microhardness, $HK_{0.025}$ (GPa)	Scratch adhesion L_c (N)	Rockwell indent quality (Daimler-Benz test)	Sliding wear coefficient K_C ($\text{m}^2 \text{N}^{-1}$)	Abrasive wear coefficient K_C ($\mu\text{m}^2 \text{N}^{-1}$)	Average friction coefficient μ	Coating structure type
TiAlCrN	25	55	1	1.22×10^{-14}	0.15	0.68	columnar monolithic
CrN	21	50	1	8.93×10^{-16}	0.77	0.49	columnar monolithic
TiAlN–CrN	32	55	1	2.38×10^{-16}	0.16	0.56	superlattice
TiAlN–VN	35	70	1	1.26×10^{-17}	0.22	0.40	superlattice
CrN–NbN	35	50	1	2.10×10^{-15}	0.61	0.63	superlattice

^a Friction coefficient and sliding wear data measured from CSEM dry pin-on-disc testing against 6 mm diameter polycrystalline Al_2O_3 at normal load 5 N, sliding velocity 0.1 m s^{-1} and radius 10 cm. Abrasive wear measured using CSEM ‘Calo-Wear’ test — 25 mm diameter ball rotating with $4 \mu\text{m}$ SiC particle aqueous suspension.

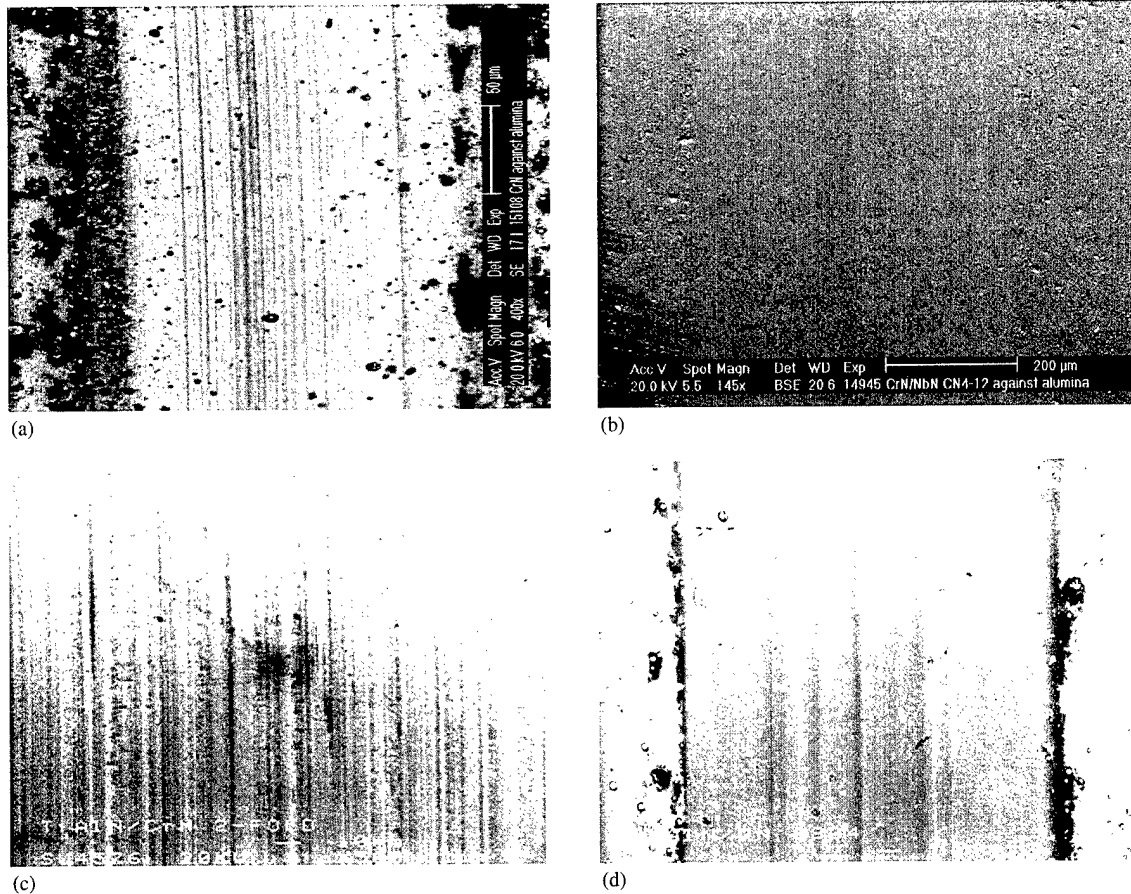


Fig. 8. Pin-on-disc wear tracks: (a) CrN film worn over 50 000 cycles (3.14 km); (b) CrN–NbN film worn over 50 000 cycles (3.14 km); (c) TiAlN–CrN film worn over 500 000 cycles (31.4 km); (d) TiAl–NVN film worn over 1.1×10^6 cycles (69 km).

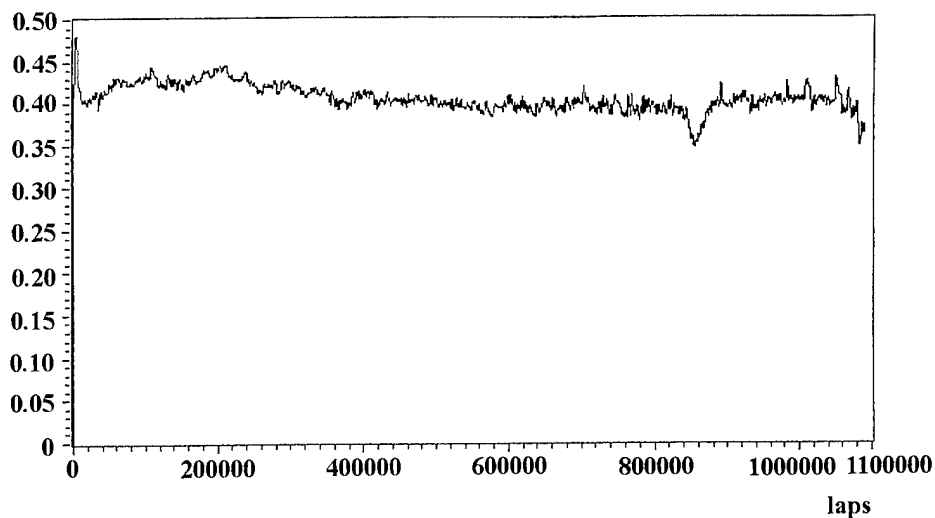


Fig. 9. Friction coefficient as a function of the sliding distance of TiAlN–VN.

It is interesting to discuss this behaviour in context with previously published results concerning XTEM investigations on the wear mechanisms of monolithically grown TiAlCrN and TiAlN–CrN superlattice coatings [23]. It has been shown that monolithically grown

coatings tended to fail during pin-on-disc testing through plastic deformation of the columnar grains at near-surface regimes due to the influence of high mechanical loads. This eventually leads to delamination and crack formation (in the literature tests of approximate length

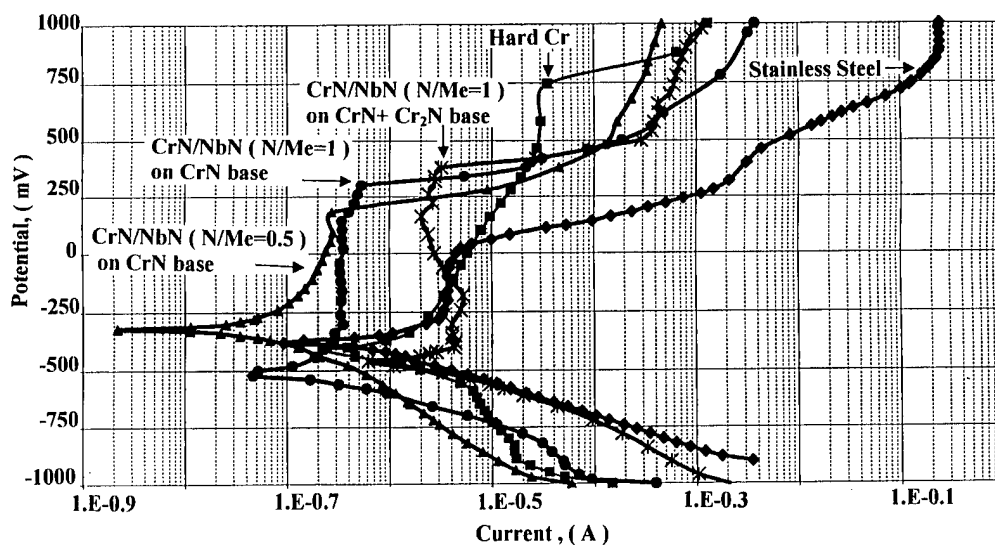


Fig. 10. Comparison of corrosion behaviour of CrN–NbN superlattice coatings with 304L SS and hard Cr plating (aerated 0.1 M acetic acid–sodium acetate buffer solution with 0.1 M added NaCl).

55 nm) beneath the worn surface followed by spallation. In the case of superlattice coatings tested under identical conditions, delamination wear was dramatically reduced (thin slices of 5–10 nm thickness) and sub-surface plastic deformation zones proved difficult to observe.

5. Corrosion behaviour

The influence of NbN on the corrosion behaviour of CrN is outlined in Fig. 10 through potentiodynamic polarisation curves produced from coated 304 SS coupons in aerated and buffered 0.1 M NaCl solution. Uncoated 304 SS was utilised as a reference material along with 20 μm thick Cr-plated SS. Three types of CrN–NbN superlattice were produced for the test: (I) CrN–NbN with an inappropriate two phase base layer; (II) sub-stoichiometric CrN–NbN ($N/Me=0.5$); (III) stoichiometric CrN–NbN with an adherent and crack-free stoichiometric CrN base layer ($N/Me=1$). It is evident from Fig. 10 that the latter two 4 μm thick coatings outperform uncoated SS and exhibit lower passive current densities than electroplated Cr. In conjunction with the higher hardness values ($HK=35$ GPa for CrN–NbN compared with $HK=10$ – 14 GPa for hard Cr plate) we may postulate from the behaviour of CrN–NbN that the system has potential to provide economically thin PVD coatings to compete in niche applications currently served by the electroplating industry. The results shown also indicate that the PVD process has to be carefully optimised or non-tolerable corrosion performance may be achieved through excessive micro-cracking or through-thickness porosity.

6. Conclusion

The results summarised in this paper indicate clearly that superlattice coatings with interesting structural and tribological properties can be currently produced under economical conditions in industrial-sized and commercially available PVD equipment. Automated process control now provides adequate stability for consistent and adjustable fine layer production, although methods for the improvement of layer intermixing and interface abruptness to increase microhardness may still require further development. The combination of appropriate processing parameters and material combinations may further allow the flexible tailoring of structural, mechanical and tribological properties to further improve component performance.

Acknowledgements

This paper has been written as a survey article. The great support of all the Surface Engineering Research Group at the Materials Research Institute of Sheffield Hallam University is gratefully acknowledged.

References

- [1] U. Helmerson, S. Todorova, S.A. Barnett, J.-E. Sundgren, L.C. Markert, J.E. Greene, *J. Appl. Phys.* 62 (2) (1987) 481.
- [2] X. Chu, M.S. Wong, W.D. Sproul, S.L. Rohde, S.A. Barnett, *J. Vac. Sci. Technol. A* 10 (1992) 1604.
- [3] X. Chu, S.A. Barnett, M.S. Wong, W.D. Sproul, *Surf. Coat. Technol.* 57 (1993) 13.

- [4] T. Hurkmans, T. Trinh, D.B. Lewis, J.S. Brooks, W.-D. Münz, *Surf. Coat. Technol.* 76–77 (1995) 159.
- [5] M. Nordin, M. Larsson, S. Hogmark, *Surf. Coat. Technol.* 106 (1998) 234.
- [6] M. Setoyama, A. Nakayama, T. Tamaka, N. Katagawa, T. Nomura, *Surf. Coat. Technol.* 86–87 (1996) 225.
- [7] W.-D. Münz, D. Schulze, F.J.M. Hauzer, *Surf. Coat. Technol.* 50 (1992) 169.
- [8] L.A. Donohue, W.-D. Münz, D.B. Lewis, J. Cawley, T. Hurkmans, T. Trinh, I. Petrov, J.E. Greene, *Surf. Coat. Technol.* 93 (1997) 69.
- [9] I. Wadsworth, I.J. Smith, L.A. Donohue, W.-D. Münz, *Surf. Coat. Technol.* 94–95 (1997) 315.
- [10] I. Petrov, P. Losbichler, D. Bergstrom, J.E. Greene, W.-D. Münz, T. Hurkmans, T. Trinh, *Thin Solid Films* 302 (1997) 179.
- [11] M. Tomlinson, S.B. Lyon, P.Eh. Hovsepian, W.-D. Münz, *Vacuum* 53 (1999) 117.
- [12] P.Eh. Hovsepian, D.B. Lewis, W.-D. Münz, S.B. Lyon, M. Tomlinson, *Surf. Coat. Technol.* (1999) in press.
- [13] H. Paritong, I. Wadsworth, L.A. Donohue, W.-D. Münz, *Trans. IMF* 76 (4) (1998) 144.
- [14] C. Schönjahn, M. Bamford, L.A. Donohue, D.B. Lewis, S. Forder, W.-D. Münz, *Surf. Coat. Technol.* (1999) in press.
- [15] W.D. Münz, I.J. Smith, D.B. Lewis, S. Creasey, *Vacuum* 48 (5) (1997) 473.
- [16] W.D. Sproul, *Surf. Coat. Technol.* 33 (1997) 73–81.
- [17] T. Hurkmans, D.B. Lewis, J.S. Brooks, W.-D. Münz, *Surf. Coat. Technol.* 86–87 (1996) 192.
- [18] P.Eh. Hovsepian, D.B. Lewis, W.-D. Münz, A. Rouzaud, P. Juliet, *Surf. Coat. Technol.* (1999) in press.
- [19] L.A. Donohue, W.-D. Münz, D.B. Lewis, I. Petrov, J.E. Greene, *Surf. Coat. Technol.* 94–95 (1997) 226.
- [20] K.L. Rutherford, I.M. Hutchings, *Surf. Coat. Technol.* 79 (1996) 231–239.
- [21] K. Noguchi, N. Kitagawa, H. Ohara, H. Animoto, 1st French and German Conference on High Speed Machining, University of Metz (1997) 407–413.
- [22] D. McIntyre, J.E. Greene, G. Håkansson, J.-E. Sundgren, W.-D. Münz, *J. Appl. Phys.* 67 (1990) 1542.
- [23] O. Luo, W.M. Rainforth, W.-D. Münz, *Wear* 225–229 (1999) 74.

Physical properties of carbon nitride films synthesized using atomic transport reactions

C. Popov^a, M.F. Plass^{a,*}, L. Zambov^a, J. Bulir^b, M.-P. Delplancke-Ogletree^b,
W. Kulisch^a

^a University of Kassel, Institute of Technical Physics, Heinrich-Plett-Str. 40, D-34109 Kassel, Germany

^b Université Libre de Bruxelles, Chemie Industrielle, 50 avenue F.D. Roosevelt, B-1050 Brussels, Belgium

Abstract

Inductively coupled plasma chemical vapour deposition (ICP–CVD) has been used for the preparing of thin CN_x films from a solid carbon source (at floating potential) and a nitrogen plasma. Volatile CN species generated via atomic transport reactions are the film forming particles. The deposited layers have a rather smooth surface; their deposition rate and thickness, respectively, depend on the substrate position due to a gradient in the precursor species concentration. The nitrogen fraction is at about 50% and exhibits almost no dependence on the deposition parameters. Emphasis was placed on a detailed study of the bonding structure by different analytical techniques. Based on these investigations, a probable structure of the CN_x films is proposed. Since no identification of tetragonally bonded carbon atoms was found, it is supposed that the bonding network is composed of imine-like units and only to a small part of nitrile-type elements. The films are insulating with resistivity of up to $10^{11} \Omega \text{ cm}$. © 2000 Elsevier Science S.A. All rights reserved.

Keywords: Bonding structure; Carbon nitride; Composition; ICP–CVD

1. Introduction

There have been numerous attempts to synthesize crystalline $\beta\text{-C}_3\text{N}_4$ which is predicted to possess a bulk modulus comparable to that of diamond [1]. Various techniques have been used for the preparation of carbon nitride: pyrolysis of nitrogen-containing organic precursors [2], r.f. sputtering [3,4], magnetron sputtering [5], electron cyclotron resonance enhanced plasma chemical vapour deposition [6], nitrogen implantation into graphite [7], chemical vapour deposition [8], and ion beam deposition [9]. Although most of the synthesized materials have nitrogen content lower than the stoichiometric for C_3N_4 (57 at.%), the new CN_x phases are of both scientific and practical interest. The properties of these materials vary depending on their composition and structure, which are strongly influenced by the deposition process. In this work we report on ICP–CVD of CN_x films utilizing transport reactions from a solid carbon source. The composition and the bonding struc-

ture of the films were studied by various analytical techniques and a probable structure of the prepared material is proposed. In addition, few optical and electrical parameters of the layers were determined.

2. Experimental

The deposition set-up for ICP–CVD of carbon nitride films utilizing transport reactions has been described in detail elsewhere [10]. In brief, the plasma tube is made of quartz, and the 13.56 MHz signal of the generator is inductively coupled into the tube via a copper coil (Fig. 1). The maximum power delivered was 100 W. The upper part of the set-up, made of stainless steel and combining the carbon source holder and the gas inlet, is at floating potential in order to prevent ion bombardment and subsequently physical sputtering of the carbon target. The lower part, consisting of a steel chamber with a substrate holder, is grounded. The base pressure was 5×10^{-4} mbar while the working pressure was between 0.3 and 1.0 mbar after introduction of nitrogen (99.999%) with a flow of 50, 100 or 200 sccm. A carbon

* Corresponding author. Tel.: +49-561-804-4205;
fax: +49-561-804-4136.

E-mail address: plass@schottky.physik.uni-kassel.de (M.F. Plass)

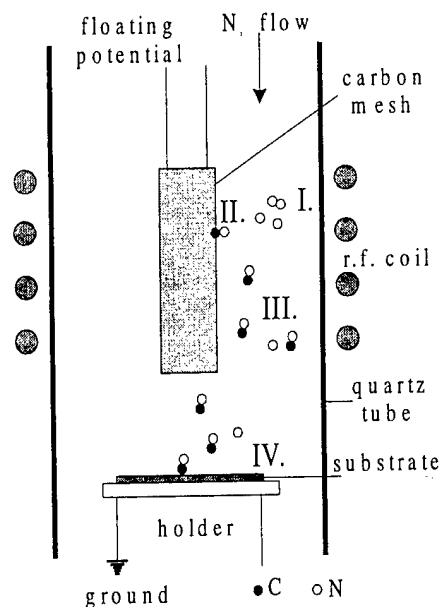


Fig. 1. Process steps of ICP-CVD of CN_x films utilizing transport reaction.

mesh of high purity was used as a carbon source. The average diameter of the carbon fibers was $5\text{ }\mu\text{m}$, thus providing a large area for interaction with the atomic nitrogen. The carbon nitride films were deposited on n-type (111) silicon substrates placed on the holder (3 cm from the carbon source). The substrate and the carbon target were at room temperature but it can be supposed that they were slightly heated by the plasma.

The process itself includes the following steps schematically presented in Fig. 1:

1. Activation of molecular nitrogen in the ICP: $\text{N}_{2(\text{g})} \rightarrow \text{N}_2^+, \text{N}, \text{N}_{(\text{g})}^+$.
2. Interaction of atomic nitrogen with the solid carbon to form carbon–nitrogen species (CN): $\text{C}_{(\text{s})} + \text{N}_{(\text{g})} \rightarrow \text{CN}_{(\text{g})}$.
3. Transport of CN species to the grounded substrate.
4. Deposition of carbon nitride film in the presence of nitrogen species from ICP: $\text{CN}_{(\text{g})} \rightarrow \text{CN}_{x(\text{s})}$.

The thickness of the films was determined by ellipsometry and cross-section scanning electron microscopy (SEM); the values obtained were used to calculate the deposition rate and the film resistivity. The surface morphology was investigated by SEM and atomic force microscopy (AFM). Auger electron spectroscopy (AES), X-ray excited photoelectron spectroscopy (XPS) and elastic recoil detection (ERD) analysis were used to study the film composition. Information on the chemical bonding structure was derived from Fourier transform infrared (FTIR) spectroscopy, Raman spectroscopy, reflection electron energy loss spectroscopy (R-EELS), XPS and AES. The refractive index of the films was determined by ellipsometry. To determine the electrical parameters (resistance and capacitance) of the CN_x

films, aluminium dot contacts were evaporated on top of the layers, which allowed current–voltage (I – V) and high frequency (1 MHz) capacitance–voltage (C – V) measurements.

3. Results and discussion

3.1. Deposition rate and surface morphology

The average deposition rate of the CN_x films was in the range of 1.0–3.5 nm/min, almost independent of the process parameters within the investigated ranges. The thickness of the films increases from the center of the substrate to the edge as shown in Fig. 2. This trend reflects the influence of the CN species concentration gradient and the gas hydrodynamics inside the reactor. The concentration of the carbon–nitrogen species decreases downstream due to depletion as a result of deposition on the wall and on the lower part of the carbon mesh. As a consequence, the deposition rate decreases in the center of the substrate right below the carbon mesh as well as with increasing distance of solid carbon source–substrate. In the latter case the nonuniformity in thickness is smaller but the average deposition rate drops down dramatically.

The deposited CN_x films have a rather smooth surface as observed by SEM and AFM (Fig. 3). The average roughness was below 1 nm, suggesting the absence of destructive processes such as resputtering or etching due to ion bombardment of the growing film.

3.2. Film composition

In Table 1 the results for the film composition obtained by surface sensitive methods (AES, XPS) are compared with those from bulk ERD analysis; the deposition conditions and the calculated nitrogen atomic fraction $\text{N}/(\text{N}+\text{C})$ are also given. For all samples the

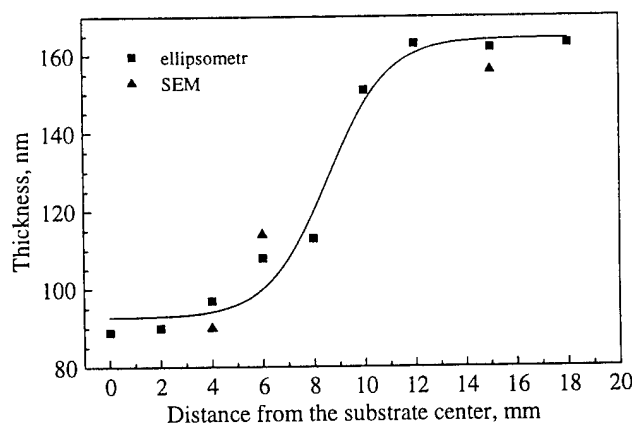
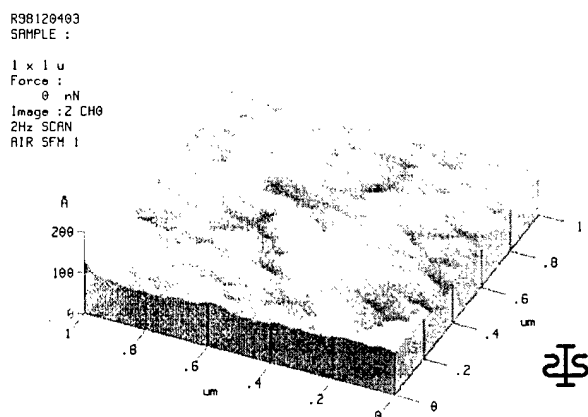


Fig. 2. Film thickness distribution across the substrate.

Fig. 3. AFM image of CN_x film.

nitrogen atomic fraction determined by AES and ERD is between 41 and 54%. The data obtained by AES are rather scattered; however, one has to keep in mind the uncertainties of the method and probably also a slight influence of the deposition conditions.

The nitrogen fraction in the bulk (ERD) is in all cases higher than at the surface, a trend already observed for CN_x films prepared by other methods [11–13]. There are three possible reasons for this observation: influence of the sampling beam (electrons, X-rays, ions) on the surface composition of the films by preferential release of loosely bonded nitrogen; sensitivity of the surface analyses results in the storing history of the samples; and loss of nitrogen from the surface region during deposition itself or during storage. The data for the elemental composition show that the nitrogen atomic fraction in all films is around 0.5. Bearing in mind the nature of the process, it can be supposed that the number of carbon atoms transported to the substrate is at the most the same as that of nitrogen atoms (if the 'free' N atoms from the plasma are not taken into account). This predetermines the nitrogen atomic fraction in the films to about 50%. The high nitrogen content is also facilitated by the relatively low substrate temperatures and by the lack of intensive ion bombardment.

Table 1
Deposition conditions and chemical composition of CN_x films

Sample no.	r.f. power (W)	N ₂ flow (sccm)	Pressure(mbar)	Composition (at.%)					N/(N+C)
				Method	N	C	O	H	
CN9	100	100	1.0	AES	43.5	55.4	1.1	–	0.44
				XPS	31.2	63.2	5.6	–	0.33
CN10	100	100	0.5	AES	39.9	57.5	2.6	–	0.41
				ERD	34.6	31.6	9.5	24.4	0.52
CN12	75	50	0.3	AES	42.6	54.1	3.3	–	0.44
				ERD	32.7	30.1	9.1	28.1	0.52
CN15	100	50	0.3	ERD	30.7	36.2	14.1	19.0	0.46
CN23	100	200	1.0	AES	52.1	47.1	0.8	–	0.53
				ERD	37.9	31.9	7.1	23.4	0.54

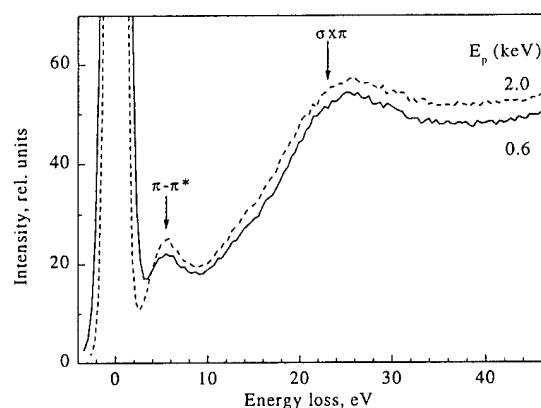
3.3. Chemical bonding structure

3.3.1. Reflection electron energy loss spectroscopy

Typical EELS spectra of the CN_x films are presented in Fig. 4. The π – π^* interband transition peak (also called π plasmon peak) appears at about 5.5 eV next to the elastically back-scattered electron peak. The σ – π plasmon energy of 22.5 eV, precisely determined from the second derivative spectrum, was used to calculate the electron density by means of the free electron approximation. An atomic density of 1.8 g cm^{-3} is obtained, assuming numbers of valence electrons of 4 and 5 for carbon and nitrogen, respectively, as the samples are approximately stoichiometric. No well defined contribution from electrons suffering two or more energy losses can be seen, indicating very broad peaks of the electron loss function due to amorphous broadening [14].

3.3.2. Auger electron spectroscopy

High resolution AES was used to study the CN_x films; a typical spectrum is presented in Fig. 5. The peak positions were calculated taking the arithmetic mean value of the maximum and minimum of the first derivative data; they are indicated by arrows in the figure. For the C_{KVV} line these peaks are at 248, 259, 265 and

Fig. 4. R-EELS spectra of CN_x films.

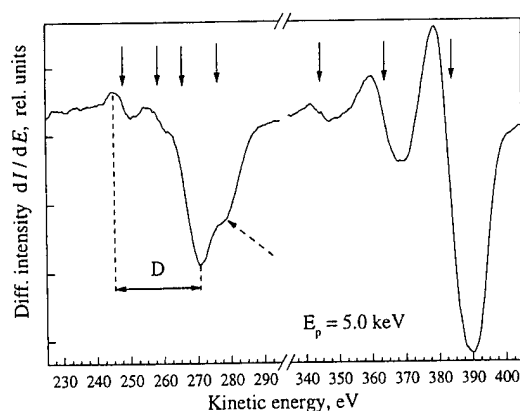


Fig. 5. C_{KVV} and N_{KVV} Auger spectra of CN_x films.

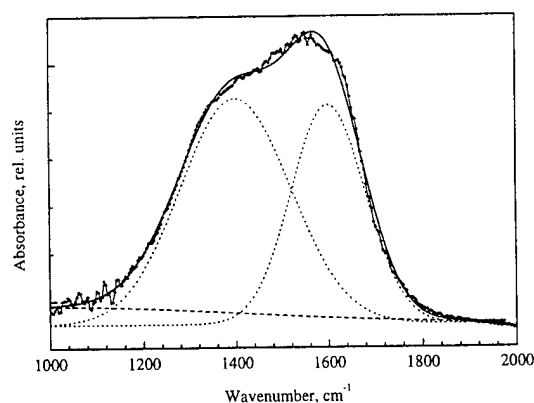


Fig. 6. Infrared absorption spectrum of CN_x films in the range 1000–2000 cm^{-1} .

277 eV. The analysis of the carbon peaks by the valence band method of Zemek et al. [15] shows a value for the D parameter of 25 eV. Comparing this result with the D parameters for diamond (14.3) and HOPG (21.1) [15] we can suppose that there are no sp^3 bonded carbon atoms in the films. A similar conclusion can be drawn by applying the graphite parameter technique [16]. The estimated graphite parameter of 15 obtained by the method of Ullmann et al. [16] is between the values for diamond (0) and sp^2 bonded a-C (38). On the high energy side of the C_{KVV} peak, an additional contribution at 277 eV appears (dashed arrow in Fig. 5). According to the discussion of Steffen [17], the great intensity of this contribution indicates sp^2 bonded carbon atoms in a disordered and heavily damaged matrix. Regarding the N_{KVV} data presented in Fig. 5, the peaks appear at 344, 364 and 384 eV. The energetic distance of 20 eV between the individual peaks is in good agreement with AES data for nitrogen in other sp^2 bonded materials, e.g. h-BN [18].

3.3.3. Fourier transform infrared spectroscopy and Raman spectroscopy

No Raman active modes were registered in the frequency range of 1000–2000 cm^{-1} as the films showed strong luminescence in this region. The infrared spectra of the films were similar to those reported for other carbon nitride materials [19,20]. The band at 2180 cm^{-1} can be attributed to the $C\equiv N$ bond stretching mode. A recent publication has shown that the main contribution to the 3200–3500 cm^{-1} absorption band is due to O–H stretching modes from adsorbed water, while only a small marginal contribution originated from N–H bonds [21]. The broad band between 1100 and 1700 cm^{-1} was deconvoluted using two Gaussian peaks at about 1400 and 1600 cm^{-1} (Fig. 6). This result shows the presence of two main modes which are similar to the Raman D and G bands of DLC which become IR active when the symmetry of the sp^2 domains is broken by incorporation of nitrogen, or to the analogous

‘semicircle’ and ‘quadrant’ stretching modes of ring structures composed of C and N atoms. The latter bands are observed for a great number of compounds containing six-member rings, e.g. triazine, pyrimidine, pyridine, etc. [22,23]. The two individual peaks in our IR spectra are rather broad indicating either a short-range compositional order and/or additional contributions of other vibrations. For example, if we assume that part of the hydrogen detected by ERD originates not only from water molecules but is bonded to nitrogen or carbon atoms, the contributions of the respective deformation modes to the broad band between 1100 and 1700 cm^{-1} must also be considered.

3.3.4. X-ray excited photoelectron spectroscopy

The infrared data were used for interpretation of the XPS results after deconvolution of the C 1s and N 1s peaks; the individual peak parameters and their assignments are summarized in Table 2.

The narrowest contributions to both peaks at 285.9 and 398.4 eV, respectively, are assigned to nitrile groups $-C\equiv N$, the presence of which was detected by FTIR. This assignment is supported by the fact that the energetic spacing of 112.5 eV between the two nitrile-type core electron binding energies (for N 1s and C 1s) is in good agreement with the value of 112.2 eV recently obtained for C_2N_2 material [24]. As supposed from the infrared spectra, most of the atoms in the films are sp^2 bonded (imine-type); the corresponding XPS peaks at 287.4 and 399.5 eV are almost twice broader than the nitrile peaks. This fact can be explained by additional amorphous broadening, by the screening effect of π electrons from conjugated or ring structures leading to additional relaxation, or by different atomic arrangements around the sp^2 carbon atoms. The third peak in the C 1s spectrum at 284.5 eV can be assigned to ‘free’ carbon or hydrocarbon contamination material on the very sample surface [25].

Table 2
XPS peak parameters for the different contributions

Core level	BE (eV)	Peak width (eV)	Chemical environment	Hybridization
C 1s	284.5	1.40 ± 0.10	C–C, C–H surface contamination	sp ²
	285.9	1.20 ± 0.05	–C≡N nitrile-type	sp
	287.4	2.30 ± 0.15	>C=N– imine-type	sp ²
N 1s	398.4	1.26 ± 0.05	N≡C– nitrile-type	sp
	399.5	2.28 ± 0.05	–N=C< imine-type	sp ²

3.3.5. Structure of the films

Based on the above composition and bonding structure studies, we can suppose that the CN_x films prepared by ICP–CVD utilizing transport reactions are ‘paracyanogen’-like with a possible structure like that given by Cuomo et al. [26] and shown in Fig. 7. In addition to this structure the presence of terminating –C≡N groups was detected by FTIR and XPS. A structure composed of bridged C–N rings is less probable bearing in mind the species involved in the film deposition.

3.4. Optical and electrical parameters

The refractive index n of the CN_x films was in the range of 1.65–1.79. It has been shown in literature that n depends on the nitrogen content in the films [27,28]. In our case the nitrogen fraction in all films is rather constant, as discussed above, which determines the almost constant value of n when changing the deposition conditions.

Fig. 8 shows a typical high frequency C – V curve of an Al/CN_x/Si MIS capacitor, indicating the insulating character of the films. For negative voltages, deep depletion is reached. The counter-clockwise hysteresis sug-

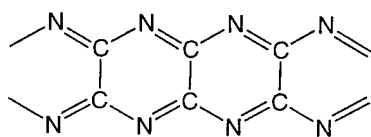


Fig. 7. Probable structure of the CN_x films prepared by ICP–CVD utilizing transport reaction.

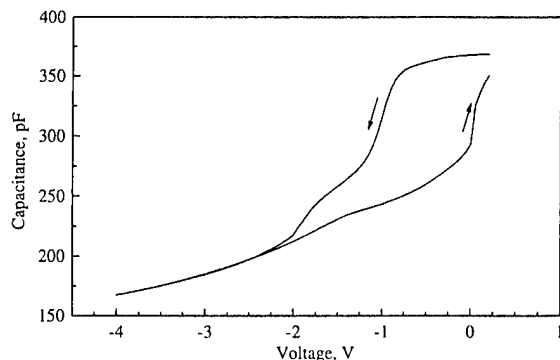


Fig. 8. High frequency (1 MHz) C – V characteristics of CN_x films.

gests the presence of some mobile ions in the CN_x films, most probably alkali and earth alkali. Their presence is not surprising since no care was taken to provide electronic-grade cleanliness during film preparation. The insulating character of the film was confirmed by I – V measurements yielding resistivities of up to $10^{11} \Omega \text{ cm}$.

4. Conclusions

Thin carbon nitride films with high nitrogen contents (in the order of 50%) have been prepared by ICP–CVD utilizing transport reactions. The deposition rate depends mainly on the substrate position. The nitrogen atomic fraction of all films is about 0.5 and not sensitive towards the deposition conditions. The structure is composed of –N=C< groups forming conjugated chains and rings. The composition and the structure of the films predetermine their insulating properties and the high value of the resistivity.

Acknowledgements

The authors gratefully acknowledge the financial support of the European Community (INCO/COPERNICUS Project IC 15CT 960757). C.P. would like to thank the Alexander von Humboldt Foundation for the awarded Research Fellowship. The authors would like to thank Prof. J. Vereecken and O. Steenhout for providing access to XPS facilities.

References

- [1] A.Y. Liu, M.L. Cohen, Science 245 (1989) 841.
- [2] T. Sekine, H. Kanda, Y. Bando, M. Yokoyama, K. Hojou, J. Mater. Sci. Lett. 9 (1990) 1376.
- [3] C.J. Torng, J.M. Siversten, J.H. Judy, C. Chang, J. Mater. Res. 5 (1990) 2490.
- [4] S. Kumar, T.L. Tansley, J. Appl. Phys. 76 (1994) 4390.
- [5] H. Sjöström, I. Ivanov, M. Johansson, L. Hultman, J.-E. Sundgren, S.V. Hainsworth, T.F. Page, L.R. Wallenberg, Thin Solid Films 246 (1994) 103.
- [6] A. Bousetta, M. Lu, A. Bensaoula, Appl. Phys. Lett. 65 (1994) 696.
- [7] A. Hoffman, I. Gouzman, R. Brenner, Appl. Phys. Lett. 64 (1994) 845.

- [8] J. Konvetakis, A. Bandari, M. Todd, B. Wilkens, N. Cave, *Chem. Mater.* 6 (1994) 811.
- [9] K.J. Boyd, D. Marton, S.S. Todorov, A.H. Al-Bayati, J. Kulik, R.A. Zuhr, J.W. Rabalais, *J. Vac. Sci. Technol. A* 13 (1995) 2110.
- [10] C. Popov, M.F. Plass, A. Bergmaier, W. Kulisch, *Appl. Phys. A* 69 (1999) 241.
- [11] W. Kulisch, M.-P. Delplancke-Ogletree, J. Bulir, M. Jelinek, K. Jurek, J. Zemek, J. Klimovic, *Diamond Relat. Mater.* 8 (1999) 1039.
- [12] R. Hauert, A. Glisenti, S. Metin, J. Goitia, J.H. Kaufman, P.H.M. van Loosdrecht, A.J. Kellock, P. Hoffmann, R.L. White, B.D. Hermsmeier, *Thin Solid Films* 268 (1995) 22.
- [13] A. Tempez, N. Badi, A. Bensaoula, J. Kulik, *J. Vac. Sci. Technol. A* 16 (1998) 2896.
- [14] L. Ley, M. Cardona, R.A. Pollack, *Photoemission in Solids II*, in: L. Ley, M. Cardona (Eds.), *Topics in Applied Physics*, vol. 27, Springer Verlag, Berlin Heidelberg, 1979, pp. 11–172.
- [15] J. Zemek, J. Zalman, A. Luches, *Appl. Surf. Sci.* 133 (1998) 27.
- [16] J. Ullmann, P. Heger, K. Pinkert, K. Baba, *Nucl. Instr. Meth. B* 106 (1995) 96.
- [17] H.J. Steffen, *Thin Solid Films* 253 (1994) 269.
- [18] K.P. Loh, I. Sakaguchi, M. Nishitani-Gamo, T. Taniguchi, T. Ando, *Phys. Rev. B* 56 (1997) 12791.
- [19] S. Veprek, J. Weidmann, F. Glatz, *J. Vac. Sci. Technol. A* 13 (1995) 2914.
- [20] S. Matsumoto, K.K. Chattopadhyay, M. Mieno, T. Ando, *J. Mater. Res.* 13 (1998) 180.
- [21] F. Alvarez, M.M. Victoria, P. Hammer, F.L. Freire Jr., M.C. dos Santos, *Appl. Phys. Lett.* 73 (1998) 1065.
- [22] H.A. Szymanski, R.E. Erickson, *Infrared Band Handbook*, vol. IIFI/Plenum, New York, 1970.
- [23] J. Weidlein, U. Müller, K. Dehnicke, *Schwingungsfrequenzen I*, Georg Thieme Verlag, Stuttgart, 1981. (in German).
- [24] F. Le Normand, A. Ababou, N. Brault, B. Carrière, L. Fayette, B. Marcus, M. Mermoux, M. Romeo, C. Speisser, *Appl. Surf. Sci.* 81 (1994) 309.
- [25] D. Marton, K.J. Boyd, A.H. Al-Bayati, S.S. Todorov, J.W. Rabalais, *Phys. Rev. Lett.* 73 (1994) 118.
- [26] J.J. Cuomo, P.A. Leary, D. Yu, W. Reuter, M. Frisch, *J. Vac. Sci. Technol.* 16 (1979) 299.
- [27] X. Wang, P.J. Martin, *Appl. Phys. Lett.* 68 (1996) 1177.
- [28] Y.F. Lu, Z.M. Ren, W.D. Song, D.S.H. Chan, *J. Appl. Phys.* 84 (1998) 2133.

Correlation between bonding structure and mechanical properties of amorphous carbon nitride thin films

C. Quirós ^{a,*}, R. Núñez ^a, P. Prieto ^a, I. Vergara ^b, D. Cáceres ^b, L. Soriano ^a,
G.G. Fuentes ^a, E. Elizalde ^a, J.M. Sanz ^a

^a Dpto. de Física Aplicada, C-XII, Universidad Autónoma de Madrid, E-28049 Madrid, Spain

^b Dpto. de Física, Universidad Carlos III de Madrid, C/ Butarque 15, E-28915 Leganés, Madrid, Spain

Abstract

Amorphous carbon nitride thin films were prepared in a dual ion beam sputtering (DIBS) system. The N/C atomic concentration ratio ranged between 0.3 and 0.5 as determined by quantitative X-ray photoelectron spectroscopy (XPS) of the surface. Fourier Transform Infrared spectroscopy (FT-IR), XPS and X-ray Absorption Spectroscopy (XAS) were used to obtain information about the different types of bonding present in the films. The hardness and the Young's modulus of the samples were determined by nanoindentation measurements. The hardness varied in the range 15–30 GPa with Young's modulus between 170 and 250 GPa. In order to explain the measured hardness, some of the films are considered as heterogeneous, in good agreement with the XPS, FT-IR and XAS data. © 2000 Elsevier Science S.A. All rights reserved.

Keywords: Carbon nitride; Dual ion beam sputtering; FT-IR; Hardness; XAS; XPS

1. Introduction

Many efforts have been made in the synthesis of carbon nitride CN_x films by several techniques. The obtained films show interesting mechanical properties that make them suitable for technological applications, e.g. low friction coefficient and high hardness [1–4]. However, there is a great spread in the results presented in the literature, and the bonding structure of the films and its relation with their mechanical properties still lacks of a definitive interpretation. In particular, the C 1s and N 1s XPS signals and IR measurements are frequently used to characterise the type of bonding present in the films [5–12], but less works report on results based on XAS [8,13,14] spectra. In this work, FT-IR, XPS and XAS measurements have been used to obtain information on the film bonding structure, and nanoindentation tests were performed in order to determine the hardness and Young's modulus of the samples.

2. Experimental

Carbon nitride films were prepared on Si (100) and KCl substrates in a Dual Ion Beam Sputtering system

(DIBS) at a base pressure of 10^{-5} Pa. A 3 cm Kaufmann-type ion gun was used to sputter a 4 in. graphite target (99.999% purity) with inert Ar^+ ions at an angle of incidence of 45° . Simultaneously, an end-Hall ion source is used to bombard the substrates at an angle of 60° off normal with reactive N_2^+ ions in order to supply nitrogen to the growing film. During the deposition time, the substrates were kept at $100^\circ C$ and rotated at 2 rpm to enhance the homogeneity. In some of the samples, a negative bias voltage was applied to the substrates in order to increase the energy of the assisting ions.

FT-IR spectra were obtained on Si (100) substrates in a Bruker IFS66V FTIR spectrometer between 7000 and 560 cm^{-1} with a resolution of 4 cm^{-1} . A previously collected spectrum of uncoated Si (100) substrate was used as reference. The Auger and XPS measurements were performed in a PHI-3027 spectrometer, equipped with a double pass CMA, using 3 keV electrons and Mg- $K\alpha$ radiation ($h\nu = 1253.6\text{ eV}$), respectively. Sensitivity factors from the manufacturer were used to determine the compositions. XAS spectra were taken in the PGM-VLS monochromator at BEESY I in the total electron yield mode with an acquisition step of 0.1 eV. The energy resolution at the N 1s edge was better than 100 meV. The spectra were normalised to the I_0 current collected from a gold mesh. The energy scale was

* Corresponding author.

calibrated according to the known position, 457.8 eV, of the first sharp peak of the Ti 2p multiplets of a TiO₂ (rutile) sample [15].

Nanoindentation experiments were made with a Nanoindenter IIs (Nano Instruments, Inc., Knoxville, TN) Mechanical Properties Microprobe. All tests were performed at room temperature with a diamond Berkovich (three-sided pyramid) indenter tip. The indenter was first loaded and unloaded three times in succession at a constant rate of 10% of the maximum depth and for three different depths; each of the unloadings terminated at 10% of the peak load to assure that contact was maintained between the specimen and the indenter. Three hold periods of 50 s were inserted at the maximum depths and another hold period of 100 s was inserted at the minimum of the final unloading. During this last hold period, the displacement of the indenter was carefully monitored to establish the rate of thermal drift in the machine for subsequent correction of the data. The load–displacement data obtained were analysed using the method of Oliver and Pharr [16] to determine the hardness and elastic modulus as a function of the displacement of the indenter.

Each specimen was also tested using the continuous stiffness measurement technique developed by Oliver and Pethica [17]. This technique enables continuous measurement of the stiffness and area contact between the indenter and the specimen during indentation. The contact stiffness, applied load and indenter displacement can then be used to determine the mechanical properties such as Young's modulus and hardness. This technique allows for measurement of the mechanical properties as a function of the indentation depth.

3. Results and discussion.

Table 1 summarises the preparation parameters of the samples studied. Three different sputtering conditions were used to obtain the flux of C atoms coming to the substrates. In order to select the assisting conditions, two effects have to be taken into account. One is

the objective of incorporating significant amounts of nitrogen to the films requires the use of high fluxes of N₂⁺ assisting ions. Conversely, to reduce the damages and resputtering phenomena that occur during the growth [18] and to obtain films with sufficient thickness to perform the nanoindentation tests, the N₂⁺ assistance must be reduced. In this way, an optimisation of the assistance conditions is required to find a compromise between these opposite trends. Table 1 shows that the assistance conditions selected led to films with N/C atomic ratios varying in the range 0 to 0.5, as stated by XPS quantification. The XPS measurements were made after a limited exposure to air (less than 5 min, similar for all the samples), so that it is to be expected that the N/C atomic ratio in the volume should be higher. It is important to indicate that low concentrations of O and W (the last coming from the filament of the assisting gun) were detected in the films (<6% and 1%, respectively). The thicknesses given in Table 1 were obtained by Auger depth profiling of the samples with reference to a film which was calibrated by RBS, and are affected by a considerable uncertainty, but they give reliable information about the relative thickness of the films.

Information about the type of bonding present in the films was obtained from FT-IR spectra of the samples, as those shown in Fig. 1. The spectra have a broad absorption band between 1000 and 1700 cm⁻¹. This band is attributed to C–C, C–N, C=C and C=N bonds present in the sample [10]. A small absorption around 2100 cm⁻¹ is also observed, especially in those samples with the highest nitrogen content. It seems that the relative intensity of this band increases with the bias voltage. The peak at this frequency can be assigned either to carbonitrile groups (–C≡N) or to the presence of carbodiimides (–N=C=N–) [9]. The changes in the background of the different spectra make difficult the quantification of the intensities of the bands.

The shape and position of the C 1s and N 1s XPS spectra can also give valuable information about the bonding structure of the sample. Fig. 2 shows the C 1s spectra for the respective samples (as labelled). At a first glance, no relevant features are observed in the

Table 1
Sputtering and assistance conditions, bias voltage, N/C atomic ratio, thickness, hardness (*H*) and Young's modulus (*E*)

Sample	Ar ⁺ sputtering		N ₂ ⁺ assistance		Bias voltage (V)	N/C (XPS)	Thickness (nm)	<i>H</i> (7 nm) (GPa)	<i>E</i> (7 nm) (GPa)
	Energy (eV)	Flux (mA/cm ²)	Energy (eV)	Flux (mA/cm ²)					
A0	500	1.0	0	0	0	0.00	240	6.5	105
A1	500	1.0	65	0.031	0	0.49	28	15	175
B1	800	3.7	87	0.077	0	0.32	–	28	240
C1	800	4.0	87	0.077	0	0.29	60	21	245
C2	800	4.0	87	0.077	–10	0.34	60	–	–
C3	800	4.0	87	0.077	–50	0.34	53	25	260
C4	800	4.0	87	0.077	–90	0.36	19	19	220

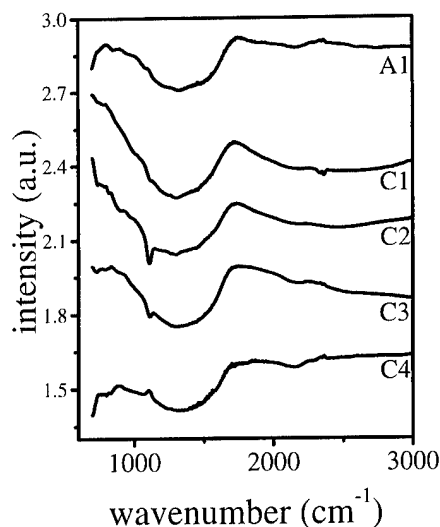


Fig. 1. FT-IR spectra of different CN_x samples as labelled (cf. Table 1).

series, except the shift of the peak maximum from the value obtained for the amorphous carbon film, 284.8 eV, up to 286.3 eV when N–C bonds are formed.

The N 1s XPS spectra show a clear dependence of the features with the bias voltage, as can be seen in Fig. 3. The N 1s peak is composed of two main contributions: the first at 400.8 eV, assigned to N–C sp^2 bonds and the second at 399.3 eV assigned to N–C sp^3 bonds [5,7,8]. In particular, increasing the bias leads to the enhancement of the low energy component. It seems that increasing the assisting energy leads to a preferential resputtering of the bonds related with the first component, i.e. N–C sp^2 . Interestingly, this component is also partially removed when the samples are subjected to heat treatments at 500°C for 2 h. This nitrogen is not firmly bonded to the film, so that it is preferentially removed or recombined by increasing the dose of assis-

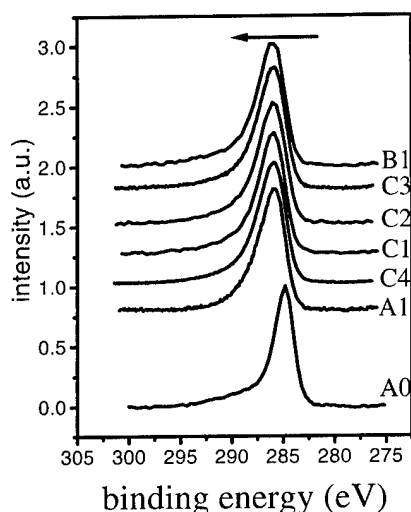


Fig. 2. C 1s XPS spectra of the CN_x films as labelled (cf. Table 1).

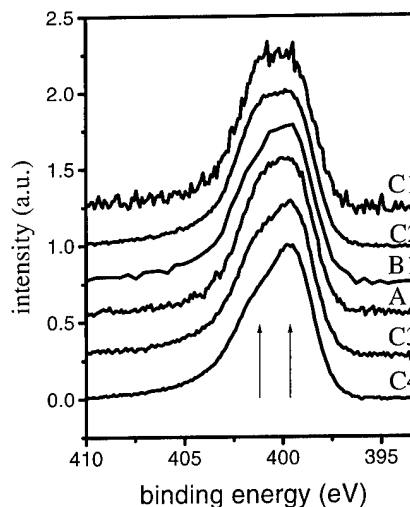


Fig. 3. N 1s XPS spectra of the CN_x films as labelled (cf. Table 1).

tance or annealing at T above 500°C. An additional small contribution is observed at binding energies close to 404 eV, usually attributed to the presence of N–O or N_2 species [5,6,8].

The previous assignment of the N 1s peaks is the most frequently accepted in the literature, but there is a great spread in the positions of the peaks that leads to ambiguous interpretation of the N 1s spectra. XAS spectra could give some complementary information for studying the role of nitrogen in the films. Fig. 4a shows the XAS N 1s spectra of the samples. The spectra have a small shoulder at 399.8 eV and two sharp features at 400.8 and 402.1 eV, all of them associated with $1\text{s} \rightarrow \pi^*$ transitions (that are related to sp and sp^2 nitrogen). Another broad peak is also present at energies close to 408.8 eV associated with $1\text{s} \rightarrow \sigma^*$ transitions (that can be produced by sp , sp^2 or sp^3 nitrogen). In Fig. 4b, the

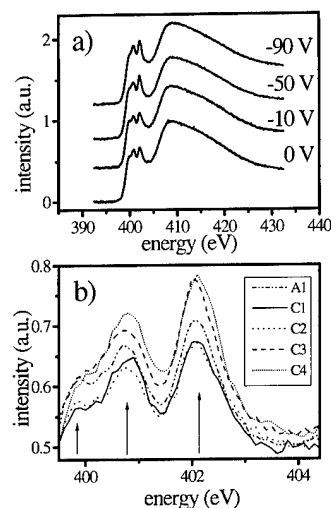


Fig. 4. XAS spectra of the N 1s edge for the CN_x films as labelled (cf. Table 1).

XAS N 1s peaks are shown normalised to the $1s \rightarrow \sigma^*$ transition in order to observe the evolution of the intensity of the $1s \rightarrow \pi^*$ transitions relative to the $1s \rightarrow \sigma^*$ transition. When the bias voltage is increased the π^* features are enhanced, which (due to the fact that sp^3 nitrogen has no π^* transitions) can be related to the decrease of the sp^3 character of the nitrogen as bias voltage is increased [13]. Interestingly, a clear correlation can be found when comparing the evolution of the low binding energy component of the N 1s XPS spectra, at 399.3 eV, and the $1s \rightarrow \pi^*$ features observed in the N 1s XAS spectra at 399.8, 400.8 and 402.1 eV. Although the assignment of the peaks is difficult, transitions at 399.8 and 402.1 eV could be generated by pyridine and pyridone (caused by surface oxidation of pyridine) functionalities, while the peak at 400.8 eV could be related to carbonitrile groups [19]. The pyridine peak in XPS is shown at 398.9 eV by some authors [12,20] and the carbonitrile at 399.5 eV [20], so the increase observed of the low energy N 1s XPS component and of the XAS N 1s features, fits with the increase of these functionalities as bias voltage is increased. In addition, FT-IR also confirms an increase of the carbonitrile contribution when bias voltage is applied.

The evolution observed in the N 1s XPS is similar to that of N 1s XAS, but is difficult to correlate with C 1s XPS evolution. A possibility to be considered is that the components observed in the XPS spectra cannot be assigned to just one type of bonding, but to the overlapping of different types giving similar binding energies.

Plotting the hardness of all the samples, independently of the sputtering conditions, versus the C 1s centroid, a clear correlation is detected (Fig. 5): the increase of the centroid position leads to measurable increases in hardness. The hardness values used in this figure were determined at low penetrations, around 7 nm, in order to enhance surface information and to facilitate the correlation with the XAS and XPS surface measurements described previously. Although the posi-

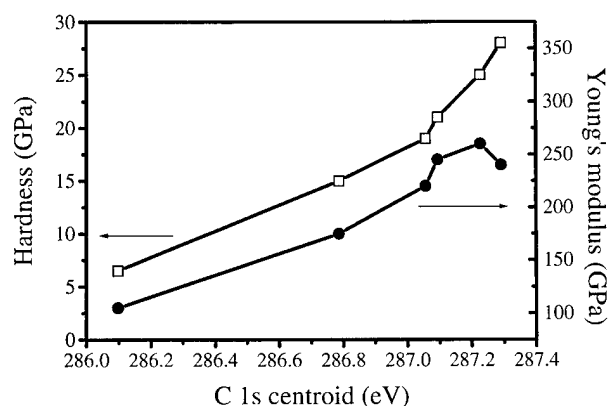


Fig. 5. Hardness and Young's modulus as a function of the C 1s centroid position of the films.

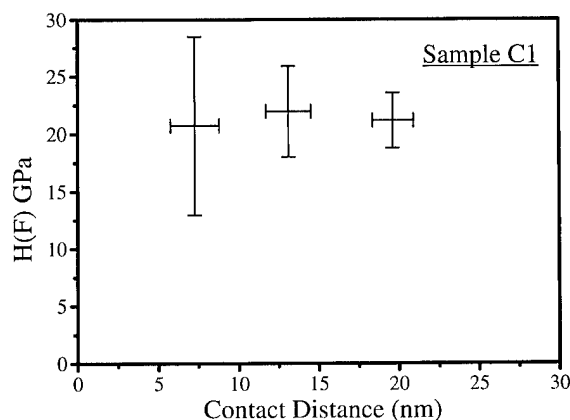


Fig. 6. Hardness of sample C1 as a function of the contact distance of the nanoindenter.

tion of the centroid cannot be unambiguously related with the C sp^3 content of the film, the general trend is that the peak shifts to higher binding energies when the C sp^3 —N fraction increases [5,7,8]. The evolution observed in the hardness measurements is consistent with the increase of the C sp^3 content as centroid position increases. In fact, EELS measurements made to these same set of samples, at the C K edge [21], showed an evolution of the sp^2/sp^3 content close to the evolution of the C 1s centroid. The dependence of the Young's modulus with the C 1s centroid is also shown in the Fig. 5. No clear dependence can be observed between the nitrogen behaviour and the mechanical properties. In fact, the hardest (B1) and the softest (A1) samples have a N 1s peak almost identical.

Fig. 6 shows the hardness data of sample C1 at three different depths corresponding to indentations in ten different areas of the film. This sample shows the highest dispersion in the surface hardness (7 nm) data, going from 13 to 28 GPa. This high dispersion suggests that the film is inhomogeneous, having areas with different C sp^2/sp^3 ratios, which are responsible for the spread in the hardness measurement. This interpretation is consistent with the intermediate position of the C 1s centroid of sample C1 in Fig. 5. In addition, its tribological performance shows the lower friction coefficient, 0.13, and the best wear resistance behaviour [21].

4. Conclusions

Thin films of carbon nitride have been prepared in a dual ion beam sputtering system. Changing the assistance conditions we were able to obtain films with N/C atomic ratios between 0 and 0.5, and thickness ranging between 19 and 240 nm. Nanoindentation tests were performed to obtain the hardness and Young's modulus of most of the films.

FT-IR, XAS and XPS measurements have shown the

presence of different nitrogen and carbon species. A clear correlation between some of the features of the XAS and XPS N 1s spectra has been evidenced, although because of the overlapping of different types of N-bonding at approximately the same binding energies, no definitive assignment can be made. The presence of pyridine and pyridone species at the surface of the films is proposed.

The measured hardnesses at depths of around 7 nm (i.e. close to the surface) show a clear correlation with the position of the centroid of the C 1s XPS peak, i.e. the hardness increases when the binding energy increases. This improvement in hardness is explained as being due to an increase of the sp^3 content of the films. The high dispersion in the values of hardness measured in some of the samples suggests the existence of inhomogeneities with different C sp^2/sp^3 ratios, in good agreement with the complex structure observed in the FT-IR, XPS and XAS measurements.

Acknowledgements

The CICYT and DGICYT of Spain (project nos. MAT96-0676 and PB96-0061) and the EU (project no. BE97-4845, and TMR Programme, contract no. ERBFMGE CT 950031 at BESSY) are acknowledged for financial support. BESSY staff are also acknowledged for their technical support.

References

- [1] H. Sjöström, S. Stafström, M. Boman, J.-E. Sundgren, *Phys. Rev. Lett.* 75 (1995) 1336.
- [2] D. Li, E. Cutiongco, Y.-W. Chung, M.-S. Wong, W.D. Sproul, *Surf. Coat. Technol.* 68–69 (1994) 611.
- [3] M. Kohzaki, A. Matsumuro, T. Hayashi, M. Muramatsu, K. Yamaguchi, *Thin Solid Films* 308–309 (1997) 239.
- [4] W.-C. Chan, B. Zhou, Y.-W. Chung, C.S. Lee, S.T. Lee, *J. Vac. Sci. Technol. A* 16 (1998) 1907.
- [5] D. Marton, K.J. Boyd, A.H. Al-Bayati, S.S. Todorov, J.W. Rabalais, *Phys. Rev. Lett.* 73 (1994) 118.
- [6] H. Sjöström, L. Hultman, J.-E. Sundgren, S.V. Hainsworth, T.F. Page, G.S.A.M. Theunissen, *J. Vac. Sci. Technol. A* 14 (1996) 56.
- [7] M. Tabbal, P. Mérel, S. Moisa, M. Chaker, A. Ricard, M. Moisan, *Appl. Phys. Lett.* 69 (1996) 1698.
- [8] S. Lopez, H.M. Dunlop, M. Benmalek, G. Tourillon, M.-S. Wong, W.D. Sproul, *Surf. Interface Anal.* 25 (1997) 827.
- [9] P. Hammer, M.A. Baker, C. Lenardi, W. Gissler, *J. Vac. Sci. Technol. A* 15 (1997) 107.
- [10] X.-A. Zhao, C.W. Ong, Y.C. Tsang, Y.W. Wong, P.W. Chan, C.L. Choy, *Appl. Phys. Lett.* 66 (1995) 2652.
- [11] K. Ogata, J.F.D. Chubaci, F. Fujimoto, *J. Appl. Phys.* 76 (1994) 3791.
- [12] Y. Taki, T. Kitagawa, O. Takai, *Thin Solid Films* 304 (1997) 183.
- [13] D.G. McCulloch, A.R. Merchant, *Thin Solid Films* 290–291 (1996) 99.
- [14] B.C. Holloway, D.K. Shuh, M.A. Kelly, W. Tong, J.A. Carlisle, I. Jimenez, D.G.J. Sutherland, L.J. Terminello, P. Pianetta, S. Hagstrom, *Thin Solid Films* 290–291 (1996) 94.
- [15] R. Brydson, H. Sauer, W. Engel, J.M. Thomas, E. Zeitler, N. Kosugi, H. Kuroda, *J. Phys.: Condens. Matter* 1 (1989) 797.
- [16] W.C. Oliver, G.M. Pharr, *J. Mater. Res.* 7 (1992) 1564.
- [17] W.C. Oliver and J.B. Pethica, U.S. Patent No. 4 848 141 (1989).
- [18] P. Hammer, M.A. Baker, C. Lenardi, W. Gissler, *Thin Solid Films* 290–291 (1996) 107.
- [19] Q. Zhu, S.L. Money, A.E. Russell, K.M. Thomas, *Langmuir* 13 (1997) 2149.
- [20] J.R. Pels, F. Kapteijn, J.A. Moulijn, Q. Zhu, K.M. Thomas, *Carbon* 33 (1995) 1641.
- [21] C. Donnet, J.M. Martin, J. Fontaine, J.C. Sánchez-López, C. Quirós, E. Elizalde, J.M. Sanz, T.C. Rojas, A. Fernandez, *Surf. Coat. Technol.* 120–121 (1999) 594.

Magnetron sputtered carbon nitride: composition and chemical bonding of as-grown and post-annealed films studied with real-time and in situ diagnostic techniques

M. Gioti *, S. Logothetidis, P. Patsalas, A. Laskarakis, Y. Panayiotatos, V. Kechagias

Department of Physics, Aristotle University of Thessaloniki, 54006 Thessaloniki, Greece

Accepted 13 October 1999

Abstract

We prepared CN_x films by reactive r.f. magnetron sputtering from a graphite target in a pure N_2 plasma, with different substrate bias voltages (V_b). We studied the optical properties of CN_x films by using the in situ spectroscopic ellipsometry (SE) in the energy region 1.5–5.5 eV. The differences in compositional and bonding configuration between CN_x films, provided by the SE data analysis, are discussed and correlated with the results obtained by Fourier Transform IR SE (FTIRSE) measurements. Post-growth annealing experiments were performed in an ultra-high vacuum (UHV) chamber, up to 900°C. The film modifications and the nitrogen evolution, were monitored in real-time using an ultra-fast 16-wavelength ellipsometer and a quadrupole mass spectrometer (QMS). In situ SE and FTIRSE measurements were also obtained on the completion of annealing. The nitrogen evolution is correlated with the carbon-nitrogen bonding and the compositional modifications in the films, as derived by FTIRSE and SE. © 2000 Elsevier Science S.A. All rights reserved.

Keywords: Carbon nitride; Chemical bonds; Ellipsometry; Reactive sputtering

1. Introduction

Nowadays carbon nitride (CN_x) is a material of high scientific and technological importance. Since Cohen and Liu [1,2] proposed that the β - C_3N_4 phase should exhibit a hardness comparable to that of diamond, CN_x has become a promising candidate as a thin film protective overcoat in the magnetic recording industry. However, the most important difficulty which faced experimentalists in producing thin films with the β - C_3N_4 phase, even using a variety of deposition techniques, is the low concentration of N (well below 57 at.%) which is incorporated in the films. Further experimental efforts in preparing and characterizing CN_x films, however, has led to the development of films with desired and unpredictable elastic properties, such as high hardness and elasticity [3]. The percentage of N in these films could be as low as 20 at.%. Thus, the enhanced elastic properties may not only be due to the existence of the β - C_3N_4 phase but also due to the formation of other phases or bonding configurations.

Indeed, HREM results identified a ‘fullerene-like’ microstructure in CN_x films [3] and theoretical calculations [3,4] support the possibility of buckling and inter-linking of graphene planes.

The structure and the bonding configuration of CN_x materials are a rather complicated subject. This is because CN_x films, like amorphous carbon films, may contain different ratios of tetrahedral sp^3 , trigonal sp^2 and linear sp^1 hybridised bonds, in contrast to the other amorphous materials of group IV (e.g. Si, Ge) which can only hybridise tetrahedrally. However, this provides the opportunity to develop films with a high degree of structural, optical and electronic tuning. Thus, CN_x can also be an alternative to amorphous silicon (a-Si) for electronic device applications [5]. The suitability of CN_x films for specific applications depends on the compositional and structural characteristics stability, adherence and tribological properties. All these properties are strongly related to the preparation conditions and the post-growth treatments of the films. Recently, we reported on the stability and adherence of CN_x films developed in an N_2/Ar gas mixture with various substrate biases, versus post-growth annealing at 300°C in

* Corresponding author. Tel.: +30-51-998189; fax: +30-51-246484.
E-mail address: mgioti@skiathos.physics.auth.gr (M. Gioti)

an inert environment [6]. In this work, we deposited magnetron sputtered CN_x films with different substrate biases in a pure N_2 plasma. We studied the film optical properties and the chemical bonding, and investigated the effect of thermal annealing up to 900°C on the films. Multi-wavelength (MW) ellipsometry, SE, FTIRSE and quadrupole mass spectrometer (QMS) were used as real time and in situ diagnostic techniques for the comparative study of the electronic dielectric response and the chemical bonding of the as-grown and annealed films.

2. Experimental

CN_x films were deposited on Si substrates by reactive r.f. magnetron sputtering technique using a graphite target in a deposition chamber with a base pressure better than 1×10^{-7} mbar. The substrates were located 65 mm above the target, and coated using a sputtering power of 100 W in a pure N_2 environment. The working pressure was 4×10^{-3} mbar. The energy and the flux of the ions reaching the growing film surface was varied by applying an external bias voltage V_b , from +20 V (floating, self bias) to -250 V, to the substrate. However, in this work we present results on two representative CN_x samples developed at low and high negative V_b — namely film #a ($V_b = -20$ V), and film #b ($V_b = -250$ V). All films were deposited at room temperature (RT) and their thickness was ~ 5000 Å.

A phase modulated ellipsometer (PME), mounted on the deposition system at an angle of incidence 70.4° , allowed in situ SE measurements of the growing films in the energy region 1.5–5.5 eV. SE is a non-destructive technique which measures the complex dielectric function $\epsilon(\omega) [= \epsilon_1(\omega) + i\epsilon_2(\omega)]$. $\epsilon(\omega)$ is directly related to the electronic properties, the chemical bonding as well as the structural and the morphological properties of the material. In the case of a thin film, the measured quantity by SE is the pseudodielectric function $\langle\epsilon(\omega)\rangle$ which accounts for the effect of substrate too. After deposition, the films were thermally annealed in a UHV chamber with a base pressure 1×10^{-10} mbar. Another PME, which was adapted on the chamber, allowed MW and SE measurements during and after annealing. MW measurements were accomplished at 16 different wavelengths in the energy range 1.54–4.32 eV. The capability of the system in its acquisition time was less than 4 s. In the same UHV chamber, an FTIRSE in the IR energy region (900 – 4000 cm^{-1}) and a QMS of 10 different detection channels were also adapted.

3. Results and discussion

The MW spectra $\langle\epsilon(\omega)\rangle$ during the annealing procedures from RT to 900°C of the #a and #b CN_x films

are presented in Figs. 1 and 2, respectively. These spectra provide a first indication concerning the stability of film #b compared to film #a. The latter film exhibits large alterations during annealing. These alterations can only be attributed to permanent modifications in microstructure, bonding configuration and film composition which occurred during annealing and not due to the temperature shift. The latter has been certified with MW and SE measurements performed when the films were cooled down to RT (see Fig. 3). SE measurements for the as-grown and annealed films were taken in the energy region 1.5–5.5 eV. In general, the CN_x films are composite materials consisting of a mixture of threefold (sp^2) and fourfold (sp^3) co-ordinated carbon and carbon–nitrogen atoms whilst with a low percentage of carbon and nitrogen atoms it is possible to constitute sp^1 hybridized chemical bonds. Consequently, as in the case of a-C [7], the electronic dielectric response (NIR-Visible-UV energy region) of the a- CN_x films is mainly due to sp^2 and sp^3 bonding and less so to sp^1 hybridized

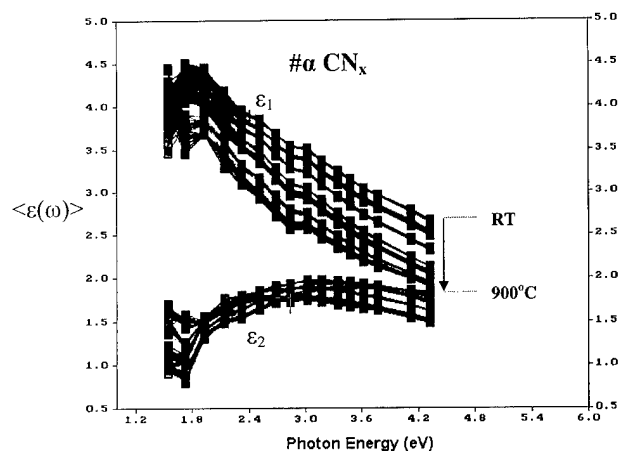


Fig. 1. Real time multi-wavelength $\langle\epsilon(\omega)\rangle$ spectra during annealing from RT to 900°C : #a CN_x film deposited with $V_b = -20$ V.

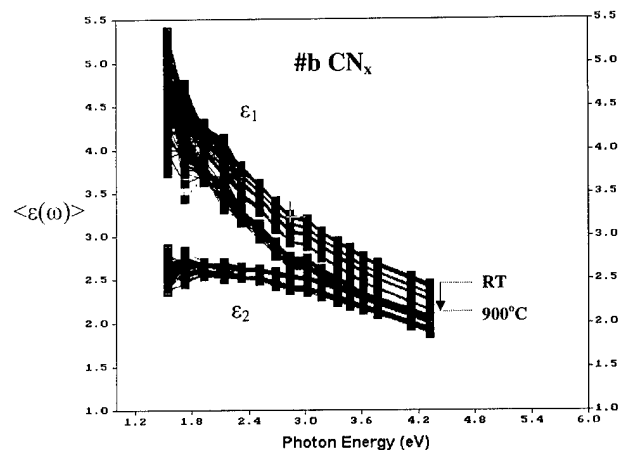


Fig. 2. Real time multi-wavelength $\langle\epsilon(\omega)\rangle$ spectra during annealing from RT to 900°C : #b CN_x film deposited with $V_b = -250$ V.

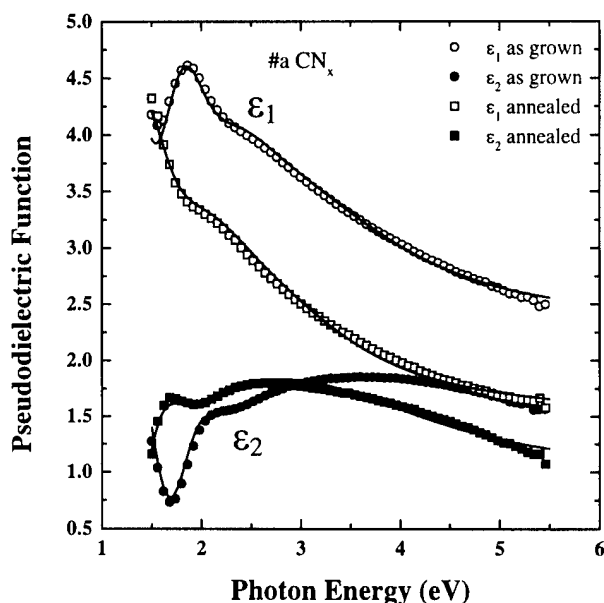


Fig. 3. The experimental (symbol) and calculated (solid line) $\langle\epsilon(\omega)\rangle$ spectra of the #a CN_x film, obtained by SE; as-grown (circles) and after annealing to 900°C (squares).

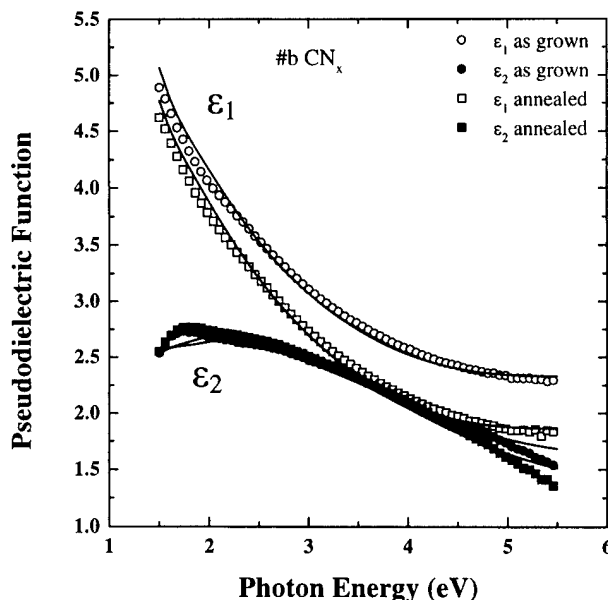


Fig. 4. The experimental (symbol) and calculated (solid line) $\langle\epsilon(\omega)\rangle$ spectra of the #b CN_x film, obtained by SE; as-grown (circles) and after annealing to 900°C (squares).

bonds and can be described with the Lorentz oscillator dispersion relations.

In order to evaluate the spectral dependence of the electronic dielectric function of CN_x films, we fit the experimental $\langle\epsilon(\omega)\rangle$ by using the modified Tauc–Lorentz (TL) model proposed by Jellison et al. [8] in combination with the three phase model (air/ CN_x film/c-Si substrate). In the TL model the imaginary part [$\epsilon_2(\omega)$] of the dielectric function is determined by multiplying the Tauc joint density of states [9] by the value of ϵ_2 obtained from the Lorentz oscillator model. So, the TL model provides the ability to determine the fundamental optical gap of the interband electronic transitions, as well as the energy, broadening and strength characteristics of each classical Lorentz oscillator [7].

In Figs. 3 and 4 are plotted the experimental (symbol) and calculated (solid line) $\langle\epsilon(\omega)\rangle$ for the #a and #b films as-grown and after annealing at 900°C , respectively. By this analysis a fundamental difference was found between the two samples concerning the number of oscillators required to describe the measured $\langle\epsilon(\omega)\rangle$ spectra. In the fitting procedure for film #a, we used two oscillators centered at ~ 3.5 eV and ~ 9.5 eV. Similar to a-C films [7], the former corresponds to π -electron transitions (sp^2 bonds, $\text{C}=\text{C}$ and $\text{C}=\text{N}$), and the latter to σ -electron transitions (sp^3 bonds, $\text{C}-\text{C}$ and $\text{C}-\text{N}$). In the case of film #b, due to its high optical absorption at low energies, in addition to the above two oscillators, an additional oscillator at 1.5 – 2.0 eV is needed to describe the experimental data. This corresponds to a semi-metallic optical behavior of film

#b. Recently [7] we have also reported that sputtered a-C films, grown with high energy ion bombardment, exhibit a similar semi-metallic optical behavior which was correlated with the formation of a dense carbon phase [10].

The calculated $\epsilon(\omega)$ spectra obtained using the optical parameters resulting from the fitting procedure, in the energy range 0 – 12 eV, are plotted for films #a and #b in Figs. 5 and 6 respectively. The non-zero optical band gap and the lower absolute values of the imaginary part

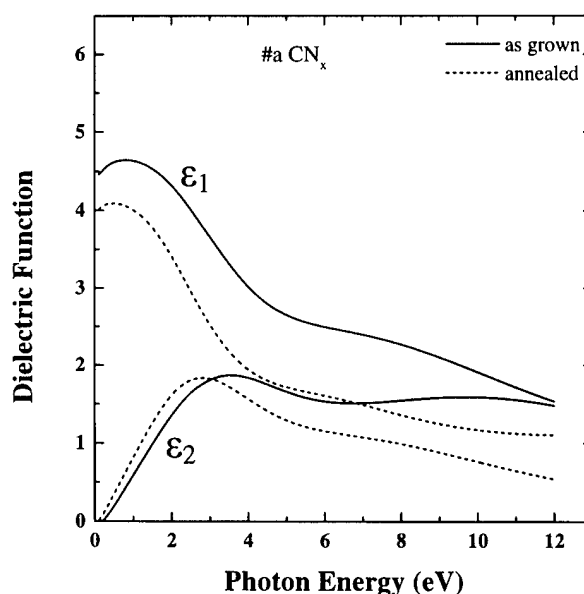


Fig. 5. The calculated $\epsilon(\omega)$ spectra of the #a CN_x film; as-grown (solid line) and annealed at 900°C (dashed line).

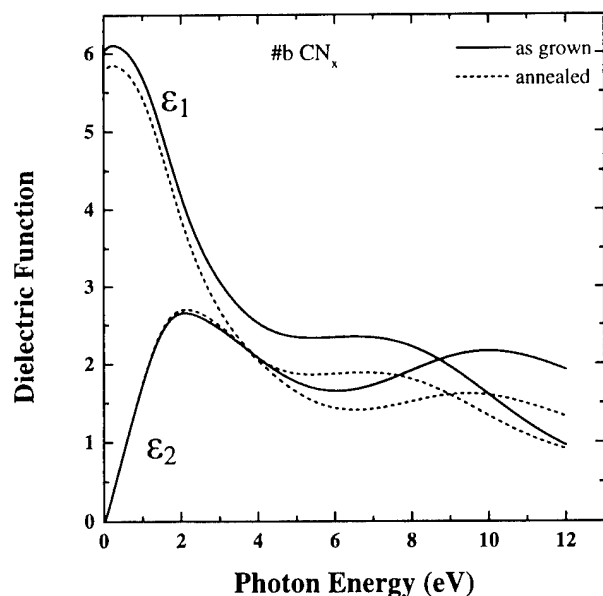


Fig. 6. The calculated $\epsilon(\omega)$ spectra of the #b CN_x film; as-grown (solid line) and annealed at 900°C (dashed line).

of dielectric function ϵ_2 (proportional to the absorption) of film #a, point to its higher optical transparency. Thereby, the comparison of the measured and calculated $\epsilon(\omega)$ spectra certify that sp^2 bonding is dominant in film #b. The alterations resulting from the annealing procedure are also clearly illustrated in Figs. 5 and 6. More specifically, in film #a (see Fig. 5) the first oscillator (~ 3.5 eV) has been shifted to lower energy (~ 3.1 eV) and the strength of the second one (~ 9 eV) has been remarkably reduced. The above suggest a redistribution of sp^2 sites and a reduction of sp^3 sites due to the evolution of N from the film. In the same mode, the strength of the oscillator centered at ~ 9 eV, in film #b, has also been reduced, but surprisingly no significant changes were deduced at low energies up to ~ 3 eV. This indicates the thermal stability of the sp^2 bonding in film #b. The electronic dielectric response (SE) does not exhibit any particular contribution of $\text{C}\equiv\text{N}$ bonds of CN_x films possibly because of their low polarizability in this energy region. Nevertheless, even though we are not able to obtain, at the moment, direct information from SE on the effect of temperature on the $\text{C}\equiv\text{N}$ bonds, we note here that the loss of nitrogen from such sites must be accompanied by the formation of microvoids. That is, the breaking of $\text{C}\equiv\text{N}$ bonds during annealing is translated into an average reduction of film optical density (lower absolute values of $\epsilon(\omega)$).

Fig. 7 shows the evolution of N_2 , as detected with QMS, during film annealing. In film #a, the evolution of N_2 initiates at $\sim 210^\circ\text{C}$, whereas in film #b it initiates at $\sim 310^\circ\text{C}$. In the latter, a saturation of N_2 partial pressure was obtained up to 600°C . In film #a, a reduction of N_2 partial pressure was detected within the

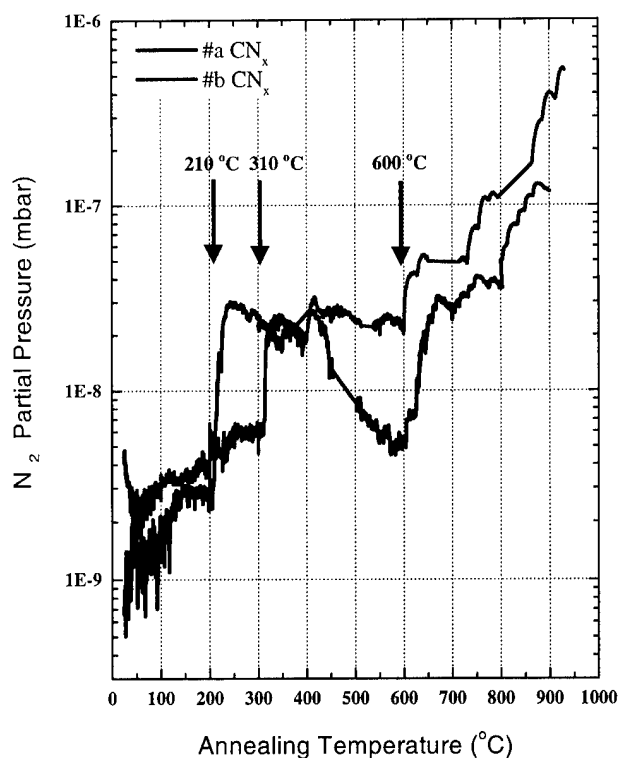


Fig. 7. The evolution of molecular nitrogen (N_2) during annealing, from RT to 900°C , of #a and #b CN_x films. The arrows indicate the characteristic temperatures where the N_2 partial pressure increases.

temperature range 420 – 600°C . This probably means that one specific, weak type of carbon–nitrogen bond was already exhausted. We expect that $\text{C}-\text{N}$ bonds start to break at lower temperatures, and the breaking of $\text{C}=\text{N}$ bonds starts afterwards due to their different degrees of freedom. Therefore, these findings suggest that the $\text{C}-\text{N}$ bonds are weaker in film #a than in film #b. However, for a more accurate definition of the characteristic temperatures at which $\text{C}-\text{N}$ and $\text{C}=\text{N}$ bonds start to break, more detailed experiments should be carried out. In both films, a gradual increase in N_2 partial pressure above 600°C was detected. This nitrogen evolution is associated with the $\text{C}\equiv\text{N}$ bonds [11,12]. We should note here that no significant changes in the partial pressures of other gases which were below 1×10^{-8} mbar, such as atomic nitrogen N, carbon C, carbon nitrogen CN, oxygen O or O_2 , etc. were detected.

Since the optical response of CN_x films was associated with chemical bonding between carbon–carbon or carbon–nitrogen atoms we studied the films using the FTIRSE technique. This technique is a powerful tool for the investigation and study of chemical bonds in amorphous materials with weak contribution. Every IR active chemical bond in the FTIRSE spectra can be described as a Lorentz oscillator. For the enhancement of the characteristic bands, the first derivative of the measured pseudodielectric function ($d\langle\epsilon\rangle/d\omega$) was cal-

culated. In this quantity, the chemical bonds can be identified by a maximum or minimum in $d\langle\epsilon_1\rangle/d\omega$ along with an inflection in $d\langle\epsilon_2\rangle/d\omega$. For the sake of simplicity, in Fig. 8 only the $d\langle\epsilon_1\rangle/d\omega$ spectra of the as-grown and annealed films are illustrated. Arrows, in the figure, denote the characteristic bands of single, double and triple chemical bonds, between carbon-nitrogen or carbon-carbon atoms, contributing in the wavenumber regions 1100–1300, 1300–1800 [13] and 2100–2250 cm^{-1} [14], respectively. The denoted C=O vibration mode at 2350 cm^{-1} is attributed to the environmental CO_2 . In film #a, two different contributions of the double bonding were identified and assigned to C=N (1530 cm^{-1}) and C=C (1670 cm^{-1}) bonds [15,16]. The question raised here is why C=C bonds are IR active only in film #a and not in film #b?

The analysis of FTIRSE spectra of the as-grown and annealed films showed that the oscillator strength for the sp^3 sites (C–N) is reduced in both films. Furthermore, the oscillator broadening of film #a is reduced by a factor of two compared to film #b, suggesting that the sp^3 bonds become more localized and their large variation in bond angles and lengths is

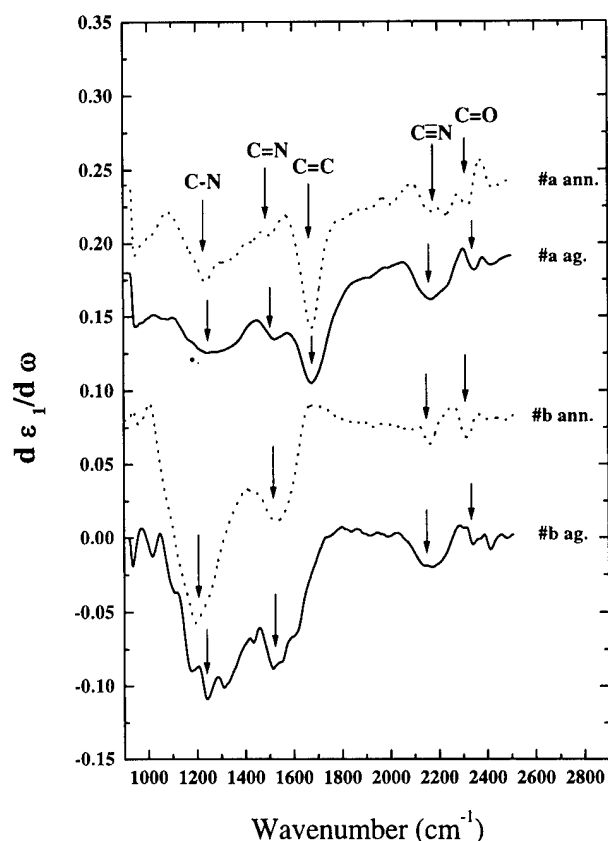


Fig. 8. The real part of the first derivative of $\langle\epsilon(\omega)\rangle$ FTIRSE spectra ($d\langle\epsilon_1\rangle/d\omega$) of the as-grown and annealed at 900°C #a and #b CN_x films. The arrows denote the characteristic bands of single, double and triple chemical bonds between carbon–nitrogen or carbon–carbon atoms, and the C=O vibration mode of environmental CO_2 .

diminished. In film #a, the effect on double bonds of annealing is a reduction of C=N and an increase of C=C bonds, whereas no significant changes are observed in film #b. This finding is in agreement with the SE results. The feature attributed to C≡N bonds seems to have the same characteristics in the films, whilst a similar reduction has been deduced in both of them after annealing. This is in agreement with the results obtained by QMS (see Fig. 7). All the above demonstrate the fundamental differences in chemical bonding configurations, and their stability during thermal annealing, between the studied CN_x films originated from the different ion energies used during their preparation. Moreover, FTIRSE spectra yield important insight into the film chemical bonding as well as the nitrogen distribution in the films; these will now be discussed.

In general, chemical bonds between carbon–carbon atoms in a-C films are not IR active [17]. In the case of CN_x films the incorporation of N in the a-C matrix breaks the symmetry and activates the carbon–carbon bonds [18]. In our first attempt to justify the observed C=C bonds in FTIRSE spectra, we suppose that this is related to the nitrogen incorporation in the amorphous carbon matrix. When the incorporated nitrogen content is high, then more N atoms are bonded into sp^2 domains and break the symmetry of sixfold rings. As a consequence, more C=C bonds may become IR active [18]. According to this assumption, the nitrogen content in film #a should be higher compared to that of film #b. On the other hand, SE data analysis revealed that film #a is more optically transparent and contains a lower percentage of sp^2 sites, compared to film #b. However, the above two arguments are in contradiction with the results reported so far, which support the increase of sp^2 sites with increasing nitrogen concentration in CN_x films [19,20]. In addition, preliminary results from X-ray photoelectron spectroscopy showed that the nitrogen concentration is similar (~20 at.%) and some small deviations cannot justify the observed differences between them.

A possible explanation of whether or not C=C bonds are activated (see Fig. 8) may be the nitrogen distribution in the films, which affects the bonding configurations. The substrate bias influences the energetic-ion bombardment and the chemistry mechanisms of the reaction kinetics in the CN_x film surface. For reactive r.f. magnetron sputtering, in the presence of a pure N plasma, where the dominant process gas ions are N^+ and N_2^+ [21], more negatively biased substrates accelerate the ions towards the growing film surface enhancing their reactivity and mobility. Thus, they can dissociate the low energy sputtered species, such as C_n or $(\text{CN})_n$ clusters, which are reaching the substrate, and form chemical bonds affecting the nitrogen distribution in the bulk of the film. In film #a, the incorporation of N in the a-C matrix is homogeneous, the N substitutes C

atoms in both sp^2 and sp^3 carbon bonded sites. In film #b, the distribution of N atoms is not homogeneous all over the film, but instead, there are regions in the a-C matrix where the local N concentration is high, and more than one N atom is incorporated per aromatic ring. This is because of the high reactivity and mobility of the nitrogen ions during deposition. If this is so, then there is a strong possibility on the formation of: (i) pentagons leading to the buckling of graphene planes; and (ii) C_3N_4 crystalline phases. The former corresponds to the transition of the graphite structure to a 'fullerene-like' one [3]. Both the 'fullerene-like' and the C_3N_4 phases exhibit high hardness and elasticity [1–3].

To verify the validation of our speculation, nanoindentation measurements were undertaken in the as-grown films. The results, not presented here, reveal that film #a is softer (~ 6 GPa) and shows a susceptibility to plastic deformation during indentation, whereas film #b is harder (~ 10 GPa) and shows a capability of elastic recovery. If we take into account that high elasticity in an examined film prevents the accurate determination of the projected area, and as result of this the accurate evaluation of the elastic properties, then the hardness of film #b is expected to be higher than 10 GPa.

4. Conclusions

CN_x films developed by r.f. magnetron sputtering in a pure N_2 plasma at RT with two different bias voltages ($V_b = -20, -250$ V) which controls the energy of N^+ and N_2^+ ions bombarding the growing film surface. We studied the optical properties and chemical bonding configurations, and the modifications occurring in post-annealing up to 900°C . The differences in the electronic dielectric response and the bonding configurations between the examined films were attributed to the nitrogen bonding and distribution in the films. That is, in the film deposited with $V_b = -20$ V (low energy ion bombardment) the nitrogen distribution is homogeneous, whereas in the film deposited with the $V_b = -250$ V (high energy ion bombardment) there are regions with a high local nitrogen concentration. This may lead either to the formation of pentagons which induces the buckling of graphene planes, or to the

formation of C_3N_4 phases. Furthermore, the CN_x film grown with high energy ion bombardment ($V_b = -250$ V) proved to be more stable during annealing, compared to that grown with $V_b = -20$ V.

Acknowledgement

This work was supported by the Greek General Secretariat for Research and Technology under the 97-YP3-211 project.

References

- [1] A.Y. Liu, M.L. Cohen, *Science* 245 (1989) 841.
- [2] A.Y. Liu, M.L. Cohen, *Phys. Rev. B* 41 (1990) 10727.
- [3] H. Siöström, S. Stafström, M. Boman, J.-E. Sundgren, *Phys. Rev. Lett.* 75 (1995) 1336.
- [4] M. Côté, M.L. Cohen, *Phys. Rev. B* 55 (1997) 5684.
- [5] P. Stumm, D.A. Drabold, P.A. Fedders, *J. Appl. Phys.* 81 (1997) 1289.
- [6] M. Gioti, S. Logothetidis, C. Charitidis, H. Lefakis, *Vacuum* 53 (1999) 53.
- [7] M. Gioti, S. Logothetidis, *Diamond Relat. Mater.* 8 (1999) 446.
- [8] G.E. Jellison Jr., F.A. Modine, *Appl. Phys. Lett.* 69 (1996) 371.
- [9] J. Tauc, R. Grigorovici, A. Vancu, *Phys. Status Solidi* 15 (1966) 627.
- [10] S. Logothetidis, M. Gioti, P. Patsalas, C. Charitidis, *Carbon* 37 (1999) 765.
- [11] A.K.M.S. Chowdhury, M. Monclus, D.C. Cameron, J. Gilvarry, M.J. Murphy, N.P. Barradas, M.S.J. Hashmi, *Thin Solid Films* 308/309 (1997) 130.
- [12] S. Veprek, J. Weidmann, F. Glatz, *J. Vac. Sci. Technol. A* 136 (1995) 2914.
- [13] J. Kouvetakis, A. Bandari, M. Todd, B. Wilkens, N. Cave, *Chem. Mater.* 6 (1994) 811.
- [14] D. Li, Y.-W. Chung, S. Yang, M.-S. Wong, F. Adibi, W.D. Sproul, *J. Vac. Sci. Technol. A* 12 (1994) 1470.
- [15] J.H. Kim, D.H. Ahn, Y.H. Kim, H.K. Baik, *J. Appl. Phys.* 82 (1997) 658.
- [16] A. Wei, D. Chen, N. Ke, S. Peng, S.P. Wong, *Thin Solid Films* 323 (1998) 217.
- [17] S. Logothetidis, H. Lefakis, M. Gioti, *Carbon* 36 (1998) 757.
- [18] J.H. Kaufman, S. Metin, D.D. Saperstein, *Phys. Rev. B* 39 (1989) 13053.
- [19] R.W.-J. Chia, E. Li, S. Sugi, G.G. Li, H. Zhu, A.R. Forouhi, I. Bloomer, *Thin Solid Films* 308/309 (1997) 284.
- [20] J. Hu, P. Yang, C.M. Lieber, *Phys. Rev. B* 57 (1998) R3185.
- [21] R. Kaltöfen, T. Sebal, G. Weise, *Surf. Coat. Technol.* 97 (1997) 131.

Carbon nitride thin films deposited by reactive plasma beam sputtering

P.Y. Tessier ^{a,*}, R. Kre N'guessan ^b, B. Angleraud ^a, V. Fernandez ^a, N. Mubumbila ^a,
G. Turban ^a

^a *Laboratoire des Plasmas et des Couches Minces, Institut des Matériaux Jean Rouxel, UMR 6502-CNRS, Université de Nantes, 44322 Nantes Cedex 3, France*

^b *Université d'Abobo-Adjamé, Abidjan, Ivory Coast*

Accepted 13 October 1999

Abstract

Carbon nitride thin films have been deposited on silicon substrates by reactive sputtering of a pure graphite target. In this process, argon plasma, generated by a hot cathode discharge, diffuses through a diaphragm into a deposition chamber towards the target which is biased at -300 V. The current density on the target is about 30 mA cm^{-2} . Nitrogen gas is injected into the deposition chamber during the sputtering. Evolution of the deposition rate is measured versus the partial N_2 pressure. The films are characterized by X-ray photoelectron spectroscopy (XPS), Fourier transform infra-red spectroscopy (FTIR) and Raman spectroscopy. The atomic ratios of N and C in films are evaluated by XPS. At high N_2 partial pressure, the atomic fraction saturates at a value of 38 at.%. The curve fitting of the C 1s and N 1s XPS peak spectra indicates that C and N atoms in films exhibit two different chemical states, representative of different C–N chemical bonds. These XPS results, combined with FTIR and Raman analysis, suggest the existence of two amorphous carbon nitride phases in films, one with a stoichiometry similar to C_3N_4 and the other with an increasing fraction of nitrogen as the total N content in the films increases. These two carbon nitride phases seem to be present as soon as nitrogen is incorporated in films, even at low atomic concentration of nitrogen. © 2000 Elsevier Science S.A. All rights reserved.

Keywords: Carbon nitride; FTIR; Raman spectroscopy; Reactive sputtering; Thin films; XPS

1. Introduction

Carbon nitride films have generated much interest since Liu and Cohen [1] predicted the existence of a metastable covalent carbon nitrogen compound ($\beta\text{-C}_3\text{N}_4$) with a bulk modulus comparable to or greater than that of diamond. This prediction motivated many researches to attempt to synthesize this material by various techniques such as laser ablation deposition [2,3], sputtering deposition [4–6], ion beam evaporation deposition [7,8], and chemical vapor deposition [9,10]. Although the nitrogen content of most of the CN_x films obtained has not yet reached the predicted value of 57 at.% of the $\beta\text{-C}_3\text{N}_4$ phase, carbon nitride has already emerged as a new material of both scientific and practical interest. For example, two main applications of these

films concern electronic field emission [11–13] and semi-conducting properties [10].

In this paper we report on experiments carried out to synthesize CN_x films by an original method using plasma beam reactive sputtering of a graphite target. Films are analyzed by X-ray photoelectron spectroscopy (XPS), Fourier transform infrared spectroscopy (FTIR) and Raman spectroscopy. The study is mainly devoted to following the evolution of the deposition rate, the composition, type of chemical bonds and structure of the deposited films versus nitrogen partial pressure injected in the reactive deposition chamber. Particular attention is paid to determine the type of chemical bonds between C and N atoms by a systematic XPS investigation.

2. Experiments details

The deposition is performed using a Sputtrion II Balzers plasma beam sputtering equipment. The experi-

* Corresponding author.

E-mail address: pierre-yves.tessier@cnrs-imn.fr (P.Y. Tessier)

mental set-up, presented in Fig. 1, is composed of an ionization chamber and a sputtering chamber. Chambers are evacuated by an 1800 l/s oil diffusion pump with a coolant baffle to a base pressure of 8×10^{-6} mbar before beginning the deposition. The ionization chamber is connected to the sputtering chamber via an aperture, through which there is a pressure drop during sputtering operation. The pressure in the ionization chamber is approximately 20 times greater than in the sputtering chamber. First, argon gas is injected into the ionization chamber, then, before deposition, nitrogen gas is injected into the sputtering chamber. The N_2 partial pressure can be adjusted between 0 and 10^{-3} mbar, whereas the Ar partial pressure is set to 10^{-3} mbar in the sputtering chamber. A heated tantalum filament emits electrons and the discharge is initiated using the auxiliary anode. An arc discharge is maintained between hot cathode and anode in the sputtering chamber. A magnetic field, generated by an external coil mounted around the sputtering chamber, forces the plasma into a beam between the aperture and anode, which results in a high concentration of ionized particles.

The target is a 60 mm diameter high purity sintered graphite (99.995%). By applying a negative voltage set at -300 V to the target, the ions of the arc plasma are accelerated towards the graphite for sputtering of the material. The current density on the target is about 30 mA cm^{-2} . Prior to each deposition, the target is sputter cleaned with a shutter shielding the substrate during this procedure. The substrates are fixed laterally 200 mm from the target center.

Substrates are p-type boron-doped silicon with (100) orientation and a resistivity of $12 \Omega \text{ cm}$. Before their introduction into the deposition system, the substrates are cleaned in acetone (5 min) then in ethanol (5 min) using an ultrasonic cleaner, and finally are dried by a N_2 flow. The last cleaning operation is Ar^+ ion bom-

bardment of substrates biased at -150 V in the deposition chamber during 5 min. For this operation, N_2 gas is not injected and the plasma beam is brought along the substrate vicinity by removing the magnetic field generated by the external coil. During deposition, substrates are connected to ground.

After deposition, the chamber is vented to atmospheric pressure under nitrogen gas and samples are immediately transferred to a Kratos Axis Ultra spectrometer for XPS ex situ analysis. The pressure in the spectrometer is around 10^{-9} mbar. This condition allows us to maintain XP spectra over a few hours with a constant C 1s, N 1s and O 1s ratio and peak shape. Monochromatic Al $K\alpha$ radiation (1486.6 eV) is used for all XPS measurements. The pass energy of the analyzer is 160 eV for wide scan XP spectra and 20 eV for detailed XPS peaks. The resolution of the spectrometer, measured by fitting a silver Fermi edge [14], is 0.47 ± 0.03 eV and 2.1 ± 0.1 eV at, respectively, 20 eV and 160 eV pass energy. Tests under electron bombardment of films during XPS measurements have revealed no shift of the binding position of the XPS peaks. This result indicates that there is no charging effect during our measurements, and correction of the binding energy is not necessary.

The transmission FTIR spectra are recorded on a Nicolet 20XSC spectrophotometer equipped with a HgCdTe detector over a range of 400 to 4000 cm^{-1} with a 4 cm^{-1} spectral resolution.

Raman measurements are carried out on a Jobin-Yvon T64000 spectrometer using the 514.5 nm line of an argon ion laser with a power of 10 mW. The width of the slit is $40 \mu\text{m}$, which gives a resolution of about 0.9 cm^{-1} .

Film thickness is measured using a Tencor Alpha Step profiler.

3. Results and discussion

The deposition rate versus nitrogen partial pressure is given in Fig. 2. A significant increase of the deposition rate is observed as the N_2 pressure increases up to 7.5×10^{-4} mbar. Measurements at 10^{-3} mbar indicate a lowering of the deposition rate. This behavior is not associated with a modification of the electrical parameters of the discharge. Particularly, the target current remains constant as the N_2 pressure increases. The increase in deposition rate with N_2 pressure has already been observed in reactive magnetron sputtering [6,15]. One possible explanation is an increase in sputtering yield of the target as the N concentration increases on the target surface due to ion bombardment. The incorporation of nitrogen atoms in the target leads to chemical reactions between N and C atoms and may reduce the cohesive energy of the carbon atoms of the target. The

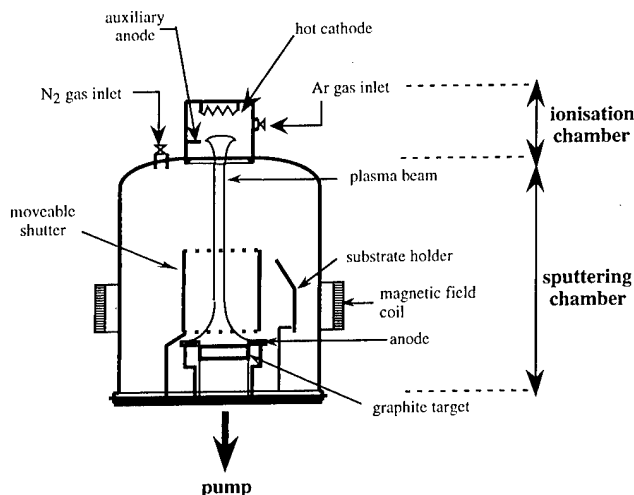


Fig. 1. Schematic diagram of the experimental set-up.

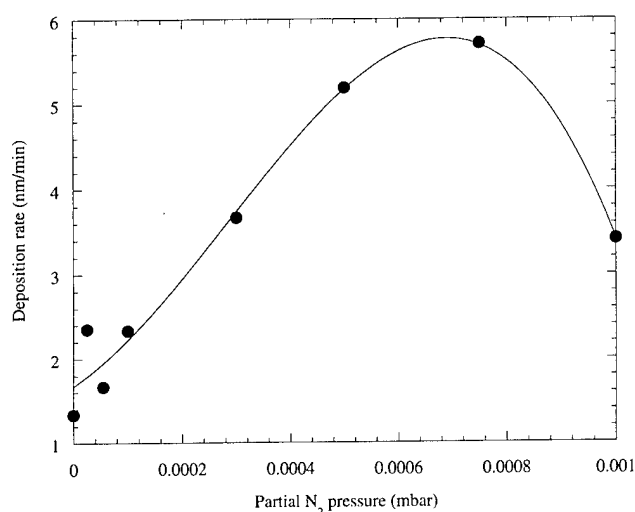


Fig. 2. Deposition rate as a function of the partial N₂ pressure.

decrease in deposition rate at high nitrogen pressure is probably due to the etching of films by nitrogen during their growth. Indeed, volatile CN compounds can be formed by chemical reaction between carbon and nitrogen at the film surface [7]. At high pressure, this etching mechanism is certainly not negligible compared with the growth one, and hence the deposition rate, which is the result of a balance between etching and growth mechanisms, must decrease.

Wide scan XP spectra indicate the presence of carbon, nitrogen and oxygen in films. The presence of oxygen is probably related to the relatively high base pressure in the deposition system. The chemical composition was obtained from the area of C 1s, N 1s and O 1s XPS peaks taking into account sensitivity factors for each constituent. The evolution of the atomic concentration of C, N and O is given in Fig. 3. A strong increase in

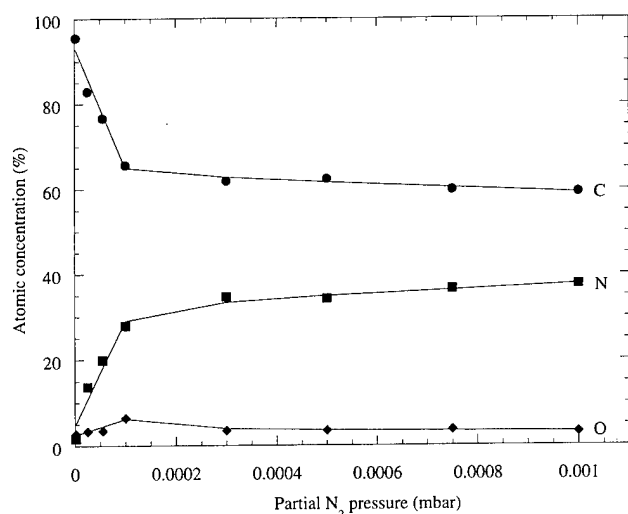


Fig. 3. Atomic concentration of C, N and O in films as a function of the partial N₂ pressure.

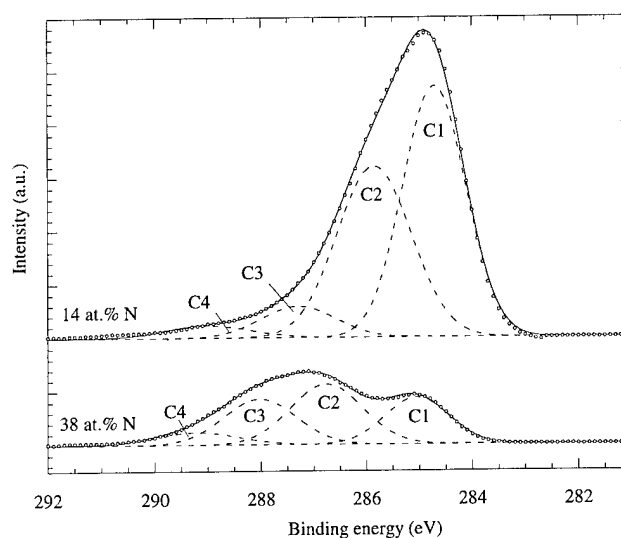


Fig. 4. C 1s spectra for films containing 14 at.% and 38 at.% concentration. The experimental data are represented by circles. The solid lines are the results of curve fitting by the Gaussian components in dotted lines.

N concentration is observed as N₂ partial pressure varies from 0 to 10⁻⁴ mbar. The N concentration saturates at high N₂ pressure and reaches 38% at 10⁻³ mbar. This saturation of the N concentration can be correlated with the observed decrease in deposition rate at high N₂ pressure. The formation of volatile CN compounds on the film surface during deposition must probably limit the incorporation of nitrogen.

The C 1s and N 1s XPS peaks are shown in Fig. 4 and Fig. 5 for two samples at 14% and 38% relative atomic nitrogen concentration. The background spectra are considered as Shirley type. The shape and the large

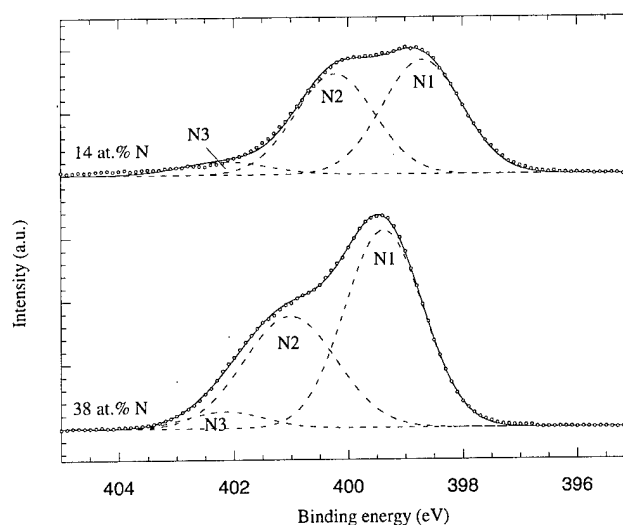


Fig. 5. N 1s spectra for films containing 14 at.% and 38 at.% N concentration. The experimental data are represented by circles. The solid lines are the results of curve fitting by the Gaussian components in dotted lines.

full-width at half-maximum (FWHM) of XPS peaks suggest different types of chemical state for carbon and nitrogen in the films. Curve fitting of spectra is achieved by adding several peaks of Gaussian shape. For all samples, the curve fitting of the C 1s spectra indicates the presence of four different chemical states of carbon (Fig. 4), whereas the N 1s spectra (Fig. 5) show three different chemical states. Results of the curve fitting are given in Table 1. All the component binding energies increase with N content. The corresponding values of FWHM are 1.4–1.6 eV for C1, C2, C3, N1, N2, N3 peaks and 1.5–1.8 eV for C4 peak. The C4 peak is attributed to C–O bonds and, similarly, the N3 peak corresponds to N–O bonds [5,9]. The C1 peak is attributed to C–C bonds; this position is at an intermediary value between the two positions of the C 1s peak attributed to C–C sp^2 bonds in graphite and C–C sp^3 bonds in diamond-like amorphous carbon. The C2 and C3 peaks are related to nitrogen incorporation and are assigned to C–N bonds. Correspondingly, in the N 1s zone, the N1 and N2 peaks are assigned to C–N bonds.

On the basis of some reports [16–18], the C2 and N2 peaks can be assigned to a type of C–N bond for which nitrogen atoms are bonded to sp^2 carbon, whereas C3 and N1 peaks correspond to C–N bonds for which nitrogen atoms are bonded to sp^3 carbon atoms. The presence of $C\equiv N$ is also not excluded since the positions of the C 1s and N 1s are, respectively, 286.7 eV and 399.6 eV in polyacrylonitriles [19]. The first value is close to the C2 peak position and the second is at an intermediary value between C2 and C3 position peaks.

The relative atomic concentration of each component, deduced from the magnitude of the component areas taking into account the XPS sensitivity factors, is shown in Figs. 6 and 7 as a function of the total nitrogen atomic concentration in films. The relative intensity of the C1 and C2 peaks decreases, whereas the C3, N1 and N2 peaks have an increasing relative intensity as the N content increases in films. Assuming two carbon nitride phases in films, phase 1 associated with C2 and N2 peaks, phase 2 associated with C3 and N1 peaks, the atomic fraction of nitrogen has been calculated in each phase. The result is shown in Fig. 8. In phase 1, the nitrogen fraction varies from 15 at.% to 39 at.% as the total nitrogen content in films increases. In phase 2, whatever the total nitrogen content in films, the fraction

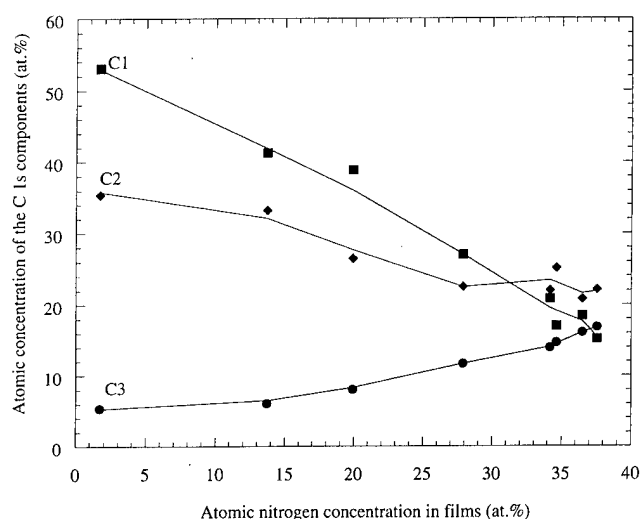


Fig. 6. Relative atomic concentration deduced of the C 1s component intensities versus total atomic nitrogen concentration in film.

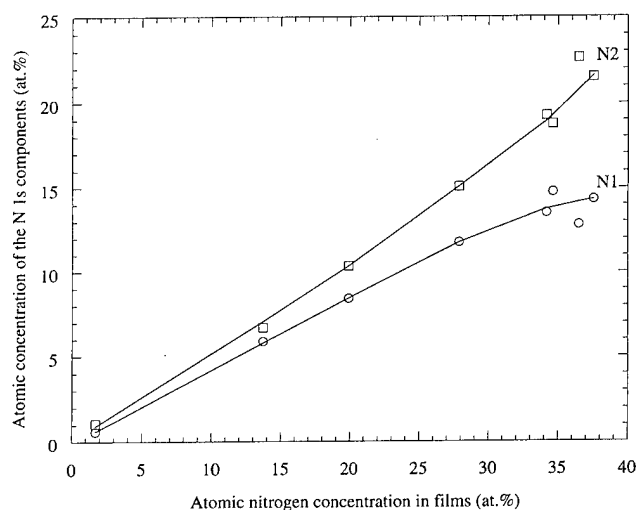


Fig. 7. Relative atomic concentration deduced of the N 1s component intensities versus total atomic nitrogen concentration in film.

of nitrogen is very close to 57 at.% which is the stoichiometry expected for C_3N_4 . This result, and the fact that the XPS peak position in phase 2 is attributed to N bonded to sp^3 C, leads us to conclude that phase 2 is a C_3N_4 phase probably in an amorphous state.

Therefore, XPS results suggest the presence of three phases in films: a carbon phase and two carbon nitride

Table 1
Results of the XP spectra curve fitting

Peak designation	C 1s core level				N 1s core level		
	C1	C2	C3	C4	N1	N2	N3
Position at low N content (eV)	284.7	286	287.3	289	398.8	400.2	402.1
Position at high N content (eV)	285.3	286.8	287.6	289.4	399.4	401	402.5

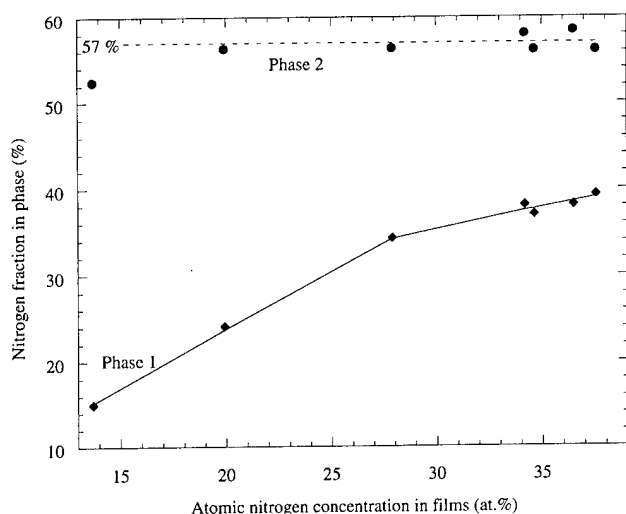


Fig. 8. Nitrogen fraction in phase 1 and in phase 2 versus total atomic nitrogen concentration in films.

phases. The first carbon nitride phase has an increasing fraction of nitrogen as the total nitrogen content increases in the films, the second one corresponds to C_3N_4 and is present as soon as nitrogen is incorporated in films.

Structural information on the deposited films is obtained using micro-Raman and FTIR spectroscopy. The Raman and FTIR spectra are analyzed in order to investigate the effect of nitrogen concentration on the film bonding structure. Whatever the N content, a broad peak between 1200 and 1700 cm^{-1} is detected, revealing the amorphous structure of the CN_x films. This peak can be resolved into two Gaussian line shapes and a constant background using curve-fitting software. The positions of the two Gaussian shapes are found around 1360 and 1560 cm^{-1} . These bands are characteristic of a mixture of graphitic (G band at 1575 cm^{-1}) and disordered sp^2 -bonded carbon (D band at 1350 cm^{-1}) [20]. With increasing nitrogen content, these bands become stronger, meaning that Raman G and D bands become more active when large amounts of nitrogen (up to 38%) are present in the film.

A weak band near 2210 cm^{-1} appears in the Raman spectra with nitrogen incorporation. Its intensity also increases as more N is incorporated in films. This band is usually attributed to the stretching vibration of $C\equiv N$ bonding. Hence the increase in this band is ascribed to an increasing amount of $C\equiv N$ bonds.

From a more precise inspection of the broad peak between 1200 and 1700 cm^{-1} , we find that the distinction between the D and G peaks becomes clearer as the nitrogen concentration in the film is raised. Indeed, at high N content (35–38%), the broad peak clearly separates into two peaks located around 1360 and 1560 cm^{-1} .

In order to quantify this behavior, we calculate the

area intensity ratio of the D and G peaks: $I(D)/I(G)$. With varying N content from 0 to 38%, the ratio $I(D)/I(G)$ varies quite linearly from 1.3 up to a limited value of 1.7–1.8. This evolution is indicative of the increase in structure disorder degree in the CN films: the translational periodicity of the atomic network of the solid is disturbed by bond-angle distortions and particle size effects caused by the nitrogen incorporation in the carbon structure. Moreover, the linear variation of $I(D)/I(G)$ as a function of nitrogen concentration shows that the shape of the Raman spectra between 1200 and 1700 cm^{-1} is clearly indicative of incorporated N amount of the CN_x films.

The Raman results can be correlated with the FTIR ones. As nitrogen is incorporated in the film, FTIR spectra exhibit characteristic bands of carbon nitrogen bonds at 2210 (stretching vibration $C\equiv N$ bond) and around 1500 cm^{-1} (stretching vibration modes of $C-N$, $C=N$, $C=C$ bonds), showing that the C and N atoms are chemically bonded in the films [18,21,22]. In particular, we can note the increase in intensity of the peak located at 2210 cm^{-1} as the N content increases in the film, showing the simultaneous increase in $C\equiv N$ bonds. The presence of $C\equiv N$ bonds is consistent with XPS results. Indeed, as noted previously, a part of the C2 peak can be attributed to $C\equiv N$ in phase 1.

4. Conclusions

This work demonstrates the ability of an original sputtering deposition process to synthesize carbon nitride films. After optimization of the deposition parameters, the N content in the deposited films reaches 38% without any ion bombardment at the substrate with an external supply. The detailed XPS results combined with FTIR and Raman measurements suggest the existence of three amorphous phases in films: a carbon phase, a carbon nitride phase with a variable fraction of nitrogen ($N-C$ sp^2 and $C\equiv N$ bonds) and another one with a stoichiometry similar to C_3N_4 in which N is bonded to C sp^3 . Future work will be devoted to the improvement of nitrogen incorporation on the films by ion bombardment of the substrate during their growth. Moreover, an attempt to determine the mechanisms involved in the CN_x phases formation will be made by studying both the transport of sputtered species and the structure of the films by analysis methods such as optical emission spectroscopy, EELS and TEM.

Acknowledgement

The authors thank J.Y. Mevellec (IMN) for his help during Raman and FTIR measurements.

References

- [1] A.Y. Liu, M. Cohen, *Phys. Rev. B* 41 (1990) 10727.
- [2] S. Lee, S.J. Park, S. Oh, W.M. Kim, J.H. Bae, B. Cheong, S.G. Kim, *Thin Solid Films* 308/309 (1997) 135.
- [3] I.N. Mihailescu, E. Gyorgy, R. Alexandrescu, A. Luches, A. Perrone, C. Ghica, J. Werkmann, I. Cojocaru, V. Chumash, *Thin Solid Films* 323 (1998) 72.
- [4] N. Axen, G.A. Botton, H.Q. Lou, R.E. Somekh, I.M. Hutchings, *Surf. Coat. Technol.* 81 (1996) 262.
- [5] W.T. Zheng, E. Broitman, H. Hellgren, K.Z. Xing, I. Ivanov, H. Sjöström, L. Hultman, J.E. Sundgren, *Thin Solid Films* 308/309 (1997) 223.
- [6] Y. Kusano, J.E. Evetts, R.E. Somekh, I.M. Hutchings, *Thin Solid Films* 332 (1998) 56.
- [7] P. Hammer, M.A. Baker, C. Lenardi, W. Gissler, *Thin Solid Films* 290/291 (1996) 107.
- [8] X.A. Zhao, C.W. Ong, Y.C. Tsang, K.F. Chan, C.L. Choy, P.W. Chan, R.W.M. Kwok, *Thin Solid Films* 322 (1998) 245.
- [9] J. Hong, G. Turban, *J. Vac. Sci. Technol. A* 17 (1) (1999) 314.
- [10] S.R.P. Silva, R.U.A. Khan, A.P. Barden, J.V. Anguita, J.M. Shannon, B.J. Sealy, A.J. Papworth, C.J. Kiely, G.A.J. Amaratunga, *Thin Solid Films* 332 (1998) 118.
- [11] J.E. Jaskie, *MRS Bull.* 21 (1996) 59.
- [12] G.A.J. Amaratunga, S.R.P. Silva, *Appl. Phys. Lett.* 68 (1996) 2529.
- [13] E.J. Chi, J.Y. Shim, D.J. Choi, H.K. Baik, *J. Vac. Sci. Technol. B* 16 (3) (1998) 1219.
- [14] A. Barrie, N.E. Christensen, *Phys. Rev. B* 14 (6) (1976) 2442.
- [15] W.T. Zheng, H. Sjöström, I. Ivanov, K.Z. Xing, E. Broitman, W.R. Salaneck, J.E. Greene, J.E. Sundgren, *J. Vac. Sci. Technol. A* 14 (5) (1996) 2696.
- [16] S. Bhattacharyya, J. Hong, G. Turban, *J. Appl. Phys.* 83 (7) (1998) 3917.
- [17] S. Kumar, K.S.A. Butcher, T.L. Tansley, *J. Vac. Sci. Technol. A* 14 (5) (1996) 2687.
- [18] A. Wei, D. Chen, N. Ke, S. Peng, S.P. Wong, *Thin Solid Films* 323 (1998) 217.
- [19] G. Beamson, D. Briggs, *High Resolution XPS of Organic Polymers*, Wiley, London, 1992, pp. 184–185.
- [20] D.S. Knight, W.B. White, *J. Mater. Res.* 4 (2) (1989) 385.
- [21] J. Shiao, R.W. Hoffman, *Thin Solid Films* 283 (1996) 145.
- [22] T.R. Lu, L.C. Chen, K.H. Chen, D.M. Bhusari, T.M. Chen, C.T. Kuo, *Thin Solid Films* 332 (1998) 74.

Synthesis and characterization of carbon nitride thin films obtained by laser induced chemical vapour deposition

A. Crunteanu^{a,b,*}, M. Charbonnier^a, M. Romand^a, F. Vasiliu^c, D. Pantelica^d,
F. Negoita^d, R. Alexandrescu^b

^a Laboratoire de Sciences et Ingénierie des Surfaces, Université Claude Bernard – Lyon 1, 69622 Villeurbanne Cedex, France

^b Lasers Department, National Institute for Lasers, Plasma and Radiation Physics, P.O. Box MG-36, R-76900 Bucharest, Romania

^c Electron Microscopy Laboratory, National Institute for Materials Physics, P.O. Box MG-7, R-76900 Bucharest, Romania

^d National Institute for Physics and Nuclear Engineering-NIPNE ‘Horia Hulubei’, P.O. Box MG-6, R-76900 Bucharest, Romania

Abstract

Carbon nitride thin films (CN_x) were produced by UV laser (ArF, $\lambda=193$ nm) induced chemical vapour deposition from C₂H₂/NH₃ mixtures, on Si and TiN/Si substrates. The surface and bulk composition of the deposited layers were investigated by X-ray photoelectron spectrometry (XPS) and elastic recoil detection analysis (ERDA), respectively. Nitrogen was found to be singly and doubly bonded to carbon, as revealed by FTIR spectrometry. Specific morphology of the films was evidenced by transmission electron microscopy (TEM), while selected area electron diffraction (SAED) confirms the presence of nano-crystallites in the layers. The calculated *d*-lattice spacings fit rather well with theoretical and experimental data for α - and β -C₃N₄. © 2000 Elsevier Science S.A. All rights reserved.

Keywords: Carbon nitride; Electron diffraction; ERDA; Laser CVD; Thin films; XPS

1. Introduction

Liu and Cohen’s prediction [1] on the existence of a new ultra-hard material based on carbon and nitrogen and having a structure equivalent to that of β -Si₃N₄ has raised great interest due to the properties that this material could have, such as hardness similar to or even higher than that of diamond, chemical and thermal stability, toughness, etc. The possible applications of this material as coatings in the semiconductor industry, for data storing media or protection have focused the efforts of the scientific community on obtaining β -C₃N₄. Since then, it has been indicated that hexagonal α -C₃N₄ [2] and other C₃N₄ phases having rhombohedral or defect zinc-blende structure [3] would be more stable than β -C₃N₄. At the same time, crystallites attributed to tetragonal and monoclinic carbon nitride were experimentally evidenced [4,5]. Different types of deposition method, such as sputtering [6,7], ion beam deposition

[8], hot filament CVD [4,5,9] or laser ablation [10,11], in reactive atmosphere have been used to synthesise carbon nitride thin films. The majority of these works have resulted in deposits with nitrogen concentration up to 40% (far from the stoichiometric value of ~57%) or failed to produce crystalline materials. However, the existence of micro-crystallites of β -C₃N₄ embedded in an amorphous CN_x matrix ($x<0.7$) was evidenced by electron diffraction [7,12] or even X-ray diffraction (XRD) [9] measurements. Recently, we have demonstrated that laser CVD (L-CVD) could be a suitable method to produce CN_x films on different substrates using carbon/nitrogen-containing gas precursors and shown that the film morphology depends on the substrate nature [13]. Also, in an earlier study, Li et al. [14] evidenced that TiN(111) substrates could play the role of a structural initiator in the nucleation of crystalline β -C₃N₄ films. Based on these observations, the present work aims at confirming the suitability of the L-CVD method to produce CN_x thin films with high nitrogen content using an ArF excimer laser, acetylene and ammonia mixtures and Si or TiN substrates.

* Corresponding author. Tel.: +401-423-1470, ext. 105;
fax: +401-423-1791.

E-mail address: aurash@ifin.nipne.ro (A. Crunteanu)

2. Experimental

The experimental set-up consists of a stainless-steel flow reactor (40 cm in diameter) equipped with a primary vacuum pump and a secondary turbo-molecular one (Leybold AG). The unfocused ArF excimer ($\lambda = 193$ nm, 20 ns) laser beam (Lambda Physics, model EMG 103 MSC) 5×25 mm² in size, enters the reactor through a CaF₂ window (purged with N₂ at ~ 150 ml/min, in order to avoid fogging and subsequent residual deposition). High purity acetylene (C₂H₂) and ammonia (NH₃) gases are selected as carbon and nitrogen donors, since both exhibit absorption at 193 nm. The acetylene and ammonia flows are maintained at 30 and 190 sccm, respectively. The gases are pre-mixed before entering the reaction cell and conducted through a nozzle over the substrate. The total pressure is settled at ~ 60 mbar. The reaction cell is pumped down to 6.6×10^{-5} mbar before admission of reactant gases. Wafers (15×20 mm² in size) of Si(100) and TiN deposited on Si are used as substrates and prior to each experiment they are ultrasonically cleaned in ethanol. The time of irradiation is varied between 30 min and 2 h.

The irradiation geometry (substrate perpendicular or parallel to the laser beam) plays an important role. First exploratory experiments have shown that the perpendicular irradiation results in scattered and non-uniform deposits in the periphery of the irradiated area with low nitrogen incorporation. Consequently, the parallel irradiation was chosen in which the laser beam and substrate are parallel and 4 mm apart. The incident laser fluence was ~ 70 mJ/cm² per pulse, at a repetition rate of 10 Hz.

The chemical composition, morphology and crystallinity of the deposited films were investigated by X-ray photoelectron spectrometry (XPS), FTIR spectrometry, transmission electron microscopy (TEM), XRD and selected area electron diffraction (SAED).

3. Results and discussion

The obtained films are yellow in colour, relatively smooth and dense, uniform and well adherent as revealed by the Scotch[®] test (European norm NF EN ISO2409: 1994). The profilometric measurements (Tencor Instrument) show that the deposition rate of the CN_x films deposited on TiN substrates is slightly higher (30 Å/min) than that of the films deposited on Si (~ 20 Å/min).

FTIR spectra of films deposited under similar experimental conditions on both types of substrate were recorded with a Nicolet 205 spectrometer in transmission mode and are presented in Fig. 1. There is no significant difference between spectra, which suggests that the composition and chemical bonding in the CN_x films deposited on TiN and Si substrates are the same. The broad

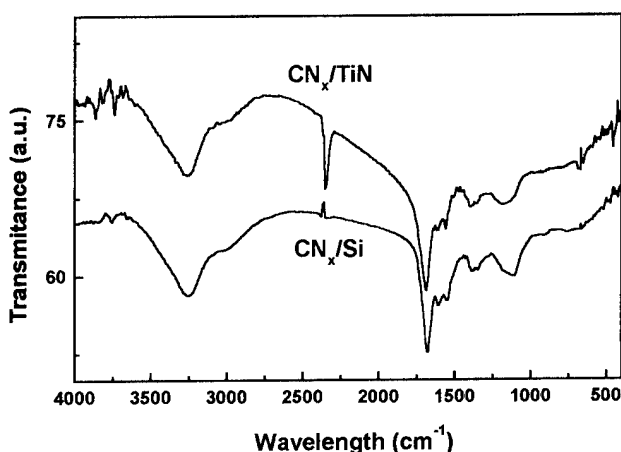


Fig. 1. FTIR transmission spectra of carbon nitride films deposited on Si and TiN substrates.

band between 3100 and 3500 cm⁻¹ can be attributed to NH₂ symmetric and asymmetric stretching modes. The shoulder in the 2800–3050 cm⁻¹ region is specific to the CH₂ symmetric and asymmetric vibrations or CH stretching modes. The low intensity features over 3600 cm⁻¹ are due to OH bonds [15]. The peaks appearing in the 1300–1700 cm⁻¹ region are representative of the existence of C=N and C–N bonds. Although it is rather difficult to distinguish between different possible chemical bonds, and despite the often contradictory reports on IR spectra of the CN_x-type films [6,10,11], the strong peak at ~ 1680 cm⁻¹ is attributed to C=C bonds and sp² graphitic domains. The small peak at ~ 1616 cm⁻¹ corresponds to NH₂ stretching modes, while the peak at ~ 1560 cm⁻¹ is attributed to C=N type bonds. The band in the 1280–1450 cm⁻¹ range, which presents a peak at ~ 1370 cm⁻¹, suggests the presence of C–N bonds. The asymmetric band in the region 1025–1270 cm⁻¹ characterises amine stretching vibrations or C–O stretching modes [15]. Furthermore, no peak belonging to the triply bonded C≡N (usually around 2200 cm⁻¹) appears in our spectra.

XPS measurements were carried out on a Riber SIA 200 instrument using a non-monochromatic Al K α (1486.6 eV) X-ray source and a MAC 2 energy analyser. The vacuum in the analytical chamber was better than 1.3×10^{-9} mbar and the electron take-off angle was 65° with respect to the sample surface. All the observed photoelectron peaks were corrected for charging effects by referencing to the C 1s peak relative to hydrocarbon species at 284.6 eV. The analyses show that both films deposited on Si and TiN contain carbon, nitrogen and a certain amount of oxygen ($\sim 10\%$) which is due to reactions involving residual oxygenated species in the reaction chamber or to air contamination. The elemental concentration of the CN_x films deposited on both types of substrate gives a N/C atomic ratio between 0.63 (film deposited for 30 min) and 0.75 (film deposited for 2 h).

The N/C ratio was calculated by taking into account the whole integrated area of the N 1s and C 1s peaks. This ratio, besides the carbon bonded to nitrogen contributions, contains information coming from other possible bonds, i.e. carbon bonded to hydrogen or oxygen and nitrogen bonded to hydrogen. Thus, we may refer to it as an overall N/C ratio. In this respect, the increase of this N/C ratio, when the deposition time increases, can be explained by the decrease of the oxygen content in the film. Such a phenomenon is the result of the consumption of the residual oxygenated species whose content decreases as a function of the deposition time. We noticed that the N/C ratio of the films deposited on TiN substrates is in all cases slightly higher (about 5%), but as it is in the limits of experimental error, we cannot affirm that there is a significant variation of N/C values with the type of substrate. The C 1s and N 1s spectra of a CN_x film deposited on a silicon substrate for 1 h irradiation (Fig. 2) are rather broad, suggesting, among others, different chemical bonds between carbon and nitrogen. A Gaussian/Lorentzian decomposition of these spectra gives peaks at 284.7, 285.7, 286.6 and 287.7 eV for the C 1s spectrum and at 398.9, 399.7 and 400.5 eV for the N 1s one. As in the case of FTIR analyses, the ill-defined nature of the films deposited (within which oxygen and hydrogen atoms are present) makes rather difficult the attribution of these peaks. Based on the literature data [8,16,17], the C 1s peak at 284.7 eV is assigned to adventitious carbon and to C–H bonds which are present in significant amount in the film as shown by FTIR and ERDA (see further). Under these conditions, it is very difficult to evaluate the contribution due to contamination. The peak at 287.7 eV suggests the existence of C=O type bonds [17]. The two other C 1s peaks at 285.7 and 286.6 eV may be attributed to carbon–nitrogen bonds and, more precisely, to sp² C–N and sp³ C–N configurations, respectively. These attributions are made by considering XPS results obtained by Gelius et al. [18,19] on graphite (sp² C peak at 284.45 eV) and diamond (sp³ C peak at 285.25 eV) and by Jackson and Nuzzo [20] on ultra-pure graphite (sp² C peak at about 284.8 eV) and diamond (sp³ C peak at

about 285.8 eV), and on amorphous carbon (sp² C and sp³ C peaks at 284.84 and 285.80 eV, respectively). In both these cases, the peak separation is 0.8–1 eV. For the CN_x films, the polarisation of the C–N bonds leads to an increase of the binding energy of the C 1s corresponding peaks. This explains the values (285.7 and 286.6 eV) determined in the present work. However, different remarks have to be made: (i) the energy difference between the sp³ C–N and sp² C–N peaks is here 0.9 eV, while higher values are given in the literature [8,16] for CN_x samples obtained by various other techniques; (ii) the presence of carbon micro-areas which do not contain nitrogen atoms must not be excluded, account being taken of the relatively low nitrogen content. As a result, trigonal C–C bonds may contribute to the peak at 284.7 eV. In the same way, tetragonal C–C bonds could participate in the peak at 285.7 eV; and (iii) the possible presence of some C–O–C and C–O–H bonds whose C 1s peak is located at a binding energy 1.5 eV higher than that corresponding to the C–H bonds could also broaden the C 1s peaks associated with C–N bonds. The decomposition of the N 1s spectrum of the CN_x film shows three peaks at 398.9, 399.7 and 400.5 eV. Their attribution is done on the basis of both theoretical and experimental literature data. According to numerical simulations [21], taking into account nitrogen atoms bonded to carbon in different hybridisation states, Hammer et al. [22,23] consider that the N 1s component at the lower binding energy (398.3 eV) is due to N–sp³ C bonds while that at higher binding energy (400.6 eV) is due to N–sp² C bonds. In addition, these authors show that a new peak due to N–H bonds appears at 399.1 eV when hydrogen is incorporated in CN_x films. Other quantum chemical calculations carried out by Sjoström et al. [24] lead to similar results with, however, a smaller energy difference (1.8 eV) between the two components. Experimental works due to Marton et al. [8,25] and Zemek et al. [26,27] confirm these calculation results. In the present work, the peak interpretation is in agreement with Hammer's model, namely N–sp³ C at 398.9 eV, N–H at 399.7 eV, and N–sp²

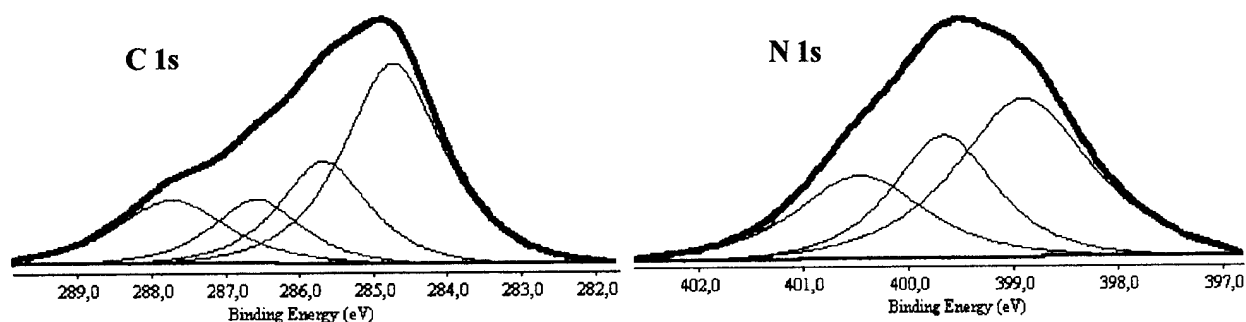


Fig. 2. C 1s and N 1s decomposed spectra for CN_x thin films deposited on Si substrates.

C at 400.5 eV, even though the energy separation between the peaks characteristic of N–C bonds is only 1.6 eV. However, this value is near to that indicated by Marton and Zemek. In conclusion, the general interpretation of the C 1s and N 1s peaks given here is made difficult because the actual structure of the films is not clearly established, as pointed out in the section dealing with the SAED results.

The bulk composition of the films deposited on Si and TiN was investigated by ERDA. The measurements were carried out at the 8.5 MV Tandem accelerator of NIPNE using an 80 MeV $^{63}\text{Cu}^{10+}$ beam. The samples were mounted in the scattering chamber with a vacuum better than 6.6×10^{-5} mbar and tilted at 15° with respect to the beam direction. The detector, which is described in detail elsewhere [28], consisted in a compact $\Delta E(\text{gas})-E(\text{solid})$ telescope placed at 30° with respect to the beam. For both types of substrate the elemental analysis of the films shows the presence of C, N, O and H along with Si and/or Ti coming from the substrate. The $\Delta E-E$ spectrum and the energy spectra of the elements for a film deposited for 1 h on a Si substrate are presented in Fig. 3. A quantitative analysis of these energy spectra using the program SURFAN [29] gives the following stoichiometric composition:

$\text{C}_{0.35}\text{N}_{0.15}\text{O}_{0.08}\text{H}_{0.42}$. As also indicated by FTIR, there is a substantial incorporation of H in the films. The amount of oxygen includes that of the oxide layer (SiO_x) at the substrate surface. The difference in the elemental composition of the films, as revealed by XPS and ERDA analysis, comes from the fact that the hydrogen is not seen in XPS, thus resulting in an overestimation of the element concentrations. In the case of CN_x films deposited on TiN, it is rather difficult to differentiate between the nitrogen signals coming from the film and from the TiN layer deposited on Si.

TEM and SAED investigations of the CN_x films deposited on Si and TiN were performed using a JEOL JEM-2000 CX transmission microscope. The specimens were obtained by mechanical stripping of the films from the substrate. The TEM images and associated SAED patterns for CN_x thin films deposited on Si and TiN substrates are presented in Fig. 4(a) and (b), respectively. The films contain polycrystalline domains, with very small grains whose dimensions are at least one order of magnitude higher for the films deposited on Si substrates. The SAED patterns confirm the nano-crystalline nature of the films and point to a better organisation of the films deposited on TiN compared to those deposited on Si. Indeed, in the latter case the diffraction rings

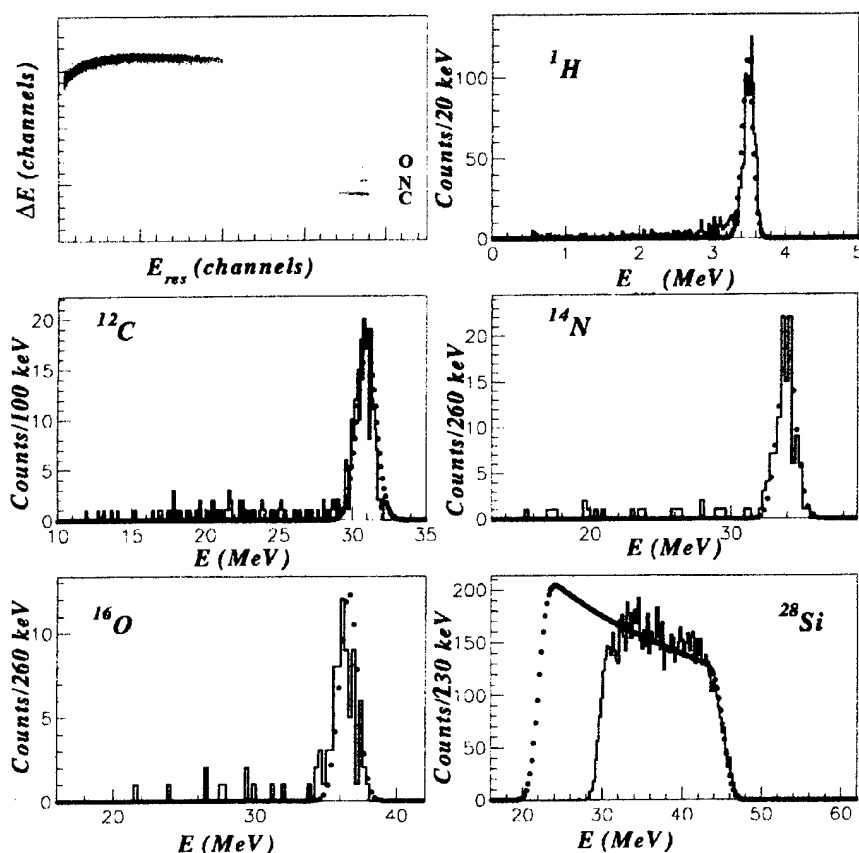


Fig. 3. $\Delta E-E$ spectrum and energy spectra for C, N, O, H and Si as recorded by ERDA for a CN_x film deposited on Si substrate along with the simulated curves (dotted lines).

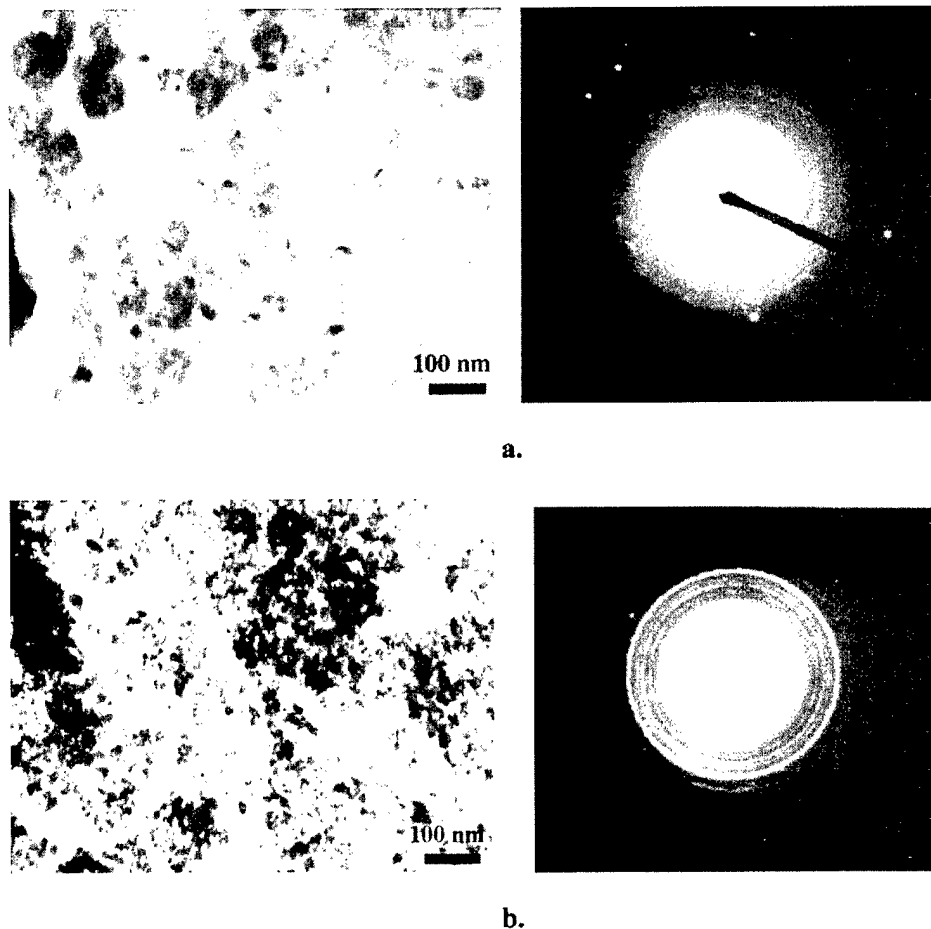


Fig. 4. TEM images and associated SAED patterns for CN_x thin films deposited on (a) Si and (b) TiN substrates.

are slightly diffuse which characterises the presence of disordered nano-crystallites. Table 1 presents, for films deposited on both substrates, the lattice spacings measured on ring patterns of Fig. 4(a) and (b), along with the theoretically predicted values for α - and β - C_3N_4 as presented in Refs. [2,12,30]. The lattice spacings marked with * and † could also come from the Si or TiN substrates as a consequence of the preparation method of the SAED specimens. It can be observed that the majority of the experimental data fit rather well the predicted pattern for both C_3N_4 phases. Although it was theoretically postulated that the α - C_3N_4 phase could be energetically preferred to the β phase [2], it is likely that non-equilibrium processes could lead to a mixture of these phases [12]. From Table 1 it can be inferred that most of the lattice spacings measured on the CN_x films deposited on Si are specific to the α - C_3N_4 phase, even though some diffraction lines calculated from the theoretical model and relative to this compound do not appear in the experimental results. Yu et al. [7] made the same observations and concluded that the absence of some diffraction lines could be attributed to the presence of oxygen and hydrogen in the films. Furthermore, the presence of two diffraction lines corre-

sponding to 2.26 and 1.82 Å and some others characteristic of both α - and β - C_3N_4 allow us to assert that the β phase is also present by the side of the α phase. The film structure is probably a mixture of the α and β phases, in which the former is predominant. For the film deposited on TiN the diffraction pattern suggests the coexistence of the same phases with, in addition, two d -spacings at 3.80 and 2.58 Å which cannot be attributed to any of the α - or β - C_3N_4 phases. Zhang et al. [9], who studied CN_x films by XRD, found similar values for two d -spacings at 3.93 and 2.55 Å and concluded that they could come from unknown CN structures.

The crystallinity of the deposited films was also investigated by XRD using a Philips PW 1340 spectrometer equipped with a Cu X-ray source ($\lambda = 1.5404$ Å) operating at 40 kV and 20 mA, but apart from the peaks belonging to the Si or TiN substrates, we could not find any peak attributable to the α - or β - C_3N_4 phases. The absence of an X-ray diffraction pattern characteristic of the films deposited is due either to the low CN_x thickness or the too small size of the crystallites (tens of nanometers, as indicated by TEM observations). It is well known that X-ray diffraction gives macroscopic infor-

Table 1

Lattice spacings of CN_x films compared with theoretical calculations for α - and β -C₃N₄. The spacings marked * and † can also be attributed to Si and TiN substrates, respectively

Experimental results				α -C ₃ N ₄						β -C ₃ N ₄					
CN _x /Si		CN _x /TiN		From Ref. [2]			From Refs. [12,30]			From Ref. [2]			From Refs. [12,30]		
<i>d</i> (Å)	I	<i>d</i> (Å)	I	<i>d</i> (Å)	<i>hkl</i>	I	<i>d</i> (Å)	<i>hkl</i>	I	<i>d</i> (Å)	<i>hkl</i>	I	<i>d</i> (Å)	<i>hkl</i>	I
		3.80	m												
3.48	m			3.55	101	s									
				3.17	110	s				3.17	110	m			
2.79*	vs	2.79*	vs	2.75	200	m	2.80	200	m	2.75	200	s	2.77	200	s
		2.58	vs												
		2.44†	s												
				2.37	201	s	2.40	201	s						
2.26	s									2.25	101	s			
		2.20	m												
		2.12†	vs	2.14	102	s	2.18	102	s						
		2.09	m	2.08	210	m	2.11	210	m	2.08	210	s	2.09	210	s
1.90	s			1.90	211	m	1.93	211	m	1.95	111	m	1.92	111	m
				1.87	112	s	1.90	112	s						
1.82	s	1.82	m							1.83	300	m	1.85	300	m
1.73	s	1.77*	s	1.77	202	w	1.73	301	m						
				1.70	301	m									
		1.64	s							1.59	211	w	1.58	211	w
		1.50†	m	1.49	103	w	1.51	103	vw	1.52	310	w	1.54	310	w
1.47	m						1.46	302	vw	1.47	301	w	1.46	301	w
		1.44	vs	1.45	311	w									
				1.31	222	m	1.33	222	m	1.33	221	w	1.33	221	w
1.24	m			1.22	321	m	1.24	321	m	1.26	320	w	1.21	410	vw

mation regarding the structure of a compound, while SAED refers to the phase structure on a microscopic scale.

4. Conclusions

Carbon nitride thin films were deposited by ArF excimer laser decomposition of NH₃/C₂H₂ mixtures, on Si and TiN substrates, at room temperature. The composition and chemical bonding of the films, as analysed by XPS and FTIR spectrometry, do not show any significant differences for the films deposited on both types of substrate. In both cases, the maximal N/C value calculated from XPS measurements goes up to 0.75. The films contain singly and doubly bonded carbon and nitrogen, hydrogen and about 10% of oxygen. ERDA measurements certify the presence of an important quantity of hydrogen in the films. The latter, deposited either on Si or TiN, are constituted of nano-crystallites embedded in an amorphous phase. The lattice spacings obtained from SAED patterns can be attributed to both α - and β -C₃N₄ phases, the α -C₃N₄ phase being predominant for the films deposited on Si. TEM images reveal that the CN_x films deposited on Si substrates are formed from grains larger than those of the films deposited on

TiN. It can be concluded that the nature of the substrate can slightly influence the microscopic structure of the deposited CN_x films, although on a macroscopic scale the differences are not observed.

Acknowledgement

One of the authors (A.C.) kindly acknowledges the French Government for his Doctoral Fellowship.

References

- [1] A.Y. Liu, M.L. Cohen, *Science* 245 (1989) 841.
- [2] Y. Guo, W.A. Goddard, *Chem. Phys. Lett.* 237 (1995) 72.
- [3] A.Y. Liu, R.M. Wentzcovitch, *Phys. Rev. B* 50 (1994) 10362.
- [4] L.P. Guo, Y. Chen, E.G. Wang, L. Li, Z.X. Zhao, *Chem. Phys. Lett.* 268 (1997) 26.
- [5] L.P. Guo, Y. Chen, E.G. Wang, L. Li, Z.X. Zhao, *J. Crystal Growth* 178 (1997) 639.
- [6] A.K.M.S. Chowdhury, M. Monclus, D.C. Cameron, J. Gilvarry, M.J. Murphy, N.P. Barradas, M.S.J. Hashmi, *Thin Solid Films* 308/309 (1997) 130.
- [7] K.M. Yu, M.L. Cohen, E.E. Haller, W.L. Hansen, A.Y. Liu, L.C. Wu, *Phys. Rev. B* 49 (1994) 5034.
- [8] K.J. Boyd, D. Marton, S.S. Todorov, A.H. Al-Bayati, J. Kulik,

- R.A. Zuhr, J.W. Rabalais, *J. Vac. Sci. Technol. A* 13 (4) (1995) 2110.
- [9] Y. Zhang, Z. Zhou, H. Li, *Appl. Phys. Lett.* 68 (1996) 634.
- [10] R. Soto, P. Gonzalez, X. Redondas, E.G. Parada, J. Pou, B. Leon, M. Perez-Amor, M.F. da Silva, J.C. Soares, *Nucl. Instrum. Meth. Phys. Res. B* 136–138 (1998) 236.
- [11] X.-A. Zhao, C.W. Ong, Y.C. Tsang, Y.W. Wong, P.W. Chan, C.L. Choy, *Appl. Phys. Lett.* 66 (20) (1995) 2652.
- [12] A.K. Sharma, P. Ayyub, M.S. Multani, K.P. Adhi, S.B. Ogale, M. Sunderaraman, D.D. Upadhyay, S. Banerjee, *Appl. Phys. Lett.* 69 (1996) 3489.
- [13] A. Crunteanu, R. Cireasa, R. Alexandrescu, I. Morjan, V. Nelea, I.N. Mihailescu, A. Andrei, *Surf. Coat. Technol.* 100/101 (1998) 173.
- [14] D. Li, X.-W. Lin, S.C. Cheng, V.P. Dravid, Y.-W. Chung, M.-S. Wong, W.D. Sproul, *Appl. Phys. Lett.* 68 (9) (1996) 1211.
- [15] G. Socrates, *Infrared Characteristic Group Frequencies*, second ed., Wiley, Chichester, UK, 1994.
- [16] S. Bhattacharyya, C. Cardinaud, G. Turban, *J. Appl. Phys.* 83 (8) (1998) 4491.
- [17] G. Beamson, D. Briggs, *High Resolution XPS of Organic Polymers*, Wiley, Chichester, UK, 1992.
- [18] U. Gelius, P.F. Heden, J. Hedman, B.J. Lindberg, R. Manne, R. Nordberg, C. Nordling, K. Siegbahn, *Phys. Scripta* 2 (1970) 70.
- [19] U. Gelius, C.J. Allan, G. Johansson, H. Siegbahn, D.A. Allison, K. Siegbahn, *Phys. Scripta* 3 (1971) 237.
- [20] S.T. Jackson, R.G. Nuzzo, *Appl. Surf. Sci.* 90 (1995) 195.
- [21] S. Souto, M. Pickholz, M.C. dos Santos, F. Alvarez, *Phys. Rev. B* 57 (1998) 2436.
- [22] P. Hammer, N.M. Victoria, F. Alvarez, *J. Vac. Sci. Technol. A* 16 (1998) 2941.
- [23] M.A. Baker, P. Hammer, *Surf. Interface Anal.* 25 (1997) 629.
- [24] H. Sjoström, S. Stafstrom, M. Boman, J.-E. Sundgren, *Phys. Rev. Lett.* 75 (1995) 1336.
- [25] D. Marton, K.J. Boyd, A.H. Al-Bayati, S.S. Todorov, J.W. Rabalais, *Phys. Rev. Lett.* 73 (1994) 118.
- [26] J. Zemek, A. Luches, G. Leggieri, A. Fejfar, M. Trchova, *J. Electron. Spectrosc. Relat. Phenom.* 76 (1995) 742.
- [27] J. Bulir, M. Jelinek, V. Vorlicek, J. Zemek, V. Perina, *Thin Solid Films* 292 (1997) 318.
- [28] M. Petrascu, I. Berceanu, I. Brancus, A. Buta, M. Duma, C. Grama, I. Lazar, I. Mihai, M. Petrovici, V. Simion, N. Mihaila, I. Ghita, *Nucl. Instrum. Meth. Phys. Res. B* 4 (1984) 396.
- [29] F. Negoita, C. Borcan, D. Pantelica, *NIPNE Sci. Rep.* (1996) 120.
- [30] D.M. Teter, R.J. Hemley, *Science* 271 (1996) 53.

Chemical analysis of pulsed laser deposited a-CN_x films by comparative infrared and X-ray photoelectron spectroscopies

T. Szörényi^{a,*}, C. Fuchs^a, E. Fogarassy^a, J. Hommet^b, F. Le Normand^b

^a CNRS-PHASE, BP 20, 67037 Strasbourg Cedex 2, France

^b IPCMS, BP 20, 67037 Strasbourg Cedex 2, France

Abstract

Amorphous carbon nitride films are deposited at room temperature on silicon substrates by ArF excimer laser (193 nm) ablation of a graphite target in nitrogen atmosphere. By tuning the process parameters, fine control of the carbon–carbon and carbon–nitrogen bond configuration is achieved in a broad range as followed by X-ray photoelectron spectroscopy (XPS) and infrared (IR) absorption spectroscopy. Based on the comparative and quantitative analysis of changes in measured IR versus XPS spectra as a function of reactive gas pressure, laser fluence and target-to-substrate distance, and on a critical review of the existing interpretation of IR data, an assignment of the components of the broad band extending from 900 to 1900 cm⁻¹ in the IR spectra to specific carbon–carbon and carbon–nitrogen bond configurations is proposed. © 2000 Elsevier Science S.A. All rights reserved.

Keywords: Carbon nitride; Infrared (IR) absorption spectroscopy; Pulsed laser deposition; X-ray photoelectron spectroscopy (XPS)

1. Introduction

The unique properties of β-C₃N₄ predicted by Liu and Cohen [1,2] motivated numerous groups to try to synthesize CN_x films with nitrogen content as close as possible to the magic 57 at.% [3–25]. Although most of the films obtained proved to be amorphous and contained much less nitrogen, as a result of these studies carbon nitride emerged as a new material possessing a great variety of properties of both scientific and practical interest.

Detailed and unambiguous description of the chemical structure of carbon nitrides prepared by different techniques and in wide ranges of process parameters is not only a challenging task but is also a prerequisite of reproducible production of films of predetermined properties appropriate for application in industrial environment. Here we report an attempt to assign individual bands of the infrared (IR) spectra to specific carbon–carbon and carbon–nitrogen bond configurations as a

result of the comparative and quantitative analysis of changes in the IR and X-ray photoelectron spectroscopy (XPS) spectra of identical thin film samples fabricated by ArF excimer laser ablation of a graphite target in nitrogen atmosphere under systematically varied experimental conditions.

2. Experimental

Carbon nitride films were deposited in a conventional PLD system in static nitrogen atmosphere of 0.1–5 mbar pressure. The beam of the ArF excimer laser (Lambda Physik, 193 nm, 22 ns, 80 Hz, maximum 240 mJ) was focused onto the surface of a rotating graphite target at normal incidence through a UV-grade quartz window. Energy density values between 6 and 16 J/cm² on the target surface were adjusted by changing the dimensions of the illuminated area.

Infrared spectra of films deposited on 0.5 mm thick silicon wafers were recorded on a Perkin–Elmer 983G spectrophotometer in the 600–2000 and 2000–4000 cm⁻¹ wavenumber domains, in the worst case at 12 cm⁻¹ and 24.5 cm⁻¹ resolution respectively. Baseline correction was performed by connecting the local

* Corresponding author. Permanent address: Research Group on Laser Physics, H-6720 Szeged, Dóm tér 9, PO Box 406, H-6701 Szeged, Hungary. Tel.: +36-62-544274; fax: +36-62-425854.

E-mail address: t.szorenyi@physx.u-szeged.hu (T. Szörényi)

minima at 900 and 1900 cm^{-1} as end points with a straight line. Though different sample-reference pairs resulted in baselines of different slopes the corrected spectra agreed fairly well. Spectra presented are averages of a minimum of three measurements made on samples prepared under identical conditions. In order to remove differences in peak heights between spectra recorded on films of different thickness, the absorbance values have been divided by the largest one in all spectra. As a result of normalization, only *relative changes* in the weight of the individual spectral components, contributing to the broad band extending from 900 to 1900 cm^{-1} , have been considered in the analysis.

In parallel experiments the surface chemical composition and structure of each film characterized by IR was determined by XPS. XP spectra were recorded by a VSW spectrometer in fixed analyzer transmission (FAT) mode at a constant pass energy of 22 eV using monochromatic Al $K\alpha$ (1486.6 eV) excitation. The overall experimental resolution was 0.75 eV. Home-made software was used for lineshape analysis of the C 1s and N 1s lines.

3. Results and discussion

3.1. IR characterization of the CN_x films

In all spectra three bands were observed. The broad feature between 3700 and 2300 cm^{-1} is associated with carbon–hydrogen and nitrogen–hydrogen bonds [3–5,7,11,13,18], the small peak at around 2200 cm^{-1} corresponds to a $\text{C}\equiv\text{N}$ stretching mode [3–7], while the other broad band between 1900 and 900 cm^{-1} comprises several components associated with different carbon–carbon and carbon–nitrogen bonding configurations [3–20]. In this paper we focus on this last feature. The interpretation of the 2200 cm^{-1} peak is clear. The role of hydrogen in influencing the chemical structure of carbon nitride films will be discussed in another paper.

Even the first glance at the full set of our spectra, and in particular at those measured on films deposited at high fluences, strongly suggested that the broad band extending from 900 to 1900 cm^{-1} was composed of at least five components. Visual examination and calculation of the second derivatives of carbon nitride spectra shown in Refs. [3–7,9–11,13,19], in some cases even contrary to the analyses of the authors [6,7], indicated the presence of a minimum of four individual bands. Clearly, a necessary prerequisite for any analysis is the identification of the individual spectral components to be assigned to the respective bond configurations. Surprisingly enough we could not find unambiguous identification of the components in the comprehensive literature [3–20]. Therefore, we used curve-fitting with four and five bands for the evaluation of the position

and intensity of the overlapping peaks that give the broad spectral feature. Though recognizing that the biggest problem with this analysis is that (with sufficiently high number of bands) different sets may give equally good fits, one may not be sure whether the respective set of parameters is unique. However, we consider that the proof of the feasibility of the curve-fitting procedure applied is that whereas four bands could not give a satisfactory fit in all cases, all the spectra within the 900–1900 cm^{-1} wavenumber domain could be perfectly fitted with five bands of full width at half maxima (FWHM) ranging from 140 to 200 cm^{-1} , peak positions at around 1080, 1230, 1375, 1510 and 1650 cm^{-1} and different intensities. All changes in the IR spectra recorded as a function of nitrogen pressure, laser energy density and target-to-substrate distance will be discussed below in terms of changes in the relative intensities of these five components numbered starting from the lowest wavenumber.

As shown in Fig. 1, changes in the pressure of the nitrogen atmosphere result in striking changes in the absorption spectra. Although peaked at $\sim 1560 \text{ cm}^{-1}$, the spectra of the films deposited at 0.1 mbar are dominated by the lower photon energy components. There is a clear contribution from the 1080 cm^{-1} band and both the 1230 and 1375 cm^{-1} components are fairly intensive. Compared with the intensity of the 1535 cm^{-1} peak, the highest photon energy component at 1630 cm^{-1} is rather weak. The second and third are well comparable to the fifth in intensity. When increasing the pressure up to 0.5 mbar the relative weight of the low and high photon energy parts of the spectrum significantly changes. While it is apparent that the two high energy components gain strength compared with the other three, it is practically impossible to follow precisely the changes in the individual components, since both the lower and the higher

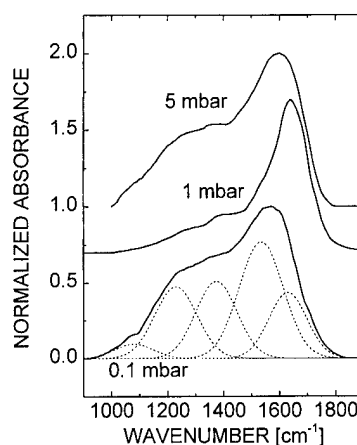


Fig. 1. Normalized absorbance spectra of carbon nitride films deposited at 0.1, 1 and 5 mbar nitrogen pressures. Laser fluence: 6 J/cm²; target-to-substrate distance: 50 mm. The curves are vertically displaced. Curve-fitting is illustrated for 0.1 mbar.

energy parts can satisfactorily be fitted with different sets of three and two bands of slightly varying FWHM and intensities respectively. Nevertheless, the shift in the peak position from 1560 to 1640 cm^{-1} indicates an increasing contribution from the highest photon energy component. A further increase from 0.5 to 1.0 mbar does not lead to significant changes in the spectra, whereas between 1.0 and 5.0 mbar changes in the opposite direction start: the low energy part recovers the losses. There is a clear increase in the strength of the low energy bands, and the maximum shifts back to approximately 1600 cm^{-1} , indicating a decrease in the contribution of the fifth component.

The most remarkable feature of the IR spectra of films deposited using pulses of higher energy densities is the clear separation of the bands, especially those in the low energy domain, between 900 and 1450 cm^{-1} (Fig. 2). This effect is a consequence of the dramatic decrease in the relative intensity of the third component, accompanied by the relative strengthening of the two other low-energy bands, particularly that peaked at around 1060 cm^{-1} . Narrowing of the individual components further amplifies this separation.

Compared with the extent of changes with nitrogen pressure and laser fluence, the influence of target-to-substrate distance is marginal. When increasing the distance from 30 to 70 mm, while keeping both the fluence and the pressure constant at 10 J/cm^2 and 1 mbar respectively, the only obvious effect is the relative decrease in the intensity of the 1375 cm^{-1} peak compared with the two bands at higher photon energies.

3.2. XPS characterization of the CN_x films

In practically all XPS studies on carbon nitride films two and three components of the N 1s and C 1s core-level lines are assumed respectively, implying two nitro-

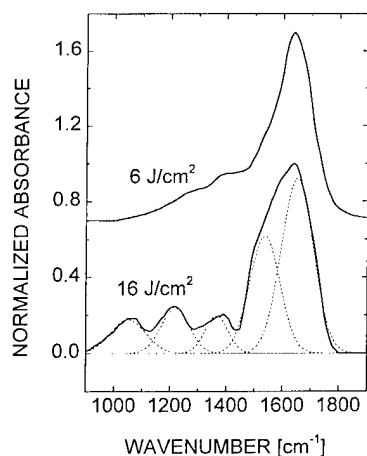


Fig. 2. Normalized absorbance spectra of carbon nitride films deposited at 6 and 16 J/cm^2 laser fluence. Nitrogen pressure: 1 mbar; target-to-substrate distance: 50 mm. The curves are vertically displaced.

gen and three carbon bonding configurations. In the interpretation of the respective contributions, however, there is no consensus yet; see Ref. [24] and references therein.

According to our assignment, the lowest energy C 1s component at around 284.6 eV originates from sp^2 -coordinated carbon atoms bonded to either carbon or nitrogen ($\text{C}=\text{C}$, $\text{C}=\text{N}$), the peak at around 286 eV from carbon atoms singly bonded to either carbon or nitrogen (sp^3 carbon: $\text{C}-\text{C}$ or $\text{C}-\text{N}$), and the highest energy component at 287–288 eV is attributed to sp^3 carbon atoms multiply bonded to nitrogen. To obtain a satisfactory agreement between the measured and fitted lines two contributions had to be assumed for the N 1s spectra. We ascribed the first component, located at around 398.5 eV, to $\text{N}=\text{C}$ bonds, and the second, at around 400 eV, to $\text{N}-\text{C}$ bonds. In the analysis the contribution of carbon and nitrogen bonded to oxygen at high binding energies has been neglected.

The lineshape analysis outlined above was performed for all samples characterized by IR spectroscopy. From the fit data the fractions of the respective components were determined as a function of process parameters. As seen in the lower part of Fig. 3, an increase in pressure from 0.1 to 0.5 mbar results in a significant decrease in the concentration of the sp^2 -coordinated carbon species. Concomitantly, the amounts of both the singly and multiply bonded carbon increase. Between 0.5 and 1.0 mbar the sp^2 -coordinated carbon fraction reaches a minimum, whereas the concentration of the sp^3 -coordinated carbon species passes through a maximum. A further increase in the nitrogen pressure leads to a slight increase in both the sp^2 -coordinated and multiply bonded carbon fraction accompanied by a

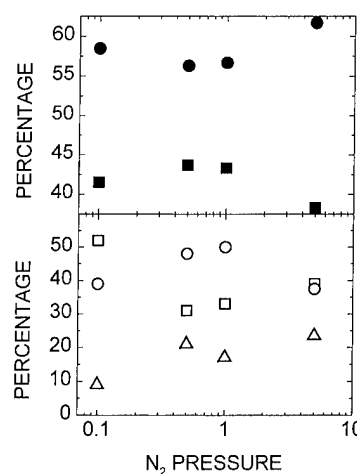


Fig. 3. Dependence of the concentration of sp^2 $\text{C}=\text{C}$ and $\text{C}=\text{N}$ bonds (open squares), sp^3 $\text{C}-\text{C}$ and $\text{C}-\text{N}$ bonds (open circles), sp^3 carbon atoms multiply bonded to nitrogen (open triangles), $\text{N}-\text{C}$ bonds (full squares) and $\text{N}=\text{C}$ bonds (full circles) on nitrogen pressure, as determined by the lineshape analysis of C 1s and N 1s photoelectron lines (open and full symbols respectively).

Table 1
Assignments of the infrared absorption bands of carbon nitride films

Wavenumber (cm ⁻¹)	Assignment	Reference
2205	C≡N triple bond	[18]
2200	nitrile (C≡N) bound to an aromatic ring	[4,5,7]
2190	C≡N triple bond	[3]
2143	nitrile (C≡N) or isocyanate (N=C=O) groups	[6]
2130	isonitrile or nitrile in an unusual environment	[4]
1689	C=N	[18]
1660	NH ₂ asymmetric bending	[3]
1650	C=C stretch	[19]
1634	C=C	[15,16]
1630	double bonded carbon	[3]
1625	C=N	[13]
1600–1650	C=N and C=C stretching vibrations	[10]
1600	C=N and C=C	[5]
1600	sp ² bonds in graphitic microdomains	[7]
1600	C=N	[9]
1570	C=C	[4]
1555	graphite-like sp ² carbon	[6]
1550	NH ₂ symmetric bending	[3]
~1540	N substituting C in graphitic microdomains	[12]
1530	C=N	[20]
1520	C=N	[19]
~1500	C=N and C–N stretching modes	[8]
1500	C=N	[15,16]
1450	CH ₂ bending	[3]
1440	C–N	[5]
1417	C–N stretching	[11]
1400	C–N stretch or disordered sp ² domains	[19]
1350–1500	C–N	[13]
1380	C–N	[9]
1370	C=C	[4]
1350	C=N and C–N stretching modes	[8]
1350	C–N	[15,16]
1300–1350	sp ² carbon	[5]
1300	sp ² bonds at the surface of graphitic microdomains	[7]
1297	disordered sp ² carbon	[6]
1265	C–N stretching	[11]
1250–1300	sp ² carbon	[12]
1250–1400	sp ³ carbon single bonded to nitrogen (C–N)	[20]
1230	C–N stretching modes	[19]
1222	C–N	[18]
1125	no assignment	[13]
1103	C–O stretching	[11]
1100	v(C–O)	[19]
1022	C–O stretching	[11]

marked decrease in the amount of carbon species in sp³ configuration. The results of the N 1s fitting are in line with those derived from the analysis of the C 1s spectra: the dependence of the concentration of both the N–C and N=C bonds on pressure shows a biphasic character (upper part of Fig. 3).

An increase in the processing fluence from 4 to 16 J/cm² results in a steep increase in the weight of the second peak at around 286 eV, i.e. in the concentration of the sp³-coordinated carbon species, at the expense of

the lowest energy C 1s component associated with sp² carbon. A significant increase in the number of multiply bonded carbon atoms at the highest binding energy contributes also to this rearrangement in the chemical structure of the films.

The changes in the XPS spectra of the films deposited by tuning the target-to-substrate distance are marginal compared with those due to changes in pressure or fluence. Nevertheless, the fraction of N–C bonds monotonously increases at the expense of the N=C bonds.

3.3. Assignment of the IR spectral components to bond configurations

From a (not complete) list of assignments compiled in Table 1 it is clear that the IR features of carbon nitrides are not very clearly identified. Our analysis cannot be considered as complete either, e.g. since bond configurations comprising hydrogen and oxygen have not been taken into account. However, by comparing the dependence of the relative intensities of the IR spectral components and the respective bond configurations as determined from the analysis of the lineshapes of the N 1s and C 1s core-level lines on reactive gas pressure, laser fluence and target to substrate distance, the corollary of our work is as follows.

(1) The IR components peaking at around 1650 and 1510 cm^{-1} can be assigned to both C=C, C–N and C=N bond configurations. The correlation between the changes in the intensity of the 1650 cm^{-1} peak and the two higher energy XPS components suggests that this band — contrary to the assignments listed in Table 1 — might be associated with sp^3 carbon singly or multiply bonded to nitrogen.

(2) The two lower energy components at around 1375 and 1230 cm^{-1} originate most probably from carbon–carbon bonds in amorphous and graphitic environments and from C=N bonds.

(3) We could not find a straight correlation between the changes in the relative intensity of the lowest photon energy IR band ($\sim 1080 \text{ cm}^{-1}$) and the respective changes in carbon–carbon and carbon–nitrogen bond configurations.

4. Conclusion

Although being an easy yet powerful technique, because of the lack of standards and reliable assignments IR spectroscopy can hardly be applied for routine characterization of carbon nitride films yet. In comparison with IR spectroscopy, XPS of carbon nitrides is a well-established analytical technique. However, even XPS cannot be directly used for calibration of IR since (i) it is extremely hard, if not impossible, to differentiate between certain chemical environments (e.g. C–C and C–N states) and (ii) owing to the complexity of the C 1s and N 1s XPS lines, there is no consensus yet in the assignment of the individual peaks to respective chemical states, as convincingly demonstrated, for example, in a recent review by Ronning et al. [24]. Detailed studies aimed at improving the weak points of both techniques by providing complementary chemical information for comparison are absolutely necessary in order to render (quantitative) IR spectroscopy appropriate for routine

characterization of carbon nitride films. Our contribution was intended as one step in this direction.

Acknowledgement

T. Szörényi is grateful to the French Ministry of Education, Research and Technology for his visiting professor fellowship.

References

- [1] A.Y. Liu, M.L. Cohen, *Science* 245 (1989) 841.
- [2] A.Y. Liu, M.L. Cohen, *Phys. Rev. B* 41 (1990) 10727.
- [3] H.-X. Han, B.J. Feldman, *Solid State Commun.* 65 (1988) 921.
- [4] J.H. Kaufman, S. Metin, D.D. Saperstein, *Phys. Rev. B* 39 (1989) 13053.
- [5] M. Ricci, M. Trinecoste, F. Auguste, R. Canet, P. Delhaes, C. Guimon, G. Pfister-Guillouzo, B. Nysten, J.P. Issi, *J. Mater. Res.* 8 (1993) 480.
- [6] N. Nakayama, Y. Tsuchiya, S. Tamada, K. Kosuge, S. Nagata, K. Takahiro, S. Yamaguchi, *Jpn. J. Appl. Phys.* 32 (1993) L1465.
- [7] X.-A. Zhao, C.W. Ong, Y.C. Tsang, Y.W. Wong, P.W. Chan, C.L. Choy, *Appl. Phys. Lett.* 66 (1995) 2652.
- [8] Z.J. Zhang, S. Fan, J. Huang, C.M. Lieber, *J. Electron. Mater.* 25 (1996) 57.
- [9] X.-M. He, L. Shu, W.-Z. Li, H.-D. Li, *J. Mater. Res.* 12 (1997) 1595.
- [10] P. Hammer, M.A. Baker, C. Lenardi, W. Gissler, *J. Vac. Sci. Technol. A* 15 (1997) 107.
- [11] Z.-M. Ren, P.-N. Wang, Y.-C. Du, Z.-F. Ying, F.-M. Li, *Appl. Phys. A* 65 (1997) 407.
- [12] K. Saito, Y. Koga, *Nucl. Instrum. Methods Phys. Res. B* 121 (1997) 400.
- [13] P. González, R. Soto, E.G. Parada, X. Redondas, S. Chiussi, J. Serra, J. Pou, B. León, M. Pérez-Amor, *Appl. Surf. Sci.* 109–110 (1997) 380.
- [14] S. Acquaviva, A.P. Caricato, M.L. De Giorgi, A. Luches, A. Perrone, *Appl. Surf. Sci.* 109–110 (1997) 408.
- [15] A. Wei, D. Chen, N. Ke, S. Peng, S.P. Wong, *Thin Solid Films* 323 (1998) 217.
- [16] A. Wei, D. Chen, N. Ke, W.Y. Cheung, S. Peng, S.P. Wong, *J. Phys. D: Appl. Phys.* 31 (1998) 1522.
- [17] Y.F. Lu, Z.M. Ren, W.D. Song, D.S.H. Chan, *J. Appl. Phys.* 84 (1998) 2133.
- [18] Z.-M. Ren, Y.F. Lu, W.D. Song, D.S.H. Chan, T.S. Low, K. Gamani, G. Chen, K. Li, *Mater. Res. Soc. Proc.* 526 (1998) 343.
- [19] I.N. Mihailescu, E. György, R. Alexandrescu, A. Luches, A. Perrone, C. Ghica, J. Werckmann, I. Cojocaru, V. Chumash, *Thin Solid Films* 323 (1998) 72.
- [20] C. Jama, V. Rousseau, O. Dessaux, P. Goudmand, *Thin Solid Films* 302 (1997) 58.
- [21] E. D'Anna, A. Luches, A. Perrone, S. Acquaviva, R. Alexandrescu, I.N. Mihailescu, J. Zemek, G. Majni, *Appl. Surf. Sci.* 106 (1996) 126.
- [22] E. Aldea, A.P. Caricato, G. Dinescu, A. Luches, A. Perrone, *Jpn. J. Appl. Phys.* 36 (1997) 4686.
- [23] R. Henck, C. Fuchs, E. Fogarassy, J. Hommet, F. Le Normand, *Mater. Res. Soc. Proc.* 526 (1998) 337.
- [24] C. Ronning, H. Feldermann, R. Merk, H. Hofsäuss, P. Reinke, J.-U. Thiele, *Phys. Rev. B* 58 (1998) 2207.
- [25] C. Vivient, J. Hermann, A. Perrone, C. Boulmer-Leborgne, *J. Phys. D: Appl. Phys.* 32 (1999) 518.

X-ray photoelectron spectroscopy study of carbon nitride films

V. Krastev ^{a,*}, P. Petrov ^b, D. Dimitrov ^c, G. Beshkov ^c, Ch. Georgiev ^b, I. Nedkov ^b

^a Institute of General and Inorganic Chemistry, Bulgarian Academy of Sciences, acad. G. Bonchev str. Bl. 11, 1113 Sofia, Bulgaria

^b Institute of Electronics, Bulgarian Academy of Sciences, Tsarigradsko Chaussee 72, 1784 Sofia, Bulgaria

^c Institute of Solid State Physics, Bulgarian Academy of Sciences, Tsarigradsko Chaussee 72, 1784 Sofia, Bulgaria

Abstract

The demand for hard and superhard coatings has inspired many investigators in their attempts to synthesise β -C₃N₄. CN_x thin films were deposited on c-silicon substrates with simultaneous nitrogen ion bombardment. An electron beam was used for graphite target evaporation, and d.c. gas discharge for creation of nitrogen ion flow. In this process, plasma that occurs in the space between electrodes and the electron beam ionises nitrogen and carbon atoms.

For characterisation of the carbon nitride films, X-ray photoelectron spectroscopy was used. A rapid change of composition occurs in the first 10–15 nm of the material, and then saturation is reached. The N/C ratio passes through the value of 1.33 (which is characteristic of C₃N₄) and reaches an even higher value at 15 nm. The N1s peak consists of four components. The number of carbon–nitrogen bonds with sp³ hybridisation goes through a minimum at 5 min sputtering time, reaches a maximum at 10 min and again decreases at 15 min. The behaviour of the area of the peak at about 400.9 eV resembles a mirror reflection through the same interval. This peak position is ascribed to C–N bonding with sp² hybridisation. The C1s peak includes five components. The area of the peak at about 287.2 eV, which is due to C–N bonds with sp³ hybridisation, passes this interval of sputtering time in parallel with the area of the N1s peak at about 399.2 eV, which is also due to this type of bonding. It is ascribed to β -C₃N₄. The area of the peak at about 286.3 eV is in parallel with the flow curve for the N1s peak at 400.9 eV, and this behaviour supports the supposition that both peaks are due to C–N bonds with sp² hybridisation.

Based on the behaviour of curves concerned with sp² and sp³ bonding which resemble a mirror reflection, the conclusion can be drawn that redistribution of C–N bonds between sp² and sp³ bonding occurs during the growth of the film, and a structure is proposed consisting of nanoclusters of β -C₃N₄ embedded in an amorphous matrix of C–N bonds with sp² hybridisation.
© 2000 Elsevier Science S.A. All rights reserved.

Keywords: Carbon nitride; Electron beam evaporation; Ion bombardment; X-ray photoelectron spectroscopy

1. Introduction

Improvements in the optical, thermal, chemical, electrical and mechanical features of materials are developing fast. At present, there is a strong demand for hard and superhard coatings. Liu and Cohen suggested in 1989 that β -C₃N₄, a carbon nitride compound with the structure of β -Si₃N₄ which does not exist in nature, should have a hardness exceeding that of c-BN and close to that of diamond [1,2].

Following theoretical predictions, different groups have tried recently to grow β -C₃N₄ on Si substrates using a variety of experimental techniques, such as chemical vapour deposition and electron cyclotron reso-

nance plasma enhanced chemical vapour deposition [3–5], ion beam and laser ablation processing [6–11], magnetron sputtering [12,13] and electron beam evaporation of carbon with nitrogen ion bombardment [14–16]. In all these approaches the β -C₃N₄ phase presented only a small fraction of the entire layer embedded in the amorphous carbon nitride matrix. The properties of carbon nitride films depend strongly on deposition and processing.

In this paper we present X-ray photoelectron spectroscopy (XPS) studies on thin CN_x layers, formed by electron beam evaporation of graphite and simultaneous nitrogen ion bombardment.

2. Experiment

Thin CN_x films were deposited on crystalline silicon substrates by electron beam evaporation of graphite and

* Corresponding author. Tel.: +359-2-774-988;
fax: +359-2-705-024.

E-mail address: vkrastev39@hotmail.com (V. Krastev)

simultaneous nitrogen ion bombardment. High purity 99.99% pyrolytic graphite targets and 99.9999% pure nitrogen gas in d.c. discharge were used. In this process, the plasma formed between the electrodes and the electron beam is responsible for nitrogen ionisation. The films were formed at electron beam powers of 0.5–1.5 kW and N^+ ion energies of 300–400 eV. The substrate holder was heated to 1150°C. The growth process cannot be described by adiabatic relations since it involves electron transfer reactions. Electrons moving from one atom to another are facing a potential barrier [17]. Passing through the barrier is assisted, in this case, by the moving nitrogen ion to which the electron belongs.

XPS analysis was carried out in an ESCALAB MkII (VG Scientific) electron spectrometer at base pressures in the preparation and analysis chamber at 2×10^{-8} and 1×10^{-8} Pa, respectively. Photoelectrons were excited by an X-ray source using Mg $K\alpha$ ($h\nu = 1256.5$ eV). When the pass energy of the analyser was 20 eV, the instrumental resolution measured as the full-width at half-maximum (FWHM) of the $Ag3d_{5/2}$ photoelectron was 1.2 eV. The surface sensitivity was estimated as 10 monolayers.

3. Results and discussion

The results of XPS measurements are shown in Figs. 1–3. The depth profile concentrations are listed in Table 1. The C1s, N1s and O1s photoelectron peaks

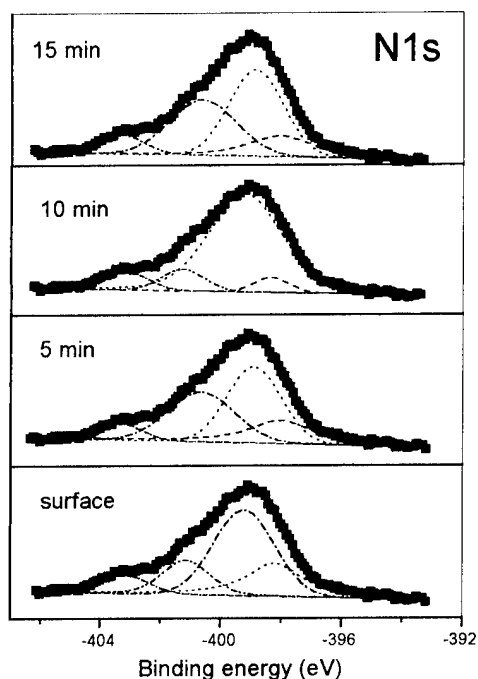


Fig. 1. Evolution of the N1s peaks with sputtering time.

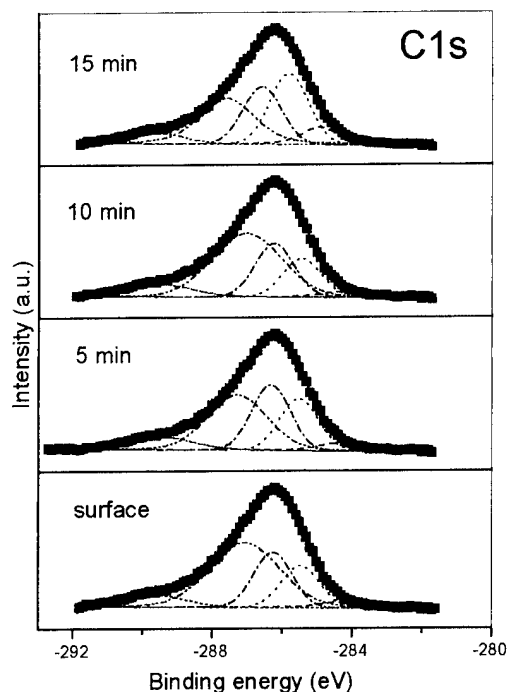


Fig. 2. Evolution of the C1s peaks with sputtering time.

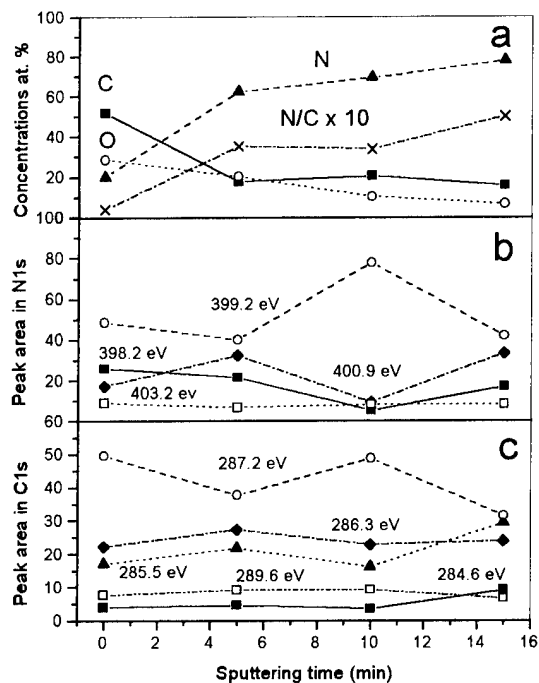


Fig. 3. (a) Depth profile of total concentrations; (b) fit results for N1s peak; (c) fit results for C1s peak.

were recorded. Their intensities were determined from the integrated C1s, N1s and O1s peak intensity, assuming a linear background. Elemental concentrations were estimated according to the approach outlined in Ref. [18]. The values of the corresponding photoionisation cross-section, σ , were taken from Ref. [19]. For a

Table 1
Concentrations and structure of C1s and N1s peaks

	Surface	5 min	10 min	15 min
C (%)	51.6	17.7	20.5	15.6
N (%)	20	62.2	69.3	77.8
O (%)	28.4	20.1	10.2	6.6
N/C	0.388	3.51	3.38	5.0
C1s-284.6 eV	3.82	4.46	3.36	9.02
C1s-285.5 eV	16.90	21.59	16.00	29.22
C1s-286.3 eV	22.17	27.23	22.75	23.77
C1s-287.2 eV	49.54	37.66	48.68	31.44
C1s-289.6 eV	7.56	9.07	9.22	6.56
N1s-398.2 eV	25.72	21.30	5.15	16.87
N1s-399.2 eV	48.53	39.85	77.68	41.78
N1s-400.9 eV	17.07	32.24	9.25	33.27
N1s-403.2 eV	8.69	6.61	7.92	8.08

detailed analysis the core-level lines obtained by XPS were fitted by Doniach–Sunjic functions, i.e. convolution of a Gaussian and a Lorentzian without additional parameters allowing asymmetry of the line [20]. In semiconducting and isolating materials this asymmetry should be zero. The secondary (inelastically scattered) electron background was assumed to be linear. During the fitting procedure all the parameters were left freely adjustable. As already mentioned in the experimental part, the resolution of the analyser of about 1 eV defines the line width of the Gaussian component of the Doniach–Sunjic functions. Due to amorphisation the line width increases. In this study we obtain line widths (FWHM) between 1.3 and 2.6 eV. As shown in Fig. 3(a), the concentration changes across the film. In our previous investigation [21], we sputtered a similar carbon–nitride film for 300 min and achieved a film thickness of 300 nm. We found that rapid changes of composition occur in the first 10–15 nm of the material, and then saturation is reached. We expect, therefore, to have reached the homogenous part of the film after penetration to a depth of 15 nm. Under the present experimental conditions, the concentration of nitrogen in the first 15 nm increases rapidly at the expense of carbon. As can be seen from Fig. 3(a), the N/C ratio exceeds the value of 1.33 (which is characteristic of C_3N_4) and reaches an even higher value at 15 nm. While the oxygen concentration is about 28 at% in the beginning, after 15 min sputtering only 6.6 at% is observed.

The evolution of the N1s and C1s peaks with sputtering time is presented in Table 1 and Figs. 1–3. The N1s peak consists of four relatively broad components with line widths (FWHM) of about 2 eV. The integrated intensity of the peak at 399.2 eV, which is characteristic of carbon–nitrogen bonds with sp^3 hybridisation [6], is minimal at 5 min sputtering time, reaches a maximum at 10 min and decreases continuously up to 15 min. The behaviour of the peak at 400.9 eV through the same time interval is

exactly the opposite. This peak is ascribed to C–N bonds with sp^2 hybridisation [6]. The peak at 398.2 eV is characteristic of C=N–C bonds [11]. The number of these bonds decreases at the expense of the formation of other C–N bonds. The low intensity peak at 403.2 eV is due to N–O bonds and is independent of time within experimental error. As shown in Table 1 and Fig. 2, the C1s peak includes five components with FWHM of 1.30 eV defined by the resolution of the analyser used in this investigation. The integrated intensity of the peak at 287.2 eV, which is due to C–N bonds with sp^3 hybridisation [6], exhibits during the sputtering time changes analogous to those observed in the N1s peak at 399.2 eV. Both peaks are ascribed to β - C_3N_4 [22]. Also the peak at 286.3 eV behaves similarly to the peak at 400.9 eV (N 1s). This behaviour strongly suggests that both peaks are due to C–N bonds with sp^2 hybridisation. The peak at 284.6 eV is assigned to bonds of graphite type [4], while the peak at 289.6 eV, which decreases slowly with thickness, is assigned to C–O bonds. The peak behaviour is additionally influenced by charge distribution due to steric interactions between adjacent atoms participating in different bonds. Based on the behaviour of peaks resembling mirror reflection and associated with sp^2 and sp^3 bonds, we conclude that redistribution of C–N bonds between sp^2 and sp^3 bonding occurs during the growth process. This is probably due to temperature changes in the substrate as a result of additional heating by the ion flow and changes in ion energy. Both factors may influence the value of Morse potential barriers hindering bond formation. We propose a structure in which tetrahedrally bonded carbon atoms of the layers are substituted by nitrogen atoms leading to a decrease in the share of the nanocrystalline diamond phase and the formation of a CN_x phase embedded in the amorphous carbon layer.

4. Conclusions

XPS was applied to investigate thin CN_x layers, deposited by electron beam evaporation of graphite and simultaneous nitrogen ion bombardment. The XP spectra show that the ratio of sp^2 to sp^3 bonds changes during the growth process and that the number of β - C_3N_4 clusters increases with increasing deposition energy and substrate temperature. In our suggested structure the tetrahedrally bonded carbon atoms of the layers are substituted by nitrogen atoms leading to a decrease in the share of the nanocrystalline diamond phase and the formation of a CN_x phase embedded in the amorphous carbon layer.

References

- [1] A.Y. Liu, M.L. Cohen, Science 245 (1989) 841.
- [2] A.Y. Liu, M.L. Cohen, Phys. Rev. B: Condens. Matter 41 (1990) 10727.

- [3] A. Bousetta, M. Lu, A. Bensaoula, A. Schultz, *Appl. Phys. Lett.* 65 (1994) 696.
- [4] J. Konvetakis, A. Bandari, M. Todd, B. Wilkens, N. Cave, *Chem. Mater.* 6 (1994) 811.
- [5] G. Beskov, D.B. Dimitrov, St. Georgiev, P. Petrov et al., *Vacuum* 51 (1998) 169.
- [6] S. Lopez, H.M. Dunlop, M. Benmalek, G. Tourillon, M. Wong, W. Sproul, *Surf. Interface Anal.* 25 (1997) 315.
- [7] Z.M. Ren, Y.-Ch. Du, Y. Qiu, J.-Da. Wu, Z.-F. Yang, X.-X. Xiong, F.-M. Li, *Phys. Rev. B* 51 (1995) 5274.
- [8] A. Hoffman, I. Gouzman, R. Brener, *Appl. Phys. Lett.* 64 (1994) 845.
- [9] K.J. Boyd, D. Marton, S. Todorov, A.H. Al-Bayati, J. Kulik, R.A. Zuhr, J.W. Rabalais, *J. Vac. Sci. Technol. A* 13 (1995) 2110.
- [10] K. Ogata, J.F. Diniz Chubaci, F. Fujimoto, *J. Appl. Phys.* 76 (1994) 3791.
- [11] C. Ronning, H. Felderman, R. Merk, H. Hofsass et al., *Phys. Rev. B* 58 (4) (1998) 2207.
- [12] H. Sjostrom, I. Ivanov, M. Johansson, L. Hultman, J. Sundgren, S.V. Hainsworth, T.F. Page, L.R. Wallenberg, *Thin Solid Films* 246 (1994) 103.
- [13] F. Fujimoto, K. Ogata, *Jpn. J. Appl. Phys.* 32 (1993) L420.
- [14] J.F. Chubaci, T. Sakai, T. Yamamoto, K. Ogata, A. Ebe, F. Fujimoto, *Nucl. Instrum. Meth. B* 80/81 (1993) 463.
- [15] P. Petrov, D.B. Dimitrov, G. Beskov, V. Krastev et al., *Vacuum* 52 (1999) 501.
- [16] I. Gouzman, R. Brener, A. Hoffman, *Surf. Sci.* 283 (1995) 331.
- [17] W. Kauzmann, *Quantum Chemistry*, Academic Press, New York, 1957.
- [18] L.T. Weng, G. Vereeke, M.J. Genet, P. Bertrand, W.E.E. Stone, *Surf. Interface Anal.* 20 (3) (1993) 179.
- [19] J. Scofield, *J. Electron Spectrosc. Relat. Phenom.* 8 (1976) 129.
- [20] S. Doniach, M. Sunjic, *J. Phys. C* 3 (1970) 285.
- [21] G. Beshkov, V. Krastev, N. Velchev, Ts. Marinova, *Mater. Sci. Eng. B* 56 (1998) 1.
- [22] M.A. Baker, P. Hammet, *Surf. Interface Anal.* 25 (1997) 301.

Near-edge X-ray absorption fine structure study of carbon nitride films

C. Lenardi ^{a,*}, M.A. Baker ^a, V. Briois ^b, G. Coccia Lecis ^c, P. Piseri ^d, W. Gissler ^a

^a Commission of the European Union, Joint Research Centre, I-21020 Ispra (VA), Italy

^b LURE, Centre Universitaire Paris-Sud, Batiment 209D, 91405 Orsay Cedex, France

^c Dipartimento di Chimica Fisica Applicata, Politecnico di Milano, via Mancinelli 7, I-20121 Milano, Italy

^d Dipartimento di Fisica, Università di Milano, via Celoria 16, I-20133 Milano, Italy

Abstract

Near-edge X-ray absorption fine structure (NEXAFS) measurements have been made on carbon nitride films containing as much as 44 at.% of nitrogen. The films have been synthesized by dual ion beam deposition (IBD) bombarding a carbon target with low-energy nitrogen ions at varying nitrogen beam energies and substrate temperatures ranging from the liquid nitrogen temperature up to 400°C. The structural changes induced by the reduction of the temperature have been previously investigated [Hammer et al., J. Vac. Sci. Technol. A 15 (1) (1997) 107; Baker et al., Surf. Coat. Technol. 97 (1997) 544]. The transition from a predominantly sp²/sp³ C–N amorphous arrangement to a more polymer-like structure has been confirmed and more deeply examined by X-ray absorption spectroscopy. In particular, for samples deposited at liquid nitrogen temperature, a relevant reduction of sp² C=C fraction has been detected. Moreover, the condensation on the growing film surface of hydrogen containing species (i.e. HCN) has been well identified by the appearance of the C–H* peak. © 2000 Published by Elsevier Science S.A. All rights reserved.

Keywords: Carbon nitride; Dual ion beam deposition; Near-edge X-ray absorption fine structure

1. Introduction

The predicted existence of a metastable covalent carbon nitride compound, β-C₃N₄ [3], having a bulk modulus comparable to that of diamond, induced many researchers to attempt to synthesize this material. Stoichiometric β-C₃N₄ was not obtained, but only films with a concentration of nitrogen not exceeding a value of 45 at.%. The formation of volatile CN compounds during the film growth can limit the nitrogen incorporation, as verified by Hammer et al.

We deposited carbon nitride films using the dual ion beam technique (DIBD). Nitrogen beams were used both to sputter a graphite target and to assist the growing films at variable energies and deposition temperatures. The target was bombarded with a 150 eV nitrogen beam. At this energy chemical sputtering is predominant and the formation of radical CN is favored [4]. The reaction of these radicals with themselves or

with adsorbed water molecules leads to formation of C₂N₂ or of HCN and HOCN. In order to increase the N content in the films we maintained the deposition temperature below the boiling point of these N-rich species, which are volatile at room temperature. Moreover, we bombarded the growing films with nitrogen ions to further increase the N content and promote the formation of the desired phase β-C₃N₄. Previous characterizations of the coatings (FTIR, XPS, AES, UV/vis spectroscopy, X-ray reflectivity, conductivity and hardness measurements) are reported in Refs. [1,2]. In the following we summarize the principal results obtained. The films deposited at high sputter beam voltages (1000–1500 V) contain up to 34 at.% of nitrogen and are opaque, conductive ($\sim 1 \Omega^{-1} \text{ cm}^{-1}$), with a density of about 2.1 g cm⁻³ and a hardness of 20 GPa. Their structure is that of sp²/sp³ amorphous carbon. Triple bonds between carbon and nitrogen (C≡N) arise above an N concentration of 20%. The films deposited at low sputter energy (150 V) and low substrate temperature ($\leq 140 \text{ K}$) have a larger N content (up to 44 at.%), exhibit a large optical band gap (up to 2.20 eV), are optically transparent, not conductive, very soft (hard-

* Corresponding author. Tel.: +39-0332-786181;
fax: +39-0332-785036.

E-mail address: cristina.lenardi@jrc.it (C. Lenardi)

ness <1 GPa) and present a density of about 1.7 g cm^{-3} . The spectroscopic analyses indicate that these properties occur as a result of a decrease of the sp^2 delocalized component substituted by localized double bonds. These groups are bound together to form a chain-like polymeric structure. No evidence of formation of the phase $\beta\text{-C}_3\text{N}_4$ was found.

The subject of this work is the investigation of the structural and electronic properties of carbon nitride films by means of near-edge X-ray absorption fine structure (NEXAFS) spectroscopy and Raman spectroscopy in order to obtain a more deep understanding of their properties. X-ray absorption is very sensitive to the chemical environment of carbon and nitrogen atoms and well suited to characterize systems having a mixing of saturated (sp^3) and unsaturated (sp^2 , sp) carbon–nitrogen bonds. Thus it represents a useful tool in determining the chemical structure and the coordination of carbon and nitrogen atoms as a function of different deposition parameters. Raman spectroscopy is very sensitive to the structural changes in carbon-based materials and information on the medium-range order can be obtained. These two spectroscopic techniques then have different bond-type sensitivity and probe different length scales [5]. Thus their combined use can provide complementary information on the nature of carbon nitride films.

2. Experimental

Film synthesis was performed in a dual ion beam sputter deposition apparatus supplied with two Kaufmann ion sources of 3 cm diameter as sputter and assisting guns. A graphite target (purity >99.99 at.%) was sputtered by nitrogen ions at different voltages between 100 and 1500 V with a total beam current of 18–35 mA. The focused assisting source was operated at voltages between 80 and 500 V with a total beam current of 1.5–8.5 mA.

The vacuum chamber was evacuated by a 450 l s^{-1} turbomolecular pump to a base pressure of $\approx 3 \times 10^{-7}$ mbar. The flow rates of the nitrogen were 5 sccm for the sputter gun and 2 sccm for the assisting gun. The working gas pressure was $\leq 4 \times 10^{-4}$ mbar.

The substrates were doubly-polished silicon (100 oriented) and sapphire. These were cleaned in an ultrasonic bath first with a tensio-active solution, then with distilled water and finally in propanol. Before the deposition the substrates were sputter cleaned by a 500 V/10 mA nitrogen beam for 2 min. A few samples were cooled down by using liquid nitrogen. The temperature was monitored by a PT100 thermocouple and the values are reported in Table 1. The samples are indicated with the same symbols used in Refs. [1,2].

The NEXAFS experiments were carried out at LURE facility (Orsay, France) on the VUV Super-ACO storage ring using the SACEMOR beamline. The monochromator was a HE-TGM with an energy resolution of 0.1 eV at the carbon K-edge. The detection of the out-coming electrons was in total electron yield (TEY) mode ($\sim 100 \text{ \AA}$ of depth sensitivity). The energy step was 0.1 eV and the collecting time was 1 s for each channel. The intensity of the incident beam I_0 was obtained from the photocurrent produced in a gold coated grid. The ratio between the collected signal from the sample I_s and the incoming intensity I_0 gives the signal of the absorption. For a detailed description of data handling (calibration and normalization) and analysis see Ref. [5].

Unpolarized Raman spectra were recorded ex situ at room temperature and backscattering geometry. An I.S.A. Jobin-Yvon triple grating spectrometer equipped with a liquid nitrogen cooled detector was utilized. The 514.5 nm line of an argon ion laser was used as excitation source.

3. Results

The Raman spectra of three CN_x films (CN42, CN54, CN67) are shown in Fig. 1. For comparison the spectra of two amorphous carbon deposits are also reported: sample C1 deposited at room temperature (Ar^+ ions, sputtering voltage 1000 V) and sample C79 deposited at 140 K (Ar^+ ions, sputtering voltage 700 V). The region between 1200 and 1650 cm^{-1} is given by the partial overlapping of the D band at $\sim 1370 \text{ cm}^{-1}$ and the G band at $\sim 1570 \text{ cm}^{-1}$. The D band is larger in CN_x films than in a-C films, giving a first qualitative indication that the incorporation of nitrogen modifies the degree of order. To compare different samples on a more quantita-

Table 1
Deposition parameters of CN_x films grown at substrate temperature between 80 and 673 K. The nitrogen content was determined by AES measurements (see Ref. [1])

Sample	Sputtering voltage U_{sputt} (V)	Sputtering current I_{sputt} (mA)	Assisting voltage U_{ass} (V)	Assisting current I_{ass} (mA)	Substrate temperature T_{sub} (K)	Deposition rate v_{dep} (nm min^{-1})	Nitrogen content (at.%)
CN42	1500	30	200	8.0	673	1.7	24
CN54	150	17	100	1.4	310	0.5	32
CN55	150	16	–	–	140	0.7	44
CN67	150	18	–	–	80	0.1	–

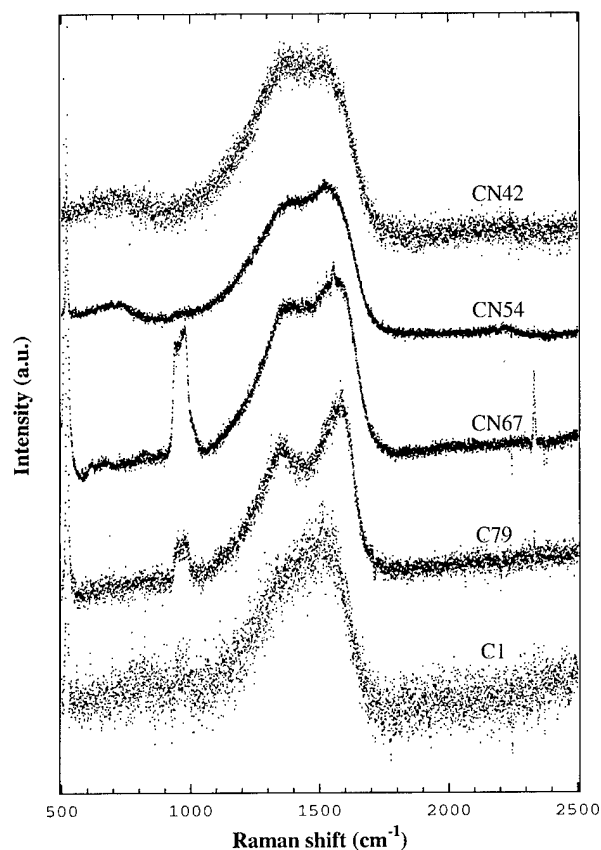


Fig. 1. Raman spectra of CN_x films. For comparison two spectra of amorphous carbon films C1 (deposition at 310 K, sputtering voltage 1000 V) and C79 (deposition at 140 K, sputtering voltage 700 V) are also reported. Due to the high optical transparency of the samples, the contribution of the silicon substrate is also detected by the peaks at $\sim 500 \text{ cm}^{-1}$ (first order) and $\sim 1000 \text{ cm}^{-1}$ (second order).

tive basis, the peaks were fitted with two Gaussian curves and the obtained values are collected in Table 2. From sample CN42 to sample CN67 both bands shift towards higher frequency and their FWHM becomes smaller as the deposition decreases. As well as the ratio of the integrated areas I_D/I_G decreases. These results indicate that the films deposited at lower temperatures have a higher degree of order. In CN_x films the feature at $\sim 2150 \text{ cm}^{-1}$ (more evident in CN54) can be related to hybridized carbon bonded to nitrogen. We recall that the presence of triple bonds ($\text{C}\equiv\text{N}$) was already unambiguously detected in FTIR measurements [1].

Table 2
Fitted values of the Raman spectra

Sample	D band position ω_D (cm^{-1})	D band FWHM Γ_D (cm^{-1})	G band position ω_G (cm^{-1})	G band FWHM Γ_G (cm^{-1})	I_D/I_G
CN42	1378	342	1559	147	1.970
CN54	1390	341	1564	146	1.515
CN67	1406	302	1584	134	1.247
C1	1385	320	1545	146	1.327
C79	1374	285	1580	129	0.861

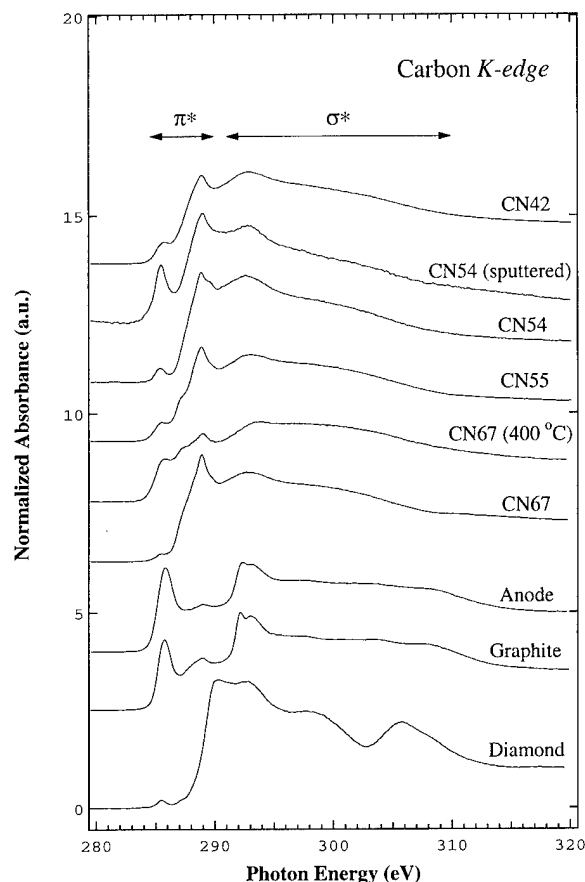


Fig. 2. The NEXAFS C K-edge spectra of the CN_x films. Two samples were treated in the experimental chamber: CN67 was heated up to 400°C for 1 h and CN54 was sputtered by an Ar^+ beam (600 V, 8 mA, for 10 min). The reference spectra of graphite, diamond and of the sample called Anode (100% sp^2) are also reported (see text).

The near-edge absorption spectra were acquired at the carbon, nitrogen and oxygen K-edges. In Fig. 2 the C K-edge NEXAFS spectra of the CN_x samples are shown. For comparison the spectra of graphite and diamond are also reported together with the spectrum indicated as 'Anode'. This is the deposit grown on the anode of a carbon cluster beam source. The highly disordered orientation of the graphitic domains in this sample makes it preferable to graphite as a reference sample for the evaluation of the sp^2 ($\text{C}=\text{C}$) content in our amorphous samples (for details see Ref. [5]). The spectra of graphite and diamond resume those reported

in the literature [6,7], even if the exciton peak of the diamond cannot be resolved. Two samples were treated in situ: CN67 was heated up to 400°C for 1 h, and CN54 was sputter etched using Ar⁺ ions (600 V, 8 mA, for 10 min).

The spectra of CN_x films show a pre-edge resonance at about 285.3 eV principally due to transitions from the C 1s level to unoccupied states of sp² (C=C) sites. Also sp (C≡C) sites contribute to this peak but the presence of triple bonds between carbon atoms seems to be negligible in the amorphous structures under investigation. Thus this peak can be used for evaluating the sp² (C=C) fraction in accordance with the method proposed by Fallon et al. [8]. The 1s→π* transitions are also present in the diamond spectrum due to a graphitic phase contained in the diamond powder, as also detected in X-ray diffraction measurements. The intensity of the peak increases both after thermal anneal (sample CN67) and after sputtering (sample CN54). This is an index of graphitization induced by these treatments, as already investigated by us and reported in Refs. [5,9]. Another relevant pre-edge resonance arises at 288.8 eV, just before the absorption edge placed at about 289.5 eV. Different transitions can contribute to this peak, as carbon bonded to an OH group. The sputtering does not evidently affect this peak, while the heating produces a relevant reduction of its intensity.

The shoulder at about 287.8 eV is assigned to C—H* transitions [10]. Fig. 3 shows the best fit of two C K-edge spectra of the sample deposited at highest temperature (CN42) and at lowest temperature (CN67). The contribution to the C—H* resonance is higher for CN67 as well as that of the peak at 288.8 eV. These increments can be originated by the possible condensation of species as HCN and OHCN on the growing film.

Possible other contributions are at 286.5 eV, related to C 1s→π* into orbitals involving C=O and C=N bonds, and at 287.2 eV related to π*_{C≡N}. In sample CN67 the contributions at 285.3 and 286.5 eV are smaller than in sample CN42. At the lowest deposition temperature the diminution of sp² sites, namely C=C and C=N, can be correlated with the loss of aromaticity in favor of a more polymeric structure with hydrogen and C≡N as terminations. This trend is confirmed by the data reported in Table 3 where the evaluated sp² (C=C) content for each CN_x film is reported. Incidentally, it is also observed that the treated samples present a relevant increment of the sp² (C=C) fraction (up to 55%).

The broad features between 290 and 320 eV are the overlap of sp, sp² and sp³ sites and reveal the amorphous nature of the films.

In Fig. 4 the nitrogen NEXAFS K-edge spectra are shown. Sample CN42 exhibits a broader structure in the pre-edge region (ionization edge at about 402.0 eV). Samples CN67 and CN55 show a shift of the maximum

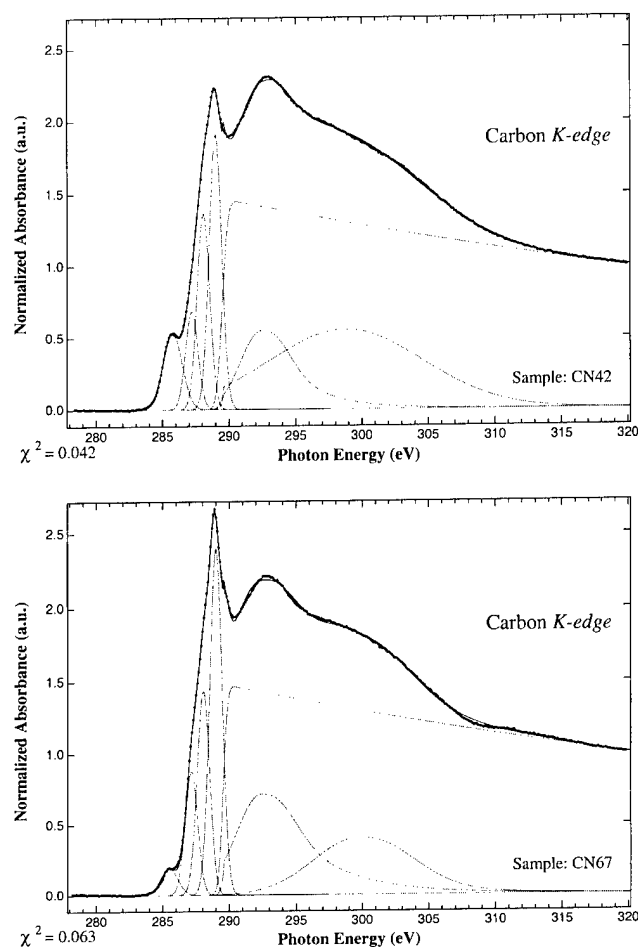


Fig. 3. Fits of the samples CN42 (673 K, 1500 V) and CN67 (80 K, 150 V). The solid line is the resulting optimized fitting curve and the dotted curves are the individual components of the deconvolution. For details regarding the fitting procedure see Ref. [6].

Table 3

Fraction of sp² (C=C) bonds evaluated from the spectra of Fig. 2 by using the procedure described in Refs. [5,8]

Sample	Fraction of sp ² (%)
Anode	100
CN42	36
CN54	13
CN54 (sputtered)	55
CN55	27
CN67	8
CN67 (400°C)	54

towards higher energies while sample CN54 is practically structureless.

The NEXAFS spectra at the oxygen K-edge are reported in Fig. 5. These data were acquired to identify the presence of bonds between carbon and oxygen given by the transition π*_{C=O} at 533.3 eV. Actually this resonance is present in every spectra but is more intense for the samples deposited at the lowest temperatures (CN55

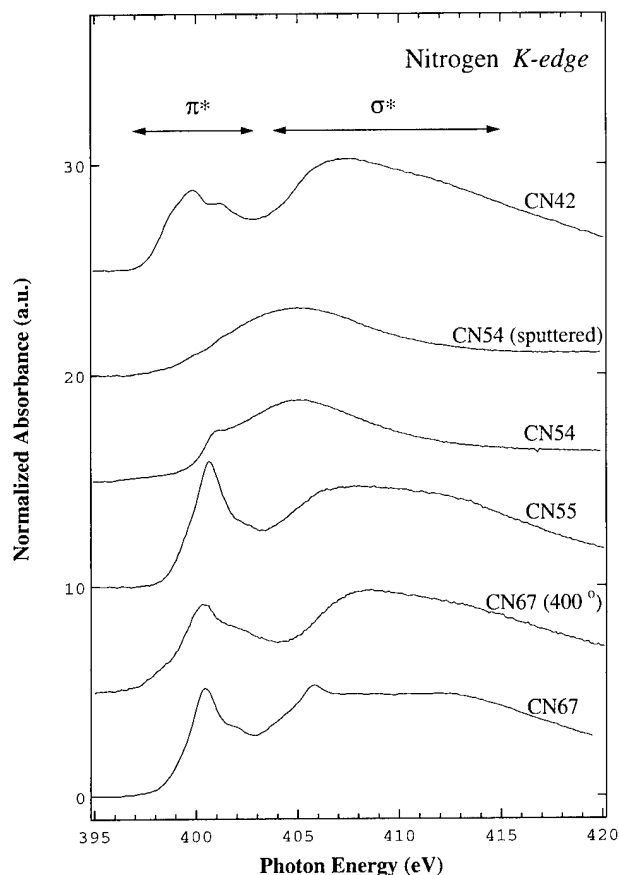


Fig. 4. The NEXAFS N K-edge spectra of the CN_x films.

and CN67). After sputtering (CN54) this peak practically disappears while after thermal anneal it is only reduced. Thus even if the oxygen is mainly a surface contaminant, it can also be incorporated in the films grown at a temperature which favors the condensation of oxygen containing species.

4. Conclusions

The combination of Raman and NEXAFS spectroscopies contributes towards a better understanding of the structure and chemical states of the carbon nitride films. From the Raman spectra we can conclude that the films are amorphous and present an increasing medium-range order as the sputtering energies and deposition temperatures decrease. Under these conditions there is also a change in the local coordination as revealed by NEXAFS data. In fact a loss of sp^2 ($C=C$) sites is detected with a concomitant increase of the peak originated by $C-H^*$ transitions and of resonances related to species containing carbon and oxygen. The incorporation of hydrogen and oxygen is favored by the low deposition temperature at which species such as HCN or OHCN can condense on the growing film.

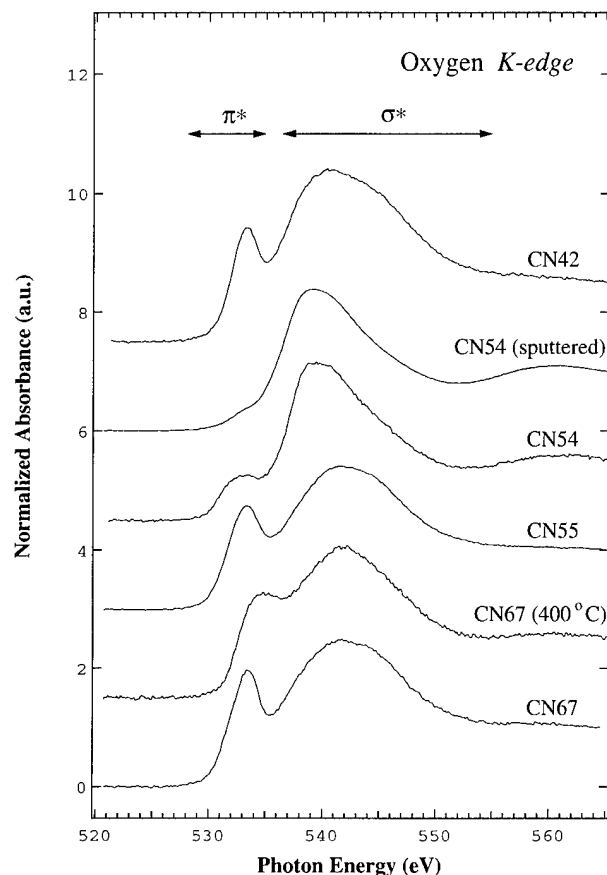


Fig. 5. The NEXAFS O K-edge spectra of the CN_x films.

Acknowledgements

The authors are indebted to P. Hammer for his valuable work on carbon nitride films carried out at the Joint Research Centre. We acknowledge C.E. Bottani and R. Pastorelli for the Raman measurements. We also wish to thank C. Laffon and Ph. Parent for their technical support at the SACEMOR beamline.

References

- [1] P. Hammer, M.A. Baker, C. Lenardi, W. Gissler, *J. Vac. Sci. Technol. A* 15 (1) (1997) 107.
- [2] M.A. Baker, P. Hammer, C. Lenardi, W. Gissler, *Surf. Coat. Technol.* 97 (1997) 544.
- [3] A.Y. Liu, M.L. Cohen, *Phys. Rev. B* 41 (1990) 10727.
- [4] P. Hammer, W. Gissler, *Diamond Relat. Mater.* 5 (1996) 1152.
- [5] C. Lenardi, P. Pseri, V. Briois, C.E. Bottani, A.L. Bassi, P. Milani, *J. Appl. Phys.* 85 (1999) 7159.
- [6] P.E. Batson, *Phys. Rev. B* 48 (1993) 2608.
- [7] J.F. Morar, F.J. Himpsel, G. Hollinger, G. Hughes, J.L. Jordan, *Phys. Rev. Lett.* 54 (1985) 1960.
- [8] P.J. Fallon, V.S. Veersamy, C.A. Davis, J. Robertson, G.A.J. Amarunga, W.J. Milne, J. Koskinen, *Phys. Rev. B* 48 (1993) 4777.
- [9] C. Lenardi, M.A. Baker, V. Briois, L. Nobili, P. Pseri, W. Gissler, *Diamond Relat. Mater.* 8 (1999) 595.
- [10] J. Stöhr, *NEXAFS Spectroscopy*, Springer, Berlin, 1992.

Hard and superhard nanocomposite coatings

J. Musil *

Department of Physics, University of West Bohemia, P.O. Box 314, 30614 Plzeň, Czech Republic

Abstract

This article reviews the development of hard coatings from a titanium nitride film through superlattice coatings to nanocomposite coatings. Significant attention is devoted to hard and superhard single layer nanocomposite coatings. A strong correlation between the hardness and structure of nanocomposite coatings is discussed in detail. Trends in development of hard nanocomposite coatings are also outlined. © 2000 Elsevier Science S.A. All rights reserved.

Keywords: Hardness; Magnetron sputtering; Mechanical properties; Nanocomposite coatings; Structure

1. Introduction

Hard coatings have been successfully used for protection of materials and particularly to enhance the life of cutting tools since the 1970s. Both the technological process of their production and their properties, i.e. hardness, wear and oxidation resistance, however, are continuously being improved. Important milestones in the development of hard coatings are briefly summarized in Table 1. This table shows a clear effort (i) to decrease the temperature T at which hard coatings are formed and (ii) to improve the properties of hard coatings, particularly to increase the hardness and oxidation resistance. The oxidation resistance should be increased up to approximately 1000°C because during high-speed machining the temperature of the tool tip can reach 1000°C and the coating should be stable at such high temperatures.

As to the hardness, the coatings are usually divided into two groups: (1) *hard coatings* having a hardness < 40 GPa, and (2) *superhard coatings* having a hardness > 40 GPa. Compared to a large number of hard materials, there are only a few superhard materials, i.e. cubic boron nitride (c-BN), amorphous diamond-like carbon (DLC), amorphous carbon nitride (a-CN_x) and polycrystalline diamond. Moreover, these superhard materials are thermodynamically unstable. This is a serious disadvantage which strongly limits their utilization in some applications. For instance, the high chemical

affinity of carbon to iron limits the applicability of diamond coated cutting tools to machining of aluminum, their alloys and wood only. Similar problems can be expected when the c-BN coating is used in cutting of steels due to the chemical dissolution of boron in iron. These problems stimulated intensive research in this field, and recently new superhard materials based on superlattices and nanocomposites were developed.

2. Hard superlattice coatings

Superlattice coatings are nanometre-scale multilayers composed of two different alternating layers with a superlattice period, i.e. the bilayer thickness of two materials, ranging from 5 to 10 nm. The bilayers of these superlattices can be metal layers, nitrides, carbides or oxides of different materials or a combination of one layer made of nitride, carbide or oxide of one metal and the second layer made of another metal. According to the composition of the bilayer, superlattice coatings can be divided into five groups: (1) metal superlattices, (2) nitride superlattices, (3) carbide superlattices, (4) oxide superlattices and (5) nitride, carbides or oxides/metal superlattices.

Experiments show that metal superlattices exhibit a relatively low hardness. On the contrary, single-crystal nitride superlattice coatings are superhard materials with a hardness ranging from 45 to 55 GPa, e.g. TiN/VN, 56 GPa [15]; TiN/(V_{0.6}Nb_{0.4})N, 41 GPa [16]; TiN/NbN, 51 GPa [17]; TiN/Nb, 52 GPa [18,19]; TiN/CN_x, 45–55 GPa [20]; ZrN/CN_x, 40–45 GPa [21];

* Tel.: +420-19-279072; fax: +420-19-279071.

E-mail address: musil@kfy.zcu.cz (J. Musil)

Table 1
Important steps in development of hard coatings

Coating	Material	H (GPa)	Main characteristics
Single layer	TiN, TiC, Al_2O_3	21, 28, 21	CVD at T around 1000°C on cemented carbides
Single layer	TiN, TiC	21, 28	PVD at $T \leq 550^\circ\text{C}$ on steel substrates
Multilayer	TiC/TiB ₂		About 10^3 phase boundaries TiC/TiB ₂ [2]
Single layer	c-BN	50 [3]	High chemical affinity of C to iron
Single layer	diamond	90 [4]	Chemical dissolution of B in iron [5]
Single layer	TiAlN		Oxidation resistance up to 800°C [6]
Single layer	DLC	65	Amorphous phase [7]
Single layer	CN _x	50–60	Substoichiometric ($x=0.2\text{--}0.35$) turbostratic structure [8,9]
Superlattices	TiN/VN, TiN/NbN, etc.	~ 50	Superlattice period 5–10 nm [10,11]
Single layer	nc-MeN/a-nitride	~ 50	Superlattice period 5–10 nm [10,11]
Single layer	nc-MeN/metal	~ 50	Nanocomposite [13]
Single layer	Ti _{0.4} Al _{0.6} N	~ 32	Nanocomposite, oxidation resistance up to 950°C [14]

TiN_x/C–N, 20–50 GPa [22,23]. The overall hardness of the superlattice coating is therefore greater than that of the materials of the individual components of the bilayer, e.g. $H_{\text{TiN/NbN}} \approx 52$ GPa, $H_{\text{TiN}} = 21$ GPa, $H_{\text{NbN}} = 14$ GPa. This hardness enhancement is a very complex phenomenon. In spite of this, several models which explain multilayers strengthening have already been developed [24–27]. The model of Shinn et al. [26] shows that (i) a difference in elastic modulus between the two layer materials is required to increase the hardness of the superlattice film, and (ii) the coherency strain at the interface between the two layers has only a minor effect. The model of Chu and Barnett [27] is based on restricted dislocation movement within and between layers in the superlattice coating. It predicts a peak in hardness when there is a difference in shear modulus between two layer materials and sharp interfaces between layers.

So far, less attention has been devoted to carbide multilayer coatings. These coatings can also be superhard, up to 55 GPa, e.g. TiC/VC, 52 GPa [28]; TiC/NbC, 45–55 GPa [29]. Considerable attention has been devoted to nitride/metal superlattice coatings. This combination of bilayer materials, i.e. the hard nitride with a more ductile metal, makes it possible to improve the toughness of the coating while retaining its relatively high hardness (≥ 30 GPa), e.g. TiN/Ti, 36.8 GPa [30]; WN/W, 34 GPa [30]; HfN/Hf, 50 GPa [30]; TiN/Ni, 35 GPa [31]; TiN/Ni_{0.4}Cr_{0.1}, 32 GPa [31]; NbN/Mo, 33 GPa [32,33]; NbN/W, 30 GPa [32,33]. An improvement in the toughness of the coating increases its adhesion to the substrate, which is of fundamental importance for coating applications.

At present, practically no data are available on oxide superlattice coatings. This is probably because the deposition rate of oxide films using both d.c. and r.f. reactive magnetron sputtering is, compared with that of metals, too low. Recently, this situation strongly changed. Considerable progress has been made in magnetron deposition of oxide films, such as Al_2O_3 , ZrO_2 , TiO_2 ,

etc. using pulsed d.c. sputtering [34,35]. For instance, the deposition rate for clear Al_2O_3 films formed using this technique can reach 78% of the metal deposition rate, which is about 25 times the rate obtainable with r.f. power [1]. Therefore, oxide films can be produced at economical rates and so we can expect that research will be intensified for oxide superlattice coatings. For instance, Sproul already reported on the deposition of multilayer nanometre-scale oxide films composed of alternating layers of Al_2O_3 and ZrO_2 at a high rate onto glass, silicon, and high-speed steel substrates [1]. Results are very encouraging because the energy delivered to the growing film during the pulse operation can stimulate film crystallization at low deposition temperatures.

In conclusion it is worthwhile to note that superhard coatings in the form of superlattices represent a very important milestone in the development of superhard materials and the understanding of the origin of the superhardness. However, the maximum hardness of the superlattice coating is very strongly dependent on the superlattice period λ , see for instance Fig. 3 presented in Ref. [15]. The strong dependence of H on λ may cause large variations in the coating hardness, H , when deposited in industrial machines because it is difficult to ensure the same thickness of all superlattice layers on all coated objects, particularly when they have a complex shape. Similar variations in H can also be caused by the interdiffusion of elements in neighbouring layers at high service temperatures. These problems can be avoided if the *superlattice* coating is replaced with a *single-layer nanocomposite* coating.

3. Nanocomposite materials

Materials are composed of grains separated by grain boundaries. The size of grains in currently produced materials, which can be called the conventional materials, varies over a wide range from about 100 nm to

several hundred millimetres, corresponding to monocrystals. This means that the number of atoms in grains is always considerably greater than that in boundary regions. The behaviour of such materials is determined mainly by the bulk of grains in which dislocations play a decisive role. Properties of these materials are continuously improved by optimizing their composition, structure and the technological processes used for their formation. No fundamental qualitative changes in properties of the conventional materials can, however, be expected.

Completely new properties are exhibited by nanocrystalline materials with a grain size of about 10 nm or less. The behaviour of these materials is determined mainly by processes in boundary regions because the number of atoms in the grains is comparable to or smaller than that in the boundary regions. Under these conditions dislocations do not exist [36], because grain boundaries prevent their formation, and the boundary regions play a decisive role in the material deformation. A new deformation mechanism, called grain boundary sliding, replaces the dislocation activity which is the dominant deformation process in conventional materials [37]. All these facts result in new unique properties of nanocrystalline materials. In the case where the size of grains decreases below 5 nm, the participation of atomic forces in material formation has to be considered and the formation of nanocrystalline subatomic structures can be expected [38].

The new unique properties of nanocrystalline materials are the main driving force stimulating their development. These materials can be prepared only by a method which simultaneously ensures a high rate of nucleation and a low growth rate of grains. This can be achieved relatively easily when the nanocrystalline materials are produced in the form of films. The most suitable method for the production of nanocrystalline films is magnetron sputtering.

4. Methods to control the size and orientation of grains in sputtered films

The main task in the development of nanocomposite materials is to master control of their growth mechanism. Therefore, further basic processes used for controlling the size and crystallographic orientation of grains in growing films are given. There are two fundamental processes: (1) low-energy ion bombardment and (2) mixing process [39,40].

4.1. Low-energy ion bombardment

The process of low-energy ion bombardment controls the growth mechanism of the film by the energy delivered to the growing film by bombarding ions. The ion

bombardment is a strongly *non-equilibrium process* which heats the growing film at an atomic level. Therefore, it is called atomic scale heating (ASH). The ion bombardment significantly differs from conventional heating because the kinetic energy of bombarding ions is transferred into very small areas of atomic dimensions and then very quickly conveyed into their close vicinity, i.e. the ASH is accompanied by extremely fast cooling rates of about 10^{14} K/s [41]. ASH can replace conventional heating and so produce dense films corresponding to zone T in the Thornton structural zone model when sputtering is carried out at low pressures of about 0.1 Pa and lower [42].

Ion bombardment of the growing film can restrict the grain growth and permit the formation of nanocrystalline films. The size and crystallographic orientation of grains can be controlled by the energy and flux of bombarding ions. This control of the film structure is, however, accompanied by *film heating* and is not convenient for all applications.

4.2. Mixing process

The mixing process is based on the addition of one or several elements to a base, one element material. As at least two elements are present in the film, *alloy films* are formed by this process. The mixing process is an efficient method convenient for production of *nanocrystalline* films. Compared with ion bombardment, *no substrate bias and heating* are necessary to form the films with nanocrystalline structure. Also, metastable high-temperature phases can be formed on unheated substrates [43]. This is connected with efficient ASH, caused by condensing sputtered atoms, and subsequent extremely fast cooling at an atomic level.

5. Nanocrystalline alloy films

The structure of alloy films depends on the amount and type of elements added to a base, one element material. Recent experiments carried out in our laboratory show that there are two groups of binary metal alloy films. The films of the first group are characterized by relatively narrow X-ray reflection lines ($\text{FWHM} \leq 1^\circ$). The films of the second group are very fine grained (nanocrystalline) or X-ray amorphous films characterized by very broad low-intensity reflections ($\text{FWHM} > 1^\circ$). Several examples are given in Table 2.

Here, together with the grain size, d , two characteristic parameters of the alloyed materials, i.e. (i) difference in atomic radii of the alloy elements and (ii) enthalpy of the alloy formation ΔH_f , are also given. These quantities are often used to predict the creation of an amorphous state [51–53]. This state is expected to be formed in the case when (i) the atomic size difference is greater

Table 2

Typical features of X-ray reflection line from selected alloy films sputtered on unheated substrates ($T = RT$) at $I_d = 1$ A, $U_s = U_n$ and $p_{Ar} = 0.5$ – 0.7 Pa

Alloy	2θ (°)	I_{hkl} (cps)	FWHM (°)	d (nm)	ΔH_f (kJ/mol)	r_A (nm)	r_B (nm)	$\Delta r/\langle r \rangle^a$	Reference
<i>Narrow reflections</i>									
NiCr (80/20 wt.%)	51.74	22642	0.2995	51.97	−4	0.1246	0.125	0.003	[44]
CrNi (60/40 wt.%)	46.50	7627	0.2788	59.94	−9				
ZrY (70/30 at.%)	46.56	89231	0.2910	49.58	14	0.160	0.181	0.123	[45]
TiSi (90/10 at.%)	52.21	756	0.3770	36.16	−65	0.144	0.1176	0.202	[46]
CuCr (60/40 at.%)	51.57	1500	0.9360	12.38	20	0.117	0.125	0.066	[47]
<i>Broad reflections</i>									
TiCu (50/50 at.%)	46.70	15	4.7020	1.79	−9.6	0.144	0.117	0.207	[48]
TiAl (60/40 at.%)	45.80	45	5.1018	1.49	−57	0.144	0.143	0.007	[49]
ZrCu (70/30 at.%)	43.55	135	9.8495	0.93	−12	0.160	0.117	0.255	[50]

^a $\Delta r/\langle r \rangle$ is the difference in atomic radii, $\langle r \rangle = (r_A + r_B)$.

than 0.15 [52] and (ii) the enthalpy of alloy formation is negative and large. As can be seen from Table 2, these two materials parameters, $\Delta r/\langle r \rangle$ and ΔH_f , are not, however, sufficient to predict the structure of binary metal alloy films formed by sputtering. At present, it is not known which combinations of these two elements will form films with narrow and broad X-ray reflection lines, respectively. Despite these problems there exists a solution which allows the preparation of nanocrystalline alloy films.

Alloy films with narrow X-ray reflection lines can be converted into films with broad X-ray reflection lines if nitrogen is added, i.e. when the nitride of the alloy film is formed, see e.g. Ref. [44]. This means that either binary metal alloys or their nitrides form nanocrystalline films. The structure of the nanocrystalline film can be controlled by the substrate bias, substrate temperature and by the amount of nitrogen incorporated into the film, i.e. by the energy delivered to the growing film.

6. Nanocomposite films based on nitrides of binary metal alloys

Nanocomposite films consist of at least two phases. Experiments show that the incorporation of N into the growing film is not sufficient to produce the nanocomposite film with fully separated phases. To achieve this, the substrate has to be heated, see for instance the formation of ZrCu–N [50], NiCr–N [44] and TiNi–N [54] nanocomposite films.

The formation of nanocomposite structures is connected with a segregation of the one-phase to grain boundaries of the second phase, and this effect is responsible for stopping of the grain growth. There are, however, two open questions. (1) What is a minimum temperature T_{seg} necessary to start the segregation process, and are there some factors which could be used to decrease T_{seg} ? (2) What is a thermal stability of nanocomposite films? Recent experiments indicate that rare-

earth elements, such as yttrium, drastically reduce the grain size in metals, see for instance Ref. [55].

7. Hard and superhard nanocomposite coatings

At present, significant effort is devoted to master the formation of nanocomposite coatings using magnetron sputtering because this technology can easily be scaled up for industrial use. The nanocomposite coatings are produced using so-called selective reactive magnetron sputtering [56]. In this deposition process, one element of the alloy is converted into nitride and the second element of the alloy is transported into the growing film unreacted.

Recently, new hard (<40 GPa) *supertough* material of the type nc-TiC/a-C [57] with a remarkable plasticity (40% during nanoindentation deformation) and new *superhard* (≥ 40 GPa) materials of the type nc-MeN/a-Si₃N₄ [12] with a high elastic recovery (up to 80%) in the form of *nanocomposite* coatings were developed; here nc- and a- denote the nanocrystalline and amorphous phases, respectively, and Me = Ti, W, V, Zr, etc. are transition metals. Even though both types of material are composed of nanocrystalline grains embedded in an amorphous matrix, they exhibit completely different physical properties. This is due to the different structures of the supertough and superhard nanocomposite coatings.

A systematic investigation carried out on systems ZrCu–N [13] and TiAl–N [49] showed that superhard nanocomposite coatings can be composed *not only* of two hard phases as proposed by Vepřek et al. [58] but also in the case when *only one* phase is hard, e.g. a nc-ZrN/Cu nanocomposite [13]. This means that there are two groups of superhard nanocomposite coatings:

1. nc-MeN/nitride (e.g. a-Si₃N₄, a-TiB₂, etc.);
2. nc-MeN/metal (e.g. Cu, Ni, Y, Ag, Co, etc.).

The hardness H of films of both groups can be continuously varied from low values of about 10 GPa to very

high values, achieving up to 50–70 GPa. Moreover, it is worthwhile to note that the hardness of nanocomposite films is strongly correlated with their structure.

7.1. Structure of superhard nanocomposite coatings

Superhard films with $H \geq 40$ GPa are formed only when their structure is close to X-ray amorphous. This structure corresponds to a transition from the crystalline structure to an amorphous one. The main factors which govern the formation of films with an X-ray amorphous structure are: the energy delivered to the growing film, the substrate temperature T_s , the type of elements forming the film [their (i) mutual solubility or immiscibility, (ii) ability to form intermetallic compounds, (iii) chemical affinity, and (iv) binding energy], gap of elements immiscibility, enthalpy of the alloy formation and the content of individual phases in the nanocomposite film, e.g. the content of soft phase in a composite of the type nc-Me/metal.

The structure of hard (<40 GPa) and superhard (≥ 40 GPa) nanocomposite coatings is significantly different. A systematic investigation of the correlation between the hardness and structure in the ZrCu–N and TiAl–N nanocomposite films showed that (a) the hard films are characterized by many reflections from polyoriented grains of both phases, (b) the superhard films are two-phase nanocomposites one phase of which has a nanocrystalline structure and the second is X-ray amorphous, and (c) the maximum hardness is achieved only when all grains are oriented in the same direction and the size of grains has an optimum value of approximately several tens of nanometres.

7.2. Classification of hard nanocomposite coatings

Till now, various different types of hard nanocomposite coating have been prepared:

1. nc-MeN/a-nitride, e.g. nc-MeN/a-Si₃N₄ (Me = Ti, W, V) [58,61], nc-TiN/a-Si₃N₄ [62];
2. nc-MeN/nc-nitride, e.g. nc-TiN/nc-BN [58];
3. nc-MeC/a-C, e.g. nc-TiC/DLC [7];
4. nc-MeN/metal, e.g. nc-ZrN/Cu [13], nc-(Ti,Al)/AlN [49,60], nc-CrN/Cu [47];
5. nc-MeN or MeC/a-boron compounds, e.g. nc-Ti(B₂O₃)/quasi-a-(TiB₂, TiB and B₂O₃) [63], Ti–B–C [64];
6. nc-WC + nc-WS₂/DLC [65];
7. nc-MeC/a-C + a-nitride, e.g. nc-Mo₂C/a-C + a-Mo₂N [59].

This survey shows that all hard nanocomposite coatings contain one or two hard crystalline phases. The second phase is more complicated. It is either amorphous (e.g. a-Si₃N₄) or crystalline (e.g. nc-BN [58]). Sometimes, the content of the second phase in the nanocomposite coating is very low at approximately 1–2 wt.% (e.g. Cu

in nc-ZrN/Cu films [13]). In such a case, it is very difficult, without a HRTEM investigation, to determine if the second phase is crystalline or amorphous because the X-ray reflections from a small quantity of grains are below the detection limit. This means that the second phase can be incorrectly interpreted as amorphous when determined from X-ray diffraction analysis only. On the basis of these facts hard nanocomposite coatings can be divided into two main groups: (1) crystalline/amorphous nanocomposites and (2) crystalline/crystalline nanocomposites.

At present, no definite methodology exists on how to select the combination of elements to produce films with nanocrystalline and/or X-ray amorphous structure. Such films can be formed from nitrides of alloys composed of elements which exhibit a wide miscibility gap and contain one element forming hard nitride, for instance nitrides of binary alloys formed of immiscible elements such as Cu–Cr, Zr–Y, etc. or transition metal nitride/boride and nitride/carbide systems [64]. A miscibility gap between intermetallics is also sufficient to produce hard nanocomposite coating, e.g. ZrCu–N film. There is also a possibility to produce the nanocomposite coating from nitrides of alloys whose elements form a solid solution, e.g. Ti_{1–x}Al_xN film. This is enabled by the existence of a gap in the alloy composition x where the structure of the film is quasi-X-ray amorphous [66].

7.3. Mechanical properties of hard nanocomposite coatings

A short survey of basic mechanical characteristics of some recently prepared nanocomposite films is given in Table 3. For comparison, the characteristics of some selected hard bulk materials and hard amorphous carbon films are also given in this table.

The hard nanocomposite coating is characterized not only by its hardness H but also by its Young's modulus E and elastic recovery W_e . The determination of these quantities for thin films is, however, difficult because they strongly vary with the load L used in their measurement. Despite these problems, Figs. 1 and 2 display H as a function $E^* = E/(1-\nu^2)$ and the elastic recovery W_e as a function H , because these dependencies were measured under the same conditions in one laboratory and on different nanocomposite systems. The high hardness of the material is only one parameter which ensures scratch and abrasion resistance. Protective overcoat films must be highly resistant also to plastic deformation during contact events. This requires a low Young's modulus E since, according to Johnson analysis, the load P_y needed to initiate plastic deformation when a rigid sphere of radius r is pressed into the coating is proportional to H^3/E^2 [74]. The ratio H^3/E^2 is a parameter which controls the resistance of materials to plastic deformation. The likelihood of plastic deformation is

Table 3
Comparison of hard bulk materials, hard single layer films and selected hard and superhard nanocomposite coatings

Material	H (GPa)	$E^* = E/(1-\nu^2)$ (GPa)	W_e (%)	H^3/E^{*2}	d (nm)	Reference
<i>Bulk materials</i>						
Diamond	100	1050		0.91		[67]
Boron	35	470		0.19		[68]
Sapphire	30	441		0.14		[69]
<i>Amorphous films</i>						
DLC	65	550	80–90	0.91		[7]
a-C (cathodic arc)	> 59	> 395		~1.3		[74]
<i>Nanocomposite single layer films</i>						
nc-TiN/Si ₃ N ₄	48	~565	— ^a	~0.34	4.5	[70]
nc-TiN/BN	69	585	—	0.96	9	[58]
nc-W ₂ N/a-Si ₃ N ₄	51	560	—	0.42	3.5	[58,70,71]
Ti-B-C	71	486	80.5	1.52	~1	[64]
Ti-B-N	54	~500	—	0.63	~1	[64]
Zr ₉₈ Cu ₂ N	54	394	81	1.03	35	[13]
W _{86.7} Ni _{8.3} N ₅	55	510	—	0.64	—	[75]
W ₆₈ Si ₁₄ N ₁₈	45	—	—	—	—	[61]
nc-Mo ₃ C/a-(C+Mo ₂ N)	49	440	67	0.61	27	[59]
Ti ₄₅ Al ₅₅ N	47	409	74	0.62	30	[49]
Ti ₆₀ Al ₄₀ N	40	650	—	0.15	—	[14]
ZrY-N	41	319	77	0.66	—	[45]
CrNi-N	32	253	74	0.50	—	[72]
Ti ₇₅ Si ₂₅ N	29	256	67	0.36	—	[46]
Ti _{0.32} C _{0.68} (TiC/a-C)	32	370	60	0.239	10–50	[73]

^a Denotes data not given in the references or not determined.

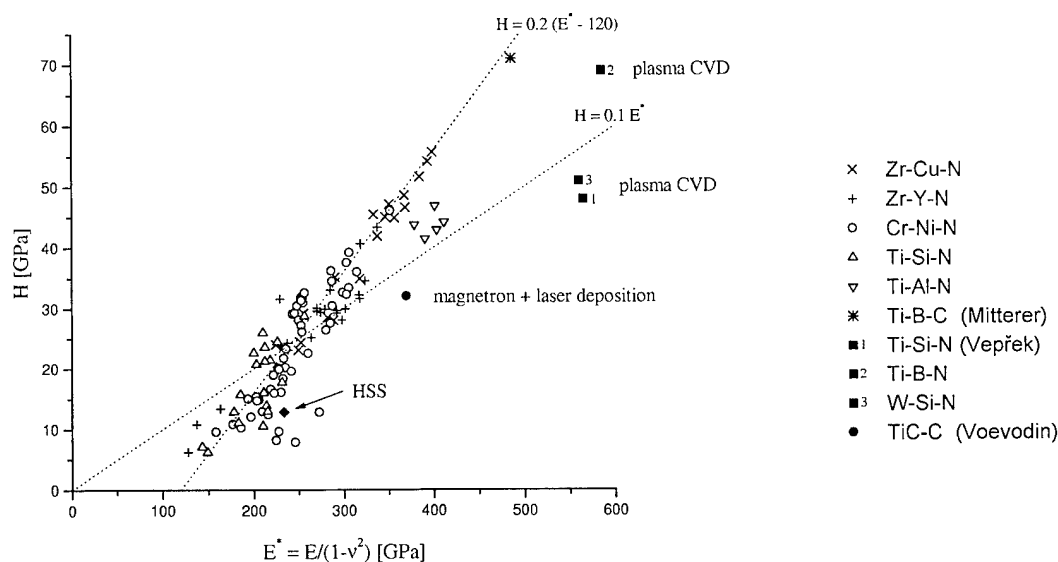


Fig. 1. H as a function of $E/(1-\nu^2)$ for Zr-Cu-N, Zr-Y-N, Cr-Ni-N, Ti-Si-N and Ti-Al-N nanocomposite films sputtered at different deposition conditions, i.e. T_s , U_s , i_s and p_{N_2} .

reduced in materials with high hardness and low modulus [74]. In general, a low modulus is also desirable as it allows the given load to be distributed over a wider area. The range H^3/E^2 of nanocomposite films spreads over a very wide range from about 0.15 to 1.52, see Fig. 3 and Table 3. Data given in Table 3 and in Figs. 1–3 show that the elastic recovery W_e and the resistance

of materials to plastic deformation can be controlled by the film hardness H and its elastic modulus E .

A spread of experimental points around the straight lines in Figs. 1–3 is connected with the variation in the film structure induced particularly by different (i) deposition conditions and (ii) chemical composition of the film. Therefore, H and E of nanocomposite coatings

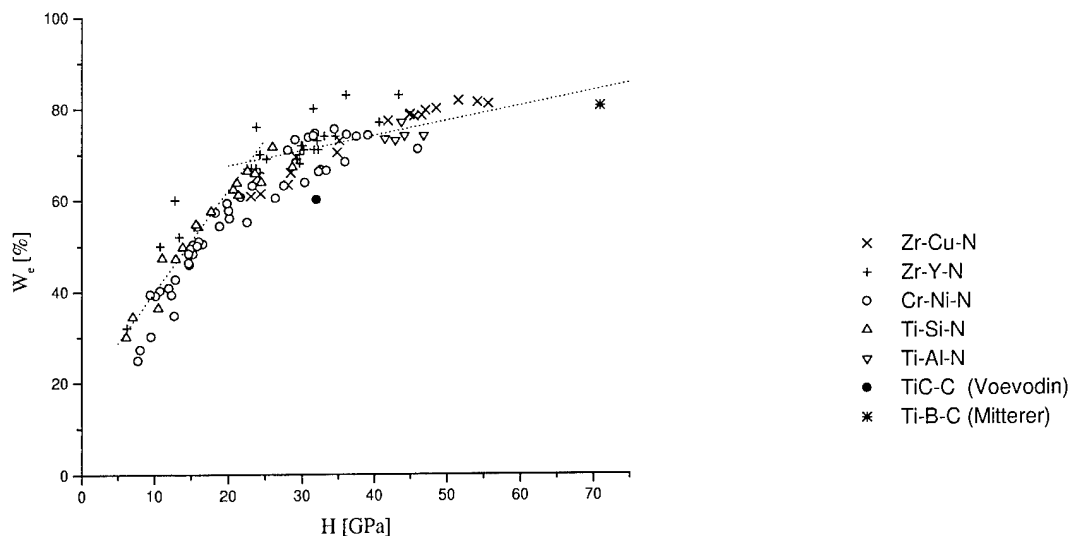


Fig. 2. Elastic recovery upon indentation W_e as a function of H for Zr-Cu-N, Zr-Y-N, Cr-Ni-N, Ti-Si-N and Ti-Al-N nanocomposite films sputtered at different deposition conditions, i.e. T_s , U_s , i_s and p_{N_2} .

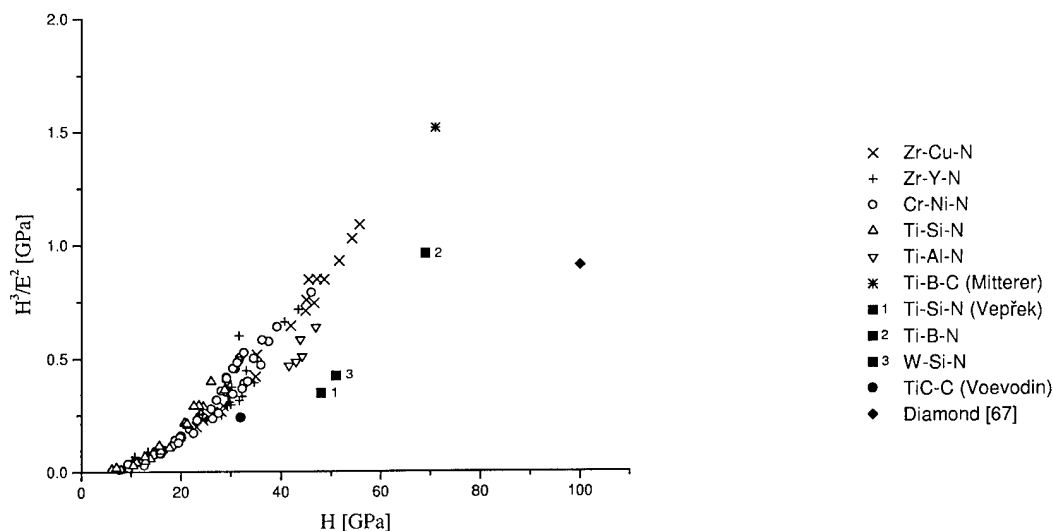


Fig. 3. The ratio H^3/E^2 characterizing the resistance of the material to plastic deformation as a function of H for Zr-Cu-N, Zr-Y-N, Cr-Ni-N, Ti-Si-N and Ti-Al-N nanocomposite films sputtered at different deposition conditions, i.e. T_s , U_s , i_s and p_{N_2} .

prepared by plasma CVD and magnetron-assisted laser deposition processes differ from those prepared by magnetron sputtering. A further systematic investigation is necessary to master the preparation of materials with prescribed properties.

8. Conclusions

The main results obtained in the development of hard and superhard nanocomposite coatings can be summarized as follows.

1. Hard (<40 GPa) coatings are characterized by a high

plastic deformation increasing with decreasing H up to about 70% for $H \approx 10$ GPa.

2. Superhard (≥ 40 GPa) coatings are characterized by a high elastic recovery increasing with increasing H up to about 85% for $H \approx 70$ GPa.
3. There are two types of superhard nanocomposite film: (1) nc-MeN/a-nitride and (2) nc-MeN/metal. This means that the superhard film can be composed either of two hard phases or of one hard phase and the second soft phase.
4. The hardness of nanocomposite coatings correlates well with their structure. A decrease of the film crystallinity, characterized by a decrease of the inten-

sity of X-ray reflection lines and by an increase of their broadening, results in an increase of hardness.

5. The structure of superhard films is close to X-ray amorphous.

The nanocomposite films are fascinating materials since novel structures and new physical properties are expected. The development of nanocomposite films is, however, only at the beginning. Many problems are unsolved and many questions remain open. Therefore, further systematic research in this field is required. Further research is focusing on the following problems: (i) understanding of the origin of superhardness; (ii) correlation between the mechanical parameters of materials and process parameters; (iii) dramatic changes in crystallographic orientation of grains in alloy films, their hardness and elastic recovery induced by incorporation of nitrogen; (iv) formation of nanocomposite films with controlled hardness, elastic modulus and elastic recovery and new functional properties; and (v) investigation of materials having very small grains of about 1 nm in size.

Acknowledgements

The author would like to thank his Ph.D. students H. Hrubý, I. Leipner, H. Poláková, F. Regent, Z. Soukup and P. Zeman for the preparation of many nanocomposite coatings of different chemical composition and Dr. R. Čerstvý and Dr. M. Kolega for X-ray characterization of these coatings. This work was supported in part by the Grant Agency of the Czech Republic under Project No. 106/96/K245 and by the Ministry of Education of the Czech Republic under Project Nos. VS 96/059 and ME 173/1999.

References

- [1] W.D. Sproul, *Science* 273 (1996) 889.
- [2] H. Holleck, Ch. Kühl, H. Schultz, *J. Vac. Sci. Technol. A* 3 (4) (1985) 234.
- [3] H. Holleck, *J. Vac. Sci. Technol. A* 4 (6) (1986) 2661.
- [4] C.A. Brookes, in: J.E. Field (Ed.), *The Properties of Diamond*, Academic Press, New York, 1979, p. 383.
- [5] B.M. Kramer, P.K. Judd, *J. Vac. Sci. Technol. A* 3 (1985) 2439.
- [6] W.D. Münz, *J. Vac. Sci. Technol. A* 4 (6) (1986) 2717.
- [7] A.A. Voevodin, J.S. Zabinski, *Diamond Relat. Mater.* 7 (1998) 463.
- [8] H. Sjöström, S. Stafström, M. Boman, J.-E. Sundgren, *Phys. Rev. Lett.* 76 (1996) 56.
- [9] H. Sjöström, L. Hultman, J.-E. Sundgren, S.V. Hainsworth, T.F. Page, G.S.A.M. Teunissen, *J. Vac. Sci. Technol. A* 14 (1996) 56.
- [10] U. Helmersson, S. Todorova, S.A. Barnett, J.-E. Sundgren, L.C. Markert, J.E. Greene, *J. Appl. Phys.* 62 (1987) 481.
- [11] X. Chu, S.A. Barnett, M.S. Wong, W.D. Sproul, *Surf. Coat. Technol.* 57 (1993) 13.
- [12] S. Vepřek, S. Reiprich, S. Li, *Appl. Phys. Lett.* 66 (20) (1995) 2640.
- [13] J. Musil, P. Zeman, H. Hrubý, P. Mayrhofer, ZrN/Cu nanocomposite film — novel superhard material, *Proc. ICMCTF'99*, April 12–18, San Diego, CA (1999), paper no. B1-2-9.
- [14] Y. Min, Y. Makino, M. Nose, K. Nogi, *Thin Solid Films* 228 (1999) 204.
- [15] U. Helmersson, S. Todorova, S.A. Barnett, J.-E. Sundgren, L.C. Markert, J.E. Greene, *J. Appl. Phys.* 62 (1987) 481.
- [16] P.B. Mirakami, L. Hultman, S.A. Barnett, *Appl. Phys. Lett.* 57 (25) (1990) 2654.
- [17] M. Shinn, L. Hultman, S.A. Barnett, *J. Mater. Res.* 7 (4) (1992) 901.
- [18] X. Chu, M.S. Wong, W.D. Sproul, S.L. Rohde, S.A. Barnett, *J. Vac. Sci. Technol. A* 10 (4) (1992) 1604.
- [19] X. Chu, S.A. Barnett, M.S. Wong, W.D. Sproul, *Surf. Coat. Technol.* 57 (1993) 13.
- [20] D. Li, X.W. Lin, S.C. Chen, V.P. Dravid, Y.W. Chung, M.S. Wong, W.D. Sproul, *Appl. Phys. Lett.* 68 (9) (1996) 1211.
- [21] M.L. Wu, W.D. Qian, Y.W. Chung, Y.Y. Wang, M.S. Wong, W.D. Sproul, *Thin Solid Films* 308/309 (1997) 113.
- [22] H. Jensen, J. Sobota, G. Sorensen, *Surf. Coat. Technol.* 94/95 (1997) 174.
- [23] H. Jensen, J. Sobota, G. Sorensen, *J. Vac. Sci. Technol. A* 16 (3) (1998) 1180.
- [24] J.E. Kryanowski, *Mater. Res. Soc. Symp. Proc.* 239 (1992) 509.
- [25] S.A. Barnett, in: M. Fracombe, J.A. Vossen (Eds.), *Physics of Thin Films*, Academic Press, New York, 1993, p. 1.
- [26] M. Shinn, L. Hultman, S.A. Barnett, *J. Mater. Res.* 7 (1992) 901.
- [27] X. Chu, S.A. Barnett, *J. Appl. Phys.* 77 (1995) 4403.
- [28] B.G. Wendler, P. Kula, K. Jakubowski, S. Fauvry, Ph. Kapsa, L. Vincent, D. Heper, *Proc. 36th Tagung der Deutschen Gesellschaft für Oberflächen- und Galvanotechnik*, October 7–9, Schwabisch Gmünd, Germany (1998) 6–11.
- [29] B.G. Wendler, M. Molinaro, *Proc. 10th Int. Summer School on Modern Plasma Surface Technology*, May 10–14, Mielno, Poland (1998) 423–436.
- [30] K.K. Shih, D.B. Dove, *Appl. Phys. Lett.* 61 (6) (1992) 654.
- [31] X. Chu, M.S. Wong, W.D. Sproul, A.S. Barnett, *Mechanical properties and microstructures of polycrystalline metal/ceramic superlattices, TiN/Ni and TiN/Ni_{0.9}Cr_{0.1}*, paper presented at ICMCTF-20, San Diego, CA, 1993.
- [32] A. Madan, X. Chu, S.A. Barnett, *Appl. Phys. Lett.* 68 (16) (1996) 2198.
- [33] A. Madan, Y.-Y. Wang, S.A. Barnett, C. Engström, H. Ljungcrantz, L. Hultman, M. Grimsditch, *J. Appl. Phys.* 84 (2) (1998) 776.
- [34] J.M. Schneider, W.D. Sproul, A.A. Voevodin, A. Matthews, *J. Vac. Sci. Technol. A* 15 (3) (1997) 1084.
- [35] J.M. Schneider, W.D. Sproul, *Reactive pulsed dc magnetron sputtering and control*, *Handbook of Thin Film Process Technology*, IOP, Bristol, 1998, pp. A5.1:1–A5.1:12.
- [36] S. Vepřek, S. Reiprich, *Thin Solid Films* 268 (1995) 64.
- [37] R.W. Siegel, *Nanophase materials: Structure, defects and properties*, *Proc. ATC Int. Symp. (ACTA)*, October 29–30, Tokyo, Japan (1996) 1.
- [38] P.Yu. Butyagin, *Colloid J.* 59 (1997) 112.
- [39] J. Musil, J. Vlček, *Czech. J. Phys.* 48 (10) (1998) 1209.
- [40] J. Musil, J. Vlček, *Magnetron sputtering of alloy and alloy-based films*, *Thin Solid Films* 343–344 (1999) 47.
- [41] K.D. Leedy, J.M. Rigsbee, *J. Vac. Sci. Technol. A* 14 (1996) 2202.
- [42] J. Musil, *Vacuum* 50 (3/4) (1998) 363.
- [43] J. Musil, A.J. Bell, J. Vlček, T. Hurkmans, *J. Vac. Sci. Technol. A* 14 (4) (1996) 2247.
- [44] J. Musil, F. Regent, *J. Vac. Sci. Technol. A* 16 (6) (1998) 3301.
- [45] J. Musil, H. Poláková, *Hard nanocomposite Zr–Y–N coatings. Correlation between hardness and structure*, 2nd Asian–European Int. Conf. on Plasma Surface Engineering, September 15–19, Beijing, China (1999), Paper No. Sat-0A3-2.

- [46] J. Musil, H. Poláková, V. Cibulka, Czech. J. Phys. 49 (3) (1999) 359.
- [47] J. Musil, I. Leipner, M. Kolega, Surf. Coat. Technol. 115 (1) (1999) 32.
- [48] J. Musil, Z. Soukup, unpublished results.
- [49] J. Musil, H. Hrubý, Superhard nanocomposite $Ti_{1-x}Al_xN$ films prepared by magnetron sputtering, Proc. 14th Int. Symp. on Plasma Chemistry, August 2–6, Praha, Czech Republic, Vol. III (1999) 1605–1610.
- [50] J. Musil, P. Zeman, Vacuum 52 (1999) 269.
- [51] W.L. Johnson, Progr. Mater. Sci. 30 (1986) 81.
- [52] G. Weigang, H. Hecht, G. von Minnigerode, Z. Phys. B 96 (1995) 349.
- [53] J.R. Ding, D.Y. Che, H.B. Yhang, K. Tao, B.X. Liu, Appl. Phys. Lett. 60 (8) (1992) 994.
- [54] M. Mišina, J. Musil, S. Kadlec, Surf. Coat. Technol. 110 (1998) 168.
- [55] Z. Liu, R. Singh, K. Poole, R.J. Diefendorf, J. Harris, K. Cannon, J. Vac. Sci. Technol. B 15 (1997) 1990.
- [56] L. May, W.R. Allen, A.L. Glower, J.C. Mabon, J. Vac. Sci. Technol. B 13 (1995) 361.
- [57] A.A. Voevodin, S.V. Prasad, J.S. Zabinski, J. Appl. Phys. Lett. 82 (2) (1997) 855.
- [58] S. Vepřek, P. Nesládek, A. Niederhofer, F. Glatz, M. Jilek, M. Šima, Surf. Coat. Technol. 108/109 (1998) 138.
- [59] M. Benda, J. Musil, Vacuum 55 (1999) 171.
- [60] Y. Min, Y. Makino, M. Nose, K. Nogi, Thin Solid Films 339 (1/2) (1999) 238.
- [61] C. Louro, A. Cavaliero, Hardness versus structure in W–Si–N sputtered coatings, 6th Int. Conf. on Plasma Surface Engineering, PSE-98, September 14–18, Garmisch-Partenkirchen, Germany (1998), paper no. ThWB5.
- [62] M. Diserens, J. Patscheider, F. Levy, Surf. Coat. Technol. 108/109 (1998) 241.
- [63] C. Mitterer, P. Losbichler, F. Hofer, P. Warbichler, W. Gissler, Vacuum 50 (3/4) (1998) 313.
- [64] C. Mitterer, P.H. Mayrhofer, M. Beschliesser, P. Losbichler, P. Warbichler, F. Hofer, P.N. Gibson, W. Gissler, H. Hrubý, J. Musil, J. Vlček, Proc. ICMCTF'99, April 12–16, San Diego, CA (1999), paper no. BP-16.
- [65] A.A. Voevodin, J.P. O'Neill, J.S. Zabinski, Surf. Coat. Technol. (1999) submitted.
- [66] U. Wahlström, L. Hultman, J.-E. Sundgren, F. Abidi, I. Petrov, J.E. Greene, Thin Solid Films 235 (1993) 62.
- [67] J.E. Field, The Properties of Diamond, Academic Press, London, 1979.
- [68] S.M. Gorbatskin, R.L. Rhoades, T.Y. Tsui, W.C. Oliver, Appl. Phys. Lett. 65 (1994) 2672.
- [69] W.C. Oliver, G.M. Pharr, J. Mater. Res. 7 (1991) 1564.
- [70] S. Vepřek, Thin Solid Films 317 (1998) 449.
- [71] S. Vepřek, Thin Solid Films 297 (1997) 145.
- [72] J. Musil, F. Regent, Structure and microhardness of magnetron sputtered nanocrystalline CrNi–N films, Proc. 14th Int. Symp. on Plasma Chemistry, August 2–6, Praha, Czech Republic, Vol. III (1999) 1617–1622.
- [73] A.A. Voevodin, J.S. Zabinski, J. Mater. Sci. 33 (1998) 319.
- [74] T.Y. Tsui, G.M. Pharr, W.C. Oliver, C.S. Bhatia, R.L. White, S. Anders, A. Anders, I.G. Brown, Mater. Res. Soc. Symp. Proc. 383 (1995) 447.
- [75] A. Cavaleiro, B. Trindale, M.T. Viera, Deposition and characterization of fine-grained W–Ni–C/N ternary films, 6th Int. Conf. on Plasma Surface Engineering, PSE-98, Garmisch-Partenkirchen, Germany, Book of Abstracts (1998) 265.

Electron beam physical vapour deposition of protective films on carbon reinforced carbon

E. Roos, K. Maile, A. Lyutovich *, S. Lauf, H. Kockelmann, A. Gusko

Staatliche Materialprüfungsanstalt (MPA) Stuttgart, University of Stuttgart, D-70569 Stuttgart, Germany

Abstract

Cr and Ti films on C/C–SiC substrates were obtained by ion assisted electron beam physical vapour deposition (IA EBPVD) and EBPVD, interrupting the deposition process and annealing the substrates. The morphology and properties of the films were studied using optical microscopy, scanning electron microscopy and X-ray diffraction (XRD) methods. Ion bombardment of the surface during the metal deposition has an influence on the structure of the grown films: by increasing the ion energy from 200 V to 700 V, the grain sizes are more uniform. X-ray investigations show that residual silicon has an influence on the initial stage of chromium deposition. XRD was also used for measurement of the residual stresses, which depend on the ion energy. © 2000 Elsevier Science S.A. All rights reserved.

Keywords: Carbon/carbon composites; Cr and Ti coatings; Ion assisted electron beam PVD; Morphology; X-ray diffraction

1. Introduction

Carbon/carbon composites (C/C) are very attractive materials because of their low density, high strength and excellent thermal resistance. C/C composites are expected to be used for heat protection and as shielding materials for spacecraft, nuclear fusion, heat exchangers, turbine engines, and for thermal radiators. The practical applications of these composites are remarkably restricted when used in an oxidative atmosphere at high temperatures because of the low resistance against oxidation. One way to protect C/C is through infiltration technology [1]. The C/C materials or C/C construction elements are immersed in molten silicon to form a SiC compound. However, to a large extent Si remains in the C/C material and, because of cracks in the SiC [2], the C/C–SiC composite cannot withstand oxidation and other types of corrosion attack. Surface modification via deposition of protective layers may considerably improve the oxidation and corrosion resistance of C/C–SiC composites.

There are some publications about chemical vapour deposition (CVD) of metals on C/C composites [3,4]. We used ion assisted electron beam physical vapour

deposition (IA EBPVD) for metal coating of C/C composites, taking into consideration that the ion bombardment gives a better control of the deposition process and the resulting adhesion, internal stress, morphology, density, and chemical composition [5–7]. Although metals have higher coefficients of thermal expansion than C/C composites, they are ductile and hence less vulnerable to crack formation.

2. Experimental details

A vacuum chamber equipped with a turbomolecular pump and a 6 kW electron beam evaporator with a 270° beam deflection by a permanent magnet and 10 kV acceleration voltage was used for the deposition of high temperature protective films. With this set-up IA EBPVD was also realised. Ions were generated by the collision of accelerated 10 keV electrons with metal flow ψ . Such interaction causes a partial (about 5%) vapour ionisation.

As coating materials, chromium and titanium were chosen because of their good anti-oxidation and anti-corrosion properties. Moreover, their carbides and silicides resist oxidation. The substrates investigated were:

- C/C–SiC infiltrated in molten Si [1];
- C/C–SiC infiltrated and heat treated [8];

* Corresponding author. Tel.: +49-711-685-3784;
fax: +49-711-685-3053.

E-mail address: lyutovich@mpa.uni-stuttgart.de (A. Lyutovich)

- C/C–SiC infiltrated and SiC covered by CVD [8].

The substrates were precleaned with acetone in an ultrasonic bath and with boiling deionised water. The dried substrates were mounted on the substrate holder. The deposition process was carried out at 600°C on a substrate with emission current of 0.2 A at 10 kV with average rate within 0.5–1 µm/min. To decrease the influence of residual stress, which ultimately causes surface damage, and to increase the maximum coating thickness by EBPVD, we used a periodically interrupting deposition process and annealing (30 min deposition, 30 min annealing without evaporation and deposition, ‘interrupting mode’ [9]). The growth rate was checked ‘in situ’ by a built-in ion detector. By IA EBPVD the bias potential was kept to one of the following levels: 0, –200 V, –500 V and –700 V.

The morphology and properties of deposited chromium and titanium films were studied using optical microscopy, scanning electron microscopy and X-ray diffraction methods. Micrographs were taken to show the overgrowth of cracks and the morphology of the films obtained. The X-ray experiments were performed with a θ –2 θ Siemens diffractometer D5000 using Cu K $_{\alpha}$ radiation of wavelength $\lambda = 1.54$ nm. X-ray diffraction methods were applied in order to study the phases formed at the interface as well as to measure the residual stresses of the metal films at room temperature by $\sin^2 \psi$ method.

2.1. Microscopic results

Optical micrographs [Fig. 1(a)–(c)] show 12 µm thick Ti films on the C/C–SiC (CVD) substrate. The cracks in SiC are partially covered with Ti in the case of EBPVD by interrupting mode and completely covered by application of IA EBPVD. The scanning electron micrographs [Fig. 2(a) and (b)] obtained using the JSM-6400 scanning electron microscope show that the ion bombardment of the surface during the metal deposition has a strong influence on the structure of the grown films: by increasing the ion energy from 200 to 700 eV, the grain sizes become more uniform.

2.2. X-ray diffraction results

The diagram in Fig. 3 presents diffraction spectra of a C/C–SiC material, which was manufactured by infiltration into molten silicon followed by heat treatment. The spectrum taken from the core material shows predominantly wide carbon diffraction peaks. Hence, it may be concluded that the bulk of the core material still consists of carbon which requires protection from oxidation at high temperatures. This protection is provided at the material’s surface by the SiC which was obtained during the carbon’s exposure to silicon. However, the spectrum taken at the surface still shows the presence

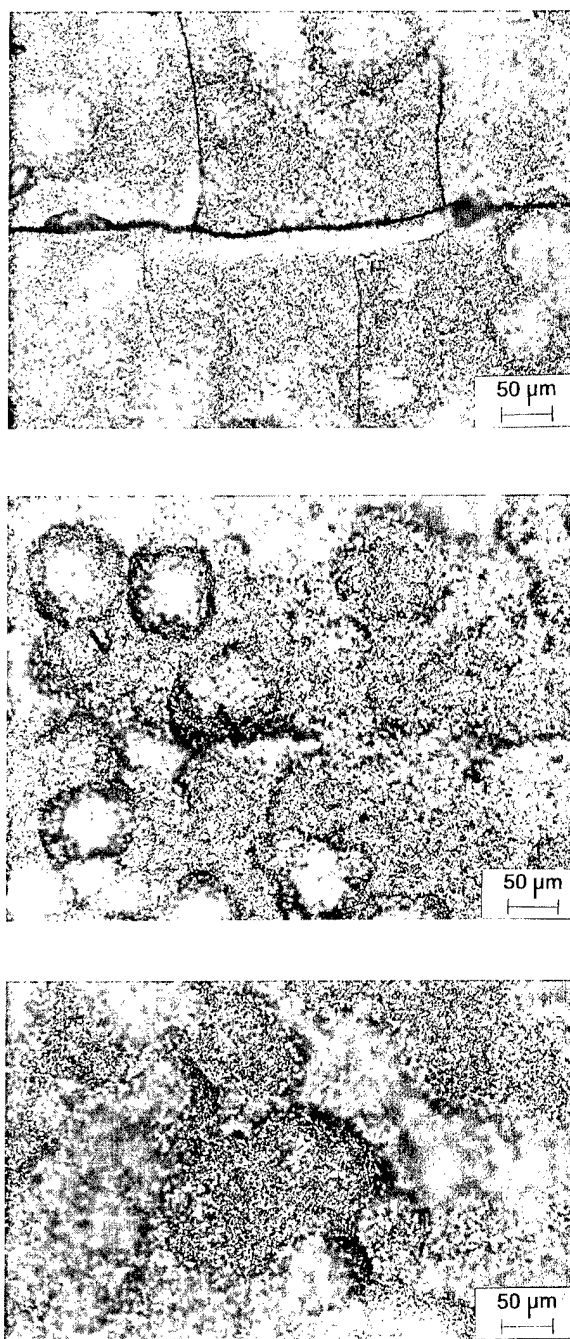


Fig. 1. Surface morphology of C/C–SiC before (a) and after (b, c) Ti coating (light microscopy). (a) C/C–SiC (CVD) before coating (note cracks). (b) C/C–SiC (CVD) Ti-coated by EB PVD with interruption (the cracks are partially covered). (c) C/C–SiC (CVD) Ti-coated by IA EB PVD, BIAS –200 V (the cracks are completely covered).

of carbon. This indicates that there are some limitations with this kind of passivation.

One of the three spectra in Fig. 4 has been taken for a sample of infiltrated C/C–SiC prior to the said heat treatment. Residual silicon may be identified at the surface besides carbon and SiC. Samples of this material were coated with 50 µm titanium and 50 µm chromium. The respective spectra have been included in the dia-

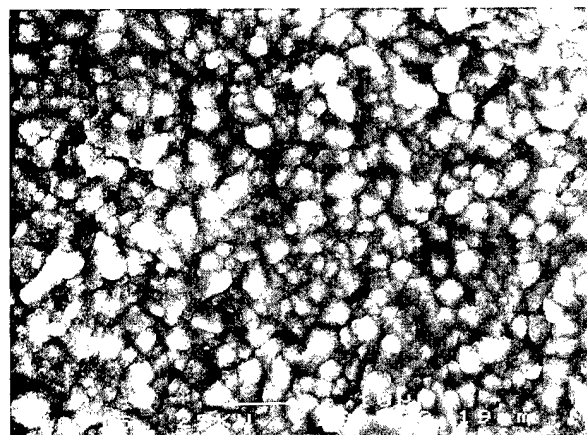
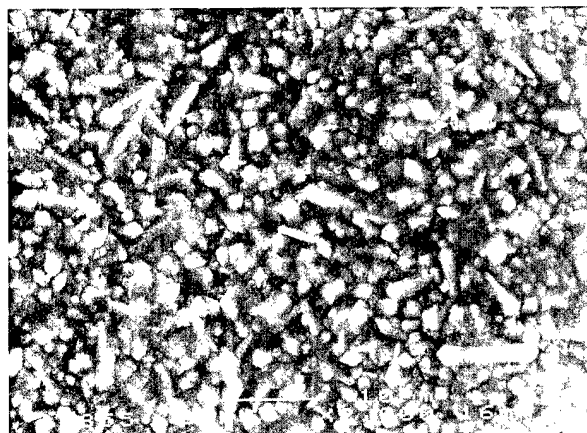


Fig. 2. Scanning electron micrograph showing influence of accelerated ions on the surface morphology of the Ti:C/C-SiC coating. (a) BIAS potential 200 V, (b) BIAS potential 700 V.

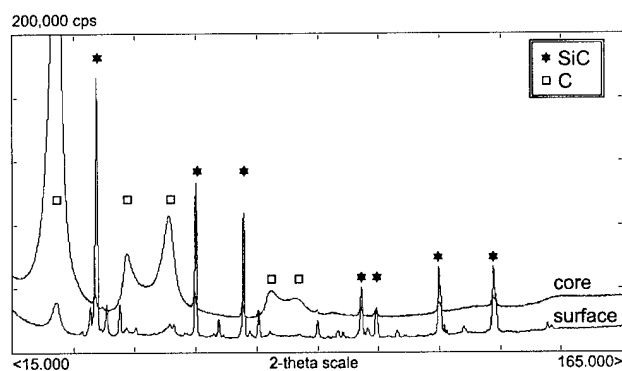


Fig. 3. Distribution of compounds in C/C-SiC X-ray diffraction data.

gram. In particular, in the region $15^\circ \leq 2\theta \leq 30^\circ$ a comparison of the spectra clearly shows that the silicon and carbon have been completely covered by the deposited metals.

In order to study the processes at the initial stage of metal deposition, thin films were deposited. Films of

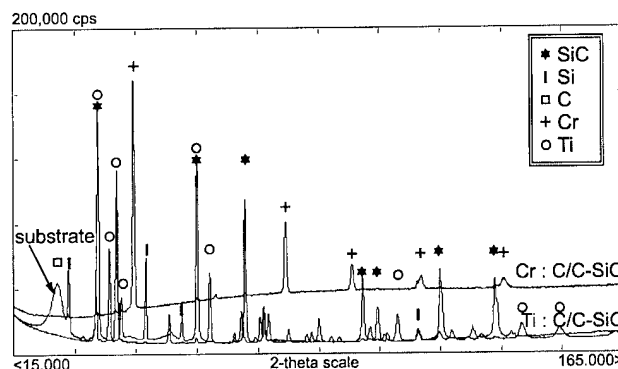


Fig. 4. Si-infiltrated C/C-SiC substrate and coatings of 50 μ m chromium and 50 μ m titanium.

1 μ m chromium were simultaneously deposited on two different substrates: infiltrated C/C-SiC and C/C-SiC additionally processed by CVD. The resulting diffraction spectra are shown in Fig. 5. While the diffraction peaks of chromium are clearly seen in the CVD processed SiC coating, they do not appear in the infiltrated only sample. This finding was confirmed by EDX investigations. It is believed that smaller amounts of chromium diffuse into the comparatively thick layer of residual silicon and evade detection in small concentrations. Chromium diffusion of the initial growth stages can promote adhesion of the metal film and a high protective quality.

Preliminary results of residual stress measurements have shown the stress decreasing in Ti films with the bias potential increasing in the range from 0 to 500 V (see Table 1).

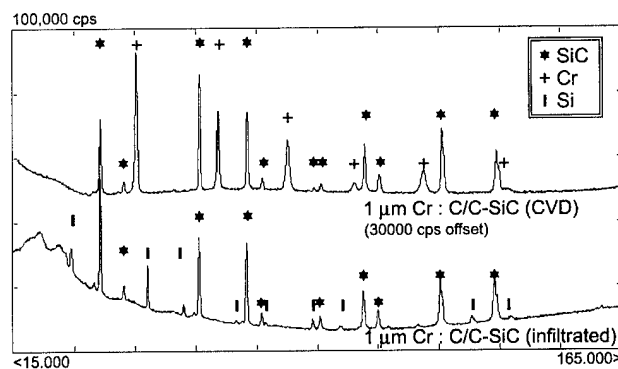


Fig. 5. Influence of residual silicon during the initial deposition of chromium.

Table 1
Residual stresses observed in titanium films

Specimen	Stress (MPa)	
12 μ m Ti: C/C-SiC, 600°C, no bias	160	± 130
12 μ m Ti: C/C-SiC, 600°C, 200 V bias	55	± 25
12 μ m Ti: C/C-SiC, 600°C, 500 V bias	60	± 10

3. Conclusions

1. Cr and Ti films were obtained on several C/C–SiC substrates using electron beam PVD with periodically interrupting deposition process and annealing as well as by accelerated ion assistance.
2. The cracks of CVD SiC coated C/C caused by different expansion coefficients are partially covered by the interrupting process and are completely covered by the ion assisted process.
3. The residual stress of 12 μm thick films on C/C–SiC (CVD) by the ion assisted process (at 200 and 500 V) are three times lower compared to those in films obtained from an ordinary EBPVD process.

Acknowledgement

The authors thank Dr. Ronald Weiss from of Schunk Kohlenstofftechnik GmbH for fruitful discussions and the provision and preparation of the C/C–SiC samples.

References

- [1] W. Krenkel, T. Reimer, Development of extremely lightweight C/C–SiC structures, ESA/estec Workshop on Thermal Protection Systems and High Temperature Materials, Stuttgart, 23–27 October, (1995).
- [2] E. Roos, K. Maile, A. Lyutovich, S. Lauf, H. Kockelmann, A. Gusko, Characterisation of Cr and Ti EB-PVD coatings by X-ray diffraction and scanning electron microscopy, Abstr. 12th Int. Conf. of the Israel Society for Quality, Jerusalem, 1–3 December (1998) 66, full report on CD-ROM.
- [3] T. Piquero, H. Vincent, C. Vincent, J. Bouix, *Carbon* 33 (4) (1995) 455–467.
- [4] Ch. Landry, A. Barron, *Carbon* 33 (1995) 381–387.
- [5] A. Lyutovich, Ionno-Aktivirovannaja Kristallizatsija Plenok (Ion Activated Films Crystallisation), Fan, Tashkent, 1982. in Russian.
- [6] A. Budrevich, A. Lyutovich, B. Oksengendler, 'Radiation Sieve' effect during epitaxy from low energy ion-molecular flow, *Phys. Status Solidi A* 119 (1989) K163–K166.
- [7] A.J. Armini, S.N. Bunker, L.A. Stelmack, Comparison of deposition technologies for ion assisted coatings, in: C.R. Clayton, J.K. Hirvonen, A.R. Srivastava (Eds.), TMS Annual Meeting, Orlando, FL, 9–13 February (1997) 79–90.
- [8] Schunk Kohlenstofftechnik GmbH, Material Data.
- [9] N. Parkansky, R.L. Boxsman, S. Goldsmith, *Surf. Coat. Technol.* 61 (1993) 268–273.

The effect of substrate temperature and biasing on the mechanical properties and structure of sputtered titanium nitride thin films

P. Patsalas *, C. Charitidis, S. Logothetidis

Department of Physics, Aristotle University of Thessaloniki, 54006 Thessaloniki, Greece

Abstract

The mechanical properties of titanium nitride (TiN_x) thin films have been investigated using depth sensing nanoindentation tests. The effects of substrate temperature (T_s) and of substrate biasing (V_b) on the mechanical properties and the microstructure of the TiN_x films were studied. T_s and V_b have strong effect on the film's microstructural characteristics such as density, grain size and orientation. It was found that deposition at high T_s and V_b promotes the growth of (002) oriented films with density close to the bulk density of stoichiometric TiN, indicating the absence of voids and the growth of stoichiometric TiN. The film hardness and elastic modulus were measured using the continuous stiffness measurements technique. It was found that there exists a direct correlation between the film's mechanical properties and microstructure. The films that exhibit the best mechanical performance are those grown along the (002) orientation and being denser and stoichiometric. © 2000 Elsevier Science S.A. All rights reserved.

Keywords: Grain growth; Nano-indentation; Sputtering; Titanium nitride; X-ray diffraction

1. Introduction

Owing to their low electrical resistivity, chemical and metallurgical stability and exceptional mechanical properties, titanium nitride (TiN_x) thin films ($[\text{N}]/[\text{Ti}]=1$) have lately gained much attention in different areas of semiconductor device technology, such as diffusion barriers, gate electrodes in field-effect transistors, contact layers in solar cells and a replacement of polycrystalline Si in very-large-scale integrated circuits (VLSI) [1–4]. For the development of new materials in microelectronic applications, in addition to their electrical properties, their mechanical characteristics may play a significant role on long-term reliability problems. In fact, new advanced metallization materials should combine good electrical properties, comparable to those of the currently used materials, with high hardness and elasticity, fine adhesion on Si and low interface stresses.

In this work, we investigate systematically the effect of deposition conditions (substrate temperature and biasing) of TiN_x thin films on their crystal structure and mechanical properties (hardness H and elastic modulus E) using X-ray diffraction (XRD) and depth sensing nanoindentation tests. It was found that a substrate

temperature (T_s) of between 27 and 400°C does not affect significantly the films' mechanical properties. On the other hand there is a direct correlation of all the mechanical properties with bias voltage (V_b), that is, hardness and elastic modulus showed increasing values with negative V_b . The variation of the TiN_x mechanical performance is correlated with the film microstructural characteristics such as composition, grain size and orientation and density/voids content.

2. Experimental

The TiN_x films were deposited on n-type c-Si(001) by DC reactive magnetron sputtering from a Ti target of purity 99.95%, using an Alcatel SCM600 deposition system. The base pressure of the deposition chamber was as low as 2×10^{-8} mbar. The Si wafers were cleaned in air using standard chemical etching (tetra-chloro-ethen/acetone/methanol/hydrofluoric acid 0.1N) and in vacuum with dry low energy Ar^+ ion etching in order to remove the native SiO_2 . The deposition was performed at target power of 450 W and with variable parameters the deposition temperature T_s (from room temperature to 400°C) and the V_b applied on the substrate (from –100 to 0 V). The film thickness was

* Corresponding author. Tel.: +30-31-998127; fax: +30-31-246484.
E-mail address: ppats@skiathos.physics.auth.gr (P. Patsalas)

calculated by spectroscopic ellipsometry (SE) and was, in all cases, ca. 100 nm. The TiN_x film composition was estimated by SE data and analysis by the Bruggeman effective medium theory (BEMT) [6,7], in combination with X-ray photoelectron spectroscopy (XPS) results; $x=[\text{N}]/[\text{Ti}]$ varied between 1 and 1.15 [5]. The working (Ar) and reactive (N_2) gasses were of 99.999% purity. During deposition, the flow rates were 15 sccm for Ar and 2.3 sccm for N_2 .

After deposition, X-ray reflectivity and diffraction (XRR/XRD) and stress measurements, by the Cantilever laser beam (CLB) technique, experiments were conducted in order to study the TiN_x density, crystal structure and internal stress, respectively. For the XRD experiments we used a Siemens D-5000 diffractometer equipped with a $\text{Cu K}\alpha$ X-ray tube, a Goebel mirror [8] and a reflectivity sample stage (RSS). The XRD experiments were performed in the form of θ - 2θ scans (Bragg-Brentano geometry) with generator current and voltage 40 mA and 40 kV, respectively. The XRR experiments were performed using RSS and were described elsewhere [9].

The hardness H and the elastic modulus E of the films were measured by nanoindentation experiments performed using continuous stiffness measurements (CSM) [10] with a nano indenter XP system. For the CSM experiments a Berkovich-type, three-sided pyramid diamond indenter with nominal angle of 65.3° between the tip axis and the faces of the pyramid was used. The CSM allows H and E to be determined as a function of depth with a single indentation [10,11]. In all CSM depth-sensing tests, a total of ten indents were averaged to determine the mean H and E values for statistical purposes. The system has load (displacement) resolution of 50 mN (<0.01 nm).

3. Results and discussion

Sputtered TiN_x films were found to exhibit exceptional mechanical performance in combination with very good electrical properties [12] making them potential candidates for metallization materials in VLSI technology. Scratch tests (not presented here) have shown that the TiN_x films are highly elastic and adherent on the Si substrates. The internal stress, measured by CLB, in the TiN_x films varies with V_b and in all cases is limited below 2 GPa providing excellent mechanical stability (no failure or changes were observed after several months).

The deposition conditions have a strong influence on the mechanical performance of the sputtered TiN_x films. Their hardness and elastic modulus range from 17 to 24 GPa and 210 to 320 GPa, respectively. The load-displacement curves, to the same contact depth, for two representative TiN_x films, 100 nm thick, measured by

single, conventional nanoindentation are shown in Fig. 1. The cross-circles correspond to a TiN_x film deposited with $V_b = -100$ V at $T_d = 400^\circ\text{C}$ and exhibit $H = 24$ GPa and $E = 320$ GPa, while the solid squares correspond to a film deposited with $V_b = -40$ V at 27°C and exhibit $H = 17$ GPa and $E = 210$ GPa. These considerable variations are attributed to the different TiN_x film microstructure developed due to the different growth mechanisms affected by the deposition conditions.

The variations of hardness and elastic modulus with V_b are presented in Fig. 2. Both quantities increase with increasing negative V_b . This is attributed to several independent strengthening mechanisms affected by:

1. the TiN_x lattice parameter and stoichiometry and the corresponding oxidation effects;
2. grain size and orientation; and

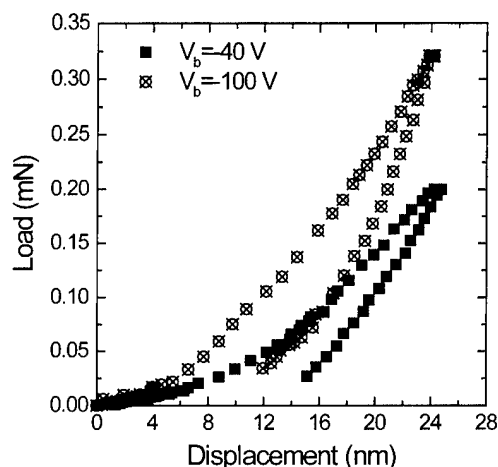


Fig. 1. Load-displacement curves from two representative TiN_x films. The soft film (\blacksquare) is deposited with $V_b = -40$ V and at 27°C while the hard film (\oplus) with $V_b = -100$ V and $T_d = 400^\circ\text{C}$.

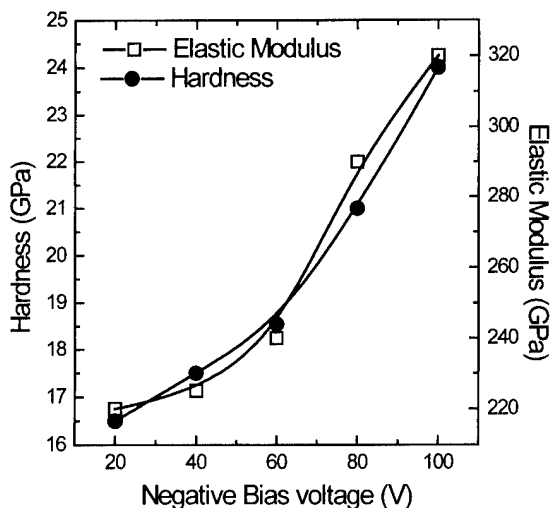


Fig. 2. The variations of the hardness H and the elastic modulus E of the TiN_x films with V_b .

3. the density increase and the elimination of voids.

All the above effects are related to the adatom mobility and the ion–solid interactions taking place close to the active growing surface during deposition of TiN_x films under negative V_b . The substrate temperature does not affect significantly the mechanical behaviour of TiN_x films (we have observed very slight increase of H , E with high dispersion of the experimental data) because of the slight changes of all the above quantities with T_s .

The quantitative study of the mechanisms contributing to the enhancement of TiN_x mechanical performance, requires a detailed study of the corresponding TiN_x microstructural characteristics. Although the fcc-structure of TiN_x films has been identified for a wide range of V_b and T_s , several microstructural characteristics such as density (or voids concentration), lattice parameter, grain size and orientation are affected by these deposition conditions. The increase of V_b and/or T_s increases the mobility of adatoms promoting closed packed structures in near thermodynamic equilibrium conditions [13]. Thus, for high adatom mobility the TiN_x films are expected to grow along the (002) orientation corresponding to that with the lowest surface free energy [14]. On the other hand, for low adatom mobility the preferred orientation is the (111) in which the highest number of atoms per unit area can be incorporated at low energy sites. Indeed, all of our films exhibited the (111) and/or (002) orientations. The amounts of grains grown along the (002) and (111) orientations play a significant role on the mechanical performance of TiN_x films, as we will discuss below.

Fig. 3 shows detailed highlights from X-ray diffractograms of the two marginal cases of the deposited TiN_x specimens, that is, a film deposited at low T_s

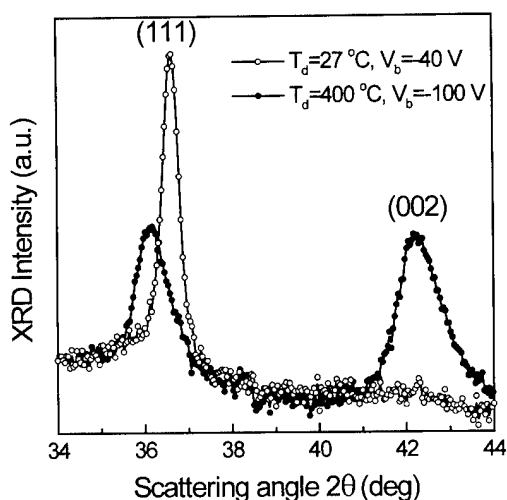


Fig. 3. Highlights from X-ray diffractograms of TiN_x films deposited at $T_d = 27^\circ\text{C}$ and $V_b = -40\text{ V}$ (○) and at $T_d = 400^\circ\text{C}$ and $V_b = -100\text{ V}$ (●).

(27°C) and V_b (-40 V) with low adatom mobility (open circles) and a film deposited at high T_s (400°C) and V_b (-100 V) with high adatom mobility (solid circles). The films exhibit considerable changes on both lattice parameter and grain orientation as it is observed by the position of the (111) reflection and by the relative strength of the (111) and (002) reflections, respectively. The film internal stresses, measured by CLB, were 0.3 and 2 GPa, respectively.

In order to study quantitatively the structural characteristics of the TiN_x films we followed a fitting procedure that includes background subtraction and simulation of the XRD reflections by Voigt curves. The fitting calculates the (111) and (002) XRD reflections' angular position/inter-planar spacing, the broadening and the area below them.

The lattice parameter a is calculated by the inter-planar spacing d_{111} of the (111) reflection through the relation $d_{111} = a\sqrt{3}^{-1/2}$. It was found that a increases from 0.424 to 0.430 nm with changing V_b from -20 to -100 V . A slight increase was observed in the lattice parameter with increasing T_s . Considering that the lattice parameter of the bulk, stoichiometric TiN is 0.424 nm [15], most of our films are in-plane compressed, in agreement with the CLB observations. This behaviour is commonly observed in physical vapour deposited TiN_x films [16,17], especially for high ion flux incorporated during film growth [13]. Although the increasing negative V_b promotes the formation of greater grains, as it was found by transmission electron microscopy (TEM) [18], the XRD reflections become broader. This is attributed to the compressive stresses causing strain in the TiN_x grains. The films with lattice parameter $\sim 0.430\text{ nm}$ were found (by XPS) to be stoichiometric ($x=1$). The intense ion bombardment of the surface atoms induces the elimination of the weakly bonded nitrogen sites around the grain boundaries contributing to the enhancement of the TiN_x mechanical performance.

In addition to the above, the observed decrease of hardness at low V_b can be attributed to oxidation of the TiN_x films deposited at low V_b [19]. The composite $\text{TiN}_x/\text{TiO}_2$ films is expected to be less hard than the stoichiometric TiN (deposited at high $|V_b|$) since the hardness of the TiO_2 is well below 15 GPa [20]. The oxidation process and its effect on the mechanical performance of TiN_x is a complicated issue and its study is beyond the scope of the present article.

The mechanical behaviour of TiN_x films is also governed by the preferred growth orientation, since TiN_x is an anisotropic material with $E_{001} > E_{111}$ [where E_{001} and E_{111} are the elastic moduli along the (001) or (002) and (111) crystallographic direction, respectively] [21]. Considering that the (111) and (002) XRD reflections are not equally strong [the (111) is 75% of (002)], we will define the normalized texture parameter T as:

$T = 0.75 I_{002} / I_{111}$, where I_{111} and I_{002} are the area below the corresponding XRD reflections that represents the fraction of grains grown along the (111) and (002) orientation, respectively. T illustrates the relative amount of grains grown along the (111) and (002) orientations. T is called 'normalized' because for $T=1$ there is no preferred orientation. For $T < 1$ the film exhibits (111) texture while for $T > 1$ exhibits (002) texture.

Fig. 4 shows the variation of the normalized texture parameter with negative V_b . There is a linear relation between T and V_b that is attributed to the higher adatom mobility for high V_b (> 50 V) promoting the growth along the (002) orientation that corresponds to the lowest surface free energy. It was also found a similar correlation between T and T_s . For $T_s < 150^\circ\text{C}$ there is pure (111) texture ($T=0$) while for $T_s > 150^\circ\text{C}$ there exist a linear relation between T and T_s . However, the effect of T_s on the growth orientation is weaker than the effect of V_b , since T is limited to below 0.4 even at 400°C . By taking into account the $T=2.7$ value (found for the film deposited at 400°C and $V_b = -100$ V) and the slope of the T versus T_s straight line, we calculate that this T value corresponds to deposition at 1930°C (close to the melting point of TiN). Thus, the effect of the ion bombardment for $V_b = -100$ V is equivalent with deposition at 1530°C .

Fig. 5 illustrates the variation of H and E with T . The increase of H and E with T can be explained by the TiN_x anisotropy or the higher value of E_{001} with respect to E_{111} . The contact area of the Berkovich-type indenter used in our experiments was calculated to be $1.5 \times 10^4 \text{ nm}^2$ while the average TiN_x column (grain) diameter was measured, by TEM [18], to be 10–30 nm; consequently, during nanoindentation experiments we

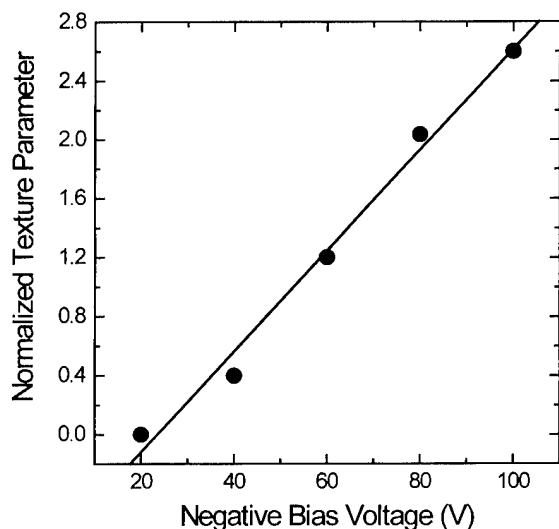


Fig. 4. The normalized texture parameter $T = I_{002}/0.75I_{111}$ versus V_b . For $V_b > 50$ V a (002) texture was observed.

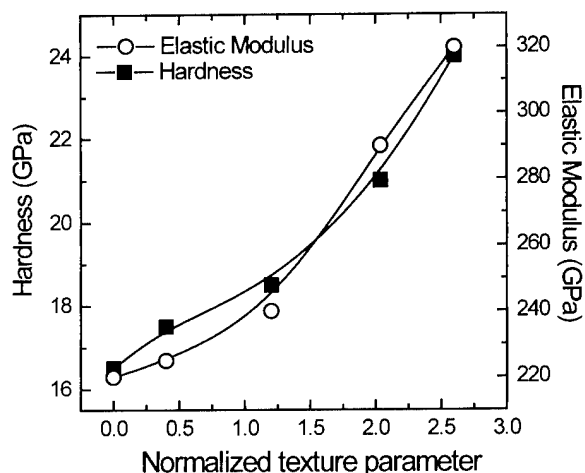


Fig. 5. The hardness and elastic modulus of TiN_x films versus the normalized texture parameter. The (002) texture promotes the enhancement of H and E values.

measure the average H and E of 20–190 grains. These average H and E values describe the mean behaviour of both (002) 'elastic' and (111) 'less-elastic' grains.

The adatom mobility during deposition has also a strong effect on TiN_x film density and voids concentration. In particular, the negative V_b or elevated T_s increase the average energy per adatom of the growing film converting the porous, columnar structure of TiN_x to a more compact stacking. Both increasing V_b and T_s result to density increase attributed to the elimination of voids. The density and voids concentration were calculated by XRR data analysis. Information on the TiN_x film density (ρ) is deduced by XRR through the dependence of the reflection coefficient on the angle of incidence [9]. The XRR measurements were analysed using a Monte-Carlo algorithm assuming a single-layer model of stoichiometric TiN on an atomically smooth c-Si(001) substrate. The maximum measured density was 5.7 g cm^{-3} for a film deposited at 400°C and $V_b = -100$ V. This value is 5% higher than the density of the bulk, unstrained, stoichiometric TiN [15]. The voids volume fraction was calculated using this maximum density as normalization constant ρ_{norm} through the relation: $\text{voids}\% = 100\% \times (\rho_{\text{norm}} - \rho_{\text{exp}}) / \rho_{\text{norm}}$, where ρ_{exp} is the experimentally measured density of each TiN_x film. In the above analysis, we assumed that the film deposited at 400°C and $V_b = -100$ V has no voids. This assumption is also supported and confirmed by SE data analysis with BEMT [7].

Fig. 6 shows the evolution of density and voids volume fraction with V_b . The density increase is attributed to the elimination of voids with V_b , as it is shown by the agreement between the independent results of XRR and SE concerning the voids. A similar variation of the density/voids was also found for the T_s . However, the effect of V_b is much stronger (variation 25%) than

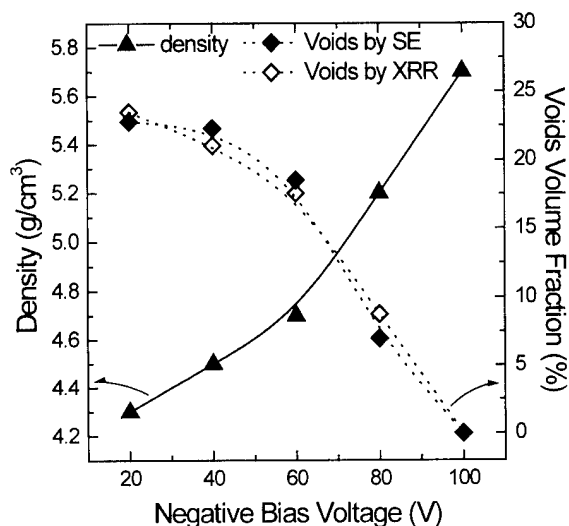


Fig. 6. The effect of V_b on the density and voids concentration of TiN_x films.

the one of T_s (variation $<10\%$ for deposition up to 400°C). TiN_x films exhibit a columnar growth, with column size and inter-columnar spacing depending on V_b and T_s [18]. The voids measured by XRR/SE are located in both inter-columnar spacing and near the grain boundaries within the columns.

The density/voids effect on the H , and E of the TiN_x is illustrated in Fig. 7. Both H and E increase linearly with density up to 24 and 320 GPa, respectively, for $\rho = 5.7 \text{ g cm}^{-3}$. Considering that further condensation of TiN_x above 5.7 g cm^{-3} cannot be achieved and that at the higher V_b values the stoichiometry does not change significantly [5,12], the measured values of H and E are close to the upper limit for TiN_x films deposited by the conventional magnetron sputtering technique. The only way to achieve further improvement

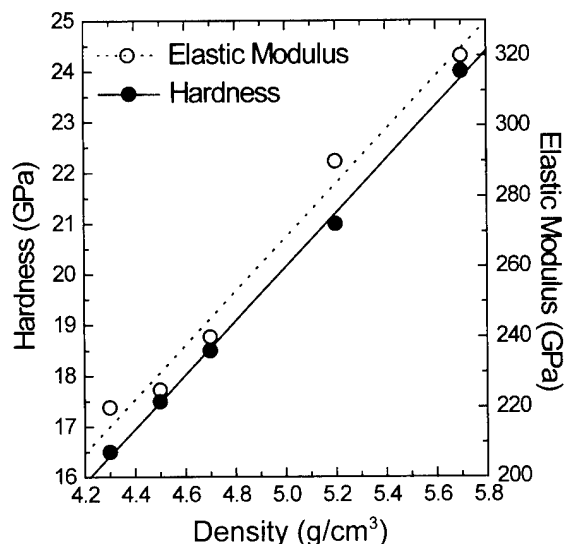


Fig. 7. The variation of H and E with TiN_x density.

of TiN_x performance could be a more oriented growth along the (002) orientation that can be achieved by higher ion flux [13].

4. Conclusions

Four independent mechanisms were found to contribute to the enhancement of the TiN_x mechanical performance:

1. TiN_x stoichiometry and lattice parameter;
2. (002) preferred growth orientation;
3. density increase (elimination of voids); and
4. prevention of oxidation.

Two of those (2 and 3) are governed by the adatom mobility during deposition that is affected by substrate temperature and biasing. Both temperature and biasing increase adatom mobility, with the bias effect being considerably stronger. Furthermore, the increase of bias results to stoichiometric ($x=1$) TiN films due to the sputtering of the weakly bonded nitrogen excess close to the grain boundaries. The lack of N-excess atoms in stoichiometric films prevents oxidation and enhances the TiN_x film's mechanical properties.

Acknowledgement

This work was supported in part by the BRITE-EURAM-CT96-0265 project.

References

- [1] M. Wittmer, B. Studer, H. Melchior, J. Appl. Phys. 52 (1981) 5722.
- [2] T. Hara, A. Yamanoue, H. Iio, K. Inoue, G. Washidzu, S. Nakamura, Jpn. J. Appl. Phys. 30 (1991) 1447.
- [3] W. Cheung, H. von Seefeld, M.A. Nicolet, F. Ho, P. Iles, J. Appl. Phys. 52 (1981) 4297.
- [4] R.C. Glass, L.M. Spellman, S. Tanaka, R.F. Davis, J. Vac. Sci. Technol. A 10 (1992) 1625.
- [5] S. Logothetidis, E. Meletis, G. Kourouklis, J. Mater. Res. 14 (1999) 436.
- [6] D.E. Aspnes, Thin Solid Films 89 (1982) 249.
- [7] P. Patsalas, C. Charitidis, S. Logothetidis, Appl. Surf. Sci. (1999) in press.
- [8] H. Schuster, H. Goebel, Adv. X-Ray Anal. 39 (1996) 1.
- [9] S. Logothetidis, G. Stergioudis, P. Patsalas, Surf. Coat. Technol. 100 (1998) 295.
- [10] W.C. Oliver, G.M. Pharr, J. Mater. Res. 7 (1992) 1564.
- [11] C. Charitidis, S. Logothetidis, P. Douka, Diamond Relat. Mater. 8 (1999) 558.
- [12] P. Patsalas, S. Logothetidis, C.A. Dimitriadis, MRS Proc. 569 (1999) 313.
- [13] J.E. Greene, J.E. Sundgren, L. Hultman, I. Petrov, D.B. Bergstrom, Appl. Phys. Lett. 67 (1995) 2928.
- [14] J.E. Greene, in: D.T.J. Hurle (Ed.), Handbook of Crystal Growth vol. 1 Elsevier, Amsterdam, 1993.

- [15] JCPDS Powder Diffraction File 38-1420.
- [16] A.J. Perry, V. Valvoda, D. Rafaja, *Thin Solid Films* 214 (1992) 169.
- [17] A.J. Perry, *Thin Solid Films* 193/194 (1990) 463.
- [18] B. Pecz, N. Frangis, S. Logothetidis, I. Alexandrou, P.B. Barna, J. Stoemenos, *Thin Solid Films* 268 (1995) 57.
- [19] S. Logothetidis, E. Meletis, G. Stergioudis, A. Adjaottor, *Thin Solid Films* 338 (1999) 304.
- [20] M.J. Mayo, R.W. Siegel, A. Narayanasamy, W.D. Nix, *J. Mater. Res.* 5 (1990) 1073.
- [21] J.O. Kim, J.D. Allenbach, P.B. Mirkarimi, S.A. Barnett, *Phys. Rev. B* 48 (1993) 1726.

Pulsed-plasma assisted magnetron methods of depositing TiN coatings

J. Walkowicz ^{a,*}, K. Miernik ^a, A. Zykov ^b, S. Dudin ^b, V. Farenik ^c

^a *Institute for Terotechnology, ul. Pulaskiego 6/10, 26-600 Radom, Poland*

^b *Kharkov State University, 31 Kurchatov avenue, Kharkov 310108, Ukraine*

^c *Scientific Center of Physical Technologies, 1 Novgorodskaya street, Kharkov 310145, Ukraine*

Abstract

Results are presented of an investigation of the deposition processes of TiN coatings by stationary magnetron discharge, with the addition of high-voltage pulses (0–2 kV) applied to the plasma source electrodes or to the substrate. Two different configurations of deposition system were investigated: (1) a hybrid plasma source, which is the combination of a direct-current (DC) magnetron with a Marshall gun; and (2) radio-frequency (RF)-sustained DC magnetron with a pulse biased processed sample. The results of studies on both the discharge characteristics and the properties of the deposited TiN coatings are presented. The influence of pulsed ion bombardment on the chemical composition of the deposited coatings is shown. © 2000 Elsevier Science S.A. All rights reserved.

Keywords: Hybrid plasma source; Pulsed discharge; RF magnetron; TiN coatings

1. Introduction

Nowadays, pulsed ion-plasma processing is finding increasingly broader application in the production of various devices and tools for microelectronics, engineering, medicine, etc. The methods of pulsed ion-plasma technology allow one to reduce the temperature of a treated sample, to increase the adhesion and density of deposited films, to improve the quality of coatings on dielectric surfaces, and to deposit multilayer coatings [1–3]. Various constructions of ion-plasma system for pulsed processing of materials are described in the scientific literature, as well as the technological processes of deposition for different coatings based on these systems. The aim of the present research was to clarify the potential capabilities of pulsed processing for the technology of TiN coatings deposition. Pulsed processing can be realized either by igniting a pulsed discharge inside the technological volume or by sustaining a stationary discharge and applying a pulsed bias to the substrate. A new hybrid plasma source (HPS) [4–6] and a radio-frequency (RF)-sustained direct-current (DC) magnetron were developed to realize both the

pulsed discharge mode and the pulsed substrate mode. The common peculiarity of these two hybrid discharges is the ability of independent plasma creation, target sputtering, and formation of plasma flows to the substrate. Owing to this feature, these devices allow wide-ranging control of the basic parameters of coating deposition processes, such as mass transfer, energy and ionization degree of material flow, power flow to the substrate, and pressure and composition of the working gas.

2. Experimental systems

Two different configurations of deposition system were investigated: the hybrid plasma source, which is the combination of a DC magnetron with a Marshall gun; and RF-sustained DC magnetron with pulse biased substrates (Fig. 1). The hybrid plasma source [Fig. 1(a)] consists of two coaxial, water-cooled titanium electrodes and a circular magnetic system (Nd–Fe–B), which is located coaxially to them. The value of the component of magnetic-field induction, parallel to the cathode surface, was 50 mT. The external electrode is a cylinder with an inside diameter of 90 mm and length of 140 mm.

* Corresponding author. Tel.: +48-484-3884; fax: +48-484-4760.

E-mail address: jan.walkowicz@itee.radom.pl (J. Walkowicz)

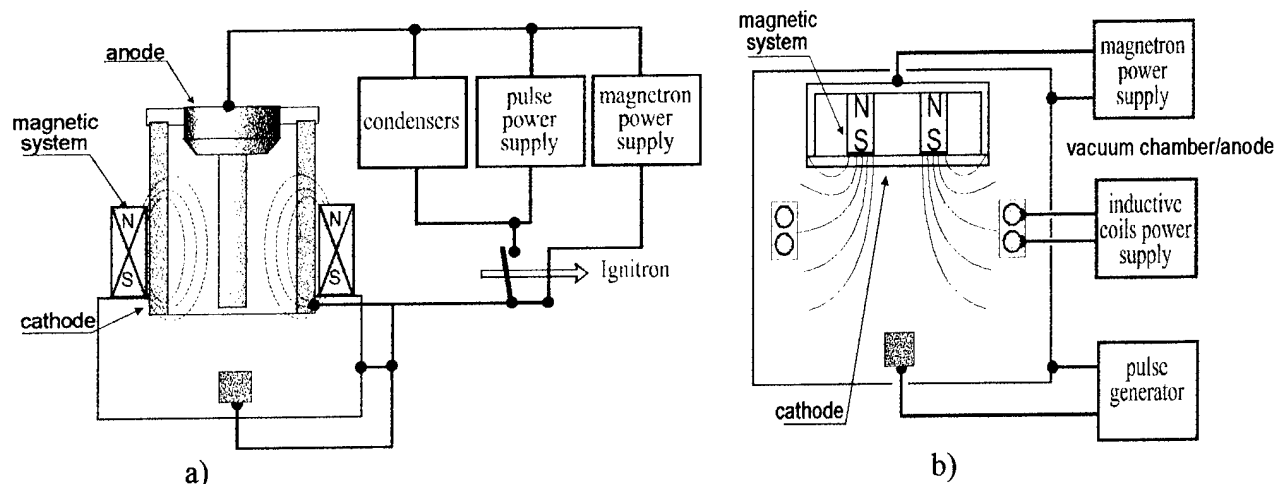


Fig. 1. Schematic illustrations of the experimental apparatus: (a) pulse hybrid plasma source; (b) RF-sustained DC magnetron with pulse bias voltage.

The internal electrode is an arbor with diameter of 18 mm and length of 140 mm. On evacuation of the chamber to a given pressure, a voltage of 300–800 V is applied to the source electrodes and the process of cathode sputtering follows. At the same time, a high voltage (1–2 kV of 0.2 Hz frequency) is applied to the electrodes. This initiates pulsed discharge in the inter-electrode area which, in turn, results in evaporation of the anode material and ejection of the discharge plasma from the source. Crystallization products were deposited on substrates located at the axis of the deposition chamber at the distance of 50, 150 and 250 mm from the source outlet.

Fig. 1(b) shows the principal scheme of the RF-sustained DC magnetron with pulse bias voltage. An ordinary planar magnetron with permanent magnets, with a titanium target of diameter 130 mm, is mounted inside the working vacuum chamber of 250 mm diameter (ambient gas pressure, 5×10^{-6} mbar). The maximum value of the radial component of magnetic-field induction at the target surface was 50 mT. The target and working chamber are cooled by a water flow. A two-coil inductor 180 mm in diameter, made from 4 mm copper tube and shielded by ceramic insulators, is located axisymmetrically inside the chamber between the target and the substrate holder in the region of weakly inhomogeneous magnetron magnetic field, with induction of 1.5–2.0 mT. The distance between the target and substrate holder was 150 mm. The substrate holder was electrically insulated from the chamber for the possibility of applying negative stationary and pulsed bias voltages. The DC magnetron power supply was provided by a 2 kW current source with falling volt-ampere characteristics and open-circuit voltage of 6 kV. RF power was applied to the inductor via a matching circuit from a 1 kW RF generator with frequency of 13.56 MHz. Substrates for the deposition of TiN coatings, made of high-speed steel, had the shape of rectan-

gular prisms with dimensions of 6 mm \times 12 mm \times 16 mm (for the hybrid source) or disks with diameter of 25 mm and thickness of 6 mm (for RF-sustained DC magnetron).

3. Results

3.1. Stationary discharge characteristics

Fig. 2 represents the volt-ampere characteristics of the cylindrical magnetron discharge in the hybrid plasma source and combined RF inductive-magnetron discharge for various values of working gas pressure.

The curves in Fig. 2(a) are typical for a cylindrical magnetron [7] and demonstrate the existence of two modes: a high-current mode at $p > 4 \times 10^{-3}$ mbar and a low-current/high-voltage mode at lower pressures. As follows from Fig. 2(b), for combined RF-sustained DC magnetron discharge, the relative magnetron contribution to ionization of the working gas is decreasing with the pressure decrease. This contribution was also found to decrease with the RF power increase. In fact, such system allows one to realize a smooth transition from the pure magnetron discharge at $p > 10^{-3}$ mbar to the combined discharge at $p < 10^{-3}$ mbar.

3.2. Substrate pulse current characteristics

In the experiments carried out, impulse bias voltage was applied to the substrates. In the case of the hybrid source, the voltage induced on the substrate was dependent on the impulse discharge voltage of the source and varied in the range of 1–2 kV. In the system with the RF-sustained DC magnetron, the bias voltage was changed in the range of 0–1.5 kV. Typical oscillograms of substrate current in the pulse hybrid plasma source

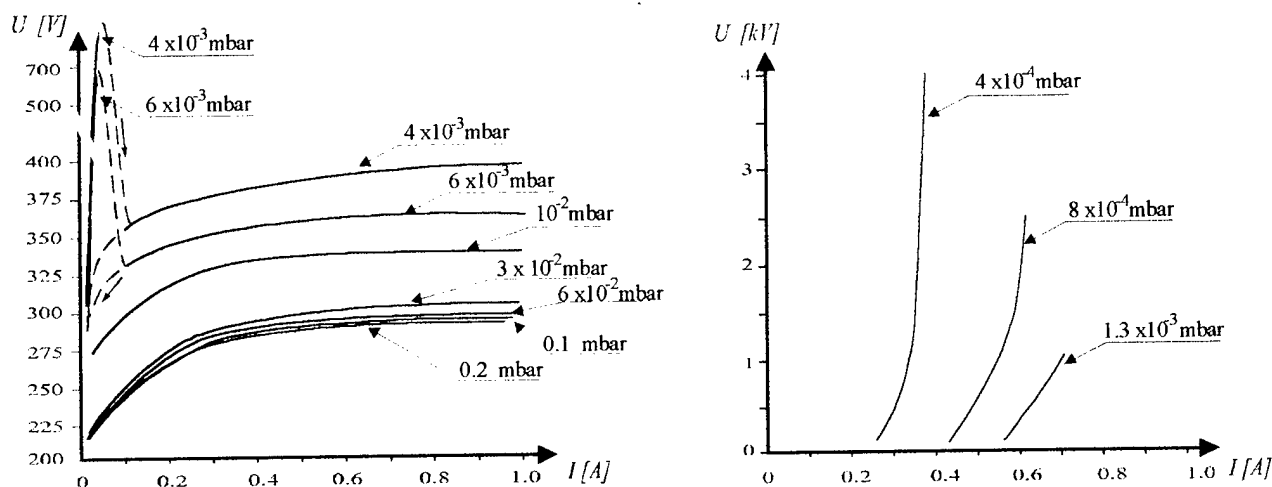


Fig. 2. Volt-ampere characteristics of the discharges (working gas: argon): (a) hybrid plasma source discharge; (b) combined RF-sustained DC magnetron discharge.

and combined RF inductive-DC magnetron discharge are shown in Fig. 3.

As can be seen from the substrate current oscillograms, the characteristic feature of both deposition methods is pulsed ion bombardment of the substrate. The pulsed ion bombardment of a film being deposited in a usual way, for example by magnetron sputtering, is desirable for surface activation and increasing the adhesion and density of the film. An important feature of the hybrid plasma source is ability to generate both flow of deposited material and pulsed flows of accelerated ions. Investigations of this feature revealed a correlation between current impulses on the substrate and voltage impulses on the anode in the high-voltage phase [8]. This appears to testify to the electrostatic nature of ion acceleration. In combined RF inductive-DC magnetron discharge deposition, a pulsed substrate bias activates chemical reactions on the substrate. This is provided by forming a flow of ions from the plasma to the substrate. If DC bias voltage is used for this purpose, the ability to control the flow is limited in as far as the voltage

magnitude is strictly defined by the activation energy of the reaction. Voltage increase shifts the growth/sputtering balance to sputtering dominance, thus decreasing the deposition rate, and also heats the substrate. Therefore, in order to optimize the processes of coating synthesis, the ability to control independently the energy and the intensity of the ion flow to the substrate is necessary. One way to realize such a possibility is to apply a pulse bias voltage to the substrate holder with a period that is less than the time of formation of a monolayer coating (in this case, the ion flow can be considered as quasi-stationary and equal to $j_0 = j_p / \delta$, where j_0 is the time-averaged ion current density, j_p is the ion pulse current density and $\delta = T/\tau$ is the off-duty factor).

3.3. Chemical composition of deposited coatings

The physical conditions of the experiment to deposit TiN coatings are given in Table 1.

The influence of deposition conditions on the thick-

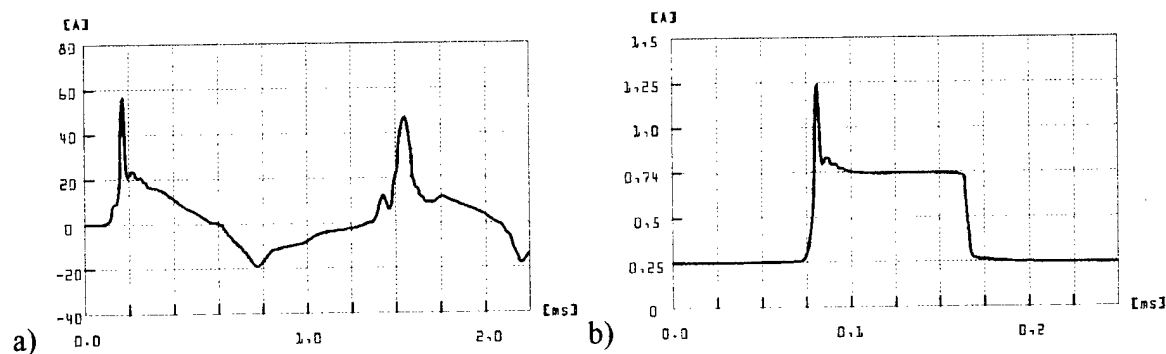


Fig. 3. Oscillograms of substrate current: (a) pulse hybrid plasma source deposition (N_2 pressure, 7×10^{-3} mbar; magnetron discharge current, 0.5 A; maximum anode voltage, 1 kV; maximum anode current, 8 kA); (b) combined RF-sustained DC magnetron discharge deposition (N_2 pressure, 5.5×10^{-5} mbar; magnetron discharge current, 0.3 A).

Table 1
Physical conditions of the deposition experiment

	Pulsed hybrid source	RF-sustained DC magnetron with pulsed bias
Composition of the atmosphere	10% N ₂ +90% Ar	10% N ₂ +90% Ar
Pressure of the atmosphere (mbar)	7×10^{-3}	$3.5 \times 10^{-5}/5.5 \times 10^{-5}$
Pulse length (μ s)	500	1–500
Pulse repeat rate	0.2 Hz	0–200 kHz
Off-duty factor	10 000	1–20
Pulse power	Up to 1 MW	Up to 4 kW
Average power (W)	20	Up to 200

ness and chemical composition of coatings obtained with the hybrid plasma source is shown in Figs. 4 and 5, respectively.

The coatings investigated were deposited in 3000 impulses in the impulse mode and in the equivalent time of 4 h 10 min in the magnetron mode. The deposition ratio reached in experimental conditions is low. The impulse plasma flow from the hybrid source exerts a distinct influence on the thickness of coatings deposited on substrates localized close to the source outlet (50 mm). This means that a small amount of sputtered material is transported by the single plasmoid ejected from the hybrid source. This observation confirms results of the authors' theoretical analysis of the hybrid source work [6]. In order to increase the amount of ejected electrode material and thus the deposition rate, the power dissipation of the magnetron discharge should be increased. Investigation of the chemical composition of the coatings, by means of the energy-dispersive

spectroscopy (EDS) method, revealed that it is constant irrespective of the distance of the substrate from the source outlet (Fig. 5). This testifies to high homogeneity of the reactive, impulse gas-metallic plasma generated in the hybrid source.

When depositing coatings with use of the combined RF-sustained DC magnetron discharge, the maximum ranges of pulse bias voltage and dimensionless off-duty factor were used [$U_b=0$ –1.5 kV, $\delta=1$ (stationary bias) to 40], the other conditions being fixed (pressure and composition of the Ar+N₂ mixture, ion pulse current density, sputtering rate of the titanium target). The average deposition rate reached with this deposition method is high: $3 \mu\text{m h}^{-1}$. Analysis of the coatings obtained by pulse and stationary bias voltages showed the following: (1) the deposition rate increased by 30% in the pulsed bias mode for bias voltage $U_b < 100$ V; and (b) for $U_b=300$ V in the stationary bias mode sputtering dominates over the deposition, whereas for pulsed bias mode deposition dominated up to 1.5 kV bias voltage. Analysis of the chemical composition of coatings deposited at high bias voltage and high off-duty factor showed the presence of carbon (up to 17%). In our opinion, the carbon incorporated in the coatings came from the steel substrates, as a result of their decarburization caused by impulse heating to high temperatures. Investigations revealed that both the stoichiometry of TiN and the amount of carbon impurities depend on the deposition conditions (Fig. 6). At lower pressure of the deposition process (3.5×10^{-5} mbar) the coating stoichiometry depends on the off-duty factor [Fig. 6(a)]. With increasing off-duty factor the titanium content in the coating decreases and it becomes more contaminated by carbon from the vacuum system. At higher pressure of the atmosphere (5.5×10^{-5} mbar), increase of the off-duty factor up to 5 has no influence on the coating's chemical composition. Further increases of the off-duty factor cause similar changes in both the titanium and carbon contents of the coating [Fig. 6(b)].

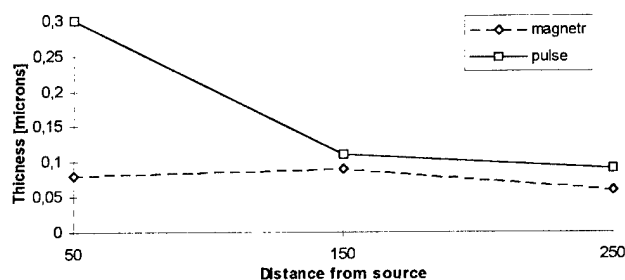


Fig. 4. Influence of the working mode of the hybrid source and substrate localization on the thickness of TiN coatings.

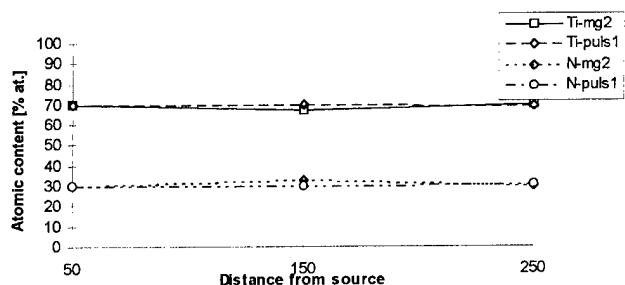


Fig. 5. Influence of the working mode of the hybrid source and substrate localization on the chemical composition of TiN coatings.

4. Discussion

Pulsed plasma generated in coaxial plasma accelerators has been used for deposition of thin hard layers

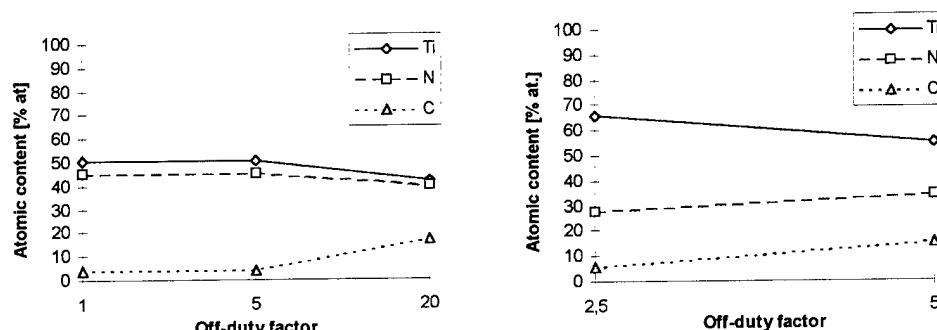


Fig. 6. Influence of deposition conditions on the chemical composition of TiN coatings obtained with use of the combined RF-sustained DC magnetron discharge: (a) at a pressure of 3.5×10^{-5} mbar; (b) at a pressure of 5.5×10^{-5} mbar.

since the late 1970s. Because of the high degree of plasma ionization, high density and high energy of the particle flux reaching the substrate, this method is particularly suitable for deposition of high-melting materials in their metastable forms. However, because of the very fast course and impulse character of the process in the classical 'Marshall gun', control of coating deposition is difficult. A group of plasmoids is generated in a single cycle. Their creation is connected with different stages of the plasma process in the accelerator, and thus both space and time distributions of the plasma components are non-homogeneous. Non-homogeneity of the distribution of pulsed plasma components also causes the distribution of crystallization products in the area of the deposition chamber to be non-homogeneous. The authors developed a new hybrid way of creating a pulsed reactive plasma, by joining the mechanism of gas-metallic plasma generation in the cylindrical magnetron system with the mechanism of electrodynamic acceleration of the plasma in an impulse coaxial accelerator system. Investigations described in this paper confirm the legitimacy of the authors' assumption that separation of the plasma generation phase from the phase of its acceleration in the proposed hybrid way of reactive impulse plasma creation will improve its homogeneity along the distance from the source. The low deposition rate can be increased by changing the ratio of power dissipation in the stationary magnetron discharge and impulse high-voltage discharge.

The influence of magnetic field on electrodeless electrical discharges has been studied for a long time, and increasing interest in this field has recently been seen in connection with broad perspectives of their technological application. Such a deposition method is executed by combined RF-sustained DC magnetron discharge investigated and described in this paper. The main advantage of technological systems this type is the possibility to decrease the working gas pressure of the RF inductive discharge down to 10^{-5} mbar without a significant effect on the power expense of ion generation. The magnetic field essentially stabilizes the RF inductive discharge and, as experiments have shown,

application of a negative voltage of significant magnitude to the target or to the substrate holder does not lead to frustration of the discharge. The investigations described herein prove that it is possible to influence the chemical composition of the coatings by proper selection of the pulsed bias parameters without changing the composition of the working gas mixture.

5. Conclusions

Results of investigations into the deposition processes of TiN coatings by stationary magnetron discharge with the addition of high-voltage pulses applied to the plasma source electrodes, or to the deposited substrate, lead us to the following conclusions:

- separation of the plasma generation phase from the phase of its acceleration in the proposed hybrid way of reactive impulse plasma creation improves the homogeneity of the plasma along the hybrid source's axis;
- the deposition rate can be increased by changing the ratio of power dissipation in the stationary magnetron discharge and the impulse high-voltage discharge of the hybrid source;
- it is possible to decrease the working gas pressure of RF-sustained DC magnetron discharge down to 10^{-5} mbar without significant effect on the power expense of ion generation; and
- it is possible to influence the chemical composition of the coatings deposited by RF-sustained DC magnetron by proper selection of the pulsed bias parameters without changing the composition of the working gas mixture.

Acknowledgements

This work was accomplished within the framework of the research project KBN No. 7 T08C 051 13 financed by The Committee for Scientific Research in Poland.

References

- [1] H. Bruzzone, H. Kelly, A. Márques, D. Lamas, A. Ansaldi, C. Oviedo, *Plasma Sources Sci. Technol.* 5 (1996) 582.
- [2] M. Sokołowski, A. Sokołowska, A. Michalski, Z. Romanowski, A. Rusek-Mazurek, M. Wronikowski, *Thin Solid Films* 80 (1981) 249.
- [3] H. Kelly, A. Lepone, A. Márques, D. Lamas, C. Oviedo, *Plasma Sources Sci., Technol.* 5 (1996) 704.
- [4] K. Miernik, J. Walkowicz, *Le Vide: science, technique et applications* 284 (1997) 227.
- [5] J. Walkowicz, K. Miernik, *Surf. Coat. Technol.* 116–119 (1999) 666.
- [6] J. Walkowicz, V.T. Barchenko, K. Miernik, *Surf. Coat. Technol.* 116–119 (1999) 685.
- [7] M.D. Gabovich, *Sov. J. Tech. Phys.* 28 (1958) 872.
- [8] M. Yamashita, *J. Vac. Sci. Technol. A* 7 (4) (1989) 2752.

Hard lubricating coatings for cutting and forming tools and mechanical components

V. Fox, A. Jones, N.M. Renevier *, D.G. Teer

Teer Coatings Ltd., 290 Hartlebury Trading Estate, Hartlebury, Worcs. DY10 4JB, UK

Abstract

Two new coatings based on graphite and MoS_2 have been developed. They combine low friction with high hardness, high load capacity and exceptionally low wear. Both coatings act as solid lubricants, providing protection for both the coated surface and any opposing uncoated surface. The coatings are finding application in improving the general performance of cutting and forming tools and also make possible high-speed machining. The graphite-based coatings have exceptional wear properties under water or oil and results from wear tests under a wide range of conditions are given. A number of practical applications are given, including the protection of artificial hip joints. The advantages offered by the use of such coatings for many mechanical components are demonstrated. © 2000 Published by Elsevier Science S.A. All rights reserved.

Keywords: Cutting tools; Forming tools; Magnetron sputtering; Solid lubricants

1. Introduction

For many years it has been possible to deposit a wide range of hard wear-resistant coatings on to steel substrates using different physical vapour deposition (PVD) techniques. These are mainly nitrides, carbides and carbonitrides of transition metals and include TiN, TiCN, TiAlN and CrN. They have proved to be very successful and are widely used in improving the performance of cutting and forming tools [1]. They have been less successful in providing protection for general wear components, such as gears and engine parts. It is interesting to speculate why this might be. One important reason is that, although coatings are routinely deposited with excellent adhesion, there is always the possibility of depositing a coating with poor adhesion. Although this is most undesirable for a coating on a cutting tool, it is not a disaster. However, if a coating fails on a critical component in an engine or in general machinery this can lead to a catastrophic failure of the whole assembly. In the opinion of the authors there are other reasons why the typical hard coatings are not used more widely. The coatings are not low friction and do not provide any protection for the opposing surface. Indeed,

the coatings are very hard and if the coated surface or the coating is rough then they can cause abrasion and rapid wear of the opposing surface. If the coating is removed then this constitutes a source of abrasive particles within the mechanism.

Diamond-like carbon (DLC) coatings [2] are also hard but also have lower friction than the hard nitride coatings. DLC coatings are starting to find application in some mechanical component applications, but their application is quite low considering the length of time since the first DLC coatings were reported [3] and also the amount of development effort that has been expended since then (e.g. see Ref. [4]). The very hard DLC coatings tend to be brittle, have poor adhesion and are unsuitable for highly loaded applications. The Me:C coatings are much softer [5] but are less brittle. They can be deposited with excellent adhesion [6] and can be used at moderately high loads. The coefficient of friction is low, typically 0.15, but again these coatings are not true solid lubricants in the sense that they do not provide an efficient transfer film on the opposing surface. Again, in the opinion of the authors, in order to provide optimum wear protection for rubbing mechanisms it is necessary to use a true solid lubricant coating with low friction and the ability to protect the opposing surface and to provide a low friction transfer film on the opposing surface. MoS_2 and graphite, both hexago-

* Corresponding author. Tel.: +44-1299-251-399,
Fax: +44-1299-250-171.

E-mail address: renevier@teercoatings.co.uk (N.M. Renevier)

nal layer lattice materials, have these properties [7], but both are soft. RF-sputtered MoS_2 coatings have been used for many years to coat bearings for aerospace applications [8], but they are not suitable for most terrestrial applications as they have poor tribological properties in humid atmospheres. Because the adhesion is poor and because the films are soft, resulting in low wear resistance, they are not suitable for highly loaded applications. Recently, two new coatings have been developed, one based on MoS_2 and one based on carbon (graphite) [9,10]. It has been proved possible to deposit these coatings whilst retaining the very low friction characteristics and to combine them with high hardness. The coatings have the high adhesion normally associated with a high ion current density magnetron sputter ion plating system [11]. The high hardness combined with low friction gives very low wear rates and the mechanical properties of the coatings combined with the good adhesion lead to very high load-bearing capacity. Also, the MoS_2 -based coating retains its desirable properties in humid atmospheres and is suitable for terrestrial applications. It is thought that these new coatings have ideal properties for a wide range of applications. This paper gives details of the deposition methods and includes a brief description of the properties of the coatings together with some of the results from a comprehensive tribological testing program. Finally, a number of existing applications are described and some early test results associated with a number of new applications are given.

2. Deposition methods

Both coatings were deposited in a Teer Coatings UDP magnetron sputter ion plating system [11].

For the MoS_2 -based coating three MoS_2 targets and one titanium target were used. A thin adhesion layer of titanium is deposited first and then the substrates are rotated to pass in front of each of the targets in turn so that a coating consisting of a mixture of MoS_2 and titanium is deposited. The MoS_2 -titanium composite coating has been registered as MoST[®] and a patent applied for [12]. The powers on the titanium and MoS_2 targets are chosen so as to give a coating with a titanium content of about 15%. The amount of metal in the coating is critical in defining the properties. The coating thickness is typically 1 μm . The titanium target is switched off at the end of the process to ensure a uniform blue-grey coloration. The temperature during the deposition process is less than 100°C.

The carbon coating procedure is similar. Here, three carbon targets and one chromium target are used. A chromium adhesion layer is deposited first and then again the substrates are rotated to pass in front of each of the targets in turn. The powers selected for the carbon and chromium targets are such as to give a coating with about 20% chromium. The coating thickness is typically 2.5 μm . The CrC-C coating has been registered as Graphit-iC[®] and a patent applied for [13]. The temperature during the deposition process is less than 250°C.

3. Coating structures and properties

The MoS_2 -titanium composite coating has a hardness of between 1200 and 2000 VHN depending on the titanium content. Initially it was thought that the method of deposition was producing a multi-layer or superlattice structure and that this was responsible for the high hardness. However, it has now been shown [Fig. 1(a)] that there is no multi-layer structure. It is

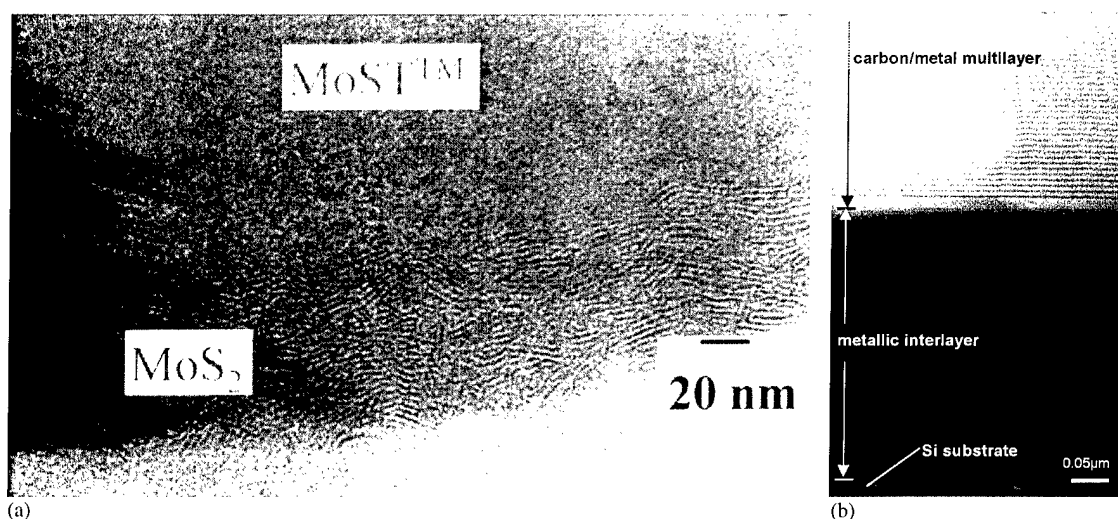


Fig. 1. Transmission electron micrographs of (a) MoST[®] and (b) Graphit-iC[®].

impossible to detect any elemental titanium within the coating, either as layers or individual particles. All the evidence indicates that the titanium is present in solution within the MoS_2 lattice and it is assumed that the strain produced within the lattice is responsible for the high hardness. The structure is amorphous or consists of very small crystallites. The adhesion is excellent and it is impossible to produce any failure in a standard scratch adhesion test up to a load of 140 N. The coefficient of friction is load dependent, but is typically 0.03 at the highest load used (100 N, contact pressure about 3.5 GPa). The maximum coefficient of friction recorded at the lower loads is about 0.1 [2 N, pin-on-disc (POD), 273 rpm, 5 mm ball WC–4%Co, 14 mm diameter track]. The friction is also dependent on humidity, but is still low at high humidity. The wear coefficient is about $10^{-17} \text{ m}^3/(\text{N m})$. (See below for typical test conditions.)

Graphit-iC[®] has a hardness of about 2500 VHN. The coating has been shown to be a CrC–C multi-layer [Fig. 1(b)], but the hardness is a property of the carbon and not an effect of the multi-layer. If the chromium is not included the coatings are of similar hardness but they are more brittle and have a lower load-bearing capacity. The coatings are electrically conducting and the structure is amorphous or consists of very small crystallites. No significant diamond content is detected in the coating and all the evidence indicates that the bonding is almost entirely sp^2 . The tribological properties are similar to those of graphite and it is thought that the structure is graphitic and that the high hardness may be due to some cross-linking between the graphite planes. The coefficient of friction is load dependent and the lowest friction, typically 0.07, is found at the highest load (contact pressure about 3.5 GPa). The wear coefficient is about $10^{-17} \text{ m}^3/(\text{N m})$ for dry rubbing. Under water the coefficient of friction is about 0.04 and the wear is so low as to be difficult to measure. (Further details below.) The wear is poor under dry nitrogen [14] and it appears that a small amount of water vapour is necessary for good wear properties, which is what has been found in many investigations of graphite.

4. Tribological tests

MoST[®] and Graphit-iC[®] coatings have been tested in POD tests at constant linear speed of 200 mm/s and at several loads (10 N, 318 rpm; 40 N, 382 rpm; 80 N, 477 rpm) and in reciprocating wear (RW) tests at a constant linear speed of 150 mm/min under 100 N load (3 mm track length-cycle of 2 s). Tests were performed in dry conditions (POD and RW), under water and oil (RW) using coated M42 steel discs (1200 SiC polishing) with 5 mm diameter WC–4%Co balls as pins.

4.1. MoST[®]

All the tests reveal the remarkable tribological properties of the MoST[®] coating. Fig. 2(a) shows a typical friction trace for an RW test under a load of 100 N and at 40% humidity. Ball craters on the wear track indicate a specific wear rate of about $3 \times 10^{-17} \text{ m}^3/(\text{N m})$. Ball-on-disc tests at a load of 10 N performed with a 9 mm diameter 52100 ball at 500 rpm and under dry nitrogen indicated a coefficient of friction of 0.005. The coating was not worn away after 1 900 000 cycles. Some tests were carried out under water and Fig. 2(b) shows the friction trace for an RW test at a load of 100 N. It can be seen that the coating fails after 2800 cycles.

4.2. Graphit-iC[®]

POD tests were performed using a 5 mm diameter tungsten carbide ball as pin and Graphit-iC[®]-coated M42 plates as the discs at loads of between 10 and 80 N. The friction coefficient varied between 0.1 and 0.06 depending on the load. The wear coefficient was typically $3 \times 10^{-17} \text{ m}^3/(\text{N m})$ [15].

Some of these test results are shown in Fig. 3(a), which plots the specific wear rate against load for typical hydrogenated Me:C coatings and for thinner Graphit-iC[®] coatings without the Cr multi-layers and for the multi layer Graphit-iC[®] coatings. The large difference in wear rate between the Graphit-iC[®] coatings and the Me:C coatings is apparent, as is the increase in the load-bearing capacity of the multi-layer Graphit-iC[®] coatings. RW tests were carried out using a 5 mm tungsten carbide ball against a Graphit-iC[®]-coated M42 steel plate at loads up to 100 N. The cycle time was 2 s and the length of each pass was 3 mm with constant sliding speed. Fig. 3(b) and (c) show a comparison of the friction trace for a Graphit-iC[®] coating and a commercially available hydrogenated Me:C coating under dry (ambient) rubbing conditions and under water at a load of 100 N. The Me:C coating failed after 6300 cycles in dry conditions and after 5400 cycles under water. The Graphit-iC[®] coating showed no sign of failure after 10 000 cycles in dry conditions and under water when the test was stopped and it was not possible to detect any measurable wear using a ball crater within the wear track. Further RW tests have been carried out on coated CoCr substrates under water in order to test the coatings for application on artificial hip joints [16]. For these tests the coefficient of friction was 0.04 and it was not possible to obtain a measurable wear rate for the coated flat discs. The wear rate on coated CoCr pins was measured after 50 000 cycles and found to be $5 \times 10^{-18} \text{ m}^3/(\text{N m})$.

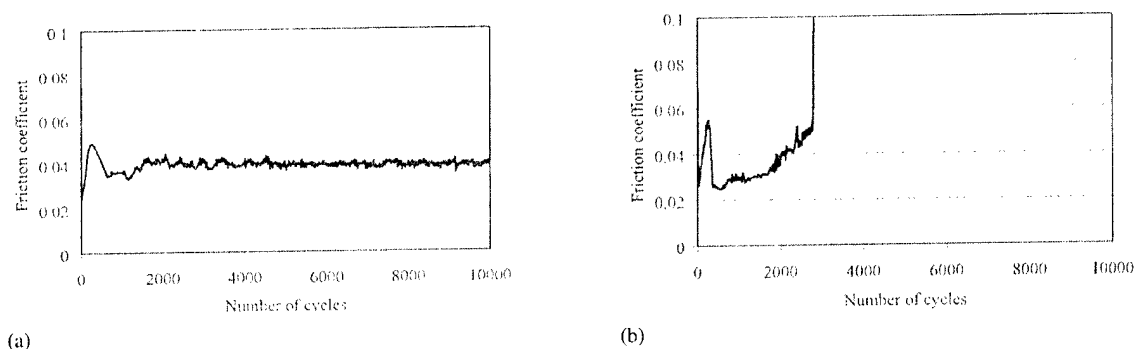


Fig. 2. 100 N RW test (a) at 41% humidity and (b) under water.

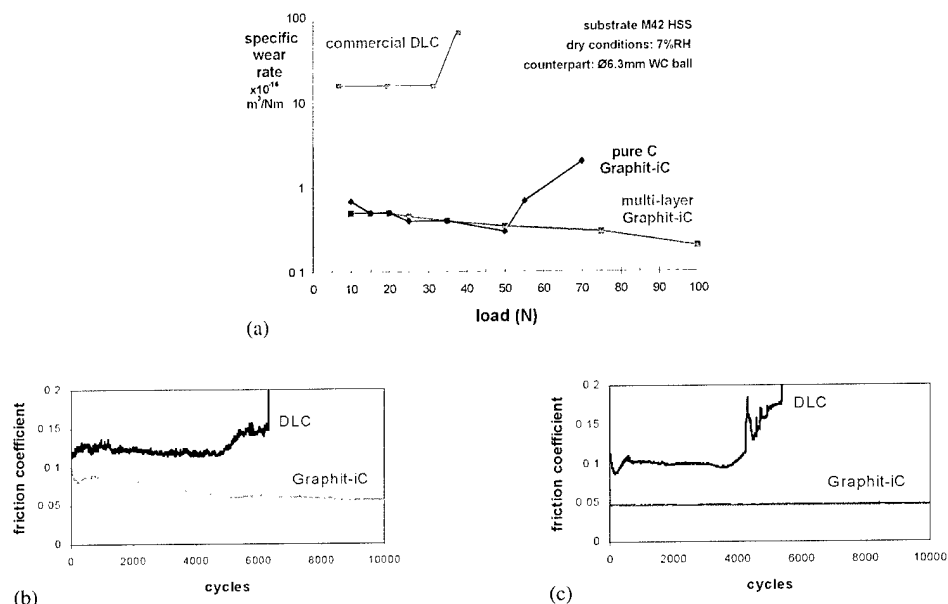


Fig. 3. Comparison of specific wear rates for Graphit-iC[®] and DLC as a function of load (a) and 100 N RW test of Graphit-iC[®] and DLC in (b) ambient conditions and (c) in de-ionised water.

5. Applications

5.1. MoST[®] on cutting and forming tools

The MoST[®] coatings have been applied extensively on cutting and forming tools with outstanding results. It is possible to include only a few examples here.

5.1.1. Perforating and piercing applications

5.1.1.1. Test 1 Rapid wear occurred when AISI D2 punches (60–62 HRC) were used for the perforating application. Punches were coated with the MoS₂–titanium composite coating and compared with the previously sprayed MoS₂ coating and uncoated punches used by the company. The application for which the punches were tested was to perforate 1.2 mm thick 409 stainless steel plate for filters without lubricant, running

at 250 pressings per minute. Previously the company had used a sprayed MoS₂ coating that enabled the punches to last for 1 day (around 80 000 pressings) without lubricant. With this sprayed coating the punch needed two to four regrinds to survive for 1 day, after which the punch was unable to function. With MoS₂–titanium composite coating, the punches were still performing after 320 000 pressings (4 days) without the need for regrinding.

5.1.1.2. Test 2 PS4 [CPM[®] M4 of Dayton Progress Corporation (USA)] (61–63 HRC) punches were coated with MoS₂–titanium composite (1.2 μ m) on top of TiCN (3–3.5 μ m of TiCN produced by arc evaporation) coating and used to perforate 12 mm HSLA steel with water-soluble lubricant (20%).

In the piercing application, use of MoS₂–titanium composite coating (Fig. 4) in lubricated conditions on the top of hard coatings such as TiCN has increased

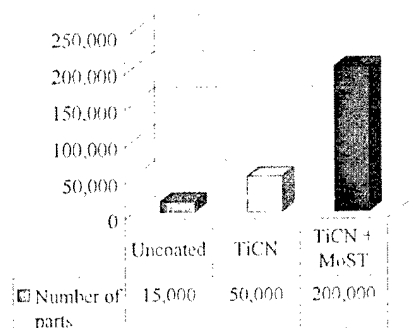


Fig. 4. Number of parts produced with MoST® in lubricated conditions (water soluble 20%).

the number of parts produced by 13 times compared with the uncoated punches and by four times compared with the punches coated with TiCN alone.

5.1.2. End mills applications

It has also been observed that MoST® coatings offer an increase of productivity. Testing of a 12 mm diameter end mill for milling a 4 mm slotting depth and 25 mm slotting width (carried out by the Institute of Advanced Manufacturing Sciences Inc. in co-operation with Multi-Arc Inc.) has shown an increase in the milling distance and a reduction in the average milling force during the test and also an improvement in the surface finish with a MoST® coating onto AISI 304 stainless steel. Both effects increase the productivity and the quality of the final product (Fig. 5).

5.1.3. Dry drilling

In this test the drills were coated with TiN, TiAlN and TiN+MoST®. These drills were tested under dry conditions and were compared with uncoated drills running dry and with emulsion. The drills were high-speed steel drills drilling into JIS S50C steel of thickness 20 mm at a speed of 30 m/min, 0.12 mm/rev with a hole depth of 18 mm. The use of MoS₂-titanium composite coating (Fig. 6) in dry conditions on the top of hard

Table 1

Preliminary results of dry drilling (1200 rpm; feed rate 0.63 mm/rev; 6 mm diameter drills; workpiece, 34CrNiMo6, 250HB)

Drill type	Uncoated	TiN	Graphit-iC®
No. of holes	4	20	77

coatings, such as TiN, has increased the number of holes produced by 2.1 times compared with TiN alone and by 2.8 times for TiAlN alone.

5.2. Graphit-iC® applications

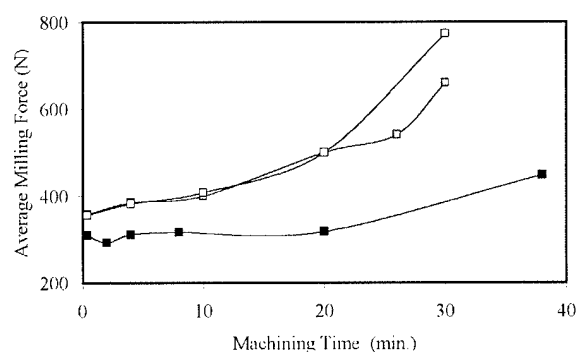
Graphit-iC® has not yet been applied widely, but the early results are very encouraging.

5.2.1. Drilling tests

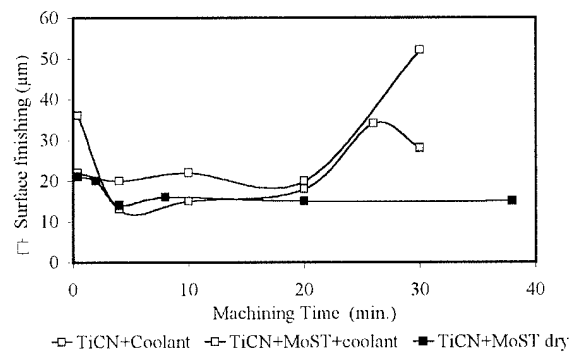
Table 1 shows the preliminary results of dry drilling tests. It can be seen that the Graphit-iC® coating has given an improvement of nearly four times over a typical TiN coating and 20 times over the uncoated drills.

5.2.2. Engine components

Both MoST® and Graphit-iC® have been subjected to long-term testing on a variety of engine components. It has been shown that they both retain their tribological properties at temperatures up to 350°C. Because of their high load bearing capacity the coatings can be used on heavily loaded gears. They are being investigated on fuel injection systems, tappets, pistons, piston rings and bearings, all with promising results. Graphit-iC® has been tested on the thrust washers of differential transmission gears. The tests were in an endurance test rig and were run at high speed/low torque and at low speed/high torque. The Graphit-iC® coating gave the best results of a number of different surface treatments included in the trials, passing all the tests. Success was also shown in reducing wear against a rubber seal lip and in rotary oil pumps.



(a)



(b)

Fig. 5. Average resultant force (a) and surface finishing (b) while end milling AISI 304 stainless steel using TiCN- (coolant) and TiCN+MoST®-coated (dry and coolant) inserts.

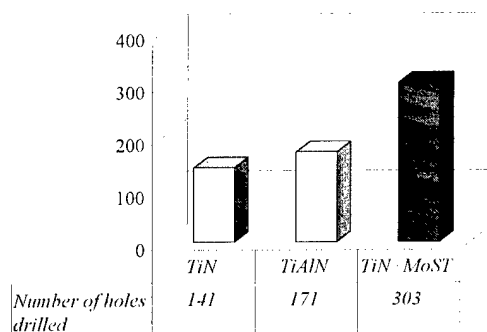


Fig. 6. Number of holes drilled before failure.

5.2.3. Medical applications

As mentioned briefly above, the Graphit-iC[®] coatings are being developed and tested for use in artificial hip joints. They have shown to present no biocompatibility problems [17]. The very low wear rate of $\sim 10^{-18} \text{ m}^3/(\text{N m})$ found in POD tests for coated CoCr compares with a rate of $\sim 10^{-15} \text{ m}^3/(\text{N m})$ found for uncoated CoCr [18]. The uncoated hip joints are claimed to have a useful life in excess of 10 years, and by taking into account the thickness of the Graphit-iC[®] coatings a life of at least 50 years seems to be possible for the coated joints. It is thought that the Graphit-iC[®] coating will also find application for knees and other joints and for items such as bone-cutting saws.

6. Discussion

The combination of hardness, wear resistance, low friction and high load-bearing capacity should result in many successful applications. The MoST[®] will be chosen for many dry applications. Both coatings have excellent properties under oil. Perhaps the most important aspect of these coatings for use in car engines or to protect other mechanical parts requiring long life is the fact that they are true solid lubricants with the ability to form transfer films and to protect the opposing surface. It is interesting to compare MoST[®] or Graphit-iC[®] with a hard coating such as TiN for use in an engine. TiN is hard and wear resistant but it does not offer any protection for the opposing surface. On the contrary, because it is hard, it can cause enhanced wear by abrasion of the opposing surface. TiN is not a low friction coating. The solid lubricant coating reduces the friction and protects both its own surface and the opposing surface. It has been shown that TiN rubbing against itself in water has a friction coefficient of 0.5 and a wear rate of the order $10^{-15} \text{ m}^3/(\text{N m})$. If the TiN coating is removed then the particles of the coating are hard and abrasive. If the solid lubricant is removed then the presence of the particles of the coating can be beneficial. It is thought that these properties and advan-

tages over conventional hard coatings will lead to widespread use of the new hard solid lubricant coatings in engines and other rubbing mechanisms. If this is so it implies a very large increase in the use of PVD coatings. The success of the coatings for cutting and forming tools is shown above. However, it is thought that the use of the hard solid lubricant coatings will continue to expand. There is a requirement to improve productivity and the speed of machining. At the very high speeds it is doubtful if the lubricants normally used are effective or if they even reach the point of cutting [19]. Dry machining techniques are required and the solid lubricant coatings have already been shown to improve the performance of high-speed machining and to allow machining without lubricants. It is confidently predicted that the hard solid lubricant coatings will find increasing use in this field. The properties of Graphit-iC[®] under water are very interesting. The coatings could be used in many existing applications such as valves, seals and washers. It can be speculated that Graphit-iC[®] coatings could be used in applications where its properties might allow the replacement of oil lubrication with water lubrication. We are presently investigating the use of Graphit-iC[®]-coated cutting tools with water lubricant/coolant. Here, we exploit the low friction and the low wear of the Graphit-iC[®], and although the water might not reach the cutting point the dry friction is still low and the presence of the water would be important in reducing the temperature of cutting tool.

7. Conclusions

The new solid lubricant coatings MoST[®] and Graphit-iC[®] offer many advantages over previous solid lubricant coatings because of their hardness, wear resistance and load-bearing capacity. They also have many advantages over conventional hard coatings because of their low friction and lubricating properties, which allows the component to be used at high speed, lowering the frictional forces and the temperature. Under dry conditions Graphit-iC[®] has a wear coefficient about ten times lower than conventional hydrogenated DLC coatings and also has a lower coefficient of friction. MoS₂-titanium composite coatings are already used to improve the performance of cutting and cold-forming tools and are beginning to be used successfully for high-speed dry machining. In cold-forming applications the use of the MoS₂-titanium composite coating has allowed the load applied during the process to be reduced. MoS₂-titanium composite coatings, in contrast to most other coatings, have allowed either the elimination or reduction of the lubricant quantity used, resulting in big cost savings, because many tools used for forming require the old oil to be cleaned off before they can be used again. Work in dry condition reduces this require-

ment. Considerable attention has been previously given to hard thin film characteristics, as is evident from numerous publications reported elsewhere. A hard coating under MoS₂–titanium composite seems to be the best choice. The exact reasons are unknown, but the improvement is probably associated with the additional support offered by the hard coating. Early tests on both coatings indicate that they will find many applications in protecting engine and other mechanical components. Both MoS₂–titanium composite coatings and Graphit-iC[®] are good candidates for a clean world process, and give greater productivity in machining, forming and for components.

Acknowledgements

The authors would like to acknowledge the support of the UK DTI through the LINK, SMART and SPUR programs. They would like to thank Multi Arc Inc. (USA) for supplying some results for MoST[®] on forming tools.

References

- [1] B. Leffler, M. Svensson, L. Lord, Behaviour of Materials in Machining, IOM Conference Proceedings, Stratford (1998) 3.
- [2] R. Messier, A.R. Badzian, T. Badzian, K. Spear, P. Bachmann, R. Roy, Thin Solid Films 153 (1987) 1.
- [3] S. Aisenberg, R. Chabot, J. Appl. Phys. 42 (1971) 2953.
- [4] Proceedings of the International Diamond Conferences, Elsevier, 1989–1998.
- [5] H. Dimigen, H. Hubsch, Philips Tech. Rev. 41 (1983–84) 186.
- [6] D. Monaghan, D.G. Teer, P.A. Logan, I. Efeoglu, R.D. Arnell, Surf. Coat. Technol. 60 (1993) 525.
- [7] W.O. Winer, Wear 10 (1967) 422.
- [8] T. Spalvins, ASLE Trans. 14 (1971) 267.
- [9] D.G. Teer, J. Hampshire, V. Fox, V. Bellido, Surf. Coat. Technol. 94–95 (1997) 572.
- [10] D. Camino, A.H.S. Jones, D. Mercks, D.G. Teer, Vacuum 52 (1999) 125.
- [11] D.G. Teer, US Patent 5 556 519, 1996.
- [12] D.G. Teer, J.H. Hampshire, V. Bellido, European Patent Appl. 96924987.9, 1996.
- [13] D.G. Teer, D. Camino, A.H.S. Jones, UK Patent Appl. GB 9725413, 1997.
- [14] R.H. Savage, J. Appl. Phys. 19 (1948) 1.
- [15] A.H.S. Jones, D. Camino, J. Jiang, D.G. Teer, J. Eng. Tribol. 212 (1998) 301–306.
- [16] A.H.S. Jones, D.G. Teer, to be presented at ICMCTF, San Diego, 1999.
- [17] J. Goodacre, G. Mellor, in preparation. Available as a private publication from Professor J. Goodacre, Lancashire Postgraduate School of Medicine & Health, UK.
- [18] R.M. Streicher, M. Semlitsch, R. Schon, H. Weber, C. Rieker, in: D. Dowson (Ed.), Advances in Medical Tribology, MEP, London, 1998, pp. 83–92.
- [19] K. Maekawa, I. Ohshima, Behaviour of Materials in Machining, IOM Conference Proceedings, Stratford (1998) 90.

PVD coating of plastic webs and sheets with high rates on large areas

S. Schiller, V. Kirchhoff, N. Schiller, H. Morgner *

Fraunhofer-Institut Elektronenstrahl- und Plasmatechnik (FEP), Winterbergstraße 28, D-01277 Dresden, Germany

Abstract

For many product applications, plastic material needs to be coated with transparent oxide layers to obtain the required properties like permeation barrier, abrasion resistance, anti-reflection and defined optical transmission for example. First of all, outstanding properties of coated material are needed in comparison to competitive technologies. Beyond this, acceptable costs for the market are decisive for the introduction of PVD technologies into production. This paper gives an overview of the great variety of applications.

The deposition rate has a strong influence on coating cost: the higher the rates, the lower the cost. High rates, especially for deposition of oxides, are often considered as being linked to poor layer quality. Plasma activation of vapor is one method to obtain high rates and acceptable properties. Hollow cathode activated deposition process (HAD) and pulsed magnetron sputtering (PMS) will be explained. Results concerning layer properties will be depicted. An outlook to the future will be derived. © 2000 Elsevier Science S.A. All rights reserved.

Keywords: Coating on plastics; Dual magnetron sputtering system (DMS); Hollow cathode activated deposition process (HAD); Large-area deposition; Pulsed magnetron sputtering (PMS) process

1. Introduction

In recent years, the importance of coating plastic surfaces with oxides and nitrides has increased. Typical applications with economical importance for transparent layers are barrier layers for packaging films, solar control and low-emissivity multilayer systems for window panes and window films, and antiabrasion layers on plastic films, plastic sheets and plastic parts.

All these applications require a coating width of more than 1 m at high quality and rather low cost. Low coating costs call for a high coating speed and high deposition rates. For the quality requirements mentioned, dense layer microstructures and therefore plasma-activated deposition processes are necessary.

For all applications mentioned above, excellent performance of coatings are needed. The layer quality will be reflected by applicatory properties.

For clear barrier layers and abrasion-resistant layers, dense microstructures and good adhesion to the plastic substrate are necessary. Moreover, for abrasion-resistant

layers, a high hardness is necessary to withstand the wear load.

Optical layers in a layer stack must have a refractive index close to that of the bulk material, dense homogeneous microstructures, smooth surfaces, good adhesion and low absorption. They have to withstand environmental influences like moisture and thermal cycling. Moreover, the demand on uniformity allows a layer thickness deviation smaller than 1–2% only for the whole coated area.

2. Coating technology and basic properties of deposited layers

2.1. HAD — *hollow cathode activated deposition process*

Fig. 1 shows the principle of the plasma-activated reactive evaporation in general. Close to the substrate, a plasma discharge is arranged, incorporating the vapor and reactive gas particle stream. The plasma promotes the chemical activity of condensing particles, mainly by excited particles. The ions will be accelerated towards the substrate in the electrical field of the plasma sheath.

* Corresponding author. Tel.: +49-35973/281-43;

fax: +49-351/2586-105.

E-mail address: morgner.h@fep.fhg.de (H. Morgner)

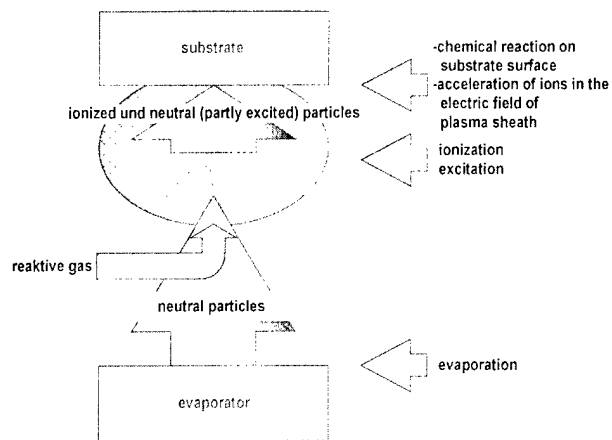


Fig. 1. Schematic of plasma-activated reactive evaporation.

For highly insulating layers, the self-bias potential will generate this field.

The HAD process is the combination of a high-rate evaporation process and a high-density plasma using the activation by hollow cathode low-voltage electron beam (LVEB). The HAD process is applicable for the coating of plastic films and plastic sheets as well.

The usage of boat evaporation is an economical way for reactive evaporation of Al in an industrial scale. Fig. 2 shows the boat evaporator with plasma activation in operation. The arrangement of the HAD process for the coating of plastic films by EB evaporation as an another example is depicted in Fig. 3 as a scheme. For coating of wide webs or sheets, the hollow cathode plasma sources are arranged side by side in a modular way without principal restriction of web width.

The very high density of the hollow cathode plasma can be explained by the electron energy distribution function (EEDF), which consists of the Maxwellian distribution of the isotropic electrons and the superimposed group of directed electrons, called the LVEB [1].

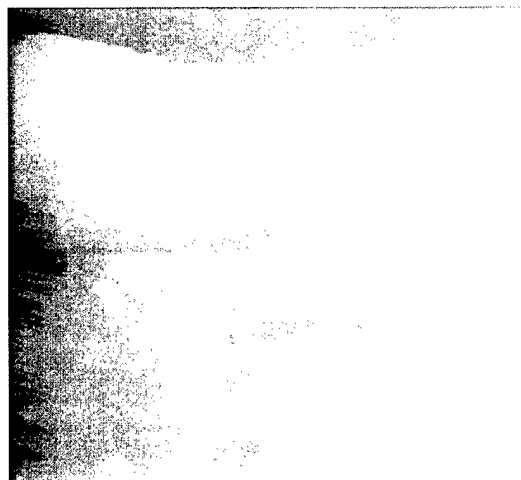


Fig. 2. Reactive HAD process with an Al boat evaporator.

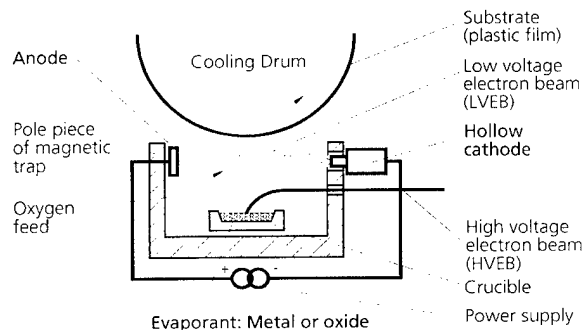


Fig. 3. Reactive evaporation of Al and plasma activation by a hollow-cathode, low-voltage electron beam.

The guidance of the plasma in a longitudinal magnetic field keeps the LVEB-electrons confined in the core region of the discharge. Only elastic electron scattering processes effect the expansion of the core region, and the plasma stays concentrated in the substrate region.

The EEDF contains a large portion of electrons that exceed the ionization energy of the particles in the vapor (e.g. 6–13 eV for the species in the aluminum oxide deposition). Therefore, a very high plasma density in the order of $10^{12}/\text{cm}^3$ can be achieved. The particle density near to the substrate amounts to about $10^{13}/\text{cm}^3$ for the reactive evaporation of Al with a deposition rate of 100 nm/s.

The energy of the tail in the electron energy distribution that charges the insulating substrate determines the self-bias potential. A self-bias potential on the insulating substrate of more than 15 V can be derived from the electron temperature in the plasma [2].

Corresponding to the ion current density, the flux of condensing particles consists of about 30% ionized particles with a relatively low kinetic energy. Fig. 4 demonstrates the change in energy distribution of the condensing particles by plasma activation.

From the deposition rate, ion current density and self-bias potential, it is possible to estimate the mean energy for the condensing particles. The ions improve the condensation of dense layers in two ways. On the

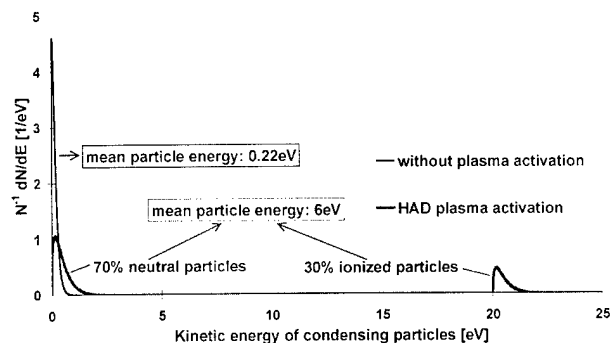


Fig. 4. Energy distribution of the condensing particles at the reactive evaporation of Al by hollow-cathode, low-voltage electron beam (LVEB).

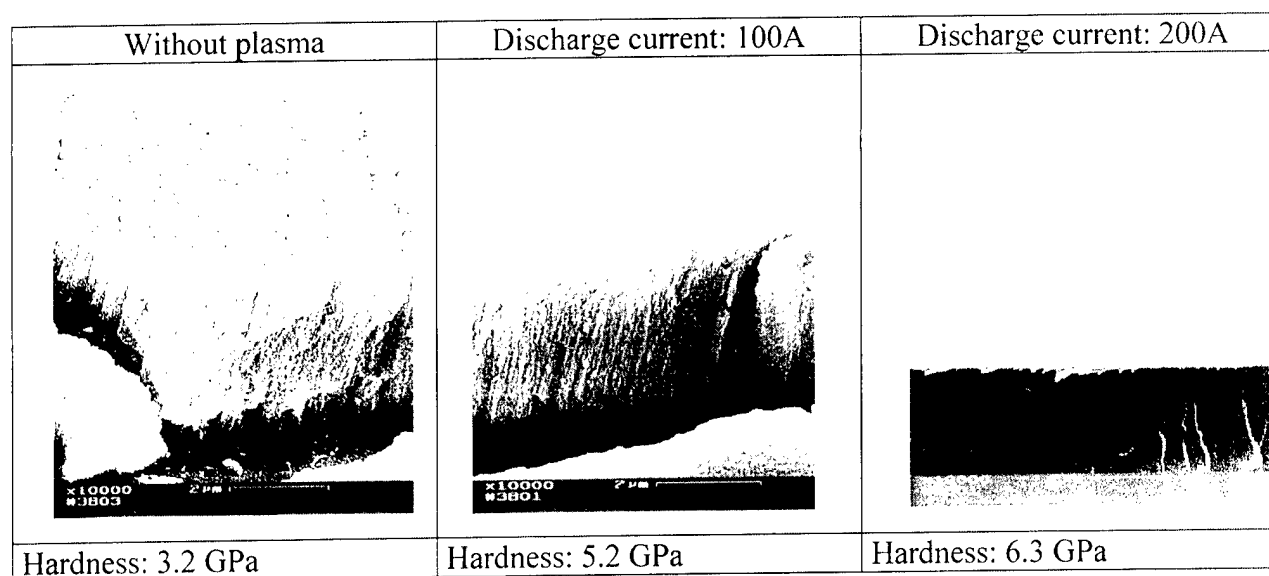


Fig. 5. Reactive EB evaporation of aluminum, plasma activation with hollow-cathode, low-voltage electron beam (HAD process). Deposition rate: 100 nm/s.

one hand, the mean kinetic energy of the condensing particles will be raised from 0.2 to about 6 eV. This enhances the mobility of the adatoms on the surface of the growing film. On the other hand, the ions impinge perpendicularly on the surface because of their acceleration in the plasma sheath, thereby avoiding geometric shadowing. In contrast, the incidence angles for the neutral particles are wide-ranged due to scatter processes in the dense vapor. Oblique incidence angles lead to more shaded particles causing porosity in the layers.

The HAD process has been developed primarily for the deposition of Al_2O_3 and SiO_x . For TiO_2 , the first experiments have been carried out. The static and dynamic deposition rates are listed in Table 1.

The layer microstructure is mostly influenced by the mean kinetic energy of condensing particles [3,4]. Without plasma activation, the particle energy ranges in the order of only several tenths of an electron-volt. This results typically in a non-dense, columnar structure that shows pronounced microcracks on the surface (see Fig. 5 left).

The microstructure improves according to the degree of plasma activation that enhances the mean kinetic energy of condensing particles. Fig. 5 demonstrates the influence of the plasma activation on microstructure

and hardness of the layer. The hardness has been measured by nanoindentation.

The best layer quality, i.e. a dense amorphous structure and a smooth surface, has been achieved with the highest degree of plasma activation at a plasma current of 200 A per hollow cathode that corresponds to the parameters in Table 1. The hardness of the dense amorphous layer amounts to 6.3 GPa. More layer property parameters can be seen in Table 2. The dense layers exhibit compressive stresses in the order of only 10 MPa. This is a very low value in comparison with other deposition processes as sputter deposition [5], where the compressive layer stress varies from several hundred megapascals up to the order of several gigapascals.

The low intrinsic stresses in dense layers that are deposited by the HAD process can be explained by the relatively low energy of the condensing particles. The energy distribution of the particles impinging the substrate consists of a Maxwellian distribution of the neutrals with 0.3...0.7 eV mean kinetic energy and of ions with kinetic energy in the range of 15...20 eV (cf. Fig. 4). The HAD process does not generate particles with a higher energy, though the mean energy of the condensing

Table 1
HAD process: static and corresponding dynamic deposition rates

Layer material	Static deposition rate (nm/s)	Dynamic deposition rate (nm m/s)
Al_2O_3	100–150	30–45
SiO_x	200–600	9–180
TiO_2	50–80	15–23

Table 2
Properties of Al_2O_3 layers by HAD process

Property	Investigation method (equipment)	Result
Transparency	Optical spectrometer	Clear, almost free of absorption
Structure	SEM, XRD	Glassy, dense, amorphous
Composition	EDX	$\text{Al}_2\text{O}_{3.0-3.1}$
Hardness	Nanoindentation	ca 6 GPa

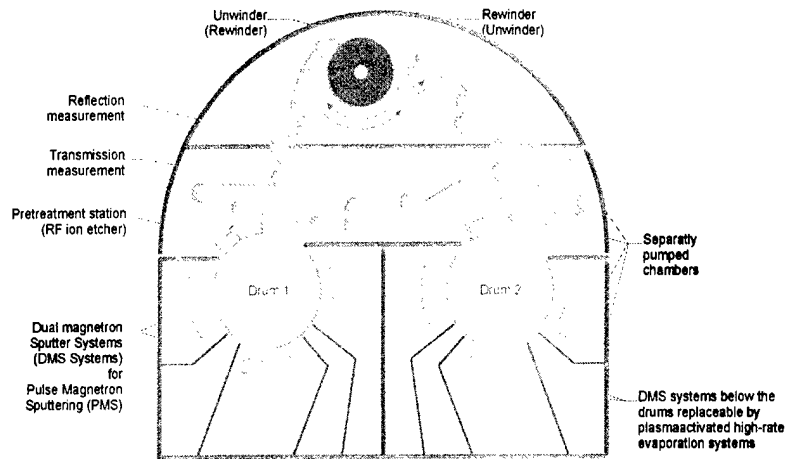


Fig. 6. Equipment scheme sputter roll coater FOSA 600 for technology development.

particles in the HAD process is within the typical range of sputter deposition. Contrary to the HAD process, the energy distribution in sputter processes contains a portion of particles with kinetic energy up to several hundred electron-volts. Based on the knowledge that the bombardment of a growing layer with high-energy particles results in compressive stress, the low stress of the HAD process that utilizes low energetic ions is understandable.

2.2. PMS — *pulsed magnetron sputtering process*

The PMS process with a dual magnetron sputtering (DMS) system is recommended for very high demands on the layer quality. The uniformity of the layer thickness of about 1.5% over the total width and the long operation time make this process a preferable method for the deposition of optical layers on plastic substrates. Table 3 shows typical layer materials that have been deposited by the PMS–DMS process and the corresponding dynamic deposition rates.

In the DMS system, two magnetron sources are connected to a bipolar pulse generator. Each magnetron alternatively acts as the cathode and the anode of magnetron discharge [6]. This process reduces arcs drastically, and reactive sputtering of oxides at high rates becomes possible.

Table 3
PMS process: layer materials and corresponding dynamic deposition rates

Layer material	Dynamic deposition rate (nm m/s)
TiO ₂	0.75
SiO ₂	2
Si ₃ N ₄	1
Al ₂ O ₃	1.3

Fig. 6 shows the sputter roll coater of FEP for web width of 600 mm. This pilot-scale machine for technological development is equipped with two cooling drums, six DMS coating stations and a station for ion pretreatment. Separated pumped sections and pumped slots between the sections reduce cross-contamination to a negligible minimum. Typically, sputtered particles already have a considerably higher kinetic energy by the nature of the particle generation process than evaporated particles. The reactive sputtering of oxides leads to negatively charged oxygen. Negatively charged particles will be accelerated in the cathode fall and impinge with a high energy on the substrate. Furthermore, the magnetic field lines in DMS system are opened towards the substrate pushing plasma to the substrate. The periodically changing plasma potential temporarily causes a high potential drop in the plasma sheath, and energetic ions impinge on the substrate surface [7]. The mean kinetic energy of all impinging particles related to the

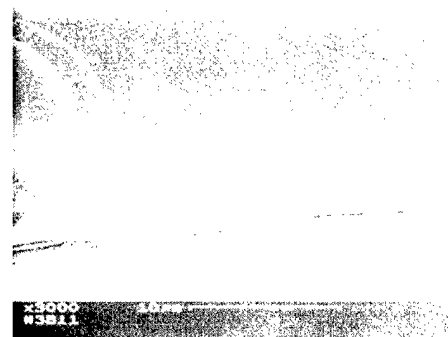
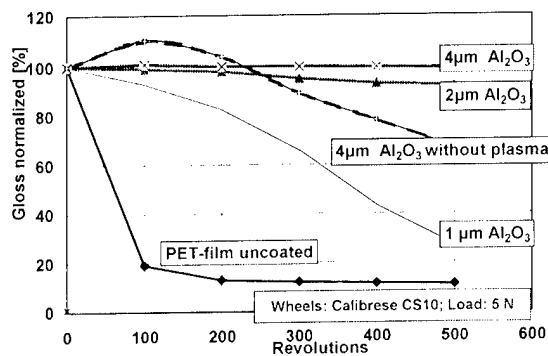
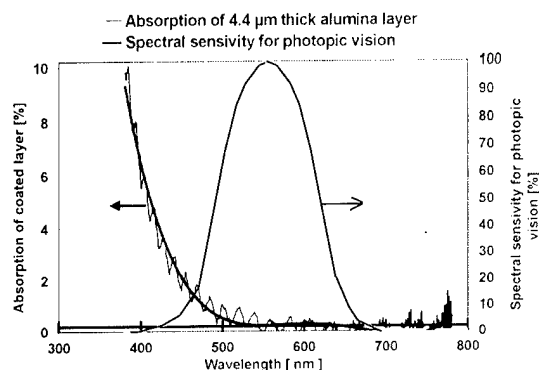


Fig. 7. Dense SiO₂ coatings by PMS process. Hardness: 6 GPa; deposition rate: 5 nm/s.

Fig. 8. Taber abrasion test for HAD- Al_2O_3 layers.Fig. 9. Absorption of HAD- Al_2O_3 layers.

condensing particles can be estimated to about 200...300 eV per condensing atom for Al_2O_3 [8]. As a result, very dense layers with a high hardness are deposited. The resulting compressive layer stress varies from several hundred megapascals up to the order of several gigapascals. Fig. 7 depicts the SEM micrograph of an SiO_2 layer with very smooth surface topography. The adhesion to substrate or sublayer improves due to surface

functionalization resp. etching effect by energetic particles. Despite the presence of energetic particles, the microstructure stays amorphous due to the low condensation temperature necessary for plastic substrates.

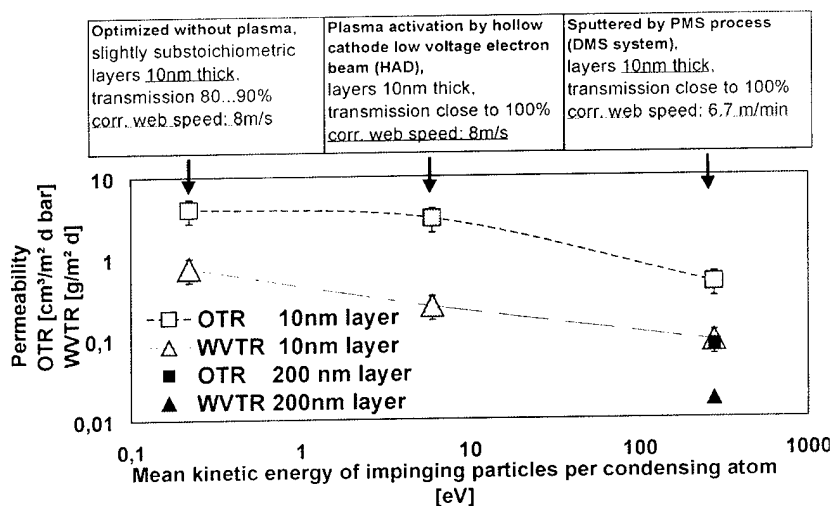
3. Applicatory properties of coated plastic substrates

The high deposition rate of HAD process makes it best suited for deposition of transparent abrasion-resistant layers and transparent barrier layers as well. For both applications, the main advantages of HAD process, the high deposition rate and consequent high productivity and low coating cost, are essential, and a layer thickness uniformity of ± 5 –10% is usually sufficient.

For optical coatings, the requirements for layer quality with respect to density, adhesion and uniformity are very high [9]. Demands for a thickness deviation less than 2% make sputtering mandatory for coating optical layers on large areas. For that purpose, the best results regarding quality and economy as well can be achieved by using DMS sputter systems. Although HAD-deposited barrier layers already have very good properties related to the requirements of food packaging, the demands on transparent barriers for flat panel application are much higher. Such requirements can be fulfilled by DMS-sputtered oxide layers. The essential lower productivity of sputtering results in a distinctively higher coating cost, which can be accepted for such special applications.

3.1. Abrasion-resistant layers

Besides the high hardness of the deposited amorphous Al_2O_3 layers that meets the hardness of bulk float glass material, the layers show a very good adhesion to

Fig. 10. Permeation of Al_2O_3 barrier layers produced by different coating technologies and their typical kinetic energy of impinging particles.

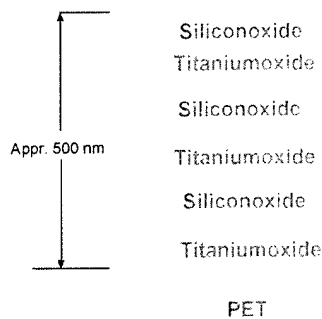


Fig. 11. Multilayer stack for greenhouse film.

the polyester film without any additional pretreatment. The result is an excellent performance of abrasion resistance for layers thicker than 2 μm in the Taber test, whereas the 4 μm layers deposited without a plasma perform poorly due to the lack of layer density (see Fig. 8). Furthermore, the transparency of the coating is excellent. The absorption in the range of the visible light is almost zero (Fig. 9).

3.2. Barrier layers

The demands on transparent barrier layers for food packaging are:

- high degree of transparency;
- oxygen transmission rate (OTR):
 $< 5 \text{ cm}^3/\text{m}^2 \cdot \text{d} \cdot \text{bar}$;
- water vapor transmission rate (WVTR):
 $< 1 \text{ g}/\text{m}^2 \cdot \text{d}$.

In principle, the main demands on transparent barrier layers can be fulfilled by optimized process without plasma activation. The plasma activation by hollow cathode LVEB improves and stabilizes the barrier properties, and the permeation barrier can be obtained even with some surplus of oxygen flow. It is not necessary to stay within a narrow process window as with a pure reactive process. This results in totally clear barrier

layers obtained with no decrease in high productivity (Fig. 10).

An essential improvement of barrier properties by more than one order of magnitude can be achieved by usage of the PMS process. The lower deposition rate and higher layer thickness reduce the productivity, but excellent permeation barrier properties can be achieved. OTR $0.08 \text{ cm}^3/\text{m}^2 \cdot \text{d} \cdot \text{bar}$ and WVTR $0.017 \text{ g}/\text{m}^2 \cdot \text{d}$ makes the layer best suited as high barrier layers for display application. The improvement in barrier properties is linked with an increase of mean particle energy of the condensing particles (Fig. 10). Furthermore, the stability of permeation barrier against elongation of the substrate film increases with plasma activation [10]. A higher particle energy results in denser microstructures and an improved adhesion.

3.3. Coatings for optical applications

Typical applications of thin films deposited by sputtering on plastic web are production of anti reflective (AR) films for CRTs or low e-films for windows, greenhouse film and bandpass-edge filters. These films typically utilize layer stacks comprising SiO_2 as a low refractive index layer and TiO_2 as a high refractive index layer. Fig. 11 shows an example of an multilayer stack of SiO_2 and TiO_2 as interference edge filter for greenhouse applications (see transmission spectrum Fig. 12). Plant growth is promoted by keeping outside near-infrared radiation. This type of coating produced by the PMS process has been used on an industrial scale.

4. Summary and outlook

The main fields of application for PVD coatings on plastic material and on large areas are barrier layers, abrasion-resistant layers and layers with an optical function. The applicatory properties depend strongly on the layer quality. It has been shown that very dense layers can be deposited by HAD and PMS processes as

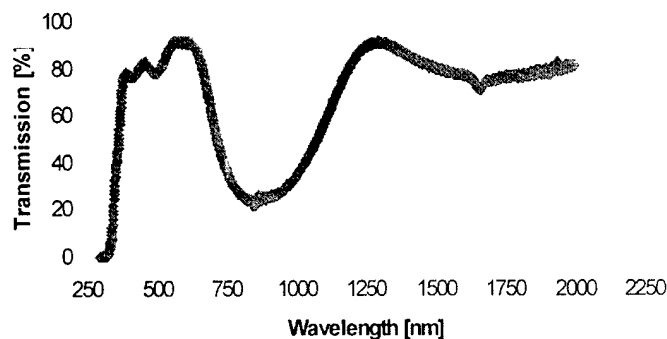


Fig. 12. Greenhouse film transmission spectrum.

well as by using plasma activation. The microstructure of these layers with smooth surface topography remains amorphous due to the low condensation temperature restriction. The choice for the right technology has to consider the demand on layer quality and on deposition cost as well. HAD as a high-rate process can be successfully applied for coating transparent abrasion-resistant layers and barrier layers for food packaging. For the deposition of optical layers and high-barrier layers, the PMS process by the DMS system is superior due to a higher kinetic energy per particle and very low thickness uniformity deviation below 2%.

The application examples shown above can also be applied to coating of plastic sheets.

References

- [1] S. Klagge, A. Lunk, *J. Appl. Phys.* 70 (1991) 99.
- [2] H. Morgner, M. Neumann, S. Straach, M. Krug, *Surf. Coat. Technol.* 108–109 (1998) 513.
- [3] A.G. Dirks, H.J. Leamy, *Thin Solid Films* 47 (1977) 219.
- [4] W. Olbrich, G. Kampschulte, *Surf. Coat. Technol.* 59 (1993) 274.
- [5] H. Schilling, G. Brauer, M. Ruske, J. Szczyrbowski, in: *Proc. Glass Processing Days*, Sept. 1997, Tampere, Finland (1997) 203.
- [6] S. Schiller, K. Goedicke, V. Kirchhoff, T. Kopte, in: *38th Annu. Tech. Conf. Proc.* (1995) 293.
- [7] S. Jäger, B. Szyszka, J. Szczyrbowski, G. Brauer, *Surf. Coat. Technol.* 98 (1998) 1304.
- [8] H. Bartzsch, Ph.D. thesis, in preparation, private commun.
- [9] H.K. Pulker, *Surf. Coat. Technol.* 112 (1999) 250.
- [10] N. Schiller, H. Morgner, M. Fahland, S. Straach, M. Rübisch, Chr. Charton, in: *Ann. Tech. Conf. (SVC)* (1999).

Condensation of silver–copper alloys in a solid–liquid domain of the phase diagram

S. Leroux ^{a,*}, J. Le Ny ^a, C. Guéneau ^a, D. Camel ^b

^a DCC/DPE/SPCP/LEPCA, Commissariat à l'Energie Atomique, Centre d'Etudes Nucléaires de Saclay,
F-91191 Gif-sur-Yvette, France

^b DTA/CEREM/DEM/SPCM, Commissariat à l'Energie Atomique, Centre d'Etudes Nucléaires de Grenoble,
F-38054 Grenoble cedex 9, France

Abstract

An experimental study of silver–copper alloys condensation with a composition entering a liquid–solid domain of the phase diagram is presented. The vapour beams were produced by two effusion cells heated by tungsten resistors and condensed on a tilted molybdenum substrate, regulated in temperature. Condensation durations were chosen to study the successive stages of the film formation. The microstructures of the quenched condensates showed that the mechanisms were similar in the case of copper rich and silver rich domains. At the beginning, droplets of condensation formed. The surface covered with the alloy increased with time. Later on, coalescences of droplets were observed and a film was established. Both droplets and film contained solid particles whose morphology was nodular. The average nodule radius and the number density of particles in the film were determined by image analysis. It was demonstrated that the cube of the average particle radius grew with time and that the number density of crystals was inversely proportional to time. These results were in good agreement with the Ostwald ripening law. © 2000 Elsevier Science S.A. All rights reserved.

Keywords: Condensation; Crystal growth; Flow; Silver–copper alloys; Solidification

1. Introduction

In the uranium enrichment process atomic vapour laser isotopic separation (SILVA), the vapour of an uranium alloy is collected on substrates. The main purpose of our work was to study the condensation and the flow of the alloy when its composition enters a solid–liquid domain of the phase diagram. The silver–copper alloy was chosen as a model for the uranium alloy. Silver and copper vapour beams were produced by two effusion cells heated by tungsten resistors, and condensed on a tilted molybdenum substrate regulated in temperature. The alloy composition on the substrate was regulated by fixing the two furnaces temperatures. In this paper, the successive stages of the film formation and the growth of the solid phase in the film were studied.

2. Experimental

2.1. Experimental procedure

The experimental equipment for co-evaporation of the two metal vapours is shown in Fig. 1.

Knudsen cells ($\Phi_{\text{cell}} = 2$ cm, $h_{\text{cell}} = 1.6$ cm, $F_{\text{hole}} = 2.5$ mm) containing silver and copper were heated by tungsten resistors, tilted at 14.5° from the vertical. A molybdenum substrate ($5.5 \times 5.5 \times 0.2$ cm), tilted at 45° from the vertical, was placed at a distance of 16 cm from the vapour sources and was regulated in temperature. The temperatures of both cells and substrate were measured by thermocouples. The vacuum in the evaporation chamber was about 10^{-6} – 10^{-5} Torr during the experiment. Prior to the experiment, the substrate was etched with an acid solution (HF, HNO₃, CH₃COOH, H₃PO₄) in order to remove surface contamination.

At the beginning of the experiment, shutters were placed above the cells and the source temperatures were allowed to reach their steady value. Next, the element

* Corresponding author. Tel.: +33-2-99-87-13-16;
fax: +33-2-99-87-13-99.
E-mail address: sylvie@emsc-rennes.fr (S. Leroux)

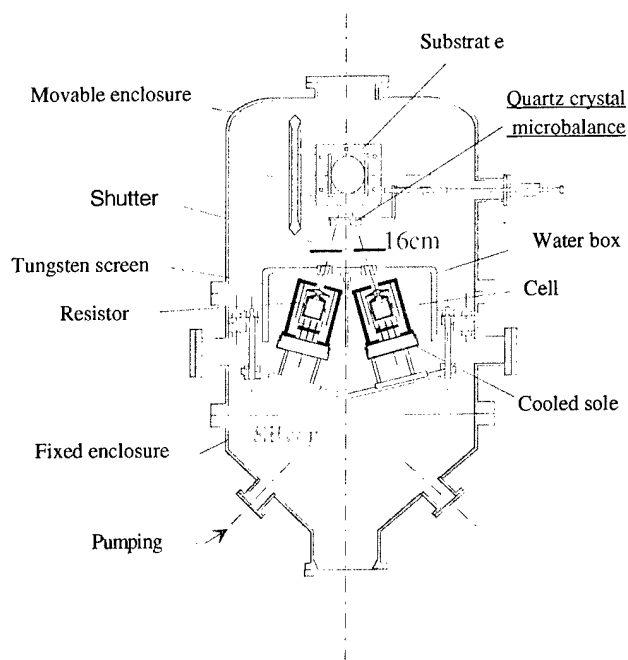


Fig. 1. Experimental equipment.

vapour fluxes were measured with a piezoelectric quartz crystal microbalance (placed at a distance of 11.2 cm from the vapour sources) and the temperatures of both cells were regulated to have the right vapour composition and flux. The incident vapour fluxes on the center of the substrate were of the order of 2×10^{-3} – $10^{-2} \text{ g h}^{-1} \text{ cm}^{-2}$. Then, the shutters were removed simultaneously and the substrate was exposed to the vapour. During condensation, in situ observations were made with a video camera. When the condensation time was over, the shutters were again placed above the cells and the condensate was quenched with nitrogen gas circulating into the substrate support (the cooling rate was of the order of 2°C/s). Finally, the element vapour fluxes were checked a second time with the piezoelectric quartz crystal microbalance before decreasing the heater temperatures.

After quenching, surface and cross-sections of specimen were observed by optical microscopy and scanning electron microscopy (SEM).

2.2. Experimental conditions

Both solid–liquid domains of the phase diagram were investigated: [liquid + copper] and [liquid + silver] (Fig. 2).

Condensation durations ranging from five to 75 min were chosen to study the successive stages of the film formation. The cell temperatures, mass deposited, average composition and condensation time are listed in Table 1. In all the tests, the alloy was collected on a molybdenum substrate regulated at a temperature

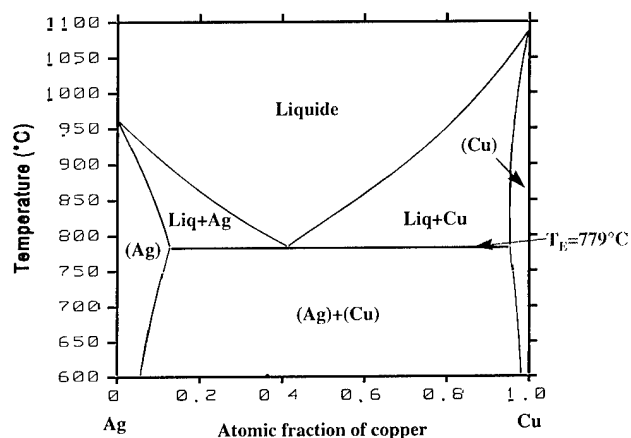


Fig. 2. Phase diagram of the silver–copper alloy.

around 810°C , just above the eutectic temperature (779°C).

3. Results and discussion

3.1. Successive stages of the film formation

Microstructures were observed on the quenched condensates for successive stages of film formation both in the copper rich and in the silver rich domains of the phase diagram (Fig. 3).

The local solid fraction during condensation before quenching was deduced from these quenched microstructures. According to the phase diagram, from 810°C primary solid fractions of silver and copper formed during cooling were equal, respectively to 30 and 12 vol.%. The cooling rate being in the order of 2°C/s and the solidification interval around 30°C , the expected secondary arm spacing of dendrites formed during the quench was around $10 \mu\text{m}$. Measured secondary spacings were in fact even lower (a few μm). So, areas (droplet or film) including dendrites corresponded to condensates which were completely liquid during condensation. On the contrary, all the crystals having a nodular shape and a size larger or equal to $10 \mu\text{m}$ were present during the experiment. The excess solid deposited during the quench then appeared as festoons in the case of silver, but was not visible in the case of copper. In case of the [copper + liquid] domain, it was also rare to observe dendritic crystals of copper near the nodules. It could be assumed that the solid deposited during the quench nucleated on the nodules.

The successive stages of the film formation were equivalent in the two [liquid–solid] domains of the phase diagram.

Initially, droplets of condensation formed on the substrate. They contained nodular crystals. Most of them were in contact with the substrate, even in the case

Table 1
Experimental conditions of alloy condensations

Test	Domain	T_{Cu} (°C)	T_{Ag} (°C)	$T_{substrate}$ (°C)	Mass deposited (g)	Average composition (at.%Cu)	Condensation time (min)
1	[liq + Cu]	1750	1427	810	0.04	56.4	5
2	[liq + Cu]	1739	1500	810	0.08	59.6	15
3	[liq + Cu]	1750	1500	809	0.20	59	30
4	[liq + Cu]	1750	1500	810	0.65	62.5	75
5	[liq + Ag]	1715	1500	817	0.63	18.9	50

of silver where the density of the solidus is higher than the density of the liquidus. Heterogeneous nucleation on the substrate was assumed. With time, the droplets grew and some coalescences occurred. After a while, the film formed. In a previous paper [1], we showed that the film forms more quickly in the presence of solid particles in contact with the substrate and that a correlation exists between the time of film formation and the solid fraction in the alloys: the time of film formation decreased when the solid fraction in the alloy increased. No film was ever formed in the purely liquid areas.

In tests 3 to 5, flows of alloy were observed. A roll formed in the bottom of the sheet. In the case of the

copper rich alloy, the nodules tend to agglomerate against the substrate, by a gravity-dependent effect, because their density is lower than the density of the liquid phase. On the contrary, in the case of the silver rich alloy the solid is heavier than the liquid. So, the nodules tend to agglomerate at the film surface.

3.2. Growth of the solid phase in the film

3.2.1. Experimental results

In the following, we study the evolution of the size and the density of crystals as a function of the duration of their stay in the film. Observation of the substrate

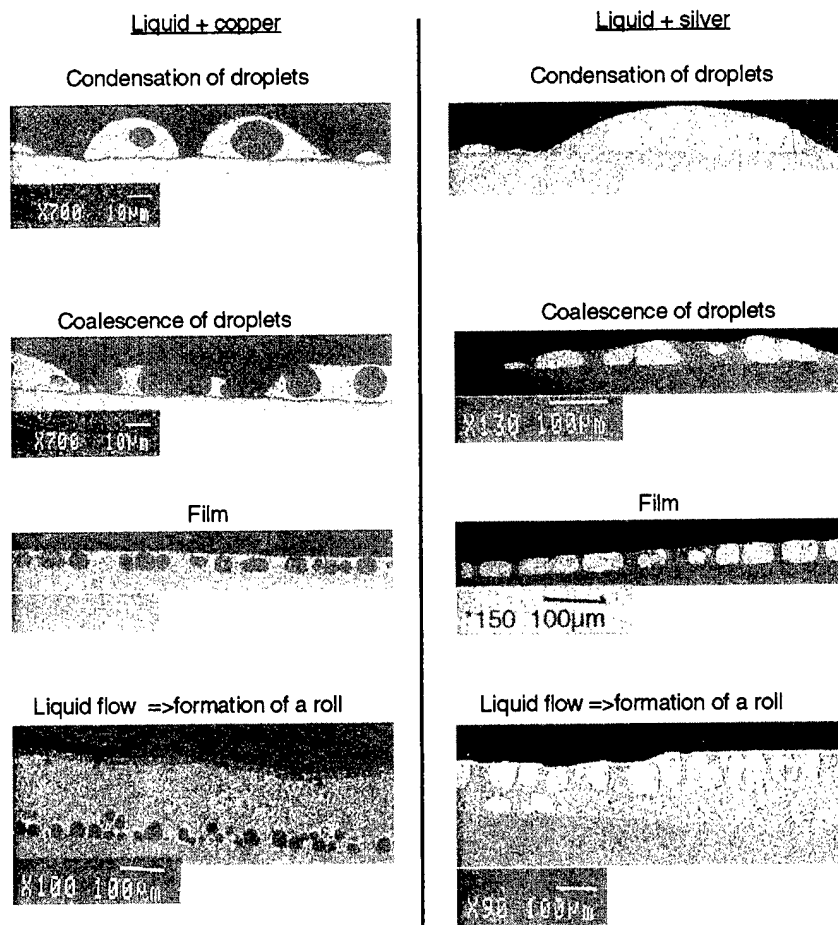


Fig. 3. Successive stages of film formation.

with the video camera during the condensation process showed that the film formed almost instantly in the bottom of the substrate, where the vapour fluxes were the most important. So we can consider that, in those parts of the substrate, the duration of the stay of crystals in the film was equal to the condensation duration. So measurements of the size and number density of particles were made for tests 2 to 5 in those areas.

To measure the mean particle radius, several micrographs were taken on cross-sections of the condensates. On each micrograph, the total surface occupied by the solid phase and the number of nodules were measured. The solid surface measured on each micrograph included the solid surface formed during the quench. So, a correction was made to obtain the total surface occupied by the solid phase during the condensation. By dividing this total solid surface by the number of nodules, and by assuming that the crystals were spherical, we could deduce the mean particle radius on each micrograph and in the total film.

To measure the number density of crystals, some parts of the film were polished superficially to reveal the solid particles. Then micrographs of the polished film surface were taken. An example is shown in Fig. 4. By image analysis, we obtained the number density of crystals per cm^2 . The areas analysed contained between 200 and 400 crystals. Finally, the number density of crystals per cm^3 was deduced by dividing the number density of crystals per cm^2 by the thickness of the film measured on cross-sections of the condensates.

The experimental radius and number density of crystals are shown in Table 2. In tests 2, 3 and 4, where the concentrations of the deposit were very close and the duration of experiment increased, the crystals size was seen to increase with time. Simultaneously, an important decrease in density was observed (compare test 2 to test 4). This indicates that the fluxes, exchanged between the solid and the liquid phases by a ripening mechanism, dominated the solidification flux due to the supply from the vapour. Fig. 5 shows that the cube of the average particle radius is proportional to time and that the

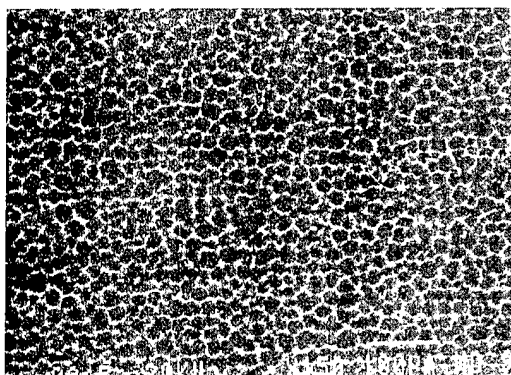


Fig. 4. Polished surface of the film (in the case of copper).

Table 2

Calculated and experimental radius and number density of crystals

Test	Number density (nodules m^{-3})		Mean radius (μm)	
	Experimental	Ostwald law	Experimental	Ostwald law
2	4.5×10^{14}	9.9×10^{14}	9.5 ± 1	11.5
3	8.5×10^{13}	1.7×10^{14}	14.7 ± 2.4	15.2
4	3.5×10^{13}	5.5×10^{13}	19 ± 2.1	20.7
5	1×10^{13}	1.9×10^{13}	55.2 ± 6.3	42.2

density of particles is inversely proportional to time. This is analysed in more detail below.

3.2.2. Discussion

We consider the case where the sites of nucleation are sufficiently numerous and so cannot be the factor which limits the density of solid particles. Then, the ripening of crystals leads to the elimination of a few crystals. Indeed in conventional solidification, that is to say in an isolated system, we can distinguish the following successive stages: nucleation, spherical growth, dendritic growth, ripening of the dendrites until they become spheres, and finally continuation of the ripening by reduction of the number of spherical crystals. In that case, the growth of the solid phase (namely, the increase of the total solid fraction) stops when the initial supersaturation of the liquid phase is consumed (i.e. at the end of the dendritic growth stage). On the other hand, in condensation growth is maintained by the supply of material to solidify from the vapour phase. However, in small time scales this constant flux is exceeded by the flux due to a ripening mechanism, this one being inversely proportional to time. Thus, there will exist a time interval after the nucleation where the Ostwald ripening overcomes the growth from the vapour phase. In this interval, the growth law of the mean particles radius r can be described by the Ostwald law. For a low volume fraction of solid particles in a bulk liquid alloy, this is written [2]:

$$r^3 - r_0^3 = \frac{8}{9} \frac{D\Gamma}{m_L(C_L - C_S)} (t - t_0), \quad (1)$$

where: D is the diffusion coefficient; Γ is the capillary constant related to the local undercooling ΔT , and the curvature, κ by: $[\Delta T = \Gamma\kappa]$; m_L is the liquidus slope; C_L and C_S , respectively, represent the composition of the liquidus and the composition of the solidus; and $(t - t_0)$ is the duration of the stay of crystals in the film.

In principle, the coarsening rate increases with the volume solid fraction [2]. But, in our case, the confining of solid crystals may lead to a slowing down of the ripening process, especially for the largest volume solid fractions, where the liquid layer covering the crystals becomes very thin.

If we assume that the solid fraction f_S is constant and

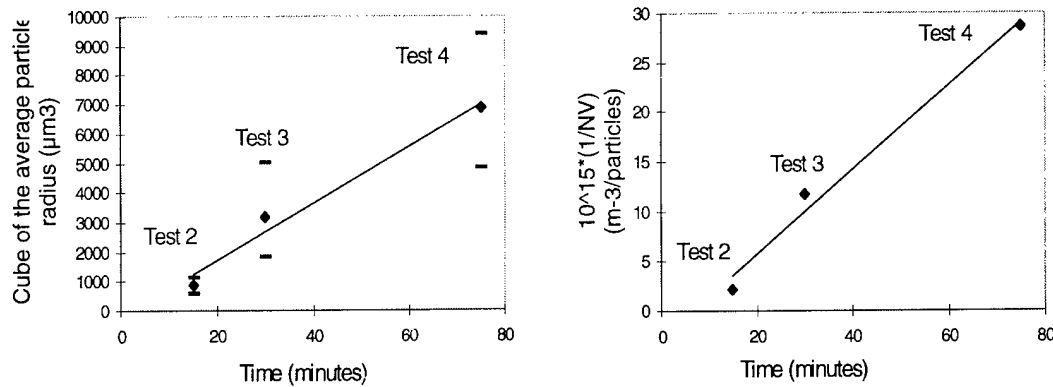


Fig. 5. Experimental radius and number density of crystals vs. time.

equal to the value given by the phase diagram, we have:

$$f_s = \frac{4\pi}{3} r^3 N_V, \quad (2)$$

where N_V is the volumic density of solid particles.

Thus, we obtain for the variation of N_V with time:

$$\frac{1}{N_V} - \frac{1}{N_{V_0}} = \frac{32}{27} \pi \frac{D\Gamma}{f_s m_L (C_L - C_S)} (t - t_0). \quad (3)$$

For most metals, Γ is of the order of 10^{-7} Km [3]. Some values are available in the literature for the silver–copper system. For a silver rich liquid, $\Gamma = 1.6 \times 10^{-7}$ Km [4]. Near the eutectic, $\Gamma = 2.5 \times 10^{-8}$ Km [5]. The diffusion coefficient D is equal to 2×10^{-9} m² s⁻¹ [4].

In our case, t_0 is the time of film formation and we have $r_0 \ll r$ and $N_{V_0} \gg N_V$ as indicated by the values of these quantities in the regions where the film has not yet been formed.

The values of r and N_V calculated for tests 2 to 5 using Eqs. 1 and 3 are compared with experimental results in Table 2. They are in the same order of magnitude. Thus, the Ostwald ripening law gives a good approximation of the variation of the particle radius and the number density of crystals as a function of the duration of the stay of crystals in the film.

4. Conclusion

In the present experimental study, silver–copper alloys with a composition entering a liquid–solid domain of the phase diagram were condensed on molybdenum substrates. The successive stages of the film formation were equivalent in the two liquid–solid domains. First, droplets of condensation formed. They contained nodular crystals, most of which were in contact with the substrate. Heterogeneous nucleation on the substrate was assumed. With time, the droplets grew and then a film formed. In the film, the Ostwald ripening process overcame the growth from the vapour phase. Thus, the cube of the average particle radius grew with time and the number density of crystals was inversely proportional to time.

References

- [1] S. Leroux, J. Le Ny, C. Guéneau, J. Granier, B. Drevet, D. Camel, *J. Cryst. Growth* 198/199 (1999) 911–916.
- [2] S.C. Hardy, P.W. Voorhees, *Met. Trans.* 19A (1988) 2713–2721.
- [3] W. Kurz, D.J. Fisher, *Fundamentals of Solidification*, Trans Tech Publications, 1998.
- [4] O. Dumas, PhD Thesis, INPG Grenoble, 1996.
- [5] P. Gressin, PhD Thesis, LTPCM Grenoble, 1982.

Determination of resputtering yields in carbon nitride films grown by dual ion beam sputtering

C. Quirós ^{a,*}, P. Prieto ^a, E. Elizalde ^a, R. Pérez-Casero ^a, V. Gómez ^b, P. Herrero ^b, J.M. Sanz ^a

^a Dpto. Física Aplicada, C-XII, Universidad Autónoma de Madrid, E-28049 Madrid, Spain

^b Instituto de Ciencia de Materiales de Madrid, CSIC, E-28049 Cantoblanco, Madrid, Spain

Abstract

Resputtering phenomena play an important role in the growth of carbon nitride films assisted with low energy N_2^+ ions. CN_x films [x ranging between 0 and 0.6, as determined by Auger electron spectroscopy (AES)] have been prepared by dual ion beam sputtering and characterized by several techniques [AES, Rutherford backscattering (RBS), Fourier transform infrared (FT-IR), transmission electron microscopy (TEM), transmission electron diffraction (TED)]. In this work we have estimated the resputtering yields of carbon and nitrogen atoms in terms of the deposition rate and the surface composition, as determined by AES depth profiling and RBS measurements. Carbon resputtering yield in the order of 0.3 carbon atoms per incident N_2^+ ions and nitrogen re-emissions higher than 90% are obtained. A threshold is found for the arrival rate ratio (ARR) of N_2^+ ions to C atoms of about 3.0. Higher values of ARR will inhibit the growth of the film. The influence of the energy of assistance and the electric properties of the substrates in the resputtering process are also discussed. © 2000 Elsevier Science S.A. All rights reserved.

Keywords: AES depth profiling; Carbon nitride; Chemical resputtering; Dual ion beam sputtering; Resputtering yields

1. Introduction

The search for the promising β - C_3N_4 phase proposed by Liu and Cohen [1] has generated many efforts in the preparation of carbon nitride films. Several techniques of synthesis have been used, however, all the approaches have shown great difficulties in incorporating nitrogen to the desired level. In particular, plasma vapour deposition (PVD) methods show a limit of around 45% for atomic nitrogen [2]. Chemical resputtering due to the formation of volatile compounds has been proposed to explain the difficulties of growing films with higher nitrogen concentrations and significant thickness [2–4], nevertheless not many works have tried to estimate the resputtering mechanisms.

Although the films do not have the required stoichiometry, their mechanical properties have technological interest for the possibility of application as hard and wear resistant coatings [5,6]. For these applications it is necessary that coatings reach sufficiently high values of

thickness. From this point of view, the quantification of the resputtering mechanisms has practical interest, since it can give information about the growth rates and thickness attainable.

2. Experimental

The films have been prepared on Si(100) and KCl substrates in a dual ion beam sputtering system (DIBS) at a base pressure of 10^{-5} Pa. The system has two ion sources. The first one, a 3 cm Kaufmann-type, is used to sputter a 4" graphite target (99.999% purity) with inert Ar^+ ions at an angle of incidence of 45° . The second one, an end-Hall ion source, is used to simultaneously bombard the substrates with reactive N_2^+ ions in order to supply nitrogen to the growing film. This reactive assistance is made at 60° off normal of the substrates. The substrates were rotated at 2 rpm to increase homogeneity, and kept at $200^\circ C$ during the deposition time (5 h for all the samples). The temperature of the substrates was determined with an iron/constantan thermocouple located in the metallic

* Corresponding author. Tel.: +34-91-397-4924;

fax: +34-91-397-3969.

E-mail address: carlos.quirós@uam.es (C. Quirós)

body of the sample holder, at 3 cm from the substrates. One of the advantages of this system, in relation to other deposition methods like magnetron sputtering, is the possibility of independent control of the carbon flux, coming from the Ar^+ sputtering of the graphite, and the nitrogen flux, coming from the N_2^+ assistance. The sputtering and assistance conditions are summarized in Table 1.

The surface composition of the samples grown on Si and KCl was determined by Auger electron spectroscopy (AES) and some additional X-ray photoelectron spectroscopy (XPS) measurements. Both were performed ex situ, after a short exposure to atmosphere, in a PHI-3027 spectrometer equipped with a double pass CMA using 3 keV electrons and Mg $K\alpha$ radiation ($h\nu = 1253.6$ eV), respectively. Sensitivity factors from the manufacturer were used to determine the compositions. FT-IR spectra were obtained on KCl substrates in a Bruker IFS66V FTIR spectrometer between 7000 and 560 cm^{-1} with a resolution of 4 cm^{-1} . A previously collected spectrum of pure KCl substrate was used as reference. The morphology and structure of the films grown on KCl substrates have also been studied by transmission electron microscopy (TEM) and transmission electron diffraction (TED) measurements that have been performed in a JEOL JEM-2000FXII microscope operating at 200 kV. This microscope is provided with an energy dispersive X-ray analysis system (EDX), LINK QX200 to obtain information about composition. The thicknesses were obtained with AES depth profiling combined with the external calibration provided by Rutherford backscattering (RBS) measurements. AES depth profiles were made with 2 keV Ar^+ ions rastered over an area of 2 mm \times 2 mm. The KLL Auger peaks of C, N and O, as well as Si LMM, were monitored as a function of sputtering time. RBS experiments were carried out using a He beam of 2 MeV and the scattered ions were detected at 165°. Random and channelling geometries were used, the latter providing better resolution for the determination of the light element amounts since it diminishes the background signal due to the silicon substrate.

3. Results and discussion

3.1. Characterization of the samples

In order to make easier the analysis of the results, the samples were deposited keeping constant the sputtering parameters, so that the flux of carbon atoms arriving at the growing film, J_C , and the total deposition time were the same for all samples. The only parameter that was changed from one sample to another was the N_2^+ flux, although, in order to achieve the different values of the N_2^+ flux, small changes were also required in the energy of these ions. The first three columns of Table 1 show these deposition parameters. The value of J_C has been deduced from the thickness of the non-assisted film, i.e. amorphous carbon film, the deposition time and the density of graphite (2.26 g/cm^3) [7]. The values of J_N and E were obtained from the current density specifications of the ion gun and the assumption that most of the nitrogen ions generated in the ion source are N_2^+ instead of N^+ .

The flux of C atoms coming from the target and arriving at the substrate (first column), and the flux of N_2^+ coming from the assisting gun and arriving at the substrates, can be combined in a magnitude, called ARR (arrival rate ratio) and shown in the fourth column of Table 1. The ARR is the number of N_2^+ ions that arrive at the growing film per C atom that reaches the film. This parameter does not take into account the effect of the ion's energy. Nevertheless, due to the fact that the range of energies employed is not very high (55–87 eV), this effect was eliminated from the discussion, although, as will be discussed later on, it has some measurable influence on the results.

The two remaining columns present the thickness and the surface composition of the films. The thickness was determined with AES depth profiling of the films grown on Si(100) substrates. All the samples were subjected to AES depth profiles under the conditions explained previously. The time required to reach the film/substrate interface was measured monitoring the CKLL, NKLL and Si LMM signals. The film/substrate interface was

Table 1
Sputtering and assistance fluxes, energy of assistance, arrival rate ratio, thickness and N/C atomic ratio of the films

Sample	J_C (C atoms/ cm^2 s)	J_N (N_2^+ ions/ cm^2 s)	E (eV)	ARR (N_2^+ ions/C atoms)	Thickness (nm)	N/C (AES)
A0	1.52×10^{14}	0	0	0	243	0.00
A1	1.52×10^{14}	1.9×10^{14}	55	1.2	143	0.23
A2	1.52×10^{14}	3.4×10^{14}	65	2.3	55	0.30
A3	1.52×10^{14}	4.1×10^{14}	71	2.7	26	0.41
A4	1.52×10^{14}	4.5×10^{14}	73	3.0	13	0.64
A5	1.52×10^{14}	4.8×10^{14}	76	3.2	1	0.81
A6	1.52×10^{14}	5.2×10^{14}	87	3.4	2	—

defined as the point in the profile at which the decay of the intensity of the C and N signals (or the increase in the Si signal) was in an equidistant position from the steady state parts of the profile. Once these etching times were determined, an external calibration was needed to translate these values to thickness in nanometres. To do this conversion one of the samples, A3, was measured with RBS. The atomic areal density obtained, 280×10^{15} atoms/cm², was used to obtain the thickness just dividing by the atomic volume density ρ . This value was provided by a bibliography search. Rossi et al. [8] have measured a density of 2.3 g/cm³ for a sample grown with the same preparation method and a composition similar to that of sample A3. The thicknesses obtained have been depicted as a function of the ARR in Fig. 1, together with the N/C atomic ratio.

The N/C atomic ratio, presented in the last column of Table 1, was determined by AES measurements of the surface of the samples grown on Si(100) substrates. The N/C compositions are shown in Fig. 1 versus the corresponding ARR values. The N/C composition of sample A6 is not presented due to the fact that it has high concentration of metallic impurities (20% as stated by XPS measurements). The origin of this contamination is the sputtering that takes place in the discharge chamber of the assistance ion gun when it works at the high power regime needed to obtain high ARR values.

The conclusion that can be obtained from Fig. 1 is that the increase of the assistance conditions, i.e. ARR, leads to the increase of the nitrogen concentration of the sample and to the progressive thinning of the films. As J_C is kept constant, the only explanation to this thinning is the existence of resputtering processes that remove material from the growing film and slow down the growth rate. In fact, Fig. 1 shows that values of ARR higher than 3.0 completely inhibit the growth of the film. The high N concentrations in the thinner films are associated with the nitridation of the silicon substrate that can be detected by AES since the probing depth is in the order of the thickness of these films.

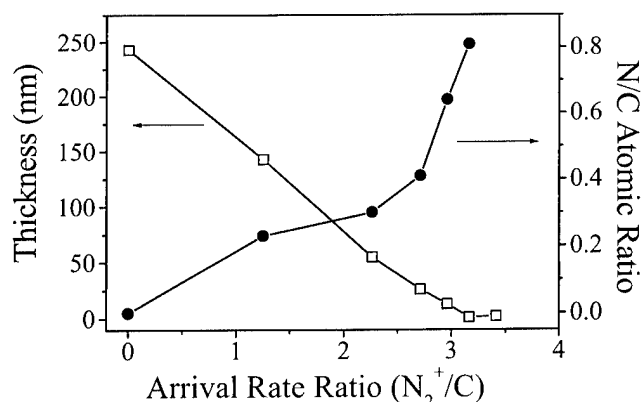


Fig. 1. Thickness and N/C atomic ratio as a function of ARR.

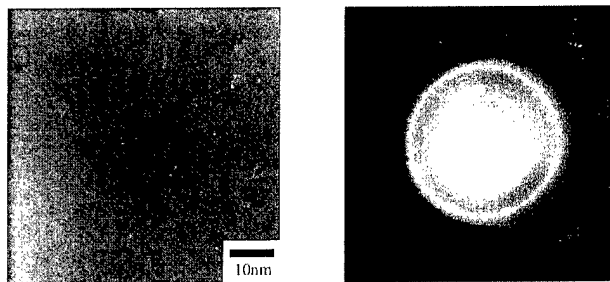


Fig. 2. (a) TEM image of sample A1, (b) electron diffraction pattern of sample A1.

TEM images and diffraction patterns have been obtained in the films grown on KCl substrates after they were floated off in water. In the case of A1, Fig. 2(a) shows a homogeneous morphology with small granulated structure. In Fig. 2(b) the corresponding electron diffraction pattern has diffuse halo rings indicating that the film is amorphous. Additional characterization of the films on KCl made by FT-IR show that they are mainly formed by C–N and C=N with increasing amounts of C≡N as ARR increases, probably associated with the incorporation of K into the films and the formation of KCN.

3.2. Determination of the resputtering coefficients

At the energies and fluxes used in this work, it is not to be expected that physical resputtering is playing a significant role [2]. However, chemical resputtering, via the formation of volatile compounds like C_2N_2 , N_2 , CNH or CNOH, has been reported like a mechanism of removing material from the growing carbon nitride films prepared in ion beam assisted systems [2–5]. In order to quantify the importance of these resputtering processes, a simple empirical growing model has been developed that, starting from the measurements of thickness and N/C composition, gives an estimation of the resputtering yields. In this model, the following variables are defined: N_i , nitrogen atoms arriving at the film; N_o , nitrogen atoms ejected from the film; N , nitrogen atoms incorporated into the film; C_i , carbon atoms arriving at the film; C_o , carbon atoms ejected from the film; C , carbon atoms incorporated into the film; r_C , resputtering yield of carbon (i.e. number of carbon atoms ejected per N_2^+ arriving ion); r_N , resputtering yield of nitrogen (i.e. number of nitrogen atoms ejected per N_2^+ arriving ion).

Taking into account that J_N is the number of N_2^+ ions arriving at the film per square centimetre per second, and that J_C is the number of carbon atoms arriving at the film per square centimetre per second, and assuming that most of the N_2^+ ions dissociate into two nitrogen atoms when they impact with the surface of the film at the energies employed (55–87 eV) [3], the

following relations can be written between the variables defined previously:

$$N_i = 2J_N; \quad N_o = J_N r_N; \quad C_i = J_C; \quad C_o = J_N r_C.$$

The number of nitrogen atoms incorporated into the film will be the difference between N_i and N_o :

$$N = N_i - N_o = 2J_N - J_N r_N.$$

Analogously, the number of carbon atoms incorporated into the film can be written as:

$$C = C_i - C_o = J_C - J_N r_C.$$

The sum of N and C gives the total number of atoms incorporated into the film per unit area and time. If this sum is divided by the atomic density of the films, the growth rate can be obtained, and for a given time of 5 h, the corresponding thickness, that can be compared with the experimental ones. This procedure is assuming again that the atomic density is not changing too much for the different stoichiometries of the samples. The growth rate is then:

$$v = \frac{N + C}{\rho} = \frac{2J_N - J_N r_N + J_C - J_N r_C}{\rho} \\ = \frac{2J_N + J_C - J_N(r_N + r_C)}{\rho}.$$

The atomic ratio N/C can be expressed as:

$$\frac{N}{C} = \frac{2J_N - J_N r_N}{J_C - J_N r_C}.$$

In these two equations only two factors are unknown, r_C and r_N . Using the experimental values of N/C and of the growth rate (i.e. thickness divided by 5 h), these resputtering yields can be obtained.

The results are shown in Fig. 3 as a function of N/C . The qualitative behaviour of these factors indicates the decrease of the resputtering yield of carbon and the increase of the resputtering yield of nitrogen with the N/C ratio of the films. The resputtering yield of carbon

under N_2^+ bombardment decreases with N/C due to the fact that when N/C increases the proportion of carbon atoms in the film decreases, and then the incoming nitrogen ions have less probability of recombination with the less abundant carbon atoms to form volatile compounds. On the contrary, the resputtering yield of nitrogen under N_2^+ bombardment increases with N/C for the opposite reason, the higher probability of recombination between the arriving ions and the more abundant nitrogen atoms in the film.

The quantitative values obtained are close to those reported by Hammer et al. [2] for r_C in a sample of carbon ($N/C=0$). They found $r_C=0.5$ for a bombardment with N_2^+ ions of 150 eV. In this work, the poorest sample in nitrogen ($N/C=0.2$) has $r_C=0.4$, and the extrapolation to $N/C=0$ gives a value similar to 0.5. In the case of nitrogen, Todorov et al. [4] have estimated re-emissions of nitrogen in the order of 80%. The values obtained in the present work point to r_N higher than 90%. These high values of the resputtering yield of nitrogen give an idea of the difficulties of incorporating nitrogen into the carbon nitride films.

3.3. Effect of the assisting energy on the resputtering process

As mentioned before, in the previous discussion the effect of the energy of the assisting ions was ignored to simplify the analysis. Nevertheless, the assistance with N_2^+ ions of different energies is to be expected to produce different results. The existence of energy thresholds in the resputtering processes (physical or chemical), and the dependence of the penetration depths and recombination probabilities of the ions with their energy, have to be taken into account to explain the effect of the energy on the assistance.

In order to quantify this effect at the energies used in this work, two samples were prepared with the same value of J_C and J_N but with different energies, 65 and 87 eV. This increase in energy of 20 eV increases the efficiency of the resputtering processes, leading to a measurable decrease in thickness of around 8%.

An additional study was made to obtain information about the influence of the insulating character of the substrate in the growth of the films. Three different substrates were used to deposit simultaneously a sample assisting with 65 eV nitrogen ions. The substrates were silicon wafers with a layer of SiO_2 of different thickness: 4 nm (native oxygen), 580 nm and 770 nm. The AES depth profiles, performed under the same conditions in the three films, indicate that the increase of the thickness of the SiO_2 layer of the substrate leads to the decrease of the thickness of the carbon nitride film grown upon it. The explanation proposed is that the increase in the oxide layer produces a more insulating substrate that accumulates higher negative surface charge during the

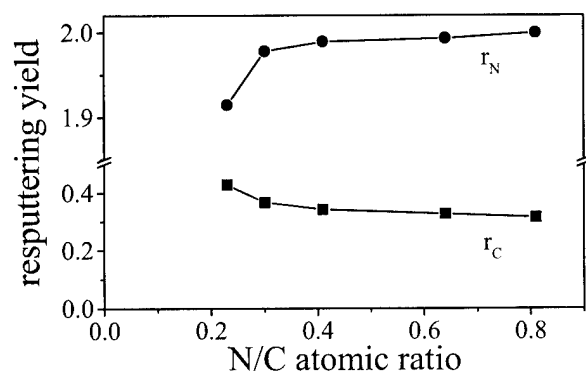


Fig. 3. Resputtering yields of carbon and nitrogen as a function of N/C atomic ratio.

assistance with positively charged nitrogen ions. This negative charge increases the energy of the incoming ions, increasing their resputtering efficiency and leading to thinner films. The N/C ratios observed are very similar for all the films, but a detailed analysis of the data shows that the thinner film has a slight increase of N/C in relation to the other two films, pointing in the same direction as the thickness data, that is, the increase of the energy of the assisting ions. These evidences confirm that the assistance conditions are not similar for substrates with different insulating properties, and that some characteristics (like thickness) of the carbon nitride coatings prepared with ion based methods can present significant changes, depending on the type of substrate employed.

4. Conclusions

Thin films of carbon nitride grown in a dual ion beam sputtering system show a strong dependence of their N/C atomic ratio and thickness on the assisting conditions. In order to quantify the intensity of the assisting conditions and to correlate the deposition parameters with the characterization measurements, the ratio of N_2^+ ions to C atoms that arrive at each film, ARR, has been determined.

The thickness of the films, obtained by AES depth profiling and RBS measurements, shows a linear decrease with ARR that indicates the presence of marked resputtering phenomena. In fact, a threshold is obtained at around 3.0 N_2^+ ions/C atoms. Growths at higher values of ARR lead to very low rates that produce films of the order of a few nanometres.

The N/C atomic ratios, obtained by AES, increase with ARR from 0 to 0.6 approximately. Higher values obtained for ARR above 3.0 N_2^+ ions/C atoms are related to the thinning of the films and the formation of silicon nitride in the interface.

In order to explain the behaviour observed for thickness and N/C data, a simple growth model has been applied taking into account and trying to quantify the resputtering processes. The values of the resputtering yields of carbon and nitrogen under N_2^+ bombardment have been determined as a function of the N/C ratios. Carbon resputtering yields in the order of 30% and nitrogen re-emissions higher than 90% are obtained. The increase of the energy of assistance produced the enhancement of the resputtering phenomena. The dependence observed of the thickness and composition of the films on the insulating character of the substrates has been related to the accumulation of negative electric charges in the surface of the film. This accumulation of electric charges increases the energy of assistance and the intensity of the resputtering processes.

Acknowledgements

The CICYT of Spain (Contract No. MAT96-0676), and the EU (Contract No. BE97-4845) are acknowledged for financial support.

References

- [1] A.Y. Liu, M.L. Cohen, Phys. Rev. B 41 (1990) 10727.
- [2] P. Hammer, M.A. Baker, C. Lenardi, W. Gissler, Thin Solid Films 290/291 (1996) 107.
- [3] R. Kaltofen, T. Sebal, G. Weise, Thin Solid Films 290/291 (1996) 112.
- [4] S.S. Todorov, D. Marton, K.J. Boyd, A.H. Al Bayati, J.W. Rabalais, J. Vac. Sci. Technol. A 12 (1994) 3192.
- [5] W.-C. Chan, B. Zhou, Y.-W. Chung, C.S. Lee, S.T. Lee, J. Vac. Sci. Technol. A 16 (1998) 1907.
- [6] H. Jensen, J. Sobota, G. Sorensen, J. Vac. Sci. Technol. A 16 (1998) 1880.
- [7] R.B. King (Ed.), Encyclopedia of Inorganic Chemistry Vol. 2, Wiley, New York, 1994, p. 554.
- [8] F. Rossi, B. Andre, A. Van Veen, P.E. Mijnders, H. Schut, F. Labohm, M.P. Delplancke, H. Dunlop, E. Anger, Thin Solid Films 253 (1994) 85.

Plasma polymer films and their future prospects

H. Biederman *, D. Slavínská

*Department of Macromolecular Physics, Charles University at Prague, Faculty of Mathematics and Physics, V Holesovickach 2,
180 00 Prague 8, Czech Republic*

Abstract

Plasma polymerization processes began their fast development in the 1950s. They have been widely recognized during the last 20 years and several successful applications have emerged. Two special groups of plasma polymers that have received increased attention in recent years are treated in detail here. First, the deposition process and basic properties such as the structure, morphology, electrical and optical properties, and ageing of metal (Ag, Ni, Mo) and semiconductor (Ge)/hard plasma polymer (C:H) composites are described consisely. The deposition process is based on unbalanced magnetron sputtering with the target operated in an argon/n-hexane working gas mixture. Second, the preparation of plasma polymer films by radio-frequency sputtering from polymeric targets is introduced and their basic properties, especially structure and morphology, are revealed. Most attention is paid to fluorocarbon plasma polymer films sputtered from polytetrafluoroethylene (PTFE). For both groups of plasma polymers, application possibilities are discussed. The whole range of plasma polymers and their future prospects are summarized, starting from those resembling conventional polymers that are prepared at low power, and ending with the new materials prepared at high power. © 2000 Elsevier Science S.A. All rights reserved.

Keywords: Plasma; Plasma polymers; Sputtering; Thin films

1. Introduction

Plasma polymerization has been studied intensively since the 1950s [1,2] and especially in the 60s [3,4]. So-called carbonaceous films were prepared by König and co-workers [1,5] in a glow discharge in benzene vapour using a parallel-plate electrode arrangement powered by singly rectified 50 Hz voltage. According to the infrared (IR) absorption spectra they fabricated not only a hydrocarbon plasma polymer, but also a hard polymer (C:H) and a material approaching an amorphous hydrogenated carbon (a-C:H). However, the first a-C:H films are related to the report by Schmellenmeier [2].

A real application of a dielectric separating film, comprising a plasma polymer prepared from styrene, was attempted by Goodman [3]. In addition, Bradley and Hammes [6] plasma-polymerized 40 'potential' monomers and prepared organic dielectric and semiconducting films.

During the last 20 years, plasma polymerization has been recognized as an established field. A number of

applications have been proposed. Several reviews and monographs have been published [7–13].

The plasma polymerization process is usually achieved by means of the two types of reactor: (1) a bell-jar type reactor with internal parallel-plate metal electrodes; and (b) a tubular-type reactor with an external coil or ring electrodes for excitation by radio-frequency (RF) discharge. In the case of the bell-jar type reactor, a direct-current (DC) or an alternating-current (AC) voltage (up to 50 kHz) is usually used. RF (100 kHz–30 MHz) voltage for the discharge excitation can also be applied. Microwave discharges have become widely used as well, with various methods of application of the microwave energy (the most frequent is the multimode cavity or 'microwave oven' mode). Magnetic fields have also been employed to assist plasma polymerization: electron cyclotron resonance (ECR) discharges and planar or cylindrical magnetrons [8–11].

The deposition rate of a plasma polymer is determined by the following parameters: the geometry of the system, the reactivity of the starting monomer and its flow rate, the working gas pressure, the power and frequency of the excitation signal and, finally, the temperature of the substrate [9–11]. We also have to take into account energetic particle bombardment from the

* Corresponding author. Tel.: +420-2-688-5095;
fax: +420-2-2-191-2360.

E-mail address: bieder@mbx.troja.mff.cuni.cz (H. Biederman)

discharge such as energetic photons, neutrals and positive ions. However, at the same time, excessive energetic bombardment changes the structure and properties of the growing film.

Several kinetic models of plasma polymerization have been proposed. The most popular are the models of Lam et al. [14], Poll et al. [15] and Yasuda [10]. These models involve a competitive ablation and polymerization mechanism (CAP). Plasma polymerization is then described by a bicyclic step-growth mechanism.

The structure of plasma polymers has been examined by IR spectroscopy, nuclear magnetic resonance spectroscopy (NMR), electron spectroscopy for chemical analysis (ESCA), Auger electron spectroscopy (AES), Rutherford backscattering spectroscopy (RBS), elastic recoil detection analysis (ERDA) and nuclear reaction analysis (NRA). Tibbitt et al. [16] postulated a possible network of plasma-polymerized ethylene using IR absorption spectra and computer analysis. The chains are short and branched, and randomly terminated with frequent crosslinks. The network has no repeating units and contains a number of various groups including trapped free radicals. This often leads to ageing when the film is exposed to the atmosphere.

The energy flux into the growing plasma polymer film is decisive for the film structure and final properties. The increase of this energy usually causes the film to be harder — it becomes more disordered and crosslinked with an excess of carbon. If the energy flux is low, a plasma polymer is created that retains more of the molecular structure of the monomer and resembles a more conventional polymer.

During the last decade, the two main directions — (1) new materials including hard coatings and composite films, and (2) plasma polymers resembling conventional polymers — were investigated. Recently, the usual plasma polymers prepared under medium energetic conditions have become the centre of attention again.

2. Plasma polymers prepared under low energy flux

The plasma polymers prepared under a low energy flux resemble conventional polymers. The approaches that may achieve enhanced control of plasma polymer film chemistry can be summarized as follows [17]: (1) minimization of the W/FM parameter (W , plasma power; F , flow rate; M , precursor molecular weight); (2) pulsing of the RF field to reduce the 'plasma-on' time; (3) use of a Faraday cage around the substrate; (4) positioning the sample downstream from the plasma zone; (5) use of monomers containing polymerizable double bonds; and (6) use of a cold substrate. Except for the last item, these procedures have been investigated extensively (for a review, see Refs. [10,11]). For example, plasma polymerization of 2-hydroxyethyl methacrylate

(HEMA), a polymerizable monomer, and acetone [18,19] was performed. In the case of HEMA, when the substrate was cooled to liquid nitrogen temperature, the resulting plasma polymers of HEMA closely resembled conventional poly(HEMA). Plasma polymers have been shown to be promising for biomedical applications [11]. Biocompatible interfaces (non-cytotoxic, non-stimulatory) have been prepared on many substrates using as an interlayer a plasma polymer of n-hexane that was coated by a plasma polymer of hexamethyldisilazane (HMDSN). Also, *N*-vinyl pyrrolidone and other compounds were used and examined as non-thrombogenic interfaces. More findings are summarized in [13,20].

Plasma polymerization of TFE outside the plasma zone was performed by Kiaei et al. [21]. They obtained films composed almost entirely of CF_2 units. These films were found by near-edge X-ray absorption fine structure (NEXAFS), using polarized X-rays, to be highly oriented normal to the substrate [22]. Similar findings are summarized in [13]. The plasma polymerization of tetrafluoroethylene (TFE), mentioned above, is a good example that substantial conventional (free radical) polymerization can occur when plasma process conditions are conveniently chosen. Similar results in obtaining 'ordered' fluorocarbon plasma polymers were achieved with use of pulsed RF discharges by Timmons et al. [23] and Badyal [24]. Successful application of these plasma polymers followed as highly water-repellent coatings on fabrics, foils, etc.

In contrast, improvement of the wettability was required, and this was achieved by means of plasma polymers containing polar groups. Investigators used as monomers both saturated [25] and unsaturated alcohols [26], amines and amides [25,27], ethylene- O_2 [28] or acetone- O_2 [29] mixtures. Some researchers [26,30,31] mixed water vapour with their monomers during plasma polymerization for enrichment of the resulting films with polar groups.

3. Plasma polymers and organic films prepared under high energy flux

When a growing hydrocarbon plasma polymer is subjected to bombardment by energetic particles it changes into a hard plasma polymer sometimes called 'C:H'. When the energy of the bombarding particles is increased further, the resulting deposit has unusual properties: high electrical resistivity (10^6 – $10^{16} \Omega \text{ cm}$), optical transparency in the infrared region (optical gap from 2.1 to 0.9 eV), hardness higher than sapphire and chemical inertness. This type of coating is the very well known amorphous hydrogenated carbon ('a-C:H') which, because of its unusual properties, is sometimes called diamond-like carbon (DLC). Coatings can be prepared easily in a parallel-plate electrode system using

RF power in an asymmetrical arrangement if the substrate is placed on a small, capacitively coupled excitation electrode while the other electrode and all metal components of the chamber are earthed [32].

A DC negative self-bias develops on the excitation electrode at a hydrocarbon gas pressure of typically several Pa. Hydrocarbon plasma polymer obtained at low biases turns into hard polymer (C:H) at an increased bias. When several hundred volts are reached, an a-C:H deposit is obtained that becomes graphitic at excessive voltages. This holds provided the substrate temperature is kept below 300°C. Above this temperature, graphitic deposits are always obtained. A DC glow discharge in a hydrocarbon gas has also been employed in a diode arrangement to deposit a-C:H films on conducting substrates placed on the cathode [33]. Deposition of a-C:H film was reported using DC post-cathode cylindrical and planar magnetrons operated in Ar–C₂H₂ mixture [34]. The stainless steel cathode is coated by carbonaceous material that is sputtered off and deposits on an electrically floating substrate together with a material from a plasma polymerization process. Simultaneous energetic bombardment is provided by neutrals reflected from the cathode when a low working gas pressure is used. For the production of hard carbonaceous coatings, the so-called unbalanced planar magnetron is also used [35–37]. In this case an amorphous hard carbon (a-C) containing no hydrogen was deposited by the sputtering of graphite in argon at a pressure of 1 Pa.

Researchers have attempted to produce materials such as a-C:F:Cl [38] and a-C:F [39] using RF diode arrangements. Films of the a-C:F:H type have received more attention [40]. In Ref. [41], DC magnetron sputtering from a glassy carbon target in an argon–hydrogen–hexafluoroethane atmosphere was reported. The films possessed low conductivity, good transparency, great hardness and low wettability. They exhibited higher density and refractive index than films deposited in a glow discharge [40,42]. In Ref. [43], a-C:H:F films were prepared in an RF discharge operated in a H₂ + C₂F₆ mixture using a reactor with a triode electrode arrangement. The films obtained were deposited on the substrate resting on the third electrode possessing temperature below 200°C and DC negative bias from 100 to 150 V. The feed gas mixture contained 5–12% C₂F₆.

Since the first report on nitrogen-doped a-C:H films by Jones and Stewart [44], hydrogenated carbon nitride films (a-C:H:N) have been prepared from a plasma of CH₄ and N₂ gases, using a cyclohexane–N₂–Ar mixture. Recently, a-C:H:N films were deposited in an RF diode system in methane–nitrogen mixtures with up to 25% N₂ at a total pressure 8 Pa and negative self-bias of 370 V. Films were deposited on silicon substrates with a thickness up to 350 nm, and also comparative a-C:H films were grown under the same conditions. The composition of the a-C:H film was 86.1 at.% carbon and

13.9 at.% hydrogen, while for a-C:H:N it was 78.1, 14.1 and 7.8 at.% for carbon, hydrogen and nitrogen, respectively. The incorporation of 7.8 at.% of nitrogen in a-C:H:N films did not change the hardness (21 GPa); however, it lowered the internal stress considerably from 2.5 GPa (a-C:H) to 1.6 GPa (a-C:H:N) [45,46].

Hard plasma polymers (C:H) can be prepared in an unbalanced planar magnetron using a mixture of a hydrocarbon gas and argon. The energetic, positive, argon-ion and hydrocarbon-fragment-ion bombardment is caused by the accelerating electric field. This field originates from the floating potential appearing on the substrate surface when it is immersed in a plasma beam directed at it by the unbalanced magnetic field of the magnetron [35–37,45]. Using the type of magnetron described, graphite was sputtered in argon and propane [45,46]. Sputtering of graphite resulted in a-C films that were electrically insulating and rather hard, but their hardness did not reach that of a-C:H. The addition of a small amount of propane to the argon caused the resulting films to be optically more transparent — their optical gap was well above 2 eV and increased with the addition of more propane.

Using this technique another class of films discussed in this section can be produced: composite metal/hard plasma polymer films (C:H) [47–50]. Generally, many more composite films (e.g., metal-doped fluorocarbon or organosilicon plasma polymer films) have been deposited and studied (for a review see, e.g., [11,51]).

Recently, in our laboratory, we studied hard plasma polymers (C:H) doped with silver [52], nickel [53,54] and molybdenum [55], prepared in a working gas mixture of argon + n-hexane. The deposition arrangement is shown schematically in Fig. 1. The unbalanced magne-

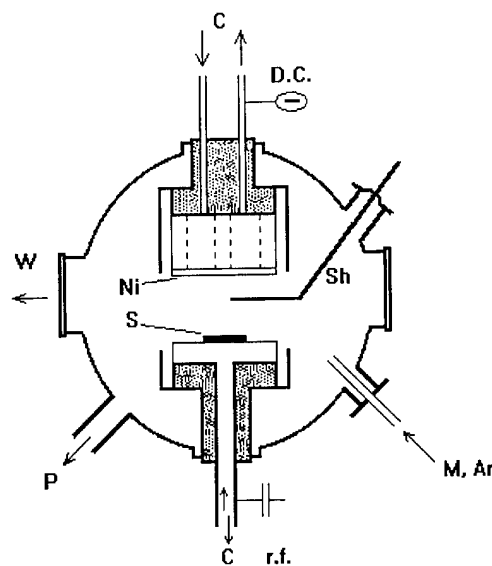


Fig. 1. The deposition arrangement: Ni, target; S, substrate; W, window; Sh, shutter; M, Ar, gas inlets; P, to pumps; C, cooling.

tron was positioned upside down and the substrate rested on a support that could be RF powered and hence develop additional DC negative self-bias. Usually we did not power this substrate holder and the accelerating field for positive ions was produced only by the floating potential of the substrate in the plasma beam from the unbalanced magnetron. This was typically -30 V (against ground.) The pressure of the working gas mixture (argon + n-hexane) was 3 mtorr, the flow of argon was $1.5 \text{ ccm (STP) min}^{-1}$, that of n-hexane $0.5 \text{ ccm (STP) min}^{-1}$, the operating voltage of the magnetron was between 300 and 500 V, and the current was always 200 mA.

In situ monitoring of the deposition process was done by optical emission spectroscopy. Also, detailed study of the deposition process was performed by using the electrically grounded aperture plate of an energy-selective mass spectrometer (Hiden Analytical-EQP 300). It was found that the grounded substrate is bombarded mainly by positive CH_3^+ , Ar^+ and Ni^+ ions, with mean energy ranging from 2 to 10 eV.

The plot of electrical resistance versus metal volume fraction, f , shows percolation behaviour. The electrical resistance ($100 \text{ G}\Omega$) of Ag/C:H for values of f below 0.2 decreases over several orders of magnitude for Ag/C:H with f approaching value 0.4. At the same value of f a decrease in resistance takes place also for Ni/C:H, but it is not so sharp. For Mo/C:H this happens at $f \sim 0.5$ and the resistance decrease is rather slow. The optical transmission in the visible range for Ag/C:H reveals so-called anomalous absorption [11], which gives the films a pink colour at low f and a violet/blue colour at higher f . This is not the case for Ni/C:H and Mo/C:H films.

Considerable effort was paid to the investigation of ageing phenomena in open air. Fig. 2 presents the sheet resistance of the three types of film: Ag/C:H, Ni/C:H and Mo/C:H, with filling factor $f \sim 0.25$. These were prepared at floating potentials of -30 V for nickel and

molybdenum composites and -12 V for the silver composite.

From Fig. 2 it may be seen that the resistance first increases and then decreases for Ag/C:H (2–10 days) and for Ni/C:H (30 days). No decrease was observed for Mo/C:H. When an additional bias was created on the substrate by RF powering the substrate holder (Fig. 1), the resistance change in open air was below 10% for samples prepared at biases of -200 V and more [53]. Observation by atomic force microscopy (AFM) showed that the increased energy of bombarding positive ions is responsible for smoother surfaces [56]. Transmission electron micrographs [52] supported the following phenomenological model [55]. During the first period of ageing of the sample, coalescence (probably of the largest metal grains) takes place, causing the nearest-neighbour distance to increase. This results in an increase of the electrical resistance. This process depends on the reactivity of the metal versus that of the C:H phase. After a certain time relaxation of the C:H matrix prevails which brings metal grains closer together (Ag/C:H and Ni/C:H), and therefore the electrical resistance decreases. The metal with the highest melting point and greatest reactivity, molybdenum, coalesces the slowest and the Mo/C:H composite does not show the resistance decrease. It has been shown [57] that, initially, the C:H component of the composite contains a large amount of frozen-in free radicals that continue post-deposition reactions. These take a minimum of 30 min. If immediately after deposition the sample is exposed to the atmosphere, the C:H matrix is oxidized as shown by Fourier transform infrared spectroscopy (FTIR) and may undergo considerable rearrangements [57]. The composition profiles of the above composites were obtained by ERDA [58], which revealed a maximum hydrogen concentration of 15 at.%. However, more accurate measurements done by NRA show that the true value of hydrogen concentration is probably up to 30 at.% [59].

Recently, we successfully deposited Ge/C:H composites [60,61] and investigated their structure, morphology, composition and main electrical properties, with the aim of applying this composite as a temperature sensor.

4. Plasma polymers prepared under mild energy flux

In recent developments, attention is again turning to plasma polymers prepared under moderate conditions. An example may be a plasma polymerization process during RF sputtering from polymeric targets such as PTFE (polytetrafluoroethylene) and PE (polyethylene) using balanced and unbalanced magnetrons. Some other polymers have also been sputtered; for a review see Ref. [64]. The deposition rate during RF sputtering of PTFE is four or five times higher than in the case of

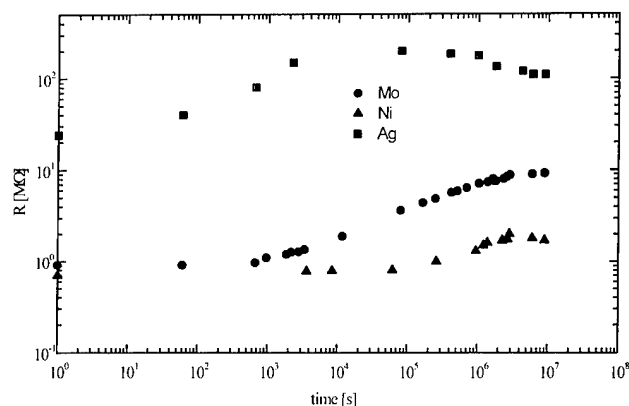


Fig. 2. Ageing of Ag/C:H, Ni/C:H and Mo/C:H composite films in open air [55].

other polymers. In unbalanced magnetron sputtering of PTFE, a hard plasma polymer is obtained (C:F). However, the substrate may be easily subjected to reactive ion etching if the energy of the positive ions is too high [63]. Deposition using RF balanced magnetron films may be applied in many fields. The simple model of the sputtered PTFE film structure may be seen in Fig. 3.

Polarized specular reflectivity spectra of the films deposited on glass substrates precoated with an aluminium layer were measured with an FTIR spectrometer. A shift of the band wavenumber with polarization was observed: $(1250 \pm 5) \text{ cm}^{-1}$ for the electric field of the radiation being perpendicular to the sample plane (reflectivity p-polarization), $(1215 \pm 10) \text{ cm}^{-1}$ for the electric vector in the sample plane (s-polarization in reflectivity and transmissivity measurements). This anisotropy could be caused by an orientation of C—C bonds (predominantly perpendicular to the sample plane) and C—F bonds (predominantly parallel to the sample plane).

5. Conclusions

The two main directions that have been followed in the field of plasma polymerization have been discussed. Plasma polymer films prepared under a low energy flux are applied successfully in the surface modification of solids (mainly conventional polymers) as protective layers (e.g., packaging) and in the biomedical field. Films prepared under high energy flux are used as protective, low-friction and hard coatings. Composite films have also been applied for optical recording. Films prepared with medium energy flux have been investigated recently and are presented here under the example of RF polymer sputtered films. These were proposed again as low-friction and protective films.

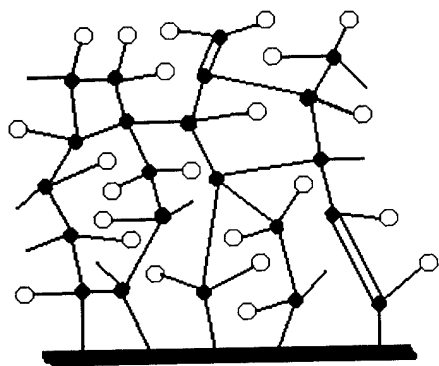


Fig. 3. Model of the fluorocarbon plasma polymer prepared by PTFE sputtering (○, fluorine; ●, carbon) [62].

Acknowledgements

The authors are indebted for support from grants OC NA100, KONTAKT 177, Aktion 923P9 and VZ 190-01/206054. The authors are also grateful to Dr. Peter Chandler and Mrs. Peggy Chandler for reading the manuscript.

References

- [1] H. König, G. Helwig, Y. Physik 129 (1951) 491.
- [2] H. Schmellenmeier, Exp. Techn. Phys. 1 (1953) 49.
- [3] J. Goodman, J. Polym. Sci. 44 (1960) 551.
- [4] L.V. Gregor, IBM Journal, March (1968) 140.
- [5] A. Brookes, H. König, Y. Physik 152 (1958) 75.
- [6] A.P. Bradley, J.P. Hammes, J. Electrochem. Soc. 110 (1963) 15.
- [7] A.T. Bell, Curr. Topics Chem. (Plasma Chem.) 43 (1980) 94.
- [8] Y. Osada, H. Biederman, Plasma Chemistry of Polymers, Advances in Polymer Science vol. 95 (1990) 342.
- [9] R. d'Agostino, Plasma Deposition, Treatment and Etching of Polymers, Academic Press, New York, 1990.
- [10] H. Yasuda, Plasma Polymerization, Academic Press, Orlando, FL, 1985.
- [11] H. Biederman, Y. Osada, Plasma Polymerization Processes, Elsevier, Amsterdam, 1992.
- [12] F.F. Shi, Surf. Coat. Technol. 82 (1996) 1.
- [13] P. Favia, R. d'Agostino, Surf. Coat. Technol. 98 (1998) 1102.
- [14] D.K. Lam, R.F. Baddour, A.F. Stancell, in: M. Shen (Ed.), Plasma Chemistry of Polymers, Marcel Dekker, New York, 1976.
- [15] H.U. Poll, M. Arty, K.H. Wickleder, Eur. Polym. J. 12 (1976) 505.
- [16] J.M. Tibbitt, M. Shen, A.T. Bell, J. Macromol. Sci. Chem. A 10 (1976) 1623.
- [17] B.D. Ratner, Polym. Preprints 34 (1993) 643.
- [18] G.P. Lopez, B.D. Ratner, J. Polym. Sci., Polym. Chem. Ed. 30 (1992) 2415.
- [19] G.P. Lopez, B.D. Ratner, Langmuir 7 (1991) 766.
- [20] R.E. Marchant, M.J. Danilich, Polym. Preprints 34 (1993) 655.
- [21] D. Kiaei, A.S. Hoffman, S.R. Hanson, J. Biomed. Mater. Res. 26 (1992) 357.
- [22] D.G. Castner, K.B. Lewis, D.A. Fischer, B.D. Ratner, J.L. Gland, Langmuir 9 (1993) 537.
- [23] L.C.M. Han, K. Rajeshwar, R.B. Timmons, Langmuir 13 (1997) 5941.
- [24] J.P.S. Badyal, Proc. IEE Seminar, Plasma polymerization-processing for the future, IEE, London (1999) 2/1.
- [25] H.J. Griesser, R.C. Chatelier, J. Appl. Polym. Sci., Appl. Polym. Symp. 46 (1990) 361.
- [26] K. Hozumi, Pure Appl. Chem. 60 (1988) 697.
- [27] R. Gombotz, A.S. Hoffman, J. Appl. Polym. Sci., Appl. Polym. Symp. 42 (1988) 285.
- [28] G.W. Prohaska, C.G. Nickson, J. Polym. Sci. A: Polym. Chem. 27 (1989) 2633.
- [29] A. Chilkoti, B.D. Ratner, D. Briggs, Chem. Mater. 3 (1991) 51.
- [30] H. Yasuda, H.C. Marsh, M.O. Bumgarner, N. Morosoff, J. Appl. Polym. Sci. 19 (1975) 2845.
- [31] H. Biederman, P. Hlíděk, J. Zemek, D. Slavínská, J. Ježek, P. Zakouřil, J. Glosik, Vacuum 46 (1995) 1414.
- [32] L. Holland, British Patent Application 1 582 231, 1976.
- [33] D.S. Whitmell, R. Williamson, Thin Solid Films 35 (1976) 255.
- [34] S. Craig, G.L. Harding, Thin Solid Films 97 (1982) 345.
- [35] N. Savvides, B. Window, J. Vac. Sci. Technol. A 3 (1985) 2386.
- [36] N. Savvides, B. Window, J. Vac. Sci. Technol. A 4 (1986) 504.
- [37] B. Window, N. Savvides, J. Vac. Sci. Technol. A 4 (1986) 453.

- [38] H. Biederman, L. Martinu, J. Zemek, *Vacuum* 35 (1986) 447.
- [39] E. Kay, *Z. Phys. D — Atoms, Molecules and Clusters* 3 (1986) 251.
- [40] R.E. Sah, B. Dischler, A. Bubenzer, P. Koidl, *Appl. Phys. Lett.* 46 (1985) 739.
- [41] D. Leidlich, A. Schuhenn, H.G. Umbach, E. Niemann, W. Beyer, *Diamond Relat. Mater.* 1 (1992) 1169.
- [42] F. Ishikawa, K. Tamahashi, M. Chigasaki, S. Onuma, M. Wakagi, T. Ohno, Y. Shimamura, C. Yamagashi, *Mater. Res. Soc. Symp. Proc.* 118 (1988) 429.
- [43] R. d'Agostino, R. Lamendola, P. Favia, A. Giquel, *J. Vac. Sci. Technol. A* 12 (1994) 308.
- [44] D.I. Jones, A.D. Stewart, *Phil. Mag.* B46 (1982) 423.
- [45] H. Biederman, R.P. Howson, I. McCabe, *Proc. of IPAT 87*, Brighton (1987) 152.
- [46] H. Biederman, K. Kohoutek, Z. Chmel, V. Sary, R.P. Howson, *Vacuum* 40 (1990) 251.
- [47] L.P. Klages, R. Memming, *Mater. Sci. Forum* 52/53 (1990) 609.
- [48] M. Grischke, K. Bevilacqua, H. Dimmigen, *Materials & Manufacturing Processes* 8 (1993) 407.
- [49] D.P. Monaghan, D.G. Teer, R.D. Arnell, I. Efoglu, W. Ahmed, *J. de Physique IV* 3 (Colloque C3) (1993) supplement au *J. de Physique II*, volume 3.
- [50] H. Ohkawa, N. Ozawa, K. Ischihara, N. Yasuda, *Proc. of ISSP'93*, Tokyo (1993) 35.
- [51] H. Biederman, L. Martinu, in: R. d'Agostino (Ed.), *Plasma Deposition, Treatment and Etching of Polymers*, Academic Press, New York, 1990.
- [52] H. Biederman, P. Hídek, J. Pešička, D. Slavínská, V. Stundzia, *Vacuum* 47 (1996) 1385.
- [53] H. Biederman, P. Hídek, J. Pešička, D. Slavínská, V. Stundzia, J. Zemek, R.J. Kingdon, R.P. Howson, *Vacuum* 47 (1996) 1453.
- [54] M. Zeuner, H. Neumann, J. Zalman, D. Slavínská, H. Biederman, *Vacuum* 51 (1996) 1453.
- [55] H. Biederman, R.P. Howson, D. Slavínská, V. Stundzia, J. Zemek, *Vacuum* 48 (1997) 883.
- [56] H. Lehmerg, H. Biederman, D. Slavínská, V. Stundzia, *Vacuum* 50 (1998) 27.
- [57] V. Stundzia, P. Bílková, H. Biederman, D. Slavínská, P. Hlídék, *Vacuum* 50 (1998) 23.
- [58] H. Biederman, V. Stundzia, D. Slavínská, P. Bílková, J. Pešička, P. Hlídék, J. Zemek, L. Martinu, J.E. Klemberg-Sapieha, S.C. Gujrathi, in: C.K. Wu (Ed.), *Proc. of ISPC 13*, Peking University Press, Beijing, 1997, p. 1165.
- [59] W. Fukarek, V. Stundzia, H. Biederman, unpublished data.
- [60] H. Biederman, V. Stundzia, D. Slavínská, J. Zalman, J. Pešička, M. Vaněček, J. Zemek, W. Fukarek, *Thin Solid Films* 351 (1999) 151.
- [61] H. Biederman, J. Zalman, D. Slavínská, J. Pešička, W. Fukarek, S. Kvasnica, F. Olcaytug, in: H. Hraborsky, H. Konrad, V. Kopecky (Eds.), *Proc. of ISPC 14*, Prague, 1–6 August (1999) 1797.
- [62] H. Biederman, P. Bílková, J. Ježek, P. Hlídék, D. Slavínská, *J. Non-Cryst. Solids* 218 (1997) 44.
- [63] H. Biederman, J. Ježek, P. Bílková, P. Hlídék, D. Slavínská, J. Zemek, in: C.K. Wu (Ed.), *Proc. of ISPC 13*, Peking University Press, Beijing, 1997, p. 1264.
- [64] H. Biederman, in: Y. Yoshino (Ed.), *Proc. of the 5th ISSP'99*, 16–18 June, S. Daikuhara, Kanazawa, 1999, p. 34.

The protection of metallic archaeological objects using plasma polymer coatings

Lidia Favre-Quattropani ^{a,*}, Pierangelo Groening ^a, Denis Ramseyer ^b,
Louis Schlappbach ^a

^a *Institut de Physique, Université de Fribourg, Pérolles, CH-1700 Fribourg, Switzerland*

^b *Service Archéologique Cantonal, Planche-Supérieure 13, CH-1700 Fribourg, Switzerland*

Abstract

One major concern of conservators and archaeologists is to limit the alteration and the corrosion of metallic archaeological objects. Organic coatings are one of the most important ways of protecting metal against corrosive agents, thanks to their diffusion barrier properties. The aim of this work was to develop effective protective coatings fitting with the specific requirements of heritage preservation (in particular the questions of reversibility and aesthetic appearance). Ultrathin (5–50 nm) polymer-like films have been deposited by plasma polymerisation in a methane or propane discharge on various metallic samples (stainless steel, Fe, Cu, Ag and Roman iron nails). Some important results are:

1. on tested substrates, except Ag, adhesion is very good;
2. concerning the reversibility of such layers, they can be totally removed in H₂ plasma;
3. the coatings are slightly coloured, which seems linked to the amount of unsaturated C=C bonds in the C layer and to a finite electrical conductivity;
4. they show interesting barrier diffusion properties to H₂S, O₂ and water vapour molecules; and
5. on silver substrates, some problems of adhesion are observed due to the diffusion of Ag ions through the organic films.

© 2000 Elsevier Science S.A. All rights reserved.

Keywords: Archaeology; Conservation; Corrosion; Plasma polymerisation; Protective coatings

1. Introduction

One major concern of conservators and archaeologists is the preservation of archaeological objects taken out of excavations and kept in museums or in depots. In the case of metallic objects, one of the problems is to stop, or to limit, surface corrosion or its alteration by the ambient atmosphere. When they are buried, these objects reach an equilibrium with the surrounding sediment and, if the conditions are favourable, they are more or less preserved until their discovery by archaeologists. Once extracted from their burial environment, this equilibrium is disturbed. Corrosion can resume and rapidly damage, or even completely destroy, the object. To preserve such an object there are three solutions [1]:

- to treat the metal to render it corrosion resistant by removing the elements which can catalyse the corrosion restart (e.g. removing the chlorides in the case of archaeological iron [2,3]);
- to treat the environment to render it non-corrosive (controlled atmosphere museum cases, storage under nitrogen environment, ...) or
- to isolate the object from the environment with a protective coating.

The last solution has the advantage of not depending on sophisticated infrastructures such as air-conditioned rooms. Organic coatings are one of the most important ways of protecting metals against corrosive agents, thanks to their diffusion barrier properties. They have been used for a long time in conservation [4,5], in particular to protect outdoor sculptures against atmospheric pollution [6–8]. In this domain, they must also satisfy specific requirements such as reversibility and aesthetic appearance (they must be as invisible as possible). These requirements imply that an ideal and

* Corresponding author. Tel.: +41-26-300-9068;

fax: +41-26-300-9747.

E-mail address: lidia.quattropani@unifr.ch (L. Favre-Quattropani)

universal protective coating does not yet exist for conservators and that research in this domain is still important.

Plasma polymerisation is a process in which gaseous organic molecules are excited in a plasma and form active species such as ions and free radicals. These active species react with themselves to form polymers in the gas phase or on surfaces exposed to the plasma. With plasma polymerisation, one can deposit reproducibly on the surface of various objects, of almost any base material, ultrathin (a few nanometers), continuous and pinhole free layers with good adhesion properties to the underlying substrate [9–11]. These layers are chemically and thermally very stable and present a high degree of cross-linking, with carbon chains limited to two or three units [12]. This explains their high chemical stability and their reduced permeability. Furthermore, they can be deposited at low temperature, below 100°C. This property is important for archaeological objects as it guarantees the preservation of metallurgical information which analysis of the object can reveal. These coatings are studied and used in material science because they give a very good corrosion protection as an effective diffusion barrier to atmospheric oxygen or water [13–15]. They are considered as protective coatings for metallic conductors in microelectronics circuits and passive electronic components [13,14] and as protectors for Ag-based optics [15]. These layers are also studied in the food packaging industry to reduce permeability to oxygen, CO₂ or water vapour of transparent plastic foils such as PET [16], or in the automotive industry to reduce the permeation of hydrocarbons in plastic fuel tanks [17].

Plasma polymerisation processes can be preceded in the same chamber by treatments in reactive or noble gas plasma for cleaning or passivating the sample surface without affecting its bulk properties [18]. In the domain of archaeology and conservation, plasma treatments have already been used for several years [19], particularly the hydrogen plasma which is often part of the cleaning and treatment processes applied to the preservation of archaeological iron [20–22]. More recently, Borrós et al. [23] used plasma techniques for the restoration of copper calcographic plates. An oxygen plasma treatment was used to remove the ink residues followed by a hydrogen plasma to reduce the oxidised surface. The copper plate was finally protected against atmospheric corrosion with an organic film deposited by plasma polymerisation of methane.

The aim of our research work was to develop effective protective coatings fitting the specific requirements of heritage preservation to prevent, or at least slow down, further corrosion of restored objects. The coatings were deposited by plasma polymerisation of methane or propane on various metallic substrates: copper, silver, iron, stainless steel and even archaeological samples (Roman iron nails). These films were characterised by X-ray

photoelectron spectroscopy concerning their thickness (for the thinnest) and their chemical composition. Their properties as protective coatings were analysed using simple corrosion tests.

2. Experiment

Test experiments were carried out on modern metallic platelets of about 0.5 to 1 cm². The chosen metals were stainless steel, iron, silver and copper. Some coatings were also deposited on pieces of restored iron nails from the second century AD (found in the Roman villa at Vallon, Fribourg, Switzerland) as example of archaeological samples. The polymer films were deposited in a high vacuum chamber (base pressure 4×10^{-8} mbar) connected to a spectrometer which enabled in situ surface analysis. The excitation of the plasma was done by microwaves at a frequency of 2.45 GHz. At low pressures, ranging from 4×10^{-4} to 10^{-2} mbar, the plasma was excited by the electron cyclotron resonance (ECR) condition realised with rare earth permanent magnets. The details of this plasma chamber have been published elsewhere [24]. Before the deposition of the protective coating, the samples were pre-treated in an H₂ plasma at a microwave power of 25 W for at least 15 min to clean their surface. The hydrogen pressure was around 10^{-3} mbar with a gas flow rate of 5.1 sccm. Ultrathin (5–50 nm) polymer-like films were then deposited by plasma polymerisation in a methane or propane discharge at a microwave power of 25 W and a pressure around 10^{-3} mbar. The gas flow rates varied between 1 and 8 sccm in the case of CH₄, and 1 and 3 sccm in the case of C₃H₈. Some depositions were also carried out in gas mixtures, with flow rates of propane, hydrogen and argon between 0 and 3 sccm and a pressure up to 2×10^{-2} mbar. A butterfly valve regulated the operating pressure independently of the gas flow rates.

X-ray photoelectron spectroscopy (XPS) was performed on a VG Escalab 5 spectrometer operating at a base pressure lower than 10^{-9} mbar. Analysis was carried out with non-monochromatized MgK α ($h\nu = 1253.6$ eV) radiation. The instrument was calibrated to the 4f_{7/2} peak of gold at $E_B = 84.0$ eV and the copper 2p_{3/2} peak at $E_B = 932.7$ eV. Survey spectra and high resolution spectra were taken with 100 and 20 eV pass energy respectively, in the constant analyser energy (CAE) mode. The X-ray source was operated at 180 W (9 kV, 20 mA).

Ageing of the coatings was evaluated by exposing the samples for different periods of time to the ambient atmosphere. Simple corrosion tests were performed in 90% relative humidity by storing the samples in a dessicator in the presence of a water container. Rapid iron corrosion was also induced by depositing a drop of deionized water at the surface of the platelet, over

some hours. In the case of silver, sulphuration tests were carried out in a dessicator which contained a 20 wt.% ammonium sulphide solution, in order to create a sulphide saturated atmosphere [25]. All tests were carried out at room temperature.

3. Results and discussion

We succeeded in depositing plasma-polymerised coatings on a variety of metallic substrates — stainless steel, iron, silver, copper, and even on restored Roman iron nails as an example of archaeological samples. For all base materials, the adhesion of the coating was good and in all cases except silver it remained at the surface of the object after exposure to ambient atmosphere for more than a year, as well as after ageing under humid conditions. XPS survey spectra of an as-deposited plasma polymer film on iron, and of similar films after exposure to the ambient atmosphere for 289 days and after exposure to 90% RH for 11 days, are shown in Fig. 1. As-deposited films consist only of hydrocarbons. After exposure to air (without or with increased humidity) the film is still present at the surface of the object, as indicated by the similarity of the XPS spectra (Fig. 1) (c) and (d) with (b) at low binding energy and by the absence of signals from the iron substrate. This shows that no delamination of the film occurs due to exposure to air or humidity. The presence of oxygen peaks (Fig. 1 spectra (c) and (d)) is due to the oxidation of the film during atmospheric exposure. XPS spectra with similar results were measured for films deposited on stainless steel, copper or Roman iron nails.

These coatings are also revealed to be very stable

when the samples are dipped in solvents, such as acetone or ethanol; they are not destroyed. However, from the conservator's viewpoint the reversibility of the treatment is especially important and the coating layers should be removable without affecting the integrity of the underlying object. These plasma polymer coatings fulfil these requirements, as they can be totally removed in H_2 plasma. Indeed a 15 min treatment is sufficient to completely remove the layers of some 10 nm thickness.

The coatings are slightly coloured, yellowish for the thinnest (~ 5 nm) and the thicker ones can be darker and more opaque. This colour can be a problem depending on the aspect of the underlying metal. Indeed, the coating colour will alter the aesthetic appearance of silver or other shiny metals, becoming visible (cf. Fig. 3(a)). On the other hand, on archaeological iron, which is always oxidised and black, a yellowish coating remains invisible.

This colour seems to be linked to the amount of double bonds in the carbon layer. Plasma polymerised propane coatings are generally darker and more opaque than plasma polymerised methane films. In the high resolution C1s XPS spectra (Fig. 2), the darker film (spectrum (c)) shows a more developed shake-up satellite peak at a binding energy of ~ 6 eV above the C1s elastic peak (at 285.0 eV). This peak is characteristic of aromatics and unsaturated $C=C$ bonds [26]. By varying the plasma parameters, for example by increasing the pressure of C_3H_8 or by adding Ar in the plasma, we can obtain lighter coloured coatings, associated with a decrease of this shake-up satellite peak. By comparison with an untreated polyethylene sample (Fig. 2 spectrum (a)), the XPS spectra measured on our coatings also

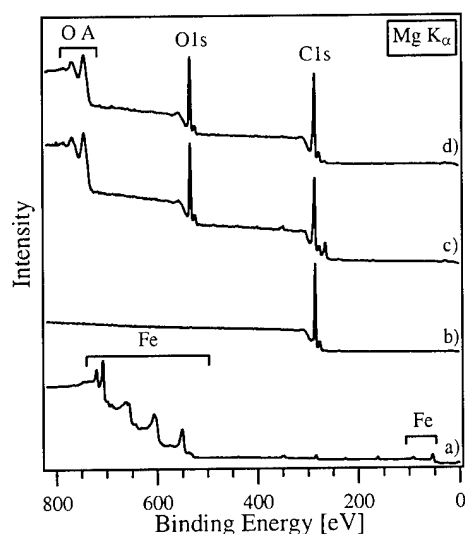


Fig. 1. XPS survey spectra of: (a) 15 min H_2 -plasma treated iron platelet; (b) as-deposited ~ 20 nm thick plasma polymer film (deposited on iron in a C_3H_8 discharge); (c) similar films after exposure to the ambient atmosphere for 289 days; (d) after exposure to 90% RH for 11 days.

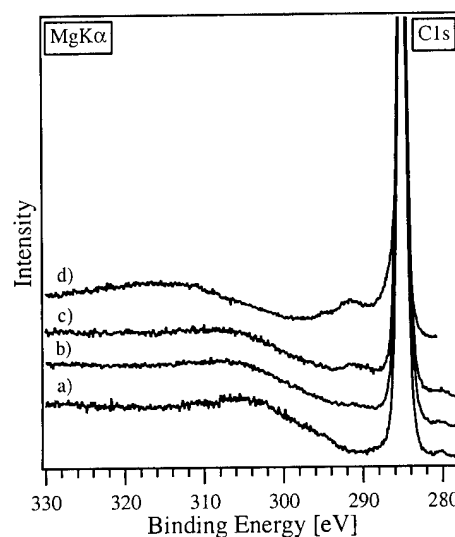


Fig. 2. High resolution C1s XPS spectra of: (a) an untreated polyethylene sample; (b) as-deposited plasma polymerised methane and (c) propane films; (d) a graphite sample. In the case of polyethylene, the sample charge was corrected by setting the C1s elastic peak at 285.0 eV.

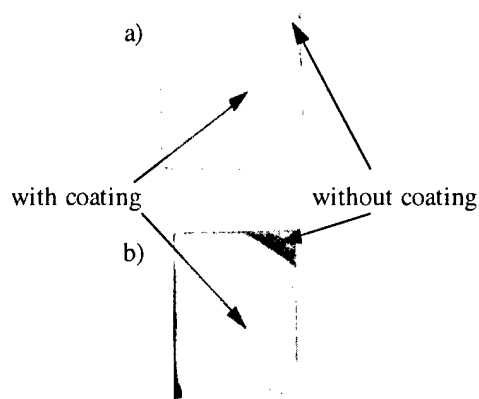


Fig. 3. Silver platelets with a ~ 10 nm thick plasma polymerised methane coating: (a) before exposure to a saturated sulphide atmosphere — the coating is visible on the main part of the platelet due to its yellowish colour; (b) after exposure to a saturated sulphide atmosphere for 5 min — the silver became dark only in the non-protected zone.

show a shift to a higher binding energy of the plasmon peak, the broad structure following the C1s elastic peak. Our coatings show more similarities with a graphite layer (Fig. 2 spectrum (d)), or with He plasma treated polypropylene films [27]. This indicates a dehydrogenation of the organic film with the formation of unsaturated C=C bonds. This dehydrogenation of a polymer sample was observed to be associated with a decrease of the electrical resistance of up to 10 orders of magnitude [27]. The probable finite conductivity of our coatings and the presence of unsaturated C=C bonds can explain the colour of the coatings. The present work aims at minimising the C=C bond amount to obtain colourless films.

The protection against corrosion was evaluated using simple tests. After deposition of a drop of water, visible red-brown corrosion marks appeared within two hours on uncoated iron samples. Protected platelets remained non-corroded during the same time. We saw that after exposure of iron samples to 90% RH for 11 days, the coating was still present. Traces of corrosion appeared, however, which are often only visible under a light microscope. At this stage of our research, it is not possible to know if this corrosion appears because the coating is oxygen- and water vapour-permeable or because there are pinholes in the film.

Protective properties of the coatings were also evaluated by exposing coated and uncoated silver platelets to a saturated sulphide atmosphere. Uncoated platelets blacken very rapidly under these extreme conditions. The silver tarnishing begins immediately after the sealing of the dessicator and total blackening is effective within less than 5 min. During the same time, protected platelets remain shiny and undamaged. This is visible on Fig. 3(b) showing a partially coated silver platelet whose coated surface has blackened only at places without a protective coating. If the exposure time is extended, coated platelets

also begin to blacken. One can observe that the resistance against tarnishing of the samples depends strongly on the coating thickness. All these results indicate interesting diffusion barrier properties of these plasma polymer coatings to H_2S .

Coatings on silver platelets exhibit some problems of adhesion. After exposure to ambient atmosphere for more than a year, no, or almost no, signals from the underlying metal are seen in the XPS survey spectra measured on films deposited on metals other than silver (Fig. 1(c) and (d)). In the case of coated silver platelets, the Ag signals in the XPS spectra become visible after only 29 days in the air. XPS measurements on the same sample at two different electron emission angles allowed us to probe different thickness of the sample surface. For an electron emission angle of 60° the probed thickness was half the thickness probed for normal emission. Fig. 4(c) and (d) show that the Ag3d to C1s peak height ratio is increased in the more surface sensitive measurement at 60° , indicating that the silver is at the sample surface. Apparently, silver diffuses at room temperature through the organic coating to the external surface. The measured quantity of silver on the polymer surface is not more than a monolayer. We guess that this mobility of the Ag ions reduces adhesion of the organic layer to the metal. In fact Ag ions, as other noble metal ions, are known to be very mobile, diffusing through metallic layers such as gold [25], or migrating inside the polymer when deposited on its surface [28]. Effective plasma polymer coatings on silver substrates will consequently attempt to stabilise the silver before the deposition of the coating. It is also possible that the H_2 plasma

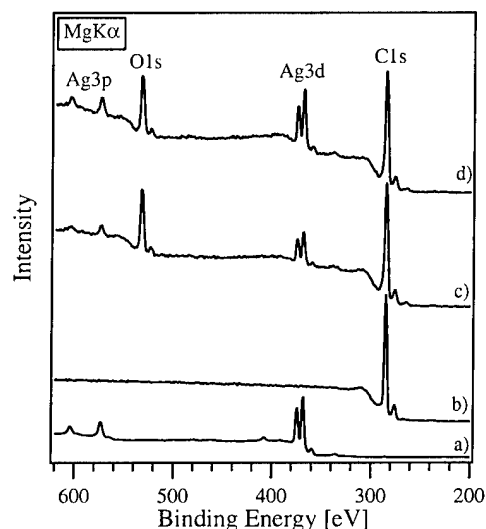


Fig. 4. XPS survey spectra: (a) of a 15 min H_2 -plasma treated silver platelet; (b) of an as-deposited ~ 30 nm thick plasma polymer film on it (deposited in a CH_4 discharge) and of the same film after exposure to the ambient atmosphere for 29 days; (c) for a normal electron emission angle; and (d) for an electron emission angle of 60° , probing half the thickness probed in spectrum (c).

treatment carried out before organic film deposition leaves an activated surface with very mobile Ag ions. Research on adequate treatments of the silver surface should be done, for example by using plasma pre-treatments in other reactive or noble gases. Diffusion of Ag ions through the organic layer could also induce the doping of the layer and partly explain the colour of the layers.

4. Conclusions and outlooks

In this work, we have shown the ability to deposit effective protective coatings on a variety of metals by plasma polymerisation of methane or propane. Except in the case of silver, the coatings have good adhesion to the underlying metal. They show interesting barrier diffusion properties to H_2S , O_2 and water vapour molecules and they are reversible in H_2 plasma. On silver substrates, some problems of adhesion are observed, due to the diffusion of Ag ions through the organic film. The coatings are slightly coloured, which seems to be linked to the presence of unsaturated $C=C$ bonds and to a finite electrical conductivity. This coloration can be a problem from a conservation point of view, however it depends on the aspect and the colour of the underlying object. Deposition conditions with weaker interaction of the plasma with the underlying substrate could favour the achievement of uncoloured coatings.

Due to their low thickness, such coatings give chemical, but not mechanical, stability to the underlying object. They do not have the consolidating effect of a resin or a wax. In this sense, they are not appropriate for objects which need to be reinforced, or which have a tendency to crumble or to lose pieces. On the other hand, they have a limited effect on the object. Their presence is barely detectable, except until now, by their colour, as a function of the substrate aspect, or by surface analysis techniques such as XPS. The thickness of such a layer is so small that it is in fact thinner than the impurity, fat or humidity layer naturally present at the surface of an object handled without gloves.

This stage of research is a feasibility study. Finer and more specific analyses should be considered, in particular by testing the permeability to corrosive agents and the resistance of the coatings to more realistic accelerated artificial ageing conditions in climatic chambers which allow variation of the temperature, the relative humidity, the presence of gaseous pollutants and the exposure to light. The efficiency of the coatings should also be regarded as a function of the sample surface roughness and its surface state. This kind of coating could also be deposited on the lacquers or varnishes already used in conservation to further improve their impermeability to corrosive agents.

Acknowledgements

The authors acknowledge fruitful discussions with François Schweizer (Laboratoire des Musées d'Art et d'Histoire, Genève, Switzerland) and Michel Menu (Laboratoire de Recherche des Musées de France, Paris, France). This work was supported by the Swiss National Science Foundation, the Research Foundation of the University of Fribourg and the Swiss Entwicklungsfonds Seltene Metalle.

References

- [1] R.T. Foley, in: B.F. Brown et al. (Eds.), *Corrosion and Metal Artefacts: A Dialogue Between Conservators and Archaeologists and Corrosion Scientists*, Special Publication 479, NBS, Washington, DC, 1977, pp. 67–76.
- [2] S. Turgose, *Studies in Conservation* 27 (1982) 97.
- [3] A. Rinuy, F. Schweizer, *Studies in Conservation* 26 (1981) 29.
- [4] E. René de la Rie, in: N.S. Allen, M. Edge, C.V. Horie (Eds.), *Polymers in Conservation*, Royal Society of Chemistry, Cambridge, 1992, pp. 62–81.
- [5] W. Mourey, in: I.D. MacLeod, S.L. Pennec, L. Robbiola (Eds.), *Metal 95, Proc. Int. Conf. Metal Conservation, Sémur en Auxois, 25–28 September, 1995*, James and James, London, 1997, pp. 225–227.
- [6] L.B. Brostoff, E. René de la Rie, in: I.D. MacLeod, S.L. Pennec, L. Robbiola (Eds.), *Metal 95, Proc. Int. Conf. Metal Conservation, Sémur en Auxois, 25–28 September, 1995*, James and James, London, 1997, pp. 242–244.
- [7] M. Pilz, H. Römmich, in: I.D. MacLeod, S.L. Pennec, L. Robbiola (Eds.), *Metal 95, Proc. Int. Conf. Metal Conservation, Sémur en Auxois, 25–28 September, 1995*, James and James, London, 1997, pp. 245–250.
- [8] V. Otieno-Alego, G. Heath, D. Hallam, D. Creagh, in: W. Mourey, L. Robbiola (Eds.), *Metal 98, Proc. Int. Conf. Metal Conservation, Draguignan-Figanières, 27–29 May, 1998*, James and James, London, 1998, pp. 309–314.
- [9] H. Yasuda, *Plasma Polymerization*, Academic Press, Orlando, 1985.
- [10] J. Patscheider, *Zeitschrift für Schweizerische Archäologie und Kunstgeschichte* 54 (1997) 22.
- [11] R.W. Jaszewski, H. Schiff, P. Gröning, G. Margaritondo, *Microelectron. Eng.* 35 (1997) 381.
- [12] P. Gröning, A. Schneuwly, L. Schlapbach, M.T. Gale, *J. Vac. Sci. Technol. A* 14 (1996) 3043.
- [13] Y. Lin, H. Yasuda, *J. Appl. Polym. Sci.* 60 (1996) 543.
- [14] C.-P. Klages, A. Dietz, T. Höing, R. Thyen, A. Weber, P. Willich, *Surf. Coat. Technol.* 80 (1996) 121.
- [15] V.Kh. Kudoyarova, A.V. Chernyshev, T.K. Zvonareva, N.B. Dzhelepova, M.B. Tsolov, *Surf. Coat. Technol.* 100/101 (1998) 192.
- [16] E.M. Moser, R. Urech, E. Hack, H. Künzli, E. Müller, *Thin Solid Films* 317 (1998) 388.
- [17] H. Gleich, O. Hoyer, *Proc. 12th Int. Symp. Swissbonding 98, Rapperswil, 12–14 May (1998)* 75–84.
- [18] P. Gröning, M. Collaud Coen, *Recent Research Developments in Macromolecules Research* 4 (1999) 211.
- [19] V.D. Daniels, L. Holland, M.W. Pascoe, *Studies in Conservation* 24 (1979) 85.
- [20] J. Patscheider, S. Veprek, *Studies in Conservation* 31 (1986) 29.
- [21] P. Arnould-Pernot, C. Forrières, H. Michel, B. Weber, *Studies in*

- Conservation 39 (1994) 232.
- [22] K. Schmidt-Ott, *Zeitschrift für Schweizerische Archäologie und Kunstgeschichte* 54 (1997) 45.
- [23] S. Borrós, Ll. Picazo, M. Pellicer, M. Alonso, J. Esteve, in: W. Mourey, L. Robbiola (Eds.), *Metal 98, Proc. Int. Conf. Metal Conservation*, Draguignan-Figanières, 27–29 May, James and James, London, 1998, pp. 202–205.
- [24] S. Nowak, P. Gröning, O.M. Küttel, M. Collaud, G. Dietler, *J. Vac. Sci. Technol. A* 10 (1992) 3419.
- [25] C. Degriigny, M. Wéry, V. Vescoli, J.M. Blengino, *Studies in Conservation* 41 (1996) 170.
- [26] G. Beamson, D. Briggs, *High Resolution XPS of Organic Polymers*, John Wiley, Chichester, 1992.
- [27] M. Collaud Coen, P. Groening, G. Dietler, L. Schlapbach, *J. Appl. Phys.* 77 (1995) 5695.
- [28] P.S. Ho, R. Haight, R.C. White, B.D. Silverman, F. Faupel, in: L.-H. Lee (Ed.), *Fundamentals of Adhesion*, Plenum Press, New York, 1991, pp. 383–406.

Mechanical properties of plasma deposited polymer coatings

F. Benítez ^{a,*}, E. Martínez ^a, M. Galán ^b, J. Serrat ^b, J. Esteve ^a

^a *Universitat de Barcelona, Departament de Física Aplicada i Òptica, Avda. Diagonal 647, Barcelona E-08028, Catalunya, Spain*

^b *TELSTAR S.A., J. Tapiolas 120, Terrassa E-08226, Catalunya, Spain*

Abstract

Thin polymeric films have been obtained by plasma polymerisation of dimethylsiloxane (DMSO). Such films are widely used as protective coatings on optical reflective surfaces and decorative parts. Thin films of polydimethylsiloxane (PDMS) have been deposited by a DC glow discharge plasma from DMSO vapour on pre-treated and untreated polycarbonate (PC) substrates, with or without previous evaporation of an additional aluminium film. A subsequent process of mineralisation by immersion in an air plasma has been applied in order to improve the PDMS films wear resistance. Polycarbonate substrates have been treated in a similar way aiming at improved adhesion of Al films. The present paper is specially focused on the surface mechanical properties of these films. These have been measured by nanoindentation and microscratch techniques and the improvement of the surface hardness and scratch resistance of PDMS films and PC substrates has been assessed. © 2000 Elsevier Science S.A. All rights reserved.

Keywords: Adhesion; Hardness; Plasma polymerisation; Surface modification

1. Introduction

Plasma deposited polymer thin films have been extensively studied because of the broad range of applications derived from the feasibility of depositing films with completely different properties. The capability of organic materials to include almost any kind of element or functional group provides such enormous versatility that it is quite easy to find a suitable material with properties closely fitting the requirements of any application. Furthermore, they are inexpensive easily processed materials and polymer thin films may be readily obtained by plasma polymerisation from a precursor vapour of most organic compounds.

General trends are encountered for the properties of plasma polymers, which may significantly differ from those obtained by conventional polymerisation methods from the same precursors: they are chemically inert, insoluble in conventional organic solvents, hydrophobic and thermally stable. Moreover, by careful control of the processing parameters, their properties may be shifted within the desired range of values.

Organosilicon plasma polymers have been essayed for a large number of applications in rather different

fields: protective coatings [1], gas barriers [2], hydrophobic layers [3], optical coatings and biocompatible films [4], moisture sensors [5], etc. We have studied plasma polymerised siloxanes as protective coatings for Al metalisations, focusing on the improvement of surface hardness and wear resistance by an SiO_x-rich modified surface layer. Such a hard layer is formed by an oxidising plasma treatment in air, or oxygen-containing atmospheres, after plasma polymerisation. In what follows, this process will be referred to as ‘mineralisation’.

2. Experimental

Thin PDMS films were deposited on commercial PC substrates by a DC glow discharge in a small commercial reactor. The reactor was pumped down to 5×10^{-3} mbar prior to the introduction of the DMSO monomer vapour at a low flow rate such as to maintain a constant 0.1 mbar pressure. The plasma was ignited by a 20 cm long and 12 mm diameter cylindrical cathode, which was negatively biased at 2200 V. The PC substrates were coated at ambient temperature, kept at a distance of 15 cm from the plasma cathode. Subsequent mineralisation of the PDMS coating was performed by a new glow discharge in a 0.1 mbar air atmosphere during shorter deposition times than those used for

* Corresponding author. Tel.: +34-93-402-1134;

fax: +34-93-402-1138.

E-mail address: fbenitez@electra.fao.ub.es (F. Benítez)

PDMS deposition. Different processing times were used in order to attain different thicknesses of polymer and SiO_x rich PDMS modified zones.

Some PC substrates were treated identically in an air atmosphere glow discharge, prior to PDMS thin film deposition. Another set of polymer films was deposited on treated and untreated PC substrates with an additional metalisation of an aluminium evaporated thin film. Mineralisation was also performed on these samples.

Mechanical characterisation of the modified polymer surfaces was carried out by the depth-sensing nanoindentation technique using a Nano Test 550 (Micro Materials) with a Berkovich indenter. This instrument allows the continuous monitoring of the applied load and the penetration of the indenter into the sample during a complete loading–unloading cycle, with resolutions better than 0.1 nm in displacement and 1 mN in load. Hardness values were calculated from the measured load–displacement hysteresis curves by means of the analysis method by Oliver and Pharr [6]. This analysis method has been extensively applied to metals and ceramic materials and some works show the validity of its application to the study of polymeric materials [7].

Microscratch measurements have been performed to evaluate the film adhesion and wear resistance, using a Rockwell diamond indenter with a tip radius of 100 μm . The scratches were produced along a scratch distance of 2 mm, starting at 0 mN normal load and increasing at a constant rate of 32.5 mN/s up to a maximum of 3000 mN. A friction sensor was added to the diamond support in order to measure tangential forces, so that real-time monitoring of the penetration depth of diamond into the coating and the diamond frictional force along the scan distance was accomplished. Both optical and scanning electron microscopy images have been obtained to compare the evolution of the friction coefficient and the resulting damage morphologies appearing along the scratch, on the different coatings.

3. Results

3.1. Hardness measurements by the nanoindentation technique

Load–displacement curves have been obtained with loading–unloading rates of 0.05 mN/s and 0.01 mN/s up to maximum loads of 5, 3, 2, 1 and 0.5 mN. The maximum penetration depths obtained lie in the range of 1000–250 nm. These penetration depth values are too large to evaluate the properties concerning the very thin modified surface layer (about 60 nm in thickness) due to the substrate softness. Nevertheless, a harder surface layer could be seen in the loading curves and hardness values increased significantly. After 90% of unloading

load, the indenter was held under such load for 15 s in order to determine the thermal drift rate of the sample during the indentation process and the data was corrected accordingly.

Fig. 1 shows two indentation curves at a 5 mN maximum load obtained for both treated and untreated polycarbonate substrates. The treated one was immersed in a 0.15 mbar air glow discharge for 5 min. Both curves are very similar in shape but there is a difference at the starting of the loading branches. The treated sample shows a different slope corresponding to a harder surface coating. A more detailed view of this part of the curve shows that the transition point between the two different slopes occurs at a maximum penetration depth of about 90 nm and at 0.3 mN of applied load. In fact, this is not the real thickness of the modified layer because the maximum penetration depth includes the deformation of the softer substrate. Different indentations performed at several peak loads showed the same variation in the slope of the loading curve. This can be seen in Fig. 2 and confirms the consistency of the results.

From the analysis of a set of these curves (five indentations at each maximum load), the evolution of the hardness values with the maximum penetration depth of the indenter could be estimated (Fig. 3, solid line). As could be already expected from the shape of the indentation curves, hardness values significantly increased with decreasing penetration of the indenter (i.e. as they approach the surface) although they do not exactly correspond to those of the modified surface. To avoid the substrate deformation effects, a maximum load of scarcely 0.3 mN should be applied, in order to restrict the penetration depth of the indenter to the initial 80 nm. Nevertheless, a minimum hardness of 440 MPa can be assumed for the plasma treated PC (and a factor of two, or even more, may be presumed from the observed trends) which means a significant

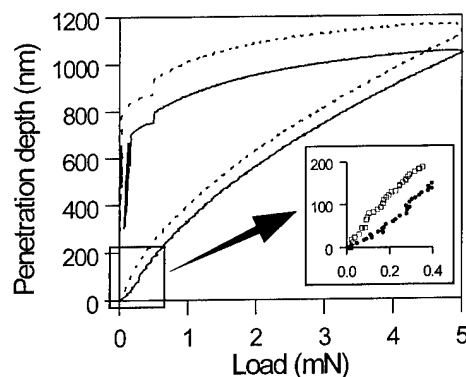


Fig. 1. Hysteresis load–displacement curves at 5 mN of maximum load for the treated polycarbonate (solid line) and for the untreated polycarbonate (dashed line). Different slopes of the curves at the initial stages of loading are found, due to the harder surface layer on the modified substrate.

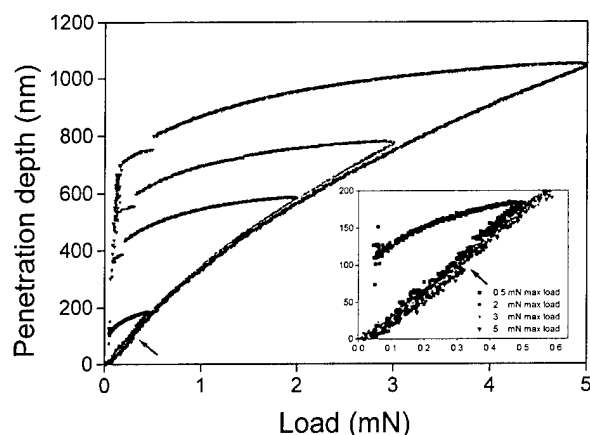


Fig. 2. Hysteresis load-displacement curves for indentations performed on the plasma treated polycarbonate at different maximum loads. All the loading branches of the curves show an inflexion point of a slope change (see the arrow in the figure) due to the different hardness of the bulk and modified surface layer.

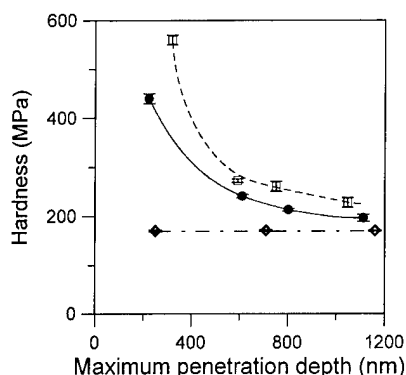


Fig. 3. Hardness vs. maximum penetration depth for the plasma modified polycarbonate (solid line) and PDMS/polycarbonate system (dashed line). The dash-dot line shows the polycarbonate hardness (without surface modification).

improvement with respect to that of bare PC substrates, i.e. 170 MPa. The values obtained are smaller and therefore consistent with those reported for ion beam surface modification of PC with 100 keV boron ions, which is ~ 1.3 MPa [8]. Although ion implantation greatly enhances tribological properties, it was also observed that densely implanted materials suffer from an increase in surface fatigue and brittle cracking, which can easily result in a decrease of wear resistance. The same argument can be applied to plasma treated polymers. Two thicker modified surface layers were obtained by increasing the immersion time in the glow discharge up to 10 and 20 min respectively without varying the remaining parameters. Both substrates were exposed to a 10 min ultrasound shaking in ethanol. The mechanical waves propagating through them were able to develop failure and detachment of the modified surface layers, to a much larger extent in the 20 min exposed one (Fig. 4). Optical microscopy images show that these

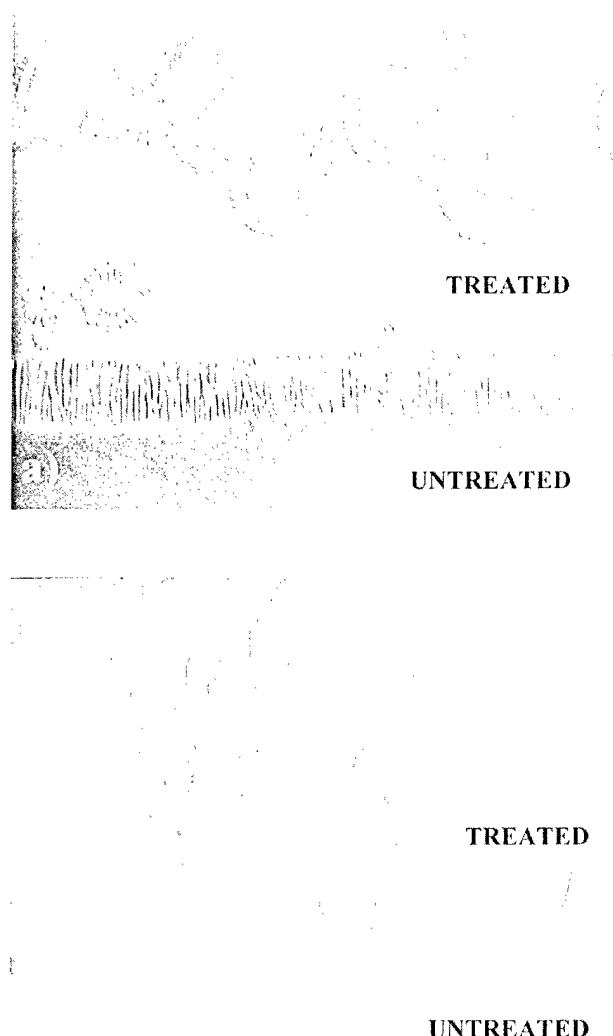


Fig. 4. Plasma treated PC substrates after 10 min ultrasound shaking. The revealed stress and detachment increases with longer exposition to plasma: (a) 10 min exposition, (b) 20 min exposition.

layers are formed with a high intrinsic compression strain. Detachment of the modified surfaces allows measurement of the modified depth by stylus profilometry. Thus, the 20 min exposed substrate develops a 220 nm thick modified surface layer.

Although the exact mechanisms responsible for such an important change in the mechanical properties are not completely understood, there is general agreement on the fact that radicals created at the surface by the removal of certain groups are easily recombined, so that a three-dimensional network of connected polymer chains is formed. The resulting cross-linked structure restrains chain movement and increases rigidity. The so called CASING cross-linking has been an important method in surface modification of polymers since it was first reported by Hansen and Schonhorn in 1966 [9].

An indentation curve at 2 mN peak load of a treated PDMS coating deposited on a PC substrate is shown in

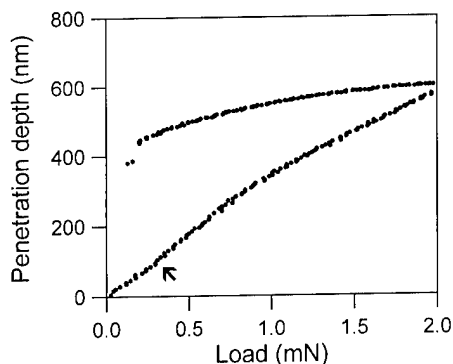


Fig. 5. Load-displacement curve obtained for a plasma modified PDMS coating of 250 nm thickness deposited on a polycarbonate substrate. The arrow shows the change of the slope in the loading curve, indicating a harder surface layer obtained with the polymerization process.

Fig. 5. A 10 min mineralisation was performed by an air plasma at 0.1 mbar. The arrow shows, again, the slope change indicating a surface harder zone of 80–90 nm thickness. Such a change of slope has also been observed and reported for other plasma and ion-beam modified polymers [8]. For highly modified polymers the change becomes a discontinuity which is related to their somewhat poorer wear performance compared to that of less modified samples.

The evolution of the system hardness (treated PDMS onto treated PC) plotted as a function of maximum penetration depth is superimposed on that of treated PC in Fig. 3 (dashed line). In this case, the hardness values are even higher than those of the uncoated polycarbonate for the same plasma treatment.

3.2. Adhesion measurements by the microscratch test

In addition to the improvement of the surface hardness, plasma modification of the polycarbonate has the effect of improving the adhesion of deposited aluminium coatings [10].

Microscratch tests performed on the untreated PC substrates show a pronounced plastic deformation of the material along the scratch. Fig. 6 shows this deformation print and the evolution of the frictional force (dashed line), which progressively increased with the scratch distance. Some debris particles can also be found at the bottom of the track. Plasma treated PC substrates show a brittle, cracked, easily delaminated surface when the load exceeds a certain threshold value. In the case of a surface mineralised layer on PDMS on a PC treated substrate, the evolution of the friction force showed an initial zone where no damage is provoked on the system, probably due to the higher hardness of the mineralised surface layer (Fig. 6). A threshold for cracking is observed, with respect to the applied load, at 150 mN (zoom in, Fig. 6(b)). Conformal cracking of the brittle

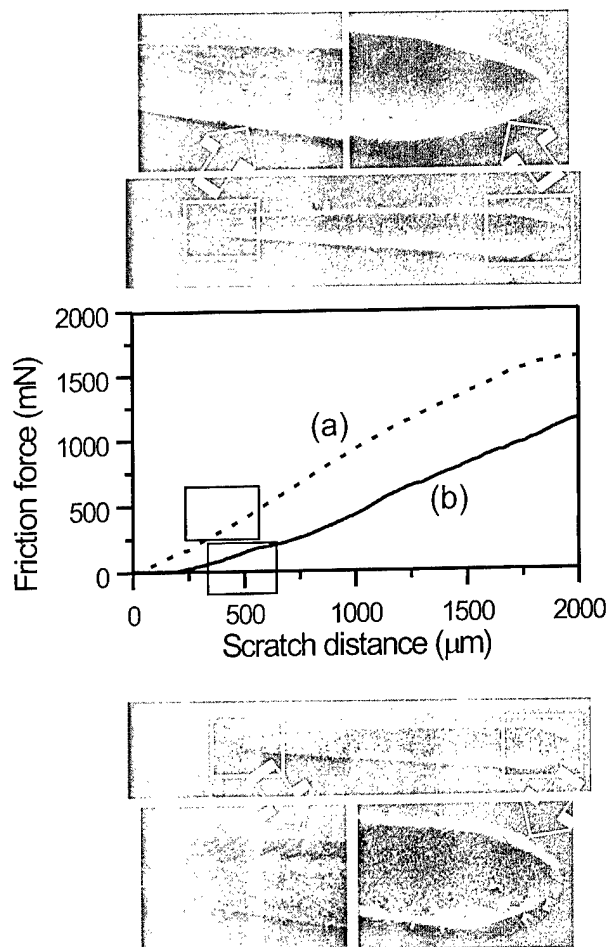


Fig. 6. Scanning electron micrographs showing scratches performed (a) on the bare polycarbonate, and (b) on a plasma treated PDMS/treated polycarbonate sample. The evolution of the friction force along the scratch is also shown for both samples.

surface layer(s) is affected by the impossibility of following the substrate plastic deformation. Increasing normal loads provoke abundant detachment and debris, which would be detrimental to the wear performance of the system. Unlike indentation measurements, untreated PDMS films show a similar behaviour in scratch tests. This could be related to the fact that plasma polymerised thin films are already highly cross-linked, due to the mechanisms responsible for its growth [11] which is not substantially altered by low energy ion bombardment.

The high penetration depths achieved at the applied loads suggest that cracking may also be due to the modified substrate layer, although no mechanical failure was observed for this sample under ultrasound shaking (unlike treated substrates) when the PDMS film is deposited.

Results for systems including an Al metalisation do not significantly differ from those without it, provided that a PDMS film has been overdeposited. Therefore, PDMS may be thought of as a fixing coating for underlying films. On the contrary, the expected improve-

ment in the adhesion of Al metalisations by plasma treatment of the substrate is easily observed. The chemical modifications induced by ions and the bonding mechanisms of Al atoms to the as-formed modified surfaces may be found elsewhere [9].

Studies aimed at improved adhesion to the substrate without reducing the film wear performance, and optimisation of the PDMS film thickness in order to diminish the accumulated internal stress, could be feasible approaches to partially solving the drawbacks encountered.

4. Conclusions

Modification of PC substrates by immersion in air plasmas produces a thin modified surface layer with significantly enhanced hardness compared to that of a bare PC substrate. The depth affected by this modification is subject to mechanical stress, and prolonged immersion times may be detrimental to the mechanical performance of the substrate. Similarly, treated plasma polymerised PDMS thin films present a harder surface layer, although the wear performance of these films is not so sensitive to this process.

With respect to Al metalisations, PDMS thin films are found to act as an overlying adhesion promoter coating while plasma treated PC surface layers would be an underlying adhesion promoter.

Acknowledgements

This study was supported by the Research Dept. of TELSTAR S.A. Acknowledgements are also due to the Serveis Científico-Tècnics Universitat de Barcelona for the SEM characterization, and the DGR of the Catalan Government.

References

- [1] H. Grünwald, R. Adam, J. Bartella, M. Jung, W. Dicken, S. Kundel, K. Nauenburg, T. Gebele, S. Mitzlaff, G. Ickes, U. Patz, J. Snyder, *Surf. Coat. Technol.* 111 (1999) 287–296.
- [2] L. Agres, Y. Segui, P. Raynaud, *J. Appl. Polym. Sci.* 61 (1996) 2015.
- [3] J. Behnisch, J. Tyczkowski, M. Gazicki, I. Pela, A. Holländer, R. Ledzion, *Surf. Coat. Technol.* 98 (1998) 872–874.
- [4] P. Favia, R. d'Agostino, *Surf. Coat. Technol.* 98 (1998) 1102–1106.
- [5] R.K. Sathir, Z.N. Sanjana, *J. Mater. Sci.* 26 (1991) 4261.
- [6] W.C. Oliver, G.M. Pharr, *J. Mater. Res.* 7 (6) (1992) 1564–1583.
- [7] E.H. Lee, Y. Lee, W.C. Oliver, L.K. Mansur, *J. Mater. Res.* 8 (2) (1993) 377–387.
- [8] H. Dong, T. Bell, *Surf. Coat. Technol.* 111 (1999) 29–40.
- [9] R.H. Hansen, H. Schonhorn, *J. Polym. Sci.* 4 (1966) 209 Polym. Lett. Ed.
- [10] C.S. Rastomjee, M. Keil, H. Sotobayashi, A.M. Bradshaw, C.L.A. Lamont, D. Gador, E. Umbach, *Appl. Surf. Sci.* 136 (1998) 280–297.
- [11] S. Sahli, Y. Segui, S.H. Moussa, M.A. Djouadi, *Thin Solid Films* 217 (1992) 17–25.

Pulsed laser deposition of crystal polyaniline thin films

Z.M. Ren ^a, Y.F. Lu ^{*}, Z.H. Mai ^a, S.C. Ng ^b, P. Miao ^b, S.I. Pang ^c, J.P. Wang ^c,
T.C. Chong ^c

^a Laser Microprocessing Laboratory Department of Electrical Engineering and Data Storage Institute, National University of Singapore,
10 Kent Ridge Crescent, Singapore 119260, Singapore

^b Department of Chemistry, National University of Singapore, 10 Kent Ridge Crescent, Singapore 119260, Singapore

^c Data Storage Institute, 5 Engineering Drive 1, Singapore 117608, Singapore

Accepted 28 June 1999

Abstract

Thin films of polyaniline (PBT), a kind of polyheterocyclic compound with hydrogen function groups, were deposited by KrF excimer ablation in a vacuum chamber. The laser pulse fluence was selected at 2 J cm^{-2} with a pulse duration of 25 ns. The polymer used in our experiments bears the basic structure and frame of many polyheterocyclic compound ramifications. The deposition of such a polymer should be helpful for future research when other kinds of function radicals are attached to polyaniline to realise different applications. The structural and topographic properties of the deposited thin films were analysed by atomic force microscope and X-ray diffraction. The deposited thin films were observed to have good crystal properties and be composed of crystalline cubes with a uniform size of $0.1 \mu\text{m}$. © 2000 Elsevier Science S.A. All rights reserved.

Keywords: AFM; Excimer laser; Polymer; Pulsed laser deposition; Thin film; XRD

1. Introduction

There is currently an increased interest in the application of conducting polymers and polymer-based optoelectronic materials due to their unique properties. The fabrication of the polymer light-emitting device (PLED) has received a lot of attention in recent years [1–4]. In many practical applications, polyheterocyclic compounds such as polyaniline (PBT) and polythiophenes are as basic materials with different kinds of function groups. In industrial applications, polymers are normally in their bulk forms of alloys and blends. Besides the bulk forms, the applications of polymers in the forms of thin-films are needed in miniaturization and integration technologies. Some fabrication methods of polymer thin films have been investigated such as vacuum evaporation [5–7], plasma polymerization [8,9], synchrotron radiation photodecomposition [10], spin coating [1–4,11], chemical vapour deposition [12], photo decomposition [13] and plasma sputtering [14] etc. Pulsed laser deposition (PLD) is another suitable deposition for fabricating polymer thin films on various kinds

of substrates [15–17]. In comparison to other methods, PLD has mainly two advantages. The first is its faithful transfer of target materials to substrate surfaces without obvious changes in composition. Since the ablated radicals normally have the same compositional ratio to the target, PLD can keep the electronic properties of the original target materials. The second concerns the energetic radicals in the ablated plume. These radicals with certain energies are beneficial to the formation of ideal crystalline structures in the deposited thin films.

In thin film deposition, polyheterocyclic compounds are usually difficult to find which are suitable solvents for spin-coating. Physical vapour deposition (PVD) always involving ion/plasma processing sometimes becomes an alternative deposition technique. However, since ion-beam processing of polymer solid surfaces can cause serious damage to polymer molecules and thus make the structures difficult to handle and affect the properties of deposited polymers, PLD seems to be an attractive deposition method since it avoids destruction of the target materials.

In our experiment, we intend to deposit a kind of polyheterocyclic compound, polyaniline (PBT), by KrF pulsed excimer laser ablation of a solid target. The chemical structure of polyaniline (PBT) used in our experiments is shown in Fig. 1.

* Corresponding author. Tel.: +65-874-2118; fax: +65-779-1103.

E-mail address: eleyflu@nus.edu.sg (Y.F. Lu)

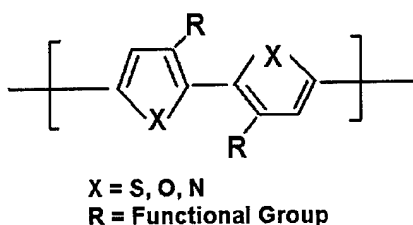


Fig. 1. Chemical structure of PBT used in the experiment.

In our compound, we have $X = \text{sulphur (S)}$. The function group is $R = \text{hydrogen (H)}$. The function group plays an important role with the electrical properties of the polymer. The conductivity and optoelectronic properties of the compound depend strongly on the selection of the functional function groups. The polymer used in our experiments has the basic frame of many polyheterocyclic compound ramifications. The deposition of such a polymer should be helpful for future research when other kinds of function groups are attached to PBT. This deposition will be targeted at fabricating polyaniline thin films with good crystal properties.

2. Experimental

Polyaniline thin films were deposited in a PLD system with a background vacuum of 1×10^{-6} Torr. The distance between the target and the substrate was 4 cm. The target was rotated by an external motor so as to provide each pulse with a fresh surface. The target was a piece of pure PBT. A KrF excimer laser with wavelength of 248 nm and a pulse duration of 25 ns was used as light source to ablate the PBT target. Its repetition rate was 10 Hz. The fluence of the KrF excimer laser was kept at 5 J cm^{-2} . The deposition rate was in the range of $50\text{--}150 \text{ nm min}^{-1}$. The thickness of the deposited thin films was in the range of $1\text{--}2 \mu\text{m}$. The substrate temperature was automatically controlled by a digital controller and can be set up to 900°C . Before deposition, the silicon substrate wafers were cleaned by acetone in an ultrasonic bath.

The measurement of the surface morphology of

deposited thin films was performed on an Autoprobe CP atomic force microscopy (AFM) system from Park Scientific Instruments. All images were obtained in a tapping mode with standard Si tips with normal radius of $10\text{--}20 \text{ nm}$. X-ray diffraction (XRD) measurements were performed on a Philips X'Pert-MRD system. $\text{Cu K}\alpha$ irradiation was used as the X-ray source in the diffraction measurements.

3. Results and discussion

The deposited PBT thin films were set for AFM measurements so as to characterise their surface morphologies and structures. The AFM results are shown in Fig. 2(a–c) corresponding to substrate temperatures of room temperature, 100°C and 200°C , respectively. The deposited thin films appear to be composed of cubic nanocrystals. The cubic nanocrystals are very obvious in Fig. 2, regardless of the different substrate temperatures. A detailed comparison among these three figures shows that the stack structure of PBT nanocrystals appears to be improved when substrate temperature is elevated to 200°C . The size distribution is very uniform for the sample deposited at a substrate temperature of 200°C while a low substrate temperature leads to some irregular crystal structures. All the cubic grains have the same size of 100 nm for the thin film deposited at a substrate temperature of 200°C whilst a substrate temperature of 100°C leads to a slightly larger size of 110 nm .

A three-dimensional AFM surface profile of the thin film deposited at a substrate temperature of 100°C is shown in Fig. 3. The cubic shapes of the nanocrystals are very obvious, demonstrating the formation of crystalline thin films. Crystal structures are seldom obtained in most depositions of polymer thin films due to the random orientation of the long molecular chains. The formation of crystalline in the deposited thin films also suggests some changes in molecular composition and structure in the resulting thin films as compared to the original target.

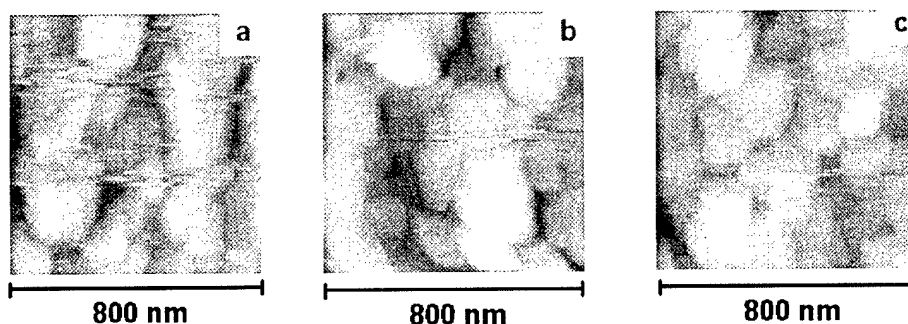


Fig. 2. AFM surface profiles of PBT thin film deposited at substrate temperatures of (a) room temperature, (b) 100°C , and (c) 200°C .

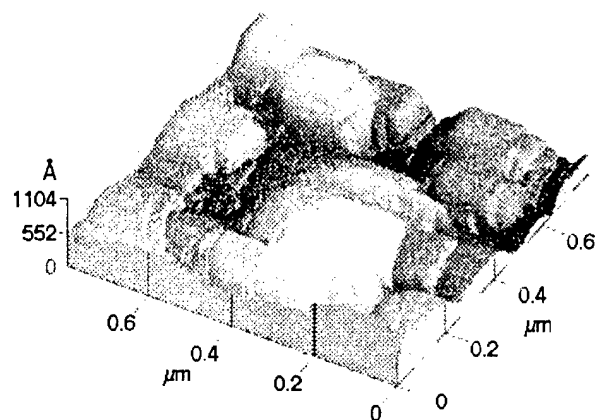


Fig. 3. Three-dimensional AFM surface scanning profile of a deposited PBT thin film.

X-ray diffraction measurements were carried out so as to assist the characterization of the deposited thin films. Fig. 4 shows the result of XRD measurements of the thin film deposited at a substrate temperature of 200°C. The diffraction peaks appear to be very sharp at $2\theta = 38.3, 44.5, 78.2$ and 82.3° . There are also two peaks from the Si(100) substrate in the spectrum. These sharp diffraction peaks confirm crystalline structures inside the deposited thin films. Some crystal orientations with different d-spacings can be calculated from these diffraction maxima: 0.24, 0.20, 0.12 and 0.11 nm, respectively. This series of d-spacings does not fit any allotropes of carbon such as graphite and diamond. The crystallines in the deposited thin films should be composed of carbon atoms and other elements such as H and S which are the functional groups in the original PBT target. The incorporation of H and S atoms into the carbon crystalline frameworks determines the lattice characters differing from other allotropes. In Fig. 4, two other broad peaks to the low end of diffraction angle at $2\theta = 12.0$ and 19.4° are also quite obvious, corresponding to

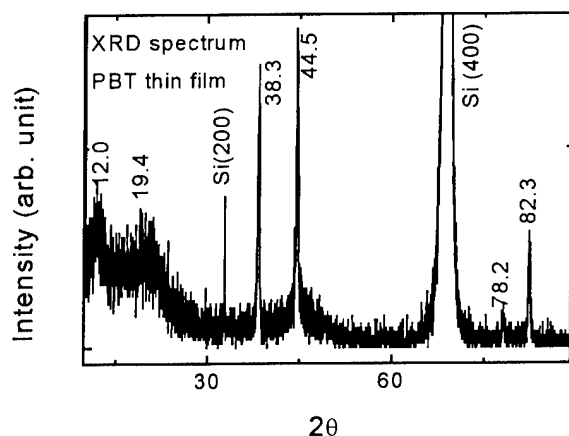


Fig. 4. XRD result of a thin film deposited at a substrate temperature of 200°C.

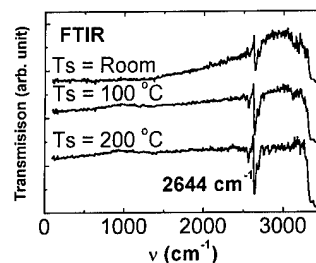


Fig. 5. FTIR spectra of deposited thin films at different substrate temperatures of room temperature, 100 and 200°C.

d-spacings of 0.74 and 0.46 nm, respectively. These two peaks with large lattice parameters possibly originate from crystal structures of polymeric compounds that can be traced to the starting PBT target.

In our deposition, despite of the random stack of micro-size cubes in the deposited thin films, the surfaces still appear to be smooth with a surface roughness < 10 nm as measured by alpha-step. The nanocrystallines inside the deposited polymer thin films exert great influence on their properties, especially conductivity and optoelectronic behaviour. The composition of uniform cubic nanocrystallines of the thin film should be easy to analyse and thus can readily control the optoelectronic and conductive properties of the PBT thin films.

The electronic properties of the deposited thin films were investigated by Fourier transform infrared (FTIR) spectroscopy. The FTIR results are shown in Fig. 5. There is no obvious difference among the three FTIR spectra of the samples deposited at room temperature, 100 and 200°C, respectively. In the spectra, the peak at 2644 cm^{-1} is related to the heterocycle composed of four carbon and one sulphur atoms. The elevating of substrate temperature therefore does not have influence on the chemical binding structures inside the polythiophene nanocrystals in the deposited thin films although it can reduce the size of the cubes as well as compress their size distributions as indicated by the previous AFM measurements.

4. Conclusions

Through our experiments, we know that thin films of PBT can be deposited on Si(100) substrates by KrF pulsed excimer laser deposition. The deposited thin films were proven to be purely composed of cubic nanocrystals instead of amorphous structures which happened in most other physical deposition of polymer thin films. The size of the nanocrystals decreases slightly with the elevating substrate temperature up to 200°C. The nanocrystals in the deposited thin films by 200°C substrate temperature have a uniform size of 100 nm. Deposited thin films exhibit good crystal properties with strong and sharp XRD peaks. The substrate temperature

does not have much influence on the chemical binding structures inside the deposited thin films.

Acknowledgements

The authors would like to express their thanks to Mr. Goh Yeow Whatt and Miss Koh Hwee Lin for their technical assistance in this research work.

References

- [1] S. Tasch, E.J.W. List, C. Hochfilzer, G. Leising, P. Schlichting, U. Rohr, Y. Geerts, U. Scherf, K. Mullen, *Phys. Rev. B* 56 (8) (1997) 4479.
- [2] K. Tada, M. Onoda, H. Nakayama, *Jpn. J. Appl. Phys. Pt 2* 37 (10A) (1998) L1181.
- [3] S.A. Carter, J.C. Scott, P.J. Brock, *Appl. Phys. Lett.* 71 (1997) 1145.
- [4] M. Benaissa, K.F. Gonsalves, S.P. Rangarajan, *Appl. Phys. Lett.* 71 (1997) 3685.
- [5] S.C.K. Misra, M.K. Ram, S.S. Pandey, B.D. Malhotra, S. Chandra, *Appl. Phys. Lett.* 61 (1992) 1219.
- [6] H. Usui, H. Koshikawa, K.J. Tanaka, *Vac. Sci. Technol. A* 13 (1995) 2318.
- [7] J.C. Bernede, H. Taoudi, E. Kodjo, *RRD Polym. Sci.* 1 (1997) 205.
- [8] M. Shen, A.T. Bell (Eds.), *ACS Symposium Series 108*, American Chemical Society, Washington, 1979.
- [9] H. Yasuda, *Plasma Polymerization*, Academic Press, Orlando, 1985.
- [10] T. Katoh, Y. Zhang, *Appl. Surf. Sci.* 139 (1999) 165.
- [11] G. Koren, *Appl. Phys. Lett.* 50 (1987) 1030.
- [12] S. Tatsuura, W. Sotoyama, T. Yoshimura, *Appl. Phys. Lett.* 60 (1992) 1661.
- [13] T. Katoh, Y. Zhang, *Appl. Phys. Lett.* 68 (1996) 865.
- [14] F. Quaranta, A. Valentinin, P. Favia, R. Lamendola, R. d'Agostino, *Appl. Phys. Lett.* 63 (1993) 10.
- [15] J. Gonzalo, P.E. Dyer, M. Hird, *Appl. Phys. Lett.* 71 (1997) 2752.
- [16] A.J. Salih, S.P. Lau, J.M. Marshall, J.M. Maud, W.R. Bowen, N. Hilal, R.W. Lovitt, P.M. Williams, *Appl. Phys. Lett.* 69 (1996) 2231.
- [17] J.K. Gibson, *J. Vac. Sci. Technol. A* 15 (4) (1997) 2107.

Catalytic behavior of plasma-sprayed Al–Al₂O₃ coatings doped with metal oxides

L.L. Pranevicius ^{a,*}, P. Valatkevicius ^b, V. Valincius ^b, C. Montassier ^c

^a *Vytautas Magnus Universitetas, 28 Daukanto gatve, 3000 Kaunas, Lithuania*

^b *Lietuvos Energijos Institutas, 3 Breslaujos gatve, 3035 Kaunas, Lithuania*

^c *LACCO, Université de Poitiers, 40 Avenue du Recteur Pineau, F-86022 Poitiers Cedex, France*

Abstract

Reactive plasma spraying of aluminum and Al(OH)₃ powders with oxide additives, CuO and Cr₂O₃, was investigated. An arc-plasma spray gun was constructed with the injection of powders into the plasma torch both internally and externally. The spraying was done at atmospheric pressure in a working gas comprising an argon/air mixture. The resulting oxide-doped Al–Al₂O₃ coatings, which were 30–50 μm thick, were investigated by X-ray diffraction and scanning electron microscopy. Their catalytic behavior was identified observing by the combustion effect of propane in a tube furnace. © 2000 Elsevier Science S.A. All rights reserved.

Keywords: Atmospheric pressure; Catalytic behavior; Oxidation; Reactive plasma spraying

1. Introduction

Significant progress has been made in recent years in the development of atmospheric-pressure plasma spraying technology [1,2]. It combines the universality of low-pressure plasma technology and the economical approaches of chemical technologies. There is great interest in the development of reactive plasma-spray deposition technology to obtain oxides of different metals introduced in a plasma in the form of powder. Oxidation may occur: (1) in flight with the solid and then with the liquid metal (the time of flight is about 1 ms); (2) at the splat surface as a liquid ($t < 20 \mu\text{s}$) and then as a solid ($t < 50 \mu\text{s}$); and (3) at beads and then the pass surface ($t \sim 0.1\text{--}3 \text{ s}$) [3].

In-flight oxidation takes place in the environment of the plasma pushed by the gas carrier from the plasma gun, which forms a torch consisting of high-velocity, high-temperature (energy) electrons, ions and neutrals. It occurs in the so-called equilibrium plasma which exists in arcs or in plasma torches at atmospheric pressure due to the great frequency of collisions between different particles. Reactive particles in the plasma,

generated by the dissociation of molecular species, react with the heated metal particles to form splats of chemical compounds.

Oxidation of the splats on the substrate leads to the oxidation of splat surfaces. Both of these processes takes place simultaneously. To obtain highly stoichiometric oxides it is important to realize the access of oxygen in the reaction zone and the mixing process of reactive species with atoms of the metal.

The goal of the present research was to study the oxidation of sprayed powders in a reactive plasma torch and on the surface of a substrate at atmospheric pressure in a working gas of argon and air, and the catalytic behavior of the coatings so obtained.

2. Experimental

A schematic representation of the plasma spray gun is shown in Fig. 1. Aluminum powder with a size distribution of 40–75 μm and Al(OH)₃, CuO and Cr₂O₃ powders of size 30–50 μm were used, and injected into the plasma torch both internally and externally. Continuously vibrating mixers controlled the dosage of the powder. The gas carrier (air/argon mixture) was

* Corresponding author. Tel: +370-7-778602; fax: +370-7-203858
E-mail address: liudas.pranevicius@tcf.ktu.lt (L.L. Pranevicius)

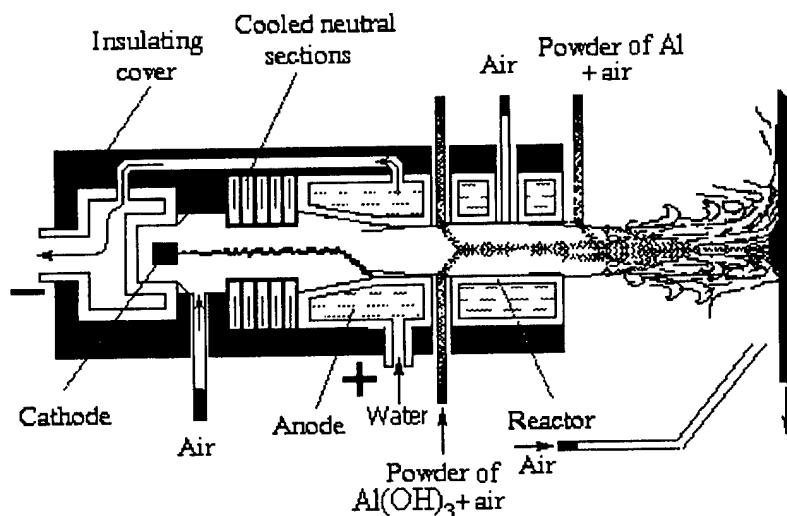


Fig. 1. Schematic representation of the plasma gun.

injected into the plasma through a 9.5 mm diameter cylindrical tube with flow rate equal to 0.4 g s^{-1} .

Al(OH)_3 powder was mixed with CuO and Cr_2O_3 oxides and injected in the direction parallel to the axis of the plasma torch along the boundary layer with the reactor. The boundary layer was cooled with an additional flow of the working gas equal to 1.2 g s^{-1} . The aluminum powder was introduced externally. The total flow rate of working gas through the plasma gun was $2.5\text{--}3 \text{ g s}^{-1}$.

The mean temperature of the gas carrier along the axis of the burning arc was 5000–6000 K, the velocity about $100\text{--}500 \text{ m s}^{-1}$. The temperature of the working gas leaving the plasma gun was 3000–3500 K and the velocity was $500\text{--}650 \text{ m s}^{-1}$. The energy flux was in the range $10^6\text{--}10^8 \text{ W m}^{-2}$ and the flux of atomic particles about $10^{21} \text{ cm}^{-2} \text{ s}^{-1}$. Deposition experiments were conducted using a 40 kW power source and the arc current was 150–200 A. Controls allowed monitoring of the working gas mixture, gas flow, power settings, mandrel motion and powder feed rate [4].

The rotation rate of the mandrel was 40 rev min^{-1} with an average axial translation speed of 5 cm s^{-1} . The separation distance between the torch and mandrel was 65 cm.

Steel sheet substrates were approximately 50 cm long and 11 cm wide, with a thickness of 0.4–45 mm. X-ray diffraction was performed from $2\theta = 30$ to 70° with $\text{Cu K}\alpha$ radiation on a Scintag XDS2000 instrument. Microstructural analysis was performed on representative samples with a JEOL JSM 840A scanning electron microscope.

The catalytic behavior of the coatings was studied in the vertical mounted tube furnace shown schematically in Fig. 2. The premixed propane/air gas stream was introduced through a stainless steel tube at the bottom

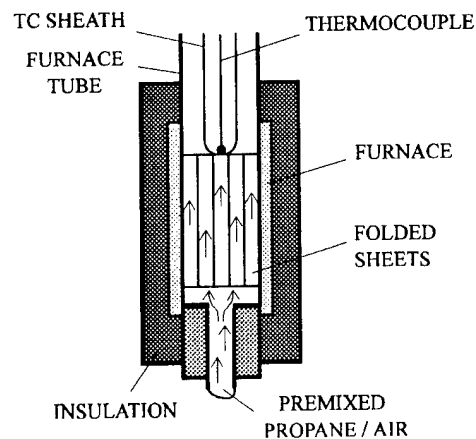


Fig. 2. Schematic illustration of the catalytic combustion tube.

of the furnace and passed through an 11 cm long active element made of doubly coated steel sheets rolled into a cylinder of diameter equal to 15 cm. The coated sheets of steel were folded and rectangular channels for flow of the propane/air were made with characteristic size equal to 7 mm. The temperature of exiting gas was monitored with a chromel–alumel thermocouple. A comparison of the temperature increase when the gas stream contains the propane/air mixture, as opposed to when it contains air only (with all other factors being kept constant), allows identification of catalytic combustion effects [5,6].

3. Results

The typical results of X-ray analysis are presented in Fig. 3 for undoped coatings [Fig. 3(a)] and coatings

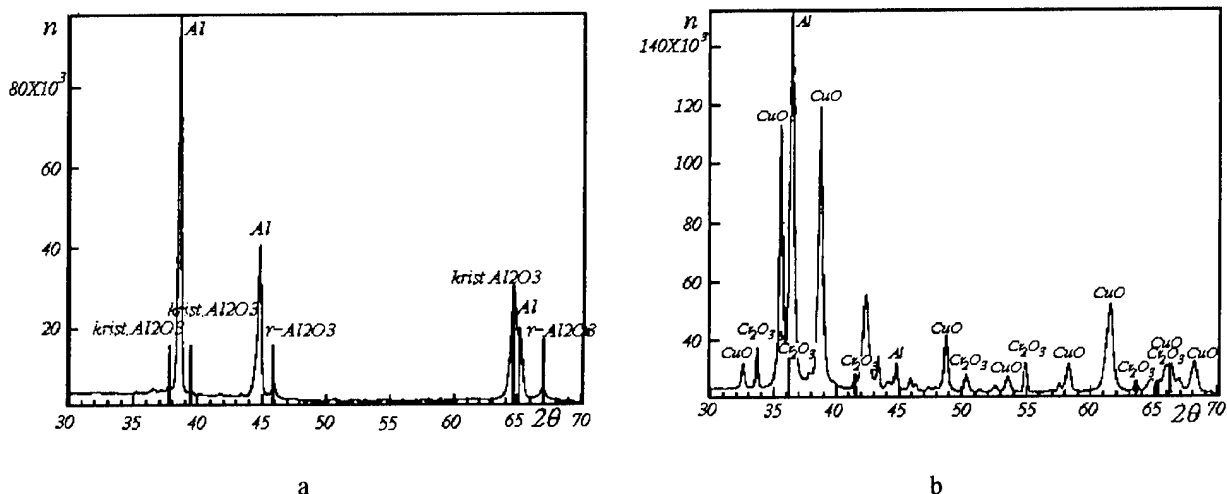


Fig. 3. X-ray analysis results of Al-Al₂O₃ coatings (a) and Al-Al₂O₃ coatings doped with the metal oxides CuO and Cr₂O₃ (b).

doped with 10% CuO and 5% Cr₂O₃ (in mass units) [Fig. 3(b)]. Aluminum coatings after deposition were thermally annealed at 520°C for 90 min. Results showed that they included about 70% Al₂O₃ γ-phase, which depends on the substrate temperature during deposition. With an increase of substrate temperature to about 290°C, a phase transition takes place from γ-Al₂O₃ to α-Al₂O₃. At the substrate temperature of 770°C, practically 100% α-Al₂O₃ is obtained. Cooling of the substrate prevented substrate heating above 290°C. The coatings obtained have a highly developed effective surface of about 100–120 m² g⁻¹ [4].

The quantity of Al₂O₃ in the coatings depends on the flow of air/argon mixture through the plasma gun. Fig. 4 presents the experimental dependence of the coating composition in relative mass units on the ratio of air and argon flows in mass units forming the working gas. It is seen that the presence of a small amount of air does not affect the quantity of oxidized aluminum. A sharp increase of Al₂O₃ in coatings is observed when the ratio of air flow to argon flow ranges between

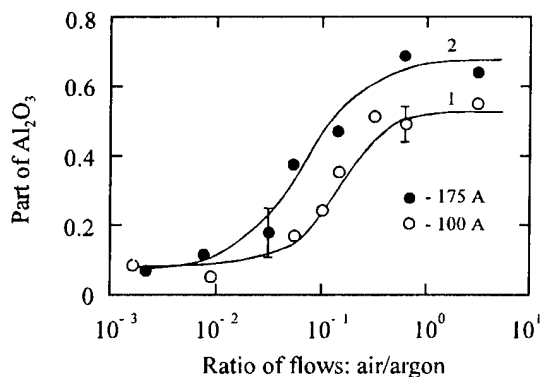


Fig. 4. Dependence of the quantity of Al₂O₃ in the deposited coating on the flow ratio of air/argon in equivalence units.

10⁻² and 2 × 10⁻¹. The quantity of Al₂O₃ saturates if the ratio of air to argon flows exceeds 10⁻¹, and it does not increase even if air is used as carrier gas without argon. The saturation level depends on the temperature of the working gas, which increases with the increase in arc current. Curve 1 in Fig. 4 corresponds to an arc current of 100 A, curve 2 to an arc current of 175 A.

The catalytic behavior of coatings obtained at atmospheric pressure in air was investigated. Fig. 5 illustrates the catalytic behavior of coatings doped with 10% CuO and 5% Cr₂O₃. Curve 1 gives the time dependence of the temperature in the furnace without propane and curve 2 the case when the equivalence ratio of propane to air is equal to 1.8. It is seen that catalytic combustion

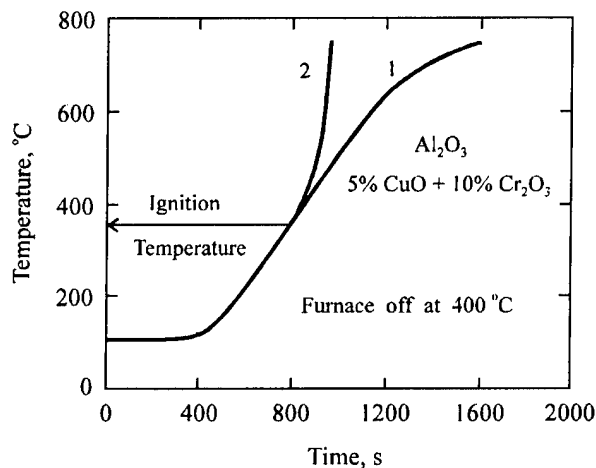


Fig. 5. Catalytic combustion behavior of Al-Al₂O₃ coatings doped with CuO and Cr₂O₃.

starts at about 350°C. Undoped coatings give the catalytic combustion effect at 710°C.

4. Conclusions

The aluminum and $\text{Al}(\text{OH})_3$ powder mixture with the addition of CuO and Cr_2O_3 powders pushed through the plasma spray gun, operating at atmospheric pressure in air, forms well adherent coatings on steel sheets including 70% $\gamma\text{-Al}_2\text{O}_3$. The quantity of the oxidized aluminum depends on the ratio of air to argon. It is shown that a sharp increase in the Al_2O_3 content of the coating starts when the equivalence ratio of air to argon exceeds 10^{-2} and saturates if that ratio exceeds 2×10^{-1} . The saturation level depends on the burning

arc current. The coatings obtained show characteristic catalytic combustion behavior.

Acknowledgement

This work was performed at the Lithuanian Energy Institute under Lithuanian Science Foundation grant N K-009.

References

- [1] R.W. Smith, Z.Z. Matasim, J. Thermal Spray Technol. 1 (1992) 57.
- [2] M. Bous, Pure Appl. Chem. 68 (1996) 1007.
- [3] P. Fauchais, J.F. Coudert, M. Vardelle, A. Denoirjean, J. Thermal. Spray Technol. 1 (1992) 117.
- [4] V. Valincius, P. Valatkevicius, L.L. Pranevicius, D. Milcius, Lithuanian Mater. Sci. 1 (6) (1998) 12.
- [5] R.L. Jones, Surf. Coat. Technol. 86–87 (1996) 127.
- [6] R.L. Jones, Surf. Coat. Technol. 94–95 (1997) 118.

Temperature and substrate influence on the structure of TiN_xO_y thin films grown by low pressure metal organic chemical vapour deposition

F. Fabreguette ^{a,b,*}, L. Imhoff ^b, J. Guillot ^b, B. Domenichini ^b, M.C. Marco de Lucas ^b,
P. Sibillot ^a, S. Bourgeois ^b, M. Sacilotti ^a

^a LPUB (Laboratoire de Physique de l'Université de Bourgogne, CNRS UPRESA 5027), Université de Bourgogne, 9 Av. Alain Savary, BP 47870, 21078 Dijon cedex, France

^b LRRS (Laboratoire de Recherches sur la Réactivité des Solides, CNRS UMR 5613, Université de Bourgogne, 9 Av. Alain Savary, BP 47870, 21078 Dijon cedex, France

Abstract

This paper presents the growth and characterization of titanium oxinitride (TiN_xO_y) films grown by low pressure metal organic chemical vapour deposition (LP-MOCVD). The film nitrogen content, obtained by Rutherford backscattering spectroscopy (RBS), increases as the growth temperature increases (from 23 at.% at 450°C to 46 at.% at 750°C). Below 550°C, the films do not show any X-ray diffraction pattern. Above 550°C, the deposited films present the (111) and (200) TiN textures. Films deposited on (100) Si exhibit a 2θ shift to higher Bragg angles, depending on the N/O ratio. These shifts are explained by using a substitutional oxygen model. Moreover, the atomic structure of such materials is described from this behaviour in terms of lattice vacancies and N/O substitutions, leading to different titanium valencies confirmed by X-ray photoelectron spectroscopy (XPS) analysis. © 2000 Elsevier Science S.A. All rights reserved.

Keywords: Rutherford backscattering spectroscopy; Thin film; TiN_xO_y ; X-ray diffraction; X-ray photoelectron spectroscopy

1. Introduction

Titanium nitride and oxide have received increasing attention over the past few years. Different chemical and physical deposition techniques have been used in the production of these films for applications in protective coatings, electrical contacts, diffusion barriers and catalytic aspects [1–4].

Moreover, the presence of oxygen in titanium nitride films leads to a promising functional range of materials, TiN_xO_y , ranging from TiN to TiO_2 with a checkable N/O ratio. Despite applications as solar selective absorbers [5], and transparent windows for infrared detectors [6,7] few works have been published concerning the production, properties and structure of these titanium oxinitride films [8–10].

In the present study, the structure of TiN_xO_y thin

films produced by LP-MOCVD is described. Both growth temperature and the nature of the substrate control the microstructure of the films. The influence of these parameters is studied.

2. Experimental procedure

The growths were performed on (100) oriented silicon, (1-102) sapphire and polycrystalline alumina substrates. The substrate temperature varied from 450 to 750°C. The growth system was a home-made low pressure (60 Torr) MOCVD one [11]. Titanium isopropoxide, $\text{Ti}(\text{OCH}(\text{CH}_3)_2)_4$, was used as both a titanium and an oxygen source [12]. Ammonia, NH_3 , was used as the nitrogen source. The structural properties of the films were observed by X-ray diffraction (XRD) on a Siemens D5000 diffractometer using the $\text{CuK}\alpha$ radiation at 1.54 Å. The film composition was quantified by XPS using a Riber Mac2 apparatus working with the $\text{AlK}\alpha$ radiation (1486.6 eV) and by Rutherford backscattering

* Corresponding author. Tel.: +33-380-39-6028;
fax: +33-380-39-5961.

E-mail address: ffabreg@u-bourgogne.fr (F. Fabreguette)

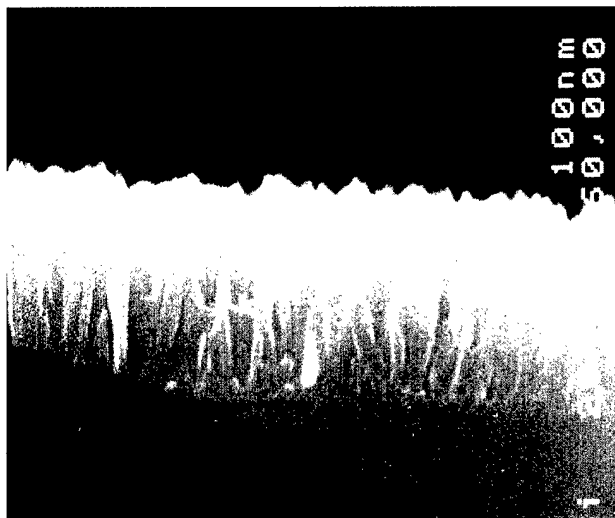


Fig. 1. SEM picture of a TiN_xO_y film grown at 500°C on (100) Si.

spectroscopy (RBS) using 2 MeV He⁺. Scanning electron microscopy (SEM) on a JEOL JSM-6400F was also used to check the film thickness and morphology.

3. Results

3.1. Film morphology

Fig. 1 shows a SEM picture of the cross-section of a TiN_xO_y film deposited at 500°C on (100) Si over 1 h. The layer presents a columnar structure, with a mean diameter of columns of about 50 nm. The growth rate obtained for this layer was about 300 nm/h. In addition, different morphologies of layers were observed while varying the growth temperature, correlated with the electrical properties [13].

3.2. Compositional analysis

The XPS spectrum for a film grown at 650°C on (100) Si is shown in Fig. 2. The signals originating from Ti 2s, O 1s, Ti 2p_{1/2}, Ti 2p_{3/2} and N 1s are easily identified at binding energies around 564, 532, 462, 456 and

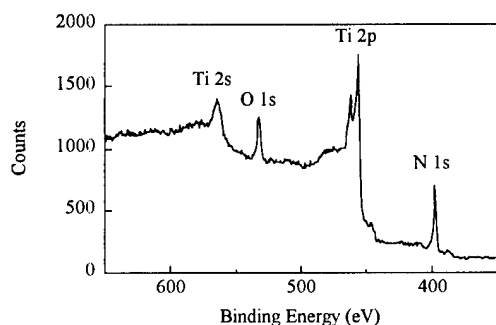


Fig. 2. XPS spectra obtained for a film deposited at 650°C on (100) Si.

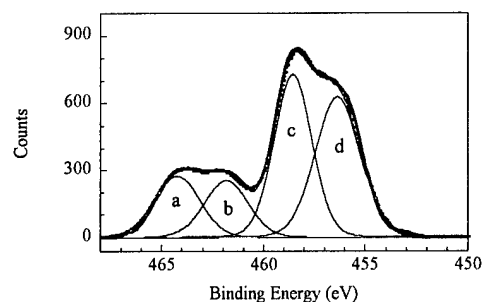


Fig. 3. Experimental (solid line) and reconstructed (dots) Ti 2p XPS line of a layer obtained at 650°C on (100) Si. The contributions of (a) Ti⁴⁺ 2p_{1/2}, (b) Ti³⁺ 2p_{1/2}, (c) Ti⁴⁺ 2p_{3/2}, and (d) Ti³⁺ 2p_{3/2} are represented.

397 eV, respectively. A few amounts of C 1s is observed at 285 eV, and disappears after a 20 min Ar⁺ bombardment at 3 keV. This behaviour corresponds to carbon surface contamination. Besides, the fit of the Ti 2p_{1/2} and Ti 2p_{3/2} signals is shown on Fig. 3. The reconstructed spectrum from the different Ti contributions is in excellent agreement with the experimental spectrum, as shown in Fig. 3. This kind of fit allowed us to obtain the Ti³⁺/Ti⁴⁺ ratio for different growth temperatures by considering, for each valency, the contribution of both 2p_{1/2} and 2p_{3/2} peaks.

In order to obtain atomic compositions, and especially the N/O ratio, RBS experiments were carried out. RBS spectra for films deposited on (100) oriented silicon at two temperatures are presented in Fig. 4. While increasing the growth temperature from 550 to 650°C, the nitrogen peak at 0.4 MeV (insert in Fig. 4) and the titanium peak at 1.25 MeV increase, which means that the contents increase as well. At the same time, the oxygen peak at 0.55 MeV (insert in Fig. 4) decreases, leading to a decrease of the oxygen content. As the width of the titanium peak is linked to the film thickness, the Si front moves back to lower energy for the thicker layer obtained at 550°C.

From 450 to 750°C, the nitrogen content increases from 23 to 45% and the oxygen content decreases from 48 to 16%. About carbon contamination, the RBS spectra confirm the XPS results since no bulk carbon contribution is observed.

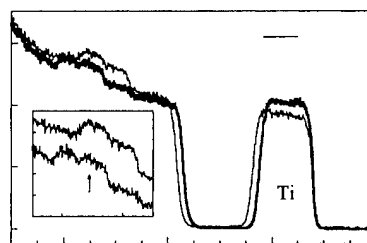


Fig. 4. RBS spectra of TiN_xO_y thin films deposited at 550 and 650°C on (100) Si.

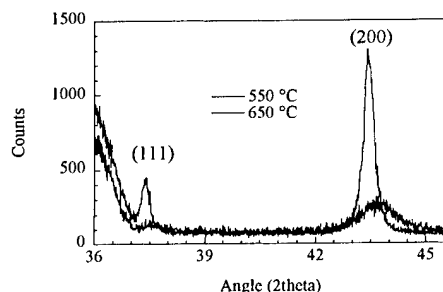


Fig. 5. X-ray diffraction patterns of TiN_xO_y films deposited at 550 and 650 °C on (100) Si.

3.3. Structural aspects

XRD patterns of two films prepared by changing the growth temperature are shown in Fig. 5. By comparing the XRD measurements with the JCPDS data, the deposited films are identified as titanium nitride films presenting a 2θ shift to higher angles when compared to theoretical positions. These films exhibit a well-crystallised (200) texture from 550 °C upwards only. For deposition temperatures below that, no diffraction spectrum is observed on silicon. The peaks observed for the layers deposited on polycrystalline alumina substrate are much more intense than those observed on (100) Si. Moreover, the broad peak present at 36° on (100) Si is probably due to substrate oxidation during the growth, since it is not present on a polycrystalline alumina substrate. The numerical values of the 2θ Bragg angles are given in Table 1, for films deposited on (100) silicon and polycrystalline alumina, and the dependence of the lattice parameter on the growth temperature is shown in Figs. 6 and 7 for the two substrates.

Concerning Si substrate, the lattice parameter increases with the deposition temperature, and the values obtained from the (111) and (200) peaks are the same. The behaviour of the films deposited on (1-102) sapphire is exactly the same than those deposited on (100) oriented silicon. On the other hand, on polycrystalline alumina there is no evolution of the lattice parameter as a function of the temperature, and two different

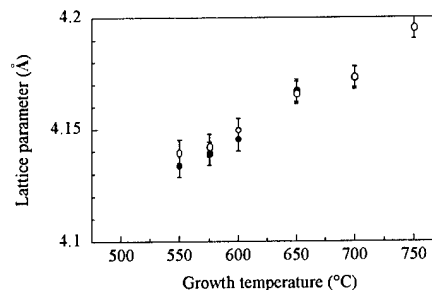


Fig. 6. Dependence of the lattice parameter on the growth temperature for layers deposited on (100) Si. Respective lattice parameters were determined from values given in Table 1 for (111) (●) and (200) (○) diffraction peaks.

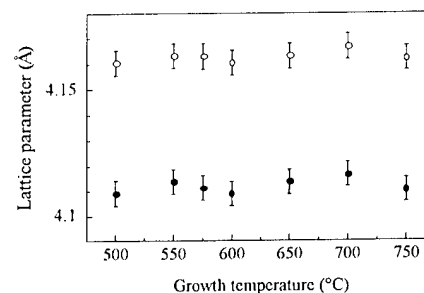


Fig. 7. Dependence of lattice parameter on the growth and temperature for layers deposited on polycrystalline alumina. Respective lattice parameters are determined from values given in Table 1 for (111) (●) and (200) (○) diffraction peaks.

values for the lattice parameter are obtained depending on the considered plane. Several hypothesis have been made concerning this behaviour, and are discussed in the following section.

4. Discussion

The XRD results indicate that the titanium oxinitride films produced by LP-MOCVD on (100) Si substrate present a structure close to the TiN one, with a 2θ shift increasing as the growth temperature decreases. Such behaviour has been previously observed by Makino et al. [10]. It has been correlated with the substitution of nitrogen by oxygen. Indeed, the oxygen ionic radius is smaller than the nitrogen radius, so while decreasing the growth temperature, the oxygen content increases as shown by RBS results, and the lattice parameter decreases. Then, using Bragg's law, it is easily understandable that the peaks move to higher 2θ .

A model has been developed to represent this substitution of nitrogen by oxygen. This model highlights the formation of Ti^{4+} while including oxygen in the structure, and also the creation of vacancies (□) in order to satisfy the electroneutrality rule:

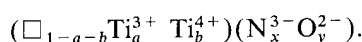


Table 1
 2θ position values of (111) and (200) diffraction peaks of layers deposited on (100) Si and polycrystalline alumina (nd = not detected)

Growth temperature (°C)	On (100) silicon		On polycrystalline alumina	
	$2\theta(111)$	$2\theta(200)$	$2\theta(111)$	$2\theta(200)$
750	37.09	43.09	37.88	43.45
700	37.30	43.33	37.82	43.40
650	37.35	43.41	37.85	43.44
600	37.55	43.59	37.90	43.47
575	37.61	43.67	37.88	43.44
550	37.66	43.70	37.85	43.44
500	nd	nd	37.90	43.47

Table 2
Composition of TiN_xO_y layers for two growth temperatures

Growth temperature (°C)	Composition
700	$(\square_{0.17}\text{Ti}_{0.57}^{3+}\text{Ti}_{0.26}^{4+})(\text{N}_{0.74}^{3-}\text{O}_{0.26}^{2-})$
650	$(\square_{0.18}\text{Ti}_{0.57}^{3+}\text{Ti}_{0.25}^{4+})(\text{N}_{0.72}^{3-}\text{O}_{0.28}^{2-})$

Using the N/O ratio obtained by RBS, and assuming that $x+y=1$, the nitrogen and oxygen contributions in the structure could be estimated. Then, using the electroneutrality $3a+4b=3x+2y$ combined with the $\text{Ti}^{3+}/\text{Ti}^{4+}$ ratio obtained from the XPS fits (Fig. 3), we tried to determine the amounts of Ti^{3+} , Ti^{4+} and vacancies. These results are shown in Table 2 for the higher growth temperatures. However, the discussion of the results obtained at temperatures lower than 600°C is difficult because of the TiO_2 presence in the layer in addition to TiN_xO_y . This fact has been shown by XPS results obtained after ionic bombardment, where the spectra were fitted with both TiN_xO_y (Ti^{3+} and Ti^{4+} peaks) and TiO_2 (equilibrium $\text{Ti}^{4+} + \text{Ti}^{2+} \leftrightarrow \text{Ti}^{3+}$) [14] contributions. This behaviour leads to an artificial increase of the oxygen amount in the TiN_xO_y films determined by RBS.

Concerning the behaviour on polycrystalline alumina substrate, several hypothesis have been considered. The polycrystallinity of this substrate may cause this behaviour. However, the growth of TiN_xO_y films on other polycrystalline substrates (Si, Ta_2O_5) showed the same 2θ shift as the one observed on (100) Si. The roughness of the alumina surface was also considered to have an influence on such a trend. In order to verify this hypothesis, depositions were carried out on polished polycrystalline alumina substrates. In that case, no 2θ shift was observed on XRD patterns. Another hypothesis concerns the ammonia treatment realised on the substrates before the growth. Thus, films were deposited without this treatment, but once again no 2θ shift was observed.

Moreover, for the three hypothesis considered, two different values of the lattice parameter were obtained depending on the (111) or (200) plane. Further investigations are being carried out in order to understand the growth on that kind of substrate.

5. Conclusion

Titanium oxinitride films obtained by LP-MOCVD were characterised by XRD, XPS and RBS methods.

The use of titanium isopropoxide $\text{Ti}(\text{OCH}(\text{CH}_3)_2)_4$ allowed us to obtain a tuneable N/O ratio dependent on the growth temperature. The XRD 2θ shift observed on (100) Si substrate was explained in terms of nitrogen substitution by oxygen. In addition, a model was developed in order to present the structure of TiN_xO_y compounds upon the growth temperature, assuming Ti^{4+} and vacancies formation. Moreover, further investigation is necessary in order to understand the behaviour observed for TiN_xO_y films deposited on polycrystalline alumina.

Acknowledgements

The authors wish to express their sincere gratitude to: Ph. Dufour and C. Josse of the Laboratoire de Recherche sur la Réactivité des Solides, Dijon, for the SEM experiments; to M. Monchanin of the Département de Physique des Matériaux, Lyon, for the RBS results; and also to the Conseil Régional de Bourgogne for the financial support.

References

- [1] W. Schintlmeister, O. Pacher, K. Pfaffinger, J. Electrochem. Soc. 123 (1976) 924.
- [2] J. Cho, S. Nam, J. Chun, J. Mater. Sci. 17 (1982) 2495.
- [3] C. Ting, Thin Solid Films 119 (1984) 11.
- [4] M. Wittmer, J. Vac. Sci. Technol. A 3 (1985) 1797.
- [5] M. Lazarov, P. Rath, H. Metzger, W. Spirkel, J. Appl. Phys. 77 (1995) 2133.
- [6] H. Tada, Y. Saito, M. Hirata, H. Kawahara, J. Appl. Phys. 83 (1993) 489.
- [7] C. Wan, F. Sulzbachand, J. Luttmer, J. Vac. Sci. Technol. B 10 (1992) 1658.
- [8] E. Vogelzang, J. Sjoecema, H. Boer, J. De Hosson, J. Appl. Phys. 61 (1987) 4606.
- [9] A. Bittar, D. Cochrane, S. Caughley, J. Vac. Sci. Technol. A 15 (1997) 223.
- [10] Y. Makino, M. Nose, T. Tanaka, M. Misawa, A. Tanimoto, T. Nakai, K. Kato, K. Nogi, Surf. Coat. Technol. 98 (1998) 934.
- [11] Ph. Babelon, PhD Thesis, Université de Bourgogne, 1997.
- [12] P. Sibillot, Ph. Babelon, M. Sacilotti, S. Bourgeois, French Patent No. 97.13043.
- [13] F. Fabreguette, L. Imhoff, B. Domenichini, M.C. Marco de Lucas, P. Sibillot, S. Bourgeois, M. Sacilotti, submitted for publication.
- [14] S. Petigny, H. Mostefa-Sba, B. Domenichini, E. Lesniewska, A. Steinbrunn, S. Bourgeois, Surf. Sci. 410 (1998) 250.

CVD of ZrO_2 , Al_2O_3 and Y_2O_3 from metalorganic compounds in different reactors

M. Pulver, W. Nemetz *, G. Wahl

*Institut für Oberflächentechnik und Plasmatechnische Werkstoffentwicklung Technische Universität Braunschweig, Bienroder Weg 53,
D 38108 Braunschweig, Germany*

Abstract

The deposition of ZrO_2 , Y_2O_3 or Al_2O_3 from the precursors $\text{Zr}(\text{tmhd})_4$, $\text{Y}(\text{tmhd})_3$ and $\text{Al}(\text{acac})_3$ is investigated in this paper. Chemical vapor deposition (CVD) experiments were carried out in the temperature range 500–1100 K at pressures between 1000 and 4000 Pa in different reactors with different temperature fields. In addition, the temperature gradient between substrate and gas was changed from negative to positive values in order to measure the influence of thermophoresis effects. The deposition rate j in the low temperature range can be described by an Arrhenius law, $j = k \exp(-E/RT)$, whereby the pre-exponential factor k and the activation energy E depend on the temperature field. It is experimentally found that the effect of a changing activation energy is partly compensated by a changing pre-exponential factor in the same direction (compensation effect). In the case of Al_2O_3 -deposition, thermophoresis effects were measured. © 2000 Elsevier Science S.A. All rights reserved.

Keywords: Alumina; Chemical vapor deposition; Metalorganic compounds; Thermophoresis; Yttria; Zirconia

1. Introduction

ZrO_2 (with and without stabilising Y_2O_3) layers are used for many applications: as heat barrier coatings in gas turbines [1]; electrolytes in high temperature fuel cells [2]; oxygen sensors [3]; ceramic at dental applications, ceramic membranes for gas separation [4,5] and as buffer layers for superconducting films [6]. Al_2O_3 layers are important as hard coatings [7] and for oxidation protection [8]. For these different applications, a large variety of structures are demanded. The aim of this study was to investigate the influence of the temperature field in the reactor on CVD processes, especially of the deposition rate and the structure. Typical forms of temperature fields are realized in cold wall (KW) and hot wall (HW) reactors. In this work however, temperature fields were studied where temperature fields were between HW and KW, and where temperatures outside the deposition substrates were higher than the temperature of the substrate — that means that positive temperature gradients were realized perpendicularly to the substrate surface. There are hints in the literature

[9] that by using different temperature gradients a large variety of structures (powder–porous–solid) can be realized. The oxides are deposited by tetramethylheptanedionate (tmhd) compounds for Y_2O_3 , ZrO_2 and by acetylacetonates (acac) for Al_2O_3 . These compounds are sufficiently stable for a CVD process and have evaporation rates high enough for CVD processes [10,11].

2. Deposition equipment

For the deposition, the CVD equipment which is described in Refs. [10–12] was used. The deposition reactor is shown in Fig. 1. Different substrate holders were available. The substrate holder shown in Fig. 1 could be cooled by an air flow (20 mol/h). By this method, the temperature of the substrate on the substrate holder could be lowered to temperatures approximately 100 K lower than the gas temperature. Another substrate holder with the same geometry could be heated to higher temperatures by a heating plate on the top of the substrate holder. Temperature differences of 500 K could be produced between the sample and the free flowing gas. As shown in Fig. 1, the reactor was heated by a resistance furnace outside the quartz tube. In a

* Corresponding author. Tel.: +49-531-391-9417;
fax: +49-531-391-9400.

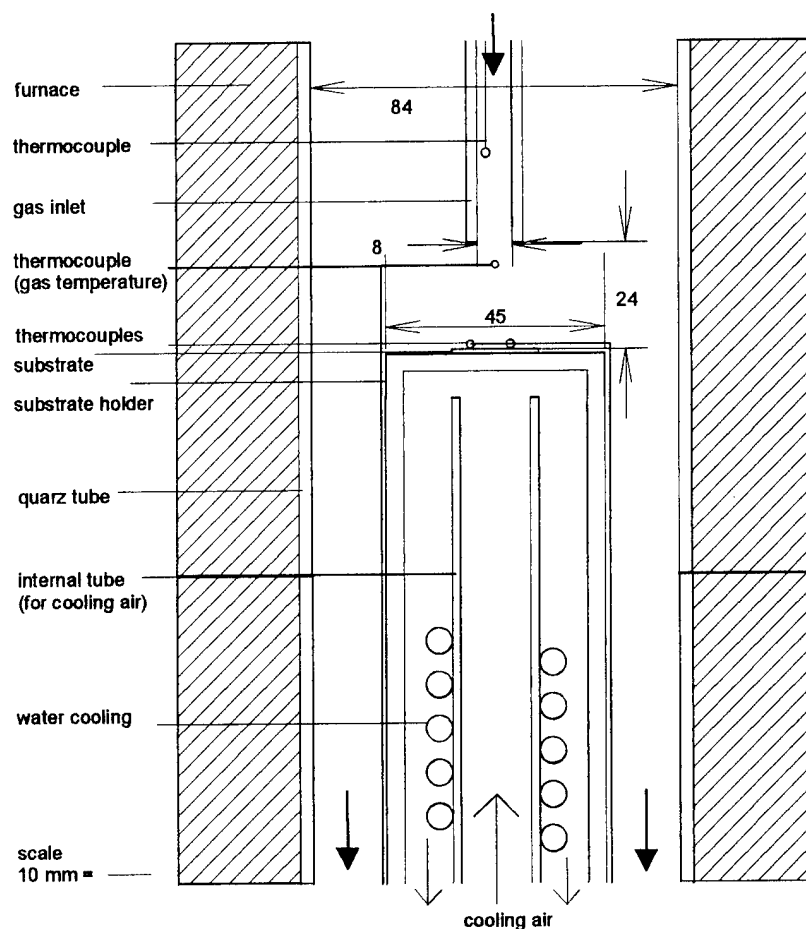


Fig. 1. Schematic diagram of the deposition reactor (unit: mm).

different arrangement the resistance furnace could be replaced by a coil for inductive heating. Then, only the substrate holder was heated. It is important to note that at all these different arrangements, with different temperature fields in the reactor, had the same geometry as shown in Fig. 1.

The temperature conditions in these reactors were defined by two temperatures: the deposition temperature T_d , and the gas temperature characterized by the wall temperature T_w . In the case of cooled substrates, the temperature T_g above the substrate was measured to characterize the temperature gradient. The position of the thermoelement for the measurement of T_g is indicated in Fig. 1. All temperatures were measured with NiCr/Ni thermoelements.

Polycrystalline Al_2O_3 wafers ($2 \times 2 \text{ cm}^2$) were used. The mass deposition density \dot{m} was determined by measuring the mass change Δm of the substrates before and after the deposition:

$$\dot{m} = \frac{\Delta m}{A \cdot t}, \quad (1)$$

where A is the area of the sample and t the deposition

time. The thickness growth rate r_{dep} and the molar deposition density j were calculated with the help of the molar masses and the mass densities of the oxides. Deposition profiles on the samples were not observed.

3. ZrO_2 and Y_2O_3 deposition

The following typical values were taken for deposition (deviations are later indicated): total pressure $p_{\text{tot}} = 1000 \text{ Pa}$; total gas flow $i_{\text{tot}} = 15 \text{ l}_n/\text{h}$; oxygen molar fraction $x_{\text{O}_2} = 0$ or 0.167 ; $\text{Zr}(\text{tmhd})_4$, $\text{Y}(\text{tmhd})_3$ molar fraction $x_{\text{Zr}(\text{tmhd})_4}$ or $x_{\text{Y}(\text{tmhd})_3} = 0 \dots 0.05$; the carrier gas was argon.

The mass deposition was always proportional to the deposition time. No incubation time was visible. The deposition time was usually $t = 1 \text{ h}$. Fig. 2 shows the deposition rate for different temperature fields.

The curves have a temperature dependence typical of CVD processes. At low temperature the deposition rate r_{dep} is described by an Arrhenius equation:

$$r_{\text{dep}} = k_0 \exp\left(-\frac{E_d}{RT_d}\right), \quad (2)$$

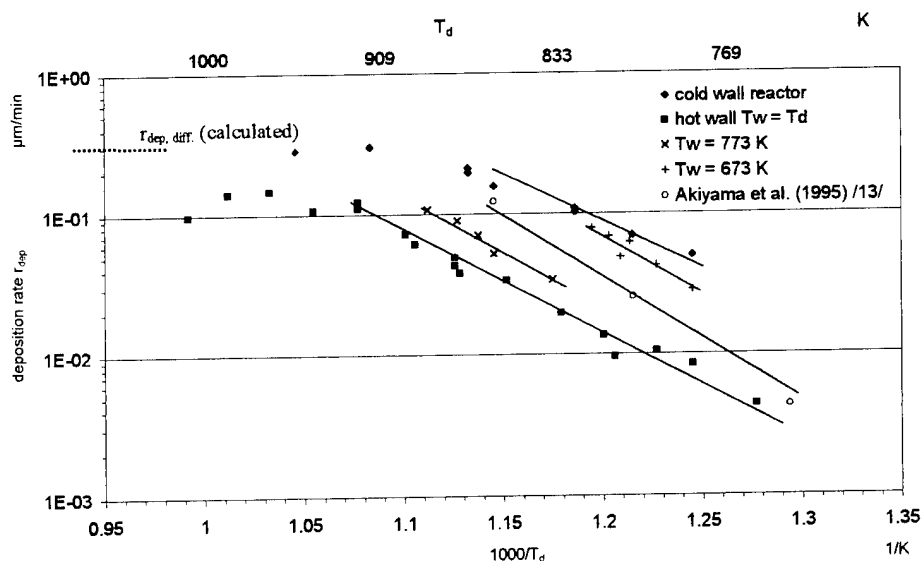


Fig. 2. Deposition rates of ZrO_2 for different reactors ($x_{\text{O}_2} = 0.167$; $x_{\text{Zr(tmhd)}} = 0.001$).

with the gas constant R , the deposition temperature T_d , the activation energy E_d and the pre-exponential factor k_0 . Fig. 3 shows the pre-exponential factors k_0 versus the activation energy E_d which were determined from Fig. 2. Also a literature value [13] which was measured in a hot wall reactor is included. The values of k_0 and E_d in Fig. 3 show that the changing activation energy is partially compensated by changing the pre-exponential factor. This effect is well known in other activated processes: e.g. catalysis [14]; desorption of adsorbed metals [15]; and evaporation of similar metalorganic tmhd compounds [12]. This compensation effect can be artificially produced if the activation energy is changed and the deposition rate is fixed at one temperature. The

scattering in Fig. 3 is, however, very large, therefore a real physical reason is suggested.

At mean temperatures (diffusion controlled part), an almost temperature-independent deposition rate exists. The deposition rate depends on the diffusion constant D of the precursor in the carrier gas. The highest deposition rates were reached in the KW reactor. The maximum value of the deposition rate compared quite well with the deposition rate, calculated by the empirical formula for the molar deposition rate j at the stagnation point, which is indicated in Fig. 2 [16,17]:

$$j = \frac{D}{d} \beta Re^{1/2} Sc^{1/3} c_{pr} \quad \beta \approx 1, \quad (3)$$

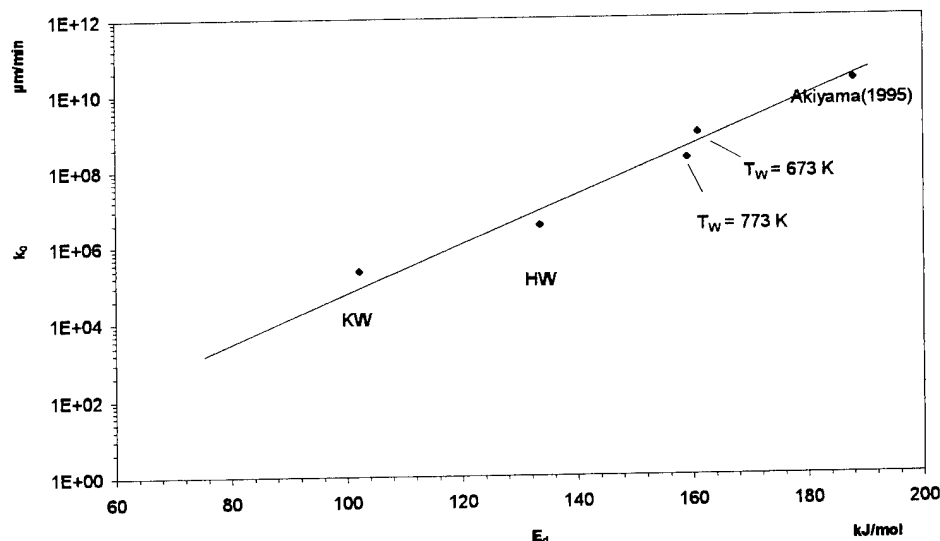


Fig. 3. Pre-exponential factor k_0 vs. activation energy E_d of ZrO_2 (KW: cold wall; HW: hot wall).

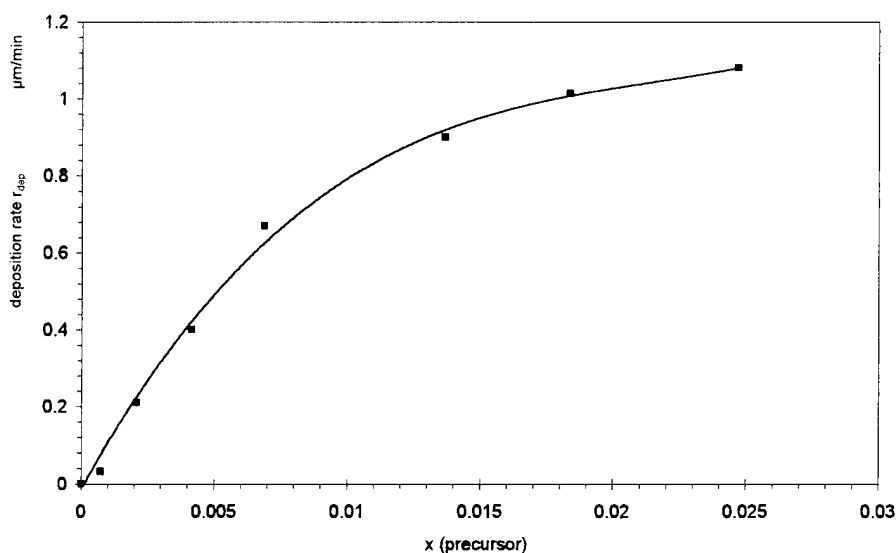


Fig. 4. Deposition rate of ZrO_2 vs. $Zr(tmhd)_4$ concentration in the gas phase (HW reactor; deposition temperature $T_d=973$ K; $x_{O_2}=0.167$).

where d is the diameter of the gas inlet, Re the Reynolds number calculated with the diameter of the gas inlet, Sc the Schmidt number for the diffusion of the precursor monomers in the gas, and c_{pr} the molar concentration of the precursor molecules in the gas phase. It is assumed that the concentration of the precursor was zero at the surface. For the gas properties, the value for Ar were taken. For the calculation of the binary diffusion coefficient D , the kinetic gas theory was used [18]. The data for the Lennard Jones parameters (energy and collision cross-section) were obtained by empirical formula given in Ref. [19]. Fig. 2 shows that, in all other temperature fields, the deposition rates were lower and that the deposition rate decreased with increasing wall temperature. The simplest explanation is the existence of homogeneous reactions in the gas phase which remove active molecules from the gas phase.

In the range of *high temperatures*, the deposition rate decreased with increasing temperature T_d . This is caused by homogeneous side reactions.

All the experiments, including positive temperature gradients, showed no powder formation. The deposition rate depended on the concentration of the precursor in the gas phase, as shown in Fig. 4. The dependence shows a saturation behaviour. Similar effects are known from other CVD systems, e.g. the deposition of BN from BB'B' trichloroborazine [20], or of SiO_2 from triethoxysilane [21]. In these examples this effect was explained by a Langmuir–Hinshelwood deposition mechanism. The saturation behaviour shown in Fig. 4 can possibly be explained by this mechanism. Another possibility, however, is the existence of homogeneous side reactions in the gas phase between the precursor molecules, which then does not take part in the deposition process.

The structure of the ZrO_2 layers were investigated on

fracture surfaces. Columnar structures were always found. Fig. 5 shows one example. The mean diameter d_g of the columns, which are deposited in the HW reactor, are plotted versus T_d in Fig. 6.

The activation energy of the straight line shown in Fig. 6 is $E_a=60$ kJ/mol. If it is assumed that the diameter of the columns is determined by diffusion, then the diameter d_g changes with the temperature according to the law:

$$d_g \approx \sqrt{D_s \tau_g} \text{ with } D_s = D_{so} \exp\left(-\frac{E_s}{RT}\right), \quad (4)$$

where τ_g is a characteristic time for the deposition process [22].

The activation energy for diffusion, $E_s=2E_a=120$ kJ/mol, is in the range of typical surface diffusion

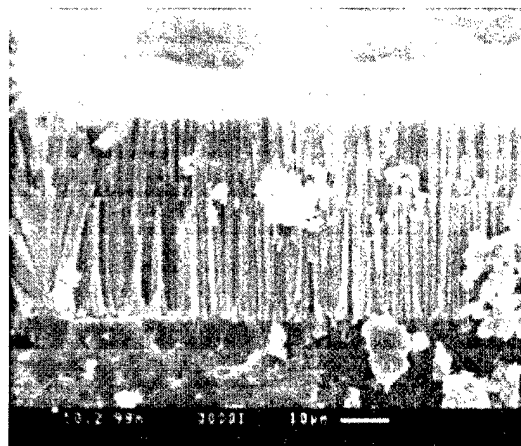


Fig. 5. SEM cross-section of ZrO_2 layer (HW reactor; $T_d=1023$ K; $x_{O_2}=0.167$; $x_{Zr(tmhd)_4}=0.05$; $t=3$ h).

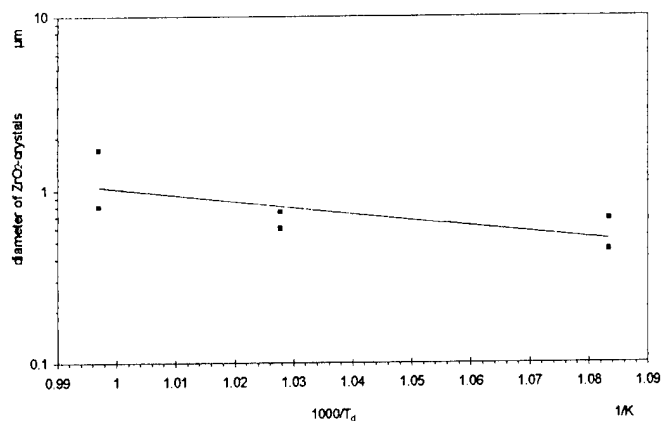


Fig. 6. Column diameter vs. deposition temperature of ZrO₂ (HW reactor; $x_{O_2}=0.167$; $x_{Zr(tmhd)4}=0.05$).

activation energies [23]. These results are in agreement with the work of Movchan and Demchishin [22].

The deposition of Y₂O₃ showed a similar temperature behaviour with an activation energy of $E_d=126$ kJ/mol measured at a wall temperature of $T_w=673$ K. A mixture of Y and Zr precursor gives yttria stabilized zirconia coatings which grows with a similar columnar structure. Deposition rate of 50 μm/h and thicknesses of 100 μm can be reached.

4. Deposition of Al₂O₃

Typical deposition conditions for the Al₂O₃ deposition were (different values are later indicated): total pressure $p_{tot}=4000$ Pa; total gas flow $i=20$ l_n/h; molar fraction of O₂ $x_{O_2}=0.5$; molar fraction of Al(acac)₃ $x_{Al(acac)3}=0.0016$. Experiments were carried out at $p_{tot}=1000$ Pa.

The temperature dependence on the deposition rate was similar to the measurements with ZrO₂ and no powder formation was observed. The dependence of the

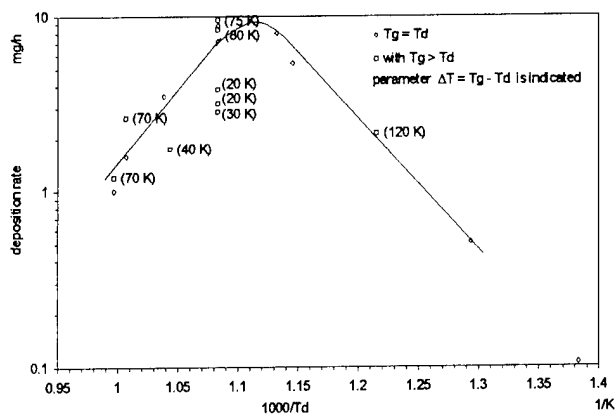


Fig. 7. Deposition rate vs. reciprocal deposition temperature T_d of Al₂O₃.

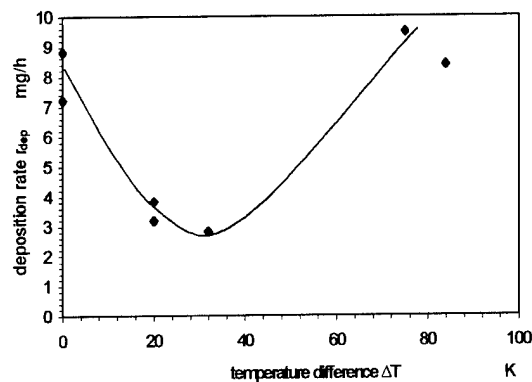


Fig. 8. Deposition rate of Al₂O₃ vs. ΔT with values from Fig. 7 at $T_d=925$ K.

deposition rate of Al₂O₃ deposited in the HW arrangement at 4000 Pa is shown in Fig. 7. This curve is typical for CVD processes with a reaction controlled range at low temperature — a maximum deposition rate at mean temperatures and a decreasing deposition rate at high temperatures, as described in connection with Fig. 2. In addition, deposition experiments at different gas temperatures are indicated. The parameter is always the difference $\Delta T=T_g-T_d$ between the gas temperature T_g and the deposition temperature T_d . It is noticeable that temperature differences only have an effect on high deposition temperature.

The experimental points show that small temperature differences of $\Delta T \approx 20$ –40 K decrease the deposition rate.

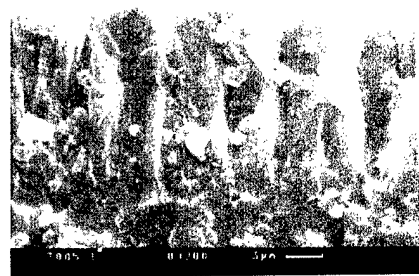


Fig. 9. SEM cross-section of Al₂O₃ with $\Delta T=0$ K.



Fig. 10. SEM cross-section of Al₂O₃ with $\Delta T=30$ K.

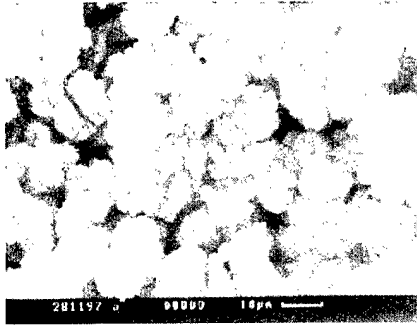


Fig. 11. SEM of the surface of the powder with $\Delta T=80$ K.

At larger temperature differences, $\Delta T=70$ – 80 K, the deposition rate is again increased, mostly to values higher than the deposition rate without gradient (Figs. 7 and 8). In the case of deposition without a temperature gradient, solid layers are always formed. An example is shown in Fig. 9. At small temperature differences, however, a mixture of powder and solid layer is formed as indicated in Fig. 10. Fig. 8 shows that these structures are formed under conditions where the deposition rate is smaller than in the case of deposition at $\Delta T=0$ K. Higher deposition rates are reached at large temperature differences. In this case, powder is deposited which does not adhere to the substrate (Fig. 11).

5. Thermodiffusion effects in the case of Al_2O_3 deposition

In the last section, the effect of positive temperature gradients on deposition was discussed. It was shown that small temperature differences decrease the deposition rate and large temperature differences increase the deposition rate. In the following, we explain this effect by the competition of diffusion effects of the molecules and the thermodiffusion of the particles formed. For the explanation, a simple deposition model is proposed which has the main properties to be discussed: A component (2) might be a carrier gas (1) with molar concentration $n_1 \gg n_2$. In the gas phase, a fraction αn_2 of the precursor is transformed into particles which contain $N \gg 1$ precursor molecules with radius $r = (3Nv_2/4\pi)^{1/3}$ where v_2 is the volume of one precursor molecule. It is assumed that the condition $r \ll \lambda$ is always fulfilled, where λ is the mean free path of the gas. The particle concentration is $n_p = \alpha n_2 / N$. The molecules of component 2 are directly deposited on the surface to form the layer. The molar fraction x_2 at the surface is $x_2(\text{surface})=0$. It is assumed also that the particles which impinge onto the surface adhere, which means that the concentration of particles near the surface is also $n_p(\text{surface})=0$. The transport of molecules and particles is principally possible by concentration diffusion and by thermophoresis through the boundary layer. We assume that all boundary layers (temperature and concentration) have the

same thickness δ . For molecules, the main transport mechanism is the concentration diffusion through the concentration boundary layer with thickness δ , the influence of thermodiffusion is negligible [6]. The molar deposition rate j is then given by:

$$j(\text{mol.diff}) = D \frac{(1-\alpha)n_2}{\delta}. \quad (5)$$

D is the binary diffusion coefficient of the precursor (component 2) in the carrier gas (component 1) [24]:

$$D = \frac{v_{th\mu}}{2\pi n \sigma_{1,2}^2}, \quad (6)$$

with the the molar gas density $n = n_1 + n_2$ and the collision radius $\sigma_{1,2}$. The mean velocity $v_{th\mu}$ of a molecule $v_{th\mu} = (8kT/\pi\mu)^{1/2}$ is described with Boltzmann constant k and the reduced mass $\mu = (m_1 m_2)/(m_1 + m_2)$.

The particle transport is possible by thermophoresis [25]. The precursor transport $j_2(\text{part. therm.})$ by particle thermophoresis is given by:

$$j_2(\text{part.therm}) = \frac{v_{th}\lambda}{8} \alpha n_2 \frac{\ln(T_g/T_s)}{\delta} \approx \frac{v_{th}\lambda}{8} \alpha \frac{n_2}{\delta} \frac{T_g - T_s}{T_s} \quad (7)$$

for $T_g \approx T_s$,

where v_{th} is the mean thermal velocity of the carrier gas molecules.

The total deposition rate j_2 is then the sum of Eqs. 5 and 7 ($T_g = T_s + \Delta T$):

$$j_2 = D_{1,2} \frac{(1-\alpha)n_2}{\delta} + \frac{v_{th}\lambda}{8} \alpha n_2 \frac{\ln[(T_s + \Delta T)/T_s]}{\delta}. \quad (8)$$

In Eq. 8 we have two competing effects. With growing powder formation at increasing T_g , the deposition rate decreases because of the first term in Eq. 8. With increasing ΔT , the powder deposition increases according to the second term. Both competitive effects produce the minimum visible in Fig. 8. In accordance with this, the powder deposition is strongly increased at the growing part of the curve as shown in Fig. 11.

6. Discussion

In the case of the ZrO_2 and Y_2O_3 deposition at $p_{\text{tot}}=1000$ Pa, columnar structures were found and no powder formation could be seen. Probably only homogeneous side reactions influence the deposition. These side reactions decrease the deposition rate of HW reactors and at higher precursor concentrations. In the case of Al_2O_3 at $p_{\text{tot}}=4000$ Pa, powder formation was detected and a large influence of a positive temperature gradient on the structure and the deposition rate was found. The deposition rate could be qualitatively under-

stood by the competition of concentration diffusion and thermophoresis of the dust particles. The structure could be strongly changed by thermophoresis (dense–porous–powder). The powder formation can be reduced by decreasing the total pressure. This result compares very well with the findings of Dekker [9] who investigated the structure of TiN deposited under different temperature fields.

Acknowledgements

This work was supported by the Deutsche Forschungsgemeinschaft and The European Commission of the Brite Euram project PROTECT — we thank them for their support.

References

- [1] H. Wang, Plasma sprayed ceramic coatings, in: J.B. Wachtman, R.A. Haber (Eds.), *Ceramic Films and Coatings*, Noyes, Park Ridge, 1992, p. 131.
- [2] B.C.H. Steele, *Electronic Ceramics*, Elsevier, London, 1991.
- [3] M. Sayer, K. Screenivas, *Science* 7 (1990) 1056.
- [4] R.J.R. Uhlhorn, *Ceramic membranes for gas separation*, PhD Thesis, Enschede, Netherlands, 1990.
- [5] Y.Sh. Lin, *Chemical and electrochemical vapour deposition of zirconia–yttria solid solutions in porous ceramic media*, PhD Thesis, Enschede, Netherlands, 1992.
- [6] L. Klippe, *Chemical vapor deposition of superconductors*, PhD Thesis, Braunschweig, 1999.
- [7] K. Holmberg, A. Matthews, *Coating Tribology*, Elsevier, 1994.
- [8] G. Bonnet, M. Silvia, S. Chevalier, J.P. Larpin, J.C. Carlson, *Surf. Coat. Technol.* 80 (1996) 76.
- [9] J.P. Dekker, *CVD techniques for the synthesis or modification of porous ceramics*, PhD Thesis, Delft, Netherlands, 1994.
- [10] M. Pulver, G. Wahl, *Electrochem. Proc.* 97 (25) (1997) 960.
- [11] M. Pulver, G. Wahl, in: P. Vincenzini (Ed.), *Advances in Inorganic Films and Coatings*, Techna Srl Faenza I, 1995, p. 167.
- [12] M. Pulver, *CVD of ZrO_2 , Y_2O_3 , Al_2O_3* , PhD Thesis, Braunschweig, 1999.
- [13] Y. Akiyama, T. Sato, N. Imaishhi, *J. Cryst. Growth* 147 (1995) 130.
- [14] E. Cremer, *Compensation effect in heterogeneous catalysis*, *Adv. Cat.* 7 (1955) 75.
- [15] G. Wahl, *Chemisorption of metals on polycrystalline tungsten surfaces*, PhD Thesis, Marburg/L., 1969.
- [16] G. Wahl, *Electrochem. Proc.* 87/88 (1987) 42.
- [17] D.T. Chin, C.H. Tsang, *J. Electrochem. Soc.* 125 (1978) 1461.
- [18] J.O. Hirschfelder, Ch. Curtiss, R.B. Bird, *Molecular Theory and Liquids*, Wiley, New York, 1964.
- [19] R.C. Reid, J.M. Prausnitz, B.E. Poling, *The Properties of Gases and Liquids*, McGraw-Hill, New York, 1987.
- [20] R. Stolle, G. Wahl, *Journal de Phys. IV Coll. C5, Suppl. Journ. Phys. II* 5 (1995) 761.
- [21] J. Arndt, G. Wahl, *Electrochem. Soc. Proc.* 97 (25) (1995) 147.
- [22] B.A. Movchan, A.V. Demchishin, *Fiz. Metalloved. translated Phys. Met. Metallogr* 28 (4) (1969) 653 Translated in *Phys. Met. Metallogr.* 28 (1969) 83.
- [23] A. Zangwill, *Physics at Surfaces*, Cambridge University Press, 1992.
- [24] E.A. Moelwyn-Hughes, *Physical Chemistry*, Pergamon Press, 1961.
- [25] N.A. Fuchs, *The Mechanics of Aerosols*, Pergamon Press, 1964.

Deposition of layered bioceramic hydroxyapatite/TiO₂ coatings on titanium alloys using a hybrid technique of micro-arc oxidation and electrophoresis

X. Nie *, A. Leyland, A. Matthews

Research Centre in Surface Engineering, University of Hull, Hull HU6 7RX, UK

Abstract

Titanium alloys have been used with some success in several bioimplant applications. However, they can suffer certain disadvantages, such as poor osteoinductive properties and low corrosive-wear resistance. Attempts to overcome the first of these drawbacks have involved coating the metal with the bioceramic material hydroxyapatite (HA), a primary component of bone and a very good osteoinductor. Since TiO₂ coatings are also known to be effective as chemical barriers against the in-vivo release of metal ions from the implants, a double layer HA–TiO₂ coating on titanium alloys with HA as the top layer and a dense TiO₂ film as the inner layer should possess a very good combination of bioactivity, chemical stability and mechanical integrity.

This paper describes efforts to improve implant biocompatibility and durability by applying a hybrid treatment of micro-arc discharge oxidation (MDO) and electrophoretic deposition. The most common structural titanium alloy (Ti-6Al-4V) was used as the substrate material. A phosphate salt solution and an HA powder aqueous suspension were used as the electrolyte for micro-arc oxidation and the solution for HA electrophoretic deposition, respectively. It is shown that a relatively thick and hard TiO₂ coating can be produced by anodic micro-arc oxidation of titanium, and an HA coating incorporated on top of the TiO₂ layer can simultaneously be formed using a combination of plasma electrolysis and electrophoresis, with the suspension held at high values of pH.

X-ray diffraction (XRD), scanning electron microscopy (SEM) and Fourier transform infrared spectroscopy (FTIR) have been used to investigate the microstructure and morphology of the coatings. The adhesive strength between the coating and substrate has been assessed using scratch adhesion testing. The corrosion resistance of the specimens was examined using potentiodynamic tests in a buffered physiological solution. The results indicate that a hybrid combination of micro-arc oxidation and electrophoretic deposition can provide a phase-pure HA top layer and anticorrosive TiO₂ interlayer, which should show good mechanical and biochemical stability in the corrosive environment of the human body. © 2000 Elsevier Science S.A. All rights reserved.

Keywords: Biomaterials; Biomedical implant; Electrophoretic deposition; Hydroxyapatite; Micro-arc oxidation; Titanium oxide

1. Introduction

Titanium alloys are proven to be potentially very suitable materials for load bearing bioimplant applications. Unfortunately, like most metals, titanium exhibits poor osteoinductive properties. This drawback has recently been addressed by coating the metal with a layer of the bioceramic HA, which is the main component of bone and thus a very good osteoinductor. Titanium oxide (TiO₂) coatings on titanium alloys have

recently demonstrated promising in vivo corrosion behaviour, acting as a chemical barrier against release of metal ions from the implant [1]. However, the chemical bond with the living bone in the body is not very strong [2], therefore a double layer HA–TiO₂ coating on titanium alloy should possess a very good combination of biochemical stability and mechanical properties, particularly if the interfacial adhesion can be enhanced, with HA as the porous, bioactive top layer and a dense TiO₂ film as the corrosion resistant inner layer.

Many techniques have been investigated for deposit-

* Corresponding author.

ing HA onto metallic surfaces, including flame, plasma and HVOF spraying, ion beam sputtering, chemical vapour deposition, dip coating, electrophoresis and electrochemical deposition [1–8]. Among these techniques, plasma spraying is the most popular method for coating implant parts with HA, but it is difficult to apply uniform coatings on implants with complex geometries. Furthermore, thermal decomposition (such as dehydroxylation) and transformation of HA can occur due to poor temperature control during deposition and the adhesion to the metallic substrate may not be sufficiently high. The purity of the HA film can also be a critical aspect with regard to increasing the *in vivo* chemical and mechanical durability of HA coatings over the lifetime of 15 years or more now required of bioimplants [9,10].

Interest in electrophoretic deposition for biomedical applications arises for a variety of reasons, not least of which is the possibility to deposit stoichiometric, high purity materials onto complex shaped components. However, high temperatures during post-treatment (e.g. firing) for increasing adhesion of such coatings may degrade their properties and those of the substrate. In previous research on electrophoretic deposition of HA, various organic liquids (rather than water) were used as the suspension media, since deposition in water is often accompanied by significant gas evolution which interrupts the transfer of suspended particles to the treated components [8,11]. Nevertheless, we have found that an aqueous electrolyte containing a small amount of organic solvent can, if combined with MDO processing, be successfully employed to produce well-adhered electrophoretically deposited coatings; this hybrid technique forms the basis of the present work.

The surface oxide film on titanium and its long term stability in biological environments plays a decisive role in the biocompatibility of titanium implants [12]. A thin (a few tens of nanometers) TiO_2 passive film on Ti alloys can form in many aqueous environments or naturally in air. Relatively thicker (20–200 nm) oxide films can be obtained by thermally enhanced oxidation in air or by anodising in an H_3PO_4 solution [13]. Chemical (sol–gel) and vapour phase techniques can also produce a range of TiO_x compositions (where x can vary through a wide range of sub-oxides up to $x=2$). Generally, corrosion resistance increases with increasing thickness of the oxide coating [13], as would be expected.

MDO represents a relatively new surface modification technique for light metals such as aluminium and titanium alloys [14,15] where thick, hard and anticorrosive oxide coatings can be easily and cost-effectively fabricated. The work reported here utilises the micro-arc discharge on titanium alloys, in simultaneous combination with electrophoretic activity from an HA suspen-

sion, to deposit double layer HA/ TiO_2 coatings for the purpose of increasing Ti-6Al-4V implant biocompatibility and durability.

2. Experimental procedure

A standard structural titanium alloy (Ti-6Al-4V) was used as the substrate material. A phosphate salt solution (8–10 g/l) was used as the electrolyte for MDO. For preparation of the HA suspension solutions for electrophoretic deposition, 3 g/l of HA powder ($\text{Ca}_{10}(\text{PO}_4)_6(\text{OH})_2$, (source: Aldrich Chemical Company, UK) and 3 ml/l ethylenediol were added to distilled water. Ethylenediamine and malonic acid were used to adjust the pH value of the solution in the range 4–11. Prior to deposition, the aqueous suspensions were stirred using an ultrasonic agitator (for 30–60 min at various values of pH) to optimise their dispersion and stability.

For the MDO treatment, the specimens were degreased in acetone and immersed (biased as an anode in the system) in a solution of a phosphate salt. A d.c. or asymmetric a.c. potential (the latter using a capacitor-based a.c. power source) of 400–450 V was applied, giving a current density of 20–40 mA/cm^2 at the work-piece and raising the bath temperature from ambient to around 75°C during treatment. After the initial oxidation treatment, the specimens were cleaned with fresh distilled water. For electrophoretic deposition, the specimens were immersed (again as the anode) in various HA suspensions and again provided with either d.c. or an unbalanced a.c. voltage of around 400 V for 5–10 min.

XRD using a Siemens D5000 with thin film attachment ($\text{CuK}\alpha$, at a glancing angle of 1°), SEM (Cambridge Instruments Stereoscan 200 with EDX attachment) and FTIR spectroscopy (Perkin-Elmer, Paragon 1000) were used to investigate the surface characteristics of the coatings. During XRD and FTIR analyses of the HA powder and as-deposited HA coatings (to check for possible degradation of the HA by the MDO process), the samples for HA powder measurement were prepared by placing pure HA powder on the TiO_2 -coated Ti alloys, by which means TiO_2 -coated Ti alloy could be used as a common background 'substrate' whilst comparing the hybrid HA/ TiO_2 coatings.

The thickness of the coatings was measured using the ball crater test. The adhesive strength between coating and substrate was assessed using a VTT scratch tester using a Rockwell 'C' indenter at 100 N/min loading rate and 10 mm/min table speed. The corrosion resistance of the specimens was investigated using a Solatron 1286 ECI system in a buffered physiological solution [13] with the following composition: NaCl 8.74 g/l; NaHCO_3 0.35 g/l; Na_2HPO_4 0.06 g/l; and $\text{H}_2\text{H}_2\text{PO}_4$

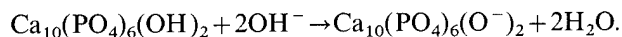
0.06 g/l. During testing Ar gas was passed through the cell to stir the solution.

3. Formation of HA/TiO₂ intermediate composite layers and HA coatings

The mechanisms for creating single-layered oxide coatings using the MDO method are described in Refs. 14–17 and will not be covered in detail here. The following paragraphs describe the formation procedure for HA/TiO₂ intermediate composite layers and HA coatings deposited by the hybrid MDO and electrophoresis treatment.

The fundamental principle of the HA/TiO₂ coating fabrication is that the MDO process is carried out in an anodic configuration (in this case the Ti alloy substrate to be treated forms the anode in the system). Using a predominantly aqueous electrolyte, if HA powder in suspension can be encouraged to develop a negative charge, and thus be attracted to the anode under the applied electrical field of the MDO process (i.e. by electrophoresis), these powders can be fixed and sintered onto the anode surface by the simultaneous (or sequential) use of the micro-arc discharge to rapidly melt and resolidify the near-surface region.

Therefore, the first objective in this work was to prepare a well dispersed HA suspension in an electrolyte also suitable for MDO treatment, and to make the HA powder negatively charged. We found that HA aqueous suspensions using ethylenediol as a dispersant could be made to stabilise for about a day. Adding small amounts of ethylenediamine to the electrolyte could be used to adjust the suspension alkalinity (pH 8–11) to control partial dissolution of the HA powder and support the repassivation mechanisms necessary for continued effective operation of the MDO process. In the alkaline suspension the reaction of the outermost HA molecules in a suspended powder is believed to proceed as follows:



Thus, the HA powder particles become negatively charged, and will be displaced towards the anode (i.e. the treated substrate) under the applied electrical field. On reaching the anode surface, the reverse reaction occurs to form the HA layer.

The hybrid treatment of MDO and electrophoresis could now be performed concurrently. Fig. 1 schematically describes the procedure of HA electrophoretic deposition with combined effects of the micro-arc discharge, which can be observed on the surface of the Ti-alloy (anode) immersed in the suspension, when the high electrode potential is applied. The whole procedure can be divided into four stages. In the first stage, the negatively charged HA powder moves towards and

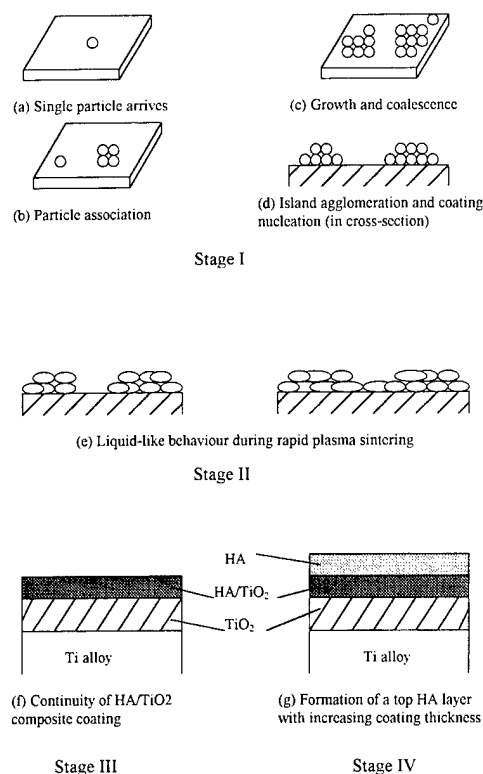


Fig. 1. Schematic diagram of the formation procedure of the HA top layer and HA/TiO₂ composite intermediate layer on a TiO₂-coated Ti alloy.

arrives at the substrate in the form of individual particles (Fig. 1(a)) under the applied electrical field. The particles diffuse around the substrate surface with a motion determined by their binding energy, which is influenced by the physical condition as well as the temperature of the substrate. After a certain time, a particle will either leave the surface or will join with another diffusing particle to form a doublet (Fig. 1(b)). In time, the doublet will be joined by other particles to form agglomerates of increasing size (Fig. 1(c)). This leads to the nucleation stage of thin film growth (Fig. 1(d)) with the formation of quasi-stable islands, each containing several tens of particles (Stage I). During the next stage, these islands grow in both size and number. At the same time, the particles in the island are heated and locally melted and resolidified within a very short period (typically on a scale of microsecond to millisecond duration) due to local micro-arc discharge breakdown of the passivating (dielectric) HA/TiO₂ film. The islands thus display instantaneous semi-molten liquid behaviour (Fig. 1(e)) and are rapidly quenched (and sintered) onto the anode surface (Stage II), an effect which can be confirmed by SEM observation (see the following section). Eventually, the growing islands meet and the film becomes continuous (Fig. 1(f), Stage III). By Stage III, the film is still relatively thin and its microstructure may be an HA/TiO₂ composite due to the combination of

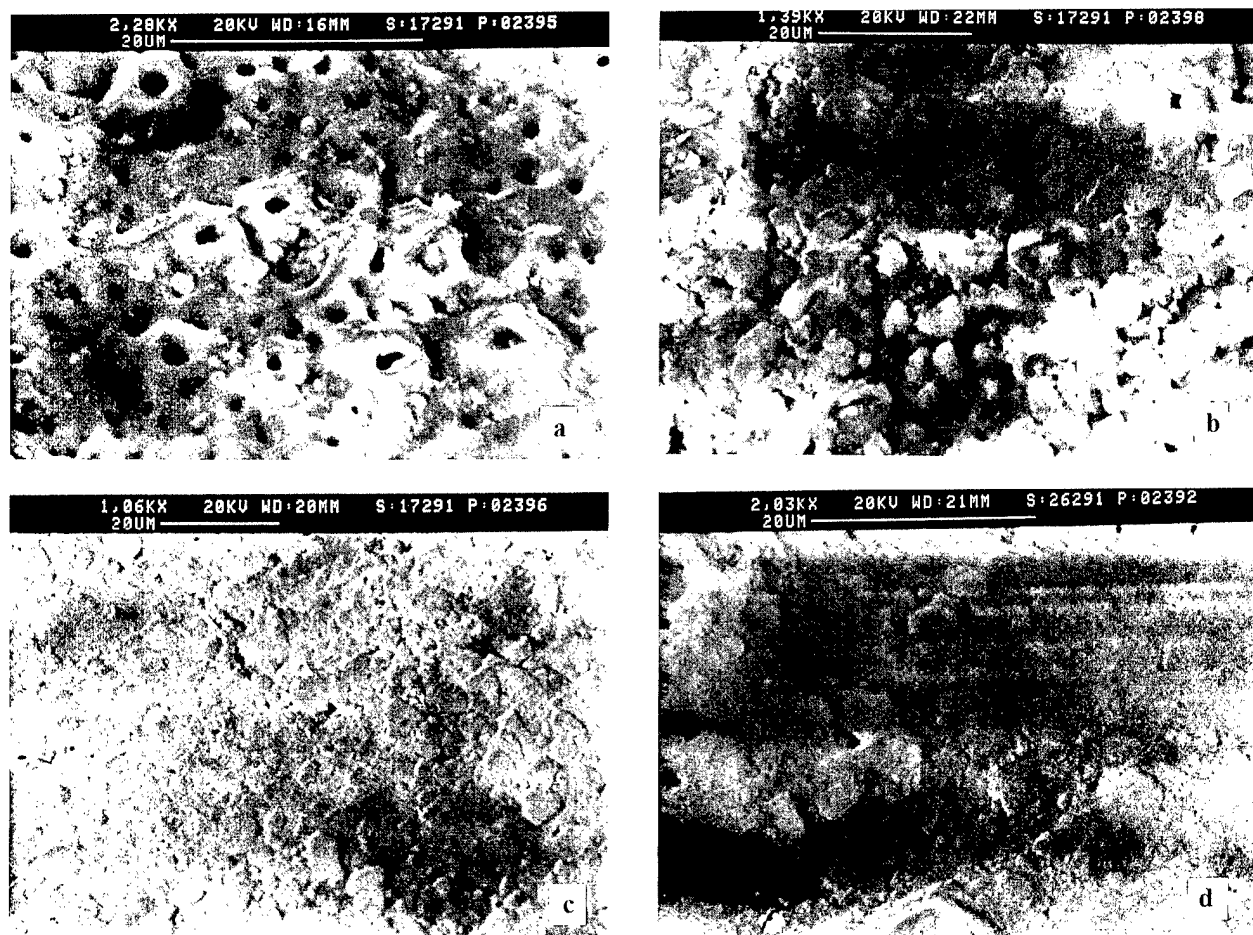


Fig. 2. SEM micrographs of the substrate surface illustrating the formation procedure of the (HA and HA/TiO₂) coatings at various stages: (a) shows the electrophoretic deposition and micro-arc sintering at the initiation stage (Stage I); the coating is HA powder and porous TiO₂ composite; (b) shows the morphology of HA powder coalescence and sintering with an increase in the treatment time (Stage II); (c) shows a continuous HA/TiO₂ composite; and (d) shows the surface of the thick sintered HA top layer of the coating.

local remelting of the TiO₂ layer and/or oxidation of the underlying Ti alloy. With increasing deposition time (and thus thickness of the HA layer), micro-arc discharging occurs increasingly only within the HA layer. As a result, the top layer and intermediate layer in a thick coating should be a single phase HA film supported by a composite of HA/TiO₂ (Stage IV). EDX and XRD analyses were used to confirm these basic assumptions regarding the microstructure of the coating.

4. Results and discussion

4.1. Morphological and microstructural analyses

MDO coatings on the Ti alloy substrate were investigated (prior to HA electrophoretic deposition) using SEM, EDX and XRD. SEM observation showed that the coating consisted of a porous surface layer and a dense inner layer, where the porous surface is probably beneficial in anchoring the suspended HA particles

during the subsequent electrophoretic deposition. EDX data showed that the coatings contained a high proportion of phosphorus, in addition to oxygen and substrate alloy components. XRD spectra indicated that the coating phase was predominantly TiO₂ (anatase). So, the microstructure of the dense oxide interlayer is thus a P-containing TiO₂ (anatase), with a typical thickness of 10–20 μm — as measured by the ball crater test.

To deposit HA onto TiO₂-coated Ti alloys, a high potential of 400 V was applied on the electrode (TiO₂-coated Ti alloy as the anode) in the alkaline suspension. While the negatively charged HA moved toward the anode a micro-arc plasma discharge could also be produced to sinter the HA powder onto the anode surface. Fig. 2 shows SEM observations of the various stages of the deposition procedure, where Fig. 2(a)–(d) correlate closely to the schematic Fig. 1(a)–(d) (Stage I), 1(e) (Stage II), 1(f) (Stage III) and 1(g) (Stage IV) confirming the proposed deposition procedure. Fig. 2(a) indicates that as the HA powder first landed on the anode, it was anchored preferentially

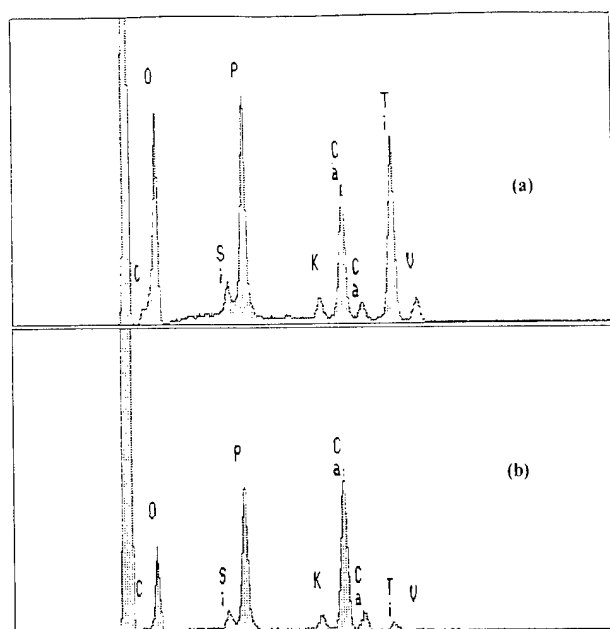


Fig. 3. EDX spectra of (a) the intermediate HA/TiO₂ composite layer, and (b) the HA top layer of the coating.

to holes in the porous oxide surface. The HA powder being redistributed by liquid-like activity during micro-arc discharge melting can be seen in Fig. 2(b) (as described in Fig. 1(e)). Fig. 2(c) demonstrates the uniform HA coating covering the anode surface, where resolidified agglomerate islands can be observed, and also their interconnection resulting from sintering caused by the micro-arc discharge can be seen. A certain degree of porosity can still be seen on the surface of thin HA coatings (Fig. 2(c)), whereas the coatings become increasingly dense with thickness (Fig. 2(d)).

Fig. 3(a) and (b) show EDX spectra of the 'thin' (about 15 μm) and 'thick' (about 30 μm) HA/TiO₂ coatings, respectively. The thin coating possesses a high titanium content (Fig. 2(a)) which may indicate that the coating consists primarily of a composite of HA/TiO₂; however the thick coating gives a very low intensity of titanium. Thus, only calcium phosphate is present in the near-surface of the thick HA coatings.

XRD spectra of the HA powder and the as-prepared HA/TiO₂ coating are shown in Fig. 4(a) and (b), where no significant difference in HA phase composition between the original powder and the coating surface can be seen. Therefore, the XRD investigation indicates that it was possible to retain the calcium phosphate as phase-pure HA in the coating.

4.2. FTIR analysis

The XRD analysis is important for phase investigation; however, the FTIR data should also be reviewed

critically, since they reveal some features which can not be observed by XRD alone [18]. An FTIR spectrum of the as-prepared HA coating on the TiO₂-coated Ti alloy is shown in Fig. 5: plot 1 where the spectrum was influenced by the TiO₂. To obtain a similar FTIR spectrum (Fig. 5: plot 2) for easy comparison to that of the HA coating, HA powder was put on the TiO₂ coated Ti alloy, to use as a common background reference. Though the spectra generated become rather complex due to the influence of the TiO₂ layer, it is not difficult to distinguish the OH⁻ and PO₄³⁻ band peaks of the HA. The OH⁻ bands at 3572 cm⁻¹ and 634 cm⁻¹, characteristic of HA, are fully developed. Also, the characteristic peaks corresponding to PO₄³⁻ in HA (560–600 cm⁻¹, 1030–1090 cm⁻¹) are clearly visible in both spectra. That is, the 1092 cm⁻¹ and 961 cm⁻¹ bands (characteristic of symmetric stretching of the PO₄³⁻ group in HA) and the bands at 598 cm⁻¹ (assigned to the deformation vibration of PO₄³⁻ ions) are still apparent in the HA coating.

The presence of OH⁻ absorption bands in the FTIR spectra of the HA/TiO₂ coatings (which are similar to those of the HA powder) indicates that little or no dehydroxylation has occurred during coating, which is quite difficult to achieve when depositing HA by plasma spraying [18]. The main reason for this benefit may be that the very short micro-arc heating time and the activity of rapid resolidification of molten phases, in conjunction with the aqueous environment (high vapour pressure), avoids the dehydroxylation of HA which would occur at atmospheric or vacuum conditions. On the other hand, it can be observed that the absorption peaks of the OH⁻ and PO₄³⁻ bands of the as-prepared HA composite coating (Fig. 5: plot 1) were weaker than those of the HA powder on TiO₂ (Fig. 5: plot 2). This may indicate some difference in HA coating condition compared to the powder, due to the sintering effects on the TiO₂-coated substrate, or could simply be due to the quantity of HA powder physically put on the TiO₂-coated substrate being higher than that contained in the as-prepared HA coating.

4.3. Hardness and scratch adhesion tests

Fig. 6 shows the surface hardness profiles of samples treated by both MDO alone, and the hybrid MDO/HA-electrophoresis treatment, and under different loadings. TiO₂ coatings possess the highest surface hardness (720 HK_{0.025}) but the hardness decrease with increasing load (and thus penetration depth) is high, due to low load support from the relatively thin coating. Since the typical hardness of HA (3–5 GPa, depending on exact composition [19]) is lower than that of TiO₂, incorporation of HA into the coating surface decreases the maximum coating hardness (570 HK_{0.025}). However,

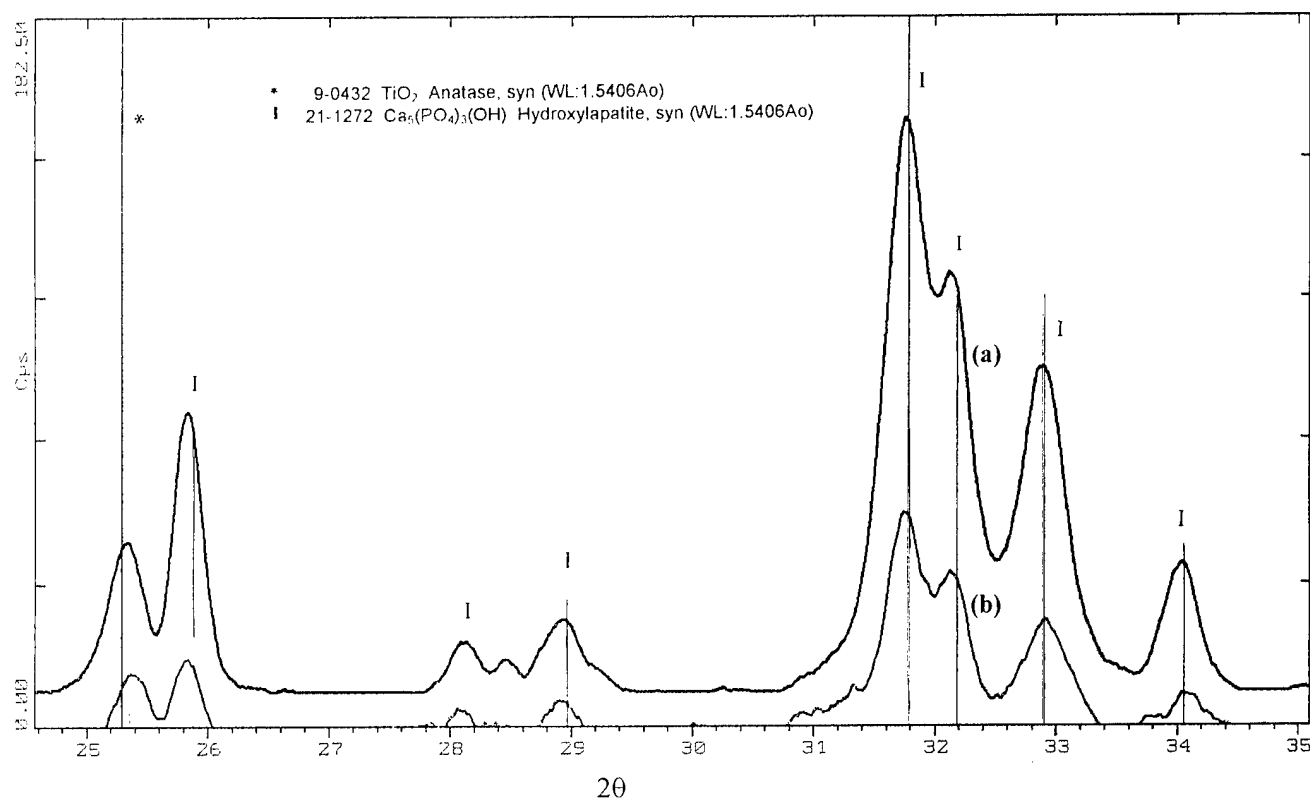


Fig. 4. XRD spectra of (a) the HA powder put on the TiO_2 coating, and (b) an as-prepared HA/ TiO_2 coating, which shows that calcium phosphate exists as a pure HA phase in the coating.

hardness decreases more slowly with increasing indentation load due to improved load support from the underlying oxide layer and the increased total coating thickness. Scratch tests indicated that the adhesion upper critical loads of the TiO_2 coating and HA/ TiO_2 coating were 8 and 10 N respectively. Furthermore, increases in critical load with increasing coating thickness were found, as expected.

4.4. Corrosion tests

The potentiodynamic polarisation curves of the TiO_2 -coated Ti alloy, HA/ TiO_2 coated Ti alloy and uncoated Ti alloy in the buffered physiological solution are plotted in Fig. 7. The TiO_2 -coated Ti alloy shows the highest corrosion potential; the HA/ TiO_2 -coated Ti alloy possesses the lowest corrosion current. However, the uncoated Ti alloy gave the lowest corrosion potential and the highest corrosion current. Therefore, the oxide-coated Ti-alloy does exhibit significantly improved corrosion resistance compared to uncoated Ti-alloys. Previous investigations [14] indicate that an MDO coating consists of three layers (porous outer layer, intermediate dense layer and inner diffusion layer). The inner diffusion layer should act as a barrier to the release of

metal ions to human body and thus avoid deleterious effects.

5. Conclusions

A relatively thick and hard TiO_2 coating can be cost-effectively produced by MDO treatment of titanium, and a pure HA coating with an intermediate HA/ TiO_2 composite layer deposited on top of the TiO_2 layer can easily be formed with excellent adhesion by hybrid MDO treatment and electrophoretic deposition using an HA suspension at high pH values. The porous surface of the TiO_2 MDO coating is helpful in anchoring the HA powder to the surface to allow sintering to occur. The HA-coated surface is also porous, which is a distinct advantage for tissue in-growth and formation of an intimate, durable bond. Dense HA coatings can, however, be formed with increasing treatment time (and thus thickness). Using the scratch test, relatively high adhesive strength compared to other techniques (conventional electrophoresis or thermal spraying, for example) was found between the coating layers and the substrate. Measurement of the corrosion resistance indicated that the duplex treatment of MDO and electrophoretic

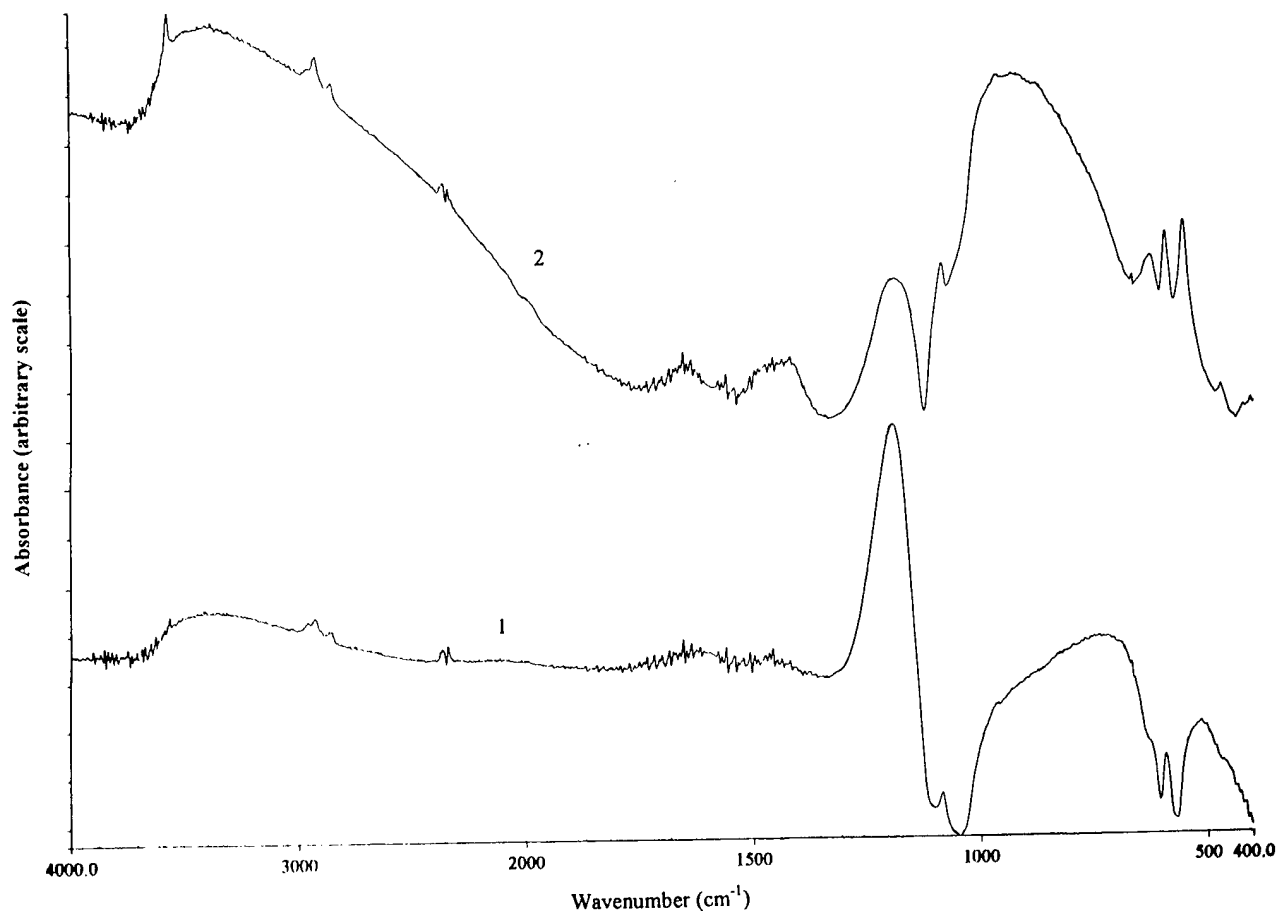


Fig. 5. FTIR spectra of (1) the as-prepared HA or HA/TiO₂ composite coating, and (2) the HA powder control, placed on the TiO₂-coated alloy surface.

Microhardness of coated and uncoated Ti alloys

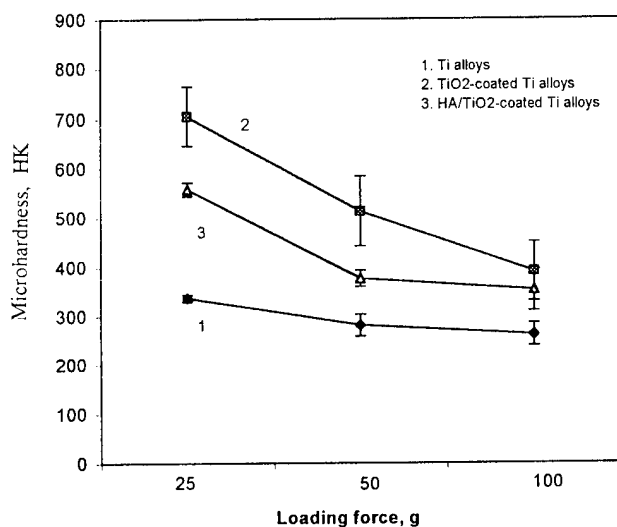


Fig. 6. 'Composite' hardness of the TiO₂-coated, HA/TiO₂-coated and uncoated Ti alloys under different loads.

deposition could provide an anticorrosive HA/TiO₂ duplex coating on Ti alloys. The hard and well-adhered coating so-produced consisted of a pure HA top layer, a composite HA/TiO₂ intermediate layer and an anticorrosive TiO₂ inner layer, which should show good in vivo biomechanical and biochemical stability.

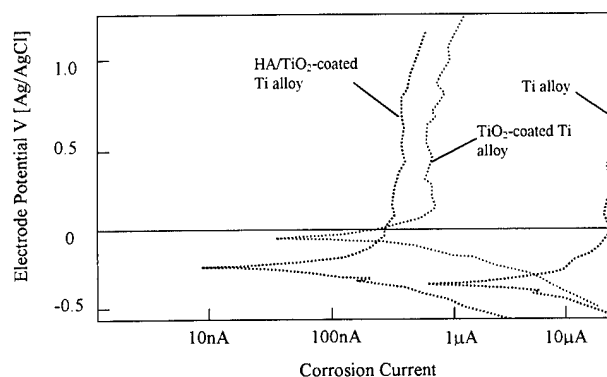


Fig. 7. Potentiodynamic polarisation curves of samples: TiO₂-coated, HA/TiO₂-coated and uncoated Ti alloys.

Acknowledgements

The authors would like to thank Dr A. Yerokhin of Tula State University, Russia for help in construction of the coating equipment. Also, Mr. X. Shen of Loughborough University is acknowledged with thanks, for constructive discussions on electrophoretic deposition. Financial support from Ion Coat Ltd is gratefully acknowledged.

References

- [1] H. Kurzweg, R.B. Heimann et al., *Biomaterials* 19 (16) (1998) 1507–1515.
- [2] P. Li, K. de Groot, T. Kokubo, J. *Sol-Gel Sci. Technol.* 7 (1998) 27–34.
- [3] X.Q. Fu, A.W. Batchelor, N.L. Loh, *Surf. Coat. Technol.* 107 (1998) 133–141.
- [4] C.Y. Yang, B.C. Wang, W.J. Chang, *J. Mater. Sci.: Mat. in Med.* 7 (1997) 167–174.
- [5] F.Z. Cui, Z.S. Luo, Q.L. Feng, *J. Mater. Sci.: Mat. in Med.* 8 (1997) 403.
- [6] J.M. Zhang, C.J. Lin, Z.D. Feng, Z.W. Tian, *Acta Physico-chimica Sinica* 14 (1998) 68–703.
- [7] S.J. Ding, C.P. Ju, J. Lin, *J. Biomed. Mater. Res.* 44 (1999) 266–279.
- [8] I. Zhitomirsky, L. Galor, *J. Mater. Sci.: Mat. in Med.* 8 (1997) 213–219.
- [9] M. Ogiso, *J. Long-term Effects of Medical Implants* 8 (1998) 193–200.
- [10] R.B. Heimann, T.A. Vu, M.L. Wayman, *Eur. J. Mineral.* 9 (1997) 597–615.
- [11] P. Sarkar, P. Nicholson, *J. Am. Ceram. Soc.* 79 (1996) 1987–2002.
- [12] J. Pan, D. Thierry, C. Leygraf, *Electrochim. Acta* 41 (1996) 1143–1153.
- [13] A. Cigada, M. Cabrini, P. Pedferri, *J. Mater. Sci.: Mat. in Med.* 3 (1992) 408–412.
- [14] X. Nie, A. Leyland, H. Song, A. Yerokhin, A. Matthews, Thickness effects on the mechanical properties of micro-arc discharge oxide coatings on aluminium alloys, *Surf. Coat. Technol.* 116–119 (1999) 1061–1064.
- [15] A.A. Vocvodin, A.L. Yerokhin, V.V. Lyubimov, M.S. Donley, J.S. Zabinski, *Surf. Coat. Technol.* 86/87 (1996) 516–521.
- [16] A.L. Yerokhin, X. Nie, A. Leyland, S.J. Dowey, A. Matthews, Review: plasma electrolysis, *Surf. Coat. Technol.* 122 (2–3) (1999) 73–93.
- [17] A.L. Yerokhin, X. Nie, A. Leyland, A. Matthews, Characterisation of oxide films produced by plasma electrolytic oxidation on Ti-6Al-4V alloy, *Surf. Coat. Technol.*, submitted for publication.
- [18] S.R. Radin, P. Ducheyne, *J. Mater. Sci.: Mat. in Med.* 3 (1992) 33–42.
- [19] A. Slosarczyk, J. Bialoskorski, *J. Mater. Sci.: Mat. in Med.* 9 (1998) 103–108.

Microstructure and properties of laser treated arc sprayed and plasma sprayed coatings

A. Pokhmurska ^{a,*}, R. Ciach ^b

^a Institute for Applied Problems of Mechanics and Mathematics, 3b Naukova Str., 290601, Lviv, Ukraine

^b Institute of Metallurgy and Material Science, 25 Reymonta Str., 30-059 Krakow, Poland

Abstract

The effect of laser melting on the microstructure, porosity, chemical homogeneity of nickel based alloy plasma sprayed and (Fe–Cr–B)+Al based electric arc sprayed coatings has been investigated. Laser melting markedly improves coating microstructure and density, and much better chemical homogeneity is obtained. Laser treatment of coatings was carried out with the help of a CW CO₂ laser ($\lambda = 10.6 \mu\text{m}$) using the graphite based antireflection coating. The results demonstrate an improvement of mechanical and corrosion properties of coatings. © 2000 Elsevier Science S.A. All rights reserved.

Keywords: Arc spraying; Electrochemical properties; Laser treatment; Microhardness; Plasma spraying; Protecting coating

1. Introduction

The high flexibility in application and ability to deposit a wide range of coating materials on various substrates have led to techniques such as thermal, electric arc, plasma spraying being widely used for coating deposition [1,2]. Such coatings have high exploitation properties and nowadays are widely used: in geometric size restoration and wear resistance increase of crank shafts in internal combustion engines, compressors, etc. However, the technology and feed materials for these methods still need to be improved. The main problems are the high porosity and poor interparticle, interface bonding and chemical inhomogeneity. Especially, porosity can degrade the corrosion resistance of the coating because it provides channels for aggressive media to penetrate the substance.

Laser treatment is used as an effective means of removing these defects and improving the properties, particularly the corrosion resistance of plasma sprayed coatings, modifying the microstructure and eliminating defects [3,4]. The aim of the present work was to investigate the microstructure and mechanical properties

of laser remelted (Fe–Cr–B)+Al based electric arc sprayed and nickel based alloy plasma sprayed coatings.

2. Materials and methods

Two chemical compositions of the alloy powders have been used for plasma sprayed coatings:

- Deloro 30: Cr 3.0–5.0%; Si 2.8–3.5%; Fe 1.0%; B 1.4–1.8%; Ni bal.
- Deloro 40: Cr 9.0%; Si 3.0%; Fe 3.0%; B 1.8%; Ni bal.

The low carbon non-alloyed steel in the form of specimens $50 \times 40 \times 10$ mm was selected as the substrate material. Coatings were plasma sprayed on the larger side of the specimens using the Jet PMR (SNMI France) equipment. The spraying parameters were: O₂ pressure 0.12 MPa; H₂C₂ pressure 0.08 MPa; air pressure 0.125 MPa; distance of gun from sample surface 200 mm; coating thickness of testing samples was from $h = 0.25$ up to $h = 1.0$ mm.

Powder wires of 1.8 mm diameter in a stainless cover were used for coating formation using the arc spraying method. The selection of small diameter electrode wires was conditioned by the stability of arc burning when using wire of a small diameter. A cover was manufactured from strip steel 0.4 mm thick. A charge was prepared from a powder (Fe–Cr–B) 60% + Al 40%. The

* Corresponding author. Tel.: +380-322-654121;
fax: +380-322-631577.

E-mail address: surface@iapmm.lviv.ua (A. Pokhmurska)

filling coefficient of wires by the charge was 18...20%. Spraying was carried out under a working voltage of 34 V, current 140 A, air pressure 0.5–0.6 MPa. Before spraying, the sample surface was finished by shot blasting.

Deposited coatings were treated under various parameter combinations of laser equipment, the basic data of which is: maximum laser beam performance 2500 W; radiation wavelength 10.6 μm ; radiation mode TEM₁₀; output beam shape ring; radiation regime continuous; working mixture CO₂ + N₂ + He; protecting gas N₂; lens focus 5".

An optical microscope and scanning electron microscope (SEM) were used to examine the surface and cross-sections of both sprayed and laser treated coatings. Rupture strength of sprayed coatings was determined at specific two-half samples.

The evaluation of corrosion resistance of samples with coatings, including those after laser treatment, was carried out on the basis of analysis of polarization curves taken in 3% NaCl solution.

3. Results and discussion

Cross-sections of as-deposited plasma sprayed coatings are shown in Figs. 1–3 for Deloro 30 and Deloro 40 alloy powders respectively. These figures show a pattern of liquid-compacted splats and deformed droplets, which indicate a variation of the temperature of droplets as they were sprayed during the plasma deposition process. Such variation must result in non-uniform cooling rates involved in solidification. Dark areas indicate considerable porosity. This is a structure typical of most plasma sprayed coatings.

In the course of laser remelting, because of laser radiation adsorption, the coating surface melts and consequently hardens due to heat removal in the core (see Figs. 2 and 4 for Deloro 30 and Deloro 40 alloy

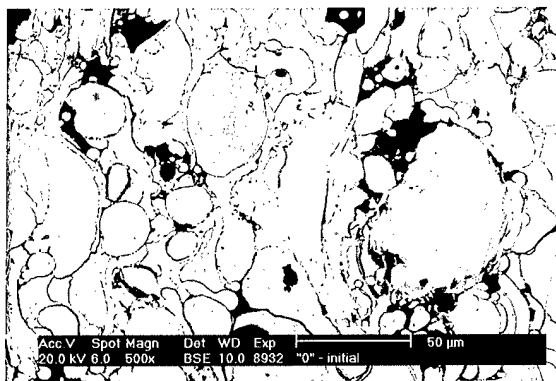


Fig. 1. A microstructure of cross-section of as-sprayed coating obtained from alloy powder Deloro 30 ($\times 500$).

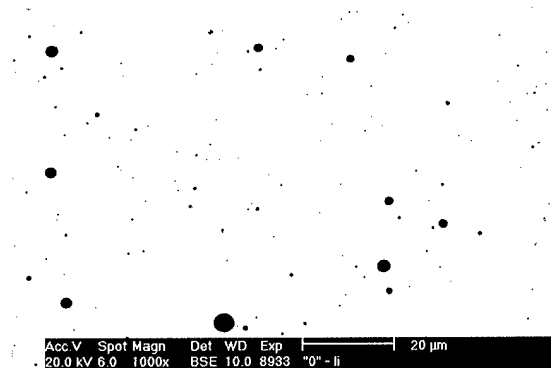


Fig. 2. A microstructure of cross-section of coating obtained from alloy powder Deloro 30 after laser remelting ($\times 1000$).

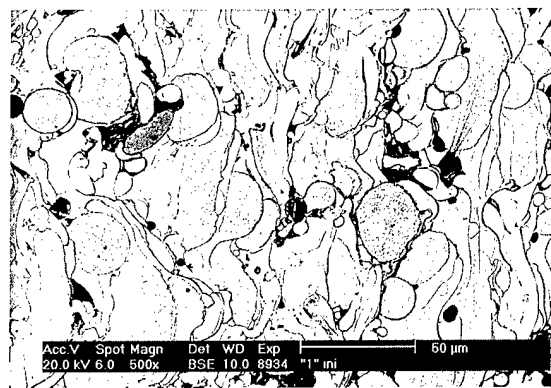


Fig. 3. A microstructure of cross-section of as-sprayed coating obtained from alloy powder Deloro 40 ($\times 500$).

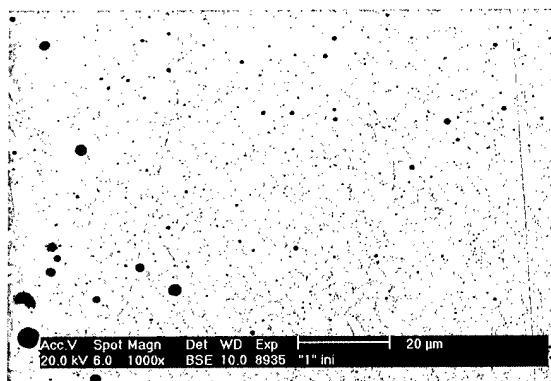


Fig. 4. A microstructure of cross-section of coating obtained from alloy powder Deloro 40 after laser remelting ($\times 1000$).

powders respectively). The aim of the surface remelting is the controlled change of coating structure after melting. Dissolving of all additives in the coating and the consequent formation of hard structure items takes place because of phase transformation in the solid phase of formation of very fine disperse phases.

The process results mainly in an increase of mechanical properties or increase of toughness when surface

hardness increases too. Depth, width and shape of melted area depend mostly on the density of adsorbed energy and interaction time. Since applied coatings have a high reflectance of light radiation, which reduces the adsorbed energy, all samples were covered with a carbon-base antireflection layer before treatment. The change of beam interaction time with layer has been achieved by a change of the sample motion rate.



Fig. 5. Structure of cross-section of as-deposited coating obtained from stainless wire of powder composition: FeCrB 60%; Al 40%, thickness 300 μm ; ($\times 300$).

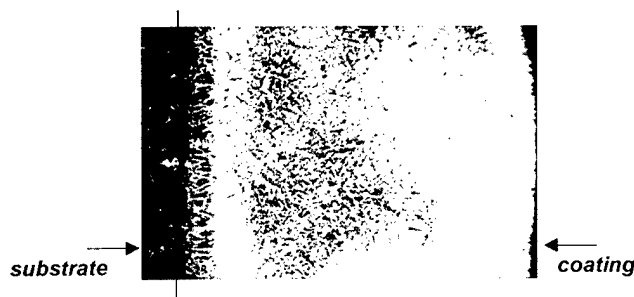


Fig. 6. Structure of cross-section of as-deposited coating obtained from stainless wire of powder composition: FeCrB 60%; Al 40%, thickness 300 μm ; after laser remelting ($\times 300$).

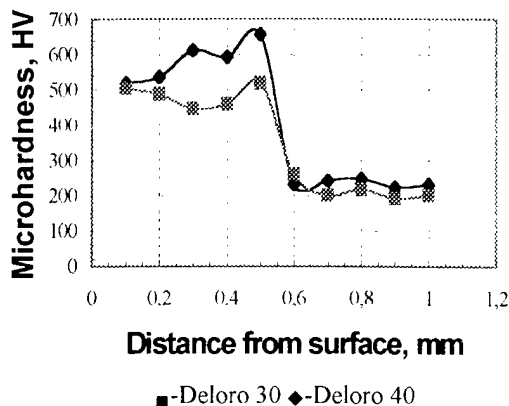


Fig. 7. Microhardness depth profiles for laser remelted plasma sprayed coatings for different chemical composition of nickel based alloy powders.

The structure and properties of arc sprayed coatings also can be changed greatly by laser treatment. Typical initial structure of a coating obtained from stainless wire of powder composition FeCrB 60%; Al 40% is presented in Fig. 5. When irradiation energies were small, structural changes generally were reduced to dispersion without noticeable features of melting. A fine dendritic structure was formed in the case when laser beam energy was increased enough to melt the coating. Its dispersion increases from the coating surface to the coating base due to more intensive heat withdrawal into the basic metal.

The best results were obtained for treatment regimes, for which a coating and a thin layer of a base was alloyed (Fig. 6). If the laser beam energy increases to values high enough not only for a coating but also for a thin layer of a base to be melted, the formation of a transition zone 75–100 μm thick is observed. Element analysis of composition in this case has shown an increase in iron concentration in the coating due to alloying with a base material. The quantity of setting defects and porosity sharply decreases.

Thus, it has been shown that laser treatment makes a better coating structure, makes it homogeneous and decreases porosity. That is why it is expected that laser treatment has positive influences on the mechanical and corrosion properties of coatings. Coating strength increases after laser treatment. For example, for a coating obtained by arc spraying of powder wire (stainless cover, charge composition: Cr 20%; B₄C 30%; SiC 30%; Al 20%) the strength determined at specific two-half samples increased from 90 to 950 MPa. To evaluate corrosion resistance of coatings, polarization curves have been measured. Character of general electrode potential variation in time, measured relative to a saturated AgCl/Ag reference electrode, indicates that laser treatment of a sample surface with coating results in a shift of its value towards positive ones almost by 100 mV. Polarization curves, taken in 3% NaCl solution for electric sprayed coatings (stainless steel cover, charge powder composition: FeCrB 60%; Al 40%) have demonstrated a decrease of corrosion current from 2.4×10^{-2} to 1.3×10^{-3} mA/cm². Determination of corrosion current density was made on the basis of experimental polarization curves by means of linear extrapolation.

Hardness depth profiles for the plasma sprayed nickel-based coatings after laser treatment are shown in Fig. 7. The hardness of the substrate was ~ 200 HV and that of the as-sprayed coating is ~ 400 HV. After laser melting, the hardness increased markedly to ~ 600 and 500 HV for the different powders, Deloro 40 and Deloro 30, respectively. This improvement indicates that laser melting makes sprayed coatings more suitable for wear resistant applications by refining their microstructure.

4. Conclusion

It has been shown that laser surface melting followed by rapid solidification of the molten coating on a non-cooled substrate allowed the achievement of a high degree of microstructure refinement. It has been shown that strength and anticorrosion properties of coatings under study can be greatly improved by laser treatment.

References

- [1] The Principle and Application Technology of Thermal Spray, American Welding Society, Miami, FL, 1985.
- [2] E. Lugscheider, H. Eschnauer, U. Miller, T. Weber, *Power Met. Int.* 23 (3) (1991) 33–39.
- [3] K. Kobylanska-Szkaradec, *Proc. Int. Thermal Spraying Conf., Germany, DVS 152* (1992) 321–324.
- [4] K. Takac, *Proc. Int. Thermal Spraying Conf., Germany, DVS 152* (1992) 231–233.

Al_2O_3 coatings on stainless steel from Al metal-organic chemical vapor deposition and thermal treatments

L. Dumitrescu, F. Maury *

Laboratoire Interfaces et Matériaux, CNRS/INPT, Ecole Nationale Supérieure de Chimie, 118 Route de Narbonne, 31077 Toulouse cedex 4, France

Abstract

Al coatings were deposited by metal organic chemical vapor deposition (MOCVD) at 573 K using tri-isobutyl aluminum (TIBA) as precursor on FeCrNi- and FeCr-type stainless steel substrates. In situ surface treatments of the substrates by TiCl_4 vapor prior to MOCVD of Al has been explored to enhance the nucleation density of the Al films and subsequently to improve their surface morphology and compactness. Further thermal treatment at 923 K of Al-coated samples under inert atmosphere (He) produces the desired $\beta\text{-FeAl}$ compound as a main layer on the substrates whereas, at lower temperature, the intermetallic phase Fe_2Al_5 is essentially formed. Al_2O_3 was grown as an outer layer on the Fe–Al diffusion coatings by annealing in the CVD reactor at 923 K under oxygen atmosphere. In these conditions, Al_2O_3 films are dense, uniform and adherent. They exhibit the cubic structure of the low temperature alumina phases. These protective coatings have been characterized by different techniques and their structure is discussed as a function of the conditions of this combined process. © 2000 Elsevier Science S.A. All rights reserved.

Keywords: Al metal organic chemical vapor deposition; Aluminium oxide coatings; Aluminizing; Fe–Al coatings; Iron aluminides

1. Introduction

Alumina layer is a good candidate for the protection of steel pieces against oxidation and chemical corrosion at high temperatures [1]. The most common reaction for direct deposition of Al_2O_3 by CVD is based on the gas mixture $\text{AlCl}_3/\text{H}_2/\text{CO}_2$ [2]. This high temperature process is applied for the growth of $\alpha\text{-Al}_2\text{O}_3$ which is used, for instance, as a wear resistant coating on cemented carbide tools. Alumina coatings can be also produced directly at lower temperature by pyrolytic decomposition of metalorganic precursors in presence of oxygen sources [3]. In these cases, γ -type or amorphous alumina films, which exhibit a lower density of pores and smaller grain sizes than $\alpha\text{-Al}_2\text{O}_3$, are generally obtained.

To be effective as a barrier layer, the oxide must be dense, strongly adherent to the metal and able to resist fracturing. For these objectives, small grain size leading to smooth surface morphologies are preferred and bond-

coat materials are required, such as iron aluminides. Combined processes, including aluminizing methods and annealing steps under an oxidant atmosphere, are extensively used to prepare such coatings which then constitute an outer layer of alumina with an inner zone of Fe–Al intermetallic phases. Among the aluminizing processes, pack cementation is well known [4] but an initial Al film can also be deposited by other methods prior to diffusion [5].

We have investigated the preparation of protective Al_2O_3 coatings on various stainless steel (SS) substrates by a multifunctional process which includes Al MOCVD, aluminizing and oxidizing treatments at moderate temperature. All the steps were carried out in the same reactor. We particularly emphasize the improvement of the morphology of the Al thin films by pretreatments of the substrate surface on one hand, and on the optimization of the experimental conditions which lead to the predominant formation of $\beta\text{-FeAl}$ as underlayer on the other hand. Indeed the similarity of the thermal expansion coefficient of iron aluminides and SS [6] and the good compatibility with the metal substrate of Fe-rich Fe–Al phases which satisfy the Pilling Bedworth condition [7] suggest that $\beta\text{-FeAl}$ is a desirable bond-coat material for Al_2O_3 .

* Corresponding author. Tel.: +33-562-885600;
fax: +33-562-885669.
E-mail address: fmaury@enset.fr (F. Maury)

2. Experimental

The samples were prepared in a horizontal cold wall MOCVD reactor previously described [8]. The substrates were placed on an SS holder and were heated inductively. The gas streams (He, H₂ and O₂ — all electronic grade) were monitored using mass flow meters. The total pressure was measured independently of the gas flow rates and was controlled automatically.

TIBA was used as the Al source. It was transported in the gas phase from a thermostated bubbler to the reactor using He as carrier gas. Prior to Al deposition, the substrates were exposed in some experiments to a TiCl₄ atmosphere as a surface pretreatment to enhance the Al nucleation density in the early stages of the growth. The mole fraction of both precursors was adjusted from the dependence of their vapor pressure on the temperature: TIBA [9] and TiCl₄ [10].

Two types of SS plates were used as substrates: an FeCrNi-type (18% Cr, 10% Ni) and a FeCr-type alloy (8.3% Cr, 0.12% Ni, 0.10% C, 0.38% Mn, 0.40% Si, 0.97% Mo, 0.08% Cu, 0.02% Al, 0.20% V, 0.07% Nb, 0.06% N, 0.01% As). They were polished down to a final root mean square surface roughness of ~4 nm. They were ultrasonically cleaned in ethanol, degreased in hot acetone, dried under an N₂ stream and rapidly put into the reactor. The MOCVD setup was purged with vacuum–H₂ pressurization cycles, then the reactor was heated at 723 K for ~20 min under an atmospheric pressure of H₂ prior to setting the deposition conditions.

Scanning electron microscopy (SEM) was used to characterize the surface morphology and the phase distribution in the depth of the coatings after staining cross-sections with an HF:HNO₃:H₂O solution (1:5:10 vol). The phases formed were identified by X-ray diffraction, XRD (CuK α), using both θ – θ and grazing incidence geometries. The coating composition was determined by electron probe microanalysis (EPMA), energy dispersive X-ray analysis (EDX) and secondary ion mass spectrometry (SIMS).

3. Results and discussion

3.1. Characterization of Al MOCVD films

Al films were deposited by MOCVD on both SS substrates using the conditions given in Table 1. These operating conditions are in agreement with those of previous works [11,12]. The temperature (573 K) and the reduced pressure (13.3 kPa) were fixed for all runs.

3.1.1. Structural features without nucleation promoter

Al thin films grown without TiCl₄ pretreatment of the steel substrates exhibit a good crystallinity. From the FWHM of XRD peaks, the crystallinity was found

Table 1

Experimental conditions used for the preparation of the Al₂O₃ coatings

<u>Al MOCVD</u>		
Temperature (K)	573	
Total pressure (kPa)	13.3	
TIBA mole fraction	3.1×10^{-3}	
TIBA bubbler temperature (K)	308	
He carrier gas flow rate (sccm)	80	
Flow velocity (cm/s)	0.5	
Stainless steel substrates (25 × 25 × 2 mm ³)	FeCrNi-type	FeCr-type
<u>Surface pretreatment of substrates</u>		
Temperature (K)	533	
Total pressure (kPa)	13.3	
TiCl ₄ mole fraction	4.9×10^{-2}	
TiCl ₄ bubbler temperature (K)	283	
H ₂ carrier gas flow rate (sccm)	50	
Duration (min)	2	
<u>Thermal post-treatments</u>		
Temperature (K)	823–923	923
Total pressure (kPa)	101	101
He flow rate (sccm)/time (min)	80/330	80/60
O ₂ flow rate (sccm)/time (min)	0	80/270
Total duration (min)	330	330

to be slightly better on FeCr- than on FeCrNi-alloy. On both types of steel the films are untextured. Those deposited on FeCrNi are constituted of individual faced grains (mean size 4–5 μ m) with porosities and their surface roughness increases with the film thickness. This undesirable rough morphology is typical of a poor Al nucleation density.

On the other hand, it is worth noting that Al layers deposited on FeCr-type steel exhibit a denser and smoother morphology. A good coalescence of the grains is observed. In addition to Ti compounds, various metal catalysts and seed layers have been used to increase the nucleation rate of Al on the surface of the substrate relative to the rate of Al growth [9]. These are possibly elements in the FeCr-type steel which are beneficial to the nucleation rate. As a consequence, the growth rate of Al films is strongly enhanced on FeCr-alloy compared to FeCrNi steel substrate (Table 2).

3.1.2. Surface pretreatment of the substrates with TiCl₄ vapor

Ti or Ti-containing compounds are known to play an important role in improving the surface morphology of MOCVD Al by increasing the nucleation density on the surface [9]. Thereby, smooth surface morphology was obtained on TiN underlayer or on SiO₂ after dipping the substrate into Ti-containing hydrofluoric acid as surface pretreatment [13]. In situ pretreatment with TiCl₄ vapor was performed on both steel substrates prior to Al deposition under the conditions used for Si wafers (Table 1) [11].

No significant improvement of the morphology of Al

Table 2

Typical features of Al MOCVD thin films deposited on the two types of steel substrates showing the influence of a surface pretreatment by TiCl_4 vapor

Substrate (pretreatment)	Growth rate ($\mu\text{m}/\text{h}$)	Thickness (μm)	Roughness (R_q , nm)	[200] texture coefficient
FeCrNi	0.5	1.5	107	1.18
FeCrNi (TiCl_4)	1.3	4.0	308	1.29
FeCr	3.1	9.5	611	1.15
FeCr (TiCl_4)	3.2	9.8	291	1.48

films grown on the both types of steel substrates was found. This pretreatment slightly favors a [200] preferential orientation. The deposition rate of Al films on TiCl_4 -pretreated FeCrNi substrates is strongly increased but such an effect was not observed for the films grown on the FeCr-type steel. In addition, EDX and XPS analyses of the substrate surface after TiCl_4 pretreatment revealed the presence of residual Ti, and especially Cl which may cause pitting corrosion, as observed by SEM. Consequently this pretreatment is unsatisfactory. It has not been applied systematically for Al films grown on FeCr-type steel since they are sufficiently uniform with a relatively smooth and compact morphology.

3.2. Annealing under inert atmosphere

Al-coated FeCrNi- and FeCr-type substrates were annealed under He atmosphere (Table 1). In the conditions explored, total diffusion was not achieved for all the samples. Since it is a diffusion process, the composition of the coatings depends on the temperature and the time of annealing, as well as on the thickness of the initial Al film.

3.2.1. Aluminizing of Al-coated FeCrNi-type stainless steel

The desired FeAl (bcc) phase is predominantly present in the coating after annealing at 923 K for 5.5 h (Fig. 1). Typically, the structure of the aluminide coatings grown on FeCrNi is SS/FeAl/ Fe_2Al_5 /Al with, in addition, significant diffusion of Cr and Ni from the substrate (Fig. 2). Such an interdiffusion was confirmed by SIMS depth profiles and was also observed on 310S type SS [5]. Traces of Fe_3Al were found by XRD at the interface with the substrate when the surface was pretreated with TiCl_4 . We believe that the stabilization of Fe_3Al is due to the presence of Ti at the interface since it is one of the elements which may increase the Fe_3Al –FeAl transition temperature above 823 K [6]. On the other hand, the roughness of Fe–Al coatings is relatively high and, as expected, related to that of the initial Al MOCVD films.

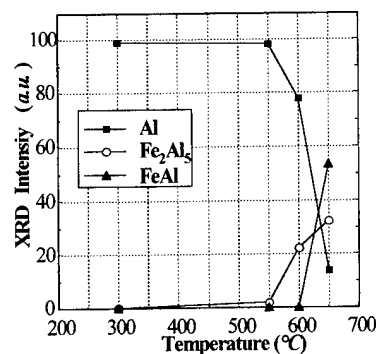


Fig. 1. Variation of the XRD intensity as a function of the annealing temperature under inert atmosphere showing the relative abundance of the phases formed from Al-coated FeCrNi steel. The XRD peaks at $\theta = 19.24$, 13.93 and 40.67° were selected for Al, Fe_2Al_5 and FeAl respectively.

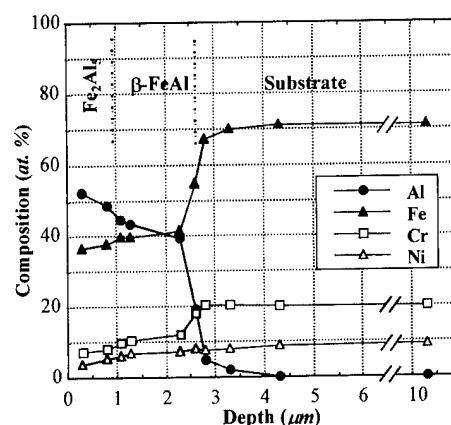


Fig. 2. EPMA analysis of a cross-section of a diffusion coating prepared by annealing under inert atmosphere (923 K; 5.5 h) of an Al-coated FeCrNi-type steel substrate.

3.2.2. Aluminizing of Al-coated FeCr-type stainless steel

The morphology of the aluminide coatings prepared on FeCr-type SS substrate is uniform and as dense as that of the initial Al film. The phase distribution in these diffusion coatings is not very different from that of the coatings prepared on FeCrNi alloy. Grazing XRD analysis has shown that Cr diffuses readily into the Al layer to form mainly Cr_5Al_8 (and/or Cr_4Al_9) at the outer surface. Next, Al-rich Fe–Al compounds are formed

below the surface (Fe_2Al_5), and phases progressively richer in Fe are formed in the inner zone, FeAl being the closest to the interface with the substrate. Typically the duplex structure is SS/FeAl/FeAl₂/Fe₂Al₅/Cr₅Al₈ as shown on Fig. 3. This structure is relatively stable since an increase of the annealing time to 15 h only slightly increases the proportion of Cr₅Al₈ to the detriment of Fe₂Al₅.

3.3. Thermal treatment under ambient O₂

Al-coated FeCr-type steel substrates were heated at 923 K under He for 1 h then under dry O₂ for 4.5 h in the CVD reactor. This oxidizing treatment was not applied to samples made with the FeCrNi steel because of the unsatisfactory morphology of the MOCVD Al film (roughness and porosity are too important).

Under these oxidizing conditions, the coatings are constituted of a thin, uniform and relatively compact Al₂O₃ outer layer and different aluminides as inner layers. As for annealing under inert atmosphere, a significant diffusion of Cr into the Al film was observed, as well as that of Fe which forms the desired β -FeAl intermetallic compound as the predominant phase (Fig. 4). The typical phase distribution in relatively thin coatings (15–20 μm) as determined by XRD is shown in Fig. 5.

Crystal morphologies of Al₂O₃ are known to be strongly dependent on the growth conditions [2,14]. All Al₂O₃ coatings prepared by this process show a very similar surface morphology constituted of small elongated grains ($\sim 1 \mu\text{m}$ long) which tend to form needles. The morphology was found to be independent of the time and thickness of the initial Al films. Al₂O₃ layers exhibit the cubic structure (η - or χ -) of the transition aluminas with a poor crystallinity (Fig. 4). From XRD

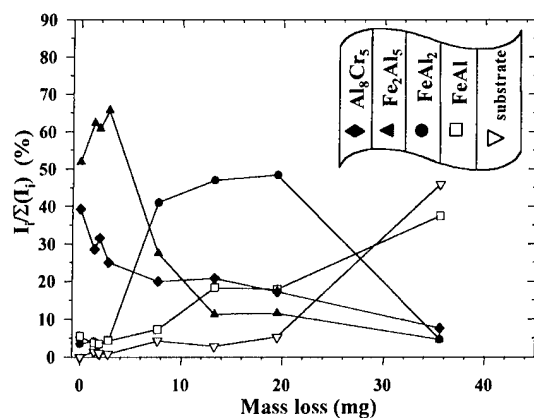


Fig. 3. Phase distribution in an aluminide coating prepared by annealing under inert atmosphere (650°C, 5.5 h) of an Al-coated FeCr-steel substrate. The ratio of the phases was determined using the relative XRD peak intensity at different levels of depth after removal the outer layers by mechanical polishing.

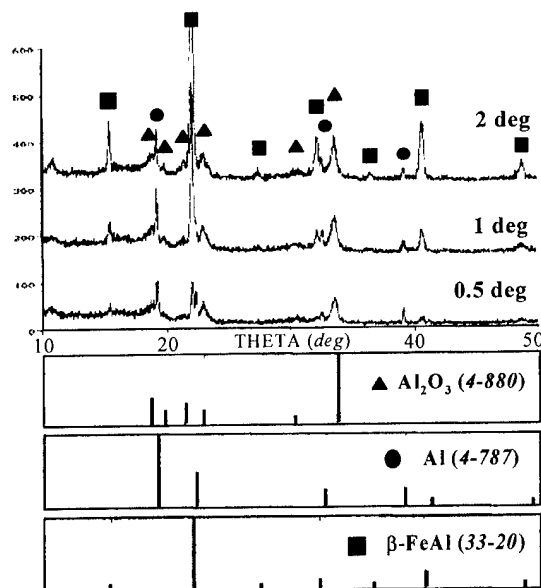


Fig. 4. XRD patterns recorded with various grazing angles of a sample prepared by thermal treatment under an O₂ atmosphere of an Al-coated FeCr steel substrate.

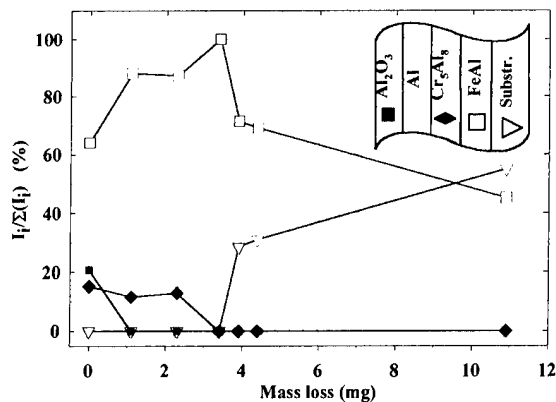


Fig. 5. Phase distribution of a diffusion coating prepared by thermal treatment (923 K) under O₂ of an Al-coated FeCr-type steel substrate. The ratio of the phases was determined using the relative intensity of representative XRD peaks at different levels of depth after a succession of polishings to remove the outer layers.

patterns, a mean crystallite size of 11–15 nm was determined and no preferential orientation was observed.

Typically, the total thickness of the diffusion coatings prepared in the conditions given in Table 1 is 35–40 μm , including 8–10 μm of α -Fe(Al) and $\sim 10 \mu\text{m}$ of β -FeAl which is still the predominant phase. Taking into account the composition of the borders between the various phases of the binary Fe–Al system, a rough scale giving the Al content in an Fe–Al matrix has been reported on the line-scan EDX analysis (Fig. 6). The structure of such coatings is mainly SS/FeAl/FeAl₂/Fe₂Al₅/Cr₅Al₈/Al₂O₃ (Fig. 6: left). Except for the presence of a white outer layer of Al₂O₃, this phase distribution is

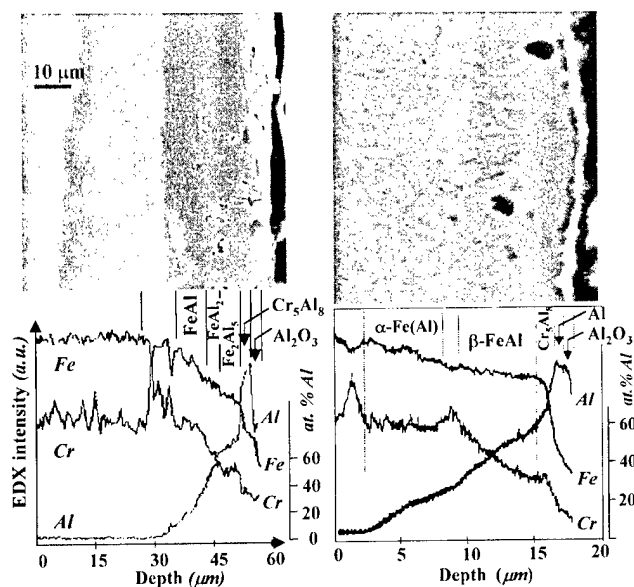


Fig. 6. SEM cross-sections and corresponding EDX line-scan analysis of coatings constituted of Al_2O_3 and diffusion layers as bond-coat materials. The samples were prepared from MOCVD Al-coated FeCr-steel treated at 923 K under O_2 atmosphere. Left: relatively thick coating ($\sim 30 \mu\text{m}$); right: thinner coating ($\sim 15 \mu\text{m}$).

very similar to that obtained by annealing under inert atmosphere (Fig. 3).

A total thickness of the diffusion coatings of only 15–20 μm can be obtained with the same post-treatment, either from thinner Al films or when the deposited Al is not totally consumed during the aluminizing process. Indeed, it was observed that surface pretreatments of the steel substrates (e.g., heating at 723 K under H_2 or in situ treatment to TiCl_4 vapor) may subsequently decrease the diffusion rate. In that way, the coatings exhibit the simpler structure SS/FeAl/ Cr_5Al_8 /Al/ Al_2O_3 where $\beta\text{-FeAl}$ ($\sim 7 \mu\text{m}$) is the major phase (Fig. 6: right). One of the differences with thicker diffusion coatings is that when Al is still present the phases FeAl_2 and Fe_2Al_5 are not detected.

For both types of coatings, Cr is mainly analyzed at the interfaces. Furthermore, we show in Fig. 6 evidence for the diffusion of Al in the SS substrate to form $\alpha\text{-Fe(Al)}$, whereas this phase has not been identified in Al-coated 310S-type SS after annealing at the same temperature [5]. In spite of the low amount of Ni (0.12%) and Mo (0.97%) in the FeCr-type SS substrate, SIMS depth profiles analysis revealed a diffusion of these metals immediately below the Al_2O_3 layer.

4. Conclusions

Dense and adherent Al_2O_3 coatings have been deposited on two types of SS substrates by a multifunctional

process which includes Al MOCVD, aluminizing and oxidizing treatments in the same reactor. In situ surface pretreatment of the substrates by TiCl_4 vapor has been investigated to enhance the nucleation density of the Al MOCVD films. However, this pretreatment was not retained because of the corrosion of the steel substrate. Moreover, satisfactory morphology of Al films was obtained on the FeCr-type alloy by optimizing the growth conditions. Then the predominant formation of $\beta\text{-FeAl}$ as a desirable bond-coat material for Al_2O_3 was successfully achieved.

Further works on these metallurgical coatings are currently in progress, in particular to control the thickness of the initial Al film, which plays an important role in the thickness and the phase distribution of the diffusion coating.

Acknowledgements

The authors gratefully acknowledge Dr. F. Schuster and Dr. C. Chabrol for fruitful discussions, and Dr. F. Senocq for his assistance in XRD analyses. This work was partially supported by CEA-CEREM, Grenoble.

References

- [1] J.-E. Sundgren, H.T.G. Hentzell, J. Vac. Sci. Technol. A 4 (1986) 2259.
- [2] B. Lux, C. Colombier, H. Altena, K. Stjernberg, Thin Solid Films 138 (1986) 49.
- [3] A.R. Barron, in: S. Rees Jr. (Ed.), CVD of Non-metals, VCH, Weinheim, 1996, pp. 282–288.
- [4] B. Nciri, L. Vandenbulcke, Thin Solid Films 139 (1986) 311.
- [5] J.E. Indacochea, I. Bloom, M. Krumpelt, T.G. Benjamin, J. Mater. Res. 13 (1998) 1834.
- [6] S.C. Deevi, V.K. Sikka, Intermetallics 4 (1996) 357.
- [7] A. Bahadur, O.N. Mohanty, Material Transaction, JIM 31 (1990) 948.
- [8] F. Maury, A. Mestari, R. Morancho, Mater. Sci. Eng. A. 109 (1989) 69.
- [9] T. Kodas, M. Hampden-Smith (Eds.), The Chemistry of Metal CVD, VCH, Weinheim, 1994, pp. 45–103.
- [10] R.C. Weast (Ed.), Handbook of Chemistry and Physics, 54th Edition, CRC Press, Cleveland, 1973, p. D187.
- [11] R.A. Levy, M.L. Green, P.K. Gallagher, J. Electrochem. Soc. 131 (1984) 2175.
- [12] T. Suzuki, J. Mater. Res. 12 (1997) 1866.
- [13] K. Sugai, H. Okabayashi, S. Kishida, T. Shinzawa, Thin Solid Films 280 (1996) 142.
- [14] T. Schmitt, H. Altena, B. Lux, in: J. Bloem, G. Verspui, L.R. Wolff (Eds.), Proc. 4th European Conf. Chemical Vapor Deposition, Philips Centre for Manufacturing Technol., Eindhoven, The Netherlands (1983) 421–427.

Titanium dioxide films prepared by photo-induced sol–gel processing using 172 nm excimer lamps

Never Kaliwoh *, Jun-Ying Zhang, Ian W. Boyd

Electronic and Electrical Engineering, University College London, Torrington Place, London WC1E 7JE, UK

Abstract

We report the growth of single- and multilayer films of titanium dioxide (TiO_2) on Si(100) substrates at low temperature by a new photo-induced sol–gel process. Polymeric TiO_2 sols prepared by the hydrolysis and condensation of titanium isopropoxide were spin-coated on the silicon substrate and then irradiated by an Xe_2^* excimer vacuum ultraviolet (VUV) lamp operating at a wavelength of 172 nm. Films with thicknesses between 10 and 200 nm were achieved readily by this technique. The effects of spin speed, irradiation time and substrate temperature on the films formed have been studied. The chemical bonding changes in the thin films were analysed by Fourier transform infrared spectroscopy (FTIR), while thickness and refractive indices were determined by ellipsometry. FTIR confirmed the removal of H_2O and OH groups after VUV irradiation for 10 min at 300°C. The refractive index reached a value of 2.4, which compares favourably with the value of 2.58 recorded for the bulk material, while optical transmittance values in the visible region of the spectrum between 85 and 95% were obtained on quartz substrates. © 2000 Elsevier Science S.A. All rights reserved.

Keywords: Ellipsometry; Excimer lamp; FTIR; Photo-induced processing; Sol–gel; Titanium dioxide thin films

1. Introduction

TiO_2 is currently attracting much interest as a nanocrystalline material for a range of potential applications, such as in dye-sensitised solar cells [1,2], as an anti-reflective coating for solar cells [3,4], as an insulator for memory devices [5], as a catalyst [6], and as a humidity and fibre-optic chemical sensor [7].

TiO_2 has been deposited by many techniques including pyrolysis [8], electron-beam evaporation of TiO_2 [9], pulsed laser deposition [10], metal–organic chemical vapour deposition (MOCVD) [11,12], molecular-beam epitaxy [13], atomic-layer deposition (ALD) [14,15], hydrothermal techniques [16,17], plasma-enhanced chemical vapour deposition (PECVD) [18], reactive sputtering [19,20] and sol–gel processes [21–23].

Sol–gel processing via the polymerisation of metal–organic compounds involves ceramic synthesis by the hydrolysis of metal alkoxides, resulting in metal oxides or hydrated oxides [21]. A gel with a continuous network is thus formed. Thin, transparent, multi-component oxide layers can be readily deposited on various sub-

strates by this process. A firing step is required to displace organic (in this case propyl) compounds and the hydroxyl groups. The method has been widely used to fabricate high-quality ceramics and glasses [24]. Advantages of this technique as compared with other processes include low cost, relative simplicity, and easier control of the composition of the deposited films [7,24].

In this work, TiO_2 produced from titanium isopropoxide [$\text{Ti}(\text{OC}_3\text{H}_7)_4$] by an excimer-lamp based photo-induced sol–gel process has been studied. The interest in ultraviolet (UV) processing and studies of the dynamics of photochemical reactions have burgeoned in recent years [25]. Photochemical processing by excimer lamps has an added advantage of a low thermal budget due to the ability of processing at low temperatures.

2. Experimental details

The excimer lamp system used comprises four lamps, employs the dielectric barrier discharge principle and is described more completely elsewhere in the literature [26]. Polymeric sols were prepared by the hydrolysis

* Corresponding author.

E-mail address: nkaliwoh@ee.ucl.ac.uk (N. Kaliwoh)

and condensation of $\text{Ti}(\text{OC}_3\text{H}_7)_4$ in $\text{C}_2\text{H}_5\text{OH}$ in the presence of HCl as shown in Fig. 1. The resulting transparent mixture was sealed in a container and stirred continuously at room temperature. The solution was spin-coated on to silicon wafers at various speeds, first after 2 h, then at 24 h intervals, and was analysed with an ultraviolet–visible (UV–VIS) spectrophotometer (Lambda 14), where the polymerisation process was monitored by observing changes in the absorbance spectra. Thickness and refractive index were measured by ellipsometry (Rudolph Auto El II) and Fourier transform infrared spectroscopy (FTIR) was used to monitor the absorption of OH and CH_3 groups to provide information on the presence and removal of H_2O and propyl radicals. Initially, substrates were irradiated with 172 nm radiation from an Xe_2^* excimer lamp for different times and at temperatures of 80, 120 and

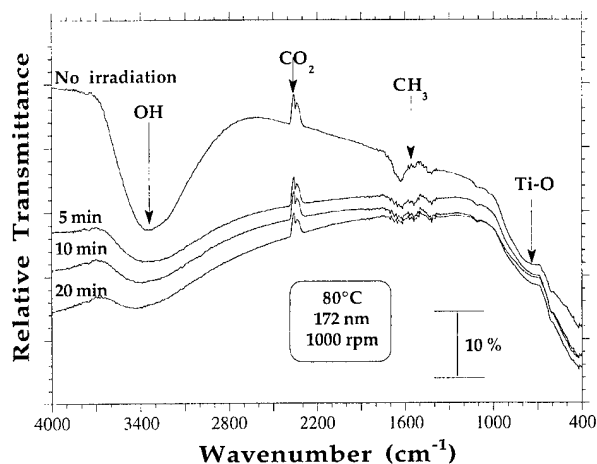


Fig. 2. FTIR spectra of films irradiated at a temperature of 80°C for exposure times of 0, 5, 10 and 20 min using 172 nm excimer lamp radiation.

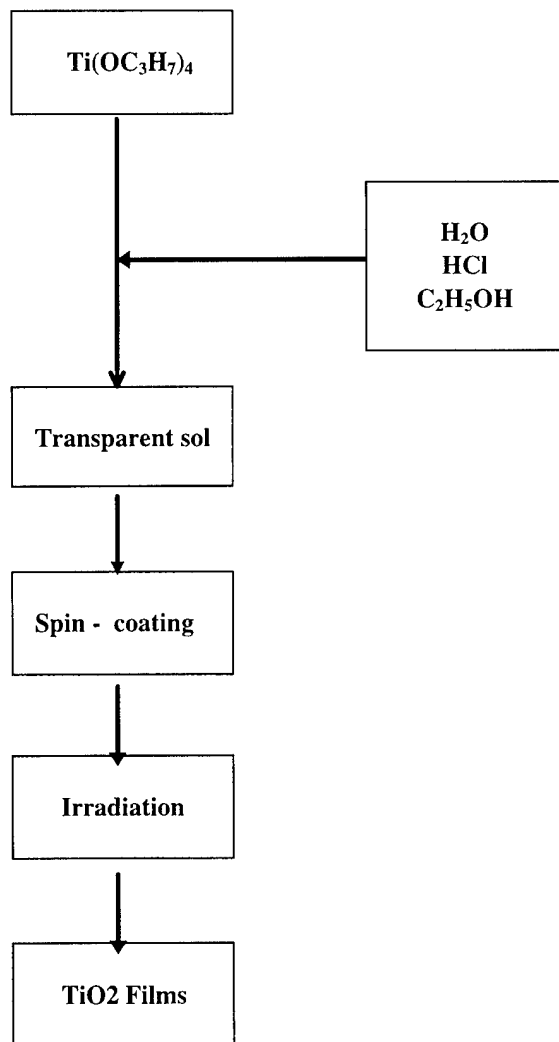


Fig. 1. Flow chart for the preparation of TiO_2 films by photo-induced sol-gel processing.

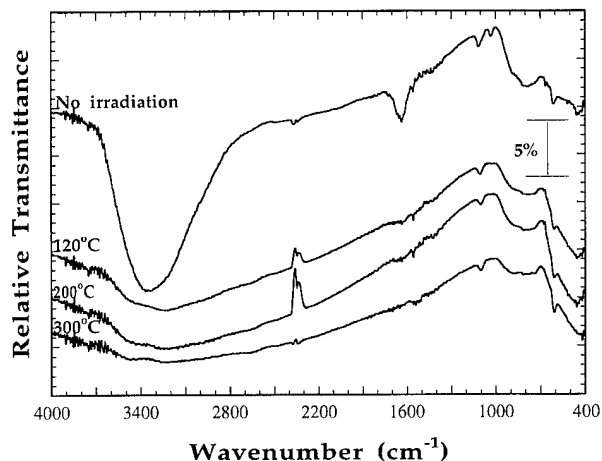


Fig. 3. FTIR spectra of films irradiated at different temperatures for a fixed exposure time of 10 min, using the 172 nm VUV irradiation.

200 and 300°C. Subsequent irradiation was carried out at 300°C for 10 min. The optical properties of the films prepared on quartz and irradiated by the 172 nm radiation were investigated using a UV–VIS spectrophotometer. TiO_2 multilayers were subsequently prepared on Si(100) in a step-wise process, with thickness and refractive index determined for every step.

3. Results and discussion

The synthesis of titanate polymers by the sol-gel process involves the hydrolysis and condensation of the starting alkoxide, in this case titanium isopropoxide, in

the following reactions:

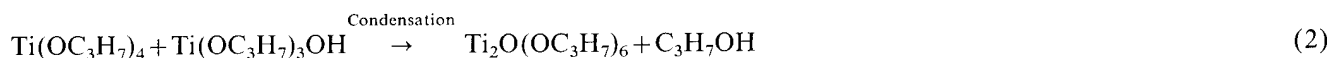


Fig. 2 shows the FTIR spectra of films irradiated at a temperature of 80°C. Changes taking place within the gel under the influence of irradiation can be observed by considering the spectral range 3100–3400 cm⁻¹ where the OH stretching vibrations of water and OH groups appear, at 550 cm⁻¹ where Ti–O vibrations occur and 1300–1500 cm⁻¹ (due to CH₃). As the irradiation time is increased from 0 to 20 min, the intensity of these bands decreases. The spectra in the 3100–3400 cm⁻¹ range show the dehydration and dehydroxylation of the polymer. The increase in temperature between 0 and 80°C results in loss of weight through the evaporation of adsorbed water and the loss of hydroxyl groups. The appearance and growth of new absorption features below 730 cm⁻¹ indicate the presence of Ti–O bonds [27]. No significant changes were observed upon raising the temperature to 200°C. At 300°C, the OH peak

disappeared, and the Ti–O peak shifted to shorter wavenumbers due to densification of the films. Fig. 3 shows the FTIR spectra of these films irradiated at different temperatures for a fixed exposure time of 10 min. The spectra show that conversion of the gel into a complex TiO₂ film takes place after irradiation for 10 min at 300°C, with the removal of OH and CH₃ groups being achieved.

TiO₂ multilayers were deposited at 2000 and 3000 rev min⁻¹ from the same solution with a 24 h time difference. These coating speeds were chosen as homogeneous films are formed at these spin-on speeds. Refractive index values ranging from 2 to 2.4 were measured for multilayers coated at 2000 and 3000 rev min⁻¹, after each irradiation step, as seen in Fig. 4. These values compare well with those for bulk material in rutile single crystals, which is reported to be 2.58 at 633 nm [28].

The multilayers deposited at the same speed exhibited a higher refractive index than the monolayers. Rao and Mohan [9] also observed an increase in refractive index with an increase in thickness of their TiO₂ films. Thicknesses of up to 200 nm were achieved for our multilayers, indicating that a predetermined thickness of film can therefore be achieved readily by employing this deposition technique to produce layers in stack form. The thin film deposited on quartz crystals showed good optical properties in the 250–1100 nm wavelength

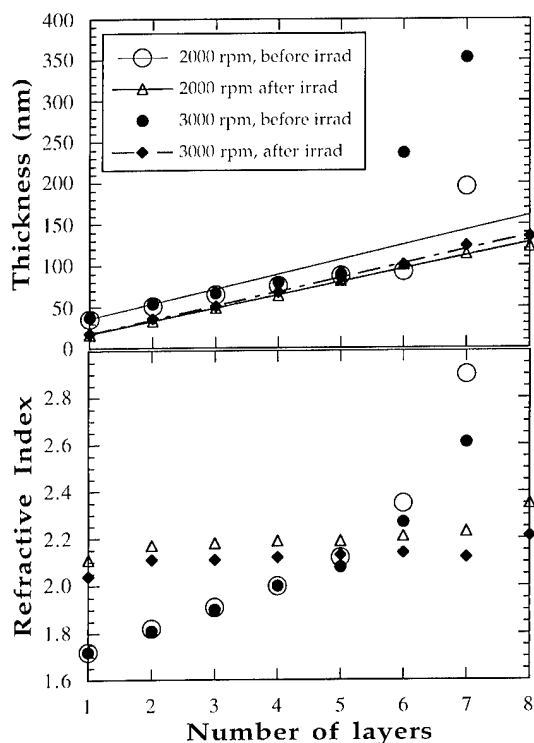


Fig. 4. Dependence of the thickness (d) and refractive index (n) of TiO₂ after irradiation at 172 nm for 10 min on spin deposition speed and number of layers.

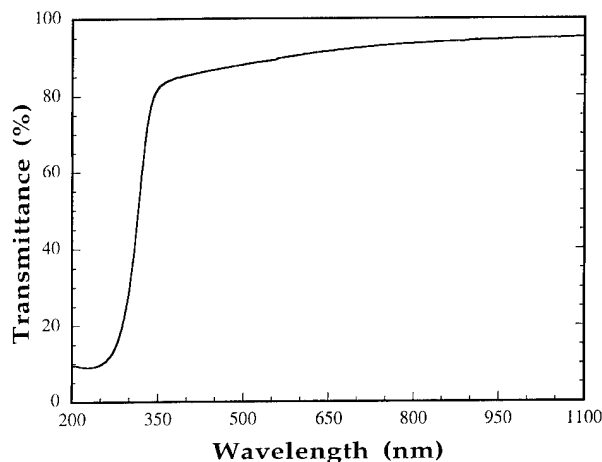


Fig. 5. Spectral transmittance of TiO₂ films deposited on quartz after irradiation at 172 nm for 10 min.

range as seen in Fig. 5. In the range 350 to 1100 nm, optical transmittance between 85 and 95% was obtained. This compares very well with films produced by other techniques.

4. Conclusion

Single- and multilayer TiO_2 films have been prepared by a new photo-induced sol–gel process using a 172 nm VUV excimer lamp. Low-temperature deposition of TiO_2 films at 300°C has been demonstrated. The refractive index of the deposited films (2.4) compares favourably with that for bulk TiO_2 (2.58). The OH groups were dispersed at 300°C and the films formed showed good optical properties with transmittance values between 85 and 90% in the visible range of the spectrum. The thickness of the films formed can readily be controlled by the spin-coating speed and the number of sequential layers deposited.

Acknowledgement

Never Kaliwot is grateful to the Scientific and Industrial Research and Development Centre of Zimbabwe for supporting his studies.

References

- [1] B. O'Regan, M. Gratzel, *Nature* 353 (1998) 737.
- [2] Y. Haga, H. An, R. Yosomiya, *J. Mater. Sci.* 32 (1997) 3183.
- [3] Y. Boukennou, B. Benyahia, M.R. Charif, A. Chikouche, *J. Phys. III, France* 5 (1995) 1297.
- [4] R. Kishore, S. Singh, B.K. Das, *Renewable Energy* 12 (2) (1997) 131.
- [5] N. Rausch, E.P. Burt, *J. Electrochem. Soc.* 140 (1993) 145.
- [6] E. Sanchez, T. Lopez, R. Gomez, Bokhimi, A. Morales, O. Novaro, *J. Solid State Chem.* 122 (1996) 309.
- [7] G.E. Badini, K.T.V. Grattan, A.C. Tseung, A.W. Palmer, *Optical Fibre Technol.* 2 (1996) 378.
- [8] P. Murugavel, M. Kalaiselvam, A.R. Raju, C.N.R. Rao, *J. Mater. Chem.* 7 (1997) 1433.
- [9] K.N. Rao, S. Mohan, *J. Vac. Sci. Technol. A* 8 (1990) 3260–3264.
- [10] C. Garapon, C. Champeaux, J. Mugnier, G. Panczer, P. Marchet, A. Catherinot, B. Jacquier, *Appl. Surf. Sci.* 96 (1996) 836–841.
- [11] H.S. Kim, D.C. Gilmer, S.A. Campbell, D.L. Polla, *Appl. Phys. Lett.* 69 (1996) 3860–3862.
- [12] A.C. Jones, T.J. Leedham, P.J. Wright, K.A. Fleeting, D.J. Otway, P. O'Brien, M. Pemble, *J. Mater. Chem.* 8 (1998) 1773–1777.
- [13] Y. Gao, Y. Liang, S.A. Chambers, *Surf. Sci.* 365 (1996) 638–648.
- [14] J. Aarik, A. Aidla, T. Vustare, *Phil. Mag. Lett.* 73 (1996) 115–119.
- [15] J. Aarik, A. Aidla, V. Sammelseg, T. Vustare, *J. Cryst. Growth* 181 (1997) 259–264.
- [16] M. Tan, G. Wang, L. Zhang, *J. Appl. Phys.* 80 (1996) 1186–1189.
- [17] Q.W. Chen, Y.T. Qian, Z.Y. Chen, Y.B. Jia, G.E. Zhou, X.G. Li, Y.H. Zhang, *Phys. Stat. Sol. A — Appl. Res.* 156 (1996) 381–385.
- [18] Y.H. Lee, K.K. Chan, M.J. Brady, *J. Vac. Sci. Technol. A* 13 (1995) 596–601.
- [19] D. Guerin, S. Ismat Shah, *J. Vac. Sci. Technol. A* 15 (1997) 712–715.
- [20] M. Georgson, A. Roos, C.G. Ribbing, *J. Vac. Sci. Technol. A* 9 (1991) 2191–2195.
- [21] C.J. Brinker, G.W. Scherer, *The Physics and Chemistry of Sol–Gel Processing*, Academic Press, London, 1990.
- [22] H. Lin, H. Hozuka, T. Yoko, *Thin Solid Films* 315 (1998) 111–117.
- [23] P. Christopolou, D. Davazoglou, C. Trapalis, G. Kordas, *Thin Solid Films* 323 (1998) 188–193.
- [24] G. Yi, M. Sayer, *Ceram. Bull.* 70 (1991) 1173.
- [25] A. Gilbert, J. Baggott, *Essentials of Molecular Photochemistry*, Blackwell Scientific Publications, Oxford, 1991.
- [26] J.Y. Zhang, L.-J. Bie, V. Dusastre, I.W. Boyd, *Thin Solid Films* 318 (1998) 252.
- [27] H. Joe, A.K. Vasudevan, G. Aruldas, A.D. Damodaran, K.G.K. Warriar, *J. Solid State Chem.* 131 (1997) 181.
- [28] E.D. Palik, *Handbook of Optical Constants of Solids*, Academic Press, Orlando, 1985, p. 800.

Author Index of Volume 125

- Adami, M., 218
Adamik, M., 147
Alexandrescu, R., 301
Amaral, A., 151
Angleraud, B., 295
Arnal, Y., 71
Aubert, P., 196
- Baborowski, J., 246
Baker, M.A., 207, 317
Bamberger, M., 40, 45
Bamford, M., 66
Baranowska, J., 30
Barna, P.B., 147
Ben Daia, M., 196
Benítez, F., 383
Benmalek, M., 35
Bertóti, I., 173
Beshkov, G., 313
Biederman, H., 371
Bourgeois, S., 396
Boxman, R.L., 257
Boyd, I.W., 424
Bozet, J.L., 196
Briois, V., 317
Brogueira, P., 151
Bulir, J., 278
- Caballero, A., 116
Cáceres, D., 284
Camacho, J., 223
Camel, D., 361
Charbonnier, M., 19, 301
Charitidis, C., 201, 335
Chevrier, J., 124
Chong, T.C., 388
Ciach, R., 415
Coccia Lecis, G., 317
Comin, F., 124
Conde, O., 141
Consiglio, R., 179
Crunteanu, A., 301
- De Rossi, S., 218
Decossas, S., 124
Delafond, J., 129
Delplancke-Ogletree, M.-P., 278
Desoyer, J.C., 129
Dessaux, O., 79
Dettenwanger, F., 89
Dévényi, A., 147
- Dimitriou, R., 157, 223, 35
Dimitrov, D., 313
Domenichini, B., 396
Donohue, L.A., 269, 66
Dudin, S., 341
Duez, N., 79
Dumitrescu, L., 419
Durand, H.-A., 111, 57
- Elizalde, E., 284, 366
Espinós, J.P., 116
Esrom, H., 19
Esteve, J., 383
Etoh, K., 111, 57
- Fabreguette, F., 396
Farenik, V., 341
Favre-Quattropiani, L., 377
Fernandez, V., 295
Filonov, K., 223, 229
Fogarassy, E., 308
Forder, S., 66
Fox, V., 347
Freudenstein, R., 190
Friess, F., 106
Fuchs, C., 308
Fuentes, G.G., 284
- Galán, M., 383
Galdikas, A., 129
Georgiev, C., 313
Gioti, M., 201, 289
Girardeau, T., 100
Gissler, W., 207, 218, 317
Goldsmith, S., 257
Gómez, V., 366
Goncharenko, I.M., 251
González-Elise, A.R., 116
Goudmand, P., 79
Grimberg, I., 257
Grimblot, J., 79
Groening, P., 377
Guéneau, C., 361
Guillot, J., 396
Günzel, R., 89
Gusko, A., 331
Gust, W., 157, 223, 229, 35
Guzman, L., 218
- Harry, E., 185
Haruta, K., 167
Heim, D., 233
- Herrero, P., 366
Holgado, J.P., 116
Holler, F., 233
Hommet, J., 308
Hones, P., 179
Hornauer, U., 89
Houdy, P., 196
Hovsepian, P.E., 269
Huang, S.M., 25
- Ignat, M., 185
Imhoff, L., 396
Ito, K., 111, 57
Ivanov, Y.F., 49
Ivanov, Y.F., 251
- Janczur, C., 1
Jehn, H.A., 212
Jones, A., 347
Juliet, P., 185
- Kaliwih, N., 424
Kaplan, W.D., 40, 45
Kataoka, I., 111, 57
Kazakevich, A., 229
Kazior, J., 1
Kechagias, V., 289
Kirchhoff, V., 354
Klett, A., 190
Klose, S., 207, 218
Kockelmann, H., 331
Kovalev, A., 223
Kövé, L., 147
Krastev, V., 313
Kre N'guessan, R., 295
Kulisch, W., 190, 278
Kuroda, K., 167
Kusinski, J., 13
- Lábár, J., 147
Labdi, S., 196
Lacoste, A., 71
Laskarakis, A., 289
Lauf, S., 331
Lavareda, G., 151
Le Cœur, F., 71
Le Normand, F., 308
Le Ny, J., 361
Le Paven-Thivet, C., 196
Lévy, F., 179
Lederemann, N., 246
Lembke, M.I., 263
- Lenardi, C., 317
Leroux, S., 361
Lewis, D.B., 263, 66
Leyland, A., 407
Logothetidis, S., 201, 289, 335
Lu, Y.F., 25, 388
Luo, X.F., 25
Lyutovich, A., 331
- Mai, Z.H., 388
Maile, K., 331
Manaila, R., 147
Mändl, S., 84, 94
Marco de Lucas, M.C., 396
Markov, A.B., 49
Martínez, E., 383
Matthews, A., 407
Maury, F., 419
McCay, M.H., 40
McCay, T.D., 40
Medres, B., 40, 45
Metzner, C., 240
Miao, P., 388
Miernik, K., 161, 341
Mitterer, C., 233
Mohai, M., 173
Molinari, A., 1
Möller, W., 89
Montassier, C., 392
Morales, J., 116
Morgner, H., 354
Mubumbila, N., 295
Münz, W.-D., 263, 269, 66
Muralt, P., 246
Musil, J., 322
Mutel, B., 79
Muzard, S., 129
- Nedkov, I., 313
Negoita, F., 301
Nemetz, W., 400
Ng, S.C., 388
Nie, X., 407
Nowacki, J., 9
Núñez, R., 284
Nunes de Carvalho, C., 151
- Ocaña, M., 116
Oliveira, J.C., 141
Orlov, P.V., 251
Ossi, P.M., 61
Ozur, G.E., 251, 49

- Panayiotatos, Y., 289
 Pang, S.I., 388
 Pantelica, D., 301
 Pastorelli, R., 61
 Patsalas, P., 289, 335
 Pauleau, Y., 185
 Pelletier, J., 71
 Pérez-Casero, R., 366
 Petrov, P., 313
 Pichon, L., 100
 Pieczonka, T., 1
 Piseri, P., 317
 Plass, M.F., 190, 278
 Pokhmurska, A., 415
 Polestchenko, K.N., 251
 Popov, C., 278
 Pranevicius, L., 129
 Pranevicius, L.L., 392
 Prieto, P., 284, 366
 Proskurovsky, D.I., 251, 49
 Przybyłowicz, J., 13
 Pulver, M., 400

 Quirós, C., 284, 366

 Rabkin, E., 157, 229
 Ramseyer, D., 377

 Randall, N., 179
 Rapoport, L., 257
 Rauschenbach, B., 84, 94
 Ren, Z.M., 388
 Renevier, N.M., 173, 347
 Reuther, H., 89
 Richter, E., 89
 Riedo, E., 124
 Romand, M., 19, 301
 Roos, E., 331
 Rotshtein, V.P., 251, 49
 Rouzaud, A., 185

 Sacilotti, M., 396
 Saka, H., 167
 Sancrotti, M., 124
 Sanz, J.M., 284, 366
 Schiller, N., 354
 Schiller, S., 240, 354
 Schlapbach, L., 377
 Schmithusen, F., 124
 Schönjahn, C., 66
 Schreck, M., 84
 Schumacher, G., 89
 Schütze, M., 89
 Schwarz, G., 106
 Seeböck, R., 19
 Sekine, K., 111, 57

 Serrat, J., 383
 Sharp, M., 40
 Shepeleva, L., 40, 45
 Shulga, J., 35
 Sibillot, P., 396
 Silvestre, A.J., 141
 Slavinská, D., 371
 Smolik, J., 134
 Soriano, L., 284
 Straboni, A., 100
 Straumal, B., 157, 223, 229, 35
 Stritzker, B., 84
 Sun, Z., 25
 Szilágyi, E., 173
 Szörényi, T., 308

 Tacikowski, J., 134
 Takatsuji, H., 167
 Teer, D.G., 347
 Tellenbach, J.-M., 246
 Templier, C., 129
 Tessier, P.Y., 295
 Thorwarth, G., 84, 94
 Tóth, J., 147
 Trampert, M., 207
 Tsuji, S., 167
 Turban, G., 295

 Üstel, F., 233

 Valatkevicius, P., 392
 Valincius, V., 392
 Vasiliu, F., 301
 Vergara, I., 284
 Vershinin, N., 157, 223, 229, 35
 Vivas, J., 35

 Wahl, G., 400
 Walkowicz, J., 134, 161, 341
 Wang, J.P., 388
 Weber, F., 207
 Weisheit, A., 45
 Weiss, B.Z., 257
 Wiener, I., 229
 Wieser, E., 89
 Wolf, G.K., 106
 Wysiecki, M., 30

 Xantopoulos, N., 246

 Yubero, F., 116

 Zambov, L., 278
 Zhang, J.-Y., 424
 Zhitomirsky, V.N., 257
 Zykov, A., 341
 Zywitzki, O., 240

Subject Index of Volume 125

- Al/Al₂O₃ multilayers
 Mechanical properties of Al/Al₂O₃ nanolaminated films: correlation to microstructure, 196
- Al₂O₃
 New coatings on metal sheets and strips produced using EB PVD technologies, 240
- CN_x films
 Structural properties and surface morphology of laser-deposited amorphous carbon and carbon nitride films, 124
- MoS₂-Ti
 XPS investigation of ion beam treated MoS₂-Ti composite coatings, 173
- SF₆
 Deposition of c-BN by ion beam assisted CVD, 106
- TiN_xO_y
 Temperature and substrate influence on the structure of TiN_xO_y thin films grown by low pressure metal organic chemical vapour deposition, 396
- Adhesion
 Deposition of c-BN by ion beam assisted CVD, 106
 Mechanical properties of plasma deposited polymer coatings, 383
- AES depth profiling
 Determination of resputtering yields in carbon nitride films grown by dual ion beam sputtering, 366
- AFM
 Structural properties and surface morphology of laser-deposited amorphous carbon and carbon nitride films, 124
 Pulsed laser deposition of crystal polyaniline thin films, 388
- Al metal organic chemical vapor deposition
 Al₂O₃ coatings on stainless steel from Al metal-organic chemical vapor deposition and thermal treatments, 419
- Alumina
 Laser induced Cu/alumina bonding: Microstructure and bond mechanism, 40
 CVD of ZrO₂, Al₂O₃ and Y₂O₃ from metalorganic compounds in different reactors, 400
- Aluminium die casting
 Application of hard coatings in aluminium die casting — soldering, erosion and thermal fatigue behaviour, 233
- Aluminium oxide coatings
 Al₂O₃ coatings on stainless steel from Al metal-organic chemical vapor deposition and thermal treatments, 419
- Aluminizing
 Al₂O₃ coatings on stainless steel from Al metal-organic chemical vapor deposition and thermal treatments, 419
- Aluminum nitride
 AlN formation by direct nitrogen implantation using a DECR plasma, 79
- Amorphisation
 Amorphisation and related structural effects in thin films prepared by ion beam assisted methods, 116
- Angular distribution
 Spatial distribution of microdroplets generated in the cathode spots of vacuum arcs, 161
- Arc
 Properties of various large-scale fabricated TiAlN- and CrN-based superlattice coatings grown by combined cathodic arc-unbalanced magnetron sputter deposition, 269
- Arc discharge
 Spatial distribution of microdroplets generated in the cathode spots of vacuum arcs, 161
- Archaeology
 The protection of metallic archaeological objects using plasma polymer coatings, 377
- Arc spraying
 Microstructure and properties of laser treated arc sprayed and plasma sprayed coatings, 415
- Atmospheric pressure
 Catalytic behavior of plasma-sprayed Al-Al₂O₃ coatings doped with metal oxides, 392
- Atomic force microscopy
 Early stage growth structure of indium tin oxide thin films deposited by reactive thermal evaporation, 151
- BF3
 Deposition of c-BN by ion beam assisted CVD, 106
- Biomaterials
 Deposition of layered bioceramic hydroxyapatite/TiO₂ coatings on titanium alloys using a hybrid technique of micro-arc oxidation and electrophoresis, 407
- Biomedical implant
 Deposition of layered bioceramic hydroxyapatite/TiO₂ coatings on titanium alloys using a hybrid technique of micro-arc oxidation and electrophoresis, 407
- Bonding structure
 Physical properties of carbon nitride films synthesized using atomic transport reactions, 278
- Boron carbide
 Influence of carbon content on the crystallographic structure of boron carbide films, 141
- Boron nitride
 Correlation between stress values of cubic boron nitride thin films and intrinsic film properties or the infrared peak position, 190
- c-BN
 Deposition of c-BN by ion beam assisted CVD, 106
- Carbon
 Effect of energy on direct ion beam deposition of carbon thin films: induced defects and graphitization, 57
 A comparative study of the nanoscratching behavior of amorphous carbon films grown under various deposition conditions, 201

- Carbon/carbon composites
 - Electron beam physical vapour deposition of protective films on carbon reinforced carbon, 331
- Carbonitriding
 - Plasma immersion ion implantation of cold-work steel, 94
- Carbon nitride
 - Physical properties of carbon nitride films synthesized using atomic transport reactions, 278
 - Correlation between bonding structure and mechanical properties of amorphous carbon nitride thin films, 284
 - Magnetron sputtered carbon nitride: composition and chemical bonding of as-grown and post-annealed films studied with real-time and in situ diagnostic techniques, 289
 - Carbon nitride thin films deposited by reactive plasma beam sputtering, 295
 - Synthesis and characterization of carbon nitride thin films obtained by laser induced chemical vapour deposition, 301
 - Chemical analysis of pulsed laser deposited a-CN_x films by comparative infrared and X-ray photoelectron spectroscopies, 308
 - X-ray photoelectron spectroscopy study of carbon nitride films, 313
 - Near-edge X-ray absorption fine structure study of carbon nitride films, 317
 - Determination of resputtering yields in carbon nitride films grown by dual ion beam sputtering, 366
- Catalytic behavior
 - Catalytic behavior of plasma-sprayed Al-Al₂O₃ coatings doped with metal oxides, 392
- Cathode sputtering
 - Influence of surface pretreatment on case formation during gaseous nitriding, 30
- Cathodic arc
 - The interface between TiAlN hard coatings and steel substrates generated by high energetic Cr₊ bombardment, 66
- Cathodic arc deposition
 - Localised oxidation defects in TiAlN/CrN superlattice structured hard coatings grown by cathodic arc/ unbalanced magnetron deposition on various substrate materials, 263
- Cemented carbides
 - Pulsed electron-beam treatment of WC-TiC-Co hard-alloy cutting tools: wear resistance and microstructural evolution, 251
- Chemical bonds
 - Magnetron sputtered carbon nitride: composition and chemical bonding of as-grown and post-annealed films studied with real-time and in situ diagnostic techniques, 289
- Chemical resputtering
 - Determination of resputtering yields in carbon nitride films grown by dual ion beam sputtering, 366
- Chemical vapor deposition
 - CVD of ZrO₂, Al₂O₃ and Y₂O₃ from metalorganic compounds in different reactors, 400
- Chlorine
 - Protection of γ -based TiAl against high temperature oxidation using ion implantation of chlorine, 89
- Chromium nitride
 - Mechanical properties of hard chromium tungsten nitride coatings, 179
- Coating on plastics
 - PVD coating of plastic webs and sheets with high rates on large areas, 354
- Coatings
 - Spatial distribution of microdroplets generated in the cathode spots of vacuum arcs, 161
 - Mechanical behaviour of hard PVD multilayered coatings, 185
- Composite coatings
 - XPS investigation of ion beam treated MoS₂-Ti composite coatings, 173
- Composite layer
 - Influence of the structure of the composite: 'nitrided layer/PVD coating' on the durability of tools for hot working, 134
- Composition
 - Physical properties of carbon nitride films synthesized using atomic transport reactions, 278
- Condensation
 - Condensation of silver-copper alloys in a solid-liquid domain of the phase diagram, 361
- Conservation
 - The protection of metallic archaeological objects using plasma polymer coatings, 377
- Copper cladding
 - Laser induced Cu/alumina bonding: Microstructure and bond mechanism, 40
- Corrosion
 - Corrosion resistance of the vacuum arc deposited Ti, TiN and TiO₂ coatings on large area glass substrates, 223
 - The protection of metallic archaeological objects using plasma polymer coatings, 377
- Corrosion resistance
 - Morphologies and corrosion properties of PVD Zn-Al coatings, 207
 - Improvement of the corrosion resistance of PVD hard coating-substrate systems, 212
 - Vapour deposited Zn-Cr Alloy coatings for enhanced manufacturing and corrosion resistance of steel sheets, 218
 - Corrosion behaviour of the protective and decorative TiN coatings on large area steel strips, 229
- Cracking
 - Mechanical behaviour of hard PVD multilayered coatings, 185
- Cr and Ti coatings
 - Electron beam physical vapour deposition of protective films on carbon reinforced carbon, 331
- Crystal growth
 - Condensation of silver-copper alloys in a solid-liquid domain of the phase diagram, 361
- Crystallographic structure
 - Influence of carbon content on the crystallographic structure of boron carbide films, 141
- Crystal orientation
 - Amorphisation and related structural effects in thin films prepared by ion beam assisted methods, 116
- Cutting tools
 - Hard lubricating coatings for cutting and forming tools and mechanical components, 347
- Deposition rate
 - Vacuum arc deposition of Ti coatings, 157
- Diamond
 - Diamond-like films formed by pulsed laser irradiation of phenylacetyne polymer, 25
- Diamond-like carbon films
 - Structural properties and surface morphology of laser-deposited amorphous carbon and carbon nitride films, 124
- Dielectric barrier discharge (DBD)
 - Surface activation of polyimide with dielectric barrier discharge for electroless metal deposition, 19
- Dual ion beam deposition
 - Near-edge X-ray absorption fine structure study of carbon nitride films, 317
- Dual ion beam sputtering
 - Correlation between bonding structure and mechanical properties of amorphous carbon nitride thin films, 284
 - Determination of resputtering yields in carbon nitride films grown by dual ion beam sputtering, 366

- Dual magnetron sputtering system (DMS)
 - PVD coating of plastic webs and sheets with high rates on large areas, 354
- Duplex treatment
 - Influence of the structure of the composite: 'nitrided layer/PVD coating' on the durability of tools for hot working, 134
- EELS
 - Structural properties and surface morphology of laser-deposited amorphous carbon and carbon nitride films, 124
- Elastic recoil detection
 - Raman study of titanium oxide layers produced with plasma immersion ion implantation, 84
- Electrochemical properties
 - Microstructure and properties of laser treated arc sprayed and plasma sprayed coatings, 415
- Electroless copper plating
 - Surface activation of polyimide with dielectric barrier discharge for electroless metal deposition, 19
- Electron beam evaporation
 - New coatings on metal sheets and strips produced using EB PVD technologies, 240
 - X-ray photoelectron spectroscopy study of carbon nitride films, 313
- Electron cyclotron resonance
 - AlN formation by direct nitrogen implantation using a DECR plasma, 79
- Electron diffraction
 - Synthesis and characterization of carbon nitride thin films obtained by laser induced chemical vapour deposition, 301
- Electrophoretic deposition
 - Deposition of layered bioceramic hydroxyapatite/TiO₂ coatings on titanium alloys using a hybrid technique of micro-arc oxidation and electrophoresis, 407
- Ellipsometry
 - Magnetron sputtered carbon nitride: composition and chemical bonding of as-grown and post-annealed films studied with real-time and in situ diagnostic techniques, 289
 - Titanium dioxide films prepared by photo-induced sol-gel processing using 172 nm excimer lamps, 424
- Epitaxy
 - The interface between TiAlN hard coatings and steel substrates generated by high energetic Cr⁺ bombardment, 66
- ERDA
 - Synthesis and characterization of carbon nitride thin films obtained by laser induced chemical vapour deposition, 301
- Erosion
 - Application of hard coatings in aluminium die casting — soldering, erosion and thermal fatigue behaviour, 233
- Erosive wear
 - Laser cladding and erosive wear of Co-Mo-Cr-Si coatings, 13
- Evaporation
 - Properties of various large-scale fabricated TiAlN- and CrN-based superlattice coatings grown by combined cathodic arc-unbalanced magnetron sputter deposition, 269
- Excimer lamp
 - Titanium dioxide films prepared by photo-induced sol-gel processing using 172 nm excimer lamps, 424
- Excimer laser
 - Pulsed laser deposition of crystal polyaniline thin films, 388
- Excimer UV lamps
 - Surface activation of polyimide with dielectric barrier discharge for electroless metal deposition, 19
- Fe-Al coatings
 - Al₂O₃ coatings on stainless steel from Al metal-organic chemical vapor deposition and thermal treatments, 419
- Film
 - A phenomenological study of the initial stages of film growth, 129
- Film stress
 - Sputtered silicon carbide thin films as protective coating for MEMS applications, 246
- Flow
 - Condensation of silver-copper alloys in a solid-liquid domain of the phase diagram, 361
- Forming tools
 - Hard lubricating coatings for cutting and forming tools and mechanical components, 347
- Fractal surface
 - Influence of ion induced surface defects on the nucleation and formation mechanisms of metallic thin films, 111
 - Effect of energy on direct ion beam deposition of carbon thin films: induced defects and graphitization, 57
- FT-IR
 - Correlation between bonding structure and mechanical properties of amorphous carbon nitride thin films, 284
- FTIR
 - Carbon nitride thin films deposited by reactive plasma beam sputtering, 295
 - Titanium dioxide films prepared by photo-induced sol-gel processing using 172 nm excimer lamps, 424
- Galvanized steel
 - New coatings on metal sheets and strips produced using EB PVD technologies, 240
- Gaseous nitriding
 - Influence of surface pretreatment on case formation during gaseous nitriding, 30
- Gold
 - A phenomenological study of the initial stages of film growth, 129
- Grain boundary
 - Formation of polycrystalline and microcrystalline composite thin films by codeposition and surface chemical reaction, 147
- Grain growth
 - The effect of substrate temperature and biasing on the mechanical properties and structure of sputtered titanium nitride thin films, 335
- Grain size
 - Early stage growth structure of indium tin oxide thin films deposited by reactive thermal evaporation, 151
- Growth
 - A phenomenological study of the initial stages of film growth, 129
- Growth modelling
 - Production of stable and metastable phases of zirconium nitrides by <di NH<ei<ee plasma nitridation and by double ion beam sputtering of zirconium films, 100
- Hall current accelerator
 - Pre-treatment of large area strips with the aid of a high power Hall current accelerator, 35
- Hard coatings
 - Improvement of the corrosion resistance of PVD hard coating-substrate systems, 212
 - Application of hard coatings in aluminium die casting — soldering, erosion and thermal fatigue behaviour, 233
- Hardness
 - Structure and hardness of vacuum arc deposited multi-component nitride coatings of Ti, Zr and Nb, 257
 - Correlation between bonding structure and mechanical properties of amorphous carbon nitride thin films, 284
 - Hard and superhard nanocomposite coatings, 322
 - Mechanical properties of plasma deposited polymer coatings, 383
- High voltage pulse

- Ion implantation by plasma immersion: interest, limitations and perspectives, 71
- Hollow cathode activated deposition process (HAD)
 - PVD coating of plastic webs and sheets with high rates on large areas, 354
- Hybrid plasma source
 - Pulsed-plasma assisted magnetron methods of depositing TiN coatings, 341
- Hydroxyapatite
 - Deposition of layered bioceramic hydroxyapatite/TiO₂ coatings on titanium alloys using a hybrid technique of micro-arc oxidation and electrophoresis, 407
- IBAD
 - Amorphisation and related structural effects in thin films prepared by ion beam assisted methods, 116
- ICP-CVD
 - Physical properties of carbon nitride films synthesized using atomic transport reactions, 278
- Implantation
 - Protection of γ -based TiAl against high temperature oxidation using ion implantation of chlorine, 89
- Impurity
 - Formation of polycrystalline and microcrystalline composite thin films by codeposition and surface chemical reaction, 147
- Indium tin oxide
 - Early stage growth structure of indium tin oxide thin films deposited by reactive thermal evaporation, 151
- Infrared (IR) absorption spectroscopy
 - Chemical analysis of pulsed laser deposited a-CN_x films by comparative infrared and X-ray photoelectron spectroscopies, 308
- Initial stages
 - A phenomenological study of the initial stages of film growth, 129
- Interface
 - The interface between TiAlN hard coatings and steel substrates generated by high energetic Cr⁺ bombardment, 66
- Ion assisted electron beam PVD
 - Electron beam physical vapour deposition of protective films on carbon reinforced carbon, 331
- Ion beam assisted deposition
 - Correlation between stress values of cubic boron nitride thin films and intrinsic film properties or the infrared peak position, 190
- Ion beam deposition
 - Production of stable and metastable phases of zirconium nitrides by NH₃ plasma nitridation and by double ion beam sputtering of zirconium films, 100
- Ion beams
 - Influence of ion induced surface defects on the nucleation and formation mechanisms of metallic thin films, 111
 - Effect of energy on direct ion beam deposition of carbon thin films: induced defects and graphitization, 57
- Ion bombardment
 - XPS investigation of ion beam treated MoS₂-Ti composite coatings, 173
 - X-ray photoelectron spectroscopy study of carbon nitride films, 313
- Ionic etching
 - Pre-treatment of large area strips with the aid of a high power Hall current accelerator, 35
- Ion implantation
 - Ion implantation by plasma immersion: interest, limitations and perspectives, 71
- IR
 - Amorphisation and related structural effects in thin films prepared by ion beam assisted methods, 116
- Iron aluminides
 - Al₂O₃ coatings on stainless steel from Al metal-organic chemical vapor deposition and thermal treatments, 419
- Iron nitrides
 - Modification of composite nitrided layers by phosphorus compounds, 9
- Iron phosphides
 - Modification of composite nitrided layers by phosphorus compounds, 9
- IR spectroscopy
 - Correlation between stress values of cubic boron nitride thin films and intrinsic film properties or the infrared peak position, 190
- Island
 - A phenomenological study of the initial stages of film growth, 129
- Kaufman source
 - Pre-treatment of large area strips with the aid of a high power Hall current accelerator, 35
- Large-area deposition
 - PVD coating of plastic webs and sheets with high rates on large areas, 354
- Laser cladding
 - Laser cladding and erosive wear of Co-Mo-Cr-Si coatings, 13
 - Laser cladding of turbine blades, 45
- Laser CVD
 - Influence of carbon content on the crystallographic structure of boron carbide films, 141
 - Synthesis and characterization of carbon nitride thin films obtained by laser induced chemical vapour deposition, 301
- Laser treatment
 - Laser induced Cu/alumina bonding: Microstructure and bond mechanism, 40
 - Microstructure and properties of laser treated arc sprayed and plasma sprayed coatings, 415
- Magnetron sputtering
 - Hard and superhard nanocomposite coatings, 322
 - Hard lubricating coatings for cutting and forming tools and mechanical components, 347
- Materials processing
 - Ion implantation by plasma immersion: interest, limitations and perspectives, 71
- Mechanical properties
 - Mechanical properties of hard chromium tungsten nitride coatings, 179
 - Hard and superhard nanocomposite coatings, 322
- Mechanical resistance
 - Vapour deposited Zn-Cr Alloy coatings for enhanced manufacturing and corrosion resistance of steel sheets, 218
- MEMS
 - Sputtered silicon carbide thin films as protective coating for MEMS applications, 246
- Metalorganic compounds
 - CVD of ZrO₂, Al₂O₃ and Y₂O₃ from metalorganic compounds in different reactors, 400
- Micro-arc oxidation
 - Deposition of layered bioceramic hydroxyapatite/TiO₂ coatings on titanium alloys using a hybrid technique of micro-arc oxidation and electrophoresis, 407
- Micro-Raman spectroscopy
 - Influence of carbon content on the crystallographic structure of boron carbide films, 141
- Microdroplets
 - Spatial distribution of microdroplets generated in the cathode spots of vacuum arcs, 161
- Microhardness
 - Microstructure and properties of laser treated arc sprayed and plasma sprayed coatings, 415

- Microstructure
 - Laser cladding and erosive wear of Co–Mo–Cr–Si coatings, 13
 - Morphologies and corrosion properties of PVD Zn–Al coatings, 207
 - Laser induced Cu/alumina bonding: Microstructure and bond mechanism, 40
- Modelling
 - A phenomenological study of the initial stages of film growth, 129
- Molybdenum
 - Influence of ion induced surface defects on the nucleation and formation mechanisms of metallic thin films, 111
- Molybdenum sulphide
 - XPS investigation of ion beam treated MoS₂–Ti composite coatings, 173
- Morphology
 - Electron beam physical vapour deposition of protective films on carbon reinforced carbon, 331
- Mössbauer spectroscopy
 - The interface between TiAlN hard coatings and steel substrates generated by high energetic Cr⁺ bombardment, 66
- Multilayers
 - Mechanical behaviour of hard PVD multilayered coatings, 185
 - Properties of various large-scale fabricated TiAlN- and CrN-based superlattice coatings grown by combined cathodic arc–unbalanced magnetron sputter deposition, 269
- Nano-indentation
 - A comparative study of the nanoscratching behavior of amorphous carbon films grown under various deposition conditions, 201
 - The effect of substrate temperature and biasing on the mechanical properties and structure of sputtered titanium nitride thin films, 335
- Nanocomposite coatings
 - Hard and superhard nanocomposite coatings, 322
- Nanoindentation
 - Mechanical properties of Al/Al₂O₃ nanolaminated films: correlation to microstructure, 196
- Nanoindentation techniques
 - Pure Al thin film protective layer to prevent stress migration in Al wiring for thin-film transistors, 167
- Near-edge X-ray absorption fine structure
 - Near-edge X-ray absorption fine structure study of carbon nitride films, 317
- Nickel
 - Influence of ion induced surface defects on the nucleation and formation mechanisms of metallic thin films, 111
 - Effect of energy on direct ion beam deposition of carbon thin films: induced defects and graphitization, 57
- Nitridation
 - AlN formation by direct nitrogen implantation using a DECR plasma, 79
- Nitrides nucleation
 - Influence of surface pretreatment on case formation during gaseous nitriding, 30
- Nitriding
 - Microstructural characterisation and properties of thermochemically treated iron-based alloys, 1
- Nitriding kinetics
 - Influence of surface pretreatment on case formation during gaseous nitriding, 30
- Nitriding of short duration
 - Modification of composite nitrided layers by phosphorus compounds, 9
- Optical properties of thin films
 - Production of stable and metastable phases of zirconium nitrides by <di NH<ei<ee plasma nitridation and by double ion beam sputtering of zirconium films, 100
- Overcoated pure aluminum thin film
 - Pure Al thin film protective layer to prevent stress migration in Al wiring for thin-film transistors, 167
- Oxidation
 - Microstructural characterisation and properties of thermochemically treated iron-based alloys, 1
 - Catalytic behavior of plasma-sprayed Al–Al₂O₃ coatings doped with metal oxides, 392
 - Protection of γ -based TiAl against high temperature oxidation using ion implantation of chlorine, 89
- Oxidation behaviour
 - Localised oxidation defects in TiAlN/CrN superlattice structured hard coatings grown by cathodic arc/ unbalanced magnetron deposition on various substrate materials, 263
- Palladium
 - Surface activation of polyimide with dielectric barrier discharge for electroless metal deposition, 19
- Palladium acetate
 - Surface activation of polyimide with dielectric barrier discharge for electroless metal deposition, 19
- Phospho-nitriding
 - Modification of composite nitrided layers by phosphorus compounds, 9
- Phosphorus in steel
 - Modification of composite nitrided layers by phosphorus compounds, 9
- Photo-induced processing
 - Titanium dioxide films prepared by photo-induced sol–gel processing using 172 nm excimer lamps, 424
- Photo-induced reduction
 - Surface activation of polyimide with dielectric barrier discharge for electroless metal deposition, 19
- Physical vapor deposition
 - Vapour deposited Zn–Cr Alloy coatings for enhanced manufacturing and corrosion resistance of steel sheets, 218
- Physical vapor deposition coating
 - Influence of the structure of the composite: 'nitrided layer/PVD coating' on the durability of tools for hot working, 134
- Physical vapour deposition
 - Morphologies and corrosion properties of PVD Zn–Al coatings, 207
- Physical vapour deposition coatings
 - Improvement of the corrosion resistance of PVD hard coating–substrate systems, 212
- Plasma
 - Plasma polymer films and their future prospects, 371
 - AlN formation by direct nitrogen implantation using a DECR plasma, 79
- Plasma-induced reduction
 - Surface activation of polyimide with dielectric barrier discharge for electroless metal deposition, 19
- Plasma activation
 - New coatings on metal sheets and strips produced using EB PVD technologies, 240
- Plasma cladding
 - Laser cladding of turbine blades, 45
- Plasma immersion
 - Ion implantation by plasma immersion: interest, limitations and perspectives, 71
 - Protection of γ -based TiAl against high temperature oxidation using ion implantation of chlorine, 89
- Plasma immersion ion implantation
 - Raman study of titanium oxide layers produced with plasma immersion ion implantation, 84

- Plasma immersion ion implantation of cold-work steel, 94
- Plasma polymerisation
 - The protection of metallic archaeological objects using plasma polymer coatings, 377
 - Mechanical properties of plasma deposited polymer coatings, 383
- Plasma polymers
 - Plasma polymer films and their future prospects, 371
- Plasma sheath
 - Ion implantation by plasma immersion: interest, limitations and perspectives, 71
- Plasma spraying
 - Microstructure and properties of laser treated arc sprayed and plasma sprayed coatings, 415
- Polyimide (PI)
 - Surface activation of polyimide with dielectric barrier discharge for electroless metal deposition, 19
- Polymer
 - Pulsed laser deposition of crystal polyaniline thin films, 388
- Polymer precursor
 - Diamond-like films formed by pulsed laser irradiation of phenylcarbyne polymer, 25
- Protecting coating
 - Microstructure and properties of laser treated arc sprayed and plasma sprayed coatings, 415
- Protective coating
 - Sputtered silicon carbide thin films as protective coating for MEMS applications, 246
- Protective coatings
 - The protection of metallic archaeological objects using plasma polymer coatings, 377
- Pulsed discharge
 - Pulsed-plasma assisted magnetron methods of depositing TiN coatings, 341
- Pulsed electron-beam treatment
 - Pulsed electron-beam treatment of WC-TiC-Co hard-alloy cutting tools: wear resistance and microstructural evolution, 251
- Pulsed electron beams
 - Physical foundations for surface treatment of materials with low energy, high current electron beams, 49
- Pulsed laser
 - Diamond-like films formed by pulsed laser irradiation of phenylcarbyne polymer, 25
- Pulsed laser deposition
 - Structural properties and surface morphology of laser-deposited amorphous carbon and carbon nitride films, 124
 - Chemical analysis of pulsed laser deposited a-CN_x films by comparative infrared and X-ray photoelectron spectroscopies, 308
 - Pulsed laser deposition of crystal polyaniline thin films, 388
- Pulsed magnetron sputtering (PMS) process
 - PVD coating of plastic webs and sheets with high rates on large areas, 354
- Pulse generator
 - Ion implantation by plasma immersion: interest, limitations and perspectives, 71
- PVD
 - Properties of various large-scale fabricated TiAlN- and CrN-based superlattice coatings grown by combined cathodic arc-unbalanced magnetron sputter deposition, 269
- PVD coatings
 - Localised oxidation defects in TiAlN/CrN superlattice structured hard coatings grown by cathodic arc/ unbalanced magnetron deposition on various substrate materials, 263
- Pyrolysis
 - Diamond-like films formed by pulsed laser irradiation of phenylcarbyne polymer, 25
- Radiation effects
 - Structural stability of irradiated metallic and non-metallic films, 61
- Raman spectroscopy
 - Carbon nitride thin films deposited by reactive plasma beam sputtering, 295
 - Raman study of titanium oxide layers produced with plasma immersion ion implantation, 84
- Reactive plasma spraying
 - Catalytic behavior of plasma-sprayed Al-Al₂O₃ coatings doped with metal oxides, 392
- Reactive sputtering
 - Magnetron sputtered carbon nitride: composition and chemical bonding of as-grown and post-annealed films studied with real-time and in situ diagnostic techniques, 289
 - Carbon nitride thin films deposited by reactive plasma beam sputtering, 295
- Resputtering yields
 - Determination of resputtering yields in carbon nitride films grown by dual ion beam sputtering, 366
- RF magnetron
 - Pulsed-plasma assisted magnetron methods of depositing TiN coatings, 341
- Roughness
 - Vacuum arc deposition of Ti coatings, 157
- Rutherford backscattering spectroscopy
 - Temperature and substrate influence on the structure of TiN_xO_y thin films grown by low pressure metal organic chemical vapour deposition, 396
- Scanning tunneling microscopy
 - Effect of energy on direct ion beam deposition of carbon thin films: induced defects and graphitization, 57
 - Influence of ion induced surface defects on the nucleation and formation mechanisms of metallic thin films, 111
- Scratch test
 - A comparative study of the nanoscratching behavior of amorphous carbon films grown under various deposition conditions, 201
- Segregation
 - Formation of polycrystalline and microcrystalline composite thin films by codeposition and surface chemical reaction, 147
- Shroud shelve
 - Laser cladding of turbine blades, 45
- Silicon carbide
 - Sputtered silicon carbide thin films as protective coating for MEMS applications, 246
- Silver-copper alloys
 - Condensation of silver-copper alloys in a solid-liquid domain of the phase diagram, 361
- Sintered materials
 - Microstructural characterisation and properties of thermochemically treated iron-based alloys, 1
- Sol-gel
 - Titanium dioxide films prepared by photo-induced sol-gel processing using 172 nm excimer lamps, 424
- Soldering
 - Application of hard coatings in aluminium die casting — soldering, erosion and thermal fatigue behaviour, 233
- Solidification
 - Condensation of silver-copper alloys in a solid-liquid domain of the phase diagram, 361
- Solid lubricants
 - Hard lubricating coatings for cutting and forming tools and mechanical components, 347
- Sputter cleaning
 - Pre-treatment of large area strips with the aid of a high power Hall current accelerator, 35

- The interface between TiAlN hard coatings and steel substrates generated by high energetic Cr^+ bombardment, 66
- Sputtering
- Pure Al thin film protective layer to prevent stress migration in Al wiring for thin-film transistors, 167
 - A comparative study of the nanoscratching behavior of amorphous carbon films grown under various deposition conditions, 201
 - Properties of various large-scale fabricated TiAlN- and CrN-based superlattice coatings grown by combined cathodic arc-unbalanced magnetron sputter deposition, 269
 - The effect of substrate temperature and biasing on the mechanical properties and structure of sputtered titanium nitride thin films, 335
 - Plasma polymer films and their future prospects, 371
- Steel
- Plasma immersion ion implantation of cold-work steel, 94
- Stress
- Correlation between stress values of cubic boron nitride thin films and intrinsic film properties or the infrared peak position, 190
- Stress migration
- Pure Al thin film protective layer to prevent stress migration in Al wiring for thin-film transistors, 167
- Structural stability
- Structural stability of irradiated metallic and non-metallic films, 61
- Structure
- Formation of polycrystalline and microcrystalline composite thin films by codeposition and surface chemical reaction, 147
 - Structure and hardness of vacuum arc deposited multi-component nitride coatings of Ti, Zr and Nb, 257
 - Hard and superhard nanocomposite coatings, 322
- Sulphurising
- Microstructural characterisation and properties of thermochemically treated iron-based alloys, 1
- Superlattices
- Properties of various large-scale fabricated TiAlN- and CrN-based superlattice coatings grown by combined cathodic arc-unbalanced magnetron sputter deposition, 269
- Superlattice structure
- Localised oxidation defects in TiAlN/CrN superlattice structured hard coatings grown by cathodic arc/ unbalanced magnetron deposition on various substrate materials, 263
- Surface activation
- Influence of surface pretreatment on case formation during gaseous nitriding, 30
- Surface binary compounds
- Structural stability of irradiated metallic and non-metallic films, 61
- Surface modification
- Mechanical properties of plasma deposited polymer coatings, 383
- Surface roughness
- Early stage growth structure of indium tin oxide thin films deposited by reactive thermal evaporation, 151
- Surface thermal treatment
- Physical foundations for surface treatment of materials with low energy, high current electron beams, 49
- Ternary compound
- Mechanical properties of hard chromium tungsten nitride coatings, 179
- Ternary nitrides
- Structure and hardness of vacuum arc deposited multi-component nitride coatings of Ti, Zr and Nb, 257
- Thermal fatigue
- Application of hard coatings in aluminium die casting — soldering, erosion and thermal fatigue behaviour, 233
- Thermochemical surface treatment
- Microstructural characterisation and properties of thermochemically treated iron-based alloys, 1
- Thermophoresis
- CVD of ZrO_2 , Al_2O_3 and Y_2O_3 from metalorganic compounds in different reactors, 400
- Thin-film transistor liquid crystal displays
- Pure Al thin film protective layer to prevent stress migration in Al wiring for thin-film transistors, 167
- Thin film
- Pulsed laser deposition of crystal polyaniline thin films, 388
 - Temperature and substrate influence on the structure of TiN_xO_y thin films grown by low pressure metal organic chemical vapour deposition, 396
- Thin films
- Influence of ion induced surface defects on the nucleation and formation mechanisms of metallic thin films, 111
 - Amorphisation and related structural effects in thin films prepared by ion beam assisted methods, 116
 - Carbon nitride thin films deposited by reactive plasma beam sputtering, 295
 - Synthesis and characterization of carbon nitride thin films obtained by laser induced chemical vapour deposition, 301
 - Plasma polymer films and their future prospects, 371
 - Effect of energy on direct ion beam deposition of carbon thin films: induced defects and graphitization, 57
- Thin films growth
- Early stage growth structure of indium tin oxide thin films deposited by reactive thermal evaporation, 151
- TiAl
- Protection of γ -based TiAl against high temperature oxidation using ion implantation of chlorine, 89
- TiN coatings
- Pulsed-plasma assisted magnetron methods of depositing TiN coatings, 341
- Titanium
- Vacuum arc deposition of Ti coatings, 157
 - Corrosion resistance of the vacuum arc deposited Ti, TiN and TiO_2 coatings on large area glass substrates, 223
 - New coatings on metal sheets and strips produced using EB PVD technologies, 240
- Titanium dioxide
- Corrosion resistance of the vacuum arc deposited Ti, TiN and TiO_2 coatings on large area glass substrates, 223
- Titanium dioxide thin films
- Titanium dioxide films prepared by photo-induced sol-gel processing using 172 nm excimer lamps, 424
- Titanium nitride
- Corrosion resistance of the vacuum arc deposited Ti, TiN and TiO_2 coatings on large area glass substrates, 223
 - Corrosion behaviour of the protective and decorative TiN coatings on large area steel strips, 229
 - The effect of substrate temperature and biasing on the mechanical properties and structure of sputtered titanium nitride thin films, 335
- Titanium oxide
- Deposition of layered bioceramic hydroxyapatite/ TiO_2 coatings on titanium alloys using a hybrid technique of micro-arc oxidation and electrophoresis, 407
 - Raman study of titanium oxide layers produced with plasma immersion ion implantation, 84
- Transition metal nitride
- Mechanical properties of hard chromium tungsten nitride coatings, 179
- Transition metals
- Structure and hardness of vacuum arc deposited multi-component nitride coatings of Ti, Zr and Nb, 257
- Tribological properties
- Mechanical properties of Al/ Al_2O_3 nanolaminated films: correlation to microstructure, 196

- Tungsten
Mechanical behaviour of hard PVD multilayered coatings, 185
- Tungsten-carbon
Mechanical behaviour of hard PVD multilayered coatings, 185
- Tungsten nitride
Mechanical properties of hard chromium tungsten nitride coatings, 179
- Turbine blade
Laser cladding of turbine blades, 45
- Unbalanced magnetron deposition
Localised oxidation defects in TiAlN/CrN superlattice structured hard coatings grown by cathodic arc/ unbalanced magnetron deposition on various substrate materials, 263
- Vacuum arc deposition
Vacuum arc deposition of Ti coatings, 157
Corrosion resistance of the vacuum arc deposited Ti, TiN and TiO₂ coatings on large area glass substrates, 223
Corrosion behaviour of the protective and decorative TiN coatings on large area steel strips, 229
Structure and hardness of vacuum arc deposited multi-component nitride coatings of Ti, Zr and Nb, 257
- Wear
Plasma immersion ion implantation of cold-work steel, 94
- X-ray diffraction
Electron beam physical vapour deposition of protective films on carbon reinforced carbon, 331
The effect of substrate temperature and biasing on the mechanical properties and structure of sputtered titanium nitride thin films, 335
Temperature and substrate influence on the structure of TiN_xO_y thin films grown by low pressure metal organic chemical vapour deposition, 396
Raman study of titanium oxide layers produced with plasma immersion ion implantation, 84
- X-ray photoelectron spectroscopy
X-ray photoelectron spectroscopy study of carbon nitride films, 313
Temperature and substrate influence on the structure of TiN_xO_y thin films grown by low pressure metal organic chemical vapour deposition, 396
- X-ray photoelectron spectroscopy (XPS)
Chemical analysis of pulsed laser deposited a-CN_x films by comparative infrared and X-ray photoelectron spectroscopies, 308
- XAS
Amorphisation and related structural effects in thin films prepared by ion beam assisted methods, 116
Correlation between bonding structure and mechanical properties of amorphous carbon nitride thin films, 284
- XPS
Structural properties and surface morphology of laser-deposited amorphous carbon and carbon nitride films, 124
XPS investigation of ion beam treated MoS₂-Ti composite coatings, 173
Correlation between bonding structure and mechanical properties of amorphous carbon nitride thin films, 284
Carbon nitride thin films deposited by reactive plasma beam sputtering, 295
Synthesis and characterization of carbon nitride thin films obtained by laser induced chemical vapour deposition, 301
- XRD
Pulsed laser deposition of crystal polyaniline thin films, 388
- Yttria
CVD of ZrO₂, Al₂O₃ and Y₂O₃ from metalorganic compounds in different reactors, 400
- Zinc alloy coatings
Vapour deposited Zn-Cr Alloy coatings for enhanced manufacturing and corrosion resistance of steel sheets, 218
- Zirconia
CVD of ZrO₂, Al₂O₃ and Y₂O₃ from metalorganic compounds in different reactors, 400
- Zirconium nitrides
Production of stable and metastable phases of zirconium nitrides by NH₃ plasma nitridation and by double ion beam sputtering of zirconium films, 100
- Zn-Al alloy
Morphologies and corrosion properties of PVD Zn-Al coatings, 207

Instructions for Authors

Submission of Papers

Manuscripts (original and two clear copies) should be submitted to one of the Editors:

for authors in the Americas

Dr. B. D. Sartwell, Surface Chemistry Branch,
Naval Research Laboratory, Code 6170, Washington,
DC 20375, USA;

and for authors elsewhere

Professor A. Matthews, Director, The Research Centre in
Surface Engineering, The University of Hull, Cottingham
Road, North Humberside, HU6 7RX, UK.

Contributions are accepted on the understanding that the authors have obtained the necessary authority for publication. Submission of a manuscript implies that it is not under consideration for publication elsewhere.

Types of contributions

- original papers
- invited or contributed reviews on specific topics
- brief communications on topics of immediate interest
- notices of meetings, symposia and short courses
- technical notes for "Current Industrial Practices" section

Languages

Papers will be published in English. Both English and US spelling are permitted, provided that spelling is consistent within an article.

Authors in Japan please note that information about how to have the English of your paper checked, corrected and improved (*before submission*) is available from: Elsevier Science K.K., Editorial Service, 1-9-15 Higashi Azabu, Minato-ku, Tokyo 106-0044, Japan; Tel.: +81 3 5561 5032; Fax: +81 3 5561 5045.

Manuscript preparation

Three copies of the manuscript should be submitted, in double-spaced typing on pages of uniform size with a wide margin on the left. The title page should be a separate sheet, bearing title, author(s)' name(s) and their full addresses, and a footnote with the corresponding author's Telephone, Fax numbers and E-mail Address.

Some flexibility of presentation will be allowed but authors are urged to arrange the subject matter clearly under such headings as Introduction, Experimental details, Results, Discussion etc. Each paper should have an abstract of 100–200 words.

References should be numbered consecutively (numerals in square brackets) throughout the text and collected together in a reference list at the end of the paper. Journal titles should be abbreviated according to the Chemical Abstracts Service Source Index, 1970 edition, and supplements. The abbreviated title should be followed by volume number, year (in parentheses) and page number.

Submission of electronic text

The final text should be submitted on a 3.5 in or 5.25 in diskette (in addition to a hard copy with original figures).

Double density (DD) or high density (HD) diskettes formatted for MS-DOS or Apple Macintosh compatibility are acceptable, but must be formatted to their capacity before the files are copied on to them. The files should be saved in the native format of the wordprocessing program used. Most popular wordprocessor file formats are acceptable. It is essential that the name and version of the wordprocessing program, type of computer on which the text was prepared, and format of the text files are clearly indicated.

Illustrations

Line drawings and cyclic or aromatic formulae should be in a form suitable for reproduction. They may be drawn in black ink on drawing paper (letter height, 3–5 mm), but the use of good quality computer-generated figures is encouraged. They should preferably all require the same degree of reduction, and should be submitted on paper of the same size as, or smaller than, the main text to prevent damage in transit. Photographs should be submitted as clear black-and-white prints on glossy paper. Each illustration must be clearly numbered.

Illustrations can be printed in colour when they are judged by the Editor to be essential to the presentation. The publisher and the author will each bear part of the extra costs involved. Further information concerning colour illustrations and the costs to the author can be obtained from the publisher.

Legends to the illustrations must be submitted in a separate list.

All tables and illustrations should be numbered consecutively and separately throughout the paper.

Proofs

Authors will receive proofs, which they are requested to correct and return as soon as possible. No new material may be inserted in the text at the time of proofreading. All joint communications must indicate the name and full postal address of the author to whom proofs should be sent.

Further information

All questions arising after the acceptance of manuscripts, especially those relating to proofs, should be directed to: Elsevier Science Ireland Ltd. Elsevier House, Brookvale Plaza, East Park, Shannon, Co. Clare, Ireland. Tel.: +353 61 709156; fax: +353 61 709107.

The full and complete instructions to authors can be found on the World Wide Web: please visit our website which is accessible via the Elsevier Surfaces and Interfaces HomePage at <http://www.elsevier.nl/locate/surfaces>

Offprints

Twenty-five offprints will be supplied free of charge to the author(s). Additional offprints can be ordered at prices shown on the offprint order form which accompanies the proofs.